WILEY-VCH

Edited by Piet W.N.M. van Leeuwen
and Matthieu Raynal

Supramolecular Catalysis

New Directions and Developments

Supramolecular Catalysis

Supramolecular Catalysis

New Directions and Developments

Edited by Piet W.N.M. van Leeuwen and Matthieu Raynal

WILEY-VCH

Editors

Prof. Piet W.N.M. van Leeuwen
INSA Toulouse
Laboratoire de Physique et Chimie des Nano-Objets
135 Avenue de Rangueil
31077 Toulouse Cedex 4
France

Dr. Matthieu Raynal
Sorbonne Université, CNRS
Institut Parisien de Chimie Moléculaire
Equipe Chimie des Polyméres
4, place Jussieu
75252 Paris Cedex 5
France

Cover Courtesy of P.W.N.M. van Leeuwen and M. Raynal

Library of Congress Card No.: applied for

British Library Cataloguing-in-Publication Data
A catalogue record for this book is available from the British Library.

Bibliographic information published by the Deutsche Nationalbibliothek
The Deutsche Nationalbibliothek lists this publication in the Deutsche Nationalbibliografie; detailed bibliographic data are available on the Internet at <http://dnb.d-nb.de>.

Print ISBN: 978-3-527-34902-9
ePDF ISBN: 978-3-527-83202-6
ePub ISBN: 978-3-527-83204-0
oBook ISBN: 978-3-527-83203-3

Typesetting Straive, Chennai, India

Printed on acid-free paper

10 9 8 7 6 5 4 3 2 1

Contents

Preface

In the first half of its history that started in 1970, supramolecular catalysis was concerned with enzyme mimicking, and in view of the synthetic problems associated with the synthesis of cavities or host molecules equipped with complex catalysts, the development was relatively slow until the mid-1990s. As the landmark starting point, we take the publication by Breslow and Overman [1] which reported the connection of a nickel catalyst complex onto a hydrophobic host molecule, α-cyclodextrin, so as to enhance the coordination of the substrate *p*-nitrophenyl acetate in the vicinity of the hydrolysis catalyst. The slow initial development of the area enabled Feiters to write a comprehensive review in 1996 containing just over 500 references [2]. The name supramolecular catalysis was coined by Lehn in 1983 and the Nobel prize in supramolecular chemistry in 1987 directed the spotlight on potential applications of this new field, catalysis being one of them. The introduction of systems smaller than the enzyme mimics by the Nobel laureates, such as the crown ether-based molecules, contributed largely to the popularity of the field. Since the late 1990s, the scope of supramolecular catalysis has considerably broadened and as yet there seems no end at this development. Thus, in the present century, a comprehensive work on the area would contain several book volumes. Our book in 2008 was based on the selected themes of a conference held in Barcelona [3], and the review in which the editors participated published in 2014 contained more than 1000 references and was limited to the most recent works and the important older publications [4]. Thus, discussing the format of a new book on the topic we realized that a full coverage of the area or even an update of the former works would be impossible within a single book volume. Thus, we worked out the idea of collecting today's strategies that were being pursued and describe those in small chapters that highlight the current trends and will shape in part the future of this branch of catalysis. We discarded heterogeneous systems such as the metal-organic frameworks because it would not be feasible to cover all in one volume. We distinguished seven broad topics, thus, "homogeneous" in nature and including both organic and metal catalysts, and we invited slightly over 40 authors making sure to arrive at the broadest possible diversity, in many ways. The response was highly positive and the plans were met with great enthusiasm. We are very grateful to all contributors for their participation and their prompt actions as most chapters were received within two months from the deadline. We would also like to

thank the Wiley teams who did a lot of the work to make this happen and especially Dr Elke Maase, who suggested "it might be timely" to think about a book in this area, and Katherine Wong.

"Supramolecular catalysis" demonstrates the power of our imaginations as typically this work comes about via design, borrowing ideas from other areas, implementing them in new systems, which is also the way it began, by mimicking enzymes.

References

1 Breslow, R. and Overman, L.E. (eds.) (1970). An "artificial enzyme" combining a metal catalytic group and a hydrophobic binding cavity. *J. Am. Chem. Soc.* 92: 1075–1077.

2 Feiters, M. C. In *Supramolecular Technology*; Reinhoudt, D. N., Ed.; Elsevier Science Ltd. Pergamon,: Elmsford, 1998; Vol. 10. Comprehensive supramolecular chemistry; Atwood, J. L., Davies, J. E. D., MacNicol, D. D., Vögtle, F., Lehn, J. M., Eds.

3 Van Leeuwen, P.W.N.M. (ed.) (2008). *Supramolecualr Catalysis*. Weinheim: Wiley-VCH Verlag GmbH.

4 (a) Raynal, M., Ballester, P., Vidal-Ferran, A., and Van Leeuwen, P.W.N.M. (2014). Supramolecular catalysis. Part 1: non-covalent interactions as a tool for building and modifying homogeneous catalysts. *Chem. Soc. Rev.* 43: 1660–1733.
(b) Raynal, M., Ballester, P., Vidal-Ferran, A., and Van Leeuwen, P.W.N.M. (2014). Supramolecular catalysis. Part 2: artificial enzyme mimics. *Chem. Soc. Rev.* 43: 1734–1787.

Toulouse, 2021
Paris, 2021

Piet W.N.M. van Leeuwen
Matthieu Raynal

A

Supramolecular Catalysis: An Introduction

Matthieu Raynal[1] *and Piet W. N. M. van Leeuwen*[2]

[1] *Sorbonne Université, CNRS, IPCM, UMR 8232, 4 Place Jussieu, 75252 Paris, Cedex 05, France*
[2] *LPCNO, Institut National des Sciences Appliquées-Toulouse, Laboratoire de Physique et Chimie des Nano-Objets, Toulouse F-31077, France*

A.0 Introduction

During the major part of its history, chemistry as a science was concerned with the separation of mixtures into pure compounds or the constituting elements, while the Greek *chimia* was interpreted as "forging together," alloying, etc. This key activity of chemistry was underscored by the Flemish mathematician and engineer Simon Stevin at the end of the sixteenth century, who worked a great deal of his life in the Northern provinces of the then *Netherlands*, by introducing the Dutch word *scheikunde*, science of separating as he did for many words with Latin/Greek origin.[1] Separation of mixtures has retained its importance in chemistry in spite of the tremendous expansion in synthetic methodologies for making new compounds in the most efficient way. This huge synthetic machinery is mainly based on the construction of covalent atom–atom bonds and to a lesser extent on ionic bonds. In the last 50 years, we have witnessed the development of supramolecular chemistry, which is concerned with the weak interactions of unlike molecules in a highly specific manner leading to organized, well-defined agglomerates [1]. The weak interactions include van der Waals forces, hydrogen bonding [2], π–π stacking [3], hydrophobic interactions [4], anion–π interactions [5], cation–π interactions [6], Lewis acid metal–ligand interactions, ion–dipole interactions [7], cation–anion attractions, Dewar–Chatt–Duncanson metal–ligand interactions, charge–transfer interactions, halogen bonding [8], etc. Some covalent bonds also share similar features because of their reversible nature [9]. Several of these forces were discovered in the last decades, but van der Waals interactions were defined already as early as 1873. The importance of non-bonding interactions in living matter was also recognized more than a century ago in 1894, when Emil Fischer described for the first time the lock-and-key interaction between enzyme and

1 Suffix+kunde (knowledge, ability) is a common way to name sciences in Dutch and German, e.g. Pflanzenkunde, German for botany.

substrate [10]. The discovery of hydrogen bonding in 1920 [11] was an important asset (see quote from Pauling [12]) for the later developments of our knowledge on the structures of peptides and DNA, and thus, supramolecular phenomena were abundant and paramount before "supramolecular chemistry" as we know it today started to develop in the 1970s, when the concepts known from biological systems were transferred to synthetic systems. The synthesis of crown ethers and the identification of their complexes with weakly binding metal ions by Pedersen, while working for Du Pont, mark the beginning of supramolecular chemistry, although Pedersen classified his work under coordination chemistry [13]. Two years later, cyclic and open-chain crown ethers were joined by bicyclic cryptands reported by Lehn et al. [14]. Cryptands form very stable complexes with selected ions, provided there is a good match with sizes of the cavities and ions, and orientation of donor atoms, as also holds for crown ethers. Although the molecules were relatively simple, yet the concepts introduced were far reaching already, such as host–guest, selective capturation, catalysis, and the like. The boom really started in the 1970s with the work on spherands by Cram's group [15], an area that was joined by many chemists, and the synthetic version of supramolecular chemistry was born. Spherands, cryptands, etc. on the man-made side and biological systems on the other side have been a source of inspiration for the design (by CPK models!) of numerous host molecules to serve as components in future applications in sensing, catalysis, light harvesting, materials, etc. Pedersen, Lehn, and Cram received the Nobel prize in 1987 for their germinal contributions, and by then, the concepts of supramolecular chemistry had been widely embraced: host–guest chemistry, molecular recognition, self-assembly, folding, to mention just the earliest ones.

Catalysis concerns the phenomenon of a substance, the catalyst, that accelerates a chemical reaction. More precisely, a catalyst is a substance (inorganic, organic, biological) that enhances the rate by which a reaction approaches equilibrium without itself being permanently incorporated. By definition, the catalyst will do so a number of times (the turnover number, TON) within a certain time, expressed as turnover frequency (TOF). A catalyst lowers the free energy barrier of a reaction by interacting with the substrates and bringing them together (if more than one reactant is involved). Catalyzed intramolecular reactions and simple substitution reactions may follow the same, if accelerated, pathway as the uncatalyzed reaction, but especially metal catalysts and organocatalysts may follow a completely different pathway [16]. Selectivity is an important additional property of a catalyst system, and this is achieved by a preferential acceleration of the pathway that leads to the desired product.

Catalyst–substrate interaction may involve the broad range of non-bonding interactions mentioned earlier in our brief introduction to supramolecular forces, but it may also include temporary covalent bonds between substrates and catalysts. As a general characteristic, catalyst and substrate "self-assemble," and thus, it would seem that catalysis is always a supramolecular phenomenon. One may ask the question then what is meant by supramolecular catalysis. While this appears a tough question, all catalysis specialists must know the answer, as out of 40+ invited contributors to this book, only one invitee had doubts about whether or not

his/her catalytic chemistry would belong to this field. Lehn, who coined the name *supramolecular catalysis* in 1983, described it initially as "molecular catalysis" taking place in a "supermolecule," i.e. a host–guest complex in which the host carries the catalyst, inside or at the rim of the cavity [17]. In 2008, taking into consideration that non-covalent interactions have been incorporated in numerous catalytic systems without being formally involved in substrate binding, the scope of the discipline has been expanded [18]. "Supramolecular catalysis" was thus referred to as any catalytic system that contains supramolecular interactions not included in the "basic" catalytic reaction, which, admittedly, leaves the matter ill-defined in a number of cases. Later [19], some of the key features expected for a catalyst to be ranked as "supramolecular" have been specified: (i) a certain degree of design has to be implemented in its structure such as recognition unit(s) dedicated to bind any of the members of the catalytic reaction, and (ii) assembly of the catalytic subunits must preferably operate by in situ mixing of the different building units. A catalyst of any nature (organometallic, organic, enzymatic) and operating through any activation mode will be defined as "supramolecular" as long as it fulfils one of the aforementioned requisites. This is the case of all catalytic systems present in the 41 chapters of this book.

Man-made supramolecular catalysis started with host–guest chemistry mimicking enzyme catalysis, with the simplified characteristic that the host containing the catalyst will convert the guest to the product, the guest being complexed via a lock-and-key principle in the host. The reactions studied were often taken from known enzymatic reactions, such as ester hydrolysis, aldehyde condensations, but also Diels–Alder reactions have also led to nice examples of accelerations and selectivity changes [20]. Most of these reactions also occur without catalyst, and the effectiveness of the supramolecular catalyst is usually measured in this field by comparing its rate with that of the uncatalyzed reaction, often present as a background reaction. The rate accelerations often stem from enhancements of local concentrations or decrease of the entropy of activation, as most of man-made supramolecular catalysts of the host–guest type do not show the typical properties of enzymes, highly active in creating "activated" complexes [21]. Organometallic catalysts cannot be compared with uncatalyzed reactions, as alkene polymerization, hydrogenation, and hydroformylation have no uncatalyzed counterparts apart from radical mechanisms in several instances. The performance of these catalysts is compared with those of simple, routine catalyst systems for the same reaction. Breslow introduced the use of natural host molecules, viz. cyclodextrins equipped with catalytically active groups as hosts for supramolecular catalysts [22]. Around 1950, 20 years well before the concepts of supramolecular chemistry and catalysis were recognized in the early 1970s, Friedrich Cramer, in his work on inclusion compounds, discovered that molecules incorporated in cyclodextrins may exhibit unusual reactivities [23]. He reported not only catalytic reactions taking place in cyclodextrin, e.g. enhanced reactions of encapsulated 1,2-di(furan-2-yl)-2-hydroxyethanone, but also reactions that were slowed down by encapsulation of one of the reacting components in cyclodextrin, named "negative catalysis" [23b]. It cannot be contested that F. Cramer gave the basis for supramolecular catalysis involving CDs [24]. The

catalytic effects of non-modified CDs on similar reactions were confirmed by others including kinetic studies performed by the Bender group [25]. Both Breslow [22a] and Tabushi [26] reported the use of cyclodextrins equipped with transition metal complexes to be used as cavities with bifunctional binding of substrates, and the suggestion was made that these could be used as catalyst for converting the doubly bound substrate, which soon followed [27]. In the same vein, an impressive rate acceleration was observed by Mock in the 1980s [28] for 1,3-dipolar cycloaddition between an azide and an alkyne inside the macrocycle cucurbit[6]uril which was attributed to the reduction of the entropic component of the free energy barrier [29]. Progress in synthetic methods also allowed the design of more elaborated synthetic hosts such as a mimic of chymotrypsin developed by Cram (35 steps!) [30], the model pyruvate oxidase system elaborated by Diederich [31], and the porphyrin cages of Sanders [32]. Probably inspired by these early works, numerous synthetic hosts have been designed and synthesized and many of them functionalized with efficient catalytic metal centers [19b]. More recently, the covalent synthetic hosts were joined by supramolecular host molecules, many based on coordination chemistry bonding motives with metal ions connecting ditopic ligand building blocks, thus forming three-dimensional metallo-cages [33]. The idea of performing catalysis in "closed-shell capsule" was put forward by Rebek in the late 1990s [34] with the "softball," a hydrogen-bonded dimer of a glycoluril derivative. These entities function merely as hosts and do not contain catalysts.

A large area of supramolecular catalysis is concerned with the construction of ligand systems by supramolecular forces, which may include hydrogen bonding, metal-anion bonding, π-stacking, etc. [19a]. Bidentate ligands are extremely common in homogeneous catalysis, but their synthesis can be tedious sometimes and the use of mixtures of two ligands had facilitated the use of combinatorial methods in the 1990s. Formation of the "hetero" ligand combination was left at chance – incidentally small–large combinations were preferred – but with the introduction of a weak binding between two monodentate ligands, preferential formation of the desired pair was made possible by Breit and Seiche, who used hydrogen bonding between DNA-like base pairs in phosphine ligands [35]. Lewis base–acid interactions and anion–cation binding were also introduced for the formation of bidentate ligands, combinatorial libraries included [36]. As we will see later, the complexity has grown enormously in supramolecular catalyst systems this century, but still thanks to the weak supramolecular interactions, the synthesis remains considerably easier than the synthesis of purely covalent systems. Self-assembly of enantioselective catalysts has been reported, and, back to the roots of the discipline, combinations of enzymes and other biomolecules have led to remarkable catalysts [37].

The chapters are divided in seven sub-areas that correspond to the main domains of supramolecular catalysis according to the editors' (necessarily subjective) categorization. This ranking must be taken with a grain of salt for two main reasons. First, this classification follows the interaction that was initially designed by the authors, which can be different from the interaction that actually occurs during the catalytic process. For example, a hydrogen bond interaction might shift from ligand

to substrate [38]. Second, some catalytic systems belong to several sub-areas as, for example, those based on CDs which may both concern catalysis in water and catalysis upon confinement. The objective is to give the reader sufficient background to fully apprehend the novelty of the various approaches depicted in this book. The description is by far not comprehensive; the reader is referred to reviews quoted in the title of each part for a more complete coverage. Only papers and reviews that highlight a specific point of the discussion will be mentioned in the main text. Previous reviews [19, 39] book chapters [37b, 40], and monographs [18, 41] addressing the topic will also offer a more general overview of the supramolecular catalysis discipline. Immobilization of catalytic systems by means of non-covalent anchoring to various supports will not be covered [42]. Similarly, the blooming fields of MOF [43] and COF [44] materials applied to catalysis are only referred to for those systems that are more supramolecular in essence, again with certain degree of subjectivity.

A.1 Ligand–Ligand Interactions, Chapters 1 and 2 [36, 45]

In the first decades of supramolecular catalysis, the science focused on biomimetic systems, and since the biocatalyst was primarily seen as a cavity capturing substrates, the focus was on host–guest supramolecular interactions that would promote catalysis, *vide infra*. Toward the end of the 1990s, it was realized that supramolecular interactions could also be used for constructing the catalyst system, the simplest one being the construction of bidentate ligands. Both homoleptic bidentate ligands and heteroleptic bidentate ligands had shown their enormous potential in homogeneous catalysis [46]. To avoid the elaborate synthesis of large numbers of bidentate ligands, the use of mixtures of monodentate ligands was introduced by Reetz, which had the additional advantage that rapid screening methods of monodentate ligand libraries could be employed [47]. Thus, Reetz discovered, shortly after the revival of monodentate chiral ligands, that also mixtures of chiral and achiral ligands could be used as enantioselective hydrogenation catalysts [48]. Mixtures of monodentate ligands will give mixtures of homo- and heteroleptic bis-ligand metal complexes. While there may be a preference for certain electronic combinations such as pyridine-phosphine in the iridium Crabtree catalyst [49], or for small–large phosphines in like ligand combinations as in the work of Reetz, supramolecular interactions offer a handle to obtain specifically the desired bidentate ligand. Interactions used include hydrogen

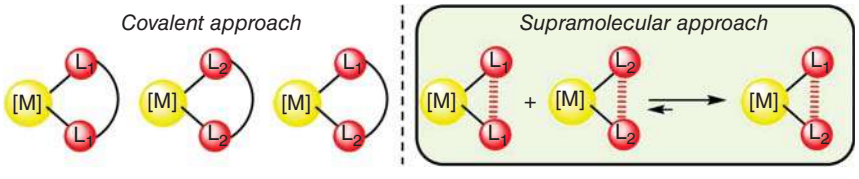

Concept A.1 Ligand–ligand complementary interactions to favor ligand heterocombination.

bonding, ionic bonding, halogen bonding, Lewis acid/base, etc. This concept was proved particularly productive and useful in a wide variety of metal complexes with a square planar coordination sphere, among which we find a large number of catalysts (Rh, Ir, Pd, Pt). In addition to square planar complexes, also the trigonal bipyramids of rhodium hydride, well-known hydroformylation catalysts, were very popular targets. Supramolecular binding effects in heteroleptic, catalytic complexes might have occurred long before it was recognized [50], as was, e.g. the case in catalysts made up from secondary phosphine oxides (SPO) exhibiting a strong hydrogen bond [51], which were reported in 1986 [52]. Its "*avant la lettre*" supramolecular nature, however, was not exploited for the formation of hetero-combinations until 2011, albeit with moderate success [53]. It is to be expected that there are more hidden examples.

The complementary nature of the supramolecular binding motive allows one to obtain purely the desired heterocombination of the two ligands in high selectivity. *In situ* formation allows fast detection of a catalytic "hit" through combinatorial methods as highlighted in *Chapter 1*. The synthetic effort is reduced drastically compared to the classic synthesis of libraries of covalent bidentate ligands. The practicality of these combinatorial methods has aroused large industrial interest in hydroformylation [54], transfer hydrogenation, and asymmetric hydrogenation as can be seen from the ample industrial support of this work (*Chapter 2*). Other suitable reactions are cyclopropanation, alkene oligomerization, Diels–Alder and aziridination; reactions that produce large quantities of salts, such as cross-coupling reactions, may be less suited for supramolecular catalysts of this group.

A.2 Self-assembled Nanostructures and Multi-component Assemblies, Chapters 3–8 [55]

The implementation of catalytic systems built upon the assembly of different building blocks has by far not been limited to the aforementioned supramolecular bidentate ligands. There is actually an infinite number of possibilities for connecting the different partners of the catalytic reactions. The thus generated supramolecular constructs are highly modular in nature such that catalytic performance can be tuned through modification of any of the building blocks. One can distinguish two main categories in this area: those that are discrete and of limited size because composed of a finite number of units (A.2a–d) and those that are macromolecular in nature, i.e. featuring a high number of building blocks or a number of larger blocks connected through non-covalent interactions (A.2e–f).

The first category encompasses a wide range of strategies that differ by the nature of the interacting species. A first sub-class refers to multi-component assemblies formed through intermolecular interactions between several functional and complementary sub-units, one of them bearing the catalytic site. The main motive of this approach was to develop modular cooperative catalysts [56] and photocatalytic dyads, including efficient catalysts for water oxidation as well as CO_2 conversion [57]. Flourishing development in the realm of photoredox catalysis also benefits from a similar strategy [58]. In a different approach, a recognition unit was

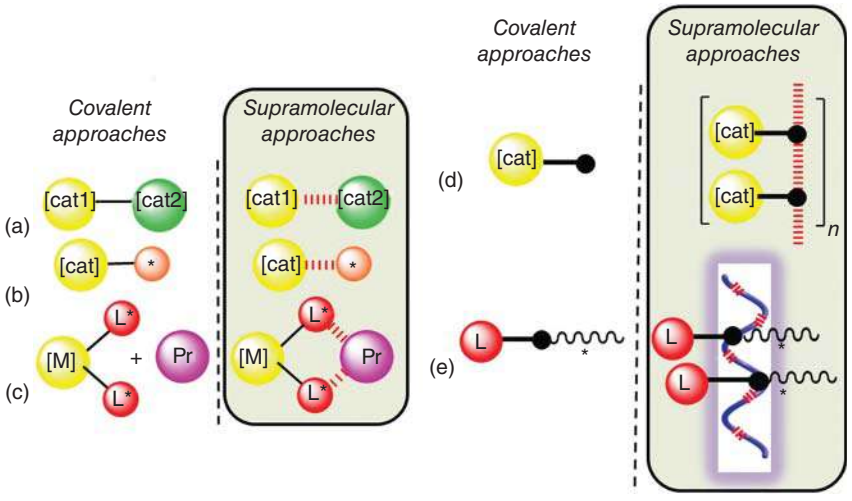

Concept A.2 Multi-component catalytic assemblies. (a) Assembled catalysts, (b) supramolecular chirogenesis, (c) auto-catalysis, (d) catalytic nanofibers, (e) catalytic nanohelices. cat = catalyst, * = chiral center or species, Pr = product.

embedded in the ligand backbone with the desired capability of interacting with a specific class of chiral molecules. These chiral molecules, named as chiral "inducers" [59], "cofactors" [60], or "sergeants" [61], depending on the system under study, transfer their chiral information to the metal center as demonstrated by appreciable enantioselectivities achieved in asymmetric transformations. Remote control of the chiral environment by means of supramolecular interactions, i.e. "supramolecular chirogenesis" [62], offers the possibility both of controlling the chiral nature of the catalytic center with limited modification of its first coordination sphere and of modulating its efficiency – notably for expanding its substrate scope – by simple variation of the chemical structure of the chiral species (*Chapter 3*). When located closer to the catalytic center, the role of this chiral additive is dual; it does not merely promote a preferential chiral environment to the catalytic center but it also controls the reactivity of the substrate as often found for chiral ions when interacting with catalytic centers [63]. It is worth indicating that non-covalent interactions between the remote part of a ligand and the product/educt of the catalytic reaction have been rarely explored; an example of such a designed auto-catalyst is presented in *Chapter 4* of the present book. In a different context, an original strategy has been developed in the early 2000s [64] in which pyridylphosphine ligand and a Zn–porphyrin unit have been combined in the same self-assembled catalyst. The metal porphyrin component does not play any "active" role in the catalytic process but acts as a "template" to modulate the reactivity and selectivity of the metal center connected to the phosphorus atom. The so-called template-ligand strategy was employed for developing a range of catalysts with non-classical reactivity, notably in rhodium-catalyzed hydroformylation reactions. The strategy was further applied to encapsulate metal catalysts (see A.4) [65]. Finally, mechanically interlocked molecules have been receiving increased attention for application in catalysis in the

last years, with a special interest for those integrating two sub-component parts: rotaxanes and catenanes (*Chapter 5*) [66]. Supramolecular interactions come into play not only for assembling the two parts but also as a tool to switch the parts between different relative positions.

The second category exploits the ability of complementary molecules to self-assemble into nanometer- or even micrometer-scale nanostructures. The most established ones, micelles and vesicles, have been intensively studied as "reaction flasks" for promoting reactions in water (see A.6). Three-dimensional metal–ligand architectures such as those found in finite coordination cages and metal-organic frameworks (MOFs) can promote reactions within their confined environment (see A.4). Alternatively, the directional assembly of small units into one-dimensional structures has been exploited to construct supramolecular catalysts that present the advantages of being both modular and stimuli-responsive [67]. Entangled fibrillar networks, such as those present in gels, make it possible to orient and confine reactive units. Hydrogels formed by the self-assembly of small peptides have been investigated as enzyme mimics and enzyme hosts [68]; their structure and functions make them "minimalistic biocatalysts" [69]. The catalytic sites located within these assemblies may experience pK_a shifts or cooperate for substrate activation leading to enhancement of the catalytic performance relatively to the non-assembled catalyst (*Chapter 6*). The designed assembly of cofactors, peptides, or DNA also yields functional "macromolecular" mimics of enzymes [70]. Finally, supramolecular chirality in these assemblies has been somewhat overlooked for the design of potent asymmetric catalysts. This is in spite of the fact that chirality in one-dimensional nanostructures, such as nanohelices and nanotubes, present very particular features. Embedding catalytic sites within these nanostructures yield a new family of catalysts with unique properties, such as the ability to promote asymmetric transformations with a very small amount of chiral inducers (*Chapter 7*) and even in absence of it (*Chapter 8*).

A.3 Ligand–Substrate Interactions, Chapters 9–14 [45f, 71]

Governing substrate reactivity by controlling its interaction with catalysts, the structure of which being far less elaborated than that of enzymes, is a long-term challenge

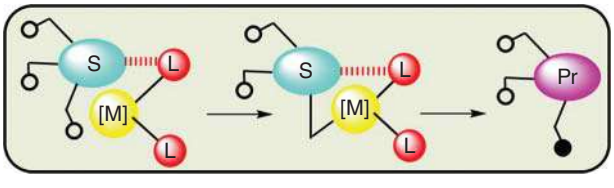

Concept A.3 Schematic representation of ligand–substrate interactions directed site selectivity. S = substrate, the empty and filled circle represents the reactive sites of the substrate and the new created function in the product, respectively.

in catalytic sciences. In conventional approaches, the favored reaction pathway is usually the one that minimizes steric repulsion; quadrant diagrams based on steric clashes between catalyst and substrate substituents often offer qualitative models for determining the stereochemical outcome in asymmetric reactions. Soon after the advent of modern asymmetric metal catalysis, attractive interactions between ligand and substrates have also been recognized as key elements to control the catalytic outcome. As an example, the combination of phthalazine or pyridazine coupled to bis-cinchona alkaloids and OsO_4 is widely used for dihydroxylation of vinyl arenes, furnishing key intermediates toward several natural products. The efficiency of this catalytic system has been attributed to π–π stacking and van der Waals interactions between the substrate and the methoxyquinoline rings of the bis-cinchona ligand as well as to edge-to-edge interaction between the substrate and the nitrogen atoms of the heterocycle [72]. It is now well established that weak interactions such as dispersive interactions play a key role in determining the preferred pathway in a range of asymmetric metal-catalyzed reactions. Even though great advances have been realized in the identification of such interactions, notably through multivariate correlations of the enantioselectivity coupled to computationally derived transition states [73], the influence of a combination of weak interactions on dictating the outcome of a catalytic reaction is still hard to determine *a priori*.

Bifunctional metal complexes combine a metal center and a functional group, the latter playing a key role in substrate binding and activation. The Noyori–Ikariya catalyst, {RuCl(η^6-benzene)[(*S*,*S*)-TsDPEN]} (Ts = tosyl, DPEN = diphenylethylenediamine), a prototypical example of this class of catalyst, has been found to be extremely efficient for hydrogenation, dehydrogenation, or transfer hydrogenation reactions [74]. It involves six-membered ring transition states in which the protonated and deprotonated form of the DPEN ligand are hydrogen-bonded to the substrate and product, respectively. The dual role of the amine/amide ligand as both hydrogen bond donor/acceptor and proton donor/acceptor is somewhat particular to this class of catalysts. The efficiency of ligands embedding N–H donors in hydrogenation and related reactions is often referred to as the "N–H effect" [75].

Alternatively, binding site(s) can be incorporated in the ligand backbone that acts as reversible recognition unit for directing the desired part of the substrate in close proximity to the metal center. A particularly interesting feature of this strategy is the possibility to achieve site selectivity, i.e. selective transformation of a given function surrounded by groups of similar reactivity. This direction was addressed by Breslow in the late 1990s by attaching cyclodextrins to the four arms of a *meso*-tetraphenylporphyrin bound to a Mn oxo center [76]. Hydroxylation of steroid substrates, decorated with *tert*-butylphenyl groups for bonding to the CD units, occurs selectively. The position of the oxidation reaction is actually dictated by geometric constraints within the CD-substrate binary assembly not by the intrinsic reactivity of the C—H bonds. A similar approach was developed later by Crabtree for the selective Mn-catalyzed C–H oxidation of ibuprofen with up to 710 turnovers [77]. Simple models in which ibuprofen is hydrogen bonded to the Kemp triacid fragment of the catalyst rationalize the selectivity outcome. Controlling substrate reactivity by means of hydrogen bonding and weak metal–ligand

interactions proved to be particularly valuable in the context of achieving selective functionalization of aromatic C—H bonds (*Chapters 9 and 10*) and aliphatic C—H bonds (*Chapter 11*), including in an enantioselective manner! The strategy has also been applied in hydroformylation reactions, providing selectivities that are out of the reach of conventional catalytic systems (*Chapters 12 and 13*). Not only product selectivity but also substrate selectivity in cross-coupling reactions can be achieved by the rational use of Zn···N interactions in the outer sphere of the Pd center (*Chapter 14*).

A.4 Catalysis Promoted by Discrete Cages, Capsules, and Other Confined Environments, Chapters 15–24 [33, 39c, 78]

Guided by the lock-and-key principles and modern description of the mode of actions of enzymes, synthetic hosts have been implemented in catalytic reactions. Confinement of substrate(s) may lead to one or several of the following specific features: (i) rate enhancement as a result of increased local concentration of the substrate in the vicinity of catalytic or functional sites, (ii) substrate desolvation and ground state destabilization, (iii) reduction of the entropy of activation thanks to favorable preorganization of the substrate(s) within the cavity, (iv) increase of substrate reactivity (e.g. by means of a higher pK_a value), (v) transition state stabilization, (vi) stabilization of reactive intermediates or catalytic species, and (vii) preferential binding of the substrate that fits the cavity interior thus leading to substrate selectivity. Remarkably, all these properties arise from secondary

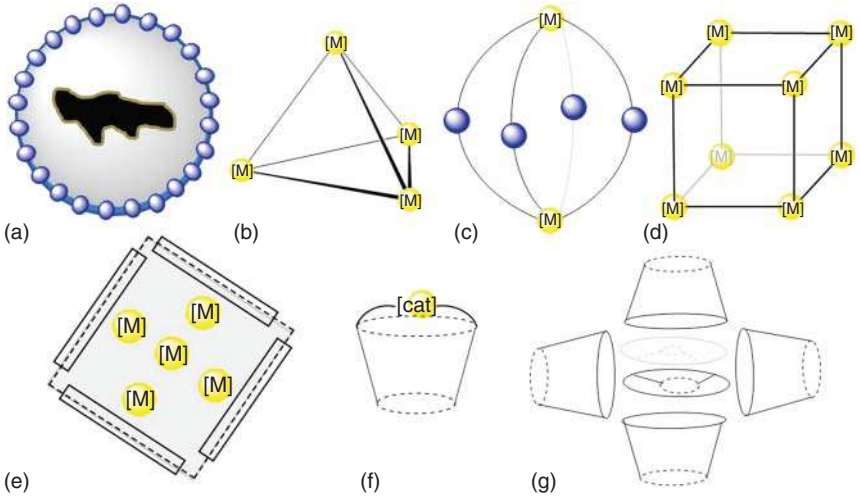

Concept A.4 Catalysis in confined space. (a) Molecularly-imprinted host. (b) Tetrahedral metal-organic cage. (c) Bimetallic coordination cage. (d) Cubic metal-organic cage. (e) Metal centers concentrated in a host. (f) Covalent host capped with a catalytic center. (g) Self-assembled hexameric capsule.

interactions between the substrate, intermediates, transition states or product, and the host, and as such, these catalysts are unarguably supramolecular in nature. In addition, reactions in the confined environment provided by synthetic hosts may follow a different pathway, i.e. that a divergence of reactivity is observed for catalysis in bulk and mediated by the host. Such behavior leading to unusual selectivities is particularly valuable in the context of increasing the scope of existing catalytic systems and develops highly selective and specific catalysts. Current limitations in many of these systems are as follows: (i) the observed rate enhancement is orders of magnitude lower than that achieved by enzymes and (ii) product inhibition of catalysis occurs because of the stronger affinity of the host for the product than for the substrate. However, host–guest systems have emerged during the last two decades that rival enzymes in terms of accelerating rates and behave as truly catalytic nanovessels.

Molecular systems that serve as hosts for catalysis may exhibit very different structural features, often based on simple elements of design. One can recognize two main distinctions depending on (i) the nature of the backbone of the host, i.e. covalent or non-covalent, and (ii) the position of the functional catalytic group, if any. The possibility of accelerating bimolecular reactions by incorporating substrate(s) mainly thanks to hydrophobic interactions in the interior of cyclodextrins [79], micelles [80], vesicles [39c], dendrimers [81], and hyperbranched polymers [82] was already probed during the second part of the last century. Alternatively, catalytic antibodies [83] and molecularly imprinted polymers (MIPs) [84], both constructed through templating of a molecule resembling the transition state of the reaction, have met with some success. Along this line, a new generation of molecularly imprinted cross-linked micelles with precise control of the structure of the internal cavity exhibit impressive selectivities including in glycan hydrolysis (*Chapter 15*). Non-covalent hosts based on coordination bonds probably represent now the most investigated class of hosts exhibiting catalytic properties. Following the seminal work of Fujita [33a] and Bergman/Raymond/Toste [78c] on catalytic octahedral and tetrahedral metallocages, respectively, the structure of catalytically potent discrete coordination cages has incredibly diversified. These metal-organic cages possess new features such as inherent polarization for the stabilization of charged species (*Chapter 16*) and ability to bind substrate and reactants both in their inner cavity and at their external surface (*Chapter 17*). Strategies for functionalizing the interior of these cages have also been disclosed recently which allows the regulation of the number and nature of catalytic sites present in the confined space (*Chapter 18*). Determining the origin of the guest reactivity at the molecular level is crucial for the development of new reaction pathways in confined environment. Advances toward this direction rely on computational methods that can adequately reproduce the different steps of catalytic reactions promoted by metal-organic cages (*Chapter 19*). Importantly, the excited state of a substrate is also deeply affected upon confinement; the outcome of photochemical reactions performed in synthetic hosts is usually drastically different from that observed in the bulk or other environments. Next to the reactivity also the enantioselectivity of photochemical processes can be

controlled upon inclusion of a substrate in a chiral guest, a strategy referred to as supramolecular (asymmetric) photochirogenesis [85].

Thanks to improved synthetic protocols, covalent cages can be functionalized more easily, at their gate with ligand or catalytic groups that point inwards or outwards the cavity interior or in their inner part thanks to endohedral functionalization [86]. Tuning the reactivity and selectivity of known organometallic catalysts upon inclusion in these discrete cages is a particularly fascinating direction. Notably, it was found that metal complexes of NHC-capped cyclodextrins display unusual reactivity and selectivity (*Chapter 20*). Likewise, a porphyrin compound with a concave diphenylglycoluril unit threads onto polybutadiene and epoxides the alkene functions, thus demonstrating a unique example of a synthetic processive catalyst (*Chapter 21*). Recent years have also witnessed the advent of hexameric hydrogen-bonded capsules of resorcinarene units as catalytic hosts. Some synthetic challenges have been addressed because organic and metal-catalyzed reactions follow unusual reaction pathways in this particular class of hosts (*Chapters 22–24*). Finally, the high modular nature of three-dimensional cages, as found in MOFs and COFs, is currently leading to impressive developments in catalysis. Confinement effects obviously play a major role, and secondary interactions can also be exploited for further improvement of the catalytic performance [87].

A.5 Supramolecular Organocatalysis and Non-classical Interactions (Chapters 25–30) [88]

The resurgence of the organocatalysis field in 2000 has led to the design of a tremendous variety of organic molecules applied as asymmetric catalysts, as

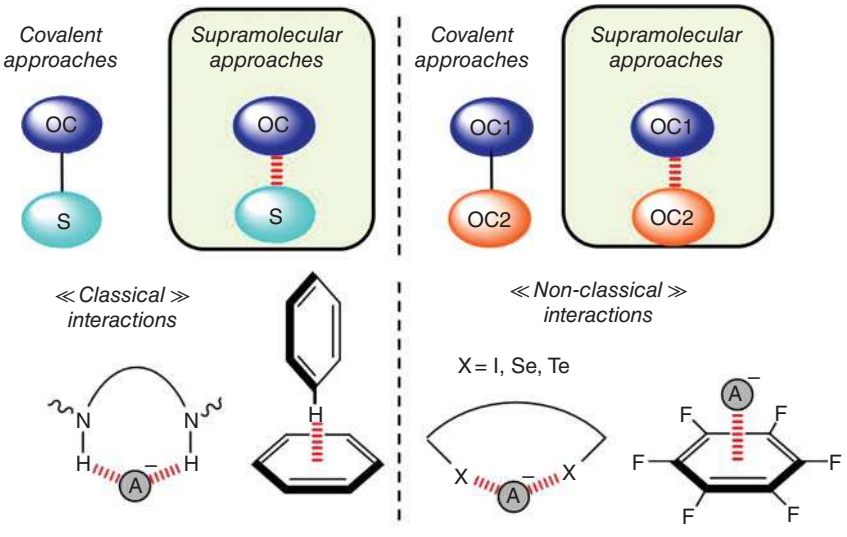

Concept A.5 Supramolecular organocatalysis.

recently recognized by the 2021 Nobel Prize awarded to MacMillan and List. Most if not all of these catalysts rely on secondary interactions for binding and activating the substrate, stabilizing reaction intermediates and transition states. Primary and secondary amines operate through reversible covalent bonds, via iminium and enamine formation, respectively, as key intermediates of the catalytic reaction. Additional interactions might also be involved as found in the Zimmerman–Traxler transition state, for which the carboxylic group of the proline is hydrogen bonded to the carbonyl group of the electrophile [89]. Non-covalent interactions are central for substrate activation in the following classes of organocatalysts: urea/thiourea/squaramide (HB donor) [90], phosphoric acids (ion-pairs) [63c], and quaternary ammonium salts (electrostatic interactions, phase-transfer catalysts) [91]. These and other functional groups are usually combined in the same chiral framework to yield bi- and multifunctional catalysts for which several types of secondary interactions act in synergy to bind and activate the substrate(s) and yield enantioenriched products with very high efficiency. In addition, confinement effects are also seen in small-molecule catalysts by subtle design of the groups surrounding the substrate binding sites [92]. Finally, the reactivity of radical intermediates can also be finely controlled by non-covalent attractive interactions involving rationally designed organocatalysts [93].

Based on the aforementioned considerations, the term "supramolecular organocatalysis" might appear as a pleonasm at first sight. Again, our feeling is that classes of organocatalysts developed by considering non-covalent interactions *a priori* as the central element of design shall endorse this denomination. For example, the well-established bidentate HBD ability of various thioureas was exploited to activate carbonyls, nitro-olefins, nitrone, imines, and so on [94]. *N*,*N*-bis[3,5-bis(trifluoromethyl)phenyl]-thiourea, known as the Schreiner thiourea, owes its efficiency (relative to other thioureas) to both the higher acidity of the N–H donors and its more rigid structure, thanks to attractive aromatic C–H···S interactions which reduce the rotation barrier of the phenyl groups. Thioureas and squaramides emerged as key elements for electrophile activation in small-molecule, asymmetric catalytic systems. Their chemistry is now very versatile as demonstrated by recently developed highly stereoselective *O*-glycosylation reactions [95]. Their scope is not limited to Lewis basic neutral electrophiles because they are also very efficient in promoting reactions involving anionic species (such as the Strecker reaction [96]) and also reactive cationic species through binding of their respective anion [97]. Such reactions particularly benefit from the interplay between HB and weaker interactions such as cation–π interactions [98] involved in their transition states (*Chapter 25*). Weaker HBD donors such as triazole derivatives actually act as strong anion receptors and very efficient anion binding catalysts when embedded in foldamer-based systems (*Chapter 26*). Simple catechol derivatives serve as hydrogen bond templates for promoting photochemical reactions in the solid state, which can be further enhanced by mechanochemistry (*Chapter 27*).

The field is also simulated by expanding the scope of weak interactions that can be employed to activate molecules. Cation–π interactions and other aromatic interactions have been detected in a high number of TS, exclusively in the presence of

(stronger) secondary interactions [99]. Matile recently demonstrated that anionic intermediates interact with electron-poor arenes acting as π-acidic surfaces [100]. Atoms of Groups 14–17 presenting a region of positive electrostatic potential can interact with the negatively charged site of a molecule, being a lone pair (n-bonding), the surface of an aromatic ring (p-bonding) or an anion. Halogen and chalcogen bonds belong to this category, and applications in catalysis [101] start to emerge (*Chapters 28 and 29*).

The possibility of achieving well-defined transition states has also motivated the design of organocatalysts for which secondary interactions are not limited to the substrate–catalyst complex. Several building blocks, e.g. monofunctional catalysts, are assembled thanks to non-covalent interactions between the complementary groups held by the blocks. The structure of such modularly designed organocatalysts (MDOs, the term was coined by Zhao [102]) can be tuned by changing the nature of the different components. Likewise, libraries of bifunctional organocatalysts can be generated in a similar fashion to the aforementioned supramolecular bidentate ligands, implemented in metal-catalyzed reactions (A.1). The possibility of achieving a high number of interactions not only between the catalyst and the substrate but also between catalysts and between substrates led to an exquisite control of the selectivity in a range of asymmetric reactions (*Chapter 30*).

A.6 Supramolecular Catalysis in Water (Chapters 31–38) [4, 103]

Shifting from organic solvents to water as reaction medium constitutes a possible strategy to reduce the environmental burden of chemical processes. On the one hand, the unique physicochemical properties of water such as its high dielectric constant and cohesive pressure, its extensive hydrogen bonding ability, and its amphoteric character may facilitate catalyst recycling and conduct to unanticipated positive effects for reactions held in presence of water or in aqueous phase. On the other hand, the poor compatibility of reagents and catalysts with water, most of them being optimized specifically for operating in (dry) organic solvents, have led to a very limited number of viable aqueous catalytic processes. Enzymes have

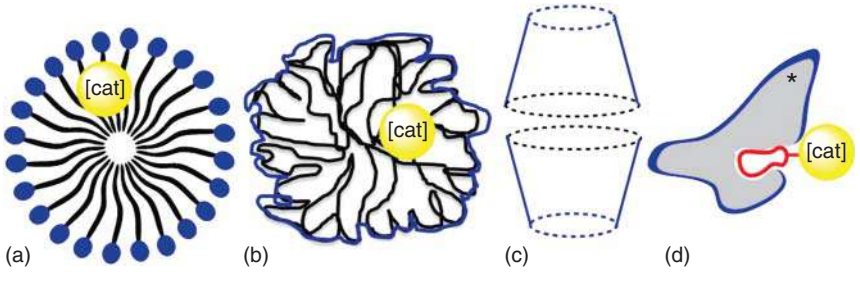

Concept A.6 Supramolecular catalysis in water. (a) Catalytic micelles. (b) Catalytic nanoparticles. (c) Self-assembled reaction capsules. (d) Supramolecular metalloenzymes.

again served as an invaluable source of inspiration; reactions usually take place in a hydrophobic pocket created by folding of the enzyme around its reactive center. Most strategies for aqueous catalytic processes involve a molecular recognition event between the host and the substrate, mostly driven by hydrophobic interactions. Other interactions can also play a role, both in the binding process and in the subsequent steps that lead to the activation and transformation of the substrate. Micelles, vesicles, dendrimers, and hyperbranched polymers constituted the oldest amphiphilic synthetic hosts that have been implemented for promoting organic reactions in aqueous phase. In the literature, "micellar effects" reflect to improved reaction rates when substrates/reactants/catalysts are incorporated in the "micellar phase" [104]. Most of the time, this effect is the consequence of an increase of the local concentrations of the reaction partners. Less frequently, specific "local" interactions might also occur within the micelles, notably involving transition states, leading to dramatic improvement in the outcome of a range of organometallic reactions (*Chapter 31*). Likewise, a set of neutral of amphiphilic surfactants, specifically designed to optimize the binding of apolar substrates, reagents, and metal catalysts, has shown impressive efficiency for a range of challenging organic and organometallic reactions. Herein, the stabilization of reactive organic/metal species and intermediates when located in micelles likely boosts the conversion allowing, for example, reactions to be conducted with ppm levels of metal species (*Chapter 32*). Significant progress in molecular design led to more elaborated amphiphilic hosts [105]. Macromolecules featuring complementary units attached to the polymer chain can be precisely programmed to fold into single-chain nanoparticles (SCNPs). Apolar substrates are converted thanks to catalytic centers located within the hydrophobic environment provided by the SCNPs (*Chapter 33*).

Cyclodextrins have undoubtedly been the most exploited water-soluble hosts [106] for reactions in biphasic aqueous media, notably because they constitute very potent additives in the hydroformylation reaction of olefins [107]. However, a catalyst that can both transform higher olefins efficiently and selectively and can be recycled is still lacking. Anchoring of a phosphine moiety to CD scaffold constitutes an attractive strategy toward this direction (*Chapter 34*). Confinement effects, as mentioned in A.4, also occur when the inner space of the water-soluble molecular host offers a suitable environment for binding and activating the substrate. Reactivity in the deep-cavity cavitands [108] is intimately related to the conformation(s) adopted by the bound substrate; for example, proximity between reactive groups enables a range of thermal and photochemical cyclization reaction including challenging macrocyclization reactions (*Chapter 35*).

Non-covalent interactions are also exploited to combine several units and construct functional catalytic systems that combine water solubility and high modularity. Assembled catalytic structures built by following this strategy can exhibit extremely diverse architectures and only a few examples will be mentioned here. The aforementioned assembled ligands (A.1) are not restricted to organic solvents; supramolecular P,N chelating ligands were formed in water upon mixing a nitrogen-functionalized CD and its complementary P-appended guest [109]. In a different area, thiols appended with different catalytic groups were grafted onto Au

nanoparticles thanks to Au–S interactions, and the catalytic groups at the surface of these monolayer-protected gold clusters were found to exhibit intriguing catalytic features such as proximity and cooperativity [110]. As mentioned in A.2, fibrillar aggregates formed by the assembly of small peptides have also attracted a lot of attention in the last decade because their aggregation pathway resembles that of protein amyloids, and moreover, they constitute structurally simple functional analogues of enzymes [69]. However, in this domain, the most impressive advances probably come from the construction of artificial systems made by combining biomacromolecules and synthetic catalytic groups [37a, 111]. Impressively, histone can be selectively modified in biological environment upon binding a synthetic version of its substrate and this can lead to the development of novel therapeutics (*Chapter 36*). Anchoring of metal complexes on proteins has been exploited for the construction of very efficient artificial metalloenzymes. Non-covalent binding of biotin-derived catalytic centers to (stret)avidin notably yielded very efficient synthetic enzymes, with an impressive scope of reactions. Other protein scaffolds as well as DNA are amenable for chemical modification; the resulting bio-hybrids catalyze new-to-nature reactions [112] such as hydroformylation (*Chapter 37*) and cyclopropanation reactions (*Chapter 38*). Important directions for the aforementioned strategies are: (i) in the realm of synthesis: the possibility of combining synthetic and biological catalysts in the same pot [113], and (ii) in the realm of biology: the development of synthetic systems that operate in cells [114] and in even more intricate biological environments.

A.7 Supramolecular Allosteric Catalysts and Replicators (Chapters 39–41) [115]

Allosteric regulation of enzyme properties (such as ligand binding and reactivity) and replication of biomolecules are fundamental mechanisms of living systems. Molecular recognition events are key for both processes. In the former case, reversible binding of an effector to the regulatory site of the enzyme triggers the conformational and functional changes, while, in the latter case, reversible interactions between the complementary units of the reactant(s) and replicator(s) are necessary to induce auto-catalysis. Integration of these effects in synthetic systems might serve as a tool to gain a deeper understanding of the complex biological

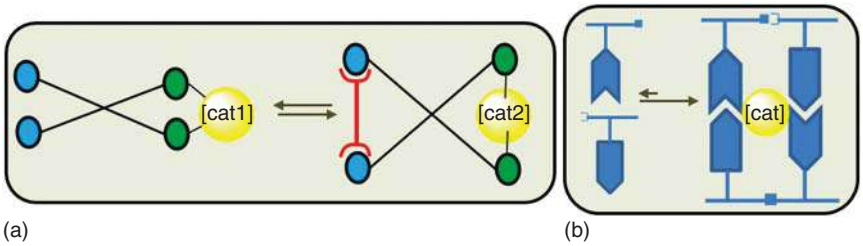

Concept A.7 Supramolecular allosteric catalysts (a) and replicators (b).

machinery at the molecular level. Alternatively, the development of catalytic systems with allosteric and replicating properties might pave the way toward the exploration of new chemical reactivities, e.g. catalysts for "non-natural" reactions in which the activity/selectivity can be stimulated and switched by the environment.

Stimuli-responsive systems were initially investigated mostly in the case of modulating the rate of intramolecular processes, e.g. racemization of 3,3′-disubstituted 2,2′-bipyridyl derivatives [116]. Later on, the effector binding site(s) and the catalytic group(s) were embedded in the same molecular framework. Most of these synthetic catalysts relied on coordination bonds to induce the conformational change that ultimately led to an alteration of the catalytic performance, but not necessarily in a reversible manner. Ligand hemilability was then exploited to vary the distance between the catalytic sites or control the substrate accessibility of a single catalytic site incorporated in molecular tweezers. This translated into truly switchable catalysts exhibiting significant rate differences between their "on" and "off" states. In the quest for efficient allosteric catalysts, non-covalent interactions must be designed that ensure the reversibility and the robustness of the conformational change. Following this idea, the dynamic nature of coordination bonds appears ideal to trigger the assembly of multi-component catalysts and promote their inter-conversion between different catalytic states (*Chapter 39*). Supramolecular triggers might also be used to induce conformational changes that lead to modulation of the selectivity of the catalytic reaction [117]. A current field of research along this direction addresses the possibility of inducing a significant level of enantioselectivity through long-range transfer of the chiral information between a chiral inducer and the catalytic site (A.2). Alternatively, more subtle alteration of the conformation of chiral ligands by means of chemical triggers was found to increase the selectivity and the scope of the resulting metal complexes (*Chapter 40*).

The first synthetic replicators exploited the auto-catalytic properties of oligonucleotides, deoxyoligonucleotides, peptides, and fatty acids. Synthetic replicators devoid of these biological synthons were designed based on simple recognition units that yield well-defined hydrogen-bonded termolecular complexes composed of the template and the two reactive sub-units. More complex systems rapidly followed. For example, self-replicators and cross-replicators are amplified from dynamic combinatorial libraries composed of interchangeable components. Further progress in this field will concern the integration of additional functions to the self-replicators. Recent work indicates that the replicator can actually promote catalytic reactions that ultimately lead to a further acceleration of its rate of formation (*Chapter 41*).

References

1 Lehn, J.M. (1990). Perspectives in supramolecular chemistry – from molecular recognition towards molecular information-processing and self-organization. *Angew. Chem. Int. Ed. Engl.* 29: 1304–1319.

2 Rebek, J. (1990). Molecular recognition with model systems. *Angew. Chem. Int. Ed. Engl.* 29: 245–255.

3 Harmata, M. and Barnes, C.L. (1990). Molecular clefts. 3. The crystal-structure of a chiral molecular tweezer and its guest. *J. Am. Chem. Soc.* 112: 5655–5657.

4 Otto, S. and Engberts, J.B.F.N. (2003). Hydrophobic interactions and chemical reactivity. *Org. Biomol. Chem.* 1: 2809–2820.

5 Giese, M., Albrecht, M., and Rissanen, K. (2015). Anion-π interactions with fluoroarenes. *Chem. Rev.* 115: 8867–8895.

6 Shepodd, T.J., Petti, M.A., and Dougherty, D.A. (1986). Tight, oriented binding of an aliphatic guest by a new class of water-soluble molecules with hydrophobic binding-sites. *J. Am. Chem. Soc.* 108: 6085–6087.

7 Pedersen, C.J. (1967). Cyclic polyethers and their complexes with metal salts. *J. Am. Chem. Soc.* 89: 2495–2496.

8 Gilday, L.C., Robinson, S.W., Barendt, T.A. et al. (2015). Halogen bonding in supramolecular chemistry. *Chem. Rev.* 115: 7118–7195.

9 Jin, Y.H., Yu, C., Denman, R.J., and Zhang, W. (2013). Recent advances in dynamic covalent chemistry. *Chem. Soc. Rev.* 42: 6634–6654.

10 Fischer, E. (1894) Einfluss der configuration auf die wirkung der enzyme. http://doi.org/10.1002/cber.18940270364.

11 Latimer, W.M. and Rodebush, W.H. (1920). Polarity and ionization from the standpoint of the Lewis theory of valence. *J. Am. Chem. Soc.* 42: 1419–1433.

12 Pauling, L. (1960). *The Nature of the Chemical Bond*, 3e. Cornell University Press "I believe that as the methods of structural chemistry are further applied to physiological problems it will be found that the significance of the hydrogen bond for physiology is greater than that of any other single structural feature".

13 Pedersen, C.J. (1967). Cyclic polyethers and their complexes with metal salts. *J. Am. Chem. Soc.* 89: 7017–7036.

14 (a) Dietrich, B., Lehn, J.M., and Sauvage, J.P. (1969). Cryptates. *Tetrahedron Lett.*: 2889–2892.
(b) Dietrich, B., Lehn, J.M., and Sauvage, J.P. (1969). Diazapolyoxamacrocycles and macrobicycles. *Tetrahedron Lett.* 10: 2885–2888.

15 Cram, D.J., Kaneda, T., Helgeson, R.C., and Lein, G.M. (1979). Spherands-ligands whose binding of cations relieves enforced electron-electron repulsions. *J. Am. Chem. Soc.* 101: 6752–6754.

16 van Leeuwen, P.W.N.M. (2004). *Homogeneous Catalysis: Understanding the Art, Chapter 1*. Dordrecht, The Netherlands: Springer.

17 (a) Hosseini, M.W., Lehn, J.M., and Mertes, M.P. (1983). Efficient molecular catalysis of atp-hydrolysis by protonated macrocyclic polyamines. *Hel. Chim. Acta* 66: 2454–2466.
(b) Lehn, J.M. (1985). Supramolecular chemistry – receptors, catalysts, and carriers. *Science* 227: 849–856.
(c) Lehn, J.M. (1986). Recent studies of supramolecular catalysis and transport processes. *Ann. New York Acad. Sci.* 471: 41–50.

18 van Leeuwen, P.W.N.M. (2008). *Supramolecular Catalysis*. Weinheim Verlag GmbH: Wiley-VCH.

19 (a) Raynal, M., Ballester, P., Vidal-Ferran, A., and van Leeuwen, P.W.N.M. (2014). Supramolecular catalysis. Part 1: non-covalent interactions as a tool for building and modifying homogeneous catalysts. *Chem. Soc. Rev.* 43: 1660–1733.

(b) Raynal, M., Ballester, P., Vidal-Ferran, A., and van Leeuwen, P.W.N.M. (2014). Supramolecular catalysis. Part 2: Artificial enzyme mimics. *Chem. Soc. Rev.* 43: 1734–1787.

20 Chao, Y. and Cram, D.J. (1976). Catalysis and chiral recognition through designed complexation of transition states in transacylations of amino ester salts. *J. Am. Chem. Soc.* 98: 1015–1017.

21 (a) Kirby, A.J. (1996). Enzyme mechanisms, models, and mimics. *Angew. Chem. Int. Ed. Engl.* 35: 707–724.
(b) Di Stefano, S., Cacciapaglia, R., and Mandolini, L. (2014). Supramolecular control of reactivity and catalysis - effective molarities of recognition-mediated bimolecular reactions. *Eur. J. Org. Chem.* 2014: 7304–7315.

22 (a) Breslow, R. and Overman, L.E. (1970). An "artificial enzyme" combining a metal catalytic group and a hydrophobic binding cavity. *J. Am. Chem. Soc.* 92: 1075–1077.
(b) Breslow, R., Doherty, J.B., Guillot, G., and Lipsey, C. (1978). β-Cyclodextrinylbisimidazole, a model for ribonuclease. *J. Am. Chem. Soc.* 100: 3227–3229.
(c) Breslow, R. (1995). Biomimetic chemistry and artificial enzymes: catalysis by design. *Acc. Chem. Res.* 28: 146–153.

23 (a) Cramer, F. (1953). Uber Einschlussverbindungen. 5. Basenkatalyse Durch Innermolekulare Hohlraume. *Chem. Ber. Recl.* 86: 1576–1581.
(b) Cramer, F. (1954). *Einschlussverbindungen*. Heidelberg: Springer-Verlag.
(c) Cramer, F. and Dietsche, W. (1958). Asymmetric catalysis by inclusion compounds. *Chem. Ind.*: 892–893.
(d) Cramer, F. and Dietsche, W. (1959). Uber einschlussverbindungen. 16. Stereospezifische reaktionen mit einschlussverbindungen. *Chem. Ber.* 92: 1739–1755.

24 Crini, G. (2014). Review: a history of cyclodextrins. *Chem. Rev.* 114: 10940–10975.

25 (a) Komiyama, M., Breaux, E.J., and Bender, M.L. (1977). The use of cycloamylose to probe the "charge-relay" system. *Bioorg. Chem.* 6: 127–136.
(b) Griffiths, D.W. and Bender, M.L. (1973). Cycloamyloses as Catalysts. *Adv. Catal.* 23: 209–261.
(c) Straub, T.S. and Bender, M.L. (1972). Cycloamyloses as enzyme models – decarboxylation of phenylcyanoacetate anions. *J. Am. Chem. Soc.* 94: 8875–8881.
(d) Straub, T.S. and Bender, M.L. (1972). Cycloamyloses as enzyme models – decarboxylation of benzoylacetic acids. *J. Am. Chem. Soc.* 94: 8881–8888.

26 Tabushi, I., Shimizu, N., Sugimoto, T. et al. (1977). Cyclodextrin flexibly capped with metal ion. *J. Am. Chem. Soc.* 99: 7100–7102.

27 (a) Tabushi, I. and Shimizu, N. 1978, Cyclodextrin metal complexes, JP 53102986. Kokai Tokkyo Koho (to Showa);
(b) Tabushi, I., Kuroda, Y., and Mochizuki, A. (1980). 1st successful carbonic-anhydrase model prepared through a new route to regiospecifically bifunctionalized cyclodextrin. *J. Am. Chem. Soc.* 102: 1152–1153.

28 (a) Mock, W.L., Irra, T.A., Wepsiec, J.P., and Adhya, M. (1989). Catalysis by cucurbituril. The significance of bound-substrate destabilization for induced triazole formation. *J. Org. Chem.* 54: 5302–5308.

(b) Mock, W.L., Irra, T.A., Wepsiec, J.P., and Manimaran, T.L. (1983). Cycloaddition induced by cucurbituril. A case of Pauling principle catalysis. *J. Org. Chem.* 48: 3619–3620.

29 (a) Goehry, C., Besora, M., and Maseras, F. (2015). Computational study on the mechanism of the acceleration of 1,3-dipolar cycloaddition inside cucurbit[6]uril. *ACS Catal.* 5: 2445–2451.
(b) Carlqvist, P. and Maseras, F. (2007). A theoretical analysis of a classic example of supramolecular catalysis. *Chem. Commun.*: 748–750.

30 Cram, D.J. (1988). The design of molecular hosts, guests, and their complexes (nobel lecture). *Angew. Chem. Int. Ed. Engl.* 27: 1009–1112.

31 Mattei, P. and Diederich, F. (1997). Catalytic cyclophanes Part XI. A flavo-thiazolio-cyclophane as a biomimetic catalyst for the preparative-scale electro-oxidation of aromatic aldehydes to methyl esters. *Helv. Chim. Acta* 80: 1555–1588.

32 Walter, C.J., Anderson, H.L., and Sanders, J.K.M. (1993). exo-Selective acceleration of an intermolecular Diels–Alder reaction by a trimeric porphyrin host. *J. Chem. Soc., Chem. Commun.* 1993: 458–460.

33 (a) Yoshizawa, M., Klosterman, J.K., and Fujita, M. (2009). Functional molecular flasks: new properties and reactions within discrete, self-assembled hosts. *Angew. Chem. Int. Ed.* 48: 3418–3438.
(b) Pluth, M.D., Bergman, R.G., and Raymond, K.N. (2009). Proton-mediated chemistry and catalysis in a self-assembled supramolecular host. *Acc. Chem. Res.* 42: 1650–1659.

34 (a) Kang, J. and Rebek, J. Jr., (1997). Acceleration of a Diels-Alder reaction by a self-assembled molecular capsule. *Nature* 385: 50–52.
(b) Kang, J., Hilmersson, G., Santamaria, J., and Rebek, J. Jr., (1998). Diels–Alder reactions through reversible encapsulation. *J. Am. Chem. Soc.* 120: 3650–3656.

35 Breit, B. and Seiche, W. (2003). Hydrogen bonding as a construction element for bidentate donor ligands in homogeneous catalysis: regioselective hydroformylation of terminal alkenes. *J. Am. Chem. Soc.* 125: 6608–6609.

36 Goudriaan, P.E., van Leeuwen, P.W.N.M., Birkholz, M.-N., and Reek, J.N.H. (2008). Libraries of bidentate phosphorus ligands; synthesis strategies and application in catalysis. *Eur. J. Inorg.Chem.*: 2939–2958.

37 (a) Boersma, A.J., Megens, R.P., Feringa, B.L., and Roelfes, G. (2010). DNA-based asymmetric catalysis. *Chem. Soc. Rev.* 39: 2083–2092.
(b) Okamoto, Y. and Ward, T.R. (2017). Supramolecular enzyme mimics. In: *Comprehensive Supramolecular Chemistry II*, vol. 4 (ed. J.L. Atwood), 459–510. Oxford: Elsevier.

38 Pignataro, L., Carboni, S., Civera, M. et al. (2010). PhthalaPhos: chiral supramolecular ligands for enantioselective rhodium-catalyzed hydrogenation reactions. *Angew. Chem. Int. Ed.* 49: 6633–6637.

39 (a) Sanders, J.K.M. (1998). Supramolecular catalysis in transition. *Chem. Eur. J.* 4: 1378–1383;

(b) Wilkinson, M.J., van Leeuwen, P.W.N.M., and Reek, J.N.H. (2005). New directions in supramolecular transition metal catalysis. *Org. Biomol. Chem.* 3: 2371–2383.
(c) Vriezema, D.M., Aragones, M.C., Elemans, J.A.A.W. et al. (2005). Self-assembled nanoreactors. *Chem. Rev.* 105: 1445–1489.
(d) Meeuwissen, J. and Reek, J.N.H. (2010). Supramolecular catalysis beyond enzyme mimics. *Nature Chem.* 2: 615–621.
(e) Dong, Z.Y., Luo, Q., and Liu, J.Q. (2012). Artificial enzymes based on supramolecular scaffolds. *Chem. Soc. Rev.* 41: 7890–7908.

40 (a) Feiters, M.C. (1998). Supramolecular Technology. In: *Comprehensive Supramolecular Chemistry*, vol. 10 (ed. D.N. Reinhoudt). Pergamon: Elmsford: Elsevier Science Ltd.; Atwood, J. L., Davies, J. E. D., MacNicol, D. D., Vögtle, F., Lehn, J. M., Eds.
(b) Ballester, P., Vidal-Ferran, A., and van Leeuwen, P.W.N.M. (2011). Chapter 2 – Modern Strategies in Supramolecular Catalysis. In: *Advances in Catalysis*, vol. 54 (eds. C.G. Bruce, K. Helmut and J. Friederike), 63–126. Academic Press.

41 (a) Baruah, J.B. (2019). *Principles and advances in supramolecular catalysis*. Boca Raton: CRC Press, Taylor & Francis Group.
(b) Wang, L. and Su, C.-Y. (eds.) (2020). *Supramolecular Catalysts: Design, Fabrication, and Applications*. World Scientific.

42 (a) Park, Y.J., Park, J.-W., and Jun, C.-H. (2008). Metal-organic cooperative catalysis in C-H and C-C bond activation and its concurrent recovery. *Acc. Chem. Res.* 41: 222–234.
(b) Fraile, J.M., García, J.I., and Mayoral, J.A. (2009). Noncovalent immobilization of enantioselective catalysts. *Chem. Rev.* 109: 360–417.

43 Bavykina, A., Kolobov, N., Khan, I.S. et al. (2020). Metal-organic frameworks in heterogeneous catalysis: recent progress, new trends and future perspectives. *Chem. Rev.* 120: 8468–8535.

44 Guo, J. and Jiang, D.L. (2020). Covalent organic frameworks for heterogeneous catalysis: principle, current status, and challenges. *ACS Central Sci.* 6: 869–879.

45 (a) Breit, B. (2005). Supramolecular approaches to generate libraries of chelating bidentate ligands for homogeneous catalysis. *Angew. Chem. Int. Ed.* 44: 6816–6825.
(b) Carboni, S., Gennari, C., Pignataro, L., and Piarulli, U. (2011). Supramolecular ligand–ligand and ligand–substrate interactions for highly selective transition metal catalysis. *Dalton Trans.* 40: 4355–4373.
(c) Bellini, R., van der Vlugt, J.I., and Reek, J.N.H. (2012). Supramolecular self-assembled ligands in asymmetric transition metal catalysis. *Isr. J. Chem.* 52: 613–629.
(d) Pignataro, L. and Gennari, C. (2016). Riding the wave of monodentate ligand revival: from the A/B concept to noncovalent interactions. *Chem. Rec.* 16: 2544–2560.

(e) Ohmatsu, K. and Ooi, T. (2015). Design of supramolecular chiral ligands for asymmetric metal catalysis. *Tetrahedron Lett.* 56: 2043–2048.
(f) Mote, N.R. and Chikkali, S.H. (2018). Hydrogen-bonding-assisted supramolecular metal catalysis. *Chem. Asian J.* 13: 3623–3646.

46 van Leeuwen, P.W.N.M. (ed.) (2008). *Supramolecular Catalysis*. Weinheim: Wiley-VCH Verlag GmbH pp. 16, 86, 153, 163, 168, 176, 186, 199, 242, 256, 266, 277, 306, 314, 334, 361.

47 Reetz, M.T., Sell, T., Meiswinkel, A., and Mehler, G. (2003). A new principle in combinatorial asymmetric transition-metal catalysis: mixtures of chiral monodentate P ligands. *Angew. Chem. Int. Ed.* 42: 790–793.

48 Reetz, M.T. and Bondarev, O. (2007). Mixtures of chiral phosphorous acid diesters and achiral P ligands in the enantio- and diastereoselective hydrogenation of ketimines. *Angew. Chem. Int. Ed.* 46: 4523–4526.

49 Crabtree, R. (1979). Iridium compounds in catalysis. *Acc. Chem. Res.* 12: 331–338.

50 Dubrovina, N.V. and Börner, A. (2004). Enantioselective catalysis with chiral phosphine oxide preligands. *Angew. Chem. Int. Ed.* 43: 5883–5886.

51 van Leeuwen, P.W.N.M., Cano, I., and Freixa, Z. (2020). Secondary phosphine oxides: bifunctional ligands in catalysis. *ChemCatChem* 12: 3982–3994.

52 (a) van Leeuwen, P. W. N. M. and Roobeek, C.F. (1983) Hydroformylation of olefins. Eur. Pat. Appl., EP 82576, Chem. Abstr., 99, 121813, (Shell Internationale Research Maatschappij B. V., Neth.).
(b) van Leeuwen, P.W.N.M., Roobeek, C.F., Wife, R.L., and Frijns, J.H.G. (1986). Platinum hydroformylation catalysts containing diphenylphosphine oxide ligands. *J. Chem. Soc., Chem. Commun.* 1986: 31–33.

53 Castro, P.M., Gulyas, H., Benet-Buchholz, J. et al. (2011). SPOs as new ligands in Rh(III) catalyzed enantioselective transfer hydrogenation. *Catal. Sci. Technol.* 1: 401–407.

54 Nurttila, S.S., Linnebank, P.R., Krachko, T., and Reek, J.N.H. (2018). Supramolecular approaches to control activity and selectivity in hydroformylation catalysis. *ACS Catal.* 8: 3469–3488.

55 (a) Jiang, J., Ouyang, G.H., Zhang, L., and Liu, M.H. (2017). Self-assembled chiral nanostructures as scaffolds for asymmetric reactions. *Chem. Eur. J.* 23: 9439–9450.
(b) Wang, T.T., Fan, X.T., Hou, C.X., and Liu, J.Q. (2018). Design of artificial enzymes by supramolecular strategies. *Curr. Opin. Struc. Biol.* 51: 19–27.

56 Park, J., Lang, K., Abboud, K.A., and Hong, S. (2008). Self-assembled dinuclear cobalt(II)-salen catalyst through hydrogen-bonding and its application to enantioselective nitro-aldol (Henry) reaction. *J. Am. Chem. Soc.* 130: 16484–16485.

57 Keijer, T., Bouwens, T., Hessels, J., and Reek, J.N.H. (2021). Supramolecular strategies in artificial photosynthesis. *Chem. Sci.* 12: 50–70.

58 Bhattacharyya, A., De Sarkar, S., and Das, A. (2021). Supramolecular engineering and self-assembly strategies in photoredox catalysis. *ACS Catal.* 11: 710–733.

59 van Leeuwen, P.W.N.M., Rivillo, D., Raynal, M., and Freixa, Z. (2011). Enantioselective supramolecular catalysis induced by remote chiral diols. *J. Am. Chem. Soc.* 133: 18562–18565.

60 Dydio, P., Rubay, C., Gadzikwa, T. et al. (2011). "Cofactor"-controlled enantioselective catalysis. *J. Am. Chem. Soc.* 133: 17176–17179.

61 Desmarchelier, A., Caumes, X., Raynal, M. et al. (2016). Correlation between the selectivity and the structure of an asymmetric catalyst built on a chirally amplified supramolecular helical scaffold. *J. Am. Chem. Soc.* 138: 4908–4916.

62 Escárcega-Bobadilla, M.V. and Kleij, A.W. (2012). Artificial chirogenesis: a gateway to new opportunities in material science and catalysis. *Chem. Sci.* 3: 2421–2428.

63 (a) Macchioni, A. (2005). Ion pairing in transition-metal organometallic chemistry. *Chem. Rev.* 105: 2039–2073.
(b) Phipps, R.J., Hamilton, G.L., and Toste, F.D. (2012). The progression of chiral anions from concepts to applications in asymmetric catalysis. *Nature Chem.* 4: 603–614.
(c) Mahlau, M. and List, B. (2013). Asymmetric counteranion-directed catalysis: concept, definition and applications. *Angew. Chem. Int. Ed.* 52: 518–533.
(d) Ye, X.Y. and Tan, C.H. (2021). Enantioselective transition metal catalysis directed by chiral cations. *Chem. Sci.* 12: 533–539.

64 Slagt, V.F., Reek, J.N.H., Kamer, P.C.J., and van Leeuwen, P.W.N.M. (2001). Assembly of encapsulated transition metal catalysts. *Angew. Chem. Int. Ed.* 40: 4271–4274.

65 Jongkind, L.J., Caumes, X., Hartendorp, A.P.T., and Reek, J.N.H. (2018). Ligand template strategies for catalyst encapsulation. *Acc. Chem. Res.* 51: 2115–2128.

66 (a) Kwamen, C. and Niemeyer, J. (2021). Functional rotaxanes in catalysis. *Chem. Eur. J.* 27: 175–186.
(b) Pan, T.Z. and Liu, J.Q. (2016). Catalysts encapsulated in molecular machines. *ChemPhysChem* 17: 1752–1758.

67 Hapiot, F., Menuel, S., and Monflier, E. (2013). Thermoresponsive hydrogels in catalysis. *ACS Catal.* 3: 1006–1010.

68 (a) Gao, Y., Zhao, F., Wang, Q.G. et al. (2010). Small peptide nanofibers as the matrices of molecular hydrogels for mimicking enzymes and enhancing the activity of enzymes. *Chem. Soc. Rev.* 39: 3425–3433.
(b) Singh, N., Kumar, M., Miravet, J.F. et al. (2017). Peptide-based molecular hydrogels as supramolecular protein mimics. *Chem. Eur. J.* 23: 981–993.
(c) Zozulia, O., Dolan, M.A., and Korendovych, I.V. (2018). Catalytic peptide assemblies. *Chem. Soc. Rev.* 47: 3621–3639.

69 Duncan, K.L. and Ulijn, R.V. (2015). Short peptides in minimalistic biocatalyst design. *Biocatalysis* 1: 67–81.

70 Liu, S.Y., Du, P.D., Sun, H. et al. (2020). Bioinspired supramolecular catalysts from designed self-assembly of DNA or peptides. *ACS Catal.* 10: 14937–14958.

71 (a) Dydio, P. and Reek, J.N.H. (2014). Supramolecular control of selectivity in transition-metal catalysis through substrate preorganization. *Chem. Sci.* 5: 2135–2145.

(b) Davis, H.J. and Phipps, R.J. (2017). Harnessing non-covalent interactions to exert control over regioselectivity and site-selectivity in catalytic reactions. *Chem. Sci.* 8: 864–877.
(c) Haldar, C., Hogue, M.E., Bisht, R., and Chattopadhyay, B. (2018). Concept of Ir-catalyzed C-H bond activation/borylation by noncovalent interaction. *Tetrahedron Lett.* 59: 1269–1277.
(d) Burg, F. and Bach, T. (2019). Lactam hydrogen bonds as control elements in enantioselective transition-metal-catalyzed and photochemical reactions. *J. Org. Chem.* 84: 8815–8836.
(e) Fanourakis, A., Docherty, P.J., Chuentragool, P., and Phipps, R.J. (2020). Recent developments in enantioselective transition metal catalysis featuring attractive noncovalent interactions between ligand and substrate. *ACS Catal.* 10: 10672–10714.
(f) Kuninobu, Y. and Torigoe, T. (2020). Recent progress of transition metal-catalysed regioselective C-H transformations based on noncovalent interactions. *Org. Biomol. Chem.* 18: 4126–4134.
(g) Trouvé, J. and Gramage-Doria, R. (2021). Beyond hydrogen bonding: recent trends of outer sphere interactions in transition metal catalysis. *Chem. Soc. Rev.* 50: 3565–3584.
(h) Vidal, D., Olivo, G., and Costas, M. (2018). Controlling selectivity in aliphatic C-H oxidation through supramolecular recognition. *Chem. Eur. J.* 24: 5042–5054.

72 Corey, E.J. and Noe, M.C. (1996). A critical analysis of the mechanistic basis of enantioselectivity in the bis-cinchona alkaloid catalyzed dihydroxylation of olefins. *J. Am. Chem. Soc.* 118: 11038–11053.

73 Sigman, M.S., Harper, K.C., Bess, E.N., and Milo, A. (2016). The development of multidimensional analysis tools for asymmetric catalysis and beyond. *Acc. Chem. Res.* 49: 1292–1301.

74 Ikariya, T., Murata, K., and Noyori, R. (2006). Bifunctional transition metal-based molecular catalysts for asymmetric syntheses. *Org. Biomol. Chem.* 4: 393–406.

75 Zhao, B.G., Han, Z.B., and Ding, K.L. (2013). The N-H functional group in organometallic catalysis. *Angew. Chem. Int. Ed.* 52: 4744–4788.

76 (a) Breslow, R., Huang, Y., Zhang, X.J., and Yang, J. (1997). An artificial cytochrome P450 that hydroxylates unactivated carbons with regio- and stereoselectivity and useful catalytic turnovers. *Proc. Natl. Acad. Sci. USA* 94: 11156–11158.
(b) Breslow, R., Gabriele, B., and Yang, J. (1998). Geometrically directed selective steroid hydroxylation with high turnover by a fluorinated artificial cytochrome P-450. *Tetrahedron Lett.* 39: 2887–2890.
(c) Yang, J. and Breslow, R. (2000). Selective hydroxylation of a steroid at C-9 by an artificial cytochrome P-450. *Angew. Chem. Int. Ed.* 39: 2692–2694.
(d) Yang, J., Gabriele, B., Belvedere, S. et al. (2002). Catalytic oxidations of steroid substrates by artificial cytochrome P-450 enzymes. *J. Org. Chem.* 67: 5057–5067.

77 (a) Das, S., Incarvito, C.D., Crabtree, R.H., and Brudvig, G.W. (2006). Molecular recognition in the selective oxygenation of saturated C-H bonds by a dimanganese catalyst. *Science* 312: 1941–1943.
(b) Das, S., Brudvig, G.W., and Crabtree, R.H. (2008). High turnover remote catalytic oxygenation of alkyl groups: how steric exclusion of unbound substrate contributes to high molecular recognition selectivity. *J. Am. Chem. Soc.* 130: 1628–1637.

78 (a) Koblenz, T.S., Wassenaar, J., and Reek, J.N.H. (2008). Reactivity within a confined self-assembled nanospace. *Chem. Soc. Rev.* 37: 247–262.
(b) Kim, K.T., Meeuwissen, S.A., Nolte, R.J.M., and van Hest, J.C.M. (2010). Smart nanocontainers and nanoreactors. *Nanoscale* 2: 844–858.
(c) Brown, C.J., Toste, F.D., Bergman, R.G., and Raymond, K.N. (2015). Supramolecular catalysis in metal-ligand cluster hosts. *Chem. Rev.* 115: 3012–3035.
(d) Morimoto, M., Bierschenk, S.M., Xia, K.T. et al. (2020). Advances in supramolecular host-mediated reactivity. *Nature Catal.* 3: 969–984.
(e) Wang, K.Y., Jordan, J.H., Hu, X.Y., and Wang, L.Y. (2020). Supramolecular strategies for controlling reactivity within confined nanospaces. *Angew. Chem. Int. Ed.* 59: 13712–13721.

79 Breslow, R. and Dong, S.D. (1998). Biomimetic reactions catalyzed by cyclodextrins and their derivatives. *Chem. Rev.* 98: 1997–2011.

80 Dwars, T., Paetzold, E., and Oehme, G. (2005). Reactions in micellar systems. *Angew. Chem. Int. Ed.* 44: 7174–7199.

81 Astruc, D. and Chardac, F. (2001). Dendritic catalysts and dendrimers in catalysis. *Chem. Rev.* 101: 2991–3023.

82 Klotz, I.M., Royer, G.P., and Scarpa, I.S. (1971). Synthetic derivatives of polyethyleneimine with enzyme-like catalytic activity (synzymes). *Proc. Natl. Acad. Sci.* 68: 263–264.

83 Mader, M.M. and Bartlett, P.A. (1997). Binding energy and catalysis: the implications for transition-state analogs and catalytic antibodies. *Chem. Rev.* 97: 1281–1301.

84 Wulff, G. and Liu, J. (2012). Design of biomimetic catalysts by molecular imprinting in synthetic polymers: the role of transition state stabilization. *Acc. Chem. Res.* 45: 239–247.

85 Yang, C. and Inoue, Y. (2014). Supramolecular photochirogenesis. *Chem. Soc. Rev.* 43: 4123–4143.

86 Yang, J., Chatelet, B., Herault, D. et al. (2018). Covalent cages with inwardly directed reactive centers as confined metal and organocatalysts. *Eur. J. Org.Chem.* 2018: 5618–5628.

87 Li, X.Z., Wu, J.G., He, C. et al. (2019). Asymmetric catalysis within the chiral confined space of metal-organic architectures. *Small* 15: 1804770.

88 (a) Knowles, R.R. and Jacobsen, E.N. (2010). Attractive noncovalent interactions in asymmetric catalysis: links between enzymes and small molecule catalysts. *Proc. Natl. Acad. Sci. USA* 107: 20678–20685.

(b) Briere, J.F., Oudeyer, S., Dalla, V., and Levacher, V. (2012). Recent advances in cooperative ion pairing in asymmetric organocatalysis. *Chem. Soc. Rev.* 41: 1696–1707.
(c) Anebouselvy, K., Shruthi, K.S., and Ramachary, D.B. (2017). Asymmetric supramolecular organocatalysis: a complementary upgrade to organocatalysis. *Eur. J. Org. Chem.* 2017: 5460–5483.

89 Allemann, C., Gordillo, R., Clemente, F.R. et al. (2004). Theory of asymmetric organocatalysis of aldol and related reactions: rationalizations and predictions. *Acc. Chem. Res.* 37: 558–569.

90 Doyle, A.G. and Jacobsen, E.N. (2007). Small-molecule H-bond donors in asymmetric catalysis. *Chem. Rev.* 107: 5713–5743.

91 Hashimoto, T. and Maruoka, K. (2007). Recent development and application of chiral phase-transfer catalysts. *Chem. Rev.* 107: 5656–5682.

92 Mitschke, B., Turberg, M., and List, B. (2020). Confinement as a unifying element in selective catalysis. *Chem* 6: 2515–2532.

93 Proctor, R.S.J., Colgan, A.C., and Phipps, R.J. (2020). Exploiting attractive non-covalent interactions for the enantioselective catalysis of reactions involving radical intermediates. *Nature Chem.* 12: 990–1004.

94 Zhang, Z. and Schreiner, P.R. (2009). (Thio)urea organocatalysis—What can be learnt from anion recognition? *Chem. Soc. Rev.* 38: 1187–1198.

95 Mayfield, A.B., Metternich, J.B., Trotta, A.H., and Jacobsen, E.N. (2020). Stereospecific furanosylations catalyzed by bis-thiourea hydrogen-bond donors. *J. Am. Chem. Soc.* 142: 4061–4069.

96 Zuend, S.J., Coughlin, M.P., Lalonde, M.P., and Jacobsen, E.N. (2009). Scaleable catalytic asymmetric Strecker syntheses of unnatural α-amino acids. *Nature* 461: 968–U223.

97 Brak, K. and Jacobsen, E.N. (2013). Asymmetric ion-pairing catalysis. *Angew. Chem. Int. Ed.* 52: 534–561.

98 Kennedy, C.R., Lin, S., and Jacobsen, E.N. (2016). The cation-pi interaction in small-molecule catalysis. *Angew. Chem. Int. Ed.* 55: 12596–12624.

99 Neel, A.J., Hilton, M.J., Sigman, M.S., and Toste, F.D. (2017). Exploiting non-covalent π interactions for catalyst design. *Nature* 543: 637–646.

100 Zhao, Y.J., Cotelle, Y., Liu, L. et al. (2018). The emergence of anion-π catalysis. *Acc. Chem. Res.* 51: 2255–2263.

101 Bulfield, D. and Huber, S.M. (2016). Halogen bonding in organic synthesis and organocatalysis. *Chem. Eur. J.* 22: 14434–14450.

102 Mandal, T. and Zhao, C.-G. (2008). Modularly designed organocatalytic assemblies for direct nitro-Michael addition reactions. *Angew. Chem. Int. Ed.* 47: 7714–7717.

103 (a) Breslow, R. (2006). The hydrophobic effect in reaction mechanism studies and in catalysis by artificial enzymes. *J. Phys. Org. Chem.* 19: 813–822.
(b) Kataev, E.A. and Müller, C. (2014). Recent advances in molecular recognition in water: artificial receptors and supramolecular catalysis. *Tetrahedron* 70: 137–167.

(c) Lipshutz, B.H., Ghorai, S., and Cortes-Clerget, M. (2018). The hydrophobic effect applied to organic synthesis: recent synthetic chemistry "in water". *Chem. Eur. J.* 24: 6672–6695.
(d) van Leeuwen, P.W.N.M. and Raynal, M. (2019). Supramolecular strategies for efficient catalysis in water. In: *Supramolecular Chemistry in Water* (ed. S. Kubik). Wiley VCH.

104 La Sorella, G., Strukul, G., and Scarso, A. (2015). Recent advances in catalysis in micellar media. *Green Chem.* 17: 644–683.

105 Lu, A. and O'Reilly, R.K. (2013). Advances in nanoreactor technology using polymeric nanostructures. *Curr. Opin. Biotechnol.* 24: 639–645.

106 Murray, J., Kim, K., Ogoshi, T. et al. (2017). The aqueous supramolecular chemistry of cucurbit[*n*]urils, pillar[*n*]arenes and deep-cavity cavitands. *Chem. Soc. Rev.* 46: 2479–2496.

107 Hapiot, F., Bricout, H., Menuel, S. et al. (2014). Recent breakthroughs in aqueous cyclodextrin-assisted supramolecular catalysis. *Catal. Sci. Technol.* 4: 1899–1908.

108 Jordan, J.H. and Gibb, B.C. (2015). Molecular containers assembled through the hydrophobic effect. *Chem. Soc. Rev.* 44: 547–585.

109 Hapiot, F., Bricout, H., Tilloy, S., and Monflier, E. (2012). Functionalized cyclodextrins as first and second coordination sphere ligands for aqueous organometallic catalysis. *Eur. J. Inorg.Chem.* 2012: 1571–1578.

110 Mancin, F., Prins, L.J., Pengo, P. et al. (2016). Hydrolytic metallo-nanozymes: from micelles and vesicles to gold nanoparticles. *Molecules* 21: 1014.

111 (a) Wang, L.X., Xiang, J.F., and Tang, Y.L. (2015). Novel DNA catalysts based on g-quadruplex for organic synthesis. *Adv. Synth. Catal.* 357: 13–20.
(b) Schwizer, F., Okamoto, Y., Heinisch, T. et al. (2018). Artificial metalloenzymes: reaction scope and optimization strategies. *Chem. Rev.* 118: 142–231.

112 Jeschek, M., Panke, S., and Ward, T.R. (2018). Artificial Metalloenzymes on the Verge of New-to-Nature Metabolism. *Trends Biotechnol.* 36: 60–72.

113 Wang, Z.J., Clary, K.N., Bergman, R.G. et al. (2013). A supramolecular approach to combining enzymatic and transition metal catalysis. *Nature Chem.* 5: 100–103.

114 Chordia, S., Narasimhan, S., Paioni, A.L. et al. (2021). In vivo assembly of artificial metalloenzymes and application in whole-cell biocatalysis. *Angew. Chem. Int. Ed.*, 60: 5913–5920.

115 (a) Kovbasyuk, L. and Krämer, R. (2004). Allosteric supramolecular receptors and catalysts. *Chem. Rev.* 104: 3161–3187.
(b) Paul, N. and Joyce, G.F. (2004). Minimal self-replicating systems. *Curr. Opin. Chem. Biol.* 8: 634–639.
(c) Vidonne, A. and Philp, D. (2009). Making molecules make themselves – the chemistry of artificial replicators. *Eur. J. Org. Chem.*: 593–610.
(d) Wiester, M.J., Ulmann, P.A., and Mirkin, C.A. (2011). Enzyme mimics based upon supramolecular coordination chemistry. *Angew. Chem. Int. Ed.* 50: 114–137.

(e) Otto, S. (2012). Dynamic molecular networks: from synthetic receptors to self-replicators. *Acc. Chem. Res.* 45: 2200–2210.

116 (a) Rebek, J. Jr.,, Costello, T., and Wattley, R. (1985). Binding forces and catalysis. The use of bipyridyl-metal chelation to enhance reaction rates. *J. Am. Chem. Soc.* 107: 7487–7493.

(b) Rebek, J. Jr., and Trend, J.E. (1978). On binding to transition states and ground states: remote catalysis. *J. Am. Chem. Soc.* 100: 4315–4316.

117 Vaquero, M., Rovira, L., and Vidal-Ferran, A. (2016). Supramolecularly fine-regulated enantioselective catalysts. *Chem. Commun.* 52: 11038–11051.

Part I

Ligand–Ligand Interactions

1

Supramolecular Construction of Bidentate Ligands Through Self-assembly by Hydrogen Bonding

Felix Bauer and Bernhard Breit

University of Freiburg, Insitute for Organic Chemistry, Fakultät für Chemie und Pharmazie, Albertstraße 21, 79104 Freiburg, Germany

1.1 Introduction

In classical transition metal catalysis, phosphine ligands have a dominant position in controlling catalysts activity and selectivity [1, 2]. Monodentate phosphine ligands show in many catalytic transformations higher catalytic activity but lower selectivity. In contrast, bidentate ligands in which two phosphorus donors are combined by a covalent backbone often show superior selectivity in many transformations. Some of these bidentate ligands were designed to achieve high selectivity in a specific reaction. However, a disadvantage is their often lower activity compared with monodentate ligands. Moreover, the synthesis of these ligands is in most cases complicated involving a multistep route to the target ligand. This is especially a drawback in the synthesis of nonsymmetrical bidentate ligands equipped with two different donor sites.

In order to overcome these limitations, supramolecular chemistry offers a powerful tool [3–5]. In this conceptually new approach, structurally less complicated monodentate ligands might self-assemble into a bidentate coordination mode in a transition metal complex by noncovalent interactions. Nature provides many noncovalent interactions such as van der Waals interactions, π-stacking, electrostatic interactions, coordinative interactions, or hydrogen bonding [3]. Among them probably the most prominent interaction is hydrogen bonding, highlighted especially in DNA where they connect the single strands of the double helix [3, 6]. This feature can be seen as an inspiration to replace covalent bonds in the backbone of a bidentate ligand (Scheme 1.1).

The high potential of this approach is beyond a simplified ligand design and lies in the inherent possibility to generate a combinatorial ligand library through simple mixing of two ligands. This means if two different ligands are coordinated to one transition metal center from n different monodentate donor ligands, a catalyst library with $(n^2 + n)/2\mathrm{ML}^x\mathrm{L}^y$ could be obtained (Table 1.1).

On the other hand, when the interaction between two ligands bound to one metal center is noncomplementary, a mixture of two homodimeric and one heterodimeric

Supramolecular Catalysis: New Directions and Developments, First Edition.
Edited by Piet W.N.M. van Leeuwen and Matthieu Raynal.

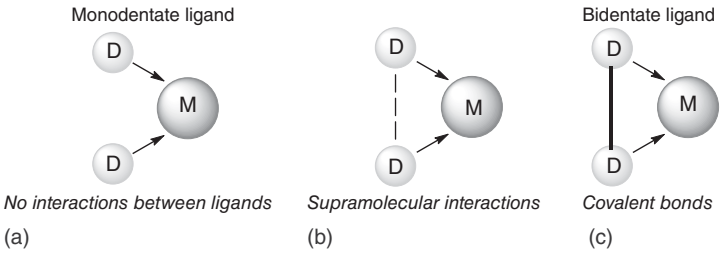

Scheme 1.1 Classical monodentate (a) and bidentate (c) ligands with a covalent-bonded backbone; self-assembled bidentate ligand by supramolecular interactions in the ligand backbone (b).

Table 1.1 Catalyst library through mixing of *n* monodentate ligands.

Ligand	**L^1**	**L^2**	**· · ·**	**L^n**
L^1	L^1 L^1			
L^2	L^1 L^2	L^2 L^2		
· · ·	· · ·	· · ·	· · ·	
L^n	L^1 L^n	L^2 L^1	· · ·	L^n L^n

ligand metal complexes will be obtained. This results in three potential catalysts present in solution (Scheme 1.2a). Only when the heterocombination is more active and selective than both homocombinations, a better catalyst could be obtained by optimization.

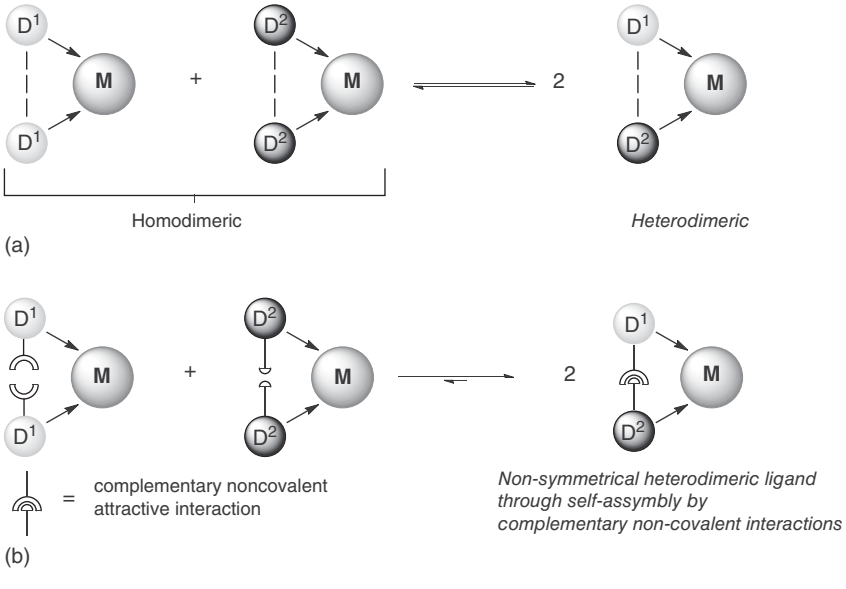

Scheme 1.2 Catalytic mixtures of two ligands D^1 and D^2 and a metal source when the ligands have noncomplementary D^1/D^2 interactions (a). Catalytic mixture of monodentate ligands with complementary binding sides in the presence of a metal source leads to single defined heterodimeric catalysts (b).

Table 1.2 Catalyst library with $m \times n$ different and defined heterodimeric ligand combinations obtained by the mixing of two sets of monodentate ligands with complementary binding sites.

Ligand	m_1	m_2	⋯	m_i
n_1	m_1n_1	m_2n_1	⋯	m_in_1
n_2	m_1n_2	m_2n_2	⋯	m_in_2
⋯	⋯	⋯	⋯	⋯
n_j	m_1n_j	m_2n_j	⋯	m_in_j

For achieving reasonable understanding in the construction of a ligand library, it is desirable that only the heterodimeric combinations are preferably formed. This problem could be solved using two sets of monodentate ligands with complementary binding sides, which enables only attractive ligand–ligand interactions in case of the heterodimeric combination (Scheme 1.2b).

Such a heterodimeric ligand system formed by complementary self-assembly could imitate classical nonsymmetrical ligand systems. If now m ligands of the set D^1 and n ligands of the set D^2 are mixed in the presence of a transition metal species, a library of $m \times n$ defined heterodimeric bidentate ligand–metal complexes is formed (Table 1.2).

In this chapter, we will focus on the results of our own research group on hydrogen bonding to construct self-assembling ligands. The concept is described and several applications in homogeneous catalysis are presented.

1.2 Formation of Bidentate Ligands Through Self-assembly via Hydrogen Bonding and Application in Hydroformylation

1.2.1 2-Hydroxypyridine/2-Pyridone Platform

In 2003, our group reported the *in situ* generation of bidentate ligands in the coordination sphere of a transition metal through self-assembly by hydrogen bonds [7]. This first example was based on the 2-pyridone (**1b**)/2-hydroxypyridine (**1a**) tautomers (Scheme 1.3). The parent system (D = H) dimerized in aprotic solvent predominantly as the symmetrical pyridone dimer **2**. However, when D is a donor group capable of coordinating a transition metal (e.g. PPh_2), it can be observed that in the presence of a transition metal, the equilibrium shifts toward the mixed hydroxypyridine/pyridone dimer **3**. This is reasonable, because only the mixture of the tautomers can benefit from the stabilization of both phosphines coordinating to the metal center and two hydrogen bonds.

In fact, for platinum and rhodium complexes of the 6-diphenylphosphanyl-2-pyridone (6-DPPon) ligand **1**, the self-assembly by hydrogen bonding could be proven in solution using NMR and in solid state by X-ray crystal structure analysis (Figure 1.1) [7, 8].

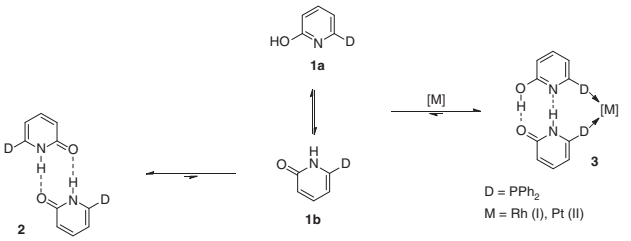

Scheme 1.3 Self-assembly of the pyridone system and in the presence of a metal source self-assembly of the 2-pyridone/2-hydroxypyridine to form bidentate complexes **3** suitable for homogeneous catalysis.

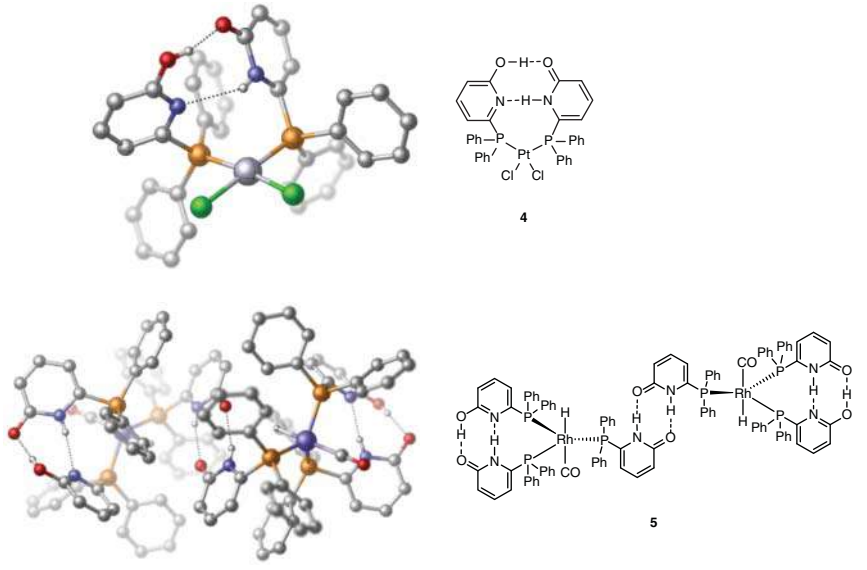

Figure 1.1 X-ray structure of a $[Cl_2Pt(6\text{-DPPon})_2]$-complex [7] (**4**) and a dimer of a $[HRh(6\text{-DPPon})_3(CO)]$-complex (**5**) (carbon-bonded hydrogen atoms are omitted for clarity) [8].

In rhodium-catalyzed hydroformylation of terminal alkenes, a catalyst based on the 6-DPPon ligand showed high selectivities for the linear aldehyde, which are typical of classical bidentate ligands [7]. However, bidentate ligands usually have lower catalytic activity compared with unselective monodentate ligands [9]. Therefore, the 6-DPPon ligand combines the advantages of mono- and bidentate ligands. This catalytic system tolerates many functional groups in the alkene substrate (Table 1.3). Among the tested substrates, some are even capable of forming hydrogen bonds such as carbamates, salicylates, or even free alcohols. If the hydrogen bonds of the ligand system are disrupted, the selectivities of the catalyst drop significantly. Potential sources for disruption are high temperatures above 110 °C, protic solvents, or acidic conditions (Table 1.3, entry 9 and 10).

Table 1.3 Regioselective rhodium-catalyzed hydroformylation of terminal alkenes with the 6-DPPon ligand.[a)]

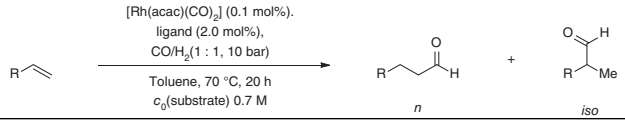

		n:iso				n:iso	
#	Substrate	6-DPPon	PPh_3	#	Substrate	6-DPPon	PPh_3
1	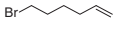	97 : 3	72 : 28	6	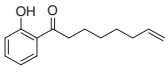	95 : 5	70 : 30
2	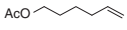	96 : 4	71 : 29	7		95 : 5	89 : 11
3	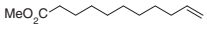	97 : 3	74 : 26	8		96 : 4	77 : 23
4	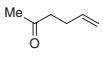	94 : 6	71 : 29	9[b)]		83 : 17	77 : 23
5	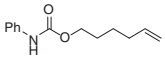	96 : 4	69 : 31	10[c)]		81 : 19	—

a) Reaction conditions: $[Rh(acac)(CO)_2]$/ligand/substrate = 1 : 20 : 1000, c_0(substrate) = 0.7 M, toluene, CO/H_2 (1 : 1, 10 bar), 70 °C. Full conversion was reached in every case after 20 hours.
b) MeOH as solvent.
c) Addition of 0.5 equiv of AcOH with respect to substrate.

The extraordinary importance of hydrogen bonding for the high activity and selectivity in rhodium-catalyzed hydroformylation was shown by detailed NMR and *in situ* IR spectroscopical investigations, ESI-MS as well as by DFT calculations [8, 10–13]. The hydrogen bonding in the ligand backbone seems to provide a flexibility that enables an easy change of coordination geometries without significant energy penalty, while on the other hand, they provide the structural stability to obtain high selectivities for the linear product.

The high activity of catalysts based on the 6-DPPon ligand in rhodium-catalyzed hydroformylation was highlighted in the first room-temperature ambient-pressure hydroformylation of terminal alkenes [14]. Using only low catalysts loading, a wide range of alkenes could be transformed into the related aldehydes in high yield and excellent selectivity (Table 1.4). In further studies of this approach, even water could be employed as a solvent, when a small amount of a specific surfactant was added [15]. This protocol is highly attractive for application in organic chemistry, because no special high-pressure equipment is necessary and the products are easily obtained in high yields and selectivity.

Although hydroformylation of terminal alkenes is a well-established transformation in homogeneous catalysis, alkynes or allenes are way less used as substrates in hydroformylation, not just because of the usual low chemo- and regioselectivity (Scheme 1.4), but also in general low activity of these substrates. However, the hydroformylation of alkynes, for example, would offer an elegant atom-economic

Table 1.4 Room-temperature/ambient-pressure regioselective hydroformylation of terminal alkenes.

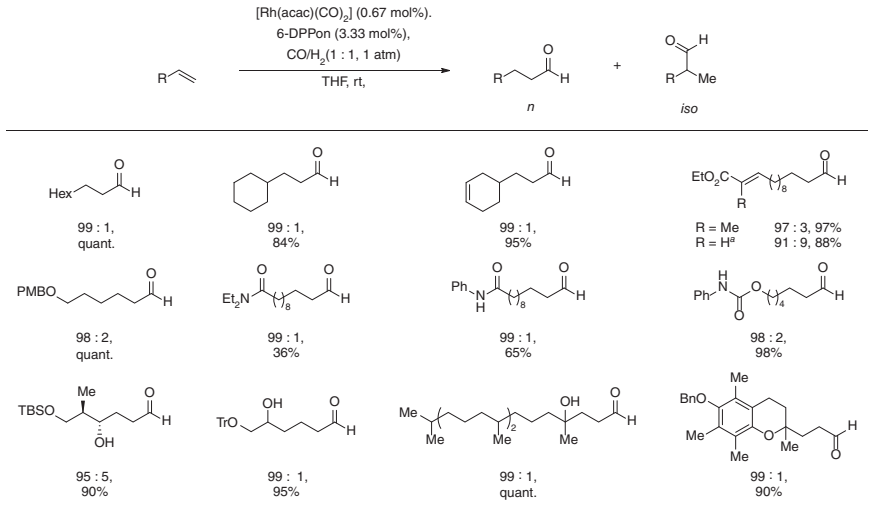

[a]Internal double bond is hydrogenated over time.

a) Internal double bond is hydrogenated over time.

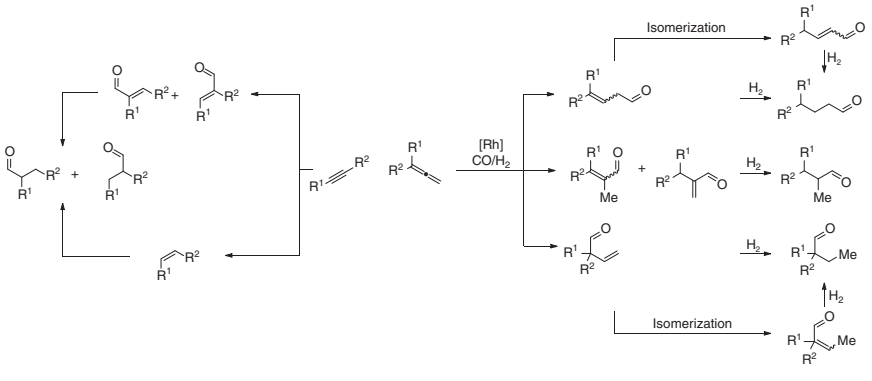

Scheme 1.4 Potential products in alkyne and allene hydroformylation.

way for the direct synthesis of enals. Major side products are the alkene and the saturated aldehydes, which are formed by either hydrogenation of the enals or hydroformylation of the alkene.

Using an electron poor derivative **6** of the 6-DPPon ligand, a huge range of internal alkynes could be used as substrate for this reaction to generate enals in high yield and excellent chemoselectivity (Scheme 1.5) [16]. Terminal alkynes were found to be a more challenging substrate, because the produced enals undergo easily hydrogenation of the conjugated double bond. Nevertheless, it was possible to generate three different enals in moderate yields, whereby a significant substrate influence on the selectivity was observed.

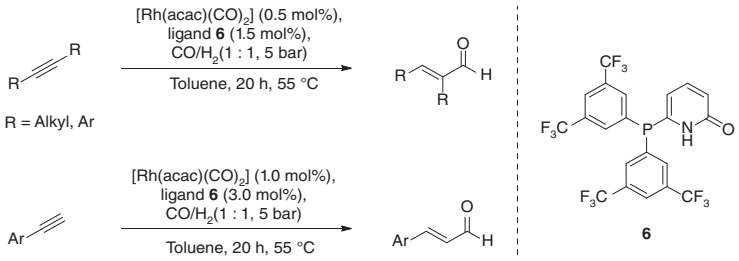

Scheme 1.5 Hydroformylation of internal and terminal alkynes.

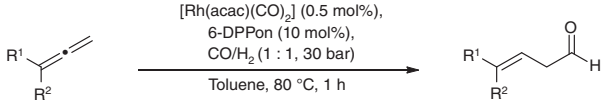

Scheme 1.6 Synthesis of γ,β-unsaturated aldehydes by allene hydroformylation.

The 6-DPPon ligand was also able to convert several 1,1-disubstituted allenes into γ,β-unsaturated aldehydes (Scheme 1.6) [17]. These unusual building blocks were obtained in high regio- and chemoselectivity. When unsymmetrically 1,1-disubstituted allenes were used as substrates, the *Z*-product was formed in up to >95% selectivity. The achieved yield was usually very high, and the catalyst can be used to synthesize the products even in gram scale. The allenes required for this protocol can be readily prepared in a simple two-step synthesis from almost any ketone [17].

1.2.2 Complementary Hydrogen Bonding for the Construction of Heterodimeric Self-assembling Ligands

The tautomers of 6-DPPon ligand **1** are indistinguishable in transition metal complexes due to a fast equilibration process [10]. This behavior is not beneficial if two pyridone ligands with different donor sites are mixed together, because mixtures of the two homodimeric and the heterodimeric complex would be obtained (Scheme 1.2). For the synthesis of a pure heterodimeric catalyst, another concept must be applied: complementary self-assembly. Inspired by the A–T base pairing of DNA, a complementary platform based on aminopyridine and isoquinolone was tailored (Scheme 1.7) to enable exclusively the synthesis of heterodimeric self-assembled ligand complexes [18].

The phosphine ligands **7** and **8** based on this platform (D = PPh_2) form in the presence of $[Cl_2Pt(COD)]$ exclusively the heterodimeric *cis*-$[Cl_2Pt(\mathbf{7})(\mathbf{8})]$ complex **10**. The complementary self-assembly of both ligands by hydrogen bonding was found in solid-state by X-ray crystal structure analysis (Figure 1.2) and in solution by a low field shift of the involved protons in the ^{1}H-NMR.

These platforms allow the selective formation of ligand libraries based on hydrogen bonding by variation of the donor group of one or both ligands (Table 1.2). Applying this concept, it was possible to identify a catalyst with outstanding activity and high regioselectivity in the rhodium-catalyzed hydroformylation of 1-octene

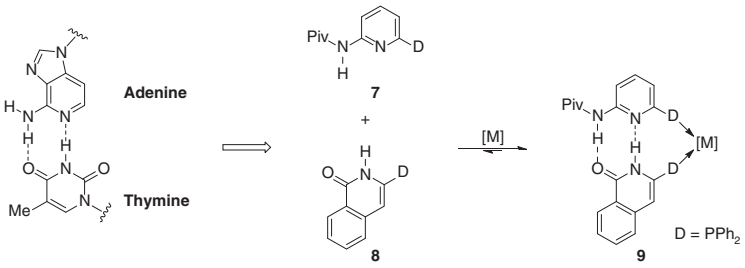

Scheme 1.7 An A–T-base pair as a model for a complementary self-assembly ligand platform via hydrogen bonds.

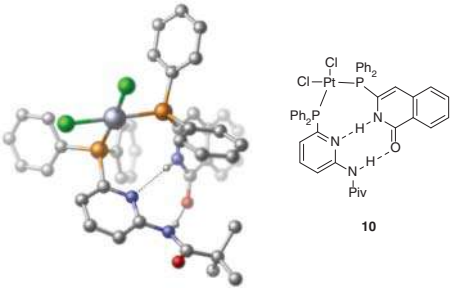

Figure 1.2 X-ray crystal structure of a [Cl_2Pt(**7a**)(**8a**)]-complex **10** (carbon-bonded hydrogen atoms are omitted for clarity) [18].

(Table 1.5) [18]. It should be highlighted that it is a nonsymmetrical combination of donor groups of the ligands.

The complementary self-assembly approach is not restricted to the aminopyridine/isoquinolone system only. The A–T base pair analogous platform could be modified as well [19]. Any modifications on this part of the ligand might affect directly the hydrogen bonding system and by that directly to ligand bite angle and coordination geometry to a metal. These parameters have a significant influence of the performance of a catalyst. In this sense, several ligands with modified hydrogen bonding systems were synthesized and explored (Scheme 1.8) [19].

Of all 10 ligand combinations [Cl_2Pt(L^{DA})(L^{AD})], complexes were prepared and studied. By ^{1}H and ^{31}P NMR spectroscopy, it was possible to show that all combinations form in solution selectively heteroleptic *cis*-complexes with hydrogen bonds. By X-ray crystal structure analysis, the defined structure could furthermore be confirmed for the solid state for the complexes of [Cl_2Pt(**13**)(**8a**)] and [Cl_2Pt(**12**)(**15**)] (Figure 1.3).

To evaluate the catalytic potential of these ligands, they were tested independently in the rhodium-catalyzed hydroformylation of 1-octene [19]. The obtained regioselectivities of all ligands were in a typical order of monodentate ligands such as PPh_3 (from 75 : 25 to 81 : 19). Afterward all 10 ligand combinations were tested under the same conditions (Table 1.6). The observed regioselectivities (89 : 11 to >99 : 1) indicate that in all cases the bidentate self-assembled ligand might be the kinetically competent catalyst.

Table 1.5 Turnover frequencies and regioselectivities for a 4 × 4 ligand matrix of aminopyridine (**7a–d**) and isoquinolone (**8a–d**) derived self-assembled bidentate ligands in the rhodium-catalyzed hydroformylation of 1-octene.

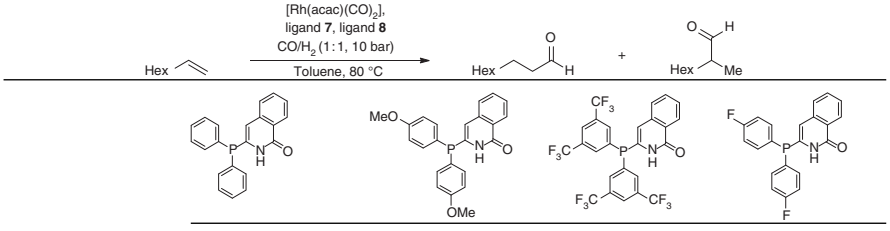

Ligand	8a	8b	8c	8d
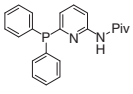 **7a**	2425 h^{-1} 94 : 6	1040 h^{-1} 94 : 6	2732 h^{-1} 96 : 4	2559 h^{-1} 95 : 5
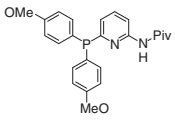 **7b**	2033 h^{-1} 93 : 7	1058 h^{-1} 92 : 8	1281 h^{-1} 96 : 4	1772 h^{-1} 94 : 6
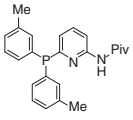 **7c**	3537 h^{-1} 94 : 6	1842 h^{-1} 93 : 7	1808 h^{-1} 96 : 4	2287 h^{-1} 94 : 6
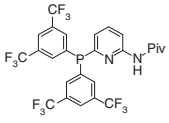 **7d**	7439 h^{-1} 96 : 4	2695 h^{-1} 95 : 5	7465 h^{-1} 94 : 6	**8643 h^{-1}** **96 : 4**

Reaction conditions: $[Rh(acac)(CO)_2] : L^{AD} : L^{DA}$: 1-octene = 1 : 10 : 10 : 7500, CO/H_2 (1 : 1, 10 bar), toluene, c_0(1-octene) = 2.91 M, 5 hours. Catalyst preformation: CO/H_2 (1 : 1, 5 bar), 30 minutes, rt to 80 °C.

Remarkably, the combinations in which the pivaloyl group of the ligands **7a** and **13** was substituted by a trifluoroacetyl group, an increase in regioselectivity was observed. This might be related to an increased strength in hydrogen bonding. Of all studied ligand combinations, the catalyst formed from **14**/**8a** and **14**/**15** showed the highest selectivity (Table 1.7). A regioselectivity for the linear aldehyde of more than 99:1 was achieved. One explanation for this improvement might be that by the change of the ring size of the six-membered aminopyridine system to the five-membered thiazole heterocycle, the accessible geometry of the system

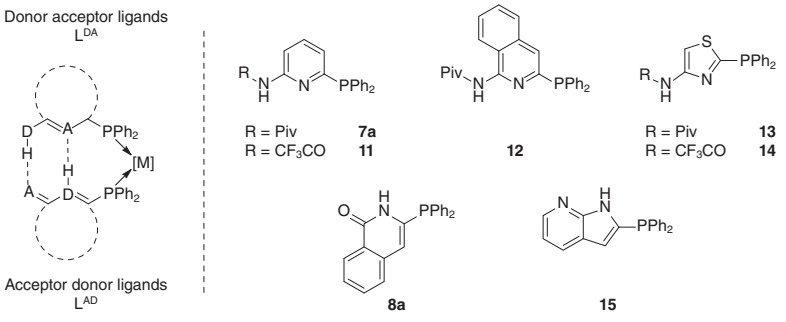

Scheme 1.8 Library of ligands with complementary hydrogen bonding platform.

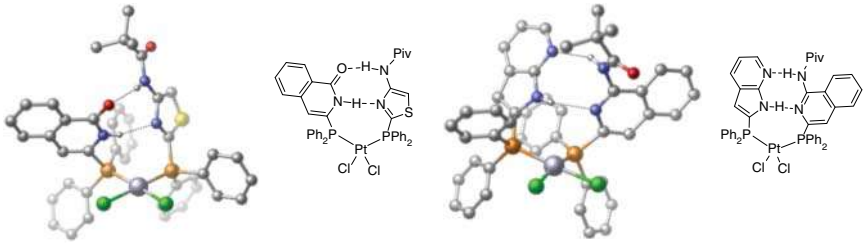

Figure 1.3 X-ray crystal structure of a [Cl_2Pt(**13**)(**8a**)]- and a [Cl_2Pt(**12**)(**15**)]-complex (carbon-bonded hydrogen atoms are omitted for clarity).

Table 1.6 Turnover frequencies and regioselectivities for a 5 × 2 ligand matrix with different combinations of DA- and AD-ligands as self-assembled bidentate ligands in the rhodium-catalyzed hydroformylation of 1-octene.

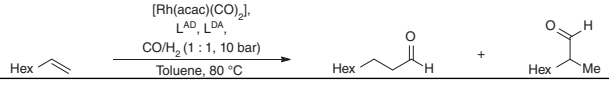

Ligand	7a	11	12	13	14
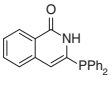 **8a**	2394 h^{-1} (93 : 7)	3396 h^{-1} (96 : 4)	2452 h^{-1} (95 : 5)	3890 h^{-1} (98 : 2)	3888 h^{-1} (**>99 : 1**)
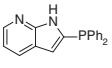 **15**	2679 h^{-1} (89 : 11)	4864 h^{-1} (96 : 4)	3205 h^{-1} (95 : 5)	3233 h^{-1} (95 : 5)	2333 h^{-1} (**99 : 1**)

Reaction conditions: [Rh(acac)$(CO)_2$] : L^{AD} : L^{DA} : 1-octene = 1 : 10 : 10 : 7500, CO/H_2 (1:1, 10 bar), toluene, 80 °C, 5 hours. Catalyst preformation: CO/H_2 (1 : 1, 5 bar), 30 minutes, rt to 80 °C.

Table 1.7 Regioselectivities of the rhodium-catalyzed hydroformylation of 1-octene in toluene or MeOH as solvent.

#	Ligands	*l* : *b* in toluene	*l* : *b* in MeOH
1	**7a**/**8a**	94 : 6	82 : 18
2	**11**/**8a**	96 : 4	79 : 21
3	**13**/**8a**	98 : 2	97 : 3
4	**14**/**8a**	99 : 1	96 : 4

Reaction conditions: $[Rh(acac)(CO)_2]$, [Rh] : L^{AD} : B1 : 1-octene = 1 : 10 : 10 : 7500, CO/H_2 (1:1, 10 bar), 80 °C; Regioselectivity: linear to branched, determined by GC-analysis and/or ^1H NMR spectroscopy.

is slightly changed. By this, more stable hydrogen bonds seem to be formed, which might yield a more rigid system. If this assumption is correct, it should be interesting to test these ligands in protic solvents such as methanol. First generation of self-assembly ligands such as 6-DPPon or **7a**/**8a** showed a significant drop of the regioselectivity in the hydroformylation of 1-octene in protic solvents [7, 18]. This sensitivity to protic solvents so far limits the application range of self-assembled ligands in homogeneous catalysis.

Therefore several ligand combinations were studied in the rhodium-catalyzed hydroformylation of 1-octene in methanol and toluene. The combinations without the thiazole-based ligands suffered a significant loss of regioselectivity in methanol. This drop in selectivity indicates a disruption of the hydrogen bonds in the backbones of these ligands, which leads to results similar to a catalyst based on PPh_3. Combinations that involve a thiazole ligand result in high regioselectivity in both toluene and methanol.

These findings clearly show that the variation of the heterocyclic platform for the hydrogen bonds has a huge influence on the resulting catalyst. Thus, new catalysts for the rhodium-catalyzed hydroformylation could be identified with a very high activity and an almost perfect regioselectivity. These catalysts could successfully be applied in protic solvents, which is a huge step for the applicability of self-assembled ligands based on hydrogen bonding.

1.3 Asymmetric Hydrogenation

1.3.1 P-chiral Self-assembly Ligands in Asymmetric Hydrogenation

To study the power of the combinatorial approach in asymmetric catalysis, a library of new chiral ligands was synthesized [20, 21], carrying the previously established platforms for complementary self-assembly via hydrogen bonding (Scheme 1.9).

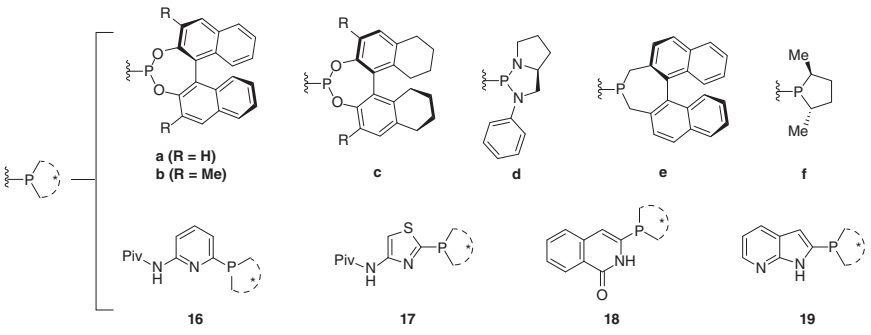

Scheme 1.9 Library of chiral self-assembly ligands.

In total, 12 AD-ligands and 10 DA ligands were prepared and tested in the asymmetric rhodium-catalyzed hydrogenation by mixing all possible ligand combinations [21]. In total, 120 catalysts are possible due to the complementary hydrogen bonding. These catalysts were investigated and seven combinations showed perfect ee and high or quantitative conversion (Table 1.8). The disadvantage of this approach is the high number of experiments to identify all promising ligand combinations.

One elegant way to overcome this drawback is a combinatorial approach using an iterative deconvolution strategy (Table 1.9). First step of this strategy is the division of all ligands of this ligand library into subgroups. Each subgroup is mixed with the corresponding other subgroups. The results of all subgroup combinations are compared and the best combination in terms of selectivity and activity is further deconvoluted by division into new subgroups. All other combinations are discarded and the process will be repeated until the most active and selective catalyst is identified. By this methodology three individual catalysts with perfect activity and enantioselectivity could be identified in only 17 reactions instead of 120 of the classical approach. This strategy not only reduces the number of reactions to be run dramatically, but also the analytical effort is reduced to the same extent.

1.3.2 Inducing Axial Chirality in a Supramolecular Catalyst

Ligands with an axial chiral backbone are among the most valuable systems used in asymmetric catalysis [22–25], but the synthesis of their inflexible backbone is often long and difficult. Recently, a new type of *in silico* designed ligand was presented [26]. This ligand is based on the 6-DPPon ligand, but carries a chiral substituent at the pyridone ring (Scheme 1.10). In transition metal complexes, this ligand self-assembles by hydrogen bonding of its tautomeric forms. However, the so formed supramolecular backbone is twisted and axially chiral, which results in two diastereomeric complexes. Rhodium and platinum complexes of these ligands were studied by ESI-MS, NMR-, UV-, and circular dichroism spectroscopy. The ratio of these complexes in solution is very sensitive to temperature and solvent effects.

Table 1.8 Parallel screening of a library of 120 self-assembled catalysts in the rhodium-catalyzed asymmetric hydrogenation by the classic approach.

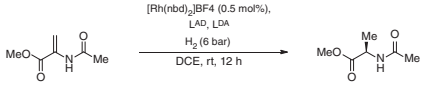

L^{DA}	L^{AD}	(*S*)-**17a**	(*S*)-**17b**	(*S*)-**17c**	(*S*)-**17d**	(*S*)-**17e**	(*S*)-**17f**	(*S*)-**16a**	(*S*)-**16b**	(*S*)-**16c**	(*S*)-**16d**	(*S*)-**16e**	(*S*)-**16f**
		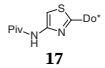 **17**						 **16**					
 **18**	(*S*)-**18a**	**99 (quant.)**	96 (quant.)	95 (quant.)	88 (quant.)	**99 (quant.)**	79 (quant.)	**99 (86)**	97 (88)	96 (89)	89 (quant.)	**99 (90)**	81 (93)
	(*S*)-**18b**	90 (quant.)	91 (99)	90 (98)	92 (quant.)	90 (quant.)	84 (quant.)	92 (84)	89 (86)	91 (85)	86 (89)	93 (86)	85 (94)
	(*S*)-**18c**	94 (quant.)	82 (98)	88 (97)	90 (quant.)	95 (quant.)	88 (quant.)	94 (83)	93 (79)	87 (78)	88 (81)	90 (84)	81 (85)
	(*S*)-**18d**	92 (quant.)	88 (quant.)	81 (quant.)	66 (quant.)	91 (quant.)	60 (quant.)	89 (quant.)	84 (98)	85 (95)	54 (90)	88 (quant.)	40 (88)
	(*S*)-**18e**	**99 (quant.)**	94 (quant.)	92 (quant.)	89 (quant.)	98 (quant.)	90 (quant.)	**99 (89)**	98 (87)	94 (86)	84 (95)	**99 (92)**	79 (95)
	(*S*)-**18f**	87 (quant.)	89 (quant.)	90 (quant.)	80 (quant.)	88 (quant.)	78 (quant.)	93 (quant.)	95 (95)	94 (89)	81 (95)	89 (87)	74 (83)
 **19**	(*S*)-**19a**	90 (quant.)	87 (94)	90 (92)	41 (96)	91 (quant.)	76 (53)	88 (85)	87 (78)	91 (81)	46 (84)	87 (90)	79 (47)
	(*S*)-**19b**	82 (quant.)	77 (72)	85 (57)	49 (80)	81 (quant.)	39 (15)	84 (81)	83 (80)	89 (59)	55 (73)	85 (81)	48 (58)
	(*S*)-**19c**	78 (quant.)	66 (89)	74 (35)	37 (77)	79 (quant.)	36 (14)	80 (82)	71 (71)	77 (65)	49 (68)	82 (85)	20 (64)
	(*S*)-**19d**	81 (quant.)	81 (84)	84 (66)	52 (98)	82 (quant.)	43 (56)	83 (88)	82 (58)	86 (67)	38 (quant.)	80 (87)	44 (78)

Reaction conditions: $[Rh(nbd)_2]BF_4$, [Rh] : L^{AD} : L^{DA} : substrate = 1 : 1.05 : 1.05 : 200, H_2 (6 bar), DCE, c_0(substrate) = 0.3 M, 12 hours, RT. Enantioselectivity was determined by chiral GC, conversion was determined by ^{1}H NMR spectroscopy.

ee

(conv.)

Table 1.9 Combinational approach to the identification of the most active and selective ligand combinations in the rhodium-catalyzed asymmetric hydrogenation.

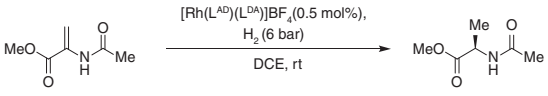

Step 1	L^{AD}	17	16
L^{DA}	Do	(*S*)-**17a**	(*S*)-**16a**
		(*S*)-**17b**	(*S*)-**16b**
		(*S*)-**17c**	(*S*)-**16c**
		(*S*)-**17c**	(*S*)-**16c**
		(*S*)-**17e**	(*S*)-**16e**
		(*S*)-**17f**	(*S*)-**16f**
18	(*S*)-**18a**	84% *ee* (quant.)	79% *ee* (quant.)
	(*S*)-**18b**		
	(*S*)-**18c**		
	(*S*)-**18d**		
	(*S*)-**18e**		
	(*S*)-**18f**		
19	(*S*)-**19a**	62% *ee* (92%)	
	(*S*)-**19b**		
	(*S*)-**19c**		
	(*S*)-**19d**		

Step 2		17		
L^{DA}	Do	(*S*)-**17a** (*S*)-**17e**	(*S*)-**17b** (*S*)-**17d**	(*S*)-**17c** (*S*)-**17f**
18	(*S*)-**18a** (*S*)-**18e**	99% *ee*	93% *ee*	87% *ee*
	(*S*)-**18b** (*S*)-**18c**	92% *ee*	89% *ee*	89% *ee*
	(*S*)-**18d** (*S*)-**18f**	82% *ee*	84% *ee*	84% *ee*

Step 3		17	
L^{DA}	Do	(*S*)-**17a**	(*S*)-**17e**
18	(*S*)-**18a**	99% *ee*	99% *ee*
	(*S*)-**18e**	99% *ee*	98% *ee*

Reaction conditions: $[Rh(nbd)_2]BF_4$, $[Rh] : L^{AD} : L^{DA}$: substrate = 1 : 1.05 : 1.05 : 200, H_2 (6 bar), DCE, c_0(substrate) = 0.3 M, 12 hours, RT. Enantioselectivity was determined by chiral GC, conversion was determined by ^{1}H NMR spectroscopy.
The shades should highlight the conditions which gave the highest yield and enantioselectivity.

At room temperature, both diastereomeric complexes are indistinguishable, but at lower temperatures, one complex is favored.

The potential of this concept was shown in rhodium-catalyzed asymmetric hydrogenation. With the ligands **20S** and **20R,** enantiomeric excess up to 90% could be achieved (Table 1.10). Control experiments in MeOH showed how crucial hydrogen bonding is to achieve enantioselectivity.

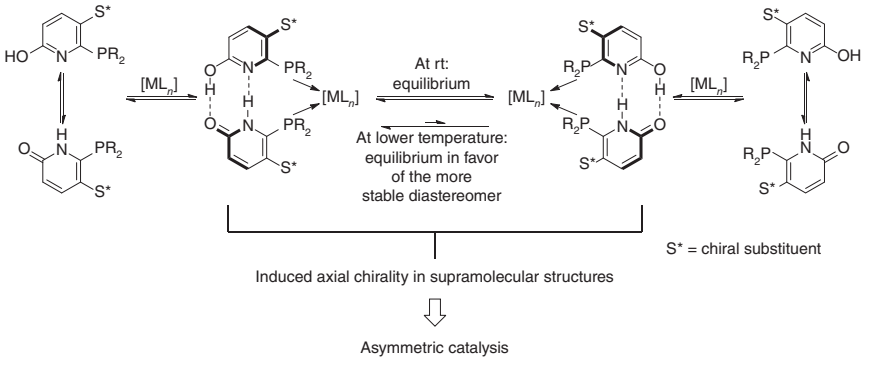

Scheme 1.10 Induced axial chirality in supramolecular structures.

Table 1.10 Asymmetric hydrogenation of methyl acetamidoacrylate.

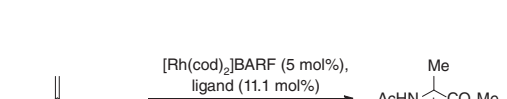

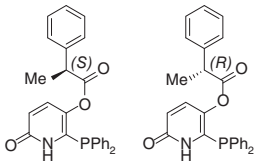

20S **20R**

#	Ligand	Solvent	Conversion (%)	*ee* (%)
1	**20S**	DCE	85	84 (*S*)
2	**20R**	DCE	81	85(*R*)
3	**20S**	*o*-DCB	93	90 (*S*)
4	**20S**	MeOH	1	*rac*.

[Rh]/L/substrate 1 : 2.2 : 20; *c*(substrate) = 0.02 M; conversion and ee determined by chiral-phase GC. BARF = *tetrakis*[3,5-*bis*(trifluoromethyl)phenyl]borate.

1.4 Other Catalytic Applications

Self-assembling ligands are not limited to rhodium-catalyzed hydroformylation or hydrogenation reactions. This methodology was successfully applied on several reactions.

1.4.1 Hydration of Alkynes

The addition of water to alkynes is an important way to install functional groups into a carbon skeleton. This transformation usually follows the Markovnikov rule [27–31]. An *anti*-Markovnikov selective hydration of a terminal alkyne would be a convenient method to generate aldehydes. For this unusual hydration mode, only few ruthenium catalysts were previously reported [32–37]. Bidentate ligands [35],

phosphinopyridine ligands [34], and the preorientation of the water molecule by hydrogen bonding [33] seemed to have positive effects in the reported processes. Self-assembling ligands also incorporate a pyridinyl-functionalized phosphine group, and they emulate bidentate ligands with their hydrogen bonding system, which might interact with water.

To obtain further insight, the hydration of 1-nonyne catalyzed by half-sandwich ruthenium complexes with different ligands was investigated [38]. With mono- or bidentate phosphine ligands, only low activity and selectivity were observed (Table 1.11, entries 1–3). The 6-DPPon ligand, which should be able to self-assemble by hydrogen bonding, showed similar results (entry 4). However, a catalyst based on the complementary self-assembling of the heterodimeric aminopyridine/isoquinolone ligands yielded the desired product in perfect selectivity with excellent catalyst activity (entry 5). By control experiments, it was shown that the heterodimeric ligand combination is responsible for the best catalyst (entries 6 and 7).

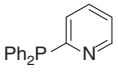
dppy


dppe

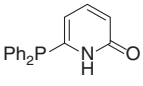
6-DPPon

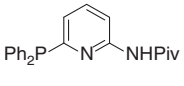
7a

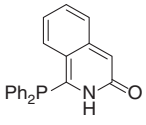
8a

Table 1.11 Ruthenium complex-catalyzed hydration of 1-nonyne.

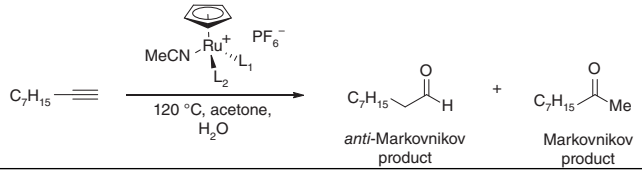

#	Cat.	L1	L2	*t* (h)	Aldehyde[a] (%)	Ketone[a] (%)
1		PPh_3	PPh_3	140	1.2	18
2[b]		dppy	dppy	168	4.0	2.4
3		dppe	—	168	2.1	20
4[b]		6-DPPon (**1**)	6-DPPon(**1**)	168	2.1	25
5		(**7a**)	(**8a**)	26	94	0
6[b]		(**7a**)	(**7a**)	72	39	3.8
7		(**8a**)	(**8a**)	48	1.9	0

a) Yield calculated from GC response factors relative to internal standard hexadecane.
b) κ^1-P, κ^2-P,N coordination of the phosphinopyridine with replacement of the acetonitrile ligand.

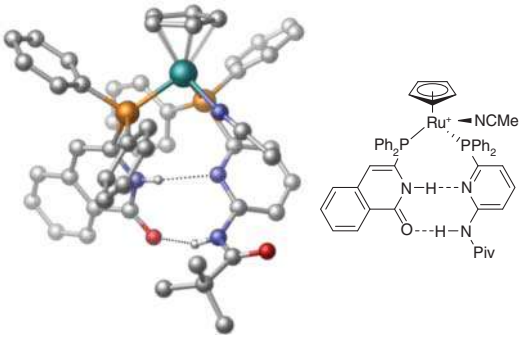

Figure 1.4 X-ray crystal structure of a [(Cp)Ru(**7a**)(**8a**)(NCMe)]$^{+}$-complex (carbon-bonded hydrogen atoms and the PF_6^- counterion are omitted for clarity.

The structure of the best catalyst was further analyzed by X-ray crystal structure analysis and the hydrogen bonding was confirmed (Figure 1.4). This catalyst was applied on a scope of 10 different alkynes with in almost all cases perfect chemoselectivity for the aldehyde and good-to-excellent activities.

1.4.2 Hydration of Nitriles

Classical hydration of nitriles to amides requires very harsh conditions [39]. Transition metal catalysis offers a powerful tool to perform this reaction under very mild conditions [40, 41]. For this reason, the hydration of nitriles to amides is an important example of an industrially important atom economic reaction [42]. After the successful application of the self-assembly ligands in the hydration of alkynes, it seemed promising to apply these ligands also to nitriles. For this reason, homo- and heterodimeric *bis*(acetylacetonato)ruthenium(II) complexes of the ligands **7a** and **8a** were prepared [43]. The structure of these complexes was investigated in solution and in solid state. Especially for the heterodimeric combination, some unusual hydrogen bonding patterns were observed involving hydrogen bonding in between the **8a** ligand and an oxygen atom of an acac ligand (Figure 1.5).

However, the homo-complex of **8a** showed the highest activity in the hydration of *p*-tolylcarbonitrile (Table 1.12).

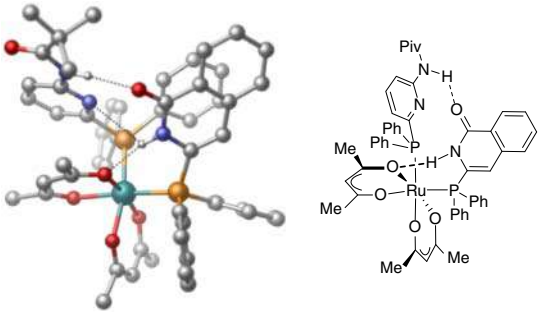

Figure 1.5 X-ray crystal structure of a [Ru(acac)$_2$(**7a**)(**8a**)]-complex (carbon-bonded hydrogen atoms are omitted for clarity) [43].

Table 1.12 Ruthenium complex-catalyzed hydration of nitriles.

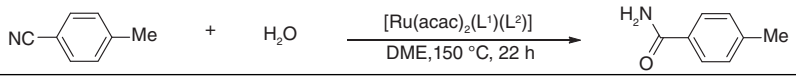

#	L^1	L^2	Conversion (%)	TOF (h^{-1})
1	**8a**	**8a**	100	20
2	**8a**	**7a**	90	5
3	**7a**	**7a**	<5	nd

Reaction conditions: $[Ru(acac)_2(L^1)(L^2)]$/substrate/water = 1 : 100 : 200, DME (1 ml), substrate (1 mmol), water (2 mmol), 150 °C, 22 hours.

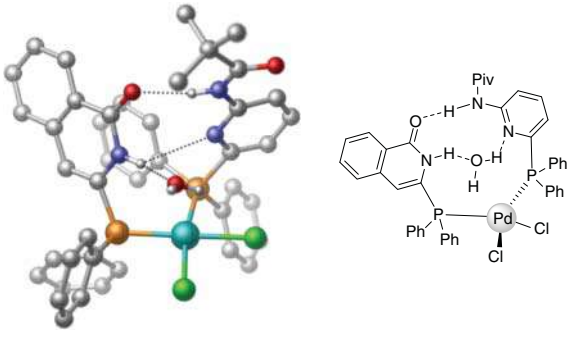

Figure 1.6 X-ray crystal structure of $[Cl_2Pd(\mathbf{8a}\cdot H_2O)(\mathbf{7a})]$ (carbon-bonded hydrogen atoms are omitted for clarity) [44].

1.4.3 Allylic Substitution with Allylic Alcohols

It was possible to synthesize crystals of a $[Cl_2Pd(\mathbf{8a}\cdot H_2O)(\mathbf{7a})]$ suitable for X-ray structure analysis (Figure 1.6) [44]. Interestingly, a single water molecule was incorporated in the hydrogen bonding system of the complementary self-assembly ligands.

Inspired by this interaction of water with the ligand backbone, it seemed reasonable that alcohols might form similar interactions [44]. Especially allylic alcohols might be directed by this interaction in a beneficial orientation with the palladium center. Indeed, it was possible to apply directly allylic alcohols as substrates in allylic substitution with water as the only by-product (Scheme 1.11). The common substrates of classic allylic substitution catalysts are in most cases allylic acetates or carbonates [45]. These substrates have to be prepared in an extra step and release always a stoichiometric amount of a coupled byproduct. The palladium-catalyzed allylic substitution with the self-assembly ligands can directly apply allylic alcohols and generates as stoichiometric by-product only water.

1.4.4 Hydrocyanation

The nitrile group is often found in many natural products as well as in different pharmaceuticals, agrochemical products, and functional materials [46]. The nitrile

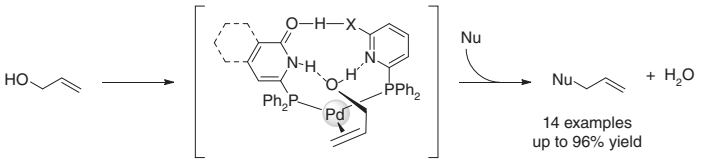

Scheme 1.11 Palladium complex-catalyzed allylic substitution of allylic alcohols directed by substrate pre-orientation through hydrogen bonding to self-assembled ligands.

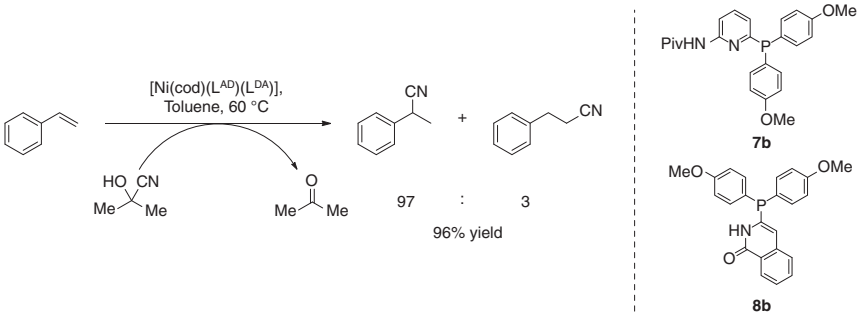

Scheme 1.12 Nickel complex-catalyzed hydrocyanation of alkenes.

group is also quite useful in organic synthesis because it can easily be transformed into different functional groups such as amines, aldehydes, ketones, and other carboxylic acid derivatives [47]. An elegant method to generate these molecules is the hydrocyanation of alkenes by the formal addition of HCN to a C=C double bond [48, 49]. Most industrial catalysts are based on (bidentate) phosphite or phosphinite ligands, but bidentate phosphine ligands showed also interesting reactivities [50]. Van Leeuwen et al. showed that electron poor bidentate ligands with bite angles around 105° seem to have positive results on the catalysts activity [51–53].

It has been demonstrated that the complementary heterodimeric self-assembly ligands can form Ni^0 complexes, which are promising catalysts in the hydrocyanation of styrenes [54]. A 5×4 ligand matrix of ligands derived from the isoquinolone and aminopyridine platform was used to identify the best ligand combination. The so found catalyst provided very high activity, perfect regioselectivity, and a good functional group tolerance in the nickel-catalyzed hydrocyanation of alkenes (Scheme 1.12). It is worth to highlight that the best ligand combination (**7b**/**8b**) bares electron-rich groups in contrast to previously reported catalysts, which seem to give better results with electron-poor ligands [52].

1.5 Concluding Remarks

In this chapter, the self-assembly of monodentate phosphine ligands in transition metal complexes by hydrogen bonding was described.

We have introduced the unique 6-DPPon ligand platform in homogeneous catalysis based on the homodimeric 2-pyridone/2-hydroxypyridine system. Catalysts

based on this platform showed an outstanding performance in rhodium-catalyzed hydroformylation of allenes, alkynes, and terminal alkenes, in some cases even at room temperature and under one atmosphere of syngas. Considering the limited accessibility of high-pressure equipment in many laboratories, this is a major advantage of this system. In addition, by introducing chiral substituents at the pyridone platform, an axial chiral self-assembled ligand system can be generated, which showed promising first results in asymmetric hydrogenation.

The A–T base pairing in the DNA inspired the complementary self-assembly of heterodimeric ligands. This approach offers easy access to the formation of structurally diverse ligand libraries. The huge advantage compared with classical bidentate ligands is that a catalyst composed of two unsymmetrical donors is easily realized just by mixing two complementary ligands together. For the synthesis of a comparable classic bidentate ligand with a covalent backbone and two unsymmetrical donor sites, a huge synthetic effort is necessary. Using these ligand libraries, it was possible to identify potent catalysts for many different transformations such as hydrocyanation, hydration of alkynes, or allylic substitution. Especially in rhodium-catalyzed hydroformylation, it was possible to generate outstanding active and selective catalysts. These catalysts enable perfect selectivity for the linear aldehyde even in protic solvents, which is an impressive proof for the stability of the supramolecular ligand backbone by hydrogen bonding. Nevertheless, large ligand libraries can still lead to a huge experimental effort to test all possible ligand combinations. In asymmetric hydrogenation, it was possible to give an example for the superiority of combinatorial methods to identify the most active catalyst, compared with the classical testing of all ligand combinations (17 instead of 120 reactions).

All those findings clearly show that the self-assembly of ligands by hydrogen bonding is a valuable tool for the synthetic chemist to use in homogeneous transition metal catalysis.

References

1 Hagen, J. (2015). Homogeneous catalysis with transition metal catalysts. In: *Industrial Catalysis: A Practical Approach*, 17–46. Weinheim, Germany: Wiley-VCH.

2 Hartwig, J.F. (2010). *Organotransition Metal Chemistry: From Bonding to Catalysis*. Mill Valley, California: University Science Books.

3 Schneider, H.-J. and Yatsimirsky, A.K. (2000). *Principles and Methods in Supramolecular Chemistry*. Chichester: Wiley.

4 Dydio, P. and Reek, J.N.H. (2014). Supramolecular control of selectivity in transition-metal catalysis through substrate preorganization. *Chem. Sci.* 5 (6): 2135–2145.

5 Lehn, J.-M. (1988). Supramolecular chemistry—scope and perspectives molecules, supermolecules, and molecular devices (nobel lecture). *Angew. Chem. Int. Ed. Engl.* 27 (1): 89–112.

6 Watson, J.D. and Crick, F.H. (1953). Molecular structure of nucleic acids; a structure for deoxyribose nucleic acid. *Nature* 171 (4356): 737–738.

7 Breit, B. and Seiche, W. (2003). Hydrogen bonding as a construction element for bidentate donor ligands in homogeneous catalysis: regioselective hydroformylation of terminal alkenes. *J. Am. Chem. Soc.* 125 (22): 6608–6609.

8 Gellrich, U., Seiche, W., Keller, M., and Breit, B. (2012). Mechanistic insights into a supramolecular self-assembling catalyst system: evidence for hydrogen bonding during rhodium-catalyzed hydroformylation. *Angew. Chem. Int. Ed. Engl.* 51 (44): 11033–11038.

9 Leeuwen, P.W.N.M. and Claver, C. (2002). *Rhodium Catalyzed Hydroformylation*. Dordrecht: Kluwer Academic Publishers.

10 Gellrich, U., Huang, J., Seiche, W. et al. (2011). Ligand self-assembling through complementary hydrogen-bonding in the coordination sphere of a transition metal center: the 6-diphenylphosphanylpyridin-2(1*H*)-one system. *J. Am. Chem. Soc.* 133 (4): 964–975.

11 Gellrich, U., Koslowski, T., and Breit, B. (2015). Full kinetic analysis of a rhodium-catalyzed hydroformylation: beyond the rate-limiting step picture. *Catal. Sci. Technol.* 5 (1): 129–133.

12 Gellrich, U., Himmel, D., Meuwly, M., and Breit, B. (2013). Realistic energy surfaces for real-world systems: an IMOMO CCSD(T):DFT scheme for rhodium-catalyzed hydroformylation with the 6-DPPon ligand. *Chemistry* 19 (48): 16272–16281.

13 Beierlein, C.H., Breit, B., Paz Schmidt, R.A., and Plattner, D.A. (2010). Online monitoring of hydroformylation intermediates by ESI-MS. *Organometallics* 29 (11): 2521–2532.

14 Seiche, W., Schuschkowski, A., and Breit, B. (2005). Bidentate Ligands by self-assembly through hydrogen bonding: a general room temperature/ambient pressure regioselective hydroformylation of terminal alkenes. *Adv. Syn. Catal.* 347 (11–13): 1488–1494.

15 Straub, A.T., Otto, M., Usui, I., and Breit, B. (2013). Room temperature ambient pressure (RTAP)-hydroformylation in water using a self-assembling ligand. *Adv. Syn. Catal.* 355 (10): 2071–2075.

16 Agabekov, V., Seiche, W., and Breit, B. (2013). Rhodium-catalyzed hydroformylation of alkynes employing a self-assembling ligand system. *Chem. Sci.* 4 (6): 2418.

17 Köpfer, A. and Breit, B. (2015). Rhodium-catalyzed hydroformylation of 1,1-disubstituted allenes employing the self-assembling 6-DPPon system. *Angew. Chem. Int. Ed. Engl.* 54 (23): 6913–6917.

18 Breit, B. and Seiche, W. (2005). Self-assembly of bidentate ligands for combinatorial homogeneous catalysis based on an A-T base-pair model. *Angew. Chem. Int. Ed. Engl.* 44 (11): 1640–1643.

19 Waloch, C., Wieland, J., Keller, M., and Breit, B. (2007). Self-assembly of bidentate ligands for combinatorial homogeneous catalysis: methanol-stable platforms analogous to the adenine–thymine base pair. *Angew. Chem.* 119 (17): 3097–3099.

20 Weis, M., Waloch, C., Seiche, W., and Breit, B. (2006). Self-assembly of bidentate ligands for combinatorial homogeneous catalysis: asymmetric rhodium-catalyzed hydrogenation. *J. Am. Chem. Soc.* 128 (13): 4188–4189.

21 Wieland, J. and Breit, B. (2010). A combinatorial approach to the identification of self-assembled ligands for rhodium-catalysed asymmetric hydrogenation. *Nat. Chem.* 2 (10): 832–837.

22 Tang, W. and Zhang, X. (2003). New chiral phosphorus ligands for enantioselective hydrogenation. *Chem. Rev.* 103 (8): 3029–3070.

23 Berthod, M., Mignani, G., Woodward, G., and Lemaire, M. (2005). Modified BINAP: the how and the why. *Chem. Rev.* 105 (5): 1801–1836.

24 Miyashita, A., Yasuda, A., Takaya, H. et al. (1980). Synthesis of 2,2′-bis (diphenylphosphino)-1,1′-binaphthyl (BINAP), an atropisomeric chiral bis(triaryl)phosphine, and its use in the rhodium(I)-catalyzed asymmetric hydrogenation of .alpha.-(acylamino)acrylic acids. *J. Am. Chem. Soc.* 102 (27): 7932–7934.

25 Miyashita, A., Takaya, H., Souchi, T., and Noyori, R. (1984). 2, 2'-bis (diphenylphosphino)-1, 1'-binaphthyl(binap). *Tetrahedron* 40 (8): 1245–1253.

26 Wenz, K.M., Leonhardt-Lutterbeck, G., and Breit, B. (2018). Inducing axial chirality in a supramolecular catalyst. *Angew. Chem. Int. Ed. Engl.* 57 (18): 5100–5104.

27 Blum, J., Huminer, H., and Alper, H. (1992). Alkyne hydration promoted by RhCl3 and quaternary ammonium salts. *J. Mol. Catal.* 75 (2): 153–160.

28 Casado, R., Contel, M., Laguna, M. et al. (2003). Organometallic gold(III) compounds as catalysts for the addition of water and methanol to terminal alkynes. *J. Am. Chem. Soc.* 125 (39): 11925–11935.

29 Mizushima, E., Sato, K., Hayashi, T., and Tanaka, M. (2002). Highly efficient AuI-catalyzed hydration of Alkynes. *Angew. Chem. Int. Ed.* 41 (23): 4563–4565.

30 Hartman, J.W., Hiscox, W.C., and Jennings, P.W. (1993). Catalytic hydration of alkynes with platinum(II) complexes. *J. Org. Chem.* 58 (26): 7613–7614.

31 Fukuda, Y. and Utimoto, K. (1991). Effective transformation of unactivated alkynes into ketones or acetals with a gold(III) catalyst. *J. Org. Chem.* 56 (11): 3729–3731.

32 Alvarez, P., Bassetti, M., Gimeno, J., and Mancini, G. (2001). Hydration of terminal alkynes to aldehydes in aqueous micellar solutions by ruthenium(II) catalysis; first anti-Markovnikov addition of water to propargylic alcohols. *Tetrahedron Lett.* 42 (48): 8467–8470.

33 Grotjahn, D.B., Incarvito, C.D., and Rheingold, A.L. (2001). Combined effects of metal and ligand capable of accepting a proton or hydrogen bond catalyze anti-Markovnikov hydration of terminal alkynes. *Angew. Chem. Int. Ed.* 40 (20): 3884–3887.

34 Grotjahn, D.B. and Lev, D.A. (2004). A general bifunctional catalyst for the anti-Markovnikov hydration of terminal alkynes to aldehydes gives enzyme-like rate and selectivity enhancements. *J. Am. Chem. Soc.* 126 (39): 12232–12233.

35 Suzuki, T., Tokunaga, M., and Wakatsuki, Y. (2001). Ruthenium complex-catalyzed anti-Markovnikov hydration of terminal alkynes. *Org. Lett.* 3 (5): 735–737.

36 Tokunaga, M., Suzuki, T., Koga, N. et al. (2001). Ruthenium-catalyzed hydration of 1-alkynes to give aldehydes: insight into anti-Markovnikov regiochemistry. *J. Am. Chem. Soc.* 123 (48): 11917–11924.

37 Tokunaga, M. and Wakatsuki, Y. (1998). The first anti-Markovnikov hydration of terminal alkynes: formation of aldehydes catalyzed by a ruthenium(II)/phosphane mixture. *Angew. Chem. Int. Ed.* 37 (20): 2867–2869.

38 Chevallier, F. and Breit, B. (2006). Self-assembled bidentate ligands for Ru-catalyzed anti-Markovnikov hydration of terminal alkynes. *Angew. Chem. Int. Ed. Engl.* 45 (10): 1599–1602.

39 Green, M.M. and Wittcoff, H.A. (2006). *Organic Chemistry Principles and Industrial Practice*, 1e. Weinheim: Wiley-VCH.

40 Ahmed, T.J., Knapp, S.M.M., and Tyler, D.R. (2011). Frontiers in catalytic nitrile hydration: Nitrile and cyanohydrin hydration catalyzed by homogeneous organometallic complexes. *Coord. Chem. Rev.* 255 (7-8): 949–974.

41 Kukushkin, V.Y. and Pombeiro, A.J.L. (2002). Additions to metal-activated organonitriles. *Chem. Rev.* 102 (5): 1771–1802.

42 Trost, B.M. (2002). On inventing reactions for atom economy. *Acc. Chem. Res.* 35 (9): 695–705.

43 Šmejkal, T. and Breit, B. (2007). Self-assembled bidentate ligands for ruthenium-catalyzed hydration of nitriles. *Organometallics* 26 (9): 2461–2464.

44 Usui, I., Schmidt, S., Keller, M., and Breit, B. (2008). Allylation of N-heterocycles with allylic alcohols employing self-assembling palladium phosphane catalysts. *Org. Lett.* 10 (6): 1207–1210.

45 Trost, B.M. and Crawley, M.L. (2003). Asymmetric transition-metal-catalyzed allylic alkylations: applications in total synthesis. *Chem. Rev.* 103 (8): 2921–2944.

46 Fleming, F.F. (1999). Nitrile-containing natural products. *Nat. Prod. Rep.* 16 (5): 597–606.

47 Larock, R.C. (1999). *Comprehensive Organic Transformations: A Guide to Functional Group Preparations*, 2e. New York, NY: Wiley-VCH.

48 Torborg, C. and Beller, M. (2009). Recent applications of palladium-catalyzed coupling reactions in the pharmaceutical, agrochemical, and fine chemical industries. *Adv. Syn. Catal.* 351 (18): 3027–3043.

49 Zhang, H., Su, X., and Dong, K. (2020). Recent progress in transition-metal-catalyzed hydrocyanation of nonpolar alkenes and alkynes. *Org. Biomol. Chem.* 18 (3): 391–399.

50 Goertz, W., Kamer, P.C.J., van Leeuwen, P.W.N.M., and Vogt, D. (1997). Application of chelating diphosphine ligands in the nickel-catalysed hydrocyanation of alk-l-enes and ω-unsaturated fatty acid esters. *Chem. Commun.* (16): 1521–1522.

51 Freixa, Z. and van Leeuwen, P.W.N.M. (2003). Bite angle effects in diphosphine metal catalysts: steric or electronic? *Dalton Trans.* (10): 1890–1901.

52 Goertz, W., Keim, W., Vogt, D. et al. (1998). Electronic effects in the nickel-catalysed hydrocyanation of styrene applying chelating phosphorus ligands with large bite angles. *J. Chem. Soc., Dalton Trans.* (18): 2981–2988.

53 Kranenburg, M., Kamer, P.C.J., van Leeuwen, P.W.N.M. et al. (1995). Effect of the bite angle of diphosphine ligands on activity and selectivity in the nickel-catalysed hydrocyanation of styrene. *J. Chem. Soc., Chem. Commun.* (21): 2177.

54 de Greef, M. and Breit, B. (2009). Self-assembled bidentate ligands for the nickel-catalyzed hydrocyanation of alkenes. *Angew. Chem. Int. Ed. Engl.* 48 (3): 551–554.

2

Self-Assembled Bidentate Ligands in Transition Metal Catalysis; From Fundamental Invention to Commercial Application

Alexander M. Kluwer[1], Xavier Caumes[1], and Joost N. H. Reek[1,2]

[1] *InCatT B.V., Science Park 904, Amsterdam, 1098 XH, The Netherlands*
[2] *University of Amsterdam, Van 't Hoff Institute for Molecular Sciences, Science Park 904, Amsterdam, 1098 XH, The Netherlands*

2.1 Introduction

From an industry point of view, there is a continuous demand for new catalysts. Different ligand parameters such as cone angle, the χ electronic parameter, and natural bite angle β_n have been developed to classify groups of ligands and providing a rationale for catalyst selection. Although these concepts have proven insightful, the development of new catalysts is often met with problems. Particularly, the fine chemical and pharmaceutical industry still faces challenges related to functional group tolerance, the desired chemo-, regio-, and enantioselectivity. In addition, the enantiomeric outcome of a reaction is often not predictable, requiring more efforts to identify the proper catalyst. The substrates to be investigated are typically decorated with various functional groups that can hinder the desired reaction, be converted under the reaction conditions, or poison the active catalyst. As a consequence, catalysts that show promising results on benchmark substrates often do not work on the actual substrate. Tackling all these hurdles is a time-consuming process which could easily require one year of research. Time to market is an important parameter for the development of catalysts for the fine chemical and pharmaceutical industry, adding relevance to protocols that lead to rapid catalyst finding. As a result of this market demand, combinatorial approaches and high-throughput experimentation (HTE) have become a dominant approach to catalyst finding [1]. To be successful, such approach relies on (i) the capacity to perform and analyze a large number of reactions in a controlled manner and in a short time and (ii) the size and the diversity of a catalyst library to cover a significant catalyst reactivity space. For the latter part, an easy starting point involves the screening of ligand libraries that are commercially available. However, if in such initial screening no catalysts are identified with the desired properties, the evaluation of new ligands is required. The rapid availability of new ligands is then the limiting factor in such scenario.

For many transformations, catalysts based on bidentate ligands outperform those based on monodentate ligands. However, in general, bidentate ligands are more

Supramolecular Catalysis: New Directions and Developments, First Edition.
Edited by Piet W.N.M. van Leeuwen and Matthieu Raynal.

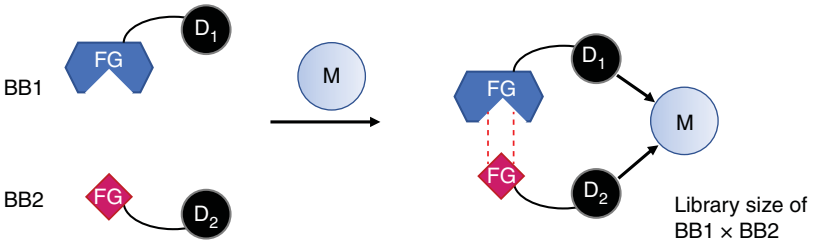

Figure 2.1 The concept of self-assembled supramolecular catalysts. The functional groups (FGs) are used to bring two ligand building blocks together by noncovalent interactions, and the donor atoms (D_1 and D_2) coordinate to the catalytically active metal (M).

tedious to prepare, especially hetero-bidentate ligands; i.e. ligands that have two different donor functionalities. As such, the preparation of libraries of bidentate ligands is very time-consuming and thus limiting the synthesis and screening protocols. In order to tackle this issue, we introduced [2], at about the same time as Breit [3] and Takacs et al. [4], the concept of supramolecular bidentate ligands, and we have developed this over the years to the extent that we now use this at InCatT B.V. at a commercial level. The idea behind supramolecular bidentate ligands is to use noncovalent interactions to self-assemble two monodentate ligands (BB1 and BB2 in Figure 2.1) into a bidentate ligand upon coordination with a metal center. The power of self-assembled bidentate ligands in the generation of new supramolecular catalysts is then twofold: (i) in general, monodentate ligands (and building blocks) are easier to prepare and (ii) the number of supramolecular bidentate ligands that can be formed by just mixing ligand building blocks grows exponentially with the number of ligand building blocks available and thus this approach is well suited to generate unprecedented large libraries of ligands. The self-assembly process can be based on hydrogen bonds, ionic interactions, or dynamic metal–ligand coordination. We have ourselves used mainly coordination chemistry and hydrogen bond motifs for our ligand designs.

The systems reported by other groups are discussed in the Introduction of this book or have been discussed in reviews that have been reported on this topic [5]. In this chapter, we will discuss how the ideas developed in our group from fundamental concept to commercially applicable systems.

2.2 Metal–Ligand Interactions, the SUPRAphos Library

We initially studied the concept of self-assembled bidentate ligands based on coordination chemistry, more specifically, pyridyl coordination to zinc(II) porphyrins as the binding motif. By simply mixing the building blocks in solution, chelating bidentate ligands are spontaneously formed by self-assembly of the complementary moieties (Figure 2.2).

The initial library, called SUPRAphos, consisted of 48 supramolecular bidentate ligands based on 14 building blocks. Six different phosphite-porphyrinato-zinc(II)

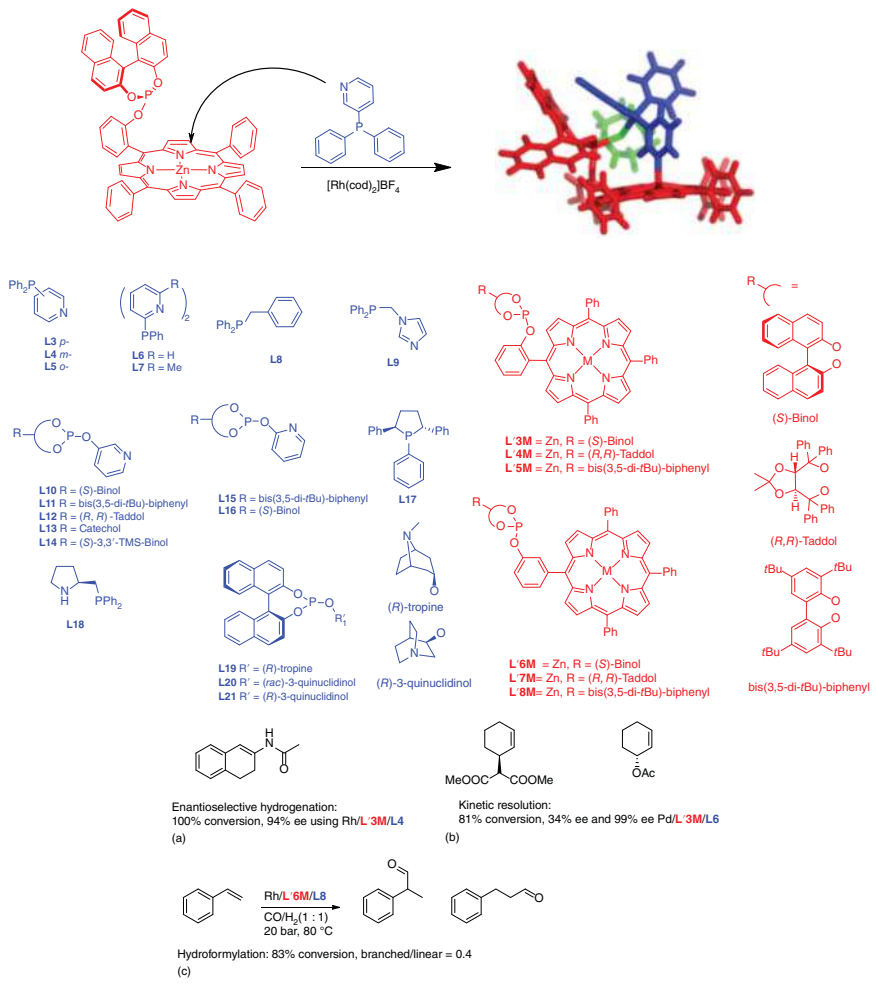

Figure 2.2 The self-assembly of bidentate ligands based on pyridyl coordination to phosphite-porphyrinato-zinc(II) compounds, leading to rhodium complexes that are suitable for hydroformylation and hydrogenation reactions (top). Displayed are some of the ligand building blocks that have been prepared (middle), and the application to (a) Rh-catalyzed asymmetric hydrogenation, (b) Pd-catalyzed kinetic resolution, and (c) Rh-catalyzed hydroformylation (bottom).

compounds were used in combination with eight nitrogen-donor-functionalized phosphine or phosphite ligands. As proof of principle, the supramolecular library was applied in palladium-catalyzed allylic alkylation [6]. The various supramolecular bidentate ligand systems gave rise to a large variety in enantioselective outcome (between 60% and 70% ee in favor of the *R*-enantiomer), providing support for the concept. The SUPRAphos library was further extended to a library of 20 by 20 matrix, implying 400 possible combinations based on 40 synthesized components. A part of this library (64 entries) was applied in the rhodium-catalyzed asymmetric hydrogenation of a challenging and industrially relevant cyclic enamide,

providing a catalyst that was the most selective catalyst at that date providing 94% enantioselectivity and outperforming traditional catalysts systems such as BIPHEP and BINAPHOS [7]. Part of the library was also successfully used in the palladium-catalyzed kinetic resolution of racemic cyclohexenyl acetate [8], and in the rhodium-catalyzed asymmetric hydroformylation of styrene [9] illustrating the versatility of this approach.

Even though commercially interesting enantioselectivities could be achieved with these supramolecular bidentate catalysts, the commercial application of these ligands was too expensive due to the difficult and non-scalable synthesis. Among the issues, the yields for the mono-phenolic porphyrin component were too low for commercial use (typically 5–8% after column chromatography).

2.3 Supramolecular Bidentate Ligands Based on Hydrogen Bonds, a Toolbox for Evolutionary Catalyst Design

A more scalable approach was realized in the supramolecular bidentate ligands based on hydrogen bonds. Although single-hydrogen bonds provide a binding energy around 3 kcal mol^{-1}, they are directional and binding energies can be increased by using an array of several hydrogen bonds. The directionality is important as orientation of the hydrogen bonds in space enhance the specificity and predictability of the assembly adding more control over the catalyst formation. The strength of a single-hydrogen bond is based on the nature of the donor and acceptor, but it also depends to a large extent on the solvent employed, meaning that catalysts based on these supramolecular bidentate ligands are more strongly solvent-dependent.

We developed and patented a new class of urea-based ligand building blocks (phosphines, chiral phosphites, and phosphoramidites), which, by self-assembly, form supramolecular bidentate ligands [10]. One main difference from the SUPRAphos library is that the both ligand building blocks contain the urea motif allowing access to both homo- and hetero-combinations, and thus extending the number of possible combinations. Urea-functionalized ligands are easily made within two to three steps synthesis by connecting three building blocks, i.e. the *ligand backbone*, *spacer*, and *urea motif*. The targeted synthons to build such ligands are sought to be either commercially available or easily accessible, which makes the approach modular and easy to build large and diverse ligand libraries. Most of these reactions are "click"-type reactions which have been performed on a Chemspeed Accelerator allowing parallel synthesis yielding 32 new ligand building blocks in a single day, highlighting the potential of this approach.

Assembly of two of such phosphine ligand building blocks allowed the formation of chelating structures in the presence of Pd and Rh complexes (Figure 2.3).

An introductory series of six structurally related ligands was explored in the asymmetric hydrogenation of prochiral substrates and high selectivities were observed (Figure 2.3) [10]. Importantly, small changes in the spacer unit between

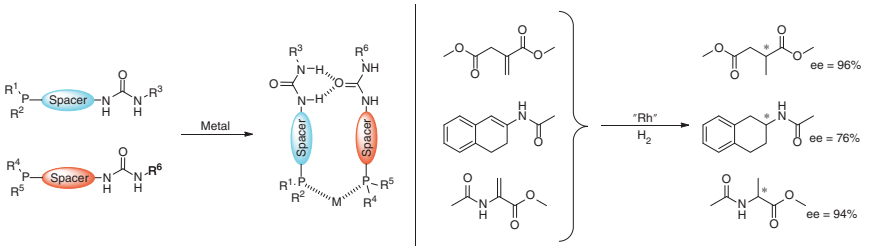

Figure 2.3 Self-assembly of UREAphos ligand systems (left) and application in asymmetric Rh-catalyzed hydrogenation of prochiral olefins (right).

the donor atom and the urea binding motif resulted in large variation in the catalytic performance of the related rhodium complex, making variation in the UREAphos structure relevant.

With the UREAphos library as toolbox, combined with optimized robotic parallel synthesis, we could develop a fast high-throughput screening and lead optimization protocol. To exemplify this, a library of urea-functionalized ligands was evaluated in an automated fashion using the 96-reactor plate of the Chemspeed Accelerator for HTE that can be used up to pressures of 100 bar and reaction temperatures between −80 and 150 °C (https://www.chemspeed.com/isynth-catscreen-96). The catalyst selection approach is based on an ***iterative elimination*** or ***evolutionary catalyst design procedure*** in which the initial screenings round evaluates a wide variety of catalysts systems that cover a very large catalytic reaction space (Figure 2.4). After analysis, a binary selection criterion (typically conversion and/or enantioselectivity) is applied on the obtained data set to identify potential new catalyst leads. These leads will be structurally refined in the second screenings round. For this, new ligand systems can be easily prepared in a parallel fashion by the modular synthetic approach providing the closely related "sibling" ligands. These new catalysts will then be evaluated in the second screenings round. This selection/elimination process is repeated until a tailor-made catalyst system can be devised that meets the required activity, selectivity criteria or performs under the pre-set reaction conditions (e.g. below 6 bar to be used in a multipurpose reactor). After having identified the best catalyst, the best reaction conditions are then evaluated in the AMTEC SPR16, a 16-parallel reactor system for which the pressure, temperature, and stirring rate can be programmed for every individual reactor. In addition, the gas-uptake curves are recorded providing the full kinetics and/or Design of Experiment (DoE) with up to eight parameters in a single overnight experiment. Further smart data processing provides more direct information regarding catalyst properties such as catalyst stability, substrate, and/or product inhibition. These tools, i.e. supramolecular bidentate catalysts, fast and efficient catalyst screening, and smart optimization procedures reduce the catalyst development times to just a number of weeks. Such screening service is highly demanded by the chemical industry to reduce the time to market.

To illustrate the evolutionary catalyst design performed at InCatT, the hydrogenation of a challenging substrate, 2,3,3-trimethyl-3*H*-indole was performed using

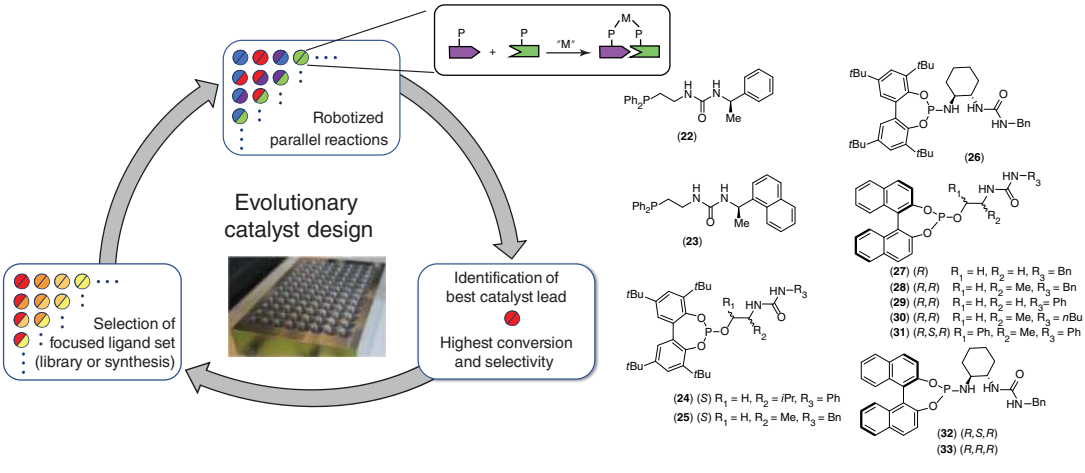

Figure 2.4 The high-throughput experimentation (HTE) and lead optimization by iterative elimination or evolutionary catalyst design procedure.

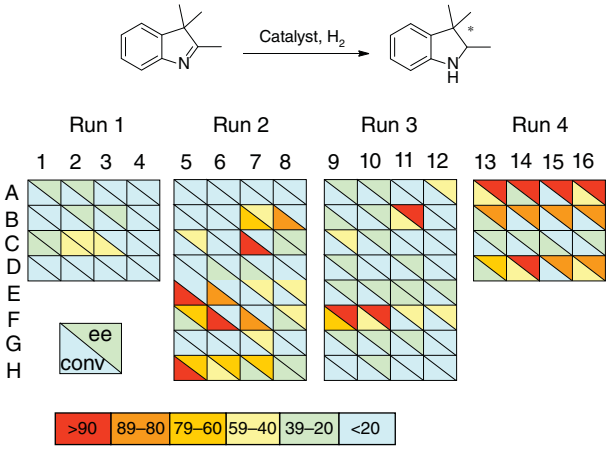

Figure 2.5 Results of the first four runs of the evolutionary catalyst design using the Chemspeed unit. Source: Kluwer et al. [11]. Reproduced with permission of John Wiley & Sons.

our ligand kit (see Figure 2.5 top) (https://www.strem.com/catalog/v/96-3740/33/ureaphos_and_metamorphos_ligand_kit_for_asymmetric_hydrogenation) [11]. In this case, the evolutionary catalyst design was performed in five rounds with a final library of 22 ligands used in 113 experiments and the results (conversion and ee) of the first four runs are shown in Figure 2.5 bottom.

The five runs proceeded as the following:

1. Sixteen ligand combinations to obtain the first lead
2. Thirty-two ligand combinations based on variation of the best results from the first lead along with metal precursor variation
3. Thirty-two homo- and hetero-combinations of the ligand family derivatives that gave the best results in run 2
4. Sixteen reactions with the best ligand combination with various additives and solvents
5. Seventeen reactions on the AMTEC unit to obtain the kinetics from the gas uptake of the reactions

Based on this screening, the best ligand combination was obtained together with kinetic data of the reaction for which the rate can be expressed as Eq. (2.1). Interestingly, the hydrogenation of the 2,3,3-trimethyl-3*H*-indole shows a second order in catalyst, a first order in hydrogen, and a zeroth order in substrate:

$$\text{Rate} = k_{\text{obs}} \cdot [\text{Catalyst}]^2 \cdot p\text{H}_2 \tag{2.1}$$

This example illustrates how high-throughput screening coupled with a supramolecular ligand library affords a fast access to a suitable catalyst for the conversion of a challenging substrate as only three runs were necessary to reach high enantioselectivity (>90%). Further experiments using gas-uptake measurement provide insight into the reaction mechanism to allow rational optimization of the reaction conditions that lead to full conversion with the highest reported enantioselectivity of 96% ee for this conversion.

2.4 Formation of Supramolecular Pincer-Type Complexes

The versatility of the urea binding motif allowed us to explore beyond the supramolecular bidentate ligands. We investigated the formation of supramolecular pincer-type complexes [12] using the participation of the urea in both ligand hydrogen bonding and the metal coordination. The urea functionalized ligand **34** possesses an acidic NH group bound via an alkyl spacer displaying a rich coordination chemistry. Depending on the metal–ligand stoichiometry and the nature of the metal precursor, P,N or P,O coordinating hemilabile bidentate ligand could be afforded by the participation of the urea motif. Complexes prepared from $[Rh(nbd)_2]BF_4$ also act as efficient catalysts for asymmetric hydrogenation reactions [12]. Interestingly, when two equivalents of ligand **34** were added to $[Rh(acac)(CO)_2]$, the ^{31}P NMR spectrum displayed an ABX pattern typical of complexes with two different phosphorus atoms coordinating to the rhodium center. Further analysis showed that the supramolecular pincer complex $[Rh(\mathbf{34})_2CO]$ with an additional hydrogen bond between the two ligands was formed (see Figure 2.6a). Although no catalysis was developed with this particular complex, it was recognized that omitting the spacer in the UREAphos ligands would provide more stable supramolecular pincer complexes.

The development of phosphinourea ligands [13], in which the spacer has been omitted from the UREAphos structure, thus directly connecting the phosphorus donor moiety to the urea group, provided well-defined stable rhodium pincer complexes such as $[Rh(\mathbf{35})_2CO]$ (Figure 2.6). The two phosphorus donor groups are in mutual trans positions after the tautomerization of the anionic ligand (see Figure 2.6b). The DFT optimized structures show that the coplanar positioning of the ligands with a NH···O distance of 1.973 Å confirms the presence of the intramolecular hydrogen bond. This complex was active in the hydroformylation of styrene yielding the branched aldehyde product with 95.6% selectivity. Mechanistic studies revealed that a ligand-assisted (cooperative) mechanism is operative in the hydrogen activation step of the hydroformylation reaction, implying an active role of this particular ligand system.

Moving from the urea to sulfonamide as binding motif, we reported and patented the METAMORPhos ligand family, a ligand that exists as a mixture of two tautomers ($N(H)–P^{III}$ and $N=P^{V}(H)$) in solution. Combining $[Rh(acac)(CO)_2]$ and ligand **36** resulted in the selective formation of a homocomplex composed of one neutral and one anionic version of **36**, as was observed by NMR and IR spectroscopy. After coordination of the ligand, the sulfonamide group is sufficiently acidic to protonate the acetylacetonate fragment (Figure 2.6c). Also, in this assembly, the P-ligands are in trans position and are held together by a single intramolecular hydrogen bond. In addition, in the presence of chiral phosphoramidite *R*-(**37**), which has a lower phosphorus basicity and only exists in the $N(H)P^{III}$ tautomer, exclusively form the heterocomplex [Rh(**37**,**36**)] [14]. Thus by the proper selection of the ligands, both the homo- and hetero-pincer complexes can be prepared by just mixing the ligands and the metal precursor. This again displays the power of the supramolecular

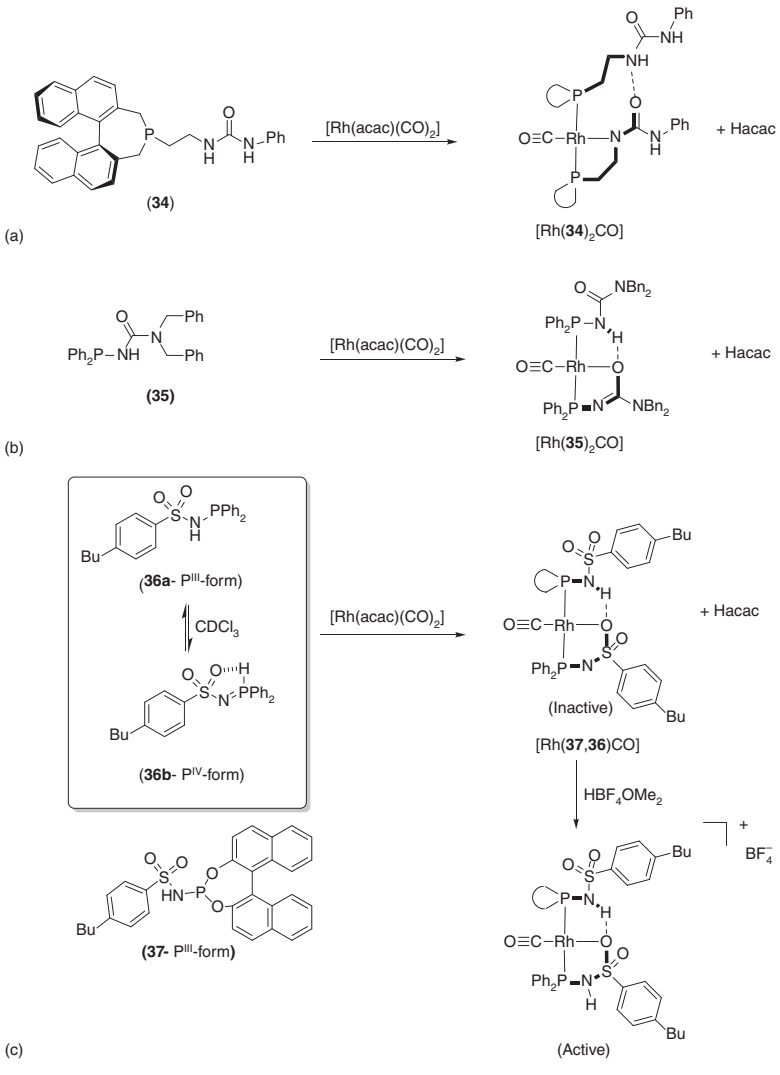

Figure 2.6 Formation of neutral supramolecular pincer complexes using (a) ureaphosphine ligand (**34**), (b) phosphinourea ligand (**35**), and METAMORPhos ligand (**36**). The neutral [Rh(**37**,**36**)] can be activated by addition of a strong acid (HBF_4) to produce the cationic [Rh(**37**)(**36-H**)]BF_4 complex.

approach giving access to a large potential pool of pincer complexes. It was found that initially homo- and heterocomplexes were not active in the asymmetric hydrogenation reaction but could be activated by the addition of a strong acid. Both heterocomplex [Rh(**37**,**36**)] and homocomplex [Rh(**36**)$_2$] displayed high levels of enantioselectivity in the hydrogenation of specific alanine precursors (up to 99% ee). Later it was found that ligand *R*-(**37**) forms dinuclear complexes that give unusual activity and selectivity in the asymmetric hydrogenation of tetrasubstituted cyclic enamides [15].

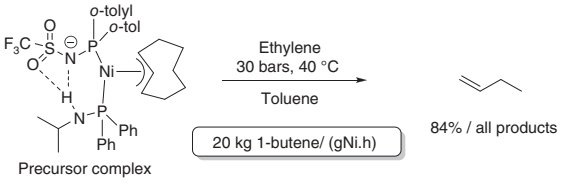

Figure 2.7 Highly active self-assembled nickel catalyst active in the ethylene dimerization reaction yielding 20 kg of 1-butene per gram nickel per hour. In the activated catalyst, the oxygen atom of the sulfonamide is proposed to be coordinating to the nickel during the catalysis forming a pincer complex.

Finally, to illustrate the potential of this family of ligands to form pincer-type complexes, it has been applied to the industrial-relevant nickel-catalyzed dimerization of ethylene (Figure 2.7). In the activated catalyst, the oxygen atom of the sulfonamide is proposed to be coordinating to the nickel during the catalysis [16]. In addition, the intramolecular hydrogen bond was essential for the complex stability. Importantly, this novel class of complexes provides highly active catalysts that display unprecedented selectivity (1-C4 > 99.0% in the C4 fraction).

2.5 From a Supramolecular Bidentate Ligand to a Catalyst with Substrate Pre-organization

Substrate pre-organization is an interesting strategy to drive the selectivity of a reaction toward the desired product (for details, see Chapter 12). In this approach, the substrate is forced to face the catalyst in a particular position through secondary noncovalent interaction. Among the potential interactions that can be used, hydrogen bonding is of particular interest for its ubiquity and directionality. In the course of the exploration of self-assembled hetero-bidentate ligands, we observed that substrate pre-organization can indeed occur in the frame of supramolecular bidentate catalysis. A small library of traditional monodentate and self-assembled bidentate catalyst systems were compared in hydrogenation of 3-hydroxy-2-methylpropionate (Roche ester) and several analogous substrates (Figure 2.8). The self-assembled bidentate ligand, formed through self-assembly between an urea-functionalized phosphine and the leucine-based phosphoramidite ligand, was found to be the most selective catalyst for this hydrogenation yielding 99% ee and outperformed the MonoPhos/PPh_3 combination, which produced the product in just 34% ee [17]. NMR and IR studies revealed the formation of a single-hydrogen bond between the –NH unit of the leucine-based phosphoramidite and the urea carbonyl group of the phosphine ligand; these results were corroborated by DFT calculations. Importantly, the characterization studies (IR and NMR spectroscopy) indicated exclusive formation of the hetero-bidentate supramolecular complex when the two monodentate ligands were mixed in a 1 : 1 ratio in the presence of a rhodium precursor such as $[Rh(cod)_2]BF_4$.

The central role of the substrate pre-organization by the self-assembled bidentate ligand was demonstrated by DFT and further experiments. The hydrogen bond

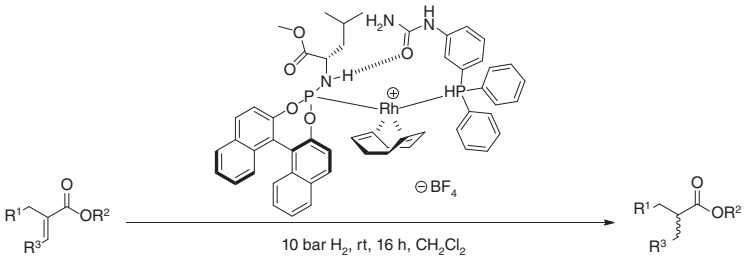

Substrate	R^1	R^2	R^3	Conversion (%)	ee (%)
S1	OH	Me	H	100	99
S2	OH	*t*Bu	H	100	99
S3	OH	Me	Ph	83	98(*S*)
S4	OMe	Me	Ph	67	25(*S*)

Figure 2.8 Formation of supramolecular bidentate complex in the presence of rhodium through a single-hydrogen bond between PN-H and the urea motif, and the results in asymmetric hydrogenation of Roche ester-type substrates.

between the ligand and the substrate is at the origin of high selectivity and steers the reaction toward the fastest and more selective pathway. This shows that catalysts based on supramolecular bidentate ligands may additionally profit from noncovalent interactions between the substrate and the catalyst, another benefit of including such strategies in combinatorial approaches and fast screening technologies.

2.6 Outlook

To know the current position of the technology and the future outlook, it is important to put the past achievements in a historical perspective. What is interesting is that at the time when the 1986 Nobel Prize was awarded to Donald Cram, Jean-Marie Lehn, and Charles Pederson for "their development and use of molecules with structure-specific interactions of high selectivities," the field of supramolecular catalysis was represented by just a handful of scientific papers. Although the supramolecular chemistry was well recognized, it required almost 10 years before the applications in catalysis became available. It is an observation that many interesting academic concepts, often inspired by examples provided by nature, come from the supramolecular chemistry community. However, application of supramolecular strategies to solve issues in transition metal catalysis, more often explored by scientist from the catalysis field, lead to inventions that are closer to application.

As an example, the field of supramolecular catalysis using self-assembled bidentate catalyst technology has matured over the past decade. New exciting developments are currently published by us and others that further enrich the toolbox for fast catalyst lead finding. The publication of a second edition of the

Supramolecular Catalysis book testifies to this. The ligand toolbox has been extended to cover a large variety of self-assembled bidentate ligands and also allows various modes of coordination to metal centers. In some of the designs, commercial aspects such as cost price, scalability, and durability are taken into account. The technology has now advanced that also more sophisticated ligand designs are being explored which include ligand cooperativity (in small molecule activation) and substrate pre-organization. These exciting developments highlight the potential of the supramolecular self-assembled ligand technology as promising solution to the demanding R&D timelines within the fine chemical and pharmaceutical industry.

References

1 Jäkel, C. and Paciello, R. (2006). High-throughput and parallel screening methods in asymmetric hydrogenation. *Chem. Rev.* 106: 2912–2942.

2 (a) Slagt, V.F., van Leeuwen, P.W.N.M., and Reek, J.N.H. (2003). Bidentate ligands formed by self-assembly. *Chem. Commun.*: 2474–2475. (b) Slagt, V.F., van Leeuwen, P.W.N.M., and Reek, J.N.H. (2003). Multicomponent porphyrin assemblies as functional bidentate phosphite ligands for regioselective rhodium-catalyzed hydroformylation. *Angew. Chem. Int. Ed.* 42: 5619–5623.

3 Breit, B. and Seiche, W. (2003). Hydrogen bonding as a construction element for bidentate donor ligands in homogeneous catalysis: regioselective hydroformylation of terminal alkenes. *J. Am. Chem. Soc.* 125: 6608–6609.

4 Takacs, J.M., Reddy, D.S., Moteki, S.A. et al. (2004). Asymmetric catalysis using self-assembled chiral bidentate P,P-ligands. *J. Am. Chem. Soc.* 126: 4494–4495.

5 Raynal, M., Ballester, P., Vidal-Ferran, A., and van Leeuwen, P.W.N.M. (2014). Supramolecular catalysis. Part 1: non-covalent interactions as a tool for building and modifying homogeneous catalysts. *Chem. Soc. Rev.* 43: 1660–1733.

6 Slagt, V.F., Röder, M., Kamer, P.C.J. et al. (2004). Supraphos: a supramolecular strategy to prepare bidentate ligands. *J. Am. Chem. Soc.* 126: 4056–4057.

7 Jiang, X.-B., Lefort, L., Goudriaan, P.E. et al. (2006). Screening of a supramolecular catalyst library in the search for selective catalysts for the asymmetric hydrogenation of a difficult enamide substrate. *Angew. Chem. Int. Ed. Engl.* 45: 1223–1227.

8 Jiang, X.-B., van Leeuwen, P.W.N.M., and Reek, J.N.H. (2007). SUPRAphos-based palladium catalysts for the kinetic resolution of racemic cyclohexenyl acetate. *Chem. Commun.*: 2287–2289.

9 Goudriaan, P.E., Jiang, X.-B., Kuil, M. et al. (2008). Synthesis of building blocks for the development of the SUPRAPhos ligand library and examples of their application in catalysis. *Eur. J. Org. Chem.*: 6079–6092.

10 (a) Sandee, A.J., van der Burg, A.M., and Reek, J.N.H. (2007). UREAphos: supramolecular bidentate ligands for asymmetric hydrogenation. *Chem. Commun.* 2: 864–866. (b) Sandee, A.J., Van Der Burg, A.M., and Reek, J.N.H (2006). Process for the production of phosphorous compounds. US7790923B2, filed 26 January 2007 and issued 7 September 2010. (c) Reek, J.N.H., Chen R., Kamer,

P.C.J., Slagt, V.F., and van Leeuwen, P.W.N.M. (2003). Coordination complex system comprising building blocks. US8216968B2, filed 24 May 2004 and issued 10 July 2012.

11 Kluwer, A.M., Detz, R.J., Abiri, Z. et al. (2012). Evolutionary catalyst screening: iridium-catalyzed imine hydrogenation. *Adv. Synth. Catal.* 354: 89–95.

12 Meeuwissen, J., Detz, R.J., Sandee, A.J. et al. (2010). Rhodium-P,O-bidentate coordinated ureaphosphine ligands for asymmetric hydrogenation reactions. *Dalton Trans.* 39: 1929–1931.

13 Meeuwissen, J., Sandee, A.J., de Bruin, B. et al. (2010). Phosphinoureas: cooperative ligands in rhodium-catalyzed hydroformylation? On the possibility of a ligand-assisted reductive elimination of the aldehyde. *Organometallics* 29: 2413–2421.

14 (a) Patureau, F.W., Kuil, M., Sandee, A.J., and Reek, J.N.H. (2008). METAMORPhos: adaptive supramolecular ligands and their mechanistic consequences for asymmetric hydrogenation. *Angew. Chem. Int. Ed.* 47: 3180–3183; (b) Sandee A.J., Van Der Burg A.M., and Reek, J.N.H. (2007). Coordination complex system comprising tautomeric ligands. WO2007086745A1, filed 26 January 2007 and issued 2 August 2007.

15 Patureau, F.W., de Boer, S., Kuil, M. et al. (2009). Sulfonamido-phosphoramidite ligands in cooperative dinuclear hydrogenation catalysis. *J. Am. Chem. Soc.* 131: 6683–6685.

16 Boulens, P., Pellier, E., Jeanneau, E. et al. (2015). Self-assembled organometallic nickel complexes as catalysts for selective dimerization of ethylene into 1-butene. *Organometallics* 34: 1139–1142.

17 Breuil, P.A.R., Patureau, F.W., and Reek, J.N.H. (2009). Singly hydrogen bonded supramolecular ligands for highly selective rhodium-catalyzed hydrogenation reactions. *Angew. Chem. Int. Ed.* 48: 2162–2165.

Part II

Self-Assembled Nanostructures and Multi-component Assemblies

3

Assembled Ionic Molecular Catalysts and Ligands

Kohsuke Ohmatsu, Daisuke Uraguchi, and Takashi Ooi

Nagoya University, Institute of Transformative Bio-Molecules (WPI-ITbM), Department of Molecular and Macromolecular Chemistry, Graduate School of Engineering, Furo-cho, Chikusa, Nagoya 464-8601, Japan

3.1 Introduction

Chiral ionic organic molecules have long been utilized as catalysts for asymmetric transformations because a majority of chemical reactions involve the generation of at least one discrete, ionic intermediate as a reactive species [1–4]. The negatively charged, anionic intermediates are necessarily accompanied by a positively charged, cationic species. Therefore, when this cation is chiral, the subsequent bond formation from the pairing anion can, in principle, proceed in an enantioselective manner [5–8]. The precise control of the bond-forming reactions that proceed via cationic intermediates can also be realized using anionic chiral molecules [9–11]. These strategies rely on the inherent effectiveness of ion-pairing for the construction of well-organized chiral molecular assemblies in the transition states and have been exploited in making great strides in the field of asymmetric catalysis.

Dating back to 1926, the concept of ion pair was introduced by Bjerrum to account for the behavior of ionophores in solvents with low permittivity [12]. Ion-pairing describes the association of oppositely charged ions, which are held together by Coulombic forces and stay longer than the time required for Brownian motion to separate noninteracting species. In addition, the association energy of ion pair with electrostatic attraction is larger than the thermal energy available to separate the individual ions. An ion pair with a common solvation shell and no solvent molecules between two ions is called a contact ion pair, of which formation is favorable in nonpolar solvents of low dielectric constant (Figure 3.1a). In a more polar environment, the ions are separated by a shared solvation shell, or each ion has its own solvation shell. These types of ion pairs are called solvent-shared and solvent-separated ion pair, respectively [13, 14].

Taking into consideration the intrinsic nature and behavior of ion pairs in a solution, we have devised two types of ionic supramolecular catalysts. One is a supramolecular chiral ligand, which is a contact ion pair consisting of ammonium–phosphine hybrid ligand and chiral anion, namely ion-paired chiral

Supramolecular Catalysis: New Directions and Developments, First Edition.
Edited by Piet W.N.M. van Leeuwen and Matthieu Raynal.

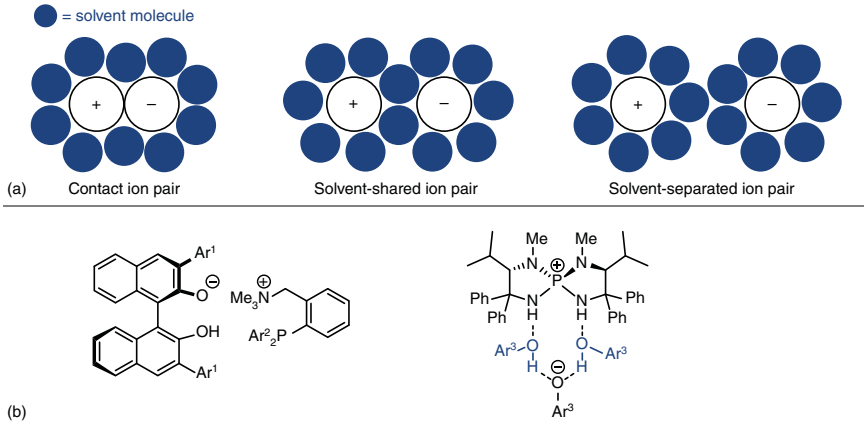

Figure 3.1 Assembled ionic molecules. (a) Different types of ion pairs. (b) Structure of ion-paired chiral ligand and assembled ion-pair catalyst generated from chiral *P*-spiro triaminoiminophosphorane and aryl hydroxides.

ligand (Figure 3.1b). Another is a higher order supramolecular catalyst like solvent-shared ion pair, which is formed from chiral *P*-spiro triaminoiminophosphorane and defined equivalents of aryl hydroxides. While the partition of cation and anion by the polar solvent is usually detrimental to the interaction of two ions, the use of appropriate polar molecules with control of stoichiometry as well as the utilization of hydrogen-bonding network enables the formation of well-defined chiral molecular assemblies that exert preeminent catalytic activity and stereocontrolling ability. In this chapter, we focus on the selected examples of these approaches toward the design of ion-paired chiral ligands and supramolecular ion-pair catalysts.

3.2 Concept of Ion-Paired Chiral Ligand

One of the keys for the development of transition-metal-catalyzed asymmetric transformations is the design of chiral ligands [15]. Conventional chiral ligands rely on the use of covalently constructed, single chiral molecules embedded with coordinative functional groups [16]. Their syntheses from each single chiral molecule often require a multi-step operation and can be complicated. For instance, the synthesis of chiral phosphines is labor-intensive because phosphorus atoms are readily oxidized during the ligand preparation. Our strategy for the design of new supramolecular chiral ligand was to divide the chiral ligand into two components, which were achiral phosphine ligand and simple chiral molecules, and to associate these components through the electrostatic interaction. We termed this type of supramolecular ionic ligands as ion-paired chiral ligands [17]. This ligand-design strategy has several advantages over the existing counterparts. For example, the synthesis of each small component is in principle much easier than that of conventional chiral ligands, and the diverse combinations of ligand components allow for facile and rapid

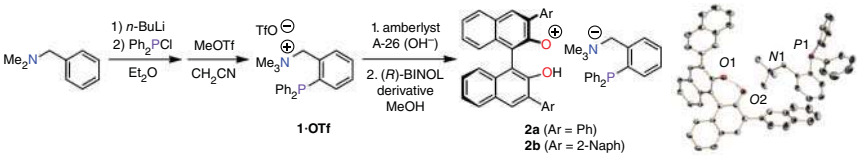

Figure 3.2 Preparation of ion-paired chiral ligands **2a** and its ORTEP diagram.

access to large libraries. In addition, steric and electronic properties of the ligands can be tuned easily by changing and modifying ligand components.

3.2.1 Design and Synthesis of Ion-Paired Chiral Ligand

As an achiral component of ion-paired chiral ligand, we designed *ortho*-diphenylphosphinobenzyl-ammonium ion **1**, termed ammonium–phosphine, because it can be readily synthesized from commercially available *N*,*N*-dimethylbenzylamine in a two-step sequence and the coordinative phosphine functionality of **1** is arranged in close proximity to the quaternary ammonium ion (Figure 3.2). The ion-paired chiral ligand **2a**, possessing (*R*)-3,3′-diarylbinaphtholate ion, was prepared through the anion exchange of ammonium triflate **1·OTf** into the corresponding hydroxide **1·OH** and the subsequent neutralization with the requisite 1,1′-bi-2-naphthol (BINOL) derivative. The X-ray diffraction analysis of **2a** confirmed that chiral binaphtholate ion was located close to the ammonium ion. In addition, the diphenyl substituents on the phosphorus center were oriented to the opposite direction from ammonium moiety probably to minimize steric repulsion, and thus the lone pair on phosphorus atom was disposed toward the ion-pairing site.

3.2.2 Application of Ion-Paired Chiral Ligand for Palladium-Catalyzed Asymmetric Allylations

The ability of **2a** as a chiral ligand was evaluated through its application to the palladium-catalyzed enantioselective allylation of α-nitrocarboxylates [18]. Since stereochemical control in the attack of a prochiral nucleophile on a π-allyl metal complex by a chiral ligand on the metal center constitutes a general challenge [19], this type of transformation is considered as a proper touchstone for the investigation of the potential of new ligands. The reaction of *tert*-butyl 2-nitropropionate with cinnamyl methyl carbonate in toluene under the influence of the catalyst generated *in situ* from $Pd_2(dba)_3$ and **2a** proceeded smoothly to give the allylated product in 78% yield with 68% ee (Figure 3.3). In contrast, no asymmetric induction was detected in the reactions using ligand **3** with a *meta*-diphenylphosphinobenzylammonium ion and ligand **4** having one carbon-elongated ammonium moiety. These results clearly indicated the critical importance of the orientational precision and spatial arrangement of the phosphine functionality and the ammonium ion moiety of **2** for exerting stereocontrolling ability. The best ligand for this allylation was ion-paired ligand **2b** possessing *para*-chlorophenyl group on phosphorus and additional phenyl substituent on the benzene linkage of the phosphinobenzylammonium ion,

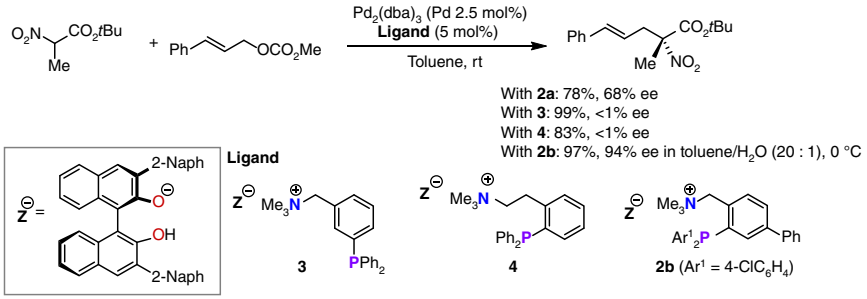

Figure 3.3 Evaluation of ion-paired chiral ligands in palladium-catalyzed asymmetric allylation of α-nitrocarboxylates.

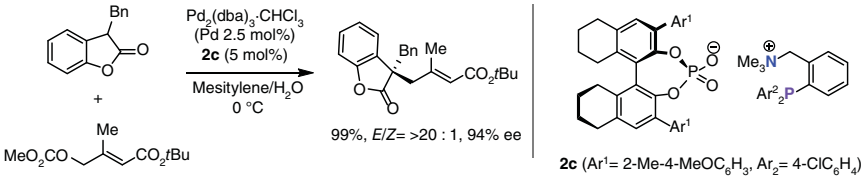

Figure 3.4 Asymmetric allylation of benzofuranone with 1,2-disubstituted allylic carbonate.

which allowed the formation of the product with 94% ee under optimized reaction conditions. Mechanistic investigations mainly based on kinetic experiments suggested that a palladium(II) complex bearing two ion-paired ligands **2b** on the palladium center acted as a reactive species in the bond-forming event.

The vast potential of ion-paired chiral ligands was further demonstrated through the realization of difficult-to-control asymmetric allylations by fully exploiting a multitude of combinations of ammonium-phosphines and readily accessible chiral anions. The use of appropriate chiral ligand **2c** comprising a BINOL-derived chiral phosphate ion enabled an unprecedented highly *E*-selective and enantioselective allylation of 3-substituted benzofuran-2(3*H*)-ones with 1,2-disubstituted allylic carbonates (Figure 3.4) [20, 21]. The origin of the high *E*-selectivity could be ascribed to the ability of **2c** to control either the distribution of syn and anti π-allyl palladium complexes or the relative rate of their bond formations.

3.2.3 *In situ* Generation of Ion-Paired Chiral Ligands and Their Combinatorial Screening

Supramolecular chiral ligands and catalysts allow the expeditious construction of structurally diverse and meaningful catalyst libraries as well as the rapid identification of the best one via combinatorial screening [22, 23]. In order to apply the ion-paired chiral ligand into combinatorial strategies, we established a method for the *in situ* generation of ion-paired chiral ligands from hydrogen sulfate salts of ammonium–phosphines and chiral Brønsted acids under phase-transfer conditions. This method was effectively utilized for the iterative deconvolution screening of ion-paired chiral ligands. After only 16 experiments, the best of 144 ligands could

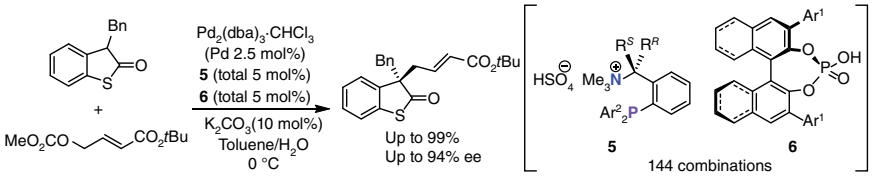

Figure 3.5 Iterative deconvolution screening for asymmetric allylation of benzylbenzothiophenone.

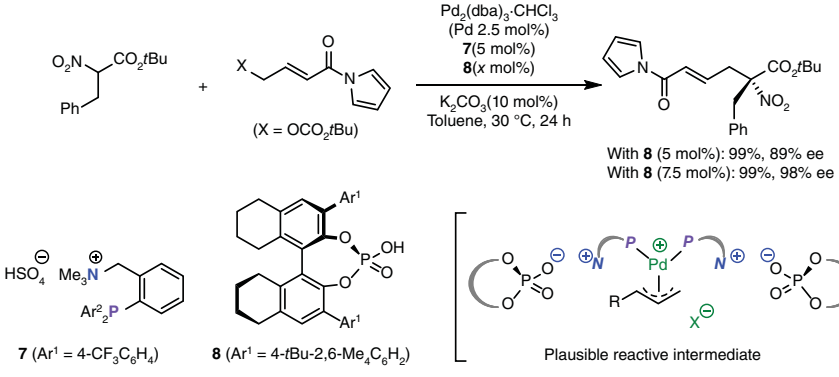

Figure 3.6 Selectivity enhancement by altering the ratio of components of ion-paired chiral ligand.

be identified to achieve the highly enantioselective allylation of benzothiophenones (Figure 3.5) [24].

The *in situ* generation of ion-paired chiral ligands provided an opportunity to develop another methodology for expanding the diversity of the corresponding supramolecular palladium complexes. When we consider the structure of the plausible intermediates in the asymmetric allylations, i.e. supramolecular complexes consisting of cationic π-allyl palladium(II) and ammonium–phosphine in a ratio of 1 : 2, up to 3 equiv of chiral anions could participate in this assembly. Therefore, the change of the ratio between ammonium–phosphine and chiral Brønsted acid could lead to the creation of different three-dimensional catalyst structures and reaction environments. Indeed, in the asymmetric allylation of α-nitrocarboxylates with functionalized allylic carbonates, the supramolecular palladium complex generated from palladium metal, hydrogen sulfate salt of ammonium–phosphine **7**, and chiral phosphoric acid **8** in a ratio of 1 : 2 : 3 exerted higher stereocontrolling ability than the 1 : 2 : 2 complex (Figure 3.6) [25].

3.3 Hydrogen-Bond-Assisted Ion-Pairing for Supramolecule Formation

Since the nature of the attractive force between a cation and an anion is electrostatic and thus nondirectional interaction, the structure of an ion pair in solution is

highly ambiguous and difficult to understand. Combination of a hydrogen bond and an ionic interaction alters the situation, and cooperative operation of the two interactions renders the ion pair discrete. A supramolecule constructed through ionic interaction and hydrogen bond is an intriguing motif for demonstrating a power of the cooperative function of the two interactions, and a variety of structurally defined supramolecules has been developed with diverse interests [26, 27]. In view of the relevance of the cooperative interaction to control the structure of ionic transition states in organic molecular catalysis, application of such supramolecules as catalysts would provide a unique opportunity for simultaneously regulating the structure of the catalyst and the transition state, yet hydrogen-bond-assisted ionic supramolecular catalysis has remained scarce.

3.3.1 Discovery of Supramolecular Ion-Pair Catalysis

As a part of our study on the cooperative catalysis of the *P*-spirocyclic chiral tetraaminophosphonium ion and the pairing organic anion [28], we attempted the preparation of a simple phenoxide salt of L-valine-derived tetraaminophosphonium ion. However, we serendipitously isolated a supramolecular ion pair consisting of the tetraaminophosphonium ion, phenoxide, and two phenols (**9a**·$(HOPh)_3$), and its molecular structure was unambiguously determined by X-ray diffraction analysis (Figure 3.7) [29]. The two phenol molecules were captured between the aminophosphonium and phenoxide ions to form a 10-membered cyclic hydrogen-bonding network. Given the inherent ability of the tetraaminophosphonium ion as a hydrogen-bond donor to organize cyclic transition-state structure for stereoselective bond-forming reactions [30–32], this salient feature of the aminophosphonium ion **9a**·H is also crucial for constructing the supramolecular ion pair. We anticipated that if **9a**·$(HOPh)_3$ could behave as an organic base, the anion generated from a substrate could replace the phenoxide to form another supramolecular assembly that participates in the transition state of a stereo-determining bond-forming event of the target reaction. As a reaction platform suitable for assessing the validity of this hypothesis, we selected the Michael addition of 2-unsubstituted azlactone to α,β-unsaturated acylbenzotriazole, in consideration of the structural similarity of the azlactone enolate to phenoxide, and examined the performance of **9a**·$(HOPh)_3$ as a catalyst (Figure 3.8) [29]. As expected, **9a**·$(HOPh)_3$ effectively promoted the reaction and afforded the desired Michael adduct in quantitative yield with 60% ee. Although the corresponding conjugate base, iminophosphorane **9a**, acted as a similarly competent base catalyst without the intervention of phenols, a significant

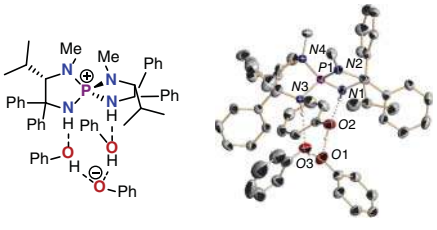

Figure 3.7 Three-dimensional structure of **9a**·$(HOPh)_3$.

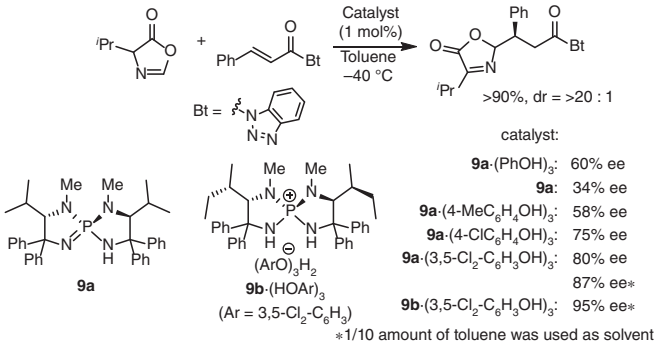

Figure 3.8 Michael addition of 2-unsubstituted azlactone to α,β-unsaturated acylbenzotriazoles under catalysis of **9**·$(HOAr)_3$. Relative stereochemistry is neither mentioned in text nor shown in the structure. (Not important in the final product, not shown.)

decrease in enantioselectivity was observed (34% ee). This observation clearly indicated that the presence of phenol affected the stereochemical outcome, which implies the unusual involvement of phenol molecules in the transition state. To confirm this possibility, we evaluated the effect of the structure of phenols and catalyst/substrate concentration on the selectivity profile. While the addition of 4-methylphenol had little influence on the enantiomeric excess of the product, the use of chlorinated phenols led to notable improvement, and 3,5-dichlorophenol was found to be an optimal catalyst component. In addition, increase in the catalyst loading or decrease in the amount of solvent, which is expected to shift the equilibrium to the supramolecular formation, also enhanced enantioselectivity. These results support the fact that the supramolecular ion pair itself functions as an active catalyst. Furthermore, the structure of the cationic component of the catalyst was revealed to be relevant to enantiocontrol, and L-isoleucine-derived aminophosphonium ion **9b**·H was particularly effective for this transformation to proceed with high stereoselectivity. Consequently, all the structural components of the supramolecular ion-pair catalyst play pivotal roles for the rigorous dictation of the stereochemical outcome of the Michael reaction.

To gain further insight into the structure of the supramolecular ion-pair catalyst in solution, we performed titration analysis using low temperature ^{31}P NMR, which revealed stepwise yet discrete formation of three different ion-pair assemblies [33]. Namely, the addition of 3,5-dichlorophenol to the L-valine-derived iminophosphorane **9a** resulted in the sequential generation of **9a**·$(HOAr)_1$, **9a**·$(HOAr)_2$, and **9a**·$(HOAr)_3$ (Ar = 3,5-$Cl_2C_6H_3$) in sharp response to the stoichiometry of added 3,5-dichlorophenol. Furthermore, each ion pair could be isolated as single crystals suitable for X-ray diffraction analysis, allowing unequivocal structural determination (Figure 3.9). More importantly, each ion pair was able to catalyze the Michael addition of 2-unsubstituted azlactone to α,β-unsaturated acylbenzotriazoles, and the observed enantioselectivity was correlated with the degree of the ion-pair assembly.

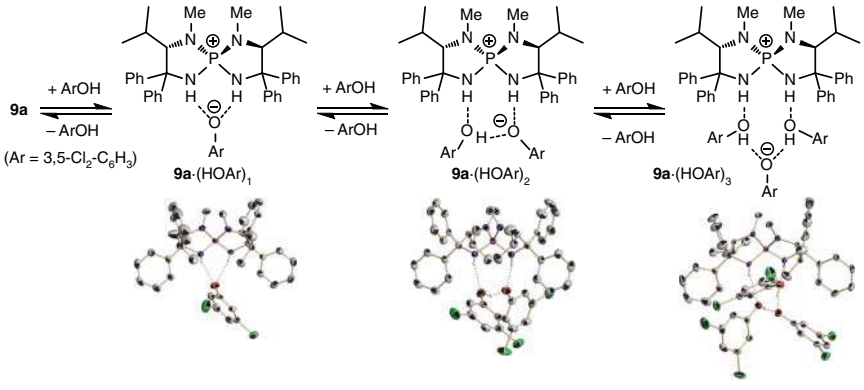

Figure 3.9 Stepwise formation of **9a**·$(HOAr)_x$ (Ar = 3,5-$Cl_2C_6H_3$).

3.3.2 Supramolecular Ion-Pair Catalysis for Michael Addition of 2-Unsubstituted Azlactone to Nitroolefins

The degree of assembly was also affected by the polarity of solvent. Low-temperature ^{31}P NMR titration study in tetrahydrofuran (THF) uncovered selective formation of the 1 : 2 assembly between the iminophosphorane **9a** and 3,5-dichlorophenol (**9a**·$(HOAr)_2$) even in the presence of an excess amount of the phenol, unlike the outcome of the analysis in toluene [34]. By taking advantage of this phenomenon, an enantioselective Michael addition of 2-unsubstituted azlactone to nitroolefins was realized under the supramolecular ion-pair catalysis enabled by **9** and 3,5-dichlorophenol (Figure 3.10). Because of the acidic nature of the product, the Michael addition to nitroolefins is prone to compete with oligomerization of the intermediary nitronate. Therefore, rapid *in situ* protonation of the nitronate is essential for suppressing the undesired oligomerization process. However, the presence of an excess amount of the phenol as a proton source was detrimental to enantiocontrol in toluene owing to the intervention of the less selective, **9**·$(HOAr)_3$-type catalyst. In contrast, by employing THF as solvent, the Michael adduct was obtained quantitatively without detectable formation of oligomeric products under the catalysis of **9b**·$(HOAr)_3$ probably because of the

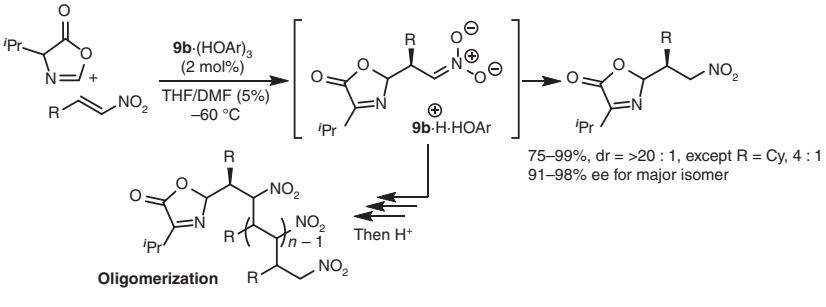

Figure 3.10 Michael addition of 2-unsubstituted azlactone to nitroolefins under catalysis of **9b**·$(HOAr)_3$ (Ar = 3,5-$Cl_2C_6H_3$).

preferable generation of more selective **9b**·$(HOAr)_2$-type assembly and the liberated 3,5-dichlorophenol contributed to the efficient protonation. Finally, slight tuning of the solvent polarity by the addition of 5% of *N*,*N*-dimethylformamide (DMF) delivered further improvement in enantioselectivity, allowing the establishment of the optimal conditions, which were applicable to the reactions with a range of nitroolefins and an excellent level of enantioselectivity was uniformly attained. These observations demonstrated that the polarity-controlled mode of assembly was of critical importance for selectively facilitating this asymmetric Michael reaction.

3.4 Conclusion

While we have developed assembled chiral ionic ligands and catalysts, the design of supramolecular chiral catalysts based on the judicious exploitation of ion-pairing is still in its infancy and there remains much room for further development. First, the search for other ionic molecular catalysts or ligands suitable for creating catalytically competent chiral supramolecules is an important task. Second, the supramolecular chiral catalysts and ligands developed so far have been applied only to the limited asymmetric transformations, such as asymmetric Michael addition and palladium-catalyzed allylic alkylation. Therefore, challenges toward the development of different types of asymmetric bond-forming reactions are essential to expand the frontiers of ionic supramolecular catalysis.

References

1 Macchioni, A. (2005). Ion pairing in transition-metal organometallic chemistry. *Chem. Rev.* 105: 2039–2073.
2 Lacour, J. and Moraleda, D. (2009). Chiral anion-mediated asymmetric ion pairing chemistry. *Chem. Commun.* 45: 7073–7089.
3 Brière, J.-F., Oudeyer, S., Dalla, V., and Levacher, V. (2012). Recent advances in cooperative ion pairing in asymmetric organocatalysis. *Chem. Soc. Rev.* 41: 1696–1707.
4 Brak, K. and Jacobsen, E.N. (2013). Asymmetric ion-pairing catalysis. *Angew. Chem. Int. Ed.* 52: 534–561.
5 Ooi, T. and Maruoka, K. (2007). Recent advances in asymmetric phase-transfer catalysis. *Angew. Chem. Int. Ed.* 46: 4222–4266.
6 Shirakawa, S. and Maruoka, K. (2013). Recent developments in asymmetric phase-transfer reactions. *Angew. Chem. Int. Ed.* 52: 4312–4348.
7 Liu, S., Kumatabara, Y., and Shirakawa, S. (2016). Chiral quaternary phosphonium salts as phase-transfer catalysts for environmentally benign asymmetric transformations. *Green Chem.* 18: 331–341.
8 Patel, N., Sood, R., and Bharatam, P.V. (2018). NL_2^+ systems as new-generation phase-transfer catalysts. *Chem. Rev.* 118: 8770–8785.

9 Lacour, J. and Hebbe-Viton, V. (2003). Recent developments in chiral anion mediated asymmetric chemistry. *Chem. Soc. Rev.* 32: 373–382.

10 Mahlau, M. and List, B. (2013). Asymmetric counteranion-directed catalysis: Concept, definition, and applications. *Angew. Chem. Int. Ed.* 52: 518–533.

11 Parmar, D., Sugiono, E., Raja, S., and Rueping, M. (2014). Complete field guide to asymmetric BINOL-phosphate derived Brønsted acid and metal catalysis: history and classification by mode of activation; Brønsted acidity, hydrogen bonding, ion pairing, and metal phosphates. *Chem. Rev.* 114: 9047–9153.

12 Bjerrum, N. (1926). Influence of ionic association on the activity of ions at moderate degrees of association. *K. Dan. Videnskab. Selsk. Mat. Fys. Medd.* 7: 1–48.

13 Winstein, S., Clippinger, E., Fainberg, A.H., and Robinson, G.C. (1954). Salt effects and ion-pairs in solvolysis. *J. Am. Chem. Soc.* 76: 2597–2598.

14 Sadek, H. and Fuoss, R.M. (1954). Electrolyte-solvent interaction. IV. Tetrabutylammonium bromide in methanol-carbon tetrachloride and methanol-heptane mixtures. *J. Am. Chem. Soc.* 76: 5897–5901.

15 Jacobsen, E.N., Pfaltz, A., and Yamamoto, H. (eds.) (1999, 2004). *Comprehensive Asymmetric Catalysis (Supplements 1 and 2)*. Springer.

16 Yoon, T.P. and Jacobsen, E.N. (2003). Privileged chiral catalysts. *Science* 299: 1691–1693.

17 Ohmatsu, K., Ito, M., Kunieda, T., and Ooi, T. (2012). Ion-paired chiral ligands for asymmetric palladium catalysis. *Nat. Chem.* 4: 473–477.

18 Sawamura, M., Nakayama, Y., Tang, W.-M., and Ito, Y. (1996). Enantioselective allylation of nitro group-stabilized carbanions catalyzed by chiral crown ether phosphine–palladium complexes. *J. Org. Chem.* 61: 9090–9096.

19 Lu, Z. and Ma, S. (2008). Metal-catalyzed enantioselective allylation in asymmetric synthesis. *Angew. Chem. Int. Ed.* 47: 258–297.

20 Ohmatsu, K., Ito, M., and Ooi, T. (2014). Ligand-controlled *E/Z* selectivity and enantioselectivity in palladium-catalyzed allylation of benzofuranones with 1,2-disubstituted allylic carbonates. *Chem. Commun.* 50: 4554-–4557.

21 Ohmatsu, K., Ito, M., Kunieda, T., and Ooi, T. (2013). Exploiting the modularity of ion-paired chiral ligands for palladium-catalyzed enantioselective allylation of benzofuran-2(3*H*)-ones. *J. Am. Chem. Soc.* 135: 590–593.

22 Wieland, J. and Breit, B. (2010). A combinatorial approach to the identification of self-assembled ligands for rhodium-catalysed asymmetric hydrogenation. *Nat. Chem.* 2: 832–837.

23 Dydio, P., Rubay, C., Gadzikwa, T. et al. (2011). "Cofactor"-controlled enantioselective catalysis. *J. Am. Chem. Soc.* 133: 17176–17179.

24 Ohmatsu, K., Hara, Y., and Ooi, T. (2014). *In situ* generation of ion-paired chiral ligands: rapid identification of the optimal ligand for palladium-catalyzed asymmetric allylation. *Chem. Sci.* 5: 3645–3650.

25 Ohmatsu, K., Hara, Y., Kusano, Y., and Ooi, T. (2016). Anion-stoichiometry-dependent selectivity enhancement in ion-paired chiral ligand–palladium complex catalyzed enantioselective allylic alkylation. *Synlett* 27: 1047–1050.

26 Rehm, T.H. and Schmuck, C. (2010). Ion-pair induced self-assembly in aqueous solvents. *Chem. Soc. Rev.* 39: 3597–3611.

27 He, Q., Vargas-Zúñiga, G.I., Kim, S.H. et al. (2019). Macrocycles as ion pair receptors. *Chem. Rev.* 119: 9753–9835.

28 Uraguchi, D., Ueki, Y., and Ooi, T. (2008). Chiral tetraaminophosphonium carboxylate-catalyzed direct Mannich-type reaction. *J. Am. Chem. Soc.* 130: 14088–14089.

29 Uraguchi, D., Ueki, Y., and Ooi, T. (2009). Chiral organic ion pair catalysts assembled through a hydrogen-bonding network. *Science* 326: 120–123.

30 Yamanaka, M., Sakata, K., Yoshioka, K. et al. (2017). Origin of high regio-, diastereo-, and enantioselectivities in 1,6-addition of azlactones to dienyl *N*-acylpyrroles: a computational study. *J. Org. Chem.* 82: 541–548.

31 Uraguchi, D., Yoshioka, K., and Ooi, T. (2017). Complete diastereodivergence in asymmetric 1,6-addition reactions enabled by minimal modification of a chiral catalyst. *Nat. Commun.* 8: 14793.

32 Uraguchi, D., Yamada, K., Sato, M., and Ooi, T. (2018). Catalyst-directed guidance of sulfur-substituted enediolates to stereoselective carbon–carbon bond formation with aldehydes. *J. Am. Chem. Soc.* 2018, 140: 5110–5117.

33 Uraguchi, D., Ueki, Y., and Ooi, T. (2011). Controlled assembly of chiral tetraaminophosphonium aryloxide–arylhydroxide(s) in solution. *Angew. Chem. Int. Ed.* 50: 3681–3683.

34 Uraguchi, D., Ueki, Y., and Ooi, T. (2012). Highly stereoselective catalytic conjugate addition of acyl anion equivalent to nitroolefins. *Chem. Sci.* 3: 842–845.

4

Self-amplification of Enantioselectivity in Asymmetric Catalysis by Supramolecular Recognition and Stereodynamics

Oliver Trapp

Ludwig Maximilian University Munich, Department of Chemistry, Butenandtstr. 5-13, 81377, Munich, Germany

4.1 Introduction

Already the Greek philosopher Aristotle had recognized that the whole is more than the sum of its parts and thus synergies result from the interaction. Such a synergy can be realized by supramolecular chemistry on the molecular level and provides completely new perspectives that would not emerge from a simple linear transfer of chemical properties. This becomes especially obvious when one proceeds to the next level apart from the question of the origin of life and asks the question of the origin of homochirality, which plays an important role in the framework of biochemical processes. This is accompanied by a spontaneous symmetry breaking and the amplification or preservation of the stereochemical configuration of individual substance classes. The occurrence of homochirality in biologically relevant structures and metabolism is considered as a signature of life [1–7]. One of the most promising concepts for asymmetric amplification is asymmetric autocatalysis [8–12]. The asymmetric autocatalysis discovered by Soai [13, 14], in which pyrimidine aldehydes are alkylated by diisopropylzinc to the corresponding chiral alcohols, is particularly compelling. The excellent and reproducible amplification of the enantiomeric excess is highly impressive.

Early mechanistic concepts of such reactions with positive nonlinear effects [15] were discussed by Noyori and coworkers [16, 17] and Kagan and coworkers [18–20]. Predominantly the formation of reversible monomer–dimer association complexes was considered. If these monomers have the same configuration, the dimers are homochiral, or if the monomers have opposite configurations, heterochiral dimers are obtained. Since these dimers are diastereoisomeric to one another, they have different intrinsic properties, which are reflected, for example, in their formation and decomposition rates, their solubilities, and their chiroptical properties. Thus, the formation of a heterochiral dimer from an enantiomerically enriched mixture can increase the enantiomeric excess of the free monomers. Ideally, this process could even lead to the result that only the main enantiomer remains monomeric in a solution and the heterochiral dimer precipitates as an insoluble solid. If the remaining

Supramolecular Catalysis: New Directions and Developments, First Edition.
Edited by Piet W.N.M. van Leeuwen and Matthieu Raynal.

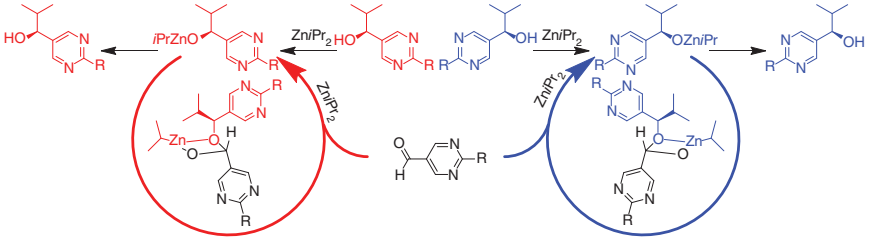

Figure 4.1 Soai's asymmetric autocatalysis with the transient zinc hemiacetalate catalyst formed during the reaction, leading to an extraordinary amplification of the initial enantiomeric excess. The structure of the hemiacetalates was confirmed by high-resolution Orbitrap mass spectrometry and kinetically monitored.

major enantiomer is catalytically active, this process can lead to the starting point of a highly efficient amplification.

Several mechanistic models were proposed to explain the extraordinary behavior of Soai's asymmetric autocatalysis [21–29]. We have been working intensively on the elucidation of the mechanism and kinetics of the Soai reaction and identified hemiacetalate zinc complexes by high-resolution mass spectrometry (cf. Figure 4.1) [30].

These complexes form supramolecular assemblies, which are highly efficient in the autocatalytic amplification of the enantiomeric excess (ee). A comprehensive kinetic analysis allowed the authors to derive a consistent kinetic model, which is even able to correctly calculate and predict ees [31].

Unfortunately, the Soai reaction is limited in its range of application with respect to the substrates that can be employed. We therefore asked ourselves whether there is a possibility of preparing an interconvertible catalyst, which, by recognizing the chirality of the desired target product, adjusts its enantioselectivity in such a way that only the desired enantiomer is formed (cf. Figure 4.2). However, this requires a completely new design. On one hand, the catalyst must be stereodynamically controllable. This means that, depending on the configuration chosen, the (*R*) or (*S*) reaction product is formed. The second prerequisite for a successful design is the decoration of the catalyst with chiral recognition units that can interact with the

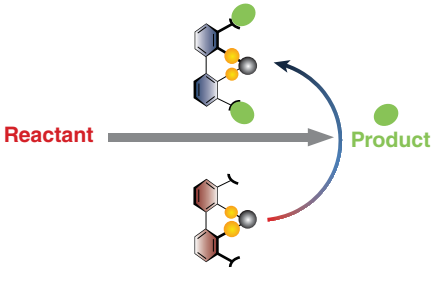

Figure 4.2 Principle of a self-amplifying asymmetric catalysis. The catalyst consists of an interconverting ligand decorated with product interaction sites. Upon noncovalent interaction of these sites with one of the product enantiomers, the ligand will be aligned in a specific configuration, which induces the enantioselective catalysis to the favored enantiomer of the reaction product.

reaction product. If the interaction is successful, the stereodynamic catalyst should then be aligned accordingly.

4.2 Design of an Enantioselective Self-amplifying Catalyst Based on Noncovalent Product–Catalyst Interactions

In contrast to Soai's asymmetric autocatalytic alkylation, of which the substrate scope is very narrow due to the formation of highly specific aggregates, the goal here is to find a general product–catalyst interaction principle that allows the assembly of self-amplifying systems "by design."

We first developed a model to identify the relevant properties of a specifically designed self-amplifying catalyst. Furthermore, this system must be tailored to the targeted catalytic application and transferred to the design of a product–catalyst pair. The principle is shown in Figure 4.3. In the first turnover of the initial catalyst, the product is formed in no or low enantioselectivity. The catalyst interacts with the initially formed product, which induces changes in the catalyst structure. The resulting product–catalyst adduct is characterized by enhanced enantioselectivity, leading to chiral self-amplification, which continues until complete conversion of the substrate. The initial steps are subjected to a dynamic process because the equilibrium of the supramolecular product–catalyst adduct is influenced by the continuous catalytic formation of the product enantiomers. An important principle is that the catalytic activity is not influenced by the product–catalyst adduct formation (principle of orthogonality).

We have developed several supramolecular catalysts decorated with chiral recognition units to recognize and transfer the chirality of the reaction product generated in the catalysis to the stereodynamic unit of the catalyst [32–40], typically consisting of a tropos biphenyl core. The interaction with the chiral reaction product induces a shift in the equilibrium of the stereodynamic catalyst by the recognized sense of chirality. In this way, it was possible to develop self-amplifying catalytic systems that dynamically adjust their configuration during catalysis to form a preferred enantiomer from the prochiral substrate [41–45].

4.3 The Stereodynamics of the Ligand Core

As mentioned earlier, the ligand core unit must be flexible so that such a system can be switched between the two enantiomeric configurations. Axially chiral biphenyl-derived ligands exhibit excellent stereoinducing properties. Moreover, by covalently linking product binding sites, the biphenyl moiety can act as part of the noncovalent interaction by forming interactions. In this way, the product enantiomers can be spatially close to the catalytic active site. We have screened many possible ligand structures including substituted 2,2′-bis(diphenylphosphino)biphenyl (BIPHEP)

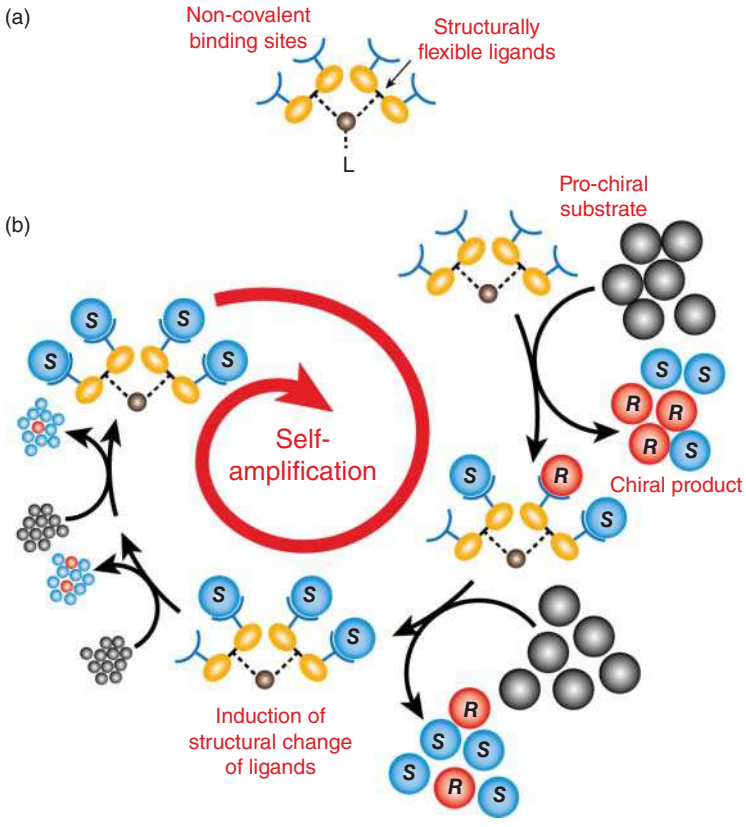

Figure 4.3 Schematic catalytic cycle of an enantioselective self-amplifying catalyst. After activation of the precatalyst, the product is formed in no or low enantioselectivity. The catalyst interacts at the product interaction sites with the initially formed product. This product–catalyst interaction induces a change in the catalyst structure, which leads to enhanced enantioselectivity in a chiral self-amplification process.

and oxidized BIPHEPO ligands (cf. Figure 4.4). It turned out that the interconversion barrier of these compounds can be tuned in the range between 85 and 100 kJ mol^{-1}, which seems to be suitable because it will provide at least some stability for some minutes. However, the problem is that the interconversion is still too slow. It seems to be counterintuitive to implement a ligand core system that is even more flexible and would allow a change in the configuration in every turnover of the catalytic process. We realized that the change of the catalyst must occur rapidly and as a result of noncovalent binding of the product as directly as possible, dynamic BIPOL-based phosphoramidite ligands were chosen, which exhibit high flexibility and low interconversion barriers. Structural changes of the ligand can result from product binding itself and in combination with rotation of the biphenyl moiety. Rhodium and iridium complexes were in the foreground of interest, as phosphoramidite complexes of these metals have already been used successfully in enantioselective hydrogenations [46, 47].

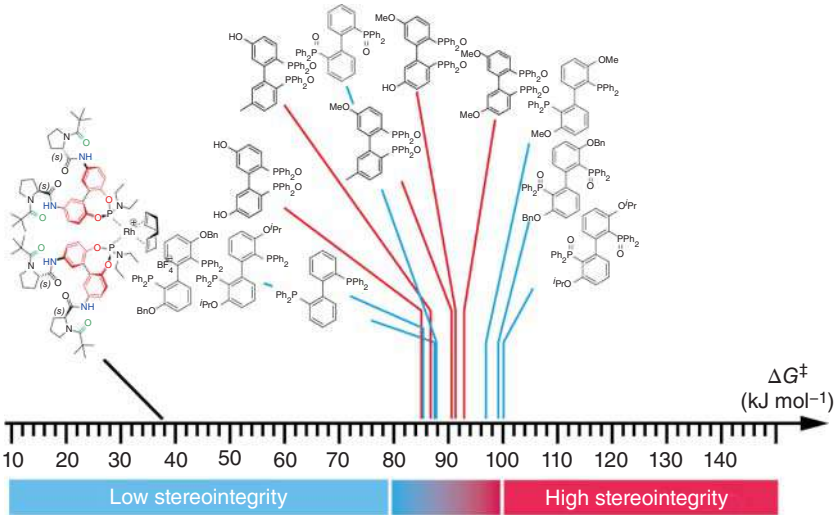

Figure 4.4 Range of the standard activation barriers $\Delta G^{\ddagger}$ of 2,2′-bis(diphenylphosphino) biphenyl (BIPHEP), the oxidized BIPHEPO, and the selector decorated biphenol phosphoramidite ligands in the rhodium(I) complex.

4.4 Design of Product–Catalyst Adducts and Catalyst Synthesis

According to the principle of orthogonality, the noncovalent interaction of the product enantiomers at the binding sites must be as strong and selective as possible. This can be realized by using the exceptionally strong, enantioselective, and noncovalent interaction between diamides such as (*S*)-*N*-pivaloylproline-3,5-dimethylanilide and (*S*)-*N*-3,5-(dinitrobenzoyl)-leucine-dimethylamide (3,5-DNB-Leu-NMe_2)) (cf. Figure 4.5) [48]. This pair of two amino acid derivatives was intensively studied by Pirkle et al. in the context of developing chiral stationary phases for liquid chromatography. The separation of racemic 3,5-DNB-Leu-NMe_2 on a stationary phase containing immobilized (*S*)-*N*-pivaloylproline-3,5-dimethylanilide proceeds with remarkable separation efficiency ($\alpha = 30.4$, $k_1' = 0.61$) [49]. The mechanism of the noncovalent interaction was studied in detail by NMR spectroscopy [50], X-ray crystallography [51], and HPLC analysis [52].

The alanine derivative 3,5-DNB-Ala-OEt represents a structurally related analog of 3,5-DNB-Leu-NMe_2 and is a noncovalently interacting catalytic product. It bears the binding sites required for interaction and can be obtained from the corresponding dehydro compound by enantioselective hydrogenation.

The dynamic phosphoramidite ligand (cf. Figure 4.6) was synthesized starting from *ortho*-biphenol, which was nitrated, allyl protected, and reduced yielding amine. Both (*S*)-*N*-pivaloylproline binding sites were introduced via amide bond formation, and the biphenol decorated with the interaction sites was obtained after deprotection. X-ray crystallographic investigation and NMR spectroscopy

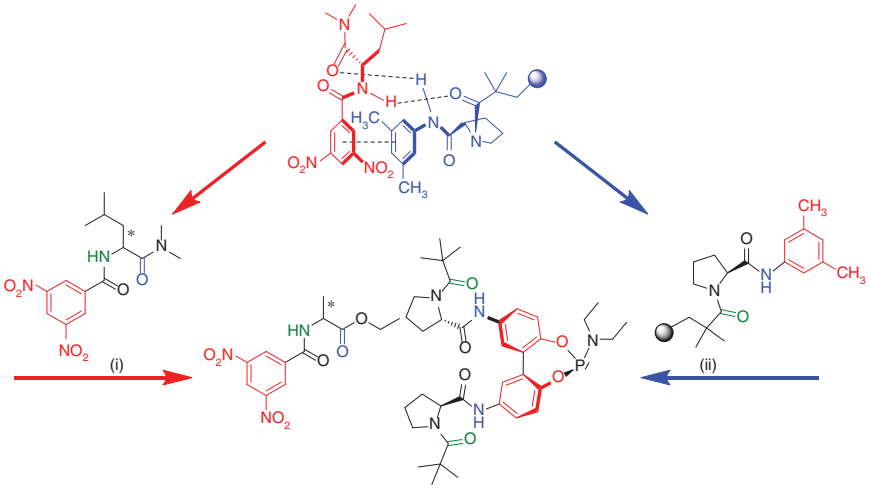

Figure 4.5 Noncovalent binding model, design of the structurally flexible ligand and the catalysis product, and synthesis of the ligands and catalysts. The extraordinary noncovalent enantioselective interaction between (*S*)-*N*-pivaloylproline 3,5-dimethyl-anilide and (*S*)-*N*-3,5-dinitrobenzoylleucine dimethylamide (3,5-DNB-Leu-NMe_2) is utilized as the product interaction site of the ligand backbone. The ligand is structurally flexible so as to induce a change in the enantioselectivity of the catalyst upon interaction with chiral molecules. Left: Interacting product design. Right: Selector-ligand design.

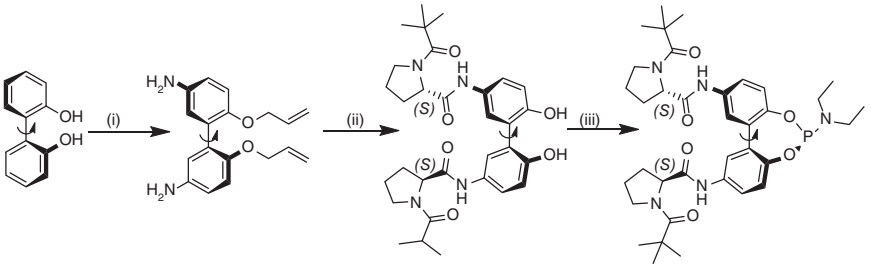

Figure 4.6 Synthesis of the phosphoramidite ligand: (i) HOAc, HNO_3; allyl bromide, K_2CO_3; $SnCl_2$; (ii) (*S*)-*N*-pivaloylproline, COMU, DIPEA; $Pd(OAc)_2$, 4-(dimethylaminophenyl) diphenylphosphine, K_2CO_3; (iii) $Cl_2P(NEt_2)$, DIPEA.

confirmed the exclusive formation of the trans-rotamer of the tertiary amide bond. Final conversion to phosphoramidite ligand was achieved using $Cl_2P(NEt_2)$. To get insights into the rotational barrier of BIPOL phosphoramidites, we performed DFT calculations at the B3LYP/cc-pVDZ level of theory. A rotational barrier of $\Delta G^{\ddagger} = 36.7\ \mathrm{kJ\,mol^{-1}}$ was determined, corroborating the structural flexibility of the targeted ligand.

The subsequent complexation of this ligand with $[Rh(COD)_2]BF_4$ yielded the cationic complex with two phosphoramidite ligands (cf. Figure 4.7).

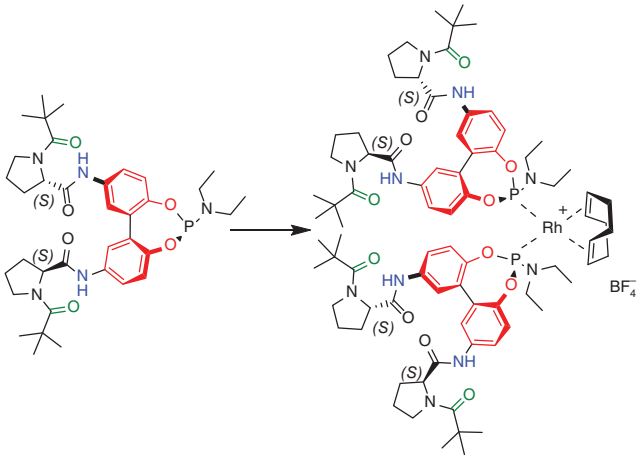

Figure 4.7 Preparation of the rhodium(I) complex utilizing the prepared ligand and $[Rh(COD)_2]BF_4$.

4.5 Noncovalent Interaction Studies via NMR Spectroscopy

The supramolecular interactions of the targeted chiral catalysis product 3,5-DNB-Ala-OEt with the phosphoramidite ligand as well as with the rhodium(I) complexes in solution were studied by NMR spectroscopy. To prove the principle of orthogonality, interactions with the substrate 3,5-DNB-ΔAla-OEt were performed to exclude its unintended binding.

The formation of noncovalent adducts was investigated by means of $^{13}C\{^1H\}$ and $^{31}P\{^1H\}$ NMR spectroscopy. Solutions of the free ligand and the Rh(I) complex in degassed anhydrous $CDCl_3$, respectively, were treated with 10 equiv of either (*R*)- or (*S*)-3,5-DNB-Ala-OEt and racemic 3,5-DNB-Ala-OEt, respectively. Indeed, huge changes in the chemical shifts were observed in $^{13}C\{^1H\}$ and $^{31}P\{^1H\}$ NMR spectra upon addition of the (*S*)-enantiomer and the racemate (50% (*S*)-enantiomer) (Δppm = 0.49 and 0.66 with (*S*)-3,5-DNB-Ala-OEt in $^{31}P\{^1H\}$ NMR spectra). In contrast, interactions with (*R*)-3,5-DNB-Ala-OEt were found to be much weaker and addition of substrate 3,5-DNB-ΔAla-OEt hardly leads to changes in chemical shifts (cf. Figure 4.8). Detailed analysis of $^{13}C\{^1H\}$ NMR spectra revealed that all carbon atoms in the proximity of the noncovalent binding sites exhibit large changes of chemical shifts (pivaloyl carbonyl group, proline heterocycle, biphenyl fragment) upon addition of (*S*)-3,5-DNB-Ala-OEt or *rac*-3,5-DNB-Ala-OEt, respectively, while other parts remain almost unchanged (*tert*-butyl group, diethylamino group), which corroborates the *by-design* interaction model. This interaction could be detected by intermolecular interactions in $^1H,^1H$ NOESY NMR. The noncovalent supramolecular association was investigated by an NMR titration experiment. The equilibrium

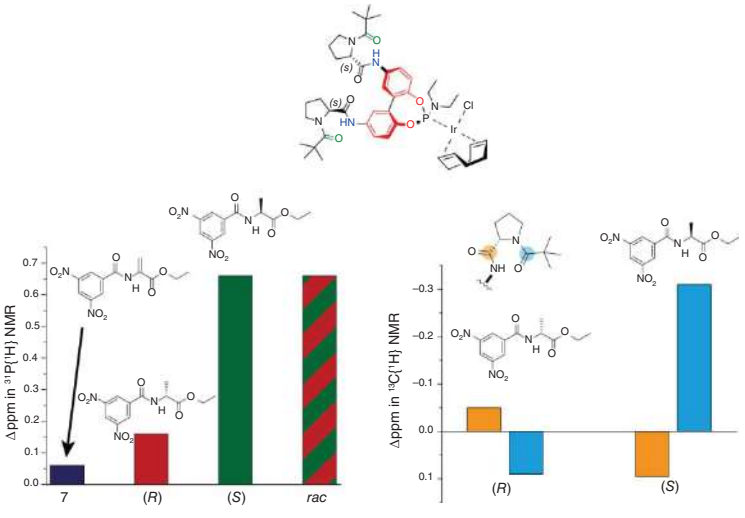

Figure 4.8 Noncovalent interactions between the product interaction site and substrate, product enantiomers, and product racemate, respectively, are demonstrated by signal shifts in $^{13}C\{^1H\}$ and $^{31}P\{^1H\}$ NMR spectroscopy. The bar graphs show the different effects of the substrate, product enantiomers, and product racemate on the phosphorus atoms of the ligand (left) and carbon atoms of the interaction site (right) upon interaction with the product enantiomers.

constant K for the adduct formation of (S)-3,5-DNB-Ala-OEt with a single binding site was estimated to be 49 l mol^{-1}.

4.6 Self-amplifying Hydrogenation of 3,5-DNB-ΔAla-OEt

To prove the self-amplifying properties of the designed catalyst, the hydrogenation of 3,5-DNB-ΔAla-OEt with the rhodium(I) catalyst was investigated in great detail. The initial enantioselectivity was differentiated from the enantioselectivity of the catalyst–product adduct by investigation of hydrogenations with different catalyst loadings. Variation of the catalyst loading over a broad range allows precise control of the TON, especially in the case of very low turnovers. In particular, the influence of different amounts of product on the product formation can be studied. Hydrogenations with an average $\frac{n_{substrate}}{n_{catalyst}} = 0.5$ (200 mol% catalyst) were performed in order to determine the initial enantioselectivity. The enantioselectivity of the catalyst–product adduct was investigated at low catalyst loadings. Hydrogenations were performed with 200, 20, 5, 2, 1, and 0.2 mol% of the Rh(I) catalyst at constant catalyst concentration to avoid dilution effects. With 200 mol% catalyst, the hydrogenation product with 53% er favoring the (R)-enantiomer was obtained. Intriguingly, lowering of the catalyst loading resulted in remarkably increased (S)-selectivity of up to 71% er favoring the (S)-enantiomer (0.2 mol% catalyst).

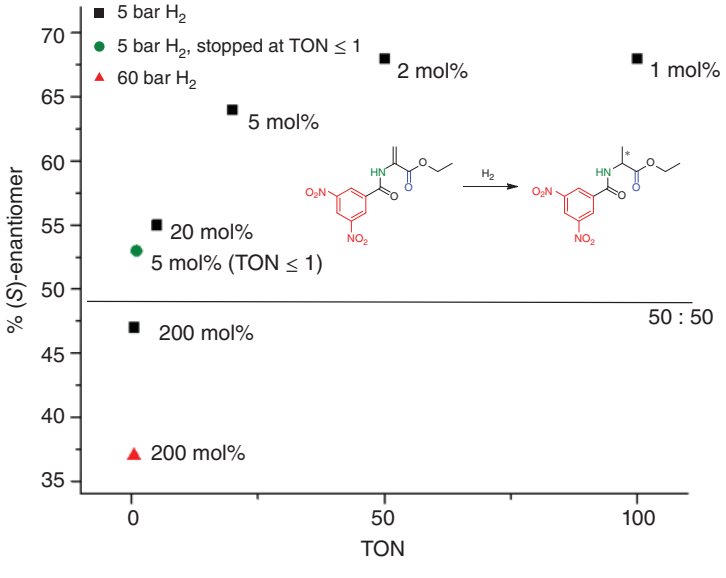

Figure 4.9 This plot shows that the product molecules formed in the hydrogenation rapidly change the enantioselectivity of the catalyst as a result of noncovalent binding of the hydrogenation product. 5 bar H_2 (black), 5 bar H_2 (green; hydrogenation stopped at TON ≤ 1), and 60 bar H_2 (red). Reaction conditions: −20 °C, DCM as solvent.

The course of the curve indicates that the first product molecules formed during catalysis rapidly alter the enantioselectivity of the catalyst by noncovalent binding of the hydrogenation product (cf. Figure 4.9).

4.7 Concluding Remarks

Here we presented our strategy and realization of a directed design of catalysts for hydrogenations that are capable of interacting with their catalysis products, a process associated with changes in enantioselectivity. The remarkable increase in enantioselectivity of the catalyst is the result of the combination of supramolecular product binding sites and structural flexibility of the ligand. The design presented here allows the study of noncovalent catalyst–product interactions and enables the straightforward implementation of interaction sites in catalysts and products. More generally, it provides insights into catalytic amplification processes in nature, which certainly played a crucial role in the emergence of homochirality on Earth.

Acknowledgments

Generous financial support by the European Research Council (ERC) (Grant No. 258740, AMPCAT) and the Max-Planck-Society is gratefully acknowledged.

References

1 Hegstrom, R.A. (1984). Parity nonconservation and the origin of biological chirality: Theoretical calculations. *Origins Life* 14: 405–411.
2 Blackmond, D.G. (2004). Asymmetric autocatalysis and its implications for the origin of homochirality. *PNAS* 101: 5732–5736.
3 Soai, K. and Kawasaki, T. (2008). Asymmetric autocatalysis with amplification of chirality. *Top. Curr. Chem.* 284: 1–33.
4 Blackmond, D.G. (2011). The origin of biological homochirality. *Philos. Trans. R. Soc. B* 366: 2878–2884.
5 Karunakaran, S.C., Cafferty, B.J., Weigert-Muñoz, A. et al. (2019). Spontaneous symmetry breaking in the formation of supramolecular polymers: implications for the origin of biological homochirality. *Angew. Chem. Int. Ed.* 58: 1453–1457.
6 Hawbaker, N.A. and Blackmond, D.G. (2019). Energy threshold for chiral symmetry breaking in molecular self-replication. *Nat. Chem.* 11: 957–962.
7 Teichert, J.S., Kruse, F.M., and Trapp, O. (2019). Direct prebiotic pathway to DNA nucleosides. *Angew. Chem. Int. Ed.* 58: 9944–9947.
8 Alberts, A.H. and Wynberg, H. (1989). The role of the product in asymmetric carbon-carbon bond formation: stoichiometric and catalytic enantioselective autoinduction. *J. Am. Chem. Soc.* 111: 7265–7266.

9 Kawasaki, T., Suzuki, K., Hakoda, Y., and Soai, K. (2008). Achiral nucleobase cytosine acts as an origin of homochirality of biomolecules in conjunction with asymmetric autocatalysis. *Angew. Chem. Int. Ed.* 47: 496–499.

10 Tsogoeva, S.B. (2010). When chiral product and catalyst are the same: discovery of asymmetric organoautocatalysis. *Chem. Commun.* 46: 7662–7669.

11 Bissette, A.J. and Fletcher, S.P. (2013). Mechanisms of autocatalysis. *Angew. Chem. Int. Ed.* 52: 12800–12826.

12 Blackmond, D.G. (2020). Autocatalytic models for the origin of biological homochirality. *Chem. Rev.* 120: 4831–4847.

13 Soai, K., Shibata, T., Morioka, H., and Choji, K. (1995). Asymmetric autocatalysis and amplification of enantiomeric excess of a chiral molecule. *Nature* 378: 767–768.

14 Shibata, T., Takahashi, T., Konishi, T., and Soai, K. (1997). Asymmetric self-replication of chiral 1,2-amino alcohols by highly enantioselective autoinductive reduction. *Angew. Chem. Int. Ed.* 36: 2458–2460.

15 Blackmond, D.G. (2010). Kinetic aspects of non-linear effects in asymmetric synthesis, catalysis, and autocatalysis. *Tetrahedron: Asym.* 21: 1630–1634.

16 Kitamura, M., Okada, S., Suga, S., and Noyori, R. (1989). Enantioselective addition of dialkylzincs to aldehydes promoted by chiral amino alcohols. Mechanism and nonlinear effect. *J. Am. Chem. Soc.* 111: 4028–4036.

17 Mikami, K., Korenaga, T., Ohkuma, K., and Noyori, R. (2000). Asymmetric activation/deactivation of racemic ru catalysts for highly enantioselective hydrogenation of ketonic substrates. *Angew. Chem. Int. Ed.* 39: 3707–3710.

18 Puchot, C., Samuel, O., Duiiach, E. et al. (1986). Nonlinear effects in asymmetric synthesis. Examples in asymmetric oxidations and aldolization reactions. *J. Am. Chem. Soc.* 108: 2353–2357.

19 Girard, C. and Kagan, H.B. (1998). Nonlinear effects in asymmetric synthesis and stereoselective reactions: ten years of investigation. *Angew. Chem. Int. Ed.* 37: 2922–2959.

20 Satyanarayana, T., Abraham, S., and Kagan, H.B. (2009). Nonlinear effects in asymmetric catalysis. *Angew. Chem. Int. Ed.* 48: 456–494.

21 Blackmond, D.G., McMillan, C.R., Ramdeehul, S. et al. (2001). Origins of asymmetric amplification in autocatalytic alkylzinc additions. *J. Am. Chem. Soc.* 123: 10103–10104.

22 Blackmond, D.G. (2006). Mechanistic study of the Soai autocatalytic reaction informed by kinetic analysis. *Tetrahedron Asymmetry* 17: 584–589.

23 Ercolani, G. and Schiaffino, L. (2011). Putting the mechanism of the Soai reaction to the test: DFT study of the role of aldehyde and dialkylzinc structure. *J. Org. Chem.* 76: 2619–2626.

24 Gehring, T., Quaranta, M., Odell, B. et al. (2012). Observation of a transient intermediate in Soai's asymmetric autocatalysis: insights from 1H NMR turnover in real time. *Angew. Chem. Int. Ed.* 51: 9539–9542.

25 Micheau, J.-C., Cruz, J.-M., Coudret, C., and Buhse, T. (2010). An autocatalytic cycle model of asymmetric amplification and mirror-symmetry breaking in the Soai reaction. *ChemPhysChem* 11: 3417–3419.

26 Micheau, J.-C., Coudret, C., Cruz, J.-M., and Buhse, T. (2012). Amplification of enantiomeric excess, mirror-image symmetry breaking and kinetic proofreading in Soai reaction models with different oligomeric orders. *Phys. Chem. Chem. Phys.* 14: 13239–13248.

27 Gridnev, I.D. and Vorobiev, A.K. (2015). On the origin and structure of the recently observed acetal in the Soai reaction. *Bull. Chem. Soc. Jpn* 88: 333–340.

28 Athavale, S.V., Simon, A., Houk, K.N., and Denmark, S.E. (2020). Demystifying the asymmetry-amplifying, autocatalytic behaviour of the Soai reaction through structural, mechanistic and computational studies. *Nat. Chem.* 12: 412–423.

29 Athavale, S.V., Simon, A., Houk, K.N., and Denmark, S.E. (2020). Structural contributions to autocatalysis and asymmetric amplification in the Soai reaction. *J. Am. Chem. Soc.* 142: 18387–18406.

30 Trapp, O., Lamour, S., Maier, F. et al. (2020). In situ mass spectrometric and kinetic investigations of Soai's asymmetric autocatalysis. *Chem. Eur. J.* 26: 15871–15880.

31 Trapp, O. (2020). Efficient amplification in Soai's asymmetric autocatalysis by a transient stereodynamic catalyst. *Front. Chem.* 8: 1173.

32 Maier, F. and Trapp, O. (2012). Stationary phase and solvent effects on the stereodynamics of tropos BIPHEP ligands revealed by a novel HPLC technique. *Angew. Chem. Int. Ed.* 51: 2985–2988.

33 Maier, F. and Trapp, O. (2013). The stereodynamics of 5,5′-disubstituted BIPHEPs. *Chirality* 25: 126–132.

34 Maier, F. and Trapp, O. (2014). Selector-induced dynamic deracemization of a selectand-modified tropos BIPHEPO-ligand: application in the organocatalyzed asymmetric double-aldol-reaction. *Angew. Chem. Int. Ed.* 53: 8756–8760.

35 Storch, G., Siebert, M., Rominger, F., and Trapp, O. (2015). 5,5′-Diamino-BIPHEP ligands bearing small selector units for non-covalent binding of chiral analytes in solution. *Chem. Commun.* 51: 15665–15668.

36 Storch, G. and Trapp, O. (2015). Temperature controlled bidirectional enantioselectivity in a dynamic catalyst for asymmetric hydrogenation. *Angew. Chem. Int. Ed.* 54: 3580–3586.

37 Storch, G., Maier, F., Wessig, P., and Trapp, O. (2016). Rotational barriers of substituted BIPHEP ligands: a comparative experimental and theoretical study. *Eur. J. Org. Chem.*: 5123–5126.

38 Storch, G., Deberle, L., Menke, J.-M. et al. (2016). A stereodynamic phosphoramidite ligand derived from 3,3′-functionalized ortho-biphenol and its rhodium(I) complex. *Chirality* 28: 744–748.

39 Storch, G., Pallmann, S., Rominger, F., and Trapp, O. (2016). Stereodynamic tetrahydro-biisoindole "NU-BIPHEP(O)"s: functionalization, rotational barriers and non-covalent interactions. *Beilstein J. Org. Chem.* 12: 1453–1458.

40 Siebert, M., Storch, G., Rominger, F., and Trapp, O. (2017). Temperature-controlled bidirectional enantioselectivity in asymmetric hydrogenation reactions utilizing stereodynamic iridium complexes. *Synthesis* 49: 3485–3494.

41 Scholtes, J.F. and Trapp, O. (2019). Supramolecular interlocked biphenyl ligands for enantioselective Ti-catalyzed alkylation of aromatic aldehydes. *Organometallics* 38: 3955–3960.

42 Scholtes, J.F. and Trapp, O. (2019). Design and synthesis of a stereodynamic catalyst with reversal of selectivity by enantioselective self-inhibition. *Chirality* 31: 1028–1042.

43 Scholtes, J.F. and Trapp, O. (2019). Enantioselectivity induced by stereoselective interlocking: a novel core motif for tropos ligands. *Chem. Eur. J.* 25: 11707–11714.

44 Scholtes, J.F. and Trapp, O. (2019). Inducing enantioselectivity in a dynamic catalyst by supramolecular interlocking. *Angew. Chem. Int. Ed.* 58: 6306–6310.

45 Scholtes, J.F. and Trapp, O. (2020). Asymmetric induction and amplification in stereodynamic catalytic systems by non-covalent interactions. *Synlett* 32: 971–980.

46 Giacomina, F., Meetsma, A., Panella, L. et al. (2007). High enantioselectivity is induced by a single monodentate phosphoramidite ligand in iridium-catalyzed asymmetric hydrogenation. *Angew. Chem. Int. Ed.* 46: 1497–1500.

47 Minnaard, A.J., Feringa, B.L., Lefort, L., and Vries, J.G.D. (2007). Asymmetric hydrogenation using monodentate phosphoramidite ligands. *Acc. Chem. Res.* 40: 1267–1277.

48 Storch, G. and Trapp, O. (2017). By-design enantioselective self-amplification based on non-covalent product-catalyst interactions. *Nat. Chem.* 9: 179–187.

49 Pirkle, W.H. and Murray, P.G. (1993). Chiral stationary phase design use of intercalative effects to enhance enantioselectivity. *J. Chromatogr.* 641: 11–19.

50 Pirkle, W.H., Murray, P.G., Rausch, D.J., and McKenna, S.T. (1996). Intermolecular ^{1}H-^{1}H two-dimensional nuclear Overhauser enhancements in the characterization of a rationally designed chiral recognition system. *J. Org. Chem.* 61: 4769–4774.

51 Pirkle, W.H., Murray, P.G., and Wilson, S.R. (1996). X-ray crystallographic evidence in support of a proposed chiral recognition mechanism. *J. Org. Chem.* 61: 4775–4777.

52 Pirkle, W.H. and Pochapsky, T.C. (1989). Considerations of chiral recognition relevant to the liquid chromatographic separation of enantiomers. *Chem. Rev.* 89: 347–362.

5

Interlocked Molecules in Enantioselective Catalysis

Carel Kwamen and Jochen Niemeyer

University of Duisburg-Essen, Faculty of Chemistry (Organic Chemistry), Universitätsstrasse 7, 45141 Essen, Germany

5.1 Introduction

Mechanically interlocked molecules (MIMs) can be defined as molecules possessing mechanical or topological bonds. A mechanical bond can exist between two subcomponents which are entangled in space and cannot be separated without breaking or distortion of covalent bonds [1]. Prototypical examples of MIMs that possess mechanical bonds are [*n*]rotaxanes [2], in which one (or more) macrocycles are confined onto one (or more) linear components with bulky substituents preventing dissociation, and [*n*]catenanes [3], where two or more macrocycles are interlocked. In comparison, topological bonds represent permanent crossing points between molecules or molecular parts, so that topological bonds cannot be broken by distortion of bonds. Thus, the bond between the subcomponents in catenanes can also be described as a topological bond. However, topological bonds can also be realized without the presence of several subcomponents, for example, in molecular knots (e.g. the trefoil knot) [4].

MIMs are commonly synthesized using supramolecular template methods, and both passive template [5, 6] and active template [7] approaches have been developed. Thus, although MIMs are not held together by weak noncovalent bonds (indeed, a covalent bond must be broken to destroy a mechanical or topological bond), they are commonly regarded as a discipline of supramolecular chemistry.

MIMs possess exceptional molecular properties like a unique three-dimensional structure which can be used to create a confined space for binding or catalysis [8] or the possibility for different co-conformations between the subcomponents which allows the design of switchable systems [9]. Also MIMs can display mechanical or topological chirality [10] which even in the absence of any classical element of chirality makes them valuable for stereoselective sensing and catalysis [11].

This has led to the application of MIMs for various applications, such as molecular machines (shuttles [12], rotors [13] and switches [14]), chemosensors [15], or molecular muscles [16]. The relevance of this fascinating field was recognized by

Supramolecular Catalysis: New Directions and Developments, First Edition.
Edited by Piet W.N.M. van Leeuwen and Matthieu Raynal.

the award of the 2016 Nobel Prize in Chemistry to Sauvage, Stoddart, and Feringa for "the design and synthesis of molecular machines" [17].

Among the inspiring applications of MIMs, their use in enantioselective catalysis has gained increasing attention in the last years [18]. Here, MIMs allow nonclassical approaches in catalysts design, such as the development of switchable chiral catalysts, the use of the mechanical bond to generate cooperative systems, or the introduction of mechanical or topological chirality.

In the upcoming parts, the enantioselective catalytic applications of molecular interlocked molecules will be described, according to the type of MIM used. Hence, examples of rotaxanes in enantioselective catalysis will be followed by those of catenanes and finally those of molecular knots.

5.2 Rotaxanes in Enantioselective Catalysis

The most extensively used class of MIMs in catalysis are rotaxanes. A number of chiral rotaxanes for application in asymmetric organocatalysis and transition metal catalysis have been developed.

The first catalytically active rotaxanes were developed by Takata and coworkers. In 2004, they presented the rotaxane (*R*)-**1** (Figure 5.1a) which features an achiral thread comprising a catalytically active thiazolium moiety and a BINOL-based macrocyclic unit introducing chirality [19]. Rotaxanes (*R*)-**1a**/**b**, which differ in the length of the thread, were employed for the asymmetric benzoin condensation of different benzaldehyde derivatives. In general, yields (10–34%) and stereoselectivities (up to 27% ee) were only moderate. The influence of the position of the BINOL unit

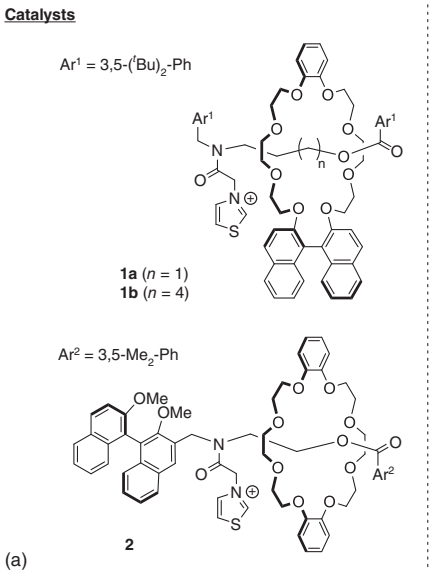

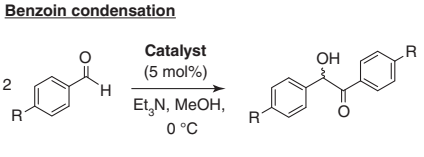

Catalyst	R	Conv. (%)	ee (%)
1a	H	34	23 (*R*)
1a	CH_3	10	25 (*R*)
1a	Cl	16	18 (*R*)
1b	H	34	16 (*R*)
1b	CH_3	10	21 (*R*)
1b	Cl	28	11 (*R*)
2	H	40	19 (*S*)
2	CH_3	10	25 (*S*)
2	Cl	22	13 (*S*)

(b)

Figure 5.1 Asymmetric benzoin condensation by *Takata's* chiral rotaxanes **1a**/**b** and **2**.

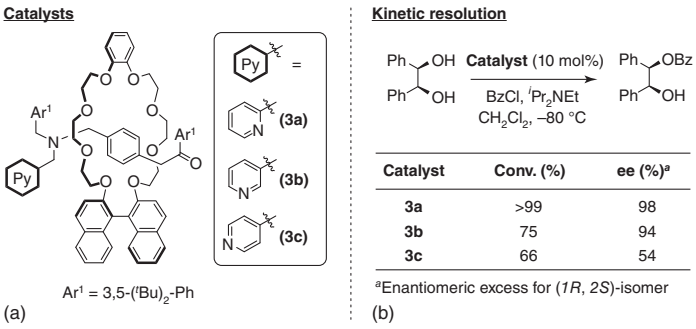

Catalyst	Conv. (%)	ee (%)[a]
3a	>99	98
3b	75	94
3c	66	54

[a]Enantiomeric excess for (*1R*, *2S*)-isomer

Figure 5.2 Asymmetric *O*-benzoylation of *meso*-1,2-diols using *Takata's* chiral rotaxanes **3a/b/c**.

on the stereoselectivity was investigated by contrasting rotaxane **2** which contains an achiral macrocycle and a chiral BINOL unit on the thread. This remarkably reversed the stereoselectivities by favoring the production of the (*S*)-products (8–25% ee), while the rotaxanes ((*R*)-**1a**/**b**) with the chiral macrocycle preferentially formed the (*R*)-products (Figure 5.1b). This work nicely showed the mechanical linking of a catalytically active unit with a chiral group on the other subcomponent can be used to achieve a chiral induction in catalysis.

This approach was extended by the same group, which later reported catalytically active rotaxanes featuring a BINOL-based crown ether macrocycle and a nucleophilic pyridine group on the thread [20]. The isomeric rotaxanes (**3a**/**b**/**c**) differ in the position of their nucleophilic nitrogen relative to the linker connecting them to the thread, while the BINOL unit is responsible for the induction of chirality (Figure 5.2a). Effectively applied for the asymmetric *O*-benzoylation of *meso*-1,2-diphenylethane-1,2-diol with benzoyl chloride (Figure 5.2b), the *ortho*- and *meta*-pyridyl containing rotaxane (**3a**/**b**) yielded excellent stereoselectivities (94–98% ee) while the *para*-pyridyl containing rotaxane (**3c**) led to a considerably lower selectivity (54% ee).

Leigh and coworkers recognized that rotaxanes which are generated by templation of a crown ether around an ammonium-based thread can be used in organocatalysis without further modification. The amine on the thread can act as a nucleophilic catalyst via iminium or enamine activation, respectively. In combination with a second binding station on the thread (e.g. a triazolium group), this gives rise to switchable catalysts that are inactive in the protonated ammonium form but can be activated by base. Several achiral versions of such rotaxane catalysts have successfully been applied [21].

In 2014, Leigh and coworkers reported the first chiral version of their switchable rotaxane catalysts [22]. They designed the rotaxane (*R*)-**4** consisting of a dibenzo-[24]-crown-8 macrocycle and an extended thread featuring a phenylalanine-derived central secondary ammonium group and a peripheral triazolium unit (Figure 5.3a). The macrocycle can station on both the ammonium group and the triazolium unit. This feature permits an effective switch of the catalyst by acid or base, between an *off*-mode ((*R*)-**[4-H]**$^+$), where the macrocycle

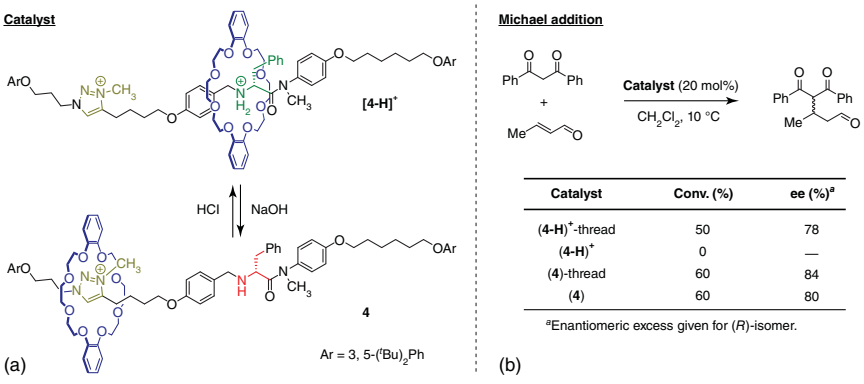

Catalyst	Conv. (%)	ee (%)[a]
(**4-H**)$^+$-thread	50	78
(**4-H**)$^+$	0	—
(**4**)-thread	60	84
(**4**)	60	80

[a]Enantiomeric excess given for (*R*)-isomer.

Figure 5.3 Asymmetric Michael addition using *Leigh's* chiral switchable rotaxane **4**.

is preferentially located on the central ammonium group thereby blocking the catalytically active group, and an *on*-mode ((*R*)-**4**) where the macrocycle sits on the permanently charged triazolium unit leaving the chiral amine sterically accessible.

This was used for the asymmetric Michael addition of 1,3-diphenyl-1,3-propanedione to (*E*)-crotonaldehyde (Figure 5.3b). The protonated catalyst (*R*)-[**4-H**]$^+$ gave no conversion after 24 hours, while the corresponding non-interlocked ammonium thread stimulates a 50% conversion with an enantioinduction of 78% ee. The deprotonated catalyst (*R*)-**4** on the other side catalysed the reaction via iminium activation of the aldehyde, delivering 60% conversion. Here, both the free thread and the catalyst (*R*)-**4** almost achieved the same enantioinduction (80% ee for (*R*)-**4** vs. 84% ee for the free thread).

Using a chiral proline-based thread, Berna and coworkers generated the rotaxanes (**5a/b**) which differ in the peripheral substitution of the macrocycle (R = H or NO_2) [23]. Here, the amide-based macrocycle is not used to achieve an *on*/*off* switching of the catalyst, but for a modulation of the steric environment of the active site. Indeed, when applied for the Michael addition of acetone to nitrostyrene, the rotaxanes **5a/b** allow for a slight stereoinduction (8–14% ee), while the thread alone does not (Figure 5.4).

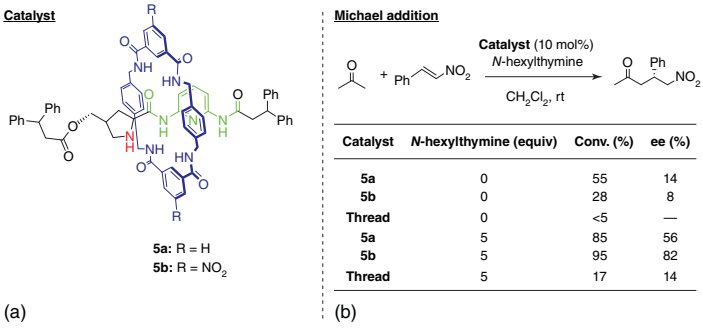

Catalyst	*N*-hexylthymine (equiv)	Conv. (%)	ee (%)
5a	0	55	14
5b	0	28	8
Thread	0	<5	—
5a	5	85	56
5b	5	95	82
Thread	5	17	14

Figure 5.4 Asymmetric Michael addition using *Berna's* prolinamine rotaxane **5**.

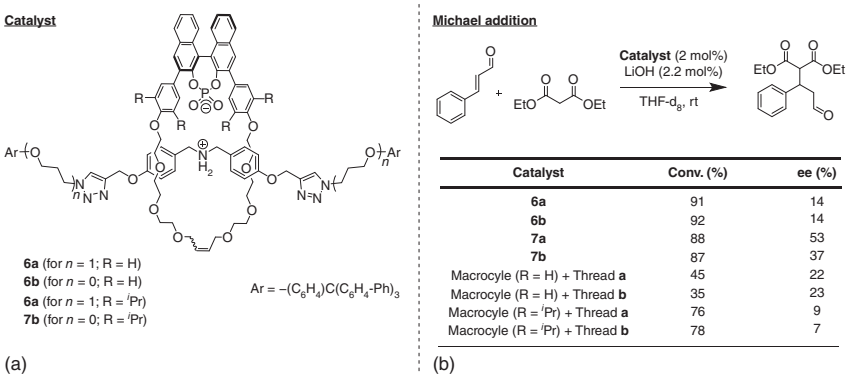

Catalyst	Conv. (%)	ee (%)
6a	91	14
6b	92	14
7a	88	53
7b	87	37
Macrocyle (R = H) + Thread **a**	45	22
Macrocyle (R = H) + Thread **b**	35	23
Macrocyle (R = ^{i}Pr) + Thread **a**	76	9
Macrocyle (R = ^{i}Pr) + Thread **b**	78	7

Figure 5.5 Asymmetric Michael addition using *Niemeyer's* chiral rotaxanes **6** and **7**. Source: Based on Pairault et al. [24].

However, the rotaxanes **5a/b** also feature an additional diaminopyridine unit on the thread. This does not act as a second binding station for the macrocycle, but for the binding of *N*-hexylthymine (HT) as a cofactor. This was designed to influence the position of the macrocycle on the thread, thus allowing an allosteric modulation of the catalyst. Indeed, in the presence of HT, a remarkable increase in conversion (85–95%) and stereoselectivity (56-82% ee) was observed for the rotaxane catalysts, while the thread only gave a slight increase in conversion (17%) and selectivity (14% ee).

The Niemeyer group recently explored the first application of a chiral acid/base-functionalized rotaxane in asymmetric catalysis. The chiral rotaxanes **6** and **7** (Figure 5.5) [24] comprise of a Brønsted acidic macrocycle based on a chiral 1,1′-binaphthyl-phosphate unit and a Brønsted basic thread featuring a central secondary amine.

Applied for the addition of diethyl malonate to cinnamaldehyde (Figure 5.5b), no significant difference was observed with a change in length of the rotaxane thread (**6a** and **6b**) on both the selectivity and rate of reaction. The introduction of bulkier substituents (**7a** and **7b**) leads to a remarkable increase in stereoselectivity (53/37% ee) associated with high reaction rates (88/87% conversion). The corresponding non-interlocked counterparts gave lower conversions (76/78%) and stereoselectivities (9/7% ee).

The reaction is assumed not to proceed via the iminium activation of the aldehyde substrate but by a Lewis acid activation of the Li-phosphate as shown by DFT calculations. It was also found that the cooperative action of the Li-phosphate and the amine/ammonium group is essential for the reaction, therefore establishing the significance of the mechanical bond for both the activity and selectivity.

Instead of using classical elements of chirality, such as centrochiral or axially chiral units on the subcomponents, interlocked molecules also allow for the generation of mechanical or topological chirality.

This concept was exploited for the first time by Leigh and coworkers in 2016, when they reported the mechanically point chiral rotaxane **8** [25]. The chirality

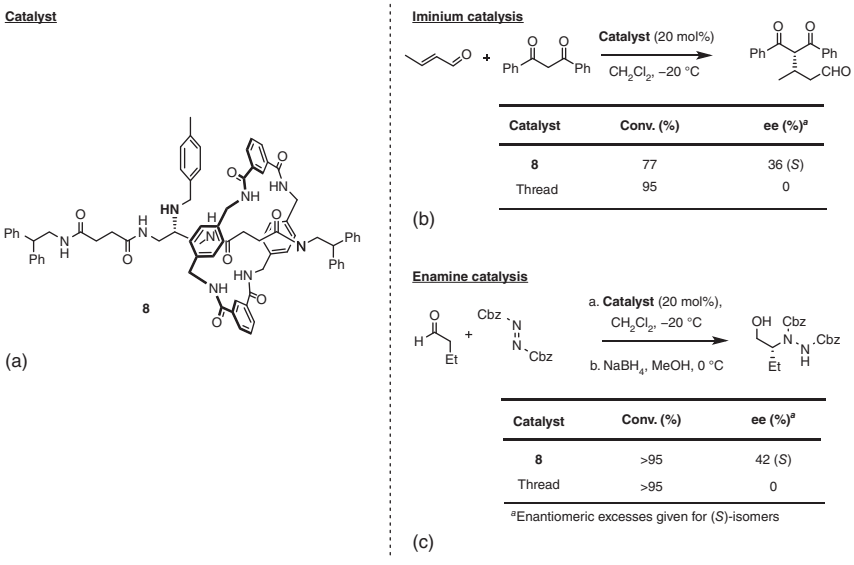

Figure 5.6 Iminium and enamine catalysis using *Leigh's* mechanical chiral rotaxane **8**.

of rotaxane **8** is brought about by threading the macrocycle on one side of the symmetrical thread (Figure 5.6). The shuttling of the macrocycle between both ends of the thread is avoided by a bulky *p*-tolyl substituent on the central amine. This prevents the interconversion of the two mechanically point chiral enantiomers and thus permits their separation (Figure 5.6a).

The enantiomerically enriched form of the rotaxane (84% ee of the (*S*)-isomer) was employed for enantioselective catalysis. Applied for iminium catalysis, the addition of 1,3-diphenyl-propane-1,3-dione to α,β-unsaturated aldehydes (Figure 5.6b) gave the Michael products with good stereoselectivity (36% ee). In enamine catalysis, the addition of aldehydes to dibenzyl azodicarboxylate (Figure 5.6c) gave the hydrazine products in good yields (>95%) and stereoselectivity (up to 42% ee). This shows that mechanical chirality can be employed to achieve significant stereoinduction in enantioselective catalysis.

Leigh and coworkers recently reported a dynamic rotaxane catalyst that allows formation of enantiomeric products upon switching [26]. The rotaxane thread features a central *syn*-2,5-disubstituted pyrrolidine together with adjacent pyridyl-acyl hydrazone and glycine amide units. This pseudo-symmetric thread is combined with a benzylic amide macrocycle to give rotaxane **9**. The rotaxane undergoes isomerization of the hydrazone unit in response to light (triggers (*E*)–(*Z*)-isomerization) or acid (triggers (*Z*)–(*E*)-isomerization), which effectively locates the macrocycle on one side of the central pyrollidine, namely either on the (*E*)-hydrazone or on the glycine amide (Figure 5.7a).

When applied for the reaction of aldehydes with vinyldisulfone, both rotaxane isomers provide higher enantioselectivities than three free threads, proving the effect of the steric shielding by the macrocycle. More importantly, the selectivities

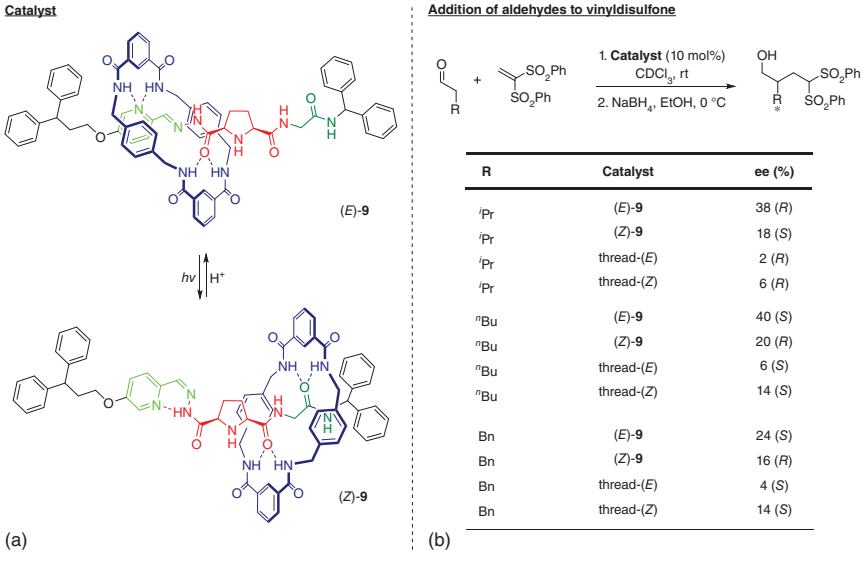

R	Catalyst	ee (%)
^{i}Pr	(*E*)-**9**	38 (*R*)
^{i}Pr	(*Z*)-**9**	18 (*S*)
^{i}Pr	thread-(*E*)	2 (*R*)
^{i}Pr	thread-(*Z*)	6 (*R*)
^{n}Bu	(*E*)-**9**	40 (*S*)
^{n}Bu	(*Z*)-**9**	20 (*R*)
^{n}Bu	thread-(*E*)	6 (*S*)
^{n}Bu	thread-(*Z*)	14 (*S*)
Bn	(*E*)-**9**	24 (*S*)
Bn	(*Z*)-**9**	16 (*R*)
Bn	thread-(*E*)	4 (*S*)
Bn	thread-(*Z*)	14 (*S*)

Figure 5.7 Rotaxane-catalyzed conjugate addition of aldehydes to vinyl sulfones using *Leigh's* switchable rotaxane **9**.

of the rotaxane pseudoenatiomers are inversed: for three different aldehydes, inverted selectivities were found (see Figure 5.7b), and the most pronounced difference was found for hexanal, giving the (*S*)-product (40% ee) with (*E*)-**9**, and the (*R*)-product (20% ee) with (*Z*)-**9**. This exciting work shows that the macrocycle can effectively control the chiral induction, thus allowing for an inversed selectivity when positioned on opposite sides of the catalytic center.

Rotaxanes have also been applied as chiral ligands in stereoselective transition metal catalysis. While those examples using axial chirality or centrochirality will not be discussed in detail here [27], a pioneering example by Goldup and coworkers has demonstrated that mechanically chiral rotaxanes can also be applied in stereoselective Au catalysis.

The mechanically planar chiral rotaxane was created by threading a nonsymmetrical axle through a directional macrocycle [28]. Based on the terminal diphenylphosphanyl group on the thread, this system was used as a monodentate ligand for Au(I). Thus, the corresponding chiral rotaxane–Au complex **10** was applied for the cyclopropanation of olefins with propargylic esters (Figure 5.8a). In the presence of Cu(I), which binds to the bipyridine unit and prevents the inhibition of the Au(I) center, the active rotaxane catalyst gave good stereoselectivities (62–92% de, 41–77% ee) for a range of different substituents (Figure 5.8b).

5.3 Catenanes in Enantioselective Catalysis

Notwithstanding the high relevance of rotaxanes as catalysts, catenanes are interesting candidates for catalyst development, although examples are still

(a)

Catalyst

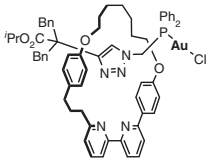

10

(b)

Cyclopropanation

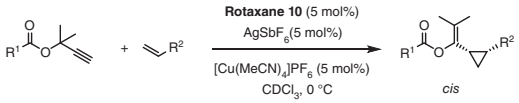

R^1	R^2	de (%)[a]	ee (%)[b]
Ph	Ph	88	57
Ph	Bn	62	42
Bn	Ph	92	54
4-CF_3-C_6H_4	Ph	92	45
4-MeO-C_6H_4	Ph	88	41
4-^{t}Bu-C_6H_4	Ph	90	74
3,5-(^{t}Bu)$_2$-C_6H_4	Ph	90	77

[a] Diastereomeric excess given for the *cis*-isomer.
[b] Enantiomeric excess given for the (*1S,2R*)-isomer.

Figure 5.8 Cyclopropanation using *Goldup's* mechanical chiral rotaxane **10**.

comparatively rare. While the synthesis of catenanes is oftentimes lower yielding than for rotaxanes, catenanes also possess a number of design advantages, such as a highly confined reaction environment at the center of the interlocked rings or the possibility for a topological chirality.

Up to date, the only described example on the use of catenanes in enantioselective catalysis was reported in 2017 by Niemeyer and coworkers. The group prepared a [2]-catenane **11** composed of two axially chiral (*S*)-1,1′-binaphthyl phosphates (Figure 5.9a) which acts as a bifunctional interlocked catalyst [29].

Applied for the asymmetric transfer hydrogenation of 2-substituted quinolines by Hantzsch esters, the optically pure bisphosphoric acid **11** in comparison to both the non-interlocked macrocycle **12** and the acyclic catalyst **13**, gave higher stereoselectivities for several substrates (Figure 5.9b). Various substituted quinolines regularly afforded high enantioselectivities with **11** (82–98% ee) but lower stereoinduction was observed with **12** and **13** (12–62% ee for **12** and 9–84% ee for **13**, respectively).

The outstanding stereoselectivities obtained for **11** are believed to be due to the catenane's interlocked nature as indicated by computational studies at the density functional theory (DFT) level. The stereodetermining transition state involves both phosphoric acids which are held together by a (mechano)intramolecular P(OH)···(O)P hydrogen bond. In case of **12** and **13**, dimerization by intermolecular hydrogen bonding is disfavored at low catalyst loadings leading to the participation of only one phosphoric acid in the transition state.

The mechanical bond in the catenane **11** is therefore believed to be crucial for the high stereoselectivities, since it both gives a high local concentration of phosphoric acids, and the necessary conformational flexibility to allow a cooperative action of the two functional groups.

In a recent mechanistic study, it was determined that the catalytic reactions with **11** and **12** also involve competing dimeric and the monomeric pathways, respectively [30]. This effect was most pronounced for catalyst **13**, which give preference for the (*S*)-enantiomer (−30% ee) of the tetrahydroquinoline product at low catalyst loading, while the (*R*)-enantiomer (+72% ee) was favored at high

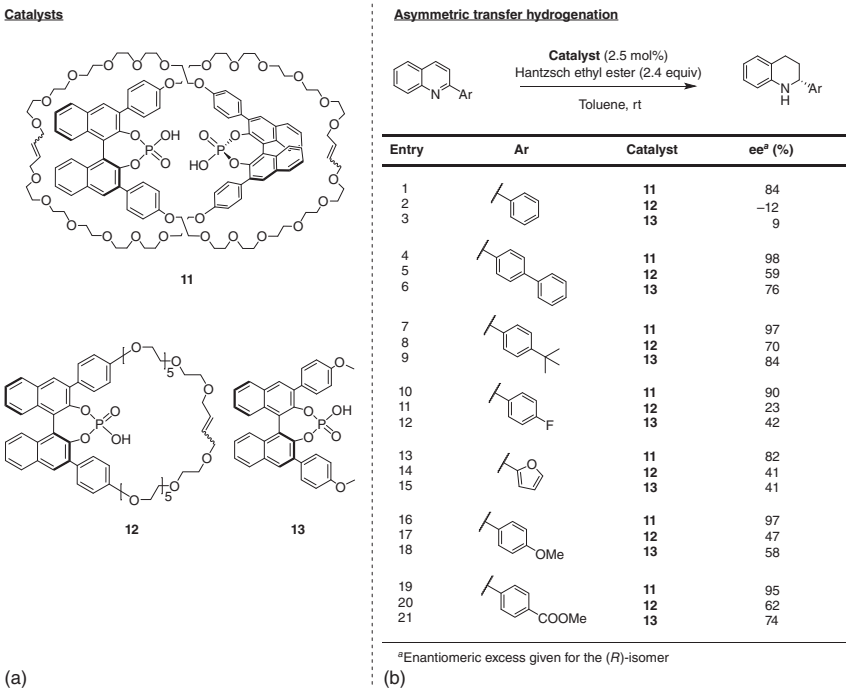

Entry	Ar	Catalyst	ee[a] (%)
1		**11**	84
2		**12**	–12
3		**13**	9
4		**11**	98
5		**12**	59
6		**13**	76
7		**11**	97
8		**12**	70
9		**13**	84
10		**11**	90
11		**12**	23
12		**13**	42
13		**11**	82
14		**12**	41
15		**13**	41
16		**11**	97
17		**12**	47
18		**13**	58
19		**11**	95
20		**12**	62
21		**13**	74

[a]Enantiomeric excess given for the (*R*)-isomer

(b)

Figure 5.9 Asymmetric transfer hydrogenation using *Niemeyer's* catenane **11** and catalysts **12** and **13**.

catalyst loading. This inversion of selectivity is caused by the competing monomeric and dimeric pathways. This demonstrates that the interlocking of both rings in catenane **11** allowed for the more stereoselective dimeric pathway to be effective even at low concentrations, thus demonstrating the benefits of interlocked catalysts for cooperative catalysis.

5.4 Molecular Knots in Enantioselective Catalysis

Molecular knots have long attracted chemists from a synthetic point of view. However, they are also highly interesting candidates for stereoselective catalysis, since they cannot only incorporate classical elements of chirality, but can also feature an inherent topological chirality.

A single example for the use of chiral knots in catalysis has been reported so far: from point chiral ligands, the Leigh group prepared the single-handed trefoil knot **14** (Figure 5.10a) [31]. The knotted structure features six centrochiral units, which lead to the exclusive formation of the Λ-coordination geometry around the central Eu ion.

Compound **15** was applied for the asymmetric Mukaiyama aldol reaction as a chiral Lewis acid catalyst. The Eu ion acts as a chiral Lewis acid inserted in the well-defined chiral environment created by the knot. The reaction of various

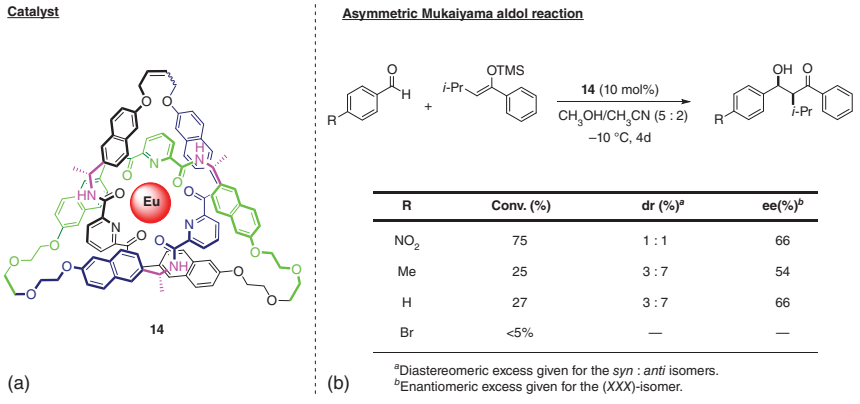

R	Conv. (%)	dr (%)[a]	ee(%)[b]
NO_2	75	1 : 1	66
Me	25	3 : 7	54
H	27	3 : 7	66
Br	<5%	—	—

[a]Diastereomeric excess given for the *syn* : *anti* isomers.
[b]Enantiomeric excess given for the (*XXX*)-isomer.

Figure 5.10 Asymmetric Mukaiyama aldol reaction using *Leigh's* chiral molecular knot **14**.

4-substituted benzaldehyde-derivatives with silyl enol ethers gave the corresponding products in up to 75% yield and 66% ee (Figure 5.10b).

5.5 Conclusion

Over the last years, there has been a huge interest in the application of interlocked molecules for catalysis, especially in enantioselective catalysis. This has opened a new chapter for the application of interlocked molecules. This research has already come a long way from the pioneering examples that included chiral elements into one of the subcomponents to the most recent works about mechanically chiral interlocked molecules for catalysis. However, it must be noted that the stereoselectivities that can be achieved with MIM catalysts are still moderate in many cases. Thus, the proof-of-concept for the use of MIMs in catalysis has now been well established, while the enantioinduction needs to be improved to justify the use of complex interlocked catalysts. However, mechanical and topological chirality can be seen as an additional design element (other than being the only source of chirality) that can help realize challenging catalytic transformations that have eluded organocatalysis so far. Beyond that, some avenues in MIM catalysis remain largely unexplored, such as the use of topological chirality in catenanes or the use of dynamic co-conformational chirality. Thus, we believe there is a bright future for the applications of MIMs in catalysis and particularly in stereoselective catalysis.

References

1 (a) Bruns, C.J. and Stoddart, J.F. (2016). *The Nature of the Mechanical Bond: From Molecules to Machines*. Hoboken, New Jersey: Wiley. (b) Mena-Hernando, S. and Pérez, E.M. (2019). *Chem. Soc. Rev.* 48: 5016–5032.

2 Xue, M., Yang, Y., Chi, X. et al. (2015). *Chem. Rev.* 115: 7398–7501.

3 (a) Gil-Ramírez, G., Leigh, D.A., and Stephens, A.J. (2015). *Angew. Chem. Int. Ed.* 54: 6110–6150. (b) Evans, N.H. and Beer, P.D. (2014). *Chem. Soc. Rev.* 43: 4658–4683.

4 (a) Forgan, R.S., Sauvage, J.-P., and Stoddart, J.F. (2011). *Chem. Rev.* 111: 5434–5464. b) Fielden, S.D.P., Leigh, D.A., and Woltering, S.L. (2017). *Angew. Chem. Int. Ed.* 56: 11166–11194.

5 (a) Ayme, J.-F., Beves, J.E., Campbell, C.J., and Leigh, D.A. (2013). *Chem. Soc. Rev.* 42: 1700–1712. (b) Lewis, J.E.M., Beer, P.D., Loeb, S.J., and Goldup, S.M. (2017). *Chem. Soc. Rev.* 46: 2577–2591. (c) Beves, J.E., Blight, B.A., Campbell, C.J. et al. (2011). *Angew. Chem. Int. Ed.* 50: 9260–9327.

6 (a) Dichtel, W.R., Miljanić, O.Š., Zhang, W. et al. (2008). *Acc. Chem. Res.* 41: 1750–1761. (b) Kay, E.R. and Leigh, D.A. (2005). *Top. Curr. Chem.* 262: 133–177. (c) Schalley, C.A., Weilandt, T., Brüggemann, J., and Vögtle, F. (2004). *Top. Curr. Chem.* 248: 141–200. (d) Spence, G.T. and Beer, P.D. (2012). *Acc. Chem. Res.* 46: 571–586. (e) Beer, P.D., Sambrook, M.R., and Curiel, D. (2006). *Chem. Commun.*: 2105–2117. (f) Meyer, C.D., Joiner, C.S., and Stoddart, J.F. (2007). *Chem. Soc. Rev.* 36: 1705–1723.

7 (a) Crowley, J.D., Goldup, S.M., Lee, A.L. et al. (2009). *Chem. Soc. Rev.* 38: 1530–1541. (b) Denis, M. and Goldup, S.M. (2017). *Nat. Rev. Chem.* 1: 0061.

8 Lewis, J.E., Galli, M., and Goldup, S.M. (2017). *Chem. Commun.* 53: 298–312.

9 van Dongen, S.F.M., Cantekin, S., Elemans, J.A.A.W. et al. (2014). *Chem. Soc. Rev.* 43: 99–122.

10 (a) Evans, N.H. (2018). *Chem. Eur. J.* 24: 3101–3112. (b) Jamieson, E.M.G., Modicom, F., and Goldup, S.M. (2018). *Chem. Soc. Rev.* 47: 5266–5311.

11 Pairault, N. and Niemeyer, J. (2018). *Synlett* 29: 689–698.

12 Balzani, V., Credi, A., and Venturi, M. (2009). *Chem. Soc. Rev.* 38: 1542–1550.

13 Kottas, G.S., Clarke, L.I., Horinek, D., and Michl, J. (2005). *Chem. Rev.* 105: 1281–1376.

14 Feringa, B.L. and Browne, W.R. (eds.) (2011). *Molecular Switches*. Weinheim, Germany: Wiley-VCH.

15 (a) Caballero, A., Zapata, F., and Beer, P.D. (2013). *Coord. Chem. Rev.* 257: 2434–2455. (b) Langton, M.J. and Beer, P.D. (2014). *Acc. Chem. Res.* 47: 1935–1949.

16 (a) Bruns, C.J. and Stoddart, J.F. (2014). *Acc. Chem. Res.* 47: 2186–2199. (b) Collin, J.-P., D-Buchecker, C., Gaviña, P. et al. (2001). *Acc. Chem. Res.* 34: 477–487.

17 (a) Feringa, B.L. (2017). *Angew. Chem. Int. Ed.* 56: 11060–11078. (b) Sauvage, J.-P. (2017). *Angew. Chem. Int. Ed.* 56: 11080–11093. (c) Stoddart, J.F. (2017). *Angew. Chem. Int. Ed.* 56: 11094–11125.

18 (a) Kwamen, C. and Niemeyer, J. (2021). *Chem. Eur. J.* 27: 175–186. (b) Mitra, R. and Niemeyer, J. (2018). *ChemCatChem* 10: 1221–1234. (c) Sluysmans, D. and Stoddart, J.F. (2019). *Trends Chem.* 1: 185–197.

19 Tachibana, Y., Kihara, N., and Takata, T. (2004). *J. Am. Chem. Soc.* 126: 3438–3439.

20 Xu, K., Nakazono, K., and Takata, T. (2016). *Chem. Lett.* 45: 1274–1276.

21 (a) Blanco, V., Carlone, A., Hänni, K.D. et al. (2012). *Angew. Chem. Int. Ed.* 51: 5166–5169. (b) Blanco, V., Leigh, D.A., Lewandowska, U. et al. (2014). *J. Am. Chem. Soc.* 136: 15775–15780. (c) Beswick, J., Blanco, V., De Bo, G. et al. (2015). *Chem. Sci.* 6: 140–143. (d) Kwan, C.-S., Chan, A.S.C., and Leung, K.C.-F. (2016). *Org. Lett.* 18: 976–979. (e) Eichstaedt, K., Jaramillo-Garcia, J., Leigh, D.A. et al. (2017). *J. Am. Chem. Soc.* 139: 9376–9381.

22 Blanco, V., Leigh, D.A., Marcos, V. et al. (2014). *J. Am. Chem. Soc.* 136: 4905–4908.

23 Calles, M., Puigcerver, J., Alonso, D.A. et al. (2020). *Chem. Sci.* 11: 3629–3635.

24 (a) Pairault, N., Zhu, H., Jansen, D. et al. (2020). *Angew. Chem. Int. Ed.* 59: 5102–5107.

25 Cakmak, Y., E-Cakmak, S., and Leigh, D.A. (2016). *J. Am. Chem. Soc.* 138: 1749–1751.

26 Dommaschk, M., Echavarren, J., Leigh, D.A. et al. (2019). *Angew. Chem. Int. Ed.* 58: 14955–14958.

27 For MIMs with axial chirality that have been used in transition-metal catalysis see: (a) Hattori, G., Hori, T., Miyake, Y., and Nishibayashi, Y. (2007). *J. Am. Chem. Soc.* 129: 12930–12931. (b) Li, Y., Feng, Y., He, Y.-M. et al. (2008). *Tetrahedron Lett.* 49: 2878–2881. For MIMs with centrochirality that have been used in transition-metal catalysis see: (c) Hoekman, S., Kitching, M.O., Leigh, D.A. et al. (2015). *J. Am. Chem. Soc.* 137: 7656–7659.

28 Heard, A.W. and Goldup, S.M. (2020). *Chem.* 6: 994–1006.

29 Mitra, R., Zhu, H., Grimme, S., and Niemeyer, J. (2017). *Angew. Chem. Int. Ed.* 56: 11456–11459.

30 Jansen, D., Gramüller, J., Niemeyer, F. et al. (2020). *Chem. Sci.* 11: 4381–4390.

31 Gil-Ramírez, G., Hoekman, S., Kitching, M.O. et al. (2016). *J. Am. Chem. Soc.* 138: 13159–13162.

6

Catalytic Supramolecular Gels

Beatriu Escuder

Universitat Jaume I, Institute of Advanced Materials, INAM, Av. Sos Baynat s/n, 12006 Castelló, Spain

6.1 Introduction

Supramolecular gels are soft materials formed by the sole concurrence of non-covalent interactions. This category includes physically crosslinked polymer gels and molecular gels, which are those formed by low-molecular weight compounds (low-molecular weight gels, LMWGs). Here, we will focus on the latter family which has received a great attention in the last two decades [1]. As a member of the supramolecular "family," LMWGs are assembled by weak interactions and present an inherent dynamic behavior and responsiveness. As shown in Figure 6.1, these materials are typically formed by the action of a trigger which provokes the solution-to-gel transition. LMWGs are usually formed by 1D aggregates that grow and crosslink leading to a 3D fibrillar network that spans the sample and precludes the motion of the solvent upon inversion of the container. Those aggregates are nothing but supramolecular polymers that grow exponentially in length thanks to the efficiency of cooperative supramolecular interactions. In addition, the incorporation of functional fragments to the basic assembling structure leads to the formation of valuable functional supramolecular materials [2].

LMWGs have received great attention in diverse fields of research such as food science, healthcare, biomedicine, drug delivery, waste and oil spills recovery, and catalysis as well [3]. The reasons for that are, among others, their synthetic simplicity, high purity, and good biocompatibility and biodegradability, compared to polymer-based gels. On the other hand, they show a high structural diversity, meaning that most of functional groups and structural fragments can be incorporated as far as they do not interfere with the assembly ability of the gelator backbone. Unfortunately, their mechanical stability is not as good as for polymer gels which could be a drawback for certain applications. However, this problem can be overcome by preparing, for instance, hybrid polymer LMWGs which may combine the properties of both types of gels.

Supramolecular Catalysis: New Directions and Developments, First Edition.
Edited by Piet W.N.M. van Leeuwen and Matthieu Raynal.

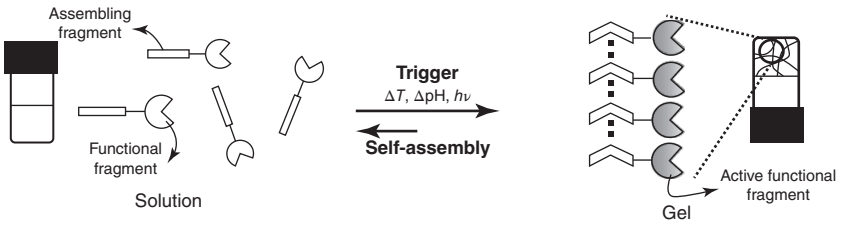

Figure 6.1 Cartoon of LMWGs self-assembly.

6.2 Catalytic LMWGs

The application of LMWGs in catalysis may be addressed from two different perspectives. In one hand, looking from a materials point of view, these gels are microporous heterogeneous systems formed by a network of thin fibers with pools of solvent entrapped within. These fibers, having a high aspect ratio, present a large available surface in which catalytic groups could be accessible to substrates in solution. On the other hand, from a molecular point of view, catalytic sites can be constructed starting from conveniently functionalized gelators. These gelators can, for instance, incorporate well-known catalytic fragments or maybe pre-catalytic moieties that become active only after self-assembly. On top of that, binding sites can be created by placing specific recognition regions in the molecular design. For instance, gelators bearing long alkyl chains or aromatic fragments have been shown to create hydrophobic pockets that if located close to the catalytic site may lead to certain substrate selectivity. In addition, the role of solvent in these catalytic systems has to be carefully considered since it will determine which intermolecular interactions will prevail in gelator–gelator assembly and gelator–substrate interaction as well.

The first mention to a potential catalytic LMWG dates back to 1990 when Inoue and coworkers observed the formation of a gel accompanying an increase in stereoselectivity of the asymmetric addition of hydrogen cyanide to *m*-phenoxybenzaldehyde in toluene catalyzed by a histidine-based cyclodipeptide [4] (Figure 6.2a). At this point, the presence of the gel was regarded as an obstacle for the analysis of results. Further studies developed by other groups revealed that catalyst self-assembly was crucial for the catalytic action [6]. However, it was not until more than 10 years later than Xu and coworkers developed the first catalytic LMWG on purpose, in particular a multitopic pyridine-based gelator to be used for the aerobic oxidation of benzyl alcohol catalyzed by Pd (Figure 6.2b) [5].

Inspired by these pioneering reports, our group started to explore the wide possibilities for LMWGs in the field of catalysis, including both organocatalysis and metallocatalysis [7]. Some selected examples will be discussed in the following sections.

6.3 LMWGs in Organocatalysis

Taking nature as inspiration, different groups including our team have foreseen the opportunity of using functional side chains of amino acids as organocatalytic

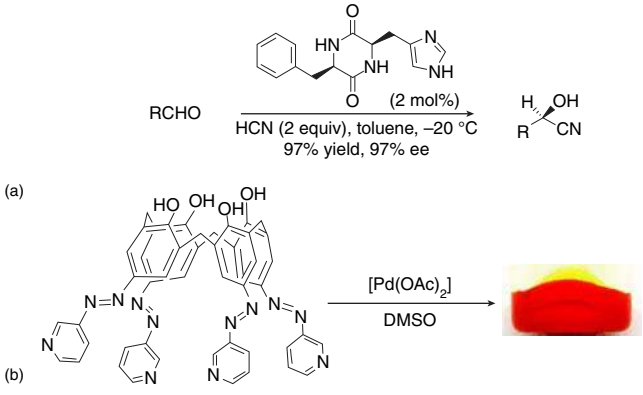

Figure 6.2 Pioneering supramolecular catalysis in gels. (a) Hydrocyanation of an aldehyde catalyzed by a self-assembled L-histidine-based cyclodipeptide in a toluene organogel. (b) Multitopic pyridine ligand that forms an orange catalytic gel in DMSO after addition of $Pd(OAc)_2$. Source: Xing et al. [5]. Reproduced with permission of John Wiley & Sons.

fragments. One of the most interesting amino acids for that purpose is histidine (H) which is found in the active site of different hydrolases, bearing an imidazole catalytic fragment. Several examples of gelators including H or imidazole moieties have been reported to form catalytic LMWGs. In our group, we have prepared compound **ImV8**, a bolaamphiphilic structure based on L-valine (V) bearing two imidazole terminal fragments (Figure 6.3a). **ImV8** forms pH-responsive hydrogels that are catalytically active for the hydrolysis of *p*-nitrophenyl acetate (PNPA) in their aggregated state [8]. The catalytic performance of **ImV8** hydrogels, which are formed in the pH range of 6–8, is superior to non-assembling analogues, in particular for the lowest pH values, and shows a Michaelis–Menten catalytic profile. We demonstrated that this improvement in catalysis is related to the combination of two effects. In one hand, a pK_a shift leads to the non-equivalence of the two imidazole moieties and a significative abundance of monoprotonated **ImV8** in the pH range 6–6.5 which could participate in a cooperative catalytic mechanism involving non-protonated and protonated imidazole residues. On the other hand, the presence of hydrophobic pockets within the gel fibers could be demonstrated with the help of 1-anilino-naphthalene-8-sulfosnate (ANS) as a hydrophobic probe. Moreover, this hydrogel was also able to hydrolyze even non-activated esters such as phenylalanine methyl esters, demonstrating the emergence of new catalytic abilities after self-assembly.

A second family of catalytic LMWGs studied in our group is based on L-proline (P). Although its side chain does not play a catalytic role in enzymes, L-proline itself and several derivatives have been widely used as abiotic mimics of Aldolase I. In particular, L-proline derivatives are described as catalysts for enamine-based C—C bond forming reactions such as aldol condensations or Michael additions among others [9]. Therefore, we have studied L-proline-based hydrogels and organogels and found once again that supramolecular self-assembly leads to unique catalytic features. Two different gelator backbones have been employed: L-valine-based bolaamphiphiles (**PVn**) (Figure 6.3a) and di/tripeptide amphiphiles

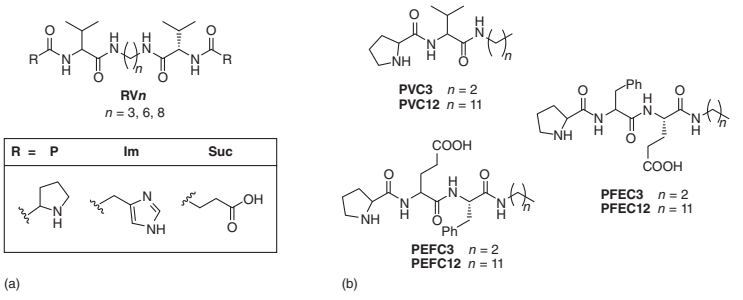

Figure 6.3 Molecular structures of compounds studied for organocatalysis: (a) bolaamphiphiles and (b) peptide amphiphiles.

(**PVC12**, **PFEC12**, **PEFC12**) (Figure 6.3b). Peptide amphiphiles were designed as a combination of a peptidic fragment able to assemble into a β-sheet like structure and a long alkyl chain that contributes to aggregation by van der Waals interactions and the hydrophobic effect in aqueous media. L-proline residue was connected at the N-terminus in order to facilitate their accessibility at the fiber–solution interphase. Compound **PVC12**, the first of the series to be studied, formed hydrogels in water with a minimum gel concentration of 2 mM and the hydrogel was used as an efficient heterogeneous catalyst for the direct aldol reaction between 4-nitrobenzaldehyde and cyclohexanone, leading to the formation of the corresponding aldol (*S*,*R*)-*anti* as a major product after 24 hours of reaction at 5 °C (99%, 92.8 dr, 88% ee) [10]. Moreover, the gel was not destroyed during the reaction and it was used in two additional runs without the loss of efficiency and stereoselectivity. The formation of enamine intermediates was confirmed and a catalytic mechanism similar to Aldolase I was proposed. Afterward, the study was extended to aliphatic methyl ketones in order to understand the potential role of the hydrophobic segments of substrates and gelator molecules [11]. Reactions between different methyl ketones and 4-nitrobenzaldehyde were performed in the presence of hydrogel **PVC12** at 25 °C during 24 hours. Polar ketones such as 1,3-dihydroxyacetone and acetone, or even 2-butanone, did not significantly react after this time. In the case of 2-pentanone, 2-hexanone, 2-heptanone, and 2-octanone, moderate yields were obtained. However, the yields were significatively improved for 2-nonanone and 2-dodecanone with conversions up to 88% and 98%, respectively. Moreover, it was noticed that the yield of reaction did not follow a linear increase with log *P*, but there was a sudden increase going from an eight-carbon to a nine-carbon ketone. This effect was associated with a tight binding of the alkyl tail into the aliphatic bilayer structure within hydrogel fibers for the longest ketone analogs. In addition to that, the same reactions were assayed with **PVC3** as catalyst, an analog which is fully soluble in water, and none of the ketones reacted in solution, revealing the determining role of supramolecular self-assembly in catalysis.

A second generation of the peptide amphiphile family was prepared in which modifications in the peptide backbone were introduced. L-valine was replaced by a dipeptide fragment including L-phenylalanine (F) and L-glutamic acid (E) with the aim to introduce additional supramolecular interactions between hydrogelator

and substrates close to the catalytic site. Thus, two tripeptide amphiphiles were prepared, **PFEC12** and **PEFC12** that self-assembled in PBS at pH 7 into hydrogels and fibrillar suspensions, respectively [12]. Their application in the direct aldol reaction between 4-nitrobenzaldehyde and cyclohexanone revealed that the relative position of F and E had an impact on the catalytic performance of the aggregated catalyst in favor of **PFEC12**. Nuclear magnetic resonance (NMR) experiments showed that after the addition of cyclohexanone to the aggregates, **PFEC12** incorporates twice of the amount of ketone to the gel phase (NMR-silent) than **PEFC12**. This was also supported by ANS binding experiments which showed a higher hydrophobicity for **PFEC12** fibers. However, kinetic studies did not show a Michaelis–Menten saturation profile but a linear increase of rate with substrate concentration, suggesting that there were no specific substrate binding and the fiber hydrophobic regions were acting as reservoirs of hydrophobic substrates as in most examples of micellar catalysis. Moreover, these catalysts were used for the synthesis of biologically relevant aldols such as tetrose derivatives with good yield and stereoselectivity.

As mentioned before, switching from aqueous media to organic solvents replaces the hydrophobic effect by other noncovalent interactions such as hydrogen bonding as the major driving forces for self-assembly. Bolaamphiphilic **PVn** derivatives (Figure 6.3a) have been shown to form organogels in acetonitrile and toluene among other solvents [13]. Structural studies suggested that, in those organic solvents, gelator molecules switched from a folded conformation in solution to extended conformations in the gel fibers stabilized by intramolecular and intermolecular H-bonding, respectively. However, the polarity of the solvent had an additional effect on the L-proline catalytic site. In the case of toluene gels, L-proline residue was able to form enamine intermediates and gels of **PV6** could be used as catalysts for the 1,4-conjugate addition of cyclohexanone to *trans*-β-nitrostyrene [14]. However, none of the acetonitrile gels of the **PVn** series was able to catalyze enamine-based reactions. In the first experiments, the gels were assayed for the direct aldol reaction between 4-nitrobenzaldehyde and acetone and compared with the catalytic activity of the gelators in solution. It is worth mentioning here that in these organogels there is a considerable fraction of gelator molecules that remain in solution in a solubility-driven equilibrium with the gel fiber. Therefore, it may happen that those molecules present some catalytic activity overlapping the gel performance. Thus, it is necessary to evaluate the catalytic activity of those solutions separately. In the case of **PVn** gels in acetonitrile, 25–50% of gelator molecules remained in solution and the yield of aldol was similar for the whole systems and for the solutions, which clearly proved that the gels were inactive as catalysts for the aldol reaction. However, it was observed that the enantiomer ratio of the aldol produced was decreasing with time when the gel was present, especially for gelators **PV6** and **PV8**. This finding was investigated and it was revealed an increase in N-terminal proline basicity of c. 3 pK_a units on going from solution to gel phase (Figure 6.4) which provoked the racemization of the aldol product. This effect could be ascribed to the close proximity of the L-proline residues on the fiber surface leading to the cooperative assistance of several basic centers in a proton relay system [15].

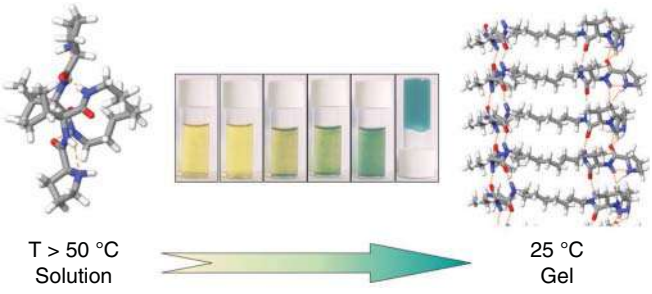

Figure 6.4 Molecular models of compound **PV8** in solution and in the gel phase and Bromothymol blue color change associated with aggregation-induced pK_a shift. Source: Rodríguez-Llansola et al. [15]. Reproduced with permission of Royal Society of Chemistry.

Moreover, we took advantage of this unexpected supramolecular basicity enhancement for the use of **PV8** gels as basic catalysts for the Henry nitroaldol reaction between nitromethane and aromatic aldehydes [16]. Very interestingly, acetonitrile could be replaced by nitromethane itself as solvent without loss of basicity and reactions within the gel phase proceeded with quantitative yields of nitroaldol product. In addition, the catalytic activity of **PV8** could be switched off simply by heating above the gel-to-solution transition temperature (T_{gel}).

6.4 LMWGs in Metallocatalysis

Those LMWGs that contain metals are known as metallogels and comprise coordination polymer gels, organometallic gelators, and self-assembled gelators that act as multitopic ligands for metals [17]. The structural role of the metal ions is different in each type. Coordination polymer gels use the metal ion coordination as the link that holds the 1D aggregates leading to strong gels; organometallic gelators incorporate the metal in the monomer and its aggregation is not directly related to coordination. In our group, we have been working since many years with the third type in which the gel fibers are preformed and the metal to be complexed is added after gel assembly [18]. For instance, compounds **PhTzVn** (Figure 6.5) have been designed based on the L-valine bolaamphiphilic backbone with phenyltriazole fragments as end groups [19]. Those groups have been selected to mimic the multitopic Cu(I) coordination by tris[(1-benzyl-1*H*-1,2,3-triazol-4-yl)methyl]amine (TBTA) which leads to an efficient catalyst for the copper-catalyzed azide-alkyne cycloaddition reaction (CuAAC) in aqueous media (Figure 6.5b). Compounds **PhTzVn** formed gels in water and alcohols and exhibited a good catalytic activity for the model reaction between phenylacetylene and benzylazide. In addition, as can be seen in Figure 6.5a, these gelators were synthesized by CuAAC of diazide precursors **N_3VnN$_3$**. Those precursors, based on a similar assembling backbone, formed gels in methanol either in the absence or presence of Cu(I). Therefore, we envisioned the possibility of developing an autocatalytic gel system in which **Cu^I-PhTzVn** gels could catalyze their own synthesis. Figure 6.5c collects the reaction rates

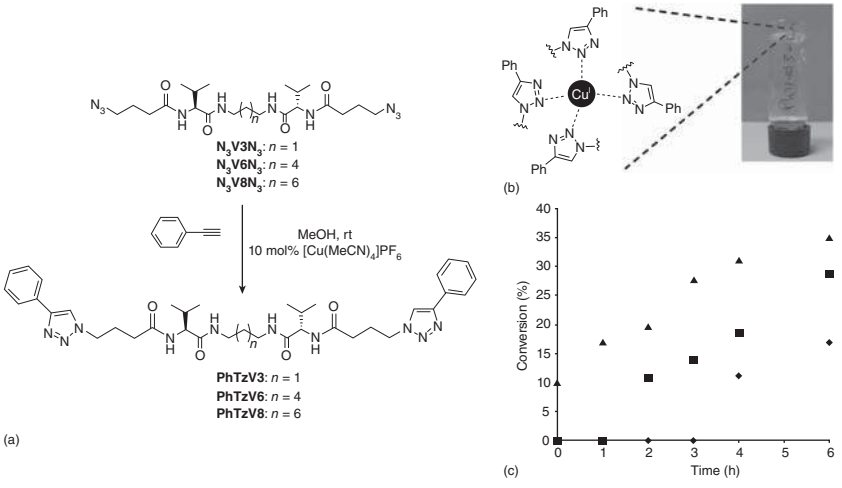

Figure 6.5 (a) Scheme of the synthesis of **PhTzVn** from diazides $\mathbf{N_3VnN_3}$. (b) Scheme of the Cu(I) coordination to the gel network and macroscopic image of the metallogel. (c) Kinetics of the CuAAC between $\mathbf{N_3VnN_3}$ and phenylacetylene in the presence of 5 mol% of $[Cu(MeCN)_4]PF_6$ (◆), 10 mol% of $[Cu(MeCN)_4]PF_6$ (■), and 10 mol% of metallogel **Cu-PhTzV3** (▲). Source: Araújo et al. [19]. Reproduced with permission of John Wiley & Sons.

for that reaction starting from **PhTzV3** gelled with $[Cu(MeCN)_4]PF_6$ and from a diazide gel containing 10% of $\mathbf{Cu^I}$**-PhTzV3**. In the absence of an initial amount of $\mathbf{Cu^I}$**-PhTzV3,** an induction time with little conversion was observed corresponding to the time required to obtain a minimum amount of gel-coordinated copper after diffusion and slow catalysis by uncoordinated $[Cu(MeCN)_4]PF_6$. In the presence of $\mathbf{Cu^I}$**-PhTzV3** the reaction started immediately.

6.5 Multicomponent Supramolecular Materials Involving Catalytic LMWGs

Multicomponent gel materials can be formed by the combination of either several LMWGs or a LMWG and another self-assembled building block. These new materials could benefit from synergies between the different constituents in terms of stability or activity [20]. For instance, a multicomponent material formed by a LMWG and a polymer physical gel may present better mechanical stability than a single LMWG which could be very interesting if a catalytic LMWG has to be applied under flow [21]. On the other hand, the combination of LMWGs with different catalytic groups may lead to materials useful for tandem catalytic reactions. In our group, we described for the first time the use of two-component hydrogels for a tandem reaction, an acetal deprotection–aldol reaction tandem process (Figure 6.6e) [22]. These catalytic hydrogels were formed by mixtures of proline-based gelators (**PV8** and **PVC12**) with an acidic gelator (**SucV8**) in aqueous media. In principle, when two different gelators are put together, they can either co-assemble into

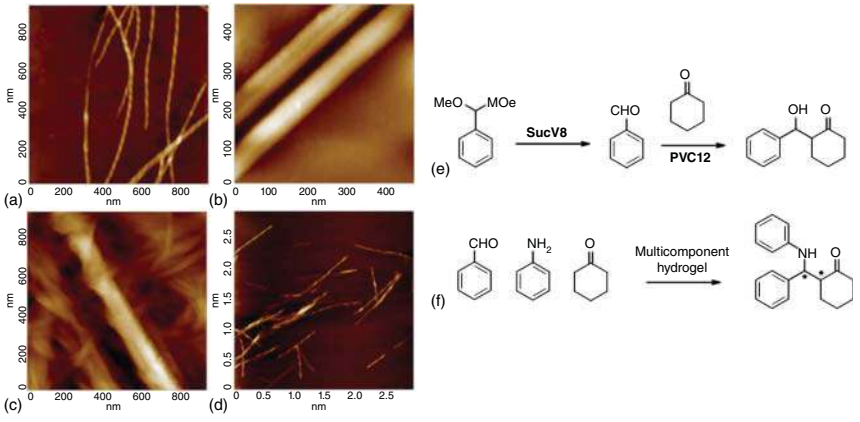

Figure 6.6 AFM images of hydrogels of (a) **SucV8**, (b) **PVC12**, (c) **PVC12**+**SucV8,** and (d) **PV8**+**SucV8**. Reaction schemes of the deacetalization–aldol tandem reaction (e) and three-component Mannich reaction catalyzed by multicomponent hydrogels. Source: Singh et al. [22]. Reproduced with permission of Royal Society of Chemistry.

a single supramolecular entity or self-sort into independent networks [23]. In our case, we prepared two different materials: **PV8** and **SucV8** present a similar bolaamphiphilic assembling backbone, so they should be prone to co-assemble; **PVC12** bears a dissimilar assembling fragment, so a self-sorted material was predicted for **PVC12** + **SucV8** mixtures. As can be seen in Figure 6.6a–d, atomic force microscopy (AFM) images of single components and mixtures confirmed our hypothesis.

Hydrogels of **SucV8** and **PVC12** showed a very distinct fibrillar network. **SucV8** gel was formed by very thin helical fibers, whereas **PVC12** gel was made of larger and more rigid rod-like fibers. Mixing of both gelators (**PVC12** + **SucV8**) resulted in a material in which the two independent networks were clearly identified. In the case of mixing **PV8** + **SucV8**, a single fibrillar network was observed, formed by shorter helical fibers. The difference between the two mixed gels was also confirmed by wide-angle X-ray diffraction (WAXD), thermal stability, and rheological studies, suggesting that **PV8** + **SucV8** were co-assembling. The spatial disposition of the functional groups in both systems may be relevant for their application in catalysis. The disposition of proline and acidic residues in close proximity may lead to the formation of salt bridges and the consequent inactivation of proline for enamine-based catalysis. This was the case when the co-assembled hydrogel **PV8** + **SucV8** was used as a catalyst: it was observed that the acetal deprotection step was successful; however, the aldol reaction did not take place. On the contrary, in the case of self-sorted hydrogel **PVC12** + **SucV8,** the tandem reaction proceeded to the final aldol product with good yield and stereoselectivity. This suggests that, in this case, the two networks were working independently in each of the two steps of the tandem process. These two-component systems were also studied for a three-component Mannich reaction (Figure 6.6f) [24]. In that case, both proline and acidic gelators were able to catalyze the reaction and a cooperation vs. competition

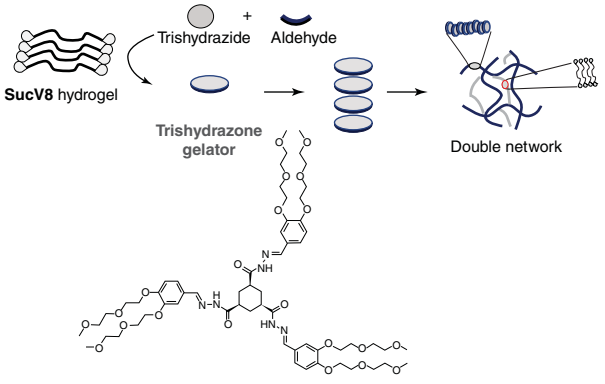

Figure 6.7 *In situ* synthesis of a double-network hydrogel catalyzed by **SucV8** hydrogel.

"social" behavior was observed depending on the relative concentration of gelators in the mixtures. Overall, this work highlights the fact that subtle molecular variations in multicomponent LMWGs may lead to diverse and complex catalytic scenarios. For instance, we have also foreseen the possibility of using a catalytic LMWG network to facilitate the *in situ* synthesis and supramolecular self-assembly of a second LMWG interpenetrated network (Figure 6.7) [25]. For that purpose, we have used acidic hydrogelator **SucV8** network as a catalyst for the synthesis of a trishydrazone gelator that self-assembles leading to a double-network hydrogel through a completely different orthogonal approach.

Finally, we recently demonstrate that catalytic LMWGs can be miniaturized to the microscale without the loss of catalytic activity. For doing so, we prepared multicomponent materials consisting of a LMWG network of compound **ImV8** encapsulated within a polymersome formed by a PEG-PBG di-block co-polymer (PEG = poly(ethyleneglycol), PBG = poly(γ-benzyl-L-glutamate)). The orthogonal self-assembly of the system could be achieved thanks to the pH responsiveness of **ImV8** that was encapsulated in a non-aggregated state at acidic pH and switched to the catalytically active aggregated state within the polymersome at pH 6–7. A fluorogenic ester substrate (pyranine acetate) was introduced together with the gelator, its hydrolysis was switched on at neutral pH, and the advance could be nicely followed by flow cytometric analysis of the catalytic particles with time [26].

6.6 Concluding Remarks

In summary, supramolecular gels made by low-molecular weight compounds offer unique opportunities in catalysis. We have shown that complex functional materials with emerging catalytic activity can be obtained by self-assembling very simple compounds. As there is no restriction on the kind of functional groups that can be incorporated in a gelator, the scope of application of LMWGs in catalysis is unlimited. Moreover, LMWGs can be combined with other self-assembling entities, leading to complex catalytic systems. The contribution of LMWGs to the field of

supramolecular catalysis is still incipient and there is a wide prospect for new applications in, for instance, catalysis in biological settings or industrial catalysis, among others.

Acknowledgments

Financial support from the Spanish Government (Grants CTQ2009-13961, CTQ2012-37735 and CTQ2017-91471-EXP), Universitat Jaume I Research Programme (Grants P1·1B2013-57 and UJI-B2017-22), and EU (Grant PITN-GA-2012-316656 – SMARTNET) is deeply acknowledged. Special thanks are given to PhD and postdoc researchers who have been sharing their enthusiasm with me working on catalytic gels during the last decade (F. Rodríguez-Llansola, C. Berdugo-Gumbau, M. Tena-Solsona, S. Díaz-Oltra, N. Singh, M. Araujo and R. Martí-Centelles).

References

1 (a) Smith, D.K. (2008). *Molecular Gels—Nanostructured Soft Materials in Organic Nanostructures* (eds. J.L. Atwood and J.W. Steed). Weinheim: Wiley-VCH. (b) Guenet, J.–.M. (2016). *Organogels. Thermodynamics, Structure, Solvent Role and Properties*. Springer. (c) Weiss, R.G. (ed.) (2018). *Molecular Gels – Structure and Dynamics*. Cambridge: Royal Society of Chemistry. (d) Segarra-Maset, M.D., Nebot, V.J., Miravet, J.F., and Escuder, B. (2013). Control of molecular gelation by chemical stimuli. *Chem. Soc. Rev.* 42: 7086–7098.

2 Escuder, B. and Miravet, J.F. (eds.) (2014). *Functional Molecular Gels*. Cambridge: Royal Society of Chemistry.

3 Draper, E.R. and Adams, D.J. (2017). Low-molecular-weight gels: the state of the art. *Chem* 3: 390–410.

4 Tanaka, K., Mori, A., and Inoue, S. (1990). The cyclic dipeptide cyclo[(*S*)-phenylalanyl-(*S*)-histidyl] as a catalyst for asymmetric addition of hydrogen-cyanide to aldehydes. *J. Org. Chem.* 55: 181–185.

5 Xing, B., Choi, M.-F., and Xu, B. (2002). Design of coordination polymer gels as stable catalytic systems. *Chem. Eur. J.* 8: 5028–5032.

6 (a) Davie, E.A.C., Mennen, S.M., Xu, Y., and Miller, S.J. (2007). Asymmetric catalysis mediated by synthetic peptides. *Chem. Rev.* 107: 5759–5812. (b) Schoenebeck, F. and Houk, K.N. (2009). Theoretical study of the catalysis of cyanohydrin formation by the cyclic dipeptide catalyst cyclo[(*S*)-His-(*S*)-Phe]. *J. Org. Chem.* 74: 1464–1472.

7 (a) Escuder, B., Rodríguez-Llansola, F., and Miravet, J.F. (2010). Supramolecular gels as active media for organic reactions and catalysis. *New J. Chem.* 34: 1044–1054. (b) Singh, N., Tena-Solsona, M., Miravet, J.F., and Escuder, B. (2015). Towards supramolecular catalysis with small self-assembled peptides. *Isr. J. Chem.* 55: 711–723.

8 Singh, N., Conte, M.P., Ulijn, R.V. et al. (2015). Insight into the esterase like activity demonstrated by an imidazole appended self-assembling hydrogelator. *Chem. Commun.* 51: 13213–13216.

9 (a) List, B. (2004). *Amine-Catalyzed Aldol Reactions in Modern Aldol Reactions*, vol. 1 (ed. R. Mahrwald). Weinheim: Wiley-VCH. (b) Enders, D., Hüttl, M.R.M., Grondal, C., and Raabe, G. (2006). Control of four stereocentres in a triple cascade organocatalytic reaction. *Nature* 441: 861–863.

10 Rodríguez-Llansola, F., Miravet, J.F., and Escuder, B. (2009). A supramolecular hydrogel as a reusable heterogeneous catalyst for the direct aldol reaction. *Chem. Commun.* 45: 7303–7305.

11 Berdugo, C., Miravet, J.F., and Escuder, B. (2013). Substrate selective catalytic molecular hydrogels: the role of the hydrophobic effect. *Chem. Commun.* 49: 10608–10610.

12 Tena-Solsona, M., Nanda, J., Díaz-Oltra, S. et al. (2016). Emergent catalytic behavior of self-assembled low molecular weight peptide-based aggregates and hydrogels. *Chem. Eur. J.* 22: 6687–6694.

13 Rodríguez-Llansola, F., Escuder, B., Hamley, I.W. et al. (2012). Structural and morphological studies of the dipeptide-based L-Pro-L-Val organocatalytic gels and their rheological behaviour. *Soft Matter* 8: 8865–8872.

14 Rodríguez-Llansola, F., Miravet, J.F., and Escuder, B. (2010). Supramolecular catalysis with extended aggregates and gels: inversion of stereoselectivity caused by self-assembly. *Chem. Eur. J.* 16: 8480–8486.

15 Rodríguez-Llansola, F., Escuder, B., and Miravet, J.F. (2009). Remarkable increase in basicity associated with supramolecular gelation. *Org. Biomol. Chem.* 7: 3091–3094.

16 Rodríguez-Llansola, F., Escuder, B., and Miravet, J.F. (2009). Switchable performance of an L-proline-derived basic catalyst controlled by supramolecular gelation. *J Am. Chem. Soc.* 131: 11478–11484.

17 (a) Wu, H., Zheng, J., Kjoniksen, A.-L. et al. (2019). Metallogels: availability, applicability and advanceability. *Adv. Mater.* 31: 1806204. (b) Zhang, J.Y. and Su, C.Y. (2013). Metal-organic gels: from discrete metallogelators to coordination polymers. *Coord. Chem. Rev.* 257: 1373–1408. (c) Tam, A.Y. and Yam, V.W. (2013). Recent advances in metallogels. *Chem. Soc. Rev.* 42: 1540–1567.

18 Miravet, J.F. and Escuder, B. (2005). Pyridine-functionalised ambidextrous gelators: towards catalytic gels. *Chem. Commun.* 41: 5796–5798.

19 Araújo, M., Díaz-Oltra, S., and Escuder, B. (2016). Triazolyl-based molecular gels as ligands for autocatalytic 'click' reactions. *Chem. Eur. J.* 22: 8676–8684.

20 (a) Buerkle, L.E. and Rowan, S.J. (2012). Supramolecular gels formed from multi-component low molecular weight species. *Chem. Soc. Rev.* 41: 6089–6102. (b) Cornwell, D.J. and Smith, D.K. (2015). Expanding the scope of gels – combining polymers with low-molecular-weight gelators to yield modified self-assembling smart materials with high-tech applications. *Mater. Horiz.* 2: 279–293. (c) Chivers, P.R.A. and Smith, D.K. (2019). Shaping and structuring supramolecular gels. *Nat. Rev. Mater.* 4: 463–478.

21 Rodon Fores, J., Criado-Gonzalez, M. et al. (2019). Supported catalytically active supramolecular hydrogels for continuous flow chemistry. *Angew. Chem. Int. Ed.* 58: 18817–18822.

22 Singh, N., Zhang, K., Angulo-Pachón, C.A. et al. (2016). Tandem reactions in self-sorted catalytic molecular hydrogels. *Chem. Sci.* 7: 5568–5572.

23 (a) Raeburn, J. and Adams, D.J. (2015). Multicomponent low molecular weight gelators. *Chem. Commun.* 51: 5170–5180. (b) Draper, E.R. and Adams, D.J. (2018). How should multicomponent supramolecular gels be characterised? *Chem. Soc. Rev.* 47: 3395–3405.

24 Singh, N. and Escuder, B. (2017). Competition versus cooperation in catalytic hydrogelators for anti-selective Mannich reaction. *Chem. Eur. J.* 23: 9946–9951.

25 Singh, N., Maity, C., Zhang, K. et al. (2017). Synthesis of a double-network supramolecular hydrogel by having one network catalyse the formation of the second. *Chem. Eur. J.* 23: 2018–2021.

26 Martí-Centelles, R., Rubio-Magnieto, J., and Escuder, B. (2020). A minimalistic catalytically-active cell mimetic made of a supra-molecular hydrogel encapsulated into a polymersome. *Chem. Commun.* 56: 14487–14490.

7

Supramolecular Helical Catalysts

Laurent Bouteiller and Matthieu Raynal

Sorbonne Université, CNRS, IPCM, UMR 8232, 4 Place Jussieu, 75252 Paris, Cedex 05, France

7.1 Introduction

Structures and functions of biomacromolecules are intimately related, and non-covalent interactions are essential to stabilize the helical scaffold adopted by, *e.g.* double-stranded DNA, enzymes, and collagen triple helix. In addition, helical scaffolds also emerge upon assembly of globular proteins as observed for the aggregation of G-actin into F-actin filaments. The structural richness of the molecules of life has undoubtedly stimulated the development of bio-hybrids and purely synthetic helical systems for a range of chirality-driven applications [1]. Molecules adopting a helical scaffold such as helicenes [2], foldamers [3], helicates [4], polypeptides [5], DNA [6], and synthetic polymers [7] have been exploited in the realm of asymmetric catalysis. It has been demonstrated that the different stereogenic elements potentially present in these catalysts, *e.g.* helical scaffold and stereogenic center located in close proximity to the reactive center, can act in concert to promote reactions with high levels of enantioselectivity [8]. Moreover, the importance of the helical conformation of the scaffold has been highlighted by the fact that achiral copper complexes intercalated into double-stranded DNA exhibited higher selectivities than those embedded into single-stranded DNA [9]. Exploiting the helical backbone as the unique source of enantiodiscrimination in a catalytic process has been addressed first with covalent polymers. Reggelin et al. showed that helical polymers devoid of stereogenic centers induced small level of enantioselectivity in various catalytic reactions [10]. Later on, Suginome and coworkers successfully demonstrated that intrinsically achiral metal centers connected to the helical scaffold of poly(quinoxaline-2,3-diyl)s promoted a range of organometallic reactions with excellent enantioselectivities [11].

From a different perspective, the assembly of complementary building blocks generates supramolecular nanostructures that can be chiral at the nano- and mesoscale [12]. Various methods exist to control the chirality of these self-assembled systems, the most common one being the incorporation of a stereogenic center in the monomer side chain. In addition, the main chain chirality of supramolecular

Supramolecular Catalysis: New Directions and Developments, First Edition.
Edited by Piet W.N.M. van Leeuwen and Matthieu Raynal.

polymers is highly sensitive to chiral perturbation and as such might be controlled by very modest chiral bias. Consequently, homochiral helical assemblies might be generated by mixing achiral and chiral monomers or non-equimolar mixtures of enantiomers [13]. Such a chirality amplification phenomenon is a particularly intriguing feature of dynamic helices. Implementing helical supramolecular assemblies as a scaffold for asymmetric reactions might seem risky at first sight given the limited stability of these objects and the usually harsh conditions required to trigger reactions [14]. However, we will show in this chapter that specifically designed helical assemblies efficiently promote asymmetric organometallic reactions. The helical scaffold confers a chiral conformation to the intrinsically achiral metal centers located at its periphery. The fact that the direction (*i.e.* configuration of the main enantiomer) and selectivity of the catalytic reaction are related to the handedness and optical purity of the helices imparts unique properties to this class of catalysts. It notably creates the possibility to engage a very low amount of chiral inducer in the catalytic reaction and to design multi-directional asymmetric catalysts.

7.2 Concept: Induction of Chirality to Metal Centers Connected to Supramolecular Helices

In 2012, we initiated a project aiming at probing whether the helical scaffold adopted by hydrogen-bonded supramolecular polymers might provide a suitable chiral environment for catalytic metal centers. M. Liu and coworkers [15] (see Chapter 8) addressed a similar approach with other types of self-assembled nanostructures. We posited that the assemblies formed upon association of benzene-1,3,5-tricarboxamide (BTA) monomers [16] constitute an ideal platform toward this goal. Indeed, BTA monomers form well-defined one-dimensional helices inside of which consecutive monomers are connected by means of three hydrogen bonds (HBs) and an aromatic interaction between the central BTA rings (Figure 7.1).

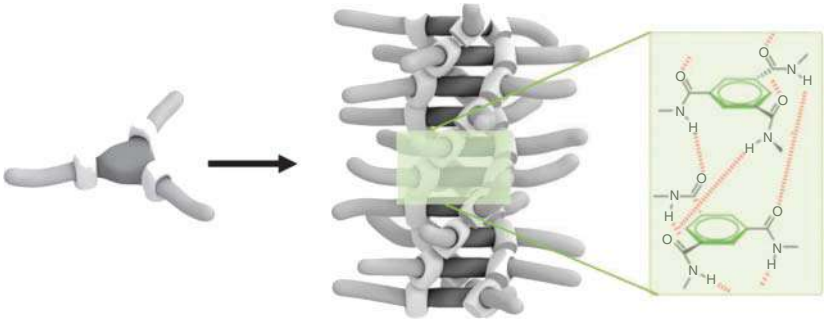

Figure 7.1 Schematic representation of the assembly of BTA monomer into one-dimensional helical structure. Source: Cantekin et al. [16]. Reproduced with permission of Royal Society of Chemistry.

The fact that complementary BTA monomers co-assemble into the same nanostructure makes this platform highly modular, a particularly important point in the context of optimizing homogeneous catalysts. Likewise, Mn-functionalized BTA helices were found to be stable during the epoxidation of stilbene performed in cyclohexane, as indicated by a precedent in the literature [17]. Even though these points constitute a solid foundation for the present objective, the ability of BTA helices to induce a chiral conformation to intrinsically achiral metal centers, a phenomenon sometimes referred to as "supramolecular chirogenesis" [18], was not demonstrated at that time.

To address this challenge, we prepared [19] a first set of BTA monomers that share the same metal binding group: a diphenylphosphino unit connected to the central BTA ring through a rigid *m*-phenylene linker (**(*S*)-BTA$^{m\text{-}PPh2}$** and **BTA$^{m\text{-}PPh2}$**, Figure 7.2). The hydrogenation of an activated olefin, dimethyl itaconate, was selected as this reaction is conveniently promoted at room temperature and low pressure of dihydrogen by phosphine rhodium complexes. BTA ligands and rhodium precursors were mixed together in dichloromethane (DCM) in order to ensure the efficient formation of the rhodium complexes, and then DCM was replaced by an apolar solvent to promote the formation of the assemblies. A similar method of preparation has been applied for all supramolecular helical catalysts mentioned throughout this chapter.

BTA ligand featuring two (*S*)-1-methylheptyl side chains, **(*S*)-BTA$^{m\text{-}PPh2}$**, yielded the hydrogenation product with 82% enantiomeric excess (ee) when the reaction was conducted in hexane (Entry 1 in Figure 7.3a). It is quite remarkable considering

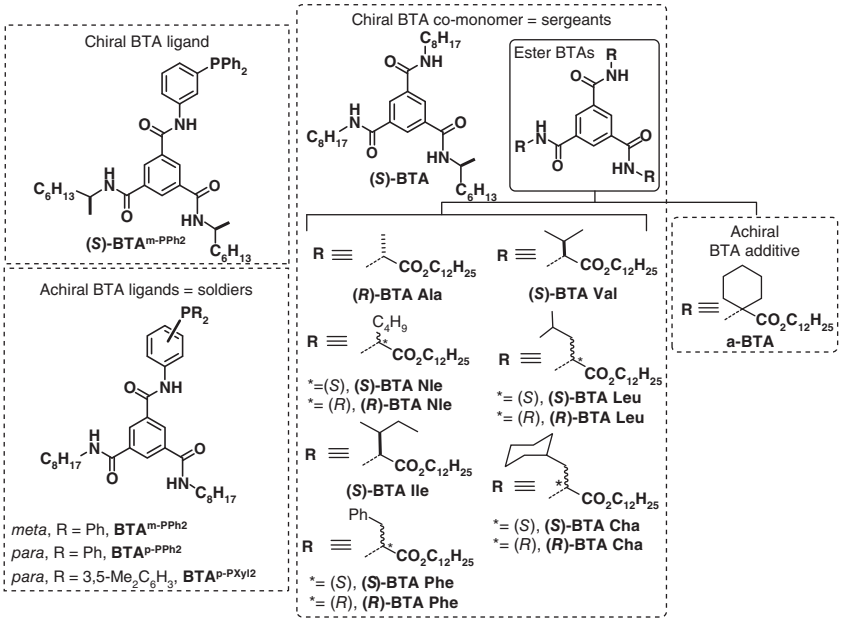

Figure 7.2 Chemical structures of the different types of BTA monomers used as building blocks of the helical catalysts mentioned in this chapter.

that the rhodium atom and the stereogenic centers are separated by 12 covalent bonds! Chirality induction at such a long distance in asymmetric catalysis has been rarely reported in the literature [21]. A series of control experiments confirmed that the observed selectivity originates from chiral assemblies, not from dissociated BTA monomers. For example, the analogue of **(*S*)-BTA$^{m\text{-}PPh2}$** for which the alkyl amide functions had been ethylated, could not assemble through HB, and consistently provided no selectivity, under otherwise identical conditions. Spectroscopic and scattering analyses unambiguously unveiled that **(*S*)-BTA$^{m\text{-}PPh2}$** forms long, helically biased and one-dimensional assemblies; chelation of a rhodium atom by two consecutive **(*S*)-BTA$^{m\text{-}PPh2}$** in the stacks is presumed (as in structure A, Figure 7.3c). We then exploited the tunable nature of this class of helical catalysts; mixing **(*S*)-BTA$^{m\text{-}PPh2}$** with **(*S*)-BTA** (an enantiopure monomer devoid of metal-binding group, Figure 7.2) generated co-assemblies that were more selective (88% ee) than the homo-assemblies of the individual components (Entry 2 in Figure 7.3a). This set of experiments confirmed our inaugural hypotheses: (i) the helical scaffold of hydrogen-bonded polymers can act as the only source of

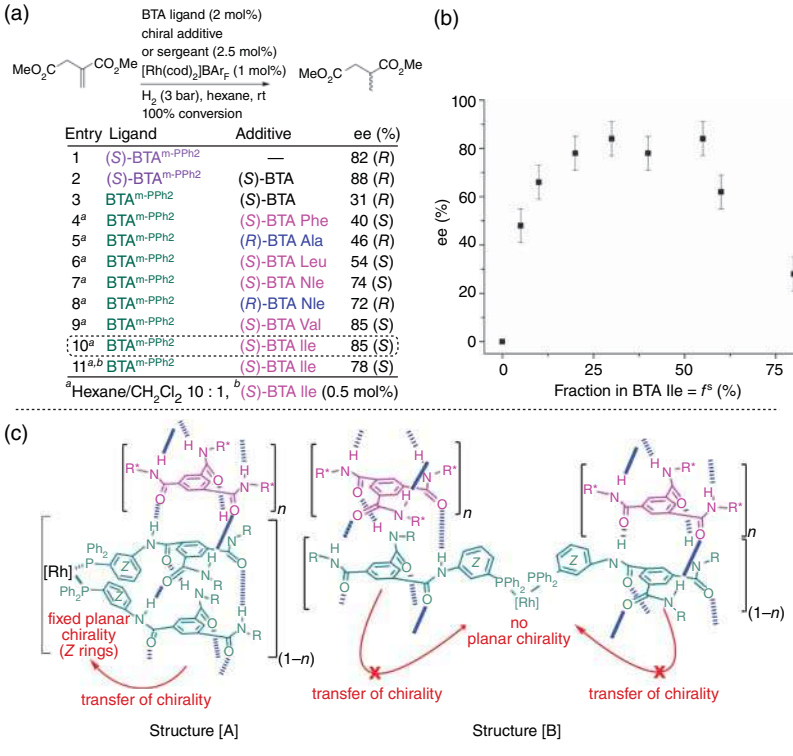

Figure 7.3 Supramolecular helical BTA catalysts for rhodium-promoted asymmetric hydrogenation of dimethyl itaconate. (a) Catalytic results. (b) Plot of the enantioselectivity as a function of the fraction of sergeant in the two-component system (BTAs form Entry 10 in (a)). (c) Plausible structures of the helical catalysts and mechanism for chirality transfer. Source: Adapted from Desmarchelier et al. [20].

enantiodiscrimination for catalytic metal centers located at its periphery and (ii) the modular nature of these assemblies can be used to tune the composition and efficiency of the metal catalysts.

7.3 Amplification of Chirality in Two-Component Supramolecular Helical Catalysts

The possibility of controlling the main chain chirality of covalent and supramolecular polymers by mixing a few chiral monomers (the "sergeants") to a large number of achiral ones (the "soldiers") is operative in a large number of systems [1]. Its implementation in asymmetric reactions faces an important challenge, *viz.* any metal catalyst that does not experience the chiral environment of the helices will significantly lower the selectivity of the reaction. In the first attempt, we found out that a mixture of the achiral ligand **BTA$^{m\text{-}PPh2}$** and **(*S*)-BTA** (Figure 7.2), with an excess of the latter component, promoted the hydrogenation reaction with a modest but encouraging 31% ee (Entry 3 in Figure 7.3a) [19]. This reflects the poor ability of **(*S*)-BTA** either to induce its preferential chirality to the co-assemblies or to incorporate into the stacks of the BTA ligand. However, it is well established that these two properties are intimately related to the structure of the sergeant. Our group notably disclosed the ability of enantiopure BTAs derived from amino esters (ester BTAs, Figure 7.2) to act as very efficient sergeants when mixed with a phosphine-free achiral BTA monomer [22]. We thus turned out to screen mixtures of **BTA$^{m\text{-}PPh2}$** and various ester BTAs, initially with a slight excess of the sergeant (f^s = fraction of sergeant = [sergeant]/[total BTA] = 55%).

Our screening (Entries 4–10 in Figure 7.3a) revealed that the selectivity varied significantly as a function of the nature of the ester BTA [20]. Control experiments indicated that the selectivity again stemmed from the formation of helical co-assemblies between the two components, even if these assemblies proved to be insoluble under catalytic conditions (as a probable result of the presence of cationic rhodium centers at their extremities). BTAs derived from Isoleucine (**BTA Ile**) or Valine (**BTA Val**) furnished the product with 85% ee, a selectivity similar to the one provided by the chiral ligand **(*S*)-BTA$^{m\text{-}PPh2}$**. This infers that these co-monomers yield significantly helically biased co-assemblies. Likewise, sergeants of opposite absolute configuration gave the opposite enantiomer of the product with identical selectivities (Entries 7 and 8) because of their ability to twist the helices in opposite directions. **BTA Ile** (Entry 10) was selected and mixed in variable amounts ($5\% < f^s < 80\%$) to **BTA$^{m\text{-}PPh2}$**, and the selectivity was determined for each mixture (Figure 7.3b). The non-linear relationship between the selectivity and the fraction of **BTA Ile** in the 0–50% range of f^s values indeed indicated that chiral amplification was at work in this system. Consequently, close to the optimal selectivity was achieved with the mixture containing only 20% of sergeant, *i.e.* one enantiopure molecule for two rhodium atoms (Entry 11). To the best of our knowledge, this was the first time that a chiral inducer could be used in a substoichiometric amount relative to a ligand without deteriorating significantly the enantioselectivity of an

organometallic transformation. Thorough characterization of these two-component mixtures helped to elucidate the following points: (i) the minimal fraction of sergeant required to get homochiral helices is 20%, consistently with the catalytic results, and (ii) the decrease of selectivity observed for f^s values >50% was not related to a decrease in the optical purity of the co-assemblies but rather to a change in the coordination mode of the rhodium centers which hampers an efficient transfer of chirality from the helical scaffold to the metal catalysts (structure B, Figure 7.3c). Structure A offers a good rationale for the mechanism of chirality induction and amplification at work in these helical systems. A preferential chiral conformation is transferred from the sergeant to the helical scaffold and from there to the *Z* rings (adopting a preferential *si*,*si* or *re*,*re* arrangement) and ultimately to the peripheral PPh_2 units.

7.4 Amplification of Chirality in Three-Component Helical Catalysts

We hypothesized that it would be easier to characterize and tune the structure of helical catalysts if they, unlike the previous systems, would remain in solution during the catalytic process. We thus decided to evaluate our BTA co-assemblies in the copper-catalyzed hydrosilylation of acetophenone derivatives, since the neutral copper intermediates involved in this reaction are expected to be soluble in apolar solvents [23]. Screening of the set of BTAs in our hands allowed us to identify **BTA$^{p\text{-}PPh2}$** (Figure 7.2), endowing a *p*-phenylene linker, as a suitable BTA ligand for promoting this reaction, and ester BTAs, bearing bulky and branched alkyl chains connected to the stereogenic center, such as **BTA Leu** and **BTA Cha**, as the most efficient chiral inducers (Entries 1–8 in Figure 7.4a) [25]. The higher efficacy of these two ester BTAs over the other sergeants was recently ascribed to their ability to intercalate into the stacks of the ligand and form very long co-assemblies [26]. Importantly, control experiments confirmed that the reaction was indeed catalyzed by fully soluble helical co-assemblies.

Various quantities of **BTA Cha** ($0.1\% < f^s < 52\%$) were added to **BTA$^{p\text{-}PPh2}$** and $[Cu(OAc)_2 \cdot H_2O]$ and evaluated in the hydrosilylation of *p*-nitroacetophenone (NPnone) [24]. The results appeared somewhat disappointing since a sizable fraction of enantiopure co-monomers ($f^s \geq 52\%$) was required to get the optimal selectivity (58% ee in NPnol at 293 K, black curve in Figure 7.4b). In other words, the magnitude of chirality amplification was weak in this initial two-component system. As ester BTAs were previously established as very efficient sergeants [22], **BTA$^{p\text{-}PPh2}$** came logically as the non-optimal partner. We hypothesized that a third component could induce a conformational change in the co-assemblies leading to a more rigid hydrogen-bonded network between the complementary monomers.

A dramatic improvement of the sergeants-and-soldiers (S&S) effect was indeed observed when the same reaction was conducted with two soldiers:

(a)

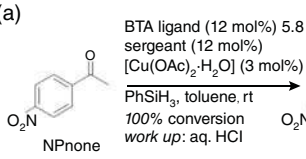

Entry	BTA ligand	Sergeant	f[a] (%)	ee (%)
1	BTA$^{p\text{-}PPh2}$	(*R*)-BTA Phe	50	8 (*S*)
2	BTA$^{p\text{-}PPh2}$	(*R*)-BTA Ala	50	20 (*S*)
3	BTA$^{p\text{-}PPh2}$	(*R*)-BTA Nle	50	43 (*S*)
4[a]	BTA$^{p\text{-}PPh2}$	(*S*)-BTA Val	52	48 (*R*)
5[a]	BTA$^{p\text{-}PPh2}$	(*S*)-BTA Ile	52	53 (*R*)
6	BTA$^{p\text{-}PPh2}$	(*R*)-BTA Leu	50	56 (*S*)
7	BTA$^{p\text{-}PPh2}$	(*S*)-BTA Cha	50	58 (*R*)
8[a]	BTA$^{p\text{-}PPh2}$	(*S*)-BTA Cha	52	58 (*R*)
9[a]	BTA$^{p\text{-}PPh2}$	(*S*)-BTA Cha	**0.5**	1 (*R*)
10[a,b]	BTA$^{p\text{-}PPh2}$	(*S*)-BTA Cha	**0.25**	50 (*R*)
11[a,c]	BTA$^{p\text{-}Xyl2}$	(*S*)-BTA Cha	**0.5**	3 (*S*)
12[a,b,c]	BTA$^{p\text{-}Xyl2}$	(*S*)-BTA Cha	**0.25**	90 (*S*)

[a]L (6 mol%) 16.3 mM, [b]+ a-BTA (6 mol%), [c]200 K.

(b)

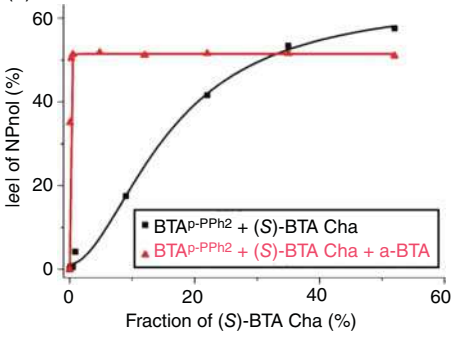

(c)

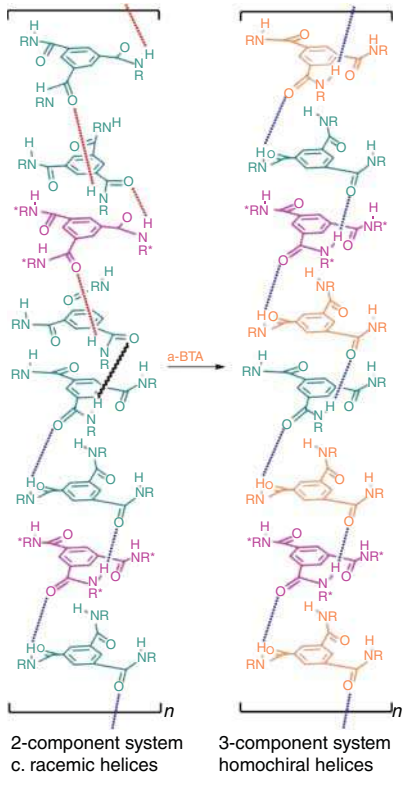

Figure 7.4 Supramolecular helical BTA catalysts for copper-promoted asymmetric hydrosilylation of NPnone. (a) Catalytic results. (b) Plot of the enantioselectivity as a function of the fraction of sergeant in the two- and three-component system (BTAs from entries 9 and 10 in (a)). (c) Representation of the helical structures with and without the achiral additive. The dark wavy bond represents a helix reversal (for clarity, only a single array of hydrogen bonds is shown). Source: Adapted from Li et al. [24].

BTA$^{p\text{-}PPh2}$ as BTA ligand and **a-BTA** as an achiral additive (Figure 7.2). For these three-component mixtures, a plateau for the enantioselectivity was reached with as little as 0.5% of **(*S*)-BTA Cha** (51% ee, red curve in Figure 7.4b). It means that the S&S effect was enhanced by more than two orders of magnitude. The addition of **a-BTA** to poorly helically biased two-component co-assemblies leads to the emergence of homochiral helices. Additional analytical techniques and determination of the energetics governing the amplification of chirality in these systems revealed that the additive both suppresses the conformational defects and stabilizes the co-assemblies (see a schematic representation of its role in Figure 7.4c). Further optimization studies (Entries 9–12 in Figure 7.4a) identified the ligand structure

(**BTA$^{p\text{-}PXyl2}$**, Figure 7.2) and the reaction temperature (200 K) as key parameters for the formation of a highly enantio-enriched product (90% ee) for a catalytic mixture containing as little as 0.25% of sergeant, *i.e.* 600 ppm of chiral co-monomers relatively to the substrate!

7.5 Switchable Asymmetric Catalysis by Reversible Assembly of Helical Catalysts

Whilst the preceding studies undoubtedly demonstrated the modular and chirally amplified nature of supramolecular BTA catalysts, their dynamic properties have not been exploited. It is worth to note that intensive research efforts are devoted to the implementation of catalysts for which the selectivity can be predictably controlled in real time. A multi-configurable catalyst would constitute an attractive synthetic tool for multi stereoblock microstructures in macromolecular catalysis [27]. As a first attempt to reach this goal, we probed the possibility of modulating the selectivity of a reaction by varying the length of helical BTA catalysts in a reversible manner.

To implement this concept, we selected the previously mentioned binary mixture between **BTA$^{p\text{-}PPh2}$** (coordinated to Cu) and **BTA Cha** in the hydrosilylation of NPnone [28]. We exploited the hydrogen bond acceptor ability of chloride anions, which are known to reduce the chain length of hydrogen-bonded supramolecular polymers [29]. In fact, addition of TPPCl (TPP, tetraphenylphosphonium) in DCM completely disassembled the helical BTA catalysts and consequently erased their selectivity. Then, we envisaged removing the chloride anions from the solution phase through a salt metathesis reaction leading to its co-precipitation with a cation. $NaNTf_2$ (NTf_2, triflimide) was found to be suitable in this regard, and its addition (in acetone, for solubility reasons) to chloride-containing mixtures leads to partial reassembly of BTA helices.

To probe the *in situ* efficiency of our method, five equivalents of NPnone were converted into NPnol in five successive runs the composition of which differed by the nature of the salts present in the catalytic mixtures. Two disassembly/reassembly cycles were thus accomplished by adding TPPCl in runs 2 and 4 and $NaNTf_2$ in runs 3 and 5 (the initial run contained no salt). As shown in Figure 7.5, the BTA catalyst promoted the reaction alternatively with a certain degree of selectivity (29–52% ee) and no or very poor selectivity (0–6% ee) as expected for the runs for which chloride ions were absent or present in solution, respectively. The length of the co-assemblies was established under conditions close to the ones employed in the first three runs. The BTA helices after salt metathesis (run 3) are indeed longer than after chloride addition (run 2), but they are actually shorter ($6 < DP_n < 15$) than the pristine co-assemblies ($DP_n \approx 250$) and this explains why the selectivity is lower for run 3 relatively to run 1. Control experiments indicated that the decrease in length and selectivity is mostly due to the presence of the polar solvents required to solubilize the salts, which by their competitive nature prevents complete reassembly. Finally, the present study reveals that a degree of polymerization of about 10 constitutes the critical length required to locate most of the copper centers in a chiral environment

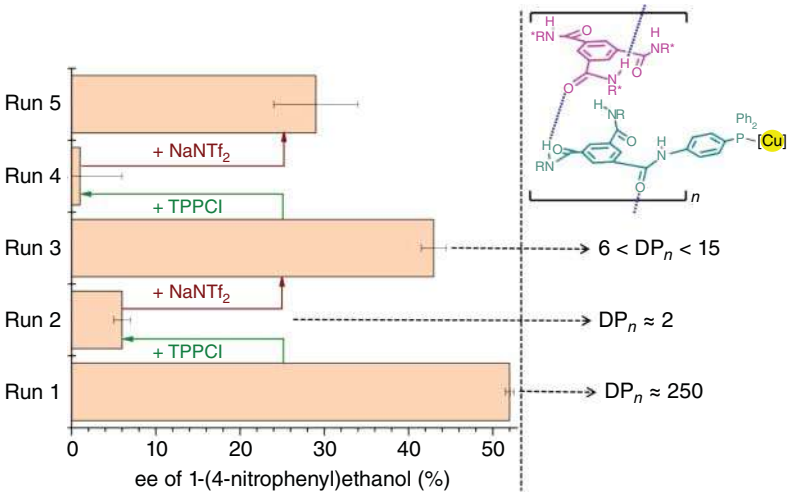

Figure 7.5 Left: Modulation of the enantioselectivity of the supramolecular catalyst involved in the hydrosilylation of five equivalents of NPnone added sequentially in the reaction mixture. Right: Representation of the helical structures with the corresponding DP_n values for runs 1–3. The catalytic system of run 1 is the one corresponding to Entry 8 in Figure 7.4a. Source: Li et al. [28]. Reproduced with permission of Royal Society of Chemistry.

suitable for asymmetric induction. The correlation between length, helical order, and asymmetric induction is a fingerprint of helical catalysts [30].

7.6 Dual Stereocontrol of an Asymmetric Reaction by Switchable Helical Catalysts

Several groups are dedicating strong efforts toward the development of enantiodivergent catalysis, *i.e.* to the possibility of obtaining both enantiomers of a reaction product with the same catalyst or close catalytic conditions. Predictable toggling between the enantiomeric states of a catalyst is usually achieved by connecting a reactive group to a chiroptical switch, the direction of which being selected *prior* to the catalytic reaction [31]. However, inverting the state of the catalyst *during* the course of a reaction faces additional challenges that have not been properly addressed yet: (i) the catalytic system should be dynamic under the reaction conditions, (ii) the stereochemical switch should be fast and lead to perfect mirrored-image environments, and (iii) the employed stimulus should preserve the catalyst integrity. The catalytic system formed by **BTA$^{p\text{-}PPh2}$** (coordinated to Cu) and **BTA Cha** proves to be particularly appealing in this context: (i) a significant level of selectivity is obtained in the hydrosilylation reaction (Figure 7.4) and (ii) the assemblies are dynamic as demonstrated by the aforementioned experiments in the presence of salts (Figure 7.5). In addition, thanks to chiral amplification effects, homochiral helices are formed even though composed of a mixture of enantiopure co-monomers (the "sergeants") and achiral monomers (the BTA ligand, the "soldiers," Figure 7.4). In the context of

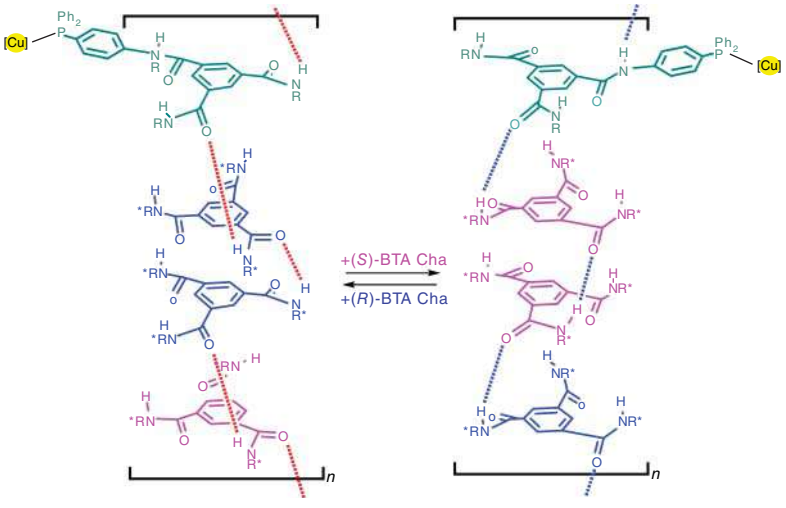

Figure 7.6 New concept to achieve dual stereocontrol in an asymmetric reaction with a supramolecular helical BTA catalyst composed of **BTA$^{p\text{-}PPh2}$** (coordinated to Cu) and a non-equimolar mixture of the enantiomers of **BTA Cha**. The handedness of the assemblies and direction of the reaction are controlled by the major enantiomer present in the co-assemblies.

switching the handedness of the helices, it is crucial to test whether homochiral helices are also obtained when a non-equimolar mixture of the co-monomer enantiomers is present in the helices. It would then be conceivable to select the direction of the catalytic reaction by changing the nature of the major enantiomer in the helical co-assemblies during the course of the reaction as represented in Figure 7.6.

We thus determined the selectivity in the hydrosilylation of NPnone displayed by three-component mixtures composed of **BTA Cha** enantiomers (−100% to 100% ee) and **BTA$^{p\text{-}PPh2}$** coordinated to Cu (f^s = 69%, Figure 7.7 left) [25]. The sigmoidal shape of the selectivity as a function of optical purity in **BTA Cha** in these mixtures indicates that chirality amplification occurs in this system. Indeed, close to optimal selectivity (*i.e.* 63% ee at 273 K) is obtained when the optical purity in **BTA Cha** is 33% ee only. The fact that purely left-handed and right-handed helices are formed when **BTA (*S*)-Cha** and **BTA (*R*)-Cha** are the respective major enantiomers in the helices makes the inversion of selectivity of the BTA catalyst a possible target. In addition, a set of experiments for which the co-monomer enantiomer (switch trigger) and phenyl silane (reaction trigger) were combined at different time intervals actually revealed that the stereochemical switch is very fast; the enantiomeric state of the catalyst is toggled in *ca*. five seconds.

To demonstrate the possibility of controlling the configuration of consecutively formed stereogenic centers, we engaged our helical BTA catalysts in the hydrosilylation of 1 : 1 mixture of NPnone and 1-(4-biphenylyl)-ethanone (PPnone). The latter substrate was selected for its far lower reactivity allowing both substrates to be converted almost consecutively. The reactions conducted with enantiopure co-monomers unsurprisingly yielded major enantiomers of NPnol and PPnol with

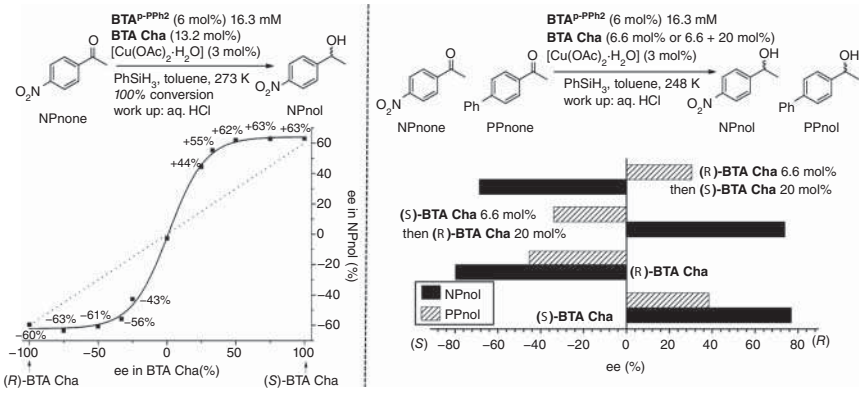

Figure 7.7 Left: Enantiomeric excess in NPnol *vs.* the optical purity in **BTA Cha**. The dotted line represents the selectivity that would have been obtained in the absence of chirality amplification. Right: Real-time control of the enantioselectivity achieved during the copper-catalyzed hydrosilylation of a 1 : 1 mixture of NPnone and PPnone. Source: Zimbron et al. [25]. Reproduced with permission of John Wiley & Sons.

the same configuration (lower two experiments in Figure 7.7 right). Then, two experiments were performed during which the nature of major co-monomer enantiomer evolved during the reaction: either **BTA (*S*)-Cha** or **BTA (*R*)-Cha** (20 mol%) was added after the conversion of NPnone. Here, the major enantiomer of NPnol and PPnol was obtained with opposite configurations, *i.e.* one was predominantly (*R*), whilst the other was (*S*). Thanks to chirality amplification governing the optical purity of the catalytic BTA helices, close to optimal selectivities were observed in all cases (70–80% ee for NPnol, 30–45% ee for PPnol at 248 K). All four possible combinations of the enantiomers can thus be generated at wish from the same system without significant dwindling of the selectivity.

7.7 Concluding Remarks

Spontaneous assembly of several components yields multi-component nanostructures with highly tunable morphology, size, and function. These systems present many advantages for implementation in catalysis if their chirality is expressed at the nanoscale and if they are dynamic thanks to the non-covalent nature of their scaffold. Mono-dimensional helical assemblies formed by BTA monomers belong to this category. Intrinsically achiral metal centers located at their peripheries experience the chiral environment of BTA helices and promote reactions with a significant level of enantioinduction. Likewise, the main chirality of these helical catalysts is sensitive to very small chiral fluctuation and can be tuned during the catalytic reaction. It offers the possibility of maintaining high levels of selectivities with ppm levels of chiral species as well as controlling the configuration of the stereogenic center formed in consecutive reactions, two properties that are out of reach for conventional catalysts. However, the true potential of this class of catalysts remains to be

discovered. For example, a better control in the position and nature of the catalytic centers would be necessary for targeting unusual reactivities, such as templating the formation of macrocycles [32] or activating reagents in a cooperative manner [33]. Finally, the major gain with these supramolecular helices is undoubtedly related to their stimuli-responsiveness and dynamic nature. Further progress is needed to develop catalysts for which the catalytic performance can be regulated at will during an intricate scheme of reactions.

Acknowledgments

All students, post-doctoral researchers, and collaborators involved in the development of the supramolecular helical BTA catalysts are deeply acknowledged for their commitment and support. Their names can be found in the related publications quoted in the chapter. French Agence Nationale de la Recherche is acknowledged for funding of projects ANR-13-BS07-0021 SupraCatal and ANR-17-CE07-0002 AbsoluCat.

References

1 Yashima, E., Ousaka, N., Taura, D. et al. (2016). Supramolecular helical systems: helical assemblies of small molecules, foldamers, and polymers with chiral amplification and their functions. *Chem. Rev.* 116: 13752–13990.

2 Narcis, M.J. and Takenaka, N. (2014). Helical-chiral small molecules in asymmetric catalysis. *Eur. J. Org. Chem.* 2014: 21–34.

3 Maayan, G., Ward, M.D., and Kirshenbaum, K. (2009). Folded biomimetic oligomers for enantioselective catalysis. *Proc. Natl. Acad. Sci. U.S.A.* 106: 13679–13684.

4 Tanabe, J., Taura, D., Ousaka, N., and Yashima, E. (2017). Chiral template-directed regio-, diastereo-, and enantioselective photodimerization of an anthracene derivative assisted by complementary amidinium-carboxylate salt bridge formation. *J. Am. Chem. Soc.* 139: 7388–7398.

5 Kelly, D.R. and Roberts, S.M. (2006). Oligopeptides as catalysts for asymmetric epoxidation. *Biopolymers* 84: 74–89.

6 Boersma, A.J., Megens, R.P., Feringa, B.L., and Roelfes, G. (2010). DNA-based asymmetric catalysis. *Chem. Soc. Rev.* 39: 2083–2092.

7 (a) Suginome, M., Yamamoto, T., Nagata, Y. et al. (2012). Catalytic asymmetric synthesis using chirality-switchable helical polymer as a chiral ligand. *Pure Appl. Chem.* 84: 1759–1769; (b) Li, Y., Bouteiller, L., and Raynal, M. (2019). Catalysts supported by homochiral molecular helices: a new concept to implement asymmetric amplification in catalytic science. *ChemCatChem* 11: 5212–5226.

8 (a) Yavari, K., Aillard, P., Zhang, Y. et al. (2014). Helicenes with embedded phosphole units in enantioselective gold catalysis. *Angew. Chem. Int. Ed.* 53: 861–865;

(b) Huerta, E., van Genabeek, B., Lamers, B.A.G. et al. (2015). Triggering activity of catalytic rod-like supramolecular polymers. *Chem. Eur. J.* 21: 3682–3690.

9 Boersma, A.J., Klijn, J.E., Feringa, B.L., and Roelfes, G. (2008). DNA-based asymmetric catalysis: sequence-dependent rate acceleration and enantioselectivity. *J. Am. Chem. Soc.* 130: 11783–11790.

10 (a) Reggelin, M., Schultz, M., and Holbach, M. (2002). Helical chiral polymers without additional stereogenic units: a new class of ligands in asymmetric catalysis. *Angew. Chem. Int. Ed.* 41: 1614–1617; (b) Reggelin, M., Doerr, S., Klussmann, M. et al. (2004). Helically chiral polymers: a class of ligands for asymmetric catalysis. *Proc. Natl. Acad. Sci. U.S.A.* 101: 5461–5466.

11 (a) Yamamoto, T. and Suginome, M. (2009). Helical poly(quinoxaline-2,3-diyl)s bearing metal-binding sites as polymer-based chiral ligands for asymmetric catalysis. *Angew. Chem. Int. Ed.* 48: 539–542; (b) Suginome, M., Yamamoto, T., and Nagata, Y. (2015). Poly(quinoxaline-2,3-diyl)s: a fascinating helical macromolecular scaffold for new chiral functions. *J. Syn. Org. Chem. Jpn.* 73: 87–101.

12 Liu, M.H., Zhang, L., and Wang, T.Y. (2015). Supramolecular chirality in self-assembled systems. *Chem. Rev.* 115: 7304–7397.

13 Palmans, A.R.A. and Meijer, E.W. (2007). Amplification of chirality in dynamic supramolecular aggregates. *Angew. Chem. Int. Ed.* 46: 8948–8968.

14 Mabesoone, M.F.J., ter Huurne, G.M., Palmans, A.R.A., and Meijer, E.W. (2020). How water in aliphatic solvents directs the interference of chemical reactivity in a supramolecular system. *J. Am. Chem. Soc.* 142: 12400–12408.

15 (a) Jiang, J., Meng, Y., Zhang, L., and Liu, M.H. (2016). Self-assembled single-walled metal-helical nanotube (M-HN): creation of efficient supramolecular catalysts for asymmetric reaction. *J. Am. Chem. Soc.* 138: 15629–15635; (b) Shen, Z.C., Sang, Y.T., Wang, T.Y. et al. (2019). Asymmetric catalysis mediated by a mirror symmetry-broken helical nanoribbon. *Nat. Commun.* 10. doi:10.1038/S41467-019-11840-3.

16 Cantekin, S., de Greef, T.F.A., and Palmans, A.R.A. (2012). Benzene-1,3,5-tricarboxamide: a versatile ordering moiety for supramolecular chemistry. *Chem. Soc. Rev.* 41: 6125–6137.

17 de Torres, M., van Hameren, R., Nolte, R.J.M. et al. (2013). Photocatalytic oxidation of stilbene by self-assembled stacks of manganese porphyrins. *Chem. Commun.* 49: 10787–10789.

18 Escárcega-Bobadilla, M.V. and Kleij, A.W. (2012). Artificial chirogenesis: a gateway to new opportunities in material science and catalysis. *Chem. Sci.* 3: 2421–2428.

19 Raynal, M., Portier, F., van Leeuwen, P.W.N.M., and Bouteiller, L. (2013). Tunable asymmetric catalysis through ligand stacking in chiral rigid rods. *J. Am. Chem. Soc.* 135: 17687–17690.

20 Desmarchelier, A., Caumes, X., Raynal, M. et al. (2016). Correlation between the selectivity and the structure of an asymmetric catalyst built on a chirally amplified supramolecular helical scaffold. *J. Am. Chem. Soc.* 138: 4908–4916.

21 (a) Le Bailly, B.A.F., Byrne, L., and Clayden, J. (2016). Refoldable foldamers: global conformational switching by deletion or insertion of a single hydrogen

bond. *Angew. Chem. Int. Ed.* 55: 2132–2136; (b) van Leeuwen, P.W.N.M., Rivillo, D., Raynal, M., and Freixa, Z. (2011). Enantioselective supramolecular catalysis induced by remote chiral diols. *J. Am. Chem. Soc.* 133: 18562–18565.

22 Desmarchelier, A., Raynal, M., Brocorens, P. et al. (2015). Revisiting the assembly of amino ester-based benzene-1,3,5-tricarboxamides: chiral rods in solution. *Chem. Commun.* 51: 7397–7400.

23 Jordan, A.J., Lalic, G., and Sadighi, J.P. (2016). Coinage metal hydrides: synthesis, characterization, and reactivity. *Chem. Rev.* 116: 8318–8372.

24 Li, Y., Hammoud, A., Bouteiller, L., and Raynal, M. (2020). Emergence of homochiral benzene-1,3,5-tricarboxamide helical assemblies and catalysts upon addition of an achiral monomer. *J. Am. Chem. Soc.* 142: 5676–5688.

25 Zimbron, J.M., Caumes, X., Li, Y. et al. (2017). Real-time control of the enantioselectivity of a supramolecular catalyst allows selecting the configuration of consecutively formed stereogenic centers. *Angew. Chem. Int. Ed.* 56: 14016–14019.

26 Martínez-Aguirre, M.A., Li, Y., Vanthuyne, N. et al. (2021). Dissecting the role of the sergeants in supramolecular helical catalysts: from chain capping to intercalation. *Angew. Chem. Int. Ed.* 60: 4183–4191.

27 Coates, G.W. and Waymouth, R.M. (1995). Oscillating stereocontrol – a strategy for the synthesis of thermoplastic elastomeric polypropylene. *Science* 267: 217–219.

28 Li, Y., Caumes, X., Raynal, M., and Bouteiller, L. (2019). Modulation of catalyst enantioselectivity through reversible assembly of supramolecular helices. *Chem. Commun.* 55: 2162–2165.

29 Pinault, T., Cannizzo, C., Andrioletti, B. et al. (2009). Anions as efficient chain stoppers for hydrogen-bonded supramolecular polymers. *Langmuir* 25: 8404–8407.

30 Flood, R.W., Geller, T.P., Petty, S.A. et al. (2001). Efficient asymmetric epoxidation of α,β-unsaturated ketones using a soluble triblock polyethylene glycol-polyamino acid catalyst. *Org. Lett.* 3: 683–686.

31 Romanazzi, G., Degennaro, L., Mastrorilli, P., and Luisi, R. (2017). Chiral switchable catalysts for dynamic control of enantioselectivity. *ACS Catal.* 7: 4100–4114.

32 Girvin, Z.C., Andrews, M.K., Liu, X., and Gellman, S.H. (2019). Foldamer-templated catalysis of macrocyle formation. *Science* 366: 1528–1531.

33 Becart, D., Diemer, V., Salaun, A. et al. (2017). Helical oligourea foldamers as powerful hydrogen bonding catalysts for enantioselective C–C bond-forming reactions. *J. Am. Chem. Soc.* 139: 12524–12532.

8

Self-Assembled Multi-Component Supramolecular Catalysts for Asymmetric Reactions

Guanghui Ouyang[1], *Jian Jiang*[2], *and Minghua Liu*[1]

[1] *Beijing National Laboratory for Molecular Science, CAS Key Laboratory of Colloid, Interface and Chemical Thermodynamics, Institute of Chemistry, Chinese Academy of Sciences, North First Street 2, Zhongguancun, Beijing, 100190, P. R. China*
[2] *CAS Center for Excellence in Nanoscience, CAS Key Laboratory of Nanosystem and Hierarchical Fabrication, National Center for Nanoscience and Technology (NCNST), No. 11, Beiyitiao, Zhongguancun, Beijing, 100190, P.R. China*

Self-assembly is one of the most efficient ways of combining molecular parts into large entities, which also facilitates the formulation of supramolecular catalysts. Besides the single component, self-assembly of two or more building blocks with distinct functions into nanostructures has many advantages [1–6]. On one hand, this is an efficient way to integrate different structural information and functions into a single system with enhanced performance owing to synergistic effects. On the other hand, multi-component building blocks can generate more complex nanostructures with different morphology, size, and even asymmetrical geometry compared with their analogs with a single component. Especially for those nanostructures with chiral characteristics, their curved surface might act as a micro-container to promote the gathering of binding species and therefore increase their local concentration, which is quite similar to some functions of the catalytic pockets of enzymes [7–9]. This feature inspired scientists to apply these chiral multi-component nanostructures as supramolecular catalysts to asymmetric catalytic reactions, and significant progresses have been achieved in the past decade [10–12].

A common strategy for the construction of multi-component catalysts is using the delicate chiral nanostructures self-assembled from chiral building blocks as supramolecular template or ligand. By partially inserting achiral catalytic species into the assembled structures or absorption of them on the curved surface, the asymmetric environment provided by assembled structures might induce chiral catalysis by these originally achiral catalytic species through steric hindrance on supramolecular level [13, 14]. The early examples adopting this strategy were reported by Feringa and coworkers. They inserted organic ligands into a DNA double helix chain and further coordination with copper ions for asymmetric reactions [15, 16]. Raynal and coworkers developed a series of supramolecular catalytic systems by utilizing helical assemblies of chiral benzene-1,3,5-tricarboxamide (BTA) as supramolecular ligands (see Chapter 7 for more details) [17, 18].

Supramolecular Catalysis: New Directions and Developments, First Edition.
Edited by Piet W.N.M. van Leeuwen and Matthieu Raynal.

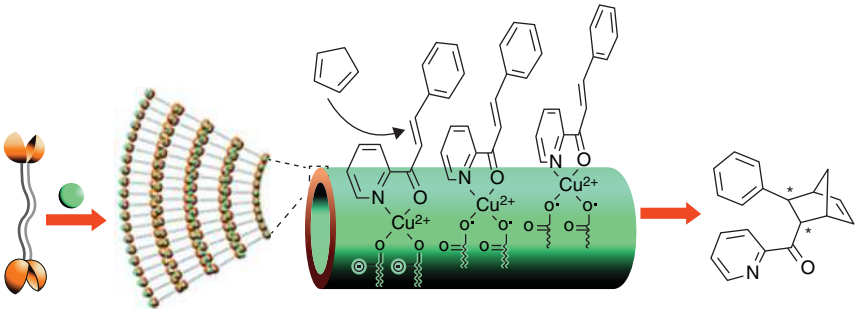

Figure 8.1 Self-assembled multi-walled nanotube as chiral scaffold for asymmetric Diels–Alder cycloaddition reaction. Source: Jin et al. [19]. Reproduced with permission of American Chemical Society.

Liu and coworkers reported the first examples of using self-assembled nanotubes from glutamic amphiphiles as chiral scaffolds for asymmetric reactions. In 2011, Liu's group reported the self-assembly of copper ion-mediated nanotube and investigated its asymmetric catalytic ability [19]. The monolayer nanotube was prepared from a low-molecular-weight bolaamphiphilic glutamic acid gelator (*N*,*N*′-hexadecanedioyl-di-L-glutamic acid, L-HDGA). In the presence of Cu^{2+}, the nanotube catalyst L-HDGA/Cu^{2+} was obtained, in which the thickness of the tubular wall was about 10 nm due to the formation of a multilayer structure. The well-arranged carboxylate groups on the outer wall of nanotube were coordinated with certain amounts of Cu^{2+} as evidenced by a series of characterization techniques. The formed L-HDGA/Cu^{2+} nanotubes showed moderate enantiomeric selectivity in Diels–Alder cycloaddition reaction, giving an ee value up to 52% (Figure 8.1). It should be noted that both the self-assembly protocol and catalytic reactions were conducted in water, which represents a good example for green catalysis. To further exemplify the role of supramolecular chirality in the catalysis process, a control experiment was designed. The authors added certain amounts of NaOH to the assembled system to destroy the L-HDGA/Cu^{2+} nanotubes. In that case, only racemic products were obtained, although the system still showed catalytic activity. These results clearly indicated that the assembled structures and their supramolecular chirality played a dominant role in the asymmetric induction process.

In the subsequent work, Liu and coworkers greatly increased the enantioselectivity and reactivity of this nanotube system by affording a single-walled helical nanotube from the same amphiphile L-HDGA as the scaffold for asymmetric reaction [20]. The assembly protocol in this case is slightly different from previous multi-walled nanotubes. Experimentally, L-HDGA was first dispersed and heated to dissolve in water. After being cooled to room temperature at ambient conditions, L-HDGA could form a transparent hydrogel, in which a nanotube with a thickness of single monolayer was obtained. These nanotubes were then dispersed into dilute solution of transition metal ions, and the mixture was stirred to promote the coordination between carboxylate groups and metal ions. Atomic force microscope (AFM) images confirmed that the tubular structures were retained after metal ions coordination. It was suggested that the metal ions are nicely located on the nanotube surface as proved by elemental mapping technology. The amount of

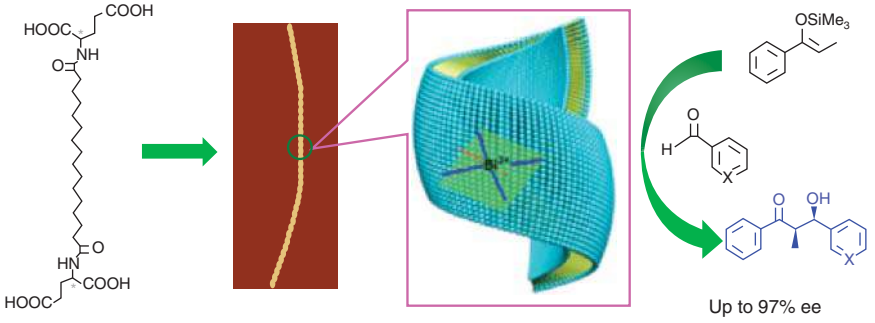

Figure 8.2 Schematic illustration of self-assembled helical single-walled nanotube and its metal ions complex for asymmetric catalysis. Source: Jiang et al. [20]. Reproduced with permission of American Chemical Society.

metal ions was found important to stabilize the nanotubes. Generally, 0.1–2% metal ions were able to form discrete metal-helical nanotube (**M-HN**), while more metal ions caused obvious aggregation of the nanotubes or even led to collapse of the tubular structures.

The catalytic activity and enantioselectivity of these **M-HN** complex were examined by two model reactions depending on the types of metal ions. The **Bi(III)-HN** (Bi^{3+}/L-HDGA, 2 mol%) was found effective in asymmetric Mukaiyama aldol reaction, which gave a moderate yield but satisfying enantioselectivity and diastereoselectivity (Figure 8.2). The *syn/anti* ratio was determined to be about 95 : 5, and an ee value up to 93% for *syn*-isomer was achieved. By optimization of reaction conditions, such as the ratio of Bi^{3+}/L-HDGA (2 mol%) and Bi^{3+}/substrate (1.2 mol%), the final yield was increased to 91% with slightly increased ee value (94%) and diastereoselectivity. Finally, the substrate scope of Mukaiyama aldol reaction catalyzed by **Bi(III)-HN** was studied with various aromatic aldehydes and aliphatic aldehydes with different substitutes. Most of the examined aldehydes gave moderate to good enantioselectivity (74–94% ee values) and good yield.

To exemplify the generality of this helical nanotube in asymmetric catalysis, helical nanotubes were combined with other types of metal ions and screened. The selected **Cu(II)-HN** was used to catalyze the asymmetric Diels–Alder reaction, giving nearly quantitative yield and up to 91% ee value. The reaction rate was unexpectedly accelerated perhaps because of the increase of local concentration of substrates nearby the reaction center. When the catalyst/substrate ratio was 0.1 mol%, the reaction could finish in 60 minutes, which is among the fastest catalysts for this reaction. Impressively, the reaction completed in just two minutes when the catalyst/substrate ratio was increased to 20 mol%, which might bring industrial application potential considering the fast reaction was processed in water (green catalysis) and the starting materials of the **Cu(II)-HN** supramolecular catalysts are cheap and easy-to-access.

A possible catalytic mechanism for the **Cu(II)-HN** system was proposed based on the experimental results and reasonable stereochemical analysis. As shown in Figure 8.3, copper ions were first coordinated with the carboxylic group on the outer surface of the nanotube and aligned in a helical way following the chirality of the nanotubes. The first substrate azachalcone was then added into

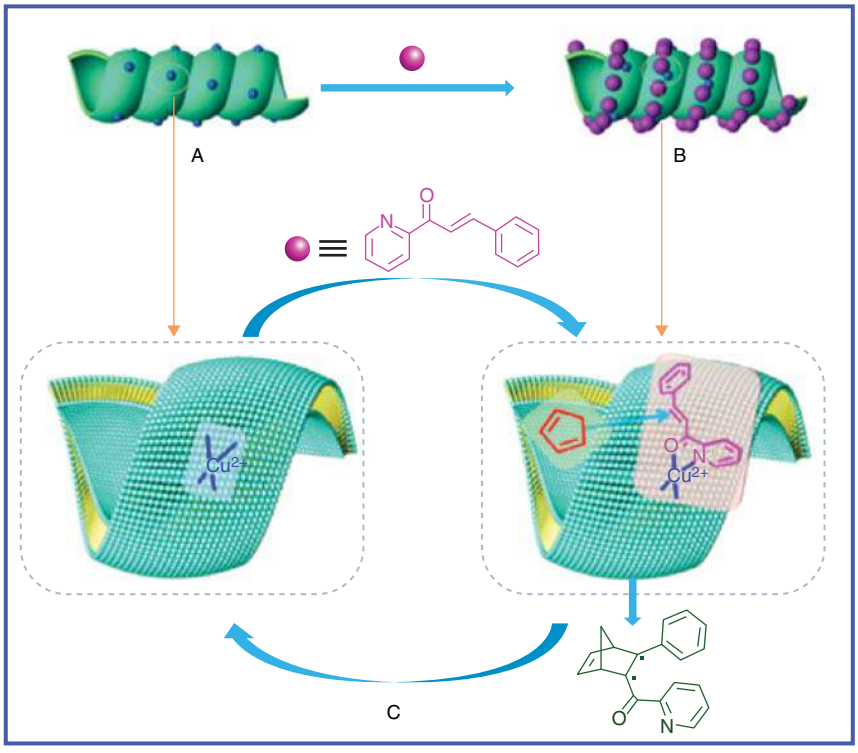

Figure 8.3 Illustration of possible catalytic mechanism for **Cu(II)-HN**-catalyzed Diels–Alder reaction. Source: Jiang et al. [20]. Reproduced with permission of American Chemical Society.

the **HN** and **Cu(II)-HN** nanotube dispersions, respectively. The mixture was then measured by circular dichroism (CD) spectrometer. Results indicated that induced CD signals assigned to the absorption band of azachalcone were observed in both **HN**/azachalcone and **Cu(II)-HN**/azachalcone systems, which indicated that azachalcone substrates were helically aligned on the surface of these nanotubes. However, the absorption band and the corresponding CD signal of azachalcone in **Cu(II)-HN**/azachalcone system showed a red shift compared with that of **HN**/azachalcone system. This suggested a coordination interaction among Cu^{2+} cations and the carboxylate acid groups on helical nanotubes. The absorbed azachalcone continue to react with the second substrate cyclopentadiene. Owing to the asymmetric steric hindrance from the curved nanotube surface, cyclopentadiene can only attack from one prochiral side of azachalcone (i.e. *re* or *si* faces), which led to high enantioselectivity.

Liu and coworkers further reported that the coordination of L-HDGA with a rhodium complex could effectively modulate the nanostructures and enantioselective catalytic activities of its self-assemblies [21]. It was found that the ratio of *cis*-$Rh_2(tfa)_2(OAc)_2$ (abbreviated as Rh_2) to L-HDGA significantly changed the morphology of the nanostructures due to different coordination mode (Figure 8.4).

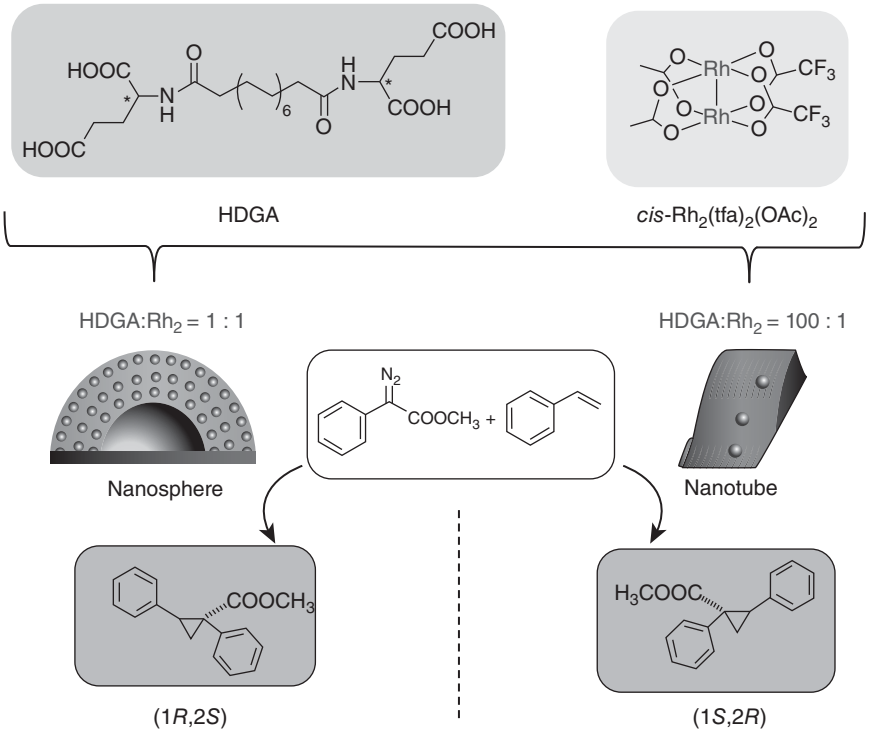

Figure 8.4 Chemical structures of bolaamphiphile (HDGA) and *cis*-$Rh_2(tfa)_2(OAc)_2$ metal complex and illustration of tunable nanostructures and asymmetric catalysis regulated by different coordination modes. Source: Yuan et al. [21]. Reproduced with permission of John Wiley & Sons.

When the ratio of HDGA/Rh_2 is 100 : 1, the morphological parameters, Fourier transform infrared spectrometry (FT-IR) and X-ray diffraction (XRD) spectra of nanotubes of HDGA/Rh_2, are nearly identical to those of pure HDGA nanotubes. These nanotube structures were gradually changed into nanospheres when increasing the ratio of Rh_2 complex to 1 : 1, as demonstrated by scanning electron microscope (SEM) and transmission electron microscope (TEM) images. FT-IR spectra indicated that the type of coordination between HDGA and Rh_2 is a bridging bidentate style according to the analysis of antisymmetric and symmetric vibration of carboxylate anions. Most importantly, the supramolecular chirality of the nanotubes and nanospheres is opposite based on the analysis results of CD spectra even though the molecular chirality of HDGA is the same. When the two different nanostructures are used as supramolecular catalysts for asymmetric cyclopropanation reaction, the products gave opposite molecular chirality, i.e. two enantiomers were obtained from the two nanostructures, respectively. This work provides a new pathway to understand the difference between molecular chirality and supramolecular chirality in asymmetric catalysis.

The above assembled multi-component catalysts are generally applied to catalyze asymmetric transformations of achiral substrates. To investigate the interactions

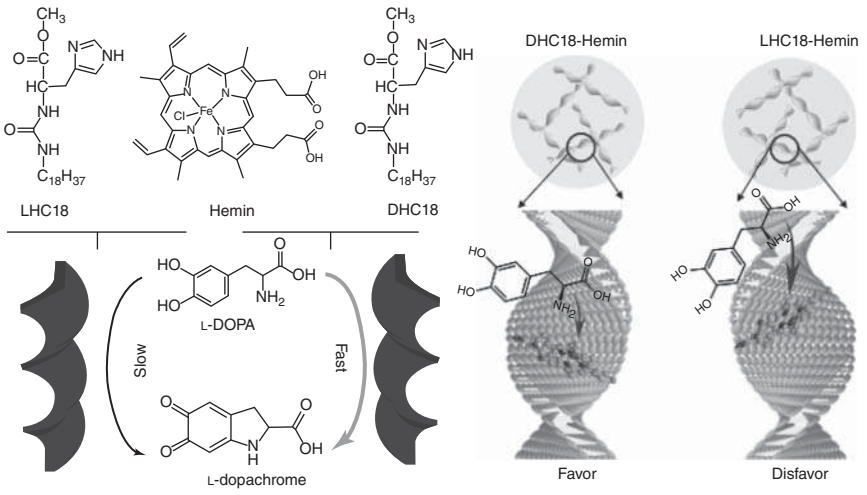

Figure 8.5 Molecular structures of LHC18 (DHC18) and hemin, and illustration of chiral recognition and catalytic conversion of hemin on the curved surface of *P*-helical and *M*-helical assemblies. Source: Wang et al. [22]. Reproduced with permission of John Wiley & Sons.

between chiral substrate and chiral assembled catalysts, Liu's group designed a two-component supramolecular gel consisting of a chiral amphiphilic histidine gelator (LHC18 or DHC18) and an originally achiral catalyst hemin [22]. During the co-assembly process, the chiral information of LHC18 or DHC18 can be transmitted to hemin, giving an unambiguously induced CD signal ascribed to hemin. The co-gel is composed of *M*-helical or *P*-helical ribbons from SEM observation, whose helicity depending on the molecular chirality of histidine gelator. The catalytic activity of these helical ribbons was tested by using 3,4-dihydroxy-L-phenylalanine (L-DOPA) as a chiral substrate. DHC18/hemin showed faster catalytic rate compared with LHC18/hemin because of a chiral recognition mechanism (Figure 8.5). This work brought fundamental understanding for chiral recognition and catalytic conversion of chiral substrates on the surface of chiral nanostructures, which might advance the application of chiral nanoenzymes in catalytic dynamic resolution of racemic compounds.

The majority of self-assembled supramolecular catalysts are originated from chiral building blocks. However, achiral motifs are also capable of forming chiral nanostructures through a mirror symmetry breaking mechanism, which might be further utilized as chiral scaffolds for catalysis and is meaningful for understanding the origin of homochirality in nature [23–25]. In this context, exploring the asymmetric catalysis mediated by mirror symmetry-broken supramolecular systems is interesting. In 2019, Liu and coworkers reported the first example of such system [26]. They synthesized an achiral BTA motif (**BTA^{BA}**) as the building block which appended with three carboxylic groups at the peripheral benzene groups (Figure 8.6a). The amide groups on **BTA^{BA}** provide H-bonding, and the carboxylic groups act as coordination sites for metal ions, which can be used as catalysis

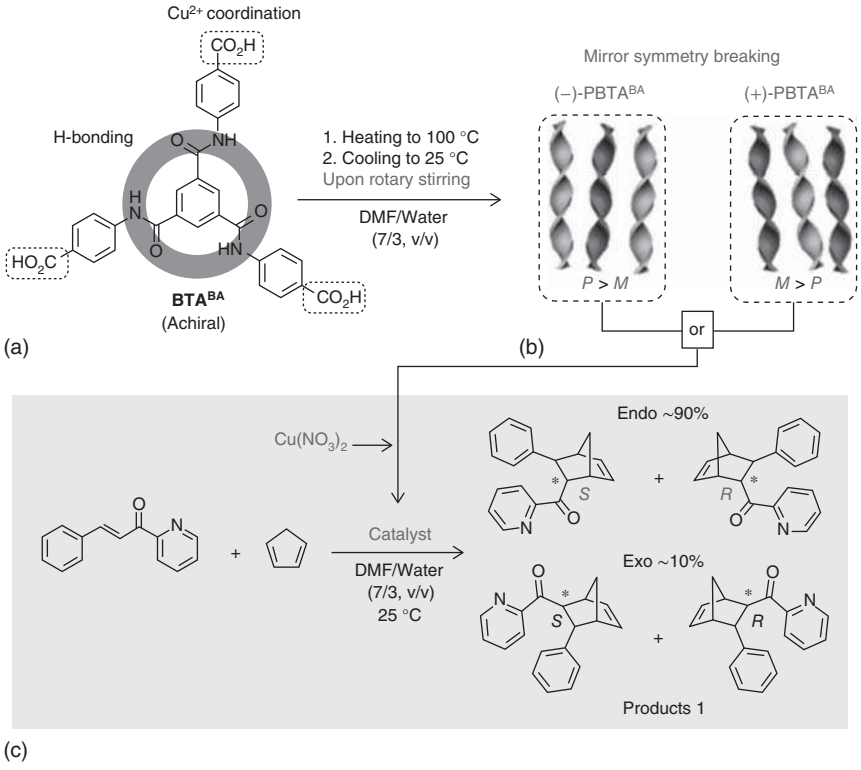

Figure 8.6 Self-assembled helical nanoribbons from achiral C3 building blocks for asymmetric Diels–Alder reaction. (a) The chemical structure of monomeric ligand. (b) Schematic illustration of mirror symmetry breaking of self-assembled helical ribbons. (c) The asymmetric Diels-Alder reaction catalyzed by metal/helical ribbon hybrid. Source: Shen et al. [26]. Reproduced with permission of Springer Nature.

centers. Through a typical heating–cooling procedure, **BTA^{BA}** was self-assembled into helical nanostructures with almost equal amounts of *M*- and *P*-helicity ribbons as demonstrated by microscopic techniques and circular dichroism analyses. It was amazing that the equilibrium of *M*- and *P*-helical nanoribbons was biased stochastically under the interference of a physical rotary field using a laboratory-used magnetic stirrer (Figure 8.6b).

The signs of CD signals of the nanoribbons are independent to the rotary direction. A random positive or negative CD signal was always obtained under clockwise or counterclockwise stirring manner. However, the CD activity is stable once emerged, which could last without fading unless the assembled structures were destroyed under heating. Besides, a chirality-controllable self-assembly process can be achieved by adding a supramolecular polymeric **BTA^{BA}** segment (**PBTA^{BA}**) as a seed into a **BTA^{BA}** solution (N,N-dimethylformamide (DMF)/water, 7 : 3 in v/v). Accordingly, (*P*)-dominant **PBTA^{BA}** seed promoted the formation of dominant *P*-helical nanoribbons with negative CD bands, while (*M*)-dominant **PBTA^{BA}** seed obtained dominant *M*-helical nanoribbons with positive CD signals. These features make the

helical nanoribbons as favorable chiral ligands for supramolecular chiral catalysis. Therefore, the authors first prepared Cu^{2+}-coordinated (−)-**PBTA^{BA}** or (+)-**PBTA^{BA}** supramolecular complex by mixing a **PBTA^{BA}** suspension (in DMF/water, 7 : 3 in v/v) and a $Cu(NO_3)_2$ solution (4.1 mM in water) at room temperature (Figure 8.6c). SEM images and CD spectra indicated that the helical nanoribbon structures of **PBTA^{BA}** were maintained after coordinating with copper ions.

The supramolecular catalysis capability of these metal complexes was carefully checked with a model Diels–Alder reaction. Typically, two substrates (azachalcone and cyclopentadiene) were successively added into a (−)-**PBTA^{BA}/Cu^{2+}** or (+)-**PBTA^{BA}/Cu^{2+}** suspension. The mixture was then stirred at room temperature for 36 hours to ensure sufficient conversion. After completion of the reaction, the organic compounds were extracted from the mixture and were analyzed on a chiral high performance liquid chromatography (HPLC) column. Both *endo* (∼90%) and *exo* (∼10%) isomers were obtained but showed an enantiomeric excess outcome. That is, (−)-**PBTA^{BA}/Cu^{2+}** and (+)-**PBTA^{BA}/Cu^{2+}** helical nanoribbons preferentially afforded (*S*)-endo and (*R*)-endo enantiomers, respectively. Repetition experiments with 76 different batches of supramolecular catalysts unambiguously confirmed the stereochemical correlation between **PBTA^{BA}/Cu^{2+}** helical nanoribbons and the products. After optimization of reaction conditions by screening the ratio of [Cu^{2+}]/[**PBTA^{BA}**] and adding a strong base to promote the anchor of copper ions to the carboxylate groups, an average *ee* value up to 46% was realized at ratios of [Cu^{2+}]/[**PBTA^{BA}**] = 1.0% and [NaOH]/[**BTA^{BA}**] = 50%. To understand the possible mechanism of asymmetrical induction of catalysis, the authors investigated the stereochemical environment of coordination pocket by binding a cationic organic dye (methylene blue, MB) and measuring its induced CD and circularly polarized luminescence (CPL) spectra. Mirror-imaged induced CD and CPL signals of organic dye were observed from mirror symmetry-broken (−)-**PBTA^{BA}**/MB and (+)-**PBTA^{BA}**/MB systems, which indirectly proved the asymmetrical nature of the carboxylate binding site. This work provided a rare example for chiral supramolecular catalysis based on a mirror symmetry-broken helical assembly of achiral building blocks, which significantly contributes to the understanding of the origin of homochirality in nature. The next challenges ahead are the preparation of enantiomeric pure helical ribbons by mirror symmetry breaking and therefore increasing the enantioselectivity to obtain chiral compounds. Together with this achievement, the emerging supramolecular catalysts generated from achiral building blocks might revolutionize the design principles of chiral catalysts and enrich synthetic methodologies.

References

1 Buerkle, L.E. and Rowan, S.J. (2012). Supramolecular gels formed from multi-component low molecular weight species. *Chem. Soc. Rev.* 41: 6089–6102.

2 Collier, J.H., Rudra, J.S., Gasiorowski, J.Z., and Jung, J.P. (2010). Multi-component extracellular matrices based on peptide self-assembly. *Chem. Soc. Rev.* 39: 3413–3424.

3 Goor, O.J.G.M., Hendrikse, S.I.S., Dankers, P.Y.W., and Meijer, E.W. (2017). From supramolecular polymers to multi-component biomaterials. *Chem. Soc. Rev.* 46: 6621–6637.

4 Li, H., Yao, Z.-J., Liu, D., and Jin, G.-X. (2015). Multi-component coordination-driven self-assembly toward heterometallic macrocycles and cages. *Coord. Chem. Rev.* 293: 139–157.

5 Tan, R., Zhu, H., Cao, C., and Chen, O. (2016). Multi-component superstructures self-assembled from nanocrystal building blocks. *Nanoscale* 8: 9944–9961.

6 Xing, P. and Zhao, Y. (2018). Controlling supramolecular chirality in multicomponent self-assembled systems. *Acc. Chem. Res.* 51: 2324–2334.

7 Deraedt, C. and Astruc, D. (2016). Supramolecular nanoreactors for catalysis. *Coord. Chem. Rev.* 324: 106–122.

8 Noble, M.E.M., Endicott, J.A., and Johnson, L.N. (2004). Protein kinase inhibitors: insights into drug design from structure. *Science* 303: 1800–1805.

9 Raynal, M., Ballester, P., Vidal-Ferran, A., and van Leeuwen, P.W.N.M. (2014). Supramolecular catalysis. Part 2: artificial enzyme mimics. *Chem. Soc. Rev.* 43: 1734–1787.

10 Jiang, J., Ouyang, G., Zhang, L., and Liu, M. (2017). Self-assembled chiral nanostructures as scaffolds for asymmetric reactions. *Chem. Eur. J.* 23: 9439–9450.

11 Raynal, M., Ballester, P., Vidal-Ferran, A., and van Leeuwen, P.W.N.M. (2014). Supramolecular catalysis. Part 1: non-covalent interactions as a tool for building and modifying homogeneous catalysts. *Chem. Soc. Rev.* 43: 1660–1733.

12 Tang, Y., He, Y., Feng, Y., and Fan, Q. (2018). Asymmetric supramolecular catalysis based on macrocyclic host molecules. *Prog. Chem.* 30: 476–490.

13 Liu, M., Zhang, L., and Wang, T. (2015). Supramolecular chirality in self-assembled systems. *Chem. Rev.* 115: 7304–7397.

14 Morrow, S.M., Bissette, A.J., and Fletcher, S.P. (2017). Transmission of chirality through space and across length scales. *Nat. Nanotechnol.* 12: 410–419.

15 Boersma, A.J., Klijn, J.E., Feringa, B.L., and Roelfes, G. (2008). DNA-based asymmetric catalysis: sequence-dependent rate acceleration and enantioselectivity. *J. Am. Chem. Soc.* 130: 11783–11790.

16 Park, S. and Sugiyama, H. (2010). DNA-based hybrid catalysts for asymmetric organic synthesis. *Angew. Chem. Int. Ed.* 49: 3870–3878.

17 Desmarchelier, A., Caumes, X., Raynal, M. et al. (2016). Correlation between the selectivity and the structure of an asymmetric catalyst built on a chirally amplified supramolecular helical scaffold. *J. Am. Chem. Soc.* 138: 4908–4916.

18 Li, Y., Hammoud, A., Bouteiller, L., and Raynal, M. (2020). Emergence of homochiral benzene-1,3,5-tricarboxamide helical assemblies and catalysts upon addition of an achiral monomer. *J. Am. Chem. Soc.* 142: 5676–5688.

19 Jin, Q., Zhang, L., Cao, H. et al. (2011). Self-assembly of copper(II) ion-mediated nanotube and its supramolecular chiral catalytic behavior. *Langmuir* 27: 13847–13853.

20 Jiang, J., Meng, Y., Zhang, L., and Liu, M. (2016). Self-assembled single-walled metal-helical nanotube (M-HN): creation of efficient supramolecular catalysts for asymmetric reaction. *J. Am. Chem. Soc.* 138: 15629–15635.

21 Yuan, C., Jiang, J., Sun, H. et al. (2018). Opposite enantioselectivity by nanotubes and nanospheres self-assembled from dirhodium(II) and an L-glutamic acid terminated bolaamphiphile. *ChemCatChem* 10: 2190–2194.

22 Wang, S., Jiang, H., Zhang, L. et al. (2018). Enantioselective activity of hemin in supramolecular gels formed by co-assembly with a chiral gelator. *ChemPlusChem* 83: 1038–1043.

23 Arlegui, A., Soler, B., Galindo, A. et al. (2019). Spontaneous mirror-symmetry breaking coupled to top-bottom chirality transfer: from porphyrin self-assembly to scalemic Diels–Alder adducts. *Chem. Commun.* 55: 12219–12222.

24 Goldanskii, V.I. and Kuzmin, V.V. (1989). Spontaneous mirror symmetry-breaking in nature and the origin of life. *Uspekhi Fizicheskikh Nauk* 157: 3–50.

25 Ribo, J.M., Hochberg, D., Crusats, J. et al. (2017). Spontaneous mirror symmetry breaking and origin of biological homochirality. *J. R. Soc. Interface* 14: 20170699.

26 Shen, Z., Sang, Y., Wang, T. et al. (2019). Asymmetric catalysis mediated by a mirror symmetry-broken helical nanoribbon. *Nat. Commun.* 10: 3976.

Part III

Ligand–Substrate Interactions

9

Harnessing Ligand–Substrate Non-covalent Interactions for Control of Site-Selectivity in Transition Metal-Catalyzed C–H Activation and Cross-Coupling

Robert J. Phipps

University of Cambridge, Department of Chemistry, Lensfield Road, Cambridge, CB2 1EW, UK

9.1 Introduction

Transition metals as catalysts for chemical reactions have provided a rich source of new and exciting reactivity which is being expanded continually. The breadth of important reactions that have been enabled by transition metals, particularly over the past half-century, is staggering. As any textbook articulates, a thorough exploration and understanding of the metal–ligand relationship is crucial to many processes and the rational design of ligands has opened many doors, including those which lead to the control of enantioselectivity. Although the most commonly used ligands primarily utilize repulsive steric interactions with which to exercise control over competing transition states, it is notable that even since the earliest days, strategies that instead use attractive interactions have been considered. Inspiration from the ways in which attractive non-covalent interactions are used so productively by enzymes at the active site has long nudged chemists to consider how such features might be incorporated into small molecule catalysts [1]. For control of enantioselectivity, this is now a fairly established strategy and is increasingly common for designs to incorporate ligand–substrate interactions, the past decades worth of advances we have recently reviewed comprehensively [2]. The challenge of inducing enantioselectivity in a reaction that by default produces a racemate is a fairly self-evident one. A parallel selectivity challenge which is perhaps more nuanced is that of controlling site-selectivity [3]. This challenge has become more important to address as transition-catalyzed methods have become more sophisticated and the reactivity manifolds have been expanded. In the later decades of the twentieth century, Breslow and coworkers carried out pioneering and visionary work on controlling the site-selective functionalization of steroid scaffolds. In most of these cases, the reactivity was achieved using free radicals to abstract hydrogen atoms from various positions – a strategy that is now receiving a great deal of attention with the popularization of photoredox catalysis and demonstrating that Breslow's work in this area was very much ahead of its time [4]. Since that time the use of transition metals to functionalize C—H bonds has progressed enormously and this has provided new

Supramolecular Catalysis: New Directions and Developments, First Edition.
Edited by Piet W.N.M. van Leeuwen and Matthieu Raynal.

tools, which can present both site-selectivity challenges and opportunities. Indeed, Breslow carried out important early work using transition metal catalysis to achieve remote steroidal C–H functionalization, the use of manganese porphyrins being a prominent example [5]. Now that reactions which functionalize C—H bonds are far more mainstream, so too is the issue of site-selectivity [6]. One of the oft-quoted advantages of C–H functionalization is that, by employing this strategy, one can now consider any C—H bond a functional handle. Therein too lies the challenge of how to choose one particular one over all of the others [7]. In many cases, the requirement for a directing group to enable reactivity may consequently dictate selectivity, but there are also numerous methods that do not require directing groups and present significant and exciting site-selectivity challenges.

9.2 C–H Borylation

At the outset of the work described herein, we were inspired by the important prior work in which ligand–substrate non-covalent interactions had been used to control regioselectivity or site-selectivity [6]. This includes strategies to control regioselectivity in rhodium-catalyzed hydroformylation, and both Reek and Breit had made important advances in this area. In Breit's case, a triarylphosphine ligand is functionalized at a remote position with an acylguanidinium functionality. The guanidine portion engages in a dual hydrogen bonding interaction with the carboxylic acid of a suitable alkene substrate and thus directs the catalysis to produce the linear product [8]. In Reek's case, a bidentate ligand site for rhodium is built into an established ion-receptor design and exerts remarkable levels of regiocontrol in the hydroformylation of alkenes that bear carboxylic acids [9].

Our goal was to apply the same principles and overall strategy as in the prior hydroformylation work but to turn to the challenge of site-selectivity in the C–H functionalization of arenes, an area in which the site-selectivity challenge (ortho, meta, and para) is evident. Much attention has been focused on arene C–H functionalization in recent years, and there is insufficient space in this highlight chapter to details of all of the strategies. In short, the methodology that we sought to utilize was the iridium-catalyzed borylation of arene C—H bonds. First developed in the early 2000s independently by Maleczka, Smith and coworkers and Hartwig, Ishiyama and coworkers, an active iridium(III) complex which typically features a bipyridine ligand is able to oxidatively add into arene C—H bonds under remarkably mild conditions in the presence of a multitude of functional groups [10–12]. Furthermore, the ensuing boron-functionalized products are hugely versatile and can be transformed to all manner of functional groups and substituents. One of the very attractive aspects of the reaction from the standpoint of applying non-covalent interactions is that the reaction typically works very well in non-polar solvents. Furthermore, it is extremely tolerant of many common functional groups and operates under the mild conditions of room temperature or only moderately elevated temperatures. A remarkable aspect of the reaction is that its regioselectivity is predominantly based on substrate steric considerations,

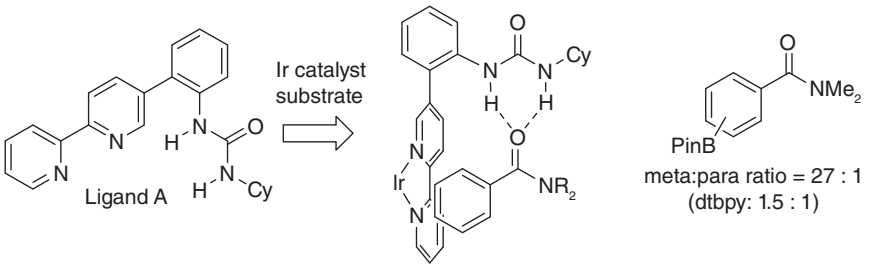

Figure 9.1 Kanai and Kuninobu's use of hydrogen bonding between ligand and substrate to control regioselectivity in Ir-catalyzed borylation.

with very little influence from electronics [13]. This has made it very well suited to the synthesis of 1,3,5-trisubstitued arenes from 1,3-disubstituted precursors. But, mixtures of regioisomers typically occur on substrates with no clear steric preference, such as mono-substituted and 1,2-disubstituted arenes. A number of creative strategies had been devised to direct borylation and overcome its native steric preference, and naturally most of these result in ortho-selective borylation [14]. We hypothesized that if we could incorporate remote functionality into the bipyridine ligand scaffold that would be able to engage in non-covalent interactions with matching functionality on the substrate, then a meta-selective borylation may be feasible. While we were in the early stages of our work, Kanai, Kuninobu and coworkers elegantly realized such a strategy by incorporating a urea group at a remote position of the bipyridine ligand such that it could interact with a carbonyl on the substrate through hydrogen bonding, resulting in meta-selective borylation (Figure 9.1) [15].

Our approach was related, but distinct. Specifically, we were curious to explore the use of an ion-pairing interaction between the bipyridine ligand and the substrate to test whether such an electrostatic interaction would be viable in distinguishing between the three possible positions of reaction on the arene. Although electrostatic interactions had been used with great success in enantioselective catalysis, there were very few examples where they were used to control site-selectivity. In the 1980s, Breslow carried out two very interesting studies on steroid functionalization using ion-pairing interactions. In the first, good site-selectivity in the functionalization of substrate containing an extended alkyl chain was obtained by using two ion-pairing interactions between it and a photoexcitable benzophenone [16]. Later work was able to utilize a single ion-pairing interaction to enable radical chlorination of a rigid quaternary ammonium-functionalized steroid with encouraging site-selectivity. In one case in the latter study, catalytic turnover, albeit low, was shown to be possible, presumably occurring via ion exchange [17].

Ion-pairing interactions are probably underexplored for the purpose of fine selectivity control due to their association with low-directionality, particularly compared with the multiple hydrogen bonding interactions that prior catalyst designs had mostly used. We posited that for the arene borylation, directionality may not be as important as obtaining the proper distance between the group on the substrate that is interacting with the ligand and the reactive iridium center.

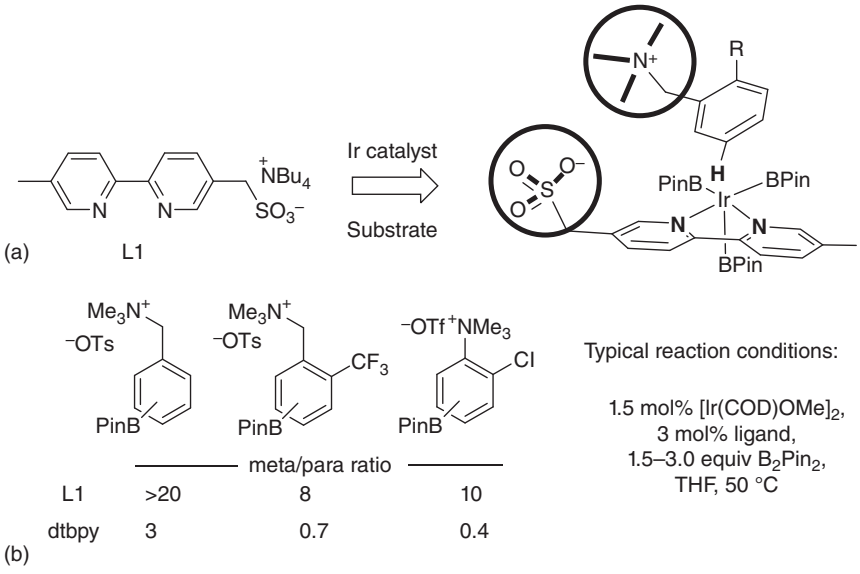

Figure 9.2 Our use of ion-pairing between ligand and substrate to control regioselectivity in Ir-catalyzed borylation. (a) Outline of hypothesis. (b) Application to aniline- and benzylamine-derived quaternary ammonium salts. Source: Adapted from Davis and Phipps [6]. Dtbpy = 4,4′-Di-*tert*-butyl-2,2′-dipyridyl.

We anticipated that with an appropriate ligand structure, meta-selective borylation may be feasible, enabled by an ion-pairing interaction (Figure 9.2a). We commenced our studies by synthesizing four bipyridine ligands bearing distal sulfonate groups at either the 4- or 5-position and separated from the bipyridine backbone by either one or two methylene linkers. These were evaluated in the borylation of a trimethylammonium salt derived from 2-chlorobenzylamine. A single ligand of the four, **L1**, gave very good levels of selectivity for borylation at the meta position, in line with our original hypothesis [18]. We found that aniline-derived ammonium salts were also borylated with high levels of meta-selectivity, and even when all four ligands were evaluated, the same ligand, **L1**, was still by far optimal (Figure 9.2b). Various control experiments demonstrated the importance of the ionic interaction between the two – closely related neutral substrates gave no selectivity whatsoever.

In our initial study, we had only examined aniline- and benzylamine-derived quaternary ammonium salts. Both of these substrate classes have very little conformational freedom, which was an ideal starting point to explore the application of poorly directional ion-pairing interactions. The concern was that if the substrates were made more flexible, such as by increasing the chain length between the arene and the ammonium group, then control of borylation regioselectivity may be harder to achieve. We were pleasantly surprised to find that even with phenethylamine-derived salts (two carbons in chain) and phenylpropylamine-derived salts (three carbons in chain), reasonably good meta-selectivity could still be obtained, although it did decrease as the chain grew longer (Figure 9.3a) [19]. We subsequently showed that our ion-pair directed

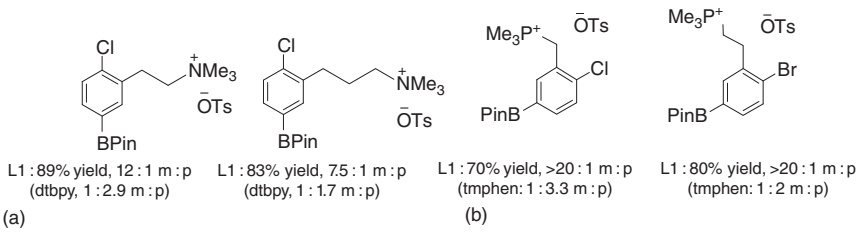

Figure 9.3 Examples of longer chain ammonium salts (a) as well as phosphonium salts (b) in ion-pair directed borylation. Tmphen = 3,4,7,8-Tetramethyl-1,10-phenanthroline.

borylation is also effective on trimethyl phosphonium salts with various chain lengths (Figure 9.3b) [20]. In all of these cases, ligand **L1** was always found to be optimal, despite variations of the design being tested.

Given the success of **L1** in ion-pair-directed borylations, we sought to use it in hydrogen bonding mode. The sulfonate group should function as a proficient hydrogen bond acceptor, and we envisioned that it should be able to engage in attractive interactions with arenes bearing amide functionality. We determined that trifluoroacetyl-protected amides worked very well, and we could tolerate a range of chain lengths between the arene and the amide with excellent meta-selectivity in the borylation (Figure 9.4a) [21]. In all cases, control experiments with non-sulfonated bipyridine ligands gave poor selectivity, as did *N*-alkylated amides, supporting the hypothesis that hydrogen bonding between ligand and substrate was crucial for the regioselective outcome. The fact that the ligand was able to operate in two different "modes" gave us the opportunity to devise some internal competition substrates between ion-pairing and hydrogen bonding, with the site of borylation determining the outcome of the competition (Figure 9.4b) [19]. As can be seen, ion-pairing was triumphant in all three cases and highlights the strong directing effect of this interaction which is arguably underused in catalysis.

All of the protocols developed thus far had resulted in meta-selective borylation by the use of ligand–substrate attractive interactions, either ion-pairing or hydrogen bonding. A goal for us was to develop a complementary ligand system that would result in para-selective borylation. Due to the significant extra reach that would be required from the ligand scaffold in order to reach over the meta position, we found it challenging to come up designs that were both synthetically feasible and effective. Ultimately, we used a different strategy in which we utilized ion-pairing to associate a bulky tetrabutylammonium cation with anionic arene substrates with the aim that borylation at the meta position would disfavored through sheer bulk of the cation. We found that a range of common building block substrates (anilines, phenols, benzylamines, benzyl alcohols) could be easily rendered anionic by conversion to their corresponding sulfamate or sulfonate salts. Borylation of these salts after tetrabutylammonium was installed as the cation uniformly resulted in excellent selectivity for the arene para position (see Figure 9.5 for example on 2-chloroaniline) [22]. A systematic evaluation of the size of the alkyl chains on the tetraalkylammonium cation correlated very well with para-selectivity.

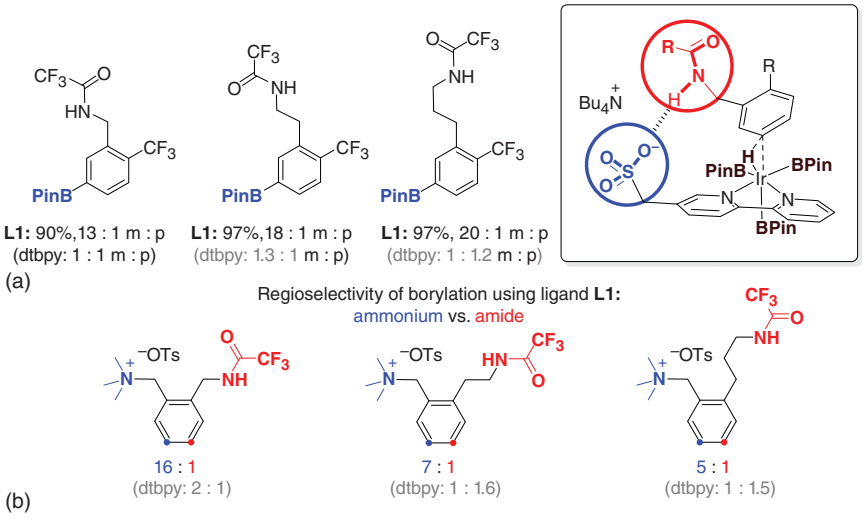

Figure 9.4 Examples of the use of ligand **L1** for hydrogen bond-directed borylation (a) and competition substrates designed to test between hydrogen bonding and ion-pairing (b).

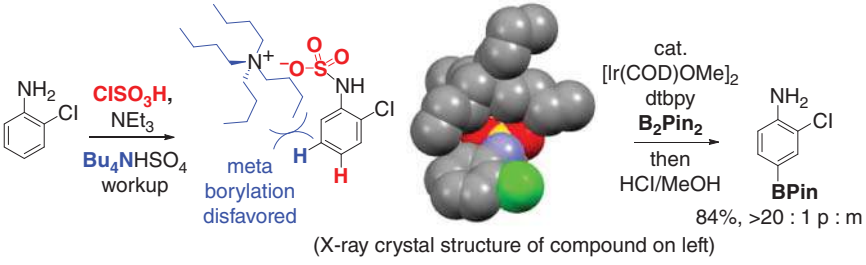

Figure 9.5 Para-selective borylation of tetrabutylammonium salts of arenes-bearing sulfamate functionality.

In the various applications of anionic sulfonate ligand **L1**, the counter cation had always been tetrabutylammonium. This was a good choice of cation to allow the ligand to be soluble in the relatively non-polar organic solvents used. In the ion-pair directed borylation, we hypothesized that counterion exchange may occur between the substrate and tetrabutylammonium, but in the hydrogen bond-directed variant, the tetrabutylammonium cation is presumably still associated with the sulfonate of the ligand during the whole process, including the rate-determining C–H activation step (see Figure 9.4, inset box). We speculated whether replacement of that tetrabutyl ammonium with a chiral quaternary ammonium cation may allow enantiodetermining C–H activation to occur in a symmetrical substrate that possessed prochiral C—H bonds (Figure 9.6a). Chiral cations have been used extensively in organocatalysis, most notably asymmetric phase-transfer catalysis, but have been only rarely incorporated into transition metal catalysis [23, 24]. One likely reason for this is that it is relatively rare for anionic metal complexes to appear

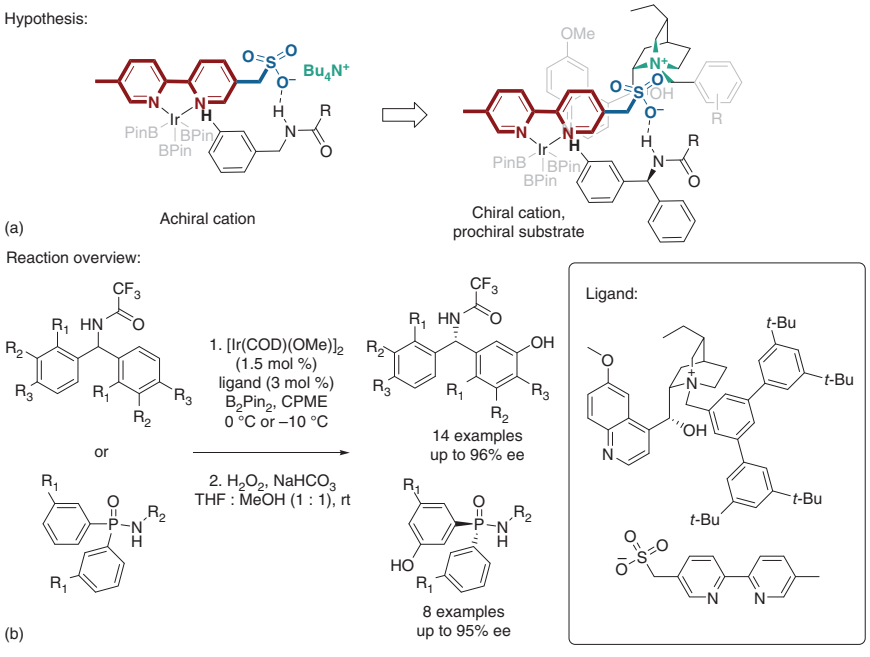

Figure 9.6 Enantioselective borylation directed by a chiral cation: (a) hypothesis and (b) overview of reaction. Source: Adapted from Fanourakis et al. [2].

in catalytic cycles; thus, the opportunities for pairing chiral cations with them are limited. In contrast, cationic metal complexes are much more widespread and have been very productively paired with chiral anions, the charge inverted strategy [25]. We reasoned that if our approach was successful, it could potentially allude to a general method for incorporating chiral cations into mainstream transition metal catalysis – attachment of a sulfonate group onto the ligand such that it does not interfere with chemistry at the metal center then provides the handle for association of the chiral cation. In important prior work, Ooi and coworkers demonstrated the charge-inverted approach, whereby a phosphine ligand is rendered cationic and a chiral anion is associated for the purposes of achieving asymmetric π-allyl chemistry under palladium catalysis [26, 27].

Paired with the sulfonated bipyridine ligand, we evaluated a number of quaternized dihydroquinine analogs where the variation was on the benzyl group which achieved the quaternization. These ion-paired catalysts were evaluated on a symmetrical benzhydrylamide substrate, not dissimilar to those that worked effectively in the meta-selective amide borylation. After a systematic exploration, we identified a large teraryl motif bearing four *tert*-butyl groups around the periphery as being optimal (Figure 9.6b, inset box). Careful optimization of solvent and temperature enabled us to obtain high enantiomeric excess in the borylated product, which was converted to the corresponding phenol via oxidation for ease of isolation and analysis [28]. We first demonstrated the scope of the enantioselective borylation on substrates which possessed no regioselectivity choice for the borylation, i.e. there

was only a single accessible position for the catalyst on each prochiral aromatic ring. We subsequently evaluated substrates which did possess a choice, mostly being 1,2-disubstitued arenes. We were pleased to find that the ion-paired ligand was able to control both regioselectivity and enantioselectivity under the optimized conditions, with only a small reduction in the latter values. Furthermore, we were able to demonstrate that this desymmetrizing borylation was effective on a quite different class of substrates allowing formation of a chiral center at phosphorous, as opposed to carbon. Symmetrical phosphinamides, which bear a hydrogen bond donor in the same position as the benzhydrylamide substrates, were subjected to the previously optimized conditions and worked very effectively. In the benzhydrylamide series, we demonstrated that the pseudoenantiomer, derived from dihydroquinidine, gave the opposite enantiomer of product with an opposite and only slightly reduced enantiomeric excess. Various control experiments highlighted the crucial need for the hydrogen bond with the substrate as well as the ion-pairing interaction between the chiral cation and the sulfonated bipyridine ligand. We are now excited to explore how widely this strategy can be applied.

9.3 Cross-Coupling

The impact that palladium-catalyzed cross-coupling has had on contemporary synthetic chemistry is hard to overstate. One of the key features of cross-coupling is its reliability and predictability as a disconnection, which is thanks to the wealth of research that has been carried out over the past half century. At first sight, there is little in the way of a site-selectivity choice in most cross-coupling reactions since the partners used typically possess one (pseudo)halide and one organometallic functionality each. Considerable advances have been made in developing highly chemoselective catalysts to discriminate between different (pseudo)halides in a single substrate [29]. But, the disadvantage here is that those (pseudo)halides must be installed in a regioselective manner, which can require significant synthetic effort. Accordingly, it could be very synthetically valuable to be able to take an arene with multiple instances of the same halide and use catalyst control to select which of those halides undergoes the cross-coupling in a site-selective manner [30, 31]. Particularly, aryl chlorides are inert to many other reaction types and can be retained over the course of numerous synthetic steps and so we embarked on a project to attempt to use non-covalent interactions to control site-selective oxidative addition to multiply chlorinated arenes.

As in our prior work on C–H borylation, we envisaged some type of non-covalent interaction between a functional group on the arene and a partner functional group on the ligand. In this case, the obvious choice of ligand class was a phosphine. In addition, we were keen to use the sulfonate group as the functionality of choice since we had seen success with this earlier and it also offers the option of using ion-pairing or hydrogen bonding interactions, or both. There are many sulfonated phosphine ligands reported in the literature in order to solubilize transition metal complexes in water, and we were particularly drawn to the sulfonated version of SPhos, sSPhos, that was reported by Anderson and Buchwald for enabling aqueous

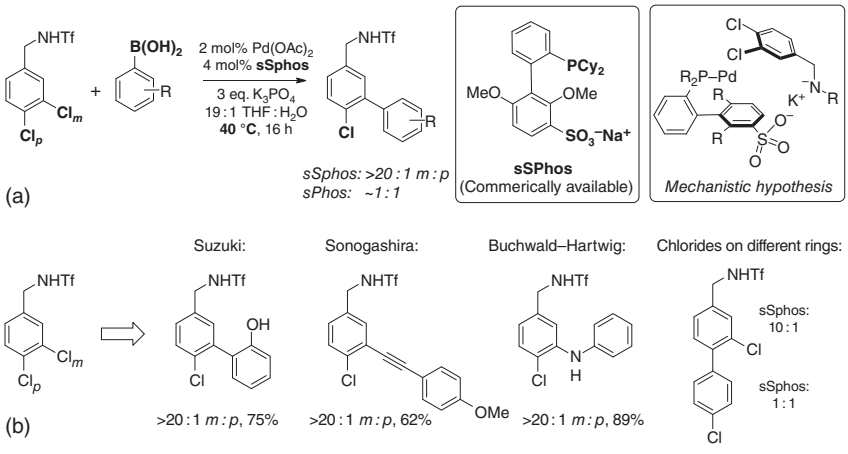

Figure 9.7 Site-selective cross-coupling using a sulfonated variant of SPhos, sSPhos: (a) reaction overview for Suzuki–Miyaura coupling, catalyst structure and mechanistic hypothesis and (b) examples of various cross-coupling protocols that are compatible.

cross-coupling [32, 33]. In sSPhos, the sulfonate is introduced on the lower, more electron-rich aryl ring in the 2-biaryldialkyl phosphine ligand scaffold. The challenge that we investigated was that involving an arene substrate bearing 3,4-dichloro substitution and with no electronic bias from the functional group at position 1. Since the chlorides in such a substrate are "remote" from the existing functionality, it is very difficult to imagine how these could be site-selectively cross-coupled using other approaches. We originally envisaged that the sulfonate group of sSPhos may engage in a hydrogen bonding interaction with a suitable hydrogen bond donor such as an amide located on the substrate. However, after optimization studies, it became apparent that a Brønsted acidic functionality was required on the substrate to obtain good results. Specifically, we found that a 3,4-dichloroarene bearing a triflamide group gave a >20 : 1 ratio preferring Suzuki–Miyaura coupling at the chloride at the meta position over the para (Figure 9.7a) [34]. After demonstrating that a broad scope of boronic acids were compatible and that Sonogashira couplings were also viable, we were pleased to find that Buchwald–Hartwig couplings of anilines could also be carried out selectively at the chloride at the meta position using a modified version of sSPhos that featured *tert*-butyl as opposed to cyclohexyl groups on the phosphorous atom (Figure 9.7b). We also demonstrated that other common Brønsted acidic groups were competent to engage in putative interaction with the ligand and showed that carboxylic acid and sulfonic acid substrates also give highly site-selective Suzuki–Miyaura coupling. We hypothesize that the inorganic base added to the reaction, K_2CO_3, deprotonates the substrate to form the potassium salt and that this potassium cation is able to engage in attractive electrostatic interactions with the sulfonate group of the ligand in the transition state for oxidative addition (see Figure 9.7a, inset box). This was supported by control experiments using crown ethers.

We next asked whether it would be possible to combine this mode of catalyst direction with a C–H activation process proceeding by the concerted-metalation–

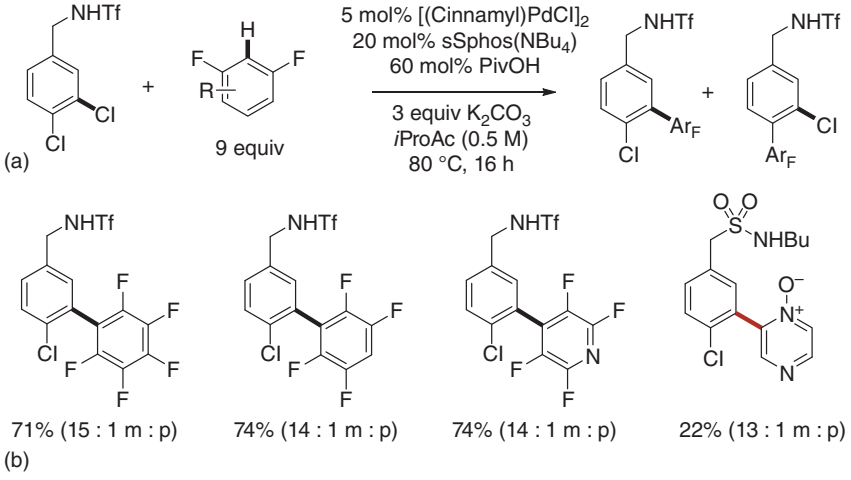

Figure 9.8 Site-selective coupling with fluoroarenes, incorporating a C–H activation step: (a) reaction overview and (b) examples of various substrates that are compatible.

deprotonation (CMD) mechanism that is at the heart of many important Pd-catalyzed C–H functionalization processes [35, 36]. Whilst the catalyst would still be responsible for controlling site-selective oxidative addition in the same way as before, transmetalation would need to be replaced by a CMD-type C–H activation step, as pioneered by Fagnou and coworkers [37, 38]. We targeted using fluorinated arenes as a substrate as these are reactive in direct arylation using aryl chlorides [39]. Taking direct inspiration from Fagnou's foundational work, we modified the conditions used before to include pivalic acid, *i*PrOAc as a solvent, and a higher reaction temperature [40]. After optimization, excellent site-selectivity could be achieved, again for the chloride at the meta position and a range of fluorinated arenes and heteroarenes were demonstrated to be compatible as well as several non-fluorinated hetercyclic *N*-oxides, albeit in low yields (Figure 9.8) [41]. We also demonstrated that further functional groups are able to engage in the electrostatic interaction with the catalyst – carboxylic acid and sulfonate, as before but now also phosphonic acid, and amine-derived sulfonates. Prior to this work, there were very few examples in which non-covalent interactions were utilized in combination with palladium-catalyzed C–H activation. We believe that there is huge potential for applying non-covalent strategies to control site-selectivity in Pd-catalyzed C–H functionalization, and our study demonstrated that the two are fundamentally compatible, with the caveat that we have not controlled site-selectivity in the C–H functionalization step itself in this particular work.

9.4 Concluding Remarks

Non-covalent interactions have been used extensively by supramolecular chemists for assembling remarkable macromolecular assemblies. The potential for

integrating discrete and targeted non-covalent interactions into transition metal complexes to direct their fantastic reactivity is obvious. Many research groups are now considering this approach when formulating designs for new catalytic systems. We, and others, have made contributions in the area of iridium-catalyzed C–H borylation and shown how powerful this approach can be, not only for the control of site-selectivity but also enantioselectivity. Whilst we do not commonly describe our approaches as "supramolecular," the presumed transition state in the latter case in which an anionic ligand, chiral cation, and substrate-bearing hydrogen bond donor are assembled through a network of electrostatic and hydrogen bonding interactions is without doubt veering toward the supramolecular end of the catalysis spectrum. We have also applied similar approaches to the challenge of site-selective cross-coupling using palladium catalysis. Our future efforts involve taking very well-utilized mainstream chemical reactions and imposing non-covalent strategies for the control site-selectivity as well as, in some cases, enantioselectivity.

Acknowledgments

I am grateful to the Royal Society for a University Research Fellowship and to all of my outstanding coworkers who have contributed to the above-mentioned studies – Holly, Madalina, Georgi, Will, Robert, Ben, James, Antti, David, Bernadette, and Violeta.

References

1 Knowles, R.R. and Jacobsen, E.N. (2010). Attractive noncovalent interactions in asymmetric catalysis: links between enzymes and small molecule catalysts. *Proc. Natl. Acad. Sci. U.S.A.* 107 (48): 20678–20685.

2 Fanourakis, A., Docherty, P.J., Chuentragool, P., and Phipps, R.J. (2020). Recent developments in enantioselective transition metal catalysis featuring attractive noncovalent interactions between ligand and substrate. *ACS Catal.* 10 (18): 10672–10714.

3 Huang, Z. and Dong, G. (2017). Site-selectivity control in organic reactions: a quest to differentiate reactivity among the same kind of functional groups. *Acc. Chem. Res.* 50 (3): 465–471.

4 Breslow, R. (1999). Chapter 6: Biomimetic reactions directed by templates and removable tethers. In: *Templated Organic Synthesis* (eds. F. Diederich and P.J. Stang), 158–188. Wiley.

5 Breslow, R., Zhang, X., and Huang, Y. (1997). Selective catalytic hydroxylation of a steroid by an artificial cytochrome P-450 enzyme. *J. Am. Chem. Soc.* 119 (19): 4535–4536.

6 Davis, H.J. and Phipps, R.J. (2017). Harnessing non-covalent interactions to exert control over regioselectivity and site-selectivity in catalytic reactions. *Chem. Sci.* 8 (2): 864–877.

7 Hartwig, J.F. (2017). Catalyst-controlled site-selective bond activation. *Acc. Chem. Res.* 50 (3): 549–555.

8 Šmejkal, T. and Breit, B. (2008). A supramolecular catalyst for regioselective hydroformylation of unsaturated carboxylic acids. *Angew. Chem. Int. Ed.* 47 (2): 311–315.

9 Dydio, P., Detz, R.J., and Reek, J.N.H. (2013). Precise supramolecular control of selectivity in the Rh-catalyzed hydroformylation of terminal and internal alkenes. *J. Am. Chem. Soc.* 135 (29): 10817–10828.

10 Ishiyama, T., Takagi, J., Ishida, K. et al. (2002). Mild iridium-catalyzed borylation of arenes. High turnover numbers, room temperature reactions, and isolation of a potential intermediate. *J. Am. Chem. Soc.* 124 (3): 390–391.

11 Cho, J.-Y., Tse, M.K., Holmes, D. et al. (2002). Remarkably selective iridium catalysts for the elaboration of aromatic C—H bonds. *Science* 295 (5553): 305–308.

12 Mkhalid, I.A.I., Barnard, J.H., Marder, T.B. et al. (2010). C–H activation for the construction of C—B bonds. *Chem. Rev.* 110 (2): 890–931.

13 Hartwig, J.F. (2011). Regioselectivity of the borylation of alkanes and arenes. *Chem. Soc. Rev.* 40 (4): 1992–2002.

14 Ros, A., Fernandez, R., and Lassaletta, J.M. (2014). Functional group directed C–H borylation. *Chem. Soc. Rev.* 43 (10): 3229–3243.

15 Kuninobu, Y., Ida, H., Nishi, M., and Kanai, M. (2015). A meta-selective C–H borylation directed by a secondary interaction between ligand and substrate. *Nat. Chem.* 7 (9): 712–717.

16 Breslow, R., Rajagopalan, R., and Schwarz, J. (1981). Selective functionalization of doubly coordinated flexible chains. *J. Am. Chem. Soc.* 103 (10): 2905–2907.

17 Breslow, R. and Heyer, D. (1983). Directed steroid chlorination catalyzed by an ion-paired template. *Tetrahedron Lett.* 24 (46): 5039–5042.

18 Davis, H.J., Mihai, M.T., and Phipps, R.J. (2016). Ion pair-directed regiocontrol in transition-metal catalysis: a meta-selective C–H borylation of aromatic quaternary ammonium salts. *J. Am. Chem. Soc.* 138 (39): 12759–12762.

19 Mihai, M.T., Davis, H.J., Genov, G.R., and Phipps, R.J. (2018). Ion pair-directed C–H activation on flexible ammonium salts: meta-selective borylation of quaternized phenethylamines and phenylpropylamines. *ACS Catal.* 8 (5): 3764–3769.

20 Lee, B., Mihai, M.T., Stojalnikova, V., and Phipps, R.J. (2019). Ion-pair-directed borylation of aromatic phosphonium salts. *J. Org. Chem.* 84 (20): 13124–13134.

21 Davis, H.J., Genov, G.R., and Phipps, R.J. (2017). Meta-selective C–H borylation of benzylamine-, phenethylamine-, and phenylpropylamine-derived amides enabled by a single anionic ligand. *Angew. Chem. Int. Ed.* 56 (43): 13351–13355.

22 Mihai, M.T., Williams, B.D., and Phipps, R.J. (2019). Para-selective C–H borylation of common arene building blocks enabled by ion-pairing with a bulky countercation. *J. Am. Chem. Soc.* 141 (39): 15477–15482.

23 Hashimoto, T. and Maruoka, K. (2007). Recent development and application of chiral phase-transfer catalysts. *Chem. Rev.* 107 (12): 5656–5682.

24 Ohmatsu, K. and Ooi, T. (2019). Cationic organic catalysts or ligands in concert with metal catalysts. *Top. Curr. Chem.* 377 (6): 31.

25 Phipps, R.J., Hamilton, G.L., and Toste, F.D. (2012). The progression of chiral anions from concepts to applications in asymmetric catalysis. *Nat. Chem.* 4: 603.

26 Ohmatsu, K., Ito, M., Kunieda, T., and Ooi, T. (2012). Ion-paired chiral ligands for asymmetric palladium catalysis. *Nat. Chem.* 4 (6): 473–477.

27 Ohmatsu, K., Ito, M., Kunieda, T., and Ooi, T. (2013). Exploiting the modularity of ion-paired chiral ligands for palladium-catalyzed enantioselective allylation of benzofuran-2(3*H*)-ones. *J. Am. Chem. Soc.* 135 (2): 590–593.

28 Genov, G.R., Douthwaite, J.L., Lahdenperä, A.S.K. et al. (2020). Enantioselective remote C–H activation directed by a chiral cation. *Science* 367 (6483): 1246–1251.

29 Fricke, C., Sperger, T., Mendel, M., and Schoenebeck, F. Catalysis with palladium(I) dimers. *Angew. Chem. Int. Ed.* 60 (7): 3355–3366.

30 Ishikawa, S. and Manabe, K. (2010). DHTP ligands for the highly ortho-selective, palladium-catalyzed cross-coupling of dihaloarenes with Grignard reagents: a conformational approach for catalyst improvement. *Angew. Chem. Int. Ed.* 49 (4): 772–775.

31 Yamaguchi, M. and Manabe, K. (2016). Ligand-controlled site-selective cross-coupling. In: *Site-Selective Catalysis* (ed. T. Kawabata), 1–25. Cham: Springer International Publishing.

32 Herrmann, W.A. and Kohlpaintner, C.W. (1993). Water-soluble ligands, metal complexes, and catalysts: synergism of homogeneous and heterogeneous catalysis. *Angew. Chem. Int. Ed.* 32 (11): 1524–1544.

33 Anderson, K.W. and Buchwald, S.L. (2005). General catalysts for the Suzuki–Miyaura and Sonogashira coupling reactions of aryl chlorides and for the coupling of challenging substrate combinations in water. *Angew. Chem. Int. Ed.* 44 (38): 6173–6177.

34 Golding, W.A., Pearce-Higgins, R., and Phipps, R.J. (2018). Site-selective cross-coupling of remote chlorides enabled by electrostatically directed palladium catalysis. *J. Am. Chem. Soc.* 140 (42): 13570–13574.

35 Ackermann, L. (2011). Carboxylate-assisted transition-metal-catalyzed C–H bond functionalizations: mechanism and scope. *Chem. Rev.* 111 (3): 1315–1345.

36 Davies, D.L., Macgregor, S.A., and McMullin, C.L. (2017). Computational studies of carboxylate-assisted C–H activation and functionalization at group 8–10 transition metal centers. *Chem. Rev.* 117 (13): 8649–8709.

37 Gorelsky, S.I., Lapointe, D., and Fagnou, K. (2008). Analysis of the concerted metalation-deprotonation mechanism in palladium-catalyzed direct arylation across a broad range of aromatic substrates. *J. Am. Chem. Soc.* 130 (33): 10848–10849.

38 Lapointe, D. and Fagnou, K. (2010). Overview of the mechanistic work on the concerted metallation–deprotonation pathway. *Chem. Lett.* 39 (11): 1118–1126.

39 Lafrance, M., Rowley, C.N., Woo, T.K., and Fagnou, K. (2006). Catalytic intermolecular direct arylation of perfluorobenzenes. *J. Am. Chem. Soc.* 128 (27): 8754–8756.

40 Lafrance, M. and Fagnou, K. (2006). Palladium-catalyzed benzene arylation: incorporation of catalytic pivalic acid as a proton shuttle and a key element in catalyst design. *J. Am. Chem. Soc.* 128 (51): 16496–16497.

41 Golding, W.A. and Phipps, R.J. (2020). Electrostatically-directed Pd-catalysis in combination with C–H activation: site-selective coupling of remote chlorides with fluoroarenes and fluoroheteroarenes. *Chem. Sci.* 11 (11): 3022–3027.

10

Supramolecular Interactions in Distal C–H Activation of (Hetero)arenes

Jyoti P. Biswas and Debabrata Maiti

Indian Institute of Technology Bombay, Department of Chemistry, Powai, Mumbai, 400076 Maharastra, India

10.1 Introduction

C–H activation has experienced tremendous growth in the recent past [1]. Direct functionalization of naturally abundant C—H bonds not only enhances step and atom economy but also gives access to important and/or exotic molecules which were previously synthetically impossible [2]. However, this strategy involves various shortcomings, which kept chemists all over the world at the edge for constant improvement. One of the major challenges associated with C–H activation is the presence of multiple chemically equivalent C—H bonds that can be activated simultaneously. Synthesis of a target molecule usually requires installation of a particular functional group at a specific position. In order to achieve such selective functionalizations, the directing group (DG) approach became popular [3–8]. However, selective distal C–H activations were found to be quite difficult to realize compared to proximal C–H functionalization. The thermodynamic instability of 10–15 membered metallacycle formation for distal C–H activation compared to the formation of five to six membered metallacycle in case of proximal position is attributed to this difficulty. Thus, proper design of directing groups along with the usage of appropriate ligands and other additives is essential to achieve an effective methodology. In this regard, our group is continuously involved in developing distal C–H activation methodologies in arene, heteroarene as well as aliphatic systems.

10.2 Distal C–H Activation of Arenes

Directing group-assisted *meta* C–H functionalization was first reported by Yu's group in 2012 [9]. A 2-benzylnitrile-based directing group was attached to benzyl alcohol through an ether linkage in order to achieve *meta* C–H olefination with activated olefins. Subsequently, various other groups including ours designed –CN-based directing groups for different substrates to reach activation of the meta position [9–15]. Unlike *ortho* C–H activation, where numerous types of directing

Supramolecular Catalysis: New Directions and Developments, First Edition.
Edited by Piet W.N.M. van Leeuwen and Matthieu Raynal.

groups could be utilized, –CN group was found to be essential till our group found an alternate and better directing group many years later. Two key reasons for this biasness are end-on binding ability of the –CN group and three-atom long straight chain which can be easily directed toward a point of interest if conformation strains are applied. Thus, it has been observed that all the –CN-directed distal C–H functionalization approaches invariably utilize conformational strains in various forms.

The other essential components of these reactions are *N*-acyl amino acid ligands and a silver salt. It is quite fascinating that in most cases, even in the presence of any other type of ligand or absence of *N*-acyl amino acids neither provides the desired product at all or very little. Thus, it has a special role in this class of reactions, which has been studied extensively both experimentally and computationally.

10.2.1 *meta* C–H Activation

In our first attempt to achieve *meta*-selective C–H olefination, 2-cyanophenyl ester of phenylacetic acid served the purpose (Figure 10.1) [16]. It was suggested according to literature precedents that the nitrile group co-ordinates with palladium catalyst and directs it toward the *meta* C—H bond. Activation of the bond provides a Pd—C bond containing intermediate which inserts into the metal-bound olefin. Subsequently, β-hydride elimination provides the desired olefinated product. Interestingly, after functionalization, the product undergoes transesterification with the alcohol solvent (hexafluoroisopropanol, HFIP). Various activated olefins as well as substitution at the arene ring were well tolerated under the reaction condition, but selectivity was an issue in a few cases. Therefore, we developed a more robust sulfonyl linker bearing a nitrile directing group (Figure 10.2) [17]. This not only solved the transesterification problem but also enhanced meta selectivity by virtue of higher conformational rigidity. Introduction of a sulfonyl linker also allowed incorporation of other functionalization such as –OH, –CN, –COOR, etc. at meta position [18, 19]. At this point, we wanted to study the detailed mechanism and role of all the reaction components both computationally and experimentally. Systematic study showed that the *N*-acyl amino acid ligand forms a bis coordinated complex with the catalyst, which in turn co-ordinates with the nitrile of the directing group. The metal then activates the nearby C—H bond, but the simultaneous abstraction of the hydrogen by the acyl group of the ligand is crucial as found in previous studies as well. This mechanism of C–H activation is termed Concerted Metalation–Deprotonation (CMD), which is proved to be lowest

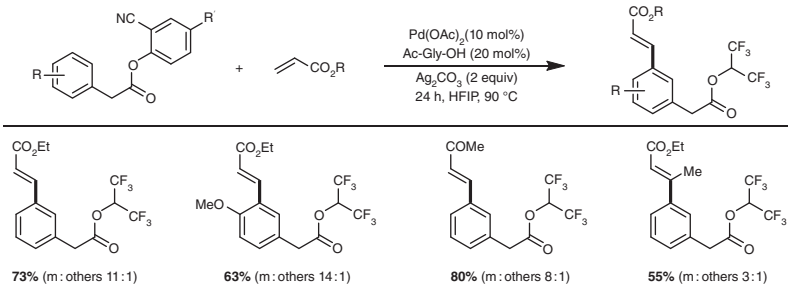

Figure 10.1 Cyanophenol directing group-assisted *meta* C–H olefination.

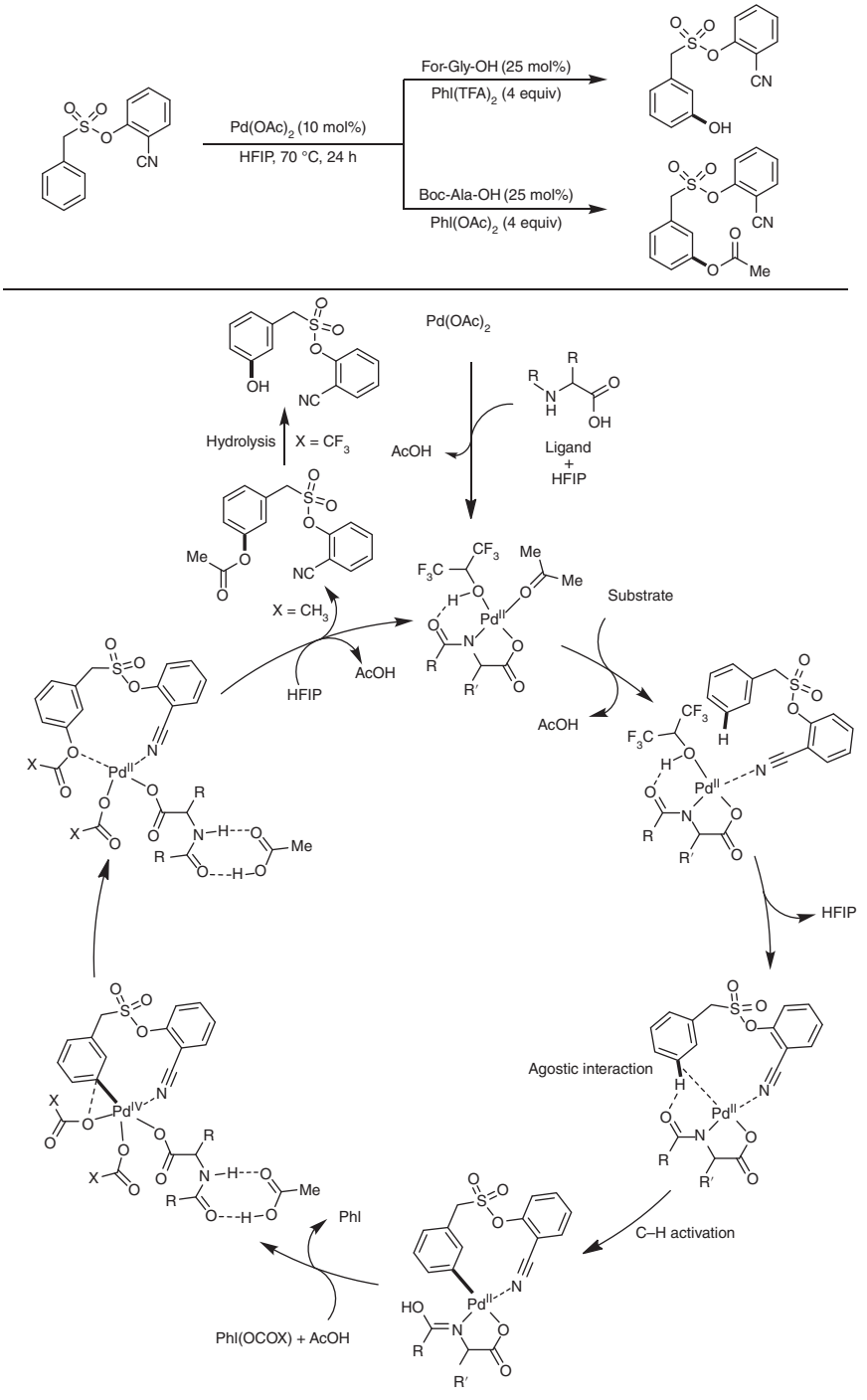

Figure 10.2 Mechanism of *N*-acyl amino acid ligand promoted palladium-catalyzed *meta* C–H activation.

in energy compared to other modes of activation under this scenario. Although the acetate ligand can also help in CMD mechanism, the bidenticity of *N*-acyl amino acids and subsequent change in electronic properties of metal probably stabilize the transition state by manifold. Once the Pd—C bond is formed, it can undergo reductive elimination with suitable ligands to provide the desired functionalization.

We further modified the linker to phosphonate ester and fascinatingly observed that olefination can be achieved at meta position at room temperature for the first time [20]. Moreover, hydroxyl and acetoxy groups can also be incorporated effectively using this DG. Notably, the optimized condition of different reactions requires different combinations of palladium salt and *N*-protected amino acids, which clearly indicates these ligands not only help in C–H activation but also have profound effect on other steps of the catalytic cycle. Combination of these was further explored to obtain *meta* selective functionalizations such as olefination, silylation of phenethyl, biaryl substrates using a cyano-directing group [21–23]. We were also able to show that the metal catalyst can be changed to Rh to obtain *meta* C–H activation [24]. However, in contrast to palladium catalysis, XPhos and copper(II) trifluoroacetate were used as ligand and oxidant, respectively.

Although the cyano-directing group laid foundation of *meta* C–H activation, we struggled to diversify in terms of types of functionalizations that would be of high scientific interest. In this regard, cyano DG failed from both yield and selectivity point of view. The reason was attributed to (i) weak nature of co-ordination by –CN, (ii) competition between end-on and side-on binding mode, and (iii) chemical insecurity under harsh condition. Thus, a stronger yet reversible coordinating DG was required to develop. We envisioned that a right heterocyclic DG might solve the stated issues. Therefore, we started with 2-(3-pyridinyl)phenol-based DG to obtain *meta* alkylation in decent selectivity and yield. Then, various other heterocycles were tested, and the pyrimidine-based biphenyl template was found to be very effective in carrying out alkylation at meta position [25]. The σ-donation and stronger π-acidity of pyrimidine due to the presence of a second nitrogen make DG-metal co-ordination stronger and the metal sufficiently electropositive for the allyl alcohol coordination. The efficacy of the pyrimidine DG is further evident from the diverse functionalizations such as cyanation, allylation, deuteration, acetoxylation, etc. of various substrates that can be achieved [26–32]. More interestingly, irrespective of the linker length (up to 20 atoms) between arene substrate and the pyrimidine DG, we obtained selective *meta* functionalization defying the high entropic barrier (Figure 10.3) [33]. Thus, there must exist a secondary interaction among the substrate, DG, and catalyst which is yet to be understood.

10.2.2 *para* C–H Activation

Meanwhile, we were also engaged in devising DGs for reaching one step further to the para position. However, the challenges were manifold viz. formation of less strained yet larger membered metallacycle, incorporation of a suitable linker that can provide perfect length as well as conformation and lastly placing the heteroatom of DG selectively closer to the *para* C—H bond. After thorough investigation, it was observed that a 2-cyanobiphenyl DG linked with diisopropylsilyl ether group is quite

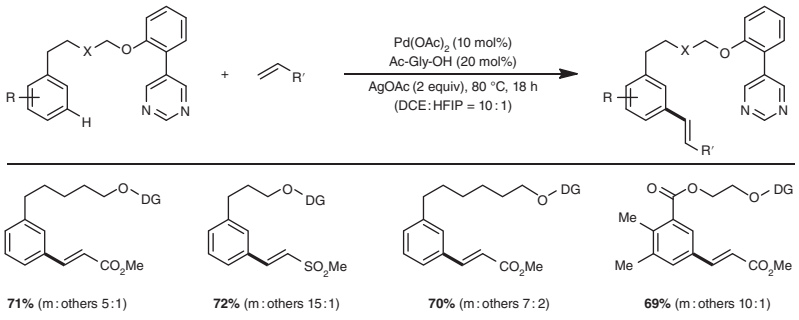

Figure 10.3 Pyrimidine DG-assisted linker length independent *meta* C–H activation.

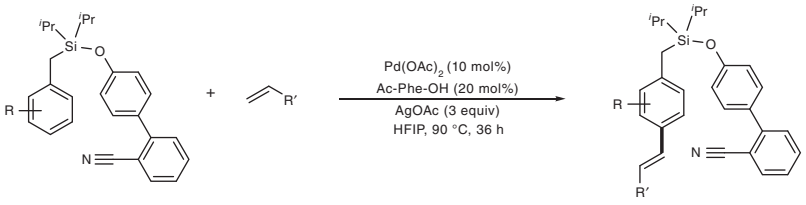

Figure 10.4 *para* C–H activation using biphenyl cyano DG.

effective in carrying out *para* olefination selectively (Figure 10.4) [34, 35]. The two isopropyl groups exert adequate Thorpe–Ingold effect to form a 17-membered cyclophane type transition state (Figure 10.5). Moreover, the rigidity of biphenyl group creates high energy barrier for the transition states corresponding to ortho and meta bond activation.

Later, it was found that substitution at the cyanophenyl by two methoxy groups drastically enhances the efficacy of para functionalization [36]. This resultant improvement was attributed to two factors, one is electronic, and the other is substrate–solvent interaction. The H-bonding interaction between HFIP was detected in NMR titration at two methoxy site as well as ether site (Figure 10.5). Arguably, (ether)O$\cdots$H–C$(CF_3)_2$ interaction adds to the steric interaction provided by the two isopropyl units. On the other hand, the rigidity provided by the methoxy–HFIP interaction probably lowers the entropic barrier at the transition state. Using this template system, various functionalizations including carbonylation, cyanation, and even rhodium-catalyzed olefination were achieved [37–39].

10.3 Distal C–H Activation of Heterocycles

Heterocycles are very important compounds both pharmaceutically and industrially. Thus, selective functionalization at a specific position of heterocycles in a one-step economic manner is highly desirable. However, the directing group approach miserably fails for heterocycles due to their ability to deactivate catalyst via coordination and lack of site for attaching directing groups. Recently, Yu's group and our group

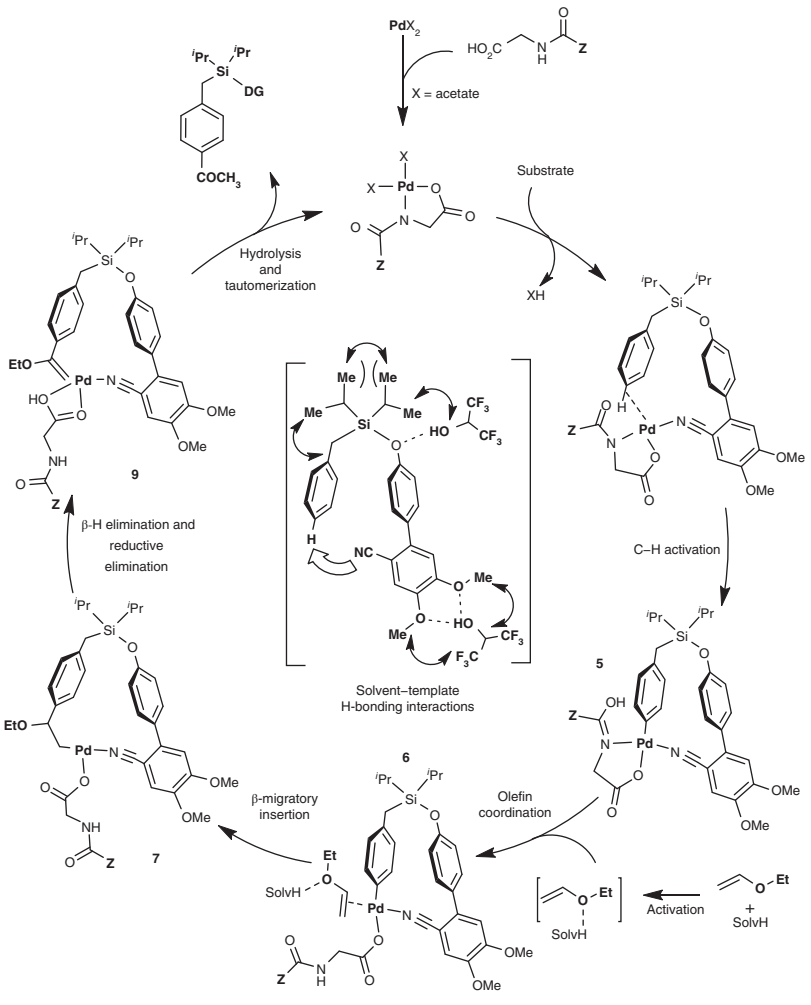

Figure 10.5 Mechanism of *para* C–H activation using second generation biphenyl cyano DG.

utilized this counterproductive coordination to form a host–guest assembly in order to activate C—H bonds at distal position.

10.3.1 Tridentate Approach

A diamide of 2,6-dipicolinic acid was synthesized with a biphenyl cyano DG appended at one side, which formed a palladium complex in acetonitrile [40]. Three coordination sites of the palladium are occupied by the three nitrogen atoms from the ligand, and the fourth site is coordinated with an acetonitrile molecule. Treatment with quinoline can easily displace the acetonitrile ligand and form a quinoline-template complex. The DG can now direct the catalyst to

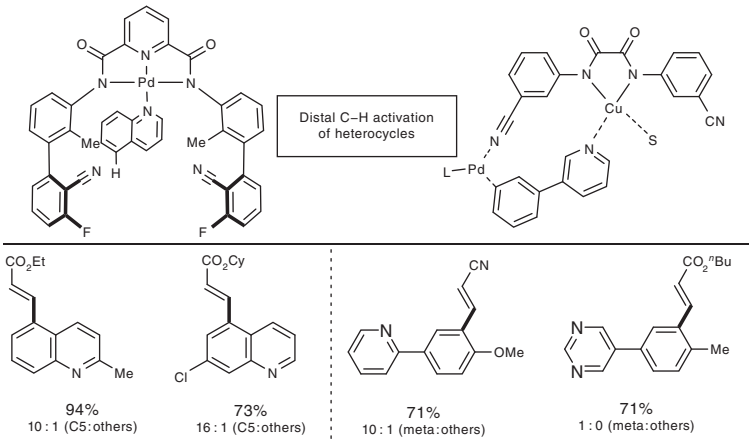

Figure 10.6 Bifunctional approach for coordination assisted distal C–H activation of heterocycles.

a distal position of quinoline for activating C—H bond selectively. The Yu group first synthesized an unsymmetrical template with biphenyl cyano DG at one side and 2,6-dimethoxyphenyl at other side of the template, which afforded selective olefination at the C-5 position of quinoline. Later, we found that a synthetically much simpler and symmetrical template with DG on both sides provided better yield and selectivity (Figure 10.6) [41]. Various quinoline derivatives, benzoxazole and benzothiazole could be olefinated at C-5 and C-7 positions, respectively. The C-7 selectivity of benzoxazole and benzothiazole is suggestive of preferable coordination of the substrate through the nitrogen center. We also found that olefination at C-5 position of thiazole can be achieved selectively which is otherwise accessible only with high difficulty [42].

Subsequently, in search of functionalization variation, we found that allyl alcohols in the presence of palladium catalyst can provide alkylation of quinoline and its derivatives at C-5 position [43]. However, an unsymmetrical template was found to be better in this case. More interestingly, the dimethoxy cyanophenyl DG which is most effective for para functionalization provided the best selectivity. Thus, template-HFIP hydrogen bonding probably has a positive impact in this case as well. In order to understand the mechanism, various intermediates have been characterized with X-ray crystallography and a plausible mechanism was depicted (Figure 10.7). Coordination of quinoline and steric push from the 3,5-di(trifluoromethyl)phenyl group onto the quinoline places the nitrile DG at close proximity of C-5 C—H bond. The nitrile then directs the catalyst in order to bring about the activation. The allyl alcohol coordinates with the catalyst and undergoes series of reaction steps namely olefin insertion, β-hydride elimination, and tautomerization to provide template-bound alkylated product. Treatment of which with *N,N*-dimethylaminopyridine releases the product by virtue of higher basicity. The parent template is obtained back upon treatment with acid and can be further utilized in the reaction.

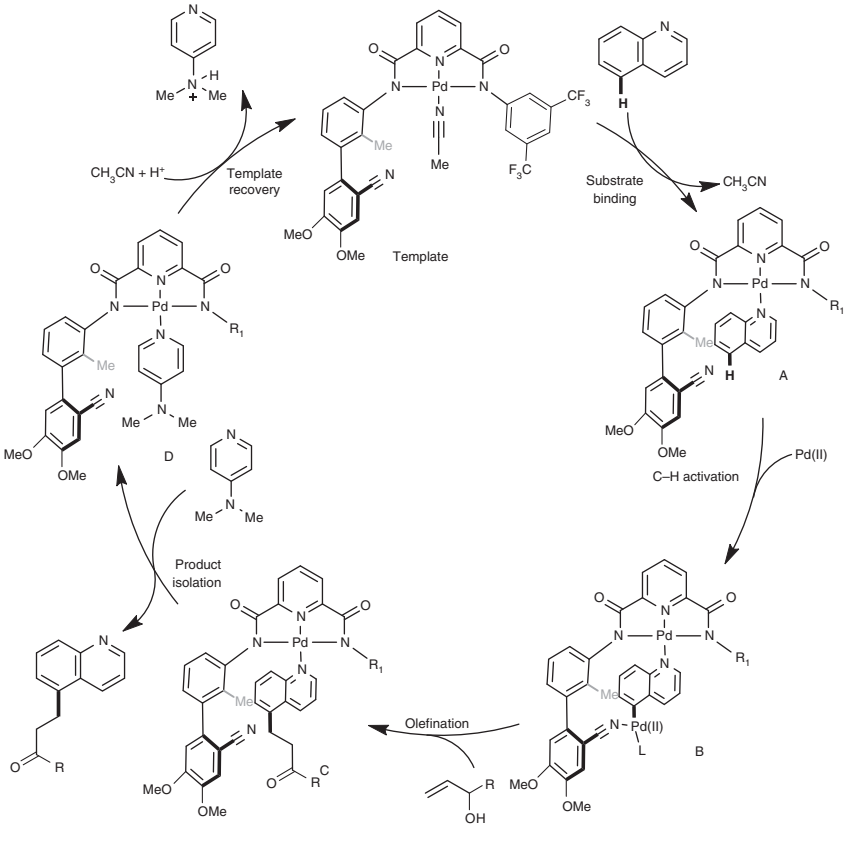

Figure 10.7 Mechanism for C-5 selective alkylation of quinolone using tridentate template.

10.3.2 Bidentate Approach

In a similar fashion, a bidentate approach was also developed simultaneously. The Yu group synthesized a pyridine-based disulfonamide ligand for the purpose. Conceptually, it was believed that under reaction conditions, copper(II) will coordinate with the amide nitrogens in a bidentate fashion and simultaneously a suitable heterocyclic substrate will also coordinate to the metal center. Thus, the DG appended on the amide ligand can direct a catalyst toward a particular distal position. Indeed, it was found that the bidentate ligand in the presence of copper acetate anchor carries out *meta* C–H olefination of 3-phenyl pyridine derivatives.

In order to simplify the approach, our group designed a synthetically far simpler and cheaper diamide ligands (Figure 10.6). The diamide synthesized from 3-cyanoaniline and oxalic acid provided the best results toward *meta* olefination of 3-phenylpyridine. During crystallization attempts, we observed that the super equivalent amount of copper forms a dimer of copper–substrate–acetate complex and lowering of copper loading decreases the yield. Therefore, the $Cu(OAc)_2$ preferably undergoes complexation with the substrate first and then co-ordinates with

the template. This is also evident from the fact that the product is only isolable after treating with Na_2S upon completion of reaction. Once the ligand–metal–substrate cluster is formed, the nitrile directs the palladium catalyst to an appropriate position and the usual steps for olefination take place.

10.4 Conclusion

It is evident from the above discussion that non-covalent interactions play an immense role in the domain of distal C–H activation. Although only a handful methods are reported in this domain which are purely based on supramolecular interactions, knowledge of influences these forces have on C–H activation at distal position even via DG approach will be crucial in designing systems solely depending on weak interactions. Achieving such goals will have huge impact on synthetic chemistry both in academics and industries.

Acknowledgments

This activity was supported by SERB, India (CRG/2018/003951). Financial support received from CSIR-India (fellowship to JPB) is gratefully acknowledged.

References

1 Crabtree, R.H. (2004). Organometallic alkane CH activation. *J. Organomet. Chem.* 689: 4083.
2 Periana, R.A., Bhalla, G.W., Tenn, J. III, et al. (2004). Perspectives on some challenges and approaches for developing the next generation of selective, low temperature, oxidation catalysts for alkane hydroxylation based on the CH activation reaction. *J. Mol. Catal. A: Chem.* 220: 7.
3 Lyson, T.W. and Sanford, M.S. (2010). Palladium-catalyzed ligand-directed C−H functionalization reactions. *Chem. Rev.* 110: 1147.
4 Kapdi, A. and Maiti, D. (2017). *Strategies for Palladium-Catalyzed Non-directed and Directed C–H Bond Functionalization*. Elsevier.
5 Bhattacharya, T., Pimparkara, S., and Maiti, D. (2018). Combining transition metals and transient directing groups for C–H functionalizations. *RSC Adv.* 8: 19456.
6 Zhu, R.-Y., Farmer, M.E., Chen, Y.-Q., and Yu, J.-Q. (2016). A simple and versatile amide directing group for C–H functionalizations. *Angew. Chem. Int. Ed.* 55: 10578.
7 Ping, Y., Wang, L., Ding, Q., and Peng, Y. (2017). Nitrile as a versatile directing group for C(sp^2)–H functionalizations. *Adv. Synth. Catal.* 359: 3274.
8 Dey, A., Agasti, S., and Maiti, D. (2016). Palladium catalysed *meta*-C–H functionalization reactions. *Org. Biomol. Chem.* 14: 5440.

9 Leow, D., Li, G., Mei, T.-S., and Yu, J.-Q. (2012). Activation of remote *meta*-C–H bonds assisted by an end-on template. *Nature* 486: 518–522.

10 Dai, H.-X., Li, G., Zhang, X.-G. et al. (2013). Pd(II)-catalyzed *ortho*- or *meta*-C–H olefination of phenol derivatives. *J. Am. Chem. Soc.* 135: 7567–7571.

11 Lee, S., Lee, H., and Tan, K.L. (2013). *meta*-Selective C–H functionalization using a nitrile-based directing group and cleavable Si-tether. *J. Am. Chem. Soc.* 135: 18778–18781.

12 Tang, R.-Y., Li, G., and Yu, J.-Q. (2014). Conformation-induced remote *meta*-C–H activation of amines. *Nature* 507: 215–220.

13 Cheng, G.-J., Yang, Y.-F., Liu, P. et al. (2014). Role of *N*-acyl amino acid ligands in Pd(II)-catalyzed remote C–H activation of tethered arenes. *J. Am. Chem. Soc.* 136: 894.

14 Yang, Y.-F., Cheng, G.-J., Liu, P. et al. (2014). Palladium-catalyzed *meta*-selective C–H bond activation with a nitrile-containing template: computational study on mechanism and origins of selectivity. *J. Am. Chem. Soc.* 136: 344.

15 Yang, G., Lindovska, P., Zhu, D. et al. (2014). Pd(II)-catalyzed *meta*-C–H olefination, arylation, and acetoxylation of indolines using a U-shaped template. *J. Am. Chem. Soc.* 136: 10807.

16 Bera, M., Modak, A., Patra, T. et al. (2014). *meta*-Selective arene C–H bond olefination of arylacetic acid using a nitrile-based directing group. *Org. Lett.* 16: 5760–5763.

17 Bera, M., Maji, A., Sahoo, S.K., and Maiti, D. (2015). Palladium(II)-catalyzed *meta*-C–H olefination: constructing multisubstituted arenes through homo-diolefination and sequential hetero-diolefination. *Angew. Chem. Int. Ed.* 54: 8515–8519.

18 Maji, A., Bhaskararao, B., Singha, S. et al. (2016). Directing group assisted *meta*-hydroxylation by C–H activation. *Chem. Sci.* 7: 3147–3153.

19 Modak, A., Mondal, A., Watile, R. et al. (2016). Remote *meta* C–H bond functionalization of 2-phenethylsulphonic acid and 3-phenylpropanoic acid derivatives. *Chem. Commun.* 52: 13916–13919.

20 Bera, M., Sahoo, S.K., and Maiti, D. (2016). Room-temperature *meta*-functionalization: Pd(II)-catalyzed synthesis of 1,3,5-trialkenyl arene and *meta*-hydroxylated olefin. *ACS Catal.* 6: 3575–3579.

21 Patra, T., Watile, R., Agasti, S. et al. (2016). Sequential *meta*-C–H olefination of synthetically versatile benzyl silanes: effective synthesis of *meta*-olefinated toluene, benzaldehyde and benzyl alcohols. *Chem. Commun.* 52: 2027–2030.

22 Maity, S., Hoque, E., Dhawa, U., and Maiti, D. (2016). Palladium catalyzed selective distal C–H olefination of biaryl systems. *Chem. Commun.* 52: 14003–14006.

23 Modak, A., Patra, T., Chowdhury, R. et al. (2017). Palladium-catalyzed remote *meta*-selective C–H bond silylation and germanylation. *Organometallics* 36: 2418–2423.

24 Bera, M., Agasti, S., Chowdhury, R. et al. (2017). Rhodium-catalyzed *meta*-C–H functionalization of arenes. *Angew. Chem. Int. Ed.* 56: 5272–5276.

25 Bag, S., Jayarajan, R., Mondal, R., and Maiti, D. (2017). Template-assisted *meta*-C−H alkylation and alkenylation of arenes. *Angew. Chem. Int. Ed.* 56: 3182–3186.

26 Bag, S., Jayarajan, R., Dutta, U. et al. (2017). Remote *meta*-C–H cyanation of arenes enabled by a pyrimidine-based auxiliary. *Angew. Chem. Int. Ed.* 56: 12538–12542.

27 Bag, S., Petzold, M., Sur, A. et al. (2019). *Chem. Eur. J.* 25: 9433–9437.

28 Achar, T.K., Zhang, X., Mondal, R. et al. (2019). Palladium-catalyzed directed *meta*-selective C–H allylation of arenes: unactivated internal olefins as allyl surrogates. *Angew. Chem. Int. Ed.* 58: 10353–10360.

29 Brochetta, M., Borsari, T., Bag, S. et al. (2019). Direct *meta*-C–H perfluoroalkenylation of arenes enabled by a cleavable pyrimidine-based template. *Chem. Eur. J.* 25: 10323–10327.

30 Porey, S., Zhang, X., Bhowmick, S. et al. (2020). Alkyne linchpin strategy for drug:pharmacophore conjugation: experimental and computational realization of a *meta*-selective inverse Sonogashira coupling. *J. Am. Chem. Soc.* 142: 3762–3774.

31 Gholap, A., Bag, S., Pradhan, S. et al. (2020). Diverse *meta*-C−H functionalization of amides. *ACS Catal.* 10: 5347–5352.

32 Bag, S., Surya, K., Mondal, A. et al. (2020). Palladium-catalyzed *meta*-C−H allylation of arenes: a unique combination of a pyrimidine-based template and hexafluoroisopropanol. *J. Am. Chem. Soc.* 142: 12453–12466.

33 Jayarajan, R., Das, J., Bag, S. et al. (2018). Diverse *meta*-C–H functionalization of arenes across different linker lengths. *Angew. Chem. Int. Ed.* 57: 7659–7663.

34 Bag, S., Patra, T., Modak, A. et al. (2015). Remote *para*-C–H functionalization of arenes by a D-shaped biphenyl template-based assembly. *J. Am. Chem. Soc.* 137: 11888–11891.

35 Patra, T., Bag, S., Kancherla, R. et al. (2016). Palladium-catalyzed directed *para* C–H functionalization of phenols. *Angew. Chem. Int. Ed.* 55: 7751–7755.

36 Maji, A., Guin, S., Feng, S. et al. (2017). Experimental and computational exploration of *para*-selective silylation with a hydrogen-bonded template. *Angew. Chem. Int. Ed.* 56: 14903–14907.

37 Maji, A., Dahiya, A., Lu, G. et al. (2018). H-bonded reusable template assisted *para*-selective ketonisation using soft electrophilic vinyl ethers. *Nat. Commun.* 9: 3582.

38 Dutta, U., Maiti, S., Pimparkar, S. et al. (2019). Rhodium catalyzed template-assisted distal *para*-C–H olefination. *Chem. Sci.* 10: 7426–7432.

39 Pimparkar, S., Bhattacharya, T., Maji, A. et al. (2020). *para*-Selective cyanation of arenes by H-bonded template. *Chem. Eur. J.* 26: 11558–11564.

40 Zhang, Z., Tanaka, K., and Yu, J.-Q. (2017). Remote site-selective C–H activation directed by a catalytic bifunctional template. *Nature* 543: 538–542.

41 Achar, T.K., Ramakrishna, K., Pal, T. et al. (2018). Regiocontrolled remote C–H olefination of small heterocycles. *Chem. Eur. J.* 24: 17906–17910.

42 Achar, T.K., Biswas, J.P., Porey, S. et al. (2019). Palladium-catalyzed template directed C-5 selective olefination of thiazoles. *J. Org. Chem.* 84: 8315–8321.

43 Ramakrishna, K., Biswas, J.P., Jana, S. et al. (2019). Coordination assisted distal C–H alkylation of fused heterocycles. *Angew. Chem. Int. Ed.* 58: 13808–13812.

11

Transition-Metal-Catalyzed, Site- and Enantioselective Oxygen and Nitrogen Transfer Enabled by Lactam Hydrogen Bonds

Finn Burg and Thorsten Bach

Technical University of Munich, Department of Chemistry and Catalysis Research Center (CRC), Lichtenbergstraße 4, 85747 Garching, Germany

11.1 Chiral Lactams as Hydrogen Bonding Sites for Enantioselective Catalysis

The perception that hydrogen bonding is largely responsible for the organization and orientation of biomolecules has led to many of today's groundbreaking discoveries in natural science [1–5]. It is therefore perhaps not surprising that hydrogen bonds play an equally important role in organic synthesis [6–10], and extensive work has been done to exploit these and other noncovalent interactions to increase the efficiency and selectivity of catalytic processes [11–16]. Our own contribution to the field of hydrogen-bond-mediated transition metal catalysis commenced approximately 10 years ago and drew inspiration from our previous work on enantioselective photocatalysis [17]. Particularly, a lactam hydrogen bonding motif had evolved to be exceptionally useful in coordinating a wide range of planar, prochiral amides, thus introducing notable enantioface differentiation. Seminal work involving chiral photosensitizers demonstrated that a catalytic turnover is possible and prompted our group to explore similar concepts for transition metal complexes [18]. It was envisioned that a catalytically active metal center could be tethered to the same established chiral lactam (Figure 11.1). Such a complex **I** can be converted with a stoichiometric reagent into its reactive form **II**, which in turn invites coordination of an eligible substrate **A**. Upon precise orientation via two-point hydrogen bonding, the supramolecular complex **III** enables the distinct transfer of a given functional group in an enantioselective fashion (e.g. in Figure 11.1, the functional group X is being transferred from the top face). Eventually, the enantiomerically enriched product **B** is released from complex **IV** whereupon the catalytic cycle is closed.

In our earlier work, chiral complexing agents such as the dextrorotatory lactam (+)-**1** and its levorotatory enantiomer (−)-*ent*-**1** were engaged in a variety of photochemical and radical reactions (Figure 11.2) [19–23]. In these transformations, the sterically demanding tetrahydronaphthalene unit blocks one of the two enantiotopic sides hence forcing any reagent to approach almost exclusively

Supramolecular Catalysis: New Directions and Developments, First Edition.
Edited by Piet W.N.M. van Leeuwen and Matthieu Raynal.

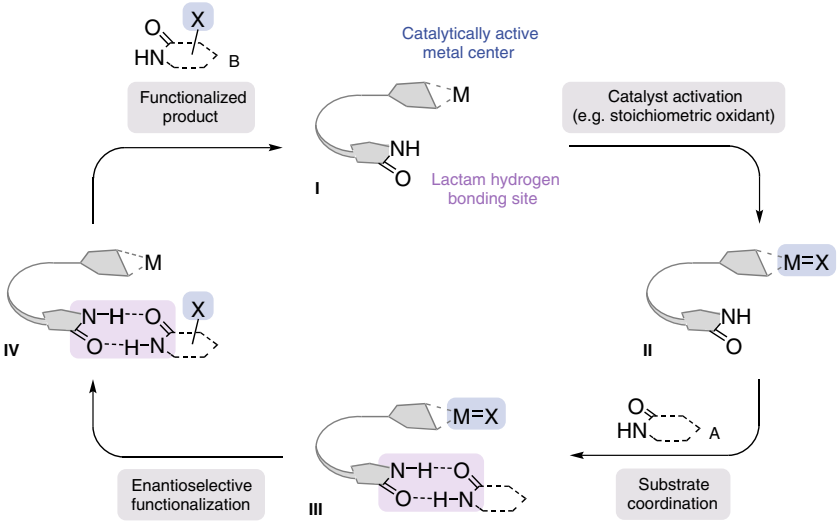

Figure 11.1 Proposed catalytic cycle for an enantioselective transition-metal-catalyzed reaction controlled by lactam hydrogen bonds.

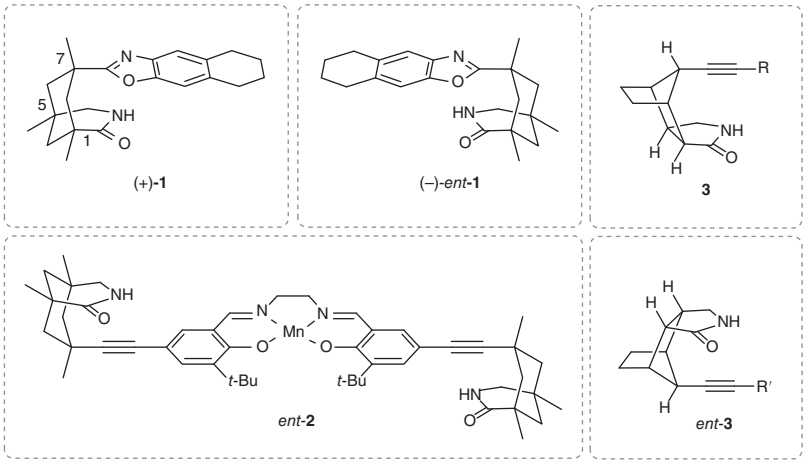

Figure 11.2 Chemical structure of the chiral complexing agent **1** and catalyst **2** with a 1,5,7-trimethyl-3-azabicyclo[3.3.1]nonan-2-one skeleton and the later applied hydrogen bonding site **3** exhibiting an octahydro-1*H*-4,7-methanoisoindol-1-one backbone.

from the more accessible face. Without any catalytic turnover, however, the chiral lactam **1** does not participate in individual reactions but solely serves the purpose to transfer its chirality to the reaction products via hydrogen bonding. Although the recovery of the complexing agent was straightforward and recovery yields were close to quantitative, the intuitive drawback correlated to the fact that significant amounts of **1** had to be added to the reaction mixture (typically 2.0–2.6 equiv) in order to achieve high enantioselectivity (>90% ee).

Our first efforts to introduce a catalytically active metal center were realized with the synthesis of the chiral manganese salen complex *ent*-**2**, which was decorated with two remote hydrogen bonding sites [24]. A preliminary study with prochiral sulfides revealed that an enantioselective sulfoxidation is feasible, and it was encouraging to observe that only 1 mol% of the catalyst *ent*-**2** was sufficient to obtain a series of optically enriched sulfoxides with up to 71% ee. Although the progress concerning hydrogen-bond-mediated transition metal catalysis was remarkable considering the unprecedented mode of action, the expectations were not yet met keeping in mind the outstanding enantioselectivity that had been previously achieved in photochemical reactions. It was anticipated that the chiral backbone of the catalyst *ent*-**2** exhibits a critical role and could possibly be the main objective for further improvement. More specifically, chiral complexing agents such as **1** were designed to provide a confined binding to the substrate, and we imagined that a catalytically active metal center required more geometrical flexibility for a functional group to be transferred. The 1,5,7-trimethyl-3-azabicyclo[3.3.1]nonan-2-one backbone **1** was envisioned as a U-shaped template, and we aimed to redesign the chiral backbone to a less rigid V-shaped scaffold. The lactam that emerged from these considerations carries an octahydro-1*H*-4,7-methanoisoindol-1-one carbon skeleton **3**, and over the past decades, several supramolecular ligands and metal complexes have proven to be valuable catalysts in a variety of enantioselective transformations (Figure 11.3).

Initially, we prepared the ruthenium porphyrin complex **3a**, in which the core is flanked by two 2,4,6-trimethylphenyl (Mes) and one phenyl moiety [25, 26]. Although sufficient for enantioselective epoxidation reactions, the electron-poor ruthenium and manganese complexes **3b** and **3c** turned out to be more robust and enabled enantioselective C(sp^3)–H oxygenation and hydroxylation reactions [27, 28]. More recently, the chiral phenanthroline ligand **3d** was prepared and applied to enantioselective silver-catalyzed C(sp^3)–H amination [29], whereas enantioselective sulfimidation reactions are currently explored in our laboratory. Similarly, the enantioselective functionalization of sulfur centers was realized by using the ruthenium pyridine-2,6-bisoxazoline (pybox) complex *ent*-**3e** [30]. Preliminary studies in the field of C(sp^3)–H amination were performed with the Rh(II) carboxylate *ent*-**3f**. However, a highly enantioselective reaction was merely observed in the case of aziridinations [31, 32].

11.2 Enantioselective Addition to Olefins

As previously stated, the ruthenium porphyrin complex **3a** marked the entry point of our studies, and the epoxidation of 3-alkenylquinolones **4** was investigated using 2,6-dichloropyridine-*N*-oxide (DCPNO) as a stoichiometric oxidant (Figure 11.4) [25, 26]. Remarkably, the oxygen transfer from the putative oxo ruthenium(VI) species proceeded in exceptionally high enantioselectivity via its bound transition state **6** [33], although one could imagine a free rotation around the C—C bond at the C-3 position. Moreover, outstanding turnover numbers (TONs) of over 350 were achieved as the simple 3-vinylquinolone **4a** was converted into the corresponding

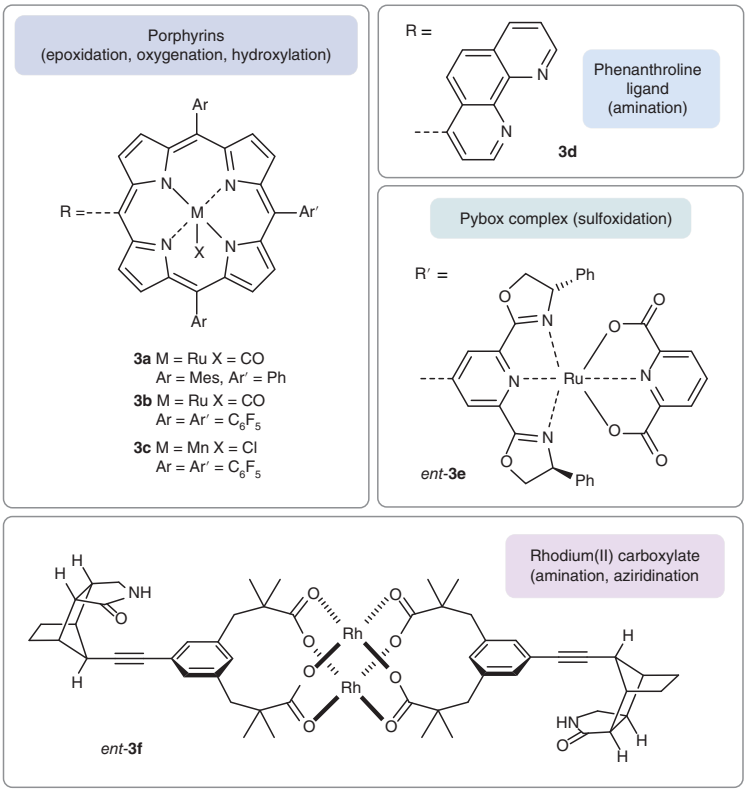

Figure 11.3 Chemical structure of supramolecular metal complexes and ligands **3** with an octahydro-1*H*-4,7-methanoisoindol-1-one backbone engaged in enantioselective transition-metal-catalyzed reactions.

epoxide **5a** with almost perfect selectivity (93% ee). Along a similar line, both electron-rich (**5c**, 98% ee) and electron-poor (**5d**, 96% ee) substituents at the C-6 position of the quinolone framework were tolerated, as well as a simple methyl substituent at the C-7 position (**5f**, 92% ee). The cyclic olefin **4b** yielded comparable results (**5b**, 92% ee), but epoxidation of a propenyl substituent resulted in a slightly diminished enantioselectivity (**5e**, 86% ee). In the presence of a second vinyl group (substrate **4g**), a ruthenium porphyrin catalyst exhibiting a *tert*-butyl group instead of the chiral lactam yielded a regioisomeric mixture of epoxides. As opposed to the racemic reaction, catalyst **3a** restored the initial reactive site and **5g** was isolated in high enantiomeric excess (88% ee, regioisomeric ratio rr = 91/9). As soon as one hydrogen bonding site at the ligand or the substrate was blocked with an *N*-methyl group, a sluggish reaction was observed and the enantioselectivity was neglectable (<5% ee), clearly highlighting the importance of precoordination to increase both the selectivity and reactivity. In addition to our studies with quinolones, it was interesting to see that to a certain extent the epoxidation was applicable to 3-alkenylpyridones (77–87% ee), although oxidation of the enamide as well as the instability of the corresponding products complicated their isolation. Even

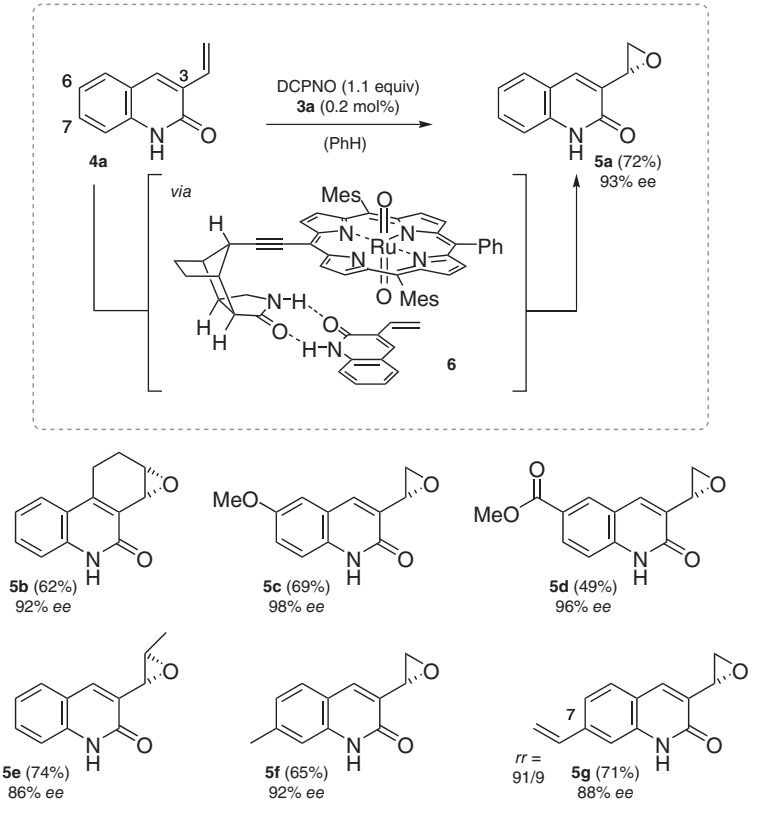

Figure 11.4 Enantioselective epoxidation of vinylquinolones **4** to epoxides **5** by the chiral ruthenium porphyrin catalyst **3a** with a remote hydrogen bonding site.

primary amides with alkene moieties showed a preferred attack from one of the two enantiotopic sides, but again with lower selectivity due to the high flexibiliy of the linear alkyl chain (45–70% ee).

Encouraged by the remarkable selectivity achieved with porphyrin complex **3a**, the dirhodium(II) carboxylate *ent*-**3f** was probed in an enantioselective aziridination reaction with structurally related 3-alkenylquinolones **4**. Preliminary experiments with bis[rhodium(α,α,α′,α′-tetramethyl-1,3-benzenedipropionic acid)] [$Rh_2(esp)_2$] as the catalyst have shown some potential [34], in as much as **4e** led to clean conversion to its corresponding aziridine as a single diastereoisomer. Due to the lability of the electron-poor aziridine, an immediate follow-up reaction occurred and an intramolecular ring opening by the adjacent nucleophilic lactam oxygen atom enabled access to dihydrobenzo[2,3-*b*]quinolones **7** [32] (Figure 11.5). This intriguing reaction sequence had not been explored previously, and we were delighted to see that 3-propenylquinolone **4e** was successfully converted into **7e** in high enantioselectivity (87% ee) with *ent*-**3f** as the catalyst (1.0 mol%). The enantioselectivity even increased upon elongation of the alkyl chain (91% ee for products **7h** and **7k**) and a variety of functional groups at the C-6 and C-7 position

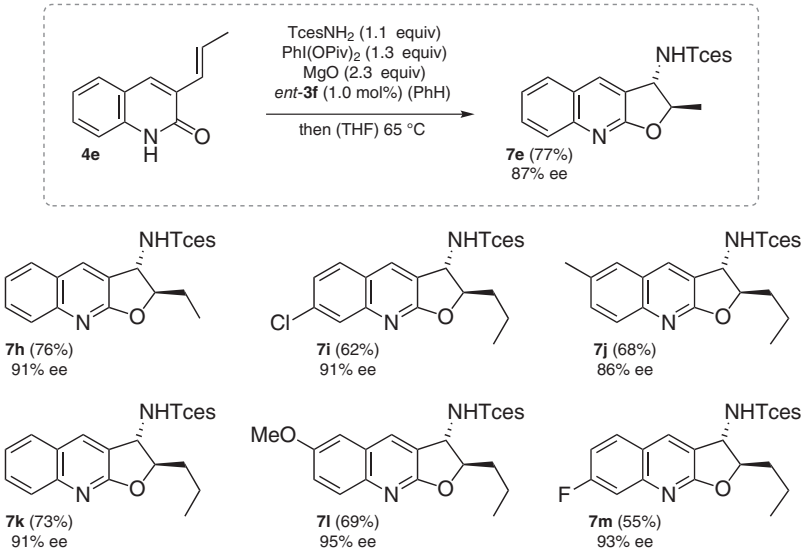

Figure 11.5 Enantioselective aziridination of vinylquinolones **4** and subsequent cyclization to dihydrobenzo[2,3-*b*]quinolones **7** catalyzed by the chiral rhodium(II) carboxylate *ent*-**3f** carrying two molecular recognition sites.

were tolerated (86–95% ee for products **7i**, **7j**, **7l**, **7m**). Eventually, facile cleavage of the 2,2,2-trichloroethoxysulfonyl (Tces) group delivered highly enantiomerically enriched amines, the absolute configuration of which was assigned by Mosher ester analysis.

11.3 Enantioselective C(sp^3)–H Functionalization

The direct enantioselective functionalization of unactivated sp^3 carbon–hydrogen (C—H) bonds lies at the forefront of modern organic synthesis, and many research groups are committed to developing innovative tools to disconnect C—H bonds in a more selective fashion [35–39]. Inspired by the remarkable efficiency of enzymes to synthesize densely oxidized secondary metabolites [40], we became interested in mimicking their unique mode of action for the selective insertion of oxygen into aliphatic C—H bonds. Spearheaded by the Breslow group [41–43], there had been several important contributions to the field of selective oxygenation reactions directed by noncovalent interactions [44–47], but the potential of hydrogen bonding to control both site- and enantioselectivity had not been investigated prior to our work [48, 49]. A low substrate turnover and the insufficient reactivity of **3a** prevented any major success for an enantioselective oxygenation, but with the preparation of the electron-deficient catalyst **3b**, a more robust catalyst was provided. Additional problems were encountered as overoxidation of the corresponding secondary alcohol deleted the newly generated stereocenter. Eventually, substrate **8** was chosen as a promising target, and it was envisioned that a desymmetrization of the prostereogenic quaternary carbon center could be realized via a selective

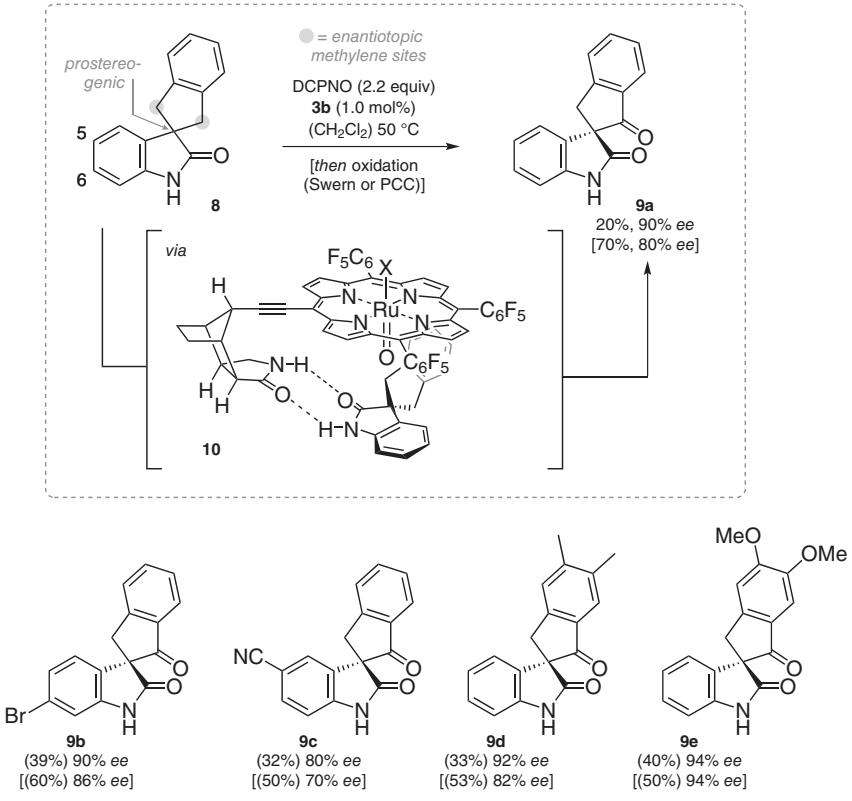

Figure 11.6 Enantiotopos-selective oxygenation of spirocyclic oxindoles **8** to ketones **9** by the revised ruthenium porphyrin complex **3b**.

oxygenation at one of the two enantiotopic methylene sites (Figure 11.6) [27]. Aside from the parent compound **9a** (90% ee), a series of highly enantiomerically enriched spirocyclic ketones **9** were prepared as the oxo ruthenium complex delivered its oxygen atom from a single enantiotopic face via its bound transition state **10**. Functional groups at both the 6- and the 5-position were tolerated (90% and 80% ee for products **9b** and **9c**) as well as derivatizing the indanone core was compatible with the oxygenation protocol (92% and 94% ee for **9d** and **9e**). In order to increase the conversion, the crude material could be subjected to an additional oxidation step (cf. yields and enantioselectivity in square brackets, PCC = pyridinium chlorochromate), although this procedure was often accompanied by a slight loss in enantioselectivity, likely due to a retro-aldol cleavage.

Since we strived for an opportunity to promote an enantioselective hydroxylation, our focus turned toward 3,4-dihydro-2-quinolones. Another important change was implemented at the porphyrin catalyst, as we introduced the manganese complex **3c** aiming to ease the catalyst synthesis and possibly preventing overoxidation to the corresponding ketone. Preliminary experiments using a simple 3,4-dihydroquinolone yielded promising results in terms of enantioselectivity

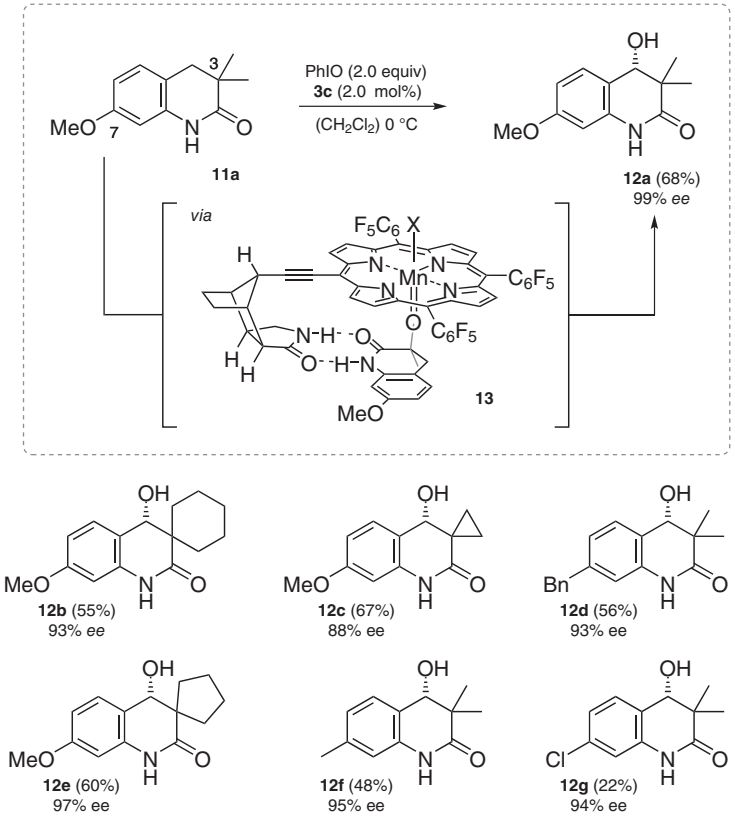

Figure 11.7 Site- and enantioselective hydroxylation of 3,3-geminal-substituted 3,4-dihydroquinolones **11** to alcohols **12** by the chiral manganese porphyrin complex **3c** with a molecular recognition site.

(96% ee), but unfortunately the major product during this transformation was identified to be the dehydrated 2-quinolone. The most straightforward solution to circumvent this problem was to introduce a geminal substitution at the C-3 position, and we subsequently explored the chemical space of this transformation [28] (Figure 11.7). The conversion of substrates **11** was found to be heavily dependent on the C-7 substituent, but in all cases the hydroxylation proceeded in outstanding enantioselectivity, almost regardless of the shape of the adjacent spirocycle (88–99% ee for products **12a–c** and **12e**). The cyclopropyl-substituted product **12c** (88% ee) was of particular interest in this study, as a competing cyclopropyl ring opening provided further evidence for a radical oxygen rebound mechanism [50]. Even in the presence of a second benzylic methylene or methane site, the reaction proceeded smoothly (93% and 95% ee for **12d** and **12f**) without any notable degree of regioisomer formation. However, electron-withdrawing substituents at the C-7 position led to a diminished yield albeit maintaining high selectivity (94% ee for **12g**).

Although it was exciting to see that a highly enantioselective hydroxylation was feasible, the major drawback was that the substrates engaged in this chemistry

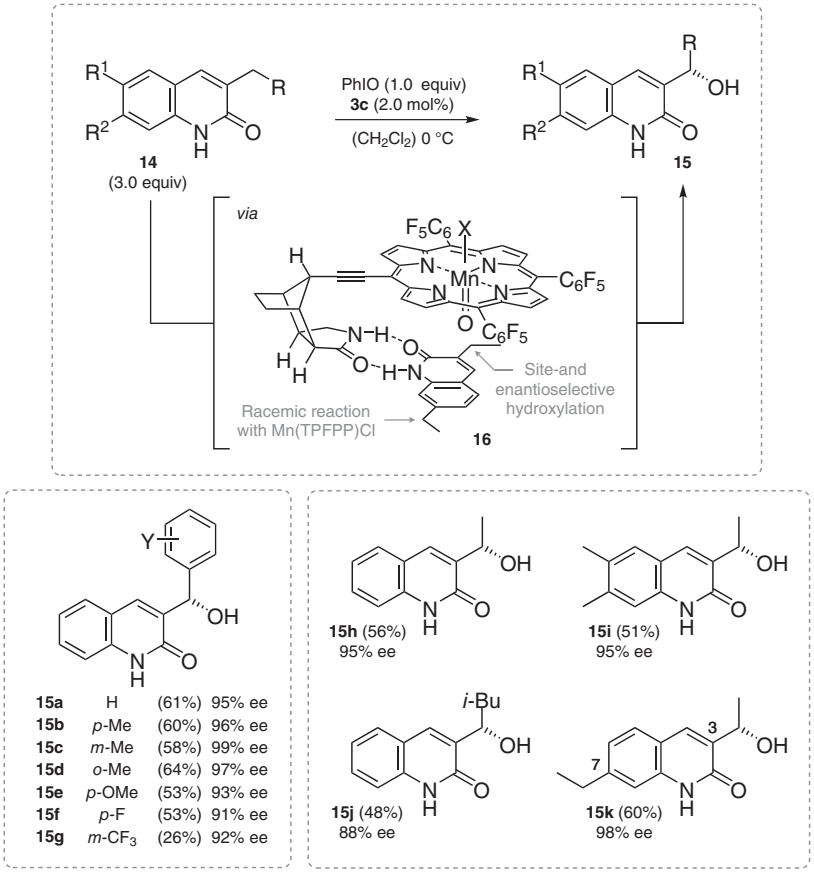

Figure 11.8 Site- and enantioselective exocyclic hydroxylation of simple quinolone analogues **14** to **15** by manganese catalyst **3c**.

were limited to an oxygenation of cyclic substrates. Our search for opportunities to increase the scope of the reaction made us revisit simple 3-substituted quinolones, similarly to our previous epoxidation studies (cf. Figure 11.4). At the beginning, we were delighted to observe an equally outstanding enantioselectivity (95% ee) when 3-(4′-methylbenzyl)quinolone **14b** was subjected to our established reaction conditions [51] (Figure 11.8). The major challenge became more apparent during careful rate profiling of the hydroxylation reaction, as it was realized that the substrate turnover did not exceed 50% conversion and the catalytic activity decreased rapidly after less than 15 minutes. Instead, the ratio of the desired alcohol **15** to its corresponding ketone deteriorated notably, and maintaining high chemoselectivity was conditional upon keeping the substrate concentration as high as possible (i.e. reducing overoxidation to its corresponding ketone). We reached the conclusion that using the oxidant as the limiting reagent (1.0 equiv) and the substrate in excess (3.0 equiv) was favorable to establish a high catalytic turnover while concomitantly minimizing the ketone concentration. Another benefit of this reaction protocol

rested on the fact that the unreacted starting material **14** can be reisolated in all cases.

Under optimized conditions, a vast number of quinolones **14** (27 examples, 80–99% ee) selectively underwent the desired transformation. For instance, several functional groups on the benzyl linker were tolerated (91–99% ee for **15a**–**15g**) and yielded similar results in terms of yield and enantioselectivity. Only the electron-poor substrate **14g** bearing a *meta*-trifluoromethyl group (26% yield, 92% ee for **15g**) suffered from a retarded conversion. As we proceeded with our study, we realized that even a simple 3-ethylquinolone **14h** can be hydroxylated in exceptionally high enantioselectivity (**15h**, 95% ee) despite the fact that it exhibits a highly flexible methylene site. Several substituents on the quinolone framework were compatible with these conditions (for instance, 95% ee for product **15i**), but an elongated, bulky alkyl chain reacted less selectively (88% ee for product **15j**). In order to probe the site selectivity, we prepared 3,7-diethylquinolone **14k** and sought to further investigate whether it behaves differently under racemic conditions. When the achiral catalyst manganese(III)-5,10,15,20-tetrakis(pentafluorophenyl)porphyrin chloride [Mn(TPFPP)Cl] was employed (2.0 mol%, 23 °C for 24 hours), we observed exclusive hydroxylation at the C-7 position (20% yield). In stark contrast, when using the porphyrin catalyst **3c,** the initial reactive site was restored and **15k** was obtained in an almost enantiomerically pure form (98% ee, crude rr = 88/12). Similar to the active site of a natural enzyme, coordination to a given substrate (complex **16**) leads to the precise exposure of a single C—H bond, while a more reactive yet undesired oxidation is prevented by spatial distance.

Fascinated by the fact that hydrogen bonding can relocate the reactive site from an intrinsically more reactive position to a geometrically favored site, we chose to target other positions on the quinolone framework. Firstly, we extended the alkyl chain at the C-3 position by two methylene units while maintaining a terminal phenyl group to activate the adjacent benzylic position (substrate **14l**, Figure 11.9). Secondly, an additional remote benzylic site was installed and spatially divided by a simple 1,4-disubstituted phenyl linker (substrates **14m** and **14n**). Again, when Mn(TPFPP)Cl was employed as an achiral catalyst under the previously applied conditions, **14o** (single regioisomer) and the remotely functionalized alcohols **14p** (crude rr = 93/7) and **14q** (crude rr = 82/18) were obtained as the major products. Remarkably, the manganese complex **3c** again reversed the site selectivity, and secondary alcohols **15l–n** were produced with exceptional selectivity (84–93% ee, crude rr for **15l** = 72/28; **15m** = 94/6; **15n** = 97/3).

Aside from successfully engaging in enantioselective hydroxylation reactions, the 3-benzylquinolones **14b** and **14e** had previously been utilized for our conceptional hydrogen-bond-mediated catalysis [31]. Indeed, the original purpose of the rhodium carboxylate *ent*-**3f** was to facilitate an enantioselective C(sp^3)–H amination inspired by seminal work of Du Bois and coworkers [52, 53]. Although a very high enantioselectivity was observed in the case of the later performed aziridination (cf. Figure 11.5), catalyst *ent*-**3f** revealed only moderate selectivity toward the initially performed functionalization (five examples, 48–74% ee).

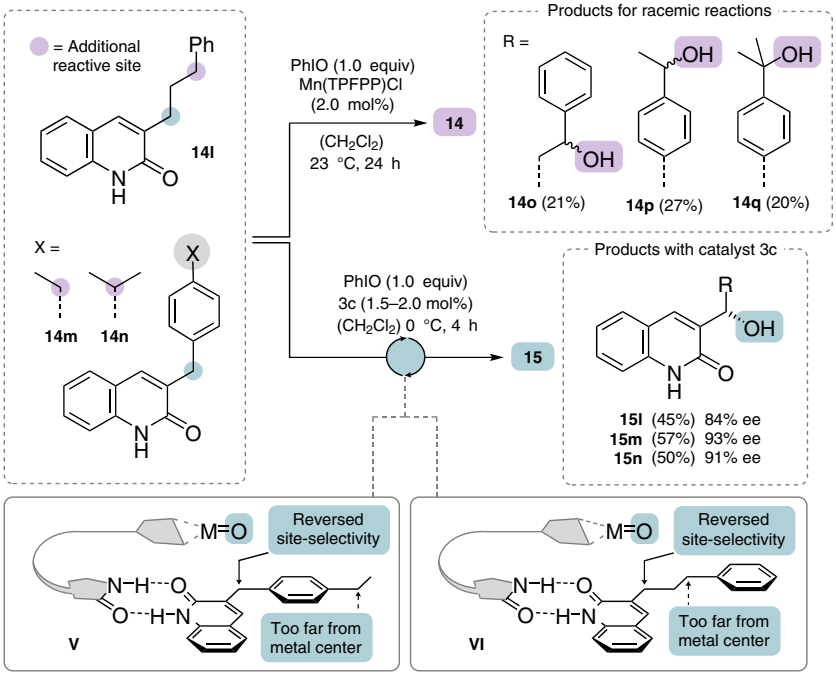

Figure 11.9 Site and enantioselective hydroxylation of quinolones **14l–14n** bearing an additional reactive site (purple) using the manganese porphyrin complex **3c** as opposed to a racemic hydroxylation reaction catalyzed by Mn(TPFPP)Cl.

Most recently, the enantioselective C(sp^3)–H amination was revisited by our group as we prepared the chiral phenanthroline ligand **3d** decorated with a lactam hydrogen bonding site. Inspired by an intriguing approach by He and coworkers [54], the silver-catalyzed amination of 7,8,9,10-tetrahydro-6(5*H*)-phenanthridinone (**17a**) was explored. Using PhINNs as a nitrene precursor (2.0 equiv), in combination with silver hexafluorophosphate (10 mol%), lactam **3d** (12 mol%), and unsubstituted 1,10-phenanthroline (10 mol%) as the co-ligand, sulfamate **18a** was isolated as a single regioisomer in very high enantioselectivity (94% ee) [29] (Figure 11.10). Under optimized conditions, the scope of this transformation was elaborated, whereupon a simple functional group tolerance was established (91% and 97% ee for **18c** and **18d**). Moreover, it was interesting to observe that the nature of the annulated aliphatic ring could be modified and **18b** and **18e** were obtained in equally high enantiomeric excess (96% and 91% ee). To our delight, the catalyst remained highly potent also for a variety of differently substituted pyridone analogues (84–95% ee for **18f–h**). Mechanistic studies were performed to shine light on the mode of action of the catalyst and the nature of the C—N bond formation step. A kinetic resolution experiment of the aminated parent compound *rac*-**18a** revealed a poor selectivity (*s* factor = 2.1) and kinetic isotope effect (KIE) measurements provided a KIE value of 1.2 for a parallel experiment (10% conversion), while a competition experiment

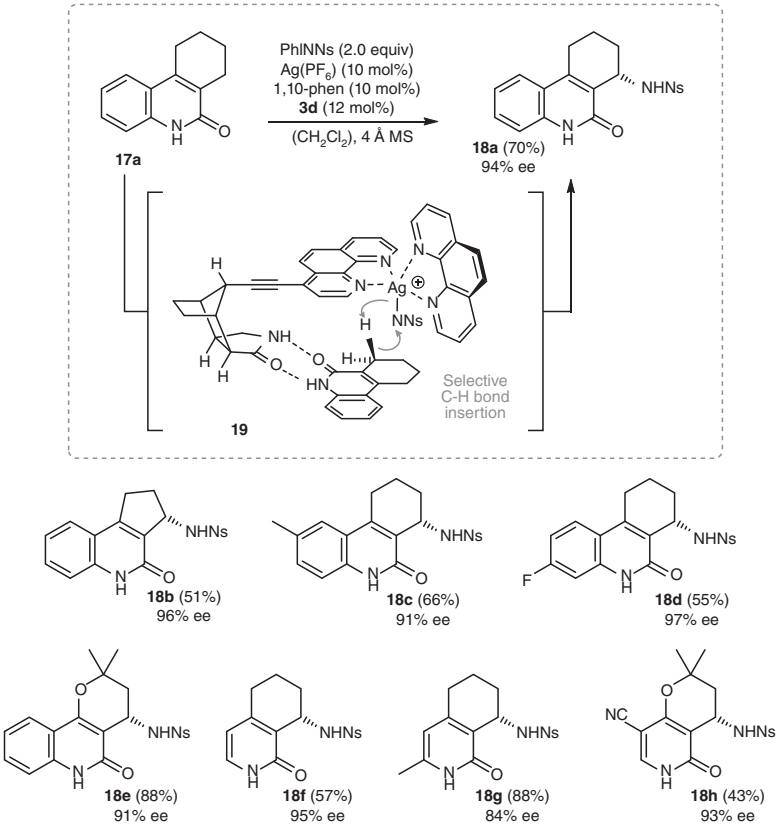

Figure 11.10 Ag-catalyzed enantioselective amination of tricyclic quinolones **17** to sulfamates **18** directed by the chiral phenanthroline ligand **3d** with a remote hydrogen bonding site. MS = molecular sieves, Ns = Nosyl (4-nitrobenzene-1-sulfonyl).

delivered a KIE value of 5.5 (30% conversion), suggesting that the C–H insertion step in complex **19** is a non-rate-determining step.

11.4 Enantioselective Oxidation of Sulfur Centers

Beyond the directed functionalization of carbon bonds, our interest expanded toward the enantioselective oxidation of sulfur centers. Within this context, the oxygenation of spirocyclic oxindoles **8** caught our attention, given that we were unable to isolate the transient secondary alcohol in reasonable enantioselectivity. We speculated that exchanging the two methylene sites by two sulfur atoms could give insight whether the oxidation process is not only selective for its enantiotopic site, but also enantioselective at this very specific atom. A set of spirodithiolanes **20** were prepared and probed in an enantioselective sulfoxidation using chiral pybox complex *ent*-**3e** equipped with the established binding site. An exceptionally selective transformation from **20a** to sulfoxide **21a** was observed (99% ee, dr > 95/5),

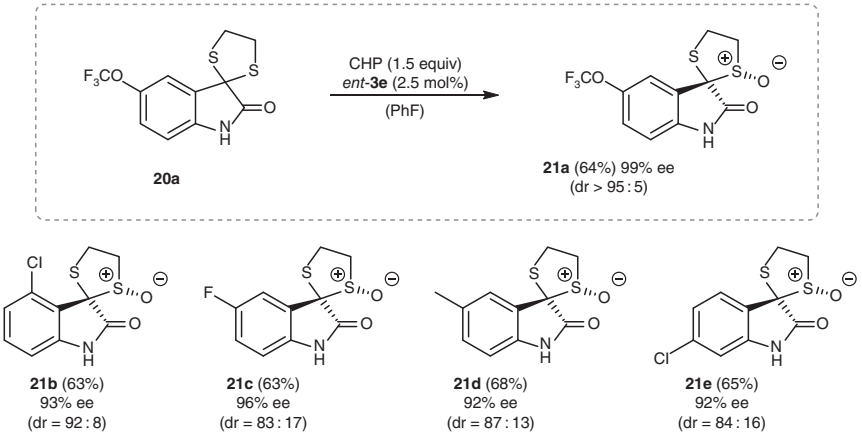

Figure 11.11 Enantio- and diastereoselective sulfoxidation of spirodithiolane-indoles **20** to sulfoxides **21** by the ruthenium pybox complex *ent*-**3e** with a molecular recognition site.

and the oxidation protocol was established for a variety of related compounds **21b**–**21e** (92–96% ee, dr 83:17–92:8) (Figure 11.11). Unlike our previous studies, in which the chirality was merely transferred by the lactam backbone, it was discovered that the two elements of chirality in ruthenium complex *ent*-**3e** work synergistically.

11.5 Concluding Remarks

Over the past decades, it was recognized that noncovalent interactions represent an intriguing opportunity to exert control over stereoselective catalysis. Within this context, several approaches such as lipophilic attraction, encapsulation, polar interaction, or ion paring have proven to be powerful strategies and accordingly are highlighted in this book. Our own contribution to this research field took inspiration from seminal molecular recognition studies spearheaded by Rebek, Deslongchamps and Diederich and rests on a chiral lactam hydrogen bonding site [55–61]. As a result, the presented chapter aims to illustrate how the precise orientation of an eligible substrate via two-point hydrogen bonding can facilitate an enantioselective transfer of electrophilic oxygen or nitrogen-containing functionalities. Perhaps even more interesting, the unique binding mode provides opportunities to override intrinsic reactivity patterns, thus opening up new avenues for unprecedented reaction sequences. Although several catalytic systems were successfully engaged in this chemistry, there are limitations that are yet to be overcome. To date, quinolone substrates persist to be the most reliable substrates for our chemistry, and along these lines the quest to develop simple, ubiquitous binding groups continues to be an exciting journey. In addition, it remains appealing to reshape and redesign both catalysts and substrates with the ultimate goal to functionalize distinct C—H bonds at a specific position of an alkyl chain at will.

Acknowledgments

Our own research on this topic was generously supported by the Deutsche Forschungsgemeinschaft (DFG), the Technical University of Munich, the Fonds der Chemischen Industrie, the Alexander von Humboldt foundation, the Studienstiftung des Deutschen Volkes, and the Elitenetzwerk Bayern. T.B. gratefully acknowledges all colleagues and coworkers who have contributed to this project and who have been instrumental to its success. Their names are provided in the references. It is due to their persistence, their continued dedication, and their intellectual input that this research topic has turned out to be so fruitful.

References

1 Pauling, L. and Corey, R.B. (1951). *Proc. Natl. Acad. Sci. U. S. A.* 37: 729.
2 Pauling, L., Corey, R.B., and Branson, H.R. (1951). *Proc. Natl. Acad. Sci. U. S. A.* 37: 205.
3 Watson, J.D. and Crick, F.H.C. (1953). *Nature* 171: 737.
4 Pauling, L. (1960). *The Nature of the Chemical Bond*. Ithaca: Cornell University Press.
5 Jeffrey, G.A. and Saenger, W. (1991). *Hydrogen Bonding in Biological Structures*. New York: Springer Science & Business Media.
6 Pihko, P.M. (2009). *Hydrogen Bonding in Organic Synthesis*. Weinheim: Wiley.
7 Yu, X. and Wang, W. (2008). *Chem. Asian J.* 3: 516.
8 Doyle, A.G. and Jacobsen, E.N. (2007). *Chem. Rev.* 107: 5713.
9 Taylor, M.S. and Jacobsen, E.N. (2006). *Angew. Chem. Int. Ed.* 45: 1520.
10 Schreiner, P.R. (2003). *Chem. Soc. Rev.* 32: 289.
11 Fanourakis, A., Docherty, P.J., Chuentragool, P., and Phipps, R.J. (2020). *ACS Catal.* 10: 10714.
12 Kuninobu, Y. and Torigoe, T. (2020). *Org. Biomol. Chem.* 18: 4126.
13 Davis, H.J. and Phipps, R.J. (2017). *Chem. Sci.* 8: 864.
14 Raynal, M., Ballester, P., Vidal-Ferran, A., and van Leeuwen, P.W.N.M. (2014). *Chem. Soc. Rev.* 43: 1660.
15 Carboni, S., Gennari, C., Pignataro, L., and Piarulli, U. (2011). *Dalton Trans.* 40: 4355.
16 Das, S., Brudvig, G.W., and Crabtree, R.H. (2008). *Chem. Commun.*: 413.
17 Burg, F. and Bach, T. (2019). *J. Org. Chem.* 84: 8815.
18 Bauer, A., Westkämper, F., Grimme, S., and Bach, T. (2005). *Nature* 436: 1139.
19 Bach, T. and Bergmann, H. (2000). *J. Am. Chem. Soc.* 122: 11525.
20 Bach, T., Bergmann, H., and Harms, K. (2000). *Angew. Chem. Int. Ed.* 39: 2302.
21 Grosch, B., Orlebar, C.N., Herdtweck, E. et al. (2003). *Angew. Chem. Int. Ed.* 42: 3693.
22 Aechtner, T., Dressel, M., and Bach, T. (2004). *Angew. Chem. Int. Ed.* 43: 5849.
23 Coote, S.C. and Bach, T. (2013). *J. Am. Chem. Soc.* 135: 14948.
24 Voss, F., Herdtweck, E., and Bach, T. (2011). *Chem. Commun.* 47: 2137.

25 Fackler, P., Berthold, C., Voss, F., and Bach, T. (2010). *J. Am. Chem. Soc.* 132: 15911.
26 Fackler, P., Huber, S.M., and Bach, T. (2012). *J. Am. Chem. Soc.* 134: 12869.
27 Frost, J.R., Huber, S.M., Breitenlechner, S. et al. (2015). *Angew. Chem. Int. Ed.* 54: 691.
28 Burg, F., Gicquel, M., Breitenlechner, S. et al. (2018). *Angew. Chem. Int. Ed.* 57: 2953.
29 Annapureddy, R.R., Jandl, C., and Bach, T. (2020). *J. Am. Chem. Soc.* 142: 7374.
30 Zhong, F., Pöthig, A., and Bach, T. (2015). *Chem. Eur. J.* 21: 10310.
31 Höke, T., Herdtweck, E., and Bach, T. (2013). *Chem. Commun.* 49: 8009.
32 Zhong, F. and Bach, T. (2014). *Chem. Eur. J.* 20: 13522.
33 Griffith, W.P. (1992). *Chem. Soc. Rev.* 21: 179.
34 Guthikonda, K. and Du Bois, J. (2002). *J. Am. Chem. Soc.* 124: 13672.
35 Saint-Denis, T.G., Zhu, R.-Y., Chen, G. et al. (2018). *Science* 359: 759.
36 Newton, C.G., Wang, S.-G., Oliveira, C.C., and Cramer, N. (2017). *Chem. Rev.* 117: 8908.
37 Zheng, C. and You, S.-L. (2014). *RSC Adv.* 4: 6173.
38 Giri, R., Shi, B.-F., Engle, K.M. et al. (2009). *Chem. Soc. Rev.* 38: 3242.
39 Davies, H.M.L. and Beckwith, R.E.J. (2003). *Chem. Rev.* 103: 2861.
40 De Montellano, P.R.O. (2015). *Cytochrome P450: Structure, Mechanism, and Biochemistry*. New York: Springer Science & Business Media.
41 Breslow, R., Zhang, X., and Huang, Y. (1997). *J. Am. Chem. Soc.* 119: 4535.
42 Breslow, R., Huang, Y., Zhang, X., and Yang, J. (1997). *Proc. Natl. Acad. Sci. U. S. A.* 94: 11156.
43 Yang, J. and Breslow, R. (2000). *Angew. Chem. Int. Ed.* 39: 2692.
44 Groves, J.T. and Neumann, R. (1987). *J. Am. Chem. Soc.* 109: 5045.
45 Groves, J.T. and Neumann, R. (1989). *J. Am. Chem. Soc.* 111: 2900.
46 Das, S., Incarvito, C.D., Crabtree, R.H., and Brudvig, G.W. (2006). *Science* 312: 1941.
47 Das, S., Brudvig, G.W., and Crabtree, R.H. (2008). *J. Am. Chem. Soc.* 130: 1628.
48 Milan, M., Bietti, M., and Costas, M. (2018). *Chem. Commun.* 54: 9559.
49 Vidal, D., Olivo, G., and Costas, M. (2018). *Chem. Eur. J.* 24: 5042.
50 Huang, X. and Groves, J.T. (2017). *J. Biol. Inorg. Chem.* 22: 185.
51 Burg, F., Breitenlechner, S., Jandl, C., and Bach, T. (2020). *Chem. Sci.* 11: 2121.
52 Espino, C.G., Fiori, K.W., Kim, M., and Du Bois, J. (2004). *J. Am. Chem. Soc.* 126: 15378.
53 Fiori, K.W. and Du Bois, J. (2007). *J. Am. Chem. Soc.* 129: 562.
54 Li, Z., Capretto, D.A., Rahaman, R., and He, C. (2007). *Angew. Chem. Int. Ed.* 46: 5184.
55 Kemp, D.S. and Petrakis, K.S. (1981). *J. Org. Chem.* 46: 5140.
56 Rebek, J. (1990). *Acc. Chem. Res.* 23: 399.
57 Lonergan, D.G., Riego, J., and Deslongchamps, G. (1996). *Tetrahedron Lett.* 37: 6109.
58 Lonergan, D.G., Halse, J., and Deslongchamps, G. (1998). *Tetrahedron Lett.* 39: 6865.

59 Lonergan, D.G. and Deslongchamps, G. (1998). *Tetrahedron* 54: 14041.
60 Castellano, R.K., Gramlich, V., and Diederich, F. (2002). *Chem. Eur. J.* 8: 118.
61 Faraoni, R., Castellano, R.K., Gramlich, V., and Diederich, F. (2004). *Chem. Commun.*: 370.

12

Supramolecular Substrate Orientation as Strategy to Control Selectivity in Transition Metal Catalysis

Joost N.H. Reek and Bas de Bruin

University of Amsterdam, Van't Hoff Institute for Molecular Sciences, Homogeneous and Supramolecular Catalysis, Sciencepark 904, 1098 XH Amsterdam, The Netherlands

12.1 Introduction

The design of transition metal catalysts traditionally relies on ligand design [1]. Typically the electronic and steric properties can be varied to optimize the activity and the selectivity of a complex. For asymmetric transformations, chiral catalysts are needed, which usually are based on chiral ligands. This approach has resulted in the enormous success of the field of homogeneous catalysis, and by now there are many successful catalysts developed at both the academic and industrial level [2]. Despite the great successes in homogeneous catalysis, there are still many reactions that cannot be performed in a selective fashion. Typically, selectivity issues can be challenging because the competing pathways follow similar pathways and the substrate does not provide electronic or steric handles to distinguish between these pathways. Even worse scenarios exist in which the desired product is only formed in minor amounts due to a natural bias for formation of the unwanted isomer. To address also these challenging catalytic conversions, novel strategies are required. One of these strategies involves substrate orientation at the metal center using supramolecular interactions between the substrate and the catalysts. This strategy has received considerable attention in the past decades, and as a result many examples have been reported in which selectivity issues have been solved using this approach [3]. Next to control over selectivity, the activity of the catalyst is generally also higher by these substrate pre-organization effects. Interestingly, the concept can be applied to many different reactions, including hydrogenation [4], hydroformylation [5], C–H activation [6], oxidation [7], and radical-type conversions [8]. In this chapter, we will focus on our contribution to supramolecular strategies in transition metal catalysis.

12.2 Asymmetric Hydrogenation

The asymmetric hydrogenation reaction is undoubtedly the most powerful asymmetric transformation for the fine chemical industry as it provides a rather

Supramolecular Catalysis: New Directions and Developments, First Edition.
Edited by Piet W.N.M. van Leeuwen and Matthieu Raynal.

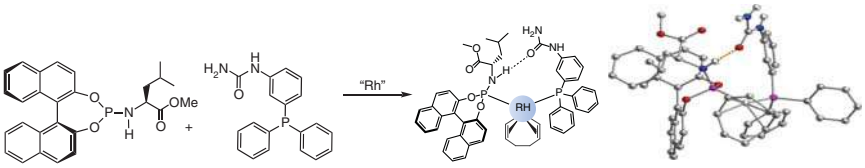

Figure 12.1 Ligand building blocks that form bidentate ligands when coordinated to rhodium based on a single hydrogen bond, indicated by dotted line in X-ray structure.

general strategy to create chiral centers in organic molecules [9]. Combinatorial chemistry approaches and high-throughput catalyst screenings are frequently used approaches to find a catalyst that induces sufficient selectivity in asymmetric hydrogenation [10]. For the generation of catalyst libraries based on chiral ligands, the use of supramolecular ligand building blocks that form bidentate ligands by self-assembly is a powerful strategy as the number of catalysts grows exponentially with the number of synthesized building blocks (see Chapter 2) [11]. We have developed ligand building blocks that can form supramolecular bidentate ligands based on a single hydrogen bond between an urea and a phosphoramidite N–H (Figure 12.1) [12]. The rhodium complexes of these ligands were shown to convert methyl 2-hydroxymethacrylate (and several of its derivatives) in very high enantioselectivities. The products form the so-called class of "Roche ester," which represent important intermediates in the preparation of biologically relevant compounds. The results in catalysis using a series of substrates suggested that hydrogen bonding between the catalyst and the substrate plays an important role achieving this high selectivity.

Detailed spectroscopic studies, in combination with kinetic analysis and DFT calculations, revealed the origin of the substrate orientation effect [12]. The characterization of the precatalyst and solvate species showed a hydrogen bond between the two ligands (Figure 12.1). In the presence of methyl 2-hydroxymethacrylate, the alkene coordinates to the rhodium center, and the hydroxyl group of the substrate is inserted in the hydrogen bond between the two ligands. The two hydrogen bonds established between the substrate and the ligands of the complex lead to a high stabilization of the diastereomeric complex in which such hydrogen bond is possible. This complex could indeed be observed during catalysis by *in situ* NMR and therefore is most likely the resting state of the reaction.

Further experiments indicate that the complex follows a lock-and-key mechanism in which the stabilizing hydrogen bonds are present in several intermediates along the pathway. The hydrogen bonds between the catalyst and the substrate lead to high enantioselectivity as the diastereoisomer of the alkene complex that leads to the dominant product is stabilized, as was demonstrated by DFT. Furthermore, the hydrogen bonds stabilize the transition state to a larger extend than the resting state, and as a result the reaction is faster for the substrate that can form the hydrogen bond. This is confirmed by kinetic analysis. The reaction follows Michaelis–Menten kinetics, and the hydrogen bonds between the substrate and the ligands lead to a stronger association (pre-complex formation) as well as a higher

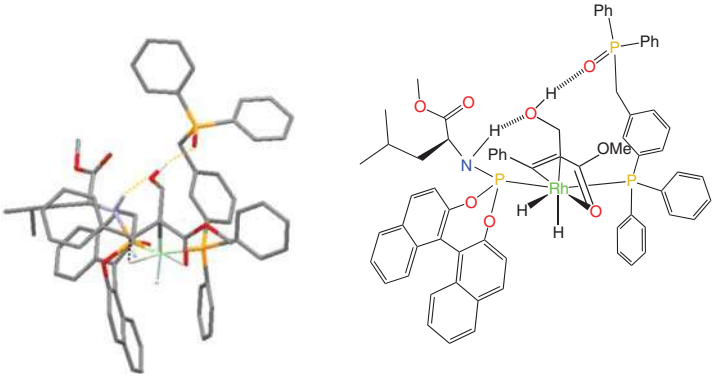

Figure 12.2 The crucial transition state using the second-generation catalyst (with phosphine oxide ligands) in the asymmetric hydrogenation reaction that is stabilized by hydrogen bonds to a larger extend than the resting state.

V_{max}. Understanding this in detail now sets the stage for implementation of such strategies in the rational design of catalysts. The redesign of the ligand building blocks was focused on changing the interactions involved in the substrate orientation [12, 13]. In this particular case, the ligand building block that contains the urea functional group was replaced by an analogue that has a phosphine oxide, which is a much stronger hydrogen bond acceptor. A mechanistic study demonstrates that also for this catalyst, two hydrogen bond interactions between the catalyst and the substrate are involved in the stabilization of a catalyst–substrate complex intermediate (Figure 12.2). Kinetic studies show that the reaction is faster when catalyzed by the phosphine-oxide-based catalysts. According to DFT calculations, the stronger hydrogen bond interactions between the catalyst and the substrate lead to a lower energy barrier by transition state stabilization, explaining the increase in rate. In addition, the product is also produced in higher selectivity (>99% ee) with the rationally optimized catalyst (Figure 12.3).

We have developed a class of bidentate ligands with an integrated binding site for anions, coined DIMPhos referring to the DIM pocket [14]. This nonchiral bidentate ligand was explored in asymmetric hydrogenation reactions, using chiral cofactors as the only source of chiral information. From the 18 cofactors evaluated, one provided a supramolecular complex that converted methyl-2-acetamido-acrylate in very high enantioselectivity. Control experiments and DFT calculations (Figure 12.4) suggest

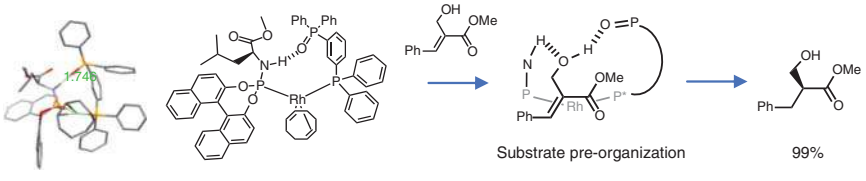

Figure 12.3 The redesign of the catalyst increaseing the binding strength between the substrate and the catalyst leads to stronger pre-organization and thus higher selectivity and reaction rates.

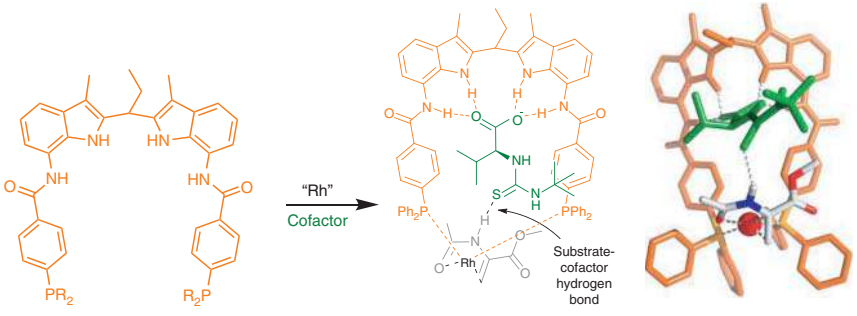

Figure 12.4 The use of DIMPhos with a chiral cofactor (green) for rhodium-catalyzed hydrogenation. The hydrogen bond established between the substrate and the bound cofactor is of crucial importance to obtain high selectivity in this reaction.

that also for this catalyst, a hydrogen bond between the substrate that is coordinated to rhodium metal center and the cofactor, which is bound in the binding pocket, is of crucial importance to achieve high enantioselectivity. So this shows that also for this system, substrate orientation plays an important role, and possibly the same mechanism as discussed above is operational.

12.3 Substrate Orientation in Hydroformylation Catalysis

The hydroformylation reaction is the formal addition of a formyl group to an alkene functional group. Usually this reaction involves a metal-catalyzed addition of CO and H_2 to the alkene. This reaction has been intensively studied, which has resulted in detailed insight in the reaction mechanism as well as many industrial applications [15]. Although many selectivity and activity issues have been solved, there are still many challenges left that have the potential to further expand the scope. These challenges mainly involve selectivity issues, including the branched selective hydroformylation, selective hydroformylation of internal alkenes, and the selective hydroformylation of tri- and tetra-substituted alkenes. Also, the asymmetric hydroformylation of terminal disubstituted alkenes is a largely unsolved issue. Some of these challenging issues can be tackled using substrate orientation strategies, as we [16] and the group of Breit [17] have demonstrated. In this section, we will discuss our approach.

The generally accepted mechanism for rhodium complexes with phosphorus ligands is displayed in Figure 12.5 [18]. For complexes that are not too electron-poor, the resting state is the rhodium(I)hydrido complex, which forms first the alkene complex (in the box). The hydride migration step that follows to either C2 or C1 leads the path to form the linear or the branched product, respectively, and most often this is the selectivity-determining step. During the migration step, the alkene rotates clockwise or anticlockwise, depending on the carbon atom to

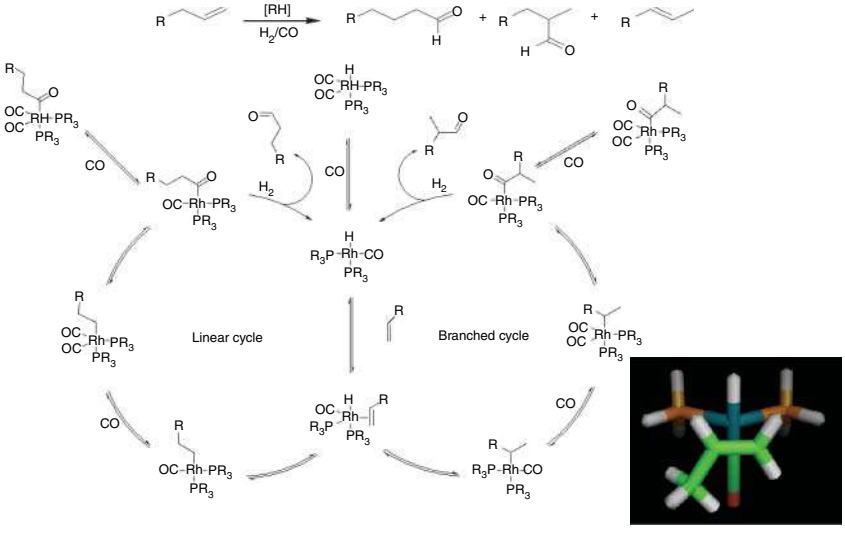

Figure 12.5 The hydroformylation reaction (top) in which alkene groups are converted to aldehyde by the addition of CO and H_2. Below the generally accepted mechanism, and in the box the hydride migration step that is often selectivity determining. Upon hydride migration (intermediate of model compound displayed), the substrate rotates clockwise, or counterclockwise, making substrate orientation by supramolecular interactions a successful strategy.

which the hydride migrates, and as such it can be intuitively be understood that supramolecular substrate orientation may be helpful in controlling the selectivity.

We have employed the aforementioned DIMPhos ligands for selective hydroformylation of alkene substrates that have carboxylate and phosphate functional groups [16]. It was shown that under hydroformylation conditions, the ligands bind to a rhodium center in a bidentate fashion forming the typical rhodium–hydride complexes that are active in hydroformylation. The metal complexes strongly bind the acetate groups in the DIM pocket, not affecting the coordination geometry around the metal. Exploration of a series of substrates in catalytic studies demonstrates that substrate preorganization results in unprecedented selectivities in hydroformylation of a broad range of terminal and internal alkenes functionalized with an anionic carboxylate or phosphate group.

Terminal unsaturated carboxylates can be hydroformylated with the phosphine analogue **L1**. 4-Pentenoate up to 10-undecenoate are converted to the aldehyde with high selectivities for the linear product (Figure 12.6). The methyl ester analogues of these substrates, which have no significant affinity of binding pocket, are converted with low selectivity supporting the effect of substrate orientation. Detailed kinetic analysis shows that these complexes convert the carboxylate substrates with a mechanism that follows Michaelis–Menten kinetics, with product inhibition. The Michaelis–Menten constant is the same as the product inhibition constant, reflecting the carboxylate binding in the DIMP pocket. We conclude from the detailed experiments that the substrate is bound first in the pocket, experiencing competition from

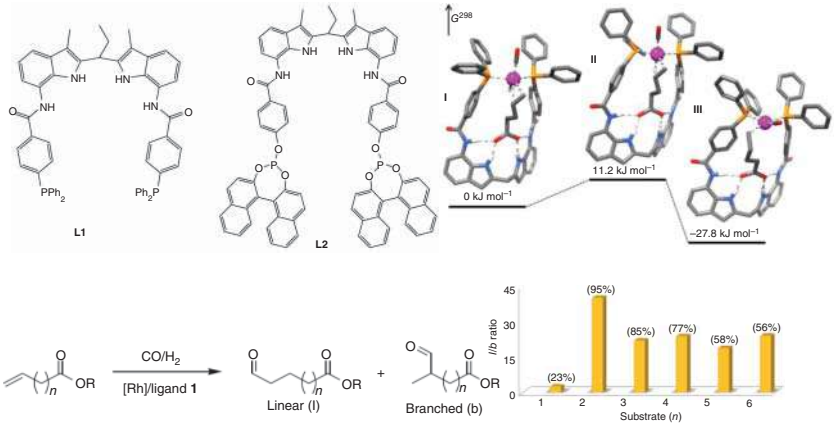

Figure 12.6 (Top)The DIMPhos ligands with aryl phosphines and with phosphites that form complexes for regioselective hydroformylation. The concept of substrate orientation is demonstrated by the DFT calculated hydride migration. Only the carbon atom close to the hydride is available for the migration as a result of the carboxylate binding in the pocket. (Bottom) Selective hydroformylation of terminal alkenes to linear aldehydes using substrate orientation. *L/B* ratio as function of the number of carbon atoms (*n*) is displayed, with the conversion in between brackets.

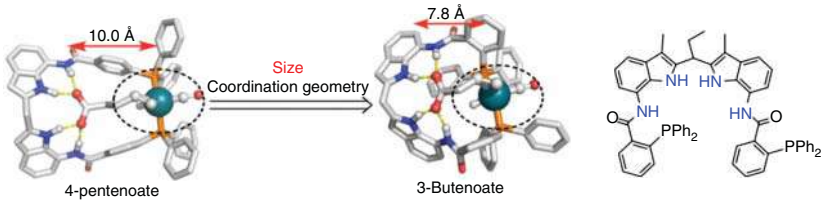

Figure 12.7 Rational design of OrthoDIMPhos as analogue of DIMPhos **L1**, changing the distance between the Rh-complex and the DIM pocket, for regioselective hydroformylation of 3-butenoic acid via substrate preorganization.

the product, and then the alkene is converted to the aldehyde. Importantly, although the mechanism is described with a model that includes product inhibition, the reaction rates are high (and accelerated by binding) and full conversion can easily be reached.

3-Butenoate ($n = 1$ in Figure 12.6) is not converted selectively using ligand **L1** since the substrate is too short to bind to the receptor moiety and the metal center simultaneously. In order to also address this substrate, we redesigned the ligand, placing the phosphines at the ortho position instead of the para position. DFT calculations show that this shortened the distance between the binding site and the rhodium complex from 10 to 7.8 Å and that this would be the ideal distance to ditopically bind 3-butenoate (Figure 12.7). Application of this ligand in the hydroformylation of 3-butenoate shows that it can convert this to yield the linear product in record high selectivity ($L/B = 84$) [19].

We have also explored supramolecular substrate orientation for internal alkenes as these are even more challenging issues. Phosphine-based DIMPhos **L1** gives

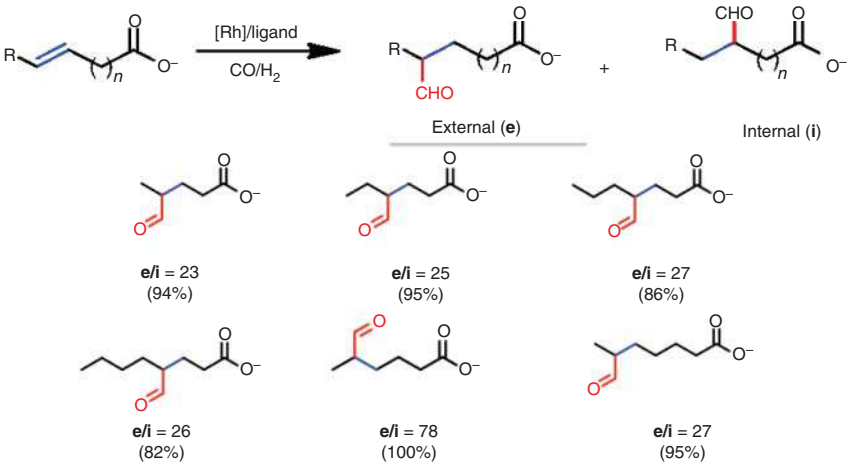

Figure 12.8 Selective hydroformylation of internal alkenes using rhodium complexes based on **L2**.

rhodium catalysts that are too unreactive to convert internal alkenes under mild conditions, but rhodium complexes based on phosphite-based DIMPhos **L2** can convert internal alkenes [20]. Also for these substrates that usually are converted to provide two products close to a 1 : 1 ratio, substrate orientation leads to highly selective processes, in which the CO inserts furthest from the carboxylate in line with the selectivity obtained for terminal alkenes. For some substrates, exceptionally high selectivities are observed, i.e. up to $o{:}i = 78$. Substrates with different distances between the alkene and the carboxylate were selectively converted with the highest selectivity obtained for the internal alkene on the 4-position (Figure 12.8).

Using the same ligand, it was demonstrated that even unprecedented reversal of selectivity can be obtained by substrate orientation, to form otherwise disfavored products in the hydroformylation of vinyl 2- and 3-carboxyarenes, with chemo- and regioselectivities up to 100%. The catalyst proved to be selective for a wide scope of substrates, allowing ample variation on the substrate [21] (Figure 12.9).

The catalyst was still selective at temperatures up to 120 °C, and also reaction could be performed at room temperature under 1 bar of syngas (although the reaction becomes more sensitive to impurities). Follow-up reactions on the formed products demonstrated the wide possible applicability, paving the way to design new synthetic routes for biorelevant compounds. Also the most challenging substrates with an internal double bond such as methyl styrene derivatives were converted with exceptional selectivity. In addition to the unusual regioselectivity, the supramolecular substrate pre-organization gives rise to very high activities. Kinetic studies and *in situ* spectroscopy reveal that the active species involves complex equilibria including dormant species. The reaction kinetics is described by a model that includes both product inhibition and substrate inhibition due to binding of the carboxylate to the binding site and to the metal center. Nonetheless, efficient formation of the desired product is observed (TOF's 2000 Mol/Mol/hour).

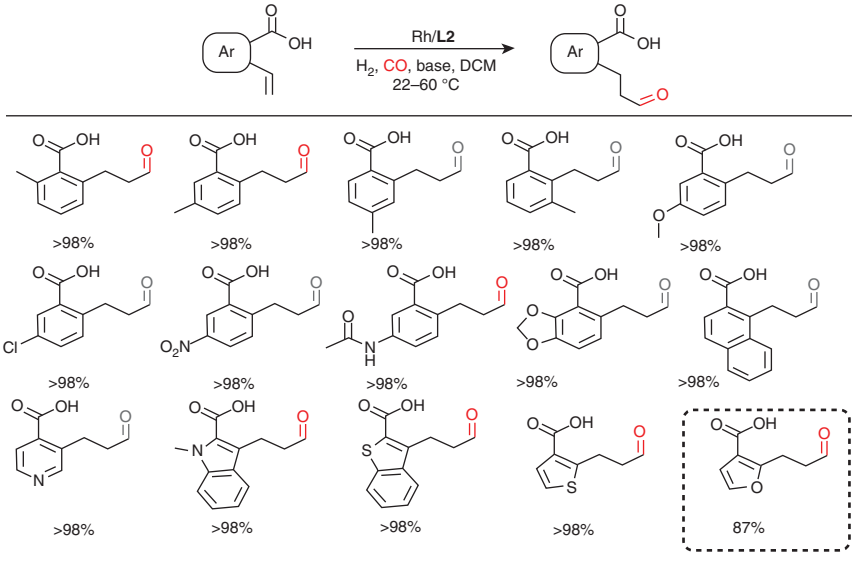

Figure 12.9 Some of the styrene derivatives that have been converted with high selectivity.

It is of general interest to develop selective hydroformylation of internal alkenes with larger distances between the directing group and the alkene, as this may result in hydroformylation catalysts that convert natural monounsaturated fatty acids (MUFAs) in a regioselective fashion, allowing broader applicability of the biofeedstock. With this in mind, we have developed a new catalyst in which the DIM binding site was at larger distance from the metal center by placing an additional phenyl group in the linker (Figure 12.10) [22]. Molecular calculations demonstrate that 9-decanoate as model for fatty acids fits reasonably when spanning the distance between the DIM pocket and the rhodium complex.

We demonstrated with this new ligand that supramolecular substrate orientation can also work when this group is remote from the reactive group, thereby increasing the scope of the approach. The hydroformylation catalyst based on the extended DIMPhos ligand converts substrates with high regioselectivity when the carboxylate directing group is remote from the alkene group, including MUFAs and their model substrates. The catalyst provides the hydroformylation product with a 10-formyl/9-formyl ratio of 2.51 for myristoleic acid, which represents the first selective catalyst for this biobased compound. These results again show that catalysts that operate via supramolecular substrate preorganization can be redesigned to provide selective catalysts for substrates of different sizes.

12.4 Substrate Orientation in C—H Borylation

Transition-metal-catalyzed CH bond activation enables the functionalization of complex molecules without the need of preactivation, allowing the introduction

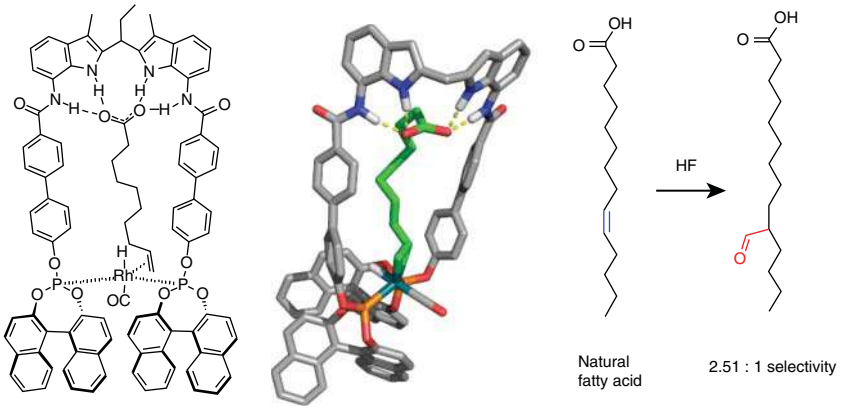

Figure 12.10 The extended DIMPhos ligand for supramolecular substrate orientation of larger substrates, that is substrates in which the distance between carboxylate and alkene is larger. Modeling picture shows the binding of 9-decanoate, the catalyst system selectively hydroformylates natural fatty acids.

of functional groups at a late stage of a synthesis sequence [23]. The direct CH borylation is of particular interest as the boron functional group allows further modification by a wide variety of transformations, including Suzuki coupling reactions, amination, hydroxylation, and halogenation, providing structural and functional molecular complexity [23]. Crucial for the application is the selectivity of the reaction, which is particularly challenging for CH bonds that are sterically and electronically deactivated in a molecule. Recently, the use of supramolecular interactions between the substrate and the ligand of metal complex has been explored to control the selectivity [24], which resulted in catalysts for selective *meta*- or *para*-CH borylation for electronically (un)activated substrates. We reported a readily accessible supramolecular iridium catalyst for ortho-selective CH borylation of valuable secondary aromatic amides, which operate via substrate pre-organization via hydrogen bonding [25] (Figure 12.11). A bipyridine ligand was functionalized with an indole amide functional group (half a DIM unit). DFT calculations of the C–H activation step show that three hydrogen bonds form between the substrate and the catalyst, to orient the substrate for ortho-selective activation. Experiments on the model substrate show that ortho-selective CH borylation can be achieved, whereas the control experiment shows on meta and para-borylated product. The scope reported included more than 26 examples of *N*-methylbenzamides and aromatic amides, including peptide-based analogues, demonstrating that this supramolecular catalyst converts a variety of secondary aromatic amides with a variety of functional groups at different positions on the aromatic ring, making the catalyst generally applicable. The supramolecular iridium catalyst has been applied at gram scale with high conversion and selectivity at elevated temperature. These experiments show that supramolecular substrate orientation is a powerful approach to control the regioselectivity in challenging CH borylation reactions. Because the ligand is easily prepared at large scale, applications of supramolecular substrate orientation in CH borylation are within reach.

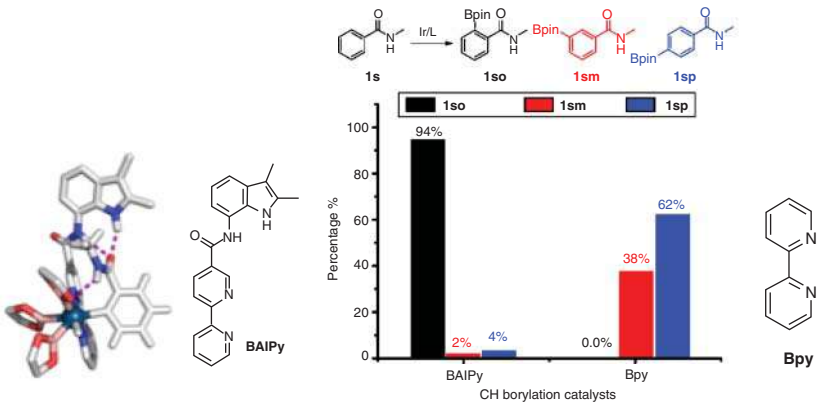

Figure 12.11 The **BAIPy** ligand with an indole amide functional group for substrate orientation for ortho-selective CH borylation of secondary aromatic amide substrates. DFT modeling of the substrate-BAIPy-trisboryl-Ir catalyst complex shows that three hydrogen bonds form between the substrate and the catalyst. A model reaction using bipyridine as the ligand (BPy) for comparison.

12.5 Second Coordination Sphere Control in Enantioselective Cobalt-catalyzed Carbene and Nitrene Transfer Reactions

Metallocarbene and nitrene radicals are important intermediates in a variety of radical-type carbene and nitrene transfer reactions mediated by cobalt(II) catalysts. Among those, chiral porphyrin complexes have shown to provide unique opportunities for the development of enantioselective radical-type reactions. Such catalysts rely on a unique combination of a unique electronic structure of the key intermediates, combined with supramolecular interactions with chiral moieties in the second coordination sphere of the catalysts. The generation of carbene and nitrene adducts at cobalt(II) leads to unique carbene and nitrene radical complexes. DFT calculations and EPR studies have confirmed that the highest spin density of the Co^{III}-carbene to be indeed located on a *p*-orbital of the carbene or nitrene moiety (Figure 12.12). The resulting carbene and nitrene radical species are key intermediates in group transfer catalysis and are reactive toward C—H, C=C, and C≡C bonds. These intermediates are best described as one-electron-reduced Fischer-type carbenes or nitrenes. Interestingly, these types of intermediates not only lead to radical-type group-transfer reactions with unique selectivity (Figure 12.12), but also provide novel opportunities to control the enantioselectivity of these radical-type reactions using hydrogen bonding interactions in the second coordination sphere (Figure 12.13). The working principle of these enantioselective reactions involves a combination of transition state stabilization and substrate orientation with respect to the chiral amide substituents in the second coordination sphere (Figure 12.13).

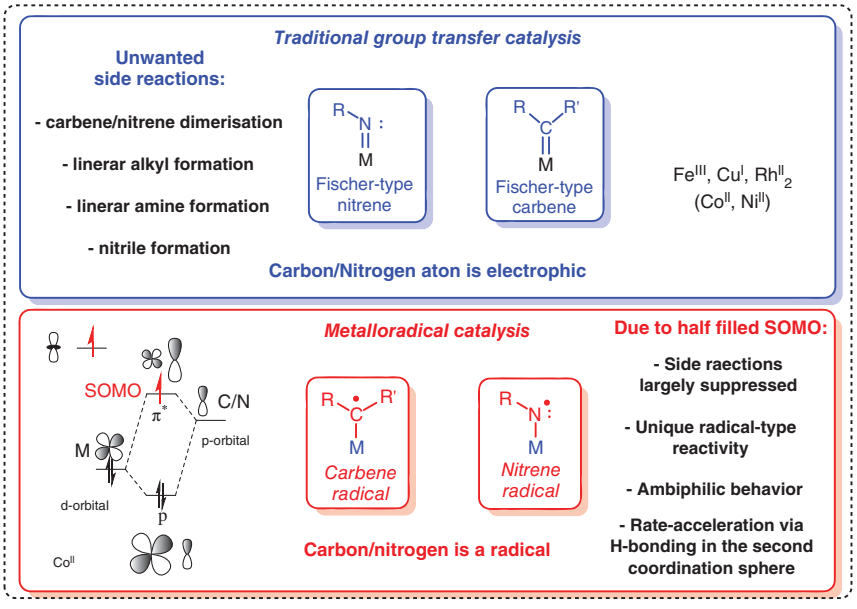

Figure 12.12 Formation of radical-type carbenes and nitrenes in cobalt(II)-catalyzed group transfer catalysis.

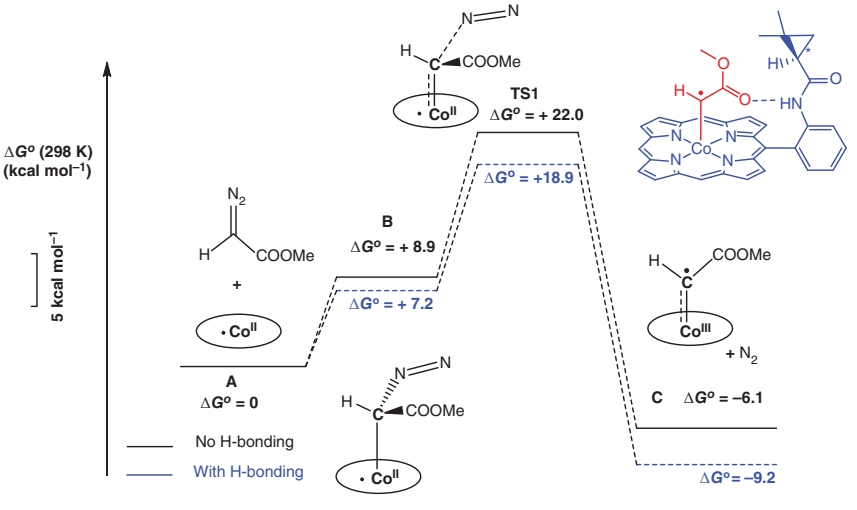

Figure 12.13 Hydrogen bonding leading to transition state stabilization in cobalt(II)-catalyzed group transfer catalysis.

Electron transfer from cobalt to the carbene or nitrene moiety results in a stronger H-bond to these hypovalent moieties than in the precursor, leading to lower transition state barriers [26, 27]. At the same time, these interactions bring the chiral information of the catalyst close to the reactive substrate.

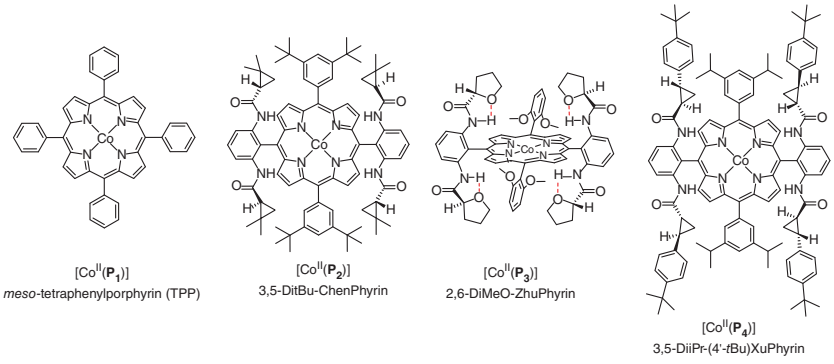

Figure 12.14 Selection of cobalt(II) porphyrins used in radical-type group transfer catalysis.

12.5.1 Applications

A selection of the several cobalt–porphyrin complexes used in carbene and nitrene transfer reactions is depicted in Figure 12.14. The commercially available non-chiral [Co^{II}(**P_1**)] (**P_1** = TPP = *meso*-tetraphenylporphyrin) and its chiral analogues allow the synthesis of a wide variety of products, among which are cyclopropanes[28–31], *2H*-chromenes [32], ketenes and β-lactams [33], *E*-aryl-dienes and dihydronaphthalenes [34], indolines [35], and sulfolane derivatives [36]. Carbene precursors for these reactions are typically diazo compounds ($R_2C{=}N_2$) and *N*-tosylhydrazones. Enantioselective carbene transfer reactions rely in many cases on complexes providing additional hydrogen bonding interactions in the second coordination sphere (Figure 12.14).

Figure 12.15 shows examples of asymmetric cyclopropanation of aromatic, aliphatic, electron-rich, and electron-deficient olefins under mild reaction conditions [37]. More recently [Co^{II}(**P_2**)] was also successfully applied in the asymmetric cyclopropanation of allyl α-diazoacetates and α-formyldiazoacetates, which were obtained in high yields and with good ee [38, 39].

Complex [Co^{II}(**P_3**)] provides a more rigid structure due to intramolecular O···H–N hydrogen bonding interactions in the ligand backbone, which enables *trans*-cyclopropanation of styrene with $HC(N_2)(Ts)$ with excellent enantioselectivity [40].

In addition to cyclopropanation, the chiral amidoporphyrin [Co^{II}(**P_4**)] is also capable of asymmetric intramolecular 1,5-C–H alkylation of α-methoxycarbonyl-α-diazosulfones to form sulfolanes in high yields and with good diastereo- and enantioselectivity (Figure 12.16) [41].

Just like radical-type carbene transfer reactions, also radical-type nitrene transfer reactions can be controlled with hydrogen bonding interactions. Most examples involve H-bonding between the amide moieties of the macrocyclic ligand

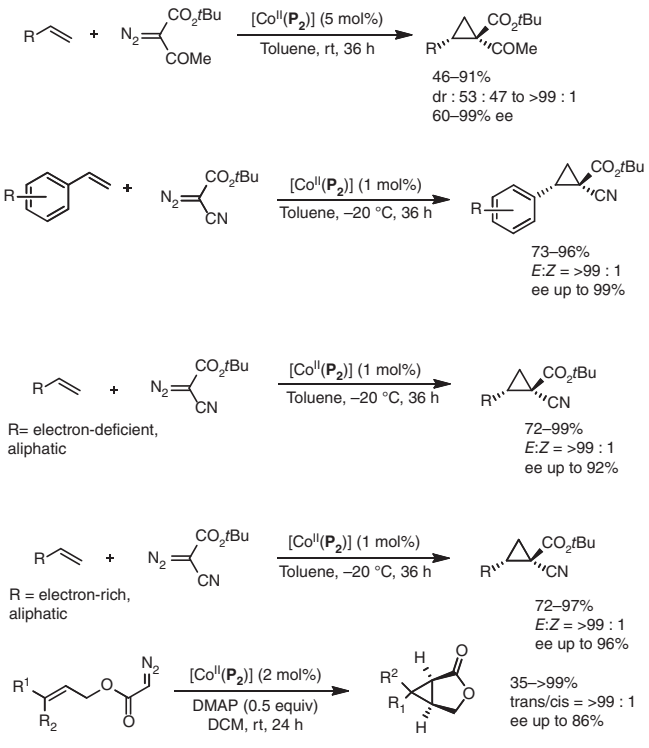

Figure 12.15 [Co^{II}(**P_2**)]-catalyzed asymmetric cyclopropanation of alkenes [37–39].

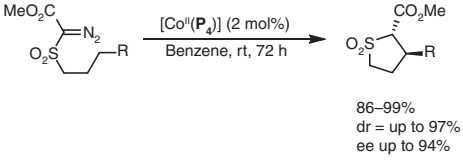

Figure 12.16 [Co^{II}(**P_4**)]-catalyzed asymmetric C–H alkylation of α-methoxycarbonyl-α-diazosulfones. R = aryl, triazole, alkenes, allene.

and activated organic azides such as RSO_2N_3, $(RO)_2P(=O)N_3$, or $ROC(=O)CN_3$ (Figure 12.17) [27].

In addition, steric interactions and van der Waals interactions in the second coordination sphere provide ample opportunities for substrate orientation, e.g. to control enantioselective intramolecular C–H amination to produce pyrrolidines from aliphatic azides [42].

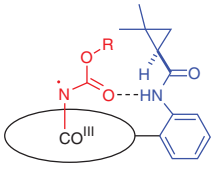

Figure 12.17 Hydrogen bonding interaction between the amide moiety of the ligand and the nitrene radical.

12.6 Concluding Remarks and Outlook

The development of catalysts by rational approaches is based on long-standing established parameters such as steric effects, electronic effects, and bite angle effects. It is now clear that supramolecular substrate orientation by using interactions between the substrate and functional groups of the catalyst provides a complementary strategy to control selectivity in transition metal catalysis. We have shown here several different examples, including hydrogenation, hydroformylation, C-H borylation, and nitrene/carbene transfer reactions. Importantly, the supramolecular catalyst can be easily prepared in some examples, and as such these can potentially be used in commercial processes. Another key advantage is that the noncovalent interactions can used as for *in silico* catalyst optimization and the design of catalysts. As such, we believe that the strategy outlined will be further developed in the next decade.

References

1 van Leeuwen, P.W.N.M. (2004). *Homogeneous Catalysis Understanding the Art*. Dordrecht: Kluwer Academic Publishers.

2 Cornils, B. and Herrmann, W.A. (eds.) (2002). *Applied Homogeneous Catalysis with Organometallic Compounds*, 2e. Wiley-VCG Verlag.

3 (a) Davis, H. and Phipps, R.J. (2016). Harnessing non-covalent interactions to exert control over regioselectivity and site-selectivity in catalytic reactions. *Chem. Sci.* 8: 864–877. (b) Dydio, P. and Reek, J.N.H. (2014). Supramolecular control of selectivity in transition metal catalysis through substrate preorganization. *Chem. Sci.* 5: 2135–2145.

4 For a recent example:Li, S., Huang, K., Cao, B. et al. (2020). Highly enantioselective hydrogenation of β,β-disubstituted nitroalkenes. *Angew. Chem. Int. Ed.* 51: 8573–8576.

5 (a) Šmejkal, T. and Breit, B. (2008). A supramolecular catalyst for regioselective hydroformylation of unsaturated carboxylic acids. *Angew. Chem. Int. Ed.* 47: 311–315. (b) Dydio, P., Dzik, W.I., Lutz, M. et al. (2011). Remote supramolecular control of catalyst selectivity in the hydroformylation of alkenes. *Angew. Chem. Int. Ed.* 50: 396–400.

6 For a recent example, Reyes, R.L., Sato, M. et al. (2020). Asymmetric remote C–H borylation of aliphatic amides and esters with a modular iridium catalyst. *Science* 369: 970–974.

7 For a recent example, Olivo, G., Farinelli, G. et al. (2017). Supramolecular recognition allows remote, site-selective C–H oxidation of methylenic sites in linear amines. *Angew. Chem. Int. Ed.* 5: 16347–16351.

8 For a recent example see:Lang, K., Torker, S., Wojtas, L., and Zhang, X.P. (2019). Asymmetric induction and enantiodivergence in catalytic radical C–H amination via enantiodifferentiative H-atom abstraction and stereoretentive radical substitution. *J. Am. Chem. Soc.* 141: 12388–12396.

9 (a) Seo, C.S.G. and Morris, R.H. (2018). Catalytic homogeneous asymmetric hydrogenation: successes and opportunities. *Organometallics* 38: 47–65. (b) Blaser, H.U., Malan, C., Pugin, B. et al. (2003). Selective hydrogenation for fine chemicals: recent trends and new developments. *Adv. Syn. Catal.* 345: 103–151.

10 Renom-Carrasco, M. and Lefort, L. (2018). Ligand libraries for high throughput screening of homogeneous catalysts. *Chem. Soc. Rev.* 47: 5038–5060.

11 (a) Wilkinson, M.J., van Leeuwen, P.W.N.M., and Reek, J.N.H. (2005). New directions in supramolecular transition metal catalysis. *Org. Biomol. Chem* 3: 2371–2383. (b) Breit, B. (2005). Supramolecular approaches to generate libraries of chelating bidentate ligands for homogeneous catalysis. *Angew. Chem., Int. Ed.* 44: 6816–6825. (c) Sandee, A.J. and Reek, J.N.H. (2006). Bidentate ligands by supramolecular chemistry—the future for catalysis? *Dalton Trans.*: 3385–3391. (d) Bellini, R., van der Vlugt, J.I., and Reek, J.N.H. (2012). Supramolecular self-assembled ligands in asymmetric transition metal catalysis. *Isr. J. Chem.* 52: 613–629.

12 (a) Breuil, P.-A.R., Patureau, F.W., and Reek, J.N.H. (2009). Singly hydrogen bonded supramolecular ligands for highly selective rhodium-catalyzed hydrogenation reactions. *Angew. Chem. Int. Ed.* 48: 2162–2165. (b)Daubignard, J., Detz, R.J., Jans, A.C.H. et al. (2017). Rational optimization of supramolecular catalysts for the rhodium-catalyzed asymmetric hydrogenation reaction. *Angew. Chem. Int. Ed.* 56: 13056–11306. (c) Daubignard, J., Lutz, M., Detz, R.J. et al. (2019). Origin of the selectivity and activity in the rhodium-catalyzed asymmetric hydrogenation using supramolecular ligands. *ACS Catal.* 9: 7535–7547.

13 Daubignard, J., Detz, R.J., de Bruin, B., and Reek, J.N.H. (2019). Phosphine oxide based supramolecular ligands in the rhodium-catalyzed asymmetric hydrogenation. *Organometallics* 38: 3961–3969.

14 Dydio, P., Rubay, C., Gadzikwa, T. et al. (2011). Cofactor-controlled enantioselective catalysis. *J. Am. Chem. Soc.* 133: 17176–17179.

15 Franke, R., Selent, D., and Börner, A. (2012). Applied hydroformylation. *Chem. Rev.* 112: 5675–5732.

16 Dydio, P. and Reek, J.N.H. (2013). Supramolecular control of selectivity in hydroformylation of vinyl arenes: easy access to valuable beta-aldehyde intermediates. *Angew. Chem. Int. Ed.* 52: 3878–3882.

17 Šmejkal, T., Gribkov, D., Geier, J. et al. (2010). Transition-state stabilization by a secondary substrate–ligand interaction: a new design principle for highly efficient transition-metal catalysis. *Chem. Eur. J.* 16: 2470–2478.

18 van Leeuwen, P.W.N.M. and Claver, C. (eds.) (2000). *Rhodium Catalyzed Hydroformylation*. Dordrecht: Kluwer Academic Publishers.

19 Bai, S.T., Sinha, V., Kluwer, A.M. et al. (2019). Rational redesign of a regioselective hydroformylation catalyst for 3-butenoic acid by supramolecular substrate orientation. *ChemCatChem.* 11: 5322–5329.

20 Dydio, P., Detz, R., and Reek, J.N.H. (2013). Precise supramolecular control of selectivity in the Rh-catalyzed hydroformylation of terminal and internal alkenes. *J. Am. Chem. Soc.* 135: 10817–10828.

21 (a) Ref. 16. (b) Dydio, P., Detz, R.J., de Bruin, B., and Reek, J.N.H. (2014). Beyond classical reactivity patterns: hydroformylation of vinyl and allyl arenes to valuable beta- and gamma-aldehyde intermediates using supramolecular catalysis. *J. Am. Chem. Soc.* 136: 8418–8429. (c) Dydio, P. and Reek, J.N.H. (2014). Scalable and chromatography-free synthesis of 2-(2-formylalkyl) arenecarboxylic acid derivatives through the supramolecularly controlled hydroformylation of vinylarene-2-carboxylic acids. *Nat. Protoc.* 9: 1183–1191.

22 Linnebank, P.R., Ferreira, S.F., Kluwer, A.M., and Reek, J.N.H. (2020). Regioselective hydroformylation of internal and terminal alkenes via remote supramolecular control. *Chem. Eur. J.* 26: 8214–8219.

23 (a) Godula, K. and Sames, D. (2006). C-H bond functionalization in complex organic synthesis. *Science* 312: 67–72. (b) Hartwig, J.F. (2012). Borylation and silylation of C–H Bonds: a platform for diverse C–H bond functionalizations. *Acc. Chem. Res.* 45: 864–873.

24 (a) Kuninobu, Y., Ida, H., Nishi, M., and Kanai, M. (2015). A meta-selective C–H borylation directed by a secondary interaction between ligand and substrate. *Nat. Chem.* 7: 712–717. (b) Davis, H.J., Mihai, M.T., and Phipps, R.J. (2016). Ion Pair-directed regiocontrol in transition-metal catalysis: a meta-selective C–H borylation of aromatic quaternary ammonium salts. *J. Am. Chem. Soc.* 138: 12759–12762. (b) Genov, G.R., Douthwaite, J.L., Lahdenperä, A.S.K. et al. (2020). Enantioselective remote C–H activation directed by a chiral cation. *Science* 367: 1246–1251.

25 Bai, S.-T., Bheeter, C.B., and Reek, J.N.H. (2019). Hydrogen bond directed ortho-selective C−H borylation of secondary aromatic amides. *Angew. Chem. Int. Ed.* 58: 13039–13043.

26 Lyaskovskyy, V., Suarez, A.I.O., Lu, H. et al. (2011). Mechanism of cobalt(II) porphyrin-catalyzed C–H amination with organic azides: radical nature and H-atom abstraction ability of the key cobalt(III)–nitrene intermediates. *J. Am. Chem. Soc.* 133: 12264–12273.

27 Olivos Suarez, A.I., Jiang, H., Zhang, X.P., and de Bruin, B. (2011). The radical mechanism of cobalt(II) porphyrin-catalyzed olefin aziridination and the importance of cooperative H-bonding. *Dalton Trans.* 40: 5697–5705.

28 Caselli, A., Gallo, E., Ragaini, F. et al. (2006). Chiral porphyrin complexes of cobalt(II) and ruthenium(II) in catalytic cyclopropanation and amination reactions. *Inorg. Chim. Acta* 359: 2924–2932.

29 Fantauzzi, S., Gallo, E., Rose, E. et al. (2008). Asymmetric cyclopropanation of olefins catalyzed by chiral cobalt(II)-binaphthyl porphyrins. *Organometallics* 27: 6143–6151.

30 Zhu, S., Ruppel, J.V., Lu, H. et al. (2008). Cobalt-catalyzed asymmetric cyclopropanation with diazosulfones: rigidification and polarization of ligand chiral environment via hydrogen bonding and cyclization. *J. Am. Chem. Soc.* 130: 5042–5043.

31 Xu, X., Zhu, S., Cui, X. et al. (2013). Cobalt(II)-catalyzed asymmetric olefin cyclopropanation with α-ketodiazoacetates. *Angew. Chem. Int. Ed.* 52: 11857–11861.

32 Paul, N.D., Mandal, S., Otte, M. et al. (2014). Metalloradical approach to 2*H*-chromenes. *J. Am. Chem. Soc.* 136: 1090–1096.

33 Paul, N.D., Chirila, A., Lu, H. et al. (2013). Carbene radicals in cobalt(II)-porphyrin-catalyzed carbene carbonylation reactions; a catalytic approach to ketenes. *Chem. Eur. J.* 19: 12953–12958.

34 te Grotenhuis, C., Das, B.G., Kuijpers, P.F. et al. (2017). Catalytic 1,2-dihydronaphthalene and E-aryl-diene synthesis via co III -carbene radical and o-quinodimethane intermediates. *Chem. Sci.* 8: 8221–8230.

35 Karns, A.S., Goswami, M., and de Bruin, B. (2018). Catalytic synthesis of indolines by hydrogen atom transfer to cobalt(III)-carbene radicals. *Chem. Eur. J.* 24: 5253–5258.

36 Cui, X., Xu, X., Jin, L.-M. et al. (2015). Stereoselective radical C–H alkylation with acceptor/acceptor-substituted diazo reagents via Co(II)-based metalloradical catalysis. *Chem. Sci.* 6: 1219–1224.

37 Zhu, S., Xu, X., Perman, J.A., and Zhang, X.P. (2010). A general and efficient cobalt(II)-based catalytic system for highly stereoselective cyclopropanation of alkenes with α-cyanodiazoacetates. *J. Am. Chem. Soc.* 132: 12796–12799.

38 Ruppel, J.V., Cui, X., Xu, X., and Zhang, X.P. (2014). Stereoselective intramolecular cyclopropanation of α-diazoacetates via Co(II)-based metalloradical catalysis. *Org. Chem. Front.* 1: 515–520.

39 Xu, X., Wang, Y., Cui, X. et al. (2017). Metalloradical activation of α-formyldiazoacetates for the catalytic asymmetric radical cyclopropanation of alkenes. *Chem. Sci.* 8: 4347–4351.

40 Zhu, S., Ruppel, J.V., Lu, H. et al. (2008). Cobalt-catalyzed asymmetric cyclopropanation with diazosulfones: rigidification and polarization of ligand chiral environment via hydrogen bonding and cyclization. *J. Am. Chem. Soc.* 130: 5042–5043.

41 Cui, X., Xu, X., Jin, L.-M. et al. (2015). Stereoselective radical C–H alkylation with acceptor/acceptor-substituted diazo reagents via Co(II)-based metalloradical catalysis. *Chem. Sci.* 6: 1219–1224.

42 Kuijpers, P.F., Tiekink, M.J., Breukelaar, W.B. et al. (2017). Cobalt-porphyrin-catalyzed intramolecular ring-closing C–H amination of aliphatic azides: a nitrene-radical approach to saturated heterocycles. *Chem. Eur. J.* 23: 7945–7952.

13

Phosphine Ligands with Acylguanidinium Groups as Substrate-directing Unit

Felix Bauer and Bernhard Breit

University of Freiburg, Insitute for Organic Chemistry, Fakultät für Chemie und Pharmazie, Albertstraße 21, 79104 Freiburg, Germany

13.1 Introduction

In nature, molecular recognition plays a crucial role in the function of enzymes as catalysts [1]. Due to the optimized structure of enzyme–substrate complexes, the transition state of chemical transformations is stabilized and the rate of a chemical reaction can be increased [2]. Enzymes also can achieve outstanding high levels of regio- and stereoselectivity, which can be explained by the preorientation of the substrate toward the reactive center by multiple noncovalent interactions. The guanidine functional group of arginine is an important group to bind substrates to enzymes [3, 4]. More than 70% of all substrates and cofactors of enzymes are negatively charged and a positively charged groups can form strong ion pairs with them [3–5]. The guanidine group is capable of forming strong hydrogen bonds to acceptor groups in enzymes [5]. However, many enzymes are quite narrow in their substrate scope, which limits their application in synthetic chemistry [6, 7].

Homogeneous transition metal catalysis is one of the most powerful tools available in modern chemistry [8]. The activity and selectivity of these catalysts are traditionally tuned by modifications of the ligand around the metallic center. In the fast-growing field of supramolecular catalysis, many groups tried to combine some of the benefits of enzyme catalysis with transition metal catalysis [9–12]. Supramolecular interactions of the substrate and specific recognition groups in the ligand sphere can be designed to generate an enzyme-like catalysts [11].

13.2 Hydroformylation of Alkenoic and Alkynoic Acids

The acylguanidine-bearing ligand **1** was synthesized to combine the structural features of a phosphine ligand with a recognition side for carboxylic acids [13]. By molecular modeling, the meta position was found to be the optimal orientation for an optimal preorientation of the substrate [14] (Scheme 13.1).

Supramolecular Catalysis: New Directions and Developments, First Edition.
Edited by Piet W.N.M. van Leeuwen and Matthieu Raynal.

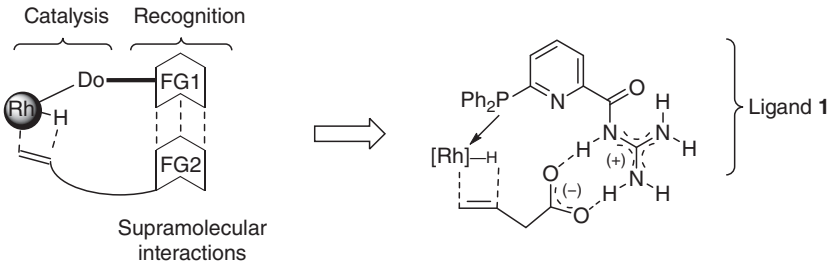

Scheme 13.1 Concept of supramolecular substrate recognition. Do = Donor; FG 1 and FG2 are complementary functional groups.

Several ligands were tested in the rhodium-catalyzed hydroformylation of unsaturated carboxylic acids (Table 13.1). As standard substrate, vinylacetic acid was chosen. PPh_3 (entry 1), an industrially relevant monodentate ligand, displayed only low activity (TOF = 30 h^{-1}) and a typical low regioselectivity (l/b = 1.3). Xantphos (entry 2), a bisphosphine ligand, with a huge bite angle showed very low activity. In the absence of a ligand, moderate selectivity for the branched product was observed (l/b = 0.6), but the activity of the catalyst was low. Whereas ligands **3** and **4** do not

Table 13.1 Hydroformylation of alkenoic acids and control experiments.[a)]

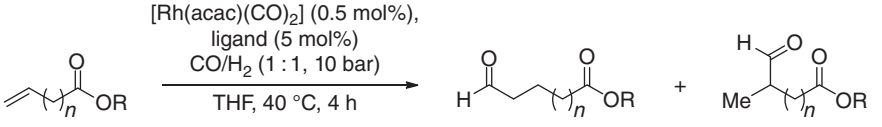

Linear Branched

#	Ligand	*n*	R	Conversion (%)	*l/b*	TOF (h^{-1})
1	PPh_3	1	H	53	1.3	30
2[b)]	Xantphos (**2**)	1	H	5	nd	nd
3	—	1	H	25	0.6	16
4	**3**	1	H	51	1.4	29
5	**4**	1	H	96	4.8	60
6	**1**	1	H	100	23	250
7	PPh_3/**5**	1	H	20	1.5	12
8	**1**	2	H	73	3.6	49
9[c)]	**1**	1	Me	50	1.1	29
10[d)]	**1**	1	Me	58	1.4	34

a) $[Rh(acac)(CO)_2]$/ligand/substrate = 1 : 10 : 200, c_0(substrate) = 0.2 M, THF (2 ml). TOF (mol aldehyde per catalyst per hour) was determined from gas consumption curve and regioselectivity was determined by ^{1}H NMR analysis of the reaction mixture.
b) $[Rh(acac)(CO)_2]$/**2**/substrate = 1 : 5 : 200.
c) Suspension of ligand **1**, without the substrate ligand has a very low solubility.
d) AcOH was added, AcOH/substrate = 1 : 1.

give an improvement either, ligand **1** showed an extraordinary high selectivity for the linear product ($l/b > 23$) as well as an outstanding activity (TOF = 250 h^{-1}). The acylguanidine **5** without a diphenylphosphine group was applied together with PPh_3. In this case, poor selectivity and low activity were observed. This shows that the molecular recognition unit and the phosphine donor group have to be in the same molecule to achieve good results. When pent-4-enoic acid was used as substrate with ligand **1,** the reaction significantly slows down and a lower linear selectivity was observed, which suggests that the distance between the carboxylic acid and the alkene group is crucial to obtain good results. The influence of the presence of the carboxylic acid group was validated by the use of methyl but-3-enoate as substrate. Without the supramolecular interactions between the substrate and recognition unit, only low conversion and selectivity was observed. This experiment was also repeated in the presence of acetic acid to exclude just a positive effect of any carboxylic acid.

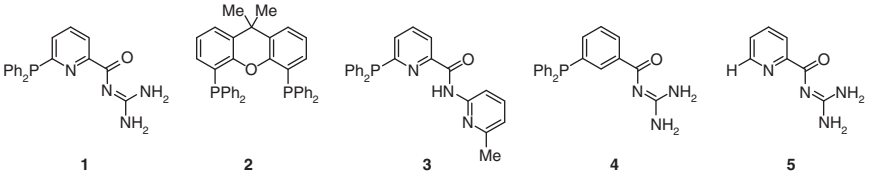

With a catalyst containing a molecular recognition unit, it is possible to differentiate between different available substrates. When a 1 : 1 substrate mixture of vinylacetic acid and another alkene was used in hydroformylation, complete conversion and excellent selectivity for the substrate with the carboxylic acid were achieved, while the unmodified alkene only showed low conversion (Scheme 13.2a).

When the unsymmetrical substrate **6** with two alkene functions at different distances to the carboxylic acid was employed, an impressive site selectivity could be observed (Scheme 13.2b). The product **7** could be isolated in 75% yield. By ^{1}H NMR

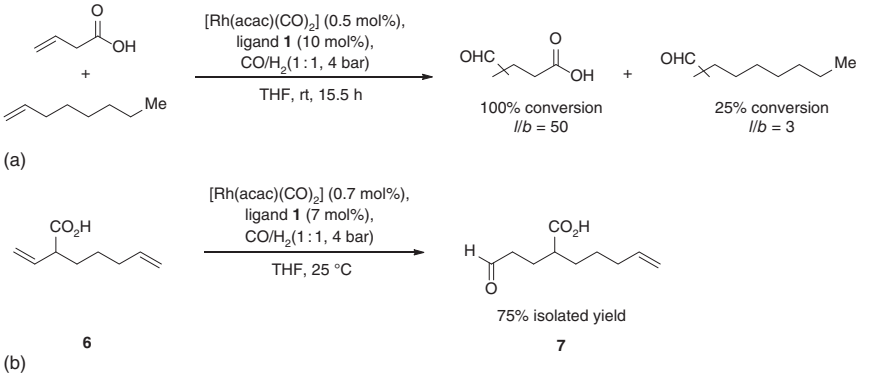

Scheme 13.2 Inter-(a) and intramolecular (b) substrate differentiation by molecular recognition.

analysis of the reaction mixture, a huge preference for the β,γ-alkene group was detected.

The coordination of the carboxyl group in the substrate by the acylguanidine unit is assumed to be responsible for the observed high catalyst activity and regioselectivity, because it might lower the activation energy in the initial hydrometalation step of the catalytic cycle. To get a better understanding for the binding mode of the ligand to the substrate in this step, density functional theory (DFT) calculations (B3LYP/3-21**) were performed on a model system, in which the phenyl groups of the ligand were substituted by hydrogen atoms to save computation time [14]. Three different binding modes between the substrate and one or both ligands were investigated. In the first considered binding mode, the substrate protonates the acylguanidine group of one ligand and is then coordinated by hydrogen bonding from both ligands before, during, and after the hydrometalation transition state (Figure 13.1). This binding mode was found lowest in energy with a ΔG for the hydrometalation of only 3.7 kcal mol^{-1}. The low-energetic barrier can be explained with the four hydrogen bonds of both ligands to the carboxyl group which perfectly preorientates the substrate for the catalytic transformation. Extra hydrogen bonds from the N–H atoms to the carbonyl group of the acylguanidine and to the pyridine nitrogen force the whole recognition unit into a flat and highly preorientated geometry, which is likely positive for the formation of stabilizing hydrogen bonds to the substrate. Another binding mode for the hydrometalation step is that the substrate protonates one ligand and then interacts only with one ligand by hydrogen bonding. The missing hydrogen bonds of the second ligand to substrate raise the energy of the hydrometalation in this binding mode to $\Delta G = 6.4$ kcal mol^{-1} [14]. If the protonated substrate interacts just with one unprotonated ligand, a $\Delta G = 11.1$ kcal mol^{-1} was observed [14].

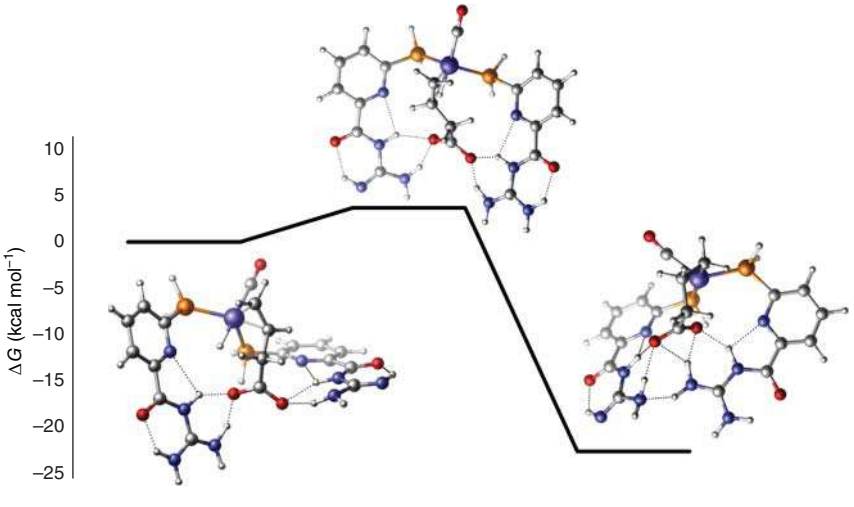

Figure 13.1 Most favorable binding mode for the hydrometalation transition state.

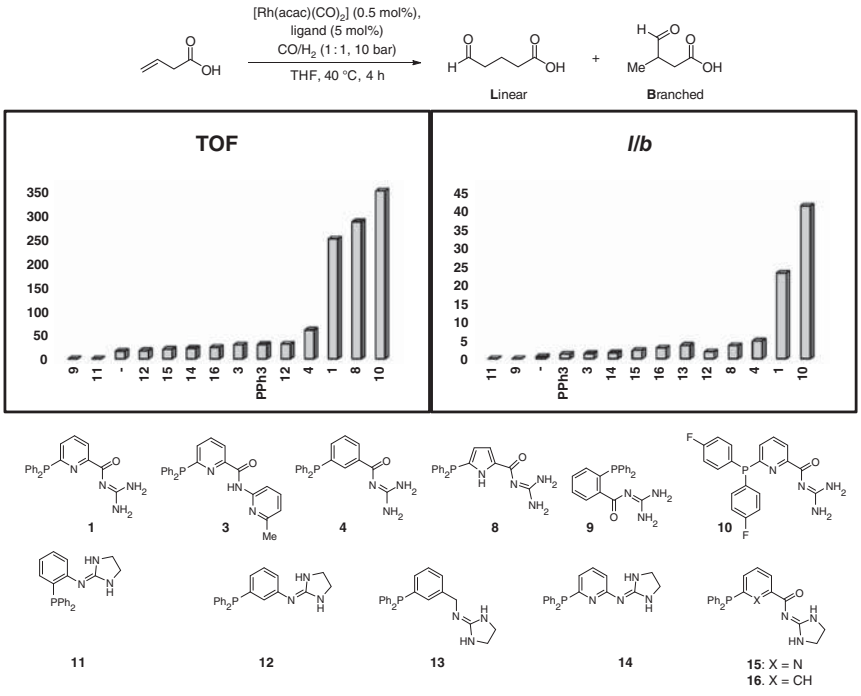

Figure 13.2 Hydroformylation of vinylacetic acid with different ligands. Reaction conditions: [Rh(acac)$(CO)_2$]/ligand/substrate = 1 : 10 : 200, c_0(substrate) = 0.2 M, THF (2 ml), CO/H_2 (1 : 1, 10 bar), 40 °C, four hours. TOF (mole aldehyde per mole catalyst per hour) was determined from gas consumption curve. Regioselectivity (*l*/*b*) was determined by ^{1}H NMR spectroscopic analysis of the crude reaction mixture.

These calculations highlight the importance of the stabilization by many low-energy interactions for this catalytic system.

For further investigations of this supramolecular-directed hydroformylation, nine new ligands were prepared and tested in the hydroformylation of vinylacetic acid (Figure 13.2) [14]. In most cases, only low activity and selectivity were observed. It was found that an acylguanidine group in the right position of the ligands seems to be crucial to obtain good activity and reactivity. All modifications at the acylguanidine unit had no positive effect on the catalyst. When ligand **1** and ligand **4** are compared, an important effect of the pyridine nitrogen atom can be seen. Interestingly, a turnover frequency (TOF) of 286 h^{-1} was achieved with ligand **8**, which has a pyrrole instead of a pyridine ring as linker of the acylguanidine unit and the diarylphosphine group. The *l*/*b* selectivity of **8** was only 3.5 which is 6.6 times lower than that of ligand **1**. The best ligand tested was electron poor ligand **10**, which showed an extraordinary high activity of 350 h^{-1} and almost doubled *l*/*b* selectivity compared to the already excellent selectivity achieved by ligand **1**.

The best three ligands were tested in the hydroformylation of (*Z*)-pent-3-enoic acid. With classical ligands, it is difficult to selectively hydroformylate the unsymmetrical internal double bond of the substrate. This can be seen with the PPh_3 ligand,

which showed only very low catalytic activity and a low selectivity toward aldehyde **19**. With ligand **1,** good regioselectivity toward aldehyde **18** (**18**/**19** = 11 : 1) was observed as well as a seven times higher catalyst activity compared to PPh_3. The best catalytic activity was observed with ligand **8** (TON = 93), but the observed selectivity was lower ((**18**/**19** = 3.9 : 1)). Finally, the electron-poor ligand **10** showed a very high catalytic activity (TON = 73), combined with an outstanding high selectivity for the aldehyde **18** (Table 13.2).

Table 13.2 Hydroformylation of (*Z*)-pent-3-enoic acid.

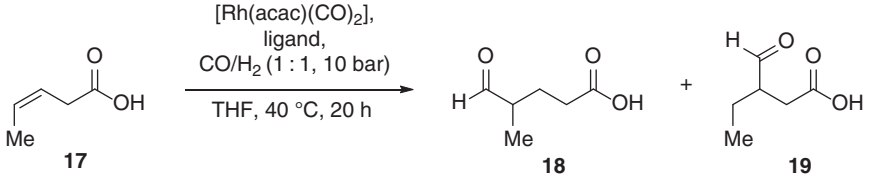

#	Ligand	Time (h)	TON[a)]	Regioselectivity 18/19
1[b)]	PPh_3	68	5.5	1 : 1.7
2[b)]	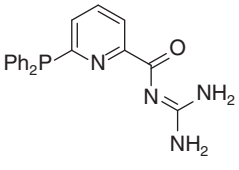	68	39	11 : 1
3[c)]	**1** 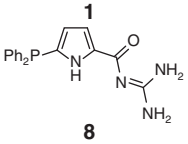 **8**	20	93	3.9 : 1
4[c)]	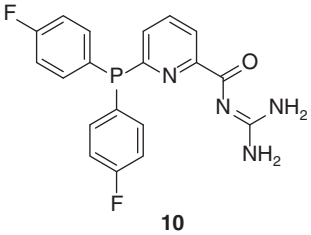 **10**	20	73	18.1 : 1

a) Turnover number = TON (mole of aldehydes per mole catalyst).
b) [Rh(acac)$(CO)_2$]/ligand/substrate = 1 : 10 : 50, c_0(substrate) = 0.2 M, THF (4 ml), CO/H_2 (1 : 1, 6 bar), rt, 68 h.
c) [Rh(acac)$(CO)_2$]/ligand/substrate = 1 : 10 : 100, c_0(substrate) = 0.2 M, THF (2 ml), CO/H_2 (1 : 1, 10 bar), rt, 20 h.

The above shown reaction requires cis-configured internal alkenes, which had to be prepared by Lindlar hydrogenation from the corresponding alkynes. To avoid this extra step, the direct use of the corresponding β-alkynoic acids as substrates seemed to be appropriate [15]. It was known from previous studies that ligands with enhanced π-acceptor ability are beneficial in the hydroformylation of alkynes [16]. Therefore, we designed a modified version of ligand **1** in which the phenyl groups are substituted by two 3,5-bis-(trifluoromethyl)phenyl groups. Indeed, this new ligand **20** was successfully applied in the hydroformylation of a broad scope of β-alkynoic acids (Scheme 13.3). In almost all cases, a saturated aldehyde product could be isolated in high yields and outstanding selectivities. It is worth to note the significance of campher sulfonic acid (CSA), since without this acid additive the conversion of the substrate dropped to around 11%. There is an example where the cyclization product of an unsaturated aldehyde was isolated and due to this, it can be assumed that the hydroformylation is the first reaction step. The initially formed unsaturated aldehyde seems to be hydrogenated to the saturated product. Control experiments could confirm the important role of the acylguanidine group. As a consequence of the easier availability of the substrate, the application range of this methodology could be broadly expanded.

After the successful use of β-unsaturated acids as substrates in supramolecular-directed hydroformylation, it was reasonable to test α-alkenoic acids [17]. Therefore, oct-2-enoic acid was used as substrate under hydroformylation conditions together with PPh_3. Only a moderate activity for the hydrogenation of the conjugated C=C double bond was observed (Scheme 13.4). When ligand **1** was used as ligand instead, the substrate was completely transformed to the saturated aldehyde **23** in perfect selectivity.

With this found untypical reactivity, it was possible to selectively reduce 16 different α-alkenoic acids into the corresponding saturated aldehydes in good to excellent yield. Control experiments indicated again the crucial role of the hydrogen bonding and the ligand design. When an isotopically labeled [1-^{13}C]-oct-2-enoic acid was employed, analysis of the reaction mixture showed complete reduction to octanal, but remarkably the isotopic labeling disappeared. Based on this finding, a reaction mechanism consisting of three consecutive steps was proposed (Scheme 13.5): In the first step, the substrate binds by hydrogen bonding to the recognition unit of the ligand(s) of the rhodium complex (accompanied by substrate deprotonation). In the second step, α-selective hydroformylation of the preorientated substrate takes place to form an α-formyl acid, which finally decarboxylates to the saturated aldehyde.

In the previously described directed hydroformylation of β-alkynoic acids, the enal intermediate gets completely hydrogenated during the reaction. When α-alkynoic acids were employed instead complex product mixtures were obtained [18]. Based on the results of the α-alkenoic acids, it seemed reasonable that by directed hydroformylation an α-formyl-alkenoic acid might be an intermediate which probably suffers from side reactions under the reaction conditions. Such an intermediate might be highly activated for a consecutive Michael addition with suitable nucleophiles. Indeed, it was possible to generate such a tandem catalytic system with ligand **20** and several aryl nucleophiles (Scheme 13.6) [18].

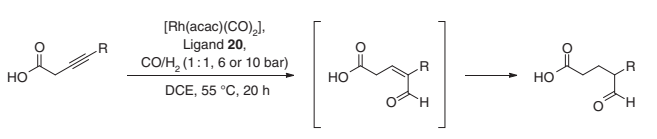

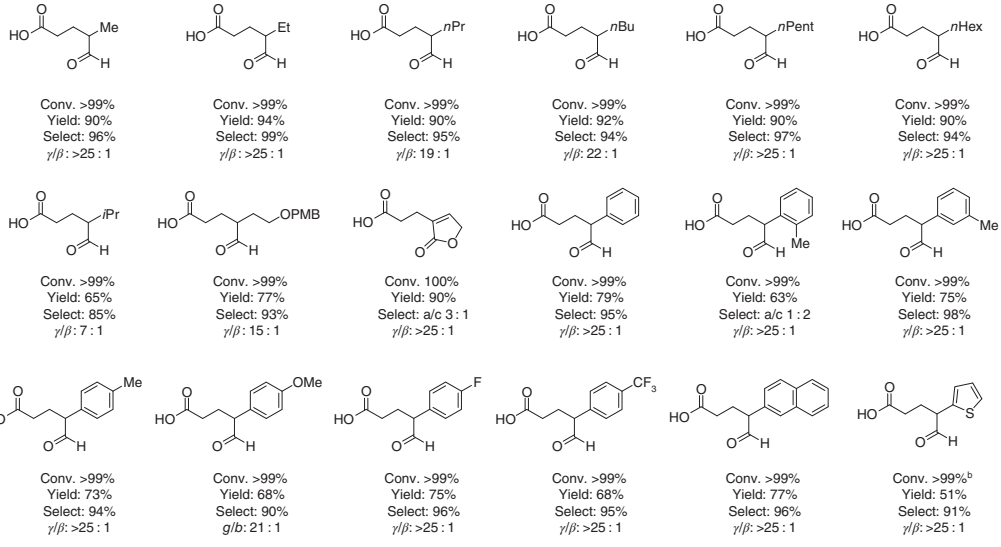

Scheme 13.3 Scope of the rhodium-catalyzed hydroformylation of β-alkynoic acid with ligand **20**. Reaction conditions: $[Rh(acac)(CO)_2]$/20/CSA/substrate = 1 : 5 : 5 : 100; c_0(substrate) = 0.5 M; 55 °C, 20 h, CO/H_2 (1 : 1, 6 or 10 bar); isolated yields; Selectivity, ratio of γ/β and conversion were determined by analysis of the reaction mixture by ^1H NMR spectroscopy. [b] CO/H_2 (1 : 1, 16 bar).

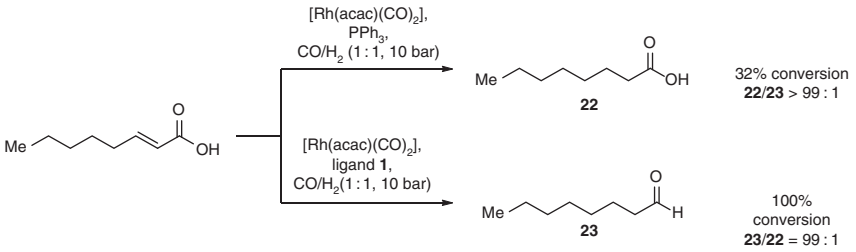

Scheme 13.4 Chemoselective reduction of oct-2-enoic acid. Conditions: $[Rh(acac)(CO)_2]$/ligand/substrate = 1 : 10 : 200, c_0(substrate) = 0.2 M, DCM (4 ml), CO/H_2 (1 : 1, 10 bar), 25 °C, 24 h.

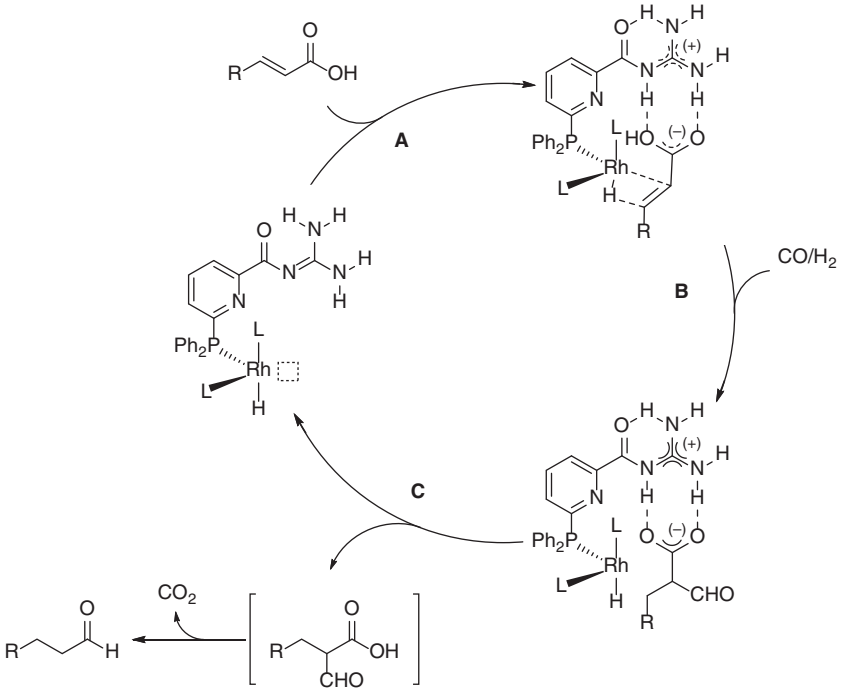

Scheme 13.5 Proposed catalytic cycle for the decarboxylative hydroformylation of α-alkenoic acids catalyzed by a rhodium complex of ligand **1**.

This methodology gives valuable β-arylaldehydes with high molecular complexity in excellent yields from easily accessible substrates and shows a high functional group tolerance. Isotopic labeling of the carboxylic acid group again excludes a mechanism in which the acid gets reduced by hydrogenation. Based on this finding and other control experiments, the mechanism shown in Scheme 13.7 was proposed [18].

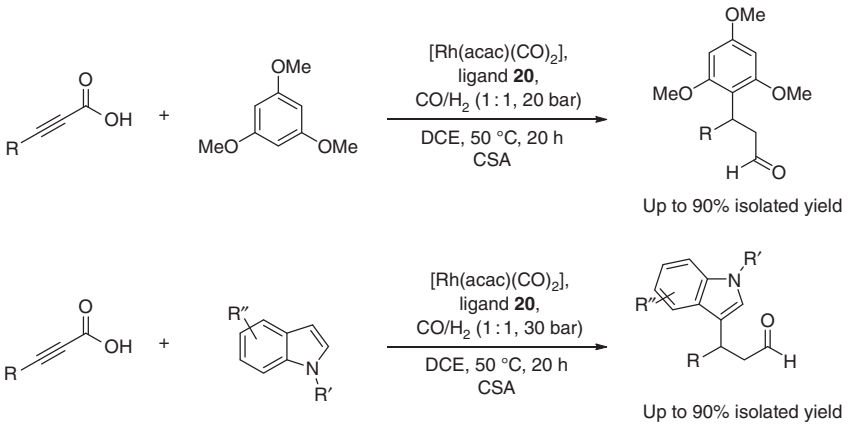

Scheme 13.6 Tandem hydroformylation/Michael addition/decarboxylation.

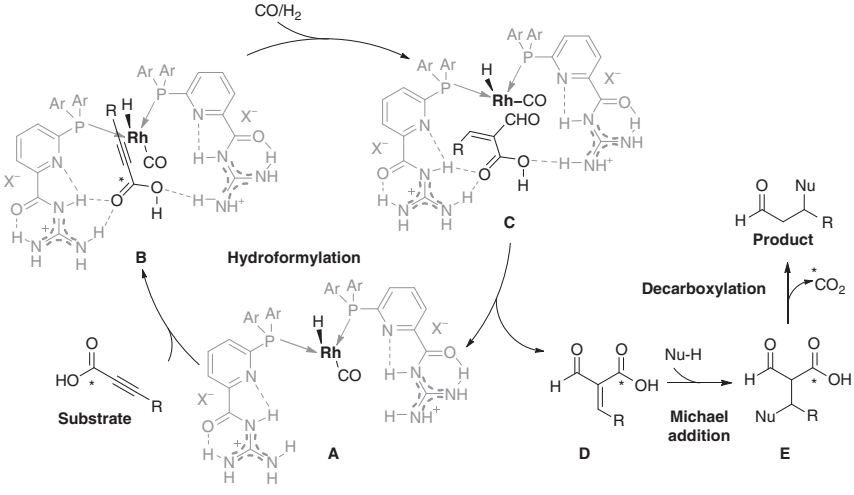

Scheme 13.7 Proposed reaction mechanism for the formation of β-arylaldehydes starting from α-alkynoic acids. It includes a rhodium-catalyzed hydroformylation, a Michael addition of the arene nucleophile and a decarboxylation.

13.3 Aldehyde Reduction and Tandem Hydroformylation–Hydrogenation

The hydroformylation of alkenes is one of the most important processes in chemical industry which is based on homogeneous catalysis, although the produced aldehydes are mostly not the final products [19, 20]. Typically, the aldehydes get reduced in an extra step to the corresponding alcohols, which have way more applications [21]. A possibility to produce the elongated alcohols in one step from the alkenes is a cobalt-catalyzed tandem hydroformylation–hydrogenation

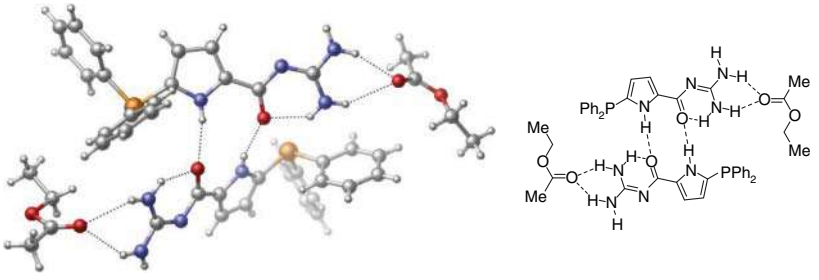

Figure 13.3 X-ray crystal structure of ligand **8**. A disordered *n*-pentane molecule is omitted for clarity.

reaction [22]. Nevertheless, the yields are only moderate and the required conditions are quite harsh [21, 22].

As shown before, acylguanidine-bearing phosphine ligands can be used to direct carboxylic acids by hydrogen bonding [13, 14]. One of the previously discussed ligands was ligand **8** with acylguanidine attached to a 5-diphenylpyrrolyl group. Single crystals of this ligand suitable for X-ray structure analysis were obtained by crystallization from ethyl acetate and *n*-pentane (Figure 13.3) [23]. In the solid state, the ligand can form two hydrogen bonds to the carbonyl group of ethyl acetate. Inspired by this, our group envisioned that also other carbonyl groups can get coordinated by the hydrogen bonding of the ligand. This coordination might decrease the energy of the lowest unoccupied molecular orbital (LUMO) of carbonyl groups and by this activate them for further transformations.

Therefore, the reaction of *n*-octanal under hydroformylation conditions (CO/H_2, 1 : 1, 20 bar) was investigated (Table 13.3) [23]. As expected, no hydrogenation of the aldehyde was observed with PPh_3 (entry 1). Using ligand **1** under similar conditions yielded in very low activity (3% conversion). A significant improvement was observed when ligand **4** (95% yield) and **8** (97% yield) were used. When the reaction with ligand **8** was performed under pure hydrogen atmosphere, the yield dropped to 27%. By this, one can assume the presence of a CO ligand in the active catalyst. The CF_3SO_3H additive had also a positive effect on the yield of the reaction, probably, due the formation of the acylguanidinium cation by protonation. The yield drops to 10% in protic solvents like MeOH, probably because the hydrogen bonds between the substrate and the catalyst are disturbed. In an experiment with phenylacylguanidine and PPh_3 as catalyst no conversion was detected, what shows that the recognition unit and the phosphine donor group must be part of the same molecule for having an effective ligand. When two of the nitrogen atoms of the ligand are blocked with a Boc group, only 10% yield were observed.

These optimized conditions were applied to several aldehyde substrates (Table 13.4) [23]. In all reactions, excellent isolated yield was achieved. Internal double bonds are not reduced or isomerized by this catalyst. α,β-Unsaturated aldehydes are way more sensitive for the reduction of the double bound. For oct-2-enal, two conditions were identified to either obtain the saturated aldehyde or the alcohol in perfect chemoselectivity (Scheme 13.8). When a β-double substituted

Table 13.3 Reduction of octanal.[a)]

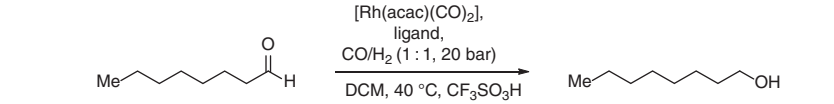

23 26

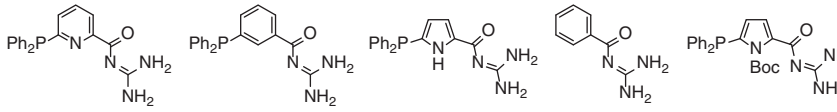

1 4 8 24 25

#	Ligand	Conversion (%)	Yield (%)
1	PPh_3	0	0
2	**1**	3	3
3	**4**	97	95
4	**8**	100	97
5[b)]	**8**	27	27
6[c)]	**8**	89	79
7[d)]	**8**		10
8	—		0
9	PPh_3/**24**		0
10	**25**		10

a) Reaction conditions: $[Rh(acac)(CO)_2]$/ligand/substrate/CF_3SO_3H = 1 : 10 : 500 : 5, DCM (2 ml), c_0(substrate) = 0.6 M, 20 h. Substrate conversion and yield determined by GC.
b) The reaction was carried out under H_2 (20 bar) without CO.
c) The reaction was carried out without CF_3SO_3H.
d) MeOH as solvent.

enal and or an α,β,γ,δ-unsaturated aldehyde were reduced, only the corresponding unsaturated allylic alcohols were obtained. Functional groups like ethers, esters, carbamates, or silylethers are well tolerated and even in the presence of a ketone the aldehyde was reduced with perfect chemoselectivity.

The proposed mechanism for the directed aldehyde reduction with ligand **8** is shown in Scheme 13.9. Starting from the rhodium complex of ligand **8**, the aldehyde substrate gets coordinated by several hydrogen bonds from the protonated acylguanidine and the pyrrole N–H. DFT calculations showed that the energy of the LUMO is decreased and the aldehyde activated by this. The catalyst is assumed to provide both an acidic proton (from the acylguanidinium) and a hydridic hydrogen atom (bond to the rhodium center) in a concerted manner. Finally, the basic acylguanidine facilitates the heterolytic cleavage of hydrogen followed by the regeneration of the active catalyst. In further DFT calculations the transition state for the hydride transfer could be identified. The energetic barrier compared to the substrate complex was only 7 kcal mol^{-1} high.

Table 13.4 Reduction of aldehydes.[a)]

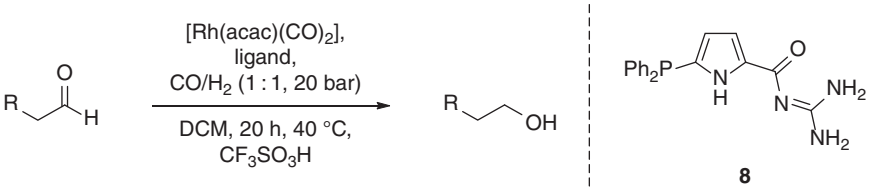

8

#	Product	Isolated yield (%)
1	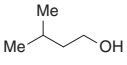	**90**
2[b)]	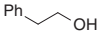	**98**
3	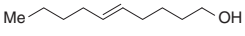	**94**
4	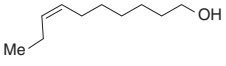	**95**
5	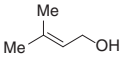	**99**
6[b)]	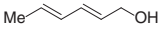	**80**
7	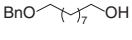	**96**
8	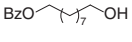	**99**
9	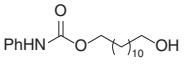	**95**
10	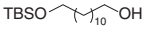	**98**
11	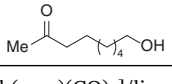	**98**

a) Reaction conditions: $[Rh(acac)(CO)_2]$/ligand/substrate/CF_3SO_3H = 1 : 10 : 500 : 5, c_0(substrate) = 0.6 M, DCM (2 ml), CO/H_2 (1 : 1, 20 bar), 20 h, 40 °C. Bn = benzyl, Bz = benzoyl, TBS, *tert*-butyldimethylsilyl.

b) $[Rh(acac)(CO)_2]$/ligand/substrate/CF_3SO_3H = 1 : 10 : 100 : 5.

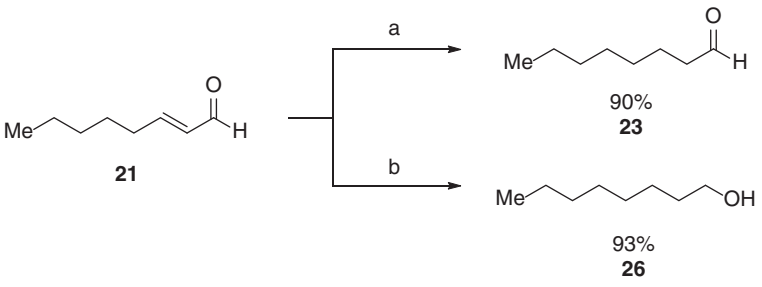

Scheme 13.8 Chemoselective reduction of octen-2-enal: (a) $[Rh(acac)(CO)_2]$/5/substrate/CF_3SO_3H = 1 : 10 : 500 : 5, c_0(substrate) = 0.6 M, DCM (2 ml) CO/H_2 (1 : 1, 20 bar), 20 h, 40 °C; (b) $[Rh(acac)(CO)_2]$/5/substrate/CF_3SO_3H = 1 : 10 : 1000 : 5, c_0(substrate) = 0.2 M, DCM (2 ml) CO/H_2 (1 : 1, 20 bar), 3 h, 40 °C. The yields are determined by GC.

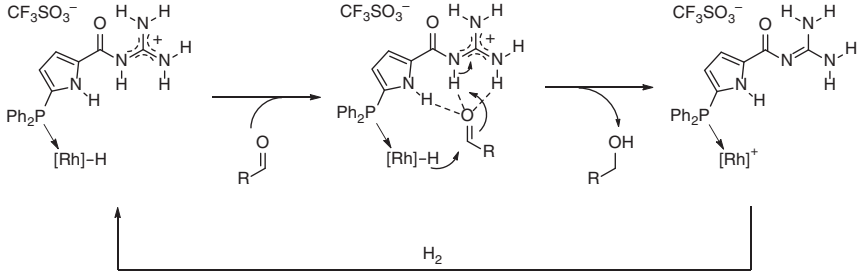

Scheme 13.9 Proposed mechanism for the aldehyde hydrogenation catalyzed by [Rh]/**8**.

This rhodium catalyst for the aldehyde hydrogenation required a CO/H_2 atmosphere, which means conditions similar to the ones in rhodium-catalyzed hydroformylation of alkenes. It seemed reasonable to combine both catalytic transformations into a tandem reaction [23, 24]. Starting from alkene substrates with a rhodium catalyst based on ligand **8**, alcohols were obtained in high yields but low regioselectivity (table 13.5, entry 1). A product distribution between linear and branched alcohol is almost similar to the ratio of aldehydes obtained using PPh_3 and corresponds to a behavior of a monodentate ligand during the hydroformylation step. Our group presented with the 6-DPPon ligand (**27**) an extremely active and selective ligand for the hydroformylation of alkenes, which is based on the self-assembly of its two tautomeric forms in transition metal complexes. A catalyst based on 6-DPPon showed no aldehyde hydrogenation at all (entry 3). It seemed therefore reasonable to use two different ligand classes at the same time to compete with rhodium present in the reaction mixture. Indeed, with such a cooperative ligand system, it was possible to yield the alcohol in 95% yield and with perfect regioselectivity (97 : 3). Using the more electron-rich ligand **30**, it was possible to get complete conversion in only 24 hours to the alcohol (entry 5), but with lower *l*/*b* selectivity (93 : 7). Electronic modifications of the 6-DPPon ligand showed that the electron poor derivative **29** in combination with **30** gave the best result (entry 7).

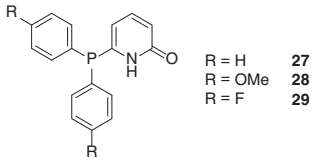

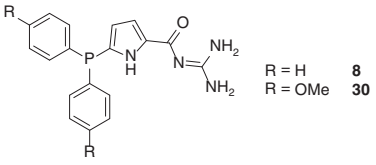

To gain deeper insights into the catalytic system, the reaction kinetics for rhodium catalysts derived from ligand **29** and **30** were studied for each step independently. The catalyst based on the self-assembling ligand **29** showed significantly higher activity and regioselectivity in hydroformylation than a catalyst based on **30**. Catalysts based on the mixture of both ligands gave the same high *l*/*b* selectivity in hydroformylation than ligand **29**. *In situ* IR experiments show vibration absorbances of an independent [HRh(**29**)$_2$(CO)$_2$] complex in the presence of ligand **30**. This supported the assumption that the [HRh(**29**)$_2$(CO)$_2$] complex might be responsible for the excellent activity and selectivity within the hydroformylation step of this catalyst system. The catalyst based on ligand **29** showed no activity at all in a hydrogenation experiment of nonanal, whereby catalysts based on ligand **30** or mixtures of **29** and **30** diplayed high activity.

Two optimized different conditions (A and B in Table 13.6) enable high yields and *l*/*b* ratios. A scope of 11 alkenes was investigated (Table 13.6). Other long-chain terminal alkenes like 1-decene gave similar results in comparison to the test substrate 1-octene (entry 2). Vinylcyclohexane could be transformed in perfect selectivity to the linear alcohol product, probably due to the increased steric demand in allylic position (entry 3). Despite the fact that hydrogen bonding is essential

Table 13.5 Tandem hydroformylation/hydrogenation of 1-octene.[a)]

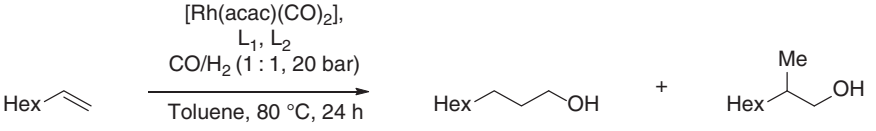

#	L_1	L_2	RCHO (%)	*l*:*b*[b)]	ROH (%)	*l*:*b*[b)]
1	**8**	—	2	—	98	81 : 19
2	**PPh$_3$**	—	99	82 : 18	0	—
3	**27**	—	99	95 : 5	0	—
4[c)]	**27**	**8**	5	—	95	97 : 3
5	**27**	**30**	1	—	99	93 : 7
6	**28**	**30**	5	33 : 67	95	91 : 9
7	**29**	**30**	5	37 : 63	95	96 : 4

a) [Rh(acac)(CO)$_2$]/L_1/L_2/substrate = 1 : 10 : 10 : 200.
b) Determined by GC analysis.
c) Reaction time was increased to 72 h.

for this catalyst system, it is compatible to many different functional groups like acetals, esters, benzyl and silylethers, carbamates and free alcohols. Furthermore, it was possible to chemoselectively convert only one terminal double bond into the C1-elongated alcohol, while an internal double bond could not be converted at all (entry 12).

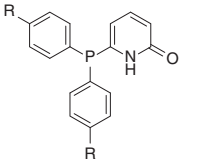

R = H **27**
R = F **29**

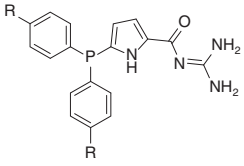

R = H **8**
R = OMe **30**

As shown before, α-alkenoic acids could be transformed into saturated aldehydes by a tandem hydroformylation/decarboxylation sequence. It seemed reasonable that by modification of the catalytic system and the reaction conditions, the aldehyde can get hydrogenated to the alcohol too, which would result into a tandem decarboxylative hydroformylation/hydrogenation reaction. As a test substrate, oct-2-enoic acid was chosen (Table 13.7) [25]. With PPh_3 as normal phosphine ligand, only hydrogenation of the conjugated alkene function was observed (entry 1). With ligand **1** in which the acylguanidine unit is attached to a pyridine ring, the main product is the saturated aldehyde (entry 2). Ligand **8** has the acylguanidine unit attached to a pyrrole ring and with this ligand the saturated alcohol was obtained as the main product (55%, entry 3), but a significant amount of the saturated carboxylic acid was observed. This carboxylic acid cannot be transformed into the aldehyde or the alcohol assuming the previously discussed mechanism of the decarboxylative hydroformylation. Ligand **9** in which the recognition unit is in ortho position to the diphenylphosphino group showed no catalytic activity under the reaction conditions (entry 4). However, ligand **4** enabled complete conversion of the substrate to the alcohol (entry 5). In previous works, the addition of the strong acid CF_3SO_3H showed a positive effect on the catalyst activity in supramolecular aldehyde reduction, so the effect of this acid with ligand **4** was studied. For this transformation, only a negative influence of this additive was found, because the reactivity changed almost completely to the saturated carboxylic acid (entry 7). Finally, different ligand mixtures were tested in this transformation. The combinations of the ligands **1** and **4** as well as **8** and **4** did not show any improved result (entry 8 and 9). However, the catalyst based on ligand **1** and **8** was significantly more active than the ones based on only one of those ligands (entry 10 and 11). With the optimized conditions, it is possible to reduce oct-2-enoic acid in quantitative yield into *n*-octanol in perfect selectivity.

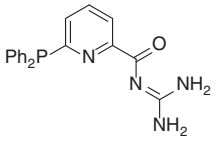

1

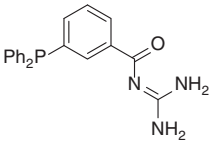

4

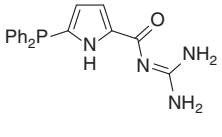

8

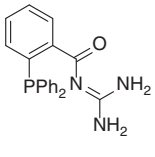

9

Table 13.6 Tandem hydroformylation–hydrogenation.

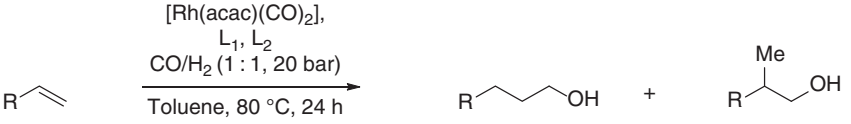

Conditions: A: L_1/L_2 = **1a**/**5a**, 72 h
B: L_1, L_2 = **1c**/**5b**, 24 h

#	Substrate	Conditions	ROH:RCO[a]	*l*:*b* (ROH)[a]	Yield (%)[b]
1	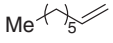	A	95 : 5	97 : 3	94[c]
		B	95 : 5	96 : 4	94[c]
2	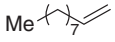	A	95 : 5	93 : 7	94
		B	99 : 1	93 : 7	99
3	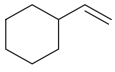	A	99 : 1	99 : 1	99[c]
		B	100 : 0	99 : 1	99[c]
4	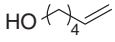	A	90 : 10	91 : 9	90[c]
		B	100 : 0	93 : 7	99[c]
5	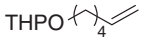	A	96 : 4	94 : 6	94[c]
		B	98 : 2	96 : 4	90
6	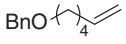	A	100 : 0	92 : 8	98[c]
		B	100 : 0	93 : 7	97[c]
7	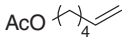	A	99 : 1	91 : 9	98
		B	99 : 1	96 : 4	99
8	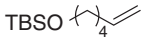	A	97 : 3	90 : 10	97[c]
		B	93 : 7	96 : 4	85
9	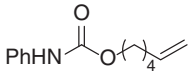	A	96 : 4	91 : 9	96
		B	99 : 1	85 : 15	99[c]
10	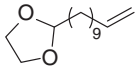	A	95 : 5	93 : 7	93
		B	97 : 3	96 : 4	87
11	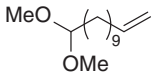	A	90 : 10	89 : 11	70
		B	99 : 1	96 : 4	90
12	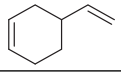	A	99 : 1	87 : 13	94[c]
		B	99 : 1	98 : 2	99[c]

a) Determined by nuclear magnetic resonance (NMR) analysis of the crude reaction mixture, except for entries 1 and 2 for which ratios were determined by GC analysis.
b) Yields of isolated products.
c) Yields determined by ^{1}H NMR spectroscopy with 1,3,5-trimethoxybenzene as internal standard. Bn = benzyl, TBS = *tert*-butyldimethylsilyl, THP = tetrahydropyranyl.

Table 13.7 Tandem decarboxylative hydroformylation–hydrogenation reaction of oct-2-enoic acid.[a)]

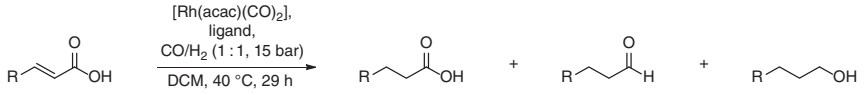

#	Ligand	M:L:S	RCO_2H[b)] (%)	RCHO[b)] (%)	RCH_2OH[b)] (%)
1	PPh_3	1 : 10 : 100	99	0	0
2	**1**	1 : 10 : 100	0	88.5	11.5
3	**8**	1 : 10 : 100	29	15	55
4	**9**	1 : 10 : 100	<1	0	0
5	**4**	1 : 10 : 100	0	0	>99
6[c)]	**4**	1 : 10 : 100	0	12	88
7[d)]	**4**	1 : 10 : 100	93	0	7
8[c)]	**4+8**	1 : 5 : 5 : 100	24	0	76
9[c)]	**1+4**	1 : 5 : 5 : 100	0	21	79
10[c)]	**1+8**	1 : 5 : 5 : 100	0	0	99
11[e)]	**1+8**	1 : 5 : 5 : 200	0	0	99

a) Conditions: c_0(substrate) = 0.2 M, DCM (2 ml), CO/H_2 (1 : 1, 15 bar), 29 h, 40 °C.
b) Determined by ^{1}H NMR of the crude reaction mixture.
c) t = 24 h.
d) The reaction was carried out with 5 equiv CF_3SO_3H.
e) t = 26 h.

Comparing the results obtained with the mixture of **1** and **8** with the results obtained separately for these ligands, one can assume that a new kinetically more active species is formed which is most likely a heteroleptic [Rh(**1**)(**8**)$(L)_x$] complex. This assumption was supported by the mixture of a platinum(II) salt in the presence of ligand **1** and **8** as well as oct-2-enoic acid. The ^{31}P NMR spectra of this reaction showed only the formation of one defined cis-coordinated heteroleptic complex. To rationalize this finding, DFT calculations were performed to compare the stability of both homoleptic complexes with the heteroleptic complex. The energies of the most stable found conformers and tautomers show indeed that the platinum complex with two different ligands is more stable than the complexes which contain only one kind of ligand (Figure 13.4).

Further, DFT calculations were done to explain the extraordinary high regioselectivity (>99 : 1) in this tandem process. The hydrometalation of the hydroformylation is most likely the step that determines the regioselectivity. Therefore, this step was analyzed for the heterodimeric rhodium complex of **1** and **8**. Indeed, the prolinear hydrometalation transition state is 5.8 kcal mol^{-1} more stable than the pro-branched one, which is in perfect agreement with the experimental observations (Scheme 13.10).

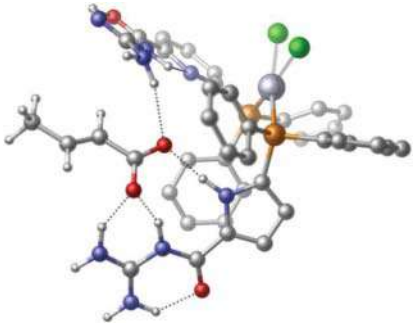

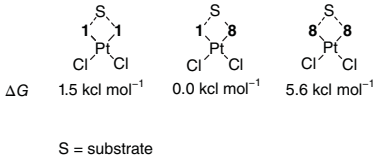

Figure 13.4 Calculated structure (PCM-B3LYP/LAN2DZ-6-31G(d,p)) of the most stable [Cl_2Pt(1)(8)] substrate complex (left; carbon bonded hydrogen atoms of the ligand are omitted for clarity). Free energy differences for the most stable complexes (right).

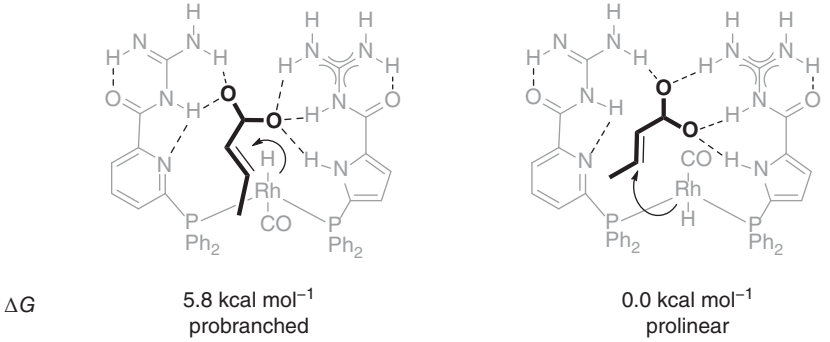

Scheme 13.10 Calculated (PCM-B3LYP/LAN2DZ-6-31G(d,p)) free energy difference for the probranched and the prolinear hydrometalation.

This strong preference can be understood by orbital control, because the calculated LUMO of a model substrate which is coordinated by hydrogen bonding to an acylguanidine had the largest coefficient in β-position to the carboxyl group [25].

13.4 Concluding Remarks

Supramolecular interactions that preorientate a specific substrate are often considered to be essential for enzyme catalysis. This preorientation can stabilize the transition state of a chemical reaction, lowering its energetic barrier and by this increasing the reaction rate. In this chapter, phosphine ligands with acylguanidine groups and their applications in homogeneous catalysis were presented.

The acylguanidine group was used as a recognition unit for certain unsaturated carboxylic acids in rhodium-catalyzed hydroformylation. By hydrogen bonding between the carboxylic acid and the ligands, an alkene or alkyne group is preorientated in a certain geometry close to the rhodium center which favors one position for the initial hydrometalation step. Depending on the substrate, the

directed hydroformylation led to saturated aldehydes or was the first step of a reaction sequence. These catalysts based on supramolecular substrate recognition showed outstanding activity and selectivity, which would be impossible to achieve by classical bidentate ligands.

Inspired by an X-ray crystal structure, it was reasonable that the acylguanidine group of such a ligand could not only interact with carboxylic acids but also with other carbonyl groups via hydrogen bonding. This could be applied in the rhodium-catalyzed hydrogenation of aldehydes, where the LUMO of the carbonyl group was lowered in energy by hydrogen bonding and therefore activated for the hydrogenation. The used catalyst required syngas and because of this, it was possible to combine it with a self-assembled hydroformylation catalyst based on the 6-DPPon ligand as a cooperative ligand system. Consequently, this enables the direct transformation of alkenes into C1-elongated alcohols in excellent yields and selectivity under mild conditions. Besides, catalysts for a sequence of directed hydroformylation, decarboxylation, and aldehyde hydrogenation were identified. Surprisingly, a mixture of two ligands gave the most active and selective catalyst, while catalysts prepared from both ligands separately gave worse results.

It was shown that ligands with recognition units for specific substrates are applicable in homogeneous catalysis. Future works might expand this concept on ligands with different recognition groups to enable new reactivities with other substrates and to other reaction types.

References

1 Robinson, P.K. (2015). Enzymes: principles and biotechnological applications. *Essays Biochem.* 59: 1–41.

2 Bruice, T.C. and Lightstone, F.C. (1999). Ground state and transition state contributions to the rates of intramolecular and enzymatic reactions. *Acc. Chem. Res.* 32 (2): 127–136.

3 Bianchi, A. (ed.) (1997). *Supramolecular Chemistry of Anions*. New York: Wiley-VCH.

4 Bowman-James, K. (ed.) (2012). *Anion Coordination Chemistry*, 1e. Weinheim: Wiley-VCH.

5 Schug, K.A. and Lindner, W. (2005). Noncovalent binding between guanidinium and anionic groups: focus on biological- and synthetic-based arginine/guanidinium interactions with phosphonate and sulfonate residues. *Chem. Rev.* 105 (1): 67–114.

6 Mander, L. (2010). *Comprehensive Natural Products II: Chemistry and Biology*. Amsterdam: Elsevier.

7 Koeller, K.M. and Wong, C.H. (2001). Enzymes for chemical synthesis. *Nature* 409 (6817): 232–240.

8 Hagen, J. (ed.) (2015). Homogeneous catalysis with transition metal catalysts. In: *Industrial Catalysis: A Practical Approach*, 17–46. Weinheim, Germany: Wiley-VCH.

9 Lehn, J.-M. (1988). Supramolecular chemistry—scope and perspectives molecules, supermolecules, and molecular devices (nobel lecture). *Angew. Chem. Int. Ed. Engl.* 27 (1): 89–112.

10 Brown, C.J., Toste, F.D., Bergman, R.G., and Raymond, K.N. (2015). Supramolecular catalysis in metal-ligand cluster hosts. *Chem. Rev.* 115 (9): 3012–3035.

11 Dydio, P. and Reek, J.N.H. (2014). Supramolecular control of selectivity in transition-metal catalysis through substrate preorganization. *Chem. Sci.* 5 (6): 2135–2145.

12 Schneider, H.-J. and Yatsimirsky, A.K. (2000). *Principles and Methods in Supramolecular Chemistry*. Chichester: Wiley.

13 Šmejkal, T. and Breit, B. (2008). A supramolecular catalyst for regioselective hydroformylation of unsaturated carboxylic acids. *Angew. Chem.* 120 (2): 317–321.

14 Smejkal, T., Gribkov, D., Geier, J. et al. (2010). Transition-state stabilization by a secondary substrate-ligand interaction: a new design principle for highly efficient transition-metal catalysis. *Chemistry (Weinheim an der Bergstrasse, Germany)* 16 (8): 2470–2478.

15 Fang, W. and Breit, B. (2018). Tandem regioselective hydroformylation-hydrogenation of internal alkynes using a supramolecular catalyst. *Angew. Chem. Int. Ed.* 57 (45): 14817–14821.

16 Agabekov, V., Seiche, W., and Breit, B. (2013). Rhodium-catalyzed hydroformylation of alkynes employing a self-assembling ligand system. *Chem. Sci.* 4 (6): 2418.

17 Šmejkal, T. and Breit, B. (2008). A supramolecular catalyst for the decarboxylative hydroformylation of α,β-unsaturated carboxylic acids. *Angew. Chem.* 120 (21): 4010–4013.

18 Fang, W., Bauer, F., Dong, Y., and Breit, B. (2019). A domino reaction for generating β-aryl aldehydes from alkynes by substrate recognition catalysis. *Nat. Commun.* 10 (1): 4868.

19 Elvers, B. and Ullmann, F. (eds.) (2011). *Ullmann's Encyclopedia of Industrial Chemistry*, 7e. Weinheim: Wiley-VCH.

20 Franke, R., Selent, D., and Börner, A. (2012). Applied hydroformylation. *Chem. Rev.* 112 (11): 5675–5732.

21 Torres, G.M., Frauenlob, R., Franke, R., and Börner, A. (2015). Production of alcohols via hydroformylation. *Catal. Sci. Technol.* 5 (1): 34–54.

22 Slaugh, L.H. and Mullineaux, R.D. (1968). Novel hydroformylation catalysts. *J. Organomet. Chem.* 13 (2): 469–477.

23 Diab, L., Šmejkal, T., Geier, J., and Breit, B. (2009). Supramolecular catalyst for aldehyde hydrogenation and tandem hydroformylation-hydrogenation. *Angew. Chem.* 121 (43): 8166–8170.

24 Fuchs, D., Rousseau, G., Diab, L. et al. (2012). Tandem rhodium-catalyzed hydroformylation-hydrogenation of alkenes by employing a cooperative ligand system. *Angew. Chem.* 124 (9): 2220–2224.

25 Diab, L., Gellrich, U., and Breit, B. (2013). Tandem decarboxylative hydroformylation-hydrogenation reaction of α,β-unsaturated carboxylic acids toward aliphatic alcohols under mild conditions employing a supramolecular catalyst system. *Chem. Commun. (Cambridge, England)* 49 (84): 9737–9739.

14

Chemical Reactions Controlled By Remote Zn···N Interactions Between Substrates and Catalysts

Jonathan Trouvé and Rafael Gramage-Doria

Univ Rennes, CNRS, ISCR-UMR6226, 35000 Rennes, France

14.1 Introduction

Homogeneous catalysis is an enabling technology for the sustainable synthesis of daily-relevant chemicals in our society [1]. Typically, small molecules, either organic ones for organocatalysis [2, 3] or inorganic ones for metal catalysis [4], have served to accelerate reactions and control the selectivity for those cases where multiple products can form. Consequently, different reactivities and different selectivities can be reached by fine-tuning of the catalysts, enhancing the stability of the catalytic system as well. In the last decades, the merger of supramolecular catalysis, that is the implementation of strategies based on supramolecular chemistry into chemical catalysis, has shown a tremendous impact in contemporary research [5]. The toolbox offered by supramolecular systems provides new possibilities to address challenges that are difficult or impossible to tackle with more classic catalysts. These tools are versatile and mainly inspired from the multiple action modes encountered in enzymes, which are Nature's catalysts. Enzymes enabled catalysis to occur under relatively mild reaction conditions with high robustness and activity mainly because the catalytically active site is well protected in hydrophobic pockets [6]. Such feature has inspired scientists to design and study chemical catalysis in confined spaces, generated by covalent chemistry, noncovalent chemistry, or coordination chemistry [7, 8].

In addition, enzymes can access key transition states and intermediates by lowering specific energetic pathways which is at the origin of their exquisite selectivity [9]. In fact, multiple reversible interactions usually based on noncovalent hydrogen bonding fix the substrate around the active site in a given geometrical conformation, thus lowering its degree of freedom and pre-organize it to reach a precise selectivity [10]. Another specificity of enzymes is the high affinity they have for the substrates with respect to the products, which translates into enhanced reaction rates as the products are straightforward released from the active site [11]. As such, kinetically labile interactions have been explored in the design of man-made catalysts for generating new ligands by self-assembly as well as for substrate pre-organization due to ligand-to-catalyst binding [12, 13]. The most

Supramolecular Catalysis: New Directions and Developments, First Edition.
Edited by Piet W.N.M. van Leeuwen and Matthieu Raynal.

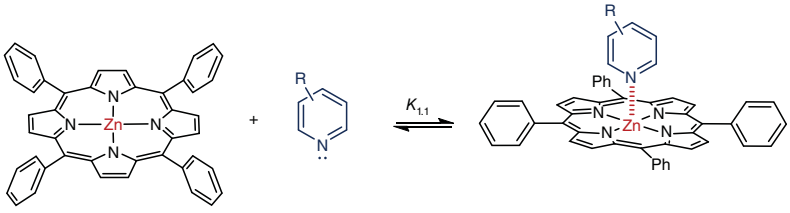

Figure 14.1 The binding of pyridine derivatives to zinc(II)-porphyrin derivatives is kinetically labile.

developed noncovalent interactions so far studied in these directions are hydrogen bonding [14] and ion pairing [15], respectively.

In supramolecular chemistry, metalloporphyrins are pivotal building blocks that lead to new dimensions and chemical space owing to their ability to apically bind to nitrogen-containing molecules (Figure 14.1) [16]. Such level of supramolecular engineering has been applied to different fields, being particular relevant for physics (energy or charge transfer, photovoltaics) and materials sciences (molecular tectonics, oligomerization, polymerization, etc.) [17–19]. The most studied interaction in this context is likely the one involving the binding of pyridine derivatives to zinc(II)-porphyrins, in which the zinc cation evolves from (almost perfect) square planar geometry to (slight distorted) square pyramidal (Figure 14.1). This type of interaction, which is *stricto sensu* a coordination bond, shares with the previously described noncovalent interactions the reversible nature of the bonding. Depending on the stereoelectronic properties of the pyridine and the zinc(II)-porphyrin derivative, this Zn···N interaction can be weaker or stronger, which results in a panel of different association constants $K_{1.1} = 10^2$–$10^6\ M^{-1}$ in general [20, 21], which are routinely measured with conventional NMR and/or UV–vis titration techniques [22]. These values are comparable to those found in hydrogen bonding, which is a noncovalent interaction well-implemented in chemical catalysis.

14.2 Organic Reactions

The exploitation of Zn···N interactions for controlling the activity and the selectivity of chemical reactions appeared promising as it was shown in the 1990s with the pioneering studies from the Sanders group (Figure 14.2) [23, 24]. They reported a number of trimeric zinc(II)-porphyrin macrocycles that served as Diels–Alderases for pyridinic substrates, with the overarching idea that the intermediates of the reaction will be accessible *via* simultaneous Zn···N interactions inside the macrocyclic structure. Because the systems were designed to fit better the transition state than the substrates and the products, enhanced reaction rates and a switch in the stereoisomerism (*exo* vs. *endo*) of the products were observed (Figure 14.2a) [25–28]. A catalytic version was developed for acyl transfer reactions between nitrogen-containing reagents (Figure 14.2b) [29]. Interestingly, these

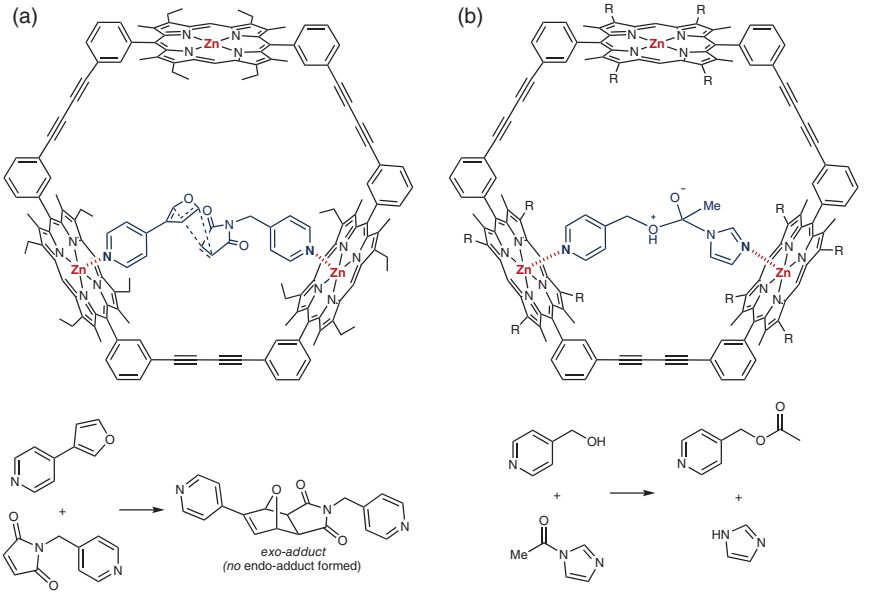

Figure 14.2 Sanders's pioneering zinc(II)-porphyrin-derived tricyclic Diels–Alderase (a) and its application in the acyl transfer reaction in a catalytic fashion (b) in which the pyridine-containing substrates react inside the cavity of the trimer.

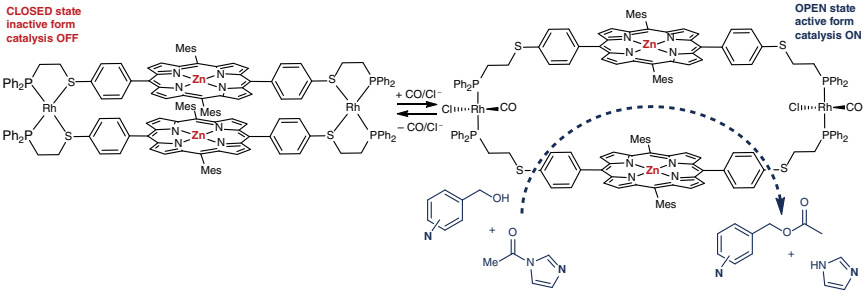

Figure 14.3 Nguyen's dimeric zinc(II)-porphyrin derivative displaying allosteric control of reactivity and substrate selectivity for acyl transfer reactions. Mes = mesitylene.

action modes mimic the tight binding of the transition state encountered in enzymes [23, 24]. Later, Nguyen and co-workers reported related catalytic versions for the acyl transfer reactions but using a dimeric zinc(II)-porphyrin macrocycle that allosterically switches on/off between open and closed conformations, the former conformation exhibits higher reactivity than the latter one (Figure 14.3) [30]. A unique substrate selectivity was observed as the 2-substituted pyridine derivatives reacted poorly with respect to the 3- and 4-isomers. Analogous observations were found when using metal–organic frameworks built up from zinc(II)-porphyrin scaffolds [31] and cyclic tetramers for the methanolysis of phosphate triesters [32].

14.3 Transition Metal Catalysis

Transition metal catalysis has enabled the streaming access to compounds that are impossible or difficult to obtain by other means [33, 34]. Indeed the combination of transition metal ions (which display multiple coordination numbers, geometries, and oxidation states) with fine-tuned ligands displaying unique stereoelectronic features offers a myriad of possibilities to tackle unprecedented challenges in terms of chemical reactivity [35]. In this context, ligands equipped with zinc(II)-porphyrins as the substrate recognition site have been rarely developed for transition metal catalysis. In principle, this type of ligands would enable labile Zn· · ·N interactions with nitrogen-containing substrates, thus preventing to some extent the undesired over-coordination of the substrates (or the products) to active metal catalysts, which is a major concern in homogeneous catalysis.

In this respect, Warnmark and co-workers developed a first approach to transition metal catalysts equipped with a substrate recognition site comprising a zinc(II)-porphyrin (Figure 14.4) [36]. The overarching idea was to achieve substrate selective catalysis, a concept reminiscent of enzymes, but difficult to implement in abiological catalysis [37]. The design was based on the combination of a substrate receptor unit and a catalytically active site *via* hydrogen bonding between donor/acceptor amide groups. The receptor unit was constituted by a zinc(II)-porphyrin equipped with peripheral 2-pyridone units and the active transition metal catalyst site (i.e. Jacobsen-type manganese epoxidation catalyst) with 2-quinolone units (Figure 14.4a). This strategy gave rise to a dynamic supramolecular catalyst expected to form a heterodimer assembly that was applied in substrate selective epoxidation reactions, in which the nitrogen-containing substrates reacted

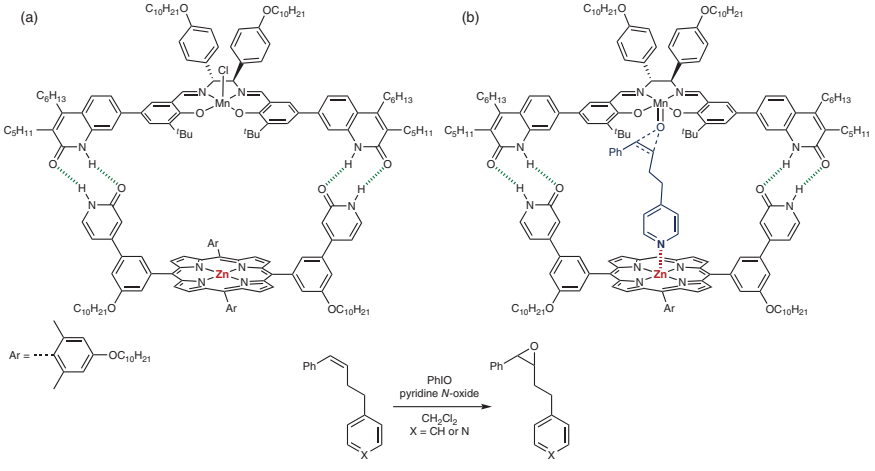

Figure 14.4 Warnmark's zinc(II)-porphyrin-based dynamic supramolecular manganese catalysts featuring substrate selectivity in epoxidation reactions *via* remote Zn· · ·N interactions between the catalyst and the substrate (a) and the corresponding postulated transition state (b). Green dashed lines indicate intermolecular hydrogen bonding.

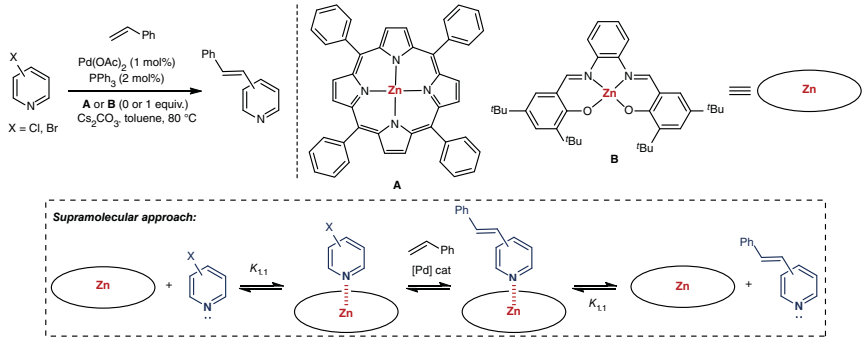

Figure 14.5 Palladium-catalyzed cross-coupling reactions with halopyridine derivatives controlled by remote Zn· · ·N interactions.

preferentially over the ones containing no nitrogen atoms. The nitrogen-containing substrates were claimed to bind inside the generated pocket of the catalyst *via* Zn· · ·N interactions while the epoxidation occurred in the olefinic site, that is, in a remote fashion (Figure 14.4b). However, due to the reversible nature in the formation of this supramolecular catalyst, different assemblies could not be discarded, such as dimers, trimers, oligomers, or even co-polymers [38, 39]. This difficulty prompted the design of more rigid supramolecular catalysts by introducing straps between the substrate recognition site and the catalytically active site with the aim to suppress to some extent unselective catalysis occurring outside of the cavity [40].

Gramage-Doria and co-workers have recently established a research line devoted to exploiting the substrate recognition properties of porphyrins in transition metal catalysis with the aim to tackle issues difficult to address with traditional stereoelectronic ligand modification. In 2017, it was shown that palladium-catalyzed cross-coupling reactions with halopyridine derivatives are controlled by the presence (or absence) of zinc(II)-containing scaffolds (Figure 14.5) [41]. Indeed, easily-accessible zinc(II)-porphyrin **A** and zinc(II)-salphen **B** were used, respectively, for Mizoroki–Heck reactions between chloro- and bromo-pyridines with styrene. In the presence of these zinc(II)-containing scaffolds, higher yields and higher reaction rates were obtained in these cross-coupling reactions except for the combination of the 2-halopyridine derivatives and zinc(II)-porphyrin **A**, in which no binding event occurs due to steric shields. The yields and reaction rates were roughly correlated with the binding strength between the zinc(II)-containing scaffolds and the halopyridines, being higher with the zinc(II)-salphen **B** than with zinc(II)-porphyrin **A**. A less pronounced effect was found in Suzuki–Miyaura cross-coupling reactions between the halopyridines and phenyl boronic acid in the presence of **A** (**B** was found unstable under the reaction conditions). Importantly, the active palladium catalyst was the same in all the cases, i.e. $Pd(OAc)_2/PPh_3$, which clearly shows that the reactivity of a trivial palladium catalyst can be indirectly controlled by this remote Zn· · ·N interaction, even at high temperatures (80 °C). In other words, the zinc(II)-containing scaffolds inhibit to some extent the

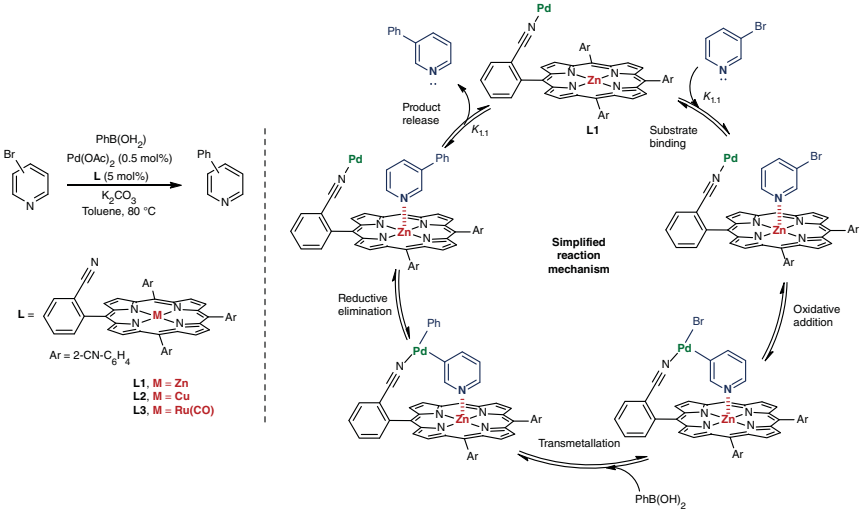

Figure 14.6 A supramolecular catalyst with an active palladium site and a substrate recognition site enabling Zn· · ·N interactions between the substrate and the catalyst, together with the postulated catalytic cycle.

undesired pathway of over-coordination to palladium by the pyridine derivatives (substrates and/or products). Such observations were made possible only in the presence of one equivalent (at least) of the zinc(II)-containing scaffold using the non-coordinating toluene as the solvent.

In subsequent studies, a truly catalytic system was designed, that is, the incorporation of the active palladium site to a ligand comprising a substrate recognition site build around a zinc(II)-porphyrin (Figure 14.6) [42]. As such, porphyrin **L**, which is appended with nitrile groups in the *ortho* position of the *meso* phenyl groups, was synthesized in a single-step operation. In this way, different metal cations (Zn, Cu, and Ru) can be embedded in the porphyrin core, thereby changing the binding ability towards pyridine derivatives as substrates, whereas the nitrile groups are available for binding catalytically active palladium cations. From the many metals incorporated inside of the porphyrin, zinc(II) revealed the most pertinent for representative Suzuki–Miyaura reactions. With this supramolecular ligand (**L1**), a unique substrate selectivity was observed since 3-bromopyridine as the substrate reacted preferentially with phenyl boronic acid over the 2- or 4-bromopyridine ones. In addition, the catalytic system displayed a remarkable substrate selectivity even in the presence of bromobenzene in competition experiments. This is a complete reversal of reactivity when compared to classical palladium catalysts that do exhibit higher reactivity for bromobenzene. A careful assessment of the origin of this unique reactivity revealed that the ideal substrate pre-organization provided by the porphyrin pocket as well as the distance and geometry between the active site and the substrate recognition site were key parameters on stabilizing the different intermediates from the catalytic cycle. Furthermore, in-depth NMR and X-ray diffraction studies indicated that the binding of palladium to the nitrile groups increased the binding strength

of the substrate to the zinc(II)-porphyrin. This is not a mere allosteric effect, but it also shows that it is possible to fine-tune the strength of the Zn· · ·N interaction in a remote fashion through coordination chemistry.

14.4 Conclusion

The last three decades have witnessed the birth and progress of the rational use of Zn· · ·N interactions between substrates and catalysts in organic reactions as well as in transition metal catalysis. Although this type of interaction is rather unconventional compared to the ones more studied, i.e. hydrogen bonding, it has already shown that unique type of reactivities and selectivities can emerge. The strength associated with the Zn· · ·N interaction is rather strong (when compared to a single hydrogen bond for example) and kinetically labile in non-coordinating solvents, even at high temperatures. All these aspects are relevant for future implementations. At this stage, this interaction has been exploited between pyridine derivatives as substrates and ligands (or catalysts) derived from zinc(II)-porphyrin or zinc(II)-salphen derivatives. Owing to the chemical robustness and synthetic versatility of these and other zinc(II)-porphyrinoids, many of them will be readily accessible for the generation of new supramolecular catalysts featuring Zn· · ·N interactions. For instance, many zinc(II)-porphyrins containing metal-appended fragments are known [43–46], but their substrate recognition properties in catalysis remain to be addressed, not to mention the possibilities to design novel ones [47]. Overall, one would expect further developments to design supramolecular catalysts based on Zn· · ·N interactions to mimic enzymatic features for man-made catalysts [48].

Acknowledgments

Financial support from the CNRS, University of Rennes 1, Agence Nationale de la Recherche (ANR), Fondation Rennes 1, Campus France, European Union's Seventh Framework Programme, Region Bretagne and Rennes Metropole is acknowledged.

References

1 Beller, M., Renken, A., and van Santen, R.A. (eds.) (2012). *Catalysis: From Principles to Applications*. Wiley-VCH.
2 Reetz, M., List, B., Jaroch, S., and Weinmann, H. (eds.) (2008). *Organocatalysis*. Springer.
3 Dalko, P.I. (ed.) (2013). *Comprehensive Enantioselective Organocatalysis: Catalysts, Reactions, and Applications*. Wiley-VCH.
4 Hartwig, J.F. (ed.) (2010). *Organotransition Metal Chemistry. From Bonding to Catalysis*. University Science Books.
5 van Leeuwen, P.W.N.M. (ed.) (2008). *Supramolecular Catalysis*. Wiley-VCH.

6 Ringe, D. and Petsko, G.A. (2008). *Science* 320: 1428–1429.
7 Raynal, M., Ballester, P., Vidal-Ferran, A., and van Leeuwen, P.W.N.M. (2014). *Chem. Soc. Rev.* 43: 1734–1787.
8 Leenders, S.H.A.M., Gramage-Doria, R., de Bruin, B., and Reek, J.N.H. (2015). *Chem. Soc. Rev.* 44: 433–448.
9 Hammes, G.G., Benkovic, S.J., and Hammes-Schiffer, S. (2011). *Biochemistry* 50: 10422–10430.
10 Zhang, X. and Houk, K.N. (2005). *Acc. Chem. Res.* 38: 379–385.
11 Houk, K.N., Leach, A.G., Kim, S.P., and Zhang, X. (2003). *Angew. Chem. Int. Ed.* 42: 4872–4897.
12 Dydio, P. and Reek, J.N.H. (2014). *Chem. Sci.* 5: 2135–2145.
13 Raynal, M., Ballester, P., Vidal-Ferran, A., and van Leeuwen, P.W.N.M. (2014). *Chem. Soc. Rev.* 43: 1660–1733.
14 Doyle, A.G. and Jacobsen, E.N. (2007). *Chem. Rev.* 107: 5713–5743.
15 Warshel, A., Sharma, P.K., Kato, M. et al. (2006). *Chem. Rev.* 106: 3210–3235.
16 Beletskaya, I., Tyurin, V.S., Tsivadze, A.Y. et al. (2009). *Chem. Rev.* 109: 1659–1713.
17 Nakamura, Y., Aratani, N., and Osuka, A. (2007). *Chem. Soc. Rev.* 36: 831–845.
18 Hosseini, M.W. (2005). *Acc. Chem. Res.* 38: 313–323.
19 Bols, P.S. and Anderson, H.L. (2018). *Acc. Chem. Res.* 51: 2083–2092.
20 Kleij, A.W. and Reek, J.N.H. (2006). *Chem. Eur. J.* 12: 4218–4227.
21 Suslick, K.S., Rakow, N.A., Kosal, M.E., and Chou, J.-H. (2000). *J. Porph. Phthalo.* 4: 407–413.
22 Thodarson, P. (2011). *Chem. Soc. Rev.* 40: 1305–1323.
23 Bonar-Law, R.P., Mackay, L.G., Walter, C.J. et al. (1994). *Pure Appl. Chem.* 66: 803–810.
24 Sanders, J.K.M. (2000). *Pure Appl. Chem.* 72: 2265–2274.
25 Waiter, C.J., Anderson, H.L., and Sanders, J.K.M. (1993). *J. Chem. Soc., Chem. Commun.* 1993: 458–460.
26 Wylie, R.S. and Sanders, J.K.M. (1995). *Tetrahedron* 51: 513–526.
27 Marty, M., Clyde-Watson, Z., Twyman, L.J. et al. (1998). *Chem. Commun.*: 2265–2266.
28 Nakash, M., Clyde-Watson, Z., Feeder, N. et al. (2000). *J. Am. Chem. Soc.* 122: 5286–5293.
29 Mackay, L.G., Wylie, R.S., and Sanders, J.K.M. (1994). *J. Am. Chem. Soc.* 116: 3141–3142.
30 Oliveri, C.G., Gianneschi, N.C., Nguyen, S.T. et al. (2006). *J. Am. Chem. Soc.* 128: 16286–16296.
31 Shultz, A.M., Farha, O.K., Hupp, J.T., and Nguyen, S.T. (2009). *J. Am. Chem. Soc.* 131: 4204–4205.
32 Kang, B., Kurutz, J.W., Youm, K.-T. et al. (2012). *Chem. Sci.* 3: 1938–1944.
33 Beller, M. and Bolm, C. (2004). *Transition Metals for Organic Synthesis*. Weinheim: Wiley-VCH.
34 de Meijere, A., Braese, S., and Oestreich, M. (2014). *Metal-Catalyzed Cross-Coupling Reactions and More*. Weinheim: Wiley-VCH.

35 van Leeuwen, P.W.N.M. (2004). *Homogeneous Catalysis: Understanding the Art*. Dordrecht: Kluwer.

36 Jonsson, S., Odille, F.G.J., Norrby, P.-O., and Warnmark, K. (2005). *Chem. Commun.* 2005: 549–551.

37 Lindback, E., Dawaigher, S., and Warnmark, K. (2014). *Chem. Eur. J.* 20: 13432–13481.

38 Jonsson, S., Odille, F.G.J., Norrby, P.-O., and Warnmark, K. (2006). *Org. Biomol. Chem.* 4: 1927–1948.

39 Odille, F.G.J., Jonsson, S., Stjernqvist, S. et al. (2007). *Chem. Eur. J.* 13: 9617–9636.

40 Lindback, E., Cherraben, S., Francoia, J.-P. et al. (2015). *ChemCatChem* 7: 333–348.

41 Kadri, M., Hou, J., Dorcet, V. et al. (2017). *Chem. Eur. J.* 23: 5033–5043.

42 Zardi, P., Roisnel, T., and Gramage-Doria, R. (2019). *Chem. Eur. J.* 25: 627–634.

43 Saito, M., Nishibayashi, Y., and Uemura, S. (2004). *Organometallics* 23: 4012–4017.

44 Harvey, P.D., Tasan, S., Gros, C.P. et al. (2015). *Organometallics* 34: 1218–1227.

45 Suijkerbuijk, B.M.J.M. and Klein Gebbink, R.J.M. (2008). *Angew. Chem. Int. Ed.* 47: 7396–7421.

46 Longevial, J.-F., Clément, S., Wytko, J.A. et al. (2018). *Chem. Eur. J.* 24: 15442–15460.

47 Trouvé, J. and Gramage-Doria, R. (2021). *Chem. Soc. Rev.* 50: 3565–3584.

48 Trouvé, J., Zardi, P., Al-Shehimy, S. et al. (2021) *Angew. Chem. Int. Ed.* 60: 18006–18013.

Part IV

Catalysis Promoted by Discrete Cages, Capsules, and Other Confined Environments

15

Artificial Enzymes Created Through Molecular Imprinting of Cross-Linked Micelles

Yan Zhao

Iowa State University, Department of Chemistry, 2438 Pammel Dr., Ames, IA 50011-3111, USA

15.1 Introduction

Micelles have long been used as mimics of enzymes [1–3]. They, however, rely on random collision for the reactants and catalysts to encounter one another, whereas enzymes possess substrate-specific active sites, which are complex-shaped, highly functionalized 3D nanospaces with optimized dynamics, solvation, and electrostatics for the catalyzed reaction. The dynamic nature of micelles makes it impossible to position a catalytic group in any given place. In contrast, the active site of an enzyme is formed through folding of the peptide chain, with multiple groups placed accurately around the substrate for efficient binding and catalysis.

This chapter summarizes our recent efforts to convert surfactant micelles into water-soluble nanoparticle catalysts with many of the features of natural enzymes. Some catalysts are simple and mostly served proof-of-concept purposes at the time of study. The learning acquired along the way, however, was essential to the design of more advanced systems with biomimetic, cooperative catalytic motifs.

15.2 Surface-Cross-Linked Micelles (SCMs)

To remove the dynamic nature of a micelle, we need to "capture" the self-assembled structure by covalent bonds. (4-Dodecyloxybenzyl)tripropargylammonium bromide **1** is prepared from the corresponding benzyl bromide and tripropargylamine by a simple S_N2 reaction. Its micelle is readily cross-linked by the highly efficient click reaction using diazide **2** and Cu(I) catalysts (Figure 15.1) [4]. The alkynyl-containing surface-cross-linked micelle (alkynyl-SCM) obtained is functionalized by another round of click reaction to afford multivalent organic nanoparticles, water- or oil-soluble depending on the surface ligands used.

Acids and bases are among the most common catalytic species in organic chemistry. Since strong acids and bases are not available in biological reactions, many enzymes have abilities to alter the pK_a of the functional groups in a remarkable

Supramolecular Catalysis: New Directions and Developments, First Edition.
Edited by Piet W.N.M. van Leeuwen and Matthieu Raynal.

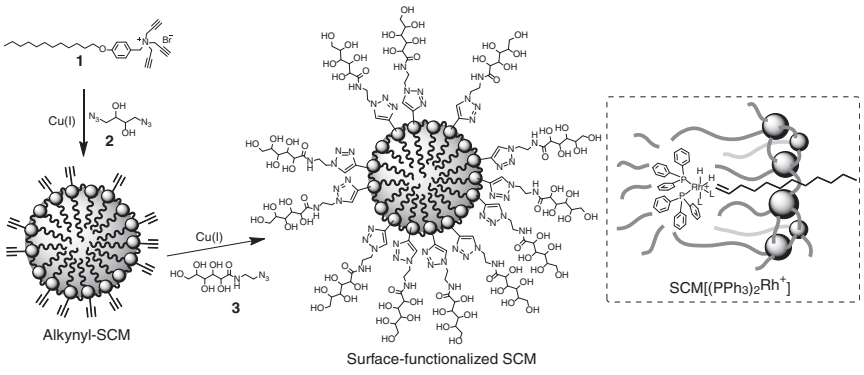

Figure 15.1 Preparation and surface functionalization of a surface-cross-linked micelle (SCM) and schematic representation of SCM[$(PPh_3)_2Rh^+$] with 1-dodecene.

fashion. The ammonium group of the active-site lysine of acetoacetate decarboxylase, for example, has a pK_a of 5.6 instead of 10.6 in an aqueous solution [5].

There are two general strategies for an enzyme to shift the pK_a of a functional group. Because an ionic group is better solvated by polar solvents, protonation of an amine or deprotonation of a carboxylic acid becomes more difficult when these groups migrate from an aqueous solution to a hydrophobic microenvironment [6]. The pK_a value is also influenced by nearby charges, with vicinal cations impeding protonation of a base and promoting deprotonation of an acid [7].

To mimic the abilities of enzymes to control local acidity and basicity, we prepared SCMs functionalized with 4-dimethylaminopyridine (DMAP) on the surface and in the interior [8]. Both SCMs are thousands to tens of thousands times more active than molecular DMAP and retain a significant activity at pH 5 when molecular DMAP is completely inactive. *p*-Nitrophenyl acetate (PNPA) hydrolyzes faster than *p*-nitrophenyl hexanoate (PNPH) in aqueous buffer, but the reactivity is reversed in the presence of DMAP-functionalized SCM that binds the more hydrophobic PNPH more strongly [8]. The SCM with internal DMAP is more active than that with DMAP on the surface, underscoring the importance of environmental control of the catalyst.

Water-soluble transition metal catalysts are often obtained by installing water-solubilizing groups such as sulfonate on the ligands. Not only does such modification complicate the ligand synthesis, the resulting catalysts are also rarely useful for highly nonpolar substrates, because of their inability to enter the aqueous phase to access the catalysts [9]. Physical entrapment of transition metal catalysts provides a potential solution, with the additional benefit of not requiring any ligand modification. SCM[$(PPh_3)_2Rh^+$] is prepared by our standard cross-linking procedure from a commercially available rhodium complex [10]. It resembles a water-soluble metalloenzyme by its catalytic metal center in a hydrophobic microenvironment.

Dodecanol is included in the preparation of SCM[$(PPh_3)_2Rh^+$] as temporary space holders, because these amphiphilic molecules occupy space in the micelle but do not participate in the cross-linking. Once removed at the end of the preparation,

they leave behind channels in the micellar core, which strongly facilitate catalytic hydrogenation of C6–C10 terminal alkenes in water. Remarkably, an increase of two carbons from 1-decene to 1-dodecene lowers the yield of hydrogenation from quantitative to ~20% – a selectivity not expected for the rhodium catalyst without SCM encapsulation. It seems the cross-linked micelle, limited by the chain length of the hydrophobic tail, can only accommodate hydrocarbon substrates below a critical length (Figure 15.1). Catalytic rhodium(I) species deactivates easily in a homogeneous solution through dimerization. Once encapsulated inside the SCM and isolated from one another, the Rh catalyst becomes highly robust and can be reused many times [10].

15.3 Molecularly Imprinted Nanoparticles (MINPs) via Double Cross-Linking of Micelles

Even though channels can be imprinted within the micellar core, the catalytic SCM described above still has a poorly defined internal structure. Once dodecanol is replaced with specially designed molecular templates, highly specific imprinted sites can be created, readily tuned through the structure of the template.

Traditional molecular imprinting starts with a mixture of template molecules dispersed in a large amount of a cross-linker and some inert solvent (i.e. porogen). Functional monomers (FMs) are often present to bind the templates by noncovalent or reversible covalent bonds. Cross-linking of the mixture creates a polymer network, with template molecules surrounded by FMs that have turned into binding groups during the imprinting process. Removal of the templates vacates the imprinted sites in the polymer network, which are complementary to the templates in size, shape, and binding functionality [11, 12].

Micellar imprinting takes place within SCMs prepared from cross-linkable surfactant **4** (Figure 15.2) [14]. The micelles are loaded with divinylbenzene (DVB, a radical cross-linker) and 2,2-dimethoxy-2-phenylacetophenone (DMPA) or 2,2′-azobis(2-methylpropionitrile) (AIBN) right in the beginning. After surface-cross-linking with **2** and surface functionalization with **3** by the click reaction, free-radical polymerization is triggered photochemically or thermally to “solidify” the micellar core around the template. The template molecules are generally amphiphilic and prefer to reside at the surfactant–water interface [13–15]. This configuration is critical to the template removal from the resulting molecularly imprinted nanoparticles (MINPs) and also makes the imprinted sites highly accessible afterwards during binding or catalysis. The surface property of MINP is controlled by the cross-linkable surfactant [16, 17] and/or surface ligands [4, 18]. FMs enable the imprinting of template molecules that are completely hydrophilic [19, 20]. MINPs have been made to bind a wide variety of molecules in water including biologically interesting small molecules [21, 22], carbohydrates [19, 20], and peptides [23, 24].

The highlight of micellar imprinting is the facile one-pot synthesis in water, completed in two days without any special techniques. MINPs as prepared resemble a

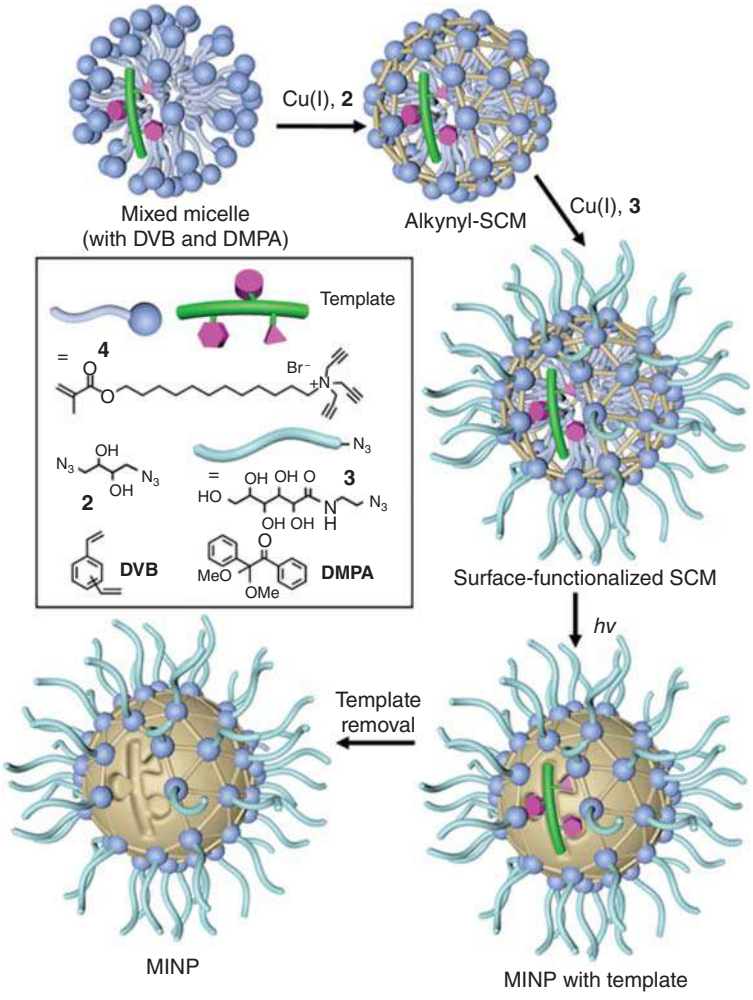

Figure 15.2 Preparation of MINP. The magenta-colored shapes on the template molecule represent hydrophobes of different size and shape. Source: Zangiabadi and Zhao [13]. Reproduced with permission of American Chemical Society.

protein receptor, having a hydrophilic surface, a hydrophobic core with a specific binding site, and a nanodimension (~5 nm). Since the surfactant aggregation number of **4** is ~50, a surfactant/template ratio of 50 : 1 translates to an average of one binding site per nanoparticle [14]. Purification requires simple precipitation into acetone and washing with organic solvents, due to the solubility properties of MINP imparted by surface ligand **3**. The overall yield of the synthesis is typically 70–80%.

To be useful for the construction of artificial enzymes, MINP needs to faithfully reproduce structural features of the template by its imprinted site. Fortunately, confinement of the polymerization and cross-linking in the nanosized SCM affords an extraordinary templating effect [25]. Imprinting factors – the imprint/nonimprint ratio in the binding constants – frequently reach hundreds [17, 24] and even

10 000 in some cases [13], much higher than those achieved traditionally. In our hands, MINPs generated for nonsteroidal anti-inflammatory drugs display cross-selectivities among analogs comparable to those of polyclonal antibodies [26]. Sequence-selective binding of peptides in water has been a long-standing challenge in supramolecular and bioorganic chemistry [27, 28]. Micellar imprinting creates a complementary array of hydrophobic indentations or "dimples" on MINPs, essentially encoding the cross-linked micelle with supramolecular information to match the hydrophobic "code" of the peptide guest that describes the size, shape, number, and distribution of hydrophobic side chains [23]. These "dimples" are highly discriminating in their binding, to the point that the shift of a single methyl in leucine and isoleucine in isomeric di- and tripeptides is distinguished, as well as phenylalanine and tyrosine. FMs can be included to target acidic/basic groups and tens-of-nanomolar dissociation constants (K_d) are frequently achieved for biological peptides with up to 18 residues [23, 24].

Another prerequisite for using MINP to create artificial enzymes is the installation of functional groups at desired locations. Template **5** has an ionic sulfonate group that anchors the molecule to the micellar surface and a methacrylate to be co-polymerized with **4** and DVB during core cross-linking (Figure 15.3). The template has a photosensitive *o*-nitrobenzyl ester bond, which cleaves cleanly inside MINP and leaves behind a pocket in the hydrophobic core, shaped exactly like **5**, with a single carboxylic acid at the far end. Soluble in DMF, the resulting MINP(**5**)-COOH can be treated as a "normal" macromolecule, activated, and functionalized to afford MINP(**5**)-CONHNaph, confirmed by fluorescence spectroscopy and isothermal titration calorimetry (ITC) by its binding properties [29].

15.4 MINP-Based Artificial Esterase

Enzymes have perfected the skills of folding a flexible peptide chain to bring multiple functional groups into a converged nanospace for binding and/or catalysis. With the ability to quickly "mold" a 3D nanospace around a template molecule inside a cross-linked micelle and functionalize the imprinted site, we now have a powerful platform to construct active sites for catalysis.

Template **6** resembles the transition state for DMAP-catalyzed PNPH hydrolysis, because part of its structure resembles the substrate and the other part enables a DMAP derivative (**7**) to be introduced through the photodeprotected carboxylic acid in the MINP binding site (Figure 15.4a) [30]. In the resulting MINP(**6**+**7**), i.e. MINP prepared with **6** as the template and **7** to functionalize the imprinted pocket, the distance of the catalytic pyridyl to the ester group of the substrate is controlled by the tether in **7**, with the best results obtained at $n = 2$.

If the DMAP-functionalized SCM mentioned earlier could only distinguish PNPH and PNPA by their hydrophobicity [8], MINP(**6**+**7**) is far more selective, hydrolyzing PNPH faster than closely related structural analogs **8**–**10** by 14–40 times. The hydrolysis follows enzyme-like Michalis–Menten kinetics, with a k_{cat} of 0.17–0.26 s^{-1} and a K_m of 0.41–0.66 mM in pH 8 HEPES buffer at 40 °C. The turnover number (TON) is >390, highlighting the longevity of the artificial enzyme.

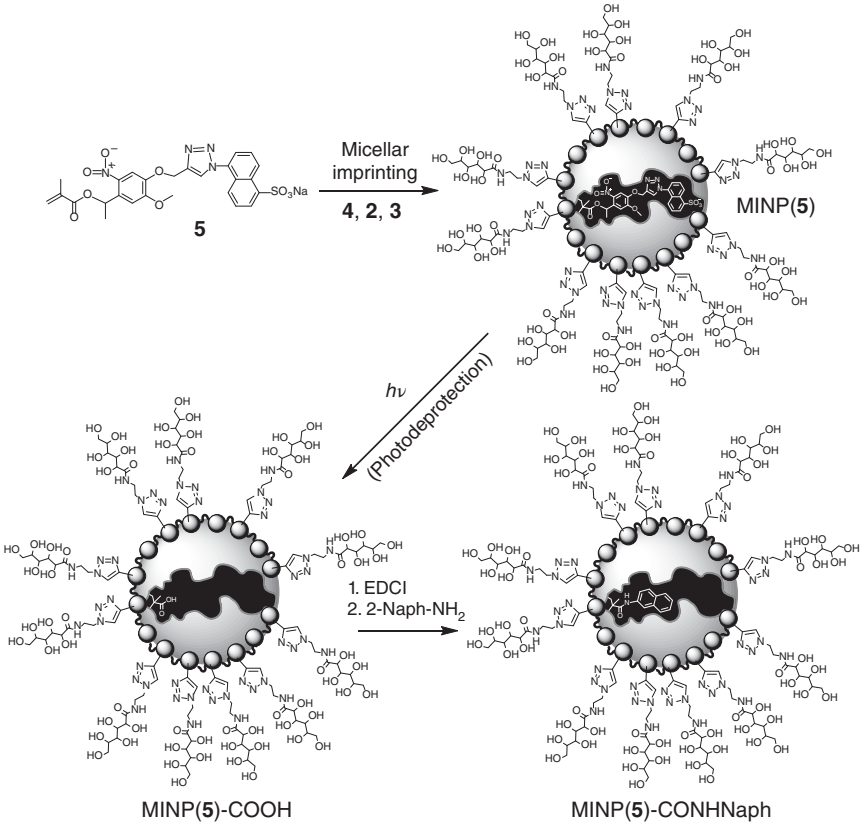

Figure 15.3 Preparation of MINP(**5**), its photodeprotection, and functionalization of the carboxylic acid inside the imprinted site.

Many hydrolytic enzymes employ zinc ions to activate water molecules for nucleophilic attacks [31]. Similar artificial zinc esterases are prepared from FM **11** and template **12a–c** (Figure 15.4b) [32]. FM **11** is a polymerizable zinc complex used as the catalytic group, and **12a–c** resemble PNPH, with their zinc-complexing amino nitrogen at different locations on the chain. The relative position of zinc to the ester group in the final catalyst can thus be tuned systematically. Among the catalysts, Zn-MINP(**12a**) hydrolyzes PNPH with remarkable selectivities among closely related analogs, even isomeric **13** with an isohexanoyl group. The selectivity of the catalyst can be controlled through using different templates such as **12d**.

Not only can covalent and metal–ligand bonds be used for catalyst construction, hydrogen bonds work as well, being stabilized by the hydrophobic environment of the micelle [33]. FM **14** binds anionic template **15**, a transition state analog for the hydrolysis of PNPH (Figure 15.4c) [34]. Through cleavage of the *o*-nitrobenzyl ester and a subsequent amide coupling with **16**, a DMAP group is introduced in the active site of MINP(**15**+**16**), with the nucleophilic/basic pyridyl nitrogen pointing at the

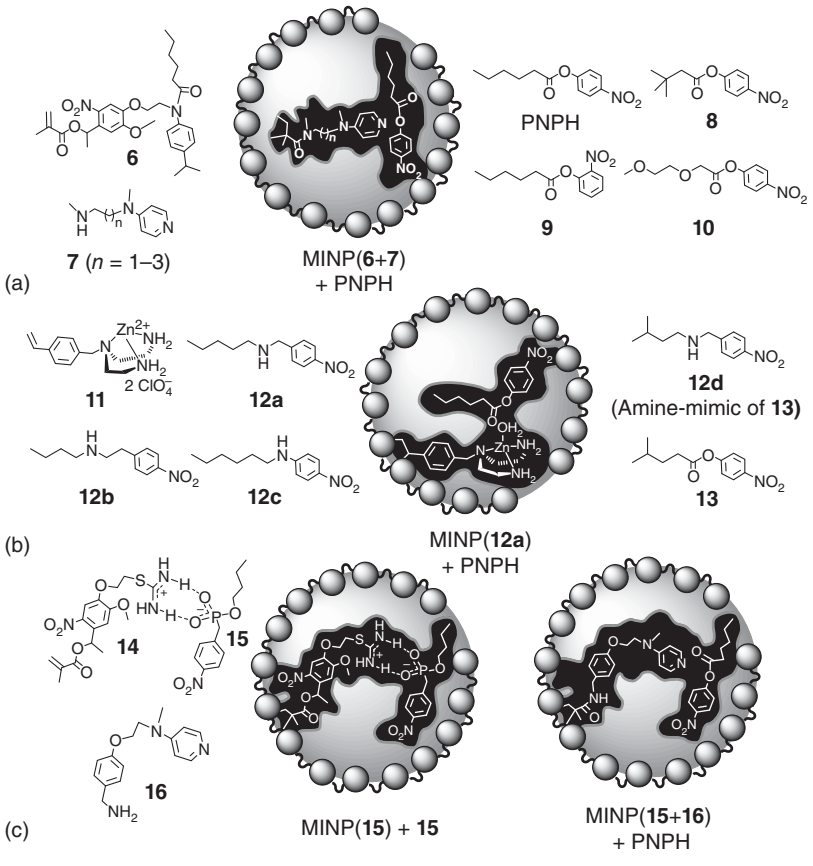

Figure 15.4 (a) MINP(**6**+**7**) prepared from template **6** and postfunctionalized with **7** for the hydrolysis of PNPH. (b) MINP(**12a**) prepared from template **12a** for the hydrolysis of PNPH. (c) MINP(**15**+**16**) prepared from template–FM complex **15**·**14** and postfunctionalized with **16** for the hydrolysis of PNPH.

ester group of the substrate. This "bait-and-switch" strategy allows one to construct different active sites quickly for different substrates [34] and install a variety of catalytic groups in the active site [35].

15.5 MINP-Based Artificial Glycosidase

As the most abundant biomolecules on earth, carbohydrates serve numerous functions including energy storage, structural support, cell signaling, and immune response. Most organisms use 1–3% of their genome to encode enzymes to process carbohydrates [36], but most of these enzymes are not readily available. In addition, enzymes generally work only under a narrow set of conditions in aqueous solutions and catalysts that tolerate harsh reaction conditions are required for challenging operations such as biomass conversion.

There are three fundamental challenges in building a synthetic glycosidase to hydrolyze a carbohydrate (or glycan) selectively [37]. First, carbohydrates are strongly solvated by water; thus, in its binding of the substrate, the catalyst needs to overcome a tremendous cost of desolvation. Second, because the biological properties of a glycan change profoundly with the inversion of a single hydroxyl, by connecting the monosaccharide building blocks through different hydroxyls, and when the (α/β) glycosidic linkages are altered, the synthetic glycosidase needs to distinguish these extremely subtle structural changes. Third, to hydrolyze an oligo- or polysaccharide at a specific position, the catalyst needs to position its catalytic group(s) precisely near the glycosidic bond to be targeted.

MINPs are excellent receptors for carbohydrates when 4-vinylphenylboronic is used as the FM to bind specific 1,2- or 1,3-diols of a sugar [20, 23, 38]. They bind monosaccharides with millimolar to submillimolar affinities in water through facile, reversible boronate ester bonds [39]. If the sugar has a hydrophobic aglycon, the binding is stronger due to added hydrophobic interactions. They distinguish common biologically important monosaccharides including glucose, mannose, and galactose with >100 : 1 selectivity [20].

Boronate **19**, synthesized from 4-vinylphenyl boronic acid and the corresponding glucoside, contains a substrate-like (yellow) and a catalyst-like (green) moiety in close proximity [40]. The resulting MINP(**19**) has a boronic acid in its imprinted site to bind the 4,6-*trans*-diol of *p*-nitrophenyl β-D-glucopyranoside (**17β**) and an adamantane-shaped hydrophobic pocket to bind acid cofactor **18a–d**. The ortho substitution on the phenyl ring of **19** ensures that the acidic group of **18a–d** resides near the exocyclic glycosidic oxygen of the bound substrate, promoting an acid-catalyzed hydrolysis (Figure 15.5).

ITC studies reveal that MINP(**19**) binds the targeted *p*-nitrophenyl β-D-glucopyranoside **17β** with $K_a = 8.59 \times 10^4\ M^{-1}$ in pH 6 MES buffer. The binding for the isomeric glycosides follows the order of **17β** > **20β** > **17α** > **21β** > **20α** ≈ **21α**. 1-Adamantanecarboxylic acid **18a** gives an even stronger binding of $K_a = 122 \times 10^4\ M^{-1}$, due to a very large hydrophobic driving force in the binding.

For the different acid cofactors, the binding follows the order of **18a** > **18b** > **18c** > **18d**. All the acid cofactors have the same adamantyl hydrophobe and thus have a similar driving force to enter the imprinted site. However, the hydrophobic binding pocket for the acid cofactor strongly favors a neutral, uncharged guest [6]. Because a stronger acid has to overcome a larger unfavorable acid–base equilibrium to enter the binding pocket in the neutral form, its binding is weakened. The weaker binding of **18b** in comparison to **18a** is most likely caused by the misfit of **18b** in the imprinted site.

Substrate selectivity is the most difficult challenge in the hydrolysis of glycans. MINP(**19a**)+**18a** catalyzes the hydrolysis of **17β** 11.4 times faster than **17α** (Figure 15.6a). Among the β anomers, the order of reactivity is glucoside (**17β**) > mannoside (**20β**) > galactoside (**21β**), consistent with the boronic acid binding. Meanwhile, all three α anomers are considerably less reactive.

Controlled, tunable selectivity for glycan hydrolysis has not been achieved by synthetic catalysts. In our case, when mannoside derivative **22** is employed as the

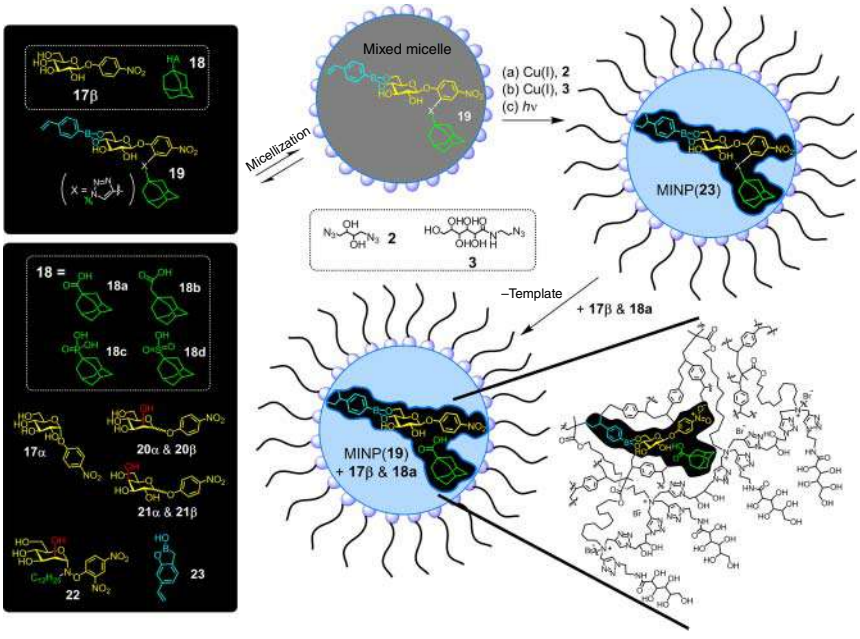

Figure 15.5 Preparation of artificial glucosidase by micellar imprinting, with a schematic representation of the cross-linked structure. Source: Li and Zhao [40]. Reproduced with permission of American Chemical Society.

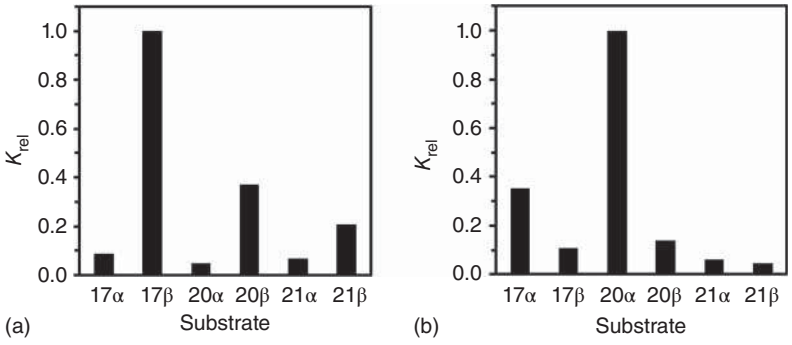

Figure 15.6 (a) Relative rates of hydrolysis of different glycosides catalyzed by MINP(**19a**)+**18a** in a 10-mM MES buffer (pH 6.0) at 40 °C. (b) Relative rates of hydrolysis of different glycosides catalyzed by MINP(**22**) + dodecanoic acid in a 10-mM MES buffer (pH 6.0) at 40 °C. [glycoside] = 100 μM. [MINP] = 5 μM. [acid cofactor] = 10 μM. Source: Li and Zhao [40]. Reproduced with permission of American Chemical Society.

template and vinylphenylboroxole **23** as the FM (Figure 15.5) [19], the resulting MINP(**22**) + dodecanoic acid complex selectively hydrolyzes the targeted **20α** with an α/β selectivity of 7.2 : 1 (Figure 15.6b) [40]. Note that significant mismatches exist between template **22** and the targeted mannoside **20α**. The *ortho*-nitro group on **22** is added mainly because the corresponding starting material is commercially available. Also, two atoms (N and O) are in between the anomeric carbon and the

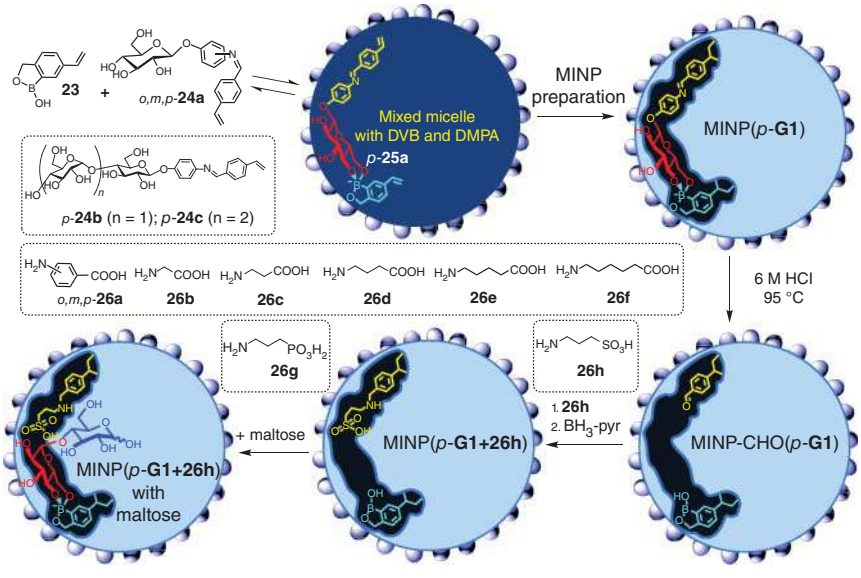

Figure 15.7 Preparation of artificial glycosidase MINP(*p*-**G1**+**26h**) and its binding of maltose. Source: Li and Zhao [41]. Reproduced with permission of Royal Society of Chemistry.

phenyl group in **22** and only one in **20α**. It is encouraging that these discrepancies are well tolerated.

The benefit of using a cofactor in the catalysis is the plug-and-play tuning of the catalytic activity. However, a higher catalytic efficiency is expected if the acid is covalently installed at the right place. Figure 15.7 shows the preparation of an artificial glycosidase using boroxole FM **23** and a glycoside *p*-**24a** as the template that contains an imine bond in the hydrophobic aglycon [41]. The imine bond in MINP(*p*-**G1**) is hydrolyzed in 6 M HCl at 95 °C, and the aldehyde group of MINP–CHO(*p*-**G1**) derivatized through reductive amination with **26a**–**f** in DMF [42]. The different tethers in **26a**–**f** enable us to vary the position and the acidity of the catalytic group and the best catalyst is found to be MINP–CHO(*p*-**G1**+**26h**).

MINP(*p*-**G1**+**26h**) is designed to bind the terminal sugar of a glucose-containing oligosaccharide (e.g. maltose or **G2**) or polysaccharide (e.g. amylose), with the sulfonic acid positioned precisely at the glycosidic bond to be targeted. Thus, it should hydrolyze the sugar chain one glucose residue at a time. In a similar fashion, MINP(*p*-**G2**+**26h**) and MINP(*p*-**G3**+**26h**) prepared from *p*-**24b** and *p*-**24c**, respectively, are designed to remove two and three glucose residues at a time.

Because these synthetic glycosidases bind both the starting sugar and the final hydrolyzed products in the active site, they display strong product inhibition. Fortunately, product inhibition can be overcome by simply performing the catalytic hydrolysis inside a dialysis membrane permeable to the desired products but impermeable to the larger starting material and the catalyst. This setup also simplifies the purification of the (*in situ* separated) products and recycling of the catalysts. Total

synthesis of carbohydrates is extremely challenging. Selective, one-step hydrolysis by rationally designed synthetic glycosidases potentially can be a powerful method to produce complex glycans from precursor oligosaccharides or polysaccharides either naturally available or prepared through enzymatic synthesis.

Substrate selectivity is one of the most important performance criteria for a synthetic glycosidase. For a monosaccharide-derived catalyst such as MINP(*p*-**G1**+**26h**), its only selectivity is for the terminal sugar at the non-reducing end and the α/β selectivity is low in the hydrolysis. For a disaccharide-derived catalyst, the situation is different because the α/β linkage between the first two sugar residues affects the binding of the substrate, as demonstrated in the catalytic hydrolysis of maltotriose and cellotriose by MINP(*p*-**G2**+**26h**) [41].

It should be mentioned that **26** is inactive outside the MINP for acid-catalyzed hydrolysis, likely due to the acid–base neutralization. Once placed inside the MINP active site, the acid becomes highly active. The main reason for the different behavior should be the tight, hydrophobic space of the active site. Intramolecular proton transfer between the acid and the amine creates a zwitterionic species. These charged groups are stabilized in solution by water molecules but are highly unstable in a hydrophobic microenvironment – a feature frequently found in enzyme active sites [5, 6].

15.6 MINP-Based Artificial Enzymes for Asymmetric Catalysis and Tandem Catalysis

Instead of solely relying on catalytic metals and ligands in their first coordination sphere, enzymes frequently employ ligands at the second coordination sphere and even remote allosteric binding sites to control catalysis. We recently reported a concept of "chiral gating" to control the passage of reactants to a chiral catalytic center to boost the latter's enantioselectivity (Figure 15.8) [43]. MINP(**28**) contains a chiral nanospace (i.e. "gate") near the hydrophobically anchored prolinamide (*S*)-**27** catalyst, which works poorly by itself in water (no reaction) or organic solvent (62% yield, 42% ee in DMSO). The nanospace is created through molecular imprinting of *p*-nitrophenylalanine on the template. With the help of MINP(**28**), (*S*)-**27** catalyzes the adol reaction between acetone and various aryl aldehydes in excellent yields, with up to 99% ee in water. The gate also endows the catalyst with size and shape selectivity, preventing "unfitted" aldehydes from reacting. Most remarkably, racemic (±)-**27** affords >70% ee for the aldol reaction in the presence of MINP(**28**), due to the latter's >100 : 1 binding selectivity for the two enantiomers of the prolinamide by its chiral imprinted pocket.

Chemists usually have to carry out their reactions using pure starting materials and isolate and purify the products before they go to the next step. If multiple reactants with the same functional group are used, a mixture of products will form unless one reactant has a much higher reactivity than the others. Enzymatic catalysts, on the other hand, routinely deal with complex mixtures but can perform

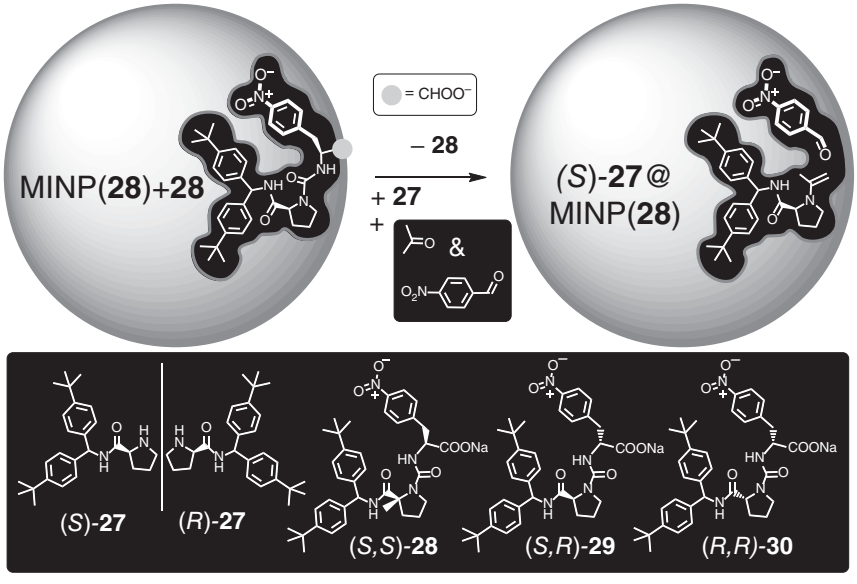

Figure 15.8 Preparation of chiral MINP for aldol reaction.

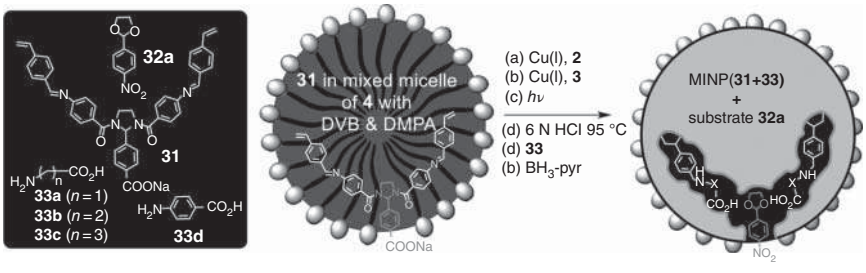

Figure 15.9 Preparation of MINP(**31**+**33**) for selective hydrolysis of acetals.

desired transformations readily. A series of enzymes often work in a tandem fashion to produce complex molecules, without any separation of intermediate products.

Template **31** has two imine bonds and is used to create an active site in the MINP with two carboxylic acids sandwiching the targeted substrate, 2-(4-nitrophenyl)-1,3-dioxolane **32a** (Figure 15.9) [44]. The tether in the amino acid **33a**–**d** tunes the distance of the acid groups to the substrate, as well as their mobility. MINP(**31**+**33b**), with a flexible tether in the amino acid in the active site, is found to be the most active for the acetal hydrolysis. MINP(**31**+**33d**), with the more rigid aromatic amino acid, is the most selective.

Keeping the acidic groups in a hydrophobic pocket enables MINP(**31**+**33b**,**d**) to retain its ability to catalyze acid-catalyzed reactions under strongly basic conditions (Figure 15.10a). With a strong selectivity for the substrate, MINP(**31**+**33d**) is able to catalyze a tandem Henry reaction from an equimolar mixture of four acetals (**32a**–**d**) (Figure 15.10b). Because acetal hydrolysis requires acidic catalysts and

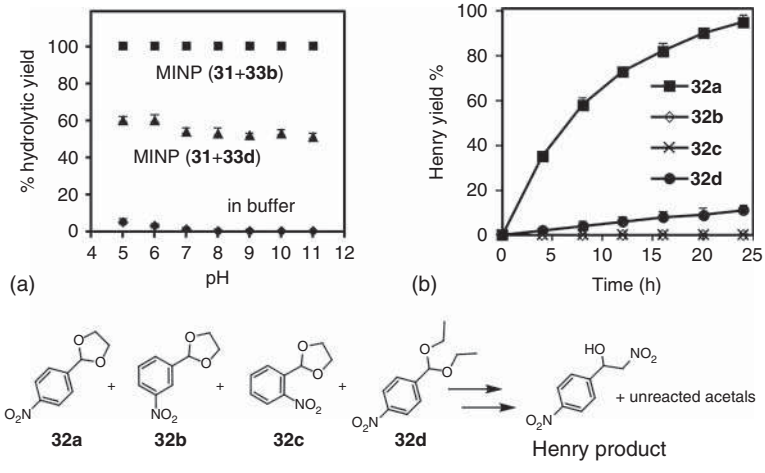

Figure 15.10 (a) Hydrolysis of **32a** as a function of solution pH after six hours at 50 °C in buffer vs. in the presence of MINP(**31**+**33b**) and MINP(**31**+**33d**). [**32a**] = 1.0 mM. [MINP] = 50 μM. (b) Yield of tandem Henry reaction at 40 °C in a 10-mM CAPS buffer (pH 10) as a function of time for an equimolar mixture of **32a–d** by MINP(**31**+**33d**). [**32a–d**] = 1.0 mM. [nitromethane] = 3.1 M. [MINP] = 50 μM. Source: Bose and Zhao [44]. Reproduced with permission of American Chemical Society.

Henry reaction basic catalysts, the two reactions generally cannot be performed in the same solution, let alone from a mixture of reactants.

15.7 Concluding Remarks

Micellar imprinting simplifies the construction of substrate-tailored active sites largely into standard organic syntheses of small molecules, followed by convenient self-assembly of double cross-linkable surfactant, covalent capture of the micelle, and postmodification of the imprinted binding sites. Strong imprinting effects in the confined minienvironment enable faithful reproduction of the structural features on the template in the imprinted site. Meanwhile, small discrepancies between the template and the substrate can be tolerated in the MINP-based artificial enzymes, affording much flexibility in the template design and synthesis.

Natural glucan 1,4-α-glucosidase hydrolyzes amylose one glucose residual at a time from the nonreducing end and β-amylase two. Our synthetic glycosidases not only have duplicated the selectivities of these enzymes but also can be designed to possess selectivity unavailable from natural biocatalysts – i.e. selective formation of maltotriose from maltohexaose or amylose. Because MINPs are cross-linked polymeric nanoparticles, they tolerate high temperatures [14, 45], organic solvent [45], and extreme pH [42], outperforming enzymes completely in these aspects. Their selectivity enables selective transformation of a reasonably complex mixture into the desired product, overriding the intrinsic activity. Although much remains to be learned, the future seems bright given what the cross-linked micelles have already accomplished.

Acknowledgments

Financial support of the research by NSF (CHE-1708526 and DMR-2002659) and NIGMS (R01GM113883 and R01GM138427) is gratefully acknowledged.

References

1 Menger, F.M. and Whitesell, L.G. (1985). A protease mimic with turnover capabilities. *J. Am. Chem. Soc.* 107: 707–708.
2 Romsted, L.S., Bunton, C.A., and Yao, J.H. (1997). Micellar catalysis, a useful misnomer. *Curr. Opin. Colloid Interface Sci.* 2: 622–628.
3 Dwars, T., Paetzold, E., and Oehme, G. (2005). Reactions in micellar systems. *Angew. Chem. Int. Ed.* 44: 7174–7199.
4 Zhang, S. and Zhao, Y. (2010). Facile synthesis of multivalent water-soluble organic nanoparticles via "surface clicking" of alkynylated surfactant micelles. *Macromolecules* 43: 4020–4022.
5 Westheimer, F.H. (1995). Coincidences, decarboxylation, and electrostatic effects. *Tetrahedron* 51: 3–20.
6 Matulis, D. and Bloomfield, V.A. (2001). Thermodynamics of the hydrophobic effect. I. Coupling of aggregation and pK_a shifts in solutions of aliphatic amines. *Biophys. Chem.* 93: 37–51.
7 Henao, J.D., Suh, Y.-W., Lee, J.-K. et al. (2008). Striking confinement effect: $AuCl_4^-$ binding to amines in a nanocage cavity. *J. Am. Chem. Soc.* 130: 16142–16143.
8 Chadha, G. and Zhao, Y. (2014). Environmental control of nucleophilic catalysis in water. *Chem. Commun.* 50: 2718–2720.
9 Cornils, B. and Herrmann, W.A. (2004). *Aqueous-Phase Organometallic Catalysis: Concepts and Applications*, 2e. Weinheim: Wiley-VCH.
10 Zhang, S. and Zhao, Y. (2012). Artificial metalloenzymes via encapsulation of hydrophobic transition-metal catalysts in surface-crosslinked micelles (SCMs). *Chem. Commun.* 48: 9998–10000.
11 Wulff, G. (2002). Enzyme-like catalysis by molecularly imprinted polymers. *Chem. Rev.* 102: 1–28.
12 Ye, L. and Mosbach, K. (2008). Molecular imprinting: synthetic materials as substitutes for biological antibodies and receptors. *Chem. Mater.* 20: 859–868.
13 Zangiabadi, M. and Zhao, Y. (2020). Molecularly imprinted polymeric receptors with interfacial hydrogen bonds for peptide recognition in water. *ACS Appl. Polym. Mater.* 2: 3171–3180.
14 Awino, J.K. and Zhao, Y. (2013). Protein-mimetic, molecularly imprinted nanoparticles for selective binding of bile salt derivatives in water. *J. Am. Chem. Soc.* 135: 12552–12555.
15 Awino, J.K. and Zhao, Y. (2014). Molecularly imprinted nanoparticles as tailor-made sensors for small fluorescent molecules. *Chem. Commun.* 50: 5752–5755.

16 Gunasekara, R.W. and Zhao, Y. (2019). Recognition and protection of glycosphingolipids by synthetic nanoparticle receptors. *Chem. Commun.* 55: 4773–4776.

17 Duan, L. and Zhao, Y. (2019). Zwitterionic molecularly imprinted cross-linked micelles for alkaloid recognition in water. *J. Org. Chem.* 84: 13457–13464.

18 Li, X. and Zhao, Y. (2012). Tunable fusion and aggregation of liposomes triggered by multifunctional surface-cross-linked micelles. *Bioconjugate Chem.* 23: 1721–1725.

19 Gunasekara, R.W. and Zhao, Y. (2017). A general method for selective recognition of monosaccharides and oligosaccharides in water. *J. Am. Chem. Soc.* 139: 829–835.

20 Awino, J.K., Gunasekara, R.W., and Zhao, Y. (2016). Selective recognition of D-aldohexoses in water by boronic acid-functionalized, molecularly imprinted cross-linked micelles. *J. Am. Chem. Soc.* 138: 9759–9762.

21 Awino, J.K. and Zhao, Y. (2017). Imprinted micelles for chiral recognition in water: shape, depth, and number of recognition sites. *Org. Biomol. Chem.* 15: 4851–4858.

22 Duan, L. and Zhao, Y. (2018). Selective binding of folic acid and derivatives by imprinted nanoparticle receptors in water. *Bioconjugate Chem.* 29: 1438–1445.

23 Awino, J.K., Gunasekara, R.W., and Zhao, Y. (2017). Sequence-selective binding of oligopeptides in water through hydrophobic coding. *J. Am. Chem. Soc.* 139: 2188–2191.

24 Fa, S. and Zhao, Y. (2019). General method for peptide recognition in water through bioinspired complementarity. *Chem. Mater.* 31: 4889–4896.

25 Chen, K. and Zhao, Y. (2019). Effects of nano-confinement and conformational mobility on molecular imprinting of cross-linked micelles. *Org. Biomol. Chem.* 17: 8611–8617.

26 Awino, J.K. and Zhao, Y. (2015). Polymeric nanoparticle receptors as synthetic antibodies for nonsteroidal anti-inflammatory drugs (NSAIDs). *ACS Biomater. Sci. Eng.* 1: 425–430.

27 Peczuh, M.W. and Hamilton, A.D. (2000). Peptide and protein recognition by designed molecules. *Chem. Rev.* 100: 2479–2494.

28 van Dun, S., Ottmann, C., Milroy, L.-G., and Brunsveld, L. (2017). Supramolecular chemistry targeting proteins. *J. Am. Chem. Soc.* 139: 13960–13968.

29 Awino, J.K. and Zhao, Y. (2015). Water-soluble molecularly imprinted nanoparticles (MINPs) with tailored, functionalized, modifiable binding pockets. *Chem. Eur. J.* 21: 655–661.

30 Hu, L. and Zhao, Y. (2018). Molecularly imprinted artificial esterases with highly specific active sites and precisely installed catalytic groups. *Org. Biomol. Chem.* 16: 5580–5584.

31 Coleman, J.E. (1998). Zinc enzymes. *Curr. Opin. Chem. Biol.* 2: 222–234.

32 Arifuzzaman, M. and Zhao, Y. (2018). Artificial zinc enzymes with fine-tuned catalytic active sites for highly selective hydrolysis of activated esters. *ACS Catal.* 8: 8154–8161.

33 Nowick, J.S., Chen, J.S., and Noronha, G. (1993). Molecular recognition in micelles – the roles of hydrogen-bonding and hydrophobicity in adenine thymine base-pairing in SDS micelles. *J. Am. Chem. Soc.* 115: 7636–7644.

34 Hu, L. and Zhao, Y. (2019). A bait-and-switch method for the construction of artificial esterases for substrate-selective hydrolysis. *Chem. Eur. J.* 25: 7702–7710.

35 Hu, L., Arifuzzaman, M.D., and Zhao, Y. (2019). Controlling product inhibition through substrate-specific active sites in nanoparticle-based phosphodiesterase and esterase. *ACS Catal.* 9: 5019–5024.

36 Davies, G.J., Gloster, T.M., and Henrissat, B. (2005). Recent structural insights into the expanding world of carbohydrate-active enzymes. *Curr. Opin. Struct. Biol.* 15: 637–645.

37 Davis, A.P. and James, T.D. (2005). *Carbohydrate Receptors*. Weinheim: Wiley-VCH.

38 Zangiabadi, M. and Zhao, Y. (2020). Selective binding of complex glycans and glycoproteins in water by molecularly imprinted nanoparticles. *Nano Lett.* 20: 5106–5110.

39 James, T.D., Phillips, M.D., and Shinkai, S. (2006). *Boronic Acids in Saccharide Recognition*. Cambridge: RSC Publishing.

40 Li, X. and Zhao, Y. (2020). Synthetic glycosidase distinguishing glycan and glycosidic linkage in its catalytic hydrolysis. *ACS Catal.* 10: 13800–13808.

41 Li, X. and Zhao, Y. (2021). Synthetic glycosidases for the precise hydrolysis of oligosaccharides and polysaccharides. *Chem. Sci.* 12: 374–383.

42 Xing, X. and Zhao, Y. (2018). Fluorescent nanoparticle sensors with tailor-made recognition units and proximate fluorescent reporter groups. *New J. Chem.* 42: 9377–9380.

43 Li, X. and Zhao, Y. (2019). Chiral gating for size- and shape-selective asymmetric catalysis. *J. Am. Chem. Soc.* 141: 13749–13752.

44 Bose, I. and Zhao, Y. (2020). pH-controlled nanoparticle catalysts for highly selective tandem Henry reaction from mixtures. *ACS Catal.* 10: 13973–13977.

45 Xing, X. and Zhao, Y. (2018). Binding-promoted chemical reaction in the nanospace of a binding site: effects of environmental constriction. *Org. Biomol. Chem.* 16: 2855–2859.

16

Bioinspired Catalysis Using Innately Polarized Pd_2L_4 Coordination Cages

Paul J. Lusby

University of Edinburgh, EaStCHEM School of Chemistry, Joseph Black Building, David Brewster Road, Edinburgh, EH9 3FJ, UK

16.1 Introduction

Over the last three decades, coordination-driven assembly has emerged as a popular approach for creating three-dimensional cage-type structures that can bind different species within their interiors. It is this property, similar to other earlier supramolecular host systems, that has led researchers to try and develop catalysts inspired by how nature uses enzymes, which also isolate substrates from the bulk using buried active sites. In this chapter, we will describe research from our own laboratory as we strive to emulate the efficiency of enzymes. We will attempt to set this into context by providing a brief comparison to previous efforts in this area.

16.2 A Coordination-Cage Host–Guest Method Based on Polar Interactions

Despite the many hundreds of coordination-cage-type assemblies that have been described in the past two decades [1], only a handful have been shown to be catalytically relevant. This lack of functional systems can perhaps be explained by considering the way that many coordination cages bind different molecular entities. Many cages are inherently soluble in aqueous media, especially those that utilize charge dense counterions, and the cavities are generally surrounded by flat aromatic surfaces, all of which lend themselves to the binding of hydrophobic species due to the expulsion of water. While this type of hydrophobic binding can be very useful for encapsulating relatively lipophilic guests, there is a lack of directional interactions to stabilize polar intermediates and transition states in the same way that enzymes use these mechanisms to deliver remarkable rate enhancements. This is a key reason that many examples of coordination cage catalysis rely on factors such as increasing effective concentration through dual binding [2], or reducing the entropy of activation using constrictive binding type mechanisms [3]. With these considerations in

Supramolecular Catalysis: New Directions and Developments, First Edition.
Edited by Piet W.N.M. van Leeuwen and Matthieu Raynal.

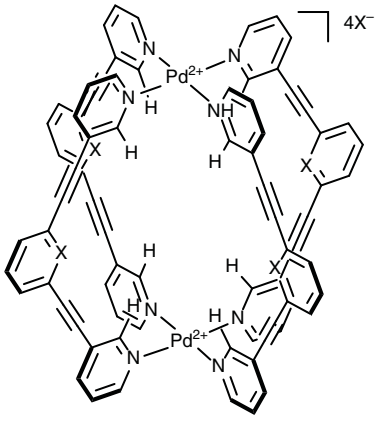

(a)

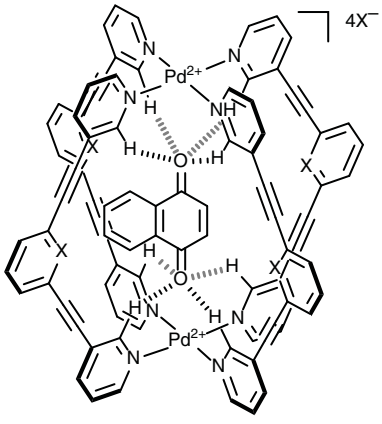

(c)

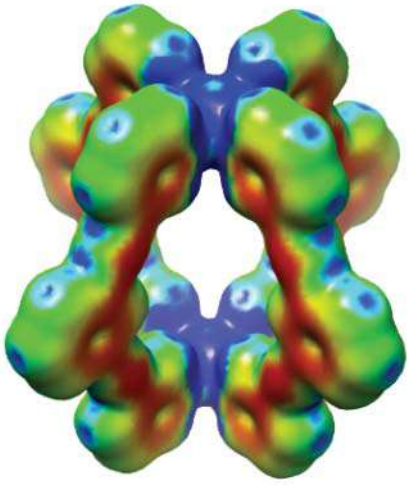

(b)

X	Solvent	K_a (M^{-1})
OTf	CD_3CN	210
OTf	CD_3OD	26
OTf	$[D_8]THF$	290
OTf	CD_2Cl_2	1 800
OTf	CD_3NO_2	2 000
BF_4	CD_3NO_2	6 500
PF_6	CD_3NO_2	13 000
SbF_6	CD_3NO_2	22 000
BArF	CD_3NO_2	50 000
BArF	CD_3OD	530
BArF	CD_3CN	1 600
BArF	CD_2Cl_2	350 000

Figure 16.1 (a) Chemical structures of the Pd_2L_4 cages described in this chapter. (b) Electrostatic surface diagram of $Pd_2\mathbf{L}^{\mathbf{CH}}{}_4$. (c) Chemical structure of naphthoquinone $\subset[Pd_2\mathbf{L}^{\mathbf{CH}}{}_4](X)_4$ and association constants as a function of counteranion and solvent. BArF = tetrakis[3,5-bis(trifluoromethyl)phenyl]borate.

mind, we sought to develop an alternative catalytic approach that would be centered on the use of electrostatic interactions. Moreover, this would exploit the inherent charge of a coordination cage and the significant polarization that this imparts on the structure, such that guests bind through the recognition of the polar surface [4].

The system we chose to develop was a very simple $Pd_2\mathbf{L}^{\mathbf{CH}}{}_4$ structure (Figure 16.1a) [4], which we have come to refer to as the "CH-cage," that had originally been reported by Hooley [5]. There were several features of this cage that appeared attractive. Most importantly, the ligands in the Pd_2L_4 structure sit

perpendicular rather than parallel to the cavity. This means that the hydrogen atoms along the edge of each ditopic ligand are directed toward the cavity – 12 in the case of $Pd_2\mathbf{L^{CH}}_4$. Furthermore, the eight hydrogen atoms that are closest to the Pd ions are significantly polarized by the charged metal, so that they collectively form two pockets of H-bond donors. This was particularly apparent in the electrostatic potential energy representation of the cage (Figure 16.1b). Moreover, these co-facial pockets of H-bond donor pockets are perfectly separated to bind quinones with virtually no distortion to the cage.

As could be expected for guest binding that relies on polar host–guest interactions, quinone encapsulation by $Pd_2\mathbf{L^{CH}}_4$ becomes stronger in more apolar, organic solvents (Figure 16.1c) [4]. However, this effect quickly plateaus even in solvents such as dichloromethane. This occurs because as the solvent polarity decreases, then ion-pairing with the counteranions becomes tighter and so does binding to the cage interior. By swapping the cage counteranions to progressively less interacting species, the association constant gradually increases. The biggest change occurs when relatively small, classically non-coordinating anions (e.g. BF_4, PF_6, etc.) are swapped to the much larger tetrakis[3,5-bis(trifluoromethyl)phenyl]borate (BArF), which is not only much less interacting but is also too large to access the cage interior. The combined use of this anion with an apolar solvent is dramatic; without changing the basic cage structure, the affinity of the same guest varies by 5 orders of magnitude. The optimized binding conditions – BArF counteranions and dichloromethane solvent – have been utilized in all subsequent catalytic studies.

16.3 From Guest Binding to Catalysis; an Artificial "Diels–Alderase"

The Diels–Alder reaction is a useful benchmark in bioinspired catalysis as it has been studied several times with very different supramolecular systems, from cyclodextrins [6] and porphyrinic receptors [7] through to H-bond [8] and metal–ligand assemblies [2]. Despite the diversity of these systems, a common concept has prevailed: the "catalyst" binds both the diene and the dienophile and accelerates the reaction due to an increased effective molarity (Figure 16.2a). The advantage of this approach is that it places the reactants in a very specific relative orientation, and this can lead to interesting types of selectivity (e.g. regio or exo vs. endo diasteroselectivity) that can be intrinsically disfavored and would be otherwise difficult to attain using simple small-molecule catalysts. The downside of the dual-encapsulation method is clear: the vast majority exhibit severe product inhibition, i.e. the reaction is not even able to release one equivalent of product (Figure 16.2a), meaning that many of these examples are not "catalysts" in the true sense of the meaning.

Consequently, we envisaged a method wherein acceleration would not be derived from dual binding, but rather the cage would electronically "activate" the bound substrate (Figure 16.2b). This activation would occur because hydrogen bonding of the Pd_2L_4 cage to the oxygen atoms of a quinone dienophile would lower its LUMO making reaction more facile, akin to the types of mechanisms that small-molecule

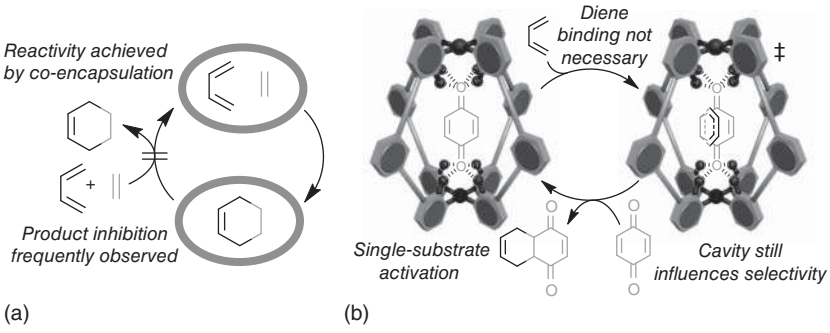

Figure 16.2 (a) Previous supramolecular Diels–Alder catalysis has relied on leveraging activity from dual encapsulation. (b) Our method uses electronic "activation" of the dienophile. Source: Martí-Centelles et al. [9]. Reproduced with permission of American Chemical Society.

H-bond donor catalysts utilize. Crucially, this type of mechanism would see one product being displaced by one substrate, both of which are held in the cavity by two pockets of H-bond donors, ensuring that turnover would be close to energetically neutral. At the same time, even though formal diene binding would not be required, this reactant would still need to access the activated quinone and so the cage structure would have opportunity to influence factors such as selectivity.

Despite our confidence in this proposal, we were unable to observe any hint of catalysis using $Pd_2\mathbf{L}^{\mathbf{CH}}{}_4$ even though we tried many different quinone–diene combinations [9]. Our rationale was that there was simply not enough room to accommodate the incoming diene. Turning to other cage structures, we decided to pursue the highly homologous *endo*-pyridyl variant, $Pd_2\mathbf{L}^{\mathbf{N}}{}_4$, now referred to in the group as the "N-cage" (Figure 16.1a), which again was a known compound, having been shown by Crowley and coworkers to encapsulate the drug molecule Cisplatin [10]. It has to be said, we were not overly confident that the N-cage would show any more promise than the CH-cage as they are so structurally similar. In fact, the results could not have been more different! The cage-mediate reaction of benzoquinone, **1**, with isoprene, **2**, using 20 mol% N-cage is finished in just over 24 hours, whereas the background reaction shows minimal conversion after days (Figure 16.3a) [9]. That the reaction had gone to completion with sub-stoichiometric cage, highlighted that product inhibition was low. This was further demonstrated by pre-loading the reaction with excess product **3** – up to 100 equivalents with respect to the benzoquinone substrate **1** (Figure 16.3b). Even with this vast excess of adduct, the catalyzed reaction is still notably quicker than the background process allowing an estimation that TON of 1000 are feasible.

One example of the subtleties of enclosed reactivity is how very small substrate changes can affect catalysis. For example, whereas the cage enhances the reactivity of C_5 dienes, isoprene, **2**, and cyclopentadiene, **4**, toward benzoquinone, **1**, by roughly similar amounts ($k_{cat}/k_{uncat} \approx 400$), it has a much greater effect on the almost identically sized pentadiene, **5**. A direct comparison of isomeric **2** and **5** (Figure 16.4) using a series of quinones (**1**, **6**–**8**) shows that the linear diene is universally superior, with k_{cat}/k_{uncat} between two and four times higher. This would suggest that the

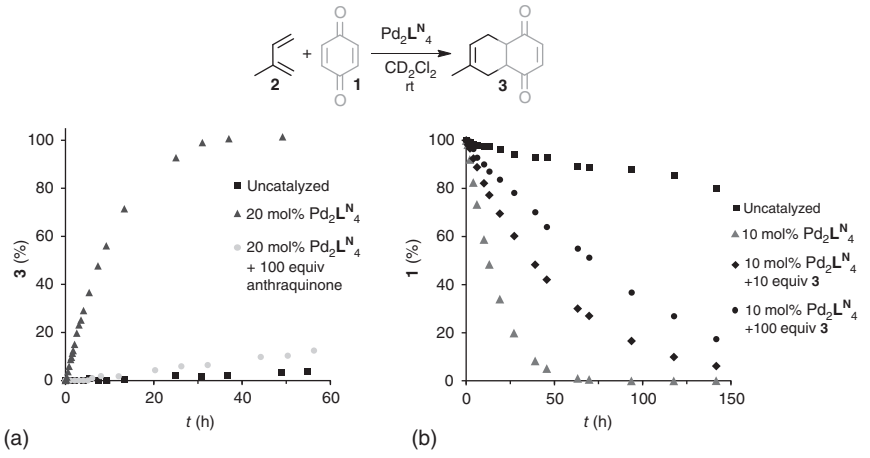

Figure 16.3 (a) Representative kinetic data for a $Pd_2\mathbf{L^N}_4$-catalyzed DA reaction. (b) Product inhibition experiment showing efficient turnover. Source: Martí-Centelles et al. [9]. Reproduced with permission of American Chemical Society.

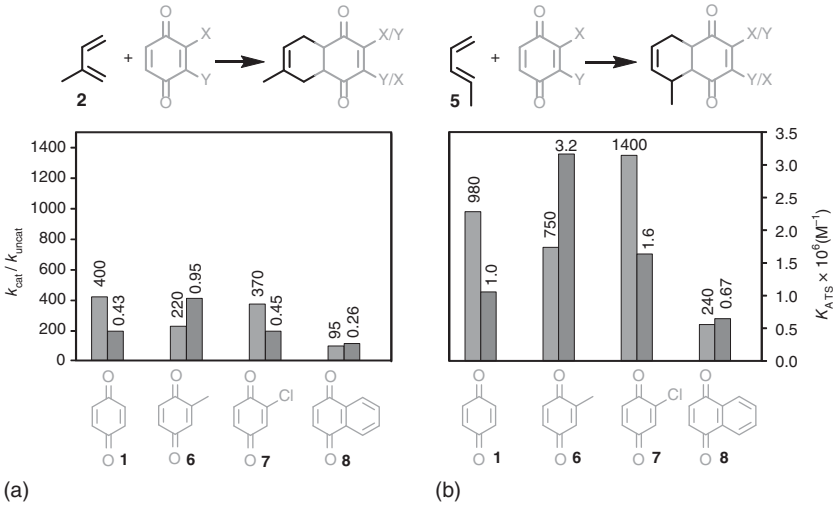

Figure 16.4 k_{cat}/k_{uncat} and transition state association constants, K_{ATS}, for a series of quinones with (a) isoprene and (b) pentadiene. Source: Martí-Centelles et al. [9]. Reproduced with permission of American Chemical Society.

incoming pentadiene **5** is able to access the frontier molecular orbitals of the bound quinone dienophile more readily (or that the TS for these series of Diels-Alder (DA) reactions is more complementary to the cage).

The significant difference in catalytic properties of the two cages can be rationalized on the basis of their relative substrate and TS binding affinities. In this regard, the benzoquinone and cyclopentadiene adduct, **9**, is a useful compound as it is a reasonable structural mimic of the TS (Figure 16.5a). Significantly, the N-cage binds the TS mimic **9** ($K_A = 11\,000\,M^{-1}$) much stronger than the CH-cage ($K_A = 550\,M^{-1}$). In addition, the N-cage shows weaker binding to the substrate ($K_A = 1100\,M^{-1}$)

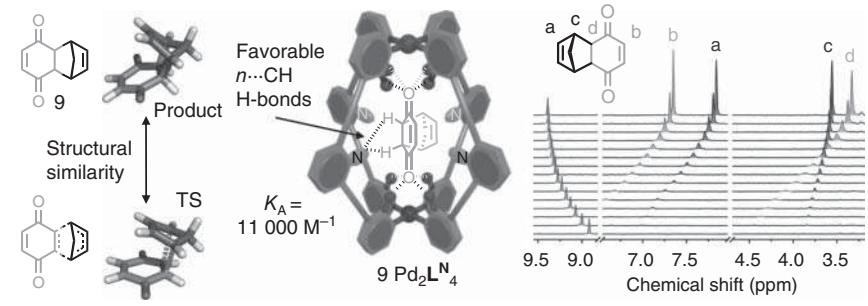

Figure 16.5 Selective TS binding can be assessed using the (a) compound **9**, that is a structural TS mimic. (b) Favorable secondary interactions are revealed using (c) NMR titration experiments. Source: Martí-Centelles et al. [9]. Reproduced with permission of American Chemical Society.

compared to the inactive CH-cage ($K_A = 8000\,M^{-1}$). The summation of a less-stabilized reactant state and a more stabilized TS (based on a mimic) gives an estimated energetic difference for the activation barrier of 3.0 kcal mol^{-1} between the two cages. Analysis of the kinetic data shows that it is even higher – several reactions reveal at least a 4 kcal mol^{-1} difference. The structural origin of this reactivity difference is more difficult to quantify, but it appears that secondary interactions are key, wherein titration data suggest several of the product H atoms form H-bonding interactions with the cage's inward facing N atoms (Figure 16.5b,c) [9]. A computational analysis indicates that the catalytic difference could also be due to a lower distortion energy associated with the N-cage at the TS [11].

The difference between TS and substrate binding energies has been used by Houk to quantify the effectiveness of different Diels–Alder non-covalent catalysts [12]. This study from 2002 showed that a catalytic antibody, 1E9, from Hilvert's group [13] was the most effective, with the TS being bound more effectively than the substrates by about 4 kcal mol^{-1}. By this measure, the N-cage is as efficient as a non-naturally occurring biological catalyst. While there are some caveats associated with this comparison – such as that the catalytic antibody binds both the diene and the dienophile, meaning that the absolute substrate and TS stabilization energies are much larger – it nonetheless highlights that the N-cage is an extremely good catalyst. Perhaps, a more direct comparison of catalytic performance is against small-molecule H-bond catalysts, which also only formally bind the dienophile. The thiourea catalyst that has been described by Schreiner [14] only shows a k_{cat}/k_{uncat} of about 40 for the reaction of methyl vinyl ketone, **10**, and cyclopentadiene, **4** (not shown) [9].

A key feature of biological catalysts is that they can select specific substrates from a pool of similar reactants. The N-cage can exhibit similar behavior. When a mixture of two dienophiles, benzoquinone, **1**, and ^{t}butylbenzoquinone, **11**, and two dienes, pentadiene, **5**, and dimethyl anthracene, **12**, are reacted competitively in the presence of a catalytic quantity of N-cage, two products, **13** and **14**, out of a possible four are formed selectively in more than 90% yield (Figure 16.6). This product distribution arises because the cage can only catalyze the formation of **13** as only **1**

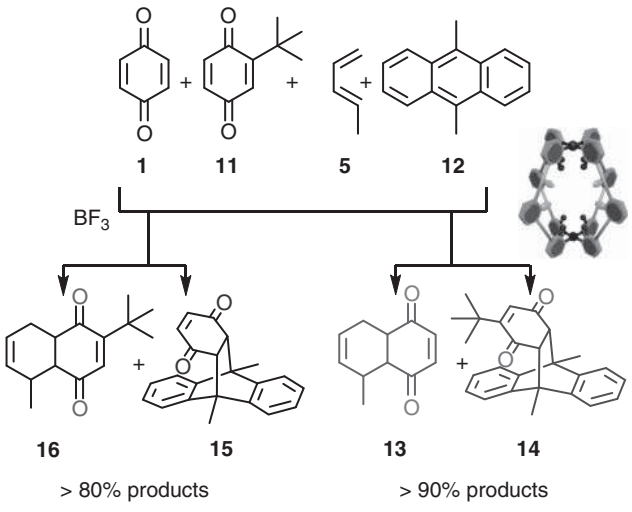

Figure 16.6 Chemoselective coordination cage catalysis. Source: Martí-Centelles et al. [9]. Reproduced with permission of American Chemical Society.

and **5** can gain access to the cavity; **14** is formed from the leftover reactants, **11** and **12**. Moreover, this product distribution deviates from intrinsic reactivity, where the more reactive dimethyl anthracene **12** and benzoquinone undergo cycloaddition fastest to give product **15** and remaining **5** and **11** generate compound **16**. This product distribution is what is obtained using a conventional Lewis acid such as BF_3, albeit it happens more quickly. Thus, the cage is able to selectively generate an inherently less-favored product, and it does this under catalytic conditions. This means that the cage is not simply behaving as a non-covalent "protecting group" to stop **12** gaining access to bound **1** but that the generation of **15** outside the cage is being out-accelerated by the cage promoted formation of **13**.

Another aspect of enzyme catalysis we have replicated is allosteric regulation [15], wherein binding of a molecule to the outside of the cage affects reactivity on the inside. Triphenylphosphine oxide interacts with the exterior pocket of four H-bond donor atoms; this binding is selective because it is size and/or symmetry mismatched to bind inside. When DA catalysis with the N-cage occurs in the presence of the triphenylphosphine oxide effector, the rate of product formation is slowed, although the factors contributing to this overall difference are subtle as both substrate and TS binding energies are weakened. This means that the activation barrier for catalysis in the presence and absence of Ph_3PO is similar ($\approx$0.2 kcal mol^{-1}), and instead, the key difference is the lower proportion of substrate bound within cage.

16.4 Base-Free Michael Addition Catalysis

Utilizing cationic cages to catalyze reactions that proceed via anionic intermediates sounds like an obvious strategy, yet it has rarely been described [16]. This is in contrast to the catalysis that has been described to Raymond, Bergman, and Toste, who

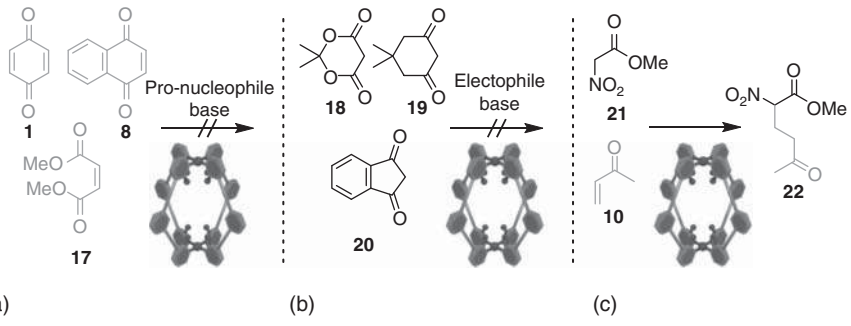

Figure 16.7 Pd_2L_4-mediated Michael addition using strongly bound (a) electrophiles and (b) pro-nucleophiles do not show any reaction, whereas using weakly binding Michael donor and acceptors leads to catalysis. Source: Wang et al. [18]. Reproduced with permission of American Chemical Society.

have used an anionic cage to catalyze several reactions that involve cationic species [17]. This disparity seems surprising, yet there may be some specific reasons, for example, anionic species (unlike cations) are less well stabilized by the flat aromatic ligands that feature in most coordination cages. Anions are also coordinating, which can lead to the possibility of cage degradation.

Using the same Pd_2L_4 cages, it was envisaged that Michael addition was an obvious starting point because a bound quinone would act as an activated Michael acceptor. The single-substrate binding strategy we had successfully employed to aid turnover with DA catalysis was also targeted for Michael addition. However, initial attempts at Michael addition using this approach mirrored our early trials with DA reactivity, namely no catalysis was observed (Figure 16.7a,b), first using quinones (e.g. **1** and **8**) and other complementary electrophiles (e.g. **17**), and then with strongly interacting pro-nucleophiles (e.g. **18**–**20**), in this latter case reasoning that catalysis would be facilitated by the cage reducing the substrate's acidity [18]. It was only when we (speculatively) tried catalysis with both weakly interacting pro-nucleophiles and electrophiles, as exemplified using methyl vinyl ketone, **10**, and methyl nitroacetate, **21**, both of which bind with association constants of less than 30 M^{-1}, that we observed clear rate enhancements. Also, this time the CH-cage delivered activity, whereas the N-cage showed none.

Our initial experiments showed that **10** and **21** react very quickly (less than 30 minutes) in the presence of both the CH-cage and organic base 1,8-Diazabicyclo(5.4.0)undec-7-ene (DBU) (0.5 equivalent with respect to cage), whereas the reaction with base only took days to complete under otherwise identical conditions. The reaction still proceeds to completion even in the presence of just CH-cage, which is remarkable since it lacks both Brønsted base and Lewis acid sites, and only interacts with the substrates using electrostatic interactions. Under the reaction conditions, using non-anhydrous dichloromethane, it appears that water deprotonates the bound pro-nucleophile. Considering that the pK_a of hydronium and **21** are −1.7 and +5.7, respectively, the CH cage activates the pro-nucleophile by the equivalent to several acidity units. Furthermore, catalysis can be significantly enhanced by stabilizing hydronium using 18-crown-6.

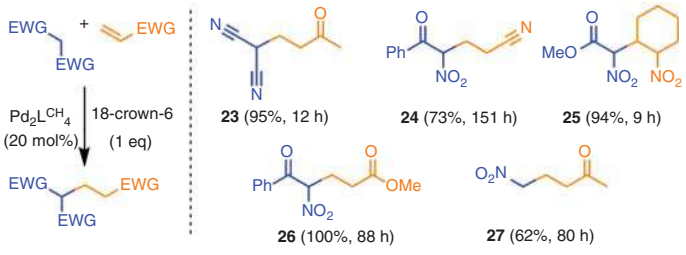

Figure 16.8 Michael addition non-covalent catalysis. The synergistic use $Pd_2\mathbf{L}^{\mathbf{CH}}{}_4$ and 18-crown-6 facilitates a wide substrate scope.

The synergistic use of the CH-cage and 18-crown-6 facilitates the Michael addition of a number of different electrophiles and pro-nucleophiles to give products **23**–**27** (Figure 16.8) [18]. Moreover, it appears that the use of weakly binding substrates is a pre-requisite for catalysis. This would imply that the cage must bind both reactants, at least transiently, which would explain why strategies involving either highly complementary electrophiles or pro-nucleophiles that block both H-bond donor pockets do not work. The use of weakly binding substrates is not a common concept in bioinspired cage catalysis, where a complementary substrate is often viewed as a key factor.

The interesting selectivity that occurs with other examples of enclosed catalysts is also observed in the catalytic Michael addition to give product **25** [18]. In this instance, catalysis with the cage leads to only two out of a possible four diastereoisomers, whereas the same reaction mediated by DBU gives all compounds in a roughly equal amount. This selectivity arises in the C—H bond forming step that follows the initial carbanion addition. Calculations suggest that the *anti*-diastereomers are favored as the pseudo-axial anionic intermediate, **25-I**$^-$, is energetically favored inside the cage and that this intermediate is setup to undergo intramolecular proton transfer (Figure 16.9).

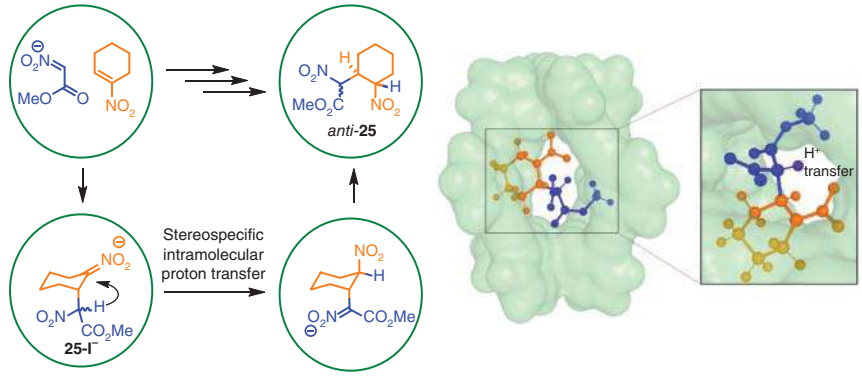

Figure 16.9 Pd_2L_4-catalyzed stereoselective Michael addition. Source: Wang et al. [18]. Reproduced with permission of American Chemical Society.

16.5 Turning Cage-Catalysis Inside Out

The basic premise of bioinspired cage catalysis is that substrates are converted into products within a well-defined microenvironment that is distinct from the bulk phase. We have recently shown a different approach, one where substrates are transformed into the products in the bulk phase, and instead the cage's interior is used to bind and alter the properties of a reagent that would otherwise be incapable of promoting a chemical transformation. This type of approach can be seen as analogous to the non-covalent manipulation of co-factors that take place in nature.

Quinones are known as reagents in organic synthesis, with electron-deficient variants such as 2,3-Dichloro-5,6-dicyano-1,4-benzoquinone (DDQ) being able to act as mild, stoichiometric $2(H^+ + e^-)$ oxidant. We have shown that binding electron-deficient quinones, in this case *p*-fluoranil, **28**, inside the CH-cage completely changes the properties of this compound; encapsulated **28** does not act as a stoichiometric oxidant but rather as a catalytic single electron acceptor [19]. This property has been used to trigger both [2+2] and [4+2] cycloaddition reactions with electron-rich substrates such as *trans*-anethole, **29**, and *N*-methylvinyl carbazole, **30**, to give a range of products, including homocyclobutyl dimers (e.g. **31** and **32**), heterocyclobutyl adducts (e.g. **33**–**36**), and cyclohexenyl compounds (e.g. **37**–**41**). In the absence of either cage or **28**, there is no reaction and similarly when the cavity is blocked by anthraquinone (Figure 16.10).

The cage plays several key roles in this catalysis. First, that cationic framework protects the semi-quinone radical-anion from being protonated; hence, why it acts as a single electron acceptor. Next, the cage dramatically shifts the reduction potential of quinone guests – by a roughly uniform 1 V. This shift corresponds to a remarkable 22 kcal mol^{-1} in radical-anion stabilization energy. It is also likely that the cationic cage promotes a radical chain reaction as back electron transfer from the encapsulated radical-anion to the radical-cationic product would necessitate interaction with the positively charged cage framework. Indeed, support for a chain-propagation

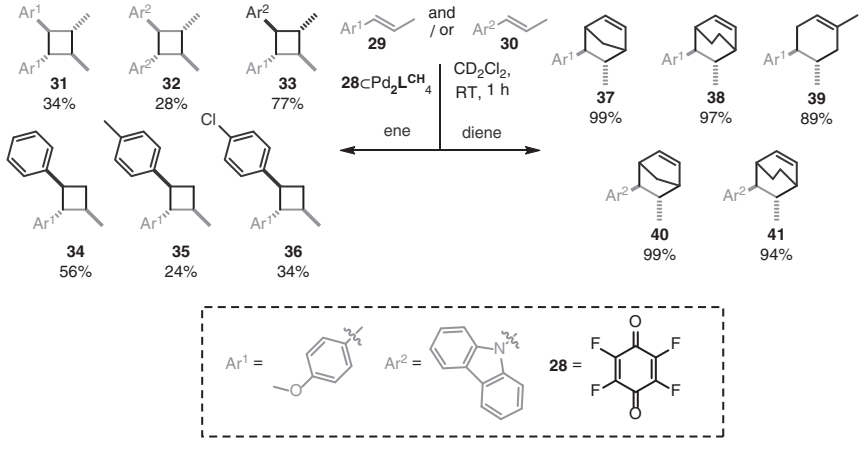

Figure 16.10 Radical-cation "exo-catalysis."

mechanism is provided by catalytic loading; the formation of compound **39** occurs in close to quantitative yield with just 1 mol% **28**⊂$Pd_2\mathbf{L}^{\mathbf{CH}}{}_4$.

16.6 Concluding Remarks

Our approach to cage catalysis – one that is underpinned by the electrostatic stabilization of intermediates and TS – has revealed several features and advantages that are distinct from many other earlier bioinspired methods. We have been able to show that this method of cage catalysis can be applied to the types of transformations that have previously been considered incompatible due to product inhibition (e.g. bimolecular fusion reactions). These processes are not only inherently more synthetically relevant, but these are also transformations where the cage's cavity can be used to influence factors such as selectivity. The catalytic activity we have observed – be it matching the selective stabilization that is observed with catalytic antibodies, or being able to promote carbanion reactions without the use of base – shows that non-covalent catalysis using supramolecular constructs can be advantageous compared to small-molecule systems that use only weak interactions. Considering that our results have been obtained by engineering simple, existing systems to unlock their catalytic properties, would suggest that there could be significant untapped potential in the many hundreds of fascinating cage structures that have appeared in the last two decades.

Acknowledgments

The catalysis that been described in this chapter has been facilitated by several funding bodies, including the EPSRC (Critical Resource Catalysis centre for doctoral training, CRITICAT, EP/L016419/1), the Leverhulme Trust (RPG-2015-232), and the University of Edinburgh via the Principal's Career Development scheme.

References

1 Chakrabarty, R., Mukherjee, P.S., and Stang, P. (2011). *Chem. Rev.* 111: 6810.
2 Yoshizawa, M., Tamura, M., and Fujita, M. (2006). *Science* 312: 251.
3 Fiedler, D., Bergman, R.G., and Raymond, K.N. (2004). *Angew. Chem. Int. Ed.* 43: 6748.
4 August, D.P., Nichol, G.S., and Lusby, P.J. (2016). *Angew. Chem. Int. Ed.* 55: 15022.
5 Liao, P., Langloss, B.W., Johnson, A.M. et al. (2010). *Chem. Commun.* 46: 4932.
6 Rideout, D.C. and Breslow, R. (1980). *J. Am. Chem. Soc.* 102: 7817.
7 Waiter, C.J., Anderson, H.L., and Sanders, J.K.M. (1993). *J. Chem. Soc., Chem. Commun.*: 458.
8 Kang, J. and Rebek, J. Jr., (1997). *Nature* 385: 50.

9 Martí-Centelles, V., Lawrence, A.L., and Lusby, P.J. (2018). *J. Am. Chem. Soc.* 140: 2862.

10 Lewis, J.E.M., Gavey, E.L., Cameron, S.A., and Crowley, J.D. (2012). *Chem. Sci.* 3: 778.

11 Young, T.A., Martí-Centelles, V., Wang, J. et al. (2020). *J. Am. Chem. Soc.* 142: 1300.

12 Kim, S.P., Leach, A.G., and Houk, K.N. (2002). *J. Org. Chem.* 67: 4250.

13 Hilvert, D. (1993). *Acc. Chem. Res.* 26: 552.

14 Wittkopp, A. and Schreiner, P.R. (2003). *Chem. Eur. J.* 9: 407.

15 Marti-Centelles, V., Spicer, R.L., and Lusby, P. (2020). *J. Chem. Sci.* 11: 3236.

16 Murase, T., Nishijima, Y., and Fujita, M. (2011). *J. Am. Chem. Soc.* 134: 162.

17 Hong, C.M., Bergman, R.G., Raymond, K.N., and Toste, F.D. (2018). *Acc. Chem. Res.* 51: 2447.

18 Wang, J., Young, T.A., Duarte, F., and Lusby, P.J. (2020). *J. Am. Chem. Soc.* 142: 17743.

19 Spicer, R.L., Stergiou, A.D., Young, T.A. et al. (2020). Host–guest-induced electron transfer triggers radical-cation catalysis. *J. Am. Chem. Soc.* 142: 2134.

17

Supramolecular Catalysis with a Cubic Coordination Cage: Contributions from Cavity and External-Surface Binding

Christopher G. P. Taylor and Michael D. Ward

University of Warwick, Department of Chemistry, Coventry, CV4 7AL, UK

17.1 Introduction: The Host Cage and Its Structure

Host–guest interactions are involved in a wide range of catalyzed reactions in biological systems, where an enzyme (host) interacts with a substrate (guest) to greatly enhance conversion to a desired product. Artificial molecular capsules within supramolecular chemistry, such as metal/ligand coordination cages, exploit similar interactions to facilitate guest binding in the interior cavity [1]. Such guest binding in a confined environment, which is quite different from that in bulk solution, can alter the reactivity of a bound guest, providing the basis for a cage-based catalytic process. This may arise in various ways including colocation of the substrate with a reaction partner leading to a higher effective concentration of reacting species; electronic effects whereby a high charge on the cage stabilizes protonated or deprotonated states of the bound guest; or conformational effects, such as folding of a flexible guest when it binds inside a geometrically constrained cavity into a conformation closely related to a reaction transition state [1].

Here we briefly describe catalytic reactions associated with an M_8L_{12} cubic coordination cage which binds hydrophobic organic guests inside its central cavity, as well as accumulating anionic species such as hydroxide ions or phenolate anions around the cationic exterior surface. This colocation of reaction partners, where the cavity-bound guest is surrounded by a shell of surface-bound anions at a high local concentration, provides the basis for the effective catalysis of the Kemp elimination reaction [2], as well as an unusual autocatalytic effect [3]. In some cases, the colocation of hydrophobic substrate and anionic reaction partner does not need to happen inside the cage cavity but can also occur at the exterior surface such that some catalysis can occur outside the cage, albeit with much lower efficiency [4, 5].

The host cage used for these studies (Figure 17.1) comprises eight Co(II) ions at the corners of an approximate cube, with twelve ditopic bis-bidentate ligands spanning the edges with each ligand connecting a pair of Co(II) ions [8, 9]. The ligands' flexibility, arising from the methylene spacers, allows them to wrap around each other such that there are extensive interligand π-stacking interactions, in

Supramolecular Catalysis: New Directions and Developments, First Edition.
Edited by Piet W.N.M. van Leeuwen and Matthieu Raynal.

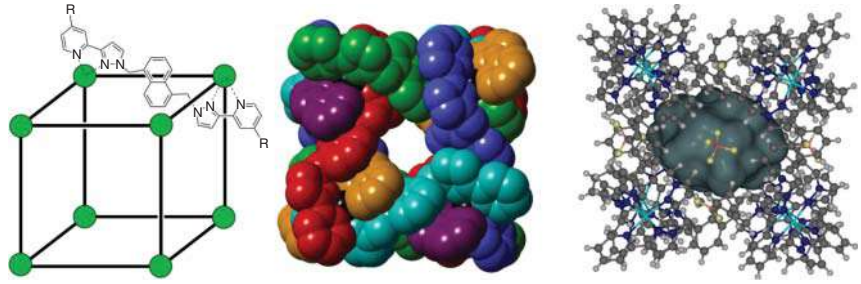

Figure 17.1 The host cages $[Co_8L_{12}]^{16+}$, abbreviated as **H** (R = H; soluble in MeCN) and $\mathbf{H^w}$ (R = CH_2OH; soluble in water), normally isolated as tetrafluoroborate salts. (a) A sketch emphasizing the cubic array of Co(II) ions and the disposition of a bridging ligand; (b) a space-filling view showing each ligand colored separately for clarity; (c) a view showing the cavity space (volume 409 Å^3). Source: (a, b) Taylor et al. [6]. CC BY 4.0, (c) Taylor et al. [7]. CC BY 4.0.

which electron-deficient (coordinated pyrazolyl-pyridine) and electron-rich (naphthyl) aromatic components alternate in the stacked arrays. The result is a robust, approximately cubic cage with a central cavity having a volume of c. 400 Å^3 and portals with a diameter of c. 4 Å in the center of each face to facilitate ingress/egress of guests. The cage (denoted **H** for "host") can be prepared using an unsubstituted pyridine ring giving a species which is soluble in polar organic solvents [8]; or with $-CH_2OH$ pendants at the C^4 position of the pyridine rings which makes the cage (denoted $\mathbf{H^w}$) soluble in water [9].

17.2 Binding of Organic Guests in the Central Cavity in Water

The ≈400 Å^3 volume of the cage cavity implies that, given Rebek's observation that an optimal guest size should be around 55 ± 9% of the cavity size for a synthetic host [10], organic molecules with a volume of 200–250 Å^3 should bind within the cage cavity subject to shape limitations. In MeCN, several polar organic species were shown to bind inside **H** via hydrogen-bonding interactions with the interior surface of the cage [9, 11]. For much stronger binding of guests, however, exploitation of the hydrophobic effect in water using isostructural host $\mathbf{H^w}$ is key, with binding constants for guests commonly in the range 10^3–10^6 M^{-1} with the exact value correlating strongly with the hydrophobic surface area of the guest [9, 12]. Based on a large number of known cage/guest binding constants, and using a molecular docking program, we could disentangle the main contributions to guest binding to the extent that we can predict binding constants of guests in water with good reliability [13].

Figure 17.2 shows the crystal structures of examples of cage/guest complexes [6, 7, 14]. In all cases, the guests have a Lewis basic site, such as carbonyl O atom of a coumarin or a ketone, which interacts with a weak H-bond donor site in a pocket within the cage interior surface that is close to the positive charge of

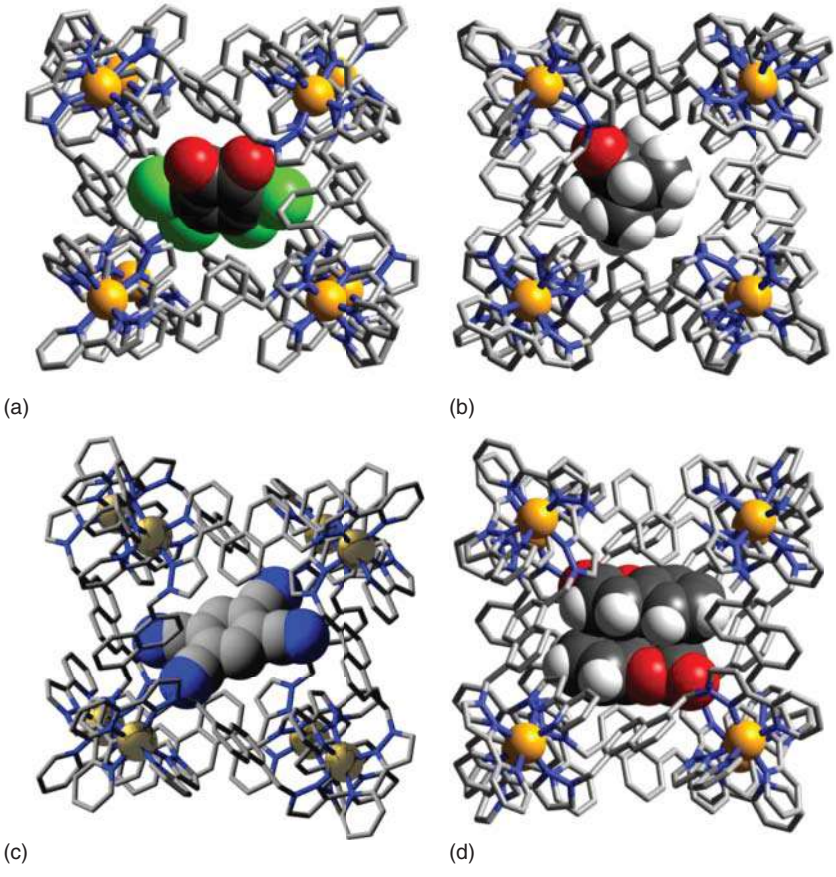

Figure 17.2 Crystal structures of some cage/guest complexes based on host cage **H** containing as guest: (a) 3,4,5,6-tetrachloroquinone [6]; (b) adamantanone [7]; (c) 1,2,4,5-tetracyanobenzene [14]; (d) two π-stacked molecules of coumarin [7]. Source: (a) Taylor et al. [6] CC BY 4.0, (b, d) Taylor et al. [7] CC BY 4.0, (c) Train et al. [14]. Reproduced with permission of American Chemical Society.

a Co(II) ion [11]. Two such binding pockets are present at diagonally opposite corners of the cavity, associated with the two octahedral metal vertices that have a *fac* tris-chelate coordination geometry. Hydrogen bonding of the guest to one of these pockets serves to orient the guest in cavity, and an appropriately sized guest such as 1,2,4,5-tetracyanobenzene (Figure 17.2c) can dock simultaneously into both pockets, spanning the long diagonal of the cage, using an opposed pair of nitrile groups as H-bond acceptor sites [14]. In some cases with planar aromatic guests (like several members of the coumarin family), a π-stacked pair of guests occupies the cage cavity in the solid state (e.g. Figure 17.2d), giving unusually high cavity occupancies of >80%. This contrasts with the behavior observed in dilute solutions where spectroscopic titrations confirm 1 : 1 binding. This indicates that the presence of a second guest in the crystals is a kinetic artifact of the "crystalline sponge" process used to prepare the crystalline host/guest complexes and does not

reflect the behavior in dilute solution where binding of the second guest is much weaker than the first ($K_2 \ll K_1$) [7].

The change in charge of acidic or basic molecules with pH has a significant effect on binding of such guests. Such a guest (that can be protonated to give a cation, as with amines; or deprotonated to give an anion, as with carboxylic acids) could undergo reversible uptake/release according to pH, with the neutral (hydrophobic) forms of the molecules showing strong binding but the charged forms being comparatively hydrophilic and therefore having binding constants that were 2–4 orders of magnitude weaker than the neutral forms [15]. With a carefully chosen mixture of three potential guests, it was possible to control the sequential uptake/release of each guest in sequence during a steady pH change [16].

17.3 Surface Binding of Anions

During our crystallographic studies on cage/guest complexes, it became apparent that a recurrent feature of the structures was the presence of anions in the windows, at the center of each face of the cage complex. Whether the anion was tetrafluoroborate, perchlorate, chloride, iodide, nitrate, or tetraphenylborate, it was clear that approximately circular portals in the face centers provide a set of CH hydrogen-bond donors that converge on each anion (Figure 17.3) [3, 8, 17].

Iodide, in particular, is a near-ideal size to occupy these portals [3], and the reader's attention is drawn to the seminal example from Lehn of a chloride ion binding very tightly in the central cavity of a pentanuclear circular helicate, based on an array of charge-assisted CH$\cdots$X interactions [18]. Figure 17.3 shows examples of the host cage with different anions in the windows, providing in every case an octahedral

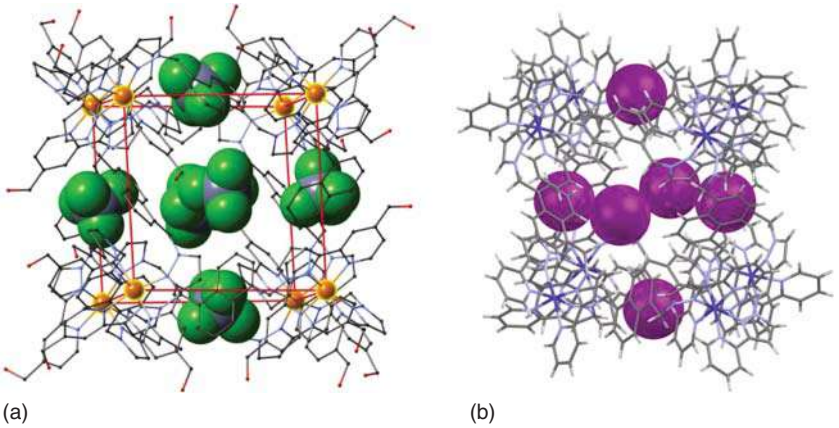

(a) (b)

Figure 17.3 Crystal structures of different salts of the host system showing the location of anions in the windows in the center of each face, giving an octahedral array of surface-bound anions surrounding the central cavity: (a) **H^{W}** as its tetrafluoroborate salt [9]; (b) **H** as its iodide salt [3]. Chloride [3] and nitrate [17] behave similarly.

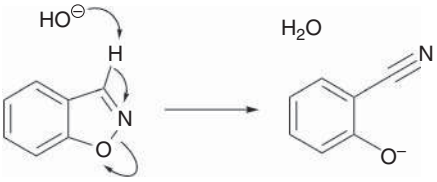

Scheme 17.1 The Kemp elimination reaction.

array of anions surrounding the cavity where the organic guest binds: this turns out to be crucial for the catalysis.

17.4 The Paradigm: Catalysis of the Kemp Elimination

Benzisoxazole is one of many small, hydrophobic organic molecules that binds in the cavity of $\mathbf{H^w}$ in water with $K \approx 4000\ M^{-1}$. Benzisoxazole has been known since the 1970s to undergo the "Kemp elimination" reaction (Scheme 17.1), an E2 elimination whereby removal of the isoxazole CH proton by base triggers rearrangement to give the 2-cyanophenolate anion [19]; the reaction has become a popular standard that has been used as a convenient way to test the efficiency of a wide range of artificial catalysts and enzyme mimics [20, 21]. We found that the Kemp elimination reaction was massively accelerated by cage $\mathbf{H^w}$ with an increase in the rate constant for the catalyzed reaction compared to the uncatalyzed background reaction by a factor of up to 2×10^5 depending on pH [2].

The mechanism for the catalytic rate enhancement is shown in Figure 17.4. The role of the cage is to bring together the two reaction partners – benzisoxazole and hydroxide ions – using orthogonal interactions: benzisoxazole binds inside the cage cavity because it is hydrophobic and hydroxide ions bind around the cationic cage surface at the portals in the faces due to an electrostatic ion-pairing effect [2, 22]. As we have seen, these surface portals are always occupied by anions in the crystal structures. Such a colocation of components implies that the concentration of hydroxide around the benzisoxazole guest is c. 1 M (approximately equivalent to a local pH of 14) [22]. The proximity of so many hydroxide ions to the cavity-bound substrate means that the benzisoxazole is readily deprotonated and the Kemp elimination occurs: crucially, as the product is anionic under the weakly basic reaction conditions, it is hydrophilic and therefore has a higher affinity for the aqueous phase than it does for the hydrophobic cavity, so can be replaced by another molecule of substrate [15, 16]. It is this change between the starting material being hydrophobic and the product being hydrophilic that allows catalytic turnover to occur, and the reaction can occur for >100 cycles without any loss of catalytic activity of the cage [2].

A detailed study of this reaction confirmed this general catalytic scheme: the results are encapsulated in Figure 17.5 [2]. First, although the background reaction (of benzisoxazole with hydroxide to give 2-cyanophenolate) is first order in $[HO^-]$ (black line in Figure 17.5), over a range of three pH units we observed no change in the rate of the cage-catalyzed reaction (red line in Figure 17.5). It follows that

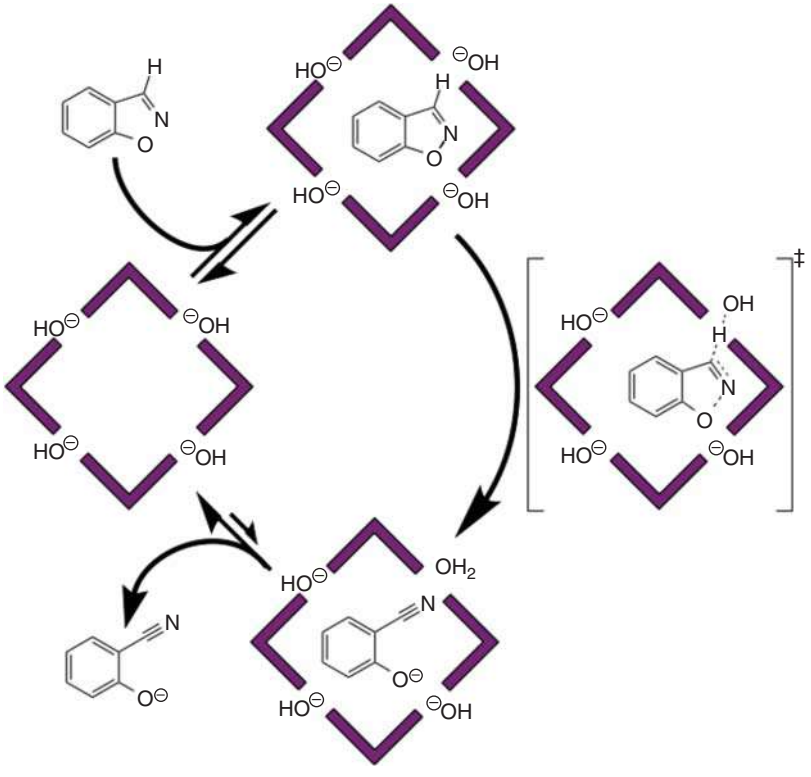

Figure 17.4 Outline of the cage-catalyzed Kemp elimination reaction, showing the role of the cage catalyst in bringing the two reaction partners together using orthogonal interactions.

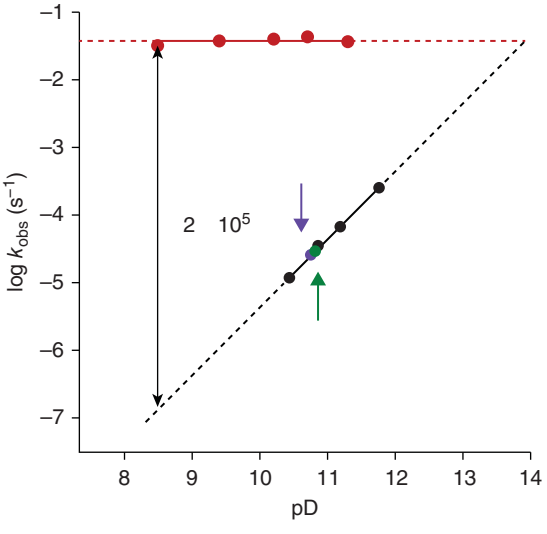

Figure 17.5 pD dependence of rate constants of the uncatalyzed Kemp elimination (black circles) and the **H**^{w}-catalyzed reaction (red circles) in D_2O at 298 K. The purple circle shows the reaction rate with catalyst, but with a competing guest (20 mM cycloundecanone) also present as an inhibitor. The green circle shows the reaction rate in the presence of catalyst, but using excess chloride as a competitor for the hydroxide binding sites.

as the bulk pH (or pD, in D_2O) drops and the background reaction gets slower, the difference between rates of catalyzed and uncatalyzed reactions increases to a value of $k_{cat}/k_{uncat} = 2 \times 10^5$ at pD 8.5: at lower pD values than this, the 2-cyanophenolate product is not fully deprotonated and therefore remains bound in the cavity in its neutral form, inhibiting further reaction.

How is it that a reaction that is first order in $[HO^-]$ can show no change in rate over three pH units? The answer is that the 16+ cage surface is so good at accumulating anions around its surface that, even at modest pH values, the cage surface is saturated with anions, and increasing the pH provides no scope for increasing the local concentration of HO^- ions around guest. The crossing point of the red and black lines in Figure 17.5 shows that the rate of the catalyzed reaction is the same as that of the uncatalyzed reaction at pD 13.8: in other words, the bound guest, surrounded by surface-bound HO^-/DO^- ions, reacts as if it were at pD 13.8 even when the pD of the bulk solution is only 8.5. This is approximately consistent (within an order of magnitude) with the estimated local concentration of HO^-/DO^- ions surrounding the guest, as mentioned earlier [22].

The implication is that the cationic cage surface is extremely effective at binding anions in dilute solutions, and indeed this accumulation of anions around positive surfaces is well known in other contexts and examples range from the Stern layer of anions around cationic micelle surfaces [23] to formation of the electrical double layer around electrodes in electrochemical experiments. Another parallel with reactions in micelles is that this cage-mediated catalysis accelerates a bimolecular reaction by an increased local concentration of the reagents, rather than greater reactivity of the reactants within the isolated micellar environment [24, 25].

Two essential control experiments confirmed the combined participation of cavity-bound benzisoxazole and surface-bound hydroxide ions in this catalytic process (Figure 17.5) [2]. First, in the presence of the competing, strongly binding but unreactive guest cycloundecanone [12], the reaction rate is reduced to the background level as the cavity is blocked and benzisoxazole cannot bind: thus, catalysis is associated with cavity binding and is stopped by a competitive inhibitor. Second, in the presence of excess chloride, the catalysis is also stopped, and the reaction rate reduced to the background level – even with the guest still bound in the cavity. This is because chloride ions, which are more easily desolvated than hydroxide ions [26], preferentially accumulate around the cationic but hydrophobic cage surface, displacing the hydroxide ions. Thus, the role of the cage catalyst in bringing both cavity-bound guest and surface-bound hydroxide ions into close proximity, via different interactions with the cage, is proven.

17.5 Effects of Anion Accumulation Around the Surface: Autocatalysis

The implication of the above results is that we can control which anions accumulate around the cage surface and therefore react with the cavity-bound guest, making the cubic cage a potentially general platform for a wide range of catalytic reactions. An

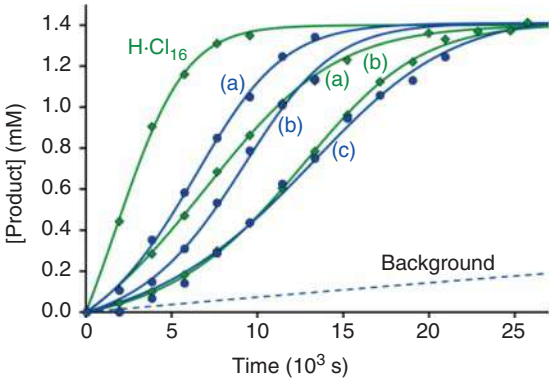

Figure 17.6 Comparison of the inhibiting effects on the **H**-catalyzed Kemp elimination of added chloride (green curves: (a) +16 mM chloride in addition to **H·Cl$_{16}$**, (b) +32 mM) and fluoride (blue curves: (a) +16 mM fluoride in addition to **H·Cl$_{16}$**, (b) +32 mM, (c) +111 mM); the sigmoidal shape of the curves at high halide concentrations indicates onset of autocatalysis.

unexpected example of this emerged when we were looking at the effects of halide (F^- and Cl^-) ions as inhibitors of the cage-catalyzed Kemp elimination, this time using unsubstituted cage **H** as the catalyst (as its chloride salt to provide the necessary water solubility) [3]. Adding either F^- or additional Cl^- slowed down the reaction due to displacement of hydroxide from the surface of the cage by the halide, with chloride showing a greater effect (smaller quantity needed for the same degree of inhibition of the Kemp elimination).

We noted, however, that as larger amounts of halide ions were added, the reaction progress not only slowed, because of the expected inhibition, but the reaction progress curve became sigmoidal in shape (Figure 17.6), which is indicative of autocatalysis, i.e. catalysis of the reaction by its product. When this occurs, the reaction starts slowly as there is no catalyst (product) present, and it gets faster as product accumulates, until all of the starting material is exhausted at which point the reaction stops. This combination of factors generates the characteristic sigmoidal shape. In this case, the product is the 2-cyanophenolate anion, and clearly it is facilitating further turnovers of the Kemp elimination on cavity-bound benzisoxazole.

As a "soft" anion (large, relatively hydrophobic and easily desolvated), we suggest that the 2-cyanophenolate anion can itself accumulate around the cage surface, in preference to both chloride and hydroxide. The consequence is that 2-cyanophenolate becomes the base (instead of a surface-bound hydroxide ion) which deprotonates another molecule of cavity-bound benzisoxazole, thereby generating more 2-cyanophenolate and perpetuating the cycle until the starting material is consumed. Thus, we have a situation that (i) when hydroxide is the surface-bound base, the (catalyzed) Kemp elimination occurs; (ii) when excess chloride or fluoride is added, hydroxide is displaced from the cage surface and the reaction slows down, but eventually (iii) 2-cyanophenolate starts to accumulate and displaces the halide ions from around the cage surface due to their easier desolvation, re-starting the reaction in an autocatalytic manner because of the basicity of the phenolate ion. Confirmation of this mechanism is provided by inhibiting the catalyzed Kemp elimination reaction using excess fluoride around the cage surface and then spiking the reaction mixture with phenolate salts of varying pK_a to re-start the reaction. The rate at which the reaction occurs after

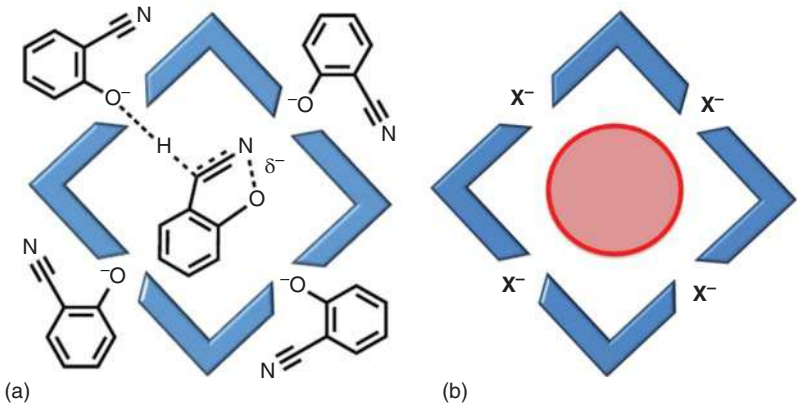

Figure 17.7 (a) The autocatalytic Kemp elimination, illustrating how surface-bound 2-cyanophenolate anions act as bases to propagate the reaction by deprotonating a bound benzisoxazole substrate; (b) a more general cartoon illustrating the role of the cage (blue) in co-locating a hydrophobic organic substrate (red) in the cavity with X^- anions that accumulate in the surface portals.

re-starting correlated well with the basicity of the phenolate anions: thus, addition of 3-chlorophenolate (pK_a 9 for the parent phenol) as the surface-bound base gave reaction progress four times faster than addition of 2-cyanophenolate (pK_a 7 for parent phenol) [3]. Thus, we can control which base (hydroxide or phenolate) binds to the cage surface and deprotonates the cavity-bound guest (Figure 17.7a), which implies that it should be possible to control catalysis more generally using different substrate/anion combinations as illustrated in cartoon form in Figure 17.7b.

17.6 Catalysis with Noncavity-Bound Guests: Phosphate Ester Hydrolysis and an Aldol Condensation

To broaden the search for types of reaction that might be catalyzed by the cage on the basis outlined above, we looked at hydrolysis of organic phosphate esters, whose toxicity has led to their use as insecticides and chemical warfare agents. As such, accelerated hydrolysis using supramolecular catalysis is an obviously appealing target for decontamination purposes.

We started with the insecticide molecule "dichlorvos" (2,2′-dichlorovinyl dimethyl phosphate) which binds weakly in the cage cavity ($K \approx 30\ M^{-1}$) in water; the crystal structure of the cage/guest complex is shown in Figure 17.8a [4]. Monitoring the hydrolysis of this by ^{31}P NMR spectroscopy at pD 7.7 showed a significant rate enhancement in the presence of $\mathbf{H^w}$: consideration of the (small) fraction of dichlorvos that would be bound inside the cage cavity of $\mathbf{H^w}$ led to the conclusion that cavity-bound dichlorvos underwent hydrolysis around 700 times faster than happened free in solution under the same conditions. Similar results were obtained for hydrolysis of 2-nitrophenyl-dimethylphosphate for which the rate acceleration in

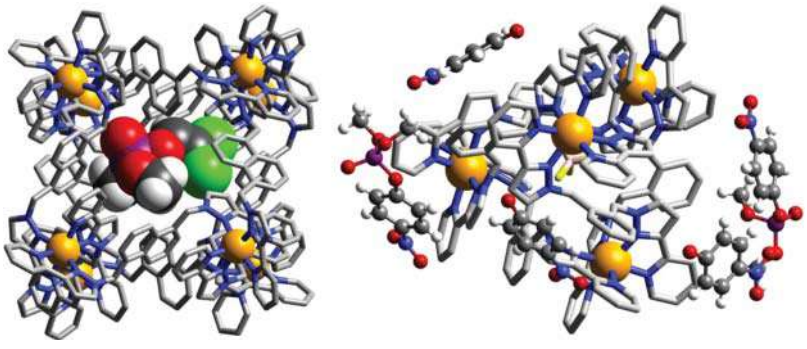

Figure 17.8 (a) Crystal structure of the complex of **H** with dichlorvos in the cavity; (b) crystal structure of a tetrahedral M_4L_6 cage incorporating in the lattice molecules of both substrate "Paraoxon-methyl" (on the left and right edges of the image) as well as hydrolyzed product (4-nitrophenolate anions). Source: Taylor et al. [4]. CC BY 4.0.

the presence of $\mathbf{H^w}$ was consistent with a 1000-fold increase in rate of hydrolysis for that fraction that is cavity-bound.

The obvious control experiment, however, yielded a quite unexpected observation: in the presence of excess cycloundecanone to block the cavity, the rate enhancements for hydrolysis of these phosphate esters did not significantly change. This implies that the catalysis does not require binding of the substrate in the cavity but could instead occur outside the cage, at the exterior surface. The same hydrophobic interaction that facilitates guest binding inside the cavity, which maximizes contacts between hydrophobic surfaces of host and guest when the guest is a good fit, will equally facilitate contacts between hydrophobic host and guest regions on the outer surface of the cage, and such contacts may be important if the guest is not actually a good fit for the cavity for size/shape reasons [6]. The same ion-pairing interaction that results in the 16+ cage surface accumulating anions around it still operates of course, and the result is that the phosphate ester substrates and the hydroxide ions are still brought into proximity by their distinct interactions with the cage exterior surface, accounting for the rate enhancement that we see (which, unsurprisingly, is substantially lower than we observed for the Kemp elimination).

This observation prompted two additional experiments which led to the same conclusion. First, the possible substrate 4-nitrophenyl-dimethylphosphate (the insecticide "Paraoxon-methyl"), which does not bind in the cavity for steric reasons, showed a very similar catalyzed rate enhancement to its isomer 2-nitrophenyl-dimethylphosphate which can bind (weakly) in the cage cavity. Second, use of a smaller tetrahedral cage with an M_4L_6 architecture whose central cavity is far too small to bind these phosphate esters also afforded a similar catalytic rate enhancement for hydrolysis of 4-nitrophenyl-dimethylphosphate to what we observed with $\mathbf{H^w}$ as the catalyst. Indeed we isolated from the NMR reaction experiment a crystal containing tetrahedral cage catalyst with both Me-paraoxon (substrate) and 4-nitrophenolate anions (product) in a single structure. Whilst

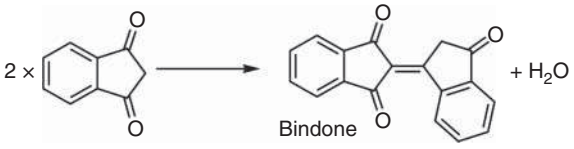

Scheme 17.2 Aldol self-condensation of indane-1,3-dione (ID) to give "bindone."

such a structure (Figure 17.8b) is not in itself an indication of the catalytically relevant species in solution, it provides a pleasing illustration of the catalyst, starting material and product in a single assembly in which no binding of substrate inside the small and nonaccessible cage cavity is possible [4].

The conclusion is unequivocal: catalysis by the cage is not solely the privilege of the central cavity but can also occur at the exterior surface where the same orthogonal interactions allow substrate and anion to be brought into proximity. The catalytic rate enhancements are much less impressive when the cavity is not involved, as the substrate is not positioned at the center of a shell of desolvated, surface-bound anions [2, 22]. However, the lack of shape/size limitations that apply to cavity binding potentially make the catalysis associated with the hydrophobic but cationic exterior surface of the cage much more general [4].

In a similar vein, we discovered that $\mathbf{H}^{\mathbf{w}}$ catalyzes an aldol condensation reaction [5]. When measuring the binding constant of the guest indane-1,3-dione ($K \approx 2000\ M^{-1}$), we noticed that solutions containing both $\mathbf{H}^{\mathbf{w}}$ and indane-1,3-dione developed a deep purple color, which is characteristic of the formation of the aldol self-condensation product "bindone" (Scheme 17.2). The CH_2 group in the saturated ring is acidic ($pK_a \approx 7$), which means that the enolate forms, and the condensation can occur, even under mild conditions. At pH 3.4, the catalyzed reaction is slow (few % conversion after several hours), but the background reaction is completely absent, and blocking the cavity with cycloundecanone resulted in no loss of catalysis, implying that reaction occurs at the exterior surface of the cage. Again, as with the phosphate esters [4], the cage acts to bring together both the hydrophobic, neutral indane-1,3-dione and its anionic enolate (a soft, easily desolvated anion which should have a high affinity for the cage surface following the discussion above), via two different types of interaction [5]. The potential generality of this is obvious, and current work is focused on the investigation of stabilization of enolate anions, and hence catalyzing reactions with them, with a variety of substrates.

17.7 Conclusion

The cubic coordination cage $\mathbf{H}^{\mathbf{w}}$ has an extremely well-developed host–guest chemistry and displays highly effective catalysis of the Kemp elimination reaction, up to 2×10^5-fold, because the cavity-bound guest (strongly bound due to the hydrophobic effect) is surrounded by a high local concentration of surface-bound hydroxide ions (due to ion-pairing around the 16+ cage), even at modest pH values. Thus, the cationic but hydrophobic cage serves to colocate the two reaction partners,

benzisoxazole and hydroxide, in a small volume using two orthogonal interactions. Accumulation of the 2-cyanophenolate product from the Kemp elimination around the cage surface can lead to autocatalysis under some conditions. More generally, the same interactions with guest molecules can operate at the cage exterior surface, allowing hydrophobic guests that do not bind strongly in the central cavity to interact with the cage exterior surface, thereby bringing them into proximity with the anionic reaction partners that concentrate around the 16+ cage. Catalysis based on this effect is much less effective than when the substrate is cavity-bound, but is still significant, and has the potential to be highly general as it is independent of the shape/size limitations of the cage cavity.

Acknowledgments

The PhD students, postdoctoral fellows, and undergraduate researchers who contributed to this work are warmly thanked; their names are in the reference list. Profs. Chris Hunter (Cambridge) and Nick Williams (Sheffield) were invaluable collaborators in understanding the host–guest chemistry of the cage, and its catalysis mechanisms, respectively. Thanks are also due to EPSRC, EU, and the Leverhulme Trust for funding.

References

1 Brown, C.J., Toste, F.D., Bergman, R.G., and Raymond, K.N. (2015). Supramolecular catalysis in metal-ligand cluster hosts. *Chem. Rev.* 115: 3012–3035.
2 Cullen, W., Misuraca, M.C., Hunter, C.A. et al. (2016). Highly efficient catalysis of the Kemp elimination in the cavity of a cubic coordination cage. *Nat. Chem.* 8: 231–236.
3 Cullen, W., Metherell, A.J., Wragg, A.B. et al. (2018). Catalysis in a cationic coordination cage using a cavity-bound guest and surface-bound anions: inhibition, activation and autocatalysis. *J. Am. Chem. Soc.* 140: 2821–2828.
4 Taylor, C.G.P., Metherell, A.J., Argent, S.P. et al. (2020). Coordination-cage-catalysed hydrolysis of organophosphates: cavity- or surface-based? *Chem. Eur. J.* 26: 3065–3073.
5 Mozaceanu, C., Taylor, C.G.P., Piper, J.R. et al. (2020). Catalysis of an aldol condensation using a coordination cage. *Chemistry* 2: 22–32.
6 Taylor, C.G.P., Train, J.S., and Ward, M.D. (2020). Interactions of small-molecule guests with interior and exterior surfaces of a coordination cage host. *Chemistry* 2: 510–524.
7 Taylor, C.G.P., Argent, S.P., Ludden, M.D. et al. (2020). One guest or two? A crystallographic and solution study of guest binding in a cubic coordination cage. *Chem. Eur. J.* 26: 3054–3064.
8 Tidmarsh, I.S., Faust, T.B., Adams, H. et al. (2008). Octanuclear cubic coordination cages. *J. Am. Chem. Soc.* 130: 15167–15175.

9 Whitehead, M., Turega, S., Stephenson, A. et al. (2013). Quantification of solvent effects on molecular recognition in polyhedral coordination cage hosts. *Chem. Sci.* 4: 2744–2751.

10 Mecozzi, S. and Rebek, J. (1998). The 55% solution: a formula for molecular recognition in the liquid state. *Chem. Eur. J.* 4: 1016–1022.

11 Turega, S., Whitehead, M., Hall, B.R. et al. (2013). Shape-, size- and functional group-selective binding of small organic guests in a paramagnetic coordination cage. *Inorg. Chem.* 52: 1122–1132.

12 Turega, S., Cullen, W., Whitehead, M. et al. (2014). Mapping the internal recognition surface of an octanuclear coordination cage using guest libraries. *J. Am. Chem. Soc.* 136: 8475–8483.

13 Cullen, W., Turega, S., Hunter, C.A., and Ward, M.D. (2015). Virtual screening for high affinity guests for synthetic supramolecular receptors. *Chem. Sci.* 6: 2790–2794.

14 Train, J.S., Wragg, A.B., Auty, A.J. et al. (2019). Photophysics of cage/guest assemblies: photoinduced electron transfer between a coordination cage containing osmium(II) luminophores and electron-deficient bound guests in the central cavity. *Inorg. Chem.* 58: 2386–2396.

15 Cullen, W., Turega, S., Hunter, C.A., and Ward, M.D. (2015). pH-dependent binding of guests in the cavity of a polyhedral coordination cages: reversible uptake and release of drug molecules. *Chem. Sci.* 6: 625–631.

16 Cullen, W., Thomas, K.A., Hunter, C.A., and Ward, M.D. (2015). pH-controlled selection between one of three guests from a mixture using a coordination cage. *Chem. Sci.* 6: 4025–4028.

17 Piper, J.R., Cletheroe, L., Taylor, C.G.P. et al. (2017). Photoinduced energy and electron-transfer from a photoactive coordination cage to bound guests. *Chem. Commun.* 53: 408–411.

18 Hasenknopf, B., Lehn, J.-M., Kneisel, B.O. et al. (1996). Self-assembly of a circular double helicate. *Angew. Chem. Int. Ed.* 35: 1838–1840.

19 Casey, M.L., Kemp, D.S., Paul, K.G., and Cox, D.D. (1973). Physical organic chemistry of benzisoxazoles. 1. Mechanism of the base-catalyzed decomposition of benzisoxazoles. *J. Org. Chem.* 38: 2294–2301.

20 Chowdhury, R. and Maranas, C.D. (2020). From directed evolution to computational enzyme engineering: a review. *AlChE J.* 66: e16847.

21 Mirata, F. and Resmini, M. (2015). Molecularly imprinted polymers for catalysis and sensing. *Adv. Biochem. Eng. Technol.* 150: 107–109.

22 Ward, M.D., Hunter, C.A., and Williams, N.H. (2018). Coordination cages based on bis(pyrazolylpyridine) ligands: structures, dynamic behaviour, guest binding and catalysis. *Acc. Chem. Res.* 51: 2073–2082.

23 Stigter, D. (1975). Micelle formation by ionic surfactants. III. Model of Stern layer, ion distribution and potential fluctuations. *J. Phys. Chem.* 79: 1008–1014.

24 Bunton, C.A., Nome, F., Quina, F.H., and Romsted, L.S. (1991). Ion binding and reactivity at charged aqueous interfaces. *Acc. Chem. Res.* 24: 357–364.

25 Bunton, C.A. and Moffatt, J.R. (1988). Micellar effects upon substitutions by nucleophilic anions. *J. Phys. Chem.* 92: 2896–2902.

26 Buurma, N.J. (2009). Kinetic medium effects on organic reactions in aqueous colloidal solutions. *Adv. Phys. Org. Chem.* 43: 1–37.

18

Transition Metal Catalysis in Confined Spaces

Joost N.H. Reek and Sonja Pullen

University of Amsterdam, Van 't Hoff Institute for Molecular Sciences, Homogeneous and Supramolecular Catalysis, Sciencepark 904, Amsterdam, 1098 XH, The Netherlands

18.1 Introduction

Biological systems represent a source of inspiration for the development of catalytic reactions. Whereas in synthetic chemical systems, we have focused for decades on single step conversions using single catalysts of low molecular weight, in natural systems, chemical conversions take place in a soup of chemical compounds. As a consequence, enzymes – Nature's catalysts – generally display high substrate and product selectivity and at the same time are highly active. For this reason, there is a huge interest to explore chemistry on the border between supramolecular and transition metal catalysis. This has resulted in many systems in which transition metal catalysts have been installed in a molecular cage mimicking to some extent the pocket around the active site of an enzyme. Catalysis in such confined nanospaces can proceed with unusual selectivity and activity as summarized in some recent reviews [1].

18.2 Template Ligand Strategies for Encapsulation of Transition Metal Catalysts

In this context, we have developed a template-ligand strategy for catalyst encapsulation, which is a general approach allowing transition metal complexes to be positioned precisely in confined spaces [2]. Relatively simple building blocks are used that function as templates for cage formation as well as ligands for coordination to a transition metal catalyst. In the first example, we have used tris-pyridyl phosphine ligands in combination with Zn(II)TPP (TPP, tetraphenyl porphyrin), which resulted in encapsulated rhodium catalysts displaying higher activity and unusual selectivity in hydroformylation reactions (Figure 18.1) [3]. We have extended this concept further to several different reactions, including gold-catalyzed transformations [4] and asymmetric hydrogenation [5]. We also reported the use of Nitschke type subcomponent self-assembled cages based on

Supramolecular Catalysis: New Directions and Developments, First Edition.
Edited by Piet W.N.M. van Leeuwen and Matthieu Raynal.

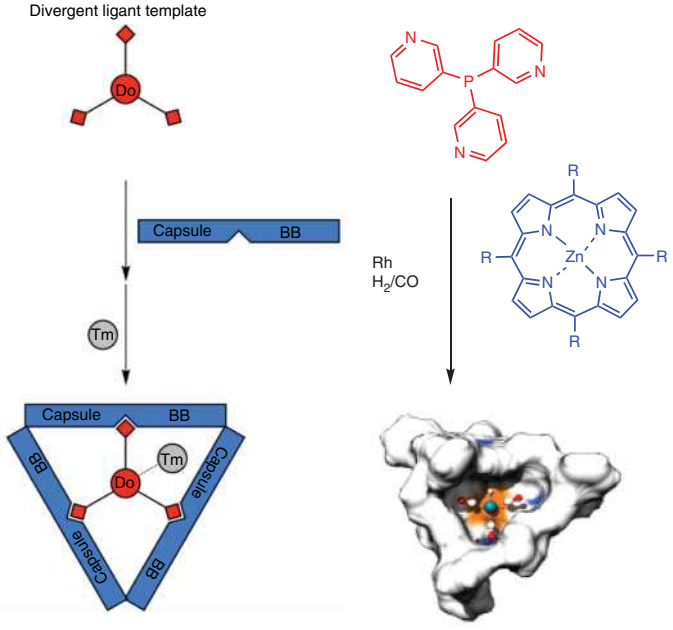

Figure 18.1 Template ligand strategy using a divergent approach leads to mononuclear complexes that are placed in well-defined cages [2]. Depicted is an example in which the self-assembly process results in a rhodium complex bound to PPy_3 (= tris-pyridyl phosphine) in confined space for hydroformylation catalysis (Do = donor, Tm = transition metal, BB = binding bridge).

Zn(II)porphyrin building blocks, which can bind catalysts via template ligands. The more rigid cage structure allows for substrate selectivity in hydroformylation catalysis [6]. Template ligands with a divergent structure lead to self-assembled architectures in which single metal complexes are formed inside of the cage. Recently, we have extended our research to convergent building blocks in which case template-ligand strategies lead to multinuclear complexes in much larger nanospheres [7]. The typical $M_{12}L_{24}$ type structures, pioneered by Fujita [8], have shown to be ideal for this purpose.

As proof-of-principle, a bent bis-pyridyl building block was functionalized with a gold(I)chloride phosphine complex (Figure 18.2) [9]. In the presence of a Pd(II) precursor, the $M_{12}L_{24}$ nanosphere forms as judged from ^{1}H-NMR, diffusion ordered spectroscopy (DOSY) NMR, and high resolution cold spray ionisation Mass spectrometry (HR-CSI-MS). Interestingly, the estimated local concentration of gold is about 1.1 M, but for catalysis, the overall concentration of the catalyst can be still at the millimolar level. The catalyst was explored in gold-catalyzed cyclization reactions, and it was established that the high local concentration of gold leads to faster catalysis.

In subsequent work, we explored the use of nanospheres in which the catalyst is bound in a non-covalent fashion. The key advantage is that the catalyst can be

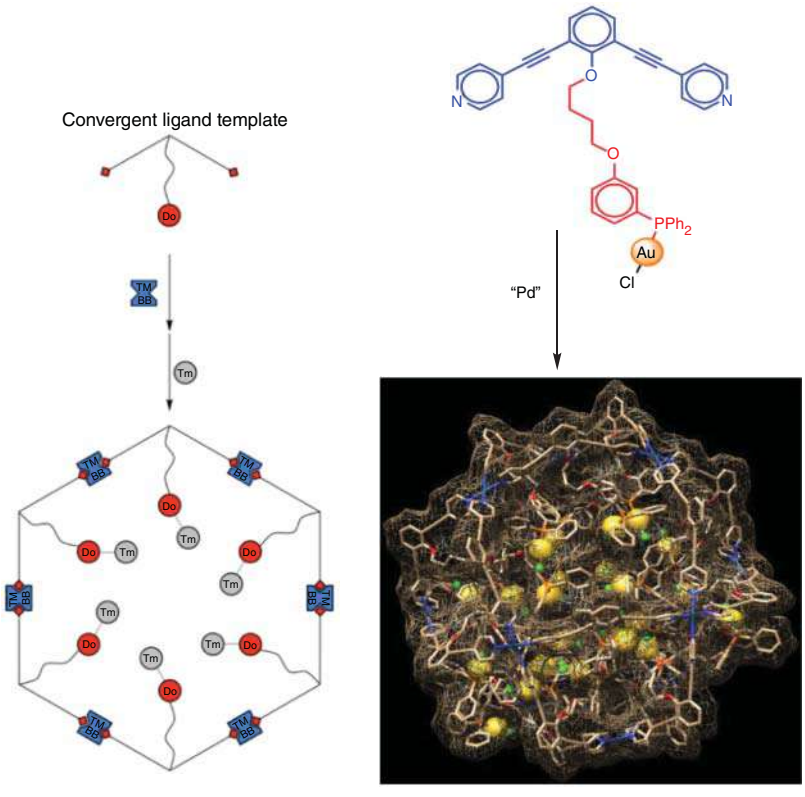

Figure 18.2 Template ligand approach using a convergent approach leads to self-assembled nanostructures with multiple metal complexes inside [2]. An example is provided in which the self-assembly process results in a $M_{12}L_{24}$ nanosphere with 24 gold catalysts inside.

independently prepared and added just before the catalytic experiment. In addition, it is very easy to vary the average local catalyst concentration inside the sphere by just varying the nanosphere/catalyst ratio. Finally, if not all binding sites are used for catalyst binding, these can be used for pre-organization of substrates in close proximity of the catalyst. This concept was first demonstrated by using building blocks containing a guanidine hydrogen bond motif (Figure 18.3) [10]. The multiple guanidinium sites in a confined space result in strong binding of sulfonate guests ($>10^5$) as the high local concentration facilitates cooperative binding. As such, the nanosphere binds up to 24 gold complexes that are supported by phosphine sulfonate ligands (TPPMS, triphenylphosphine monosulfonate). In contrast, carboxylate guests display much weaker binding (10^3). This difference makes these nanospheres perfect vehicles for substrate/catalyst pre-organization: four sulfonate-containing Au catalysts ($TPPMSAu^+$) were strongly bound within the sphere and acetylenic carboxylate substrates were pre-organized by adjacent guanidinium sites for efficient cyclization to the enol lactone. The neutral analog of the

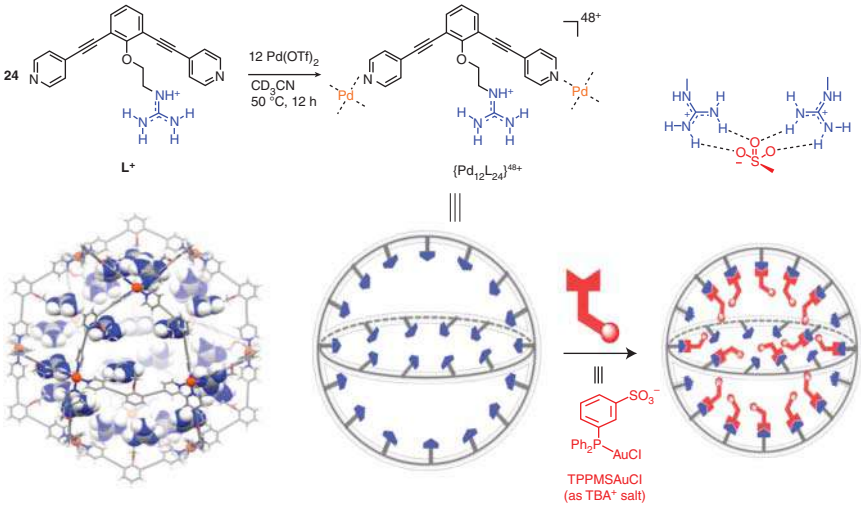

Figure 18.3 Formation of a self-assembled $M_{12}L_{24}$ nanosphere with guanidine binding sites for the non-covalent binding of catalysts that are functionalized with a sulfonate group. Binding to the guanidine is ditopic and therefore strong. An example is provided in which 24 gold complexes are bound inside the nanosphere.

substrate, acetylenic acid, has no driving force to go inside, and as such is converted slowly by the sphere-encapsulated catalysts. Base-triggered co-encapsulation of the substrates within the sphere increases the rate 40-fold.

In subsequent work, the same guanidinium cage was used to control the selectivity of cycloisomerization reactions [11]. In the gold-catalyzed transformation of 2-alkynyl benzoic acid (Figure 18.4), the five- and the six-membered ring product can be formed. When only a small number of gold catalysts are uploaded in the nanosphere (2–12 equiv), the six-membered ring product is the dominant product, whereas at high loading (18, 24 equiv), the five-membered ring product is formed.

Next to substrate/catalyst pre-organization, the same nanosphere can also be used to facilitate reactions. We recently found that the Cu(I)(Xantphos)-catalyzed cycloisomerization of 4-pentynoic acid to the corresponding enol lactone involves a bimetallic activation of the substrate [7]. Therefore, the reaction usually needs relatively high catalyst loading. Interestingly, pre-organization of copper catalysts based on SXantphos (a sulfonated analog) in a guanidinium-functionalized $M_{12}L_{24}$ nanosphere leads to high local concentrations of catalysts and results in an improved reaction rate (turnover frequency [TOF] increases by a factor of 5).

18.3 Catalyst Encapsulation Strategies for Solar Fuel-Related Reactions

In the preceding part, we have outlined template-ligand strategies for the encapsulation of transition metal complexes and we highlighted important examples of

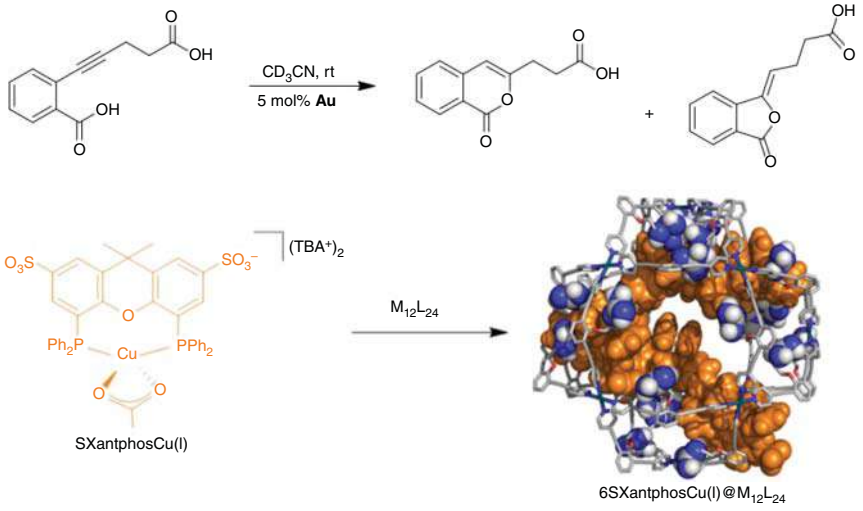

Figure 18.4 Cyclization reaction in which product formation depends on local gold catalyst concentration (24 complexes in nanosphere gives five-membered ring), and the encapsulation of six SXantphosCu(I) complexes in the nanosphere leading to faster cyclization reactions. Source: from Ref. [7]. Reproduced with permission of The Royal Society of Chemistry.

transition metal-catalyzed chemical transformations that clearly benefit from such an approach. In the following, we will briefly discuss the role of supramolecular chemistry in improving catalysis for solar fuel production – artificial photosynthesis.

Artificial photosynthesis is a discipline that aims to mimic principles of natural photosynthesis in order to convert the energy from sunlight into chemical fuels. The dominant strategy is to use sunlight as energy source to efficiently split water into molecular oxygen, protons, and electrons. Electrons released in this process are either used for the reduction of protons to form molecular hydrogen, or for the reduction of carbon dioxide, or other substrates. For water splitting driven by light, three important steps are necessary: (i) light harvesting, (ii) charge separation, and (iii) redox catalysis [12] (Figure 18.5).

A general artificial photosystem combines a light-harvesting unit (= photosensitizer) with a redox catalyst. In the eventual device, light-driven water-oxidation catalysis, using a photosensitizer catalyst pair immobilized on an electrode, should be combined with a (light-driven) reduction reaction. Such a device is referred to as dye-sensitized photo-electrochemical cells (DC-PECs). In such a setup, a photocathode based on p-type semiconductor (e.g. NiO) is functionalized with reduction catalysts and dyes as photosensitizers and the photoanode consists of a n-type semiconductor, typically TiO_2, functionalized with water oxidation catalyst and dye molecules. The properties of the different components, such as oxidation/reduction potentials, should be carefully chosen. So far, the efficiencies are limited by charge recombination processes, and by the properties of the catalysts. A recent review describes in detail the challenges associated with DC-PECs, and how supramolecular strategies can overcome these limitations [13]. In general,

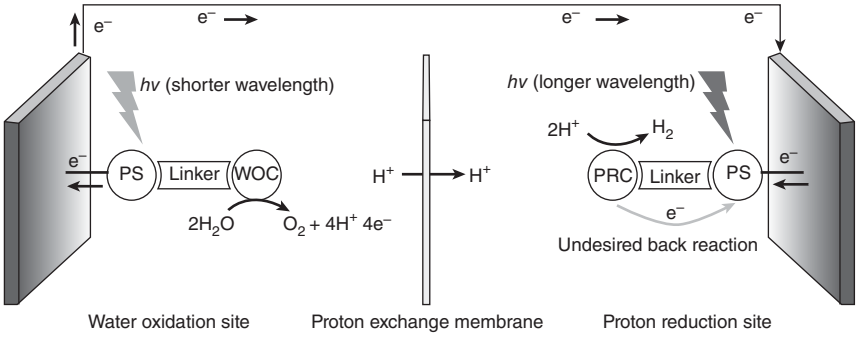

Figure 18.5 A schematic picture of an artificial photosynthetic device with an anode for light-driven water oxidation (PS = chromophore, WOC = catalyst) and a cathode for light-driven proton reduction catalysis (PS = chromophore, PRC = catalyst). Next to productive forward reaction, charge recombination takes place (light gray arrow), compromising the efficiency.

challenges that are faced for the development of the catalysts are (i) the rate of the catalysts should be sufficient (to keep pace with the photon flux), (ii) the overpotential, that is extra potential compared to the thermodynamic potential to drive the reaction, should be minimal as this directly translates into losses, and (iii) the stability of the catalyst should be high. Next to this, strategies to implement molecular components into devices should be developed. We found that molecular encapsulation can positively affect the key parameters of the redox catalysts at stake, and the use of metal–organic frameworks (MOF's), which in fact represent the heterogeneous analog of molecular capsules, may provide a useful strategy to implement such capsule strategies in devices. We will discuss these approaches in this part of the chapter. One should keep in mind that fully operational DC-PECs are the final goal, but that key properties of catalysts can be explored by evaluation of half-reactions using electrochemistry, or by applying sacrificial oxidants to study, for example, water oxidation catalysts. In a similar fashion, light-driven reactions can be studied using photosensitizers and sacrificial reductants (in case of reduction catalysts).

18.3.1 Molecular Cages for Water Oxidation Catalysis

One of the bottlenecks in artificial photosynthesis lies still in redox catalysis, especially water oxidation. Among the best molecular water oxidation catalysts known in literature are ruthenium-based complexes like $Ru(bda)(pic)_2$ (see the structure in the right in Figure 18.6). Water oxidation with these catalysts can proceed either via the oxyl radical mechanism (I2M) or via the water nucleophilic attack (WNA) mechanism (Figure 18.6). The latter follows a mononuclear pathway and, because of scaling relations, often requires a larger overpotential. The I2M has a dinuclear pathway, usually leading to higher catalytic rates at milder overpotential. However, this dinuclear pathway can be slow at low catalyst concentrations (higher order in catalyst), and the oxo-radical intermediate can lead to catalyst decomposition as it may oxidize the ligand.

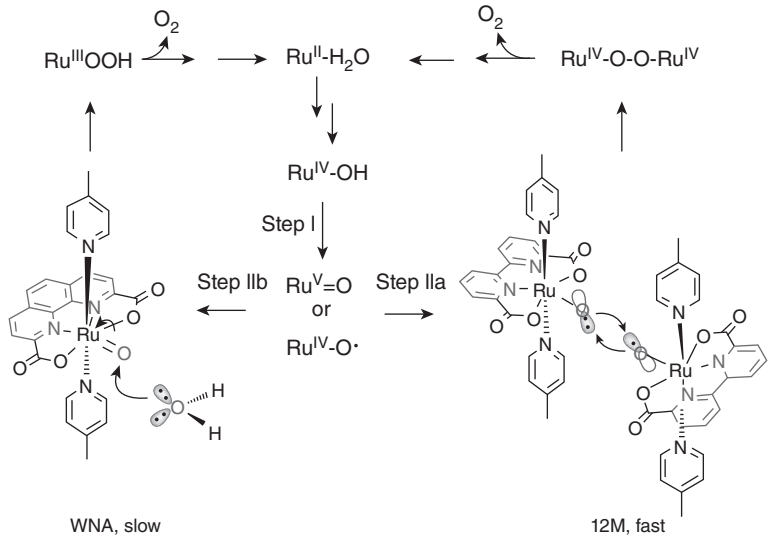

Figure 18.6 Water oxidation with ruthenium-based catalyst can follow two different reaction pathways. After two proton-coupled electron transfers, a ruthenium oxo species is formed which can be subjected either to water nucleophilic attack (WNA) or dinuclear coupling pathway. Depending on the type of ligand, either the mononuclear (phenanthroline) or dinuclear (bipyridine) pathway is preferred. Source: from Ref. [14]. Reproduced with permission of John Wiley & Sons.

As the dinuclear pathway is facilitated by high concentrations, we anticipated that using the guanidinium-functionalized $M_{12}L_{24}$ nanospheres to generate high local concentrations, as discussed in the previous section (18.2, see also Figure 18.3 and 18.4), would increase reaction rates for water oxidation catalysts such as Ru(bda)$(pic)_2$ that follow the I2M pathway. Therefore, analogs were prepared that contained sulfonated pyridine ligands for binding to the guanidinium units, leading to high local concentration of these ruthenium catalysts at typical low overall concentrations used in electrochemical experiments [14]. As indicated by electrochemical studies, confinement in the nanosphere allowed an increase in reaction rate by a factor of 140 as a result of local concentration effects. In contrast, using the phenanthroline derivative of the catalyst, which proceeds via mononuclear WNA, did not change the reaction rate by binding in the cage (see Figure 18.7). These experiments clearly demonstrate that the local concentration only plays a role for the catalyst following the I2M mechanism.

18.3.2 Molecular Cages for Proton Reduction Catalysis

[FeFe] hydrogenase are Nature's most efficient catalysts for proton reduction with TOFs reaching 9000 s^{-1} [15]. Figure 18.8 depicts a crystal structure of an [FeFe] hydrogenase that has been isolated from *Clostridium pasteurianum* in 1998 [16]. The active site consists of a dinuclear iron complex (H-cluster) bridged by a dithiolate ligand. Further three CO and two CN- ligands are coordinated to the two iron centers.

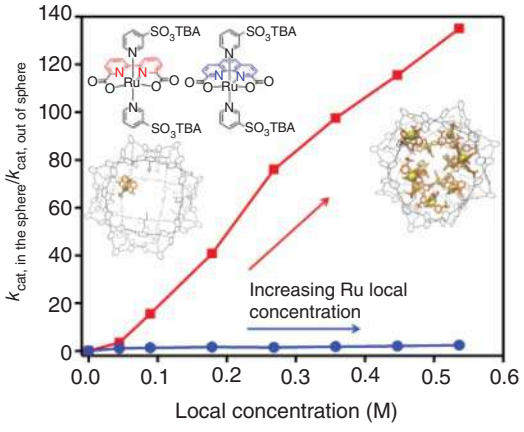

Figure 18.7 Relative rate in electrochemical water oxidation using two different catalysts. The local concentration only affects the catalysts that follow the I2M pathway (in red). Source: from Ref. [14]. Reproduced with permission of John Wiley & Sons.

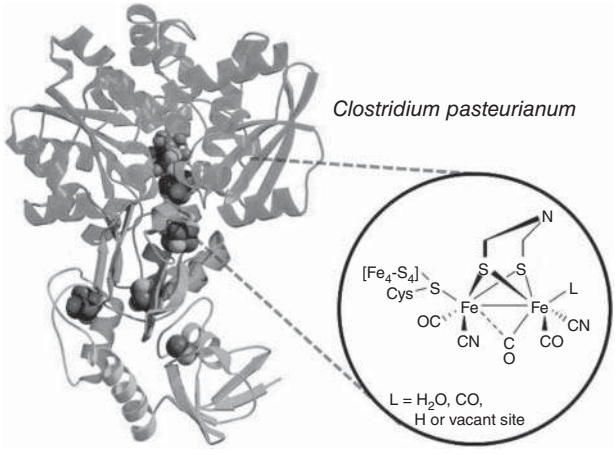

Figure 18.8 Crystal structure of [FeFe] hydrogenase extracted from *Clostridium pasteurianum*. Source: Adapted from Ref. [16].

The H-cluster is bound to a cubic $[Fe_4S_4]$ cluster via a cysteine linker. Notably, amino acid residues, sitting in the protein pocket in proximity to the H-cluster, interact with the ligands, holding one of the CO ligands in a bridging position [17]. Thereby, an open coordination site is made available, where proton reduction takes place via terminal hydride formation. This so-called *rotated geometry* is probably one of the reasons for the high activity of [FeFe] hydrogenases, since it prevents the formation of less reactive bridging hydrides [18]. In the past decades, a vast amount of model complexes has been reported, but they all show by far lower activity than the enzyme [19]. Also, it is still a major challenge to observe terminal hydrides in model complexes. Recently, synthetic complexes have been introduced to the *apo-HydA1*, which is one of the hydrogenases in algae of the type *Chlamydomonas reinhardtii* [20]. The resulting metallo-enzyme showed comparable activities as native hydrogenases, unambiguously demonstrating the power of the protein matrix around the active site. The question is whether positioning mimics of the active site in molecular

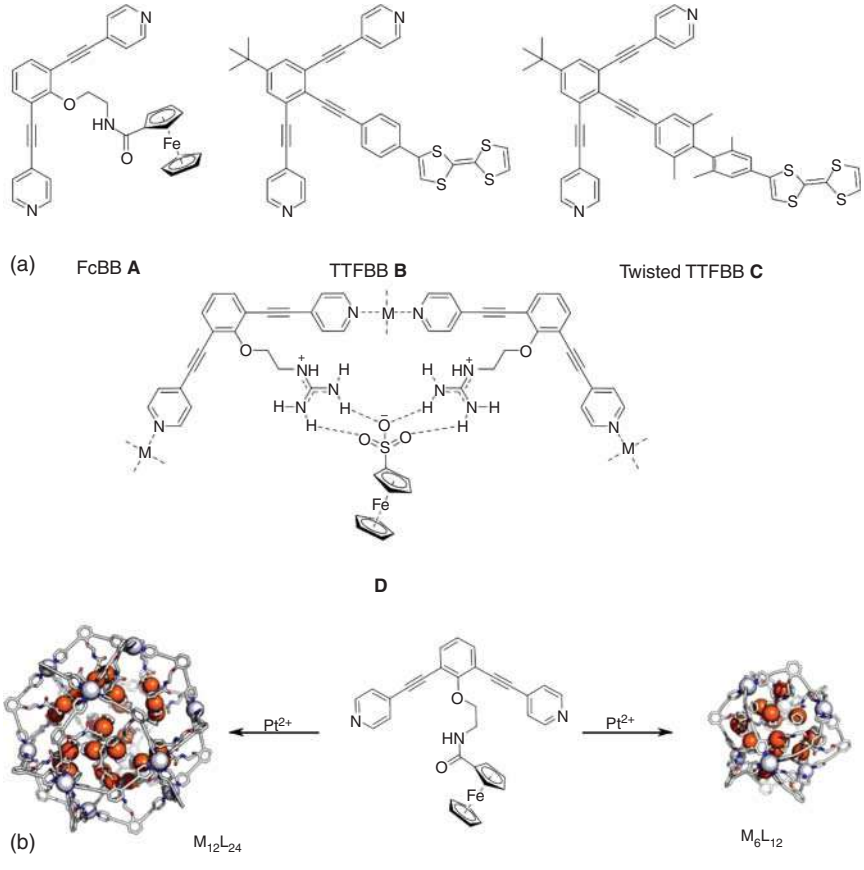

Figure 18.9 (a) Ligands containing redox-active functionalities in endohedral position. (b) Assembly or $M_{12}L_{24}$ nanosphere with Pd(II) and M_6L_{12} nanosphere with Pt(II). Source: from Ref. [21]. Reproduced with permission of American Chemical Society.

cages would have a similar positive effect on the catalytic properties of the mimic in terms of activity, stability, and overpotential required for catalysis. In addition to the previously mentioned interactions of protein residues with the active site, there are further advantages of the protein: Proton channels ensure efficient supply with substrate, and additional $[Fe_4S_4]$ clusters shuttle electrons to the active site. Produced hydrogen is released via channels in the protein. It would be interesting to design cages in which electron transport pathways are controlled.

With such a goal in mind, we recently studied electron transfer rates from heterogeneous electrodes to redox-active species attached to ligands in endohedral position in supramolecular nanospheres of the structure M_6L_{12} and $M_{12}L_{24}$ (M = Pd, Pt) [21]. Different linkers have been prepared as depicted in Figure 18.9, where a redox-active TTF building block was attached in a rigid fashion, using a conjugated and non-conjugated linker, and a ferrocene redox probe was attached via a flexible linker. In addition, we encapsulated ferrocene sulfonate into the $M_{12}M_{24}$ nanosphere via

non-covalent interactions with guanidine residues. In all cases, the thermodynamics of electron transfer were not significantly affected by encapsulation. In contrast, it was demonstrated that the type of linker and the number of incorporated species determine the rate of electron transfer. Thus, careful design allows to tune the reaction rate electron transfer.

Having established that redox chemistry within these spheres is possible, we introduced a [FeFe] hydrogenase mimic via a flexible linker. Template-ligand assembly resulted in endohedral-functionalized $Pd_{12}L_{24}$ nanospheres with 5 [FeFe] mimics on average (Figure 18.10a,b) [22]. These encapsulated catalysts showed electrocatalytic proton reduction at 250 mV more favorable potential, at the expense of the reaction rate that was about 100 times lower compared to the free mimic. Interestingly, mixed ligand nanospheres with ligands containing ammonium salts resulted in encapsuled systems in which the substrate (proton) is pre-organized to the mimic. Also, for these systems, proton reduction catalysis is displayed at significantly lower overpotential (250 mV), but now at about the same rate as the free mimic. This shows that these nanospheres are perfect vehicles to mimic second coordination sphere effects and to pre-organize protons, as a mimic for the proton channels observed in hydrogenase enzymes.

We were also interested in the evaluation of a second coordination sphere on the properties of a single hydrogen mimic. In order to study this, we used the ligand-template approach to encapsulation. The [FeFe](tfbdt)$(CO)_5(PPy_3)$ complex (tfbdt = 3,4,5,6-tetrafluoro-1,2-benzenedithiol, PPy_3 = tris pyridine-3-yl-phoshine) with the PPy_3 as template-ligand building block was encapsulated into self-assembled subcomponent molecular cage that contains six Zn(II) porphyrin units connected via redox-innocent triazole ligands coordinated to Fe(II) (Figure 18.10c) [23]. It was shown that the cationic cage decreases the reduction potential of the encapsulated catalyst by 30 mV. Furthermore, in combination with the weak acid $HNEt_3PF_6$, electrochemical proton reduction proceeds at 150 mV lower overpotential compared to the free catalyst. Probably, the cationic cage stabilizes anionic intermediates of the proton reduction catalyst. In addition, a common deactivation pathway for [FeFe] hydrogenase active site mimics is the disproportionation of the free catalyst. This process is prevented when the catalyst is isolated by encapsulation within the cage, leading to improved stability of the catalyst system.

In light-driven reactions, molecular catalysts often suffer from limited stability. Furthermore, electron transfer rates between photosensitizer and catalyst need to be improved. In Nature, light-harvesting units and reaction sites are assembled in a supramolecular fashion. In a similar way, supramolecular chemistry can serve as a valuable tool for improving artificial photosynthesis, for example, by pre-organizing photosensitizers. In the first attempt to mimic such precise molecular pre-organization, we have used a hydrogenase mimic with a phosphine-pyridyl ligand as template ligand. We demonstrate light-driven proton reduction catalysis; however, the obtained self-assembled photocatalyst was rather unstable [24]. In a subsequent study, we prepared a [FeFe] hydrogenase active site mimic containing a pyridyl-phosphole ligands which was encapsulated into a smaller Nitschke-type

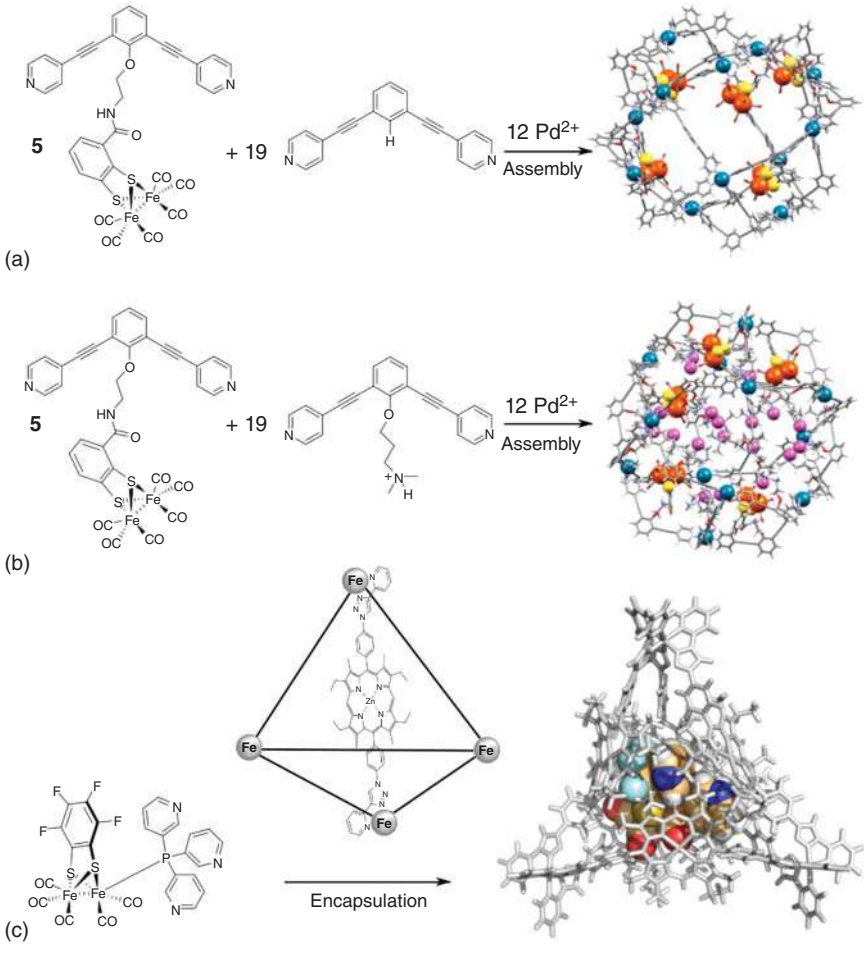

Figure 18.10 (a and b) Encapsulation of [FeFe] hydrogenase mimics in $M_{12}L_{24}$ nanospheres (L = mixture of [FeFe]-functionalized and unfunctionalized ligands) [22], (c) template-ligand approach for the encapsulation of a hydrogenase mimic in a self-assembled sub-component molecular cage [23].

cage based on Zn(II) porphyrin ligands [25]. The porphyrin ligands take up a dual role in this assembly: on the one hand, coordination of the pyridyl ligands to the Zn(II) center ensures tight binding of the catalyst in the cage. On the other hand, the porphyrin acts as a photosensitizer, driving photochemical proton reduction. Light-driven proton reduction catalysis was achieved in the presence of TFA as the proton source and 4-mercaptobenzoic (SED1) acid as the sacrificial electron donor. The limited stability of the Zn(II) porphyrin allowed only the presence of small amounts of acid, leading to relatively low turnover numbers. Importantly, after the reaction, a second batch of substrate was added to the reaction mixture, demonstrating that the catalyst was still photoactive, showing the stabilization effect of encapsulation.

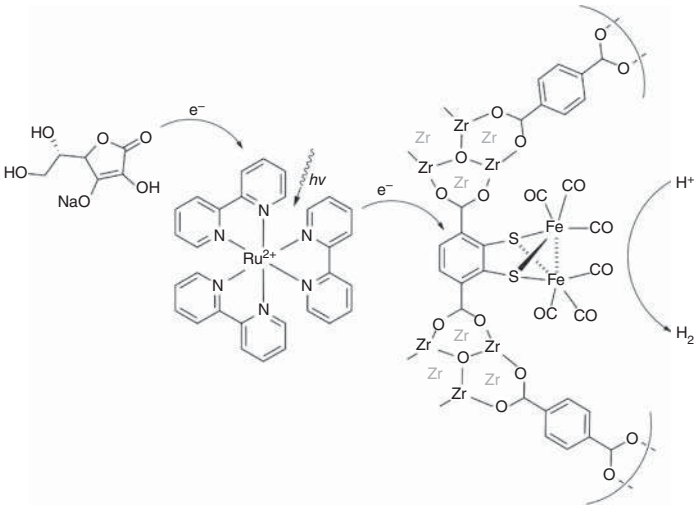

Figure 18.11 Photochemical proton reduction using [FeFe]-UiO-66, $[Ru(bpy)_3]^{2+}$ as a photosensitizer and sodium ascorbate as a sacrificial reductant [27].

18.3.3 Proton Reduction Catalysis Using MOFs

These studies together clearly demonstrate the high potential of supramolecular coordination cages and nanospheres as interactive hosts for molecular catalyst. Also, MOFs have been considered as scaffolds for molecular catalysts, and there are numerous examples in literature, where catalysts relevant for artificial photosynthesis have been incorporated into MOFs [26]. In contrast to discrete, homogeneous coordination cages, MOFs are heterogeneous materials with high porosity and surface area. Catalysts can either be incorporated as building block or be encapsulated in the pores of the MOFs. The large variety of organic ligands that can be used for MOF synthesis offers high potential for the preparation of mixed-linker MOF catalysts, taking advantage of second coordination sphere effects. Internal channels in MOFs can potentially provide similar substrate and product diffusion as channels in proteins.

[FeFe] hydrogenase active site mimics have previously been encapsulated into MOFs. In a seminal paper, Pullen and Fei *et al.* introduced [FeFe](dcbdt)$(CO)_6$ (dcbdt = 1,4-dicarboxylbenzene-2,3-dithiolate) as ligand to chemically stable UiO-66 (Figure 18.11) [27]. The resulting MOF catalyst showed to be significantly more stable and active as proton reduction catalyst than the homogeneous analog, when irradiated in the presence of $[Ru(bpy)_3]^{2+}$ as a photosensitizer and ascorbate as a sacrificial reductant in an aqueous buffer at pH 5. It was concluded that the incorporated catalysts are unable to undergo unproductive dimerization and disproportionation. In contrast to the supramolecular cage, incorporation of the catalyst as a ligand to UiO-66 does not seem to affect the catalysts' reduction potential, as shown for thin films on FTO (fluorine-doped tin oxide)-conducting glass electrodes [28].

More similar to the ligand-template strategy used for supramolecular cage encapsulation, Feng and coworkers introduced a pyridine-tagged [FeFe] complex

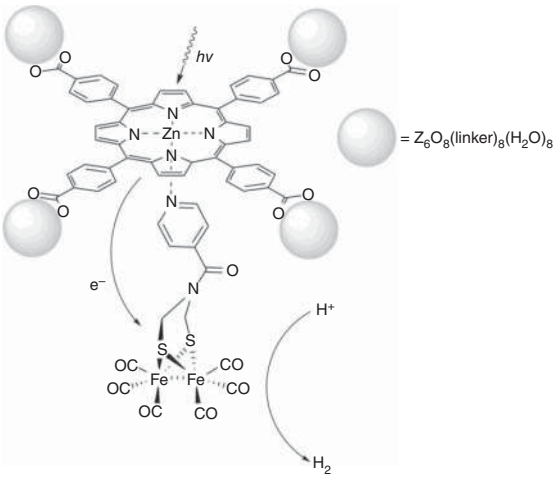

Figure 18.12 Schematic representation of the [FeFe] complex bound to Zn(II)porphyrin MOF [29].

to a MOF consisting of Zn(II)TPP (TCPP, [tetra-(4-carboxyphenyl)porphyrin]) ligands [29]. This MOF catalyst showed to be active in photochemical proton reduction without addition of external photosensitizer as in the previous example (Figure 18.12). However, due to the weaker binding of the catalyst in comparison with rigidly incorporated [FeFe] in UiO-66, the material showed limited stability and all catalysts were decomposed after the first run. In an alternative approach, MIL-125(Ti)-NH_2 has been used as a photoactive MOF for the encapsulation of [Co]-oxime diamine as proton reduction catalyst. The catalyst was built-up within the MOF pores, effectively using a "ship-in-a-bottle" strategy. Photochemical proton reduction with this material produced decent yields, and the material was recycled up to three times by simple filtration, again showing stabilization effects of the catalyst thanks to encapsulation [30].

Catalysts can be encapsulated in supramolecular cages and MOFs, showing not only similarities but there are also some differences. In a supramolecular cage, each encapsulated catalyst is well-accessible by substrates and the reaction is only dependent on host–guest exchange. The homogeneous nature of supramolecular cages allows their study by standard electrochemical techniques as well as spectroscopy in solution. In MOFs, diffusion of substrates through the cavities plays a major role and can be a limiting factor on reaction rates [31]. A clear advantage of MOFs is their easy separation from the reaction mixture and recyclability [32]. Importantly, MOFs can be mounted on electrodes, and in this manner, it gives an entry in implementation into solar-to-fuel devices. Even though there is an obvious overlay between supramolecular coordination cages and MOFs as hosts for catalysts, both research fields have so far been mostly treated independently in the context of artificial photosynthesis [33]. Only recently, Choi and coworkers compared the performance of a CO_2-reduction catalyst Re(dcbpy)$(CO)_3$Cl incorporated into a Zr-based supramolecular cage with an analogous MOF-catalyst UiO-67. This study clearly demonstrated that the discrete supramolecular cage is more active than the MOF [34].

18.4 Concluding Remarks and Outlook

In this chapter, we have outlined different strategies to provide transition metal catalysts with a chemical environment that is mimicking the second coordination sphere of active sites in metalloenzymes. The ligand-template strategy allows programmed assembly of supramolecular architectures around catalytically active metal complexes. The resulting catalysts benefit from improved selectivity, enhanced reaction rates, and better stability. More specifically, nanospheres containing guanidinium residues in endohedral position have proven to be useful hosts for the encapsulation of catalysts. Increased local concentration due to encapsulation of multiple catalysts allows efficient catalysis. Mixed ligand nanospheres have shown great potential for introducing second coordination sphere effects. [FeFe] hydrogenase active sites mimics have been investigated heavily both in supramolecular cages and MOFs. While these [FeFe] complexes present a much-appreciated example, the concepts described in this chapter have been and will even more be applied for other transition metal catalysts. Future research on the relation between MOFs and cages as catalyst supports will ultimately lead to improved mechanistic understanding and improved catalysis.

References

1 (a) Leenders, S.H.A.M., Gramage-Doria, R., de Bruin, B., and Reek, J.N.H. (2015). Transition metal catalysis in confined spaces. *Chem. Soc. Rev.* 44: 433–448. (b) Brown, C.J., Toste, F.D., Bergman, R.G., and Raymond, K.N. (2015). Supramolecular catalysis in metal-ligand cluster hosts. *Chem. Rev.* 115: 3012–3035. (c) Catti, L., Zhang, Q., and Tiefenbacher, K. (2016). Advantages of catalysis in self-assembled molecular capsules. *Chem. Eur. J.* 22: 9060–9066. (d) Raynal, M., Ballester, P., Vidal-Ferran, A., and van Leeuwen, P.W.N.M. (2014). Supramolecular catalysis. Part 2: Artificial enzyme mimics. *Chem. Soc. Rev.* 43: 1734–1787. (e) Koblenz, T.S., Wassenaar, J., and Reek, J.N.H. (2008). Reactivity within a confined self-assembled nanospace. *Chem. Soc. Rev.* 37: 247–262.

2 Jongkind, L.J., Caumes, X., Hartendorp, A.P.T., and Reek, J.N.H. (2018). Ligand template strategies for catalyst encapsulation. *Acc. Chem. Res.* 51: 2115–2128.

3 Slagt, V.F., Reek, J.N.H., Kamer, P.C.J., and van Leeuwen, P.W.N.M. (2001). Assembly of encapsulated transition metal catalysts. *Angew. Chem. Int. Ed.* 40: 4271–4274.

4 Gramage-Doria, R., Bellini, R., Rintjema, J., and Reek, J.N.H. (2013). Supramolecular ligands in gold(I) catalysis. *ChemCatChem* 5: 1084–1087.

5 Bellini, R. and Reek, J.N.H. (2012). Supramolecular hybrid bidentate ligands in asymmetric hydrogenation. *Eur. J. Inorg. Chem.* 2012: 4684–4693.

6 Nurttila, S.S., Brenner, W., Mosquera, J. et al. (2019). Size-selective hydroformylation by a rhodium catalyst confined in a supramolecular cage. *Chem. Eur. J.* 25: 609–620.

7 Gonell, S., Caumes, X., Orth, N. et al. (2019). Self-assembled $M_{12}L_{24}$ nanospheres as a reaction vessel to facilitate a dinuclear Cu(I) catalyzed cyclization reaction. *Chem. Sci.* 10: 1316–1321.

8 Harris, K., Fujita, D., and Fujita, M. (2013). Giant hollow M_nL_{2n} spherical complexes: structure, functionalisation and applications. *Chem. Commun.* 49: 6703–6712.

9 Gramage-Doria, R., Hessels, J., Leenders, S.H.A.M. et al. (2014). Gold(I) Catalysis at Extreme Concentrations Inside Self-Assembled Nanospheres. *Angew. Chem. Int. Ed.* 53: 13380–13384.

10 Wang, Q.-Q., Gonell, S., Leenders, S.H.A.M. et al. (2016). Self-assembled nanospheres with multiple endohedral binding sites pre-organize catalysts and substrates for highly efficient reactions. *Nat. Chem.* 2016 (8): 225–230.

11 Gonell, S. and Reek, J.N.H. (2019). Gold-catalyzed cycloisomerization reactions within guanidinium $M_{12}L_{24}$ nanospheres: the effect of local concentrations. *ChemCatChem* 11: 1458–1464.

12 Balzani, V., Credi, A., and Venturi, M. (1997). Photoprocesses. *Curr. Opin. Chem. Biol.* 1: 506–513.

13 Keijer, T., Bouwens, T., Hessels, J., and Reek, J.N.H. (2021). Supramolecular strategies in artificial photosynthesis. *Chem. Sci.* 103: 15729.

14 Yu, F., Poole, D., Mathew, S. et al. (2018). Control over electrochemical water oxidation catalysis by preorganization of molecular ruthenium catalysts in self-assembled nanosphere. *Angew. Chem. Int. Ed.* 57: 11247–11251.

15 Frey, M. (2002). Hydrogenases: hydrogen-activating enzymes. *ChemBioChem* 3: 153–160.

16 Peters, J.W., Lanzilotta, W.N., Lemon, B.J., and Seefeldt, L.C. (1998). X-ray crystal structure of the Fe-only hydrogenase (CpI) from *Clostridium pasteurianum* to 1.8 Ångstrom resolution. *Science* 282: 1853–1858.

17 Finkelmann, A.R., Stiebritz, M.T., and Reiher, M. (2014). Inaccessibility of the μ-hydride species in [FeFe] hydrogenases. *Chem. Sci.* 5: 215–221.

18 Liu, C., Peck, J.N.T., Wright, J.A. et al. (2011). Density functional calculations on protonation of the [FeFe]-hydrogenase model complex $Fe_2(\mu\text{-pdt})(CO)_4(PMe_3)_2$ and subsequent isomerization pathways. *Eur. J. Inorg. Chem.* 2011: 1080–1093.

19 (a) Tard, C. and Pickett, C.J. (2009). Structural and functional analogues of the active sites of the [Fe]-, [NiFe]-, and [FeFe]-hydrogenases. *Chem. Rev.* 109: 2245–2274. (b) Li, Y. and Rauchfuss, T.B. (2016). Synthesis of diiron(I) dithiolato carbonyl complexes. *Chem. Rev.* 116: 7043–7077.

20 Berggren, G., Adamska, A., Lambertz, C. et al. (2013). Biomimetic assembly and activation of [FeFe]-hydrogenases. *Nature* 499: 66–69.

21 Zaffaroni, R., Bobylev, E.O., Plessius, R. et al. (2020). How to control the rate of heterogeneous electron transfer across the rim of M_6L_{12} and $M_{12}L_{24}$ nanospheres. *J. Am. Chem. Soc.* 142: 8837–8847.

22 Zaffaroni, R., Orth, N., Ivanović-Burmazović, I., and Reek, J.N.H. (2020). Hydrogenase mimics in $M_{12}L_{24}$ nanospheres to control overpotential and activity in proton-reduction catalysis. *Angew. Chem. Int. Ed.* 59: 18485–18489.

23 Nurttila, S.S., Zaffaroni, R., Mathew, S., and Reek, J.N.H. (2019). Control of the overpotential of a [FeFe] hydrogenase mimic by a synthetic second coordination sphere. *Chem. Commun.* 55: 3081–3084.

24 Kluwer, A.M., Kapre, R., Hartl, F. et al. (2009). Self-assembled biomimetic [$2Fe_2S$]-hydrogenase-based photocatalyst for molecular hydrogen evolution. *Proc. Natl. Acad. Sci. U.S.A.* 106: 10460–10465.

25 Nurttila, S.S., Becker, R., Hessels, J. et al. (2018). Photocatalytic hydrogen evolution by a synthetic [FeFe] hydrogenase mimic encapsulated in a porphyrin cage. *Chem. Eur. J.* 24: 16395–16406.

26 Cohen, S.M., Zhang, Z., and Boissonnault, J.A. (2016). Toward "metallo-MOFzymes": Metal–Organic Frameworks with Single-Site Metal Catalysts for Small-Molecule Transformations. *Inorg. Chem.* 55: 7281–7290.

27 Pullen, S., Fei, H., Orthaber, A. et al. (2013). Enhanced photochemical hydrogen production by a molecular diiron catalyst incorporated into a metal–organic framework. *J. Am. Chem. Soc.* 135: 16997–17003.

28 Fei, H., Pullen, S., Wagner, A. et al. (2015). Functionalization of robust Zr(IV)-based metal-organic framework films via a postsynthetic ligand exchange. *Chem. Commun.* 51: 66–69.

29 Sasan, K., Lin, Q., Mao, C., and Feng, P. (2014). Incorporation of iron hydrogenase active sites into a highly stable metal-organic framework for photocatalytic hydrogen generation. *Chem. Commun.* 50: 10390–10393.

30 Nasalevich, M.A., Becker, R., Ramos-Fernandez, E.V. et al. (2015). Co@NH_2-MIL-125(Ti): cobaloxime-derived metal–organic framework-based composite for light-driven H_2 production. *Energy Environ. Sci.* 8: 364–375.

31 Roy, S., Pascanu, V., Pullen, S. et al. (2017). Catalyst accessibility to chemical reductants in metal–organic frameworks. *Chem. Commun.* 53: 3257–3260.

32 Bozal-Ginesta, C., Pullen, S., Ott, S., and Hammarström, L. (2020). Self-recovery of photochemical H_2 evolution with a molecular diiron catalyst incorporated in a UiO-66 metal–organic framework. *ChemPhotoChem* 4: 287–290.

33 Pullen, S. and Clever, G.H. (2018). Mixed-ligand metal-organic frameworks and heteroleptic coordination cages as multifunctional scaffolds – a comparison. *Acc. Chem. Res.* 51: 3052–3064.

34 Lee, H.S., Jee, S., Kim, R. et al. (2020). A highly active, robust photocatalyst heterogenized in discrete cages of metal–organic polyhedra for CO_2 reduction. *Energy Environ. Sci.* 13: 519–526.

19

Catalysis by Metal–Organic Cages: A Computational Perspective

Giuseppe Sciortino, Gantulga Norjmaa, Jean Didier Maréchal, and Gregori Ujaque

Universitat Autònoma de Barcelona, Centro de Innovación en Química Avanzada (ORFEO-CINQA), Departament de Química, Cerdanyola del Vallès, Catalonia, 08193, Spain

19.1 Introduction

Supramolecular chemistry has evolved into an interdisciplinary field across different areas as applied chemistry, biology, and nanoscience [1]. Application of this field is very broad going from detecting of harmful environmental contaminants to regulating biochemical processes, or using them as supramolecular catalysts. Host–guest interactions are at the heart of this fascinating field since they are responsible for the binding of substrates to molecular receptors [1]. These include noncovalent interactions that comprise electrostatic forces, hydrogen bonding and van der Waals forces, among others. The rational control of these interactions is the main objective of any supramolecular chemist.

A myriad of synthetic hosts has been designed and prepared during the past decades, largely enriching the toolbox of available supramolecules. One of the most exciting developments is the so-called metallocages, supramolecular organometallic complexes (SOCs) or metal–organic cages (MOCs) [2]. MOCs are molecular entities obtained by self-assembly of metal ions or clusters with organic ligands that are driven mainly by coordination rules [2a, 3]. Interestingly, they account for a variety of topologies and well-defined shapes at the nanoscale. The cavities of these supramolecular architectures are appealing for hosting small molecules with high selectivity and specificity. The capability for tailoring the cavities of the MOCs has led to develop many applications such as molecular recognition [4], purification of product mixtures [5], gas sorption [6], drugs or photosensitizers carriers, and catalysis [7].

Hosseini and Lehn defined supramolecular catalysis as "the chemical transformation of a bound substrate, for which complexation and recognition steps are prerequisites" [8]. Coordination cages can behave as molecular flasks by benefiting from the cavity to control a chemical reaction between encapsulated reactants. Among all catalytic processes employing MOCs, we selected those that have been

Supramolecular Catalysis: New Directions and Developments, First Edition.
Edited by Piet W.N.M. van Leeuwen and Matthieu Raynal.

analyzed by theoretical methods with special interest in deepening the molecular vision given by computation.

The use of computational techniques is essential to acquire a meaningful understanding at a molecular level of catalytic processes [9, 10]. They comprise the methods adequate to examine the bond-forming and bond-breaking processes. Moreover, they should also be appropriate to analyze the host–guest interactions. Up to now, few theoretical studies on the rate acceleration by supramolecular hosts have been reported [11].

The purpose of the present chapter is to provide the reader with an overview of the chemical processes catalyzed by MOCs that have been investigated by a computational point of view. A specific section will be devoted to a general overview on the theoretical methods employed, as well as their combinations, followed by a section that gathers the cases that have been studied so far. Finally, some hints about the future directions on the field will be briefly discussed.

19.2 Looking for a Robust Computational Framework to Study MOCs

The study of catalytic processes, where chemical bonds are formed and broken, requires the use of quantum mechanics (QM). Working with MOCs, indeed, involves working with systems commonly close to the size limit that these methods can afford (today ~300 atoms); inclusion of explicit solvent molecules makes the issue even more unaffordable. On top of that, the possible flexibility and the large number of possible configurations (for both hosts and guests) make the systems suitable for the use of statistical methods [12]. Thus, in most of the cases not a single methodology, but a combination of methods (multi-level) is required. Here we summarize the methods, or combination of methods employed so far in the literature.

The use of QM has been generalized, particularly those based on density functional theory (DFT). [13] QM approaches describe the molecular system at electronic level allowing predicting the structure, energy and fine molecular properties with great accuracy. They are widely used in inorganic and organometallic chemistry because of the complexity introduced by metals and has been applied to catalytic metallocages [9, 10].

Despite the increase in the computational power, QM methods are computationally expensive; thus, several strategies have been employed to deal with catalytic metallocages from a QM perspective. The most drastic one consists in cutting out part of the cage generating cluster models without considering the entire size of the system. A highly valuable alternative is the use of Hybrid Quantum Mechanics/Molecular Mechanics (QM/MM) methods in which part of the system is treated under QM formalism, generally the reactive part, while the rest is treated at MM level [14]. Alternatively, Semi-empirical Quantum Mechanical (SQM) methods have been also employed because they are several orders of magnitude faster than *ab initio*. Recent advances include the modifications of density functional tight

binding (DFTB) method like GFN-xTB [15] that has been developed for large molecular systems, or the development of PM7 [16], among others [17]. Finally, MM approaches, routinely used on structural studies of organic and biological systems [18], could be applied to metallocages by including custom-generated metal parameters in their force-fields [19], though they are not suitable to study reactivity.

Catalytic reactions with MOCs take place in solution; therefore, the effects of the medium can be fundamental and should be considered. Bulk effects can be modeled by using explicit, implicit, or hybrid explicit–implicit solvation models. Including full explicit solvation shells in metallocages dramatically increase the number of the atoms restricting this description to SQM- or MM-based methods. From a QM point of view, the hybrid model including a reduced number of explicit solvent molecules along with continuum models results in a good balance between accuracy and computational time. One of the widely used popular implicit schemes is the self-consistent reaction field (SCRF) that treats the solute–solvent interaction as a classical electrostatic problem [20]. Among the most employed methods there are polarizable continuum model (PCM) [20], solvation model based on density (SMD) [21], and conductor-like screening model (COSMO) [22].

A proper description of the host and guest dynamics (including noncovalent interactions as well as the flexibility of the partners) is essential for a complete understanding of how host–guest interactions take place. The use of statistical methods is then required to properly account for these effects. In this sense, the experience acquired on the biochemical systems will be of great help to this field. Molecular dynamics (MD) represents one of the most powerful tools for studying dynamic processes of molecular systems. In the context of supramolecular catalysis by metallocages, MDs can deal with conformational changes of the cages, even induced for substrates binding, and can describe the accommodations of the guests into the cavities. MD simulations of host−guest adducts have been combined with QM methods for studying MOCs catalytic processes, as shown in Section 19.3.

Classical MDs based on MM force-fields, despite their high potentiality, as commented above, lack appropriate parameterization for metals that are essential in MOCs [18, 19]. A part of including custom-generated metal parameters in the force-fields (bonded model), the cationic dummy atom approach (CADA) [23] has been recently applied in the field of metallocages [24]. The approach consists in describing the metal ion as a hard sphere with dummy particles of negligible dimension placed in the coordination vacancies and bonded to the central atom. The total charge of the metal (n^+) is distributed between the dummies that result with partial positive charge (δ^+) and can interact by electrostatic contacts with the surrounding.

The time scales for interesting events in supramolecular chemistry, due to the huge amount of conformational sampling required, are very often not accessible. For these cases, employing enhanced sampling techniques is indispensable. Several methods have been developed such as replica-exchange MD, metadynamics, and simulated annealing [25]. Among other properties, they proportionate very valuable information on how the reactants motion evolve and are accommodated inside the cavity.

The force-field limitations could be overcome by combining QM methods with dynamics methods, by employing QM/MM-MD or *ab initio* molecular dynamics (AIMD) methods. The latter is an alternative to the force-field classical approach consisting in computing the forces of each configuration generated along the trajectory using first principles [26]. Dealing with transition metals-based metallocages, the most convenient electronic structure method in AIMD simulations is DFT. With these methods, the explicit solvent can be incorporated along with a proper description of the dynamic behavior of the system. The major drawback, however, is the computational cost.

Besides the computational methods commented above, there are other tools very helpful to interpret in chemical language the results of these calculations. One of the most appealing ones is the noncovalent interaction (NCI) analysis (as implemented in the NCIPlot software) [27]. It is a DFT-based analysis enabling the identification of intra- and inter-molecular NCIs, thus becoming quite appropriate to analyze host–guest interactions. The employment of energy decomposition analysis can be also very informative [11c, 28]. The computation of guests as well as cavity volumes is also very useful, in combination with the Rebek rule of 55% for the occupancy factor (packing coefficient) [29].

Finally, development of automatic protocols for designing and screening MOCs are starting to be developed (i.e. cgbind) [30]. They aim to facilitate the construction, characterization, and prediction of functional MOCs, including their use as catalysts.

19.3 Applications of Modeling to Confined Catalysis

Molecular modeling is emerging as a fundamental complement to experiments in order to achieve a full characterization and understanding of the MOCs-mediated catalysis at the atomic level.

In a recent work, Reek and coworkers reported the hydroformylation of terminal alkenes by encapsulating a Rh-phosphine complex into a $Fe_4(Zn\text{-}L)_6$ tetrahedral metallocage (Figure 19.1a) [31]. Computational techniques were used at different stages of the research. Volume exploration of the host cavity and the catalysts guest for several species showed that $[HRh(CO)_2(L^3)_2]$ where L^3 = tris(4-pyridyl)phosphine fills 53% of the cavity. It is a trigonal bipyramid complex leaving sufficient space inside the cavity to accommodate the substrates. Encapsulation has been confirmed by cold spray ionization mass spectrometry, UV–vis titrations, and 1D and 2D NMR spectroscopy. Tight-binding quantum chemical simulations (GFN-xTB) [32] were used to obtain the molecular structure of the encapsulated complexes $Fe_4(Zn\text{-}L)_6$ by comparing the three possible isomers of $[HRh(CO)_2(L)_2]$. Computational results showed that the isomer with both pyridylphosphines in the equatorial plane, Rh1, was the most stable one; the L^3 ligand is able to coordinate each Zn^{II} of the walls of the MOC (Figure 19.1b). This finding was confirmed by high-pressure IR spectroscopy and GFN-xTB frequencies comparing the CO stretching of encapsulated complex with its free form. Finally, in the hydroformylation of terminal aromatic and aliphatic alkenes, $Rh1\subset Fe_4(Zn\text{-}L)_6$

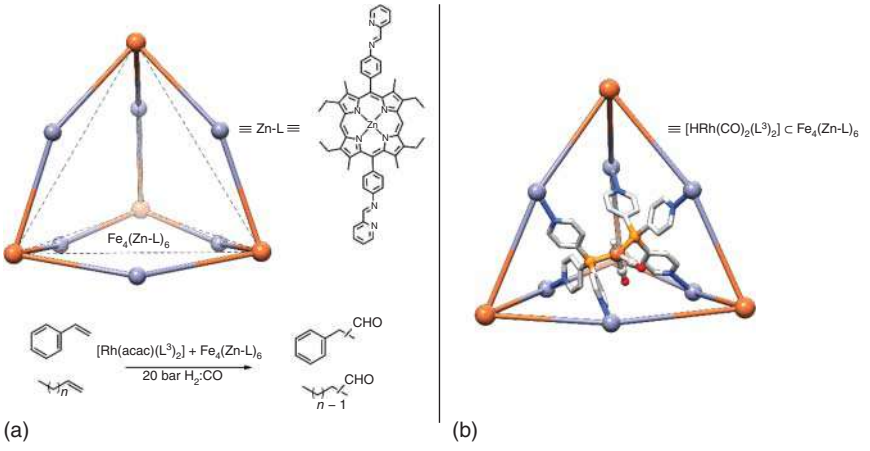

Figure 19.1 Representation of: (a) $Fe_4(Zn\text{-}L)_6$ host tetrahedral metallocage on the top, and hydroformylation catalyzed reaction on the bottom; (b) active $[HRh(CO)_2(L^3)_2]\subset Fe_4(Zn\text{-}L)_6$ inclusion complex, Rh1.

displayed a clear selection toward small substrates due to the low dimension of its window aperture upon inclusion of Rh1. Interestingly, hydroformylation of linear aliphatic alkenes showed an odd–even effect (conversion of even chains larger than odd ones). This effect was rationalized optimizing the structure of inclusion complex (Rh1, alkene)$\subset Fe_4(Zn\text{-}L)_6$ by GFN-xTB, followed by a single point energy at DFT level. The energy differences between the folded and linear states for the alkenes highlighted that for odd-numbered alkenes the folded state inside the cage is energetically less demanding than that for the even-numbered ones.

Self-assembled tetrahedron supramolecular metallocage, $K_{12}[Ga_4L_6]$, developed by the Raymond group, has been employed to accelerate several chemical reactions up to 10^7 times compared to the bulk process (Figure 19.3a) [33]. The metallocage assembles as a racemic mixture of ΔΔΔΔ and ΛΛΛΛ diastereomers and forms a highly anionic host $[Ga_4L_6]^{12-}$ in solution that encapsulates cationic and neutral guests. The rate constants measured for the association and dissociation of Me_4N^+ in both ΔΔΔΔ and ΛΛΛΛ hosts were the same within error, indicating diastereomers do not affect the binding process of this symmetric guest. Full DFT calculations of both diastereomeric MOCs showed that their relative Gibbs energies were very similar in implicit methanol solvent [34].

Despite the increasing interest in this supramolecular host, only few computational investigations of its catalytic behavior have been reported so far. A summary of those studies is presented in Figure 19.2. The origin of the catalytic hydrolysis of orthoformate catalyzed by $[Ga_4L_6]^{12-}$ in basic solution was investigated by Warshel's group [35]. They used the empirical valence bond (EVB) and free energy perturbation (FEP) approaches to reproduce the catalytic process showing that the catalytic effect can be entirely attributed to the electrostatic contributions. The analysis also revealed a significant encapsulation of the H_3O^+ ion, causing a very low "local pH" condition inside the cavity even in basic bulk solution.

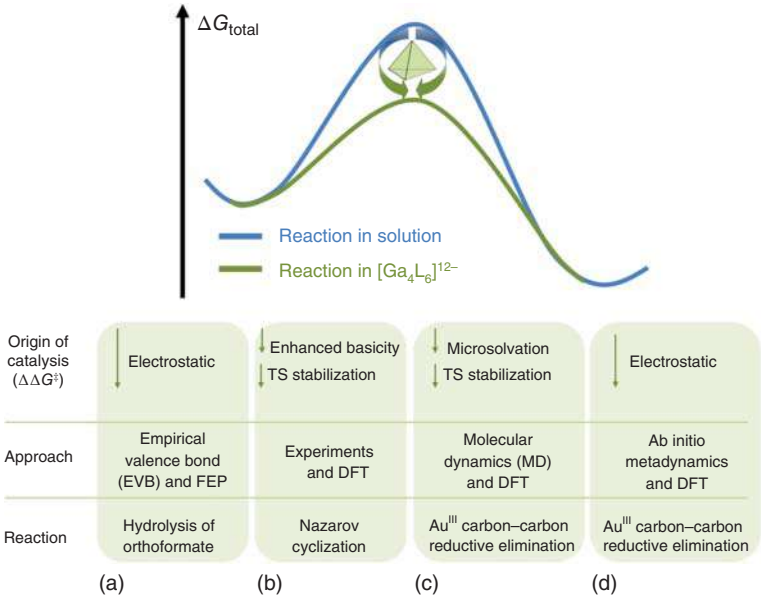

Figure 19.2 Summary of the studies on the origin of the catalysis performed for $[Ga_4L_6]^{12-}$ MOC. Source: (a) Ref. [35], (b) Ref. [36], (c) Refs. [34, 37], and (d) Refs. [38, 39].

In 2010, the Bergman and Raymond groups reported a mechanistic analysis of the Nazarov cyclization in the confined space of $[Ga_4L_6]^{12-}$ by combining kinetic and ^{18}O-incorporation studies with DFT calculations for the process in solution [36]. From their analysis, they suggested that protonation of the substrate occurs along with its rapid and reversible binding, in agreement with the encapsulation of the H_3O^+ ion in the metallocage reported by the Warshel group for the hydrolysis of orthoformates. The results indicated that electrocyclization is the rate-limiting step in the uncatalyzed reaction; in the metallocage-catalyzed reaction, however, the water loss from substrate and the electrocyclization are both rate-determining. The activation parameters were also determined, obtaining $\Delta H^{\ddagger}$ values of 15.6(6) and 14.8(8) kcal·mol^{-1} and $\Delta S^{\ddagger}$ values of −47(2) and −20(3) e.u. for the uncatalyzed and the MOC-catalyzed reactions, respectively.

Their previous studies on the basicity enhancement of MOC-bound guests showed that the protonation equilibria of amines in the $[Ga_4L_6]^{12-}$ were shifted by up to 4.5 order of magnitude [40]. Therefore, they estimated that the acidity of the protonated pentadienol encapsulated by $[Ga_4L_6]^{12-}$ is four pK_a units higher than that of nonencapsulated one. Based on those data, the rate acceleration of the MOC-catalyzed Nazarov cyclization is not only due the transition state stabilization but also to the increase of the basicity induced by the confined space.

The aza-Cope reaction performed inside the $[Ga_4L_6]^{12-}$ was investigated by means of QM/MM calculations where the reactants and the metallocage were described at QM level, whereas the counterions were described at MM level. The reaction pathways leading to the formation of R- and S-enantiomers were evaluated

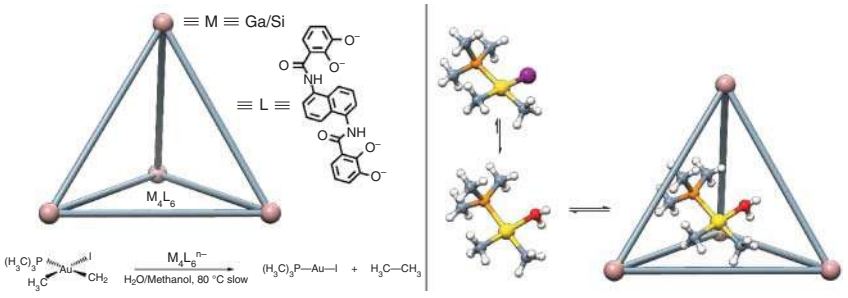

Figure 19.3 Representation of: (a) $M_4L_6{}^{n-}$ host tetrahedral metallocage on the top and alkyl–alkyl bond reductive elimination catalyzed reaction on the bottom; (b) representation of the equilibrium $[Au^{III}P(CH_3)_3(CH_3)_2I] \rightleftharpoons [Au^{III}P(CH_3)_3(CH_3)_2(H_2O)]^+$ and the $[Au^{III}P(CH_3)_3(CH_3)_2(H_2O)]^+ \subset M_4L_6{}^{n-}$ resting state identified by DFT.

showing that the former is favored in agreement with experiment. The origin of chiral differentiation was attributed, in addition to the relative stability of the prochiral substrate, to the difference in the barrier associated to the rearrangement for each enantiomer. This was related to the host–guest shape complementarity; for the S-pathways, the reactant substituent (isopropyl) was found to be more distorted than for the R-pathway [41].

The origin of the rate acceleration in the carbon–carbon reductive elimination from the Au(III) complex, $R_3PAuI(CH_3)_2$, has been investigated by two independent groups (Figure 19.2c,d). The Teresa Head-Gordon group initially studied the carbon–carbon reductive elimination in the $[Ga_4L_6]^{12-}$ and in the $[Si_4L_6]^{8-}$ MOCs by static DFT simulations [38], ascertaining that the resting state of the reaction is the $[AuP(CH_3)_3(CH_3)_2]^+$ dissociated form of the complex (Figure 19.3b). The analysis of $\Delta E_{binding}$ of the $[AuP(CH_3)_3(CH_3)_2]^+$ complex on both MOCs showed the preference for the most charged metallocage $[Ga_4L_6]^{12-}$, as can be expected from electrostatic considerations. Moreover, the differences in the activation barriers computed inside both anionic metallocages was computed to be ~19 kcal·mol^{-1}, mainly attributed to electrostatic interactions. In a later work, the same group [39] addressed the role of electric field in this process by means ab initio meta dynamics (AIMetaMD) calculations including the water solvent explicitly. The activation barrier inside $[Ga_4L_6]^{12-}$ was ~9 kcal·mol^{-1} lower than that in the bulk. The electrostatic contribution to the barrier was estimated to be ~5 kcal mol^{-1}, while the further ~50% of the transition state stabilization was attributed to the presence of the coordinated water molecule in the encapsulated complex $[Au(H_2O)P(CH_3)_3(CH_3)_2]^+ \subset Ga_4L_6{}^{12-}$.

The same process was also evaluated by Norjmaa et al. using DFT calculations in combination with classical MD simulations [34, 37]. The MD simulations allowed the authors to determine the average number of solvent molecules encapsulated in the $[Ga_4L_6]^{12-}$, using MeOH as in the experiment. Simulations were performed on the host–guest complexes in a cubic periodic box with more than 3500 explicit methanol solvent molecules and counter ions to neutralize the system. The results from the MD simulations guided the models selected for the DFT calculations.

First, they identified that the effect on the Gibbs energy barrier of the counter ions outside the cavity was negligible: the encapsulated system is somehow isolated from outside effects [34]. The full DFT calculations showed that the Gibbs energy barrier decreases by the presence of the metallocage can be related to two different factors: microsolvation (removing explicit solvent molecules around the Au(III) complex) and encapsulation (performing the reaction inside the cavity). The overall reduction of the Gibbs energy barrier was ∼9 kcal·mol^{-1}, with 5.7 kcal·mol^{-1} reduction due to microsolvation and 3.1 kcal·mol^{-1} due to encapsulation [34]. The same authors also performed a comparative analysis of the reductive eliminations for $[Et_3PAu(MeOH)(CH_3)_2]^+$ and $[Me_3PAu(MeOH)(CH_3)_2]^+$ complexes [37]. The subtle difference of the phosphine ligand modify their behavior in the $[Ga_4L_6]^{12-}$ metallocage although very little in solution. The MD simulations indicated that for the Au(III) complex with the PMe_3 ligand, there is on average one additional MeOH solvent molecule inside the cavity of the metallocage compared to the complex with the PEt_3 ligand; this is behind the fact that this system shows lower increase in the reaction rate, since microsolvation for both complexes is different inside the cavity. Interestingly, the energy decomposition analysis showed that the transition state stabilizations within the MOC for the reductive eliminations for the $[Me_3PAu(MeOH)(CH_3)_2]^+$ and $[Et_3PAu(MeOH)(CH_3)_2]^+$ complexes are 2.8 and 7.8 kcal·mol^{-1}, respectively (Figure 19.3). Overall, encapsulated solvent molecules in the cavity of the $[Ga_4L_6]^{12-}$ are playing a crucial role in modifying the energy barrier of this process.

Duarte, Lusby and coworkers have recently reported a complete characterization of the Diels–Alder catalytic activity of two Pd_2L_4 homolog metallocages ($[Pd_2L^N{}_4]^{4+}$ and $[Pd_2L_4{}^{CH}]^{4+}$, where L^N = 2,6-bis(3′-pyridylethynyl)pyridine and L^{CH} = 1,3-bis(3′-pyridylethynyl)benzene) with different quinones (Figure 19.4a). The proposed multistep methodology, including classical MD in explicit solvent and DFT, has been benchmarked toward experimental host–guest binding affinities and catalytic performance of the MOCs with the aim to establish a general and portable computational protocol [24]. In the first instance, the flexibility of the metallocages has been assessed by classical MD in explicit solvent using the CADA for Pd^{2+} [23b]. Slight differences have been observed in the Pd···Pd distances, while more interesting was the helical flexibility of the cages during MDs. As a following point, the binding energies ($\Delta E_{binding}$) of anthraquinone, **aq**, and benzoquionone, **bq**, have been estimated by static DFT simulations *in vacuum* and in solvent using implicit method (SMD). Inclusion of solvent effects is fundamental to reproduce the experimental highest affinity of both substrates toward $[Pd_2L^N{}_4]^{4+}$. The method was also tested for the relative affinity of 14 additional guests toward both metallocages using among DFT(M06) method with success (mean absolute deviation (MAD) of 2.2 and 1.7 kcal·mol^{-1}, respectively). The use of semi-empirical PM7 [16] and tight-binding GFN-xTB [32] gave poor correlation with experimental values. The generally higher affinities of quinones toward $[Pd_2L^{CH}{}_4]^{4+}$ were also rationalized by analyzing the host–guest interaction separating the host in two parts: $[Pd(pyridine)_4]^{2+}$ describing the top and the bottom and [pyridine$_4$] (or [benzene$_4$]) representing the central part of the metallocage. As a result, the CH(**bq**)-N($\mathbf{L^N}$) bonds become irrelevant under

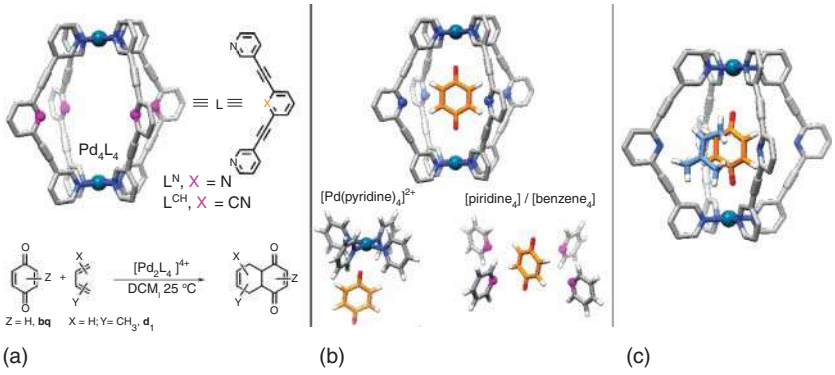

Figure 19.4 Representation of: (a) $Pd_2L_6^{4+}$ host cylindrical metallocage on the top, and Diels–Alder catalyzed reaction on the bottom; (b) representation of the inclusion complex **bq**⊂$[Pd_2L_4]^{4+}$ on the top and fragmentation scheme on the bottom; and (c) representation of the TS between **d1** and **qb**⊂$[Pd_2L^N{}_4]^{4+}$.

dielectric continuum model, while the CH(**bq**)-π(**L**$^{\mathbf{CH}}$) interactions contribute positively to the binding energy (Figure 19.4b).

Finally, the authors computed the Diels–Alder reaction between **bq** and isoprene, **d1**, inside both homologous metallocages. The formation of either the inclusion complex **d1**⊂$[Pd_2L_4]^{4+}$ or (**d1**+**bq**)⊂$[Pd_2L_4]^{4+}$ resulted in an unfavorable process. Computational investigation highlights an intermolecular mechanism between **bq**⊂$[Pd_2L_4]^{4+}$ and **d1** (Figure 19.4c). The reaction between **bq**⊂$[Pd_2L_4]^{4+}$ and **d1** lowers the barrier by 4.7 kcal·mol^{-1} compared to the Diels–Alder reaction in bulk, with an activation energy barrier of 18.8 kcal·mol^{-1} (in concordance with the experimental data, 20.4 kcal·mol^{-1}). Both cages enhance the electrophilicity of the encapsulated **bq** by decreasing the energy of the lowest occupied molecular orbital (LUMO). Nevertheless, whereas $[Pd_2L^N{}_4]^{4+}$ shows catalytic activity, $[Pd_2L_4{}^{CH}]^{4+}$ does not. To analyze this difference an energy distortion/interaction decomposition along with a NCI analysis was performed [27]. They realized that a significant distortion of the cage was taking place at the geometry of the TS. Nevertheless, a smaller distortion for the $[Pd_2L^N{}_4]^{4+}$ was needed compared to $[Pd_2L_4{}^{CH}]^{4+}$. Moreover, the NCI analysis revealed the larger steric clashes for $[Pd_2L_4{}^{CH}]^{4+}$, and the favorable CH···N hydrogen bonds for $[Pd_2L^N{}_4]^{4+}$. In order to explore a wide range of substrates, the authors proposed an approximation method: computing the *real* TSs *in vacuum* and using this geometry for calculating a *pseudo* TS inside the cage by optimizing the structure freezing the distances found in the *in vacuum* simulations. The proposed scheme, benchmarked in a data set of six quinones and five dienes achieved the 80% of accuracy in prediction of the Diels–Alder catalytic performance of Pd_2L_4 metallocages.

Pavan and coworkers [42], using classical MD and metadynamics, characterized the main molecular factors determining the *trans* → *cis* isomerization process of several azobenzenes inside the highly flexible $[(Pd\text{-}L^1)_6L^2{}_4]^{12+}$ metallocage [43], [L^1 = *N*,*N*,*N*′,*N*′-tetramethylethylenediamine, and L^2 = 1,3,5-tris(1-imidazolyl)

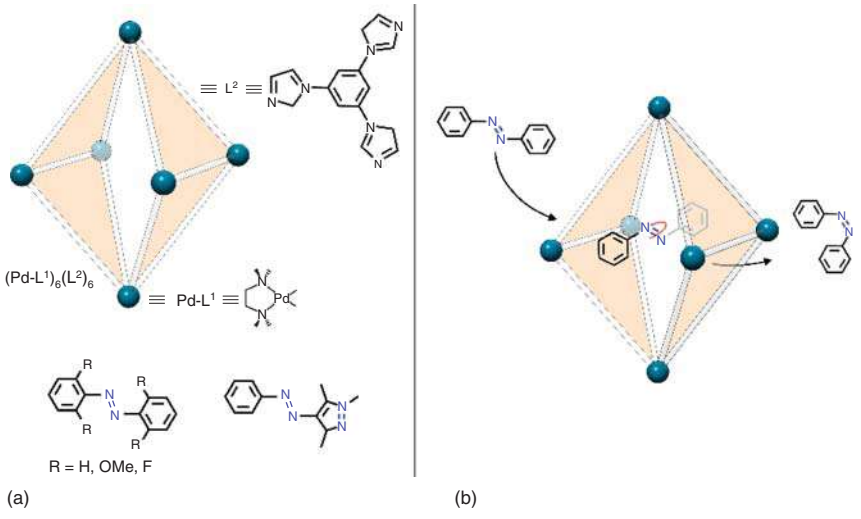

Figure 19.5 Representation of: (a) $[(Pd\text{-}L^1)_6L^2{}_4]^{12+}$ host octahedral metallocage on the top, and azobenzenes series on the bottom; (b) isomerization process proposed in the confined space of $[(Pd\text{-}L^1)_6L^2{}_4]^{12+}$.

benzene] (Figure 19.5a). As a result of a first series of MDs and metadynamics, the distortion of the cage on its axial and equatorial axes has been established within ∼1.4 to1.9 and ∼0.9 to 1.3 nm, respectively, in agreement with the high deformations observed experimentally (Figure 19.5b) [44]. The behavior of the MOC in the presence of several substrates (in their *cis* and *trans* forms) was analyzed following a similar strategy. The substrates remained bound within the cage during the whole MD simulation times. Comparing the behavior of encapsulated and empty cages, they observed that the metallocage loses flexibility upon encapsulation; moreover, to incorporate the guest, the MOC must undergo structural rearrangements, which requires a Gibbs energy cost. The energy penalty is similar for both *cis* and *trans* forms, indicating that there is not an additional Gibbs energy cost in terms of host deformation. The *cis–trans* isomerization process within the metallocage was simulated using a model for excited *trans*-azobenzenes. In this model, the potential term for the central CN=NC dihedral of azobenzene unit was derived from QM calculations on the excited state. During the MD simulations, the *trans*-azobenzene guest (which is assumed to reach the excited state) undergoes spontaneous *trans* → *cis* isomerization. Nevertheless, this observation is not enough to draw conclusions on whether the isomerization process takes place inside or outside the metallocage. To obtain a complete picture of the transition mechanism, and on the stability of the guest inside the host before and after the transition, additional metadynamics simulations on the guest encapsulation were performed. They found that formation of the host–guest *cis* isomers complex is energetically favored in all the tested cases ($\Delta G_{binding}$ from −3.6 up to −7.9 kcal·mol^{-1}) with slight lower activation barriers ($\Delta G_{encapsulation}{}^{\ddagger}$ about 0.3–2.8 kcal·mol^{-1}). These findings showed higher residence times of the *trans* isomers with respect to the isomerization

times, suggesting that the isomer conversion takes place preferentially inside the metallocage (Figure 19.5c). Finally, the deceleration of isomerization times with the increasing of the guests' volume was also investigated. They also found a similar relationship by artificially increasing the atomic radii of the guests, thus suggesting that the process could be hindered in highly crowded systems.

Other computational studies on supramolecular metallocages have almost exclusively focused on structural aspects [45].

19.4 Future Directions

To foresee the forthcoming of a research field always consists in a delicate exercise. The present topic is not an exception. Despite the application of computational chemistry to supramolecular catalysis is in its infancy, we are convinced that it is assured of a brilliant future. Such evolution is very likely to be associated with multiscaling methodologies, a necessary combination of methods from different grounds. To be reliable indeed, the study of the reactivity requires QM-based methods, either pure or QM/MM. On the other hand, these systems are quite large to perform systematic studies at this level of theory. Moreover, in addition to the size issues, working with these systems involves dealing with a huge number of possible host–guest configurations, which is even much larger when explicit solvent is included. Overall, they can make the computational simulation quite troublesome. The use of QM, MM, and MD simulations, as well as the proper combination of them, seems to be the most practical way to afford the computational investigation on MOCs and their application to catalysis. To deal with huge systems, other methods (as Coarse Grain models) can be also employed, although in those cases reactivity issues cannot be afforded.

Finally, the developments of automatic protocols for designing MOCs with tailored cavities are starting to appear (i.e. cgbind). They attempt to facilitate the construction, characterization, and prediction of functional metallocages. Their potential for rational design of new MOCs with defined properties is out of doubt, but reactivity issues once again are more challenging.

References

1 (a) Atwood, J.L. (2017). *Comprehensive Supramolecular Chemistry II*. Elsevier. (b) Steed, J.W. and Atwood, J.L. (2013). *Supramolecular Chemistry*. Wiley.

2 (a) Cook, T.R. and Stang, P.J. (2015). Recent developments in the preparation and chemistry of metallacycles and metallacages via coordination. *Chem. Rev.* 115 (15): 7001–7045. (b) Yoshizawa, M., Klosterman, J.K., and Fujita, M. (2009). Functional molecular flasks: new properties and reactions within discrete, self-assembled hosts. *Angew. Chem. Int. Ed.* 48 (19): 3418–3438.

3 (a) Zhang, D., Ronson, T.K., and Nitschke, J.R. (2018). Functional capsules via subcomponent self-assembly. *Acc. Chem. Res.* 51 (10): 2423–2436. (b) Cook,

T.R., Zheng, Y.-R., and Stang, P.J. (2013). Metal–organic frameworks and self-assembled supramolecular coordination complexes: comparing and contrasting the design, synthesis, and functionality of metal–organic materials. *Chem. Rev.* 113 (1): 734–777. (c) Brown, C.J., Toste, F.D., Bergman, R.G., and Raymond, K.N. (2015). Supramolecular catalysis in metal–ligand cluster hosts. *Chem. Rev.* 115 (9): 3012–3035. (d) Ballester, P., Fujita, M., and Rebek, J. (2015). Molecular containers. *Chem. Soc. Rev.* 44 (2): 392–393. (e) Ibáñez, S., Poyatos, M., and Peris, E. (2020). N-heterocyclic carbenes: a door open to supramolecular organometallic chemistry. *Acc. Chem. Res.* 53: 1401–1413.

4 Voloshin, Y., Belaya, I., and Krämer, R. (2016). *The Encapsulation Phenomenon: Synthesis, Reactivity and Applications of Caged Ions and Molecules*. Springer.

5 García-Simón, C., Garcia-Borràs, M., Gómez, L. et al. (2014). Sponge-like molecular cage for purification of fullerenes. *Nat. Commun.* 5 (1): 5557.

6 Li, J.-R. and Zhou, H.-C. (2010). Bridging-ligand-substitution strategy for the preparation of metal–organic polyhedra. *Nature Chem.* 2 (10): 893–898.

7 (a) Van Leeuwen, P.W.N.M. (2008). *Supramolecular Catalysis*. Wiley. (b) Morimoto, M., Bierschenk, S.M., Xia, K.T. et al. (2020). Advances in supramolecular host-mediated reactivity. *Nat. Chem.* https://doi.org/10.1038/s41929-020-00528-3.

8 Hosseini, M.W. and Lehn, J.-M. (1991). Supramolecular catalysis of adenosine triphosphate synthesis in aqueous solution mediated by a macrocyclic polyamine and divalent metal cations. *J. Chem. Soc., Chem. Commun.* (7): 451–453.

9 (a) Eisenstein, O., Ujaque, G., and Lledós, A. (2020). What makes a good (computed) energy profile? *Top. Organomet. Chem.* 67: 1–38. (b) Harvey, J.N., Himo, F., Maseras, F., and Perrin, L. (2019). Scope and challenge of computational methods for studying mechanism and reactivity in homogeneous catalysis. *ACS Catal.* 9 (8): 6803–6813. (c) Tantillo, D.J. (2016). Faster, Catalyst! React! React! Exploiting computational chemistry for catalyst development and design. *Acc. Chem. Res.* 49 (6): 1079–1079.

10 Lledós, A. and Ujaque, G. (2020). *Topics in Organometallic Chemistry: New Directions in the Modeling of Organometallic Reactions*. Springer Nature Switzerland AG.

11 (a) Pahima, E., Zhang, Q., Tiefenbacher, K., and Major, D.T. (2019). Discovering monoterpene catalysis inside nanocapsules with multiscale modeling and experiments. *J. Am. Chem. Soc.* 141 (15): 6234–6246. (b) Chakraborty, D. and Chattaraj, P.K. (2018). Confinement induced thermodynamic and kinetic facilitation of some Diels–Alder reactions inside a CB[7] cavitand. *J. Comput. Chem.* 39 (3): 151–160. (c) Daver, H., Harvey, J.N., Rebek, J., and Himo, F. (2017). Quantum chemical modeling of cycloaddition reaction in a self-assembled capsule. *J. Am. Chem. Soc.* 139 (43): 15494–15503. (d) Goehry, C., Besora, M., and Maseras, F. (2015). Computational study on the mechanism of the acceleration of 1,3-dipolar cycloaddition inside cucurbit[6]uril. *ACS Catal.* 5 (4): 2445–2451. (e) Kim, S.P., Leach, A.G., and Houk, K.N. (2002). The origins of noncovalent catalysis of intermolecular Diels–Alder reactions by cyclodextrins, self-assembling capsules, antibodies, and RNAses. *J. Org. Chem.* 67 (12): 4250–4260.

12 Frederix, P.W.J.M., Patmanidis, I., and Marrink, S.J. (2018). Molecular simulations of self-assembling bio-inspired supramolecular systems and their connection to experiments. *Chem. Soc. Rev.* 47 (10): 3470–3489.

13 Koch, W. and Holthausen, M.C. (2015). *A chemist's Guide to Density Functional Theory*. Wiley.

14 Chung, L.W., Sameera, W.M.C., Ramozzi, R. et al. (2015). The ONIOM method and its applications. *Chem. Rev.* 115 (12): 5678–5796.

15 Grimme, S., Bannwarth, C., and Shushkov, P. (2017). A robust and accurate tight-binding quantum chemical method for structures, vibrational frequencies, and noncovalent interactions of large molecular systems parametrized for all spd-block elements (Z = 1–86). *J. Chem. Theory Comput.* 13 (5): 1989–2009.

16 Stewart, J.J.P. (2013). Optimization of parameters for semiempirical methods VI: more modifications to the NDDO approximations and re-optimization of parameters. *J. Mol. Model.* 19 (1): 1–32.

17 (a) Thiel, W. (2014). Semiempirical quantum–chemical methods. *WIREs Comput. Mol. Sci.* 4 (2): 145–157. (b) Christensen, A.S., Kubař, T., Cui, Q., and Elstner, M. (2016). Semiempirical quantum mechanical methods for noncovalent interactions for chemical and biochemical applications. *Chem. Rev.* 116 (9): 5301–5337.

18 Li, P. and Merz, K.M. (2017). Metal ion modeling using classical mechanics. *Chem. Rev.* 117 (3): 1564–1686.

19 (a) Seminario, J.M. (1996). Calculation of intramolecular force fields from second-derivative tensors. *Int. J. Quantum Chem.* 60 (7): 1271–1277. (b) Li, P. and Merz, K.M. (2016). MCPB.py: a python based metal Center parameter builder. *J. Chem. Inf. Model.* 56 (4): 599–604. (c) Zheng, S., Tang, Q., He, J. et al. (2016). VFFDT: a new software for preparing AMBER force field parameters for metal-containing molecular systems. *J. Chem. Inf. Model.* 56 (4): 811–818.

20 Tomasi, J., Mennucci, B., and Cammi, R. (2005). Quantum mechanical continuum solvation models. *Chem. Rev.* 105 (8): 2999–3094.

21 Marenich, A.V., Cramer, C.J., and Truhlar, D.G. (2009). Universal solvation model based on solute electron density and on a continuum model of the solvent defined by the bulk dielectric constant and atomic surface tensions. *J. Phys. Chem. B* 113 (18): 6378–6396.

22 Klamt, A. and Schüürmann, G. (1993). COSMO: a new approach to dielectric screening in solvents with explicit expressions for the screening energy and its gradient. *J. Chem. Soc., Perkin Trans.* (5): 799–805.

23 (a) Aaqvist, J. and Warshel, A. (1989). Calculations of free energy profiles for the staphylococcal nuclease catalyzed reaction. *Biochemistry* 28 (11): 4680–4689. (b) Duarte, F., Bauer, P., Barrozo, A. et al. (2014). Force field independent metal parameters using a nonbonded dummy model. *J. Phys. Chem. B* 118 (16): 4351–4362. (c) Liao, Q., Kamerlin, S.C.L., and Strodel, B. (2015). Development and application of a nonbonded Cu^{2+} model that includes the Jahn–Teller effect. *J. Phys. Chem. Lett.* 6 (13): 2657–2662. (d) Liao, Q., Pabis, A., Strodel, B., and Kamerlin, S.C.L. (2017). Extending the nonbonded cationic dummy model to account for ion-induced dipole interactions. *J. Phys. Chem. Lett.* 8 (21): 5408–5414.

24 Young, T.A., Martí-Centelles, V., Wang, J. et al. (2020). Rationalizing the activity of an "artificial Diels–Alderase": establishing efficient and accurate protocols for calculating supramolecular catalysis. *J. Am. Chem. Soc.* 142 (3): 1300–1310.

25 Bernardi, R.C., Melo, M.C.R., and Schulten, K. (2015). Enhanced sampling techniques in molecular dynamics simulations of biological systems. *Biochim. Biophys. Acta* 1850 (5): 872–877.

26 (a) Marx, D. and Hutter, J. (2009). *Ab Initio Molecular Dynamics: Basic Theory and Advanced Methods*. Cambridge: Cambridge University Press. (b) Vidossich, P., Lledós, A., and Ujaque, G. (2016). First-principles molecular dynamics studies of organometallic complexes and homogeneous catalytic processes. *Acc. Chem. Res.* 49 (6): 1271–1278.

27 Contreras-García, J., Johnson, E.R., Keinan, S. et al. (2011). NCIPLOT: a program for plotting noncovalent interaction regions. *J. Chem. Theory Comput.* 7 (3): 625–632.

28 Fernández, I. and Bickelhaupt, F.M. (2014). The activation strain model and molecular orbital theory: understanding and designing chemical reactions. *Chem. Soc. Rev.* 43 (14): 4953–4967.

29 Mecozzi, S. and Rebek, J. (1998). Julius, the 55% solution: a formula for molecular recognition in the liquid state. *Chem. Eur. J.* 4 (6): 1016–1022.

30 Young, T.A., Gheorghe, R., and Duarte, F. (2020). cgbind: A python module and web app for automated metallocage construction and host–guest characterization. *J. Chem. Inf. Model.* 60 (7): 3546–3557.

31 Nurttila, S.S., Brenner, W., Mosquera, J. et al. (2019). Size-selective hydroformylation by a rhodium catalyst confined in a supramolecular cage. *Chem. Eur. J.* 25 (2): 609–620.

32 Bannwarth, C., Caldeweyher, E., Ehlert, S. et al. (2021). Extended tight-binding quantum chemistry methods. *WIREs Comput. Mol. Sci.* 11: e01493.

33 Hong, C.M., Bergman, R.G., Raymond, K.N., and Toste, F.D. (2018). Self-assembled tetrahedral hosts as supramolecular catalysts. *Acc. Chem. Res.* 51 (10): 2447–2455.

34 Norjmaa, G., Maréchal, J.-D., and Ujaque, G. (2019). Microsolvation and encapsulation effects on supramolecular catalysis: C–C reductive elimination inside $[Ga_4L_6]^{12-}$ metallocage. *J. Am. Chem. Soc.* 141 (33): 13114–13123.

35 Frushicheva, M.P., Mukherjee, S., and Warshel, A. (2012). Electrostatic origin of the catalytic effect of a supramolecular host catalyst. *J. Phys. Chem. B* 116 (45): 13353–13360.

36 (a) Hastings, C.J., Pluth, M.D., Bergman, R.G., and Raymond, K.N. (2010). Enzymelike catalysis of the Nazarov cyclization by supramolecular encapsulation. *J. Am. Chem. Soc.* 132 (20): 6938–6940. (b) Hastings, C.J., Pluth, M.D., Bergman, R.G., and Raymond, K.N. (2014). Origins of large rate enhancements in the Nazarov cyclization catalyzed by supramolecular encapsulation. *Chem. Eur. J.* 20: 3966–3973.

37 Norjmaa, G., Maréchal, J.-D., and Ujaque, G. (2020). Reaction rate inside the cavity of [Ga4L6]12− supramolecular metallocage is regulated by the encapsulated solvent. *Chem. Eur. J.* 26 (31): 6988–6992.

38 Vaissier Welborn, V. and Head-Gordon, T. (2018). Electrostatics generated by a supramolecular capsule stabilizes the transition state for carbon–carbon reductive elimination from gold(III) complex. *J. Phys. Chem. Lett.* 9 (14): 3814–3818.

39 Welborn, V.V., Li, W.-L., and Head-Gordon, T. (2020). Interplay of water and a supramolecular capsule for catalysis of reductive elimination reaction from gold. *Nat. Commun.* 11 (1): 415.

40 Pluth, M.D., Bergman, R.G., and Raymond, K.N. (2009). Proton-mediated chemistry and catalysis in a self-assembled supramolecular host. *Acc. Chem. Res.* 42 (10): 1650–1659.

41 Ootani, Y., Akinaga, Y., and Nakajima, T. (2015). Theoretical investigation of enantioselectivity of cage-like supramolecular assembly: the insights into the shape complementarity and host–guest interaction. *J. Comput. Chem.* 36 (7): 459–466.

42 Pesce, L., Perego, C., Grommet, A.B. et al. (2020). Molecular factors controlling the isomerization of azobenzenes in the cavity of a flexible coordination cage. *J. Am. Chem. Soc.* 142 (21): 9792–9802.

43 (a) Samanta, D., Mukherjee, S., Patil, Y.P., and Mukherjee, P.S. (2012). Self-assembled Pd_6 open cage with triimidazole walls and the use of its confined nanospace for catalytic Knoevenagel- and Diels–Alder reactions in aqueous medium. *Chem. Eur. J.* 18 (39): 12322–12329. (b) Samanta, D., Gemen, J., Chu, Z. et al. (2018). Reversible photoswitching of encapsulated azobenzenes in water. *Proc. Natl. Acad. Sci. U.S.A.* 115 (38): 9379–9384.

44 Samanta, D., Galaktionova, D., Gemen, J. et al. (2018). Reversible chromism of spiropyran in the cavity of a flexible coordination cage. *Nat. Commun.* 9 (1): 641.

45 (a) Murase, T., Horiuchi, S., and Fujita, M. (2010). Naphthalene Diels–Alder in a self-assembled molecular flask. *J. Am. Chem. Soc.* 132 (9): 2866–2867. (b) Horiuchi, S., Murase, T., and Fujita, M. (2011). Diels–Alder reactions of inert aromatic compounds within a self-assembled coordination cage. *Chem. Asian J.* 6 (7): 1839–1847. (c) Ibáñez, S. and Peris, E. (2019). A rigid trigonal-prismatic hexagold metallocage that behaves as a coronene trap. *Angew. Chem. Int. Ed.* 58 (20): 6693–6697. (d) Ibáñez, S. and Peris, E. (2020). Dimensional matching versus induced-fit distortions: binding affinities of planar and curved polyaromatic hydrocarbons with a tetragold metallorectangle. *Angew. Chem. Int. Ed.* 59 (17): 6860–6865. (e) García-Simón, C., Colomban, C., Çetin, Y.A. et al. (2020). Complete dynamic reconstruction of C60, C70, and (C59N)2 encapsulation into an adaptable supramolecular nanocapsule. *J. Am. Chem. Soc.* 142 (37): 16051–16063.

20

N-heterocyclic Carbene (NHC)-Capped Cyclodextrins for Cavity-Controlled Catalysis

Sylvain Roland and Matthieu Sollogoub

Sorbonne University, Parisian Institute of Molecular Chemistry, UMR CNRS 8232, 4 place Jussieu, 75005 Paris, France

20.1 Introduction: NHC-Capped Cyclodextrin Metal Complexes

Cyclodextrins (CDs) are naturally occurring cyclic oligo-glucopyranosides composed of 6, 7, or 8 sugar units forming α-, β-, and γ-CDs, respectively. They have been seen as potential enzyme mimics as early as the 1950s by Cramer because they are both water-soluble and characterized by a hydrophobic cavity that can include substrates [1]. Very early on, they also have been associated to a metal center [2, 3] and such a conjugate was then described for the first time by Breslow as an "artificial enzyme" [4]. A plethora of biomimetic reactions catalyzed by CDs was then described [5]. Metal coordination by CD-based ligands has thrived over the past years [6]. Phosphorus [7], nitrogen [8], sulfur [9], or carbon [10]-based ligands were attached to the CD to coordinate the metal at the entrance of the cavity who can potentially play the role of second coordination sphere. In 2013, we came out with a different design: the CD was capped with an *N*-heterocyclic carbene (NHC) ligand pointing toward the inside of the cavity leading upon complexation, to full encapsulation of the metal inside the cavity of the CD, which now plays the role of both first and second coordination sphere [11, 12]. With this design, the substrates are therefore forced to interact with the cavity to access a reactive metal center. This encapsulation allowed us to isolate reactive species. This design also induced a modification of the shape of the cavity, and we showed that this shape was at the origin of various selectivities in different catalytic reactions that will be exposed here.

The synthesis of this family of ligands is straightforward. Starting from native CDs, a benzylation/regioselective debenzylation sequence gave diols **1α**, **1β**, and **1γ** [13]. It was followed by a bis-mesylation to afford the bis-mesylated α-, β-, and γ-CDs (**2α**, **2β**, and **2γ**), which were capped with imidazole to form the corresponding imidazoliums (α-, β-, and γ-ICyD)HCl that could be metallated into (α-, β-, and γ-ICyD)MCl [11]. ICyD stands for imidazol-2-ylidene-capped-benzylated CD; it is

Supramolecular Catalysis: New Directions and Developments, First Edition.
Edited by Piet W.N.M. van Leeuwen and Matthieu Raynal.

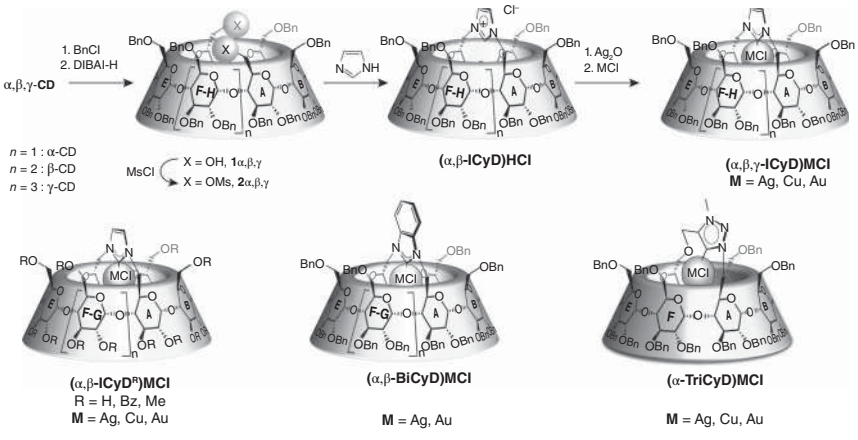

Figure 20.1 Synthesis and structural variation of the NHC-capped CDs.

preceded by the nature of the CD (α, β, or γ). We also varied the functionalization of the CD hydroxyls: free hydroxyls, benzoates, and methyls, and called the corresponding derivatives α-ICyD^{H}, α-ICyD^{Bz}, and α- and β-ICyD^{Me}, respectively [11, 14, 15]. We also explored other carbenes: benzimidazolylidene-capped-benzylated CD called BiCyD and triazolylidene-capped CDs complexes called TriCyD [14]. α-BiCyD^{Me} was subsequently synthesized by others (Figure 20.1) [16].

In (**ICyD**)MCl complexes, the inside of the CD cavity is lined with protons of the different glucosyl units that can interact with the metal center and the halogen atom. The main interactions are those of H-5s with the metal center and of H-3s with the chloride (Figure 20.2). This was first observed by NMR where these protons were strongly deshielded compared to the corresponding imidazoliums (ICyD)HCl. This effect was first attributed to anagostic interactions between H-5s and the metal and weak hydrogen bonding between H-3 and the chloride [14]. In-depth theoretical study of this system now makes us qualify the C–H· · ·M interaction as contra-electrostatic H-bonds [17].

Subsequent NMR [14], X-ray [15], and modeling studies on (α-**ICyD**)AuCl showed that the cavity adopted a different shape than that of the native CD and that the closer the proton was from the metal or the chloride the more deshielded

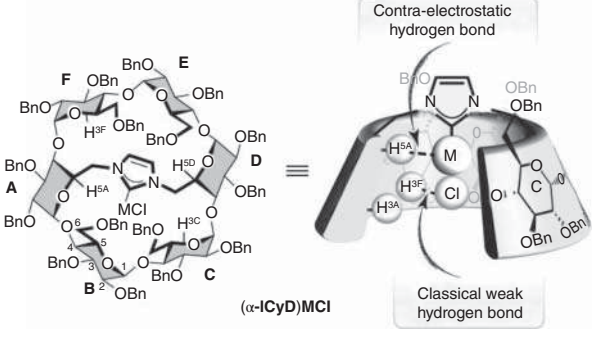

Figure 20.2 H-3s and H-5s interact with the metal-halogen unit inside the cavity.

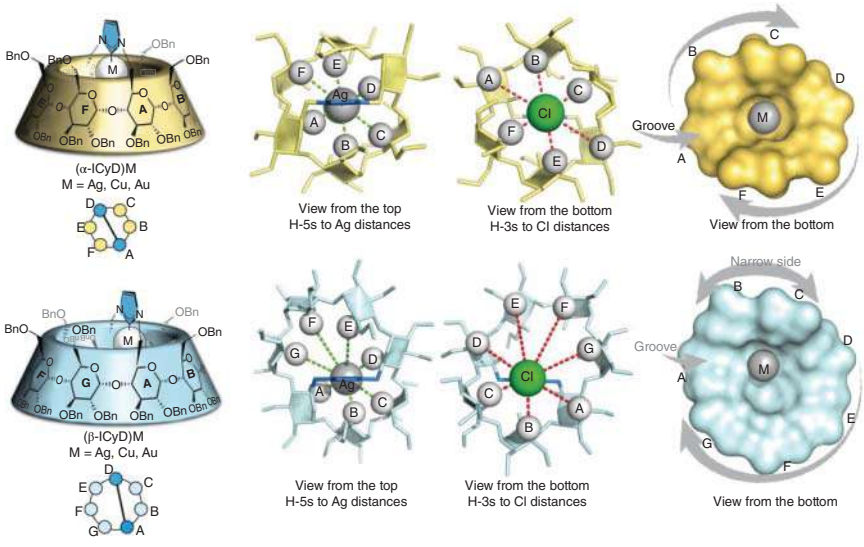

Figure 20.3 Shapes of α-**ICyD** and β-**ICyD** linked to the H-3s and H-5s respective distances to MCl.

it is. This observation allowed to determine the shapes of the other complexes (β- and γ-ICyD)MCl. In all cases, the NHC bridging induces a tilting of the glucose units bearing the NHC and an asymmetric deformation of the macrocycle but quite distinct according to the nature of the CD. For instance, the cavity of the α-**ICyD** wraps tightly the metal and adopts a helical shape as a (*M*)-helix. In the cases of β-**ICyD**, the cavity is more open, a pit is visible next to the metal, furthermore one side of the cavity forms some sort of a steep wall, while the other side adopts a (*M*)-helical shape. Thus, while a lateral approach to the metal by a substrate is conceivable in the case of β-**ICyD**, it seems to be excluded in the case of α-**ICyD** (Figure 20.3) [14].

Capping of CDs with NHCs gives access to (α- and β-**ICyD**)MCl complexes that possess different chiral shapes for their cavities. We therefore wondered whether, as in the case of enzymes, these topographically well-defined cavities could account for the selectivity of various catalytic reactions.

20.2 Orientation of Cyclization Reactions – Five vs. Six-Membered Cycle

CD-NHC-based **ICyD** ligands have been mainly studied in catalysis with group 11 metals. We first investigated the properties of **ICyDAuCl** gold(I) complexes in cycloisomerization reactions where a significant effect of the shape/size of the CD cavity on the reaction outcome was observed. For instance, gold(I)-catalyzed cycloisomerization reactions of enynes, such as **3**, were found to give different sizes of cycle depending on whether the α-CD- or the β-CD-based gold complex is used [11, 14].

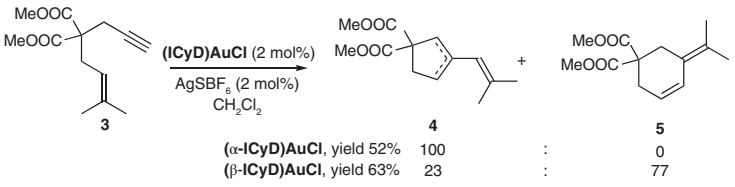

Figure 20.4 Effect of the CD cavity on the outcome of gold-catalyzed cyclization reactions.

(α-**ICyD**)**AuCl** induces the formation of a five-membered cyclopentene ring **4** as the sole isomer, whereas with (β-**ICyD**)**AuCl**, a six-membered ring **5** is obtained as the major isomer (ratio 77 : 23) (Figure 20.4).

With an encapsulated reactive gold center, the stability of the reaction intermediates and transition states, which are bound to the metal deep inside the cavity, is significantly affected by the nature of the CD. In gold-catalyzed cycloisomerization reactions, the enyne initially reacts with a cationic [(α-**ICyD**)**Au**]$^+$ or [(β-**ICyD**)**Au**]$^+$ complex to form a gold cyclopropyl intermediate of similar structure for both complexes. However, density-functional theory (DFT) calculations showed that different conformers of the gold cyclopropyl intermediate were favored in α- or β-CD-based ligands (Figure 20.5) [14]. In α-**ICyD**, only one conformer **A** is observed which leads rapidly to the formation of the cyclobutene intermediate that rearranges in the five-membered-ring product **4**. In β-**ICyD**, two different conformers **B** and **C** are accessible but **B** is more stable by 4.08 kcal mol^{-1} than **C** and it leads to the formation of the cyclohexene **5** and cyclopentene product **4**, from **B** and **C**, respectively. Consequently, the different shapes of their cavities lead to two different major fragmentation pathways for (α-**ICyD**)**AuCl** or (β-**ICyD**)**AuCl**, providing two different cyclization products (Figure 20.5).

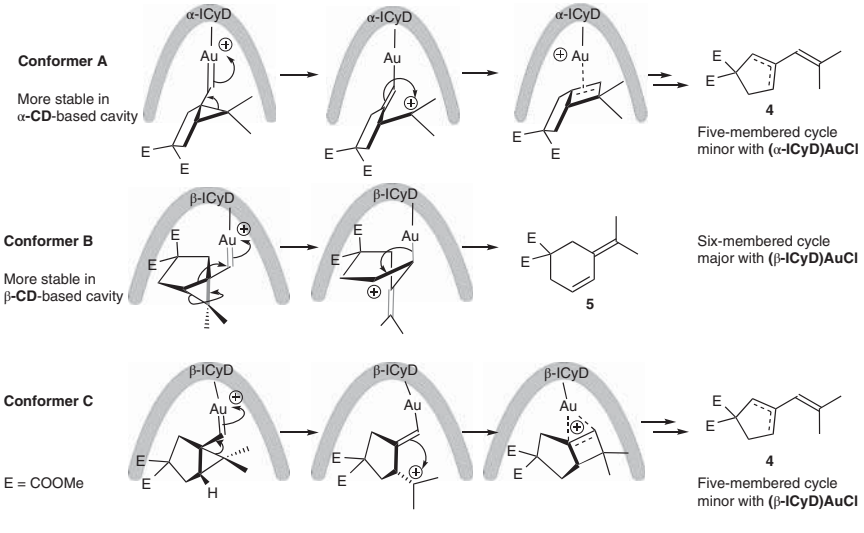

Figure 20.5 Different stabilizations of gold cyclopropyl intermediate conformers by the CD cavity.

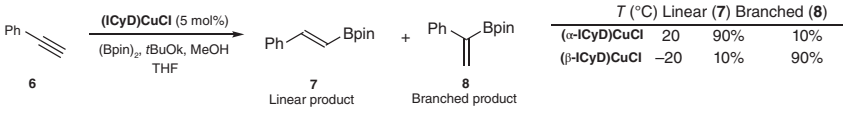

Figure 20.6 Cavity-directed regioselective copper-catalyzed hydroboration.

20.3 Control of Regioselectivity

Another interesting cavity effect was observed in the copper-catalyzed formal hydroboration of alkynes in the presence of $(Bpin)_2$ [18, 19] which was investigated with (α- and β-**ICyD**)**CuCl** complexes. A dramatic inversion of regioselectivity was observed when one complex or the other was used. Starting from the same alkyne, for example phenylacetylene **6**, with (α-**ICyD**)**CuCl**, the linear adduct **7** is formed as the major isomer, whereas the opposite regioselectivity is obtained with (β-**ICyD**)**CuCl**, leading to the branched adduct **8** as the major one (Figure 20.6) [20]. The reaction is faster with the β-CD-based catalyst having a larger cavity. In this case, the reaction was run at −20 °C to optimize regioselectivity.

Calculations showed that two different cavity-induced approaches are responsible for the different regioselectivities observed with α-**ICyD** and β-**ICyD**. With conventional NHCs, the mechanism involves a "parallel" or "anti-parallel" lateral approach of the alkyne to the NHC—Cu—B bond [19, 21], and the regioselectivity of the reaction is governed by the relative orientation of both partners (Figure 20.7a). With β-**ICyD** ligands, only the less hindered CH side of the terminal alkyne can be placed deep inside the cavity to react with the copper center through a "parallel" approach. This classical parallel approach, which is controlled by steric factors (the Ph group is outside the cavity), leads to the formation of the branched adduct (**8**) preferentially (Figure 20.7b). It is worth noting that classical NHCs with alkyl substituents would rather give the linear product for reasons more linked to electronic properties of the ligand as demonstrated by Hoveyda and coworkers [19]. With α-CD-based copper complexes having a smaller cavity, the penetration of the alkyne inside the cavity was shown to be very disfavored, and a "perpendicular" approach at the entrance of the cavity was proposed. This approach allows alkyne/metal interaction to take place and induces the formation of the linear isomer (**7**) as the major one (Figure 20.7c). Examination of inter-atomic distances in the corresponding transition state in α-**ICyD** (**TSα** linear) showed that the Cβ—B bond was rather short (1.7 Å), whereas the Cα—Cu bond was long (2.16 Å), leading to the development of a negative charge at Cα, which is stabilized by delocalization in the aromatic group which accounts for the regioselectivity here (Figure 20.7d).

Another example of cavity-induced switch in regioselectivity was observed in the copper-catalyzed formal reduction of α,β-unsaturated ketones, such as benzylideneacetone **9**, in the presence of silanes. In this reaction, α-**ICyDCuCl** gave the 1,2 reduction product **10** as the major one, whereas β-**ICyDCuCl** gave 1,4 reduction (**11**) or full reduction (**12**) products depending on the amount of $PhSiH_3$ used (Figure 20.8) [22].

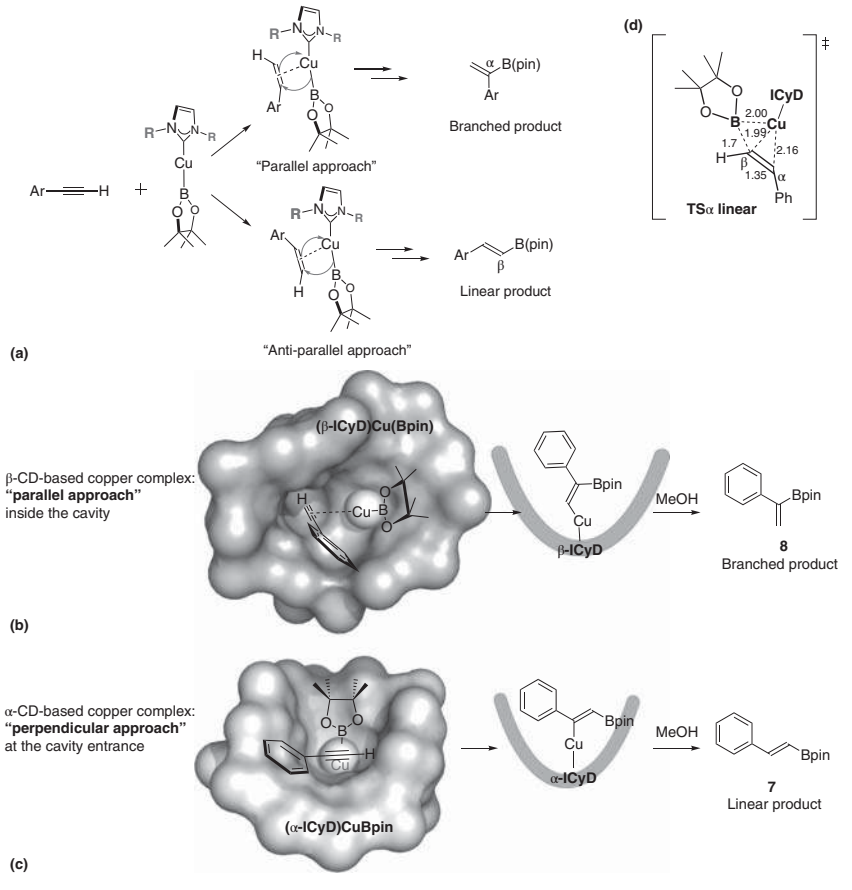

Figure 20.7 Schematic representations of a perpendicular or parallel approach of the alkyne in CD-NHC–copper complexes (**ICyD** ligands).

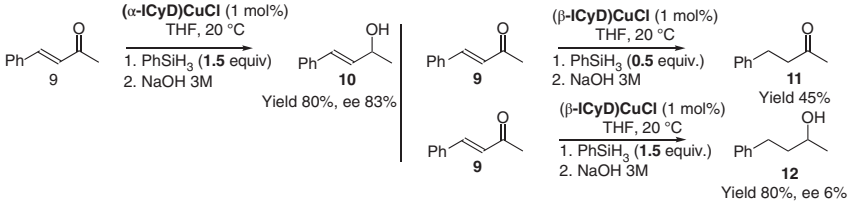

Figure 20.8 Switch in regioselectivity in the formal reduction of α,β-unsaturated ketones.

Calculations showed that the transition state for the 1,2-addition is favored in α-ICyD, whereas that of the 1,4-addition is significantly lower in energy in the cavity of the larger β-CD-based ligand. Concerning the 1,2-addition, it appears that the energies of the transition states **TS-α-1,2** and **TS-β-1,2** are very similar. However, for the 1,4-addition, which requires ketone activation, the cavity effect is much more important and a difference in energy of 8.5–8.9 kcal mol^{-1} was calculated between

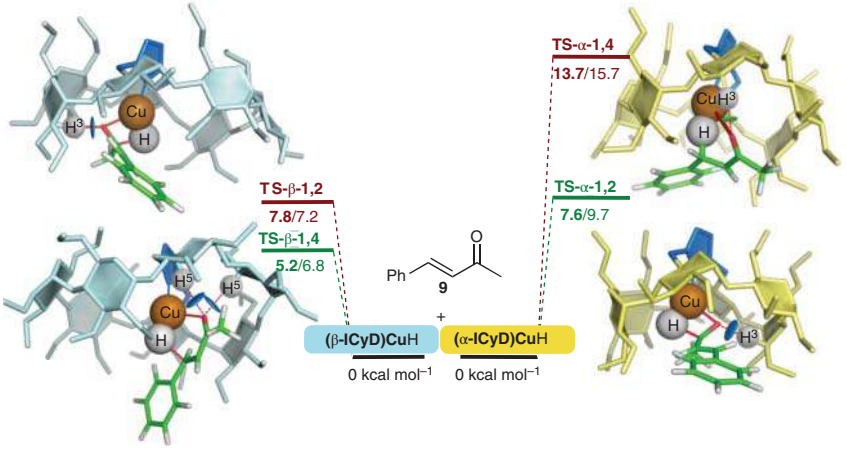

Figure 20.9 View of the two key transition states for each **ICyD** ligand, highlighting the interaction between the substrate and the CD moiety as found by NCI. (Color code for NCI analysis: red: repulsive, green: weakly attractive, blue: attractive).

TS-α-**1**,**4** and **TS**-β-**1**,**4**, the latter being the most stable. These models showed that in **TS**-α-**1**,**4**, the distance between the copper and oxygen atoms was 3.6 Å compared to 2.3 Å in **TS**-β-**1**,**4**. Hence, it is likely that the 1,4-addition is more concerted in β-**ICyD** than in α-**ICyD** and thus favored in the former case. Here again, the difference in stability between the different TSs is linked to the shape of the cavity. In the case of α-**ICyD**, the substrate lies at the entrance of the cavity, perpendicular to the Cu–H, a behavior reminiscent of the one found for cuproboration reaction discussed earlier. In contrast, with β-**ICyD**, the substrate has the space to penetrate further inside the cavity. Furthermore, non-covalent interaction (NCI) analyses suggest that the difference in energy between **TS**-α-**1**,**4** and **TS**-β-**1**,**4** might result from two stabilizing C = O···H-5 attractive interactions in **TS**-β-**1**,**4** compared to one weakly attractive C = O···H-5 interaction in **TS**-α-**1**,**4**. When comparing **TS**-α-**1**,**2** and **TS**-α-**1**,**4**, we can also observe a strong stabilizing C=O···H-3 attractive interactions in **TS**-α-**1**,**2**, which is rather weak in **TS**-α-**1**,**4**. For β-**ICyD**, there are two stabilizing interactions with the cavity in TS1,4 and only one in TS1,2. We therefore clearly demonstrate the role of the cavity in the chemoselectivity of this reaction, which is linked not only to steric repulsion but also to stabilizing interactions. Here, the second sphere of coordination plays a stabilizing role for the transition state, much like in enzymes (Figure 20.9).

20.4 Control of Enantioselectivity by the CD Chiral Cavity

Both the chiral cavities of α-**ICyD** and β-**ICyD** ligands have been shown to induce significant enantioselectivity in metal-catalyzed reactions. The first example was reported in 2013 in the gold-catalyzed cycloisomerization reaction of enynes (**13** and **14**) that gave up to 80% ee (Figure 20.10) [11]. The β-CD-derived ligand

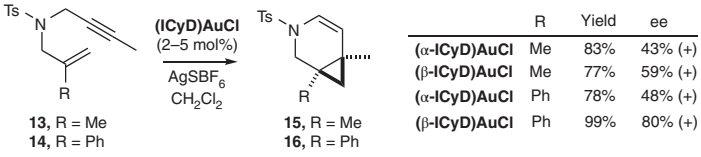

	R	Yield	ee
(α-ICyD)AuCl	Me	83%	43% (+)
(β-ICyD)AuCl	Me	77%	59% (+)
(α-ICyD)AuCl	Ph	78%	48% (+)
(β-ICyD)AuCl	Ph	99%	80% (+)

Figure 20.10 CD-induced enantioselectivity in a gold-catalyzed cycloisomerization reaction.

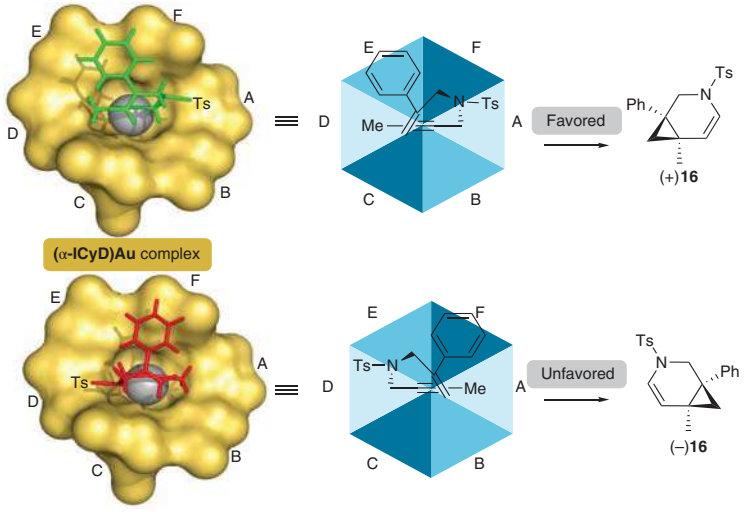

Figure 20.11 Models of the different conformers of enyne **14** in the cavity of α-**ICyD** ligand. The favored approach leading to the major enantiomer is shown on the left.

β-**ICyD** was found to induce better control of enantioselectivity than the α-CD-based one. This is a general trend that has been consistently observed in gold catalysis so far. Note that reactions are also usually slower with α-CD-based catalysts than with β-CD-based catalysts, and therefore, higher temperatures are required to get similar reaction rates.

Interestingly, the chiral cavities of α-**ICyD** and β-**ICyD** ligands, although different in shape, induce the formation of the same major enantiomer, although the discrimination is better in the cavity of β-CD-based ligands (Figure 20.11).

A good approximation of the shape of the CD cavity in a series of **ICyD** metal complexes could be obtained from NMR studies and calculations. Study of the approach of the alkyne in the cavity by using these shapes allowed to rationalize the enantioselectivity. This selectivity stems from the approach of the alkene on the gold-activated alkyne. The two possible approaches are shown in Figure 20.11. The alkyne is positioned in flattest area of the ligands, then the enyne can adopt two conformations, and the major isomer is obtained when the aryl attached to the alkene is less hindered by the helical shape of the cavity. For a better understanding, we can schematize the shape of the CD by replacing each sugar unit by a blue triangle and differentiate the triangles according to their inclination, the flatter they

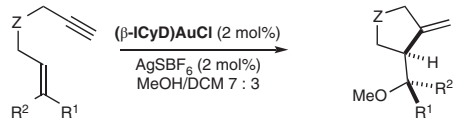

3, Z = $C(CO_2Me)_2$, $R^1 = R^2$ = Me
17, Z = NTs, $R^1 = R^2$ = Me
18, Z = NTs, R^1 = Ph, R^2 = H

19, Z = $C(CO_2Me)_2$, $R^1 = R^2$ = Me, 95%, ee 94% (–)
20, Z = NTs, $R^1 = R^2$ = Me, 79%, ee 84% (–)
21, Z = NTs, R^1 = Ph, R^2 = H, 58%, ee 86% (–)

Figure 20.12 Enantioselective gold-catalyzed alkoxycyclization and hydroxycyclization reactions with β-CD-based ligands.

are the lighter blue. The phenyl group is thus better accommodated in a lighter blue triangle. This simple model made by hand was confirmed by DFT calculation. We therefore clearly show how the shape of the cavity induced by the capping of the CD induces enantioselectivity (Figure 20.11) [14].

The best control of enantioselectivity by the β-CD cavity was observed in gold-catalyzed alkoxycyclization and hydroxycyclization reactions. In a MeOH/DCM mixture, the alkoxycyclization of enyne **3** gave **19** with an enantioselectivity reaching 94% ee using 2% of (β-**ICyD**)**AuCl** [23], which is very competitive compared to previous reports [24]. When the initial double bond of the enyne is substituted by three different groups, as in **18**, two stereogenic centers are formed simultaneously in **21** (Figure 20.12).

From the proposed mechanism, it appears that the first stereo-determining step is the cyclization of the enyne **3**. This suggests that a highly favored cyclization reaction, which is cavity-controlled, takes place from π-complex **D** (Figure 20.13). This step leads to an intermediate chiral gold cyclopropylcarbene intermediate **B** (the same as in Figure 20.5) with high control of stereoselectivity. Intermediate **B** reacts with small alcohol nucleophiles such as MeOH to give alkoxycyclization products while keeping stereoselectivity. Here also, we have proposed models based on the shape of the β-**ICyD** cavity to rationalize the enantioselectivity (Figure 20.13) [23].

In 2020, we reported highly enantioselective gold-catalyzed cycloisomerization and hydroxycyclization reactions in neat water by using water-soluble **ICyD^{Me}** ligands derived from permethylated α- or β-CD [14]. In the cycloisomerization reaction of enyne **13**, α- and β-**ICyD^{Me}** led to the same cyclized product **15** with 60% and 81% ee, respectively. As in organic solvents, α- and β-CD-derived ligands led to the same major enantiomer, and the enantioselectivity is better with the β-CD-derived ligand. In hydroxycyclization reactions, a more dramatic effect of the nature of the cavity both on reactivity and on enantioselectivity was observed. In the presence of (α-**ICyD^{Me}**)**AuCl**, the reaction with enyne **3** is very difficult under standard conditions (without silver salts), even at 50 °C, leading to virtually no conversion. Addition of silver salts ($AgSbF_6$) was required for the reaction to take place, leading to the cyclized product **22** with 74% conversion (after 18 hours) and a moderate enantioselectivity (54% ee). In contrast, with (β-**ICyD^{Me}**)**AuCl**, a conversion of **3** into **22** in 74% yield was obtained at 50 °C without activation by silver salts. In addition, a very high enantioselectivity was observed with an ee reaching 96%. The enantioselectivity with β-**ICyD^{Me}** could be further improved by running the reaction at a lower

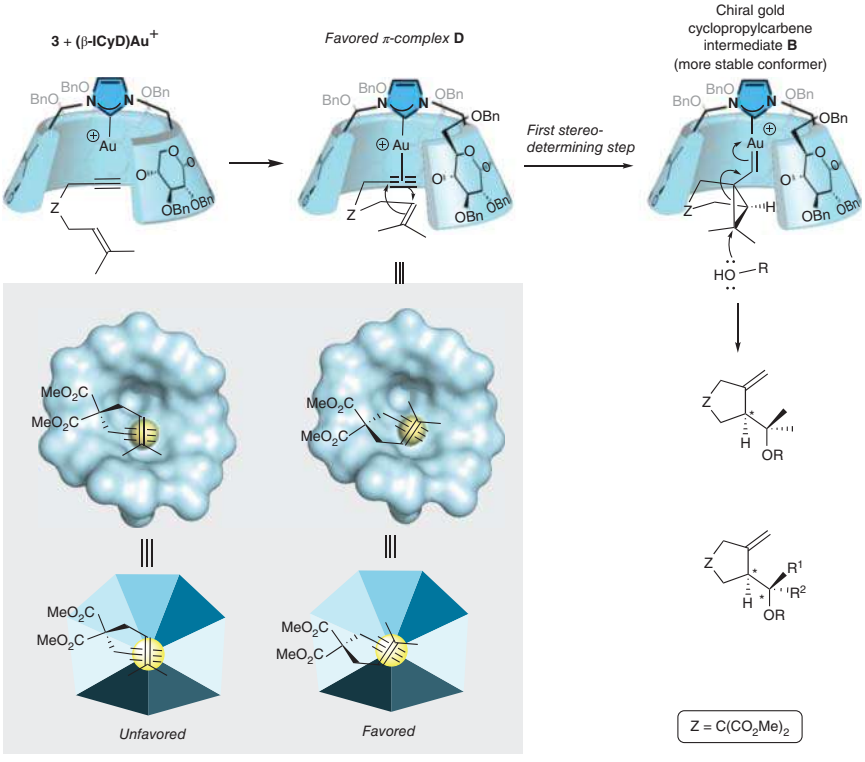

Figure 20.13 Cavity-controlled favored formation of a chiral gold cyclopropyl intermediate in (β-ICyD)Au complexes and enantioselective alkoxycyclization reactions.

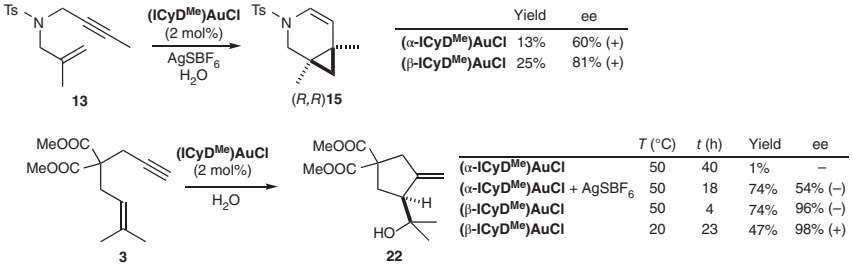

Figure 20.14 Enantioselective gold-catalyzed reaction in water with water-soluble α-**ICyD^{Me}** and β-**ICyD^{Me}** ligands.

temperature (20 °C) at which an ee of 98% was measured, a value which was not reached so far with other systems (Figure 20.14).

20.5 Substrate Selectivity

In gold-catalyzed alkoxycyclization reactions catalyzed by (β-**ICyD^{Me}**)**AuCl**, we observed that the size of the alcohol involved in the reaction affected the reaction

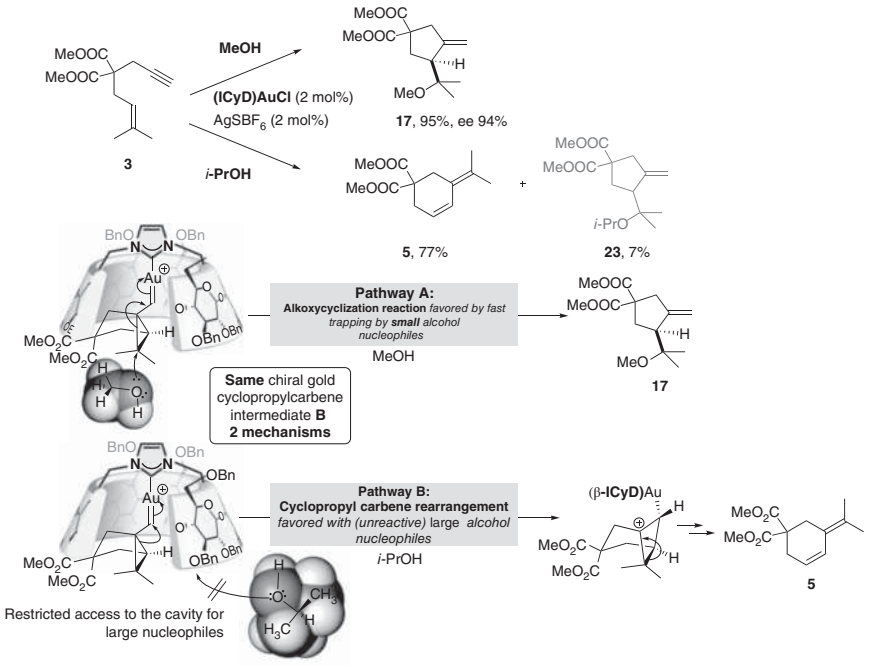

Figure 20.15 Control of reaction pathways by the size of the substrate.

pathway [23]. Actually, the alkoxycyclization reaction of **3** was found only to take place as the major reaction when small alcohol nucleophiles such as MeOH are used affording **17**. The experiments showed that increasing the size of the alcohol to *i*-PrOH, for example, led to the gradual emergence of a competitive enyne cyclization product **5** in which the alcohol was not involved. This result demonstrated that the cavity of the β-CD-derived ligands was able to select substrates of different sizes to interact with reactive intermediate **B** in the cavity. When a small nucleophile is used, its addition to the gold cyclopropyl intermediate **B** is presumably fast enough to favor pathway A over the cyclopropylcarbene rearrangement (pathway B). Steric clash between large nucleophiles and the β-CD cavity in **B** slows down the alkoxycyclization reaction (pathway A), and gold cyclopropylcarbene rearrangement becomes favorable (pathway B) to afford cyclohexene **5**. (Figure 20.15) This is yet another consequence of the encapsulation of the metal center inside the CD cavity.

20.6 Protection of Metal Centers and Promotion of Reactive Species

In some metal-catalyzed reactions, the protective role of the CD cavity to maintain catalytic activity could be clearly demonstrated. For instance, comparison of α- and β-CD-derived **ICyD^{Me}** ligands in silver-catalyzed hydration reactions of alkynes in water showed a dramatic difference in conversion (Figure 20.16), the larger

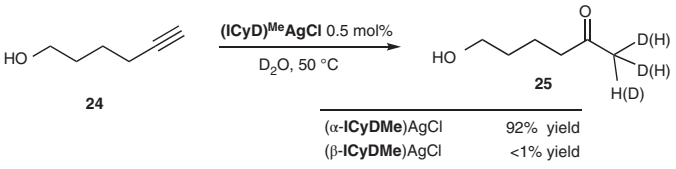

Figure 20.16 (ICyD^{Me})AgCl-catalyzed hydration of alkynes.

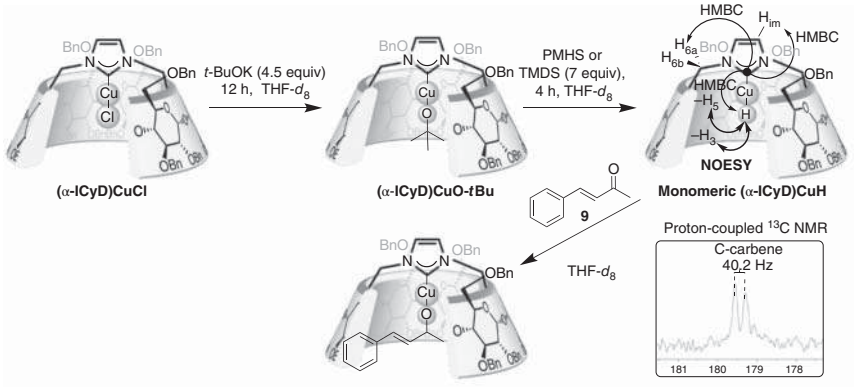

Figure 20.17 Synthesis, characterization, and reactivity of the monomeric (α-**ICyD**)**CuH**.

(β-**ICyD^{Me}**)**AgCl** complex being virtually inactive [15]. NMR experiments showed that in water at 50 °C, the β-CD-based silver catalyst was decomposing, whereas, in contrast, the α-CD-based catalyst (α-**ICyD^{Me}**)**AgCl** was stable, allowing the hydration reaction to take place. This demonstrates the high stabilizing effect of the small α-CD cavity compared to that of the β-CD.

The CD cavity was also exploited to capture reactive species that could not be isolated using more conventional NHCs. For instance, copper hydride species, which has the propensity to aggregate, has never been isolated as a monomeric species, although it has been seen in equilibrium with its dimer by Bertrand and coworkers [25]. By using α-**ICyD** ligands, we could isolate and characterize a monomeric (L)CuH complex on its own in solution [22], an unprecedented result which was attributed to the high protecting and stabilizing effect of the α-CD cavity preventing dimerization and further oligomerization. To do so, we first reacted (α-**ICyD**)**CuCl** with *t*-BuOK to give (α-**ICyD**)**CuO*t*-Bu**, which under the action of polymethylhydrosiloxane (PMHS) afforded a single product as evidenced by NMR monitoring. The monomeric state of this product was spectroscopically evidenced, following Bertrand's characterization [25]. The carbene signal was found as a doublet at ~180 ppm in the proton-coupled ^{13}C NMR, with a coupling constant of 40.2 Hz, characteristic of a trans $^{2}J(^{13}C\text{-}^{1}H)$ coupling, clearly revealing the monomeric character of the complex. Further characterization used HMBC experiment that showed cross-correlations between this carbene and protons of the imidazole ring, H-6s of the sugars attached to the NHC and a proton at 1.5 ppm which was attributed to the hydride. In addition, intra-cavity cross-correlations

between the hydride and intra-cavity H-5 and H-3 protons confirmed that the hydride was indeed inside the cavity. Furthermore, we studied the reactivity of this hydride by adding the benzylideneacetone **9**. We obtained the product of 1,2-addition, confirming that the monomeric (**ICyD**)**CuH** is the reactive species in the catalytic reduction described earlier (Figure 20.17).

20.7 Concluding Remarks

The family of NHC-capped CDs, ICyDs, has proven to be very effective in reactions catalyzed by gold, copper, and even silver. The reactive center is deeply encapsulated within the CD cavity, and this unique property has allowed the isolation of reactive species such as the monomeric Cu–H. In addition, the capping of the CD induces a deformation of the cavity giving it a well-defined asymmetrical shape. This asymmetry resulted in enantioselective reactions with very high ees, in some cases, even better than with classical phosphines. Moreover, the shape of the cavity is very different between α-ICyD and β-ICyD. This difference could be exploited to operate ligand-controlled regioselective copper-catalyzed hydroboration or chemoselective α,β-unsaturated ketone reduction. We also showed that the cavity acted as a second sphere of coordination which was involved in the selectivity of the reactions studied by the stabilization of TSs. This set of features, stabilization of reactive species through encapsulation, shape-induced regio-, enantio-, and chemo-selectivities, closely resembles those of metalloenzymes.

Acknowledgments

The authors thank all the students and colleagues who participated in this adventure.

References

1 Cramer, F. (1953). Über Einschlußverbindungen, V. Mitteil.: Basenkatalyse durch innermolekulare Hohlräume. *Chem. Ber.* 86: 1576–1581.
2 Engeldinger, E., Armspach, D., and Matt, D. (2003). Capped cyclodextrins. *Chem. Rev.* 103: 4147–4174.
3 Cyclodextrin catalysis as a model for enzyme action. I. Tabushi (1982). *Acc. Chem. Res.* 15: 66–72.
4 Breslow, R. and Overman, L.E. (1970). "Artificial enzyme" combining a metal catalytic group and a hydrophobic binding cavity. *J. Am. Chem. Soc.* 92: 1075–1077.
5 Breslow, R. and Dong, S.D. (1998). Biomimetic reactions catalyzed by cyclodextrins and their derivatives. *Chem. Rev.* 98: 1997–2012.
6 Gramage-Doria, R., Armspach, D., and Matt, D. (2013). Metallated cavitands (calixarenes, resorcinarenes, cyclodextrins) with internal coordination sites. *Coord. Chem. Rev.* 257: 776–816.

7 Reetz, M.T. and Rudolph, J. (1993). Synthesis of a phosphine-modified cyclodextrin and its rhodium complex. *Tetrahedron: Asymm.* 4: 2405–2406. Reetz, M.T. and Waldvogel, S.R. (1997). β-Cyclodextrin-modified diphosphanes as ligands for supramolecular rhodium catalysts. *Angew. Chem. Int. Ed.* 36: 865–867. Wong, Y.T., Yang, C., Ying, K.-C., and Jia, G. (2002). Synthesis of a novel β-cyclodextrin-functionalized diphosphine ligand and its catalytic properties for asymmetric hydrogenation. *Organometallics* 21: 1782–1787. Engeldinger, E., Poorters, L., Armspach, D. et al. (2004). Diastereospecific synthesis of phosphinidene-capped cyclodextrins leading to "introverted" ligands. *Chem. Commun.*: 634–635. Tran, D.N., Legrand, F.-X., Menuel, S. et al. (2012). Cyclodextrin–phosphane possessing a guest-tunable conformation for aqueous rhodium-catalyzed hydroformylation. *Chem. Commun.* 48: 753–755.

8 Yang, C., Cheung, Y.K., Yao, J. et al. (2001). Palladium and platinum complexes with a β-cyclodextrin-functionalized phosphine ligand. *Organometallics* 20: 424–429. Heck, R. and Marsura, A. (2004). A new symmetrically modified α-cyclodextrin tripode: selective metal complexation and fluorescence properties. *Tetrahedron Lett.* 45: 281–284. Sechet, D., Kaya, Z., Phan, T.-A. et al. (2017). Aza-capped cyclodextrins for intra-cavity metal complexation. *Chem. Commun.* 53: 11717–11720.

9 Benmerad, B., Clair, P., Armspach, D. et al. (2006). Sulfur-capped cyclodextrins: a new class of cavitands with extroverted as well as introverted donor functionalities. *Chem. Commun.* 25: 2678–2680.

10 Legrand, F.-X., Ménand, M., Sollogoub, M. et al. (2011). An N-heterocyclic carbene ligand based on a β-cyclodextrin–imidazolium salt: synthesis, characterization of organometallic complexes and Suzuki coupling. *New J. Chem.* 35: 2061–2065. Guitet, M., Marcelo, F., de Beaumais, S.A. et al. (2013). Diametrically opposed carbenes on an α-cyclodextrin: synthesis, characterization of organometallic complexes and Suzuki–Miyaura coupling in ethanol and in water. *Eur. J. Org. Chem.*: 3691–3699.

11 Guitet, M., Zhang, P., Marcelo, F. et al. (2013). NHC-capped cyclodextrins (ICyDs): insulated metal complexes, commutable multicoordination sphere, and cavity-dependent catalysis. *Angew. Chem. Int. Ed.* 52: 7213–7218.

12 Roland, S., Suárez, J.M., and Sollogoub, M. (2018). Confinement of metal-*N*-heterocyclic carbene complexes to control reactivity in catalytic reactions (minireview). *Chem. Eur. J.* 24: 12464–12473.

13 Lecourt, T., Pearce, A.J., Herault, A. et al. (2004). Triisobutylaluminium and diisobutylaluminium hydride as molecular scalpels: the regioselective stripping of perbenzylated sugars and cyclodextrins. *Chem. Eur. J.* 10: 2960–2971.

14 Zhang, P., Tugny, C., Suárez, J.M. et al. (2017). Artificial chiral metallo-pockets including a single metal serving as structural probe and catalytic center. *Chem* 3: 174–191.

15 Zhu, X., Xu, G., Chamoreau, L.-M. et al. Permethylated NHC-capped α- and β-cyclodextrins (ICyDMe). Regioselective and enantioselective gold-catalysis in pure water. *Chem. Eur. J.* 2020, 26: 15901–15909.

16 Kaya, Z., Andna, L., Matt, D. et al. (2018). Benzimidazolium- and benzimidazolilydene-capped cyclodextrins: new perspectives in anion encapsulation and gold-catalyzed cycloisomerization of 1,6-enynes. *Chem. Eur. J.* 24: 17921–17926.

17 dos Passos Gomes, G., Xu, G., Zhu, X. et al. (2021). Mapping C–H...M interactions in confined spaces: (α-ICyD^{Me})Au, Ag, Cu complexes reveal "contra-electrostatic H-bonds" masquerading as anagostic interactions. *Chem. Eur. J.* 27: 8127–8142.

18 Yun, J. (2013). Copper(I)-catalyzed boron addition reactions of alkynes with diboron reagents. *Asian J. Org. Chem.* 2: 1016–1025. Barbeyron, R., Benedetti, E., Cossy, J. et al. (2014). Recent developments in alkyne borylations. *Tetrahedron* 70: 8431–8452. Fujihara, T., Semba, K., Terao, J., and Tsuji, Y. (2014). Regioselective transformation of alkynes catalyzed by a copper hydride or boryl copper species. *Catal. Sci. Technol.* 4: 1699–1709. Yoshida, H. (2016). Borylation of alkynes under base/coinage metal catalysis: some recent developments. *ACS Catal.* 6: 1799–1811.

19 Jang, H., Zhugralin, A.R., Lee, Y., and Hoveyda, A.H. (2011). Highly selective methods for synthesis of internal (α-) vinylboronates through efficient NHC–Cu-catalyzed hydroboration of terminal alkynes. Utility in chemical synthesis and mechanistic basis for selectivity. *J. Am. Chem. Soc.* 133: 7859–7871.

20 Zhang, P., Suárez, J.M., Driant, T. et al. (2017). Cyclodextrin cavity-induced mechanistic switch in copper-catalyzed hydroboration. *Angew. Chem. Int. Ed.* 56: 10821–10825. Wen, Z., Zhang, Y., Roland, S., and Sollogoub, M. (2019). Carboboration of alkynes with cyclodextrin-encapsulated N-heterocyclic carbene copper complexes. *Eur. J. Org. Chem.*: 2682–2687.

21 Moon, J.H., Jung, H.-Y., Lee, Y.J. et al. (2015). Origin of Regioselectivity in the Copper-Catalyzed Borylation Reactions of Internal Aryl Alkynes with Bis(pinacolato)diboron. *Organometallics* 2151–2159.

22 Xu, G., Leloux, S., Zhang, P. et al. (2020). Capturing the elusive monomeric (L)CuH in NHC-capped cyclodextrins (ICyDs): cavity-controlled chemoselective hydrosilylation of α,β-unsaturated ketones. *Angew. Chem. Int. Ed.* 59: 7591–7597.

23 Tugny, C., del Rio, N., Koohgard, M. et al. (2020). β-cyclodextrin-NHC-gold(I) Complex (β-ICyD)AuCl: a chiral nanoreactor for enantio- and substrate-selective alkoxycyclization reactions. *ACS Catal.* 10: 5964–5972.

24 Charruault, L., Michelet, V., Taras, R. et al. (2004). Functionalized carbo- and heterocycles via Pt-catalyzed asymmetric alkoxycyclization of 1,6-enynes. *Chem. Commun.*: 850–851.

25 Romero, E.A., Olsen, P.M., Jazzar, R. et al. (2017). Spectroscopic evidence for a monomeric copper(I) hydride and crystallographic characterization of a monomeric silver(I) hydride. *Angew. Chem. Int. Ed.* 56: 4024–4027.

21

Supramolecular Catalysis by Metallohosts Based on Glycoluril

Jeroen P.J. Bruekers, Johannes A.A.W. Elemans, and Roeland J.M. Nolte

Radboud University, Institute for Molecules and Materials, Department of Molecular Chemistry, Heyendaalseweg 135, Nijmegen 6525 AJ, The Netherlands

21.1 Introduction

Since the discovery of the first enzyme (diastase) by Anselme Payen and Jean-Francois Persoz in 1833 [1] and Emil Fischer's attempt in 1894 to explain the mechanism of the action of enzymes, chemists have been intrigued by nature's catalytic systems and have tried to mimic them. According to Fischer's proposal [2], an enzyme possesses an indentation or cleft in which one particular substrate fits preferentially and is converted by nearby catalytically active groups. With the advent of supramolecular chemistry in the early 1970s, this relatively simple concept has been worked out to form the basis for the design of catalysts that contain a cavity in which a molecule can be bound and transformed by one or more adjacent reactive functions. In the last decades, a variety of cavity molecules have been designed and synthesized, including cavitands [3], cyclodextrins [4], calixarenes [5], pillararenes [6], and cucurbiturils [7]. These cavity molecules have been used for different purposes, such as the construction of catenanes and rotaxanes [8], but also for applications such as biochemical sensing [9] and substrate-selective catalysis [10]. For the latter application, our group has developed cavity-containing compounds derived from the concave molecule diphenylglycoluril to which aromatic side walls are attached, often referred to as molecular clips (**1**, Figure 21.1). These molecular clips act as hosts for phenol and dihydroxybenzene derivatives (association constants $K_a = 10–10^5\ M^{-1}$), which bind a guest via hydrogen bonding, π–π stacking interactions, and a "cavity effect," i.e. the entropically favorable filling of the cavity by the guest [11, 12]. They have been further functionalized with (aza)crown ethers to provide the diphenylglycoluril-based derivatives **2**, which have a basket-shaped structure (Figure 21.1) [11, 13]. Baskets **2** have a strong affinity for small cations (e.g. K^+, $K_a = 4.2 \times 10^8\ M^{-1}$), diammonium salts, or cationic aromatic guests such as methyl viologen (**Me_2V**, $K_a = 5.7 \times 10^4\ M^{-1}$) [11, 14]. In the following sections, we will describe supramolecular catalysts derived from baskets **2** and the functionalisation of clip **1** with a porphyrin roof via ethyleneoxy linkers, resulting

Supramolecular Catalysis: New Directions and Developments, First Edition.
Edited by Piet W.N.M. van Leeuwen and Matthieu Raynal.

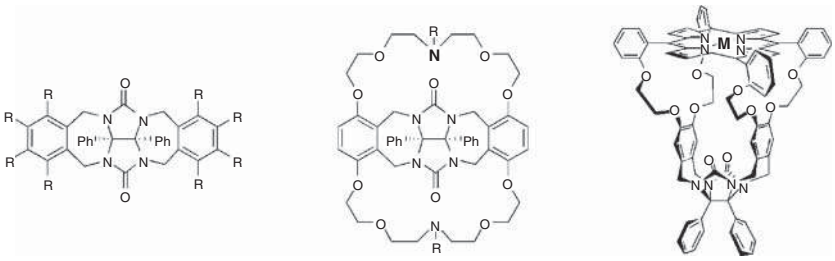

Figure 21.1 General structures of molecular clips (**1**), baskets (**2**), and cages (**3**).

in cage catalyst **3** (Figure 21.1). The latter compound has a more defined cavity than compounds **1** and **2**. Cage compound **3** is also able to bind dihydroxybenzenes and viologen derivatives with high affinities (up to $K_a = 10^7\ M^{-1}$). Its manganese derivative has been studied as a distributive epoxidation catalyst, i.e. a catalyst in which the substrate binds and is converted into product in one single reaction, and as a processive epoxidation catalyst, i.e. a catalyst that after binding a (polymeric) substrate converts it multiple times at different locations on the substrate, without detaching [15]. The ruthenium derivative of **3** has been applied as a catalyst for the coupling of α-diazoesters [16].

21.2 Rhodium-Based Catalytic Baskets

Rhodium catalysts are well-known hydrogenation, hydroformylation, and isomerization catalysts. Our group has combined a tetrakis(triphenylphosphite)rhodium(I) hydride complex with molecular basket **2** to obtain the cavity-containing catalyst **4** (Figure 21.2a). Compound **4** was able to isomerize **5**, a guest molecule that binds to **2** (R = benzyl) with $K_a = 90\ M^{-1}$, the products being the corresponding *cis*- and *trans*-methylstyrenes in a ratio of circa 1 : 3. The isomerization rate was circa 5 times higher than the rate of isomerization of the nonbinding allylbenzene (66% and 12% conversion after two hours, respectively). This is in sheer contrast to the conversion of these substrates by the noncavity containing catalyst $HRh(CO)[P(OPh)_3]_3$, which does not show any difference in rates [18]. Catalyst **4** is able to distinguish between substrates **5–7** (Figure 21.2b), which bind with different binding strengths in its cavity, **5**: $K_a = 90\ M^{-1}$, **6**: no binding, and **7**: $K_a = 2200\ M^{-1}$. Under a hydrogen atmosphere, **4** is able to convert these substrates into the corresponding β-methylstyrenes (isomerization) or propyl derivatives (hydrogenation). The initial reaction rates of this catalyst were compared to those of $HRh[P(OPh)_3]_4$. The rates of hydrogenation measured for the non-binding substrate **6** decreased going from $HRh[P(OPh)_3]_4$ to **4** ($v_{initial}(HRh[P(OPh)_3]_4)/v_{initial}(\mathbf{4}) = 12$), whereas the hydrogenation rates for the binding substrates **5** and **7** increased with ratios of 2.2 and 4.7, respectively. The ratio between isomerization and hydrogenation for substrates **5**–**7** also changed when employing basket **4**, i.e. from 1.2 (**5**), 10.1 (**6**), and 0.9 (**7**) for $HRh[P(OPh)_3]_4$ to 4.8 (**5**), 5.7 (**6**), 1.3 (**7**) for **4**. Further detailed kinetic studies gave the following insights

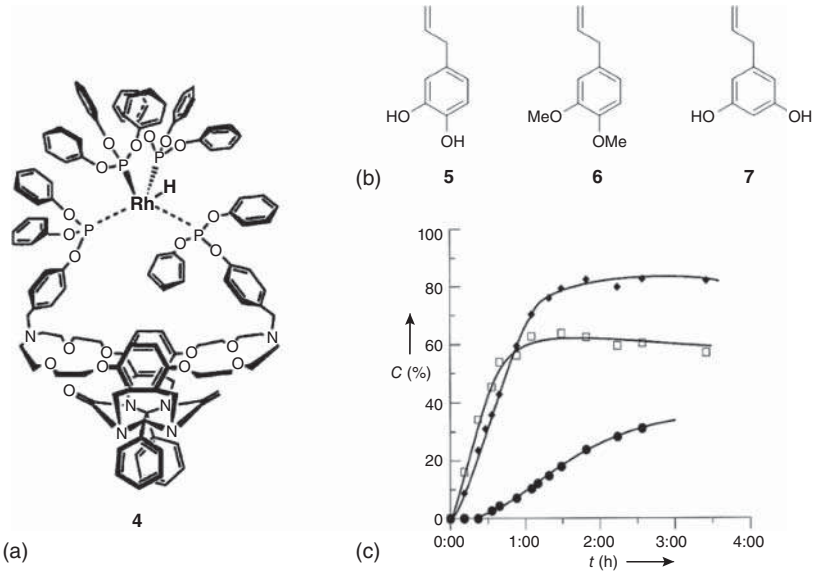

Figure 21.2 (a) Rhodium-based catalytic basket **4**. (b) Substrates **5**–**7**. (c) Plots of the conversions of the substrates over time by catalyst **4** in a competition experiment, **5** (♦), **6** (•), **7** (□). Source: Reproduced with permission from The American Chemical Society [17].

into this supramolecular catalytic system: (i) stronger binding inside the host results in faster conversions, (ii) the Rh center is not completely shielded from the solution and is still accessible to nonbinding substrates, (iii) hydrogenation preferentially takes place inside the cavity of **4**, while the isomerization reaction primarily occurs on the outside of **4**, and (iv) the rate-limiting step for the hydrogenation reaction is the addition of H_2 to the Rh-phosphite complex, in a similar way as known for $HRh[P(OPh)_3]_4$ [17].

The reaction between **4** and substrates **5**–**7** was also investigated under competitive conditions (3 equiv of substrates **5**–**7**, 0.4 atm. of H_2, Figure 21.2c). The conversion of **7** started immediately, while **5** and **6** experienced a lag period of 3 and 22 minutes, respectively. Substrate **6** did not react until about 50% of **5** and 75% of **7** had reacted. This experiment shows that the supramolecular system is a substrate selective catalyst. Interestingly, the conversion rate of **5** was not significantly decreased by the presence of **7** in this mixture, which one would have expected based on the binding constants of the two guest substrates. This effect was ascribed to cooperative binding of both substrates **5** and **7** in the cavity of **4**. This phenomenon was investigated further by studying the rates of the conversion of **5** in the presence of the coguest resorcinol. This additive had no effect on the activity of the rhodium center itself, but the conversion rates of **5** increased almost ninefold (from $v_{initial}$ 3.4 to 29.8 $\mu M\ s^{-1}$) after an induction period of 25 minutes. This rate enhancement was not observed for the model catalyst $HRh[P(OPh)_3]_4$, supporting the idea of a cooperative binding effect in the case of **4** [17].

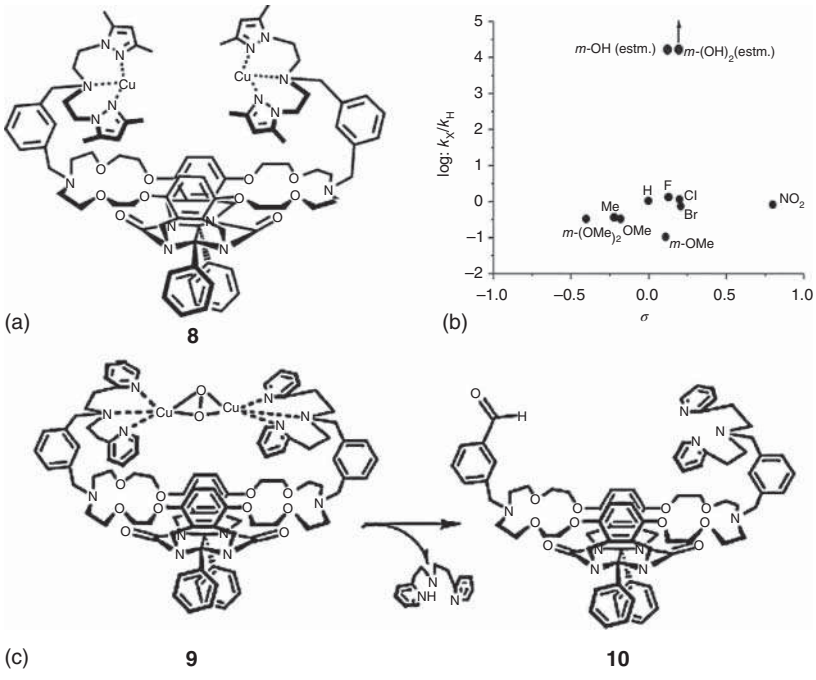

Figure 21.3 (a) Copper-pyrazole basket **8**. (b) Hammett plot for the oxidation of substituted benzylic alcohols with **8**. (c) Copper–pyridine–oxygen basket **9** and its self-oxidation reaction, leading to catalyst destruction. Source: Reproduced with permission from The American Chemical Society [19].

21.3 Copper-Based Catalytic Baskets

Via a similar approach as described for the supramolecular hydrogenation and isomerization catalysts, basket **2** was converted into a supramolecular oxidation catalyst. This was achieved by providing **2** with pyrazole ligands and treating the resulting functionalized compound with $Cu(ClO_4)_2$ to give the bis-Cu(II) basket **8** (Figure 21.3a). Since the cavity of basket **2** was designed to bind (di)hydroxybenzenes, the ability of copper basket **8** to oxidize (hydroxy)benzyl alcohols to the corresponding aldehydes was investigated [19]. In this reaction, which is stoichiometric, the Cu(II) center is irreversibly reduced to Cu(I). In preliminary experiments oxidation of 3-hydroxybenzyl alcohol and 3,5-dihydroxybenzyl alcohol by **8** turned out to be much faster than the oxidation of benzyl alcohol. Detailed kinetic studies with a large series (10 examples) of substituted benzyl alcohols provided a Hammett plot (Figure 21.3b), from which it was clear that the higher rates ($>4\times10^4$ fold) of the hydroxyl-substituted benzyl alcohols was not the result of a simple electronic effect, but caused by complexation of these substrates in the cavity of **8** [19].

Unfortunately, the copper-catalyzed reaction is stoichiometric, and the system did not show turnover. In an effort to develop a truly catalytic system, which moreover

uses molecular oxygen as the oxidant, the pyrazole ligands in basket **8** were changed for pyridine ligands and Cu(I) was used as the metal center, yielding bis-Cu(I) basket **9** (Figure 21.3c). Low-temperature experiments showed that **9** binds molecular oxygen in a side-on fashion, i.e. a bent μ-η^2:η^2 mode, in a similar way as copper enzymes do [20, 21]. Basket **9** still had the ability to bind guest substrate molecules, but was not able to oxidize these with molecular oxygen. Separate experiments showed that this was caused by degradation of the supramolecular catalyst, i.e. oxidation of one of the ligands of **9** yielding the benzaldehyde-functionalized basket **10** (Figure 21.3c). Theoretical calculations revealed that in **9** the xylylene spacer groups and the reacting benzylic positions are very close to the Cu_2O_2 complex (shortest distance ~2.3 Å), leading to a rapid ligand oxidation and destruction of the catalyst [20, 21].

21.4 Porphyrin Cage Catalysts

21.4.1 Epoxidation of Low-Molecular-Weight Alkenes

Functionalizing molecular clip **1** with a porphyrin roof via four ethyleneoxy spacers results in porphyrin cage **3** (M = 2H, Figure 21.1). This compound was first prepared in low yield via a nine-step synthesis in 1998 [22–24], but the procedure could recently be optimized resulting in a considerably increased overall yield (including up to 58% for the final cage forming step) [25]. Cage compound **3** is relatively rigid and has a cavity with a diameter of 9 Å, in which dihydroxybenzenes can be bound in a similar way as in the parent clip compound **1**, as well as viologen derivatives [23]. Yet, its structure is flexible enough to stretch the cavity a bit when needed. This is revealed in the allosteric binding of $\mathbf{Me_2V}$ in the porphyrin double cage compound **11** (Figure 21.4). Binding of the viologen guest in the first cavity of **11** proceeds with a high association constant ($K_a = 7 \times 10^7\ M^{-1}$), but subsequent binding of another viologen guest in the second cavity occurs with a considerably decreased binding affinity (~three orders of magnitude, $K_a = 5 \times 10^4\ M^{-1}$). As a result of the binding of the first viologen the side walls of the cavity slightly move outward to accommodate the guest. This in turn causes pinching of the empty cavity, leading to a decreased binding of the second viologen guest [26].

When a Mn(III) center is inserted into the porphyrin ring of **3**, this host system becomes catalytically active. The activity of catalyst **Mn3** was compared to that of manganese(III)tetraphenyl porphyrin **MnTPP** and its ortho-methoxy-substituted derivative **MnTMPP** in the epoxidation of alkenes using sodium hypochlorite as the oxidant and pyridine (Py) as an axial ligand in a two-phase organic solvent water system. Binding of a pyridine ligand to **MnTPP** is known to enhance the catalytic activity of the manganese center. It is proposed that the electron donating character of the ligand facilitates the formation of the active Mn-oxo species and increases its stability. Due to the relatively low association constant ($K_a < 1000\ M^{-1}$), 500 equiv of Py are needed for optimal results in the case of **MnTPP**. However, employing **Mn3** required only 1 equiv of Py, since this ligand binds strongly inside the cavity of this host (K_a with **Zn3** $= 1.1 \times 10^5\ M^{-1}$), while simultaneously enhancing the

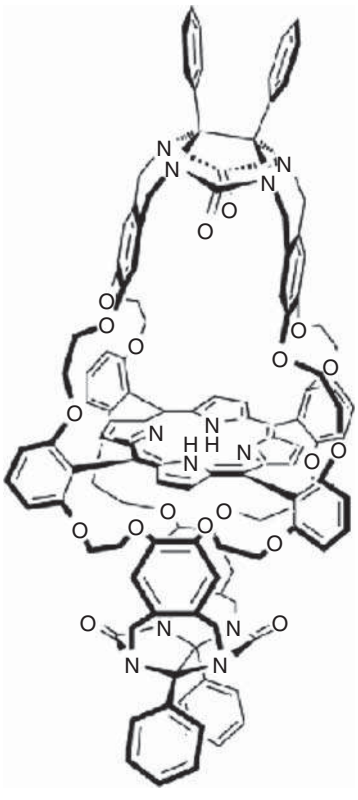

Figure 21.4 Structure of porphyrin double cage compound **11**.

11

epoxidation reaction rate 5–10-fold [27]. This enhancement is not caused by electronic or steric effects of the alkoxy spacer groups in **Mn3**, as **MnTMPP** displayed even lower epoxidation rates than **MnTPP**. *trans*-Stilbene as a substrate exclusively yielded the *trans*-epoxide, while the epoxidation of *cis*-stilbene yielded both *cis*- and *trans*-epoxide, the cis/trans ratios being 94 : 4 and 65 : 35 for **Mn3** and **MnTPP**, respectively. For the latter catalyst, this ratio could be improved further by adding more ligand. This enhancement in selectivity was rationalized by the strong coordination of the axial ligand pulling the metal center further into the plane of the porphyrin, thereby sterically hindering the rotation around the C—C bond of the substrate coordinated to the other face of the porphyrin in the transition state [24, 27].

A drawback of the use of **MnTPP** and **MnTMPP** is their instability. In the course of the catalytic reaction, the mixture gradually decolorizes, especially in a later stage when the amount of unreacted alkene diminishes. This is attributed to the formation of μ-oxo-bridged Mn(IV) dimers, which are inactive and rapidly decompose. This instability was also observed in the case of **Mn3** when 1 equiv of Py is present. To prevent the formation of these dimers of **Mn3**, a bulky axial ligand, i.e. 4-*tert*-butylpyridine (Bupy), which does not fit inside the cavity was employed. This eliminated the decomposition of the catalyst, as shown by the fact that the color was

retained and new additions of alkenes resulted in similar epoxidation rates, thus affording high turnover numbers per **Mn3** molecule (>1000). This stabilization by Bupy was not observed in the case of **MnTPP** and **MnTMPP**, which decomposed rapidly. The use of Bupy also forces the reaction to preferably occur inside the cavity of **Mn3**, rather than on the outside, which is the case when pyridine is present as an axial ligand. This difference in reaction site allows the system to differentiate between substrates: *trans*-stilbene is converted twice as fast as *cis*-stilbene inside **Mn3**, whereas these rates are similar when the reaction occurs outside of this cage catalyst. Molecular modeling revealed that the bulkier *cis*-stilbene experiences severe steric hindrance when confined inside the host, while this hindrance for the near flat *trans*-stilbene is negligible [24, 27].

In an effort to obtain a more chemically stable catalyst that does not form the proposed μ-oxo-bridged dimer, which eventually results in the destruction of the catalyst, the manganese derivative of **11**, i.e. **Mn11**, was prepared and studied [26, 28]. In this catalyst, the porphyrin is shielded from both sides by a diphenylglycoluril-based clip, which makes it impossible to form a μ-oxo-bridged species. Furthermore, cage catalyst **Mn11** can be activated with just 1 equiv of Py, just like **Mn3**, which is an advantage. The initial epoxidation rate of alkenes by **Mn11** indeed could be increased by the addition of 1 equiv pyridine, but subsequent addition of more Py caused the rate to decrease. This is likely due to the binding of pyridine in the second cavity, where it inhibits the formation of the active oxo-species [28]. The epoxidation of *cis*-stilbene inside the cavity of **Mn11** (1 equiv of Py present) was circa 22 times slower than the epoxidation of this substrate inside the cavity of **Mn3** (500 equiv of Bupy present) and for *trans*-stilbene the rate was 12 times slower**.** This suggests that the (second) cavity of **Mn11** is sterically less accessible, in line with the host–guest binding studies mentioned above. The conversion of *cis*-stilbene by **Mn11** resulted in a substantial amount of *trans*-stilbene oxide product (c/t = 40 : 60 when 1 equiv of Py is present), indicating that the pseudo-rotaxane geometry of the catalyst–substrate complex in **Mn11** imposes steric constraints on the bulky reaction intermediate in the transition state, causing its partial isomerization. Although the reaction rates of **Mn11** were low compared to **Mn3** and other manganese porphyrins, the reaction always went to completion without any catalyst decomposition. The addition of a new batch of substrate resulted in the same reaction rate and again in a complete conversion. This remarkable difference in catalyst stability can be attributed to the shielding of the manganese porphyrin by the two diphenylglycoluril-based cavity molecules, preventing μ-oxo dimer formation to occur (see above) [28].

Since the biphasic epoxidation system described above with sodium hypochlorite as oxidant is not conveniently scaled up, the possibility of employing molecular oxygen in combination with a co-reductant, e.g. isobutyraldehyde, in a single-phase system in the epoxidation of alkenes catalyzed by **Mn3** was investigated [29]. This approach has the added advantage of being more environmentally friendly and cost effective. For a series of different substrates, high conversions were obtained with 0.5 mol% of **Mn3** and excess of Bupy (Table 21.1). The catalytic reaction proceeded most smoothly in chlorinated solvents, such as dichloromethane and

Table 21.1 Aerobic epoxidation of alkenes by catalysts **Mn3** and **MnTPP**.[a)]

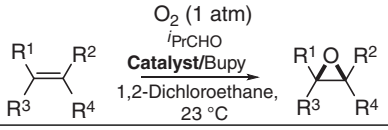

Entry	Catalyst	Substrate	Product	Time (h)	Yield (%)	*cis/trans*
1	**Mn3**			4	94	
2	**Mn3**			4	89	
3	**Mn3**	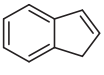	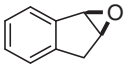	4	72	
4	**Mn3**	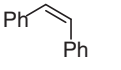		4	91	95 : 5
	MnTPP			4	86	90 : 10
5	**Mn3**	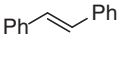	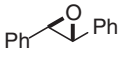	8	32	<1 : 99
	Mn3[b)]			24	45	<1 : 99
	MnTPP			8	30	5 : 95
6	**Mn3**	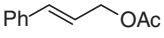	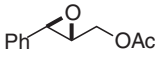	8	67	<1 : 99
	MnTPP			8	61	3 : 97
7	**Mn3**		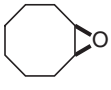	24	48	
	MnTPP			8	89	
8	**Mn3**	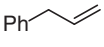	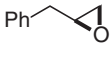	4	96	
9	**Mn3**	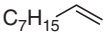	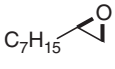	4	95	

a) Reaction conditions: olefin (0.2 mmol), isobutyraldehyde (2.0 mmol), Bupy (1.0 mmol), catalyst (1.0 μmol), dichloroethane (4 ml), O_2-balloon bubbling, 23 °C.

b) 1 mol% of catalyst was used.

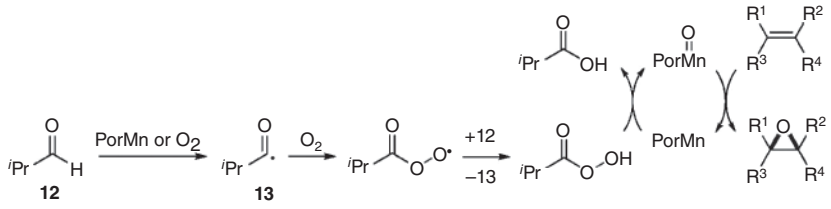

Scheme 21.1 Mechanism proposed for the aerobic epoxidation of alkenes catalyzed by **Mn3** using molecular oxygen as the oxidant and isobutyraldehyde as a co-reductant.

1,2-dichloroethane, in which the cage catalyst dissolved easily. The reaction is likely to take place inside the cavity of **Mn3**, as can be concluded from the reaction of the bulky substrate cyclooctene, which is much slower with **Mn3** than with **MnTPP** (entry 7 of Table 21.1).

Based on spectroscopic studies and trapping experiments with radical scavengers, a plausible mechanism was proposed for the **Mn3**-catalyzed epoxidation reaction (Scheme 21.1) [29]. First, an acyl radical is formed via hydrogen atom abstraction from the aldehyde. This step can occur without mediation of the manganese porphyrin; however, the conversion of cyclohexene in the absence of the catalyst was rather low, suggesting that the manganese porphyrin plays a role. A subsequent reaction between the acyl radical and O_2 generates an acyl peroxy radical. Hydrogen atom abstraction from a second equivalent of aldehyde produces a peracid and another acyl radical. Once the peracid is formed, it decomposes in the presence of manganese porphyrin. According to UV–vis studies one of the products of this reaction is a high-valent manganese oxo species, either a Mn(IV)-oxo or Mn(V)-oxo complex, which can readily oxidize the alkene to the epoxide, while it is being reduced itself. This process repeats until all manganese-oxo species eventually are decomposed to μ-oxo dimeric manganese porphyrin and other catalytically inactive species [29].

21.4.2 Epoxidation of Polymeric Alkenes

In the previous section, cage catalyst **Mn3** was studied as a distributive catalyst, i.e. a catalyst that converts a substrate after which the components separate and the catalyst starts a new round of catalysis. Because of the toroidal-like structure of **Mn3**, it was investigated whether it could also function as a processive epoxidation catalyst [15], i.e. a catalyst that threads onto a polymeric substrate containing alkene double bonds, and while gliding along it converts these double bonds into epoxide functions.

In a separate series of experiments, the threading of **3** onto the model polymers **14–16** was studied (Figure 21.5a). To this end, one side of the polymer was provided with a di(*tert*-butyl)phenyl blocking group and close to this group with a viologen trap, which has a high affinity for the cavity of **3**. This design forces **3** to enter the polymer from the open side and traverse the entire chain before it can complex to the viologen trap (Figure 21.5c). Cage compound **3** is fluorescent, but when it is bound to the viologen its fluorescence is quenched. Studying the fluorescence over time

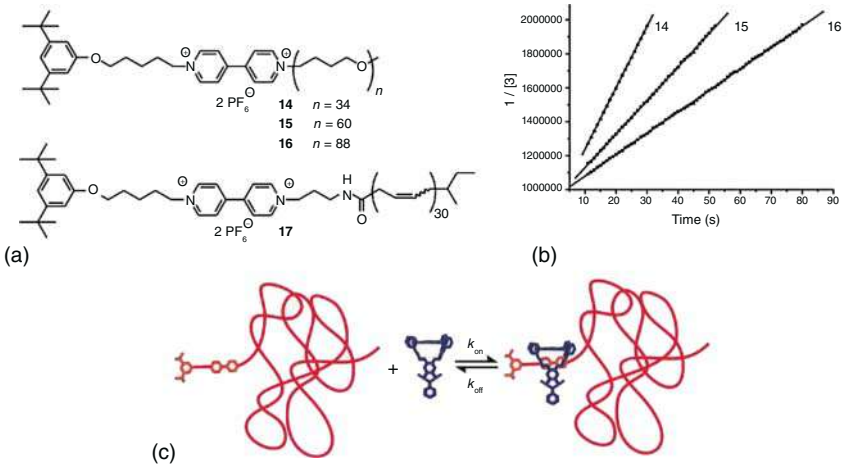

Figure 21.5 (a) Structure of one-side-blocked polymers **14–17**. (b) Second-order rate plots for the threading of porphyrin cage compound **3** onto polymers **14–16**. (c) Schematic representation of the threading process. Source: Reproduced with permission from The National Academy of Sciences [30].

after the addition of the polymer allows one to obtain information about the kinetics of threading. The experiments revealed that threading indeed occurs and that it is a second-order process, as expected (Figure 21.5b). The reversed de-threading process followed first-order kinetics. From these experiments, it became clear that longer polymer chains resulted in slower threadings and that an energetic barrier of 61 J nm^{-1} needs to be overcome to reach the viologen trap [30]. The mechanism for this threading process is thought to be similar to the translocation of a DNA chain through a hole in a virus particle [31].

Further experiments to elucidate the threading mechanism revealed that the porphyrin cage compound can either directly bind to the open end of the polymer chain and thread (Figure 21.6a) or first binds with its outside to the viologen-binding site, after which the polymer open end enters the cavity via an intramolecular looping process (Figure 21.6b) [32]. Both processes are possible and were shown to occur, depending on the chain length of the polymer. A mechanism via a folded chain (Figure 21.6c) could be discarded based on threading studies with model compounds [33].

Similar experiments as described for the polytetrahydrofuran-derived polymers **14–16** were also performed with the one-side-blocked polybutadiene chain **17**. From the experiments, the translocation speed of **3** along polymer **14** was estimated to be 750 pm/s and 14 pm/s along the polybutadiene derivative **17**, which is bulkier than **14** [30]. Epoxidation experiments were performed with **Mn3** and a polybutadiene (PB) of high molecular weight (M_W 200 000–300 000; 98% cis-double bonds) [34]. In the presence of excess Bupy and using iodosylbenzene as the oxygen donor, the relative conversions of polybutadiene to polybutadieneepoxide (PE) by **Mn3** were compared to those by the reference catalyst **MnTMPP**. **Mn3** appeared to react 2.2 times more slowly, and this feature was ascribed to the forced reaction on the inside

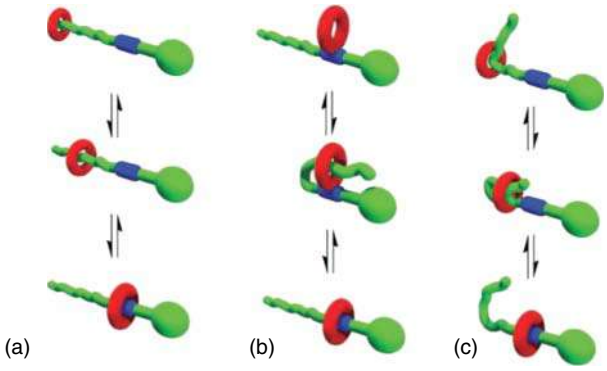

Figure 21.6 Possible mechanisms of threading cage compound **3** onto a polymer chain. (a) Direct threading. (b) Intramolecular looping path. (c) Threading via a folded chain. Source: Reproduced with permission from AAAS [32].

of the cavity of **Mn3**, while this restriction is not present for **MnTMPP**. When the cavity of **Mn3** was blocked by adding 1 equiv of $\mathbf{Me_2V}$, the reaction rate dropped by ~40%, while under this condition **MnTMPP** became even more activated, i.e. with an increase in rate of 20%. Interestingly, **Mn3** produced 80% *trans*-epoxide and 20% *cis*-epoxide from the predominantly *cis*-alkene double bonds in PB, while the reference catalyst **MnTMPP** yielded predominantly the *cis*-epoxide (78%). This is another indication that the epoxidation of the double bonds in the polymer occurs inside the cavity of **Mn3**. An alternative mechanism would be a reaction on a fold in the polymer chain, which enters the cavity of **Mn3**. Based on molecular modeling, this reaction pathway was proven to be very unlikely due to the large amount of steric hindrance involved. To further exclude such a mechanism, a polybutadiene fragment (50–100 repeat units) was synthesized containing **Mn3** attached to it in a rotaxane fashion and blocking groups on both ends of the polymer. A reaction on a folded chain, as mentioned above, is not possible in this case. In the presence of Bupy, the double bonds in this rotaxane polymer were still found to be epoxidized and even faster than the epoxidation of PB by **Mn3**, because no initial threading is required [34]. The rate of epoxidation of PB by **Mn3** was calculated and compared to the rate of threading of **3** onto polymer **17**, see above. From the comparison, i.e. an epoxidation rate of 1 pm s^{-1} and a threading rate 14 pm s^{-1}, it could be concluded that the processive reaction is not taking place in a sequential stepwise manner, but is a hopping process in which the catalyst moves randomly along the polymer chain to eventually epoxidize all alkene double bonds (Figure 21.7). When the epoxidation conditions were changed to molecular oxygen and isobutyraldehyde as co-reductant, epoxidation of a similar PB led to mainly *cis*-polyepoxide, which is in sharp contrast to the reaction with iodosylbenzene as oxygen donor [29, 34]. Apparently, under the different epoxidation conditions different reactive species (Mn(V)oxo vs. Mn(IV)oxo) are operative, but further studies have to substantiate this [29].

An attempt was made to reduce the amount of axial ligand required in the epoxidations of the polymer substrate. To this end, porphyrin cage catalyst **Mn18** was

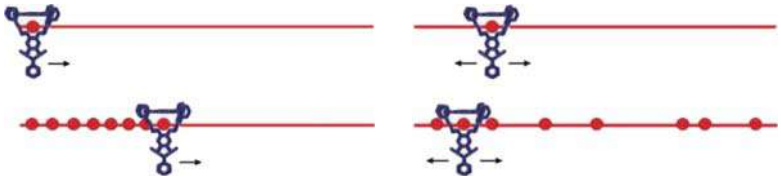

Figure 21.7 Schematic representation of **Mn3** epoxidizing a polybutadiene chain via (a) sequential processive mechanism and (b) a hopping process. Source: Reproced with permission from The National Academy of Sciences [30].

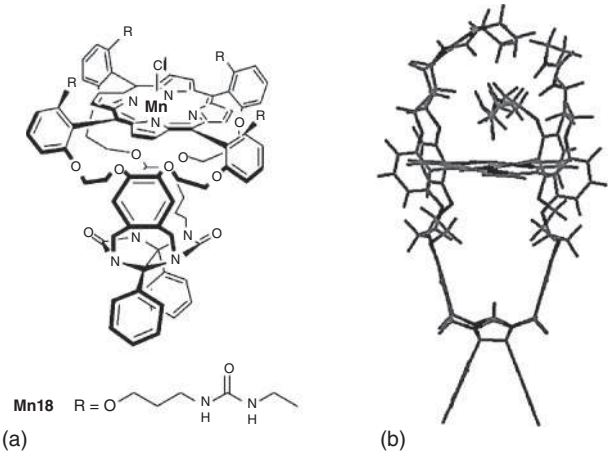

Figure 21.8 (a) Structure of the urea-functionalized manganese cage catalyst **Mn18**. (b) Model based on NMR studies on the zinc derivative **Zn18**. Source: Reproduced with permission from the American Chemical Society [35].

designed and synthesized (Figure 21.8a). It carries 4 ethylureapropoxy tails on the outer ortho-positions of the porphyrin *meso*-phenyl groups. These tails can simultaneously activate the catalyst and protect it from decomposition. Studies with **Mn18** and the zinc analog of this compound (**Zn18**) revealed that the tails adopt a folded conformation over the porphyrin roof (Figure 21.8b) with the urea groups displaying coordinative interactions with the zinc center [35, 36]. The catalytic properties of this protected catalyst **Mn18** were investigated under the previously described conditions using iodosylbenzene as the oxygen donor, with and without pyridine present. **Mn18** converted PB (M_w = 200 000; 98% cis) to the polyepoxide with 100% conversion and a cis/trans ratio of 30/70 independent of the presence or absence of the pyridine ligand. The catalyst turned out to be very stable: employing 8000 alkene equivalents relative to the catalyst resulted in complete conversions after 96 hours. Under similar conditions using **Mn3** as the catalyst, the epoxidation reaction halted after a turnover number of 1800. The stability of **Mn18** was further confirmed by its ability to convert additional batches of substrate [35].

21.4.3 Carbenoid Transfer Reactions with α-Diazoesters

Ruthenium porphyrins are known to catalyze a variety of carbenoid transfer and carbon–carbon coupling reactions. To enter this field, we synthesized the ruthenium derivative of **3** (**Ru3)** and employed it in the homodimerization of diazoacetates **19** and **20** to yield fumarate or maleate esters (Figure 21.9) [16]. When **Ru3** was treated with 2 equiv of **19**, the only product observed was homodimer **23**. This product was also formed when the reference compound **RuTPP** was used as a catalyst. Interestingly, when a large excess of **19** (50 equiv with respect to **Ru3**) was applied, rotaxane **Ru21** was obtained in 50% yield, in addition to **23**. Apparently, in the case of **Ru3**, reactions can take place both at the outside and the inside, leading to a homodimer and rotaxane, respectively. Similar reactions of **Ru3** with **20** (50 equiv) led to rotaxane **Ru22** (40%) and additionally to products in which more molecules of **20** (up to four fragments) were inserted into the axle of the rotaxane, leading to branched compounds. Such branched compounds were not observed in the case of **Ru21**. NMR and mass spectrometric studies revealed that the branched products are the result of C=C and C–H insertion reactions. Reference catalyst **RuTPP** did not display such post-modification abilities, suggesting that in the case of rotaxane **Ru22** the branching is the result of an effective molarity effect, making that additional reactions with new molecules of **20** readily can take place on the freely movable axle because it

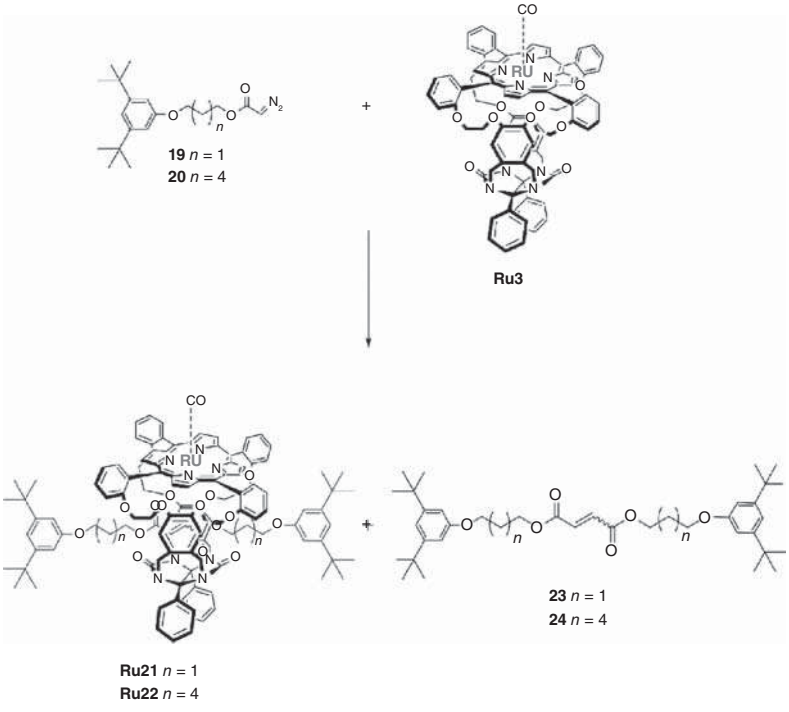

Figure 21.9 Formation of rotaxanes **Ru21** and **Ru22** and the carbon–carbon coupled products **23** and **24** from diazoacetates **19** and **20** catalyzed by **Ru3**. Source: Reproduced with permission from Elsevier [16].

is close to the Ru center. The observation that **Ru21** does not display such insertion reactions was ascribed to steric hindrance, as it has a much tighter structure in which the blocking groups limit the access of additional molecules of **19** to the axle, which is buried inside the cavity of **Ru21** [16].

21.5 Outlook

As shown in this chapter, diphenylglycoluril is a versatile concave building block for the construction of supramolecular catalysts containing a cavity and a nearby catalytic metal center. Different catalytic reactions have been studied, and the analysis of the reaction mechanisms suggests some parallels with the reactions catalyzed by enzymes in nature. Features such as selective and cooperative binding in a cavity and as a result a higher selectivity and reaction rate could be demonstrated. A relatively new aspect in catalysis is processivity, i.e. the phenomenon that a catalyst performs several rounds of catalysis without detaching from the substrate. This was shown to be possible with porphyrin cage catalyst **Mn3**, which is able to epoxidize the alkene double bonds in a polybutadiene chain while gliding along it. This processive catalytic system opens interesting possibilities for further research. We are developing it in the direction of a catalytic system that can write and store digital information on a polybutadiene chain in the form of chiral epoxide functions: (*R*,*R*)-epoxide = digit 1, (*S*,*S*)-epoxide = digit 0 [37]. To this end, we have synthesized chiral glycoluril porphyrin cages that contain a Feringa motor that can be controlled by light (see **Zn25**, Figure 21.10) [38]. Preliminary experiments show that the conformation and properties of **Zn25** can be switched by light and furthermore that the porphyrin motor cage can thread onto polymer chains. Switching with light also changes the chiral conformation of **Zn25**, and future experiments will be directed to perform enantioselective epoxidation, i.e. writing, on polybutadiene chains with a manganese derivative of **Zn25** controlled by light [38].

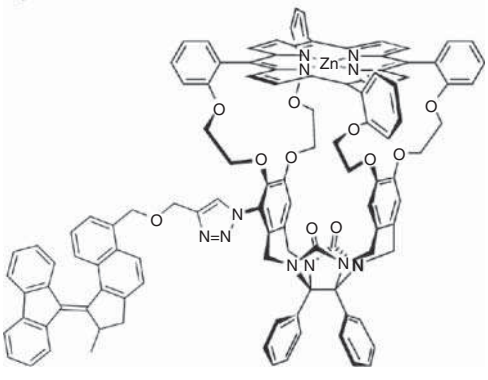

Zn25

Figure 21.10 Structure of porphyrin cage compound **Zn25**, which contains an attached light-switchable Feringa motor.

Acknowledgments

This work was funded by the European Research Council (ERC Advanced Grant No. 74092 to R.J.M.N.) and by the Dutch Ministry of Education, Culture, and Science (Gravitation program 024.001.035).

References

1 Payen, A. and Persoz, J.-F. (1833). Mémoire sur la diastase, les principaux produits de ses réactions et leurs applications aux arts industriels. *Annales de Chimie et de Physique* 2nd series, 53: 73–92.
2 Fischer, E. (1894). Einfluss der configuration auf die wirkung der enzyme. *Berichte der Deutschen Chemischen Gesellschaft zu Berlin* 27: 2985–2993.
3 Biros, S.M. and Rebek, J. Jr., (2007). Structure and binding properties of water-soluble cavitands and capsules. *Chem. Soc. Rev.* 36: 93–104.
4 Crini, G., Sophie Fourmentin, S., Fenyvesi, E. et al. (2018). Cyclodextrins, from molecules to applications. *Env. Chem. Lett.* 16: 1361–1375.
5 Kobayashi, K. and Yamanaka, M. (2015). Self-assembled capsules based on tetra-functionalized calix[4]resorcinarene cavitands. *Chem. Soc. Rev.* 44: 449–466.
6 Ogoshi, T. (2012). Synthesis of novel pillar-shaped cavitands "pillar[5]arenes" and their application for supramolecular materials. *J. Incl. Phenom. Macrocycl. Chem.* 72: 247–262.
7 Assaf, K.I., Werner, M., and Nau, W.M. (2015). Cucurbiturils: from synthesis to high-affinity binding and catalysis. *Chem. Soc. Rev.* 44: 394–418.
8 Bruns, C. J., Stoddart, J. F. (2017) The nature of the mechanical bond: from molecules to machines. Wiley on Line Library, Online ISBN: 9781119044123.
9 Pinalli, R., Pedrini, A., and Dalcanale, E. (2018). Biochemical sensing with macrocyclic receptors. *Chem. Soc. Rev.* 47: 7006–7026.
10 Pappalardo, A., Puglisi, R., and Trusso Sfrazzetto, G. (2019). Catalysis inside supramolecular capsules: recent developments. *Catalysts* 9: 630.
11 Rowan, A.E., Elemans, J.A.A.W., and Nolte, R.J.M. (1999). Molecular and supramolecular objects from glycoluril. *Acc. Chem. Res.* 32: 995–1006.
12 Reek, J.N.H., Priem, A.H., Engelkamp, H. et al. (1997). Binding features of molecular clips. Separation of the effects of hydrogen bonding and π-π interactions. *J. Am. Chem. Soc.* 119: 9956–9964.
13 Smeets, J.W.H., Van Dalen, L., Kaats-Richter, V.E.M., and Nolte, R.J.M. (1990). Functionalized basket-shaped hosts. Synthesis and complexation studies with (alkali) metal and ammonium and diammonium Ions. *J. Org. Chem.* 55: 454–461.
14 Schenning, A.P.H.J., Bruin, B., de Rowan, A.E. et al. (1995). Strong binding of paraquat and polymeric paraquat derivatives by basket-shaped hosts. *Angew. Chem. Int. Ed. Engl.* 34: 2132–2134.
15 van Dongen, S.F.M., Elemans, J.A.A.W., Rowan, A.E., and Nolte, R.J.M. (2014). Processive catalysis. *Angew. Chem. Int. Ed.* 53: 11420–11428.

16 Van den Boomen, O.I., Coumans, R.G.E., Akeroyd, N. et al. (2017). Carbenoid transfer reactions catalyzed by a ruthenium porphyrin macrocycle. *Tetrahedron* 73: 5029–5037.

17 Coolen, H.K.A.C., Meeuwis, J.A.M., van Leeuwen, P.W.M.N., and Nolte, R.J.M. (1995). Substrate selective catalysis by rhodium metallohosts. *J. Am. Chem. Soc.* 117: 11906–11913.

18 Coolen, H.K.A.C., Leeuwen, P.W.N.M., and van Nolte, R.J.M. (1992). A Rh^{I}-centered cage compound with selective catalytic properties. *Angew. Chem. Int. Ed. Engl.* 31: 905–907.

19 Martens, C.F., Klein Gebbink, R.J.M., Feiters, M.C., and Nolte, R.J.M. (1994). Shape-selective oxidation of benzylic alcohols by a receptor functionalized with a dicopper(II) pyrazole complex. *J. Am. Chem. Soc.* 116: 5667–5670.

20 Klein Gebbink, R.J.M., Martens, C.F., Kenis, P.J.A. et al. (1999). Synthesis, structure, and reactivity of copper dioxygen complexes derived from molecular receptor ligands. *Inorg. Chem.* 38: 5755–5768.

21 Sprakel, V.S.I., Feiters, M.C., Meyer-Klaucke, W. et al. (2005). Oxygen binding and activation by the complexes of PY2- and TPA-appended diphenylglycoluril receptors with copper and other metals. *Dalton Trans.*: 3522–3534.

22 Rowan, A.E., Aarts, P.P.M., and Koutstaal, K.W.M. (1998). Novel porphyrin–viologen rotaxanes. *Chem. Commun.* 5: 611–612.

23 Elemans, J.A.A.W., Claase, M.B., Aarts, P.P.M. et al. (1999). Porphyrin clips derived from diphenylglycoluril. Synthesis, conformational analysis, and binding properties. *J. Org. Chem.* 64: 7009–7016.

24 Elemans, J.A.A.W., Bijsterveld, E.J.A., Rowan, A.E., and Nolte, R.J.M. (2007). Manganese porphyrin hosts as epoxidation catalysts – activity and stability control by axial ligand effects. *Eur. J. Org. Chem.*: 751–757.

25 Gilissen, P.J., Swartjes, A., Spierenburg, B. et al. (2019). Rapid and scalable synthesis of chiral porphyrin cage compounds. *Tetrahedron* 75: 4640–4647.

26 Thordarson, P., Bijsterveld, E.J.A., Elemans, J.A.A.W. et al. (2003). Highly negative homotropic allosteric binding of viologens in a double-cavity porphyrin. *J. Am. Chem. Soc.* 125: 1186–1187.

27 Elemans, J.A.A.W., Bijsterveld, E.J.A., Rowan, A.E., and Nolte, R.J.M. (2000). A host–guest epoxidation catalyst with enhanced activity and stability. *Chem. Commun.*: 2443–2444.

28 Thomassen, P.J., Varghese, S., Bijsterveld, E.J.A. et al. (2015). A double-cavity-containing porphyrin host as a highly stable epoxidation catalyst. *Eur. J. Org. Chem.*: 5246–5253.

29 Bernar, I., Rutjes, F.P.J.T., Elemans, J.A.A.W., and Nolte, R.J.M. (2019). Aerobic epoxidation of low-molecular-weight and polymeric olefins by a supramolecular manganese porphyrin catalyst. *Catalysts* 9: 195.

30 Coumans, R.G.E., Elemans, J.A.A.W., Nolte, R.J.M., and Rowan, A.E. (2006). Processive enzyme mimic: kinetics and thermodynamics of the threading and sliding process. *Proc. Natl. Acad. Sci. USA* 103: 19647–19651.

31 Muthukumar, M. (2001). Translocation of a confined polymer through a hole. *Phys. Rev. Lett.* 86: 3188–3191.

32 Deutman, A.B.C., Monnereau, C., Elemans, J.A.A.W. et al. (2008). Mechanism of threading a polymer through a macrocyclic ring. *Science* 322: 1668–1671.

33 Deutman, A.B.C., Varghese, S., Moalin, M. et al. (2015). Slippage of a porphyrin macrocycle over threads of varying bulkiness: implications for the mechanism of threading polymers through a macrocyclic ring. *Chem. Eur. J.* 21: 360–370.

34 Thordarson, P., Bijsterveld, E.J.A., Rowan, A.E., and Nolte, R.J.M. (2003). Epoxidation of polybutadiene by a topologically linked catalyst. *Nature* 424: 915–918.

35 Monnereau, C., Hidalgo Ramos, P., Deutman, A.B.C. et al. (2010). Porphyrin macrocyclic catalysts for the processive oxidation of polymer substrates. *J. Am. Chem. Soc.* 132: 1529–1531.

36 Hidalgo Ramos, P., Saisaha, P., Elemans, J.A.A.W. et al. (2016). Conformational analysis and binding properties of a cavity containing porphyrin catalyst provided with urea functions. *Eur. J. Org. Chem.* 2016: 4487–4495.

37 Rutten, M.G.T.A., Vaandrager, F., Elemans, J.A.A.W., and Nolte, R.J.M. (2018). Encoding information into polymers. *Nat. Rev. Chem.* 2: 365–381.

38 Gilissen, P.J., White, P.B., Berrocal, J.A. et al. (2020). Molecular motor-functionalized porphyrin macrocycles. *Nat. Commun.* 11: 5291.

22

Catalysis Inside the Hexameric Resorcinarene Capsule: Toward Addressing Current Challenges in Synthetic Organic Chemistry

Leonidas-Dimitrios Syntrivanis[1,2] *and Konrad Tiefenbacher*[1,3]

[1] *University of Basel, Department of Chemistry, Mattenstrasse 24a, CH-4058, CH-4056 Basel, Switzerland*
[2] *University of Illinois at Urbana-Champaign, Department of Chemistry, 600 South Mathews Avenue, Urbana, IL 61801, USA*
[3] *ETH Zurich, Department of Biosystems Science and Engineering, Mattenstrasse 26, CH-4058 Basel, Switzerland*

22.1 Introduction

The first examples of molecular capsules, supramolecular assemblies formed from the spontaneous association of smaller components, were reported in the early 1990s [1]. Such capsules can accommodate smaller molecules of appropriate size and shape in their cavities. The analogy to an enzyme's active site therefore raised the question of whether such supramolecular assemblies could act as a catalyst to promote organic reactions. The first such example was reported by the Rebek group in 1992: the dimeric "softball" capsule was found to promote the Diels–Alder reaction between *p*-quinone and cyclohexadiene [2, 3]. Since then numerous additional examples have appeared in the literature and are summarized in excellent reviews [4–9]. Our interest in the field has been focused on the potential application of supramolecular capsule catalysis to current challenges in synthetic organic chemistry. In this chapter, we summarize our results from this adventure of applying the supramolecular resorcinarene capsule as catalyst for challenging organic transformations, which started in 2012.

22.2 Background

The resorcinarene capsule **I** (Scheme 22.1a), originally reported by Atwood in 1997 [10], self-assembles from six resorcinarene monomers **1** and eight water molecules in apolar solvents to enclose a cavity with a volume of approximately 1375 Å^3 [11–13]. The capsule is able to stabilize cationic guests within its cavity through cation–π interactions with the aromatic walls. Its potential as a container for a separate catalyst was first recognized by the groups of Scarso and Reek: in their seminal paper in 2011, they encapsulated a gold(I) catalyst and demonstrated the altered reactivity of

Supramolecular Catalysis: New Directions and Developments, First Edition.
Edited by Piet W.N.M. van Leeuwen and Matthieu Raynal.

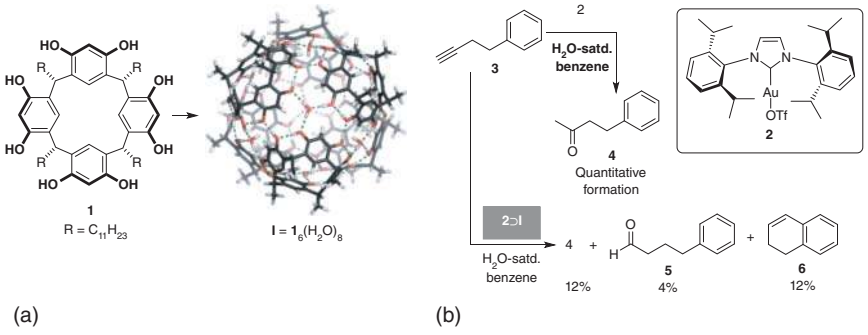

Scheme 22.1 (a) Formation of hexameric capsule **I** by the self-assembly of monomer **1**. (b) Altered reactivity of gold(I) catalyst **2** when encapsulated in capsule **I**.

the entrapped catalytic species on 4-phenyl butyne (Scheme 22.1b) [14]. Although the rates were reduced as compared to the solution control experiments, they clearly demonstrated that beside hydration, cyclization also becomes competitive inside the container.

Motivated by this result, my group started investigating the resorcinarene hexamer and the closely related pyrogallolarene hexamer [15–17] in 2012. Inspired by the paper of Scarso and Reek, we initially investigated the possibility of promoting iminium catalysis inside the capsule. The intermolecular reaction we initially chose to study turned out to be quite challenging and required extensive optimization. However, these initial experiments revealed an aspect of the resorcinarene hexamer that had so far been overlooked, its intrinsic acidity. Specifically, we found that the capsule behaves as a Brønsted acid, with a pK_a of approximately 5.5–6 [18]. This relatively high acidity may be rationalized on the basis of the following three points: (i) Protonation of a guest leads to more stable complexes by virtue of cation–π interactions. (ii) The resulting capsule anion is stabilized by extensive delocalization as the charge can be shifted between the 48 phenolic groups and 8 water molecules of the assembly by proton migration. (iii) Attractive Coulomb interactions between the positively charged protonated guest and the negatively charged capsule could also be a contributing factor.

These findings were then translated to a first synthetic application [18], by using the capsule **I** as a catalyst in the hydrolysis of acetals. Smaller acetals were hydrolyzed faster than larger ones, an effect attributed to easier encapsulation (Figure 22.1). This allowed the selective hydrolysis of 1,1-diethoxyethane (**7**) in the presence of 1,1-diethoxydodecane (**8**) (98 : 2 selectivity at 85% conversion). In a control experiment, a comparable acid (acetic acid, pK_a = 4.8) led to no conversion,

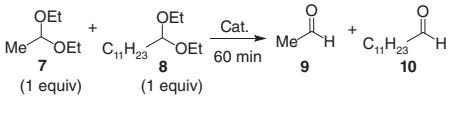

Cat.	Conversion ratio **9 : 10**	
10 mol% I + 0.1 mol% HCl	85%	98 : 2
400 mol% TFA	33%	37 : 63
10 mol% AcOH	—	
0.1 mol% HCl	—	

Figure 22.1 Acetal hydrolysis catalyzed by capsule **I** and comparison with Brønsted acids.

indicating the crucial role of the capsule cavity in the hydrolysis. The much stronger trifluoroacetic acid had to be used in large excess (4 equiv) to get comparable rates and gave a mixture of the two hydrolysis products (37 : 63). Later studies [19] found that traces of HCl, present in the capsule due to its preparation under aqueous acidic conditions or in regular chloroform due to photodegradation, were necessary for the reaction inside capsule **I** to take place. Importantly, however, HCl functions only as a cocatalyst; reaction with the same amount of HCl but in the absence of capsule failed to provide any hydrolysis product.

22.3 Application to Terpene Cyclization

The tail-to-head terpene (THT) cyclization [20] gives rise to the myriad of terpene structures encountered in nature, starting from only a few linear precursors. In nature the THT cyclization is catalyzed by class I cyclases, enzymes possessing a hydrophobic reaction pocket equipped with a metal(II) cation that triggers cleavage of the pyrophosphate leaving group, and aromatic amino acid residues that have been proposed to stabilize cationic transition states [21, 22]. Reproducing this reactivity in solution with man-made catalysts has however historically been extremely challenging, due to premature quenching of reactive intermediates, for example, by molecules of solvent.

Inspired by the analogy between the aromatic amino acids lining the active sites of terpene cyclases and the aromatic walls of capsule **I**, we investigated the capability of the capsule to catalyze the THT cyclization of linear precursors. The reaction of nerol (**11**) in the presence of capsule **I** led to the formation of the cyclic terpenes α-terpineol (**13**) and eucalyptol (**14**) (Scheme 22.2a) [23]. Interestingly, this was the first report about the direct one-pot cyclization to eucalyptol starting from an acyclic terpene in a nonenzymatic setting. This result clearly indicated the application potential of **I** for challenging organic transformations for the first time. As α-terpineol and eucalyptol derive from the capture of cationic intermediates by the cleaved leaving group, it was hypothesized that the product selectivity might be changed by using a leaving group displaying a lower nucleophilicity. This proved to be the case, as subjecting geranyl acetate (GOAc **15**, Scheme 22.2b) to the capsule-mediated reaction provided mainly α-terpinene (**17**). The cisoid cation **16**, resulting from isomerization of the transoid cation formed after ionization of GOAc, cyclizes to the α-terpinyl cation **12**. α-Terpinene is then presumably formed from the α-terpinyl cation via an 1,2-hydride shift followed by elimination. The formation of α-terpinene represents a "non-stop" THT cyclization, which is difficult to achieve in solution. As mentioned previously for the acetal hydrolysis studies, it was discovered that the presence of small amounts of HCl was essential for the reaction to take place [24]. This indicates that the acid acts in a synergistic fashion with the capsule to catalyze the reaction, in analogy with the role played by cofactors in natural enzymes. Importantly, no reaction was observed when HCl was added in the absence of the capsule. Additional control experiments provided strong evidence that the THT cyclization takes place within the capsule's cavity.

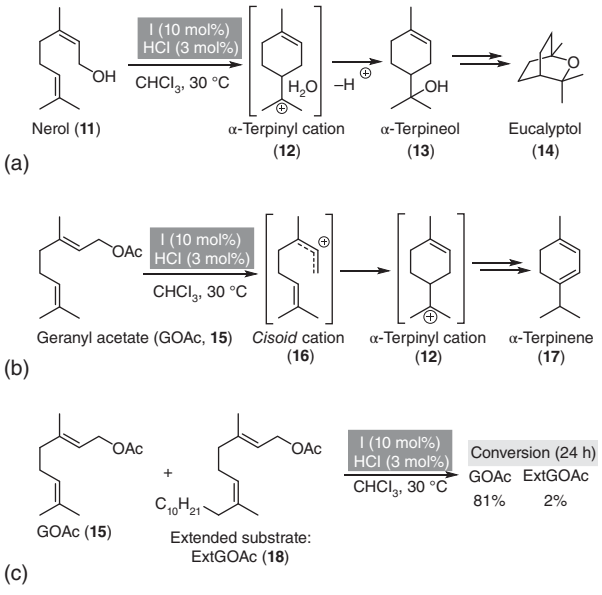

Scheme 22.2 THT cyclization of (a) nerol and (b) geranyl acetate in capsule **I**; (c) control experiment involving reaction of extended substrate.

No cyclization was observed when the capsule's cavity was blocked by a strongly binding guest (Bu_4NBr), despite the increase of the capsule's acidity associated with binding of the ammonium guest [18]. Most importantly, a size competition experiment between the regular substrate **15** and the extended version **18** provided strong evidence for the reaction taking place inside the capsule. The uptake of the extended substrate is disfavored due to its size, leading to a highly selective conversion of the substrate **15** (81% vs. 2% conversion, Scheme 22.2c). Additionally, several Brønsted and Lewis acids were tested for the cyclization of GOAc, but in all cases, only traces of cyclic monoterpene products were formed.

The cyclization of GOAc was investigated in detail to learn more about the catalytic mechanism [24]. Capsule **I** is protonated rapidly by the HCl cocatalyst, as indicated by ^{1}H NMR experiments. Encapsulation of the substrate is evident by NMR experiments, and we hypothesized that after encapsulation the substrate is activated by protonation. The measured positive entropy of activation, together with the normal secondary kinetic isotope effect ($k_H/k_D = 1.22$) observed in the cyclization of 1,1-D_2-GOAc, pointed to cleavage of the leaving group as the rate-limiting step for the reaction. The origin of the alcohol group in the α-terpineol formed was also studied: experiments with ^{18}O-labeled linalool indicated that the alcohol group in the terpineol formed is derived for the most part (approximately 75%) directly from the leaving group.

The capsule can also catalyze the cyclization of sesquiterpene substrates [25]. In this case, however, linear substrates give rise to a considerably more complex reaction profile due to the larger number of different cyclization modes possible. When subjected to capsule **I**, commercially available (2*E*, 6*E*)-farnesol

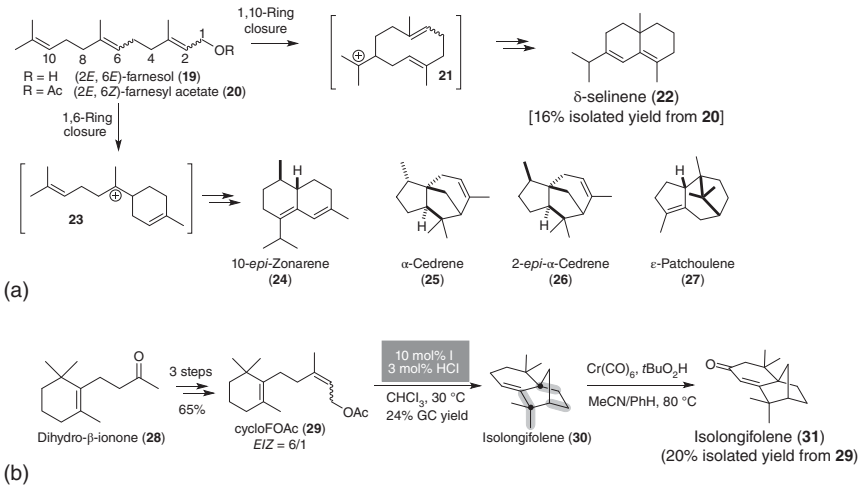

Scheme 22.3 Capsule-mediated THT cyclizations of (a) linear sesquiterpenes and application to the total synthesis of δ-selinene; (b) a conformationally constrained sesquiterpene and application to the synthesis of isolongifolene and isolongifolenone (new bonds and quaternary centers formed in the cyclization are highlighted).

(**19**, Scheme 22.3a) gives a mixture of polycyclic products including δ-selinene (**22**), 10-epi-zonarene (**24**), α-cedrene (**25**) 2-epi-α-cedrene (**26**), and ε-patchoulene (**27**). Of the other bond isomers, (2*E*, 6*Z*)-farnesyl acetate (**20**) was found to provide the most selective cyclization, forming δ-selinene and 10-*epi*-zonarene in 18% and 10% yield, respectively. This selectivity for δ-selinene indicates that the 6*Z* double-bond geometry gives rise to a preference for an initial 1,10-cyclization. In contrast, an alternative 1,6-cyclization operates with substrates bearing the 2*Z* double-bond geometry. The cyclization of (2*E*, 6*Z*)-farnesyl acetate was employed in the first total synthesis of δ-selinene: the substrate was prepared on gram scale in a six-step sequence, then subjected to capsule-catalyzed cyclization to give **22** in 16% isolated yield [26].

Interestingly, the rate-limiting step in the cyclization of sesquiterpenes was found to no longer be the cleavage of the leaving group, but rather the encapsulation of the substrate [26]. It is also important to note that in literature experiments that employed Brønsted or Lewis acids, the dominant species formed was the monocyclic cyclohexane derivative bisabolene [27–29]. Polycyclic products were only formed in low yields, largely deriving from reprotonation of the monocyclic intermediate under harsher acidic conditions [30, 31].

The results obtained from these cyclization studies indicated that conformational control of the substrate is important in achieving selectivity for a specific product. Incorporation of one ring in the structure of the precursor was employed as a way to constrain its conformational flexibility. The cyclization of cyclofarnesyl acetate (cycloFOAc, **29**) inside capsule **I** displayed better product selectivity than the acyclic precursors, as (*Z*)-**29** and (*E*)-**29** formed the tricyclic sesquiterpene isolongifolene (**30**) in 29% and 23% yield, respectively (Scheme 22.3b) [25]. Overall,

this transformation accomplishes the construction of four C—C bonds and two quaternary carbon centers in one step. This allowed the shortest total synthesis of isolongifolene to date: cycloFOAc was synthesized in three steps from inexpensive, commercially available dihydro-β-ionone (**28**) and converted to isolongifolene via the capsule-catalyzed cyclization. In this way, racemic isolongifolene was prepared in 11% overall yield over four steps (85% GC purity). Although the product obtained after regular column chromatography is not analytically pure, it can serve as the substrate for further functionalization: allylic oxidation of isolongifolene obtained in this way gave the natural product isolongifolenone (**31**), which was isolable as a pure compound (13% overall yield from **28** in five steps). As was the case for the cyclization of acyclic sesquiterpenes, literature experiments with cyclofarnesyl substrates did not lead to the isolongifolene product observed inside the capsule. In solution, different rearrangements were favored and cationic intermediates quenched by nucleophiles [32, 33].

The mechanism of the isolongifolene formation was investigated by a combination of DFT and isotopic labeling studies [25]. On that basis, the following mechanism can be proposed: Initial cyclization of the cycloFOAc substrate gives spirocyclic intermediate **32** (Scheme 22.4); in the case of (*E*)-cycloFOAc, an isomerization of the double bond has to occur before the cyclization can take place. The spirocyclic intermediate then undergoes a 3,7-ring closure, that, according to DFT calculations, is concerted with a Wagner–Meerwein alkyl shift, providing intermediate **33**. From here an 1,2-alkyl shift followed by an 1,3-hydride shift and a second 1,2-alkyl shift (the latter two steps being a concerted process according to DFT calculations) lead to cation **36**; methyl shift and elimination then delivers isolongifolene (**30**).

While the selective synthesis of isolongifolene was a significant advance, it still did not represent a solution to an unmet challenge in synthesis, as isolongifolene is a commercially available compound. Application of the capsule catalyst **I** to the synthesis of compounds that are difficult to access through other means was highly desirable. The biomimetic synthesis of presilphiperfolan-1β-ol (**44**, Scheme 22.5) is such an example [34]. Presilphiperfolan-1β-ol is a tricyclic sesquiterpene natural product that exhibits antimycobacterial properties [35]. Its complex structure renders its synthesis challenging: the only previously reported total synthesis consisted of 13 steps [36].

The proposed biosynthesis of presilphiperfolan-1β-ol [37] involves initial cyclization of farnesyl pyrophosphate (**38**) to humulenyl cation **39** (Scheme 22.5), followed

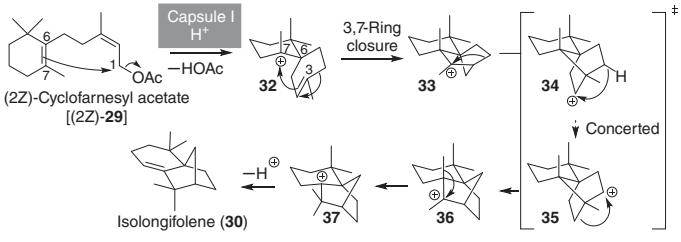

Scheme 22.4 Proposed mechanism for the capsule-catalyzed formation of isolongifolene.

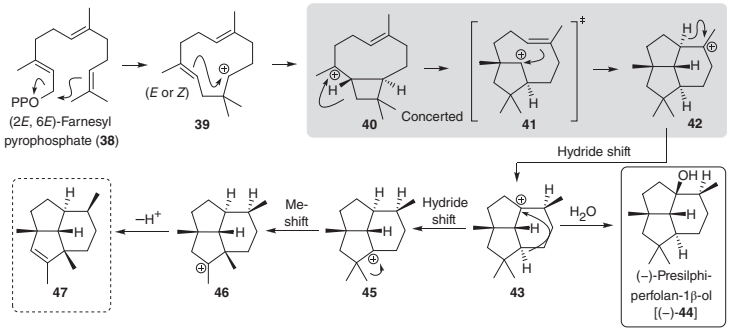

Scheme 22.5 Proposed biosynthesis of presilphiperfolan-1β-ol and formation of rearranged alkene **47**.

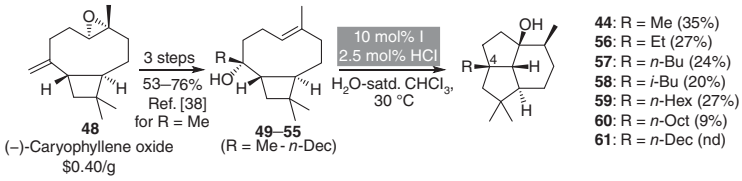

Scheme 22.6 Capsule-catalyzed synthesis of presilphiperfolan-1β-ol and unnatural derivatives.

by formation of caryophyllenyl cation **40**. A concerted 1,2-alkyl shift/cyclization cascade then leads to structure **42**. A 1,2-hydride shift, followed by capture by water, gives presilphiperfolan-1β-ol (**44**). The proposed intermediacy of the caryophyllenyl cation led us to hypothesize that generating this cation within the confines of the capsule would allow the subsequent cascade to take place. Caryophyllenyl alcohol **49** (Scheme 22.6) was therefore prepared from inexpensive, commercially available (−)-caryophyllene oxide (**48**) following a literature procedure [38]. When subjected to the capsule catalyst in regular chloroform, the formation of presilphiperfolan-1β-ol was observed, together with alkene **47**. The latter is presumably formed from intermediate **43** via an 1,3-hydride shift followed by a methyl shift and elimination. Alkene **47** represents, to our knowledge, a novel sesquiterpene skeleton. Reaction with HCl in the absence of capsule, or with capsule blocked by a strongly binding ligand (Bu_4NBr) did not form presilphiperfolan-1β-ol, providing evidence for the reaction taking place within the cavity of the capsule. A number of additional Brønsted and Lewis acids were also assayed for their capacity to promote the reaction, but none provided any detectable traces of presilphiperfolan-1β-ol, further underlining the unique chemical environment present within the capsule. This is also consistent with previous literature aimed at producing the presilphiperfolanol scaffold from caryophyllene or its derivatives, none of which provided a natural presilphiperfolanol [37].

The use of water-saturated chloroform – instead of regular chloroform – as the solvent suppressed the formation of rearranged alkene **47**, providing presilphiperfolan-1β-ol in 42% GC yield. These findings were then applied to the synthesis of the

natural product: precursor caryophyllenyl alcohol **49** was subjected to cyclization in preparative scale using optimized conditions to give presilphiperfolan-1β-ol in 35% isolated yield (Scheme 22.6). This represents the shortest synthesis of presilphiperfolan-1β-ol to date, in four steps from commercially available starting material.

This approach also allowed the synthesis of a number of unnatural derivatives of presilphiperfolan-1β-ol (Scheme 22.6). Substrates **50**–**55**, bearing different alkyl substituents at the C4 position, were subjected to the cyclization reaction. Derivatives **56**–**59**, bearing Et, *n*-Bu, *i*-Bu and *n*-Hex side chains, were isolated in 20–27% yield. Increasing the size of the substituent led to a decrease in the reaction rate. Accordingly, the octyl-substituted derivative **60** was isolated in only 9% yield, while the decyl-substituted precursor **55** did not form any appreciable amount of product. This trend is consistent with a specific size limit for the reaction to take place inside the capsule. The formation of unnatural presilphiperfolan-1β-ol derivatives **56**–**60** is significant, as they would not be available via the biomachinery and thus demonstrate an advantage of the supramolecular catalyst over the natural enzyme: even if the enzyme that produces presilphiperfolan-1β-ol was identified, it would be unlikely to give access to these unnatural derivatives of the natural product.

We anticipate that capsule **I** will enable a series of further terpene cyclizations that are difficult to perform via alternative means in the laboratory.

22.4 Elucidating the Prerequisites for Catalytic Activity Inside the Resorcinarene Capsule

Interestingly, unlike capsule **I**, the related pyrogallolarene capsule [15] **II** (Scheme 22.7) is catalytically incompetent with regard to the THT cyclization. The additional phenol groups present in monomer **62** participate in the hydrogen-bond network, so that six monomers assemble into capsule **II** without the incorporation of water molecules. To determine the reason behind the catalytic inactivity of capsule **II**, and obtain further insight into the origin behind the catalytic activity of

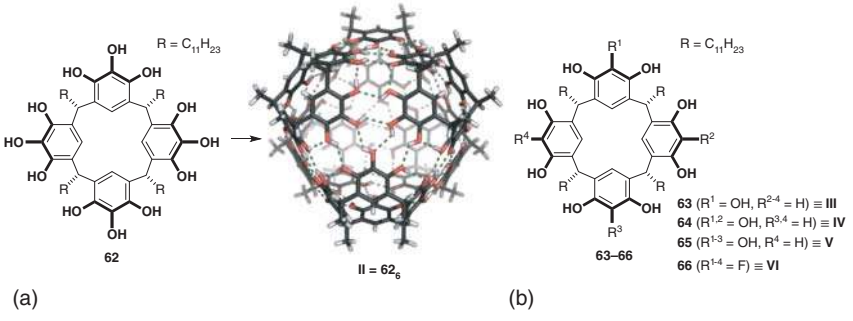

Scheme 22.7 (a) Formation of pyrogallolarene capsule **II** from the assembly of six monomers **62**. (b) Structures of macrocycles **63**–**66** and their assembly into hexamers **III**–**VI**.

capsule **I**, we prepared a series of related macrocycles **63**–**66** with varying patterns of hydroxyl substitution on the aromatic rings (Scheme 22.7) [39]. These were found to self-assemble into the corresponding hexameric assemblies **III**–**VI**. Assemblies **III** and **IV**, bearing one and two additional hydroxyl group per monomer, respectively compared to **I**, were able to catalyze the THT cyclization of geranyl acetate to α-terpinene, albeit in a lower yields than **I**. Assembly **V**, like **II**, was catalytically inactive, while assembly **VI** displayed very slow conversion.

Substrate encapsulation was determined not to be the crucial factor for catalytic activity, as all assemblies demonstrated uptake of a saturated substrate analog. The ability to encapsulate ion pairs, f.i. the protonated substrate ion pair, was also found not to be the critical factor: while catalytically inactive assembly **II** cannot encapsulate ion pairs, assembly **V**, which is also catalytically inactive, was found to be able to do so. On the other hand, protonation of the assembly by added acid, determined by broadening of the phenolic signals in ^{1}H NMR, was found to correlate well with catalytic activity. Assemblies **I**, **III**, **IV**, and **VI** were all protonated by added HCl, while catalytically inactive assemblies **II** and **V** were not. The incorporation of water as part of the assembly was also found to correlate with catalytic activity: DOSY-NMR titration experiments indicated that water is part of the hydrogen bond network for assemblies **I**, **III**, **IV**, and **VI** but not for **II** and **V**. Quantum mechanics/molecular mechanics (QM/MM) molecular dynamics (MD) simulations of capsule **I** containing encapsulated geranyl acetate and external HCl point to the following mechanism for substrate protonation: First, protonation of a water molecule at the capsule's surface by HCl takes place. The chloride ion of the resulting H_3O^+/Cl^- ion pair is stabilized by coordination to the phenol groups of the surrounding resorcinarene molecules, replacing the hydronium ion, which then activates the encapsulated substrate.

Overall, these results suggest that incorporation of water in the hydrogen-bond network of the capsule is essential for protonation of the substrate and therefore for catalytic activity in the context of terpene cyclization reactions. The water molecule acts as a shuttle to deliver a proton from the external acid to the encapsulated substrate. Hosts that do not incorporate water in their assembly are unable to participate in this mechanism of protonation, explaining their catalytic inactivity. The incorporation of the chloride anion at the capsule surface, suggested by the calculations, may also explain why it does not interfere with the reaction by quenching reactive intermediates.

22.5 Further Applications of Capsule I as Catalyst

Aside from the THT cyclization, capsule **I** can promote a number of additional transformations that are otherwise difficult to achieve in solution. For example, it can encapsulate the iminium species formed from an unsaturated aldehyde (such as **67**) and organocatalyst **69** (Scheme 22.8a) [40, 41]. The encapsulated iminium species can then be reduced to the corresponding saturated aldehyde using Hantzsch ester **68** as reductant [42]. With proline as the organocatalyst, a significant increase in

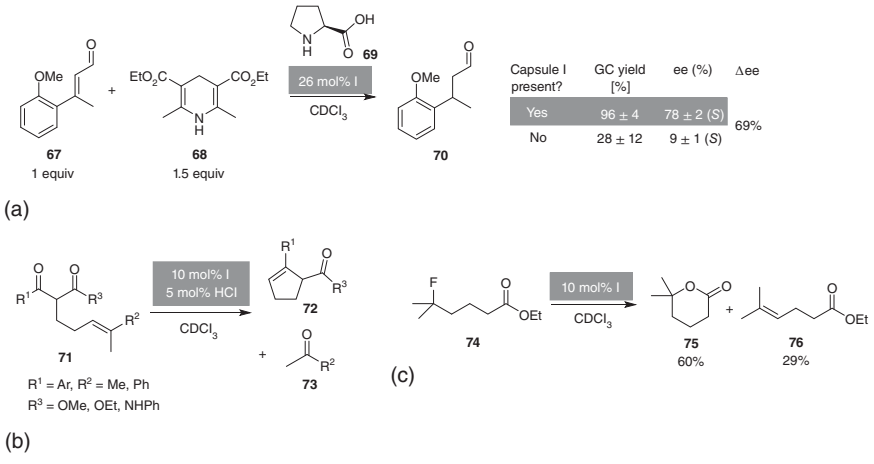

Scheme 22.8 (a) Example for the organocatalytic reduction of aldehyde **67** in the presence and in the absence of capsule **I**. (b) Carbonyl–olefin ring closing metathesis catalyzed by capsule **I**. (c) Example for the activation of a tertiary alkyl C—F bond by capsule **I**.

enantiomeric excess was observed when the reaction was carried out in the presence of the capsule as opposed to its absence, with Δees of up to 92% being achieved. This increase in enantioselectivity is noteworthy as no chiral information is added with the capsule. This effect can be rationalized as arising from steric shielding of one side of the encapsulated iminium species, resulting from interaction with the aromatic walls of the capsule.

Capsule **I** in combination with HCl was also found to catalyze the carbonyl–olefin metathesis of substrates **71** (Scheme 22.8b) [43]. Notably, this is the first example of a Brønsted acid-catalyzed carbonyl–olefin metathesis reaction, as most known methods rely on use of Lewis acids [44, 45]. Importantly, HCl by itself is not able to promote the reaction [46]. For many of the substrates tested, this capsule/HCl cocatalytic system provides yields comparable to the $FeCl_3$-catalyzed method reported by the Schindler group [46–48], and therefore represents a potentially useful alternative.

Recently, we also discovered that the capsule is able to activate C—F bonds [49]. Due to the strength of the C—F bond, harsh conditions are required in solution for its activation [50, 51]; an example that employs milder conditions involves use of the enzyme isopenicillin N synthase [52]. When tertiary alkyl fluorides were subjected to the capsule, generation of the tertiary carbocation was followed by elimination or by cyclic ether formation (Scheme 22.8c). Additionally, activation of benzylic fluorides allowed their use in Friedel–Crafts alkylation reactions inside the capsule. Unlike the THT cyclization or carbon-olefin metathesis reactions, in this case, HCl is not required as a co-catalyst.

22.6 Concluding Remarks

In this chapter, we highlighted some first examples from our laboratory that demonstrate that catalysis inside supramolecular capsules is indeed able to address

current challenges in synthetic organic chemistry. Especially noteworthy are the terpene cyclization results, particularly the four-step synthesis of the sesquiterpene natural product presilphiperfolan-1β-ol. It was enabled by mimicking the proposed biomimetic key cationic cyclization/rearrangement cascade reaction inside the supramolecular capsule – a reaction that was investigated intensively but failed under regular solution conditions so far. Moreover, this strategy enabled the facile access to unnatural derivatives of this natural product that would not be available from the biomachinery. We are very optimistic that further exciting applications of supramolecular capsule catalysis to current synthetic challenges will be discovered soon.

Acknowledgments

This work was supported by funding from the European Research Council Horizon 2020 Programme (ERC Starting Grant 714620-TERPENECAT) and the Swiss National Science Foundation as part of the NCCR Molecular Systems Engineering. L.-D.S. is supported by the European Union's Framework Programme for Research and Innovation Horizon 2020 (2014–2020) under the Marie Skłodowska-Curie Grant Agreement No. 836024-PROTEAS.

References

1 Conn, M.M. and Rebek, J. (1997). Self-assembling capsules. *Chem. Rev.* 97 (5): 1647–1668.
2 Kang, J. and Rebek, J. (1997). Acceleration of a Diels–Alder reaction by a self-assembled molecular capsule. *Nature* 385 (6611): 50–52.
3 Kang, J., Hilmersson, G., Santamaría, J., and Rebek, J. (1998). Diels–Alder reactions through reversible encapsulation. *J. Am. Chem. Soc.* 120 (15): 3650–3656.
4 Hong, C.M., Bergman, R.G., Raymond, K.N., and Toste, F.D. (2018). Self-assembled tetrahedral hosts as supramolecular catalysts. *Acc. Chem. Res.* 51 (10): 2447–2455.
5 Zhu, Y., Rebek, J. Jr., and Yu, Y. (2019). Cyclizations catalyzed inside a hexameric resorcinarene capsule. *Chem. Commun.* 55 (25): 3573–3577.
6 Zhang, Q., Catti, L., and Tiefenbacher, K. (2018). Catalysis inside the hexameric resorcinarene capsule. *Acc. Chem. Res.* 51 (9): 2107–2114.
7 Borsato, G., Rebek, J. Jr., and Scarso, A. (2011). Capsules and cavitands: synthetic catalysts of nanometric dimension. In: *Selective Nanocatalysts and Nanoscience*, 105–168. Wiley-VCH.
8 Gaeta, C., Talotta, C., De Rosa, M. et al. (2019). The hexameric resorcinarene capsule at work: supramolecular catalysis in confined spaces. *Chem. Eur. J.* 25 (19): 4899–4913.
9 Zhang, D., Ronson, T.K., and Nitschke, J.R. (2018). Functional capsules via subcomponent self-assembly. *Acc. Chem. Res.* 51 (10): 2423–2436.

10 MacGillivray, L.R. and Atwood, J.L. (1997). A chiral spherical molecular assembly held together by 60 hydrogen bonds. *Nature* 389 (6650): 469–472.

11 Avram, L. and Cohen, Y. (2002). Spontaneous formation of hexameric resorcinarene capsule in chloroform solution as detected by diffusion NMR. *J. Am. Chem. Soc.* 124 (51): 15148–15149.

12 Shivanyuk, A. and Rebek, J. (2001). Reversible encapsulation by self-assembling resorcinarene subunits. *Proc. Natl. Acad. Sci. U.S.A.* 98 (14): 7662.

13 Avram, L., Cohen, Y., and Rebek, J. Jr., (2011). Recent advances in hydrogen-bonded hexameric encapsulation complexes. *Chem. Commun.* 47 (19): 5368–5375.

14 Cavarzan, A., Scarso, A., Sgarbossa, P. et al. (2011). Supramolecular control on chemo- and regioselectivity via encapsulation of (NHC)-Au catalyst within a hexameric self-assembled host. *J. Am. Chem. Soc.* 133 (9): 2848–2851.

15 Gerkensmeier, T., Iwanek, W., Agena, C. et al. (1999). Self-assembly of 2,8,14,20-tetraisobutyl-5,11,17,23-tetrahydroxyresorc[4]arene. *Eur. J. Org. Chem.* 1999 (9): 2257–2262.

16 Atwood, J.L., Barbour, L.J., and Jerga, A. (2001). Hydrogen-bonded molecular capsules are stable in polar media. *Chem. Commun.* 22: 2376–2377.

17 Shivanyuk, A. and Rebek, J.J. (2001). Hydrogen-bonded capsules in polar, protic solvents. *Chem. Commun.* 22: 2374–2375.

18 Zhang, Q. and Tiefenbacher, K. (2013). Hexameric resorcinarene capsule is a Brønsted acid: investigation and application to synthesis and catalysis. *J. Am. Chem. Soc.* 135 (43): 16213–16219.

19 Köster, J.M. and Tiefenbacher, K. (2018). Elucidating the importance of hydrochloric acid as a cocatalyst for resorcinarene-capsule-catalyzed reactions. *ChemCatChem* 10 (14): 2941–2944.

20 Pronin, S.V. and Shenvi, R.A. (2012). Synthesis of highly strained terpenes by non-stop tail-to-head polycyclization. *Nat. Chem.* 4 (11): 915–920.

21 Lesburg, C.A., Zhai, G., Cane, D.E., and Christianson, D.W. (1997). Crystal structure of pentalenene synthase: mechanistic insights on terpenoid cyclization reactions in biology. *Science* 277 (5333): 1820.

22 Starks, C.M., Back, K., Chappell, J., and Noel, J.P. (1997). Structural basis for cyclic terpene biosynthesis by tobacco 5-epi-aristolochene synthase. *Science* 277 (5333): 1815.

23 Zhang, Q. and Tiefenbacher, K. (2015). Terpene cyclization catalysed inside a self-assembled cavity. *Nat. Chem.* 7 (3): 197–202.

24 Zhang, Q., Catti, L., Pleiss, J., and Tiefenbacher, K. (2017). Terpene cyclizations inside a supramolecular catalyst: leaving-group-controlled product selectivity and mechanistic studies. *J. Am. Chem. Soc.* 139 (33): 11482–11492.

25 Zhang, Q., Rinkel, J., Goldfuss, B. et al. (2018). Sesquiterpene cyclizations catalysed inside the resorcinarene capsule and application in the short synthesis of isolongifolene and isolongifolenone. *Nat. Catal.* 1 (8): 609–615.

26 Zhang, Q. and Tiefenbacher, K. (2019). Sesquiterpene cyclizations inside the hexameric resorcinarene capsule: total synthesis of δ-selinene and mechanistic studies. *Angew. Chem. Int. Ed.* 58 (36): 12688–12695.

27 Gutsche, C.D., Maycock, J.R., and Chang, C.T. (1968). Acid-catalyzed cyclization of farnesol and nerolidol. *Tetrahedron* 24 (2): 859–876.

28 Sakane, S., Fujiwara, J., Maruoka, K., and Yamamoto, H. (1983). Chiral leaving group. Biogenetic-type asymmetric synthesis of limonene and bisabolenes. *J. Am. Chem. Soc.* 105 (19): 6154–6155.

29 de Meireles, A.L.P., Costa, M.d.S., da Silva Rocha, K.A., and Gusevskaya, E.V. (2015). Heteropoly acid catalyzed cyclization of nerolidol and farnesol: synthesis of α-bisabolol. *Appl. Catal., A* 502: 271–275.

30 Ohta, Y. and Hirose, Y. (1972). Electrophile induced cyclization of farnesol. *Chem. Lett.* 1 (3): 263–266.

31 Andersen, N.H. and Syrdal, D.D. (1972). Chemical simulation of the biogenesis of cedrene. *Tetrahedron Lett.* 13 (24): 2455–2458.

32 Tanimoto, H., Kiyota, H., Oritani, T., and Matsumoto, K. (1997). Stereochemistry of a unique tricarbocyclic compound prepared by superacid-catalyzed cyclization. *Synlett* 1 (01): 121–122.

33 Fráter, G., Müller, U., and Kraft, P. (1999). Synthesis of tricyclic ketones with sesquiterpene skeletons by acid-catalyzed rearrangement of β-monocyclofarnesol. *Helv. Chim. Acta* 82 (4): 522–530.

34 Syntrivanis, L.-D., Némethová, I., Schmid, D. et al. (2020). Four-step access to the sesquiterpene natural product presilphiperfolan-1β-ol and unnatural derivatives via supramolecular catalysis. *J. Am. Chem. Soc.* 142 (12): 5894–5900.

35 Pinto, S.C., Leitao, G.G., de Oliveira, D.R. et al. (2009). Chemical composition and antimycobacterial activity of the essential oil from anemia tomentosa var. anthriscifolia. *Nat. Prod. Commun.* 4 (12): 1675–1678.

36 Hong, A.Y. and Stoltz, B.M. (2012). Enantioselective total synthesis of the reported structures of (-)-9-epi-presilphiperfolan-1-ol and (-)-presilphiperfolan-1-ol: structural confirmation and reassignment and biosynthetic insights. *Angew. Chem. Int. Ed.* 51 (38): 9674–9678.

37 Hong, A.Y. and Stoltz, B.M. (2014). Biosynthesis and chemical synthesis of presilphiperfolanol natural products. *Angew. Chem. Int. Ed.* 53 (21): 5248–5260. and references therein.

38 Shankar, S. and Coates, R.M. (1998). Solvolysis of caryophyllen-8β-yl derivatives: biomimetic rearrangement–cyclization to 12-nor-8α-presilphiperfolan-9β-ol. *J. Org. Chem.* 63 (25): 9177–9182.

39 Merget, S., Catti, L., Piccini, G., and Tiefenbacher, K. (2020). Requirements for terpene cyclizations inside the supramolecular resorcinarene capsule: bound water and its protonation determine the catalytic activity. *J. Am. Chem. Soc.* 142 (9): 4400–4410.

40 Bräuer, T.M., Zhang, Q., and Tiefenbacher, K. (2016). Iminium catalysis inside a self-assembled supramolecular capsule: modulation of enantiomeric excess. *Angew. Chem. Int. Ed.* 55 (27): 7698–7701.

41 Bräuer, T.M., Zhang, Q., and Tiefenbacher, K. (2017). Iminium catalysis inside a self-assembled supramolecular capsule: scope and mechanistic studies. *J. Am. Chem. Soc.* 139 (48): 17500–17507.

42 Yang, J.W., Hechavarria Fonseca, M.T., List, B., and Metal-Free Transfer, A. (2004). Hydrogenation: organocatalytic conjugate reduction of α,β-unsaturated aldehydes. *Angew. Chem. Int. Ed.* 43 (48): 6660–6662.

43 Catti, L. and Tiefenbacher, K. (2018). Brønsted acid-catalyzed carbonyl-olefin metathesis inside a self-assembled supramolecular host. *Angew. Chem. Int. Ed.* 57 (44): 14589–14592.

44 Ludwig, J.R. and Schindler, C.S. (2017). Lewis acid catalyzed carbonyl–olefin metathesis. *Synlett* 28 (13): 1501–1509.

45 Becker, M.R., Watson, R.B., and Schindler, C.S. (2018). Beyond olefins: new metathesis directions for synthesis. *Chem. Soc. Rev.* 47 (21): 7867–7881.

46 Ludwig, J.R., Phan, S., McAtee, C.C. et al. (2017). Mechanistic investigations of the iron(III)-catalyzed carbonyl-olefin metathesis reaction. *J. Am. Chem. Soc.* 139 (31): 10832–10842.

47 Ludwig, J.R., Zimmerman, P.M., Gianino, J.B., and Schindler, C.S. (2016). Iron(III)-catalysed carbonyl-olefin metathesis. *Nature* 533 (7603): 374–379.

48 McAtee, C.C., Riehl, P.S., and Schindler, C.S. (2017). Polycyclic aromatic hydrocarbons via iron(III)-catalyzed carbonyl–olefin metathesis. *J. Am. Chem. Soc.* 139 (8): 2960–2963.

49 Köster, J.M., Häussinger, D., and Tiefenbacher, K. (2019). Activation of primary and secondary benzylic and tertiary alkyl (sp3)C-F bonds inside a self-assembled molecular container. *Front. Chem.* 6: 639.

50 Amii, H. and Uneyama, K. (2009). C−F bond activation in organic synthesis. *Chem. Rev.* 109 (5): 2119–2183.

51 Shen, Q., Huang, Y.-G., Liu, C. et al. (2015). Review of recent advances in CF bond activation of aliphatic fluorides. *J. Fluorine Chem.* 179: 14–22.

52 Grummitt, A.R., Rutledge, P.J., Clifton, I.J., and Baldwin, J.E. (2004). Active-site-mediated elimination of hydrogen fluoride from a fluorinated substrate analogue by isopenicillin N synthase. *Biochem. J.* 382 (2): 659–666.

23

Supramolecular Organocatalysis Within the Nanospace of Resorcinarene Capsule

Carmine Gaeta[1], Carmen Talotta[1], Margherita De Rosa[1], Annunziata Soriente[1], Antonio Rescifina[2], and Placido Neri[1]

[1] *Università di Salerno, Dipartimento di Chimica e Biologia "A. Zambelli", Via Giovanni Paolo II 132, I-84084 Fisciano (Salerno), Italy*
[2] *Università di Catania, Dipartimento di Scienze del Farmaco e della Salute, V.le A. Doria 6, I-95125 Catania, Italy*

23.1 Introduction

In the late 1990s, researchers showed that small organic molecules could catalyze the chemical reactions by a biomimetic approach [1]. Starting from these foundational works, organocatalysis was conceptualized as a new field of research and since then has had a rapid diffusion thanks to the economic and environmental benefits offered by the employment of organocatalysts [1]. In this field, different generic modes of substrate activation have been identified that can act on different classes of substrates. The most important modes are [1]: iminium catalysis, enamine catalysis, hydrogen-bonding catalysis, acid–base organocatalysis, and more recently, singly occupied molecular orbital (SOMO) catalysis. In the last decade, much attention has been focused on the field of supramolecular organocatalysis in which covalent hosts [2–8] or self-assembled H-bonded capsules [9–14] are employed as catalysts or nanovessels in organic reactions.

The main feature of supramolecular organocatalysis is that the generic modes of activation based on secondary interactions can work on specific substrates and in confined spaces, like in the active site of natural enzymes [15]: *thus, in supramolecular organocatalysis, molecular recognition of the substrate plays a pivotal role*.

In this regard, supramolecular systems bearing an internal hydrophobic cavity are the most promising candidates as supramolecular organocatalysts. The first examples were designed starting with covalent hosts, usually cyclodextrin macrocycles [16], which were endowed with an internal hydrophobic cavity adorned with catalytically relevant functional groups.

More recently, many efforts have been focused on performing organocatalysis by exploiting the internal cavity in noncovalent hosts such as H-bonded self-assembled capsules [17]. Self-assembled capsules can be easily prepared by reversible self-assembling of simple molecular components, and they show a large

Supramolecular Catalysis: New Directions and Developments, First Edition.
Edited by Piet W.N.M. van Leeuwen and Matthieu Raynal.

internal cavity. Consequently, they can accommodate large substrates and permit bimolecular reactions. In addition, their dynamic self-assembly can ensure the catalytic turnover, and their inner cavity is usually able to stabilize transition states and intermediates by secondary interactions [18]. The most astonishing aspect of catalysis in confined spaces is that reactions can show unusual mechanisms due to the conformational control of the substrates, steric constrictions, stabilization of species, and solvent exclusion [11, 17]. Consequently, the classical rules of organic reactivity are often violated [11]. The most widespread nanoconfined spaces are formed by self-assembling molecular components driven by metal–ligand interactions [14] or hydrogen-bonding interactions [9–13]. In this regard, the H-bonded self-assembled capsules have played a crucial role in supramolecular chemistry [9–13]. In particular, the hexameric resorcinarene capsule $\mathbf{C}_R$ (Figure 23.1), reported by Atwood and MacGillivray [19], has gained relevance in supramolecular organocatalysis [9–13].

The structural features of hexameric capsule $\mathbf{C}_R$ make it able to perform catalytic functions operating by the generic modes of substrate activation such as iminium catalysis [20–22] and H-bonding catalysis in which the self-assembled capsule acts as

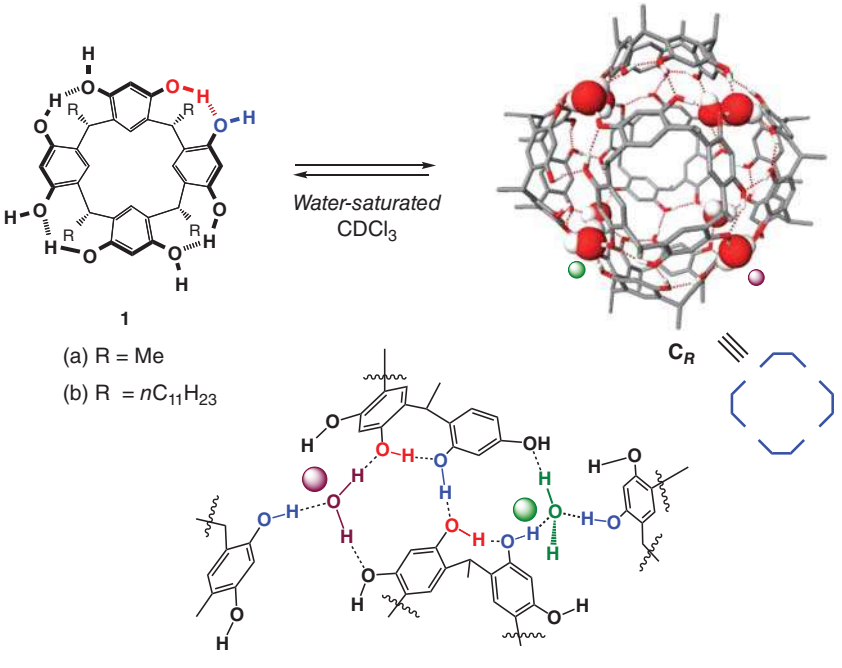

Figure 23.1 The self-assembling equilibrium for the formation of hexameric capsule $\mathbf{C}_R$. In the chemical drawing of resorcinarene **1**, the OH group in red is involved in intramolecular H-bond, while that in blue establishes intermolecular H-bonds leading to the assembly of $\mathbf{C}_R$. Inset: partial chemical drawing of the capsule representing bridging water molecules with one H-bond donating free valence (in green) and complete valence (in purple).

H-bonding donor [23–26]. In addition, thanks to its cavity, the hexameric capsule can act as an organocatalyst and operates by the substrate and product selectivity [9–13].

23.2 The Hexameric Resorcinarene Capsule

The hexameric capsule $\mathbf{C}_{\boldsymbol{R}}$ (Figure 23.1) is obtained by self-assembly of six resorcinarene **1** molecules and 8 water molecules, sealed by 60 (O—H···O) H-bonds [19], in water-saturated $CHCl_3$ (or $CDCl_3$) or wet-benzene solution [27]. The cavity of the resorcinarene capsule shows an internal volume of 1375 Å^3 and can host about six to eight molecules of chloroform or benzene [28]. The capsule is stabilized by a belt of 60 hydrogen bonds between the eight bridged water molecules and the six resorcinarene molecules. In particular, $\mathbf{C}_{\boldsymbol{R}}$ bears eight water molecules located to the corners of a cube, which establish three H-bonds each one (Figure 23.1). Four of these bridging water molecules donate two H-bonds (Figure 23.1, H_2O drawn in purple), completing their H-bond donating valence and act as acceptors of a single H-bond. The other four bridging water molecules donate a single H-bond (Figure 23.1, green) and act as double H-bond acceptors; in this way, each one remains with a *H-bond donating free valence*. The capsule shows a π-electron-rich aromatic cavity that can bind cationic guests by cation–π interactions. Rebek first reported NMR evidence of the encapsulation of ammonium guests inside $\mathbf{C}_{\boldsymbol{R}}$ in solution [29].

The hexameric capsule behaves as a mild Brønsted acid with a pK_a value of about 5.5–6.0 [30–32], thanks to the stabilization of the resulting anion by delocalizing the negative charge onto the phenolic groups and water molecules of the assembly. Semiempirical calculations estimated a pK_a of ≈2.5 for the four bridged-water molecules with *H-bond donating free valence* (Figure 23.1, green) and a mean pK_a of 6.1 for all OH groups of $\mathbf{C}_{\boldsymbol{R}}$ [23], in excellent agreement with the experimental value [30].

Thanks to all these structural features, the capsule can perform supramolecular organocatalysis [9–13] through the following mechanisms:

(a) *H-bond organocatalysis* – The bridging water molecules of $\mathbf{C}_{\boldsymbol{R}}$ with *H-bond donating free valence* (Figure 23.1, in green) may act as H-bond donating groups for the activation of substrates hosted inside the capsule [23–25].

(b) *Brønsted acid organocatalysis* – The aforementioned remarkable Brønsted acidity of $\mathbf{C}_{\boldsymbol{R}}$ (p$K_a \approx 5.5$–6.0 measured in water-saturated $CDCl_3$ relative to the reported pK_a values of amines in water) has been exploited in catalysis of organic reactions [30–32].

(c) *Iminium catalysis (with cocatalyst)* – The internal volume (1375 Å^3) of $\mathbf{C}_{\boldsymbol{R}}$ is large enough to easily allow the coencapsulation of the reactants and a cocatalyst. By exploiting this approach, interesting examples of iminium catalysis have been obtained [20–22].

(d) *Halogen-bond catalysis (with cocatalyst)* – With the same approach, a halogen-bond (XB) catalyst can be coencapsulated with the reactants that allow their activation toward nucleophiles [26].

23.3 The Hexameric Capsule as H-bonding Organocatalyst

The hexameric capsule itself can act as a H-bonding organocatalyst thanks to the presence of bridged water molecules with *H-bond donating free valence* (Figure 23.1, in green). This ability was exploited in the catalysis of Friedel–Crafts (FC) benzylation of arenes and heteroarenes [23] (Scheme 23.1). In particular, the benzylation of *N*-methylpyrrole **2** proceeds with high efficiency (80% total yield after 16 hours) and unusual β-regioselectivity inside the capsule $\mathbf{C_R}$ (52% mol) in water-saturated $CDCl_3$ at 50 °C (Scheme 23.1). When the reaction was performed in the bulk solution in the absence of $\mathbf{C_R}$, no hint of products **4** was detected. Quantum-mechanics calculations (Scheme 23.1, bottom) and experimental evidence have shown that the H-bonding interaction between benzyl chloride and one bridged water molecule of $\mathbf{C_R}$ plays a crucial catalytic role in the activation of the C—Cl bond (**I** in Scheme 23.1). The unusual β-regioselectivity was also rationalized by Quantum mechanics (QM) calculations (Scheme 23.1), which clearly indicate that the α-attack of *N*-methylpyrrole to the activated benzyl chloride inside the capsule led to cationic intermediate **II** (Scheme 23.1) that can directly evolve to the less favored α-**4** regioisomer. The more abundant β-**4** is formed through a [1,2]-benzyl shift to form intermediate **III** (Scheme 23.1) that undergoes a [1,2]-H shift to give **IV**, which is re-aromatized to β-**4**. Finally, the encapsulated product β-**4**@$\mathbf{C_R}$ is thermodynamically more stable than α-**4**@$\mathbf{C_R}$, and in the long run, the reaction exclusively provides the thermodynamic product β-**4**.

The catalytically relevant role of the bridging water molecules of $\mathbf{C_R}$ was also demonstrated in the conjugate addition of *N*-methylpyrrole and indoles to

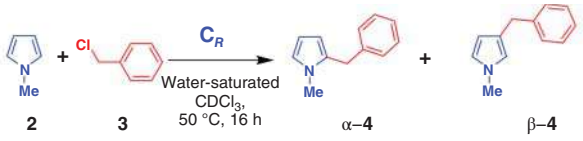

Mechanism of the FC-benzylation inside the capsule proposed by QM calculations:

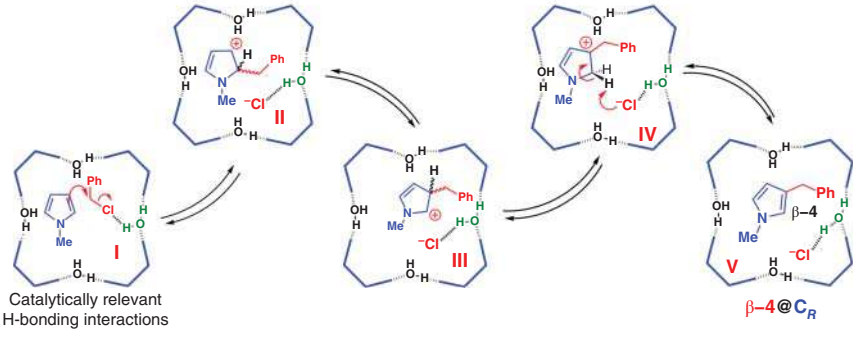

Scheme 23.1 The hexameric capsule $\mathbf{C_R}$ acts as a H-bonding organocatalyst in a mild Friedel–Craft benzylation of *N*-methylpyrrole.

nitroalkenes [24]. When the reaction between **2** and β-nitrostyrene was performed in the absence of $\mathbf{C}_R$ in water-saturated $CDCl_3$, no hint of products was detected. Differently, the conjugate addition between **2** and β-nitrostyrene occurs in high yield in the presence of the capsule. The crucial role played by H-bonding interactions involving the bridging water molecules in the activation of the electrophile was also highlighted by QM-calculations.

The ability of hexameric capsule to work as H-bond organocatalyst was recently exploited in a sustainable metal-free synthesis of amidopyrroles [25]. In particular, when a mixture of *N*-methylpyrrole and phenyl isocyanate was reacted in the presence of $\mathbf{C}_R$, the amidopyrrole product was formed in excellent yield, while no traces were detected in the absence of capsule. In addition, in this case, the authors highlighted the catalytically relevant role of the H-bonding interactions for the activation of isocyanate.

23.4 The Hexameric Capsule as Brønsted Acid Organocatalyst

The inherent Brønsted acidity of the hexameric capsule ($pK_a \approx 5.5$–6.0) can play a crucial role in the organocatalytic formation of imine derivatives [33]. In fact, when benzaldehyde **6** and *p*-chloroaniline **5** were mixed in an equimolar ratio (42.3 mM) in water-saturated $CDCl_3$ at 30 °C in the presence of capsule $\mathbf{C}_R$ (1 equiv), imine **8** was formed in 34% after two hours. This demonstrated that the inherent Brønsted acidity of $\mathbf{C}_R$ is sufficient to catalyze the rate-limiting dehydration step for the imine bond formation. Interestingly, in the presence of a mixture of aldehydes, $\mathbf{C}_R$ performed a kinetic and thermodynamic modulation of the corresponding imine dynamic covalent library (DCL) (Scheme 23.2). The DCL of imine **8** and **9**, obtained by combining *p*-chloroaniline **5**, benzaldehyde **6**, and *p*-CF_3-benzaldehyde **7**, adapts its composition in the presence of $\mathbf{C}_R$ capsule (Scheme 23.2). Imine **8**, obtained by benzaldehyde, was formed faster than **9** after 0.5 hour, but after two hours this selectivity was reversed. Finally, after 24 hours, the **8**/**9** ratio reached the value of 15/60 and remained constant (48 hours). The two imines **8** and **9** were formed in 1 : 1 ratio under the same conditions but in the absence of capsule. These results indicated that **8** was the kinetically favored product, while **9** was the thermodynamic one.

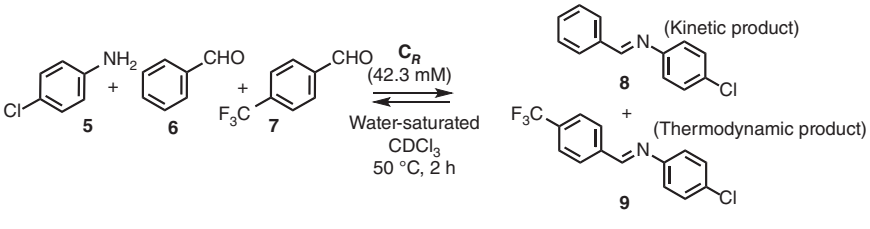

Scheme 23.2 Modulation of dynamic imine library (DCL) of constituents **8** and **9** in the presence of capsule $\mathbf{C}_R$.

The inherent Brønsted acidity of $\mathbf{C_R}$ was exploited for the formation of bis(heteroaryl)methanes from pyrroles or indoles and α-ketoesters or aldehydes (Scheme 23.3) [34]. The reaction takes place in the nanoconfined space inside the capsule, which shows a double catalytic function. In fact, $\mathbf{C_R}$ acts as a H-bond catalyst for the initial activation of the carbonyl function and, more importantly, as a Brønsted acid catalyst for the intermediate alcohol dehydration. Thus, the *N*-methylpyrrole **2** (4 equiv) and ethyl pyruvate **10** (0.16 mmol) were reacted in the presence of $\mathbf{C_R}$ (0.26 equiv) in water-saturated $CDCl_3$ at 30 °C to give meso-α,α-substituted dipyrromethane **11** (Scheme 23.3) in 60% yield, accompanied by 10% and 28% of α,β-linked dipyrromethane **12** and monoalkylated adduct **13**, respectively [34].

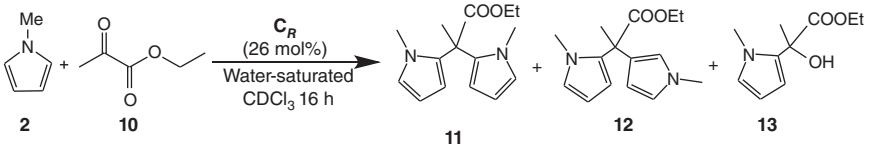

Scheme 23.3 Synthesis of bis(heteroaryl)methanes by Brønsted acid organocatalysis by $\mathbf{C_R}$. No reaction takes place in the absence of capsule.

The Brønsted acid organocatalysis by $\mathbf{C_R}$ was used in an intramolecular hydroalkoxylation of unactivated hydroxyolefins to give cyclic ethers (Scheme 23.4) [35]. This reaction occurs in the bulk solution in the presence of strong Brønsted acids (like triflic acid), while, surprisingly, milder conditions are sufficient inside the hexameric capsule thanks to the confinement effect. The inherent acidity of $\mathbf{C_R}$ is not sufficient by itself, and the addition of HCl (3%) is required.

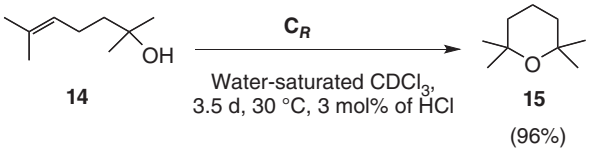

Scheme 23.4 Intramolecular hydroalkoxylation of unactivated hydroxyolefins to give cyclic ethers organocatalyzed inside $\mathbf{C_R}$.

The hydroxy olefin **14** was converted to **15** in 96% yield after 3.5 days at 30 °C in the presence of $\mathbf{C_R}$ (3.3 mM) and HCl as cocatalyst (3 mol%) [35]. The hydroalkoxylation of **14** was slowed down by the addition of Bu_4NBr to the reaction mixture. The competitive tetrabutylammonium guest, occupying the cavity of $\mathbf{C_R}$, inhibits its catalytic activity. Analogously, no conversion of **14** to **15** was observed in the absence of $\mathbf{C_R}$. The catalysis in Scheme 23.4 is due to an initial protonation of the substrate inside the cavity of $\mathbf{C_R}$, favored by the presence of HCl as cocatalyst, and to the stabilization of the cationic intermediates and transition states by cation· · ·π interactions with the aromatic walls of the hexameric capsule.

The scope of this approach has been further expanded with a range of amazing transformations of natural products providing interesting mimics of cyclase enzymes (see Chapter 15).

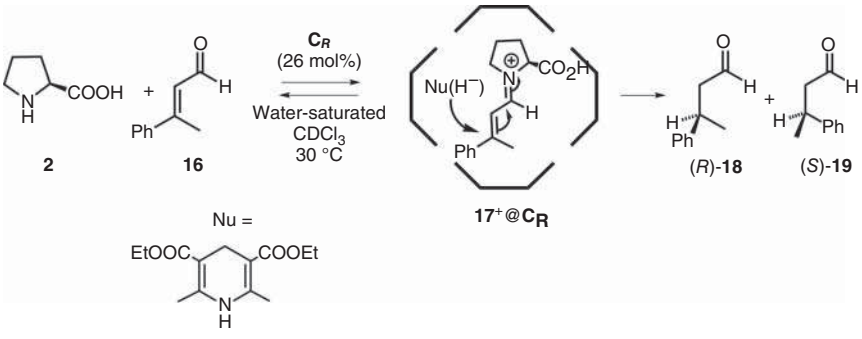

Scheme 23.5 Iminium catalysis inside the hexameric capsule for the biomimetic reduction of the unsaturated aldehyde **16** in the presence of cocatalyst L-proline and Hantzsch ester.

23.5 Iminium Catalysis with a Coencapsulated Cocatalyst

The first example of iminium catalysis inside the hexameric capsule $\mathbf{C}_R$ was reported in 2016 [20]. As outlined in Scheme 23.5, cocatalyst L-proline **2** and α,β-unsaturated aldehyde **16** were mixed in water-saturated $CDCl_3$ at 30 °C in the presence of 26 mol% of $\mathbf{C}_R$. Under these conditions, the iminium derivative $\mathbf{17}^+$ was encapsulated inside the capsule thanks to stabilizing cation· · ·π interactions.

By detailed control experiments [20, 21], the authors showed that the two *E*- and *Z*-$\mathbf{17}^+$ stereoisomeric iminium species were first formed in solution and then encapsulated inside $\mathbf{C}_R$, where the iminium *Z*-$\mathbf{17}^+$ was rapidly isomerized to *E*-$\mathbf{17}^+$. Finally, the coencapsulation of iminium *E*-$\mathbf{17}^+$ and Hantzsch ester, as NADH-like artificial-cofactor, led to the formation of **18** in 93% yield.

Interestingly, excellent enantioselectivity (74% of ee) was observed in favor of the (*S*)-enantiomer of **18**, a value significantly higher than that observed in the bulk solvent in the absence of capsule (9% of ee for *S*, Δee = 65%, 27% yield). In particular, the authors postulated that in the confined space, the iminium *E*-$\mathbf{17}^+$ adopts a specific orientation establishing more favorable cation· · ·π interactions with the aromatic walls of $\mathbf{C}_R$ from the less hindered face. Consequently, the reduction occurs from the face in *syn* with respect to the encumbering COOH group. Naturally, when the reaction in Scheme 23.5 is performed in bulk solution, in the absence of capsule, the attack from the face in *syn* to COOH group is unfavored for steric reasons.

Another example of iminium catalysis inside the confined space of the hexameric capsule $\mathbf{C}_R$ was also reported for a 1,3-dipolar cycloaddition (1,3-DC) [22]. The cycloaddition between nitrone **19** and (*E*)-crotonaldehyde **20** (Scheme 23.6) can give the two 4- and 5-formyl regioisomers (**23** and **24**, respectively) both as *endo* and *exo* diastereomers, each in two possible enantiomeric forms. In the bulk solvent, in the presence of L-proline methyl ester **21a** as cocatalyst, the 1,3-DC reaction led to the formation of the products in 42% yield, a value significantly lower than that obtained in the presence of $\mathbf{C}_R$ (88%). In addition, the reaction performed in confined space inside the capsule favored the formation of the *endo*-stereoisomer of **23**, with an

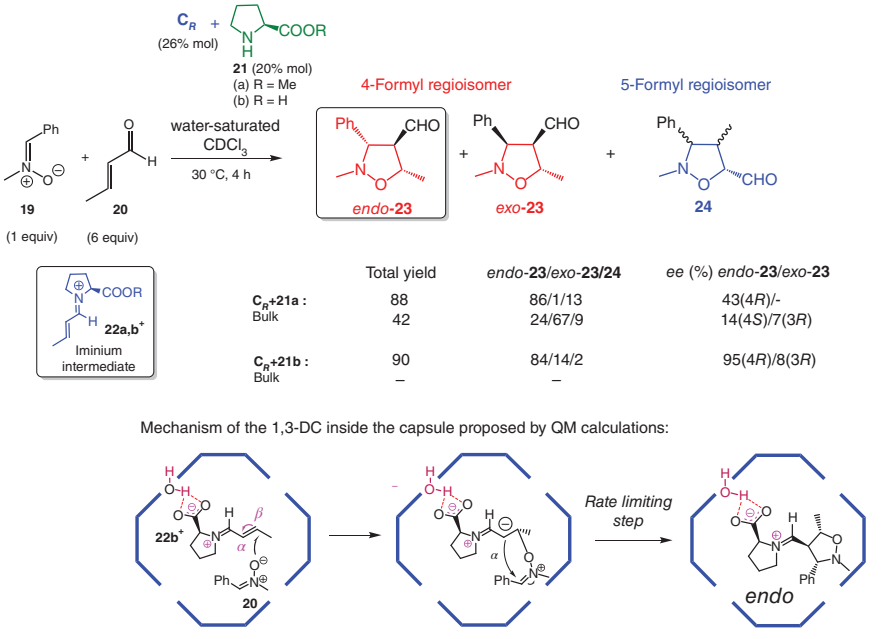

Scheme 23.6 An example of iminium-catalyzed 1,3-dipolar cycloaddition inside the cavity of $\mathbf{C}_R$.

endo/*exo* ratio of 86/1, while in the bulk medium, *exo*-**23** was the major product (24/67 *endo*/*exo*).

Interestingly, the (4*R*)-enantiomer of *endo*-**23** was preferentially formed with 43% ee in the presence of $\mathbf{C}_R$, while in its absence, (4*S*)-one was formed preferentially with 14% ee. These experimental results clearly indicate that inside the confined space of $\mathbf{C}_R$, the 1,3-DC occurs with different stereo- and regiochemical outcomes with respect to the bulk medium. These results were rationalized by QM calculations using L-proline **21b** as cocatalyst (Scheme 23.6, bottom), which gave similar experimental results (90% yield) to **21a**. The 1,3-DC takes place inside $\mathbf{C}_R$ by a stepwise mechanism in which the iminium $\mathbf{22b}^+$ was formed and stabilized by cation$\cdots\pi$ interactions. The calculations indicated that the acidity of the capsule plays a crucial role in the formation of the iminium intermediate.

A H-bonding interaction was found between the carboxylic function of L-proline and a bridging water molecule of $\mathbf{C}_R$. The formation of iminium intermediate $\mathbf{22b}^+$ (Scheme 23.6) inside the capsule and its stabilization by cation$\cdots\pi$ interactions caused a substantial lowering of the LUMO of the aldehyde, which explains the very low activation free energy for the Michael-type addition with nitrone **19**.

In conclusion, these results clearly showed that the confinement effect of the reactants **19** and **20** inside the capsule determines different regiochemical and stereochemical outcome compared to the reaction in bulk solvent.

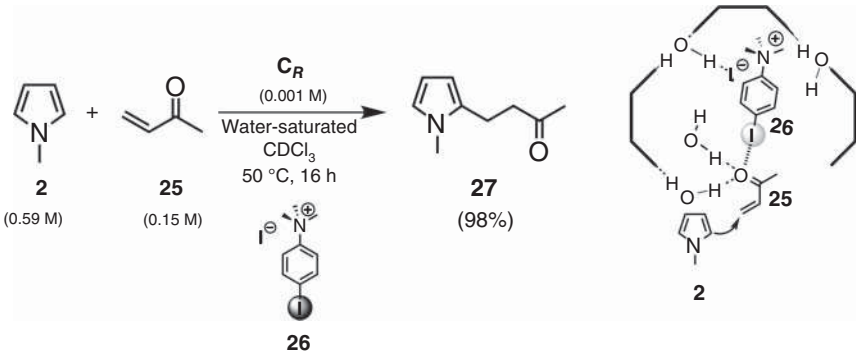

Scheme 23.7 (Left) Michael reaction between *N*-methylpyrrole **2** and methylvinylketone **25** inside the pentameric capsule $\mathbf{C}_{R'}$ catalyzed by XB-catalyst **26**. (Right) The catalytically active species in which the substrate **25** is activated by XB interactions (thick dashes) with XB catalyst **26** and H-bonding interactions (thin dashes) with the bridging water molecules.

23.6 Halogen-bond (XB) Catalysis with a Coencapsulated Cocatalyst

Another example of exploitation of encapsulated cocatalyst (*i.e.*, XB catalyst **26**) is provided by the Michael reaction between *N*-methylpyrrole **2** and methylvinylketone **25** inside $\mathbf{C}_{R}$ (Scheme 23.7) [26]. In this reaction, the carbonyl substrate was activated by a synergic interplay between halogen-bonding (XB) and H-bonding interactions (Scheme 23.7, right). As a XB donor group, the *p*-iodophenyltrimethyl-ammonium salt **26** was used, which bears an ammonium group acting as a Trojan horse to drive the XB catalyst inside the capsule. The capsular water molecules acted as synergic H-bonding donor groups. The yield of the reaction between **2** and **25** in the presence of $\mathbf{C}_{R}$ and XB catalyst **26** was very high (98%). QM calculations clearly indicated that the carbonyl group of **25** was activated by the synergistic action of halogen bonding with **26** and H-bonding with bridging water molecules, inside an open pentameric resorcinarene capsule $\mathbf{C}_{R'}$. This highlights the dynamic nature of $\mathbf{C}_{R}$ and how the action of the binding of the reactants can influence the structure of the cavity itself.

Further examples of coencapsulated cocatalyst are provided by a range of interesting catalytically active metal complexes (see Chapter 17).

23.7 Concluding Remarks

In conclusion, in this chapter, we have examined the literature data regarding the organocatalytic abilities of hexameric resorcinarene capsule. The examples here described clearly show that $\mathbf{C}_{R}$ is a valid supramolecular organocatalyst able to host a discrete number of reactants inside its cavity, including cocatalyst(s). The reactions

are then activated by typical organocatalytic mechanisms, such as H-bonding catalysis, Brønsted acid catalysis, iminium catalysis, and halogen-bonding catalysis. The regio- and stereochemistry of the reactions occurring inside the confined space of the capsule can diverge with respect to the analogous reactions in the bulk solvent. These phenomena can be ascribed to the confinement effect on substrates and transition states due to conformational control, steric constrictions, species stabilization by secondary interactions, and solvent exclusion. It can be envisioned that future efforts will be directed to fine control of the inner space geometry and to the exploitation of different catalytic functions.

Acknowledgment

This work was supported by the University of Salerno (FARB and PhD funding).

References

1 McMillan, D.W.C. (2008). The advent and development of organocatalysis. *Nature* 455: 304–308.
2 Raynal, M., Ballester, P., Vidal-Ferran, A., and van Leeuwen, P.W.N.M. (2014). Supramolecular catalysis. Part 1: non-covalent interactions as a tool for building and modifying homogeneous catalysts. *Chem. Soc. Rev.* 43: 1660–1733.
3 De Rosa, M., La Manna, P., Talotta, C. et al. (2018). Supramolecular organocatalysis in water mediated by macrocyclic compounds. *Front. Chem.* 6: 84.
4 Floresta, G., Talotta, C., Gaeta, C. et al. (2017). γ-Cyclodextrin as a catalyst for the synthesis of 2-methyl-3,5 diarylisoxazolidines in water. *J. Org. Chem.* 82: 4631–4639.
5 De Simone, N.A., Meninno, S., Talotta, C. et al. (2018). Solvent-free enantioselective michael reactions catalyzed by a calixarene-based primary amine thiourea. *J. Org. Chem.* 83: 10318–10325.
6 La Manna, P., Soriente, A., De Rosa, M. et al. (2019). Green, mild, and efficient Friedel–Crafts benzylation of scarcely reactive arenes and heteroarenes under on-water conditions. *ChemSusChem* 12: 1673–1683.
7 De Rosa, M., La Manna, P., Soriente, A. et al. (2017). A simple tetraminocalix[4]arene as a highly efficient catalyst under "On-Water" conditions through hydrophobic amplification of weak hydrogen bonds. *Chem. Eur. J.* 23: 7142–7151.
8 De Rosa, M., La Manna, P., Soriente, A. et al. (2016). Exploiting the hydrophobicity of calixarene macrocycles for catalysis under "on-water" conditions. *RSC Adv.* 6: 91846–91851.
9 Catti, L., Zhang, Q., and Tiefenbacher, K. (2016). Advantages of catalysis in self-assembled molecular capsules. *Chem. Eur. J.* 22: 9060–9066.

10 Gaeta, C., Talotta, C., De Rosa, M. et al. (2019). The hexameric resorcinarene capsule at work: supramolecular catalysis in confined spaces. *Chem. Eur. J.* 25: 4899–4913.

11 Gaeta, C., La Manna, P., De Rosa, M. et al. (2021). Supramolecular catalysis with self-assembled capsules and cages: what happens in confined spaces. *ChemCatChem* 13: 1638–1658.

12 Borsato, G., Rebek, J. Jr., and Scarso, A. (2011). *From Selective Nanocatalysts and Nanoscience* (eds. A. Zecchina, S. Bordiga and E.E. Groppo), 105–168. Weinheim, Germany: Wiley-VCH Verlag GmbH & Co. KGaA.

13 Leenders, S.H.A.M., Gramage-Doria, R., de Bruin, B., and Reek, J.N.H. (2015). Transition metal catalysis in confined spaces. *Chem. Soc. Rev.* 44: 433–448.

14 Hong, C.M., Bergman, R.G., Raymond, K.N., and Toste, F.D. (2018). Self-assembled tetrahedral hosts as supramolecular catalysts. *Acc. Chem. Res.* 51: 2447–2455.

15 Kirby, A.J. and Hollfelder, F. (2009). *From Enzyme Models to Model Enzymes*. Cambridge: RSC Publishing.

16 Breslow, R. (1982). Artificial enzymes. *Science* 218: 532–537.

17 See the special issue and Toste, D. (2018). Supramolecular chemistry in confined space and organized assemblies. *Acc. Chem. Res.* 51: 2980–2981.

18 Bollinger, J.L. (2017). *Effects of Nanoconfinement on Catalysis* (ed. R. Poli), 17–48. Berlin: Springer.

19 MacGillivray, L.R. and Atwood, J.L. (1997). A chiral spherical molecular assembly held together by 60 hydrogen bonds. *Nature* 389: 469–472.

20 Bräuer, T.M., Zhang, Q., and Tiefenbacher, K. (2016). Iminium catalysis inside a self-assembled supramolecular capsule: modulation of enantiomeric excess. *Angew. Chem. Int. Ed.* 55: 7698–7701.

21 Bräuer, T.M., Zhang, Q., and Tiefenbacher, K. (2017). Iminium catalysis inside a self-assembled supramolecular capsule: scope and mechanistic studies. *J. Am. Chem. Soc.* 139: 17500–17507.

22 La Manna, P., De Rosa, M., Talotta, C. et al. (2018). The hexameric resorcinarene capsule as an artificial enzyme: ruling the regio and stereochemistry of a 1,3-dipolar cycloaddition between nitrones and unsaturated aldehydes. *Org. Chem. Front.* 5: 827–837.

23 La Manna, P., Talotta, C., Floresta, G. et al. (2018). Mild Friedel–Crafts reactions inside a hexameric resorcinarene capsule: C–Cl bond activation through hydrogen bonding to bridging water molecules. *Angew. Chem. Int. Ed.* 130: 5521–5526.

24 Gambaro, S., De Rosa, M., Soriente, A. et al. (2019). A hexameric resorcinarene capsule as a hydrogen bonding catalyst in the conjugate addition of pyrroles and indoles to nitroalkenes. *Org. Chem. Front.* 6: 2339–2347.

25 La Manna, P., Talotta, C., De Rosa, M. et al. (2020). An atom-economical method for the formation of amidopyrroles exploiting the self-assembled resorcinarene capsule. *Org. Lett.* 22: 2590–2594.

26 La Manna, P., De Rosa, M., Talotta, C. et al. (2020). Synergic interplay between halogen bonding and hydrogen bonding in the activation of a neutral substrate in a nanoconfined space. *Angew. Chem. Int. Ed.* 59: 811–818.

27 Avram, L. and Cohen, Y. (2002). Spontaneous formation of hexameric resorcinarene capsule in chloroform solution as detected by diffusion NMR. *J. Am. Chem. Soc.* 124: 15148–15149.

28 Shivanyuk, A. and Rebek, J. Jr., (2003). Assembly of resorcinarene capsules in wet solvents. *J. Am. Chem. Soc.* 125: 3432–3433.

29 Shivanyuk, A. and Rebek, J. Jr., (2001). Reversible encapsulation by self-assembling resorcinarene subunits. *Proc. Natl. Acad. Sci. USA* 98: 7662–7665.

30 Zhang, Q. and Tiefenbacher, K. (2013). Hexameric resorcinarene capsule is a Brønsted acid: investigation and application to synthesis and catalysis. *J. Am. Chem. Soc.* 135: 16213–16219.

31 Köster, J.M. and Tiefenbacher, K. (2018). Elucidating the importance of hydrochloric acid as a cocatalyst for resorcinarene-capsule-catalyzed reactions. *ChemCatChem* 10: 2941–2944.

32 Zhang, Q., Catti, L., and Tiefenbacher, K. (2018). Catalysis inside the hexameric resorcinarene capsule. *Acc. Chem. Res.* 51: 2107–2114.

33 Gambaro, S., Talotta, C., Della Sala, P. et al. (2020). Kinetic and thermodynamic modulation of dynamic imine libraries driven by the hexameric resorcinarene capsule. *J. Am. Chem. Soc.* 142: 14914–14923.

34 Gambaro, S., La Manna, P., De Rosa, M. et al. (2020). The hexameric resorcinarene capsule as a Brønsted acid catalyst for the synthesis of bis(heteroaryl)methanes in a nanoconfined space. *Front. Chem.* 7: 687.

35 Catti, L. and Tiefenbacher, K. (2015). Intramolecular hydroalkoxylation catalyzed inside a self-assembled cavity of an enzyme-like host structure. *Chem. Commun.* 51: 892–894.

24

Resorcin[4]arene Hexamer: From Nanocontainer to Nanocatalyst

Giorgio Strukul, Fabrizio Fabris, and Alessandro Scarso

Università Ca' Foscari di Venezia, Dipartimento di Scienze Molecolari e Nanosistemi, via Torino 155, 30123 Mestre Venezia, Italy

24.1 Introduction

Homogeneous catalysis is witnessing a radical change in perspective, with an increasing awareness that a clear understanding of the nanometric tridimensional space where the reactions take place plays a key role in controlling both the activity and even more importantly the different selectivities of chemical transformations. The understanding of what happens at this level during a catalytic process can spur further achievements in deciphering biological phenomena such as enzyme activity. Supramolecular interactions are currently considered in homogeneous catalytic reactions, and a better definition of the nano-space around the active site is the target for developing more active and selective systems.

Nanoconfinement effects in chemical transformations [1] and supramolecular strategies in catalysis are gaining momentum [2]. Encapsulation phenomena in catalysis have been broadly described in the recent years, in particular for self-assembling capsules held together by metal–ligand coordination operating in water where the hydrophobic effect represents a powerful driving force to promote encapsulation. Much less investigated are encapsulation phenomena in catalysis in organic media where the recognition of the reactive species involves weaker supramolecular interactions.

The resorcin[4]arene unit reported in Figure 24.1 bearing long alkyl chains to impart solubility in apolar solvents is a typical easy-to-synthesize product that can be obtained in multigram scale with no particular instrumental requirements, starting from simple reagents using hydrochloric acid as catalyst. Moreover, its supramolecular self-aggregation in apolar media, leading to the formation of hexameric capsules where the resorcin[4]arene are held together with eight water molecules through a seam of overall 60 hydrogen bonds, makes this capsule a real benchmark host for supramolecular applications.

Its large pseudo-spherical cavity of about ~1375 $Å^3$ with an internal diameter of ~13 Å provides sufficient space for the co-encapsulation of different species such as

Supramolecular Catalysis: New Directions and Developments, First Edition.
Edited by Piet W.N.M. van Leeuwen and Matthieu Raynal.

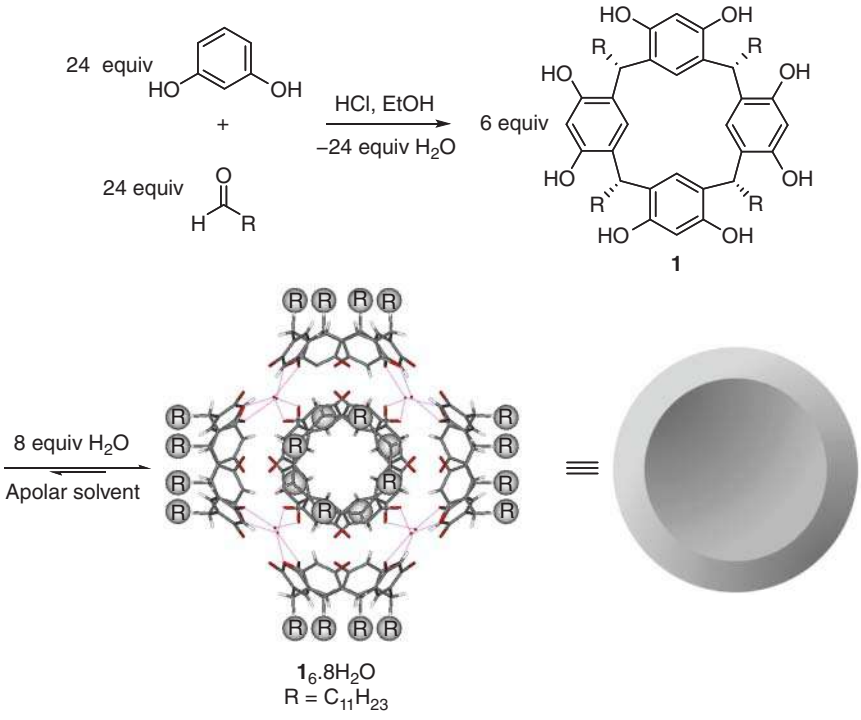

Figure 24.1 Synthesis of resorcin[4]arene **1** and its self-assembly in organic media forming $\mathbf{1}_6 \cdot 8H_2O$ driven by the formation of 60 hydrogen bonds involving 8 water molecules leading to the hexameric capsule.

substrates, reagents, or catalysts. The aromatic electron-rich panels that adorn the cavity not only promote the quantitative binding of cationic guests of suitable size and shape but can also be exploited to stabilize transient cationic or electron-poor intermediate species typical of several organic transformations. Many of these opportunities have been investigated by us and other research groups [3]. In Sections 24.2 and 24.3, our contribution to the field is described classifying the role of the capsule initially as a nanoreactor, where stoichiometric or catalytic reactions take place with confinement effects on substrate and product selectivity, and later reporting examples in which the capsule itself catalyzes organic transformations due to stabilization of intermediate species within the electron-rich cavity.

24.2 Resorcinarene Capsule as Nanoreactor

The rigid cavity of the capsule, in combination with its slow in–out of guests on the NMR timescale, makes the hexamer a perfect nanocontainer to investigate confinement effects. The high affinity of the capsule for cationic guests spurred our interest in considering this nanoreactor for the amide condensation between aliphatic carboxylic acids and primary aliphatic amines mediated by a common cationic coupling agent 1-ethyl-3-(-3-dimethylaminopropyl)carbodiimide hydrochloride **2**. The latter

species showed quantitative encapsulation in the hexameric capsule leaving a residual space in the cavity that was exploited to impart substrate preferences in the amide coupling reaction [4].

Specifically, when combining hexanoic acid with equimolar amounts of octyl and butyl amines in the absence of the capsule, the reaction led to the formation of the shorter amide in 2.5 times larger amounts with respect to the longer one. The selectivity was further steered toward the shorter products when running the reaction with the condensing agent hosted within the hexameric capsule. Similarly, the reaction of hexadecylamine with equimolar amounts of hexanoic and dodecanoic acid showed a 1,2 preference for the shorter amide product when the reaction was run in solution, while in the presence of the capsule, the selectivity increased up to 28 : 1 for the shorter amide product. For all tested competitive experiments, the capsule showed to favor the combination of shorter substrates. A competitive experiment involving butylamine and octylamine with hexanoic and dodecanoic acid is reported in Figure 24.2. While in the absence of the capsule the four possible amide products

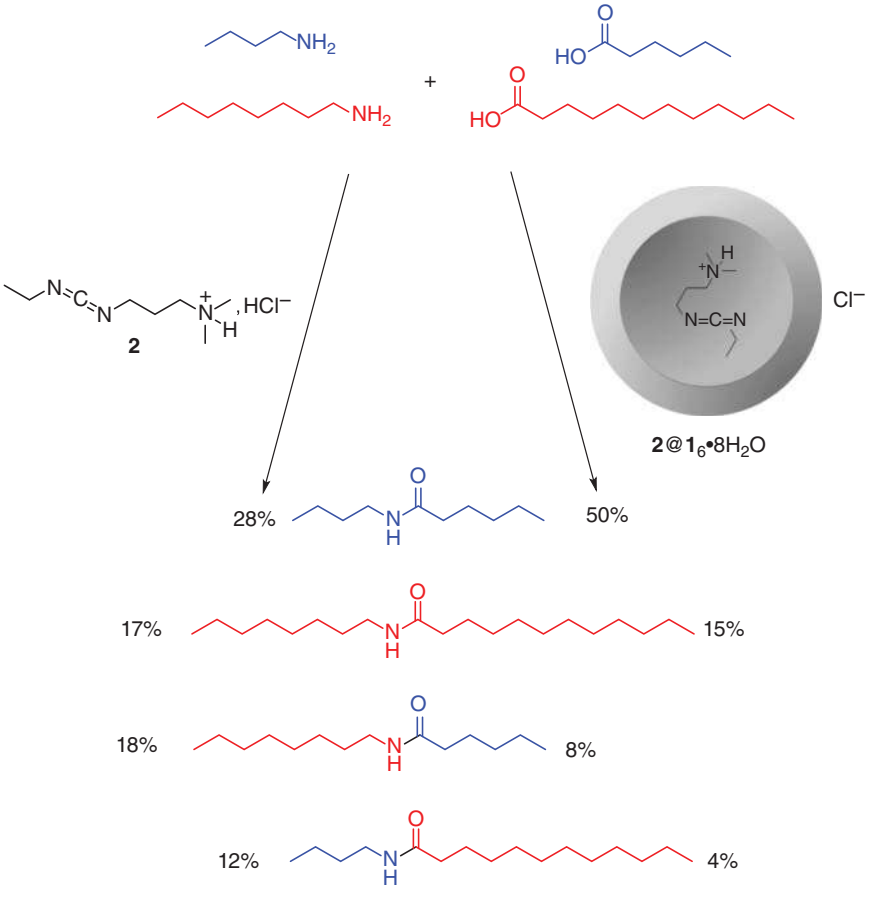

Figure 24.2 The encapsulation of the cationic carbodiimide steers the substrate selectivity in amide coupling toward the shorter combination of amines and carboxylic acids.

were obtained with comparable yields in the range 28% to 12%, in the presence of the capsule as nanocontainer in which the reaction takes place, the shorter amide product was obtained in 50% yield, while the longer one in only 4% yield.

The nanoreactor properties of the hexameric capsule were further investigated in combination with cationic transition metal catalysts. In consideration of its nice matching of size and shape, the encapsulation of $[Ru(bpy)_3]^{2+}\cdot(OTf)_2$ **3** was investigated.

By ^{1}H NMR (nuclear magnetic resonance) and DOSY (diffusion ordered spectroscopy) experiments, it was observed that the metal species could be quantitatively encapsulated in one equivalent of capsule, and it could be released back in solution using an excess of a competitive cationic guest such as tetraethylammonium. The reversible binding of the complex was exploited to modulate the catalytic properties of the metal catalyst, which is well known as a sensitizer under visible light irradiation to activate triplet oxygen to the corresponding singlet species to oxidize thioethers to the corresponding sulfoxides (Figure 24.3) [5]. Thanks to the above-mentioned reversibility, it was possible to modulate off/on the activity of the metal catalyst using the hexameric capsule initially as a trap with immediate interruption of the sulfoxide formation, further releasing the catalyst in solution with reactivation of the sulfoxidation reaction using an excess of tetraethylammonium. In this case, the role of the capsule corresponds to caging on-demand the catalyst that assumes an off-state, while it returns in the on-state when displaced back into solution by a competitive guest.

The OH moieties present on the rim of the resorcin[4]arene could act as coordinating ligands for hard metal catalysts, while soft metal catalysts and complexes do not interfere with the hydrogen-bonding seam. Based on this, we selected the carbene-based Au(I) metal complex **4** reported in Figure 24.4 as a suitable catalyst that showed quantitative encapsulation in the presence of one equivalent of capsule. The catalyst is well known for its ability to activate terminal alkynes promoting their rapid hydration to the corresponding ketone products. Using 4-phenyl-butyne as substrate, when the catalyst is free in solution only the formation of the corresponding methyl ketone is observed, while the encapsulated catalyst showed unexpectedly the additional formation of the aldehyde and 1,2-dihydronaphthalene (Figure 24.4) [6].

The aldehyde is a completely unprecedented product for Au(I)-catalyzed terminal alkyne hydrations, while the formation of the cyclic product is known for reaction under dry conditions. Overall, the encapsulation of **4** can change the product distribution of the reaction, probably affecting the transition state of the reaction, demonstrating the fundamental role of confinement effects, even if with loss of regioselectivity in the present case.

The effect of the encapsulation of **4** was also investigated in terms of substrate selectivity for a series of homologous aliphatic or aromatic terminal alkynes (Figure 24.5) [7]. The reaction of a mixture of equimolar amounts of 1-dodecyne, 1-octyne, and the isomeric ethynyl-cyclohexane with the free catalyst in solution showed a slight preference in terms of rate of reaction in favor of the latter substrate probably because it is slightly more electron rich compared to the other two.

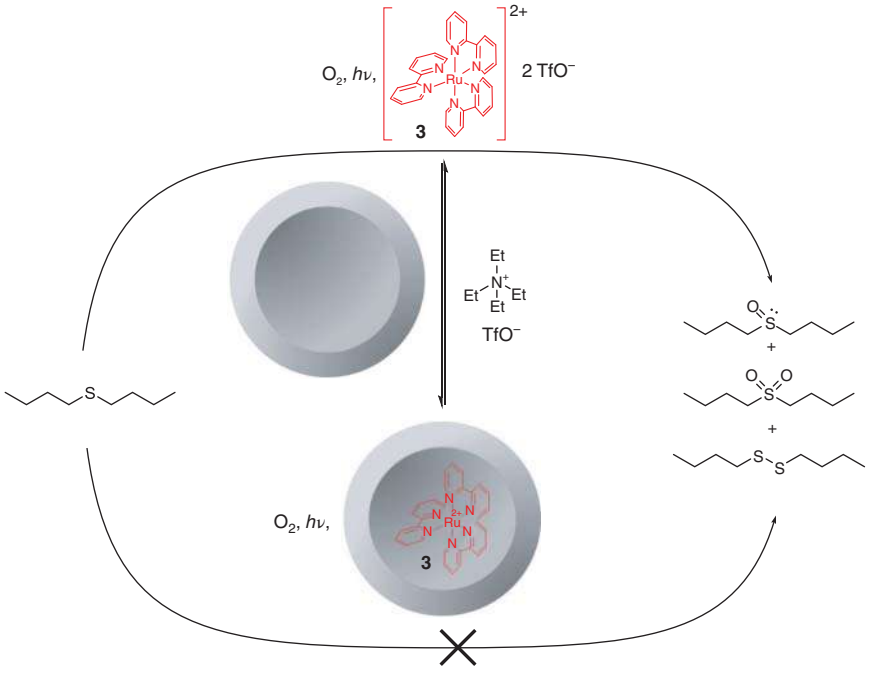

Figure 24.3 Under visible light and in the presence of O_2, $[Ru(bpy)_3](OTf)_2$ provides singlet oxygen that oxidizes dibutyl sulfide mainly to sulfoxide. The activity of the catalyst can be triggered off and on by encapsulation and release from the capsule.

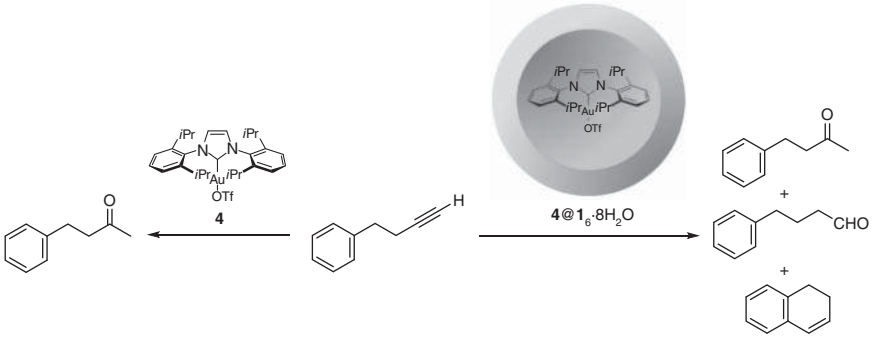

Figure 24.4 The cationic Au(I) catalyst **4**, that in solution promotes the Markovnikov hydration of 4-phenyl butyne, once encapsulated leads to the formation also of the corresponding aldehyde and 1,2-dihydronaphthalene.

The reaction under identical experimental conditions with **4** hosted within the capsule showed an increased preference for the cyclic substrate whose conversion after 155 minutes was 48%, compared to 25% and 21% for 1-octyne and 1-dodecyne, respectively (Figure 24.5a). Similar competitive experiments were run using rigid phenylacetylene derivatives characterized by small size differences, observing an inversion of the substrate selectivity trend when the reaction was carried out

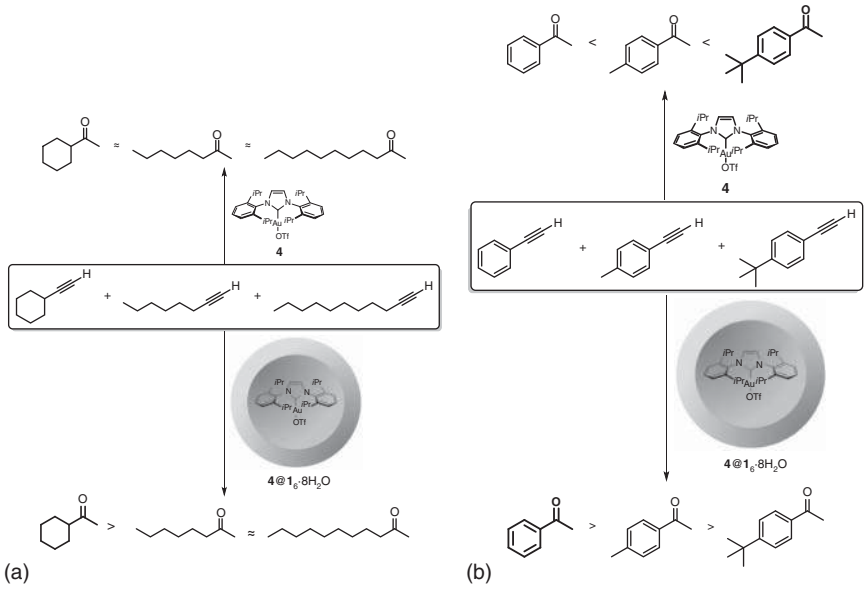

Figure 24.5 The substrate selectivity for the free and encapsulated Au(I) catalyst **4** was investigated with (a) aliphatic terminal alkynes and (b) aromatic terminal alkynes.

with the encapsulated **4**. In fact, using the three phenyl acetylene derivatives reported in Figure 24.5b, the reaction with the free catalyst in solution showed a decreasing order of activity from the more electron-rich *tert*-butyl derivative to the phenylacetylene substrate. On the contrary, with the encapsulated catalyst, the reactivity order was reversed with the smaller phenylacetylene reacting faster than the methyl and *tert*-butyl substituted analogues. Once again, the capsule imparts a steric selection on the substrates leading to the preferential conversion of the smaller derivatives with respect to the longer ones, even though the differences in size are rather small.

24.3 Resorcin[4]arene Capsule as Nanocatalyst

One unusual activation mechanism imparted by the hexameric capsule involves hydrogen peroxide. This molecule can substitute one of the eight water molecules in the hydrogen-bonding network of the capsule. This effect provides an electrophilic activation of the oxidant that enabled the oxidation of electron-rich substrates such as thioethers, leading to the formation of the corresponding sulfoxides with high chemoselectivity (Figure 24.6) [8].

More in detail, while the reaction in the absence of the capsule was sluggish with just 10% product formation after 90 minutes, in the presence of 10 mol% of the hexameric capsule, the reaction was complete in 65 minutes. Control experiments using resorcinol to mimic the hydrogen-bonding properties of the resorcin[4]arene or acetic acid to simulate the Brønsted acidity of the capsule, all showed marked

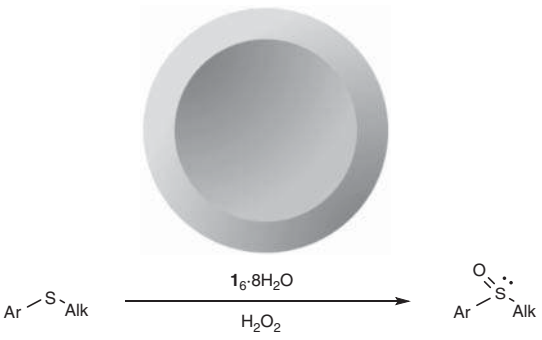

Figure 24.6 The hexameric capsule activates hydrogen peroxide for the electrophilic oxidation of thioethers forming selectively the corresponding sulfoxides.

decrease of activity. These results further confirmed that the capsule acted as a true organocatalyst activating the oxidation toward dialkyl, aryl-alkyl, and diaryl thioethers (Figure 24.6). Several substrates were tested observing in all cases large inactivation of the catalytic activity of the capsule when using a competitive guest, which suggests a stabilizing effect imparted by the electron-rich cavity on the polar transition state derived by the combination of the oxidant and the substrate. In all cases only the sulfoxide product was observed, indicating a good chemoselectivity of the reaction with short reaction time representing one of the most effective organocatalyst for sulfoxidation reaction with hydrogen peroxide.

Some of the specific properties of the hexameric capsule such as a weak Brønsted acidity and the presence of water molecules on the edges of the aggregate as H-bond donors pointing inside the cavity spurred the investigation of some classical organic transformations known to be sensitive to this kind of activation process. Epoxide isomerization leading to carbonyl compounds is a typical reaction that can be promoted under homogeneous conditions by a wide range of catalysts such as metal species, protic acids, and H-bonding units. The hexameric capsule proved to promote this reaction but only with activated substrates such as epoxides bearing aryl substituents directly connected to the C atoms of the oxirane ring or α-pinene oxide and norbornene oxide (Figure 24.7). For example, the reaction with styrene oxide was complete forming the isomerization product phenyl acetaldehyde in 18 hours using 13 mol% of capsule. Control experiments confirmed that the activation imparted by the capsule was not due to just Brønsted acidity or mere H-bonding [9].

The accepted mechanism for epoxide isomerization involves the formation of carbocationic species. It is likely that the electron-rich inner cavity of the capsule can stabilize these charged intermediate species, thus explaining the acceleration observed. It is also interesting to observe that α-pinene oxide, which by isomerization can provide a wide range of possible isomers, led to the formation of the campholenic aldehyde with 82% yield with minor isomeric by-products after only four-hour reaction.

The stabilizing properties provided by the inner surfaces of the cavity of the capsule could be exploited, in combination with protic acids, to promote the organocatalytic hydration of terminal alkynes (Figure 24.8). The reaction was investigated on aromatic terminal alkynes using catalytic amounts (10 mol%) of the capsule and of

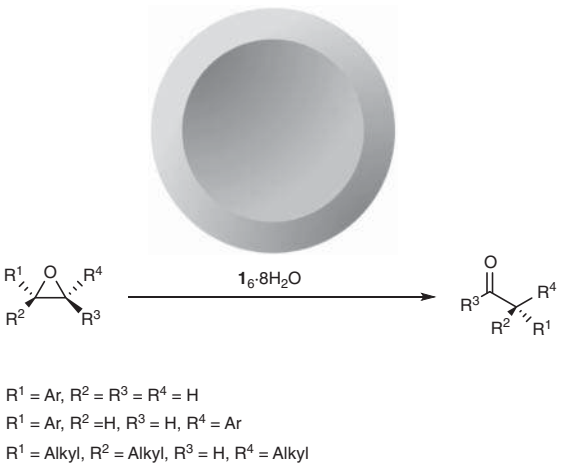

Figure 24.7 The hexameric capsule promotes the isomerization of epoxides to the corresponding carbonyl compounds.

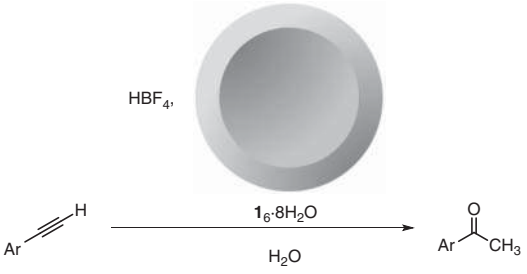

Figure 24.8 The capsule, in combination with HBF_4 as strong Brønsted acid, promotes the Markovnikov hydration of terminal aromatic alkynes to methyl aryl ketones.

HBF_4 (50 mol%) observing the formation of the corresponding methyl ketones in a few hours at 60 °C [10].

The scope of the reaction was limited to phenylacetylene derivatives bearing activating aliphatic or alkoxy substituents on the aromatic ring; larger substrates such as 9-ethynyl-phenanthrene and 1-ethynyl-4-phenoxybenzene showed much lower conversion into the corresponding methyl ketones. Since in this reaction, the protonation is likely to be the rate-determining step, the stabilizing nano-environment provided by the capsule for the protonated substrate efficiently favors the reaction.

The electronic properties of the capsule turned out to efficiently promote encapsulation of neutral compounds such as isonitrile derivatives characterized by a particular electronic configuration of the R-NC moiety, with a predominant carbenic behavior and electrophilic character of the C atom (Figure 24.9a). Several alkyl and aryl isonitrile derivatives were investigated showing in all cases spontaneous encapsulation within the cavity of the hexameric capsule, as observed by the appearance of new upfield shifted resonances on the ^1H NMR spectra in slow exchange with the external isonitrile. It was also observed that within a few hours at 60 °C, the isonitrile compounds could be transformed into the corresponding formylamide hydration product (Figure 24.9a) [11].

The general mechanism for the reaction involves protonation of the terminal carbenic C atom forming a cationic intermediate that is stabilized by the cavity

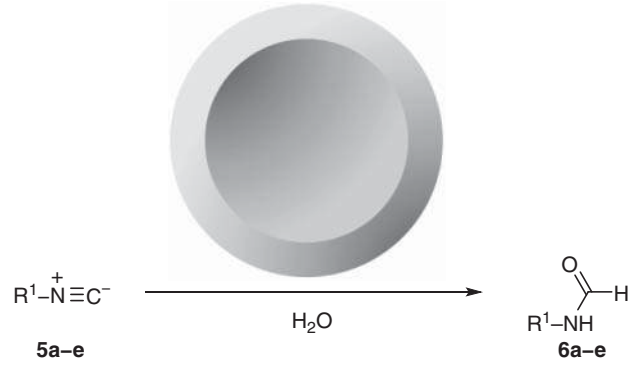

5a–e **6a–e**

a: R^1 = Cy; **b**: R^1 = *i*Pr; **c**: R^1 = *t*-Bu; **d**: R^1 = Bn; **e**: R^1 = 2,6-Me_2Ph

(a)

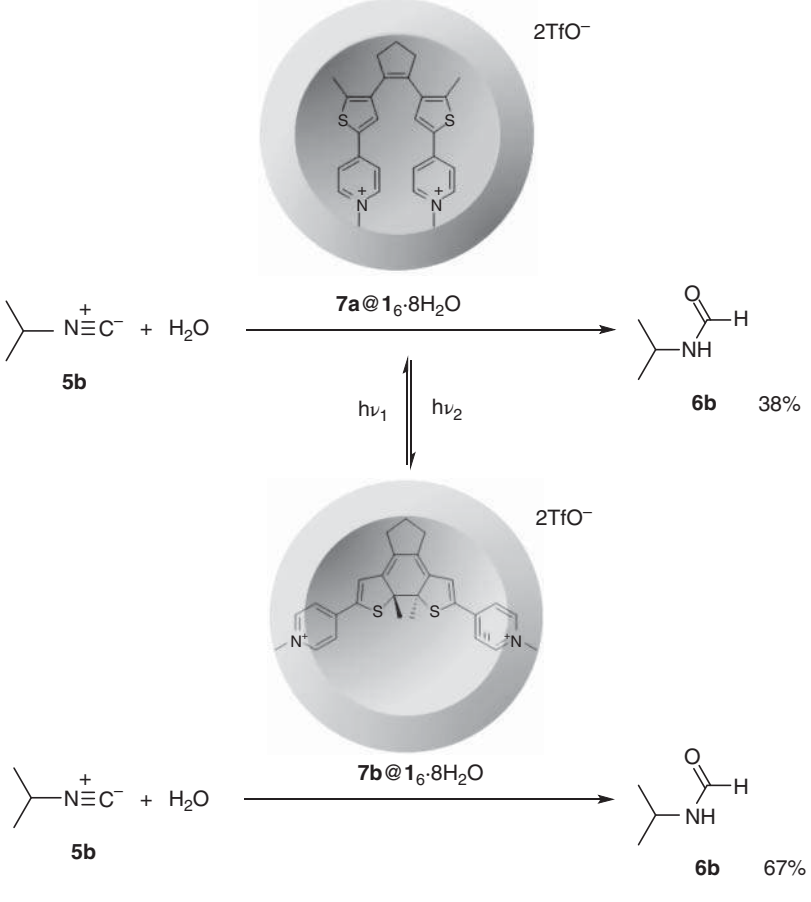

(b)

Figure 24.9 (a) Neutral isonitriles **5a–e** can be efficiently encapsulated within the hexameric capsule leading to the formation of the corresponding formyl amides **6a–e**. (b) The encapsulation of a photo-modulable cationic guest **7a** or **7b** provides different catalytic activity to the capsule.

of the capsule and that further reacts with water leading to the corresponding formylamides. The catalytic activity of the capsule was further modulated by the co-encapsulation of a photo-switchable bis-cationic diarylethene guest reported in Figure 24.9b whose geometry can be regulated by irradiation at a proper wavelength. In particular, both open **7a** and closed **7b** isomeric forms of the photo-switchable cationic guests demonstrated to be fully encapsulated with a stoichiometric amount of capsule. The inner volume of the cavity left accessible by the diarylethene guest showed to favor the co-encapsulation of the isonitrile and its hydration, even though with lower rate and conversion. In particular, it is worth to notice that the open isomer **7a** led to higher inhibition of the hydration reaction with respect to the closed isomer **7b**, probably because the latter, being more rigid, leaves more space for the isonitrile reagent. The different inhibition activity of the open and closed forms of the cationic guest was better observed running the two separate experiments at room temperature for seven days observing 38% with **7a** and 67% with **7b** for the corresponding *N*-isopropylformylamide, respectively.

Spurred by the unprecedented host properties of the resorcin[4]arene capsule for isonitriles as neutral guests, we investigated other reactions involving this class of reagents in combination with trimethylsilyl azide for the formation of the corresponding 1-substituted 1*H*-tetrazole cycloaddition products (Figure 24.10) [12].

In the absence of the capsule, the reaction was sluggish even at 60 °C for five hours, while with 10 mol% of the hexameric capsule, the reaction between cyclohexyl isonitrile and trimethylsilyl azide led quantitatively to the corresponding 1*H*-tetrazole, demonstrating the good catalytic effect of the capsule considering that this reaction is usually carried out under harsh conditions with strong acids and at high temperature. Control experiments allowed to rule out a simple Brønsted acid role of the capsule and further confirmed that encapsulation of the isonitrile was a key aspect of the activation observed, with almost no tetrazole products observed when the cavity was occupied by a competitive guest. Moreover, the capsule showed a certain degree of substrate selectivity between two competitive substrates preferring the aliphatic reagent cyclohexyl isonitrile with respect to benzyl isonitrile, forming the corresponding products in a 2.2 ratio, while the reaction catalyzed by a strong acid led to the two products in 0.4 ratio. This is a clear consequence of the preferential encapsulation dictated by the cavity of the capsule.

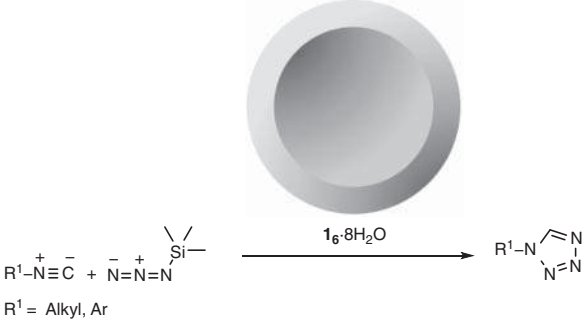

Figure 24.10 Isonitriles in the presence of trimethylsilyl azide are converted selectively into the corresponding tetrazoles by the activation provided by the hexameric capsule.

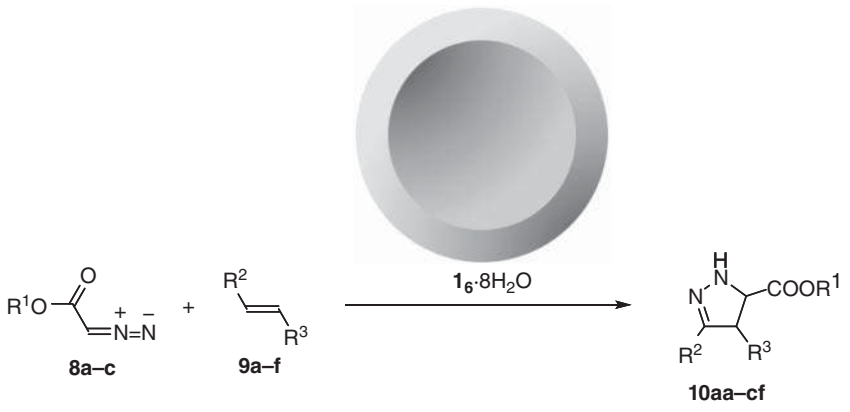

8a: R^1 = Et; **8b**: R^1 = *t*-Bu; **8c**: R^1 = Bn
9a: R^2 = CHO, R^3 = H; **9b**: R^2 = CN, R^3 = H; **9c**: R^2 = CHO, R^3 = Me;
9d: R^2 = CHO, R^3 = *n*–Pr; **9e**: R^2 = COOMe, R^3 = H; **9f**: R^2 = COO*n*-Bu, R^3 = H

Figure 24.11 Neutral diazoacetate esters **8a–c** show encapsulation within the hexameric capsule and together with electrophilic dipolarophiles **9a–f** lead to the corresponding 4,5-dihydro-1*H*-pyrazoles **10** promoted by the supramolecular capsule.

The investigation of possible alternative neutral compounds showing affinity for the cavity of the capsule led to the discovery that ethyl, *tert*-butyl, and benzyl diazoacetate esters **8a–c** are suitable guests thanks to their carbene-like properties and an electron-poor character. ^{1}H NMR confirmed the encapsulation of this class of compounds showing in all cases new upfield shifted resonances for the encapsulated diazoacetate esters. The capsule was exploited to promote the atom-efficient 1,3 dipolar cycloaddition reaction between diazoacetate esters **8** and dipolarophiles **9** such as acrolein, acrylonitrile, acrylate esters, and many others to form 4,5-dihydro-3*H*-pyrazoles as primary products that underwent further tautomerization to the corresponding more stable 4,5-dihydro-1*H*-pyrazoles **10** (Figure 24.11) [13].

Also in this case, substantial inhibition of the catalytic activity was observed by employing competitive guests such as tetraalkylammonium ions to fill the cavity of the capsule or using resorcinol as a mimic of the H-bonding properties of the capsules. The observation that encapsulation of the reagents was fundamental for the reaction was further evidenced by the preferential combination of acrylonitrile with respect to the longer *trans*-crotonaldehyde and *trans*-2-hexenal for the reaction with *tert*-butyl-diazoacetate **8b**.

24.4 Concluding Remarks

In recent years, the resorcin[4]arene hexameric capsule emerged as one of the most versatile self-assembled nano-aggregates that can be exploited either as a nanoreactor or as a nano-organocatalyst. Taking advantage of its electron-rich cavity, we

reported several applications of this capsule as a well-defined environment, roomy enough to host cationic substrates or metal catalysts. This led to several examples in which the limited space available can greatly affect the approach of the substrates changing their relative rate of reaction, or it can impart steric requirements leading to unexpected product distributions. These confinement effects are gaining momentum and will help to shed light on much more complicated systems such as the active site of enzymes. Moreover, we demonstrated that the hexameric capsule, with its particular electronic properties, can greatly accelerate a wide range of organic reactions characterized by the formation of cationic intermediates that inside the cavity experience marked stabilization. In combination with its weak intrinsic Brønsted acidity or aided by added protic acids, the capsule demonstrated to activate several reactions ranging from epoxide isomerization, isonitrile and alkyne hydration, diazoacetate cycloaddition reactions with unsaturated carbonyl compounds and tetrazole synthesis from isonitriles, as well as hydrogen peroxide activation toward sulfides leading to the corresponding sulfoxide products. More reactions driven by similar mechanistic profiles are likely to be disclosed, leading to better levels of selectivity and activity: these are intriguing challenges for future investigations. The full understanding of the potential of this host is far from being complete.

Acknowledgments

Financial support for this research from Università Ca' Foscari Venezia, Ministero Università e Ricerca and Fondazione CARIPARO SELECT project is gratefully acknowledged.

References

1 Grommet, A.B., Feller, M., and Klajn, R. (2020). Chemical reactivity under nanoconfinement. *Nat. Nanotechnol.* 15: 256–271.
2 Wang, K., Jordan, J.H., Hu, X.-Y., and Wang, L. (2020). Supramolecular strategies for controlling reactivity within confined nanospaces. *Angew. Chem. Int. Ed.* 59: 13712–13721.
3 Borsato, G. and Scarso, A. (2016). Catalysis within the self-assembled resorcin[4]arene hexamer. In: *Organic Nanoreactors* (ed. S. Sadjadi), 203–234. Elsevier.
4 Giust, S., La Sorella, G., Sperni, L. et al. (2015). Substrate selective amide coupling driven by encapsulation of a coupling agent within a self-assembled hexameric capsule. *Chem. Commun.* 51: 1658–1661.
5 Bianchini, G., Scarso, A., La Sorella, G., and Strukul, G. (2012). Switching the activity of a photoredox catalyst through reversible encapsulation and release. *Chem. Commun.* 48: 12082–12084.
6 Cavarzan, A., Scarso, A., Sgarbossa, P. et al. (2011). Supramolecular control on chemo- and regioselectivity via encapsulation of (NHC)-Au catalyst within a hexameric self-assembled host. *J. Am. Chem. Soc.* 133: 2848–2851.

7 Cavarzan, A., Reek, J.N.H., Trentin, F. et al. (2013). Substrate selectivity in the alkyne hydration mediated by NHC–Au(I) controlled by encapsulation of the catalyst within a hydrogen bonded hexameric host. *Catal. Sci. Technol.* 3: 2898–2901.

8 La Sorella, G., Sperni, L., Strukul, G., and Scarso, A. (2016). Supramolecular activation of hydrogen peroxide in the selective sulfoxidation of thioethers by a self-assembled hexameric capsule. *Adv. Synth. Catal.* 358: 3443–3449.

9 Caneva, T., Sperni, L., Strukul, G., and Scarso, A. (2016). Efficient epoxide isomerization within a self-assembled hexameric organic capsule. *RSC Adv.* 6: 83505–83509.

10 La Sorella, G., Sperni, L., Ballester, P. et al. (2016). Hydration of aromatic alkynes catalyzed by a self-assembled hexameric organic capsule. *Catal. Sci. Technol.* 6: 6031–6036.

11 Bianchini, G., La Sorella, G., Canever, N. et al. (2013). Efficient isonitrile hydration through encapsulation within a hexameric self-assembled capsule and selective inhibition by a photo-controllable competitive guest. *Chem. Commun.* 49: 5322–5324.

12 Giust, S., La Sorella, G., Sperni, L. et al. (2015). Supramolecular catalysis in the synthesis of substituted 1*H*-tetrazoles from isonitriles by a self-assembled hexameric capsule. *Asian J. Org. Chem.* 4: 217–220.

13 La Sorella, G., Sperni, L., Strukul, G., and Scarso, A. (2015). Supramolecular encapsulation of neutral diazoacetate esters and catalyzed 1,3-dipolar cycloaddition reaction by a self-assembled hexameric capsule. *ChemCatChem* 7: 291–296.

Part V

Supramolecular Organocatalysis and Non-classical Interactions

25

The Aryl-Pyrrolidine-*tert*-Leucine Motif as a New Privileged Chiral Scaffold: The Role of Noncovalent Stabilizing Interactions

Daniel A. Strassfeld and Eric N. Jacobsen

Harvard University, Department of Chemistry and Chemical Biology, 12 Oxford Street, Cambridge, MA, 02138, USA

25.1 Introduction

On the surface, the conditions for achieving high selectivity and broad generality in enantioselective catalysis may appear to be directly at odds: the former requires energetic differentiation between transition structures differing only in their spatial arrangement, whereas the latter requires accessible reaction rates despite major structural variations in the reacting partners. Indeed, limited generality is characteristic of many biocatalytic reactions, which often induce exquisite enantioselectivity but only rarely display promiscuity in substrate scope [1]. However, one of the crucially important features of asymmetric catalysis that emerged from pioneering studies is that small-molecule chiral catalysts can in fact promote highly enantioselective reactions across significant variations to substrate structure [2]. In certain cases, such generality has enabled access to entire classes of chiral synthetic building blocks and has proven enormously enabling in stereoselective synthesis [3].

A different and even more unanticipated type of generality in small-molecule asymmetric catalysis has been identified wherein given chiral catalyst frameworks can be applied with high enantioselectivity across an assortment of mechanistically distinct reactions [4]. Such so-called "privileged" catalyst scaffolds have become invaluable tools in the discovery of new reactions. The factors that make possible the attainment of high enantioselectivity across unrelated reactions are intriguing and not fully understood. Some of the privileged chiral systems identified to date are rigid, multidentate C_2-symmetric chiral ligands that create well-defined, sterically differentiated reactive sites at metal centers. However, these features are neither sufficient, nor necessary, to render a particular chiral scaffold privileged. For example, cinchona alkaloid derivatives lack any of those characteristics, and it is evident that these scaffolds induce stereocontrol by a wide variety of mechanisms. Indeed, entirely new applications of these templates in asymmetric catalysis continue to be discovered [5]. The identification of new privileged chiral scaffolds and the elucidation of the factors responsible for their generality present enormous

Supramolecular Catalysis: New Directions and Developments, First Edition.
Edited by Piet W.N.M. van Leeuwen and Matthieu Raynal.

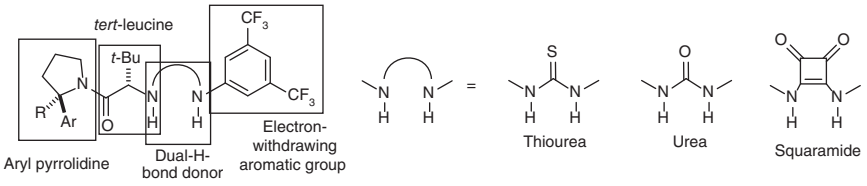

Figure 25.1 The aryl-pyrrolidino-*tert*-leucine HBD-catalyst framework, with its essential components highlighted.

challenges and would certainly advance the field of enantioselective catalysis in both practical and fundamental ways.

Over the past two decades, our group has sought to discover and develop new classes of organocatalysts based on dual H-bond donors (HBDs) such as ureas, thioureas, guanidinium ions, and squaramides [6]. Over the course of these studies, we identified the scaffold depicted in Figure 25.1 as a remarkably general, broadly applicable chiral catalyst framework. This chapter provides an overview of the discoveries that led to the identification of the critical components of this new family of privileged catalysts, the broad range of transformations it enables, and our emerging understanding of how the aryl-pyrrolidine-*tert*-leucine motif is able to induce high levels of enantioselectivity across diverse reaction mechanisms.

25.2 Foundational Studies

Our group's efforts in enantioselective HBD catalysis sprung from an unexpected discovery made during efforts to apply combinatorial strategies to the discovery of catalytically active chiral ligand–metal complexes [7] (Figure 25.2). One of the libraries we investigated proved to be both active and enantioselective in a model imine hydrocyanation (Strecker) reaction, even in the absence of added metal ions. Optimization of the metal-free systems led to the identification of **1b** as an enantioselective catalyst for Strecker reactions of both aromatic and aliphatic aldimines. The

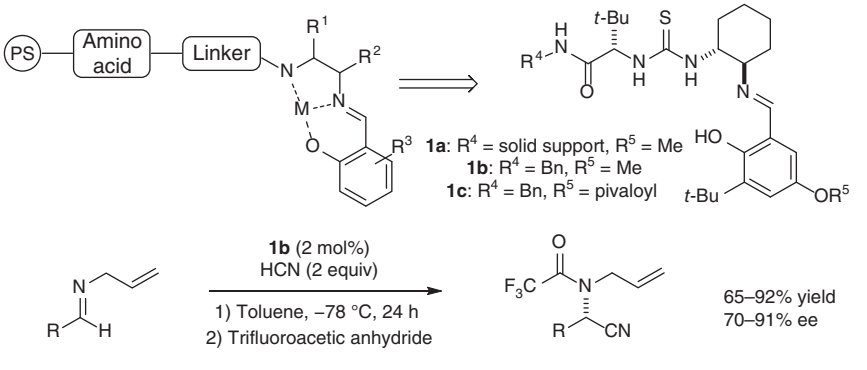

Figure 25.2 Initial discovery that amino-acid-derived thioureas catalyze enantioselective Strecker reactions.

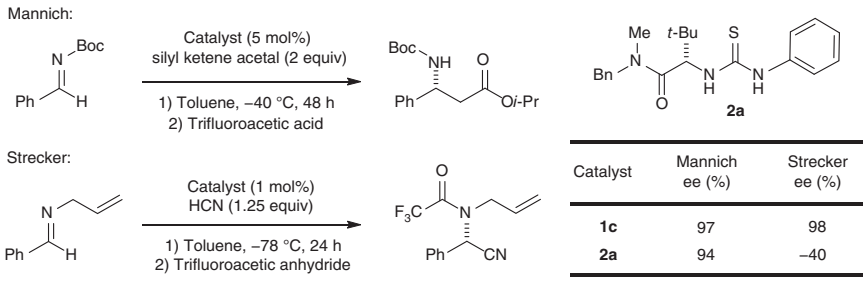

Catalyst	Mannich ee (%)	Strecker ee (%)
1c	97	98
2a	94	–40

Figure 25.3 Identification of a simplified catalyst for the enantioselective Strecker and Mannich reactions.

amino acid component of the catalyst was shown to have a pronounced effect on the enantioselectivity, with the highest levels achieved with the sterically demanding, nonnatural amino acid *tert*-leucine. This chiral building block would prove to be a key component of the privileged catalyst scaffold.

Subsequent studies of Strecker [8] and Mannich [9] reactions catalyzed by **1b** and closely related derivatives revealed that the thiourea (or urea) component was the sole catalytic engine of these compounds. Thus, the Schiff base motif of **1** could be excised completely, as in **2a**, with little detrimental effect on enantioselectivity in the Mannich reaction (Figure 25.3) [10].

While catalyst **2a** was effective in the model Mannich reaction, it was poorly enantioselective in the Strecker reaction of benzaldehyde *N*-allyl imine (Figure 25.3) [10]. It was also intriguing that the opposite absolute configuration of product was obtained to that formed with catalyst **1c**, suggesting that the catalysts possessing or lacking the Schiff base rely on fundamentally different mechanisms of enantioinduction in the Strecker reaction. Fortunately, efforts to reoptimize the Strecker reaction with catalysts possessing the simplified structure of **2** proved relatively straightforward. The introduction of the 3,5-bis(trifluoromethyl)aryl substituent on the HBD, as in **2b**–**2f** (Figure 25.4a), was found to enhance the reactivity of the catalysts substantially [11]. This motif, which was originally applied by Schreiner in the context of achiral HBD catalysis [12] and subsequently extended to enantioselective reactions by Takemoto [13], increases the acidity of the HBD by 2–3 pK_a units relative to the phenyl analogue [14], thereby increasing the strength of the HBD [15]. The "half-Schreiner" catalyst motif has subsequently been applied successfully in the majority of reactions catalyzed by this class of simplified catalysts.

With *N*-benzhydryl aldimines as substrates, it was found that introduction of aryl substituent(s) on the *tert*-leucine amide had a pronounced positive impact on the enantioselectivity of the reaction (Figure 25.4a) [11]. Both the presence and configuration of the arene(s) were impactful, with the benzhydryl amide **2f** providing the highest levels of enantioselectivity. Catalyst **2f** proved highly effective and broadly applicable in the Strecker reaction across a wide variety of aryl and aliphatic aldimine substrates. Detailed experimental and computational studies pointed to a mechanism involving enantiodetermining catalyst-promoted proton transfer to generate diastereomeric iminium/cyanide ion pairs that are bound to

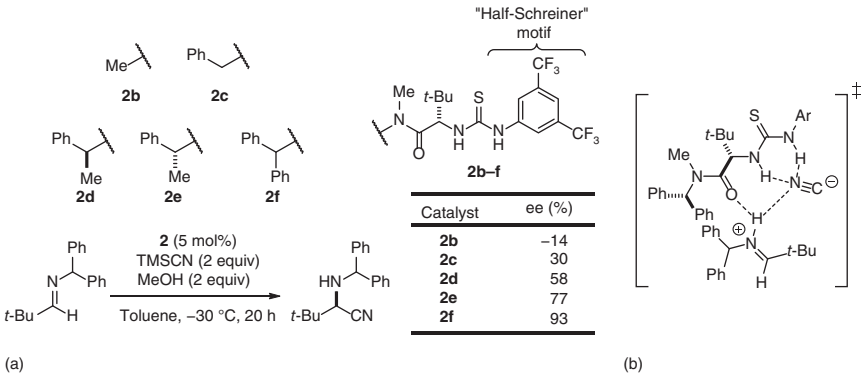

Figure 25.4 (a) The "half-Schreiner" motif, and impact of the aryl substituent on the *tert*-leucine amide on enantioselectivity in the Strecker reaction of *N*-benzhydryl pivalaldimine. (b) Proposed attractive NCIs in the enantiodetermining transition state.

the catalyst through multiple noncovalent interactions (NCIs) (Figure 25.4b) [16]. Enantioselectivity was proposed to result from greater stabilization of one diastereomeric transition state due to differential H-bonding between the *tert*-leucine amide and the incipient iminium ion, with the hindered amide playing a steric role in destabilizing transition states leading to the minor enantiomeric product.

Several crucial insights were attained in the development of the HBD-catalyzed Strecker reaction and other imine addition reactions [17] that proved foundational in our subsequent efforts. Simple and modular 4-component structures such as **2** were proven capable of inducing high enantioselectivity in synthetically valuable reactions. The discovery that such weakly acidic dual-HBDs could promote reactions via anion-binding pathways held great implications for the engagement of cationic electrophilic intermediates in enantioselective processes. Finally, the observed interplay between aryl substituents and the *tert*-leucine amide in dictating reaction enantioselectivity suggested that interesting and completely unexplored modes of enantioinduction in small-molecule catalysis may be accessible.

25.3 Development of the Aryl-Pyrrolidino-*tert*-Leucine Catalyst Motif

In efforts to extend the anion-binding catalysis principle beyond iminium ion chemistry, our group was especially interested in the possibility of achieving enantioselective nucleophilic additions to oxocarbenium ions [18]. Catalysts such as **2b**–**2f** were indeed found to promote the model alkylation reaction in Figure 25.5, albeit with only moderate enantioselectivity. A discernable role for the presence and configuration of aryl substituents on the amide component was again noted (e.g. **2d** vs. **2e**), giving rise to the hypothesis that conformationally constrained aryl-substituted amides derived from cyclic amines might allow for improved enantiocontrol. Indeed, aryl-pyrrolidino-*tert*-leucine thioureas **3b** and **epi-3b**

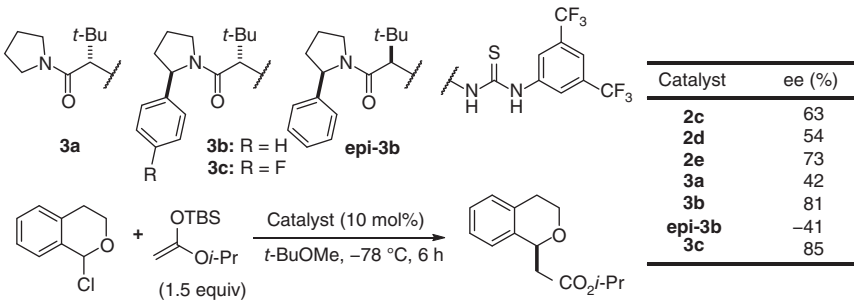

Catalyst	ee (%)
2c	63
2d	54
2e	73
3a	42
3b	81
epi-3b	–41
3c	85

Figure 25.5 Identification of aryl-pyrrolidine-*tert*-leucine HBDs as particularly effective chiral catalysts.

produced a magnification of the stereochemical matching and mismatching effects observed with **2d** and **2e**. Ultimately, the fluoro-substituted **3c** was identified as the optimal catalyst.

Extensive mechanistic studies were performed on the oxocarbenium alkylation reaction, revealing that the aryl-pyrrolidino thiourea catalyst **3c** is engaged in a complex set of on- and off-cycle aggregation phenomena and exists as a roughly 1 : 1 mixture of slowly interconverting E- and Z-amide rotamers (Figure 25.6) [19]. While the Z-amide positions the aryl substituent in close proximity to the HBD binding pocket of the catalyst, the E-rotamer locates the arene away from the active site, limiting its ability to contribute to enantioinduction. Thus, to the extent that the catalyst in the E-amide rotamer may be catalytically active, it was expected to promote product formation with different – and presumably lower – enantioselectivity than the Z-conformer. Accordingly, we sought to modify the catalyst in order to disfavor population of the E-rotamer [20]. Computational modeling predicted that the introduction of a methyl group at the 2-position of the 2-aryl-pyrrolidine would lead to a severe steric repulsive interaction with the *tert*-leucine in the E-amide rotamer, and thus, strongly favor the desired Z-rotamer. This hypothesis was confirmed through NMR analysis of catalysts containing the appropriate methylated aryl-pyrrolidino-*tert*-leucine fragments (**Me-3**). Gratifyingly, this modification also led to measurable increases in reactivity and enantioselectivity relative to the nonmethylated analogue in the oxocarbenium ion alkylation reaction. These same trends have been observed in multiple other systems, with the methylated aryl pyrrolidines frequently outperforming their nonmethylated analogues (for examples, see [21–24]).

In the studies of oxocarbenium alkylation reactions, modification of the aryl substituent had measurable effects on enantioselectivity, with 4-fluorophenyl pyrrolidine **3c** outperforming phenyl pyrrolidine **3b**, albeit only slightly (Figure 25.5). However, this effect of aryl-pyrrolidine modification paled in comparison to that observed during the course of catalyst optimization in the thiourea-catalyzed cation-olefin polycyclization reaction depicted in Figure 25.7 [25]. The phenyl-pyrrolidine derivative **3b** promoted the reaction in low yields and with low enantioselectivity. While introduction of simple substituents on the

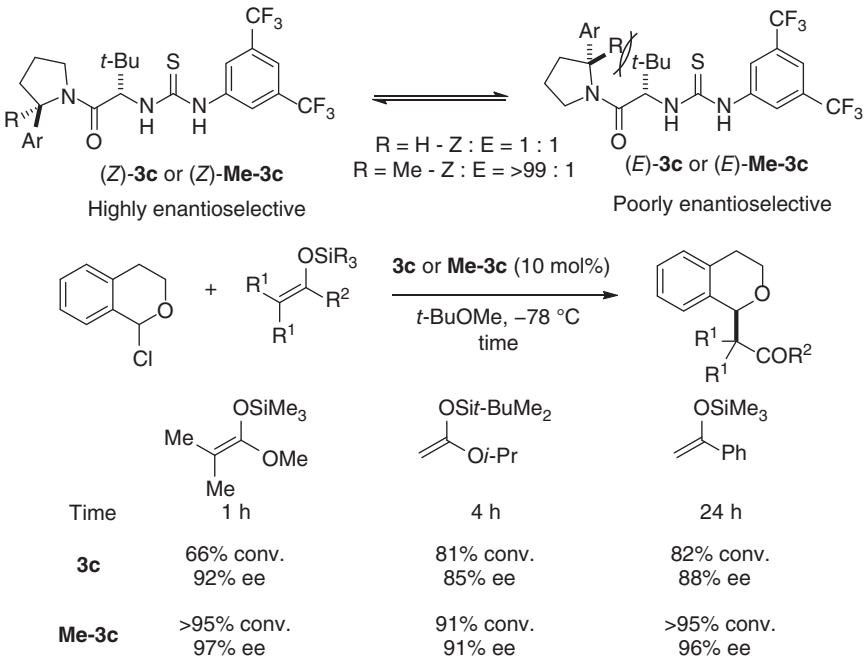

Figure 25.6 Conformational control of the aryl-pyrrolidino-*tert*-leucine amide improves enantioselectivity and yield in the oxocarbenium alkylation reaction.

phenyl group had little effect (data not shown), the incorporation of incrementally more expansive aromatic substituents had a remarkably favorable impact on both reactivity and enantioselectivity. Mechanistic studies revealed that enantioselectivity (expressed as $\Delta\Delta G^{\ddagger} = -\mathrm{RTln(er)}$) was enthalpically controlled and correlated linearly with the polarizability of the arene substituent. These observations provided strong evidence that differential, stabilizing cation–π interactions [26] play a direct role in enantioinduction. On a broader level, this study provided definitive proof that modification of the aryl substituent on the pyrrolidine component of this class of HBDs could serve as a powerful tool for catalyst design and optimization.

25.4 Scope of Enantioselective Reactions and Mechanisms Promoted Effectively by Aryl-Pyrrolidine-*tert*-Leucine HBD Catalysts

In the years since the discovery of the utility of HBD catalysts bearing the aryl-pyrrolidino-*tert*-leucine motif, we and others have demonstrated their applicability in a wide variety of enantioselective reactions. Although these transformations all involve HBD catalysis, they have been revealed to proceed through several fundamentally different mechanisms (e.g. ion-pairing vs. direct substrate activation and one vs. two catalyst units in the enantiodetermining transition state [19]). However,

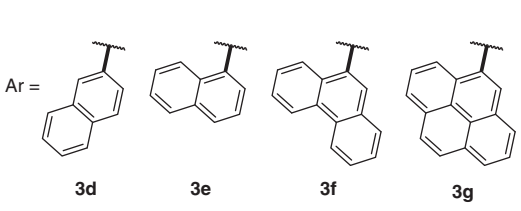

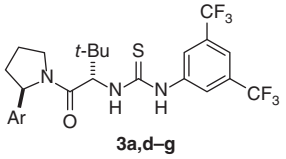

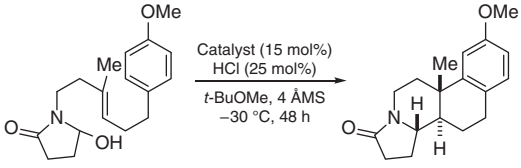

Catalyst	Yield (%)	ee (%)
3a	12	25
3d	33	61
3e	46	60
3f	52	87
3g	78	95

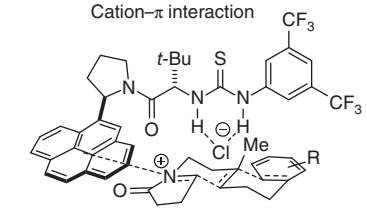

Eyring analysis of enantioselectivity

Catalyst	$\Delta\Delta H^{\ddagger}$ (kcal/mol)	$\Delta\Delta S^{\ddagger}$ (cal/mol • K)
3e	–1.12 ± 0.07	–2.0 ± 0.3
3f	–1.87 ± 0.08	–2.8 ± 0.3
3g	–3.95 ± 0.17	–8.9 ± 0.7

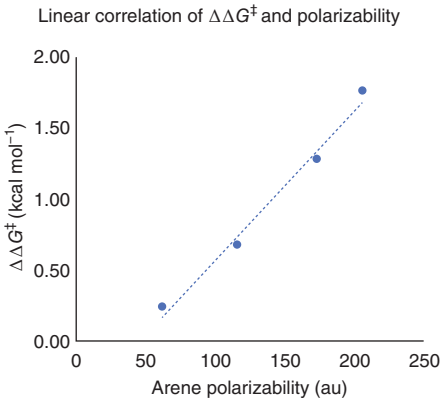

Figure 25.7 The dramatic effect of extended aromatic groups on enantioselectivity and yield in a cation-olefin polycyclization reaction catalyzed by **3**.

a consistent theme that has emerged is that the identity of the aryl pyrrolidine component can be a – if not *the* – critical factor in optimizing and controlling enantioselectivity.

The broadest application of the aryl-pyrrolidino-*tert*-leucine motif in HBD catalysis so far has been in the context of enantioselective additions to iminium ions. In these reactions, the catalyst is proposed to promote generation of a reactive chiral ion pair by associating to the counterion of the iminium ion (typically generated *in situ*) [17]. In this manner, aryl-pyrrolidino-HBD catalysts have proven effective at promoting highly enantioselective inter- and intramolecular additions of allyl silanes and silyl ketene acetals to *N*-aryl [27], *N*-acyl [28], and *N*-carbamoyl [29, 30] iminium ions (Figure 25.8). An aryl-pyrrolidino-squaramide-catalyzed Pictet–Spengler reaction was also featured as the key step in an asymmetric total synthesis of (−)-arborisidine and 19-*epi*-(−)-arborisidine [31].

Aryl-pyrrolidino-HBDs have also proven effective in activation of other classes of electrophiles via anion-binding catalysis (Figure 25.9). In addition to the asymmetric alkylations of oxocarbenium ions discussed above [18], this family of catalysts

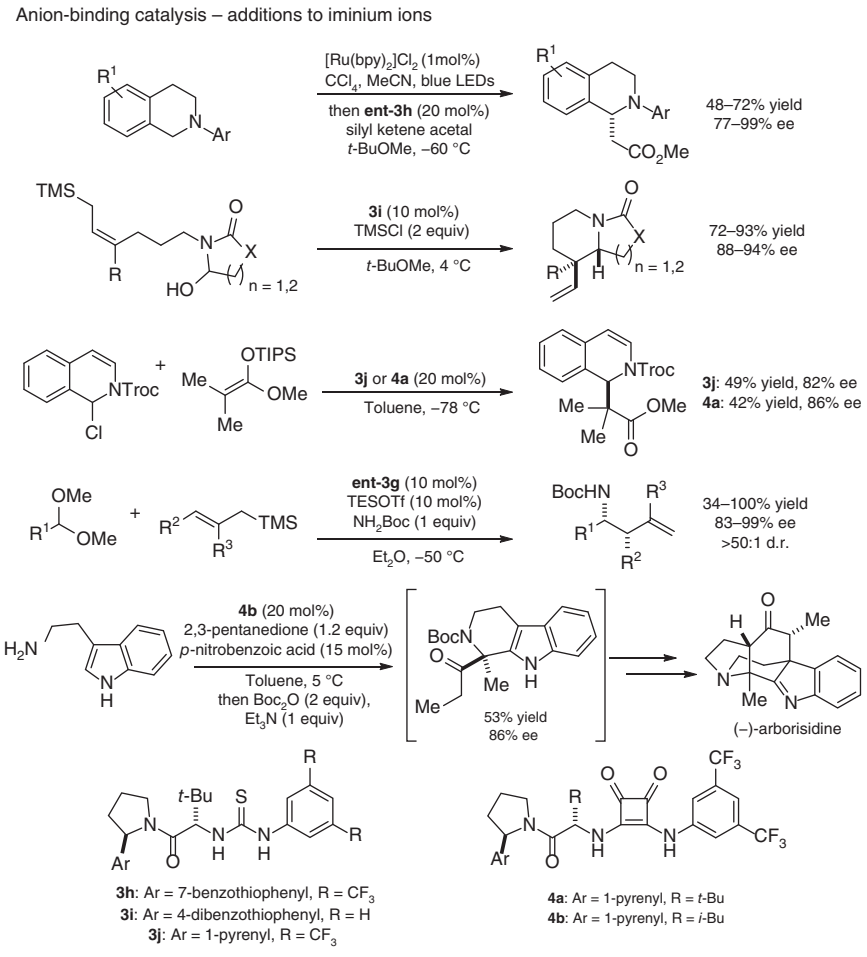

Figure 25.8 Examples of highly enantioselective additions to iminium ions promoted by aryl-pyrrolidino HBD catalysts.

has been shown to promote enantioselective Friedel–Crafts alkylations of indoles with pyrone-derived vinylogous oxocarbenium ions [32] and to activate silyl Lewis acids to enable asymmetric Mukaiyama aldol reactions of aryl acetals and [4+3] cycloadditions to oxyallyl cations [33]. Moreover, this strategy is not limited to additions to polar π-systems, as aryl pyrrolidino HBDs have proven capable of controlling enantioselective additions of indoles to *meso*-episulfonium ions [34] and promoting asymmetric selenocyclizations via dynamic kinetic resolutions of seleniranium ions [35].

In the reactions outlined in Figures 25.8 and 25.9, the catalyst-bound anion in the key ion-pair intermediate is often the leaving group in the original substrate and always a spectator in the enantioselective addition. Enantioselective anion delivery is an alternative mode of anion-binding catalysis wherein the catalyst-bound anion in the ion-pair intermediate is the reactive nucleophilic partner in the addition to the

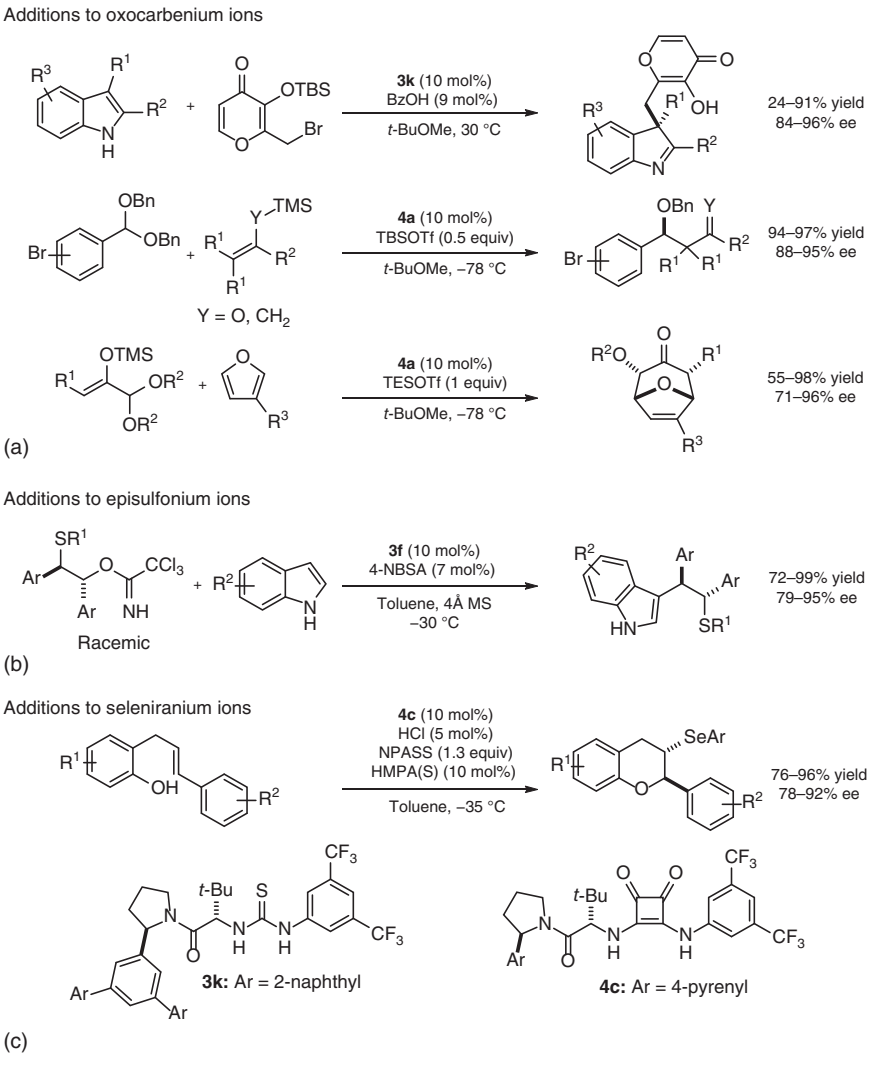

Figure 25.9 Anion-binding catalysis with aryl-pyrrolidino HBDs in reactions of (a) oxocarbenium ions, (b) episulfonium ions, and (c) seleniranium ions.

cationic electrophile (see [23] and references therein). These pathways thus differ fundamentally in the role of the catalyst in the enantiodetermining step relative to conventional ion-pairing catalysis. Nonetheless, aryl-pyrrolidino-*tert*-leucine-HBDs have been shown to be highly effective at controlling enantioselective delivery of anionic nucleophiles to cationic electrophiles in the context of both enolate additions to *N*-acyl pyridinium intermediates [36] and in ring openings of activated oxetane intermediates with halides (Figure 25.10a) [23]. The same family of catalysts has also been shown to induce high enantioselectivity in another mechanistically distinct class of reactions wherein proton transfer has been established as the stereodetermining event (Figure 25.10b). In particular, aryl-pyrrolidine

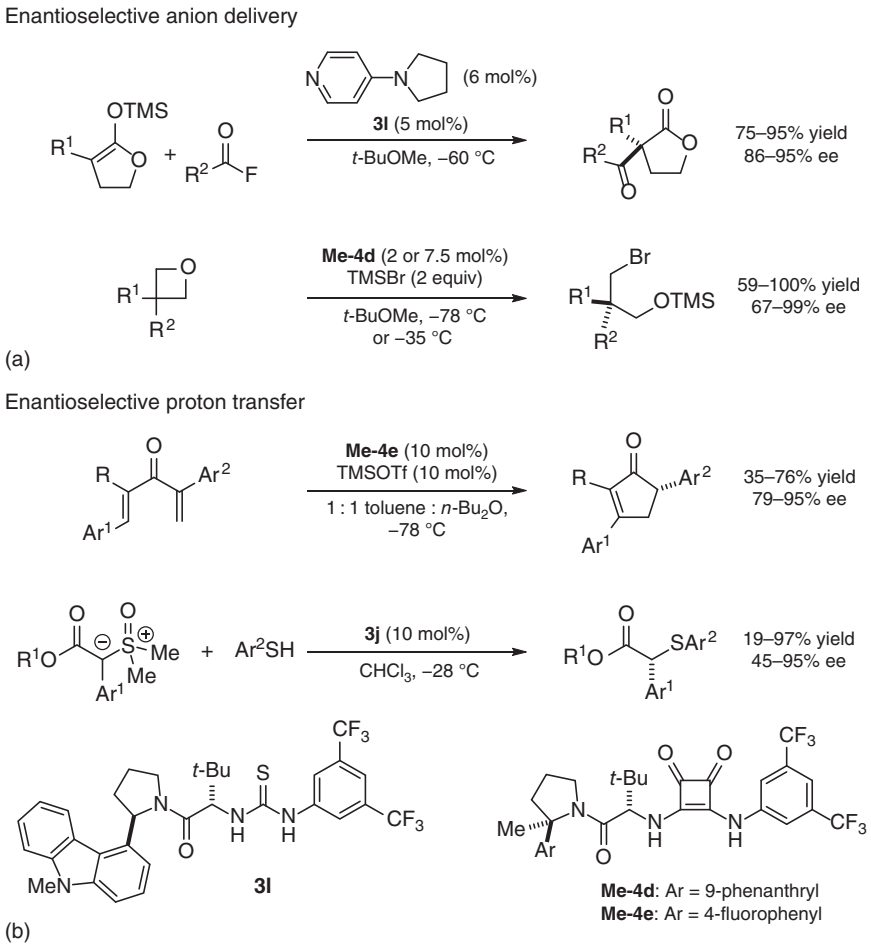

Figure 25.10 Other reaction mechanisms promoted by aryl-pyrrolidino HBD catalysts: (a) enantioselective anion delivery and (b) enantioselective proton transfer.

squaramides have been shown to promote enantioselective Nazarov cyclizations via an enantiodetermining formal [1, 4] proton shift [24] and enantioselective S–H insertions into sulfoxonium ylides [37].

In addition to ion-pairing catalysis via anion binding, HBD catalysts can promote reactions through LUMO lowering by direct association to Lewis-basic functionality on the electrophile [12, 38]. The aryl-pyrrolidine-*tert*-leucine motif has proven highly effective in reactions proceeding through these manifolds as well (Figure 25.11a), allowing for the development of enantioselective nitro-Mannich reactions [39] and 1,3-dipolar cycloadditions of hydrazones to nitro-olefins [40]. In the former reaction, the authors propose that H-bond donation from the catalyst acidifies the nitroalkane, catalyzing nitronate formation. In the 1,3-dipolar cycloadditions, it is proposed that H-bonding to the nitro-olefin activates it toward nucleophilic attack by the hydrazone. Similarly, this family of catalysts has been

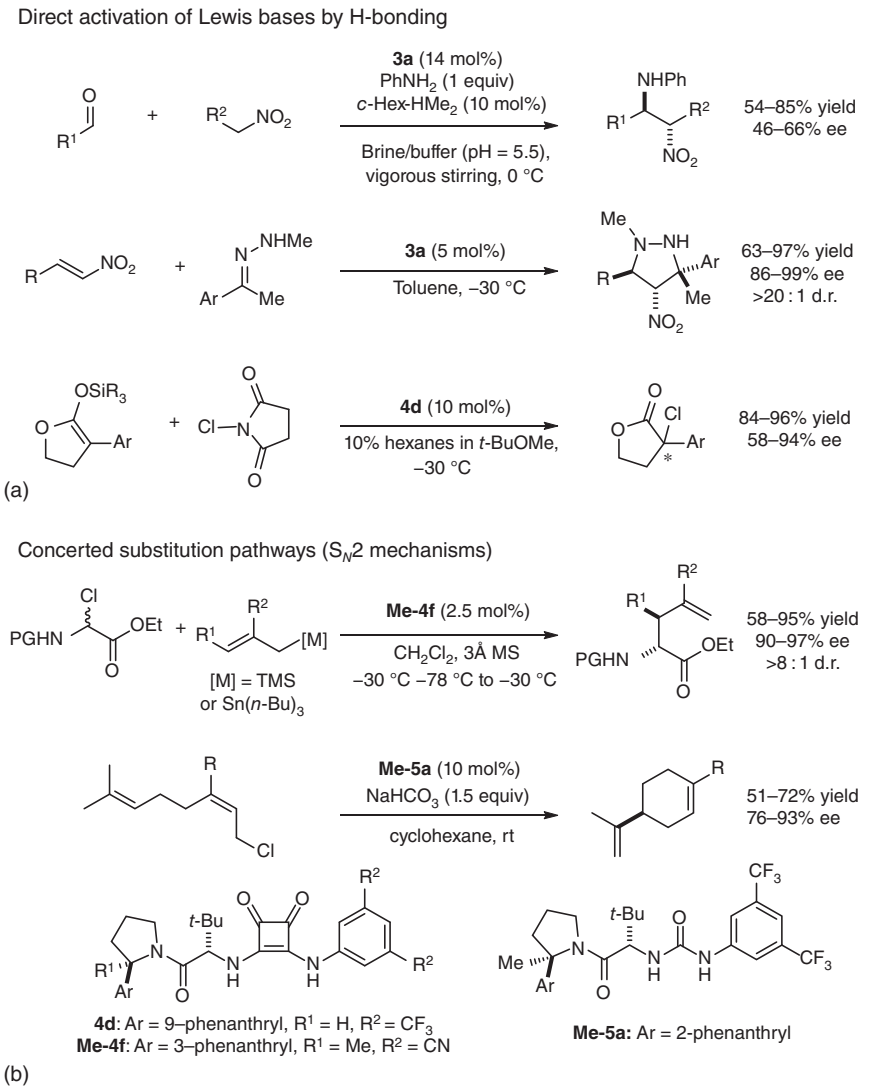

Figure 25.11 Yet other reaction mechanisms promoted with high enantioselectivity by aryl-pyrrolidino HBD catalysts. (a) Direct electrophile activation. (b) Concerted substitution pathways.

shown to activate *N*-chlorosuccinimide as a chloronium transfer reagent for the enantioselective chlorination of silyl enol ethers via proposed H-bond association to the succinimide carbonyl [41]. In addition to the direct activation of π-bonds, aryl-pyrrolidine HBDs have been demonstrated to catalyze enantioselective S_N2 substitutions via chloride-abstraction catalysis in the asymmetric alkylation of α-chloro glycinates [21] and in enantioselective tail-to-head carbocyclizations [22] (Figure 25.11b).

25.5 Mechanisms of Enantioinduction by Aryl-Pyrrolidine-*tert*-Leucino-H-Bond-Donor Catalysts: Case Studies

The successful application of aryl-pyrrolidino-*tert*-leucine-derived HBDs in highly enantioselective reactions that occur through a wide variety of distinct mechanisms clearly establishes this class of compounds as a privileged chiral catalyst scaffold. However, these catalysts are structurally quite different from other privileged frameworks identified previously [4] and operate exclusively through relatively weak NCIs that have shallow dependencies on geometry and distance [42]. As such, elucidation of the basis for stereoinduction with these catalysts may prove highly enabling for the design of new small-molecule noncovalent catalysts. Our understanding of how this family of catalysts induces high levels of enantioselectivity across a broad range of reactions and mechanisms is emerging gradually. Case studies on the mechanisms of enantioinduction for three reactions – the enantioselective addition of indoles to episulfonium ions [34], asymmetric oxetane openings with TMSBr [23, 43], and multicomponent aza-Sakurai allylations of acetals [30] – offer important insights.

An analysis of the mechanism of enantioinduction in thiourea-catalyzed additions of indoles to *meso*-episulfonium ions (Figure 25.9b) provided crucial insight into the role of differential cation–π interactions induced by the aryl-pyrrolidino-*tert*-leucine motif in HBD catalysts such as **3** [34]. As was the case in the thiourea-catalyzed cation-olefin polycyclization reaction (Figure 25.7), a strong correlation was observed in this reaction between enantioselectivity and the expanse of the aromatic group, and the source of this effect was probed experimentally. Rate studies with different aryl-pyrrolidino-*tert*-leucine-derived thioureas revealed that the most enantioselective catalysts were also the most reactive, consistent with enantioselectivity being the result of selective stabilization of the major transition state rather than destabilization of the minor pathway (Figure 25.12a). Binding studies with a substrate analog provided evidence for a catalyst-ion-pair complex that localized the episulfonium ion under one face of the phenanthryl group as a result of a stabilizing cation–π interaction.

Examination of the scope of the episulfonium opening reaction provided additional insight into the mechanism of enantioinduction [34]. While the use of indole as the nucleophile afforded product in 93% ee in the model reaction, *N*-methyl indole formed nearly racemic product, suggesting that the ability of the nucleophile to serve as a HBD might be critical for obtaining high levels of enantioselectivity. The enantioselectivity of the reaction did not correlate with indole pK_a, suggesting that any H-bonding interaction with the nucleophile is comparable in the major and minor transition states, but a correlation was observed between the pK_a of the N—H bond and the rate acceleration induced by the catalyst (Figure 25.12b). On the basis of these data, as well as reduced reactivity observed with the thioamide analogue of **3a** relative to the oxo-amide, it was proposed that the indole undergoes general-base activation by the *tert*-leucine amide during the indole addition step. In addition to providing rate acceleration, nucleophile activation provides an additional anchoring

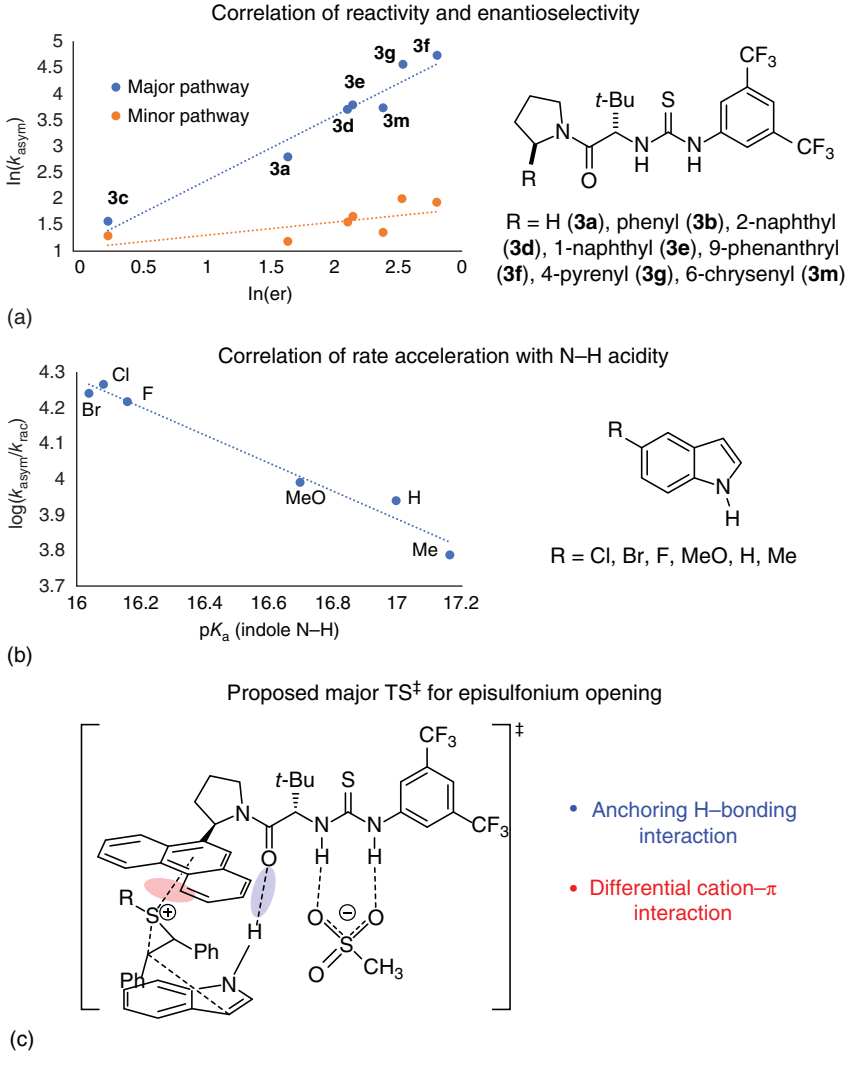

Figure 25.12 Mechanistic studies of the enantioselective opening of episulfonium ions with indoles. (a) Correlation of rate vs. enantioselectivity with different pyrrolidino-*tert*-leucine-derived catalysts. (b) Correlation of rate with the pK_a of the indole reacting partner. (c) Qualitative transition-state model, depicting the key cation–π interaction responsible for enantioinduction.

interaction that is critical to rigidifying the catalyst-transition state complex and enabling enantiodiscrimination by the catalyst through differential stabilization of the episulfonium by the aforementioned cation–π interaction (Figure 25.12c).

The second case study to be discussed here concerns enantioselective ring-opening additions to oxetanes with TMSBr catalyzed by squaramide HBDs (Figure 25.10a) [23]. Detailed study of this system proved highly illuminating with respect to the factors that may underlie the broad applicability of

aryl-pyrrolidino-*tert*-leucine-derived catalysts in transformations occurring via different reaction mechanisms [43].

Ironically, problems with reaction reproducibility provided the first clues into the almost uncanny generality of catalyst **Me-4d**. The reaction of 3-phenyloxetane with TMSBr was found to proceed with reproducibly high enantioselectivity but highly variable rates, particularly when carried out at different scales. Furthermore, other catalysts in the same class (**Me-4**) that afforded suboptimal enantioselectivities were shown to promote the ring opening with highly irreproducible ee's [23]. These observations suggested that product formation may arise from multiple mechanisms. A careful mechanistic analysis revealed that the catalysts promote oxetane opening through both TMSBr and HBr activation pathways, the latter reagent being generated in catalytic quantities by adventitious water present in varying concentrations depending on external conditions and reaction scale [43]. The bromohydrin product generated by HBr addition undergoes silylation under the catalytic conditions, such that both pathways result in the formation of same silylated product (Figure 25.13). Under small-scale laboratory conditions, both mechanisms contribute significantly, but variably, to product formation. In order to evaluate the impact of each pathway on the overall reaction enantioselectivity, acid-only and acid-free reaction conditions were developed that restricted the transformation to either one of the two mechanisms. Only the optimal squaramide **Me-4d** proved capable of catalyzing both pathways with high enantioselectivity, affording 94% ee in the model reaction of 3-phenyloxetane via the Lewis-acid pathway and 97% ee through the Brønsted-acid mechanism. All other chiral squaramide catalysts examined promote the two pathways with very different levels of enantioselectivity, with some catalysts even favoring opposite enantiomers of product for oxetane openings with HBr and TMSBr (Figure 25.14). Thus, catalyst **Me-4d** displayed a remarkable feature critical to its identification as the optimal catalyst: the ability to induce high enantioselectivity across two very different mechanisms that happen to form the same product. Given

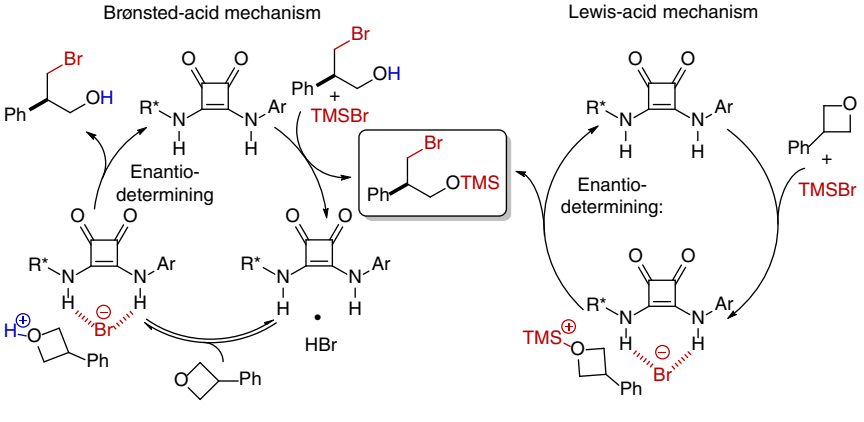

Figure 25.13 Competing, Brønsted- and Lewis-acid mechanisms in squaramide-catalyzed oxetane openings. Both pathways are operative and are induced with high enantioselectivity by catalyst **Me-4d**.

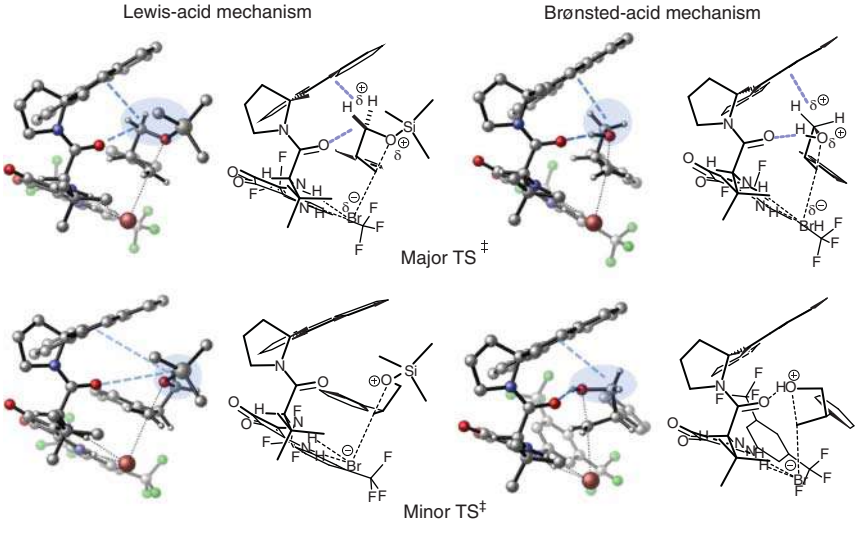

Arene structure-enantioselectivity relationship

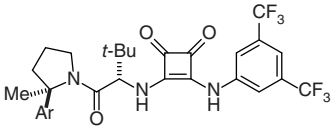

Arene	ee (%) - Lewis acid	ee (%) - Brønsted acid
9-phenanthryl (**Me-4d**)	94	97
1-naphthyl (**Me-4g**)	66	96
2-naphthyl (**Me-4h**)	74	91
phenyl (**Me-4i**)	48	92
4-fluorophenyl (**Me-4e**)	2	72
3,5-difluorophenyl (**Me-4j**)	0	54
3,4,5-trifluorophenyl (**Me-4k**)	–42	18

Catalyst electrostatic potential

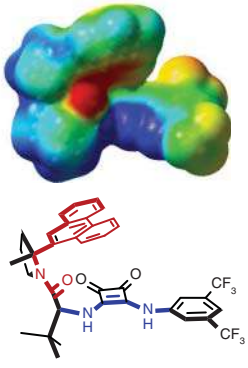

Figure 25.14 Computed transition states and supporting data for the squaramide-catalyzed enantioselective oxetane opening reaction. The region in the transition state bearing significant partial positive charge is highlighted in blue and the proposed stabilizing interactions are depicted with blue dotted lines.

that generality across mechanisms is at the heart of what makes chiral frameworks "privileged," we anticipated that an in-depth analysis of the enantioselective oxetane opening reaction with **Me-4d** might offer a unique opportunity to shed light on factors that make such generality possible.

Kinetic isotope effect studies established bromide delivery as the enantiodetermining step for both the Lewis- and Brønsted-acid mechanisms [23, 43]. The geometries of the relevant transition states were derived using density functional theory (Figure 25.14) [43]. The silylated and protonated oxetane intermediates possess dramatically different steric properties, yet the computational models share notable features. In particular, the lowest energy transition states leading to the major enantiomer of product for both mechanisms orient the incipient α-silyloxy

or α-hydroxy methylene group under the phenanthrene in position for stabilizing C–H–π interactions. In contrast, in the lowest energy transition states leading to the disfavored enantiomer of product, that methylene is oriented away from the phenanthrene. There is significant positive charge buildup on that methylene during the ring-opening event, so the models suggest that differential transition state stabilization through cation–π interactions with that group play a key role in enantioinduction. This hypothesis was supported experimentally by results obtained with (poly)fluorophenyl pyrrolidines **Me-4e**, **Me-4j**, and **Me-4k**, which revealed that diminution of the ability of the arene to engage in cation–π interactions through fluorination [26, 44] led to pronounced decreases in enantioselectivity for both mechanisms.

The computational models also point to stabilizing NCIs involving the *tert*-leucine amide in both the Lewis- and Brønsted-acid-promoted pathways, although the nature of the interactions with the amide differs between the two reaction mechanisms [43]. The transition state models for the Lewis-acid mechanism implicate the amide in a stabilizing charge–dipole interaction with the silylated oxonium and the α-oxymethylene. This interaction is computed to stabilize the major transition state preferentially, although the effect on enantioselectivity is clearly secondary to the cation–π interaction as evidenced by the effects of the aryl substituent shown in Figure 25.14. For the Brønsted-acid mechanism, the computational model reveals an explicit H-bond interaction between the *tert*-leucine amide and the protonated oxetane. The H-bond would be expected to be stronger and more directional than the charge–dipole interaction in the Lewis acid mechanism, allowing it to play a more significant role in enantioinduction. Indeed, higher enantioselectivities are observed in the Brønsted-acid pathway for the opening of 3-phenyloxetane.

What underlies the unique ability of **Me-4d** to promote both pathways with high enantioselectivity? Inspection of an electrostatic potential map of the catalyst in its reactive conformation (Figure 25.14) reveals that the positive polarization (in blue) in the HBD site is partially enclosed within a "chiral pocket" of negative electrostatic potential (in red) created by the amide carbonyl and the highly polarizable aryl substituent on the pyrrolidine [43]. Dipolar transition states with a range of different steric and functional properties may thus be accommodated enantioselectively within that chiral environment. These catalyst features may also account for the remarkably broad scope of the enantioselective ring-opening reaction across different 3-substituted oxetanes [23].

The third case study of the mechanism of enantioinduction with aryl-pyrrolidino-*tert*-leucine-derived HBD catalysts concerns chiral thiourea/TESOTf co-catalyzed multicomponent aza-Sakurai allylations of acetals (Figure 25.8). Analysis of this reaction provides a compelling illustration of the fact that the same chiral motif can induce stereoselectivity in different reactions by engaging in fundamentally different types of interactions with transition states [30].

The enantioselective, multicomponent aza-Sakurai reaction displays certain characteristics that are rarely encountered in anion-binding catalysis with HBDs. Even though the dual-HBD was found to be essential for high ee's, very similar enantioselectivities are obtained with thiourea (**3**), squaramide (**4**), and urea (**5**)

analogs of the same aryl-pyrrolidino-*tert*-leucine motif (Figure 25.15). Also, high ee's are obtainable in relatively polar solvents such as CH_2Cl_2 [30], whereas other ion-pairing reactions typically require very nonpolar media to attain optimal stereoselectivities [6]. These observations suggested that secondary interactions may be involved in the enantiodetermining iminium allylation transition state that are not common to other ion-pairing catalysis pathways. Computational modeling of the iminium allylation step revealed a key H-bonding interaction between the iminium and the catalyst amide [30]. The proposed interaction was probed experimentally by comparing the oxo-amide catalyst **3f** to its thioamide analog. Under reaction conditions where **3f** afforded product in 91% ee, the thioamide yielded nearly racemic product, consistent with an H-bond to the amide playing a key role in enantioinduction.

Variation of the pyrrolidine aryl substituent on the catalyst revealed a trend similar to that observed previously, wherein more expansive arene substituents on the aryl-pyrrolidine group afforded higher levels of enantioselectivity. In those prior studies, the effect was ascribed to differential stabilization of the major and minor transition states through cation–π interactions [25, 34, 43]. The signature test for such interactions is the effect of fluorine substitution on the aromatic ring [26, 44]. As demonstrated in Figure 25.14, catalysts bearing highly fluorinated aromatic groups were very poorly enantioselective in the oxetane-opening reaction, consistent with the crucial role of differential, stabilizing cation–π interactions in the enantiodetermining transition state [43]. In sharp contrast, all three of the fluorinated catalysts examined in the aza-Sakurai reactions afforded the product in higher levels of ee than phenyl-pyrrolidine thiourea **3b** [30]. Computational modeling indicates that the phenyl ring of the substrate engages in a face-face π-stacking interaction with the extended aromatic substituent of the aryl pyrrolidine in the transition state leading to the major enantiomer of product (Figure 25.15). However, the anchoring H-bonding interaction between the iminium and the amide forces the substrate and catalyst aryl groups to adopt a T-shaped interaction in the pathway leading to the minor enantiomer of product. The face-face π-stacking geometry is predicted to be more stabilizing with extended aromatic substituents [45], and thereby, provides a mechanism for preferential stabilization of the major transition state.

Although the mechanisms of enantioinduction differ significantly across the three reactions discussed earlier, several common features emerge. In particular, these studies all implicate cooperative transition state stabilization by the arene and the amide of the aryl-pyrrolidino-*tert*-leucine fragment. This cooperativity is manifested in different ways. In the episulfonium ion ring-opening chemistry and the aza-Sakurai reaction, H-bonding interactions with the *tert*-leucine amide are critical for enantioselectivity and appear to play an essential role in rigidifying and enhancing energetic differentiation between diastereomeric transition states. However, the arene is engaged in transition state stabilization through different mechanisms, either cation–π stabilization or dispersive face-to-face π-interactions. In the oxetane-opening chemistry, cation–π interactions stabilize and position the highly polarized addition complex. The transition state is intrinsically rigidified by

Comparable enantioselectivities with varied H-bond donor motifs

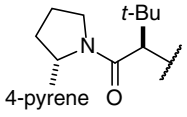

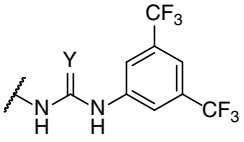

ent-3g: Y = S, 95% ee
ent-5b: Y = O, 95% ee

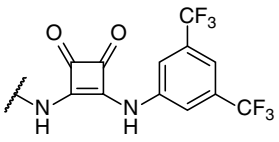

ent-4c 93% ee

Arene structure-enantioselectivity relationship

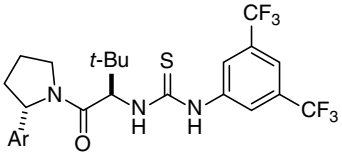

Arene	ee (%)
4-pyrenyl (**ent-3g**)	95
1-pyrenyl (**ent-3j**)	89
9-phenanthryl (**ent-3f**)	91
1-naphthyl (**ent-3e**)	81
2-naphthyl (**ent-3d**)	66
phenyl (**ent-3b**)	60
4-fluorophenyl (**ent-3c**)	68
3,5-difluorophenyl (**ent-3n**)	68
3,4,5-trifluorophenyl (**ent-3o**)	71

Major TS‡

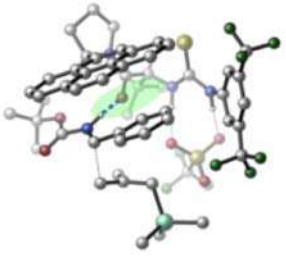

Minor TS ‡

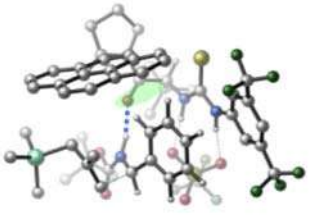

Figure 25.15 Computed transition states and supporting data for the asymmetric 3-component aza-Sakurai allylation of acetals. The proposed H-bond is depicted with a blue dotted line and the proposed π-stacking interaction is shown in green.

the delivery of the HBD-bound anionic nucleophile to the electrophilic ring carbon. Still, the amide carbonyl plays an essential role, interacting with the activated electrophile through either H-bonding or dipole stabilization. The combination of the amide and arene with the HBD active site serves to create a dipolar chiral pocket that can accommodate a wide variety of dipolar transition states. Given the wide variety of polar mechanisms of importance in organic reactions, we anticipate that the aryl-pyrrolidine-*tert*-leucine motif will continue to prove effective at inducing high levels of enantioselectivity in new applications, including reactions that do not involve HBD catalysis.

25.6 Concluding Remarks

The concept of privileged chiral catalysts and scaffolds has proven highly enabling for the development of new enantioselective transformations [4]. While novel

applications are identified at an increasing pace, new insights into the fundamental principles that underlie selectivity [42, 46] and generality [47] in asymmetric catalysis are emerging only gradually. Early mechanistic analyses of effective systems drew on relatively simple models such as sterically differentiated quadrants at metal reactive sites, with transition states involving covalent or coordinative association of the catalyst to the substrate [48]. Insofar as the mechanisms of enantioinduction could be elucidated for these transformations, they were understood to rely on destabilization of transition states leading to the minor enantiomer of product through steric repulsion or strain. More recently, noncovalent catalysis has emerged as an alternative principle for enantioinduction with small-molecule catalysts, with selectivity achieved through selective stabilization of the transition state(s) leading to the major enantiomer of product [42]. We suggest that steric destabilization and noncovalent stabilization strategies ultimately rely on distinct structural features of chiral catalysts. For catalysts that control enantioselectivity by destabilizing all of the transition states leading to the minor enantiomer of product, symmetry elements in the catalyst simplify the problem by reducing the number of competing pathways [4, 49]. If the catalyst operates by stabilizing a single transition state leading to the major enantiomer of product, symmetry elements may be less essential. It is notable that cinchona alkaloid derivatives and aryl-pyrrolidino-*tert*-leucine-derived-HBD catalysts, along with essentially all enzymes, possess only C_1 symmetry and have been proposed to operate via selective transition state stabilization (vide supra, and [50]). Instead, the engagement of multiple recognition elements and cooperative networks of stabilizing interactions are essential in these systems [42]. Functional groups that can engage in many different types of interactions – for example, (i) arenes, which can participate in charge-dominated (cation–π or anion–π) attractive interactions, dispersion-dominated (π-stacking) attractive interactions, or repulsive (steric) interactions and (ii) carbonyl groups, which can engage in H-bonding, dipole stabilization, or other stabilizing interactions [51] – may be especially conducive to generality by allowing catalysts to recognize a wide range of transition states. This certainly seems to be the case for the privileged aryl-pyrrolidino-*tert*-leucine motif, for which the presence of the *tert*-leucine amide has proven essential and variation of the aryl substituent has been the most important strategy for catalyst optimization. It is our hope that the continued application and study of this and other privileged chiral scaffolds will facilitate the development of new catalytic, asymmetric methods and enhance understanding of the molecular properties and specific interactions that enable both selectivity and generality in asymmetric catalysis.

Acknowledgments

This program in H-bond-donor asymmetric catalysis has received financial support since its inception from the NIH (GM43214). We thank Dr. Shao-Liang Zheng (Harvard X-ray Laboratory) for X-ray crystallographic structure determinations. Sincere thanks are also given to all the extraordinary group members who contributed to this program both directly and indirectly over the past two decades.

References

1 Koshland, D.E. (1958). Application of a theory of enzyme specificity to protein synthesis. *Proc. Natl. Acad. Sci. U.S.A.* 44: 98–104.

2 Knowles, W.S. (2002). Asymmetric hydrogenations (Nobel lecture). *Angew. Chem. Int. Ed.* 41: 1998–2007.

3 Jacobsen, E.N., Pfaltz, A., and Yamamoto, H. (eds.) (2004). *Comprehensive Asymmetric Catalysis*. Berlin: Springer-Verlag.

4 Yoon, T.P. and Jacobsen, E.N. (2003). Privileged chiral catalysts. *Science* 299: 1691–1693.

5 Marzijarani, N.S., Lam, Y.-H., Wang, X. et al. (2020). New mechanism for cinchona alkaloid-catalysis allows for an efficient thiophosphorylation reaction. *J. Am. Chem. Soc.* 142: 20021–20029.

6 (a) Taylor, M.S. and Jacobsen, E.N. (2006). Asymmetric catalysis by chiral hydrogen-bond donors. *Angew. Chem. Int. Ed.* 45: 1520–1543. (b) Doyle, A.G. and Jacobsen, E.N. (2007). Small-molecule H-bond donors in asymmetric catalysis. *Chem. Rev.* 107: 5713–5743. (c) Brak, K. and Jacobsen, E.N. (2013). Asymmetric ion-pairing catalysis. *Angew. Chem. Int. Ed.* 52: 534–561.

7 Sigman, M.S. and Jacobsen, E.N. (1998). Schiff base catalysts for the asymmetric Strecker reaction identified and optimized from parallel synthetic libraries. *J. Am. Chem. Soc.* 120: 4901–4902.

8 (a) Sigman, M.S., Vachal, P., and Jacobsen, E.N. (2000). A general catalyst for the asymmetric Strecker reaction. *Angew. Chem. Int. Ed.* 39: 1279–1281. (b) Vachal, P. and Jacobsen, E.N. (2000). Enantioselective catalytic addition of HCN to ketoimines. Catalytic synthesis of quaternary amino acids. *Org. Lett.* 2: 867–870. (c) Vachal, P. and Jacobsen, E.N. (2002). Structure-based analysis and optimization of a highly enantioselective catalyst for the Strecker reaction. *J. Am. Chem. Soc.* 124: 10012–10014.

9 Wenzel, A.G. and Jacobsen, E.N. (2002). Asymmetric catalytic Mannich reactions catalyzed by urea derivatives: enantioselective synthesis of β-aryl-β-amino acids. *J. Am. Chem. Soc.* 124: 12964–12965.

10 Wenzel, A.G., Lalonde, M.P., and Jacobsen, E.N. (2003). Divergent stereoinduction mechanisms in urea-catalyzed additions to imines. *Synlett* (12): 1919–1922.

11 Zuend, S.J., Coughlin, M.P., Lalonde, M.P., and Jacobsen, E.N. (2009). Scaleable catalytic asymmetric Strecker syntheses of unnatural α-amino acids. *Nature* 461: 968–970.

12 (a) Schreiner, P.R. and Wittkopp, A. (2002). H-bonding additives act like Lewis acid catalysts. *Org. Lett.* 4: 217–220. (b) Lippert, K.M., Hof, K., Gerbig, D. et al. (2012). Hydrogen-bonding thiourea organocatalysts: the privileged 3,5-bis(trifluoromethyl)phenyl group. *Eur. J. Org. Chem.*: 5919–5927.

13 Okino, T., Hoashi, Y., and Takemoto, Y. (2003). Enantioselective Michael reaction of malonates to nitroolefins catalyzed by bifunctional organocatalysts. *J. Am. Chem. Soc.* 125: 12672–12673.

14 Jakab, G., Tancon, C., Zhang, Z. et al. (2012). (Thio)urea organocatalyst equilibrium acidities in DMSO. *Org. Lett.* 14: 1724–1727.

15 (a) Huynh, P.N.H., Walvoord, R.R., and Kozlowski, M.C. (2012). Rapid quantification of the activating effects of hydrogen-bonding catalysts with a colorimetric sensor. *J. Am. Chem. Soc.* 134: 15621–15623. (b) Nödling, A.R., Jakab, G., Schreiner, P.R., and Hilt, G. (2014). ^{31}P NMR spectroscopically quantified hydrogen-bonding strength of thioureas and their catalytic activity in Diels–Alder reactions. *Eur. J. Org. Chem.*: 6394–6398.

16 Zuend, S.J. and Jacobsen, E.N. (2009). Mechanism of amido-thiourea catalyzed enantioselective imine hydrocyanation: transition state stabilization via multiple non-covalent interactions. *J. Am. Chem. Soc.* 131: 15358–15374.

17 Raheem, I.T., Thiara, P.S., Peterson, E.A., and Jacobsen, E.N. (2007). Enantioselective Pictet–Spengler-type cyclizations of hydroxylactams: H-bond donor catalysis by anion binding. *J. Am. Chem. Soc.* 129: 13404–13405.

18 Reisman, S.E., Doyle, A.G., and Jacobsen, E.N. (2008). Enantioselective thiourea-catalyzed additions to oxocarbenium ions. *J. Am. Chem. Soc.* 130: 7198–7199.

19 (a) Ford, D.D., Lehnherr, D., Kennedy, C.R., and Jacobsen, E.N. (2016). On- and off-cycle catalyst cooperativity in anion-binding catalysis. *J. Am. Chem. Soc.* 138: 7860–7863. (b) Ford, D.D., Lehnherr, D., Kennedy, C.R., and Jacobsen, E.N. (2016). Anion-abstraction catalysis: the cooperative mechanism of α-chloroether activation by dual hydrogen-bond donors. *ACS Catal.* 6: 4616–4620.

20 Lehnherr, D., Ford, D.D., Bendelsmith, A.J. et al. (2016). Conformational control of chiral amido-thiourea catalysts enables improved activity and enantioselectivity. *Org. Lett.* 18: 3214–3217.

21 Bendelsmith, A.J., Kim, S.C., Wasa, M. et al. (2019). Enantioselective synthesis of α-allyl amino esters via hydrogen-bond-donor catalysis. *J. Am. Chem. Soc.* 141: 11414–11419.

22 Kutateladze, D.A., Strassfeld, D.A., and Jacobsen, E.N. (2020). Enantioselective tail-to-head cyclizations catalyzed by dual-hydrogen-bond donors. *J. Am. Chem. Soc.* 142: 6951–6956.

23 Strassfeld, D.A., Wickens, Z.K., Picazo, E., and Jacobsen, E.N. (2020). Highly enantioselective, hydrogen-bond-donor catalyzed additions to oxetanes. *J. Am. Chem. Soc.* 142: 9175–9180.

24 Metternich, J.B., Reiterer, M., and Jacobsen, E.N. (2020). Asymmetric Nazarov cyclizations of unactivated dienones by hydrogen-bond-donor/Lewis acid co-catalyzed enantioselective proton-transfer. *Adv. Synth. Catal.* 362: 4092–4097.

25 Knowles, R.R., Lin, S., and Jacobsen, E.N. (2010). Enantioselective thiourea-catalyzed cationic polycyclizations. *J. Am. Chem. Soc.* 132: 5030–5032.

26 (a) Ma, J.C. and Dougherty, D.A. (1997). The cation–π interaction. *Chem. Rev.* 97: 1303–1324. (b) Kennedy, C.R., Lin, S., and Jacobsen, E.N. (2016). The cation–π interaction in small-molecule catalysis. *Angew. Chem. Int. Ed.* 55: 12596–12624.

27 Bergonzini, G., Schindler, C.S., Wallentin, C.-J. et al. (2014). Photoredox activation and anion binding catalysis in the dual catalytic enantioselective synthesis of β-amino esters. *Chem. Sci.* 5: 112–116.

28 Park, Y., Schindler, C.S., and Jacobsen, E.N. (2016). Enantioselective aza-Sakurai cyclizations: dual role of thiourea as H-bond donor and Lewis base. *J. Am. Chem. Soc.* 138: 14848–14851.

29 Attard, J.W., Osawa, K., Guan, Y. et al. (2019). Silanediol anion binding and enantioselective catalysis. *Synthesis* 51: 2107–2115.

30 Ronchi, E., Paradine, S. M. and Jacobsen, E. N. (2021). Enantioselective, multicomponent synthesis of homoallylic amines enabled by hydrogen-bonding and dispersive interactions. *J. Am. Chem. Soc.* 143: 7272–7278.

31 Andres, R., Wang, Q., and Zhu, J. (2020). Asymmetric total synthesis of (–)-arborisidine and (–)-19-*epi*-arborisidine enabled by a catalytic enantioselective Pictet–Spengler reaction. *J. Am. Chem. Soc.* 142: 14276–14285.

32 Yeung, C.S., Ziegler, R.E., Porco, J.A. Jr., and Jacobsen, E.N. (2014). Thiourea-catalyzed enantioselective addition of indoles to pyrones: alkaloid cores with quaternary carbons. *J. Am. Chem. Soc.* 136: 13614–13617.

33 Banik, S.M., Levina, A., Hyde, A.M., and Jacobsen, E.N. (2017). Lewis acid enhancement by hydrogen-bond donors for asymmetric catalysis. *Science* 358: 761–764.

34 Lin, S. and Jacobsen, E.N. (2012). Thiourea-catalyzed ring opening of episulfonium ions with indole derivatives by means of stabilizing non-covalent interactions. *Nat. Chem.* 4: 817–824.

35 Zhang, H., Lin, S., and Jacobsen, E.N. (2014). Enantioselective selenocyclization via dynamic kinetic resolution of seleniranium ions by hydrogen-bond donor catalysts. *J. Am. Chem. Soc.* 136: 16485–16488.

36 Birrell, J.A., Desrosiers, J.-N., and Jacobsen, E.N. (2011). Enantioselective acylation of silyl ketene acetals through fluoride anion-binding catalysis. *J. Am. Chem. Soc.* 133: 13872–13875.

37 Momo, P.B., Leveille, A.N., Farrar, E.H.E. et al. (2020). Enantioselective S–H insertion reactions of α-carbonyl sulfoxonim ylides. *Angew. Chem. Int. Ed.* 59: 15554–15559.

38 Curran, D.P. and Kuo, L.H. (1994). Altering the stereochemistry of allylation reactions of cyclic α-sulfinyl radicals with diarylureas. *J. Org. Chem.* 59: 3259–3261.

39 Cruz-Acosta, F., de Armas, P., and Garcia-Tellado, F. (2013). Water-compatible hydrogen-bond activation: a scaleable and organocatalytic model for the stereoselective multicomponent aza-Henry reaction. *Chem. Eur. J.* 19: 16550–16554.

40 Lykke, L., Carlsen, B.D., Rambo, R.S., and Jørgensen, K.A. (2014). Catalytic asymmetric synthesis of 4-nitropyrazolidines: an access to optically active 1,2,3-triamines. *J. Am. Chem. Soc.* 136: 11296–11299.

41 Liu, R.Y., Wasa, M., and Jacobsen, E.N. (2015). Enantioselective synthesis of tertiary α-chloro esters by non-covalent catalysis. *Tetrahedron Lett.* 56: 3428–3430.

42 Knowles, R.R. and Jacobsen, E.N. (2010). Attractive noncovalent interactions in asymmetric catalysis: links between enzymes and small molecule catalysts. *Proc. Natl. Acad. Sci. U.S.A.* 107: 20678–20685.

43 Strassfeld, D. A., Algera, R. F., Wickens, Z. K. and Jacobsen, E. N. (2021). A case study in catalyst generality: simultaneous, highly-enantioselective Brønsted- and

Lewis-acid mechanisms in hydrogen-bond-donor catalyzed oxetane openings. *J. Am. Chem. Soc.* 143: 9585–9594.

44 (a) Mecozzi, S., West, A.P., and Dougherty, D.A. (1996). Cation–π interactions in simple aromatics: electrostatics provide a predictive tool. *J. Am. Chem. Soc.* 118: 2307–2308. (b) Zhong, W., Gallivan, J.P., Zhang, Y. et al. (1998). From *ab initio* quantum mechanics to molecular neurobiology: a cation–π binding site in the nicotinic receptor. *Proc. Natl. Acad. Sci. U.S.A.* 95: 12088–12093.

45 Grimme, S. (2008). Do special noncovalent π–π stacking interactions really exist? *Angew. Chem. Int. Ed.* 47: 3430–3434.

46 (a) Jacobsen, E.N. and MacMillan, D.W.C. (2010). Organocatalysis. *Proc. Natl. Acad. Sci. U.S.A.* 107: 20618–20169. (b) Mahlau, M. and List, B. (2013). Asymmetric counteranion-directed catalysis: concept, definition, and applications. *Angew. Chem. Int. Ed.* 52: 518–533. (c) Neel, A.J., Hilton, M.J., Sigman, M.S., and Toste, F.D. (2017). Exploiting non-covalent π interactions for catalyst design. *Nature* 543: 637–646.

47 Ford, D.D., Nielsen, L.P.C., Zuend, S.J. et al. (2013). Mechanistic basis for high stereoselectivity and broad substrate scope in the (salen)Co(III)-catalyzed hydrolytic kinetic resolution. *J. Am. Chem. Soc.* 135: 15595–15608.

48 Walsh, P.J. and Kozlowski, M.C. (2009). *Fundamentals of Asymmetric Catalysis*. Sausalito: University Science Books.

49 Whitesell, J.K. (1989). C_2 symmetry and asymmetric induction. *Chem. Rev.* 89: 1581–1590.

50 (a) Jencks, W.P. (1989). *Catalysis in Chemistry and Enzymology*. New York: McGraw Hill. (b) Krenske, E.H. and Houk, K.N. Aromatic interactions as control elements in stereoselective organic reactions. *Acc. Chem. Res.* 2013 (46): 979–989.

51 Newberry, R.W. and Raines, R.T. (2017). The $n \rightarrow \pi^*$ interaction. *Acc. Chem. Res.* 50: 1838–1846.

26

Chiral Triazole Foldamers in Enantioselective Anion-Binding Catalysis

Alica C. Keuper and Olga García Mancheño

Organic Chemistry Institute, University of Münster, Corrensstraße 36, Münster, 48149, Germany

26.1 Introduction

Foldamers presenting a well-defined conformation upon recognition of a substrate constitute a unique platform for the design of novel, highly efficient catalysts with enzyme-like specificity and reactivity control. In this regard, helical foldamer structures have been identified as very suitable scaffolds, allowing for an anticipated spatial organization of catalytic active functionalities within the structure. Consequently, the helicity and specific arrangement of these structures can be used as the origin of chirality transfer in catalytic processes [1]. Moreover, numerous foldamer-based systems (discrete or polymeric) are already known to selectively recognize and complex anionic species [2], which represents an attractive alternative for the development of innovative strategies in catalysis involving anions.

26.2 Triazoles as Anion Receptors

1,2,3-Triazoles are intriguing heterocycles due to their interesting properties such as a large dipole moment ($\mu = 4.38$ D) [3], highly polarized C—H bond [4] and relative acidity of the hydrogens at the C4- and C5-positions compared to alkenes or other aromatic compounds (Figure 26.1, top) [5]. Moreover, these structures are readily accessible through the copper(I)-catalyzed azide-alkyne cycloaddition (CuAAC), one of the most relevant transformations within the so-called *click chemistry* [6]. On the basis of these special characteristics, triazoles were successfully applied in supramolecular chemistry, particularly in the selective recognition of anions [7]. In this regard, many triazole-based anion receptors have been reported in the last decade [8–13], ranking from simple to highly preorganized supramolecular foldamer [10], macrocyclic [10c, 11], molecular rotor [12], and rotaxane [13] structures containing two or more triazole units. Among them, the early triazole-foldamer systems developed by Hecht [10a], Craig [10b], and Flood [10c] in 2008 (Figure 26.1, bottom) can be highlighted, which present high selectivity and anion-binding affinities (up to $k_a = 1.7 \times 10^4$ M^{-1} with A$^-$ = Cl$^-$ [10b]).

Supramolecular Catalysis: New Directions and Developments, First Edition.
Edited by Piet W.N.M. van Leeuwen and Matthieu Raynal.

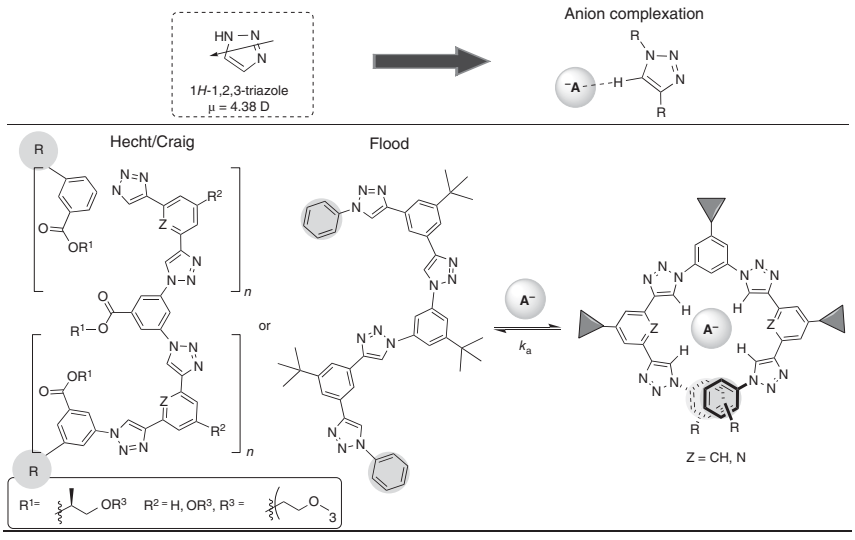

Figure 26.1 1,2,3-Triazoles and some representative foldamer triazole anion-receptors.

26.3 Design of Foldamer Triazoles as Hydrogen Bond Donors for Anion-Binding Catalysis

Inspired by the high efficiency of foldamer triazoles to selectively bind anions [10], as well as the emerging field of asymmetric anion-binding catalysis [14], we decided to merge both research fields aiming at providing new, powerful alternatives. Considering that the concept of anion-binding organocatalysis relies on the formation of a chiral contact ion-pair upon binding of the catalyst to the counteranion of a cationic substrate, we envisioned the effective formation of triazole receptor (host):ionic substrate (guest) ion-pair complexes (Figure 26.2), which could compete to the mainly explored (thio)urea and squaramide-type anion receptor catalysts [15].

In early work, we first proved that a family of bidentate bis-triazoles could be used as weak hydrogen-bond (HB) donors in catalysis [16]. However, in order to translate this finding to asymmetric catalysis few key features had to be considered. First, the chirality in the catalyst was introduced by an extension of the system to four triazoles on a chiral *trans*-1,2-diamine backbone, thus allowing to build a defined chiral helical supramolecular structure upon complexation to an anion. Second, the efficient formation of the tight chiral ion-pair responsible of the chirality transfer

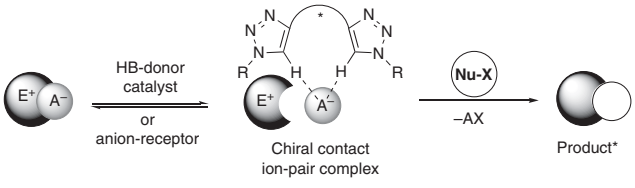

Figure 26.2 Concept of anion-binding catalysis with envisioned triazole anion-receptors.

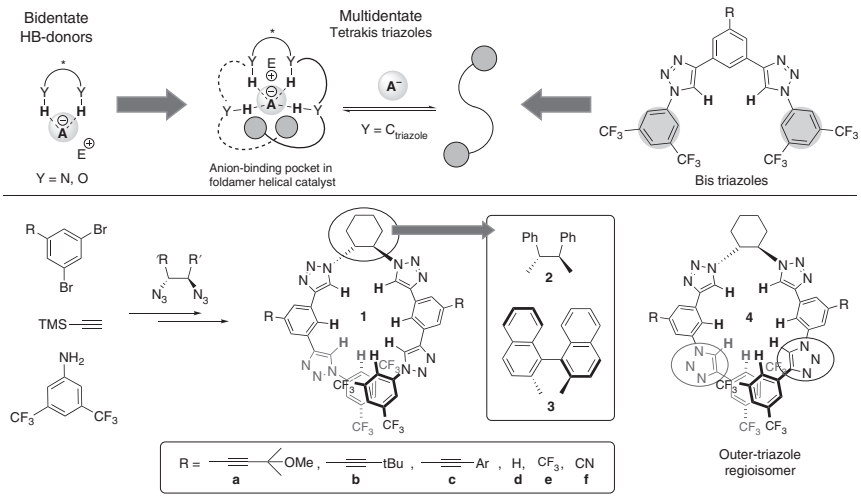

Figure 26.3 Designed triazole-based helical foldamer catalysts with chiral anion-binding pocket.

should take place. In this case, the polarized C—H bonds of triazoles are still weak HB-donors, for that reason a typical bidentate fixation might not be sufficient. Thus, a cooperative interaction of a catalyst presenting multidentate sites to bind not only the anion (by HB) but also to fix the cationic substrate (through the triazole *N*-atoms or polar groups in the side-chain) was embraced. In 2014, we described the first generation of chiral tetrakis-triazoles (TetraTri) based on this design (Figure 26.3, top) [17]. A straightforward synthesis for the TetraTri **1**–**4** was developed by sequential Sonogashira cross-couplings and CuAAC-cycloadditions, where the central chiral backbone is introduced in the last click reaction with the corresponding chiral azide such as (1*R*,2*R*)-1,2-diazidocyclohexane (Figure 26.3, bottom). Besides the more step-economic symmetrical systems, regioisomeric structures on the outer triazoles were also synthetized since in some cases those were reported to present higher halogen affinities (Figure 26.3, right bottom) [9].

26.4 Anion-Binding-Catalyzed Enantioselective Reissert-Type Reaction with Silylketene Acetals

The asymmetric Reissert reaction implies the dearomatization of *N*-heteroarenes by first substrate activation via *N*-acylation to generate the corresponding *N*-acyliminium species, which then reacts with a nucleophile to form the corresponding enantioenriched heterocyclic product. A paradigm work in this area was developed by Shibasaki et al., who employed a chiral 1,1′-Bi-2-naphthol (BINOL)-derived aluminum catalyst with various heteroarenes [18]. Particularly, in the field of anion-binding catalysis [14], the group of Jacobsen reported pioneering work applying a bifunctional thiourea catalyst in the *N*-acyl Mannich reaction

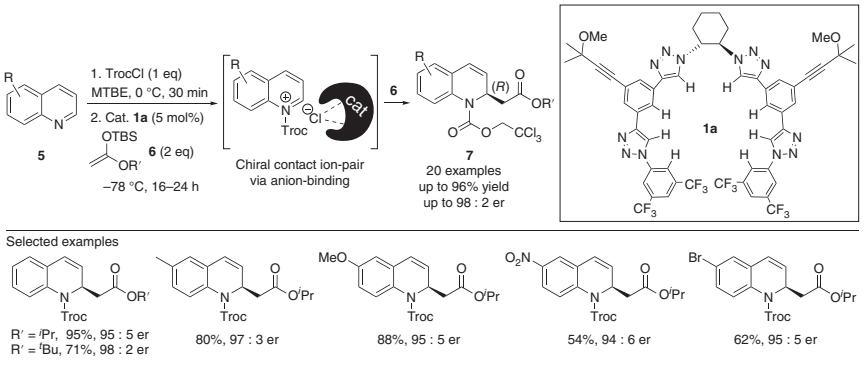

Scheme 26.1 Enantioselective anion-binding-catalyzed Reissert reaction with quinolines.

of isoquinolines [19]. The HB-donor organocatalyst is able to bind effectively to the counterion of the *N*-acyliminium salt [20], leading to a chiral anion–catalyst complex that takes part in the formation of the key contact ion-pair involved in the stereoselectivity-determining step.

Encouraged by the previous reports [19], the designed foldamer chiral triazole-based catalysts **1**–**4** were employed in the Reissert reaction of quinoline derivatives **5** with silylketene acetals **6** as nucleophiles, which allow access to synthetically valuable 2-substituted chiral 1,2-dihydro-quinolines **7** (Scheme 26.1) [17]. The selection of the appropriate solvent is of prime importance, since it influences the formation of the contact ion-pair [21]. Therefore, nonpolar solvents such as ethers or aromatics (e.g. toluene) are generally optimal for this transformation. Moreover, the acylating agent plays an important role to achieve good enantioselectivities. Thus, 2,2,2-trichloroethoxycarbonyl chloride (TrocCl) turned out to be the best choice, which introduces an additional π–π or π–halogen interaction within the three-body ion-pair system (catalyst-Cl^- complex/quinolinium) [22]. Moreover, bulky-medium size groups at the silyl ketene acetal (such as *tert*-Butyldimethylsilyl (TBS) and O^{i}Pr or O^{t}Bu) led to the best results. Thus, the use of 5 mol% of catalyst **1a** in methyl *tert*-butyl ether (MTBE) at −78 °C in the reaction with different substituted quinolines provided excellent enantioselectivities (up to 98 : 2 er). However, the substitution at the C3- and C8-positions of the quinoline ring was not well-tolerated, providing lower inductions and no reactivity, respectively. This observation suggests important steric effects hampering the nucleophile approach, as well as the need for the rotation of the Troc-group to make space around the reactive C2-position.

The extension to other *N*-heteroarenes was also possible employing this catalytic system (Figure 26.4). Consequently, the reaction with isoquinolines (a) was performed under identical conditions [23]. However, less efficient chirality transfer was observed, in which the highest enantioselectivities were obtained with the regioisomeric TetraTri catalyst **4a** (**8**, up to 90 : 10 er). The more challenging pyridine substrates, which are prompt to react in a non-regiospecific way at both the C2 and C4 positions and are less reactive than (iso)quinolines [24], could be

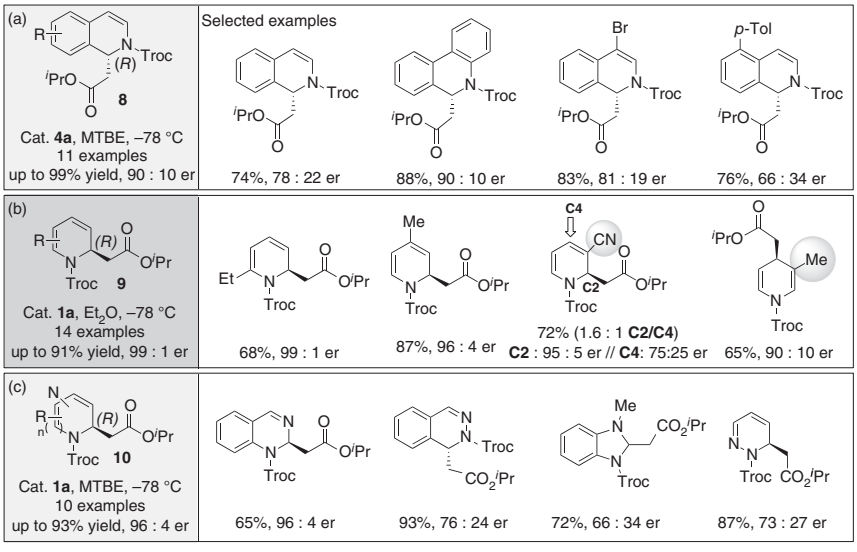

Figure 26.4 Extension of the asymmetric Reissert reaction to other *N*-heteroarenes: (a) isoquinolines; (b) pyridines, and (c) diazarenes.

successful dearomatized in the presence the triazole-catalyst **1a** (Figure 26.4b) [25]. After a short optimization, acylation with TrocCl and 5 mol% of catalyst **1a** in Et_2O at −78 °C was employed. Thus, good to excellent enantiomeric ratios (up to 99 : 1 er) and regioselectivities toward the C2-addition products **9** were reached in most cases. However, the substitution at C3 again led to interesting results. Hence, mixtures of C2 and C4 (with small substituents such CN) or a complete inversion of the regioselectivity to the C4-addition products (with larger groups, e.g. CH_3) were observed, in which the C4-products showed significantly lower enantioselectivities (up to 90 : 10 er) than the C2-addition adducts.

Finally, this Reissert-type reaction could be expanded to the dearomatization of diazarenes, which present a larger number of reactive sites respect to their two nitrogen atoms (Figure 26.4c) [26]. Fortunately, for quinazoline a high regioselectivity and enantiomeric ratio of 96 : 4 was observed. For other diazarenes, lower chirality inductions were obtained, but this method allows their fast transformation into chiral di- or tetrahydro diazaheterocycles **10**, which are important building blocks in natural and bioactive compounds.

26.5 Reaction with Different Nucleophiles

Based on the high efficiency of the chiral TetraTri catalysts in the Reissert-type reaction with silylketene acetals, their applicability with other types of nucleophiles was also explored with quinoline as benchmark substrate (Figure 26.5). Various carbon- [27] and heteroatom-based [28] reagents presenting different *N*-values according to the Mayr's reactivity scale [29] showed that a nucleophilicity of around

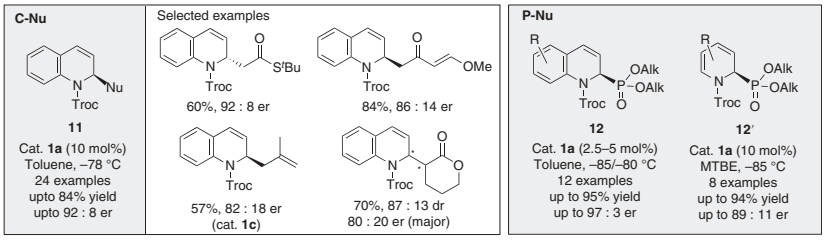

Figure 26.5 Scope with other (a) C- and (b) phosphorus nucleophiles.

$N = 10$ was the most suitable one. Thus, far lower N-values (<5) led to no reactivity, whereas strong nucleophiles like Grignard reagents provided racemic or complex mixtures. Accordingly, among the screened C-nucleophiles, silyl ketene thioacetals, some silyl enol ethers and allyl-Sn reagents within $N = 7$–11 provided high (**11**, up to 92 : 8 er) or promising results under noncompletely optimized conditions in toluene at −78 °C employing **1a** as catalyst. More interestingly, phosphorus nucleophiles such as alkyl phosphites $(EtO)_3P$ or $(n BuO)_2$P-OTMS [30] with an $N \sim 10$ proved to be more effective, allowing the enantioselective synthesis of chiral cyclic α-amino phosphonic acid derivatives **12/12′** [31]. Hence, the reaction at −85 to −80 °C in toluene or MTBE, depending on the quinoline or pyridine substrate, led to the desired products in good to excellent yields and enantioselectivities (up to 97 : 3 er) [28].

26.6 Nucleophilic Dearomatization of Pyrylium Derivatives

This triazole-based foldamer system also proved to be efficient for the enantioselective synthesis of oxygen heterocycles from *in situ* generated pyrylium-type derivatives from 4-(benzo)pyranones **13**, giving easy access to chiral chromanones and dihydropyrones **14** (Scheme 26.2) [32]. The asymmetric nucleophilic dearomatization of pyrylium salts represent a significant challenge due their intrinsic nature [33], often leading to ring-opening or decomposition of the final products. Moreover, pyrylium salts are less reactive than nonconjugated oxonium ions and their stereoelectronic properties are difficult to be fine-tuned in contrast to the related N-derivatives. Nevertheless, our group accepted the challenge, aiming at a high stereocontrol by an efficient substrate recognition upon multidentate coordination with the catalyst.

We started the studies with commercially available 4-chromenone as a model substrate and silyl ketene acetals as nucleophiles. After optimization of the reaction conditions, the active benzopyrylium ion species was generated *in situ* by treatment with TBSOTf as the silylating reagent. This was performed in the presence of 1 mol% of our best TetraTri anion-binder **1a** and a catalytic amount of 2,4,6-collidine at 60 °C in toluene, prior to the addition of the nucleophile at −78 °C. To our delight, we observed excellent enantioselectivities up to 98 : 2 er for the desired chiral

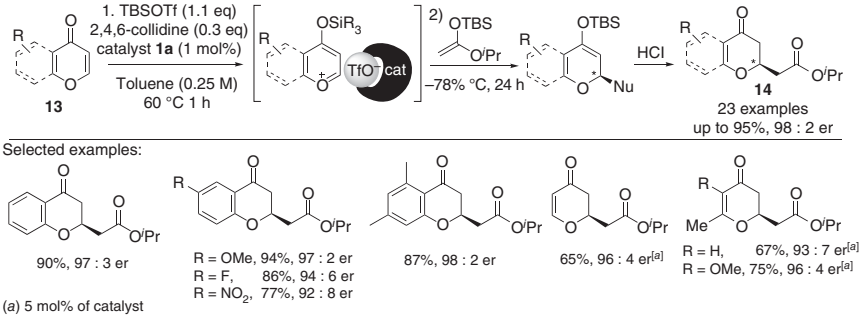

Scheme 26.2 Dearomatization reaction of pyrylium derivatives.

chromanones **14**. Remarkably, the high performance of the catalyst allowed low loadings of 0.05 mol%. Furthermore, the reaction was also possible with the more demanding 4-pyrones, leading to the desired heterocycles with up to 96 : 4 er, although in this case 5 mol% of the catalyst was needed for an optimal outcome.

26.7 Folding and Cooperative Multi-Recognition Mechanism

Aiming at gaining some insight into the mechanism of action of the TetraTri catalyst **1a**, a combined experimental and computational study was carried out [34]. The circular dichroism (CD) titration of the TetraTri catalyst **1a** with tetrabutylammonium chloride (TBACl) revealed the formation of a chiral helical anion-catalyst complex in the presence of the chloride anion. Additionally, the first steps of the folding mechanism, implying the capture of the chloride anion and the first conformational changes, were investigated using Born–Oppenheimer molecular dynamic (BOMD) simulations with Me_4NCl as substrate (Figure 26.6). This study showed a fast complexation process, which is initiated by the anion recognition through H-bonding between the chloride anion and the C—H bonds of the two-upper central triazoles, and leads to a conformational structure change into a pseudo-helical conformer. Thus, one arm of the catalyst first opens to better allocate the ionic substrate in the binding cavity, which then proceeds its closure toward the folded 1 : 1 complex.

Nonlinear-effect analysis within a model reaction suggested that this type of catalyst stays mainly monomeric during the catalytic process. Furthermore, ^{1}H NMR and isothermal calorimetry (ITC) titrations with several tetrabutylammonium (TBA) salts as anion sources indicate a 1 : 1 stoichiometry of the catalyst (host):guest complexes, which present a relatively small anion-binding energy of ~3–4 kcal mol^{-1} and moderate affinities of $k_a \sim 500$ and ~700 M^{-1} for chloride and benzoate, respectively. Next, the interactions and cooperative nature of the multidentate H-bonding structure were addressed with a model Reissert reaction with *N*-Troc-pyridium salt, for which the possible transition state (**TS**) was computed in Et_2O at −78 °C (Figure 26.7). Interestingly, we could determine that both the

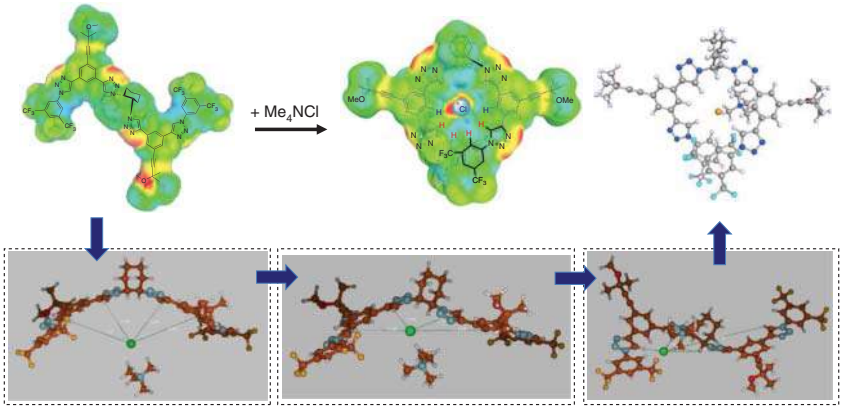

Figure 26.6 Computed structures and folding of chiral catalyst **1a** with Me_4NCl as substrate (BOMD at DFT-M06-2X/defSV(P) level).

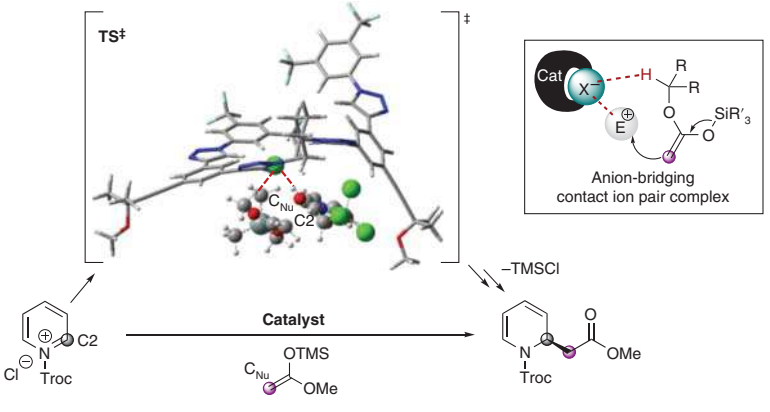

Figure 26.7 Catalyst–chloride H-bond bridging interactions in the transition state (**TS**), computed at M06-2X/def2tzvp//AM1 level of theory.

pyridinium and nucleophile are stabilized by HB-interactions with the chloride anion as bridging unit. The nucleophilic attack with transfer of the chirality then requires a small barrier of 2.0 kcal mol^{-1} toward the final product upon subsequent elimination of TMSCl and regeneration of the catalyst.

26.8 Design of Catalytic Transformations Based on Anion-Template Strategies

Encouraged by the finding of the interesting role of the anion as bridging motif between the catalyst and nucleophile in the **TS** [34], we envisioned that nucleophiles able to interact via H-bonding with the anions of the contact ion-pair complex will open new possibilities in this field. Hence, embracing this idea, we

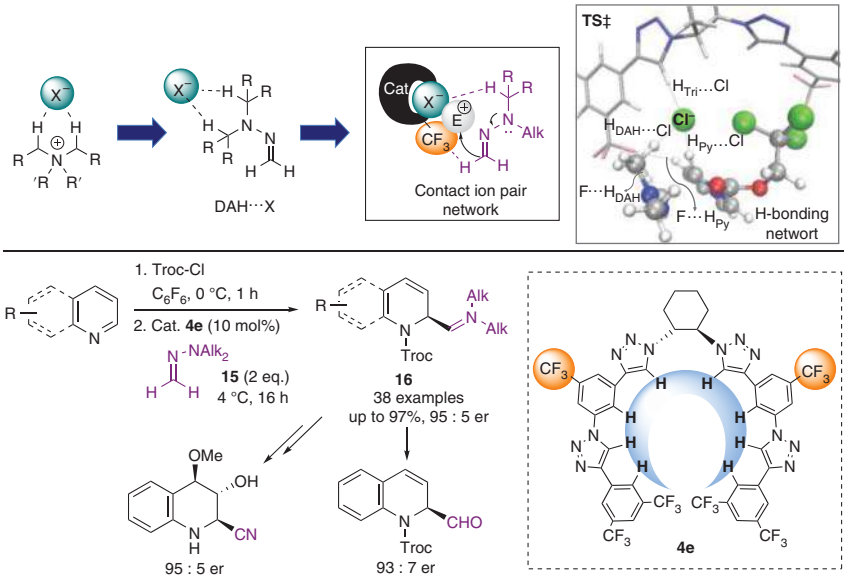

Figure 26.8 Design and application of contact ion-pair HB-network with DAHs.

recently developed a novel asymmetric anion-binding organocatalytic approach with *N,N*-dialkylhydrazones (DAHs) **15** as versatile polarity-reversed (umpolung) nucleophiles in organocatalysis [35] (Figure 26.8). Inspired by the anion-binding and catalytic properties of ammonium salts by H-bonding with their α–C—H bonds [36], we reasoned that DAHs could likewise recognize anions and build a defined HB-network toward a superior stereocontrol. Thus, we used the multidentate triazole-based H-donor **4e** bearing CF_3 groups in the central aromatic units to enhance the anion affinity (~3100 vs. 500 M^{-1} for **1a**), allowing the formation of a supramolecular tight chiral contact ion pair complex by a highly ordered HB-network between the catalyst, ionic substrate and nucleophilic hydrazone. To test our hypothesis, the asymmetric Reissert-type reaction of quinolines was again selected as model process, providing enantiomerically enriched hydrazones **16** in up to 95 : 5 er (in C_6F_6 at 4 °C), which can easily be derivatized into value-added heterocycles with up to three stereocenters [37].

26.9 Concluding Remarks

The TetraTri H-donor foldamer catalysts have shown a high performance in several Reissert-type enantioselective dearomatization reactions of *N*- and *O*-heteroarenes. Combined experimental and computational studies on the monomeric TetraTri catalysts showed a typical initial S-shape, which change the conformation into a pseudo-helical 1 : 1 host:guest complex in the presence of an ionic substrate upon a fast-anion uptake and folding process. Small binding energies of 3–4 kcal mol^{-1} and moderate constants were, however, sufficient for attaining the observed good

reactivity and high enantioselectivity. Moreover, we have noticed a favorable anion-bridging effect between the catalyst, substrate, and nucleophile that can further be modulated by introducing other coordinating groups in the side chains, bringing together all reaction components in a proper orientation for achieving high chirality transfer. This offers new possibilities with challenging reactants that might lead to further ground-breaking strategies in the field of anion-binding catalysis.

Acknowledgments

The Deutsche Forschungsgemeinschaft (DFG) (GA 1594/5-1 and SFB858) and the European Research Council (ERC-CG 724695) are gratefully acknowledged for financial support for this research. Special thanks are given to S. Beckendorf, whose initial explorations into triazole-based anion receptors led to the design of the chiral helical TetraTri catalysts.

References

1 Girvin, Z.C. and Gellman, S.H. (2020). Foldamer catalysis. *J. Am. Chem. Soc.* 142: 17211–17223.
2 John, E.A., Massena, C.J., and Berryman, O.B. (2020). Helical anion foldamers in solution. *Chem. Rev.* 120: 2759–2782.
3 Jug, K., Chiodo, S., Calaminici, P. et al. (2003). Electronic and vibrational polarizabilities and hyperpolarizabilities of azoles: a comparative study of the structure–polarization relationship. *J. Phys. Chem. A.* 107: 4172–4183.
4 Vargas, R., Garza, J., Dixon, D.A., and Hay, B.P. (2002). How strong is the Cα–H···O=C hydrogen bond? *J. Am. Chem. Soc.* 122: 4750–4755.
5 (a) Matulis, V.E., Halauko, Y.S., Ivashkevich, O.A., and Gaponik, P.N. (2009). CH acidity of five-membered nitrogen-containing heterocycles: DFT investigation. *THEOCHEM* 909: 19–24. (b) Shen, K., Fu, Y., Li, J.N. et al. (2007). What are the pK_a values of C–H bonds in aromatic heterocyclic compounds in DMSO? *Tetrahedron* 63: 1568–1576.
6 (a) Kolb, H.C., Finn, M.G., and Sharpless, K.B. (2001). Click chemistry: diverse chemical function from a few good reactions. *Angew. Chem. Int. Ed.* 40: 2004–2021. (b) Hein, J.E. and Fokin, V.V. (2010). Copper-catalyzed azide–alkynecycloaddition (CuAAC) and beyond: new reactivity of copper(I) acetylides. *Chem. Soc. Rev.* 39: 1302–1315.
7 Lehn, J. (1993). Supramolecular chemistry. *Science* 260: 1762–1763.
8 Beer, P.D. and Gale, P.A. (2001). Anion recognition and sensing: the state of the art and future perspectives. *Angew. Chem. Int. Ed.* 40: 486–516.
9 (a) Hua, Y. and Flood, A.H. (2010). Click chemistry generates privileged CH hydrogen-bonding triazoles: the latest addition to anion supramolecular chemistry. *Chem. Soc. Rev.* 39: 1262–1271. (b) Haridas, V., Sahu, S., Praveen Kumar, P.P., and Sapala, A.P. (2012). Triazole: a new motif for anion

recognition. *RSC Adv.* 2: 12594–12605. (c) Schulze, B. and Schubert, U.S. (2014). Beyond click chemistry – supramolecular interactions of 1,2,3-triazoles. *Chem. Soc. Rev.* 43: 2522–2571.

10 (a) Meudtner, R.M. and Hecht, S. (2008). Helicity inversion in responsive foldamers induced by achiral halide ion guests. *Angew. Chem. Int. Ed.* 47: 4926–4930. (b) Juwarker, H., Lenhardt, J.M., Pham, D.M., and Craig, S.L. (2008). 1,2,3-Triazole CH···Cl^- contacts guide anion binding and concomitant folding in 1,4-diaryl triazole oligomers. *Angew. Chem. Int. Ed.* 47: 3740–3743. (c) Li, Y. and Flood, A.H. (2008). Strong, size-selective, and electronically tunable C–H···halide binding with steric control over aggregation from synthetically modular, shape-persistent [3_4] triazolophanes. *J. Am. Chem. Soc.* 130: 12111–12122.See also:(d)Wang, Y., Bie, F., and Jiang, H. (2010). Controlling binding affinities for anions by a photoswitchable foldamer. *Org. Lett.* 12: 3630–3633. (e) Parks, F.C., Liu, Y., Debnath, S. et al. (2018). Allosteric control of photofoldamers for selecting between anion regulation and double-to-single helix switching. *J. Am. Chem. Soc.* 140: 17711–17723.

11 (a) Flood, A.H. (2016). Creating molecular macrocycles for anion recognition. *Beilstein J. Org. Chem.* 12: 611–627. (b) Shad, M.S., Santhini, P.V., and Dehaen, W. (2019). 1,2,3-Triazolium macrocycles in supramolecular chemistry. *Beilstein J. Org. Chem.* 15: 2142–2155. See also: (c) Li, Y. and Flood, A.H. (2008). Pure CH hydrogen bonding to chloride ions: a pre-organized and rigid macrocyclic receptor. *Angew. Chem. Int. Ed.* 47: 2649–2652. (d) Mungalpara, D., Valkonen, A., Rissanen, K., and Kubik, S. (2017). Efficient stabilisation of a dihydrogenphosphate tetramer and a dihydrogenpyrophosphate dimer by a cyclic pseudopeptide containing 1,4-disubstituted 1,2,3-triazole moieties. *Chem. Sci.* 8: 6005–6013. (e) Liu, Y., Zhao, W., Chen, C.-H., and Flood, A.H. (2019). Chloride capture using a C–H hydrogen-bonding cage. *Science* 365: 159–161.

12 Dorel, R. and Feringa, B.L. (2020). Stereodivergent anion binding catalysis with molecular motors. *Angew. Chem. Int. Ed.* 59: 785–789.

13 (a) White, N.G. and Beer, P.D. (2013). A rotaxane host system containing integrated triazole C–H hydrogen bond donors for anion recognition. *Org. Biomol. Chem.* 11: 1326–1333. (b) Eichstaedt, K., Jaramillo-García, J., Leigh, D.A. et al. (2017). Switching between anion-binding catalysis and aminocatalysis with a rotaxane dual-function catalyst. *J. Am. Chem. Soc.* 139: 9376–9381.

14 (a) Zhang, Z. and Schreiner, P. (2009). (Thio)urea organocatalysis – what can be learnt from anion recognition? *Chem. Soc. Rev.* 38: 1187–1198. (b) Beckendorf, S., Asmus, S., and García Mancheño, O. (2012). H-donor anion acceptor organocatalysis – the ionic electrophile activation approach. *ChemCatChem* 4: 926–936. (c) Brak, K. and Jacobsen, E.N. (2013). Asymmetric ion-pairing catalysis. *Angew. Chem. Int. Ed.* 52: 534–561. (d) Mahlau, M. and List, B. (2013). Asymmetric counteranion-directed catalysis: concept, definition, and applications. *Angew. Chem. Int. Ed.* 52: 518–533.

15 (a) Doyle, A.G. and Jacobsen, E.N. (2007). Small-molecule H-bond donors in asymmetric catalysis. *Chem. Rev.* 107: 5713–5743. (b) Limnios, D. and Kokotos, C.G. (2015). Chapter 19: Ureas and thioureas as asymmetric organocatalysts.

In: *Sustainable Catalysis: Without Metals or Other Endangered Elements*, RSC Green Chemistry Series, Part 2 (ed. M. North), 196–255. Royal Society of Chemistry (RSC) Publishing. (c) Alemán, J., Parra, A., Jiang, H., and Jørgensen, K.A. (2011). Squaramides: bridging from molecular recognition to bifunctional organocatalysis. *Chem. Eur. J.* 17: 6890–6899.

16 (a) Beckendorf, S., Asmus, S., Mück-Lichtenfeld, C., and García Mancheño, O. (2013). "Click" bis-triazoles as neutral C–H···anion acceptor organocatalysts. *Chem. Eur. J.* 19: 1581–1585. (b) Asmus, S., Beckendorf, S., Zurro, M. et al. (2014). Influence of the substitution and conformation of C–H-bond-based bis-triazole acceptors in anion-binding catalysis. *Chem. Asian J.* 9: 2178–2186. (c) Zurro, M. and García Mancheño, O. (2017). 1,2,3-Triazole-based catalysts: from asymmetric metal catalysis to anion-binding organocatalysis. *Chem. Rec.* 17: 485–498.

17 Zurro, M., Asmus, S., Beckendorf, S. et al. (2014). Chiral helical oligotriazoles: new class of anion-binding catalysts for the asymmetric dearomatization of electron-deficient *N*-heteroarenes. *J. Am. Chem. Soc.* 136: 13999–14002.

18 (a) Takamura, M., Funabashi, K., Kanai, M., and Shibasaki, M. (2000). Asymmetric Reissert-type reaction promoted by bifunctional catalyst. *J. Am. Chem. Soc.* 122: 6327–6328. (b) Ichikawa, E., Suzuki, M., Yabu, K. et al. (2004). New entries in Lewis acid–Lewis Base bifunctional asymmetric catalyst: catalytic enantioselective Reissert reaction of pyridine derivatives. *J. Am. Chem. Soc.* 126: 11808–11809.

19 Taylor, M.S., Tokunaga, N., and Jacobsen, N.E. (2005). Enantioselective thiourea-catalyzed acyl-Mannich reactions of isoquinolines. *Angew. Chem. Int. Ed.* 44: 6700–6862.

20 (a) Wu, P. and Nielsen, T.E. (2017). Scaffold diversity from *N*-acyliminium ions. *Chem. Rev.* 117 (12): 7811–7856. (b) Lee, Y.S., Alam, M., and Keri, R.S. (2013). Enantioselective reactions of *N*-acyliminium ions using chiral organocatalysts. *Chem. Asian J.* 8: 2906–2919.

21 (a) Mayer, U. (1976). Solvent effects on ion-pair equilibria. *Coord. Chem. Rev.* 21: 159–179. (b) Valeriani, C., Camp, P.J., Zwanikken, J.W. et al. (2010). Ion association in low-polarity solvents: comparisons between theory, simulation, and experiment. *Soft Matter* 6: 2793–2800.

22 (a) Neel, A.J., Hilton, M.J., Sigman, M.S., and Toste, F.D. (2017). Exploiting non-covalent π interactions for catalyst design. *Nature* 543: 637–646. (b) Wang, D.-X. and Wang, M.-X. (2013). Anion–π interactions: generality, binding strength, and structure. *J. Am. Chem. Soc.* 135: 892–897.

23 Zurro, M., Asmus, S., Bamberger, J. et al. (2016). Chiral triazoles in anion-binding catalysis: new entry to enantioselective Reissert-type reactions. *Chem. Eur. J.* 22: 3785–3793.

24 (a) Bull, J.A., Mousseau, J.J., Pelletier, G., and Charette, A.B. (2012). Synthesis of pyridine and dihydropyridine derivatives by regio- and stereoselective addition to *N*-activated pyridines. *Chem. Rev.* 112: 2642–2713. (b) Sowmiah, S., Esperança, J.M.S.S., Rebelo, L.P.N., and Afonso, C.A.M. (2018). Pyridinium salts: from synthesis to reactivity and applications. *Org. Chem. Front.* 5: 453–493.

25 Asmus, S., Zurro, M., Fischer, T., and García Mancheño, O. (2015). Highly enantioselective nucleophilic dearomatization of pyridines by anion-binding catalysis. *Angew. Chem. Int. Ed.* 54: 8823–8827.

26 Fischer, T., Bamberger, J., and García Mancheño, O. (2016). Asymmetric nucleophilic dearomatization of diazarenes by anion-binding catalysis. *Org. Biomol. Chem.* 14: 5794–5805.

27 Duong, Q.-N., Schifferer, L., and García Mancheño, O. (2019). Nucleophile screening in anion-binding Reissert-type reactions of quinolines with chiral tetrakis(triazole) catalysts. *Eur. J. Org. Chem.*: 5452–5461.

28 Fischer, T., Duong, Q.-N., and García Mancheño, O. (2017). Triazole-based anion-binding catalysis for the enantioselective dearomatization of *N*-heteroarenes with phosphorus nucleophiles. *Chem. Eur. J.* 23: 5983–5987.

29 Ofial, A.R. and Mayra, H. (2008). Do general nucleophilicity scales exist? *Phys. Org. Chem.* 21: 584–595.

30 (a) Guin, J., Wang, Q., van Gemmeren, M., and List, B. (2015). The catalytic asymmetric Abramov reaction. *Angew. Chem. Int. Ed.* 54: 355–358. (b) Choudhury, A.R. and Mukherjee, S. (2016). Enantioselective dearomatization of isoquinolines by anion-binding catalysis en route to cyclic α-aminophosphonates. *Chem. Sci.* 7: 6940.

31 Kukhar, V.P. and Hudson, H.R. (2000). *Aminophosphonic and Aminophosphinic Acids: Chemistry and Biological Activity*. Chichester, UK: Wiley.

32 Fischer, T., Bamberger, J., Gómez-Martínez, M. et al. (2019). Helical multi-coordination anion-binding catalysts for the highly enantioselective dearomatization of pyrylium derivatives. *Angew. Chem. Int. Ed.* 58: 3217–3221.

33 (a) Balaban, T.S. and Balaban, A.T. (2003). Pyrylium salts. In: *Hetarenes and Related Ring Systems, Six-Membered Hetarenes with one Chalcogen*, Science of Synthesis, Houben-Weyl Methods of Molecular Transformations, vol. 14, 11–200. Stuttgart: Thieme. (b) Katritzky, A.R. and Boulton, A.J. (2010). *Pyrylium Salts: Synthesis. Advances in Heterocyclic Chemistry*, 241. New York: Academic Press.

34 Piekarski, D.G., Steinforth, P., Gómez-Martínez, M. et al. (2020). Insight into the folding and cooperative multi-recognition mechanism in supramolecular anion-binding catalysis. *Chem. Eur. J.* 26: 17598–17603.

35 (a) Lazny, R. and Nodzewska, A. (2010). *N,N*-Dialkylhydrazones in organic synthesis. From simple *N,N*-dimethylhydrazones to supported chiral auxiliaries. *Chem. Rev.* 110: 1386–1434. (b) Retamosa, M.G., Matador, E., Monge, D. et al. (2016). Hydrazones as singular reagents in asymmetric organocatalysis. *Chem. Eur. J.* 22: 13430–13445.

36 (a) Shirakawa, S., Liu, S., Kaneko, S. et al. (2015). Tetraalkylammonium salts as hydrogen-bonding catalysts. *Angew. Chem. Int. Ed.* 54: 15767–15770. (b) Nakamura, T., Okuno, K., Nishiyori, R., and Shirakawa, S. (2020). Hydrogen-bonding catalysis of alkyl-onium salts. *Chem. Asian J.* 15: 463–472.

37 Gómez-Martínez, M., Pérez-Aguilar, M.C., Piekarski, D.G. et al. (2021). *N,N*-Dialkylhydrazones as versatile umpolung reagents in enantioselective anion-binding catalysis. *Angew. Chem. Int. Ed.* 60, 5102–5107.

27

Supramolecular Catalysis via Organic Solids: Templates to Mechanochemistry to Cascades

Shweta P. Yelgaonkar and Leonard R. MacGillivray

University of Iowa, Department of Chemistry, 230 N. Madison Street, Iowa City, IA 52242, USA

27.1 Template Approach for [2+2] Photocycloadditions

Solid-state reactions that employ auxiliary molecules as templates to direct chemical reactivity represent supramolecular approaches to achieve stereo- and regio-controlled formation of complex molecules as products. Our research group has introduced a general supramolecular strategy that utilizes small-molecule ditopic receptors as templates to assemble and preorganize functionalized olefins into the prerequisite geometry for an intermolecular [2+2] photoreaction in the solid state (Scheme 27.1a). For a [2+2] photodimerization to occur in a solid, reactive centers are generally required to adhere the topochemical postulates of Schmidt, being parallel and separated by 4.2 Å [1]. The template-directed method exploits weak, noncovalent bonds to preorganize the alkenes into suitable positions to react, being effectively forced into a parallel orientation.

As an example, *trans*-1,2-bis(4-pyridyl)ethylene (**4,4′-bpe**) is photostable as a pure component in the solid state. When the olefin is cocrystallized with the ditopic hydrogen-bond donor resorcinol (**res**), the alkene is assembled via O–H···N hydrogen bonds into a discrete, four-component assembly. The carbon–carbon double (C=C) bonds are aligned parallel and separated by 3.65 Å. Ultraviolet (UV) radiation of a crystalline sample results in the stereo-controlled formation of tetrakis(4-pyridyl)cyclobutane (**4,4′-tpcb**) in 100% yield and gram quantities. The pairs of 4-pyridyl groups that interact with each template are, thus, cisoid in the cyclobutane photoproduct. Subsequent removal of the **res** template by basic extraction allows for the isolation of **4,4′-tpcb** (Scheme 27.1b) [2].

In addition to resorcinol, we have employed several other templates that operate by hydrogen bonding [3–5], halogen bonding [6], and coordination-driven self-assembly [7] to direct the [2+2] photodimerization. The method has also been extended to the assembly and reactivity of dienes and trienes, as well as several other symmetrical and unsymmetrical olefins, to synthesize cyclobutane products that are otherwise challenging to obtain in solution such as ladderanes [8] and [2.2]cyclophanes [9, 10].

Supramolecular Catalysis: New Directions and Developments, First Edition.
Edited by Piet W.N.M. van Leeuwen and Matthieu Raynal.

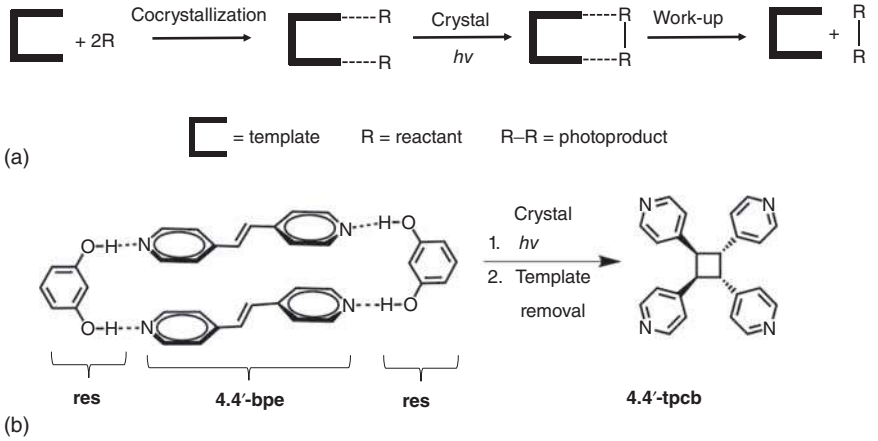

Scheme 27.1 (a) Template approach to control photoreactivity in solid state and (b) formation of **4,4′-tpcb** using hydrogen-bond donor template (**res**).

Accordingly, our chapter will begin with the introduction to our template-directed solid-state strategy that makes use of ditopic receptor molecules to control the [2+2] photodimerization in solid state. An initial highlight will be on the field of mechanochemistry. We will discuss template-directed solid-state [2+2] photoreactions using the application of solvent-free and liquid-assisted grinding (LAG). We will then discuss our efforts to use the ditopic receptors as small-molecule supramolecular catalysts to direct the photodimerization. We address a role of mechanochemistry to achieve catalytic turnover and describe a technique based on vortex mixing. The vortex method allows for simultaneous grinding and UV irradiation of a solid sample in a single pot and can be applied to both organic (i.e. cocrystals) and inorganic materials (e.g. metal–organic frameworks, MOFs). We also discuss our efforts to achieve mechanochemically mediated cascade reactions that combine molecular-and-supramolecular chemistry in a single pot.

27.2 State of Mechanochemistry

Mechanochemistry is the application of mechanical energy to achieve chemical transformations. Mechanochemistry holds a central place in the development of solvent-free chemistry and has introduced new perspectives in areas of organic and inorganic syntheses, supramolecular chemistry, organometallics, pharmaceuticals, materials science, and crystal engineering [11, 12]. Benefits to perform mechanochemistry include reducing time for synthesis, cost, and waste generation. In 2019, mechanochemistry was recognized by the IUPAC as one of the top 10 emerging chemical technologies [13, 14]. It should be noted that work of Toda in the 1980s spurred interest in the use of grinding and milling reactions as a green approach to perform environmentally friendly and solvent-free chemistry in connection to ideas of the organic solid state [15]. Synthetic advantages of

molecular mechanochemistry are becoming established, furnishing ready access and improved yields to diverse organic reactions that include C—C bond formations, metal-catalyzed couplings, copper-catalyzed 1,3-dipolar cycloadditions, and C–H activation reactions [16]. It is within the past decade that supramolecular chemistry has provided developments in the areas of cocrystals, capsules, catenanes, and rotaxanes so as to provide platforms to expand the synthetic potential of mechanochemistry. Supramolecular chemistry by milling or grinding is now a viable means to generate supramolecular complexes, coordination metal complexes, molecular and supramolecular cages, open frameworks, and interlocked architectures [17].

27.2.1 Our Studies in Mechanochemistry

In 2008, we demonstrated that mortar-and-pestle grinding can be used to assemble ditopic template molecules and olefins into photoactive cocrystals composed of discrete four-component hydrogen-bonded assemblies [18]. We employed hydrogen-bond donor [**res** and **res**-derivatives: **R-res**] and hydrogen-bond acceptor [2,3-bis(4-methylenethiopyridyl)naphthalene (**2,3-nap**), and 1,8-bis(4-pyridyl)naphthalene (**1,8-dpn**)] templates to generate photoreactive assemblies via both dry and LAG (Scheme 27.2).

Hydrogen-bond donor templates – Co-grinding of **res** with **4,4′-bpe** in a mortar-and-pestle generated the photoactive cocrystal (**res**)·2(**4,4′-bpe**) in quantitative yield. The assemblies were determined to form and react, using powder X-ray diffraction (PXRD) and ^{1}H NMR spectroscopy, within periods as little as 15 minutes. To generalize the approach, we used **res**-based templates to assemble symmetrical **2,2′-bpe** and unsymmetrical *trans*-1-(2-pyridyl)-2-(4-pyridyl)ethylene (**2,4′-bpe**). Dry grinding of **R-res** (5-methoxy; 5-cyano; 4,6-dichloro) with **4,4′-bpe** afforded 2(**R-res**)·2(**4,4′-bpe**) in approximately 15 minutes. Likewise, cocrystals 2(**res**)·2(**2,2′-bpe**), and 2(**4-Cl-res**)·2(**2,4′-bpe**) formed rapidly. UV irradiation of the solids generated the corresponding cyclobutane photoproducts stereospecifically and in up to 100% yield.

Hydrogen-bond acceptor templates – We also demonstrated that hydrogen-bond acceptor templates **2,3-nap** and **1,8-dpn** form photoactive solid-state assemblies with fumaric acid (**fum**). In contrast to the hydrogen-bond donor templates based on **res**, however, 2(**2,3-nap**)·2(**fum**) and 2(**1,8-dpn**)·2(**fum**) formed only using LAG. In general, co-grinding of fum with either **2,3-nap** or **1,8-dpn** with a small aliquot of ethyl acetate for approximately 10 minutes afforded cocrystals 2(**2,3-nap**)·2(**fum**) and 2(**1,8-dpn**)·2(**fum**), respectively, as confirmed by PXRD.

27.3 Organic Catalysis and Mechanochemistry

The ability of small molecules to catalyze organic reactions with efficiencies akin to enzymes has advantages such as lower toxicity, better tolerance to moisture and

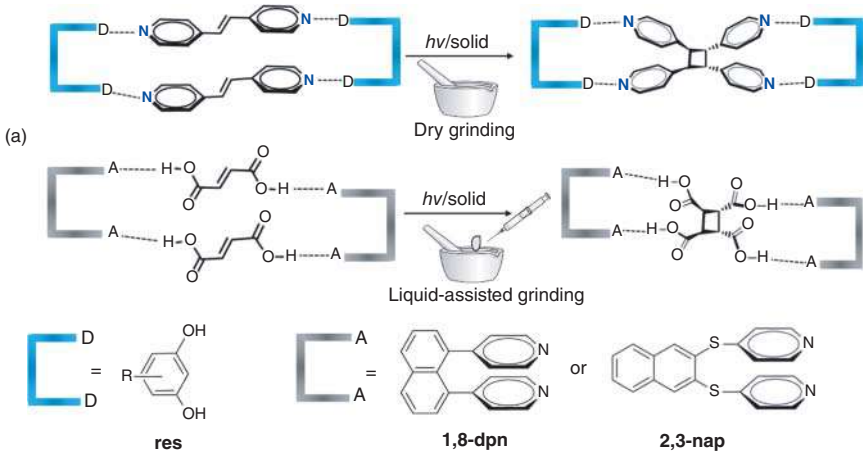

Scheme 27.2 Hydrogen-bond-assisted [2+2] photodimerizations via grinding: (a) hydrogen-bond donor templates using dry grinding and (b) hydrogen-bond acceptor templates using LAG.

air compared to transition metal analogs, excellent compatibility, and scope for high stereoselectivity [19]. During the past 20 years, an area of catalysis that has grown in relation to applications of mechanochemistry is organocatalysis. The area uses small organic molecules to catalyze organic reactions under solvent-free conditions (e.g. ball milling, microwave, and ultrasound irradiation) [20]. The growth has allowed mechanochemistry to be considered a platform to conduct organocatalytic transformations. The use of solvent-free ball milling for organocatalytic reactions can feature higher yields, shorter reaction times, and improved and/or new selectivities compared to analogous reactions in solution [21]. Pioneering work of Bolm, in this regard, has demonstrated the ability of 10 mol% (*S*)-proline to catalyze an asymmetric aldol reaction under solvent-free conditions [20]. The reaction proceeded efficiently with shorter times and in high yield to give the *anti*-aldol products with up to 99% enantiomeric excess (ee). Several other organocatalyzed transformations (e.g. Michael addition, Baylis–Hillman reaction, Mannich reaction) have also been similarly reported [22].

27.3.1 Supramolecular Catalysis by Ditopic Receptors

The concept of supramolecular catalysis generally embraces molecular recognition, templating, and host–guest chemistry to achieve a transformations catalyzed by organic molecules [23]. The field originated with a desire to understand how Nature uses enzymes to catalyze highly efficient and selective biochemical reactions from a structural viewpoint [24]. Supramolecular catalysis is different from classical catalysis, as the binding step in supramolecular catalysis relies on molecular recognition

and organization to facilitate transformation to product. Thus, in supramolecular catalysis, noncovalent interactions such as hydrogen bonding, cation-/anion–π interactions, hydrophobic effects, and halogen bonding play important roles to form organized and geometrically enforced catalyst–substrate complexes.

To increase the rate and/or selectivity of organic transformations, approaches to design supramolecular catalysts based on concepts of molecular recognition were introduced. In this context, examples have reported on uses of molecular templates to catalyze chemical reactions in solution by participating in hydrogen bonds with substrates. The first small-molecule ditopic receptor that served as a supramolecular catalyst was reported by Kelly in 1989. The work described molecular-oriented substrates that participated in an S_N2 alkylation of an amine by an alkyl halide. Later, Bassani described the use of a ditopic catalyst to direct a [2+2] photodimerization of a cinnamic acid in solution. The works of Kelly and Bassani required on the order of stoichiometric amounts of catalyst owing to effects of solvation and entropy on structure that is inherent to the liquid phase [25].

27.3.2 Our Studies in Supramolecular Catalysis and Mechanochemistry

In 2010, we turned to determine if small-molecule ditopic receptors based on **res** could function as supramolecular catalysts mechanochemically in the organic solid state. It was unclear whether supramolecular catalysis could be achieved given that diffusion rates of molecules in the crystalline state are in the order of 10^{-15} m^2 s^{-1}, which is at least 6 orders of magnitude less than in solution. Catalysis was achieved by dry mortar-and-pestle grinding. 4,6-Dichlororesorcinol (**4,6-diCl-res**) acted as a supramolecular catalyst of a [2+2] photodimerization of **4,4′-bpe** to form **4,4′-tpcb**. The cyclobutane photoproduct was generated stereospecifically and in high yield (i.e. >90%) (Scheme 27.3) [26]. Turnover was facilitated by the dry grinding using 50%, 20%, and 10% catalyst "loadings." Each grinding step resulted in crystallization of the photoproduct in a solid mixture. DFT calculations performed on the hydrogen-bonded assemblies before and after photoreaction

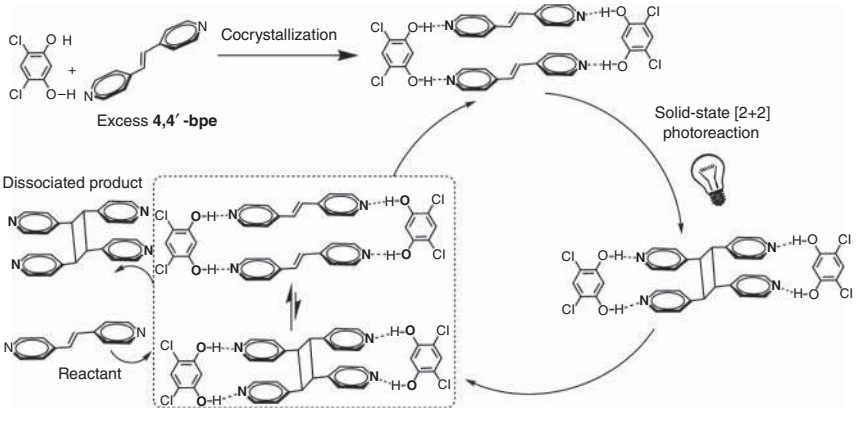

Scheme 27.3 Supramolecular catalysis of the [2+2] photodimerization using 4,6-**diCl-res**.

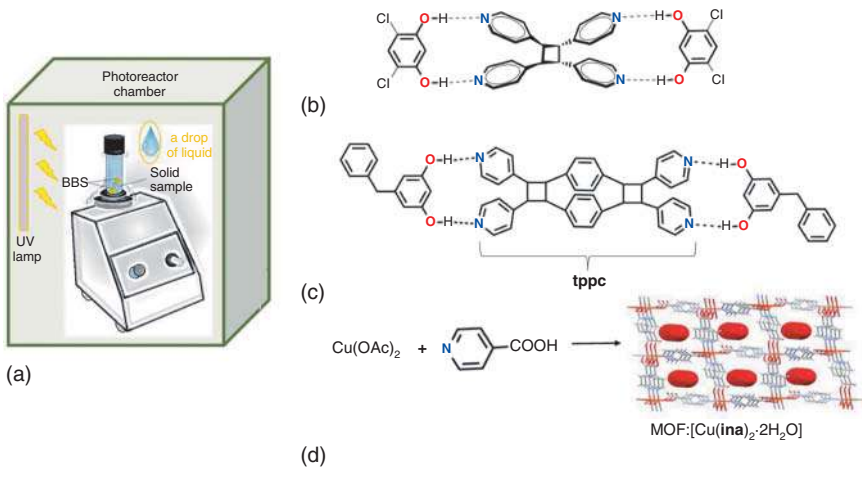

Scheme 27.4 Schematics depicting: (a) vortex grinding apparatus with application of UV radiation and use to generate (b) **4,4′-tpcb**, (c) **tppc**, and (d) 2D MOF [Cu**(ina)**$_2$]·2H$_2$O. Source: Reproduced from Ref. [28] with permission from the Royal Society of Chemistry.

revealed that the binding energy of the photoproduct within the hydrogen-bonded assembly is relatively low. A weaker C–H···N interaction and a tendency of the assembly to assume a helical twisted conformation was considered to destabilize the photoreacted structure by approximately 1.1 kcal mol^{-1}. The scope of the supramolecular catalysis was expanded by demonstrating boronic acids to function as small-molecule hydrogen-bond donor catalysts [27].

We later reported a modification to catalyze the [2+2] photodimerization under grinding conditions. We showed the efficiency of the supramolecular catalysis to be improved using automated vortex grinding (Scheme 27.4). An apparatus was developed based on a sample vial and small metal ball bearings (BBs) that allowed for simultaneous grinding and UV irradiation using a vortex mixer (Scheme 27.4a) [28]. Simultaneous grinding and UV radiation of **4,4′-bpe** with 50 mol% of **4,6-diCl-res** using vortex mixing afforded **4,4′-tpcb** in 97% yield in a period of one day (Scheme 27.4b). The catalysis achieved using the vortex grinding technique was on the order of four times faster versus mortar-and-pestle grinding. The simultaneous exposure of the sample to mechanical stress, induced by collisions with the BBs, and to internal build-ups of stress in the crystalline state as a result of the photodimerization was considered to support the enhanced reactivity and catalysis.

We expanded the scope of vortex grinding for the one-pot syntheses of the tetra(4-pyridyl)[2.2]paracyclophane (**tppc**) under LAG conditions (Scheme 27.4c). [2.2]Cyclophanes are a general class of layered aromatic compounds with applications in areas ranging from chemical synthesis (e.g. catalysis) to materials science (e.g. optical materials). We demonstrated that when the small molecule template 4-benzyl-resorcinol (**4-benz-res**) and diene *p*-di[2-(4-pyridyl)ethenyl]benzene (**1,4-bpeb**) were subjected to vortex grinding and in the presence of UV light

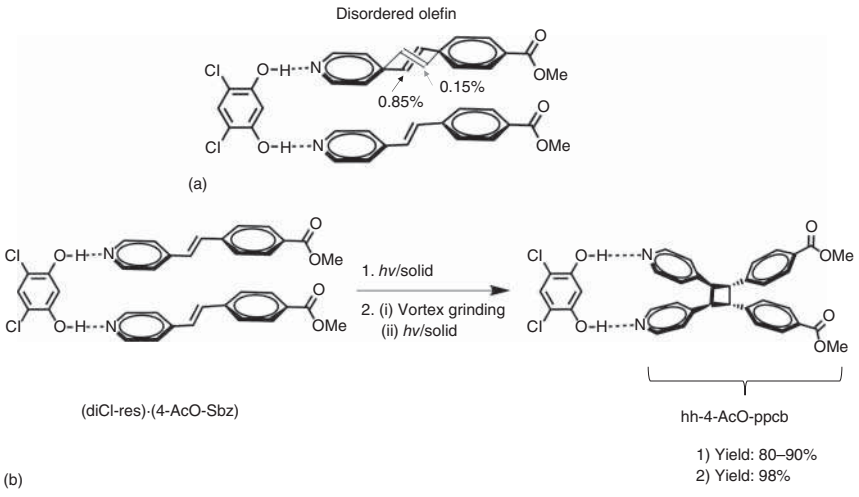

Scheme 27.5 Schematics depicting: (a) disordered (**4,6-diCl-res**)·2(**4-AcO-Sbz**), and (b) post-application of vortex grinding applied to **hh-4-AcO-ppcb** to improve product yield.

and small amount of solvent, the [2.2]paracyclophane **tppc** was generated stereoselectively in quantitative yield [29]. We also demonstrated application of the vortex method to form a MOF. Vortex grinding of copper acetate monohydrate and isonicotinic acid (HINA) afforded the two-dimensional (2D) MOF [Cu(**ina**)$_2$]·2H$_2$O (where: **ina** = isonicotinate) as confirmed by PXRD (Scheme 27.4d).

In 2016, vortex grinding was used to improve the yield of a solid-state [2+2] photodimerization. The grinding was employed to overcome detrimental effects of static disorder [30]. To demonstrate the utility of the approach, the template-directed [2+2] photodimerization of the ester-functionalized stilbazole (**4-AcO-Sbz**) was studied (Scheme 27.5). Cocrystallization of **4,6-diCl-res** and **4-AcO-Sbz** generated the three-component hydrogen-bonded assembly (**4,6-diCl-res**)·2(**4-AcO-Sbz**) with the two olefins stacked head-to-head with the C=C bonds separated by 3.86 Å. A C=C bond of one olefin was disordered, such that the C=C bonds of the two stacked alkenes were in a criss-cross geometry (occupancies 0.85 and 0.15). UV irradiation of the solid generated the corresponding head-to-head cyclobutane (**hh-4-AcO-ppcb**) in 80–90% yield. The suppressed yield was attributed to static disorder of the C=C bonds that prohibits the misaligned C=C bonds to react (Scheme 27.5a). When the solid was subjected to vortex grinding, enhanced reactivity (i.e. increase in yield) was realized to produce **hh-4-AcO-ppcb** in quantitative yield (Scheme 27.5b).

27.4 Cascade Reactions and Mechanochemistry

The idea that two or more reactions can operate in sequence, or as cascade reactions, has inspired chemists to develop organic reactions that occur in sequence and, in doing so, generate complex products (e.g. natural products). Cascade reactions are

critical for biological processes where molecular recognition capabilities of enzymes convert substrates to products. Natural enzymes are, thus, now more regularly integrated into cascade processes in the field of biotechnology, and organic catalysts are exhibiting prominent roles in the development of organocascade processes.

In 2020, we hypothesized that a small-molecule ditopic template could be integrated into a cascade reaction. We developed a template that combines organic synthesis, supramolecular chemistry, and solid-state photochemistry in a single pot [31]. Our work resulted in a mechanochemically mediated Diels–Alder reaction to generate the hydrogen-bond donor template **dat** (Scheme 27.6). **Dat** was generated *in situ* by vortex grinding in the presence of a small amount of water. The resulting dicarboxylic acid then acted as a ditopic template to assemble stacking of **4,4′-bpe** in the cocrystal 2(**dat**)·2(**4,4′-bpe**). The stacked olefins photodimerized to generate **4,4′-tpcb** in quantitative yield. Moreover, we showed that the Diels–Alder reaction to form **dat**, the cocrystallization to form 2(**dat**)·2(**4,4′-bpe**), and the photodimerization to generate **4,4′-tpcb** occurs in a one-pot cascade process using vortex grinding. In a broader sense, mechanical approach performed via the organic solid state was akin to cascade reactivity conducted in the liquid phase. The method combined molecular and supramolecular processes in the form of covalent synthesis

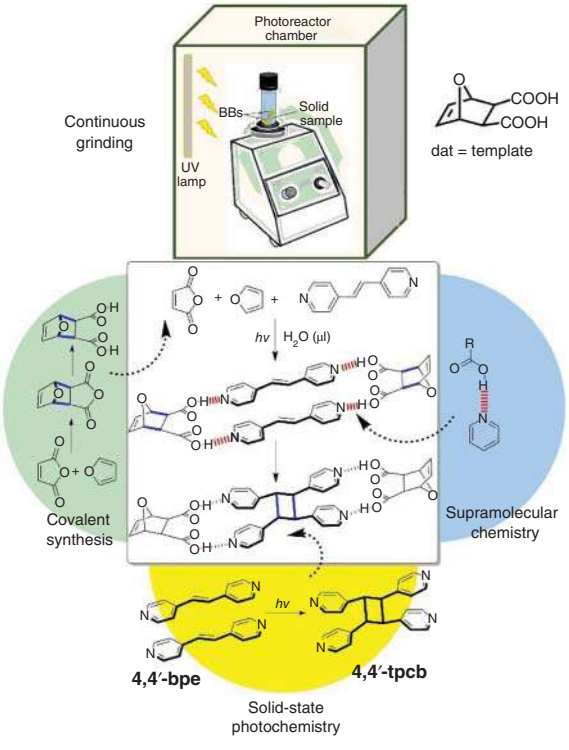

Scheme 27.6 Mechanochemical cascade with template **dat** that generates **4,4′-tpcb**. Source: Reproduced from Ref. [31] with permission from the Royal Society of Chemistry.

(molecular), self-assembly (supramolecular synthesis), and crystal engineering (solid-state photochemistry) to generate **4,4′-tpcb**.

27.5 Concluding Remarks

In this chapter, we have described a supramolecular strategy that utilizes small-molecule ditopic templates to preorganize olefins into the prerequisite geometry for a reaction in the solid state. The templates have been developed as small-molecule supramolecular catalyst to direct the [2+2] photodimerization by grinding or mechanochemical conditions. The method overcomes low-diffusion rates of molecules in solids with the catalysis occurring in crystalline environments to generate products in quantitative yield. Examples that demonstrate mechanochemistry as a mean to generate synthetic targets of architecturally rich molecules such as substituted cyclobutanes, ladderanes, and [2.2]cyclophanes have been presented. The approach has also been developed to support multi-step and one-pot cascade reactivity.

Acknowledgments

We acknowledge the National Science Foundation for funding of the work (LRM DMR-1708673).

References

1 Cohen, M., Schmidt, G., and Sonntag, F. (1964). 384. Topochemistry. Part II. The photochemistry of *trans*-cinnamic acids. *J. Chem. Soc.*: 2000–2013.
2 MacGillivray, L.R., Reid, J.L., and Ripmeester, J.A. (2000). Supramolecular control of reactivity in the solid state using linear molecular templates. *J. Am. Chem. Soc.* 122: 7817–7818.
3 Bhattacharya, S., Stojakovic, J., Saha, B.K., and MacGillivray, L.R. (2013). A product of a templated solid-state photodimerization acts as a template: single-crystal reactivity in a single polymorph of a cocrystal. *Org. Lett.* 15: 744–747.
4 Papaefstathiou, G.S., Duncan, A.J., and MacGillivray, L.R. (2014). Two act as one: unexpected dimers of catechol direct a solid-state [2+2] photodimerization in a six-component hydrogen-bonded assembly. *Chem. Commun.* 50: 15960–15962.
5 Macgillivray, L.R., Papaefstathiou, G.S., Friščić, T. et al. (2008). Supramolecular control of reactivity in the solid state: from templates to ladderanes to metal–organic frameworks. *Acc. Chem. Res.* 41: 280–291.
6 Sinnwell, M.A., Blad, J.N., Thomas, L.R., and MacGillivray, L.R. (2018). Structural flexibility of halogen bonds showed in a single-crystal-to-single-crystal [2+2] photodimerization. *IUCrJ* 5: 491–496.

7 Chu, Q., Swenson, D.C., and MacGillivray, L.R. (2005). A single-crystal-to-single-crystal transformation mediated by argentophilic forces converts a finite metal complex into an infinite coordination network. *Angew. Chem. Int. Ed.* 44: 3569–3572.

8 Gao, X., Friščić, T., and MacGillivray, L.R. (2004). Supramolecular construction of molecular ladders in the solid state. *Angew. Chem. Int. Ed.* 43: 232–236.

9 Elacqua, E., Friščić, T., and MacGillivray, L.R. (2012). [2.2]Paracyclophane as a target of the organic solid state: emergent properties via supramolecular construction. *Isr. J. Chem.* 52: 53–59.

10 Friščić, T., Elacqua, E., Dutta, S. et al. (2020). Total syntheses supramolecular style: solid-state construction of [2.2]cyclophanes with modular control of stereochemistry. *Cryst. Growth Des.* 20: 2584–2589.

11 Agarwal, J., Rani, R., and Peddinti, R.K. (2017). Mechanochemical grinding Diels–Alder reaction: highly efficient and rapid access to bi-, tri-, and tetracyclic systems. *Synlett* 28: 1336–1340.

12 Do, J.-L. and Friščić, T. (2017). Chemistry 2.0: developing a new, solvent-free system of chemical synthesis based on mechanochemistry. *Synlett* 28: 2066–2092.

13 Friščić, T., Mottillo, C., and Titi, H.M. (2020). Mechanochemistry for synthesis. *Angew. Chem. Int. Ed.* 59: 1018–1029.

14 Beyer, M.K. and Clausen-Schaumann, H. (2005). Mechanochemistry: the mechanical activation of covalent bonds. *Chem. Rev.* 105: 2921–2948.

15 Tanaka, K. and Toda, F. (2000). Solvent-free organic synthesis. *Chem. Rev.* 100: 1025–1074.

16 Tan, D. and Friščić, T. (2018). Mechanochemistry for organic chemists: an update. *Eur. J. Org. Chem.* 2018: 18–33.

17 Friščić, T.J.C.S.R. (2012). Supramolecular concepts and new techniques in mechanochemistry: cocrystals, cages, rotaxanes, open metal–organic frameworks. *Chem. Soc. Rev.* 41: 3493–3510.

18 Atkinson, M.B., Bučar, D.-K., Sokolov, A.N. et al. (2008). General application of mechanochemistry to templated solid-state reactivity: rapid and solvent-free access to crystalline supermolecules. *Chem. Commun.*: 5713–5715.

19 Zhou, Q.L. (2016). Transition-metal catalysis and organocatalysis: where can progress be expected? *Angew. Chem. Int. Ed.* 55: 5352–5353.

20 Bruckmann, A., Krebs, A., and Bolm, C. (2008). Organocatalytic reactions: effects of ball milling, microwave and ultrasound irradiation. *Green Chem.* 10: 1131–1141.

21 Kristofikova, D., Modrocká, V., Mečiarová, M., and Sebesta, R.J.C. (2020). Green asymmetric organocatalysis. *ChemSusChem* 13: 2828–2858.

22 Hernández, J., Avila-Ortiz, C., and Juaristi, E. (2014). Useful chemical activation alternatives in solvent-free organic reactions. In: *Comprehensive Organic Synthesis*, 2e, vol. 9 (eds. G.A. Molander and P. Knochel), 287–314. Oxford: Elsevier.

23 Raynal, M., Ballester, P., Vidal-Ferran, A., and van Leeuwen, P.W.N.M. (2014). Supramolecular catalysis. Part 1: Non-covalent interactions as a tool for building and modifying homogeneous catalysts. *Chem. Soc. Rev.* 43: 1660–1733.

24 Vriezema, D.M., Comellas Aragonès, M., Elemans, J.A. et al. (2005). Self-assembled nanoreactors. *Chem. Rev.* 105: 1445–1490.

25 Ma, D.-Y. and Wärnmark, K. (2010). Mechanoassisted supramolecular catalysis in solid state synthesis. *ChemCatChem* 2: 1059–1060.

26 Sokolov, A.N., Bučar, D.K., Baltrusaitis, J. et al. (2010). Supramolecular catalysis in the organic solid state through dry grinding. *Angew. Chem. Int. Ed.* 122: 4369–4373.

27 Campillo-Alvarado, G., Brannan, A.D., Swenson, D.C., and MacGillivray, L.R. (2018). Exploiting the hydrogen-bonding capacity of organoboronic acids to direct covalent bond formation in the solid state: templation and catalysis of the [2+2] photodimerization. *Org. Lett.* 20: 5490–5492.

28 Stojaković, J., Farris, B.S., and MacGillivray, L.R. (2012). Vortex grinding for mechanochemistry: application for automated supramolecular catalysis and preparation of a metal–organic framework. *Chem. Commun.* 48: 7958–7960.

29 Stojaković, J., Farris, B.S., and MacGillivray, L.R. (2014). Liquid-assisted vortex grinding supports the single-step solid-state construction of a [2.2]paracyclophane. *Faraday Discuss.* 170: 35–40.

30 Elacqua, E., Kummer, K.A., Groeneman, R.H. et al. (2016). Post-application of dry vortex grinding improves the yield of a [2+2] photodimerization: addressing static disorder in a cocrystal. *J. Photochem. Photobiol. A* 331: 42–47.

31 Yelgaonkar, S.P., Swenson, D.C., and MacGillivray, L.R. (2020). Supramolecular chemistry under mechanochemical conditions: a small molecule template generated and integrated into a molecular-to-supramolecular and back-to-molecular cascade reaction. *Chem. Sci.* 11: 3569–3573.

28

Exploration of Halogen Bonding for the Catalysis of Organic Reactions

Revannath L. Sutar and Stefan M. Huber

Ruhr-University Bochum, Faculty for Chemistry and Biochemistry, University Street, 150, Bochum, 44801, Germany

28.1 Introduction

Even though it was not recognized at that time, Colin's discovery of a 1 : 1 complex between molecular iodine and ammonia in 1814 [1] eventually lead to the introduction of a further noncovalent interaction to organic chemistry. This binding between electrophilic halogen substituents and Lewis bases was later defined as halogen bonding (XB) [2, 3]. It was investigated only scarcely for a long time, with renewed interest emerging in the 1990s [4], particularly in the context of crystal engineering [5]. Meanwhile, the use of molecular iodine for promoting numerous organic transformations was already introduced in 1915 [6]. Although the exact mode of activation was rather unclear for a long time, its excellent performance has attracted attention as a sustainable and relatively inexpensive alternative to transition metal catalysis [7]. Out of three possible modes of activation (as Brønsted acid, as Lewis acid and via I^+), the Lewis acid catalysis represents one noteworthy application of XB in solution [8]. The interaction of I_2 with common Lewis bases has also been systematically quantified [9].

Elemental iodine, however, lacks any options of further modification, and thus increased attention has been directed to organic XB donors. Based on fundamental studies on their Lewis acidity [10], this class of compounds has by now been successfully introduced in organocatalysis. In general, electronegative or polarizing groups are required to polarize the halogen. This includes cationic ones – mainly triazolium, (benz)imidazolium or iodonium derivatives (cf. Figures 28.1 and 28.2) – and those with neutral backbones like polyfluorinated alkyl/aryl moieties or alkynes (see Figure 28.3). In particular, 1,2,3-triazolium derivatives are very attractive due to the ease of the synthesis and their stability [11].

Weakly Lewis basic compounds like ketones, aldehydes, or esters usually only weakly associate with iodine and other halogen bond donors. However, solid-state studies have shown that this coordination to carbonyl compounds is indeed possible even in a bidentate fashion [12], which should be sufficient for activation and

Supramolecular Catalysis: New Directions and Developments, First Edition.
Edited by Piet W.N.M. van Leeuwen and Matthieu Raynal.

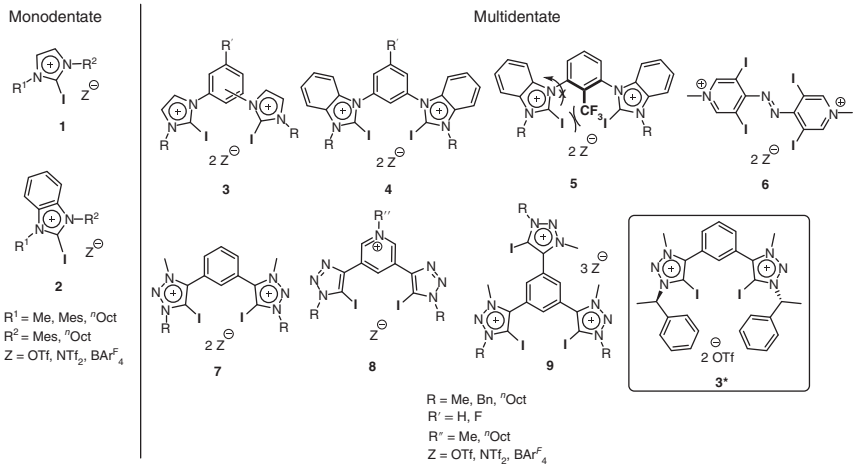

Figure 28.1 Cationic XB donors.

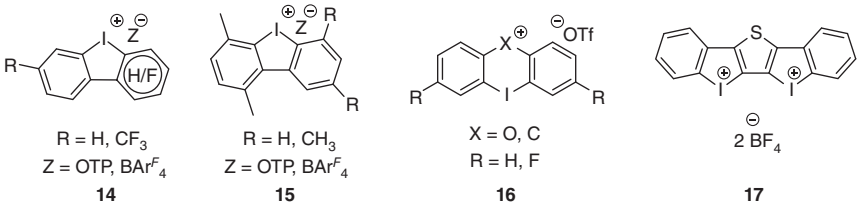

Figure 28.2 Iodine(III)-derived XB donors.

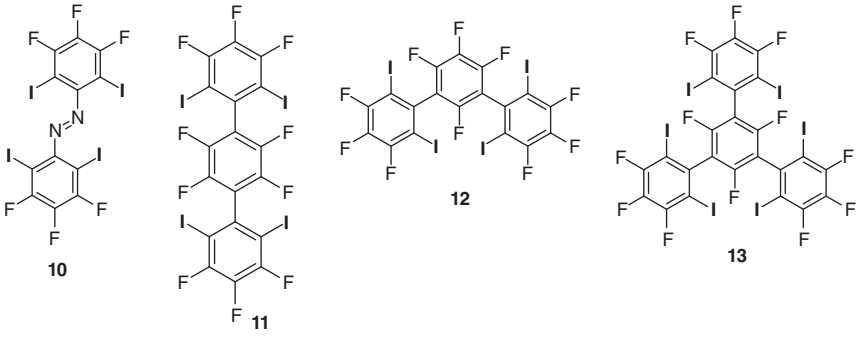

Figure 28.3 Neutral multidentate XB donors.

catalysis. In fact, halogen bonding results in the activation of both the halogen bond donor and the acceptor, and both effects have been used in synthesis [13]. Based on the strength of the interaction and the stability of the formed adduct, the interaction can be transient or non-transient. In the former case, the R—X bond of the XB donor is cleaved in the course of the reaction, often with transfer of X^+ to a substrate, and thus all classical halogenation reactions fall under this category. Here, we

will focus on the second alternative, in which a non-transient XB is formed between an XB donor and a substrate, with the former then acting as a stable noncovalent organocatalyst.

The first report on this method was published by Bolm and coworkers, who suggested the involvement of XB between perfluoroalkyl iodides (as catalysts) and quinolines during a Hantzsch ester reduction [14]. Although the exact mode of catalysis is still under discussion [7i, 15], this case introduced the concept of polarized organohalogen compounds performing the catalytic function of molecular iodine. In the last decade, many new examples of this catalysis have been introduced and the mode of activation has been clarified by several mechanistic and theoretical studies [15, 16]. Most cases can be placed in one of two different types of activation, which will be discussed in more detail below: halide abstraction reactions and activations of organic functional groups.

28.2 Halide Abstraction Reactions

There are many crystal engineering reports on the interaction of mono- and multidentate halogen bond donors with halides [17]. In the solution phase, this phenomenon can be used to abstract halides from the substrate (or to remove them from an equilibrium) in order to induce nucleophilic substitution reactions (Figure 28.4a). With this hypothesis in mind, a series of neutral and cationic mono- and multidentate halogen bond donors were tested as promoters in a benchmark reaction of halide abstraction – the Ritter-type solvolysis of benzhydryl bromide in acetonitrile (Scheme 28.1a) [18, 19a, b, e]. In this halide abstraction reaction, the multidentate cationic (triflate salts of **3**, **6**, **7**; Figure 28.1) and neutral XB donors (**11**; Figure 28.3) were expectedly more efficient than their monodentate analogs (triflate salts of **1**, **2**). For structurally similar XB donors, the cationic variant (**6**) was far more active than the corresponding neutral analog (**10**) due to charge assistance [20]. For those XB donors featuring a benzene core, meta-substituted dicationic donors were more active than their para-substituted counterparts (for example **3**) due to the more appropriate bite angle. However, in the more challenging solvolysis of benzhydryl chlorides, these meta-substituted dicationic donors (**3.OTf**) showed inferior activity compared to iodine(III) derivatives (like **14**, **15**) [18b, d]. Recently, a few of these iodine(III) derivatives were screened for the effect of structural variations on the catalytic performance, and it was observed that the five membered iodolium derivatives especially those with the electron withdrawing fluorine substituents (**14**) are more active than the six-membered iodininium compounds (**16**) [18d]. The key role of halogen bonding in the mechanism of this reaction was supported by NMR studies, single-crystal X-ray analyses of adducts between XB donors and halides as well as by a series of comparison experiments. The reaction is driven by the formation of a stable XB donor/halide adduct, and thus the former is needed in stoichiometric amounts to induce the desired transformation. Not only the non-halogenated analogs of the XB donors, but also one of the most promising electrophilic hydrogen-bonding organocatalyst (Schreiner's thiourea) [19b], were

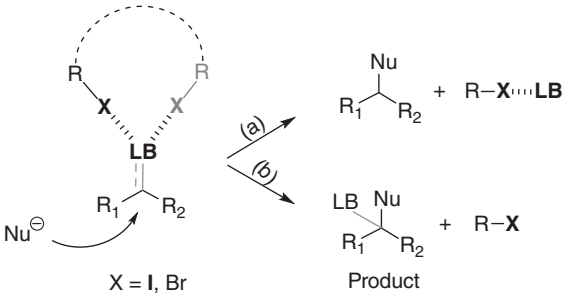

Figure 28.4 General representation of halogen-bonding catalysis: (a) halide abstraction and (b) activation of organic functional groups.

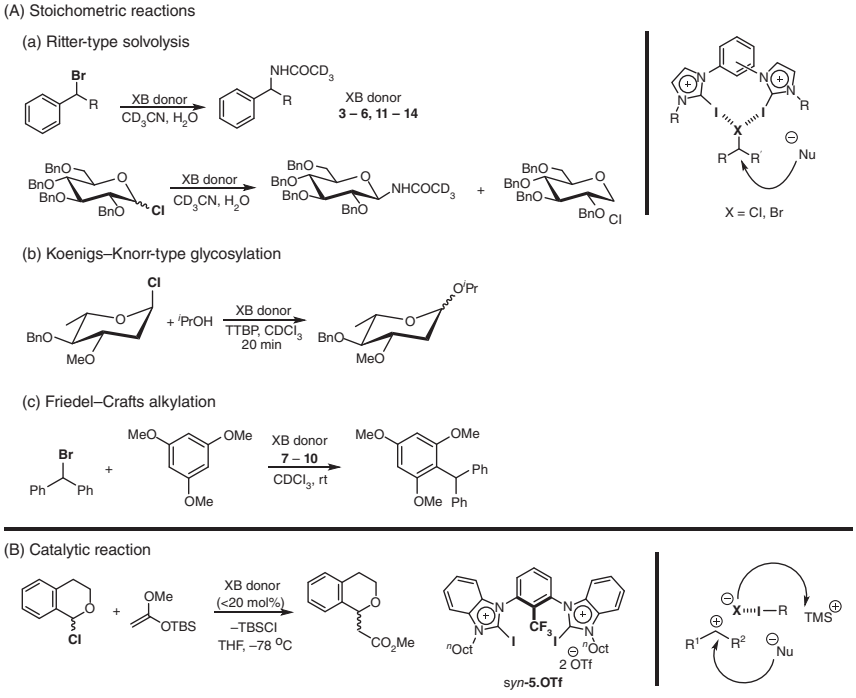

Scheme 28.1 XB-induced halide abstraction reactions.

markedly less active than the halogen-based Lewis acids. This peculiar catalytic activity of imidazolium-based halogen bond donors has recently been attributed to the combined effect of halogen bonding and lone pair···π interactions [18c]. Unfortunately, a 5-iodo-1,2,3-triazolium-based chiral halogen bond donor (**3***; Figure 28.1) did not induce any enantioselectivity in this reaction [19a].

Not only the just-mentioned solvolysis, but also the nucleophilic addition of isopropanol to a glycosyl chloride [19c] was achieved using this protocol (Scheme 28.1b). Lately, the use of halogen-bonding catalysis in glycosylation

reactions has been further extended to much more complex examples by Loh and coworkers [21].

The binding strengths of haloimidazolium-based bidentate halogen bond donors (**3**) to different halides (Cl, Br, I) were systematically investigated by isothermal calorimetric titrations [22]. The binding affinity showed little dependency on the weakly coordinating counteranions but was affected by the temperature and the bite angle. Thus, stronger binding was noted at higher temperature and also the meta-substituted dicationic donors showed higher binding constants than the para-substituted analogs.

As mentioned above, cationic XB donors showed higher Lewis acidy than neutral (poly- or perfluorinated) ones as a consequence of charge assistance (cationic XB donor, anionic substrate). Iodolium-based species (like **14**) in addition feature two perpendicular electrophilic axes which allow biaxial binding [23c]. On the other hand, halogen bonding can be strong enough to overcome charge repulsion, as has recently been demonstrated in two examples of "anti-electrostatic" XB [23a, b]. In these cases, the XB donor unit is overall negative even though the iodine-bearing substituent may be positively charged (as in the cyclopropenium system reported [23a]).

Cationic XB donors, however, suffer from issues such as low solubility due to ion pairing in nonpolar solvents, and sometimes also low stability. Thus, an increased cationic charge of these XB donors and the resulting strong coordination of counterions ($OTf^- > NTf_2^- > BAr^F{}_4^-$) may even reduce their Lewis acidity and catalytic activity. For instance, almost comparable activity was observed for bidentate dicationic (**7**) and monocationic XB donors (**8**) in a Friedel–Crafts alkylation reaction (Scheme 28.1c) [19d]. Further investigations dealing with the binding of these two XBs with halides indicated that this identical activity is the result of the compensation of a more favorable enthalpic contribution in **7** with a more favorable entropic contribution in **8**. These cationic XB donors generally have good stability in nonpolar solvents and at low temperature. The issue of low solubility of these donors in nonpolar solvents is typically resolved using long-chain alkyl substituents, which otherwise have a negligible effect on the catalytic activity.

One of the ways to avoid inhibition of the XB donors in halide abstraction reactions seems to be *in situ* dissociation of the XB donor–halide adducts. Owing to the strong affinity of silyl cations to halides, these could be efficient traps for the latter. Accordingly, the reaction between silyl enol ethers and 1-chloroisochroman was tested in the presence of various mono- and multidentate XB donors (Scheme 28.1B) [24]. Out of several monocationic (**1. Otf** and **2. OTf**), bidentate neutral (**11**, **12**, and **13**) [24a] or dicationic (**3. OTf**, **6. OTf**, **7. Otf**, and **5. OTf**) XB donors, a syn-preorganized one (*syn*-**5.OTf**) was found most active even at only 0.5 mol% loading [24b]. The high catalytic activity of this bidentate XB donor (*syn*-**5.OTf**), which results from the preorganization of the Lewis acidic iodine sites, was further corroborated by ITC titrations and the catalytic performance of structurally related non-preorganized XB donors in the same and a few other reactions (Ritter-type solvolysis, Friedel–Crafts alkylation, Michael addition, and Diels–Alder reaction) [25]. All the above studies indicated that the binding strengths of XB donors can be increased by the use

of multiple binding sites and particularly by syn-preorganization [24b, 25, 26]. The latter also helps to achieve asymmetric induction due to the formation of a rigid and confined chiral space (see below) [26d,e].

28.3 Activation of Organic Functional Groups

As discussed above, solid-state studies demonstrated the coordination of comparably weakly Lewis basic organic functional groups through halogen bonding (Figure 28.4) [12], which could be utilized for noncovalent organocatalysis. In fact, this weak coordination has the advantage of likely avoiding XB donor inhibition and thus enabling catalysis (unless other nucleophilic species deactivate the XB donor). Next to Bolm's initial report on possibly XB-based quinoline activation [14], this concept was first attempted for activating a carbonyl group – one of the most important functional groups in organic chemistry – in the Diels–Alder reaction between methyl vinyl ketone (MVK) and cyclopentadiene. Owing to the low Lewis basicity of this group, a strong dicationic halogen bond donor with non-coordinating $BAr^F{}_4$ counterions (**3.BAr$^F{}_4$**) was required (Scheme 28.2a) [27a]. The involvement of XB between the carbonyl group of MVK and the XB donor was rigorously supported by multiple control experiments. Recently, Wang's group used tripodal neutral XB donors similar to **13** as a model in DFT calculations and showed the competitive involvement of hydrogen and halogen bonding in this and related reactions [27b]. Later, the catalytic activity of variously substituted mono- and bidentate iodine(III) compounds was also exploited in this reaction [18b]. Monodentate iodine(III) compounds (e.g. **14** and **15a.BAr$^F{}_4$** (R = H)) showed comparable activity to that of bidentate dicationic organoiodine(I) XB donor (**3.BAr$^F{}_4$**). Notably, a bidentate iodine(III)-based XB donor (**17**) was found more active in a more challenging variant of this reaction involving 1,3-cyclohexadiene and MVK [28].

Next, the Michael addition of indole to *trans*-crotonophenone was attempted using these XB donors as catalyst. Consistent with earlier results on halide abstraction organocatalysis [24b], a syn-preorganized XB donor (*syn*-**5.BAr$^F{}_4$**) performed the best (Scheme 28.2b) [29a]. Meanwhile, Breugst's group screened the salts of various monodentate iodobenzimidazolium derivatives (OTf, NTf_2, BF_4, BPh_4, $BAr^F{}_4$ salts of **2**) [29b] and somewhat unexpectedly suggested the possibility of using coordinating anions (triflate) in this reaction. Later Scheidt and coworkers used chiral XB donors (**19**, **20**) and an achiral XB donor (**18**) in combination with chiral anions as catalysts for promoting this reaction, although without enantioselectivity [15a]. Based on these results and additional experiments, they doubtfully proposed the preference of a Brønsted-acid-catalyzed pathway over the XB activation. In a recent study, the activation of a doubly unsaturated ketone was performed through XB catalysis (Scheme 28.2c) [30]. Once again, the screening of several mono- and bidentate neutral and cationic XB donors indicated the best catalyst to be the syn-preorganized dicationic XB donor with non-coordinating

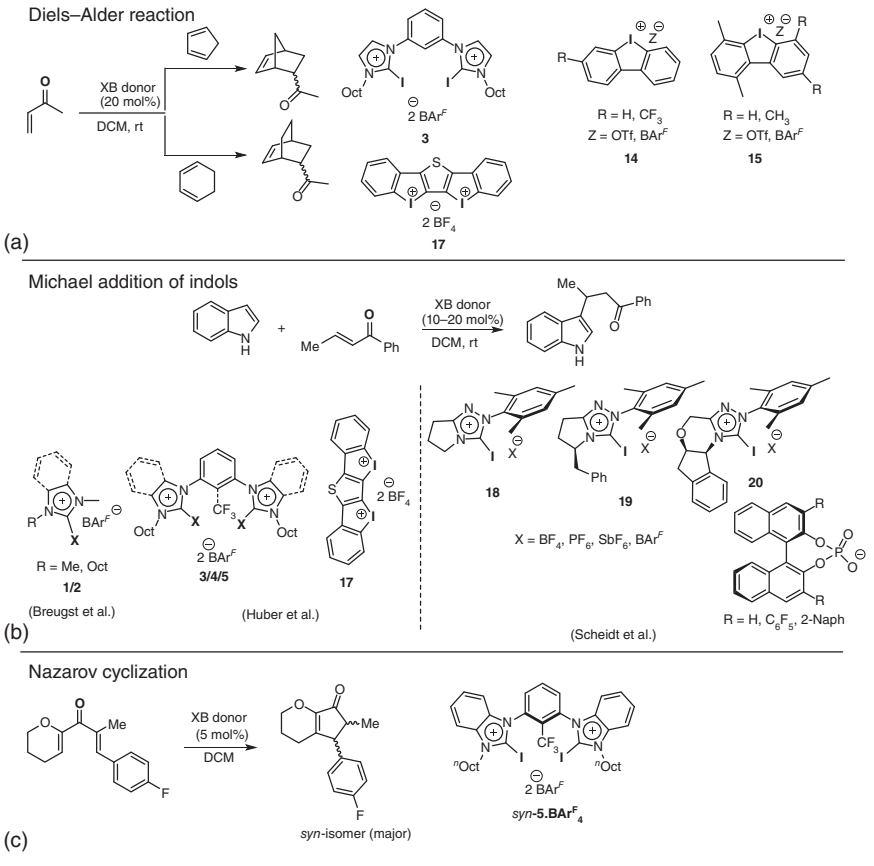

Scheme 28.2 XB-catalyzed reactions of conjugated carbonyl compounds.

$BAr^F{}_4$ anions (*syn*-**5.BAr$^F_4$**) [30b]. Thus, the results are consistent with all earlier examples of α,β-unsaturated carbonyl activation. In this Nazarov reaction, the main role of the XB donor is to induce the electrocyclization; the later step (keto-enol tautomerization) is likely independent of the catalyst.

Not only unsaturated carbonyls but also simple aldehydes undergo XB-donor-catalyzed nucleophilic addition reactions. Shibata and coworkers used powerful neutral XB donors bearing a C(sp^3)—I bond attached to a strongly electron-withdrawing fluorobis(sulfonyl) methane scaffold (**21** and **22**) for catalyzing a Mukaiyama aldol reaction [31a] (Scheme 28.3a). The involvement of halogen bonding as the main driving force was confirmed by NMR titrations, single-crystal XRDs, and DFT calculations. Recently, they attempted the asymmetric version of this reaction using a chiral fluorobis(sulfonyl) scaffold (**23**); however, no enantioselectivity has been obtained [31c]. Lately, this reaction was performed with an unprecedentedly low loading of above-mentioned bidentate XB donor *syn*-**5.BAr$^F_4$** as the catalyst

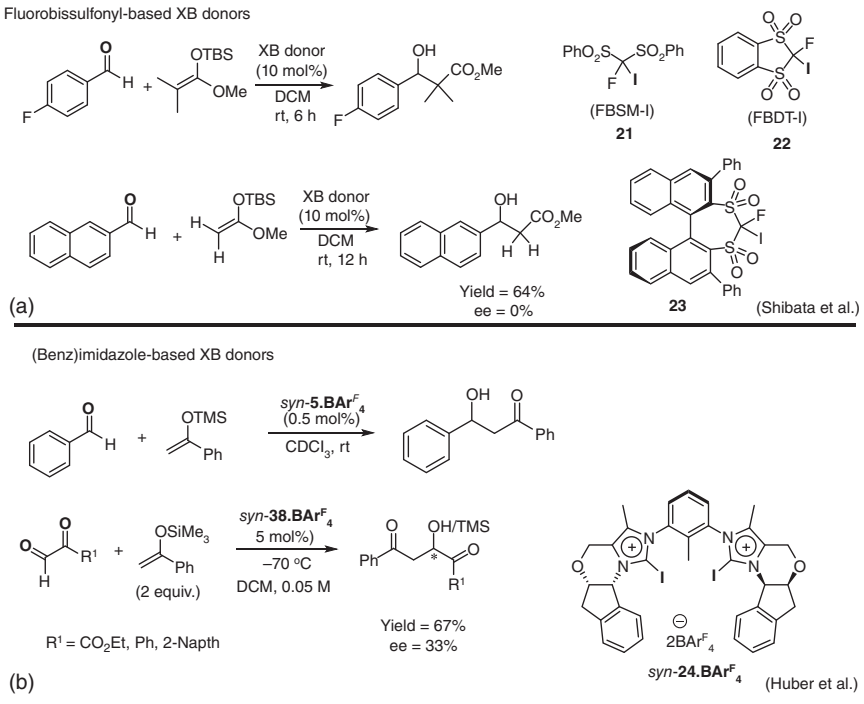

Scheme 28.3 XB-induced Mukaiyama aldol reactions.

at room temperature (Scheme 28.3b) [31b]. Once again, the involvement of XB by the catalyst (and not by traces of elemental iodine) with the carbonyl compound was established by various comparison experiments and theoretical calculations. Interestingly, this catalyst is stable in the reaction mixture for a couple of days and it works three times in a row without any loss in catalytic activity. In an enantioselective version of this reaction, a syn-preorganized chiral bidentate halogen bond donor (*syn*-**24.BAr$^F_4$** was used. The rigidification caused by the syn-preorganization and the chiral side arms of the XB donor induces moderate enantioselectivity (33% ee) when glyoxal derivatives are used as electrophiles [26d,e]. This is the first example in which asymmetric induction was observed solely through halogen bonding. However, no asymmetric induction was observed when monocarbonyl compounds (benzaldehyde and anisaldehyde) were used. During this work, a clear enantio discrimination of *trans*-1,2-diphenyl ethylene diamine was also achieved. This spatial enantiodifferentiation of the enantiomers in the complexed state (as XB adducts) was corroborated by DFT calculations and NCI plots, and it is in correlation with the observed enantioselectivity in the dicarbonyl reaction.

Very recently, the activation of another functional group, the nitro group, was achieved using a rather strong bidentate iodine(III)-based XB donor (**17**) (Scheme 28.4) [28]. This catalyst (5 mol%) promoted the Michael addition between 5-methoxyindole and *trans*-β-nitrostyrene at room temperature, whereas the most active iodine(I)-based XB donor *syn*-**5.BAr$^F_4$** was completely inactive.

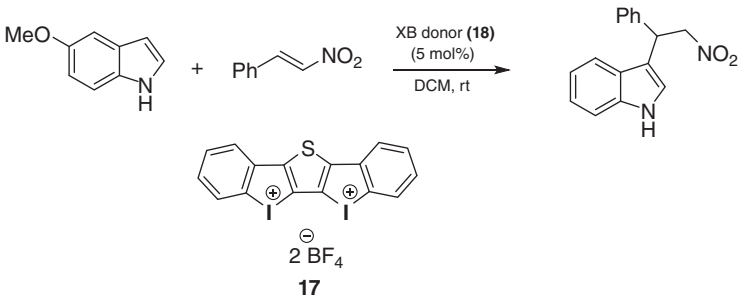

17

Scheme 28.4 Halogen-bonding-catalyzed nitro-Michael addition.

28.4 Activation of a Metal–Halogen Bond

In addition to the activation of carbon–halogen bonds mentioned in part 28.2, recently the XB-induced abstraction of chloride from metal pre-catalyst was reported as the main driving force for gold-catalyzed cycloisomerization reactions (Scheme 28.5) [32]. Based on the trends in the rate enhancement of the cyclizations, on ^{31}P NMR measurements and on DFT calculations, this role of XB was supported. Out of several mono- and bidentate XB donors tested as catalysts for this reaction, *syn*-**5.BAr$^F_4$** performed best. This still represents mostly a proof-of-principle case, however, as the more easily accessible NaBAr$^F_4$ provided superior performance as activator.

28.5 Conclusion

Inspired by the use of halogen bonding in the solid state and in anion recognition, the application of halogen bonding has now also been realized in organic transformations through the activation of functional groups such as organohalides, carbonyls, nitro groups, and even metal catalysts. The involvement of XB as the main driving force in promoting these reactions has been rigorously supported by experimental and theoretical means. Earlier studies demonstrated that the syn-preorganization of two iodine substituents could produce a highly active iodine(I)-based XB donor. However, recent results indicate the iodine(III)-based XB donors, particularly structurally rigid bidentate ones, are even more active catalysts, which will help to eliminate some doubts associated with halogen-bonding catalysis. There are many other interesting examples continuously emerging in which new modes of activation and catalysis are developed. These include, for instance, π-activation [33], aqueous catalysis [34], highly efficient glycosylation reactions [21], and the supramolecular rigidification of ligands around a metal center [35]. Even though halogen bonding catalysis now seems equally promising than its close analog – hydrogen-bonding organocatalysis – many challenges still remain. Examples of these are the application of XB catalysis to synthetically more relevant reactions and reaction environments as well as overcoming the sometimes weak

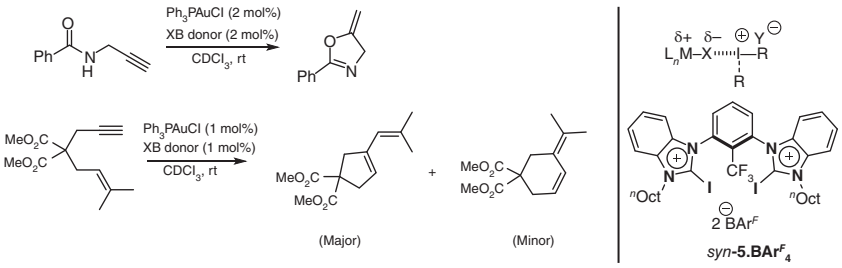

Scheme 28.5 XB-induced cleavage of a Au—Cl bond to generate an activated metal catalyst.

interaction with oxyanions and the occasionally low stability of cationic XB donors. Given the progress that has been achieved in this field in the last 10 years, these issues seem more than solvable.

References

1 Colin, J.J. (1814). Note sur quelques combinaisons de l'Iode. *Ann. Chim.* 91: 252–272.

2 Desiraju, G.R., Ho, P.S., Kloo, L. et al. (2013). Definition of the halogen bond (IUPAC recommendations 2013). *Pure Appl. Chem.* 85: 1711–1713.

3 For general reviews on halogen bonding, see (a) Gilday, L.C., Robinson, S.W., Barendt, T.A. et al. (2015). Halogen bonding in supramolecular chemistry. *Chem. Rev.* 115: 7118–7195. (b) Wang, H., Wang, W., and Jin, W.J. (2016). σ-Hole bond vs π-hole bond: a comparison based on halogen bond. *Chem. Rev.* 116: 5072–5104. (c) Cavallo, G., Metrangolo, P., Milani, R. et al. (2016). The halogen bond. *Chem. Rev.* 116: 2478–2601. (d) Costa, P.J. (2017). The halogen bond: nature and applications. *Phys. Sci. Rev.* 2: 2017–0136.

4 (a) Legon, A.C. and Warner, H.E. (1993). Isolation of stable intermediates in reactive gas mixtures: rotational spectrum of $H_3P\ldots Cl_2$ in a pulsed jet. *J. Chem. Phys.* 98: 3827–3832. (b) Weiss, R., Rechinger, M., and Hampel, F. (1994). Concerning the mechanism of α-elimination: hypervalent ion pairing in an iodocarbenium iodide. *Angew. Chem. Int. Ed.* 33: 893–895. (c) Legon, A.C. (1995). Mulliken n.aσ and bπ.aσ complexes $B\ldots Cl_2$ in the gas phase: rules for predicting angular geometries and nature of the interaction. *Chem. Phys. Lett*. 237: 291–298.

5 (a) Mukharjee, A., Tothadi, S., and Desiraju, G.R. (2014). Halogen bonds in crystal engineering: like hydrogen bonds yet different. *Acc. Chem. Res.* 47: 2514–2524. (b) Berger, G., Soubhye, J., and Meyer, F. (2015). Halogen bonding in polymer science: from crystal engineering to functional supramolecular polymers and materials. *Polym. Chem.* 6: 3559–3580. (c) Teyssandier, J., Mali, K.S., and Feyter, S.D. (2020). Halogen bonding in two-dimensional crystal engineering. *ChemistryOpen* 9: 225–241.

6 Hibbert, H. (1915). Use of iodine as dehydrating and condensing agent. *J. Am. Chem. Soc.* 37: 1748–1763.

7 (a) Banerjee, A.K., Vera, W., Mora, H. et al. (2006). Iodine in organic synthesis. *J. Sci. Ind. Res.* 65: 299–308. (b) Togo, H. and Iida, S. (2006). Synthetic use of molecular iodine for organic synthesis. *Synlett*: 2159–2175. (c) Das, S., Borah, R., Devi, R.R., and Thakur, A.J. (2008). Molecular iodine in protection and deprotection chemistry. *Synlett*: 2741–2762. (d) Jereb, M., Vražič, D., and Zupan, M. (2011). Iodine-catalyzed transformation of molecules containing oxygen functional groups. *Tetrahedron* 67: 1355–1387. (e) Parvatkar, P.T., Parameswaran, P.S., and Tilve, S.G. (2012). Recent developments in the synthesis of five- and six-membered heterocycles using molecular iodine. *Chem. Eur. J.* 18: 5460–5489. (f) Ren, Y.-M., Cai, C., and Yang, R.-C. (2013). Molecular iodine-catalyzed multicomponent reactions: an efficient catalyst for organic synthesis. *RSC Adv.* 3: 7182–7204. (g) Finkbeiner, P. and Nachtsheim, B.J. (2013). Iodine in modern oxidative catalysis. *Synthesis* 45: 979–999. (h) von der Heiden, D., Bozkus, S., Klussmann, M., and Breugst, M. (2017). Reaction mechanism of iodine-catalyzed Michael additions. *J. Org. Chem.* 82: 4037–4043. (i) Breugst, M. and von der Heiden, D. (2018). Mechanism in iodine catalysis. *Chem. Eur. J.* 24: 9187–9199.

8 Paolo, T.D. and Sandorfy, C. (1974). On the hydrogen bond breaking ability of fluorocarbons containing higher halogens. *Can. J. Chem.* 52: 3612–3622.

9 (a) Laurence, C. and Gal, J.-F. (eds.) (2010). *Lewis Basicity and Affinity Scales: Data and Measurement*, 1e. Chichester, UK: Wiley. (b) Laurence, C., Graton, J., Berthelot, M., and El Ghomari, M.J. (2011). The diiodine basicity scale: toward a general halogen-bond basicity scale. *Chem. Eur. J.* 17: 10431–10444.

10 (a) Cametti, M., Raatikainen, K., Metrangolo, P. et al. (2012). 2-Iodo-imidazolium receptor binds oxoanions *via* charge-assisted halogen bonding. *Org. Biomol. Chem.* 10: 1329–1333. (b) Schulz, N., Sokkar, P., Engelage, E. et al. (2018). The interaction modes of haloimidazolium salts in solution. *Chem. Eur. J.* 24: 3464–3473.

11 (a) Kaasik, M., Kaabel, S., Kriis, K. et al. (2017). Synthesis and characterisation of chiral triazole-based halogen-bond donors: halogen bonds in the solid state and in solution. *Chem. Eur. J.* 23: 7337–7344. (b) Borissov, A., Lim, J.Y.C., Brown, A. et al. (2017). Neutral iodotriazole foldamers as tetradentate halogen bonding anion receptors. *Chem. Commun.* 53: 2483–2486. (c) Kaasik, M., Kaabel, S., Kriis, K. et al. (2019). Synthesis of chiral triazole-based halogen bond donors. *Synthesis* 51: 2128–2135.

12 Syssa-Magalé, J.L., Boubekeur, K., and Schollhorn, B. (2005). First molecular self-assembly of 1,4-diiodo-tetrafluoro-benzene and a ketone via (O···I) non-covalent halogen bonds. *J. Mol. Struct.* 737: 103–107.

13 (a) Guha, S., Kazi, I., Nandy, A., and Sekar, G. (2017). Role of Lewis base-coordinated halogen(I) intermediates in organic synthesis: the journey from unstable intermediates to versatile reagents. *Eur. J. Org. Chem.*: 5497–5518. (b) Sutar, R.L. and Huber, S.M. (2019). Catalysis of organic reactions through halogen bonding. *ACS Catal.* 9: 9622–9639.

14 Bruckmann, A., Pena, M.A., and Bolm, C. (2008). Organocatalysis through halogen-bond activation. *Synlett*: 900–902.

15 (a) Squitieri, R.A., Fitzpatrick, K.P., Jaworski, A.A., and Scheidt, K.A. (2019). Synthesis and evaluation of evaluation of azaolium-based halogen bond-donors. *Chem. Eur. J.* 25: 10069–10073. (b) Ser, C.T., Yang, H., and Wong, M.W. (2019). Iodoimidazolinium-catalyzed reduction of quinoline by Hantzsch ester: halogen bond or Brønsted acid catalysis. *J. Org. Chem.* 84 (16): 10338–10348.

16 For more reviews on the application of halogen bonding in catalysis see(a)Schindler, S. and Huber, S.M. (2014). Halogen bonds in organic synthesis and organocatalysis. In: *Halogen Bonding II*. *Topics in Current Chemistry*, vol. 359 (eds. P. Metrangolo and G. Resnati), 167–203. (b) Bulfield, D. and Huber, S.M. (2016). Halogen Bonding in Organic Synthesis and Organocatalysis *Chem. Eur. J.* 22: 14434–14450. (c) Breugst, M., von der Heiden, D., and Schmauck, J. (2017). Novel Noncovalent Interactions in Catalysis: A Focus on Halogen, Chalcogen, and Anion-π Bonding. *Synthesis* 49: 3224–3236.(d) Bamberger, J., Ostler, F., and Mancheño, O.G. (2019). *ChemCatChem* 11: 1–15.(e) Yang, H. and Wong, M.W. (2020). Application of halogen bonding to organocatalysis: a theoretical perspective. *Molecules* 25: 1045.

17 Metrangolo, P., Resnati, G., Pilati, T., and Biella, S. (2008). Halogen bonding in crystal engineering. In: *Halogen Bonding*. *Structure and Bonding (Berlin)*, vol. 126 (eds. P. Metrangolo and G. Resnati), 105–136.

18 (a) Walter, S.M., Kniep, F., Herdtweck, E., and Huber, S.M. (2011). Halogen-bond-induced activation of a carbon–heteroatom bond. *Angew. Chem. Int. Ed.* 50: 7187–7191; *Angew. Chem*. 123: 7325–7329. (b) Heinen, F., Engelage, E., Dreger, A. et al. (2018). Iodine(III) derivatives as halogen bonding organocatalysts. *Angew. Chem. Int. Ed.* 57: 3830–3833; *Angew. Chem*. 130: 3892–3896. (c) Wang, Y. and Su, P. (2020). Why can cationic halogen bond donors activate the Ritter-type solvolysis of benzhydryl bromide but cationic hydrogen bond donors can not? *ACS Omega* 5: 21862–21872. (d) Reinhard, D.L., Heinen, F., Stoesser, J. et al. (2021). Tuning the halogen bonding strength of cyclic diaryliodonium salts. *Helv. Chim. Acta* 104: e2000221.

19 (a) Kniep, F., Rout, L., Walter, S.M. et al. (2012). 5-Iodo-1,2,3-triazolium-based multidentate halogen-bond donors as activating reagents. *Chem. Commun.* 48: 9299–9301. (b) Kniep, F., Walter, S.M., Herdtweck, E., and Huber, S.M. (2012). 4,4′-Azobis-(halopyridinium) derivatives: strong multidentate halogen-bond donors with a redox-active core. *Chem. Eur. J.* 18: 1306–1310. (c) Castelli, R., Schindler, S., Walter, S.M. et al. (2014). Activation of glycosyl halides by halogen bonding. *Chem. Asian J.* 9: 2095–2098. (d) Dreger, A., Engelage, E., Mallick, B. et al. (2018). The role of charge in 1,2,3-triazol(ium)-based halogen bonding activators. *Chem. Commun.* 54: 4013–4016. (e) Perera, M.D. and Aakeröy, C.B. (2019). Organocatalysis by a multidentate halogen-bond donor: an alternative to hydrogen-bond based catalysis. *New J. Chem.* 43: 8311–8314.

20 Walter, S.M., Jungbauer, S.H., Kniep, F. et al. (2013). Polyfluorinated versus cationic multidentate halogen-bond donors: a direct comparison. *J. Fluorine Chem.* 150: 14–20.

21 (a) Xu, C. and Loh, C.C.J. (2019). A multistage halogen bond catalyzed strain-release glycosylation unravels new hedgehog signaling inhibitors. *J. Am. Chem. Soc.* 141: 5381–5391. (b) Xu, C., Bhaskara Rao, V.U., Weigen, J., and Loh, C.C.J. (2020). A robust and tunable halogen bond organocatalyzed 2-deoxyglycosylation involving quantum tunneling. *Nat. Commun.* 11: 4911.

22 Walter, S.M., Kniep, F., Rout, L. et al. (2012). Isothermal calorimetric titrations on charge-assisted halogen bonds: role of entropy, counterions, solvent, and temperature. *J. Am. Chem. Soc.* 134: 8507–8512.

23 (a) Holthoff, J.M., Engelage, E., Weiss, R., and Huber, S.M. (2020). "Anti-electrostatic" halogen bonding. *Angew. Chem. Int. Ed.* 59: 11150–11157; *Angew. Chem*. 132: 11244–11251. (b) Maxson, T., Jalilov, A.S., Zeller, M., and Rosokha, S.V. (2020). Halogen bonding between anions: association of anion radicals of tetraiodo-*p*-benzoquinone with iodide anions. *Angew. Chem. Int. Ed.* 59: 17197–17201; *Angew. Chem*. 132: 17350–17354. (c) Heinen, F., Engelage, E., Cramer, C.J., and Huber, S.M. (2020). Hypervalent iodine(III) compounds as biaxial halogen bond donors. *J. Am. Chem. Soc.* 142: 8633–8640.

24 (a) Kniep, F., Jungbauer, S.H., Zhang, Q. et al. (2013). Organocatalysis by neutral multidentate halogen-bond donors. *Angew. Chem. Int. Ed.* 52: 7028–7032; *Angew. Chem*. 125: 7166–7170. (b) Jungbauer, S.H. and Huber, S.M. (2015). Cationic multidentate halogen-bond donors in halide abstraction organocatalysis: catalyst optimization by preorganization. *J. Am. Chem. Soc.* 137: 12110–12120.

25 Voelkel, M.H.H., Wonner, P., and Huber, S.M. (2020). Preorganization: a powerful tool in intermolecular halogen bonding in solution. *ChemistryOpen* 9: 214–224.

26 (a) Zapata, F., Caballero, A., Molina, P. et al. (2014). Open bis(triazolium) structural motifs as a benchmark to study combined hydrogen- and halogen-bonding interactions in oxoanion recognition processes. *J. Org. Chem.* 79: 6959–6969. (b) Tepper, R., Schulze, B., Görls, H. et al. (2015). Preorganization in a cleft-type anion receptor featuring iodo-1,2,3-triazoles as halogen bond donors. *Org. Lett.* 17: 5740–5743. (c) Riel, A.M.S., Decato, D.A., Sun, J. et al. (2018). The intramolecular hydrogen bonded–halogen bond: a new strategy for preorganization and enhanced binding. *Chem. Sci.* 9: 5828–5836. (d) Sutar, R.L., Engelage, E., Stoll, R., and Huber, S.M. (2020). Bidentate chiral bis(imidazolium)-based halogen-bond donors: synthesis and applications in enantioselective recognition and catalysis. *Angew. Chem. Int. Ed.* 59: 6806–6810; *Angew. Chem*. 132: 6872–6877.

27 (a) Jungbauer, S.H., Walter, S.M., Schindler, S. et al. (2014). Activation of a carbonyl compound by halogen bonding. *Chem. Commun.* 50: 6281–6284. (b) Kee, C.W. and Wong, M.W. (2016). In silico design of halogen-bonding-based organocatalyst for Diels–Alder reaction, Claisen rearrangement, and Cope-type hydroamination. *J. Org. Chem.* 81: 7459–7470.

28 Heinen, F., Reinhard, D., Engelage, E., and Huber, S.M. (2020). A bidentate iodine(III)-based halogen bond donor as powerful organocatalyst. *Angew. Chem. Int. Ed.* 60: 5069–5073.

29 (a) Gliese, J.P., Jungbauer, S.H., and Huber, S.M. (2017). A halogen-bonding-catalyzed Michael addition reaction. *Chem. Commun.* 53: 12052–12055. (b) von der Heiden, D., Detmar, E., Kuchta, R., and Breugst, M. (2018). Activation of Michael acceptors by halogen-bond donors. *Synlett* 29: 1307–1313.

30 (a) Koenig, J.J., Arndt, T., Gildemeister, N. et al. (2019). Iodine-catalyzed Nazarov cyclizations. *J. Org. Chem.* 84: 7587–7605. (b) Dreger, A., Wonner, P., Engelage, E. et al. (2019). A halogen-bonding-catalysed Nazarov cyclisation reaction. *Chem. Commun.* 55: 8262–8265.

31 (a) Matsuzaki, K., Uno, H., Tokunaga, E., and Shibata, N. (2018). Fluorobissulfonylmethyl iodides: an efficient scaffold for halogen bonding catalysts with an sp^3-hybridized carbon–iodine moiety. *ACS Catal.* 8: 6601–6605. (b) Sutar, R.L., Erochok, N., and Huber, S.M. (2021). Mukaiyama aldol reaction catalyzed by (benz)imidazolium-based halogen bond donors. *Org. Biomol. Chem.* 19: 770–774. (c) Uno, H., Matsuzaki, K., Shiro, M., and Shibata, N. (2020). Design and synthesis of a chiral halogen-bond donor with a sp^3-hybridized carbon–iodine moiety in a chiral fluorobissulfonyl scaffold. *Molecules* 25: 4539.

32 Wolf, J., Huber, F., Erochok, N. et al. (2020). Activation of a metal-halogen bond through halogen bonds. *Angew. Chem. Int. Ed.* 59: 16496–16500; *Angew. Chem.* 132: 16638–16643.

33 (a) Kuwano, S., Suzuki, T., Yamanaka, M. et al. (2019). Catalysis based on C–I···π halogen bonds: electrophilic activation of 2-alkenylindoles by cationic halogen-bond donors for [4+2] cycloadditions. *Angew. Chem. Int. Ed.* 58: 10220–10224; *Angew. Chem.* 131: 10326–10330. (b) Suzuki, T., Kuwano, S., and Arai, T. (2020). Non-bonding electron pair versus π-electrons in solution phase halogen bond catalysis: Povarov reaction of 2-vinylindoles and imines. *Adv. Synth. Catal.* 362: 3208–3212.

34 Bergamaschi, G., Lascialfari, L., Pizzi, A. et al. (2018). A halogen bond-donor amino acid for organocatalysis in water. *Chem. Commun.* 54: 10718–10721.

35 (a) Carreras, L., Serrano-Torne, M., van Leeuwen, P.W.N.M., and Vidal-Ferran, A. (2018). XBphos-Rh: a halogen-bond assembled supramolecular catalyst. *Chem. Sci.* 9: 3644–3648. (b) Carreras, L., Benet-Buchholz, J., Franconetti, A. et al. (2019). Halogen bonding effects on the outcome of reactions at metal centres. *Chem. Commun.* 55: 2380–2383.

29

Chalcogen-Bonding Catalysis

Wei Wang and Yao Wang

School of Chemistry and Chemical Engineering, Shandong University, No. 27 Shanda South Road, Jinan 250100, China

29.1 Introduction

Chalcogen-bonding interaction, the noncovalent bonding between a chalcogen atom in a molecular entity and an electron donor in the same or another molecular entity, is an evolutionary force that is exploited by nature to modulate the conformation of proteins [1]. While the divalent chalcogens bearing lone pair electrons are conventionally considered as electron donors [2], the observation of chalcogen-bonding interaction reveals a converse fact that these divalent chalcogens could act as electron acceptors. This counterintuitive phenomenon indicates that electron density is distributed around the divalent chalcogens in an anisotropic way [3]. Theoretical calculation suggests there are regions of positive molecular electrostatic potential, the so-called "σ-hole," orienting along the extension of the axis of covalent bond [4]. The presence of "σ-hole" is a general character in molecules containing group 14–17 elements [5] and the relevant interactions are known as tetrel, pnictogen, chalcogen, and halogen bond, respectively. The origin of chalcogen bonding is the subject of extensive theoretical studies and yet remains debated [6]. Beyond the contribution from electrostatic potential, theoretical investigation on various chalcogen-bonding interactions suggest that charge transfer and disperse forces could also play a significant role in the formation of this type of noncovalent interactions [6].

While the presence of chalcogen bonding has been noticed by scientists for several decades [7], the translation of this noncovalent force into chemical applications relatively lags behind. Chalcogen bonding has been mainly found to play a significant role in crystal engineering [8, 9]. Furthermore, this type of interactions has been demonstrated to be of significance for the modulation of conformation in drug discovery [10] and Lewis base catalysis [11–15]. Until recently, chalcogen-bonding interactions were applicable to anion recognition/transport [16–22], and noncovalent catalysis [23, 24]. While significant advances have been made in the application of chalcogen-bonding interactions, the exploitation of this noncovalent force in

Supramolecular Catalysis: New Directions and Developments, First Edition.
Edited by Piet W.N.M. van Leeuwen and Matthieu Raynal.

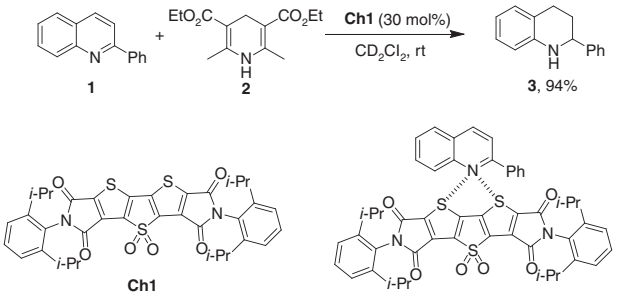

Figure 29.1 S···N bonding catalysis of reduction of quinoline with Hantzsch ester [25].

solution yet remains underdeveloped. This chapter highlights significant advances in the area of chalcogen-bonding catalysis.

29.2 Challenges in Chalcogen-Bonding Catalysis

While chalcogen-bonding interaction has been demonstrated to be a valuable tool in rigidifying conformation in Lewis base catalysis, the mere employment of this weak interaction to drive a chemical reaction is a substantial challenge. Matile et al. discovered that the S···N bonding could promote the reduction of quinoline **1** with Hantzsch ester **2** to give tetrahydroquinoline **3** (Figure 29.1) [25], thus demonstrating the feasibility of the concept of chalcogen-bonding catalysis. In line with the strength of a chalcogen bond, a Se···N bonding activation approach to achieving this reaction was subsequently found to be more efficient [26]. Huber et al. proved that chalcogen bonding can activate bromide **4** to facilitate the Ritter-type reaction albeit with stoichiometric amount of promoter (Figure 29.2) [27]. A catalytic addition reaction between 1-chloroisochroman and a ketene silyl acetal involving Se···Cl bonding activation was afterward proven feasible [28]. While these discoveries demonstrate chalcogen bond is applicable to activate organic molecules, the intrinsic weak interaction poses a great challenge to catalyze less reactive reactions beyond the scope of fundamental transformations. From the viewpoint of a sustainable development, the discovery of highly reactive catalysts that show superior/comparable efficiency in contrast to the other catalysis disciplines is one of the major challenges. To emerge as a general catalysis tool, chalcogen-bonding catalysis should be capable of playing as a valuable platform to develop new reactions and to solve synthetic problems which otherwise are difficult to find a solution using conventional approaches.

29.3 Discovery of Efficient Chalcogen-Bonding Catalysts

The strength of a chalcogen bond depends on several factors, including (i) the electron-donating ability of Lewis bases, (ii) the polarizability of the specific chalcogen atom (Te > Se > S > O), (iii) the substituent adjacent to the chalcogen atom,

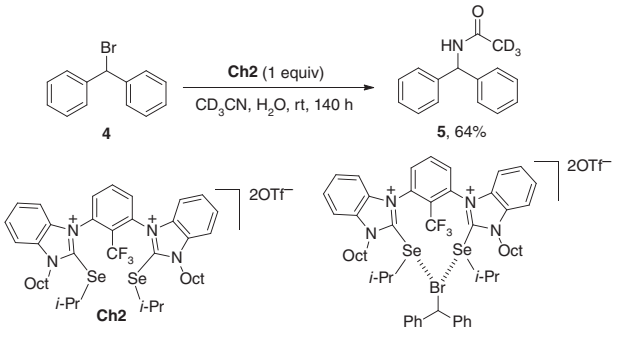

Figure 29.2 Se···Br bonding activation approach to achieving Ritter-type reaction [27].

and (iv) the steric environment around a chalcogen atom. Taking into account the factors that affect the strength of a chalcogen bond, Wang et al. developed a class of highly reactive catalysts (i.e. **Ch3** type) that have been demonstrated to be capable of catalyzing a range of distinctive chemical reactions [29–31]. The properties of the chalcogen-bonding interactions shown in the solid-state structures of these catalysts are in consistence with the notions of theoretical investigation.

Theoretical computation suggests that the electron density distributes around the divalent chalcogen in an anisotropic manner, thus indicating that the divalent chalcogen (i.e. **Ch**) can serve as either an electron donor or electron acceptor. Therefore, in principle, a "like attracting like" **Ch**···**Ch** bonding between the same or similar chalcogen-containing molecules is allowed (Figure 29.3). In consistence with this theoretical notion, the investigation by Parthasarathy et al. showed the presence of "like attracting like" S···S interactions with high directionality [32]. In the solid-state structure of **Ch3**, the distance between two selenium atoms is 3.76 Å, while Se1 approaches Se2 in the direction of the axis of the covalent bond C2–Se2 (i.e. C2–Se2···Se1 166.7°), suggesting the presence of a Se···Se bonding

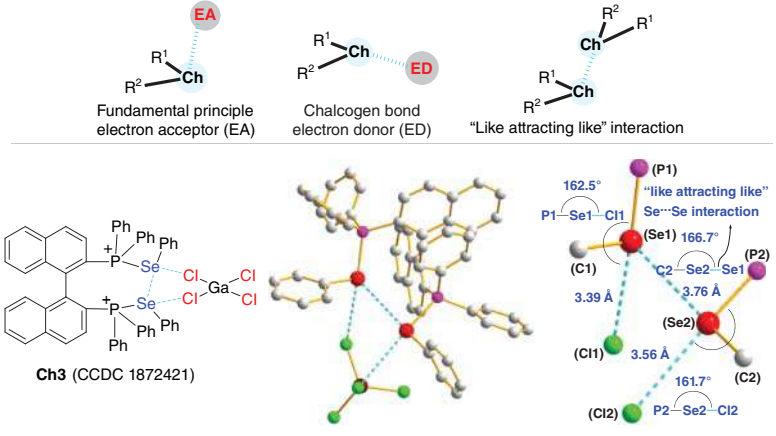

Figure 29.3 Se···Se and Se···Cl bonding interactions in solid-state structure of **Ch3** [30].

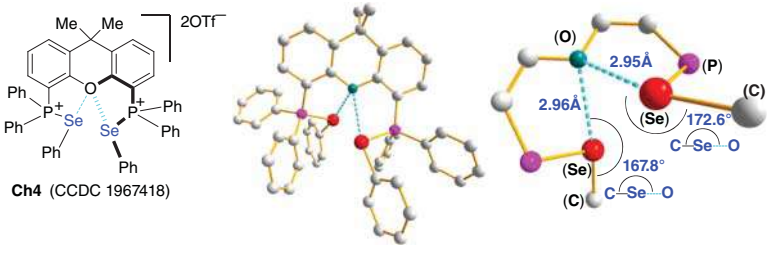

Figure 29.4 Intramolecular Se···O bonding interaction in solid-state structure of **Ch4** [30].

interaction. This observation indicates the dual electronic character of selenium atoms in **Ch3**-type molecules.

Theoretically, there are two σ holes along the axis of the covalent bonds of the divalent chalcogen compounds, thus potentially allowing the formation of two chalcogen bonds. This notion is supported by the observation in the solid-sate structure of **Ch3** as the same selenium (i.e. Se2) can form two chalcogen bonds with selenium (i.e. Se1) and chlorine (Cl2), respectively.

Beyond the observation of Se···Se and Se···Cl interactions, the solid-state structure of **Ch4** shows the presence of the intramolecular Se···O bonding interaction (Figure 29.4). Moreover, the intermolecular Se···O interaction between **Ch3** and 1,4-dioxane was observed, suggesting this type of chalcogen-bonding donor can attract neutral organic molecule (Figure 29.5). Except the noncovalent interactions between the divalent selenium atoms and the lone pair of electron donors, Se···π bonding between such selenium and π-electron donor was observed in the crystal structure of the complex of **Ch3** and 1,4-dioxane. The concurrent presence of Se···O and Se···π interactions indicates that different types of chalcogen-bonding interactions can be formed with the same chalcogen atom. Beyond the observation of chalcogen-bonding interactions in the solid-state structures of **Ch4**-type molecules, the presence of noncovalent interactions between these molecules and Lewis bases in solution was demonstrated through the implementation of ^{77}Se, ^{31}P, and ^{13}C NMR experiments. The results of these nuclear magnetic resonance (NMR) experiments suggest the presence of Se···O bonding interactions between this type of chalcogen-bonding donors and Lewis bases in solution. The observations from the solid-state structures and the experimental results in solution provide

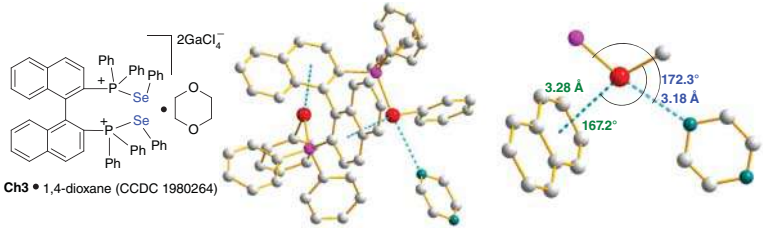

Figure 29.5 Chalcogen-bonding interactions in solid-state structure of the complex of **Ch3** and 1,4-dioxane [31].

significant basis for translating this type of noncovalent interactions into the power of catalysis.

29.4 Chalcogen–Chalcogen Bonding Catalysis

Upon using nitrogen- or halogen-containing Lewis basic substrates, the chalcogen-bonding donors tend to bind strongly the halide intermediates or amine products, thus limiting the turnover of catalyst. To solve this problem, a fast equilibrium between chalcogen-bonding donor and product/intermediate is necessary to achieve an efficient catalysis process. In this context, chalcogen–chalcogen bonding catalysis approach was envisioned to provide a general solution to the intrinsic limitations of this type of noncovalent catalysis. To demonstrate the feasibility of chalcogen–chalcogen bonding catalysis, Wang et al. developed an assembly reaction of indole derivatives **6** and β-ketoaldehyde **7** (Figure 29.6) [29]. In the presence of a **Ch5**-type catalyst, β-ketoaldehyde **7** was activated by Se···O interaction, thus triggering the condensation of 3-alkylated indole **6** and β-ketoaldehyde **7**. The *in situ* generated enone **M1** further undergoes a Michael addition process with a Se···O bonding activated β-ketoaldehyde to give intermediate **M2** with multiple carbonyl groups. Subsequently, under Se···O bonding catalysis, an aldol condensation reaction occurs to give intermediate **M3** bearing a suitably positioned aldehyde group which further undergoes an intramolecular cyclization to generate N-heterocycle **M4**. Finally, a dehydration process takes place to deliver the stable product **8** with a newly formed seven-membered ring.

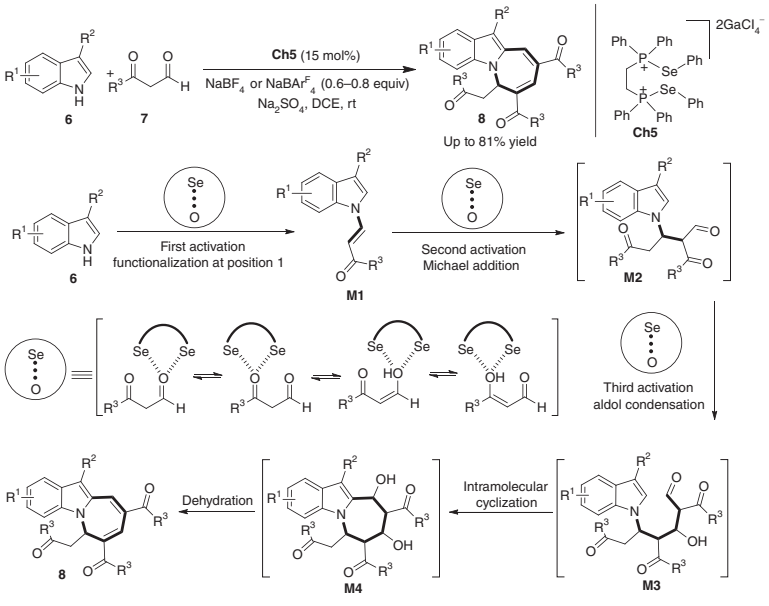

Figure 29.6 Assembly reactions of indole derivatives and β-ketoaldehydes enabled by Se···O bonding interaction [29].

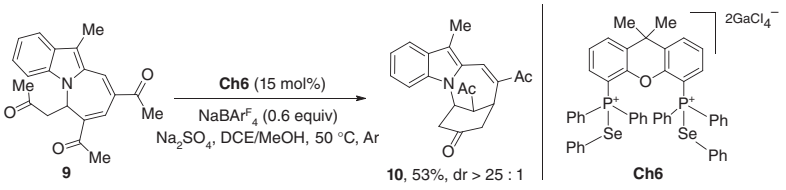

Figure 29.7 Se···O bonding catalysis of an intramolecular cyclization reaction [29].

Under the optimized conditions, the N-heterocyclic products **8** were obtained with moderate to good yields. Comprehensive control experiments demonstrate Se···O bonding interaction is the driving force of this transformation.

Generally, it was considered to be a challenge to generate enol from linear aliphatic ketones by a noncovalent force such as hydrogen bonding and halogen bonding interactions. Given the fact that the Se···O bonding interaction between **Ch6**-type chalcogen donors and ketones leads to a remarkable chemical shift of ^{13}C signal of carbonyl group, an attempt to cyclization of N-heterocycle **9** bearing methyl ketone moiety through the generation of enol by Se···O bonding activation was implemented (Figure 29.7) [29]. Significantly, under Se···O bonding catalysis, N-heterocycle **9** can undergo an intramolecular enol addition reaction to give bridged N-heterocycle **10**. In contrast, under classical base-promoted conditions, such as Cs_2CO_3 and KHMDS, this cyclization reaction is not productive. These results expand the capability of noncovalent forces.

To further demonstrate the potential of this catalysis concept, an intermolecular aza-Michael addition reaction of 3-alkylated indole with α,β-unsaturated ketone was achieved under neutral conditions [29]. It is known that the nucleophilicity of nitrogen in 3-alkylated indole is weak under neutral conditions. As a result, to achieve an intermolecular aza-Michael addition reaction using indole derivative as a nucleophile, deprotonation of NH in the presence of a strong base to generate more nucleophilic nitrogen anion was required [33]. In the presence of **Ch6**, it was found that the aza-Michael addition reaction between 3-methylindole **11** and enone **12** proceeded smoothly under neutral condition to give N-alkylated indole **13** enabled by Se···O bonding interaction (Figure 29.8). The new reactivity demonstrates that chalcogen-bonding catalysis approach can provide an alternative solution to synthetic issues in organic synthesis.

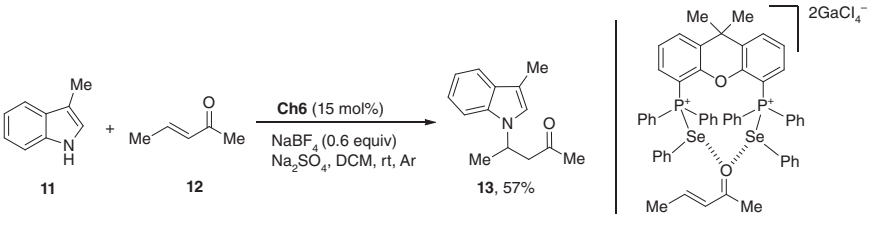

Figure 29.8 Se···O bonding catalysis of the aza-Michael addition reaction between 3-methylindole and enone [29].

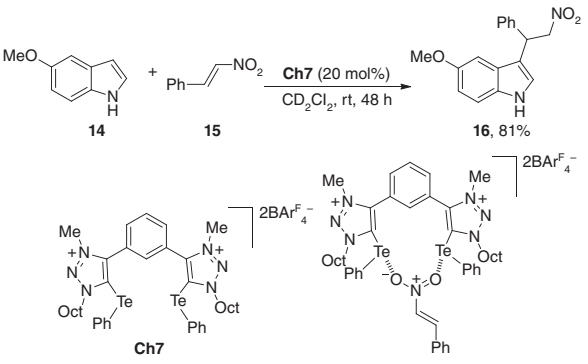

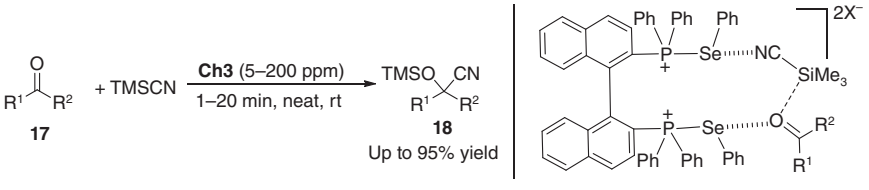

Figure 29.9 Te···O bonding catalysis of Michael addition reactions [34].

Figure 29.10 ppm-Level chalcogen-bonding catalysis [31].

Beyond the scope of divalent sulfur and selenium bonding catalysis, Te···O bonding catalysis was also established. Huber et al. found that the double Te···O bonding interaction between catalyst **Ch7** and nitro group could activate nitro olefin **15**, thus facilitating a Michael addition using indole derivative **14** as a nucleophile (Figure 29.9) [34]. In consistence with the strength of chalcogen-bonding donors that follows the order of S < Se < Te, the selenium as well as sulfur counterpart did not exhibit catalytic activity. In addition, the same research group reported that Te···O bonding interaction could activate carbonyl group to achieve a Michael addition reaction between indole and enone [35].

While chalcogen bonding has found significant application in catalysis, the efficiency remains a major concern as a relative high catalyst loading was required to promote chemical transformation. Wang et al. found that the chalcogen-bonding catalysis approach can be extremely efficient for specific reactions. To show such an example, a cyanosilylation of ketones in the presence of **Ch3**-type chalcogen-bonding donor was implemented [31]. The experimental results revealed that the reactions can be achieved even in the presence of ppm-level catalyst loading, while the reactions were finished within several minutes (Figure 29.10). This chalcogen-bonding catalysis approach gives up to 10^6/hour turnover frequency numbers.

29.5 Dual Chalcogen–Chalcogen Bonding Catalysis

To further develop chalcogen-bonding catalysis, the application of this noncovalent interaction in less reactive reactions with an emphasis on solving synthetic problems

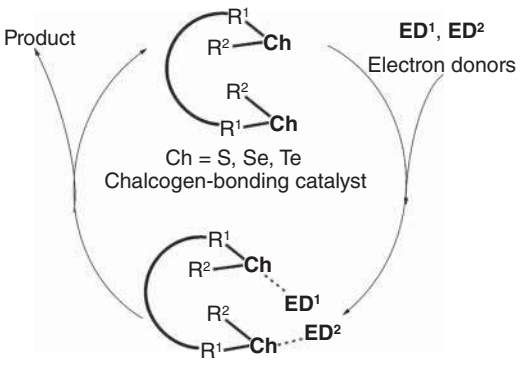

Figure 29.11 Dual chalcogen–chalcogen bonding catalysis [30].

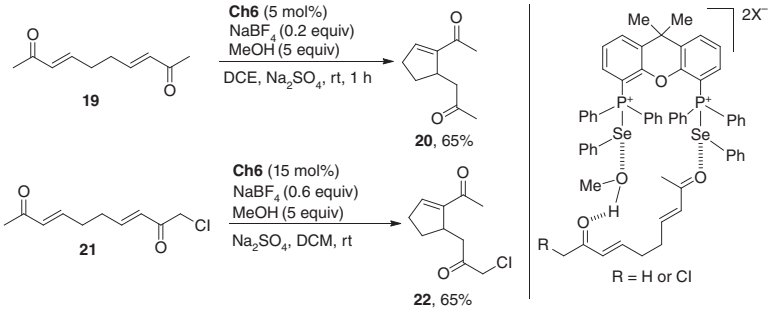

Figure 29.12 Dual Se···O bonding catalysis approach to the Rauhut–Currier-type reaction [30].

is an essential research goal. In this context, Wang et al. introduced the strategy of dual chalcogen–chalcogen bonding catalysis for the simultaneous interaction between a bidentate chalcogen-bonding catalyst and two chalcogen-based electron donors, thus driving chemical reactions in a distinct way (Figure 29.11) [30].

To demonstrate this strategy, the Rauhut–Currier-type reaction was employed as a benchmark reaction. Conventionally, Rauhut–Currier-type reactions were promoted by the strongly nucleophilic Lewis bases such as trialkyphosphines [36–38]. As shown in Figure 29.12, in a distinct approach, the dual Se···O bonding interaction between a bidentate chalcogen-bonding catalyst **Ch6** and two electron donors, i.e. an enone **19** and methanol, enables the achievement of Rauhut–Currier-type reaction at room temperature in the presence of 5 mol% of **Ch6** [30]. As a specific example, the trialkylphosphine approach (i.e. n-Bu_3P) could not tolerate a specific chloro-containing enone **21**, while the Se···O bonding catalysis approach can tolerate this functional group.

To probe the mechanism of the dual catalysis, the authors developed an effective strategy that involves "promoter as inhibitor" as well as "substrate as inhibitor" (Figure 29.13). If a dual catalysis mechanism is in operation, the proper concentrations of substrate enone and promoter methanol is necessary to generate the reactive equilibrium species **M5** that the bidentate catalyst simultaneously interacts with the substrate and promoter. In this context, the inappropriately high

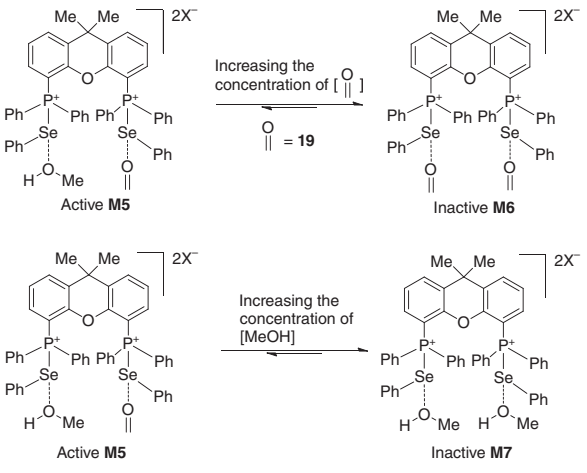

Figure 29.13 Demonstration of dual Se···O bonding catalysis mechanism [30].

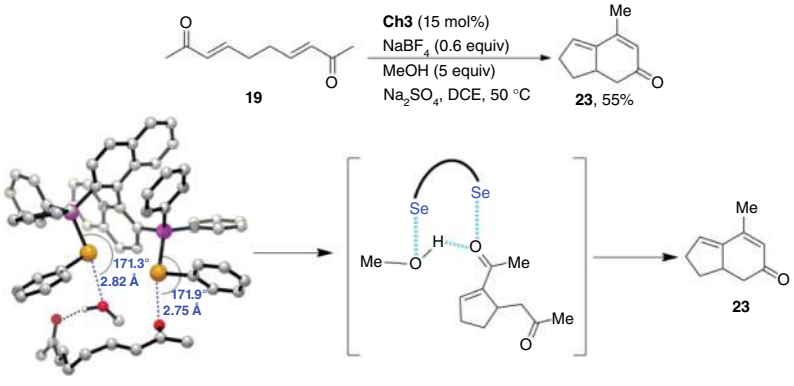

Figure 29.14 Consecutive cyclization enabled by dual Se···O bonding catalysis mechanism [30].

concentration of either the substrate enone or promoter would suppress the reactive equilibrium species by competitive generation of inactive **M6** or **M7**, thus resulting in the inhibition of the reaction process. Upon maintaining the concentration of the catalyst **Ch6** unchanged, the experimental results reveal that an inappropriately high concentration of either enone or methanol causes a substantial suppression of the Rauhut–Currier reaction, indicating a dual catalysis mechanism.

As shown in Figure 29.14, catalysis with dual Se···O bonding interaction enables the achievement of a consecutive cyclization to give bicyclic products [30]. The simultaneous Se···O bonding interaction between a bidentate chalcogen-bonding catalyst and an enone and methanol gave cyclization product **20** bearing an enone moiety, which further undergoes an intramolecular cyclization to deliver the bicyclic product **23**. Mechanistic investigation indicates that the simultaneous interaction of catalyst with both enone **20** and methanol is essential to give rise to the catalytic activity.

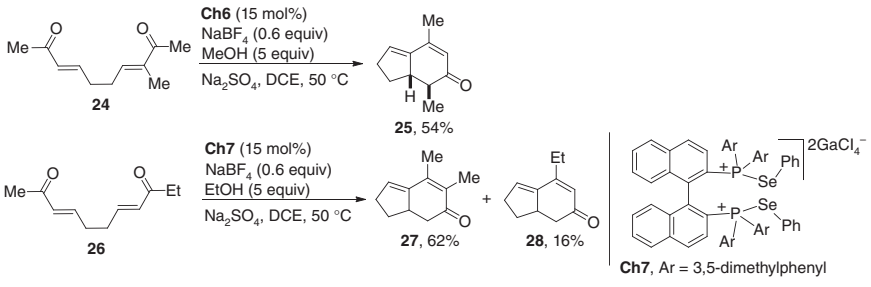

Figure 29.15 Dual Se···O bonding catalysis approach to solving reactivity and selectivity issues [30].

As depicted in Figure 29.15, with α-methyl substituted enone **24** as reactant, the reactivity of enone will significantly decrease owing to both the electronic and steric effect. As a result, no reaction occurred under *n*-Bu_3P catalysis using **24** as a substrate [39]. In contrast, the dual Se···O bonding catalysis strategy can address this reactivity issue to give bicyclic product **25**. To highlight the potential of chalcogen-bonding catalysis, further investigation reveals that this dual Se···O bonding catalysis approach can even differentiate similar groups such as methyl and ethyl incorporated in substrate **26** to achieve moderate regioselectivity. In contrast, a conventional *n*-Bu_3P approach could not differentiate significantly such similar groups.

29.6 Conclusion Remarks

Chalcogen-bonding interactions have been explored in the research fields of crystal engineering, drug discovery, anion recognition/transport, and catalysis. While significant advances have been made in the understanding and exploiting this type of noncovalent interactions, the investigation of chalcogen-bonding interactions in solution is still in a very early stage. The recent study on chalcogen-bonding catalysis shows the feasibility of this concept; however, a sustainable development of this catalysis method needs to meet several challenges. As chalcogen-bonding interaction is comparatively weak, the discovery of reactive catalysts and new strategies to drive chemical reactions in an efficient way is a critical problem. In contrast to the other established catalysis disciplines, the advantages of catalysis with chalcogen bonding need more convincible evidences to elucidate. Meanwhile, for a sustainable development of this area, the application of chalcogen-bonding interactions to solve elusive problems in organic synthesis which otherwise are inaccessible by the other methods is one of the major research objects. Last but not least, the enantioselective chalcogen-bonding catalysis has not been achieved and research toward this direction is highly desirable. It is expected that the extensive study on chalcogen-bonding interaction would provide a fruitful platform to solve synthetic problems.

Acknowledgments

Financial support for this research under grants from the National Natural Science Foundation of China (21772113, 21971147, and 22022105) and the Natural Science Foundation of Shandong Province (ZR2019JQ08) is gratefully acknowledged.

References

1 Scheiner, S. (ed.) (2015). *Noncovalent Forces*. Cham: Springer International Publishing.
2 Vedejs, E. and Denmark, S.E. (eds.) (2016). *Lewis Base Catalysis in Organic Synthesis*. Weinheim: Wiley.
3 Bauzá, A., Mooibroek, T.J., and Frontera, A. (2015). The bright future of unconventional σ/π-hole interactions. *ChemPhysChem* 16: 2496–2517.
4 Murray, J.S., Lane, P., Clark, T., and Politzer, P. (2007). σ-Hole bonding: molecules containing group VI atoms. *J. Mol. Model.* 13: 1033–1038.
5 Clark, T. (2013). σ-Holes. *WIREs Comput. Mol. Sci.* 3: 13–20.
6 Pascoe, D.J., Ling, K.B., and Cockroft, S.L. (2017). The origin of chalcogen-bonding interactions. *J. Am. Chem. Soc.* 139: 15160–15167.
7 Bent, H.A. (1968). Structural chemistry of donor-acceptor interactions. *Chem. Rev.* 68: 587–648.
8 Mahmudov, K.T., Kopylovich, M.N., Guedes da Silva, M.F.C., and Pombeiro, A.J.L. (2017). Chalcogen bonding in synthesis, catalysis and design of materials. *Dalton Trans.* 46: 10121–10138.
9 Gleiter, R., Haberhauer, G., Werz, D.B. et al. (2018). From noncovalent chalcogen−chalcogen interactions to supramolecular aggregates: experiments and calculations. *Chem. Rev.* 118: 2010–2041.
10 Beno, B.R., Yeung, K.S., Bartberger, M.D. et al. (2015). A survey of the role of noncovalent sulfur interactions in drug design. *J. Med. Chem.* 58: 4383–4438.
11 Birman, V.B., Li, X., and Han, Z. (2007). Nonaromatic amidine derivatives as acylation catalysts. *Org. Lett.* 9: 37–40.
12 Leverett, C.A., Purohit, V.C., and Romo, D. (2010). Enantioselective, organocatalyzed, intramolecular aldol lactonizations with keto acids leading to bi- and tricyclic β-lactones and topology-morphing transformations. *Angew. Chem. Int. Ed.* 49: 9479–9483.
13 Robinson, E.R.T., Fallan, C., Simal, C. et al. (2013). Anhydrides as α,β-unsaturated acyl ammonium precursors: isothiourea-promoted catalytic asymmetric annulation processes. *Chem. Sci.* 4: 2193–2200.
14 Robinson, E.R.T., Walden, D.M., Fallan, C. et al. (2016). Non-bonding 1,5-S···O interactions govern chemo- and enantioselectivity in isothiourea-catalyzed annulations of benzazoles. *Chem. Sci.* 7: 6919–6927.

15 Young, C.M., Elmi, A., Pascoe, D.J. et al. (2020). The importance of 1,5-oxygen· · ·chalcogen interactions in enantioselective isochalcogenourea catalysis. *Angew. Chem. Int. Ed.* 59: 3705–3710.

16 Zhao, H. and Gabbaï, F.P. (2010). A bidentate Lewis acid with a telluronium ion as an anion-binding site. *Nat. Chem.* 2: 984–990.

17 Garrett, G.E., Gibson, G.L., Straus, R.N. et al. Chalcogen bonding in solution: interactions of benzotelluradiazoles with anionic and uncharged Lewis bases. *J. Am. Chem. Soc.* 137: 4126−−4133.

18 Lim, J.Y.C., Marques, I., Thompson, A.L. et al. (2017). Chalcogen bonding macrocycles and [2]rotaxanes for anion recognition. *J. Am. Chem. Soc.* 139: 3122–3133.

19 Borissov, A., Marques, I., Lim, J.Y.C. et al. (2019). Anion recognition in water by charge-neutral halogen and chalcogen bonding foldamer receptors. *J. Am. Chem. Soc.* 141: 4119–4129.

20 Benz, S., Macchione, M., Verolet, Q. et al. Anion transport with chalcogen bonds. *J. Am. Chem. Soc.* 138: 9093–9096.

21 Macchione, M., Tsemperouli, M., Goujon, A. et al. (2018). Mechanosensitive oligodithienothiophenes: transmembrane anion transport along chalcogen-bonding cascades. *Helv. Chim. Acta.* 101: e1800014.

22 Lee, L.M., Tsemperouli, M., Poblador-Bahamonde, A.I. et al. (2019). Anion transport with pnictogen bonds in direct comparison with chalcogen and halogen bonds. *J. Am. Chem. Soc.* 141: 810–814.

23 Bamberger, J., Ostler, F., and Mancheño, O.G. (2019). Frontiers in halogen and chalcogen−bond donor organocatalysis. *ChemCatChem* 11: 5198–5211.

24 Vogel, L., Wonner, P., and Huber, S.M. (2019). Chalcogen bonding: an overview. *Angew. Chem. Int. Ed.* 58: 1880–1891.

25 Benz, S., López-Andarias, J., Mareda, J. et al. (2017). Catalysis with chalcogen bonds. *Angew. Chem. Int. Ed.* 56: 812–815.

26 Benz, S., Mareda, J., Besnard, C. et al. (2017). Catalysis with chalcogen bonds: neutral benzodiselenazole scaffolds with high-precision selenium donors of variable strength. *Chem. Sci.* 8: 8164–8169.

27 Wonner, P., Vogel, L., Düser, M. et al. (2017). Carbon-halogen bond activation by selenium-based chalcogen bonding. *Angew. Chem. Int. Ed.* 56: 12009–12012.

28 Wonner, P., Vogel, L., Kniep, F., and Huber, S.M. (2017). Catalytic carbon-chlorine bond activation by selenium-based chalcogen bond donors. *Chem. Eur. J.* 23: 16972–16975.

29 Wang, W., Zhu, H., Liu, S. et al. (2019). Chalcogen-chalcogen bonding catalysis enables assembly of discrete molecules. *J. Am. Chem. Soc.* 141: 9175–9179.

30 Wang, W., Zhu, H., Feng, L. et al. (2020). Dual chalcogen-chalcogen bonding catalysis. *J. Am. Chem. Soc.* 142: 3117–3124.

31 Bao, L., Kong, X., and Wang, Y. (2020). Noncovalent chalcogen-bonding catalysis using ppm-level catalyst loading to achieve cyanosilylation of ketones. *Asian J. Org. Chem.* 9: 757–760.

32 Guru Row, T.N. and Parthasarathy, R. (1981). Directional preferences of nonbonded atomic contacts with divalent sulfur in terms of its orbital orientations.

2. Sulfur· · ·sulfur interactions and nonspherical shape of sulfur in crystals. *J. Am. Chem. Soc.* 103: 477–479.

33 Yang, J., Lia, T., Zhou, H. et al. (2017). Potassium hydroxide catalysed intermolecular aza-Michael addition of 3-cyanoindole to aromatic enones. *Synlett* 28: 1227–1231.

34 Wonner, P., Dreger, A., Engelage, E., and Huber, S.M. (2019). Chalcogen bonding catalysis of a nitro-Michael reaction. *Angew. Chem. Int. Ed.* 58: 16923–16927.

35 Wonner, P., Steinke, T., Vogel, L., and Huber, S.M. (2020). Carbonyl activation by selenium- and tellurium-based chalcogen bonding in a Michael addition reaction. *Chem. Eur. J.* 26: 1258–1262.

36 Kürti, L. and Czako, B. (eds.) (2005). *Strategic Applications of Named Reactions in Organic Synthesis*. Amsterdam: Elsevier.

37 Wang, L.C., Luis, A.L., Agapiou, K. et al. (2002). Organocatalytic Michael cycloisomerization of bis(enones): the intramolecular Rauhut–Currier reaction. *J. Am. Chem. Soc.* 124: 2402–2403.

38 Frank, S.A., Mergott, D.J., and Roush, W.R. (2002). The vinylogous intramolecular Morita–Baylis–Hillman reaction: synthesis of functionalized cyclopentenes and cyclohexenes with trialkylphosphines as nucleophilic catalysts. *J. Am. Chem. Soc.* 124: 2404–2405.

39 Thalji, R.K. and Roush, W.R. (2005). Remarkable phosphine-effect on the intramolecular aldol reactions of unsaturated 1,5-diketones: highly regioselective synthesis of cross-conjugated dienones. *J. Am. Chem. Soc.* 127: 16778–16779.

30

Asymmetric Supramolecular Organocatalysis: The Fourth Pillar of Catalysis

Kengadarane Anebouselvy, Kodambahalli S. Shruthi, and Dhevalapally B. Ramachary

University of Hyderabad, Catalysis Laboratory, School of Chemistry, Prof. CR Rao Road, Gachibowli, Hyderabad 500 046, India

30.1 Introduction

Asymmetric catalysis receives sustenance from enzyme catalysis [1], metal catalysis [2], organocatalysis [3–5], and recently from supramolecular organocatalysis also [6]. There has always been a continuous flourishing of ways for substrate activation using a myriad of chiral catalysts for synthesizing enantiomerically pure organic compounds. Originally, extraordinarily functionalized natural enzymes inspired scientists through their great capability in delivering enantiomerically pure products from simple starting materials in the biochemical reactions. This led to the design of various catalyst systems for the desired processes and thriving of transition metal catalysis, organocatalysis, etc. The spark for the bonfire of organocatalysis [3–5], which uses small organic molecules to catalyse asymmetric transformations, originated definitely from enzyme catalysis.

Over the past few decades, organocatalysts with numerous advantages like easy availability, cheap, environmentally friendly, stable, etc., have been exercised in various asymmetric transformations and exhibited to deliver the desired products with excellent reactivity, selectivity, and sustainability. However, at times, especially in the case of certain substituted substrates, they were found to be inadequate and unsuccessful. This brought forward the branching of organocatalysis into supramolecular organocatalysis, which uses more than one organic compound for catalysing a particular reaction to generate the necessary products effectively and selectively. This synergistic cooperation of two or more organocatalysts, harnessing various potentially weak interactions along with the covalent bonds, resulting in a conformationally rigid pre-transition state, so as to produce the enantiopure products with very high reactivity and selectivity presents the present highlight.

This supramolecular organocatalysis, also known as modularly designed organocatalysis/synergistic catalysis, has proven advantages like rapid access to a vast library of catalyst systems (by simple mixing of two or more single catalysts), and the availability of a maximum number of interactions in the pre-transition state,

Supramolecular Catalysis: New Directions and Developments, First Edition.
Edited by Piet W.N.M. van Leeuwen and Matthieu Raynal.

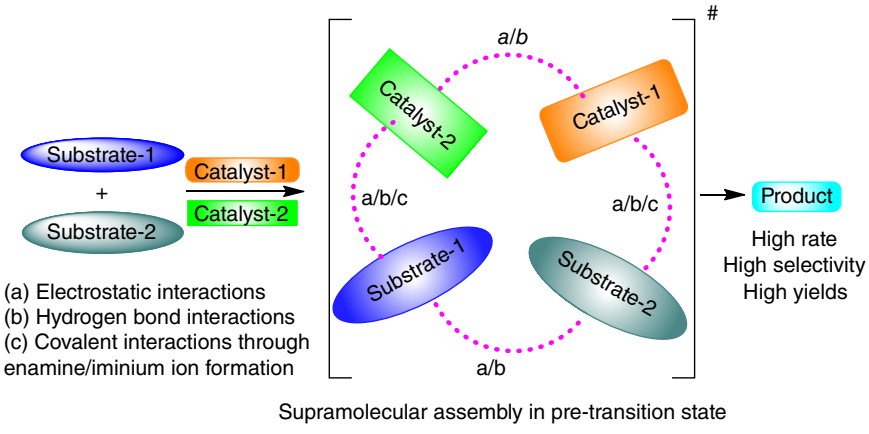

Figure 30.1 Directing as well as role-playing crucial and diverse, catalyst–catalyst, substrate–catalyst, and substrate–substrate interactions that are found to exist in the pre-transition state of a particular ASO reaction.

like H-bonding, van der Waals interaction, electrostatic interaction, and covalent bond between the substrates and the catalysts, creating more rigidity so as to afford highest reactivity and selectivity possible for the chosen product.

The formation, controlling, and stabilizing of spatially organized three-dimensional pre-transition state structures are orchestrated by the covalent as well as various noncovalent interactions among the substrates and the catalysts, thereby imparting rate acceleration and excellent stereocontrol for the intended chemical asymmetric transformations (Figure 30.1). The fascinating prominent aspect of supramolecular organocatalysis resides in how these interactions among the substrates and catalysts govern the reactivity as well as selectivity of chemical reactions. This contrivance of the spatial arrangement of the corresponding reaction partners through supramolecular organocatalysts and ultimately how the proximity of the appropriate reaction centers drives the reaction in a particular way to provide high rate and excellent stereoselectivity as they unfolded are presented here (Figure 30.1).

30.2 Asymmetric Michael Additions

Asymmetric Michael addition between aldehydes or ketones and nitroalkenes is a well-known and potentially useful organocatalytic reaction [7] for the synthesis of versatile γ-nitrocarbonyl compounds, but the single organocatalyst L-proline is ineffective in catalyzing the asymmetric reaction.

First, in 2012, we illustrated an exemplary approach for the asymmetric synthesis of highly substituted spirodihydrocoumarins **7** possessing a quaternary stereocenter, through neighboring *ortho*-hydroxyl group-induced sequential Michael–lactonization reactions on 2-(2-nitrovinyl)phenols **2** with alkyl cyclopentanone-2-carboxylates **1** in the presence of a catalytic amount of quinine thiourea **3a** (Scheme 30.1) [8]. Despite the employment of a single catalyst in this

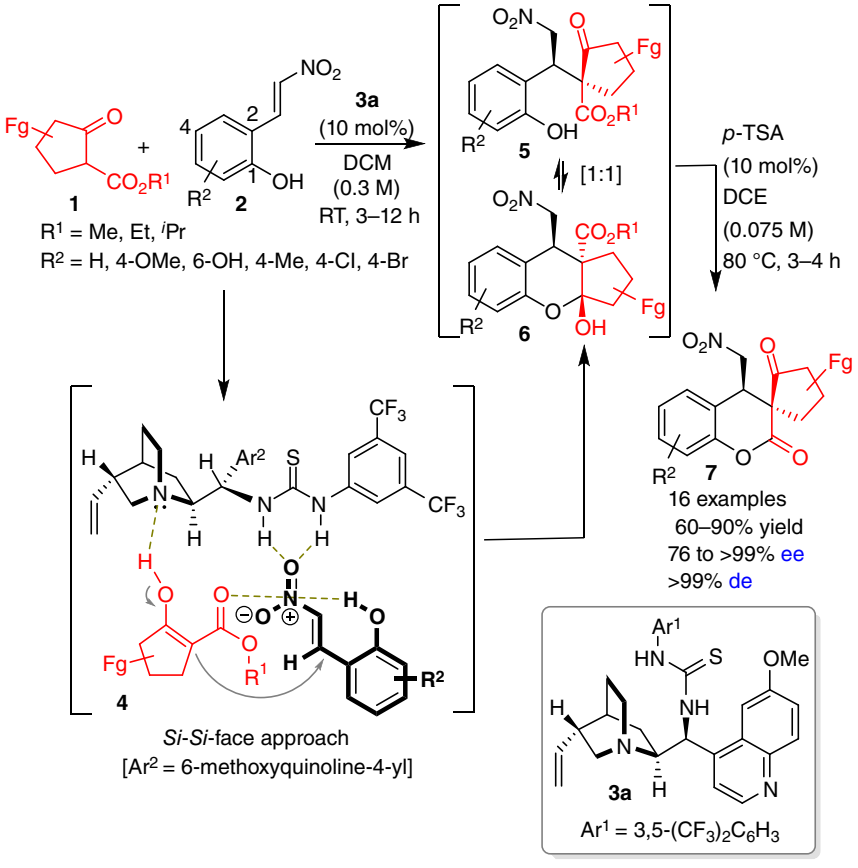

Scheme 30.1 Asymmetric sequential Michael lactonization reaction for the synthesis of spirodihydrocoumarins **7** via self-assembled supramolecular arrangement between quinine thiourea **3a** and substrates **1/2**.

reaction, this work is discussed here due to the inducement from the cooperation of two substrates, and one catalyst in forming the supramolecular cyclic assembly through hydrogen bond interactions, as exhibited in the pre-transition state cluster **4**.

Sequential Michael–lactonization reaction of alkyl cyclopentanone-2-carboxylates **1** with 2-(2-nitrovinyl)phenols **2** using 10 mol% of quinine thiourea **3a** as catalyst in dichloromethane (DCM) at 25 °C for three hours furnished the products **5**/**6** (which were found to be in fast dynamic equilibrium), which on further lactonization with *p*-TSA catalyst furnished *cis*-(−)-**7** in good yield with excellent "ee" and "de" (Scheme 30.1). Control experiments revealed that the outcome of the product selectivity and reactivity was controlled by neighboring group participation of Ar–O–H through hydrogen bonding with the carbonyl group of alkyl cyclopentanone-2-carboxylates **1** in the pre-transition state along with the catalyst. The reaction was productive for various neutral, electron-withdrawing and electron-donating substituted 2-(2-nitrovinyl)phenols **2** and furnished the products with excellent yields, ee's and de's. The neighboring *ortho*-hydroxyl group

involvement in the reaction through a 21-membered supramolecular assembly was elucidated as shown in Scheme 30.1. The reaction most likely proceeded via the pre-transition state **4**, where the less hindered *Si*-face of 2-(2-nitrovinyl)phenols **2** approached the *Si*-face of the *in situ* generated enol, to furnish the products **5**/**6** with excellent yields, ee's and de's.

We subsequently demonstrated the application of supramolecular organocatalysis for the asymmetric Michael reaction of cyclohexanone **8a** with 2-(2-nitrovinyl) phenols **2**, which were found to be nonreactive under simple organocatalysis, and produced the hexahydroxanthenols **12** with high yield, ee and de values (Scheme 30.2) [9]. The reaction in the presence of both 5 mol% of D-proline **9a** and quinine thiourea **3a** in DCM at 25 °C for five hours yielded a 1 : 1 ratio of the lactol products (+)-**11** in quantitative yield with 97% ee and 92–95% de, which got enriched after the reductive etherification to furnish product (−)-**12** in 90% yield with 94% de and >99% ee. For the opposite catalyst combination of L-proline **9b** and quinidine thiourea **3b**, the reaction yielded the opposite enantiomer (+)-**12**. Shuffled catalyst combinations resulted in strong mismatching of catalysts. Besides, the pre-catalyst components either **9a** or **3a**, when used alone, were not effective

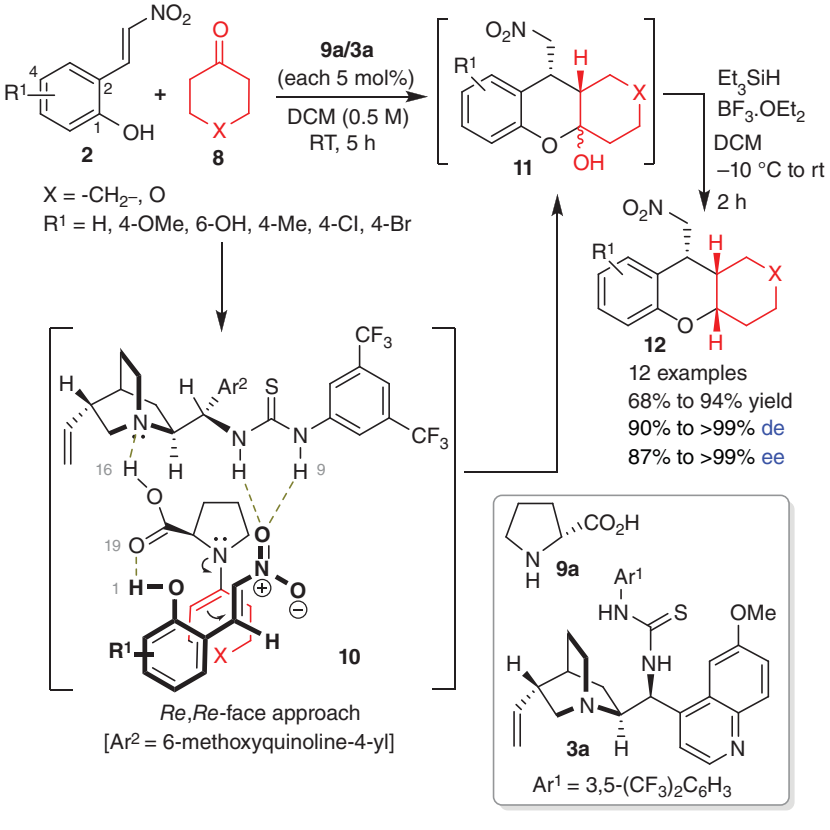

Scheme 30.2 D-Proline **9a**-quinine thiourea **3a** as supramolecular organocatalyst for asymmetric Michael addition of ketone **8** to *ortho*-hydroxy nitrostyrene **2**.

in promoting the reaction. Control experiments proved that hydrogen-bonding interaction between *ortho*-phenolic OH group of 2-(2-nitrovinyl)phenol **2** and carbonyl group of D-proline **9a** is decisive in determining the magnitude of asymmetric induction for the Michael product. The existence of the proposed 19-membered cyclic pre-transition state supramolecular assembly was strongly supported by evidence through electrospray ionization with high-resolution mass spectrometry (ESI-HRMS) technique, thereby establishing the mechanism (Scheme 30.2).

As per the elucidated mechanism, the reaction most likely proceeded through the pre-transition state **10** (Scheme 30.2), with four important interactions among the substrates and the catalysts, carboxylic group of D-proline **9a** undergoing proton exchange with quinoline moiety of quinine thiourea **3a**, two NH groups of quinine thiourea **3a** hydrogen bonding with NO_2 group of 2-(2-nitrovinyl)phenol **2**, secondary amine group of D-proline **9a** forming *syn*-enamine with cyclohexanone **8a**, and lastly phenolic OH group of 2-(2-nitrovinyl)phenol **2** protonating carbonyl group of D-proline **9a**, consequently forming the rigid 19-membered supramolecular cyclic pre-transition state to control the facial selectivity. A series of substituted 2-(2-nitrovinyl)phenols **2** furnished the products in excellent yields, de and ee values, tolerating the electronic and steric influence of the substrates. Remarkably, simple acetone **8b** also gave the chiral product in 93% yield with >99% de and 94% ee.

In 2014, we reported an asymmetric synthetic process for functionalized tetrahydroquinolines by Michael reaction of functionalized 1-azido-2-(2-nitrovinyl)benzene **13** with acetone **8b** through supramolecular organocatalysis, using L-phenylalanine **14a**/quinidine thiourea **3b** followed by reductive amination (Scheme 30.3) [10].

As the initial reaction screening with L-phenylglycine **14b**/quinidine thiourea **3b** and D-proline **9a**/quinine thiourea **3a** supramolecular catalyst assemblies did not deliver the desired results, different supramolecular organocatalysts assembled *in situ* from a library of two sets of organocatalysts were screened (Scheme 30.3). The best catalyst combination was found to be quinidine thiourea **3b** with L-phenylalanine **14a** in DCM, which gave the product keto azides **16** in good to high yields and excellent ee's within 72 hours. Various functionalized 1-azido-2-(2-nitrovinyl)benzenes **13** underwent the reaction with acetone **8b** to furnish the chiral keto azides **16** in good yields and excellent ee's, which were then transformed into medicinally significant functionalized tetrahydroquinolines through reductive amination (Scheme 30.3).

Control experiments proved that along with NO_2, N_3 also involved in hydrogen bonding with the N–H group of the catalyst **3b**, and so the position of N_3 on the aryl was crucial for achieving high rate and selectivity in the reaction. By using ESI-HRMS technique, we identified the catalytic pre-transition state intermediates and proposed that the mechanism proceeded through conformationally flexible cyclic 22-membered pre-transition state supramolecular assembly **15**, by **14a**/**3b**-catalysis as represented in Scheme 30.3. The interactions that held together the 22-membered pre-transition state were the CO_2H group hydrogen bonding with the *tert*-amine group of **3b**, NH groups of **3b** hydrogen bonding with both N_3 and NO_2 groups, the primary amino group of **14a** forming enamine with acetone, and finally the NO_2 group hydrogen bonding with the enamine NH.

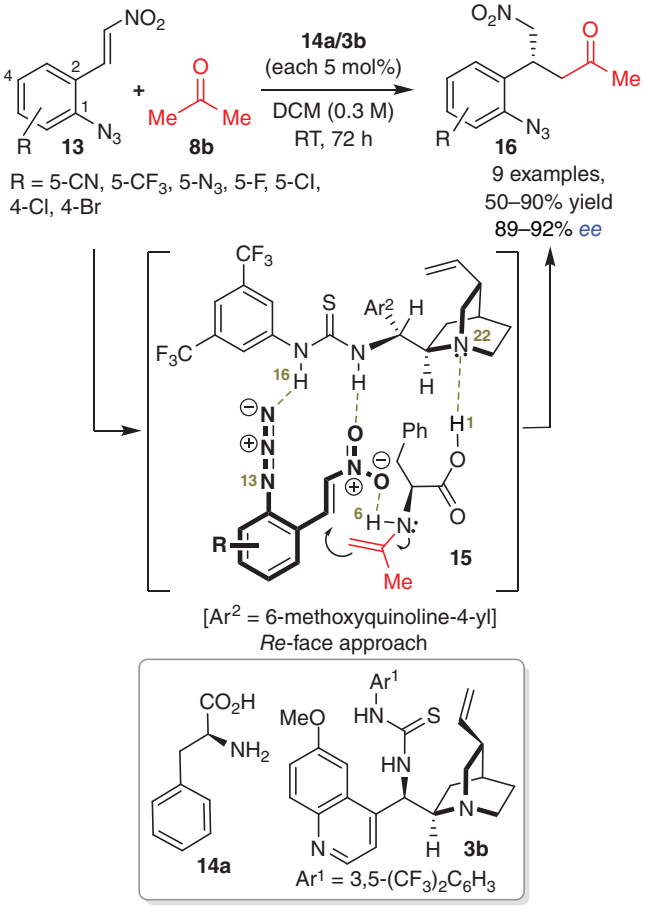

Scheme 30.3 L-Phenylalanine **14a**-quinidine thiourea **3b** as supramolecular organocatalyst assembly for asymmetric Michael addition of acetone **8b** to 1-azido-2-(2-nitrovinyl)benzene **13**.

Subsequently, in the next year, yet again an efficient supramolecular organocatalyst was illustrated for the asymmetric Michael reaction of various cyclic/acyclic ketones **8** with functionally rich *N*-benzyloxycarbonyl-N-*H*-(*E*)-2-(2-nitrovinyl) anilines **17** to furnish the chiral carbamates **19** in excellent yields with excellent enantioselectivity, diastereoselectivity, and chemoselectivity (Scheme 30.4) [11]. Though the presence of *N*-protected amino group on the aryl ring of (*E*)-2-(2-nitrovinyl)anilines rendered them inactive under standard organocatalysis, amazingly, fruition was attained with newly emerging supramolecular organocatalysts, wherein D-proline **9a** and quinine thiourea **3a** (each 5 mol%) were used in CH_2Cl_2 at 25 °C, to furnish the chiral products **19** in high yields with excellent ee's and de's. Remarkably, different N-protected-*N*-*H*-(*E*)-2-(2-nitrovinyl)anilines **17** were accepted for the reaction. Opposite enantiomer of the product **19** was obtained from the catalyst combination of L-proline **9b** and quinidine thiourea **3b**

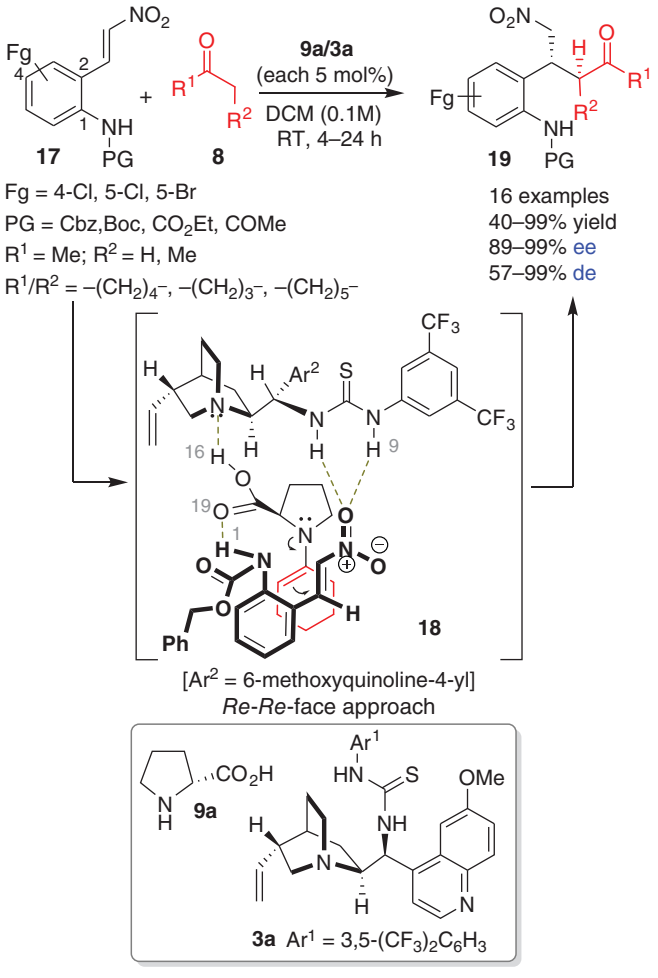

Scheme 30.4 D-Proline **9a** and quinine thiourea **3a** as supramolecular organocatalyst for asymmetric Michael addition of ketones **8** to (*E*)-2-(2-nitrovinyl)anilines **17**.

in moderate yield with excellent ee and de. Various simple as well as functionalized cyclic/acyclic ketones were subjected to the reaction to furnish the products **19** in good to excellent yields with good to excellent de and ee values. Diverse substituents on the aryl ring of N-protected-*N*-*H*-(*E*)-2-(2-nitrovinyl)anilines **17** were tolerated in the reaction. Based on control experiment results, the mechanism was explained through *in situ* formation of a cyclic supramolecular self-assembled 19-membered pre-transition state and the reaction most likely proceeded via pre-transition state **18** as depicted in Scheme 30.4. Four essential interactions among the two substrates and the two catalysts governed the formation of cyclic 19-membered pre-transition state **18** and efficiently facilitated the highly enantioselective Michael adduct formation. Experimental evidence was gathered for the supramolecular 19-membered pre-transition state by investigating the ongoing reaction using HRMS (ESI), which

revealed the presence of self-assembled pre-transition state [**18**·H^+] from the very start of the reaction.

30.3 Concluding Remarks

For the asymmetric synthesis of specially functionalized complex organic molecules, supramolecular organocatalysis has become a significant tool, due to the limitless potential of successfully working catalyst systems that can be assembled. The various observed interactions that held together the reaction partners, by means of the involved catalysts, contribute to a great deal to achieve high rate as well as high selectivities for diverse reactions. This study has also shed some light on the mechanistic studies and methods of identifying and supporting the pre-transition states. We hope that this compilation would gather more audiences and provide a good reinforcement for further extensions and explorations of many more reactions in the future.

Acknowledgments

This work was made possible by a grant from the Department of Science and Technology (DST), SERB, New Delhi [Grant No.: EMR/2015/000860]. KSS thanks Council of Scientific and Industrial Research (CSIR), New Delhi for her research fellowship.

References

1 (a) Friedrich, S. and Hahn, F. (2015). *Tetrahedron* 71: 1473–1508. (b) Wee, E.J.H. and Trau, M. (2014). *Nat. Chem.* 6: 756–757. (c) Scott, L.T. (2014). *Nat. Chem.* 6: 177–178. (d) Oroz-Guinea, I. and García-Junceda, E. (2013). *Curr. Opin. Chem. Biol.* 17: 236–249. (e) Benkovic, S.J. and Hammes-Schiffer, S. (2003). *Science* 301: 1196–1202.

2 (a) Pellissier, H. (2016). *Adv. Synth. Catal.* 358: 2194–2259. (b) Gensch, T., Hopkinson, M.N., Glorius, F., and Wencel-Delord, J. (2016). *Chem. Soc. Rev.* 45: 2900–2936. (c) Souillart, L. and Cramer, N. (2015). *Chem. Rev.* 115: 9410–9464. (d) Mo, J., Wang, L., Liu, Y., and Cui, X. (2015). *Synthesis* 47: 439–459. (e) Zhang, X.-S., Chen, K., and Shi, Z.-J. (2014). *Chem. Sci.* 5: 2146–2159.

3 (a) Huang, Y.-Y., Cai, C., Yang, X. et al. (2016). *ACS Catal.* 6: 5747–5763. (b) Lear, M.J. and Hayashi, Y. (2013). *ChemCatChem* 5: 3499–3501. (c) Memeo, M.G. and Quadrelli, P. (2012). *Chem. Eur. J.* 18: 12554–12582. (d) Bartoli, G. and Melchiorre, P. (2008). *Synlett* 12: 1759–1772. (e) Erkkila, A., Majander, I., and Pihko, P.M. (2007). *Chem. Rev.* 107: 5416–5470.

4 (a) Desmarchelier, A., Coeffard, V., Moreau, X., and Greck, C. (2014). *Tetrahedron* 70: 2491–2513. (b) Ramachary, D.B. and Reddy, Y.V. (2012). *Eur. J. Org. Chem.* 2012: 865–887. (c) Mukherjee, S., Yang, J.W., Hoffmann, S., and

List, B. (2007). *Chem. Rev.* 107: 5471–5569. (d) List, B. (2004). *Acc. Chem. Res.* 37: 548–557. (e) Hagiwara, H. (2004). *Mini-Rev. Org. Chem.* 1: 169–182. (f) Notz, W., Tanaka, F., and Barbas, C.F. III, (2004). *Acc. Chem. Res.* 37: 580–591.

5 (a) Serdyuk, O.V., Heckel, C.M., and Tsogoeva, S.B. (2013). *Org. Biomol. Chem.* 11: 7051–7071. (b) Siau, W.-Y. and Wang, J. (2011). *Catal. Sci. Technol.* 1: 1298–1310. (c) Hideto, M. and Yoshiji, T. (2008). *Bull. Chem. Soc. Jpn.* 81: 785–795. (d) Abigail, G.D. and Eric, N.J. (2007). *Chem. Rev.* 107: 5713–5743. (e) Mark, S.T. and Eric, N.J. (2006). *Angew. Chem. Int. Ed.* 45: 1520–1543. (f) Peter, R.S. (2003). *Chem. Soc. Rev.* 32: 289–296.

6 (a) Srivastava, M., Rai, P., Singh, J. et al. (2016). *Curr. Organocatal.* 3: 32–38. (b) Brown, C.J., Toste, F.D., Bergman, R.G., and Raymond, K.N. (2015). *Chem. Rev.* 115: 3012–3035. (c) Kenny, R. and Liu, F. (2015). *Eur. J. Org. Chem.* 2015: 5304–5319. (d) Inamdar, S.M., Shinde, V.S., and Patil, N.T. (2015). *Org. Biomol. Chem.* 13: 8116–8162. (e) Liu, J., Chen, L., Cuis, H. et al. (2014). *Chem. Soc. Rev.* 43: 6011–6061. (f) Hapiot, F., Bricout, H., Menuel, S. et al. (2014). *Catal. Sci. Technol.* 4: 1899–1908. (g) Raynal, M., Ballester, P., Vidal-Ferran, A., and van Leeuwen, P.W.N.M. (2014). *Chem. Soc. Rev.* 43: 1660–1733. (h) Woods, P.A. and Smith, A.D. (2012). Supramolecular organocatalysis, Chapter 4. In: *Supramolecular Chemistry: From Molecules to Nanomaterials*, vol. 1 (eds. J.W. Steed and P.A. Gale), 1383–1414. Wiley. ISBN: 978-0-470-74640-0. (i) Brière, J.-F., Oudeyer, S., Dalla, V., and Levacher, V. (2012). *Chem. Soc. Rev.* 41: 1696–1707. (j) Meeuwissen, J. and Reek, J.N.H. (2010). *Nat. Chem.* 2: 615–621. (k) Bella, M., Schietroma, D.M.S., Cusella, P.P. et al. (2009). *Chem. Commun.*: 597–599. (l) Rao, K.R., Nageswar, Y.V.D., Krishnaveni, N.S., and Surendra, K. (2005). *Adv. Org. Synth.* 1: 301–339. (m) Desiraju, G.R. (1995). *Angew. Chem.* 107: 2541–2558, *Angew. Chem. Int. Ed.* 34: 2311–2327.

7 (a) Faisca Phillips, A.M. (2016). *Curr. Org. Synth.* 13: 687–725. (b) Jusseau, X., Chabaud, L., and Guillou, C. (2014). *Tetrahedron* 70: 2595–2615. (c) Bhanja, C., Jena, S., Nayak, S., and Mohapatra, S. (2012). *Beilstein J. Org. Chem.* 8: 1668–1694. (d) Vicario, J.L., Badia, D., and Carrillo, L. (2007). *Synthesis* 14: 2065–2092. (e) Sulzer, M.S. and Alexakis, A. (2007). *Chem. Commun.* 30: 3123–3135. (f) Rele, D. and Trivedi, G.K. (1993). *J. Sci. Industrial Research* 52: 13–28.

8 Ramachary, D.B., Madhavachary, R., and Prasad, M.S. (2012). *Org. Biomol. Chem.* 10: 5825–5829.

9 Ramachary, D.B., Sakthidevi, R., and Shruthi, K.S. (2012). *Chem. Eur. J.* 18: 8008–8012.

10 Ramachary, D.B. and Shruthi, K.S. (2014). *Org. Biomol. Chem.* 12: 4300–4304.

11 Ramachary, D.B., Shruthi, K.S., and Madhavachary, R. (2015). *Eur. J. Org. Chem.* 2015: 6413–6418.

Part VI

Supramolecular Catalysis in Water

31

Metal Catalysis in Micellar Media

Giorgio Strukul, Fabrizio Fabris, and Alessandro Scarso

Università Ca' Foscari di Venezia, Dipartimento di Scienze Molecolari e Nanosistemi, via Torino 155, Mestre Venezia 30123, Italy

31.1 Introduction

The use of micellar media is receiving increasing attention in transition metal catalysis for a number of reasons involving both practical and fundamental issues, such as the possibility to get rid of large amounts of organic solvents as reaction media and simplify work-up operations involved in product isolation, thus resulting in a significant improvement from the point of view of environmental acceptability. This is an important motivation from a practical point of view and in the perspective of possible industrial applications. Equally important are some extra advantages imparted by micelles, some of them hardly predictable when this field started being systematically explored. These include remarkable reaction rate acceleration, substrate, and product selectivities, all depending on the choice of the appropriate surfactant. These effects are basically due to the weak, yet very effective, supramolecular interactions between catalyst, substrate, and surfactant, occurring inside the confined nano space present in a micelle [1, 2]. These features are typical of the behavior observed in biological systems and more specifically in enzymes, which are an unlimited source of inspiration, so that micellar catalysis with transition metals can be viewed also as a bridge between traditional homogeneous catalysis and enzymatic catalysis.

The field has been reviewed a few times over the years [3–6] and has been particularly successful thanks to the use of neutral designer surfactants [7] introduced by the work of Lipshutz et al. [8], with which some remarkable results have been obtained in a series of classical C–C forming reactions (Heck, Stille, Suzuki-Miyaura, etc.) involved in the synthesis of active pharmaceutical ingredients. The interest in this area stemmed mainly from the seminal work of Engberts reported some 30 years ago [9], but it was not before 2004 that systematic evaluation of micellar systems for transition metal catalysis started being investigated.

Supramolecular Catalysis: New Directions and Developments, First Edition.
Edited by Piet W.N.M. van Leeuwen and Matthieu Raynal.

When we stepped in the field we had been working in catalytic oxidations with hydrogen peroxide for about 25 years, dealing with two-phase systems made of water (for hydrogen peroxide) and an immiscible organic solvent (generally 1,2-dichloroethane [DCE] or dichloromethane [DCM]) to dissolve both catalysts and substrates, observing that much better results in terms of activity and selectivity could be achieved with respect to single phase systems using, e.g. THF to dissolve all reaction ingredients. At that time we were mainly interested in finding an easy way to separate soluble catalysts from the reaction medium, this being our main motivation to test micellar media, with the idea of confining the catalyst inside the micelle dispersed in water, then extracting the products with a water immiscible solvent at the end of the reaction. Since the beginning we opted to use commercially available surfactants for a number of reasons: (i) the easy availability of a wide range of cationic, anionic, zwitterionic, and neutral surfactants with different chemical composition; (ii) their generally low cost; and (iii) their already wide use in industry (albeit for different purposes) that will eventually pave the way in case of possible practical applications. Also the choice of the transition metal is critical because it must withstand the presence of water without being inactivated. This excludes early transition metals. On the other hand, simple ions (e.g. Co^{2+}, Mn^{2+}, Zn^{2+}) may be good to mimic biochemical reactions, but they behave as simple Lewis acids catalysts and do not possess the kaleidoscope of properties exhibited by organometallic complexes. Looking for the appropriate class of catalysts, the choice is therefore limited mainly to noble metal complexes because many of them do not suffer from inactivation by water.

31.2 Oxidation Reactions

Our first bet in micellar catalysis was in enantioselective oxidation for several reasons: (i) because it is involved in the synthesis of important drugs like, e.g. the proton pump inhibitor Esomeprazole, the anticancer Taxol, or the anti-HIV Indinavir and (ii) because it allows one to check the effects of the reaction medium on reactivity and on whole array of selectivities (chemo-, regio-, enantio-), all at the same time.

Our initial tests were in the sulfoxidation of different thioanisoles with hydrogen peroxide using the cationic dimeric Pt complex **1** as catalyst [10]. Some representative data are shown in Figure 31.1.

As shown, the choice of the appropriate surfactant is crucial (anionic in this case) to improve both reactivity as well as the sulfoxide/sulfone ratio and the enantioselectivity of the former. Another important point was the optimization of the surfactant concentration described in Figure 31.2 because this has a dramatic effect on both the activity (initial rate) and the enantioselectivity. This is an operation that must be done with any micellar system.

Key features observed were (i) easy isolation of the products from the catalyst by simple diethyl ether/water SDS two phase separation, (ii) use of green and inexpensive hydrogen peroxide as oxidant, (iii) catalyst loading as low as 1 mol%, (iv) good yields, sulfoxide/sulfone ratios larger than 200, and enantioselectivities up to 88%, and (v) use of mild experimental conditions.

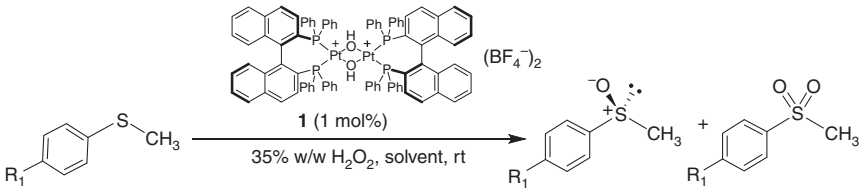

R_1	conv. (%)	**so/so$_2$** ratio	ee (%)	Solvent
H	99	80	16	CH_2Cl_2
NO_2	41	25	26	CH_2Cl_2
H	16	31	5	H_2O/CTAB
H	20	56	0	H_2O/Triton-X100
H	98	> 200	40	H_2O/SDS
NO_2	63	90	88	H_2O/SDS

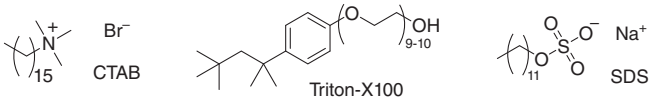

Figure 31.1 Stereoselective oxidation of thioanisoles in different micellar media with **1**.

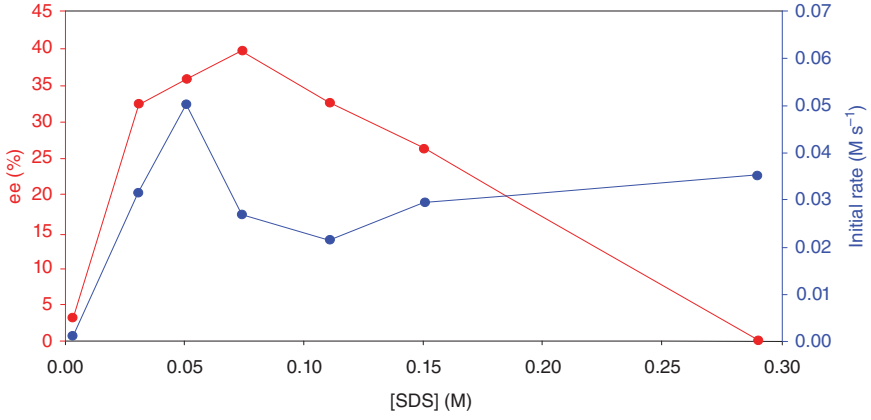

Figure 31.2 Effect of SDS concentration on the initial rate and ee in the sulfoxidation of thioanisole with **1**.

Similar results were found also in the enantioselective epoxidation of terminal alkenes [11] still using hydrogen peroxide and a cationic Pt complex **2** as the catalyst (see some data in Figure 31.3). In this case, a neutral surfactant proved to be the best choice. It was also possible to separate and recycle the Pt^{II} catalyst for at least three times without loss of activity and enantioselectivity.

However, it was in the Baeyer–Villiger oxidation of ketones that some surprising results were observed. Our initial attempts involved bis-cationic Pt complexes as catalysts in the desymmetrization of meso cyclic ketones [12]. In the case of 4-substituted cyclohexanones, the use of SDS in water as the reaction medium compared to DCE allowed significant amplification of the enantioselectivity but at the

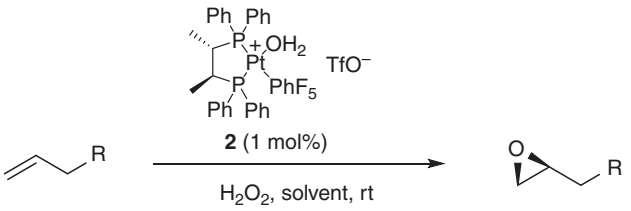

R = *n*-(C_3H_7), *n*-(C_5H_{11}), *n*-(C_9H_{19}), *iso*Pr, *iso*Bu, 3,4-$(MeO)_2$Ph

R	Solvent	Yield (%)	ee (%)
*iso*Pr	$ClCH_2CH_2Cl$	56	58
*iso*Pr	H_2O/Triton-X100	51	84

Figure 31.3 The enantioselective epoxidation of 4-methyl-1-pentene with **2**: comparison between the use of an organic solvent and a micellar medium.

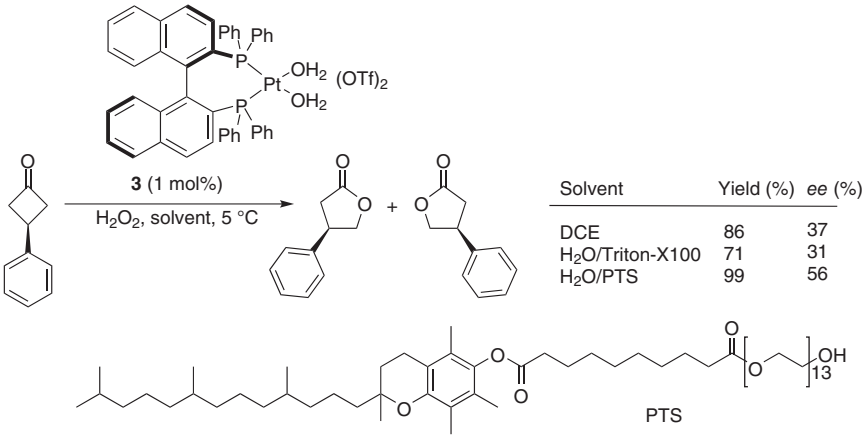

Figure 31.4 Effect of the surfactant in the asymmetric Baeyer–Villiger oxidation of meso 3-phenyl-cyclobutanone in micellar media with **3**.

expense of a much lower product yield, whereas with 3-substituted cyclobutanones (Figure 31.4) a neutral surfactant like PTS in water showed both an improvement in product yield and a much better asymmetric amplification.

However, the most striking effect on a catalytic reaction due to the supramolecular interactions induced by micelles was observed in the Baeyer–Villiger oxidation of a substituted cyclobutanone (Figure 31.5) [13]. The Co^{III} catalyst **4** used is commercially available and virtually useless in this reaction if tested in DCE, but once dissolved in water with the aid of the neutral surfactant Triton-X114, good catalytic activity, high regioselectivity, and a jump in enantioselectivity were observed. All that is simply due to the reaction occurring inside the micelles.

Overall, the use of surfactants in the oxidation reactions studied implies the partition of all reaction components (substrate, oxidant, and catalyst) between the micelle, bulk water, and the interphase between the two. Moreover, the lipophilicity of all species is crucial to rationalize their positioning in the micellar system,

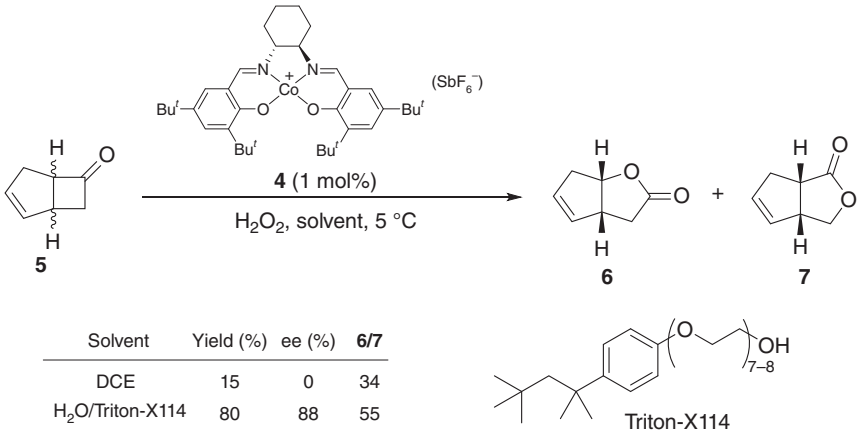

Solvent	Yield (%)	ee (%)	6/7
DCE	15	0	34
H_2O/Triton-X114	80	88	55

Figure 31.5 Striking effect on the activity and the enantioselectivity due to the micellar medium in the Baeyer–Villiger oxidation of a substituted cyclobutanone catalyzed by a Co^{III} catalyst **4**.

and as a general observation, more hydrophilic substrates gave better results in neutral surfactants, whereas anionic micelles were preferred for more lipophilic substrates. Analogously, a general increase in enantioselectivity was observed for more apolar substrates in water–surfactant medium compared with reaction in chlorinated solvent. The supramolecular control exerted by the micelle on the conformation/configuration of the catalyst–substrate adduct is not possible in common organic solvents, because simple solvation leads to a lower order of the molecules around the catalyst. A similar principle is observed in several enzymes, in which the binding of substrates and their juxtaposition in the hydrophobic active site is driven by the hydrophobic effect.

31.3 C—C and C—X Bond Forming Reactions

The use of micellar media was extended to a variety of catalyzed C—C and C—heteroatom bond forming reactions. The first category includes hydroformylation [14], C=C double bond isomerization [15], Diels–Alder reaction [16], and Heck coupling [17]. A summary of the essential results obtained in these catalytic processes is shown in Figure 31.6.

In hydroformylation (Figure 31.6a), the micellar system containing a bis-cationic Pt catalyst modified with a large-bite angle diphosphine shows catalytic activity comparable, and in some cases better, than traditional Pt–Sn systems, with excellent linear to branched selectivities that can rival with the best Rh catalysts. The catalytic system can be successfully applied to a large range of substrates characterized by terminal or internal cis double bonds and even with the latter high selectivities to the most desired linear aldehydes is observed thanks to a prior isomerization process. The catalyst can be recycled up to four times employing 1 mol% as the catalyst loading with only a modest decrease in activity and no effect on selectivity.

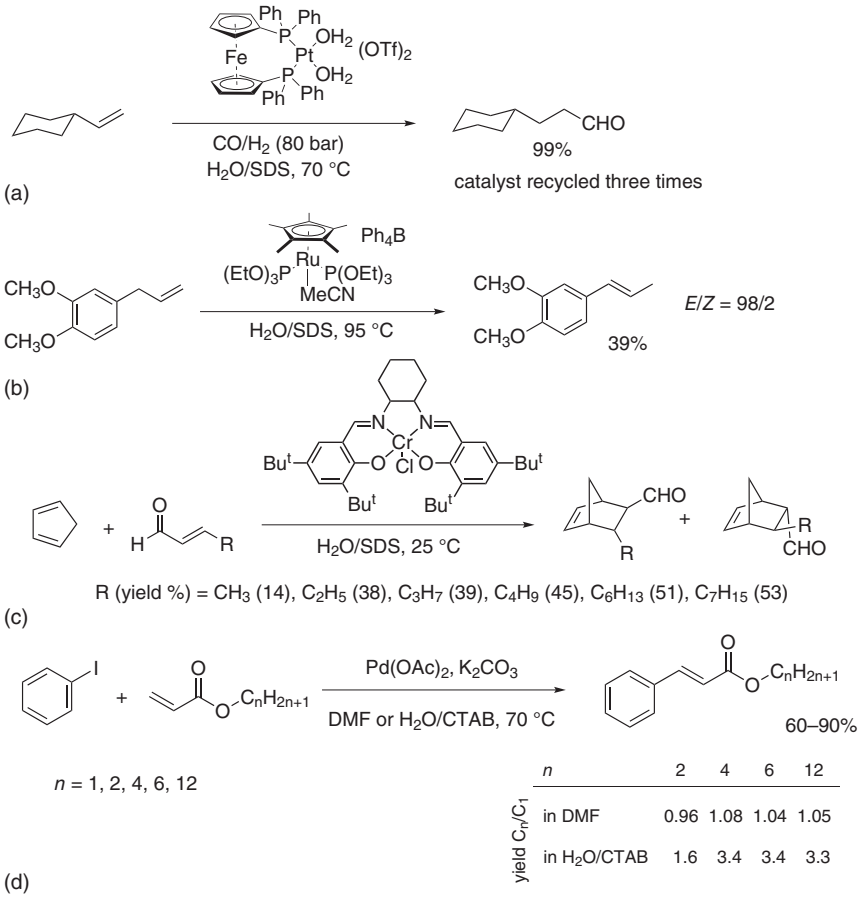

Figure 31.6 An overview of the results obtained in hydroformylation (a), C=C double bond isomerization (b), Diels–Alder reaction (c), and Heck coupling (d) in catalytic experiments carried out under micellar conditions.

In isomerization (Figure 31.6b), a cationic Ru complex in water/SDS was applied to a series of allylbenzenes that are precursors to fragrances showing excellent E-isomer selectivity and overall good performance with respect to the use of organic solvents. The latter was retained even when the reaction was scaled up to substrate in gram quantities.

In the Diels–Alder reaction (Figure 31.6c) between cyclopentadiene and a series of α,β-unsaturated aldehydes bearing aliphatic chains of variable length, a Cr^{III}(salen)Cl catalyst embedded into a H_2O/SDS supramolecular aggregate can display substrate selectivity. It was observed that while in $CHCl_3$ there is virtually no difference in yields when using the variable length dienophiles in competitive experiments, in the micellar system an up to 3.5 increase in activity in favor of longer substrates compared to the shorter ones was observed.

A similar effect was observed in the Pd-mediated Heck coupling between iodoaryl substrates and linear acrylic esters in water (Figure 31.6d) to yield cinnamyl

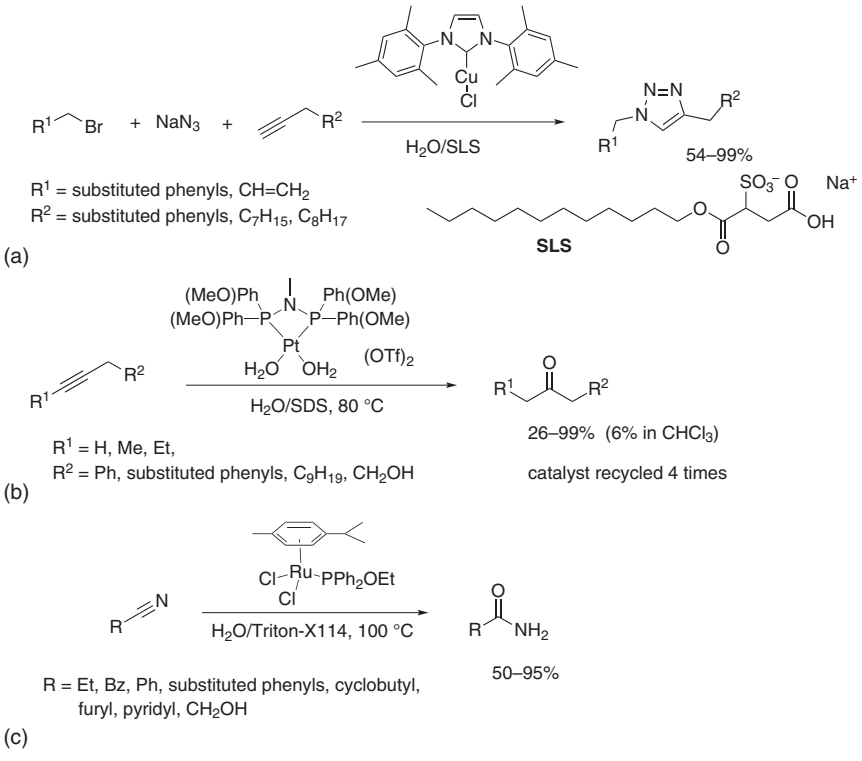

Figure 31.7 An overview of the results obtained in the synthesis of 1,2,3 triazoles (a), the hydration of alkynes (b), and the hydration of nitriles (c).

esters of different length. Here some competitive experiments were carried out by reacting methyl acrylate (C_1) and longer length *n*-alkyl acrylates (C_n) in pairs and taking the ratio in yields between C_n and C_1 as a parameter to evaluate substrate selectivity. While no difference was observed operating in DMF as the solvent, in water/cetyltrimethylammonium bromide longer acrylates give much better yields in cinnamyl esters with respect to shorter ones.

In the latter examples for Diels–Alder and Heck reactions, the selection rule is imparted by the hydrophobic effect that forces the more lipophilic substrates to migrate inside the micelle and get in contact with the catalyst. The results obtained underline the importance of hydrophobic interactions and mimic the behavior observed with natural catalysts such as enzymes. Substrate selectivity has often been observed in confined spaces such as molecular capsules [1, 2], but only rarely in micellar media.

The C—X bond forming reactions studied were the following: the synthesis of 1,2,3-triazoles [18], the hydration of alkynes [19], and the hydration of nitriles [20]. A summary of the main features is reported in Figure 31.7.

A very simple and efficient regioselective multicomponent synthesis of 1,4-disubstituted 1,2,3-triazoles starting from organic bromides, sodium azide, and alkynes catalyzed by 1 mol% of a Cu^I catalyst modified with a substituted

imidazole-2-ylidene ligand was accomplished in one pot, operating in water at room temperature and in the presence of surfactants (Figure 31.7a). The micellar medium obtained by the addition of commercially available SLS or TPGS-750-M surfactants in water favors the *in situ* formation of the organic azide, thus avoiding its separate synthesis and storage. The micellar medium is also responsible for the consecutive positive interaction between the organic azide and the alkyne mediated by the organometallic Cu^{I} catalyst. This system could be applied to a wide range of combinations of organic bromides and alkynes, obtaining overall more than 20 different 1,2,3-triazoles in high yields. In one case, the reaction was scaled up to 2 mmol of product. The triazole products could be easily isolated by means of simple extraction with ethyl acetate. The multicomponent reaction can be carried out in a greener way and is competitive in terms of yields and selectivities with respect to an isolated organic azide, thus avoiding the manipulation of these noxious chemicals and with the advantage of carrying out the whole procedure in one pot.

Alkyne hydration was achieved thanks to a new class of monomeric bis-cationic Pt complexes bearing a series of small bite angle diphosphinamine PNP ligands operating in water under micellar conditions selectively yielding the corresponding ketones (Figure 31.7b). The micellar medium enables a large improvement in catalytic activity compared to the reaction performed in homogeneous binary solvent mixtures like acetone-water, dioxane-water, or biphasic 1 : 1 $CHCl_3$/water. The specific role played by the micellar aqueous medium is to favor the formation of catalytically active Pt^{II} species bearing σ-vinyl moieties, while in organic media with water the reaction stops at forming the π-coordinated alkyne species. The strong interaction between the bis-cationic catalyst and the anionic micelles allows catalyst recycling for four times without significant loss of catalytic activity. The Pt^{II} catalytic system remains confined in the aqueous phase, while the product was isolated by extraction with hexane.

Efficient nitrile hydration to the corresponding amide derivatives was observed in water using poorly soluble $[RuCl_2(\eta^6\text{-arene})(PR_3)]$ catalysts with the aid of surfactants to ensure substrate and catalyst solubilization, thus enabling a ligand effect study on catalytic activity (Figure 31.7c). Neutral surfactants showed the best catalytic activity, probably because they do not interfere (as charged species do) with ligand exchange on the catalyst, allowing high amide yields with a large variety of nitrile substrates. In this case, micellar media enabled the screening of common monophosphine ligands, like in classical organometallic chemistry studies, and it was observed that neither electron-rich nor electron-poor phosphines ensured high catalytic activity, but rather an appropriate balance of steric and electronic features is required. In general, with respect to the use of intrinsically water soluble catalysts, the micellar approach can, in principle, be applied to exploit libraries of existing catalysts for libraries of reactions without the need to synthesize specific water-soluble catalysts for each reaction.

31.4 Metal Nanoparticles in Micellar Media

The micellar media approach to catalysis was not limited to organometallic catalysts, and we tested also a facile and inexpensive method for the preparation of Pd nanoparticles (Pd-NP) in water stabilized by anionic sulfonated surfactants as shown in Figure 31.8 [21]. These were obtained by stirring aqueous solutions of $Pd(OAc)_2$ with commercial anionic surfactants **8**–**11** and further treating under hydrogen atmosphere for variable amounts of time (Figure 31.8a). The Pd-NPs

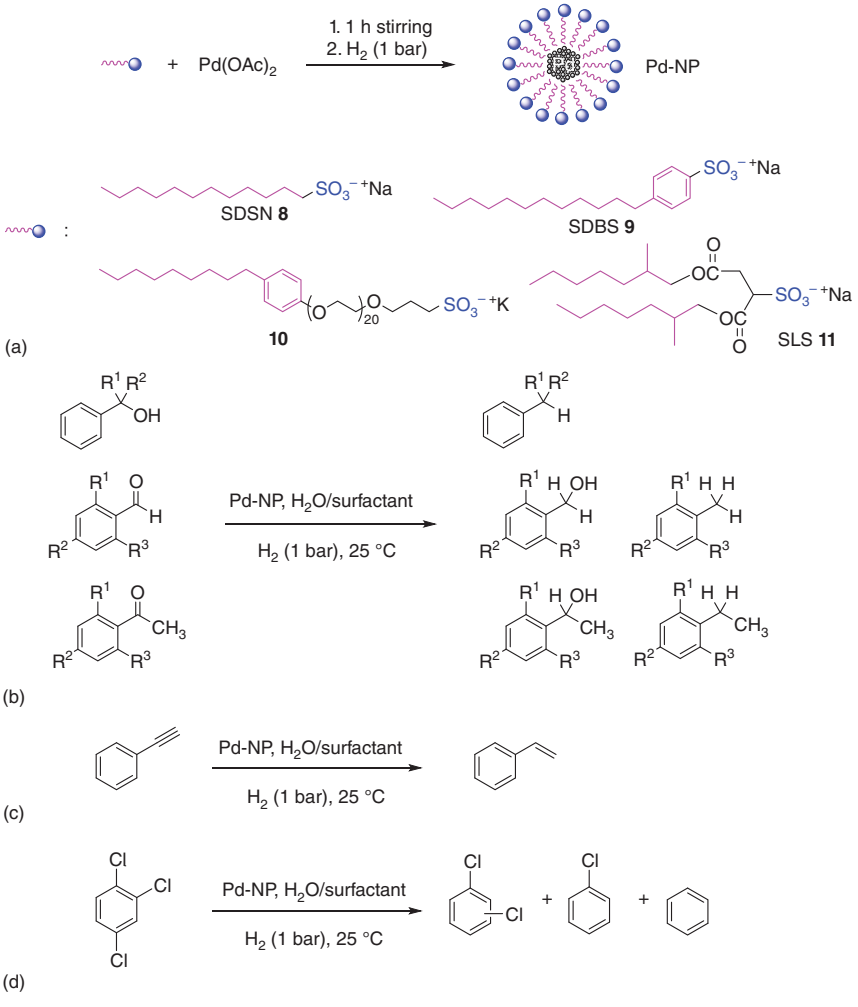

Figure 31.8 Preparation of Pd nanoparticles with different sulfonated anionic surfactants **8**–**11** and their reactivity in a series of hydrogenation reactions.

showed similar size range and distribution but different morphologies as a function of the nature of the surfactant employed as well as its concentration and experimental conditions.

The aqueous Pd nanoparticle solutions were tested in the selective hydrogenolysis of aryl-alcohols, leading to complete conversion to the deoxygenated products even in the absence of strong Brønsted acids as well as in the hydrogenation of aromatic aldehydes and ketones (Figure 31.8b). Their activity and selectivity could be modulated by choosing the appropriate surfactant; thus, with **10** the hydrogenation of benzaldehyde and other aromatic derivatives showed a very high chemoselectivity toward the formation of the corresponding benzyl alcohols, whereas Pd/C as a comparison was more difficult to control, causing the formation of deoxygenation reaction products. Similarly, with sodium dodecylsulfonate **8** and with sodium lauryl sulfosuccinate **11** complete hydrogenolysis was observed and deoxygenation of secondary and tertiary alcohols could be achieved with quantitative conversion.

Surfactant sodium dodecylbenzene sulfonate **9** gave a catalytic system with controlled activity in the semi-hydrogenation reactions of alkynes to alkenes (Figure 31.8c) with a particular affinity for compounds containing aromatic rings, probably due to π–π supramolecular interactions between the surfactant and the substrates.

To demonstrate the generality of the catalytic system developed in water, we studied also the application of these systems to the decomposition of hazardous chlorinated aromatic compounds directly in water (Figure 31.8d). With this purpose, the catalytic activity of Pd-NP stabilized by the sulfonated anionic surfactant **10** was checked in the reaction of 1,2,4-trichlorobenzene. Pd-NP could convert quantitatively the substrate under mild conditions in water, and recycling of the catalytic system was possible without detrimental effects on its activity and selectivity.

In this system, the role of the surfactant is crucial to ensure the necessary stability to Pd-NP under the catalytic conditions applied. In spite of the fact that the reaction environment is always the same (water, surfactant, and hydrogen), the type of substrate analyzed in the individual cases can completely change the stability of the metal system; for example, surfactant **9** leads to Pd metal precipitation with aldehydes while giving the best catalyst with acetylenes. In some cases, the delicate balance between catalytic activity and stability can be quite significant as in the case of the hydro-dechlorination reaction with surfactant **10** that can even be recycled.

In all these reactions, criteria like particle size/particle distribution were poorly helpful to rationalize catalytic activity and selectivity; rather, intriguing and somehow unpredictable "ligand" effect by the different surfactants capping the Pd-NP could be invoked to explain, at least in part, the sometimes large differences in activity observed. What is interesting is also that a benchmark catalyst like Pd/C can often be surpassed in activity and/or selectivity in the reactions tested by simply switching to the appropriate cheap and commercially available surfactant, thereby providing an easy to use, flexible, and practical catalytic system capable of efficiently addressing a variety of synthetically significant hydrogenation reactions.

Pd-NP stabilized by **8** showed also a remarkable example of substrate selectivity in the selective hydrogenation of a series of α,β-unsaturated aldehydes (Figure 31.9)

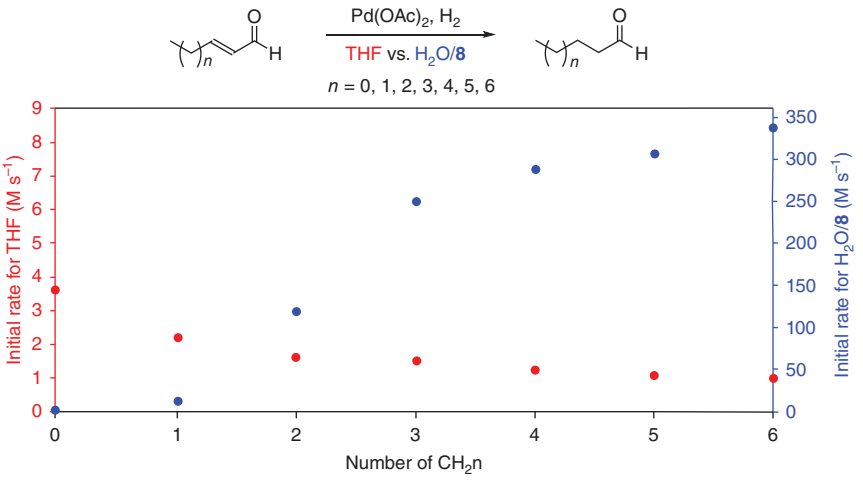

Figure 31.9 Substrate selectivity in the hydrogenation of a series of α,β-unsaturated aldehydes catalyzed by Pd metal in different media.

[22]. The Pd metal catalyst was generated either by treating a THF solution of $Pd(OAc)_2$ with hydrogen or as in Figure 31.8 in water containing **8**. A competitive experiment was performed in both reaction media by feeding seven α,β-unsaturated aldehydes from C_4 to C_{10} all together into the catalytic system. Substrate selectivity was determined by calculating the relative initial rates for all aldehydes with respect to the slowest one. As shown in Figure 31.9, in THF the relative rates decreased from C_4 to C_{10} with a maximum selectivity factor of 3.6 for the shortest aldehyde. When the same experiment was carried out in the micellar medium, not only the trend was reversed, but the substrate selectivity showed a 330-fold increase on going from C_4 to C_{10}.

Here again the selection rule corresponds to the affinity between the aldehyde and the micelles generated by **8**. These competitive experiments demonstrate that this driving force can greatly amplify selection issues even in simple systems like the present ones as shown by the large preference for longer lipophilic substrates that outperform the shorter more hydrophilic ones by a factor of two orders of magnitude.

31.5 Catalyst Surfactant Interactions

In conclusion, commercial surfactants can be profitably exploited for carrying out in water a variety of catalytic reactions using well-known transition metal complexes already optimized in traditional homogeneous catalysis for working in organic solvents. The advantages of micellar media are the following:

- They drastically reduce the use of large amounts of organic solvents that in the industrial practice can be recycled only to a minor extent.
- They improve the separation and recycling of the catalyst. Although this is not always possible, we have observed that it depends on catalyst robustness, on the

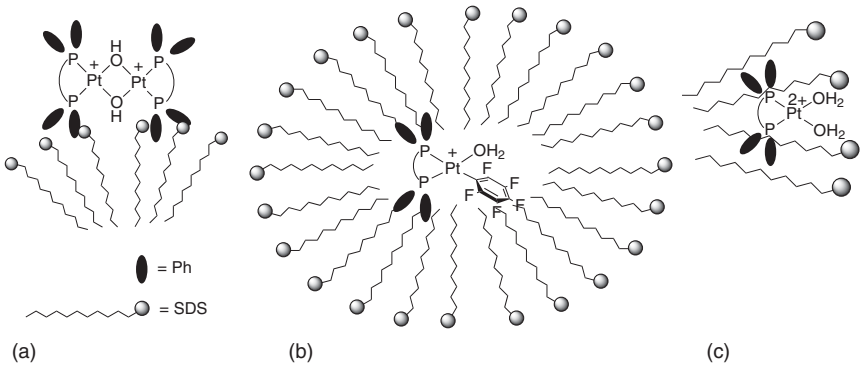

Figure 31.10 Positioning of cationic (diphosphine)Pt complexes in SDS micelles in different oxidation reactions with hydrogen peroxide: sulfoxidation (a), epoxidation (b), Baeyer–Villiger oxidation (c).

nature of the organic solvent used for extraction, on the hydrophobic nature of reaction products, and on the nature of the surfactant. From our experience, ionic surfactants tend to favor separation.

- They increase catalytic activity, partly because of an increase in concentration inside the micelle by an order of magnitude with respect to an organic solution and partly because of the interactions between the micelle and the transition state of the reaction in the micelle confined space.

The latter argument is crucial also for selectivity and has not been adequately addressed in the literature at least for micellar catalysis. In studying catalytic oxidation reactions, we have observed that, even with a very simple surfactant like sodium dodecyl sulfate, quite similar cationic Pt^{II} complexes exhibit different positioning (Figure 31.10) inside the surfactant, driven essentially by the gradient of polarity present in the micelle on going from the hydrophilic surface to the hydrophobic core. This nano environment influences differently the steric and electronic requirements necessary to stabilize the transition state of the catalyzed reaction, thus affecting both the activity and selectivity.

The extent of this stabilization can be easily evaluated from the ee in the case of enantioselective reactions and can be very high. For example in the Baeyer–Villiger oxidation shown in Figure 31.5, there is no difference in energy between the diastereomeric transition states when working in DCE (ee = 0%), while in water/Triton-X114, the two diastereomeric transition states differ by $-6.82\ kJ\ mol^{-1}$ (ee = 88%), a large discrimination effect solely due to the interactions with the micelle.

From an industrial point of view, all together these factors imply a drastic decrease in the E-factor associated with the individual reactions, an improvement of yields in the desired product, milder reaction conditions, ease in catalyst and products separation, a decrease in energy consumption, a shortening of operation times, and eventually a cut in production costs.

Acknowledgments

Financial support for this research from Università Ca' Foscari Venezia, Ministero Università e Ricerca and Fondazione CARIPARO SELECT project is gratefully acknowledged.

References

1 Wang, K., Jordan, J.H., Hu, X.-Y., and Wang, L. (2020). Supramolecular strategies for controlling reactivity within confined nanospaces. *Angew. Chem. Int. Ed.* 59: 13712–13721.
2 Grommet, A.B., Feller, M., and Klajn, R. (2020). Chemical reactivity under nanoconfinement. *Nat. Nanotechnol.* 15: 256–271.
3 La Sorella, G., Strukul, G., and Scarso, A. (2015). Recent advances in catalysis in micellar media. *Green Chem.* 17: 644–683.
4 Scarso, A. (2016). Micellar nanoreactors. In: *Encyclopedia of Inorganic and Bioinorganic Chemistry* (ed. D.A. Atwood), 1–16. Chichester, UK: Wiley.
5 Scarso, A. and Strukul, G. (2019). Transition metal catalysis in micellar media: much more than a simple green chemistry promise. In: *Green Synthetic Processes and Procedures* (ed. R. Ballini). London: The Royal Society of Chemistry.
6 Sar, P., Ghosh, A., Scarso, A., and Saha, B. (2019). Surfactant for better tomorrow: applied aspect of surfactant aggregates from laboratory to industry. *Res. Chem. Intermed.* 45: 6021–6041.
7 Lorenzetto, T., Berton, G., Fabris, F., and Scarso, A. (2020). Recent designer surfactants for catalysis in water. *Catal. Sci. Technol.* 10: 4492–4502.
8 Lipshutz, B.H., Ghorai, S., and Cortes-Clerget, M. (2018). The hydrophobic effect applied to organic synthesis: recent synthetic chemistry "in water". *Chem. Eur. J.* 24: 6672–6695.
9 Engberts, J.B.F.N. (1992). Catalysis by surfactant aggregates in aqueous solution. *Pure Appl. Chem.* 64: 1653–1660.
10 Scarso, A. and Strukul, G. (2005). Asymmetric sulfoxidation of thioethers with hydrogen peroxide in water mediated by platinum chiral catalyst. *Adv. Synth. Catal.* 347: 1227–1234.
11 Colladon, M., Scarso, A., and Strukul, G. (2007). Towards a greener epoxidation method: use of water-surfactant media and catalyst recycling in the platinum-catalyzed asymmetric epoxidation of terminal alkenes with hydrogen peroxide. *Adv. Synth. Catal.* 349: 797–801.
12 Cavarzan, A., Bianchini, G., Sgarbossa, P. et al. (2009). Catalytic asymmetric Baeyer–Villiger oxidation in water by using PtII catalysts and hydrogen peroxide: supramolecular control of enantioselectivity. *Chem. Eur. J.* 15: 7930–7939.
13 Bianchini, G., Cavarzan, A., Scarso, A., and Strukul, G. (2009). Asymmetric Baeyer–Villiger oxidation with Co(Salen) and H_2O_2 in water: striking supramolecular micelles effect on catalysis. *Green Chem.* 11: 1517–1520.

14 Gottardo, M., Scarso, A., Paganelli, S., and Strukul, G. (2010). Efficient platinum(II) catalyzed hydroformylation reaction in water: unusual product distribution in micellar media. *Adv. Synth. Catal.* 352: 2251–2262.

15 Sperni, L., Scarso, A., and Strukul, G. (2017). Micellar promoted alkenes isomerization in water mediated by a cationic half-sandwich Ru(II) complex. *Inorg. Chim. Acta* 455: 535–539.

16 Trentin, F., Scarso, A., and Strukul, G. (2011). Micellar-driven substrate selectivity in Cr(salen)Cl catalytic Diels–Alder reaction in water. *Tetrahedron Lett.* 52: 6978–6981.

17 La Sorella, G., Bazan, M., Scarso, A., and Strukul, G. (2013). Competitive micellar induced substrate selectivity in the Pd mediated heck coupling between iodoaryl substrates and linear acrylic esters in water. *J. Mol. Catal. A: Chem.* 379: 192–196.

18 Tasca, E., La Sorella, G., Sperni, L. et al. (2015). Micellar promoted multi-component synthesis of 1,2,3-triazoles in water at room temperature. *Green Chem.* 17: 1414–1422.

19 Trentin, F., Chapman, A.M., Scarso, A. et al. (2012). Platinum(II) diphosphinamine complexes for the efficient hydration of alkynes in micellar media. *Adv. Synth. Catal.* 354: 1095–1104.

20 Cavarzan, A., Scarso, A., and Strukul, G. (2010). Efficient nitrile hydration mediated by Ru(II) catalysts in micellar media. *Green Chem.* 12: 790–794.

21 La Sorella, G., Sperni, L., Canton, P. et al. (2018). Selective hydrogenations and dechlorinations in water mediated by anionic surfactant-stabilized Pd nanoparticles. *J. Org. Chem.* 83: 7438–7446.

22 La Sorella, G., Canton, P., Strukul, G., and Scarso, A. (2014). Surfactant-induced substrate selectivity in the palladium-nanoparticle-mediated chemoselective hydrogenation of unsaturated aldehydes in water. *ChemCatChem* 6: 1575–1578.

32

Surfactant Assemblies as Nanoreactors for Organic Transformations

Margery Cortes-Clerget, Joseph R.A. Kincaid, Nnamdi Akporji, and Bruce H. Lipshutz

University of California, Department of Chemistry & Biochemistry, Building 557, Mesa road, Santa Barbara, CA 93 106, USA

32.1 Introduction

Performing chemistry in organic solvents will eventually become an embarrassing memory; a relic from a time when sustainability and mitigation of the environmental impact associated with organic synthesis was hardly a consideration. That's the future, at least if we have any say in the matter.

Growing environmental concerns over conventional methods used for organic synthesis have led to a boom in new green methodologies over the last few decades. Organic solvents, in particular, have garnered much of the attention as they constitute the bulk of waste generated by the chemical enterprise, and c. 80% within the pharmaceutical industry, according to the ACS Green Chemistry Institute [1]. Organic solvents themselves represent a considerable threat to both human and environmental health, many of them being toxic, carcinogenic, harmful to reproductive health, and/or flammable. Additionally, the solvent waste stream is problematic, as most is either burned (thereby releasing climate-altering greenhouse gases directly to the atmosphere) or buried where it can potentially breach containment and contaminate groundwater sources; i.e., an ecological catastrophe waiting to happen. If health and safety concerns are not enough to catalyze a switch to alternative solvent systems, perhaps the inevitable exhaustion of petroleum resources (estimated at 43 years from now) [2] will be the catalyst. Alternatively, an increasing number of regulations imposed by world governments will force the switch, e.g., the Registration, Evaluation, Authorization and Restriction of Chemicals (REACH) [3] regulation in the European Union, which seeks to mitigate health and environmental concerns related to bulk chemicals, including solvents. Whatever the driving force, it is imperative that the chemical industry adopt greener alternatives to conventional organic solvents.

Several such alternatives have materialized over the years and found niche applications to synthetic challenges, but ultimately the solution to the solvent problem will not come in the form of ionic liquids, fluorous media, or supercritical

Supramolecular Catalysis: New Directions and Developments, First Edition.
Edited by Piet W.N.M. van Leeuwen and Matthieu Raynal.

CO_2, but rather from Nature's chosen solvent: water. For billions of years, Nature has made use of water as the medium for the synthesis of staggeringly complex natural products. Water is nontoxic, nonflammable, nonvolatile, inexpensive, and omnipresent. If it is the obvious choice to replace harmful organic solvents, why hasn't it?

Historically, concerns over both solubility and the moisture sensitivity of reagents have led to apprehension toward, or flat-out refusal to consider, the use of water as a reaction medium for the majority of chemical transformations. This has led to the parochial convention that water should be avoided at all costs. However, just as biological systems make use of the lipophilic interior of phospholipid-derived vesicles to "dissolve" otherwise water-insoluble compounds, chemists can make use of self-assembling amphiphiles (e.g., surfactants) dissolved in water to provide a lipophilic microenvironment inside of which chemical transformations can take place. Additionally, water sensitivity presents a smaller obstacle to aqueous chemistry than previously thought, as illustrated by a number of reactions involving water-sensitive reagents (e.g., acyl chlorides [4], organolithium [5], and Grignard [6] reagents) that can be used smoothly *in water*. The key is the presence of a suitable lipophilic environment within the aqueous solution, such as surfactant-derived nanomicelles or suspended droplets of hexane, which provide a hydrophobic pocket to rapidly sequester reagent molecules before they have an opportunity to interact with the surrounding water.

Toward the goal of normalizing water as an alternative to conventional organic solvents, our group focuses on development and use of "designer" surfactants that enable chemistry in water under mild conditions. Our flagship surfactant, TPGS-750-M [7], is derived from biodegradable vitamin E (which serves as the lipophilic moiety) and hydrophilic poly(ethylene glycol) (PEG) monomethyl ether attached via a succinate linker. With this representative surfactant in hand, we have developed a growing portfolio of alternative surfactants that address particular synthetic needs (e.g., MC-1 for polar polypeptide synthesis in water) [8], as well as a library of synthetic methodologies using water as the global reaction medium. These technologies include Pd-catalyzed cross-couplings requiring only ppm levels of catalyst in Suzuki–Miyaura [9], Sonogashira [10], and amination reactions [11], ppm Au-catalyzed transformations (e.g., asymmetric lactonizations [12] and alkyne hydrations [13]), and reactions involving water-sensitive organozinc intermediates, generated in situ, that go on to participate in Negishi-like cross-couplings [14], to name just a few. However, this chapter is not intended as a comprehensive guide to chemistry in water; rather, our goal is to showcase the nanomicelles that have enabled those reactions and to highlight a series of synthetic transformations that can only be performed in the presence of aqueous surfactants.

32.2 Micellar Catalysis: Concepts

Surfactants are amphiphilic molecules, meaning that each is composed of both hydrophilic and lipophilic subsections. As such, when dissolved in water, they

self-assemble into entropically driven nanostructures (e.g., micelles or vesicles) with the hydrophilic heads directed outward toward the aqueous environment, and the lipophilic portions forming an inner core that excludes water. When appropriate surfactants are dissolved in water, the resulting nanoparticles (NPs) can be exploited to accommodate substrates and catalysts to perform numerous organic transformations. Because the total volume of the lipophilic core is very small compared to the total reaction volume, and because most substrates reside therein, while a typical reaction may have a 0.5 M concentration with respect to water, the concentration inside the micelles tends to be substantially greater. This high local concentration leads to increased interactions between reactants, thereby typically affording increased reaction rates at lower temperatures compared to less concentrated reactions in organic solvents.

The nature of the solute(s) also determines its (their) location within the micellar medium. While nonpolar compounds preferentially dissolve within the core of the micelles, hydrophilic molecules such as short alcohols or amines tend to concentrate at the surface of the aggregate [15, 16].

Our group has designed a number of efficient nonionic surfactants for organic transformations in water, each with enabling capabilities for various applications, the most versatile of which is TPGS-750-M [7]. The diameter of micellar aggregates made from TPGS-750-M was determined by cryo-TEM experiments and lies between 40 and 60 nm. This diameter does not coincide with the length of two amphiphiles placed end to end, which would lead to micelles with diameters between 15 and 20 nm, or three times smaller than what is observed. Density functional theory (DFT) calculations confirmed that the assembly is not a single micelle, but rather 30–40 individual, smaller (c. 10 nm) micelles forming compartmentalized NPs (Figure 32.1) [17]. DFT calculations also demonstrated that very little water is present in the core of the individual micelles, confirming the existence of hydrophobic inner cores, while a considerable amount of water is present in the PEG regions. In this model, the external interface with bulk water is stabilized by the variable amounts of vitamin E succinate impurity present in the surfactant [17]. This complex structural array facilitates transfer of chemical entities between micellar cores by involving shorter distances and less contact with water. This explains why some highly water-sensitive species, such as organozinc reagents, can be accommodated in such an aqueous environment. The average assembly size associated with TPGS-750-M is c. 46 nm at pH = 4.

A less expensive alternative to TPGS-750-M, "Nok," is constructed from plant-derived β-sitosterol rather than tocopherol and may offer similar or greater yields for transition-metal-catalyzed coupling reactions [18].

In some reactions involving polar substrates that may be distributed in large measure outside the micelles, achieving high conversion can be problematic. To address this issue, MC-1 [8], a surfactant inspired by the polar aprotic solvent dimethylsulfoxide (DMSO), was developed to facilitate peptide synthesis in water. By incorporating a sulfone along the lipophilic chain of the surfactant (Figure 32.1), polar substrates are accommodated inside the lipophilic core, thus leading to greater levels of conversion and ultimately, higher yields.

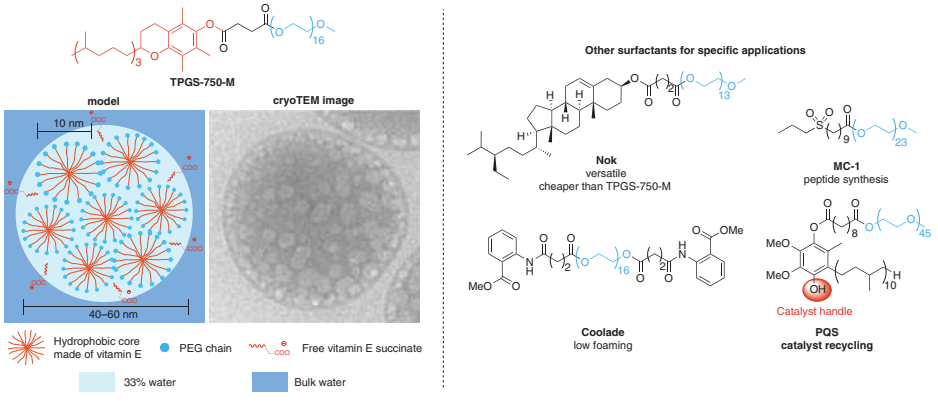

Figure 32.1 Designer surfactants and micelle-in-micelle assembly enabling organic transformations in water.

Surfactant design is often matched directly to the intended industrial application for which it is to be applied. In reactions that involve or generate gas, surfactant solutions have a propensity to foam, thereby limiting their utility especially at scale. Foaming of aqueous surfactant solutions is known to linearly decrease with decreasing length of the lipophilic moiety [19]. This led us to develop Coolade [20], a low-foaming designer surfactant constructed from a PEG chain in between two methyl anthranilate units. This design maintains the requisite hydrophilic–lipophilic balance to form micelles, but the short lipophilic chains limit foaming. Coolade is the surfactant of choice in reductions of *gem*-dibromocyclopropanes, nitro group and azide reductions, and in the preparation of Pd NPs.

Since these surfactants are engineered to remain in water during filtration or extraction of products, the aqueous layer can be reused multiple times upon addition of either fresh catalyst and/or starting materials. For the sake of recycling, a surfactant that can incorporate a catalyst covalently bound within its structure has also been developed. For example, polyethylene glycol ubiquinol succinate (PQS) [21], a platform made from the dietary supplement ubiquinol, has been used to attach proline [22] (for organocatalytic transformations), ruthenium carbenes (for olefin metathesis reactions), and an iridium catalyst (for photoredox applications) [23], within the lipophilic core of its nanomicelles.

Switching from organic solvents to aqueous surfactant solutions is not a simple media replacement. We discovered (and keep discovering) "new rules" along the way, specific to this type of technology [24]. Developing a good appreciation for these rules allows for better design elements for both surfactants and catalysts, leading to higher efficiencies for a given process.

32.3 Ligand Design

The world's declining supply of palladium has necessitated the development of highly effective palladium catalysts that function at low loadings, offer high functional group tolerance, reactivity and efficiency, and can be used under mild conditions. This is especially relevant to the pharmaceutical industry as targeted Active Pharmaceutical Ingredients (APIs) tend to increase in complexity while pressures to reduce drug prices mount. Added constraints arise from strict FDA guidelines requiring low levels of residual palladium ($\leq$10 ppm per dose) [25]. Typical conditions for Pd-catalyzed Suzuki–Miyaura cross-couplings (SMCs) involve the use of toxic organic solvents and rely on palladium loadings in the 1–5 mol % range. By increasing the lipophilicity of the ligand, however, catalyst residence time (i.e., its binding constant) within the micelle increases. Hence, given the high (usually $\geq$2 M) local concentration of substrates, lower levels of catalyst are required for these same C—C bond-forming transformations. With this new rule having been uncovered, EvanPhos, a *meta*-biaryl phosphine-containing platform constructed in only two steps, was developed as a highly active catalyst for SMCs [26]. By utilizing $Pd(OAc)_2$ and pre-activation of the derived ligated palladium(II) complex, the resulting

$(EvanPhos)_2Pd$ catalyst was effective at loadings in the ppm (0.1–0.5 mol%) range, an order of magnitude lower than traditional organic methods (Figure 32.2). Although designed for micellar systems, the catalyst system is also amenable to a typical use in the greener organic solvent EtOAc, affording coupled products in excellent yields.

Among the many advantages of this new catalytic system is the modular nature of the ligand. Its facile synthesis allows for derivatization of the skeletal structure, enabling development of new variants based on the need for more active species while maintaining the same benefits. The limited activity of $(EvanPhos)_2Pd$ toward aryl chlorides prompted the design of N_2Phos, a biaryl phosphine ligand that, likewise, enables ppm level SMCs in water [27].

DFT calculations illustrate that the greater steric congestion associated with N_2Phos induces increased steric crowding around the palladium center. This steric effect helps to destabilize the 2 : 1 ligand-Pd(0) complex derived from N_2Phos and $Pd(OAc)_2$, thereby favoring formation of the far more active 1 : 1 ligand-Pd(0) species. This new system is amenable to a wide array of aryl/heteroaryl halides and employs lower palladium loadings compared to EvanPhos. Most notably, highly functionalized aryl chlorides afford products at loadings of palladium in the 0.25 mol % range (Figure 32.2).

Palladacycles, which are characterized as among the most powerful precatalysts due to their ability to form highly active monoligated Pd(0) species, have been investigated as a means of achieving even lower palladium loadings [28–31]. To increase the efficacy of palladacycles in micellar systems, modifications were made to increase solubilization by increasing their affinity for the lipophilic core of the micelles, thereby greatly reducing the amount of Pd and ligand needed to facilitate cross-coupling reactions in water. Novel-substituted palladacycles have been prepared incorporating HandaPhos as ligand, wherein the palladacycle contains lipophilic *tert*-butyl, CF_3, or isopropyl residues. The di-isopropyl-substituted HandaPhos palladacycle proved to be the most effective when applied to Suzuki–Miyaura couplings needing only 300 ppm loadings of palladium for aryl bromides (Figure 32.3) [32]. Some coupling reactions could be performed at levels of palladium down to 25–100 ppm, showcasing the efficacy of this new precatalyst system. Reaction partners containing electron-donating and/or -withdrawing groups, in addition to heterocycles, were well-tolerated, as were less reactive aryl chlorides when loadings of 500 ppm palladium were employed.

It was found that the most effective palladacycle precatalyst contained isopropyl residues on both the aryl ring and on the nitrogen within the biaryl array. When paired with readily available and inexpensive EvanPhos and triflate as counterion, this new precatalyst shows increased efficacy toward highly valued reactions such as Heck and Sonogashira couplings at loadings of palladium in the 500–1500 ppm range [33]. Ligand development along these lines has proven to impart considerable catalytic activity to the resulting palladium complexes. This approach, which takes advantage of the simple notion of "like dissolves like" associated with micellar catalysis, opens new possibilities for sustainable processes applicable to syntheses of complex agrochemicals (e.g., Arylex, Rinskor) [34], APIs (e.g., sonidegib) [4], and other fine chemicals.

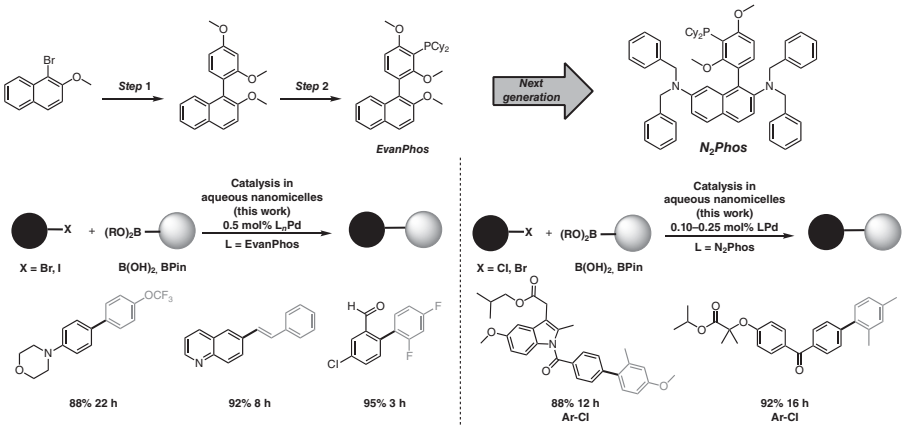

Figure 32.2 Ligand design and application to Suzuki–Miyaura cross couplings.

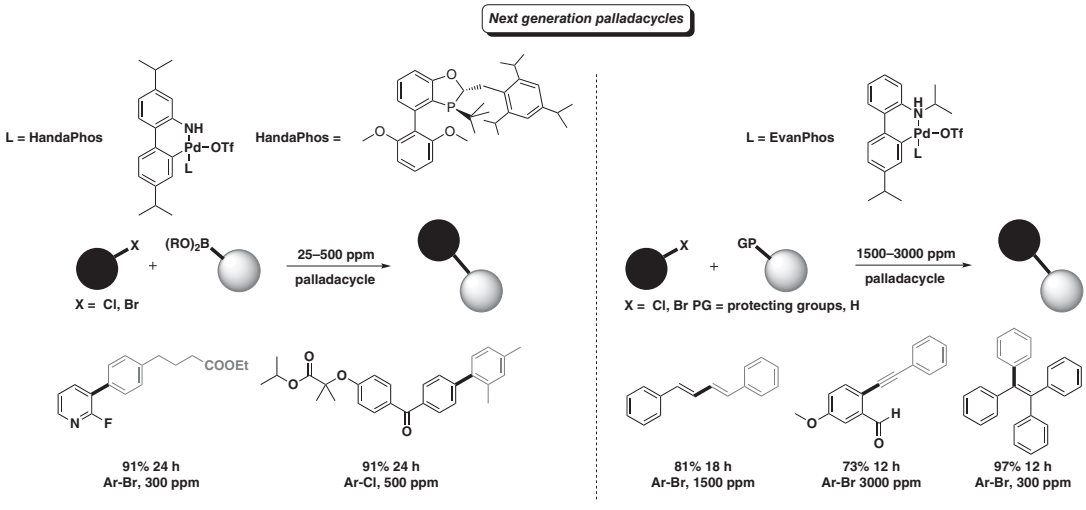

Figure 32.3 Next-generation palladacycles for cross couplings.

32.4 The "Nano-to-Nano" Effect

The use of transition metal-containing NPs has emerged as an alternative method for catalysis that relies on only ppm level quantities of catalyst. However, two important complications may arise when considering use of such NPs in aqueous surfactant solutions: (i) deactivation of the catalyst due to aggregation (which reduces the catalytic surface area) and (ii) transporting the substrate from the lipophilic core of the micelle to the aqueous phase containing the metal NPs. Fortunately, both complications are obviated when PEG-containing surfactants such as TPGS-750-M and Nok are used due to the "nano-to-nano" effect. This refers to the tendency of polyether PEG chains to act as stabilizing ligands on metal NPs, thus preventing aggregation [35, 36]. Moreover, the observation that PEG associates with the NPs means that the nanomicelles containing lipophilic substrates agglomerate around the catalyst NPs (hence "nano-to-nano"), effectively acting as an internal delivery system (Figure 32.4a–c). The unexpectedly high rates of reaction, mild reaction temperatures, and need for only ppm levels of metal catalyst to achieve the desired conversions are, therefore, attributed to the increased proximity of the substrates to the catalyst.

In 2015, a new platform was disclosed for delivering metal catalysts to aqueous nanomicelles: Fe/ppm Pd NPs [9]. These NPs are formed by the reduction of $FeCl_3$ containing ppm amounts of palladium, with MeMgCl. This process resulted in a solid, spherical nanomaterial that contained mostly metal salts and THF in which the NPs are made. Attempts to use this material as a catalyst for Mizoroki–Heck reactions [37] *in organic solvents* did not lead to any conversion. However, when dissolved in a 2 wt % aqueous solution of TPGS-750-M, the NPs acted as a highly effective catalyst. Cryo-TEM images of the nanomaterial before and after dissolution in aqueous surfactant demonstrated a remarkable change in shape and size (from micron-sized spheres to 50 nm rods; Figure 32.4). This effect, referred to as "water sculpting," is thought to be the result of salts being pulled out from the originally fashioned NPs and into the surrounding water, leaving the Pd-containing active catalyst behind. The images also demonstrate the nano-to-nano effect in action as the Fe/ppm Pd nanorods can be seen exclusively aggregated around the surfactant-derived nanomicelles.

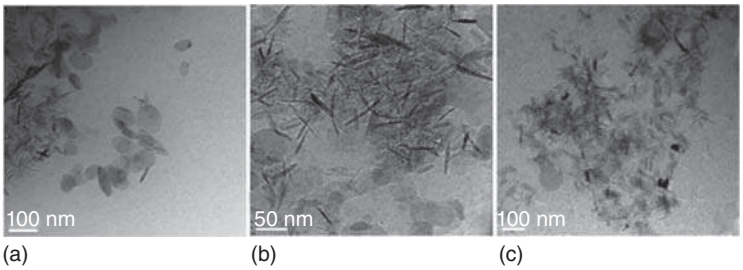

Figure 32.4 Cryo-TEM images; three different views (a–c) of TPGS-750-M-derived nanomicelles aggregated around Fe/ppm Pd nanorods.

The benefits of the "nano-to-nano" effect have been applied to numerous reaction types using different transition metal-containing NPs. The first of these was for Lindlar-like reductions of alkynes to *Z*-olefins using Pd NPs [38]. Several have been developed for Fe/ppm Pd NPs, including Suzuki–Miyaura [9] and Sonogashira cross-couplings [39]. NPs containing other transition metals have also been developed, including Fe/ppm Ni NPs which have demonstrated greater efficiency in the reduction of nitroarenes to their corresponding anilines compared to those using Fe/ppm Pd NPs [40], and Fe/ppm Cu NPs which effect highly efficient azide-alkyne click reactions [41]. In addition to the benefits regarding reaction rate, temperature, and low levels of catalyst loading, an important benefit of these NPs is recyclability. While heterogeneous catalysts containing lipophilic ligands (*vide supra*) may be partially or fully removed upon extraction of products, NP catalysts remain bound to the exterior of nanomicelles and can be reused in subsequent batches without the need for new catalyst. Another important consideration in pharmaceutical applications are the low levels of residual metals found in the final product. In all cases using Fe/ppm Pd/Cu/Ni NPs, residual metals have been shown to be well below the FDA-approved limits.

32.5 Reservoir Effect

Biocatalysis has emerged as a versatile and sustainable approach to generating chemo-, regio-, and stereoselective products with high levels of efficiency. The recent Nobel Prize for directed evolution highlights the potential of this methodology in the realm of organic synthesis and method development [42]. As powerful as this new tool is, most biolytic transformations, with the exception of some classes of lipases, require a buffered aqueous medium due to organic solvents' propensity to denature proteins, thereby diminishing their activity, or halting it entirely [43]. While greener alternatives have been developed to assuage this obstacle (e.g., eutectic solvents and ionic liquids), sterically demanding and larger lipophilic substrates often exhibit poor conversion in these media due to their poor solubility [44–47]. In an effort to expand the utility of biocatalysis, without the need for an additional organic solvent (e.g., DMSO), the compatibility of enzymatic systems under micellar conditions was investigated [48].

The well-studied oxidoreductase (i.e., alcohol dehydrogenase [ADH]) was investigated on a number of aryl ketones (Figure 32.5). All reactions were performed in a phosphate buffer at pH = 7 both with and without 2 wt % TPGS-750-M/H_2O. Enzymatic super activity was observed in the surfactant solutions as the lipophilicity of the substrates increased, implying a synergistic effect. In the case of the larger more lipophilic 2-ethylhexyl acrylate (Figure 32.5), the reduction reached 82% conversion after 24 hours, while slope discontinuity at 25% was observed after one hour in just buffered media, indicating enzyme saturation.

The rationale for this phenomenon is that under typical conditions, entrance into the enzyme active site is eventually hindered by the accumulation of water-insoluble substrates and products, thus leading to incomplete conversion in the buffered aqueous medium. In the presence of micelle-containing media, however, the

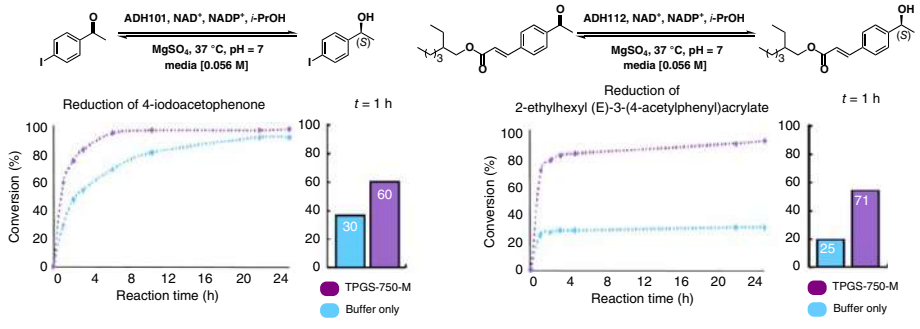

Figure 32.5 Positive effect of TPGS-750-M on enzymatic activity, exemplified by reduction of aryl ketones by ADH112.

micelles function as a "solvent" for the substrates and products, compartmentalizing them and acting as a reservoir. The dynamic nature of micellar environments allows for a slow release of organic molecules into the aqueous phase where the enzyme is present so that the biocatalytic transformation can occur. Thus, micelles in the buffer help to control both substrate and product concentrations in the aqueous medium, providing a measured supply that does not overcrowd and, in turn, lead to enzymatic inhibition, allowing for higher rates of conversion. Other enzyme classes are currently being investigated and a similar outcome has been observed, indicating that the effect may be general, thereby opening the door to new transformations that can be performed biocatalytically.

32.6 Access to Opportunities for Telescoping Sequences

Synthetic sequences to APIs regularly involve several steps; therefore, having the ability to telescope several of them, i.e., perform multiple synthetic steps in a single pot, can substantially reduce solvent waste both by limiting the total volume of reaction solvents as well as eliminating multiple purification processes. On the multi-kilogram scale, this translates into considerable cost savings, both monetarily and environmentally. Unfortunately, it is rare that chemists who employ traditional synthetic methods in organic solvents have the luxury of telescoping reactions since these sequences typically require steps that occur in different solvent media. Fortunately, the nondiscriminatory nature of aqueous nanomicelles provides an alternative that not only makes tandem sequences possible, but also affords an opportunity to telescope reactions under mild conditions using only water as the global reaction medium.

Several demonstrations of tandem sequences have already been described, including the industrially relevant one-pot, three-step sequence leading to the fungicide boscalid (Scheme 32.1) [4]. This multistep process not only improved upon prior

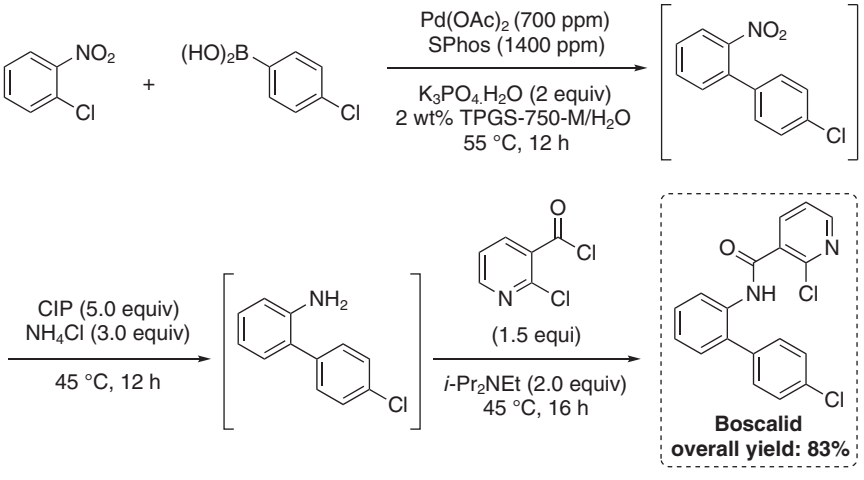

Scheme 32.1 Synthetic path toward boscalid.

methods en route to this target by reducing catalyst loading and temperature (as a result of the high local concentration within the micelles, as discussed previously) but also required only 9.0 ml of water containing very little surfactant for the three steps performed on a 5 mmol scale.

Another example of a one-pot, multistep sequence in an aqueous surfactant medium is the tandem deprotection/coupling of Cbz-protected oligopeptides (Scheme 32.2) [49]. Amide bond formation is one of the most heavily utilized transformations in the chemical enterprise, including the synthesis of oligo- and polypeptides. However, common methods for their syntheses typically involve copious quantities of environmentally egregious organic solvents (e.g., DMF, DMSO) and coupling reagents which often lead to E Factors upward of 250–1000. The tandem procedure now available avoids this by replacing organic solvents with an aqueous surfactant solution and replacing harmful coupling reagents such as HOBt and piperidine with the comparatively mild (1-cyano-2-ethoxy-2-oxoethylidenaminooxy)dimethylamino-morpholino-carbenium hexafluorophosphate (COMU) and 2,6-lutidine. Moreover, both the deprotection and coupling steps are combined into a sequential, 1-pot procedure. Using this method, E Factors as low as 10 have been obtained. The decapeptide Cbz-D-Phe-Pro-Val-Orn(Boc)-Leu-D-Phe-Pro-Val-Orn(Boc)-Leu-OMe (the linear precursor of the antibiotic gramicidin S) was synthesized via both an [8 + 2] and a [5 + 5] convergent strategy, leading to 82% and 72% yields, respectively. Shorter peptides such as Cbz-Phe-Leu-OEt were obtained in nearly quantitative yields.

An especially interesting prospect enabled by micellar catalysis involves tandem chemo-/bio-catalytic sequences. Because enzymes are oftentimes restricted to an aqueous environment, telescoping bio-catalyzed reactions with traditional chemo-catalyzed transformations in organic solvents is possible but requires removal of the organic medium and replacement by an aqueous buffer solution. This exchange is avoided by use of an aqueous surfactant reaction medium for effecting both bio- *and* chemo-catalysis. For instance, several telescoped sequences have been developed for the enzyme ADH such as a tandem ppm Pd, Cu-free Sonogashira cross-coupling followed by ADH-catalyzed asymmetric ketone reduction (Scheme 32.3), and the ppm Au-catalyzed alkyne hydration followed by ketone reduction by ADH (Scheme 32.4) [48].

Both reaction types gave rise to good overall yields and excellent enantioselectivities, while the enzyme was unaffected by residual metal catalysts and salts leftover from each of these prior transformations, a phenomenon further exemplified by the three-step, one-pot sequence shown in Scheme 32.5. This process generates relatively large quantities of metal and salt impurities, and yet the enzymatic reduction proceeds unimpeded, presumbly a result of the nanomicelles present that accomodate the ligated metals. Tandem processes using different enzymes such as ene-reductase and lipase, as well as sequences where the biocatalytic step precedes the chemo-catalytic step, are currently under study.

With the recent advances in aqueous micellar catalysis, there is no longer any question over whether telescoping reactions is possible, and the focus is shifting now toward how best to design these sequences to minimize waste and maximize efficiency.

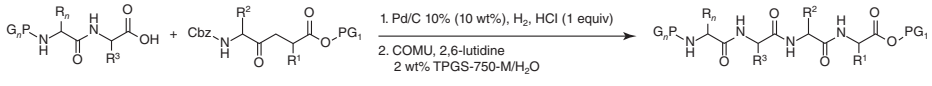

Scheme 32.2 Tandem peptide deprotection/coupling.

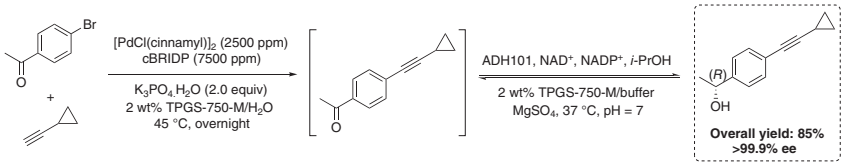

Scheme 32.3 ppm Pd, Cu-free Sonogashira coupling, then ADH.

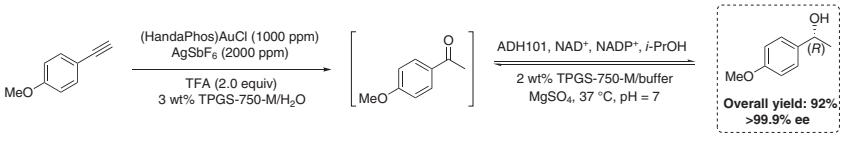

Scheme 32.4 ppm Au-catalyzed alkyne hydration, then ADH.

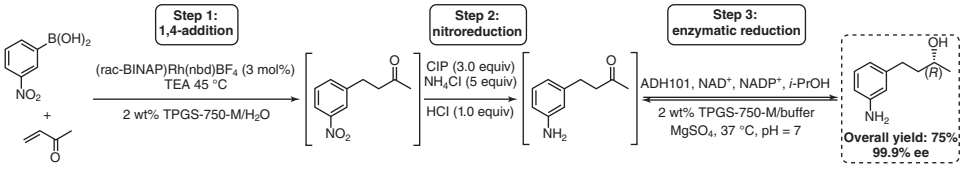

Scheme 32.5 Three-step, 1-pot sequence involving both chemo- and biocatalysis.

32.7 Industrial Applications

While recent discoveries regarding micellar catalysis and the "new rules" that govern it are exciting from an academic standpoint, the greatest real-world impact is observed when reactions are increased to an industrial scale. As discussed, chemistry in water offers obvious economic and productivity benefits such as lower cost associated with waste management, higher reaction rates, selectivities, and yields, and importantly, improved safety compared to organic solvents. Also noteworthy is that micellar catalysis improves greatly on the environmental impact of industrial syntheses. One key metric used to evaluate the greenness of chemical processes is process mass intensity (PMI), which is calculated as the mass of materials used divided by the mass of the final product, with lower PMIs indicating greener processes.

An example of an industrial application of micellar catalysis comes from Novartis, which developed several multistep, one-pot syntheses in water. The example illustrated in Scheme 32.6 involves a four-step, one-pot process featuring a selective S_NAr, a Suzuki–Miyaura cross-coupling, a nitro group reduction using ppm Pd-containing NPs, and lastly, amide bond formation [50]. All steps were performed in a single pot without isolation of intermediates using only an aqueous solution of TPGS-750-M and a small amount of cosolvent. The final product was accessed with 48% overall yield (vs. 43% in organic solvents), and the overall PMI was estimated at 161 (vs. 238).

Lippincott et al. demonstrated a Suzuki–Miyaura cross-coupling reaction under micellar catalysis conditions between a dichloropyridine and a bromoaniline [51].

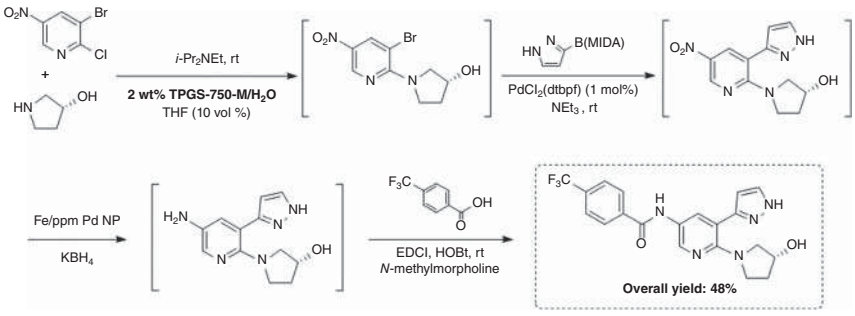

Scheme 32.6 Industrial example of a 4-step, 1-pot synthesis toward an API.

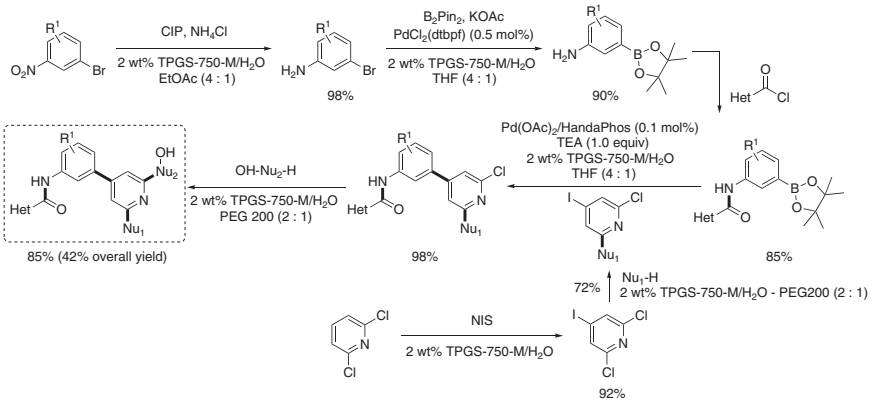

Scheme 32.7 Multistep synthesis enabled by micellar catalysis in water.

A higher selectivity (vs. oversubstitution) was observed when the initially used toluene was replaced by a 2 wt% aqueous solution of TPGS-750-M. Owing to the high lipophilicity of the newly introduced ligand HandaPhos, catalyst loadings as low as 1000 ppm (0.1 mol %) were sufficient to afford the desired product in >95% yield. Optimization of the reaction scheme by judiciously adjusting the polarity of each starting material led to a convergent five-step synthesis involving nitro reduction, borylation, iodination, Suzuki–Miyaura coupling, and finally, an S_NAr reaction, all in the same aqueous solvent system, with an overall yield of 42% (Scheme 32.7).

Recently, Bailey at Takeda Pharmaceuticals received the 2020 Peter J. Dunn Award for the synthesis of a 5-HT_4 receptor agonist, made predominantly in water, where use of TPGS-750-M was crucial for several key steps [52]. The initial route as developed involved five different organic solvents and led to a 35% overall yield with a production mass intensity (PMI) of 350. The new route afforded the product in 56% yield and featured a PMI as low as 79 with identical purity (Scheme 32.8). Operating in water also allowed adjustment of the workup pH, thus facilitating precipitation of the desired intermediates/product.

These selected examples are illustrative of the opportunities that micellar technology offers to the industrial arena, as well as the benefits to be realized using this approach to synthesis. Use of micellar catalysis makes sense, not only from an

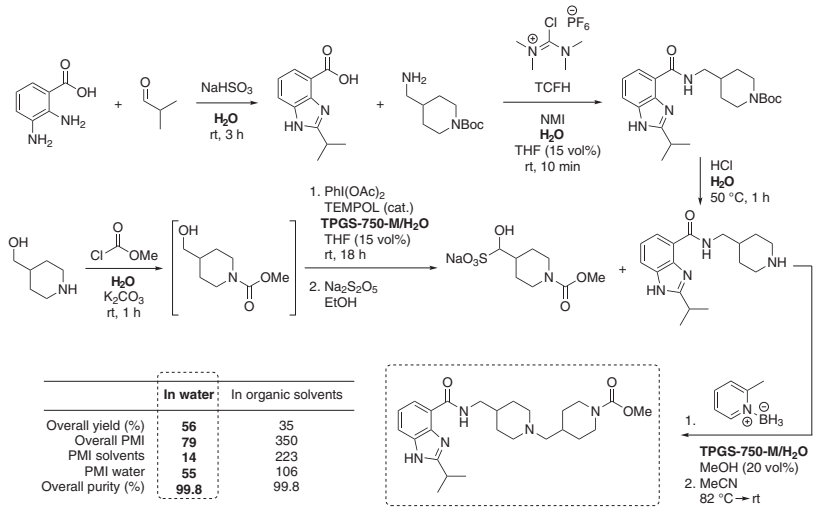

Scheme 32.8 Takeda's synthesis of a 5-HT4 receptor agonist in water.

environmental point of view but also from an economic perspective. Generating less waste, using a single medium over multiple steps, lowering catalyst loadings, and accessing greater yields under milder conditions are all facilitated by surfactant technology.

32.8 Conclusions

Not long ago, performing a multitude of organic reactions in water was unthinkable; but with advancements associated with newly engineered "designer" surfactants, Nature's solvent has proven itself to be a powerful alternative to environmentally egregious organic solvents. The nanoreactors generated upon dissolution of very small amounts of surfactant in water lead to concentrated solutions of water-insoluble substrates and catalysts within their lipophilic cores, thereby enabling lower reaction temperatures and catalyst loadings compared to those required using organic solvents. This technology has been applied to industrial targets and is readily amenable to multi-step, one-pot reactions affording lower PMI outcomes and hence, a significant reduction in associated waste generation. The nanoreactors' role as substrate/product reservoirs has enabled biocatalysis involving lipophilic substrates in water by minimizing enzymatic inhibition, thus allowing for access to greater levels of conversions and thus greater yields compared to those seen in conventional aqueous buffers. Using aqueous surfactant solutions as a common medium for both bio- and chemo-catalysis enables tandem processes, saving costly workup between steps. The affinity between metal NPs and the MPEG moiety of surfactants gives rise to the nano-to-nano effect, delivering substrate-filled nanomicelles directly to nanoparticle catalysts. None of these features exist in conventional organic solvents and are only possible because of the unique properties of

nanomicelles and aqueous media. There is no longer any question whether water is a suitable "solvent" for organic reactions; while counter-intuitive, it is the *preferred* medium for organic synthesis of the future.

References

1 Dunn, P., Henderson, R., Mergelsberg, I., and Wells, A. (2009). *Moving towards Greener Solvents for Pharmaceutical Manufacturing An Industry Perspective*. ACS CGI Pharmaceutical Roundtable.

2 World Oil Statistics – Worldometer (2020). https://www.worldometers.info/oil/.

3 Understanding REACH – ECHA (2012). https://echa.europa.eu/regulations/reach/understanding-reach.

4 Takale, B.S., Thakore, R.R., Mallarapu, R. et al. (2020). A sustainable 1-pot, 3-step synthesis of boscalid using part per million level pd catalysis in water. *Org. Process Res. Dev.* 24 (1): 101–105.

5 Dilauro, G., Dell'Aera, M., Vitale, P. et al. (2017). Unprecedented nucleophilic additions of highly polar organometallic compounds to imines and nitriles using water as a non-innocent reaction medium. *Angew. Chem. Int. Ed.* 56 (34): 10200–10203.

6 Cicco, L., Sblendorio, S., Mansueto, R. et al. (2016). Water opens the door to organolithiums and Grignard reagents: exploring and comparing the reactivity of highly polar organometallic compounds in unconventional reaction media towards the synthesis of tetrahydrofurans. *Chem. Sci.* 7 (2): 1192–1199.

7 Lipshutz, B.H., Ghorai, S., Abela, A.R. et al. (2011). TPGS-750-M : a second-generation amphiphile for metal-catalyzed cross-couplings in water at room temperature. *J. Org. Chem.* 76 (11): 4379–4391.

8 Cortes-Clerget, M., Spink, S.E., Gallagher, G.P. et al. (2019). MC-1. A "designer" surfactant engineered for peptide synthesis in water at room temperature. *Green Chem.* 21 (10): 2610–2614.

9 Handa, S., Wang, Y., Gallou, F., and Lipshutz, B.H. (2015). Sustainable Fe–ppm Pd nanoparticle catalysis of Suzuki–Miyaura cross-couplings in water. *Science* 349 (6252): 1087.

10 Jin, B., Gallou, F., Reilly, J., and Lipshutz, B.H. (2019). ppm Pd-catalyzed, Cu-free Sonogashira couplings in water using commercially available catalyst precursors. *Chem. Sci.* 10 (12): 3481–3485.

11 Zhang, Y., Takale, B.S., Gallou, F. et al. (2019). Sustainable ppm level palladium-catalyzed aminations in nanoreactors under mild, aqueous conditions. *Chem. Sci.* 10 (45): 10556–10561.

12 Handa, S., Lippincott, D.J., Aue, D.H., and Lipshutz, B.H. (2014). Asymmetric gold-catalyzed lactonizations in water at room temperature. *Angew. Chem. Int. Ed.* 53 (40): 10658–10662.

13 Klumphu, P., Desfeux, C., Zhang, Y. et al. (2017). Micellar catalysis-enabled sustainable ppm Au-catalyzed reactions in water at room temperature. *Chem. Sci.* 8 (9): 6354–6358.

14 Krasovskiy, A., Duplais, C., and Lipshutz, B.H. (2010). Stereoselective negishi-like couplings between alkenyl and alkyl halides in water at room temperature. *Org. Lett.* 12 (21): 4742–4744.

15 Otto, S. (1998). Catalysis of Diels–Alder reactions in water. PhD thesis. Rijksuniversiteit Groningen, Groningen, Netherlands.

16 Jobe, D.J., Reinsborough, V.C., and White, P.J. (1982). Solubilization sites in micellar sodium octylsulphate solutions by ultrasonic spectroscopy. *Can. J. Chem.* 60 (3): 279–284.

17 Andersson, M.P., Gallou, F., Klumphu, P. et al. (2018). Structure of nanoparticles derived from designer surfactant TPGS-750-M in water, as used in organic synthesis. *Chem. – A Eur. J.* 24 (26): 6778–6786.

18 Klumphu, P. and Lipshutz, B.H. (2014). "Nok": A phytosterol-based amphiphile enabling transition-metal-catalyzed couplings in water at room temperature. *J. Org. Chem.* 79 (3): 888–900.

19 Tamura, T., Takeuchi, Y., and Kaneko, Y. (1998). Influence of surfactant structure on the drainage of nonionic surfactant foam films. *J. Colloid Interface Sci.* 206 (1): 112–121.

20 Lee, N.R., Cortes-Clerget, M., Wood, A.B. et al. (2019). Coolade. A low-foaming surfactant for organic synthesis in water. *ChemSusChem* 12 (13): 3159–3165.

21 Lipshutz, B.H. and Ghorai, S. (2009). PQS: A new platform for micellar catalysis. RCM reactions in water, with catalyst recycling. *Org. Lett.* 11 (3): 705–708.

22 Lipshutz, B.H. and Ghorai, S. (2012). Organocatalysis in water at room temperature with in-flask catalyst recycling. *Org. Lett.* 14 (1): 422–425.

23 Bu, M., Cai, C., Gallou, F., and Lipshutz, B.H. (2018). PQS-enabled visible-light iridium photoredox catalysis in water at room temperature. *Green Chem.* 20 (6): 1233–1237.

24 Lipshutz, B.H. (2018). Synthetic chemistry in a water world. New rules ripe for discovery. *Curr. Opin. Green Sust. Chem.* 11: 1–8.

25 Purdie, F.P. (2018) Elemental impurities in drug products guidance for industry. https://www.fda.gov/media/98847/download .

26 Landstrom, E.B., Handa, S., Aue, D.H. et al. (2018). EvanPhos: a ligand for ppm level Pd-catalyzed Suzuki–Miyaura couplings in either organic solvent or water. *Green Chem.* 20 (15): 3436–3443.

27 Akporji, N., Thakore, R.R., Cortes-Clerget, M. et al. (2020). N2Phos – an easily made, highly effective ligand designed for ppm level Pd-catalyzed Suzuki–Miyaura cross couplings in water. *Chem. Sci.* 11 (20): 5205–5212.

28 Huang, Z., Yang, Q.-Z., Khvostichenko, D. et al. (2009). Method to derive restoring forces of strained molecules from kinetic measurements. *J. Am. Chem. Soc.* 131 (4): 1407–1409.

29 Bruno, N.C., Tudge, M.T., and Buchwald, S.L. (2013). Design and preparation of new palladium precatalysts for C–C and C–N cross-coupling reactions. *Chem. Sci.* 4 (3): 916–920.

30 Bruno, N.C. and Buchwald, S.L. (2013). Synthesis and application of palladium precatalysts that accommodate extremely bulky di-*tert*-butylphosphino biaryl ligands. *Org. Lett.* 15 (11): 2876–2879.

31 Bruno, N.C., Niljianskul, N., and Buchwald, S.L. (2014). *N*-substituted 2-aminobiphenylpalladium methanesulfonate precatalysts and their use in C–C and C–N cross-couplings. *J. Org. Chem.* 79 (9): 4161–4166.

32 Takale, B.S., Thakore, R.R., Handa, S. et al. (2019). A new, substituted palladacycle for ppm level Pd-catalyzed Suzuki–Miyaura cross couplings in water. *Chem. Sci.* 10 (38): 8825–8831.

33 Thakore, R.R., Takale, B.S., Gallou, F. et al. (2019). *N*,*C*-disubstituted biarylpalladacycles as precatalysts for ppm Pd-catalyzed cross couplings in water under mild conditions. *ACS Catal.* 9 (12): 11647–11657.

34 Takale, B.S., Thakore, R.R., Irvine, N.M. et al. (2020). Sustainable and cost-effective Suzuki–Miyaura couplings toward the key biaryl subunits of Arylex and Rinskor active. *Org. Lett.* 22 (12): 4823–4827.

35 Lipshutz, B.H. (2017). The 'nano-to-nano' effect applied to organic synthesis in water. *Johnson Matthey Technol. Rev.* 61 (3): 196.

36 Hou, Z., Theyssen, N., Brinkmann, A., and Leitner, W. (2005). Biphasic aerobic oxidation of alcohols catalyzed by poly(ethylene glycol)-stabilized palladium nanoparticles in supercritical carbon dioxide. *Angew. Chem. Int. Ed.* 44 (9): 1346–1349.

37 Pang, H., Hu, Y., Yu, T. et al. (2021). Water-sculpting of a heterogeneous nanoparticle pre-catalyst for mizoroki-heck couplings under aqueous micellar catalysis conditions. *J. Am. Chem. Soc.* 143: 3373–3382.

38 Slack, E.D., Gabriel, C.M., and Lipshutz, B.H. (2014). A palladium nanoparticle–nanomicelle combination for the stereoselective semihydrogenation of alkynes in water at room temperature. *Angew. Chem. Int. Ed.* 53 (51): 14051–14054.

39 Handa, S., Jin, B., Bora, P.P. et al. (2019). Sonogashira couplings catalyzed by fe nanoparticles containing ppm levels of reusable Pd, under mild aqueous micellar conditions. *ACS Catal.* 9 (3): 2423–2431.

40 Pang, H., Gallou, F., Sohn, H. et al. (2018). Synergistic effects in Fe nanoparticles doped with ppm levels of (Pd + Ni). A new catalyst for sustainable nitro group reductions. *Green Chem.* 20 (1): 130–135.

41 Adenot, A., Landstrom, E.B., Gallou, F., and Lipshutz, B.H. (2017). Fe/ppm Cu nanoparticles as a recyclable catalyst for click reactions in water at room temperature. *Green Chem.* 19 (11): 2506–2509.

42 Arnold, F.H. (2018). Directed evolution: bringing new chemistry to life. *Angew. Chem. Int. Ed.* 57 (16): 4143–4148.

43 Castro, G.R. and Knubovets, T. (2003). Homogeneous biocatalysis in organic solvents and water-organic mixtures. *Crit. Rev. Biotechnol.* 23 (3): 195–231.

44 Hoang, H.N. and Matsuda, T. (2017). Chapter 1 - Biotransformation using liquid and supercritical CO_2. In: *Future Directions in Biocatalysis*, 2e (ed. T. Matsuda), 3–25. Amsterdam: Elsevier.

45 van Rantwijk, F. and Sheldon, R.A. (2007). Biocatalysis in ionic liquids. *Chem. Rev.* 107 (6): 2757–2785.

46 Itoh, T. (2017). Ionic liquids as tool to improve enzymatic organic synthesis. *Chem. Rev.* 117 (15): 10567–10607.

47 Paul, C.E. and Fernández, V.G. (2016). Chapter 2 – Biocatalysis and biotransformation in ionic liquids. In: *Ionic Liquids in Lipid Processing and Analysis* (eds. X. Xu, Z. Guo and L.-Z. Cheong), 11–58. AOCS Press.

48 Cortes-Clerget, M., Akporji, N., Zhou, J. et al. (2019). Bridging the gap between transition metal- and bio-catalysis via aqueous micellar catalysis. *Nat. Commun.* 10 (1): 1–10.

49 Cortes-Clerget, M., Berthon, J.-Y., Krolikiewicz-Renimel, I. et al. (2017). Tandem deprotection/coupling for peptide synthesis in water at room temperature. *Green Chem.* 19 (18): 4263–4267.

50 Gallou, F., Isley, N.A., Ganic, A. et al. (2016). Surfactant technology applied toward an active pharmaceutical ingredient: more than a simple green chemistry advance. *Green Chem.* 18 (1): 14–19.

51 Lippincott, D.J., Landstrom, E., Cortes-Clerget, M. et al. (2020). Surfactant technology: with new rules, designing new sequences is required! *Org. Process Res. Dev.* 24 (5): 841–849.

52 Bailey, D.J., Helbling, E., Mankar, A. et al. (2021). Beyond organic solvents: synthesis of a 5-HT4 receptor agonist in water. *Green Chem.* 23: 788–795.

33

Compartmentalized Polymers for Catalysis in Aqueous Media

Fabian Eisenreich and Anja R.A. Palmans

Eindhoven University of Technology, Laboratory of Macromolecular and Organic Chemistry, Department of Chemical Engineering and Chemistry, Den Dolech 2, 5600 MB Eindhoven, The Netherlands

33.1 Introduction

A century after Staudinger's landmark contribution "*Über Polymerisation*" [1], the field of polymer science has advanced to a point where precise control over a polymer's chain length, dispersity, topology, and thermal/mechanical properties permits to create materials that affect every aspect of our daily lives. In addition, rapid developments in the field of transition-metal-based homogeneous catalysis resulted in a vast variety of bond making and breaking reactions in which metals such as Rh [2, 3], Ru [2, 4], and Pd [5] have played a prominent role when combined with suitable ligands. Such organometal complexes are highly efficient and selective, with often near perfect stereoselectivities when chiral ligands are applied. Despite their broad applicability, the reuse of the organometal complexes has remained a point of attention, as well as the capability to perform reactions in benign solvents such as water [6, 7].

Over the years, a variety of synthetic macromolecules have been evaluated as homogeneous carriers of ligands for metal-based catalysts, with the aim to facilitate reuse of the catalyst by introducing phase-selective solubility of the polymer support [8]. These polymeric supports have expanded the scope of reaction media by compatibilization of reactions traditionally performed in organic media to aqueous conditions [9]. Access to perfectly branched dendrimers [10], star polymers [11, 12], polymer-based micellar system [13], and helical (supramolecular) polymers [14, 15] as catalyst carriers increased control over the localization of the catalysts and allowed to tune its direct environment. In turn, this resulted in a high control over the selectivity of reactions as well as the ability to perform reactions in aqueous media.

Despite all the progress achieved in controlling the primary structures and hereby properties of synthetic macromolecules to improve their role in developing reusable catalysts, their catalytic power still lags far behind that of enzymes. Enzymes are dynamically folded macromolecules with a perfectly defined three-dimensional

Supramolecular Catalysis: New Directions and Developments, First Edition.
Edited by Piet W.N.M. van Leeuwen and Matthieu Raynal.

(3D) structure, which results in a high activity and selectivity in converting substrates into products. Enzymes function efficiently in highly competitive, crowded media as a direct result of their defined 3D structure, and with the help of directed evolution techniques they can be altered to catalyze a range of non-natural reactions as well [16]. Nowadays, enzymes are applied in many industrial chemical processes because of their high selectivity, the mild reaction conditions required, and their low environmental impact [17, 18].

Organometal complexes have an unprecedentedly wide scope in their ability to catalyze bond-forming (and breaking) reactions and are tolerant to many different types of substrates. However, they are not always compatible with aqueous conditions. In addition, it has been challenging to combine them with enzymes in cascade or tandem reactions [19, 20]. This is a result of the incompatibilities that arise between organometal complexes and protein-based catalysts since amino acid residues tend to bind the metal, whereas metals can irreversibly inhibit enzyme active sites, resulting in a mutual decrease (or even loss) of activity. Such a combination, however, would be highly advantageous to shorten reaction sequences and increase selectivity in multistep procedures. Thus, proper compartmentalization of the different catalytic sites is required to enhance the complementarity and compatibility between these intrinsically different catalytic systems.

A viable way to achieve this would be the ability to control the 3D conformations of synthetic polymers, which normally adopt random coil conformations in good solvents or dense globular structures in poor solvents. Control over a synthetic polymer's global conformation can provide proper shielding and stabilization of a metal-based catalyst in challenging environments. In addition, an enhancement in substrate specificity and product selectivity can be achieved. Inspired by the beautiful work that unraveled how a polypeptide chains fold into an active and functional nanostructure [21–26], we have set out to design and study amphiphilic synthetic polymers, in which a high degree of control over their 3D structure is viable. We refer to these polymer-based scaffolds as single chain polymeric nanoparticles (SCPNs). Herein, a *single* polymer chain compacts in water into a particle of nanometer-sized dimensions as a result of hydrophobic and hydrogen-bond-based intramolecular interactions, sometimes combined with metal–ligand interactions. The compaction can result from a *collapse*, driven by hydrophobic interactions, and a *folding* process, driven by hydrogen-bonding interactions. The term dynamic SCPN is used when this compaction constitutes a reversible process that responds to temperature and other external cues. This results in the formation of a compartmentalized particle with a hydrophilic exterior and a hydrophobic interior. Ideally, when catalysts or ligands are suitably attached, the local polarity around the catalyst is controlled, as well as the nature of the scaffold surrounding the catalytically active site. This catalytic site can be of organic origin, or can be a transition metal complexed to suitable ligands. We here summarize the progress we have made in achieving green conversions in water and/or bio-orthogonal catalysis in complex aqueous media by developing conformationally restricted polymers with ligands and/or catalysts attached.

33.2 Folding a Polymer Chain in Water into a Compact Structure

The first step in folding a polymer chain around a catalytic site is the ability to relate its primary structure (degree of polymerization [DP], molar mass dispersity, microstructure, and backbone flexibility) to conformational preference in solution, and hereby guide and control its conformational flexibility. Initial works on this topic were presented by the groups of Hawker and Fréchet, Morishima, and Ramakrishnan, where control over the polymer conformation was achieved by intrachain cross-linking [27, 28], hydrophobic collapse [29], or π-stacking interactions [30], respectively. Following these pioneering contributions, many exciting procedures were developed to prepare polymer particles with restricted conformations, as summarized in recent reviews [31–36]. In these, covalent bonds [28], reversible covalent bonds [37], non-covalent bonds [38, 39], and combinations hereof [40, 41] were applied to confine the conformational flexibility of a single polymer chain in solution. Such control over global conformations is possible in organic solvents as well as in water.

In analogy to protein folding, the term *"folding"* in the context of SCPN formation is used when a polymer's conformational freedom is restricted by applying non-covalent or dynamic covalent interactions. The term *"collapse"* refers to restricting the conformational freedom of a polymer chain due to solvophobic or hydrophobic effects. The global conformation of a single polymer chain can also be locked by the formation of intramolecular covalent bonds [31], but then SCPNs lose their adaptability to changes in the environment and no longer respond to chemical/physical triggers (pH, temperature, light). In addition, this does not constitute a "folding process" as more optimal conformations cannot be attained in response to changes in the environment. We have focused on *collapse* induced by hydrophobic interactions and *folding* induced by directional hydrogen-bond formation.

To elucidate the details of the reversible folding and unfolding of the polymers into SCPNs, we have mostly used the well-studied benzene-1,3,5-tricarboxamide (BTA) motif [42]. This supramolecular motif forms helical superstructures stabilized by threefold hydrogen bonds. When stereogenic centers are introduced in the alkyl side chains, one helical sense is biased, permitting to use chiroptical techniques such as circular dichroism (CD) to assess the degree of aggregation. We reasoned that attaching BTAs to a polymer chain would permit to follow the folding process by tracking the signature CD signal that arises when BTAs aggregate into non-racemic helical stacks. In combination with scattering techniques, which provide information on size, shape, and intermolecular aggregation of the particles, the folding process of single polymer chains into dynamic SCPNs in water can then be unveiled.

In 2011, we reported on a series of polymethacrylate-based graft copolymers **P1–P7** comprising oligo(ethylene glycol) (oEG) grafts, aliphatic dodecyl grafts, and grafts with a chiral BTA-based hydrogen-bonding motif (Figure 33.1a) [43]. The oEG graft was selected to impart water solubility, whereas the dodecyl and BTA comprising grafts were added to induce a hydrophobic collapse and directional hydrogen bonds, respectively. Importantly, the different types of grafts were

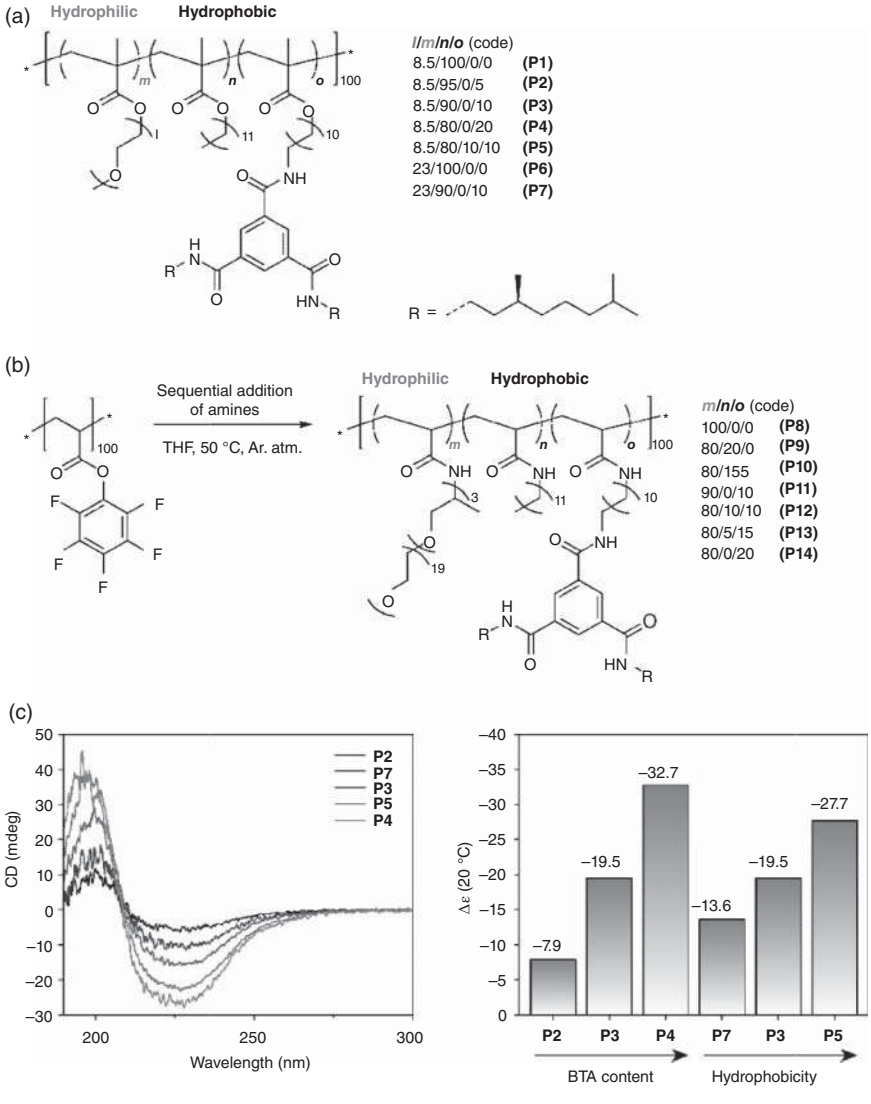

Figure 33.1 Chemical structures of (a) polymethacrylate-based polymers **P1–P7** obtained via direct copolymerization and (b) polyacrylamide-based polymers **P8–P14** obtained by post-functionalization of poly(pentafluorophenyl acrylate) by the sequential addition of the appropriate amines. (c) CD spectra of polymers **P2–P7** in water at $c_{BTA} = 50\,\mu M$ and at $T = 20\,°C$ (left) and molar circular dichroism $\Delta\varepsilon$ measured at $\lambda = 225\,nm$ at $T = 20\,°C$ (right).

randomly distributed over the polymer chain. With the help of CD spectroscopy, aqueous solutions of these amphiphilic copolymers showed a pronounced negative Cotton effect with an extremum at 223 nm (Figure 33.1c). Similar "free" BTAs aggregated into *M*-helical superstructures in apolar alkane solvents, showed an identically shaped Cotton effect [44–46]. The presence of this Cotton effect in the copolymers indicated that BTAs attached to an amphiphilic polymer chain

are indeed capable of forming arrays of hydrogen bonds, but now in water. Interestingly, when calculating the molar CD $\Delta\varepsilon$, a concentration-independent measure for the CD effect, it became clear that an increase of the BTA loading from 5 (**P2**), to 10 (**P3**) and 20% (**P4**) resulted in an increase of the $|\Delta\varepsilon|$ value from 7.9 to 19.5 and 32.7 l/(mol cm). Interestingly, adding 10% dodecyl grafts (**P5**) in addition to 10% BTAs grafts (**P3**) resulted in an increase of the $|\Delta\varepsilon|$ value from 19.5 to 27.7 l/(mol cm), despite BTA loading on the polymer remaining identical (Figure 33.1c). Conversely, increasing the number of the ethylene glycol units on the grafts from 8.5 (**P3**) to 23 (**P7**) reduced $|\Delta\varepsilon|$ from 19.5 to 13.6 l/(mol cm). Since only aggregated BTAs contribute to the CD effect, this observation suggests a higher propensity for ordered hydrogen-bond formation in the presence of additional hydrophobic dodecyl units and shorter polar side chains. Heating the solutions resulted in a loss of the CD effect. The loss was completely reversible upon cooling, and no hysteresis was observed. Additional small-angle X-ray and light scattering experiments showed that nanometer-sized particles were formed that consisted of only one polymer chain, especially with lower amounts of BTAs. Compared to the homopolymer with only oEG grafts (**P1**), the copolymers with 10% BTA grafts showed a smaller hydrodynamic radius, R_H, which was explained by the formation of more compact particles.

All in all, we concluded from the combined evidence of hydrogen-bond formation between BTAs in water, the formation of nanometer-sized particles consisting of one polymer chain and the responsive nature of the hydrogen bonds that amphiphilic heterograft copolymers with BTA grafts intramolecularly and reversibly fold into SCPNs. The presence of a hydrophobic interior, and therefore a compartmentalized structure, was corroborated by using the solvatochromic dye Nile Red [41]. In pure water Nile Red displayed a low fluorescence intensity with an emission maximum at 660 nm. The addition of copolymers comprising either BTAs, dodecyl grafts, or both resulted in a blue shift of 27 nm for the emission wavelength of Nile Red in water. The fluorescence intensity increased significantly in the presence of the polymers. The solutions of polymers with attached BTAs showed a stronger increase in fluorescence intensity compared to solutions of polymers with only dodecyl grafts. This suggested that a more pronounced hydrophobic environment was present upon incorporation of BTAs in the copolymer. The observations corroborated the presence of hydrophobic pockets in all polymer solutions.

Initially, we naively assumed that after folding in water, the SCPNs would adopt a more or less spherical shape. Detailed scattering studies performed on a homopolymer with only oEG grafts (**P1**) and a copolymer with an additional 10% BTA grafts (**P3**), however, revealed this was not the case [47]. **P3** formed particles with an elongated shape, a result of the intramolecular BTA self-assembly that "stretched" the particle by the formation of helical, elongated aggregates. In contrast to our expectations, the shape of the SCPNs based on **P3** was ellipsoidal. Increasing the DP of the polymer from 100 to 500, and keeping the amount of BTA grafts constant at 10 mol%, resulted in an increase of the longitudinal dimension of the particle while the cross-sectional dimension remained constant [48]. We also expected to obtain particles of higher density by the internal cross-linking of the interior of the SCPN

by the BTA units, but the opposite was the case. The specific densities of the SCPNs with (**P3**) and without BTAs (**P1**) were found to be 0.93 and 1.19 g/ml, respectively, at 25 °C. This suggests that polymers with only BTA grafts have a less dense structure in water [47]. For catalysis, a more elongated, less dense structure of SCPNs could allow for substrates and products to enter and exit the active site of the particle more easily, but it could also mean that the catalytic site would be more exposed.

The question thus remained how to code the primary structure of the copolymer to enhance its propensity to form compact, more spherical SCPNs with a well-defined, hydrophobic interior. To this end, a library of heterograft copolymers **P8–P14** was screened, in which the amount of BTAs grafts was systematically increased (0%, 5%, 10%, and 20%) and dodecyl grafts were added (0%, 5%, 10%, and 15%) as well (Figure 33.1b) [49]. In this series, a polyacrylamide backbone was selected, a result of the post-functionalization approach applied, which permitted to keep the DP and molar mass dispersity ($Đ$) identical between all members of the library. Higher amounts of BTA grafts increased the intermolecular aggregation of the particles. In fact, copolymers with 20% BTA grafts predominantly formed multiple chain polymeric nanoparticles (MCPNs) rather than SCPNs. This was in agreement with results from Terashima and coworkers who found that amphiphilic polymers with randomly distributed hydrophobic dodecyl grafts always form MCPNs above 40% of hydrophobic grafts [50]. Since one BTA graft has a similar hydrophobic content as three dodecyl grafts, 20% of BTAs is well above this limit. Interestingly the combination of BTA and dodecyl grafts enhanced the propensity to form compact SCPNs. In fact, **P13** with 15% dodecyl and 5% BTA grafts showed the most compact, structured particles with the most globular shape, which for catalysis applications is expected to be the most advantageous design. All in all, the results of this study showed that the primary structure of the copolymer guides the nature and shape of the formed particles (Figure 33.2). In case of BTA and dodecyl groups present, spherical SCPNs were obtained. When only BTAs were present,

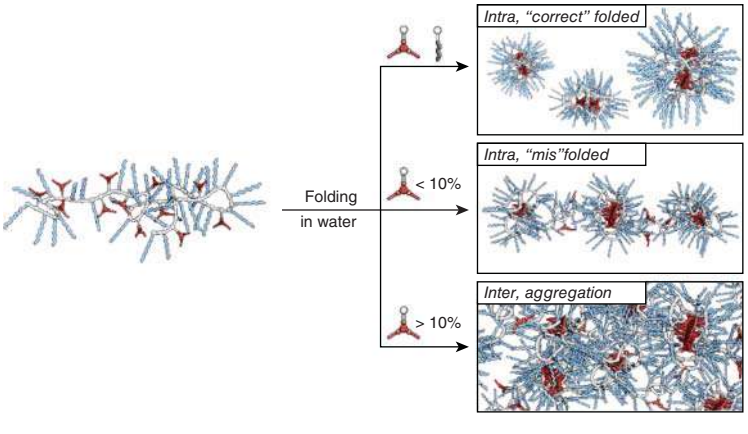

Figure 33.2 Schematic representation of how the primary structure and the content of BTA and dodecyl groups affect the size and shape of nanoparticles formed in water.

elongated SCPNs were formed. In the presence of high amounts of BTA, >10%, MCPNs were obtained.

Finally, we would like to make some comments on the preparation and stability of SCPNs in water. Solubilizing amphiphilic copolymers in water requires very specific and controlled preparation protocols, which for each different type of polymer needs to be optimized. Especially when the hydrophobic content increases, the propensity of the particles to cluster increases. In addition, changing the water-compatible grafts from oEG or Jeffamine@1000 to saccharides alters the hydrophobic/hydrophilic balance and enhances MCPN formation [51]. However, once present as SCPNs, the stability of the particles is high, and no clustering is observed over at least one week [49].

33.3 Polymer-Supported Ru(II) Catalysis in Water

The formation of well-defined and compartmentalized polymeric nanoparticles provides a unique platform to perform organic reactions, which are challenging to realize in aqueous media due to the lack of water solubility of the substrate and/or the catalyst. Initially, we focused on enabling transition-metal catalysis in water by the controlled folding of the polymeric chain around the catalytic site and thereby shielding it from the aqueous environment. To this end, we prepared amphiphilic polymethacrylates via living radical polymerization with DP ~ 100, which were decorated with hydrophilic poly(ethyleneglycol) methyl ether (PEGMA, $DP_{PEG} \sim 8.5$) and 9% hydrophobic chiral BTA substituents. The polymer backbone was additionally functionalized with 5% triphenylphosphine ligands, which form stable complexes with transition metals, in this case ruthenium(II) (Figure 33.3). The metal complexation was achieved either by a one-pot approach using a Ru-catalyst for the polymerization [43] or by post-loading the polymer with $RuCl_2(PPh_3)_3$ [41]. Both strategies resulted in a quantitative complexation of ruthenium analyzed by NMR spectroscopy and inductively coupled plasma atomic emission spectroscopy. Upon

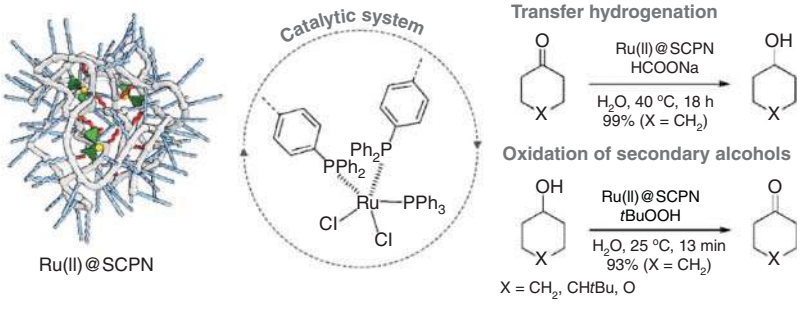

Figure 33.3 Illustration of Ru(II)-loaded SCPNs based on amphiphilic polymethacrylates with DP ~ 100 based on poly(ethyleneglycol) methyl ether (PEGMA, $DP_{PEG} \sim 8.5$) with 9% hydrophobic chiral BTA substituents and 5% triphenylphosphine ligands, as used for transfer hydrogenation and oxidation reactions in water.

exposure to water the polymer chains collapse into compact SCPNs with hydrodynamic radii R_H of around 5–10 nm measured by dynamic light scattering. Importantly, the ruthenium complexation did not negatively affect the folding of single polymer chains to defined nanoreactors. In fact, it supports the folding event as a secondary type of cross-linking. Furthermore, CD spectroscopy confirmed the formation of helical BTA stacks within the interior of the SCPNs.

The catalytic activity of Ru(II)@SCPNs was investigated in a transfer hydrogenation reaction of cyclohexanone as a model substrate and sodium formate as the hydrogen source at 40 °C in pure water as the solvent. The reduction to cyclohexanol was quantitative after 18 hours at a [substrate]/[Ru] ratio of 200/1. Even at lower catalyst concentrations ([substrate]/[Ru] = 1000/1), the polymer-bound catalyst showed a high efficacy (conversion of 98% in 50 hours). The apparent TOF of our catalytic system was around 10–20 h^{-1} and is in good agreement with other water-soluble Ru-complexes reported in literature [52–57]. The Ru(II)@SCPNs also demonstrate a high robustness under the applied reaction conditions as the helical BTA assemblies were still intact and neither decomposition nor hydrolysis of the polymer structure were observed. Further detailed analysis on how the nature of the hydrophobic side chains influences the catalytic activity of Ru(II)@SCPNs revealed that BTAs and long alkyl chains are equally sufficient to create a hydrophobic interior. The additional feature of helical stacks in the vicinity of catalytic sites is not further improving the catalytic activity since the Ru catalyst is already tightly shielded by the metal–ligand coordination.

Interestingly, the Ru(II)@SCPNs system shows a selectivity toward more hydrophobic substrates. In a competing reaction, three different substrates with increasing hydrophobicity, namely tetrahydro-4*H*-pyran-4-on, cyclohexanone, and 4-*tert*-butylcyclohexanone, were applied and conversions of 30%, 70%, and >99%, respectively, were determined [58]. The same selectivity was observed for the reverse reaction – the oxidation of secondary alcohols to ketones in the presence of *t*BuOOH. These results showcase how the conversion rate of more hydrophobic substrates increases, based on the more pronounced accumulation and thus higher local concentrations within the catalytically active nanoparticles.

33.4 Polymer-Supported Cu(I) and Pd(II) Catalysis in Water

The development of bio-orthogonal reactions is an intriguing research field as it allows for the selective modification of biologically active molecules in their native cellular environment. Well-known reactions, which have been explored in a cellular context, are Cu(I)-catalyzed azide–alkyne cycloadditions (CuAAC) [59, 60] and Pd(II)-catalyzed depropargylations [61]. In addition, seminal works by Zimmerman and coworkers showed that Cu(I)-based SCPNs can show unprecedentedly high rates in click reactions, even in complex cellular media [62–64]. In order to perform bio-orthogonal chemical transformations based on dynamic amphiphilic polymeric nanoparticles, we synthesized a series of polymers functionalized with different

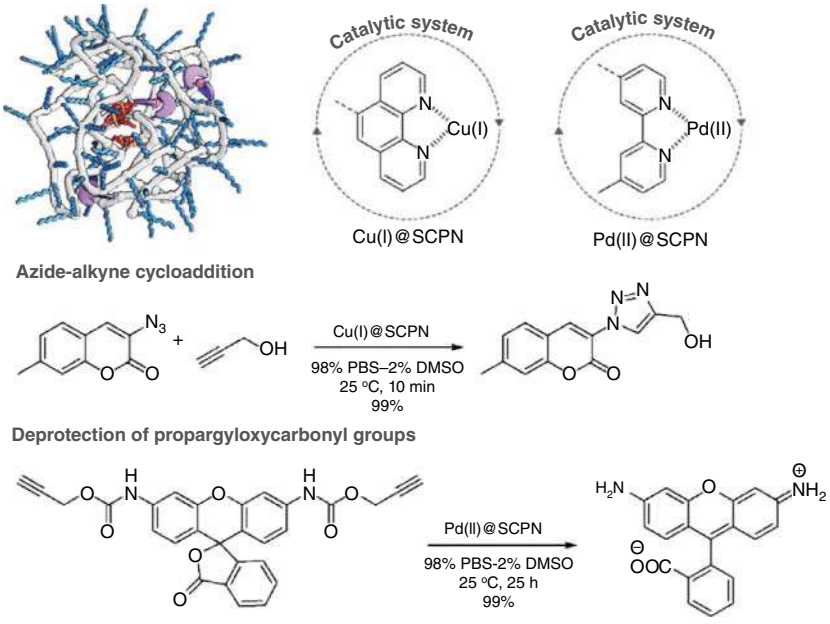

Figure 33.4 Illustration of Cu(I)- and Pd(II)-loaded SCPNs employed in azide-alkyne cycloaddition and propargyl deprotection reactions in PBS buffer solution.

metal-binding motifs (Figure 33.4) [65]. The polymer backbone was decorated with nitrogen-containing ligands, such as (benzimidazoylmethyl)-bis(pyridylmethyl) amine (Bimpy), phenanthroline (Phen), and 2,2′-bipyridine (Bipy), along with BTA pendants and Jeffamine as water-soluble side chains. First, CuAAC reactions at dilute concentrations were performed with 3-azido-7-hydroxycoumarin and propargyl alcohol as azide and alkyne substrates. Cu(I) was generated in situ using $CuSO_4$ and sodium ascorbate in phosphate buffer at a physiological pH of around 7.4 and the ligand-containing polymers were subsequently added to obtain catalytically active Cu(I)@SCPNs. The Cu(I)@SCPNs with Bimpy and Phen as ligands showed rapid full conversions after 10 and 25 minutes, respectively. The water-soluble Pd(II)@SCPNs catalytic system was formed by mixing $Pd(OAc)_2$ with the Bipy-containing polymer under buffered conditions. *N*-Propargyloxycarbonyl-caged rhodamine was chosen as the fluorogenic substrate and full conversion to the free rhodamine was reached after 25 hours. In both reactions, highly fluorescent products were generated, thus their formation could conveniently be followed by fluorescence spectroscopy.

As both metal-mediated reactions were successful in buffered aqueous solutions, we were highly interested in going one step further toward bio-orthogonal catalysis in living cells [66]. Therefore, it is of major importance to analyze the toxicity of SCPNs to living cells. After developing strategies to deliver SCPNs into intracellular locations, such as lysosome and cytosol, and extracellular space of HeLa cells, we could demonstrate that the native SCPN architecture is non-toxic and thus biocompatible. The outer oligo(ethylene glycol)-based layer of SCPNs is most likely

preventing harmful cell interactions. More importantly, still no or only minor cytotoxicity could be observed when Cu(I) and Pd(II) were coordinated to the SCPN scaffolds. The metal-loaded polymers were applied in a series of deprotection reactions of propargyloxycarbonyl protected rhodamine dyes in the extracellular matrix of living cells. The product formation reached a plateau after 24 hours, and the desired fluorescent molecule was capable of crossing the cell membrane. This demonstrates that the SCPNs only have to be present in the extracellular space and not inside living cells to activate a potential prodrug and convert it to an active drug, which is promising for cancer therapy.

33.5 Polymer-Supported Organocatalysis in Water

Organocatalysis has gained an immense amount of attention since the late 1990s, and evolved to a powerful tool to synthesize molecules in a highly enantioselective and efficient fashion. The amino acid L-proline (L-Pro) is one of the most prominent small molecule organocatalysts capable of catalyzing a plethora of organic reactions. Since L-Pro-catalyzed reactions go through complex transition states directed by the carboxylic acid, we were interested in how the folding of an amphiphilic polymer around a proline catalytic moiety would influence its reactivity [67]. In addition, the efficiency and selectivity of L-Pro in water are typically poor because of the lack of hydrophobic shielding, which can be circumvented by anchoring proline to the backbone of SCPNs and thus providing a hydrophobic pocket. To this end, a series of SCPNs with L-Pro (5%), chiral BTA (10%), and PEGMA (85%) functionalities were prepared and the L-Pro@SCPNs were applied in a model aldol addition between cyclohexanone and 4-nitrobenzaldehyde in water (Figure 33.5a). Quantitative conversion to the aldol product was obtained after a reaction time of 120 hours at room temperature with high diastereoselectivity (de ~ 90%) and moderate enantioselectivity (ee ~ 70%). When the L-Pro content in the polymer is increased to 10%, the catalytic system showed even at very low catalyst loading conditions of 0.05 mol% unprecedentedly high activity for a synthetic polymer. This can be attributed to the concentrator effect within the compartmentalized particles, which results in high local substrate concentrations. Remarkably, the presence of helical BTA stacks in the vicinity of proline catalysts is fundamental for a successful aldol reaction. SCPNs that were functionalized with dodecyl groups instead of chiral BTA moieties did not show any conversion under identical conditions. This showcases that a structuring and conformationally adaptive element, such as helical BTA assemblies, can create an optimal microstructure for efficient catalysis.

Instead of linking L-Pro directly to the SCPN scaffold, we alternatively pursued a modular approach by covalently attaching the organocatalyst to a chiral (*S*)-BTA monomer structure ((*S*)-BTA-L-Pro), which can coassemble into the supramolecular stacks of an achiral BTA functionalized SCPN (Figure 33.5a) [68]. Mixing (*S*)-BTA-L-Pro with the achiral polymer in water showed a negative Cotton effect

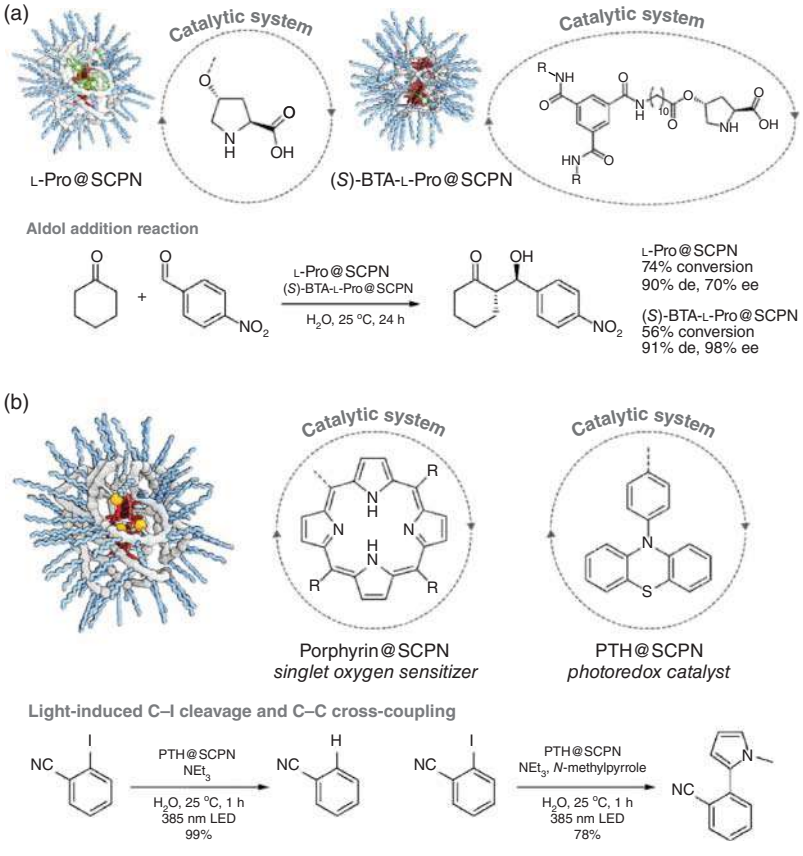

Figure 33.5 (a) Illustration of SCPNs, which either contain covalently bound L-proline or supramolecularly incorporated (*S*)-BTA-L-proline. Both catalytically active SCPNs were used for enantioselective aldol reactions in water. R = (*S*)-3,7-dimethyloctyl. (b) Illustration of light-responsive SCPNs containing either porphyrin photosensitizer for singlet oxygen generation or phenothiazine for light-induced reduction and cross coupling reactions in water. R = 4-(methoxycarbonyl)phenyl.

in CD spectroscopy experiments, which confirms the formation of stacks with a preferred *M*-helical sense as well as successful coassembly. A direct comparison of this modular approach with the covalent system discussed above toward the model aldol reaction unveils clear differences. While the covalent L-Pro@SCPN system showed high conversion at the cost of moderate enantioselectivity, the modular (*S*)-BTA-L-Pro@SCPN approach results in high enantioselectivity (ee > 94%) but lower activity (56% conversion after 24 hours). The elevated selectivity strongly suggests that the organocatalyst is better shielded from the aqueous surrounding when directly embedded in the supramolecular assembly within the hydrophobic pocket. This strategy illustrates how a desired functionality, in this case catalytic activity, can conveniently be introduced into SCPNs.

33.6 Polymer-Supported Photocatalysis in Water

Light is an excellent external trigger to steer chemical transformations based on its high spatio-temporal resolution, simple and safe handling with the advent of LED technology, precise energy tuning in terms of light intensity and wavelength, and orthogonality by selectively exciting chromophores according to their absorbance profile. Porphyrins are a well-known class of highly colored chromophores, which in their excited triplet state can interact with molecular oxygen and form reactive oxygen species, for instance singlet oxygen [69]. This light-induced process is a key step in photodynamic therapy as the produced singlet oxygen causes oxidative damage and leads to cell death only in the illuminated areas. Porphyrins are, however, poorly water soluble and prone to aggregate due to their large π-system, which results in self-quenching of the excited triplet states and thus diminishes their potential as photosensitizers [70]. Linking porphyrins to the polymer backbone of SCPNs bypasses their lack of solubility and additionally prevents clustering of the chromophores (Figure 33.5b) [65]. Irradiation of porphyrin@SCPNs in water with blue light (420 nm) led to the generation of singlet oxygen as was shown by the characteristic luminescence of $^1O_2$ at 1275 nm in infrared emission spectroscopy. In addition, the in situ produced $^1O_2$ could be exploited to cleave an amino-acrylate linker, which connects a fluorogenic model compound to the SCPNs. The light-triggered release of small molecules can be applied for drug delivery strategies by employing biologically active compounds. Moreover, the singlet oxygen generation successfully caused cell death by internalizing porphyrin@SCPNs in living HeLa cells and subsequent light illumination, paving the way toward their use in photodynamic therapy [66].

Photoredox catalysis is another aspiring research field in synthetic chemistry and is based on exceptionally high reduction or oxidation potentials of chromophores in their excited state. Examples of photoredox catalysis in aqueous media are still scarce due to the poor solubility of aromatic chromophores in water [71, 72]. Thus, we anchored phenothiazine (PTH), a metal-free photocatalyst with a high reduction potential of $E^*_{red} = -2.1$ eV [73], to the polymer backbone of SCPNs and studied the cleavage of carbon-halogen bonds in pure water (Figure 33.5b) [74]. The reduction of (hetero)aryl-iodide substrates was achieved within one hour of light irradiation (385 nm LED), thereby displaying high tolerance toward a variety of functional groups. Employing electron-poor substrates (e.g. 2-iodobenzonitrile) resulted in quantitative product formation, while more demanding electron-rich compounds expectedly showed lower conversions, such as 2-iodoaniline with 11% conversion. The presence of triethylamine is a prerequisite for a successful outcome as it regenerates the catalyst after the light-induced SET event. Besides, the PTH@SCPNs were conveniently recycled and used in consecutive reductions (up to five cycles) without loss of activity. The course of the reaction could be halted and continued at will by turning the light source repeatedly OFF and ON and thus demonstrating a high degree of temporal control. Moreover, the benzene radical species, which is formed after the heterolytic bond cleavage, can be trapped with electron-rich reagents. The C–C cross-coupling reaction between 2-iodobenzonitrile and *N*-methylpyrrole

turned out to be efficient in aqueous medium (78% conversion). Due to the high local concentration of substrates within the hydrophobic interior of SCPNs, only five equivalents of the coupling partner were sufficient, which is significantly less compared to reports in organic solvents [75] and thereby reduces the amount of waste. The combination of efficient photoredox catalysis and amphiphilic polymeric nanoparticles has tremendous potential for late-stage modifications of drug compounds or decomposition of toxic halogen-rich pollutants in water.

33.7 Outlook and Conclusions

Combining the lessons learned from protein folding – both in experimental work and in molecular simulations – with a fundamental understanding on how the primary structure of a synthetic polymer (monomer sequence, distribution, and chain length) relates to function, have been crucial steps to achieve active and versatile synthetic catalysts that can compete or cooperate with Nature's enzymes. The next step in designing functional polymeric systems for advanced catalysis applications requires a high degree of architectural and structural precision, reliable and scalable preparation methods, and control over the dynamic interactions on molecular and macroscopic scale. Hereby, precision polymer synthesis in combination with strict control over the non-covalent inter- and intramolecular interactions will play an important role to regulate the vicinity of the catalytically active site even more. What is currently lacking, is the ability to visualize the 3D structure of the SCPNs as well as to determine the internal structure of the functional particles. High-resolution microscopy in combination with sophisticated molecular dynamics simulations will hopefully become possible in the near future, which will undoubtedly further increase our level of understanding these synthetic systems.

Our approach to combine scattering and spectroscopic studies to fundamentally understand the folding of amphiphilic polymers into single-chain polymeric nanoparticles proved fruitful as a first step to achieve enzyme-like activity and selectivity in synthetic catalysts. In addition, the selected approach allowed us to devise ways to fold these amphiphilic polymers around catalytic sites, hereby enhancing their stability and compatibility with complex media. As a result, we are able to conduct a range of catalytic reactions in water and complex media thermally, but also by using light as a source of energy. These conversions are of interest in green chemistry approaches especially since the recyclability of the catalyst is possible and may also contribute to degrade persistent organic pollutants. Access to highly active, selective, as well as stable catalysts will also allow us to achieve conversions in complex cellular media as needed for prodrug activation or to complement the catalytic repertoire of Nature by non-natural catalytic reactions in concert with natural catalytic reactions. On the long term, access to such highly active catalysts may even lead to the possibility to replace enzymes that no longer fulfil their natural functions in cells. All in all, the integration of catalysis, supramolecular chemistry, and polymer chemistry with biological systems is a powerful combination to access increasingly sophisticated catalysts, with a catalytic power approaching that of natural enzymes.

Acknowledgments

The authors acknowledge financial support from The Netherlands Organization for Scientific Research (NWO) and F.E. acknowledges the Alexander von Humboldt Foundation for providing a Feodor Lynen research fellowship.

References

1 Staudinger, H. (1920). Über Polymerisation. *Ber. Dtsch. Chem. Ges.* 53: 1073–1085.
2 Noyori, R. (2002). Asymmetric catalysis: science and opportunities. *Angew. Chem. Int. Ed.* 41: 2008–2022.
3 Knowles, W.S. (2002). Asymmetric hydrogenations. *Angew. Chem. Int. Ed.* 40: 1998–2007.
4 Grubbs, R.H. (2006). Olefin-metathesis catalysts for the preparation of molecules and materials (nobel lecture). *Angew. Chem. Int. Ed.* 45: 3760–3765.
5 Johansson Seechurn, C.C.C., Kitching, M.O., Colacot, T.J., and Snieckus, V. (2012). Palladium-catalyzed cross-coupling: a historical contextual perspective to the 2010 nobel prize. *Angew. Chem. Int. Ed.* 51: 5062–5085.
6 Lipshutz, B.H. (2018). Synthetic chemistry in a water world. New rules ripe for discovery. *Curr. Opin. Green Sustain. Chem.* 11: 1–8.
7 Lipshutz, B.H. (2017). When does organic chemistry follow nature's lead and "make the switch"? *J. Org. Chem.* 82: 2806–2816.
8 Bergbreiter, D.E. (2014). Soluble polymers as tools in catalysis. *ACS Macro Lett.* 3: 260–265.
9 Bhowmick, S., Mondal, A., Ghosh, A., and Bhowmick, K.C. (2015). Water: the most versatile and nature's friendly media in asymmetric organocatalyzed direct aldol reactions. *Tetrahedron: Asymmetry* 26: 1215–1244.
10 Astruc, D. and Chardac, F. (2001). Dendritic catalysts and dendrimers in catalysis. *Chem. Rev.* 101: 2991–3024.
11 Ouchi, M., Terashima, T., and Sawamoto, M. (2009). Transition metal-catalyzed living radical polymerization: toward perfection in catalysis and precision polymer synthesis. *Chem. Rev.* 109: 4963–5050.
12 Ren, J.M., McKenzie, T.G., Fu, Q. et al. (2016). Star polymers. *Chem. Rev.* 116: 6743–6836.
13 van Oers, M.C.M.M., Abdelmohsen, L.K.E.A.E.A., Rutjes, F.P.J.T.J.T., and van Hest, J.C.M.M. (2014). Aqueous asymmetric cyclopropanation reactions in polymersome membranes. *Chem. Commun.* 50: 4040–4043.
14 Suginome, M., Yamamoto, T., and Nagata, Y. (2015). Poly(quinoxaline 2 ,3 diyl)s: a fascinating helical macromolecular scaffold for new chiral functions. *J. Synth. Org. Chem. Japan* 73: 1141–1155.
15 Raynal, M., Portier, F., van Leeuwen, P.W.N.M., and Bouteiller, L. (2013). Tunable asymmetric catalysis through ligand stacking in chiral rigid rods. *J. Am. Chem. Soc.* 135: 17687–17690.

16 Chen, K. and Arnold, F.H. (2020). Engineering new catalytic activities in enzymes. *Nat. Catal.*: 1–11.

17 Schmid, A., Dordick, J.S., Hauer, B. et al. (2001). Industrial biocatalysis today and tomorrow. *Nature* 409: 258–268.

18 Schmid, A., Hollmann, F., Park, J.B., and Bühler, B. (2002). The use of enzymes in the chemical industry in Europe. *Curr. Opin. Biotechnol.* 13: 359–366.

19 van As, B.A.C., van Buijtenen, J., Heise, A. et al. (2005). Chiral oligomers by iterative tandem catalysis. *J. Am. Chem. Soc.* 127: 9964–9965.

20 van Buijtenen, J., van As, B.A.C., Meuldijk, J. et al. (2006). Chiral polymers by iterative tandem catalysis. *Chem. Commun.* 30: 3169–3171.

21 Onuchic, J.N., Luthey-Schulten, Z., and Wolynes, P.G. (1997). Theory of protein folding: the energy landscape perspective. *Annu. Rev. Phys. Chem.* 48: 545–600.

22 Finkelstein, A.V. (2018). 50+ years of protein folding. *Biochemistry* 83: S3–S18.

23 Dobson, C.M. (2003). Protein folding and misfolding. *Nature* 426: 884–890.

24 Rose, G.D., Fleming, P.J., Banavar, J.R., and Maritan, A. (2006). A backbone-based theory of protein folding. *Proc. Natl. Acad. Sci.* 103: 16623–16633.

25 Schönfelder, J., De Sancho, D., and Perez-Jimenez, R. (2016). The power of force: insights into the protein folding process using single-molecule force spectroscopy. *J. Mol. Biol.* 428: 4245–4257.

26 Anfinsen, C.B. (1972). The formation and stabilization of protein structure. *Biochem. J.* 128: 737–749.

27 Bosman, A.W., Vestberg, R., Heumann, A. et al. (2003). A modular approach toward functionalized three-dimensional macromolecules: from synthetic concepts to practical applications. *J. Am. Chem. Soc.* 125: 715–728.

28 Harth, E., Van Horn, B., Lee, V.Y. et al. (2002). A facile approach to architecturally defined nanoparticles via intramolecular chain collapse. *J. Am. Chem. Soc.* 124: 8653–8660.

29 Morishima, Y., Nomura, S., Ikeda, T. et al. (1995). Characterization of unimolecular micelles of random copolymers of sodium 2-(acrylamido)-2-methylpropanesulfonate and methacrylamides bearing bulky hydrophobic substituents. *Macromolecules* 28: 2874–2881.

30 Ghosh, S. and Ramakrishnan, S. (2005). Small-molecule-induced folding of a synthetic polymer. *Angew. Chem. Int. Ed.* 44: 5441–5447.

31 Mavila, S., Eivgi, O., Berkovich, I., and Lemcoff, N.G. (2016). Intramolecular cross-linking methodologies for the synthesis of polymer nanoparticles. *Chem. Rev.* 116: 878–961.

32 Hanlon, A.M., Lyon, C.K., and Berda, E.B. (2016). What is next in single-chain nanoparticles? *Macromolecules* 49: 2–14.

33 Altintas, O. and Barner-Kowollik, C. (2016). Single-chain folding of synthetic polymers: a critical update. *Macromol. Rapid Commun.* 37: 29–46.

34 Sanchez-Sanchez, A. and Pomposo, J.A. (2014). Single-chain polymer nanoparticles via non-covalent and dynamic covalent bonds. *Part. Part. Syst. Char.* 31: 11–23.

35 Gonzalez-Burgos, M., Latorre-Sanchez, A., and Pomposo, J.A. (2015). Advances in single chain technology. *Chem. Soc. Rev.* 44: 6122–6142.

36 Terashima, T. (2014). Functional spaces in star and single-chain polymers via living radical polymerization. *Polym. J.* 46: 664–673.

37 Murray, B.S. and Fulton, D.A. (2011). Dynamic covalent single-chain polymer nanoparticles. *Macromolecules* 44: 7242–7252.

38 Seo, M., Beck, B.J., Paulusse, J.M.J. et al. (2008). Polymeric nanoparticles via noncovalent cross-linking of linear chains. *Macromolecules* 41: 6413–6418.

39 Foster, E.J., Berda, E.B., and Meijer, E.W. (2009). Metastable supramolecular polymer nanoparticles via intramolecular collapse of single polymer chains. *J. Am. Chem. Soc.* 131: 6964–6966.

40 ter Huurne, G.M., Voets, I.K., Palmans, A.R.A., and Meijer, E.W. (2018). Effect of intra- versus intermolecular cross-linking on the supramolecular folding of a polymer chain. *Macromolecules* 51: 8853–8861.

41 Artar, M., Terashima, T., Sawamoto, M. et al. (2014). Understanding the catalytic activity of single-chain polymeric nanoparticles in water. *J. Polym. Sci. Part A Polym. Chem.* 52: 12–20.

42 Cantekin, S., de Greef, T.F.A., and Palmans, A.R.A. (2012). Benzene-1,3,5-tricarboxamide: a versatile ordering moiety for supramolecular chemistry. *Chem. Soc. Rev.* 41: 6125.

43 Terashima, T., Mes, T., De Greef, T.F.A. et al. (2011). Single-chain folding of polymers for catalytic systems in water. *J. Am. Chem. Soc.* 133: 4742–4745.

44 Smulders, M.M.J., Buffeteau, T., Cavagnat, D. et al. (2008). C3-symmetrical self-assembled structures investigated by vibrational circular dichroism. *Chirality* 20: 1016–1022.

45 Smulders, M.M.J., Schenning, A.P.H.J., and Meijer, E.W. (2008). Insight into the mechanisms of cooperative self-assembly: the "sergeants-and-soldiers" principle of chiral and achiral C3-symmetrical discotic triamides. *J. Am. Chem. Soc.* 130: 606–611.

46 Stals, P.J.M., Smulders, M.M.J., Martín-Rapún, R. et al. (2009). Asymmetrically substituted benzene-1,3,5-tricarboxamides: self-assembly and odd-even effects in the solid state and in dilute solution. *Chem. Eur. J.* 15: 2071–2080.

47 Gillissen, M.A.J., Terashima, T., Meijer, E.W. et al. (2013). Sticky supramolecular grafts stretch single polymer chains. *Macromolecules* 46: 4120–4125.

48 Stals, P.J.M., Gillissen, M.A.J., Paffen, T.F.E. et al. (2014). Folding polymers with pendant hydrogen bonding motifs in water: the effect of polymer length and concentration on the shape and size of single-chain polymeric nanoparticles. *Macromolecules* 47: 2947–2954.

49 ter Huurne, G.M., de Windt, L.N.J., Liu, Y. et al. (2017). Improving the folding of supramolecular copolymers by controlling the assembly pathway complexity. *Macromolecules* 50: 8562–8569.

50 Terashima, T., Sugita, T., Fukae, K., and Sawamoto, M. (2014). Synthesis and single-chain folding of amphiphilic random copolymers in water. *Macromolecules* 47: 589–600.

51 Abdouni, Y., ter Huurne, G., Yilmaz, G. et al. Self-assembled multi and single chain glyconanoparticles and their lectin recognition. *Biomacromolecules* 22: 661–670.

52 Wu, X. and Xiao, J. (2007). Aqueous-phase asymmetric transfer hydrogenation of ketones ? A greener approach to chiral alcohols. *Chem. Commun.* 2449: 2449–2466.

53 Liu, J., Zhou, Y., Wu, Y. et al. (2008). Asymmetric transfer hydrogenation of ketones with a polyethylene glycol bound Ru catalyst in water. *Tetrahedron: Asymmetry* 19: 832–837.

54 Li, X., Wu, X., Chen, W. et al. (2004). Asymmetric transfer hydrogenation in water with a supported Noyori–Ikariya catalyst. *Org. Lett.* 6: 3321–3324.

55 Schlatter, A., Kundu, M.K., and Woggon, W.-D. (2004). Enantioselective reduction of aromatic and aliphatic ketones catalyzed by ruthenium complexes attached to β-cyclodextrin. *Angew. Chem. Int. Ed.* 43: 6731–6734.

56 Zeror, S., Collin, J., Fiaud, J.-C., and Zouioueche, L.A. (2006). A recyclable multi-substrates catalytic system for enantioselective reduction of ketones in water. *J. Mol. Catal. A: Chem.* 256: 85–89.

57 Arakawa, Y., Chiba, A., Haraguchi, N., and Itsuno, S. (2008). Asymmetric transfer hydrogenation of aromatic ketones in water using a polymer-supported chiral catalyst containing a hydrophilic pendant group. *Adv. Synth. Catal.* 350: 2295–2304.

58 Artar, M., Souren, E.R.J., Terashima, T. et al. (2015). Single chain polymeric nanoparticles as selective hydrophobic reaction spaces in water. *ACS Macro Lett.* 4: 1099–1103.

59 Rostovtsev, V.V., Green, L.G., Fokin, V.V., and Sharpless, K.B. (2002). A stepwise huisgen cycloaddition process: copper(I)-catalyzed regioselective "ligation" of azides and terminal alkynes. *Angew. Chem. Int. Ed.* 41: 2596–2599.

60 Kolb, H.C., Finn, M.G., and Sharpless, K.B. (2001). Click chemistry: diverse chemical function from a few good reactions. *Angew. Chem. Int. Ed.* 40: 2004–2021.

61 Li, J., Yu, J., Zhao, J. et al. (2014). Palladium-triggered deprotection chemistry for protein activation in living cells. *Nat. Chem.* 6: 352–361.

62 Bai, Y., Feng, X., Xing, H. et al. (2016). A highly efficient single-chain metal–organic nanoparticle catalyst for alkyne–azide "click" reactions in water and in cells. *J. Am. Chem. Soc.* 138: 11077–11080.

63 Chen, J., Wang, J., Li, K. et al. (2019). Polymeric "clickase" accelerates the copper click reaction of small molecules, proteins, and cells. *J. Am. Chem. Soc.* 141: 9693–9700.

64 Chen, J., Wang, J., Bai, Y. et al. (2018). Enzyme-like click catalysis by a copper-containing single-chain nanoparticle. *J. Am. Chem. Soc.* 140: 13695–13702.

65 Liu, Y., Pauloehrl, T., Presolski, S.I. et al. (2015). Modular synthetic platform for the construction of functional single-chain polymeric nanoparticles: from aqueous catalysis to photosensitization. *J. Am. Chem. Soc.* 137: 13096–13106.

66 Liu, Y., Pujals, S., Stals, P.J.M. et al. (2018). Catalytically active single-chain polymeric nanoparticles: exploring their functions in complex biological media. *J. Am. Chem. Soc.* 140: 3423–3433.

67 Huerta, E., Stals, P.J.M., Meijer, E.W., and Palmans, A.R.A. (2013). Consequences of folding a water-soluble polymer around an organocatalyst. *Angew. Chem. Int. Ed.* 52: 2906–2910.

68 Huerta, E., Van Genabeek, B., Stals, P.J.M. et al. (2014). A modular approach to introduce function into single-chain polymeric nanoparticles. *Macromol. Rapid Commun.* 35: 1320–1325.

69 Allison, R.R., Downie, G.H., Cuenca, R. et al. (2004). Photosensitizers in clinical PDT. *Photodiagn. Photodyn. Ther.* 1: 27–42.

70 Jang, W.-D., Nishiyama, N., Zhang, G.-D. et al. (2005). Supramolecular nanocarrier of anionic dendrimer porphyrins with cationic block copolymers modified with polyethylene glycol to enhance intracellular photodynamic efficacy. *Angew. Chem. Int. Ed.* 44: 419–423.

71 Pfund, B., Steffen, D.M., Schreier, M.R. et al. (2020). UV light generation and challenging photoreactions enabled by upconversion in water. *J. Am. Chem. Soc.* 142: 10468–10476.

72 Giedyk, M., Narobe, R., Weiß, S. et al. (2020). Photocatalytic activation of alkyl chlorides by assembly-promoted single electron transfer in microheterogeneous solutions. *Nat. Catal.* 3: 40–47.

73 Discekici, E.H., Treat, N.J., Poelma, S.O. et al. (2015). A highly reducing metal-free photoredox catalyst: design and application in radical dehalogenations. *Chem. Commun.* 51: 11705–11708.

74 Eisenreich, F., Meijer, E.W., and Palmans, A.R.A. (2020). Amphiphilic polymeric nanoparticles for photoredox catalysis in water. *Chem. Eur. J.* 26: 10355–10361.

75 Ghosh, I., Ghosh, T., Bardagi, J.I., and König, B. (2014). Reduction of aryl halides by consecutive visible light-induced electron transfer processes. *Science* 80 (346): 725–728.

34

Phosphines Modified by Cyclodextrins for Supramolecular Catalysis in Water

Sébastien Tilloy and Eric Monflier

Univ. Artois, CNRS, Centrale Lille, Univ. Lille, UMR 8181, Unit of catalysis and solid state chemistry (UCCS), Faculty of Sciences, Rue Jean Souvraz, Lens, 62300, France

34.1 Introduction

Native cyclodextrins (CDs) are cyclic oligosaccharides composed of six (α-CD), seven (β-CD) or eight (γ-CD) α-1,4-linked D-glucopyranose units (Figure 34.1).

This cyclic arrangement forms a hydrophobic cavity, whereas the external surface is hydrophilic. CDs can form inclusion complexes with numerous organic compounds and so have found numerous applications in various fields, such as analytical chemistry, agrochemistry, pharmaceuticals, foods, cosmetics, and catalysis [1, 2]. More precisely concerning this last topic, CDs are of great interest to elaborate ligands for organometallic catalytic processes. Indeed, the application of various CDs modified by phosphine moieties in organometallic catalysis was described in the literature [3–41]. However, these CD-phosphines are poorly soluble or insoluble in water, restricting their application in aqueous organometallic catalytic processes. This is regrettable, since these water-soluble CD-modified phosphines are potentially bifunctional compounds. Indeed, they could simultaneously act as ligands for transition metal and as molecular recognition agents during aqueous biphasic catalytic processes. More precisely, the transition metal can be coordinated by the phosphine moiety to be efficiently immobilized in water, and the hydrophobic cavity can include the substrate and therefore improve the mass transfer (Figure 34.2).

Nevertheless, such modified CDs must have precise specifications: (i) possess coordination properties, (ii) be sufficiently soluble in water to maintain the organometallic catalyst in aqueous phase, (iii) have an available cavity to include the guest, and (iv) finally, they must act as mass transfer agents. In this chapter, we describe our pathway from 2010 to elaborate four CD-modified di- or triphenylphosphines (Figure 34.3) acting both as ligands and/or as mass transfer agents and their applications in aqueous hydroformylation reaction.

Supramolecular Catalysis: New Directions and Developments, First Edition.
Edited by Piet W.N.M. van Leeuwen and Matthieu Raynal.

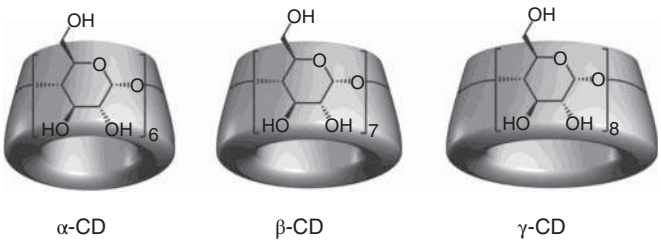

Figure 34.1 Representation of native CDs.

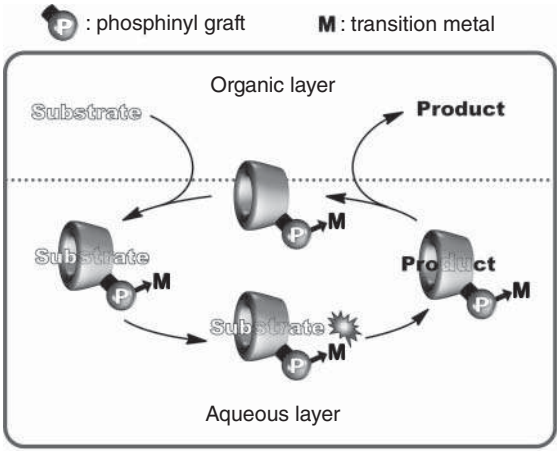

Figure 34.2 Coordinating property and substrate recognition ability of a CD-phosphine during a metal-catalyzed reaction in aqueous biphasic system.

34.2 Synthesis and Properties of CD-Phosphine 1 (CD-P-1)

The first attempt described the synthesis of a diphenyl monophosphine CD (**CD-P-1**) [42]. Indeed, some examples in the literature were relative to diphosphines CDs bearing four or six phenyl groups, but the presence of these hydrophobic groups leads to an insolubility in pure water requiring the addition of a co-solvent (such as DMF or methanol) for application in the hydroformylation reaction [34, 39]. Unfortunately, the presence of a co-solvent led to a loss of the organometallic species in organic layer and a decrease in recognition capacity of CD moiety. So, the synthesis of a monophosphine CD was envisaged to reduce the global hydrophobicity. **CD-P-1** was prepared in three steps from β-CD. β-CD was treated with tosyl chloride to give mono(6-*O*-tosyl)-β-CD which was then permethylated. The last step was a treatment with $KPPh_2$ to produce **CD-P-1**. **CD-P-1** is soluble in water up to 3 mM (at 20 °C). Concerning the inclusion capacity, NMR 2D T-ROESY experiments were performed in water and a self-inclusion phenomenon was observed. Indeed, one phenyl group is included into the cavity (Figure 34.4a). Such phenomena can be a drawback, since the inclusion capacity can be limited. To estimate the strength of this self-inclusion, an assay was performed to include an external guest (Figure 34.4b). Sodium 1-adamantanecarboxylate (ACNa) was chosen because it is known to form

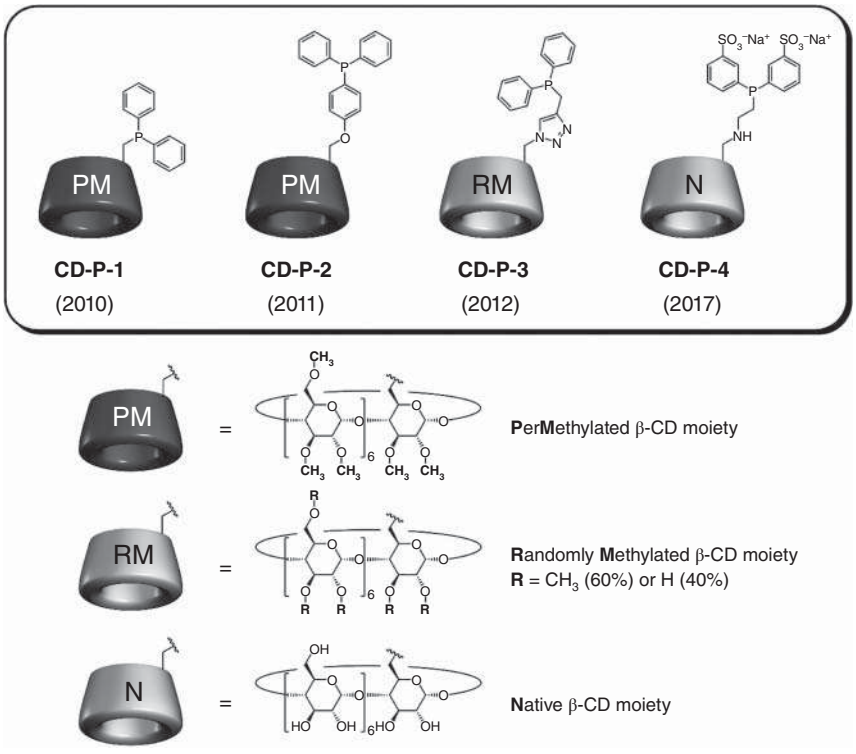

Figure 34.3 Representation of the four CD-phosphines (CD-P).

very stable inclusion complexes with β-CD series. The association constant between ACNa and **CD-P-1** was found equal to 265 M^{-1}. For comparison, the value of the association constant between ACNa and permethylated β-CD is equal to 10 700 M^{-1}. This value, 40 times higher than that of **CD-P-1**, means that the self-inclusion complex is very strongly stabilized, and the occupation of the cavity of **CD-P-1** by the aromatic moiety will prevent the formation of stable inclusion complexes.

Nevertheless, we were then interested in the performance of **CD-P-1**, as ligand, in the hydroformylation in water (Table 34.1). As the cavity is not available, methyl 4-pentenoate was chosen as model substrate, since it is not able to form an inclusion complex with **CD-P-1** and it is soluble in water. With the combination Rh/**CD-P-1**, high conversion (96%) was reached after two hours (Table 34.1, entry 1; Experimental conditions: substrate/**CD-P-1**/Rh: 500/4/1; P(CO/H_2) 50 bar; $T = 80\,°C$). The aldehyde selectivity was 99%, which shows that no isomerization or hydrogenation of the double bound occurred. The ratio of linear to branched aldehydes (*l*/*b*) was 1.8. Although its cavity was only very slightly available, **CD-P-1** was also evaluated as ligand and mass transfer agent during aqueous biphasic hydroformylation reaction of 1-decene (Table 34.1, entry 2; Experimental conditions: substrate/**CD-P-1**/Rh: 500/4/1; P(CO/H_2) 50 bar; $T = 80\,°C$). High conversion was reached, but a leaching of the catalyst in the organic layer was evidenced. This

behavior was expected, since **CD-P-1** is partially soluble in organic medium such as cyclohexane or heptane.

So, **CD-P-1** is able to act as ligand but does not possess the requirements expected for applications as mass transfer agent, since its cavity is not available and it is partially soluble in organic medium.

34.3 Synthesis and Properties of CD-Phosphine 2 (CD-P-2)

In order to prevent the self-inclusion phenomenon observed for **CD-P-1**, we have decided to insert a rigid connection (a phenyl group) between the CD and diphenylphosphino moieties [43]. **CD-P-2** was synthesized in two steps from mono(6-*O*-tosyl)-β-CD, which was first permethylated and then engaged with cesium 4-(diphenylphosphino)phenoxide to give **CD-P-2**. Unfortunately, the introduction of an additional phenyl group has increased the hydrophobic character. Indeed, solubility tests have shown that **CD-P-2** was poorly soluble in water (0.01 mM at 20 °C), whereas it was highly soluble in organic solvents such as methanol or chloroform (100 mM at 20 °C). Inspite of this low water solubility, NMR 2D T-ROESY experiments were performed in water and interestingly, no correlation between the aromatic protons and the CD protons were observed. These experiments demonstrated that the cavity is available since neither intermolecular nor intramolecular complexation phenomena were evidenced. In Figure 34.4, the equilibrium (a) was not observed. So, the inclusion properties of **CD-P-2** were investigated in the presence of ACNa. NMR experiments showed that ACNa was included in the CD cavity (Figure 34.4b). Interestingly, a hydrophilic assistance was observed

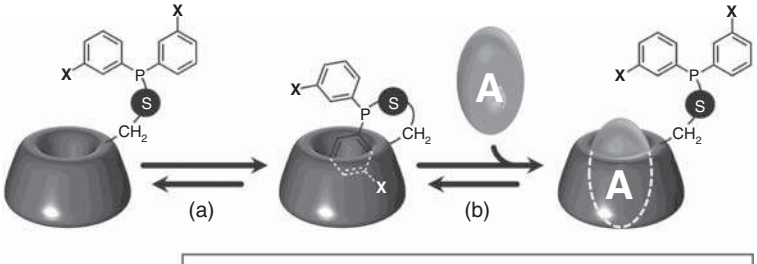

	CD-P-1	CD-P-2	CD-P-3	CD-P-4
S : spacer group	–	–O–	–N N=N CH2–	–NH–CH2–CH2–
X	–H	–H	–H	$-SO_3^-Na^+$
β-CD moiety	**PM**	**PM**	**RM**	**N**

Figure 34.4 (a) Equilibrium between free form and self-inclusion form of a **CD-P** and (b) inclusion of an adamantane derivative (**A**) (**PM** = permethylated; **RM** = randomly methylated; **N** = native).

Table 34.1 Rhodium-catalyzed hydroformylation of various substrates using **CD-P** as ligand.[a)]

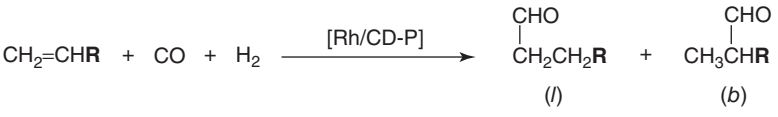

–R = **–(CH$_2$)$_2$CO$_2$Me**, **–(CH$_2$)$_8$CO$_2$Na** or **–(CH$_2$)$_n$CH$_3$** (*n* = 7, 9, 11, 13, 15)

Entry	CD-P	Substrate (—R)	Time (h)	Conversion[b)] (%)	Selectivity[c)] (%)	*l*/*b*[d)]
1	**CD-P-1**	–(CH$_2$)$_2$CO$_2$Me	2	96	99	1.8
2	**CD-P-1**	–(CH$_2$)$_7$CH$_3$	2	97	98	2.8
3	**CD-P-2**	–(CH$_2$)$_8$CO$_2$Na	0.25	99	98	2.9
4[e)]	**CD-P-2**	–(CH$_2$)$_8$CO$_2$Na	0.25	80	98	3.2
5[f)]	**CD-P-2**	–(CH$_2$)$_8$CO$_2$Na	0.25	32	98	3.1
6	**CD-P-2**	–(CH$_2$)$_7$CH$_3$	2	96	98	2.8
7	**CD-P-3**	–(CH$_2$)$_2$CO$_2$Me	6	99	99	0.67
8	**CD-P-3**	–(CH$_2$)$_7$CH$_3$	6	5	95	2.6
9	**CD-P-4**	–(CH$_2$)$_7$CH$_3$	3	47	81	2.3
10	**CD-P-4**	–(CH$_2$)$_7$CH$_3$	24	99	84	2.4
11[e)]	**CD-P-4**	–(CH$_2$)$_7$CH$_3$	3	26	80	2.6
12[h)]	**CD-P-4**	–(CH$_2$)$_7$CH$_3$	3	45	78	2.5
13[i)]	**CD-P-4**	–(CH$_2$)$_7$CH$_3$	3	42	75	2.5
14	**CD-P-4**	–(CH$_2$)$_9$CH$_3$	3	55	61	2.5
15	**CD-P-4**	–(CH$_2$)$_{11}$CH$_3$	3	47	57	2.6
16	**CD-P-4**	–(CH$_2$)$_{13}$CH$_3$	3	32	58	2.6
17	**CD-P-4**	–(CH$_2$)$_{15}$CH$_3$	3	29	58	2.5

a) Experimental conditions: [Rh(acac)(CO)$_2$] (1.94×10^{-3} mmol), **CD-P** (7.76×10^{-3} mmol for **CD-P-1**, **CD-P-2**, and **CD-P-3**; 9.7×10^{-3} mmol for **CD-P-4**), substrate (0.97 mmol), water (6 ml); 1500 rpm; *T*: 80 °C; P(CO/H$_2$): 50 bar.
b) Olefin conversion.
c) Aldehydes selectivity (byproducts are issued from isomerization of the C—C double bond).
d) Ratio of linear to branched aldehyde products.
e) Substrate/ACNa/**CD-P-2**/Rh: 250/250/4/1.
f) Substrate/ACNa/**CD-P-2**/Rh: 50/450/4/1.
g) Substrate/ACNa/**CD-P-4**/Rh: 500/4/4/1.
h) Performed using the aqueous phase recovered from entry 9.
i) Performed using the aqueous phase recovered from entry 12.

since this inclusion increased the water solubility by a factor 30 (from 0.01 to 0.3 mM). To evaluate the capacity of **CD-P-2** to form water-soluble rhodium species, [Rh(acac)(CO)$_2$] was mixed in water with three equivalents of **CD-P-2** under 1 bar of H$_2$ during eight hours. [HRh(CO)(**CD-P-2**)$_3$] was formed and its water solubility was determined to 0.5 mM. Therefore, in this favorable context, the catalytic

behavior of the Rh/**CD-P-2** combination was investigated in aqueous hydroformylation reaction of sodium 10-undecenoate, a water-soluble substrate. This substrate was chosen because it is able to be included in the available cavity of **CD-P-2**. High conversion (99%) and selectivity (98%) were reached with a linear to branched ratio of 2.9 (Table 34.1, entry 3; Experimental conditions: substrate/**CD-P-2**/Rh: 500/4/1; P(CO/H_2) 50 bar; $T = 80\,^{\circ}C$). In order to validate the positive effect of the inclusion, the influence of a competitor inside **CD-P-2** cavity was evaluated during the catalytic process. So, the hydroformylation reactions of sodium 10-undecenoate was also performed in the presence of ACNa. Expectedly, the conversion dramatically decreased when the ACNa concentration increased (compare the conversion values: 99%, 80%, and 32% obtained for substrate/ACNa/**CD-P-2**/Rh ratios equal to 500/0/4/1, 250/250/4/1, and 50/450/4/1, respectively; Table 34.1, entries 3–5). However, the chemoselectivity and regioselectivity were similar. These results clearly demonstrate that the presence of a free recognition site near the catalytic center greatly improves the catalytic activity when the substrate is able to be included. **CD-P-2** was also evaluated as ligand and mass transfer agent during aqueous biphasic hydroformylation reaction of 1-decene. High conversion (97% in two hours) was reached. Unfortunately, a leaching of the catalytic species was observed in the organic layer (Table 34.1, entry 6; Experimental conditions: substrate/**CD-P-2**/Rh: 500/4/1; P(CO/H_2) 50 bar; $T = 80\,^{\circ}C$). This high catalytic activity was due to the solubility of the organometallic species in 1-decene layer and not to mass transfer properties. It was expected since **CD-P-2** is partially soluble in organic medium such as methanol, chloroform, or heptane. This behavior is a major drawback preventing the recycling of the aqueous catalytic layer. So, **CD-P-2** can be used as a ligand in pure water but not in an aqueous organic biphasic medium.

34.4 Synthesis and Properties of CD-Phosphine 3 (CD-P-3)

From **CD-P-1** to **CD-P-2**, the presence of a spacer group between CD and diphenylphino moieties prevented the self-inclusion phenomenon. Nevertheless, the water solubility of **CD-P-2** is not sufficient to allow an aqueous biphasic catalysis process. In order to circumvent this drawback, we have synthetized by click chemistry a CD-phosphine with a triazole group as spacer and a platform based on randomly methylated-β-CD (RAME-β-CD) [44]. Indeed, the water solubility of RAME-β-CD is at least twice higher than that of permethylated-β-CD. The **CD-P-3** was synthesized from borane-protected diphenylpropynylphosphine and randomly methylated mono-6-azido-6-deoxy-β-CD by a copper-catalyzed azide–alkyne cycloaddition reaction followed by a borane-deprotection reaction. The water solubility of **CD-P-3** was equal to 15 mM (at 20 °C). Two-dimensional NMR experiments based on the T-ROESY sequence evidenced only slight dipolar contacts between the phenyl protons and the CD inner protons. The value of association constant with ACNa is equal to 46 600 M^{-1} signifying that the CD cavity is able to include an adamantane derivative (Figure 34.4).

The catalytic properties of the combination between a rhodium species and **CD-P-3** were studied in hydroformylation reaction. In order to evaluate the behavior of **CD-P-3** as ligand, the first experiments were performed with methyl 4-pentenoate. This substrate is water-soluble and not included in the CD cavity. When **CD-P-3** was used as a ligand, total conversion was reached after six hours with a linear to branched aldehyde ratio (*l*/*b*) equal to 0.67 (Table 34.1, entry 7; Experimental conditions: substrate/**CD-P-3**/Rh: 500/4/1; P(CO/H_2) 50 bar; $T = 80\,°C$). In a second time, 1-decene was envisaged as water-insoluble substrate able to form an inclusion complex with β-CD derivatives. Only 5% of conversion was obtained after six hours with a linear to branched aldehyde ratio (*l*/*b*) equal to 2.6 (Table 34.1, entry 8; Experimental conditions: substrate/**CD-P-3**/Rh: 500/4/1; P(CO/H_2) 50 bar; $T = 80\,°C$). No leaching of organometallic catalyst in 1-decene layer was observed owing to the higher water solubility of **CD-P-3** compared to **CD-P-1** and **CD-P-2**. Nevertheless, this poor conversion is surprising, as experiments conducted with ACNa as competitive guest have suggested that the phenyl moiety could be removed from the cavity by another guest. One explanation could be that the molecular recognition of free **CD-P-3** is different than that of **CD-P-3** coordinated to rhodium species. In particular, the phosphine-coordinated hydrophobic rhodium carbonyl hydride moiety could be included more strongly in the hydrophobic cavity than a phenyl ring, decreasing the inclusion capacity for 1-decene.

To resume, we have successfully prepared a valuable water-soluble CD-phosphine for aqueous organometallic catalysis, but the recognition capacity of Rh/**CD-P-3** species is too low for an efficient phase transfer effect.

34.5 Synthesis and Properties of CD-Phosphine 4 (CD-P-4)

In order to reduce the self-inclusion of a hydrophobic phenyl moiety inside the hydrophobic cavity, the introduction of hydrophilic-sulfonated phenyl was envisaged [45]. Indeed, the presence of a sulfonate group on the aromatic ring leads to a highly hydrophilic character. For example, the water solubility of the tris(3-sodium sulfonatophenyl)phosphine sodium salt (TPPTS-P(m-$C_6H_4SO_3Na)_3$) is equal to $1100\,g\,l^{-1}$ [46]. So, the product of the sulfonation of 2-(diphenylphosphino) ethylamine was put in reaction with mono-6-iodo-6-deoxy-β-CD to give **CD-P-4**. The introduction of a hydrophilic moiety was successful, since the water solubility was determined to 40 mM. Unfortunately, intra- and intermolecular inclusion processes of one of the two sulfophenyl groups into the β-CD cavity were identified in water by NMR 2D T-ROESY experiments. However, this inclusion of a sulfophenyl group was weak, since **CD-P-4** possesses a great affinity for adamantanol with a value of $40\,000\,M^{-1}$ for the association constant (Figure 34.4b). So, this CD seems possess the requirements for application in aqueous organic biphasic medium. Rh-catalyzed hydroformylation of 1-decene under aqueous biphasic conditions was carried out using **CD-P-4** in the presence of $Rh(CO)_2(acac)$. This catalytic species was able to convert 99% of 1-decene into aldehydes with a chemoselectivity of 84%

and a *l*/*b* ratio of 2.4 after 24 hours (Table 34.1, entries 9 and 10; Experimental conditions: substrate/**CD-P-4**/Rh: 500/5/1; P(CO/H_2) 50 bar; $T = 80\,^{\circ}C$). In order to highlight the beneficial effect of the cavity, catalytic tests were performed in the presence of ACNa. A decrease in conversion was observed indicating the competition between ACNa and 1-decene (Table 34.1, compared entries 9 and 11). Indirectly, it also proves the inclusion of the substrate into **CD-P-4** cavity during the catalytic process. The catalytic system has been recycled twice and only a slight decrease of the conversion and selectivity was noticed (Table 34.1, compared entries 9, 12, and 13). This phenomenon was due to the partial oxidation of **CD-P-4**. Interestingly, this system was also able to hydroformylate higher olefins such as 1-dodecene, 1-tetradecene, 1-hexadecene, and 1-octadecene (Table 34.1, entries 14–17). For the same time (three hours), the increase in the chain length led to a lower conversion.

The main advantages of **CD-P-4** compared to other **CD-P** are, on the one hand, the possibility to act as mass transfer agent and, on the other hand, the easy separation of the product containing organic phase and the catalyst-containing aqueous phase, leading to its reusability.

34.6 Concluding Remarks

In this chapter, we showed that the road to elaborate a CD-phosphine acting both as ligand and as mass transfer during hydroformylation reaction was long and filled with obstacles. The specifications of the ideal CD-phosphine are water solubility, coordination ability, available cavity, and mass transfer properties. All these goals were reached for **CD-P-4**, but a weak self-inclusion phenomenon was still present and probably decreased its efficiency. In our opinion, a challenge remains the synthesis of a CD-phosphine based on a RAME-β-CD bearing a TPPTS, as represented in Figure 34.5 (left side). Indeed, the rigid sulfophenyl spacer will prevent the self-inclusion and RAME-β-CD moiety will be efficient for mass transfer. In order to obtain a higher linear to branched aldehydes ratio, another challenging synthesis is a CD-phosphine based on a RAME-β-CD bearing a sulfonated nixantphos [47] (a bidentate ligand – Figure 34.5 – right side). These syntheses are under progress.

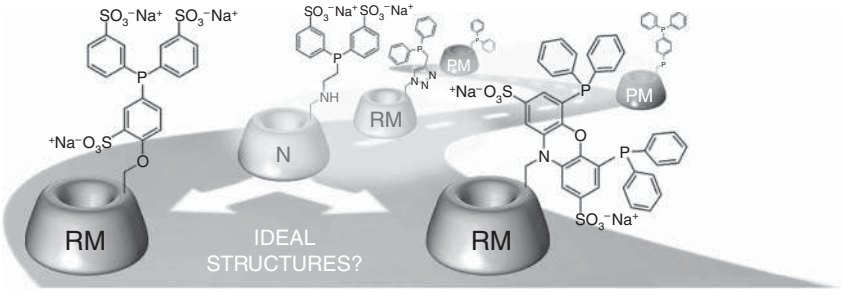

Figure 34.5 Pathway for the elaboration of the **CD-P** ideal structure.

References

1 Szejtli, J. (1998). Introduction and general overview of cyclodextrin chemistry. *Chem. Rev.* 98 (5): 1743–1753.

2 Hedges, A.R. (1998). Industrial applications of cyclodextrins. *Chem. Rev.* 98 (5): 2035–2044.

3 Matt, D. and Harrowfield, J. (2021). Phosphines and other P(III)-derivatives with cavity-shaped subunits: valuable ligands for supramolecular metal catalysis, metal confinement and subtle steric control. *ChemCatChem* 13: 153–168.

4 Matsinha, L.C., Siangwata, S., Smith, G.S., and Makhubela, B.C.E. (2019). Aqueous biphasic hydroformylation of olefins: from classical phosphine-containing systems to emerging strategies based on water-soluble nonphosphine ligands. *Catal. Rev.* 61 (1): 111–133.

5 Tilloy, S., Bricout, H., Menuel, S. et al. (2016). Cyclodextrins modified by metal-coordinating groups for aqueous organometallic catalysis: what remains to be done? *Curr. Organocatalysis* 3 (1): 24–31.

6 Jouffroy, M., Gramage-Doria, R., Semeril, D. et al. (2014). Phosphinocyclodextrins as confining units for catalytic metal centres. Applications to carbon–carbon bond forming reactions. *Beilstein J. Org. Chem.* 10: 2388–2405.

7 Jouffroy, M., Gramage-Doria, R., Armspach, D. et al. (2014). Confining phosphanes derived from cyclodextrins for efficient regio and enantioselective hydroformylation. *Angew. Chem. Int. Ed.* 53 (15): 3937–3940.

8 Hapiot, F., Bricout, H., Menuel, S. et al. (2014). Recent breakthroughs in aqueous cyclodextrin-assisted supramolecular catalysis. *Catal. Sci. Technol.* 4 (7): 1899–1908.

9 Takashima, Y., Uramatsu, K., Jomori, D. et al. (2013). Ring-opening metathesis polymerization by a Ru phosphine derivative of cyclodextrin in water. *ACS Macro Lett.* 2 (5): 384–387.

10 Jouffroy, M., Semeril, D., Armspach, D., and Matt, D. (2013). Phosphane–phosphite chelators built on a α-cyclodextrin scaffold: application in Rh-catalysed asymmetric hydrogenation and hydroformylation. *Eur. J. Org. Chem.* 2013 (27): 6069–6077.

11 Gramage-Doria, R., Armspach, D., Matt, D., and Toupet, L. (2012). Non-conventional coordination of cavity-confined metal centres. *Dalton Trans.* 41 (29): 8786–8796.

12 Gramage-Doria, R., Armspach, D., Matt, D., and Toupet, L. (2012). TRANSDIP: a trans-chelating ligand tailor-made for probing unusual Pd0 and PdII intermediates. *Chem. Eur. J.* 18 (35): 10813–10816.

13 Tilloy, S., Binkowski-Machut, C., Menuel, S. et al. (2012). Phosphane-based cyclodextrins as mass transfer agents and ligands for aqueous organometallic catalysis. *Molecules* 17 (11): 13062–13072.

14 Armspach, D., Matt, D., Poorters, L. et al. (2011). Ditopic binding of cyclodextrin-included ligands in trigonal silver(I) complexes. *Polyhedron* 30 (4): 573–578.

15 Zaborova, E., Deschamp, J., Guieu, S. et al. (2011). Cavitand supported tetraphosphine: cyclodextrin offers a useful platform for Suzuki–Miyaura cross-coupling. *Chem. Commun.* 47 (32): 9206–9208.

16 Gramage-Doria, R., Rodriguez-Lucena, D., Armspach, D. et al. (2011). Regioselective double capping of cyclodextrin scaffolds. *Chem. Eur. J.* 17 (14): 3911–3921.

17 Gramage-Doria, R., Armspach, D., Matt, D., and Toupet, L. (2011). A cavity-shaped diphosphane displaying "Oschelating" behavior. *Angew. Chem. Int. Ed.* 50 (7): 1554–1559.

18 Guieu, S., Zaborova, E., Bleriot, Y. et al. (2010). Can hetero-polysubstituted cyclodextrins be considered as inherently chiral concave molecules? *Angew. Chem. Int. Ed.* 49 (13): 2314–2318.

19 Poorters, L., Armspach, D., Matt, D. et al. (2007). A metallocavitand functioning as a container for anions: formation of noncovalent linear assemblies mediated by a cyclodextrin-entrapped NO^{3-} ion. *Angew. Chem. Int. Ed.* 46 (15): 2663–2665.

20 Poorters, L., Armspach, D., Matt, D. et al. (2007). Synthesis and properties of TRANSDIP, a rigid chelator built upon a cyclodextrin cavity: is TRANSDIP an authentic trans-spanning ligand? *Chem. Eur. J.* 13 (34): 9448–9461.

21 Poorters, L., Armspach, D., Matt, D., and Toupet, L. (2007). α-TEPHOS: a cyclodextrin-derived tetraphosphine for multiple metal binding. *Dalton Trans.* 29: 3195–3202.

22 Hapiot, F., Tilloy, S., and Monflier, E. (2006). Cyclodextrins as supramolecular hosts for organometallic complexes. *Chem. Rev.* 106 (3): 767–781.

23 Engeldinger, E., Poorters, L., Armspach, D. et al. (2004). Diastereospecific synthesis of phosphinidene-capped cyclodextrins leading to "introverted" ligands. *Chem. Commun.* (6): 634–635.

24 Engeldinger, E., Armspach, D., Matt, D., and Jones, P.G. (2003). Cyclodextrin phosphanes as first and second coordination sphere cavitands. *Chem. Eur. J.* 9 (13): 3091–3105.

25 Poorters, L., Armspach, D., and Matt, D. (2003). Selective tetrafunctionalisation of α-cyclodextrin using the supertrityl protecting group – synthesis of the first C-2-symmetric tetraphosphane based on a cavitand (α-TEPHOS). *Eur. J. Org. Chem.* 2003 (8): 1377–1381.

26 Engeldinger, E., Armspach, D., and Matt, D. (2003). Capped cyclodextrins. *Chem. Rev.* 103 (11): 4147–4173.

27 Engeldinger, E., Armspach, D., Matt, D. et al. (2002). Synthesis of large chelate rings with diphosphites built on a cyclodextrin scaffold. Unexpected formation of 1,2-phenylene-capped α-cyclodextrins. *C.R. Chim.* 5 (5): 359–372.

28 Reetz, M.T., Kostas, I.D., and Waldvogel, S.R. (2002). Synthesis of a gold(I) complex with a (thio)phosphine-modified β-cyclodextrin. *Inorg. Chem. Commun.* 5 (4): 252–254.

29 Engeldinger, E., Armspach, D., Matt, D. et al. (2002). A cyclodextrin diphosphane as a first and second coordination sphere cavitand: evidence for weak C–H···Cl–M hydrogen bonds within metal-capped cavities. *Angew. Chem. Int. Ed.* 41 (14): 2593.

30 Wong, Y.T., Yang, C., Ying, K.-C., and Jia, G. (2002). Synthesis of a novel β-cyclodextrin-functionalized diphosphine ligand and its catalytic properties for asymmetric hydrogenation. *Organometallics* 21 (9): 1782–1787.

31 Reetz, M.T., Rudolph, J., and Goddard, R. (2001). Diastereotopic group recognition in the solid state – a unique intramolecular β-cyclodextrin inclusion complex. *Can. J. Chem.* 79 (11): 1806–1811.

32 Engeldinger, E., Armspach, D., and Matt, D. (2001). Cyclodextrin cavities as probes for ligand-exchange processes. *Angew. Chem. Int. Ed.* 40 (13): 2526.

33 Yang, C., Cheung, Y.K., Yao, J. et al. (2001). Palladium and platinum complexes with a β-cyclodextrin-functionalized phosphine ligand. *Organometallics* 20 (3): 424–429.

34 Armspach, D. and Matt, D. (1999). Metal-capped α-cyclodextrins: the crowning of the oligosaccharide torus with precious metals. *Chem. Commun.* (12): 1073–1074.

35 Reetz, M.T. and Frombgen, C. (1999). Chemoselective reduction of halo-nitro aromatic compounds by β-cyclodextrin-modified transition metal catalysts in a biphasic system. *Synthesis* 1999 (9): 1555–1557.

36 Deshpande, R.M., Atsushi, F., and Masaru, I. (1999). Novel phosphinite capped cyclodextrin-rhodium catalysts in substrate selective hydroformylation. *Chem. Lett.* 28 (1): 13–14.

37 Reetz, M.T. (1998). Supramolecular transition metal catalysts in two-phase systems. *Catal. Today* 42 (4): 399–411.

38 Reetz, M.T. (1998). New supramolecular transition metal catalysts. *J. Heterocycl. Chem.* 35 (5): 1065–1073.

39 Reetz, M.T. and Waldvogel, S.R. (1997). β-Cyclodextrin-modified diphosphanes as ligands for supramolecular rhodium catalysts. *Angew. Chem. Int. Ed. Engl.* 36 (8): 865–867.

40 Reetz, M.T. and Rudolph, J. (1993). Synthesis of a phosphine-modified cyclodextrin and its rhodium complex. *Tetrahedron Asymmetry* 4 (12): 2405–2406.

41 Sawamura, M., Kitayama, K., and Ito, Y. (1993). Synthesis and properties of a new chiral diphosphine ligand bearing a cyclodextrin-based molecular recognition site and its palladium(II) complex. *Tetrahedron Asymmetry* 4 (8): 1829–1832.

42 Machut-Binkowski, C., Legrand, F.X., Azaroual, N. et al. (2010). New phosphane based on a β-cyclodextrin, exhibiting a solvent-tunable conformation, and its catalytic properties. *Chem. Eur. J.* 16 (33): 10195–10201.

43 Legrand, F.X., Six, N., Slomianny, C. et al. (2011). Synthesis, rhodium complexes and catalytic applications of a new water-soluble triphenylphosphane-modified β-cyclodextrin. *Adv. Synth. Catal.* 353 (8): 1325–1334.

44 Tran, D.N., Legrand, F.X., Menuel, S. et al. (2012). Cyclodextrin-phosphane possessing a guest-tunable conformation for aqueous rhodium-catalyzed hydroformylation. *Chem. Commun.* 48 (5): 753–755.

45 Leblond, J., Potier, J., Menuel, S. et al. (2017). Water-soluble phosphane-substituted cyclodextrin as an effective bifunctional additive in hydroformylation of higher olefins. *Catal. Sci. Technol.* 7 (17): 3823–3830.

46 Cornils, B. and Kuntz, E.G. (1995). Introducing TPPTS and related ligands for industrial biphasic processes. *J. Organomet. Chem.* 502: 177.

47 van der Veen, L.A., Keeven, P.H., Schoemaker, G.C. et al. (2000). Origin of the bite angle effect on rhodium diphosphine catalyzed hydroformylation. *Organometallics* 19 (5): 872–883.

35

Water-Soluble Yoctoliter Reaction Flasks

Yahya A. Ismaiel and Bruce C. Gibb

Tulane University, Department of Chemistry, 2015 Percival Stern Hall, 6400 Freret St., New Orleans, LA 70118, USA

35.1 Introduction

A major facet of Gibb group research is the study of chemical reactivity inside structurally precise yocto-liter containers. There are two motivations for this work. The first is to develop an understanding of organic chemistry within such small volumes. Two of the "Holy Grails" of chemistry involve controlling reactions using interfacial electric fields [1] and the development of artificial enzymes [2, 3]. These grails are interrelated by their common use of noncovalent interactions to control the transformation of matter. Thus, while the use of scanning tunneling microscopy to carefully shape and orient electric fields can be viewed as singularly concerned with charge-based forces [1, 4], enzyme catalysis – while still dominated by Coulombic interactions [5–8] – also involves the gamut of directional noncovalent interactions such as hydrogen bonding, and the subtilties of van der Waals interactions. Noting these points, our research asks a variety of questions around the ideas of chemical entrapment, controlling guest conformational sampling, and more generally how the orchestration of noncovalent interactions in a host–guest complex can be used to affect chemical reactivity.

Our second motivation is environmental. Water, the greenest of solvents, is society's ideal medium for performing chemistry [9]. However, as every chemist knows, using water as a solvent is often fraught with difficulties. Contemporary chemistry side-stepped these issues by using organic solvents. This has been an exceptionally successful strategy, but one that disregards environmental cost, ignores the economic benefits of using ubiquitous water, and entirely overlooks the benefits that the hydrophobic effect [10–18] can bring to chemical synthesis. For example, in enzyme catalysis, it controls protein folding, substrate binding, and reaction turnover, and at a higher level, compartmentalization and localization. Thus in our mind, aiming to master the transformation of matter and aiming to minimize the environmental costs of chemistry share much common ground.

The self-assembling cavitands described here utilize the hydrophobic effect to thermodynamically drive their assembly into capsules that complex guest molecules

Supramolecular Catalysis: New Directions and Developments, First Edition.
Edited by Piet W.N.M. van Leeuwen and Matthieu Raynal.

within their inner spaces. The focus here is on dimeric capsular complexes, although larger assemblies have been reported [19–20]. The yocto-liter (10^{-24} l) inner space of the capsules is a far smaller volume than typically utilized in the lab and can have a profound effect on guest conformation and reactivity. Moreover, as we describe, the anisotropy of the inner space, and the strong electrostatic potential field (EPF) generated by the water-solubilizing groups of the hosts, also contribute to controlling how these complexes function as yocto-liter reaction flasks. Before discussing these points, we briefly introduce the requisite cavitands, the thermodynamic and kinetic aspects of their assembly, and the general rules governing guest motif once entrapped.

35.2 Deep-Cavity Cavitands

The group has reported a range of water soluble deep-cavity cavitands with cationic [21], anionic [22], and uncharged coats [23] that assemble into well-defined supramolecular capsules. Central to this short review are octa-acid (OA) **1**, *tetra-endo*-methyl octa-acid (TEMOA) **2**, and octa-quaternary ammonium Positand-1 (**3**) (Figure 35.1). These hosts possess a deep-nonpolar pocket for guest binding, a nonpolar rim to the pocket that promotes dimerization, and an outer "coating" of water-solubilizing groups. OA **1** and TEMOA **2** are studied in basic solutions to form nominally octa-anionic hosts, whereas Positand-1 (**3**) is soluble across the pH range.

35.3 The Thermodynamic and Kinetic Features of the Capsular Complexes

Host **1**–**3** form dimeric complexes in the presence of suitable nonpolar guests. Directly measuring the thermodynamic stability of such complexes is complicated by the low solubility and aggregation of guests. That noted, at low concentrations, strongly fluorescent guests such as pyrene (Py) can yield overall stability constants

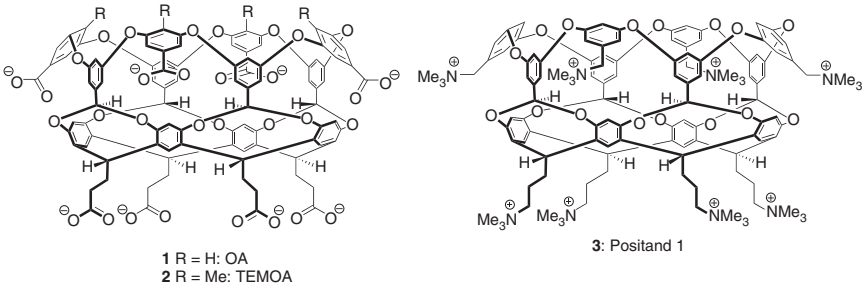

Figure 35.1 Structures of octa-acid **1** and TEMOA **2** (shown as their conjugate carboxylates) and Positand-1 (**3**).

for the formation of 2 : 1 host–guest complexes. For example, β_{21} ($= K_{11} \times K_{21}$) for Py binding to $\mathbf{1}_2$ was measured at $3.19 \times 10^{12}\,M^{-2}$ [24]. More generally, the absence of free host at the correct host–guest stoichiometries, and the fact that even small guests such as propane form slow-exchanging (on the nuclear magnetic resonance [NMR] timescale) complexes, both point toward considerable thermodynamic stability. Despite this, these complexes do allow the relatively fast entry and egress of small solutes; a key point in their ability to act as reaction vessels. The first evidence of this came from collaborative work with the Ramamurthy and Turro groups, which revealed $^3O_2$ could enter the capsule formed by OA **1** and excited (*) sensitizer dimethyl benzil (*DMB), undergo energy transfer, and then egress the complex in the singlet state (vide infra) [25]. Quenching rate constants for this system were 7.9 and $8.7 \times 10^7\,M^{-1}\,s^{-1}$ as determined by phosphorescence and T–T absorption experiments, respectively, values much slower than the diffusion rate constant ($\sim 10^9\,M^{-1}\,s^{-1}$). It was subsequently shown that $^3O_2$ entry and quenching of an excited state complex is highly guest-dependent but is generally on the microsecond timescale [26].

Using Py as a guest for OA **1**, the Bohne group assessed the formation/dissociation kinetics of capsule formation and hence were the first to unambiguously differentiate between the kinetics of capsular "breathing" to allow small guest entry, and the kinetics of capsule formation/disassembly in its own right [24]. Thus, the Bohne group showed that the I^- quenching rate constant of *Py in the capsule OA $\mathbf{1}_2$ ($5.9 \times 10^5\,M^{-1}\,s^{-1}$) was similar to that of the $^3O_2/\mathbf{1}_2$.*Py system ($5 \times 10^5\,M^{-1}\,s^{-1}$) [26], i.e. much slower than the $^3O_2/\mathbf{1}_2$.*DMB system and some four orders of magnitude slower than diffusion-controlled quenching. Furthermore, using stopped-flow fluorescence experiments the Bohne group were able to determine a K_{11} value of $4.5 \times 10^5\,M^{-1}$ and hence a K_{21} value of $7 \times 10^6\,M^{-1}$ ($\beta_{21} = K_{11} \times K_{21}$). The fact that $K_{11} < K_{21}$ points to why 1 : 1 complexes are not generally observed; the portal region of the complex consists of a large area of nonpolar surface which, combined with any exposed guest surface, greatly favors capsule formation. Global fitting of fluorescence data as a function [OA 1] gave rates constants for the assembly of the 1 **:** 1 complex to the 2 : 1 capsular species of $\boldsymbol{k_{21}^+} = 2.6 \times 10^6\,M^{-1}\,s^{-1}$, and $\boldsymbol{k_{21}^-} = 0.37\,s^{-1}$; the latter corresponding to a lifetime of 2.7 seconds for the $\mathbf{1}_2$.Py complex. Hence the "breathing" process is at least 10^5 times faster than the rate of the complete dissociation of the complex.

35.4 Assembly State of OA 1 and TEMOA 2 and Guest Packing Motifs Within

Studies with homologous series of *n*-alkane guests have revealed how guest size influences the assembly state of OA **1** and TEMOA **2** [27–29]. The relationship between the assembly of OA **1** and guest size is straightforward: methane does not bind, ethane forms 1 : 1 complexes, propane through *n*-octane form 2 : 2 host–guest capsular complexes; and larger guests (up to C26) form 2 : 1 host–guest complexes [27, 28]. In contrast, TEMOA **2** displays a more complex, non-monotonicity between

assembly state and guest size [29]. Molecular simulations by the Ashbaugh group demonstrate how the *endo*-methyls of $\mathbf{2}_2$ disfavor dimer formation and crowd alkanes within its capsule to engender this non-monotonicity [30]. Parenthetically, this reduced predisposition of TEMOA **2** to dimerize is also manifest with alkanes longer than C14, where, depending on the charges state of each cavitand [20], 4 : 2 and even 6 : 3 host–guest complexes can form [31, 32].

Using cavitands as yoctoliter reaction flasks has to date focused on dimer capsules, and studies on *n*-alkane complexation has revealed much about the motif of the entrapped guest within $\mathbf{1}_2$ and $\mathbf{3}_2$. The truncated, conical pocket of these cavitands is comprised of aromatic rings and is approximately 8 Å in diameter at the rim and 8 Å deep. The aromatic nature of the walls and the conical cross section of the binding site results in considerable anisotropy within the inner space, and this in turn means that ^{1}H NMR spectroscopy is an excellent technique to probe the average conformation, or binding motif, of the guest. Unfortunately, the relatively high freezing point of aqueous solutions means that it is not possible to slow guest movement sufficiently to observe individual binding motifs; whereas guest entry and egress is generally slow on the NMR timescale, its movement within the inner space is relatively fast.

^{1}H NMR analysis reveals a succession of motifs within $\mathbf{1}_2$ as a function of increasing guest length (Figure 35.2a). The inner space of the dimer is approximately the same length as the fully extended chain of *n*-dodecane. As a result, *n*-nonane to *n*-dodecane adopt extended motifs with each terminal methyl forming Me$\cdots\pi$ interactions with the set of four, polar-positioned aromatic rings at the two extrema of the inner space. This pulls the mainchain of the guest into an extended form rich in anti dihedral angles. With slightly longer guests the extended motif compresses somewhat into a helical, gauche-enriched motif, but as the guest is increased in size further this situation ultimately becomes untenable. Thus, around *n*-heptadecane and *n*-octadecane a guest instead adopts a turn in its mainchain to form a J- or

Figure 35.2 (a) Three *n*-alkane motifs within the OA dimer $\mathbf{1}_2$. Left: The gauche-enriched extended/compressed motif as illustrated by *n*-tridecane. Center: The J-motif exemplified by *n*-heptadecane. Right: The spinning-top motif displayed by *n*-tetracosane. An example of the fully extended motif of, for example, *n*-decane is not shown. (b) Schematic representations of the complexes of naphthalene, anthracene, and tetracene within the OA dimer $\mathbf{1}_2$. Naphthalene and anthracene form 2 : 2 complexes, and in the latter the two guests are forced to $\pi-\pi$ stack in an out-of-register manner. In contrast, tetracene is large enough such that only one guest can be encapsulated.

U-motif where one extrema of the inner space is occupied by a terminal methyl, and the other by the hairpin turn in the mainchain. Finally, for guests longer than *n*-tricosane, the capsule reaches capacity and a motif resembling a spinning top is adopted, with the two termini of the guest again located in opposing extrema and a hairpin turn partially exposed to water. These different motifs were corroborated by molecular simulations, dihedral principle component analysis, and gauge invariant atomic orbital calculations [33]. As we will discuss, these different motifs have a profound effect on guest reactivity.

35.5 Photochemistry

The first studies of reactions within the yoctoliter inner space of the capsule $\mathbf{1}_2$ focused on photochemistry. In collaboration with the Ramamurthy group, the capsule formed by OA **1** was shown to bring selectivity to a wide range of reactions [34]. We begin with an example of stopping a reaction inside the OA **1** capsule, because it graphically illustrates the level of control possible in yocto-liter spaces. The example in question concerns the guests, naphthalene, anthracene, and tetracene (Figure 35.2b) [35]. In free aqueous solution, naphthalene shows only monomer emission at a concentration of 10^{-4} M. In contrast, in the presence of OA **1**, a red-shifted monomer emission and an excimer emission are observed. ^{1}H NMR spectroscopy confirmed the cause for this; naphthalene forms a 2 : 2 complex with OA **1**. Thus, within the inner space of $\mathbf{1}_2$, each naphthalene molecule experiences an effective concentration of ~3 M, but there is some free space in the complex so that the guests are not permanently held close to one another. As a result, both monomer and excimer emissions are observed. Tetracene represents the opposite extreme. In free solution, it shows monomer and excimer emissions and readily undergoes photochemical-induced dimerization. However, in the presence of OA **1**, the corresponding 2 : 1 host–guest complex is formed. As a result, only monomer emission is observed, and no dimerization occurs.

Anthracene represents an interesting intermediate case. Excitation of anthracene in free solution results in a rapid and quantitative dimerization. The efficiency of this process means that its emission spectrum reveals monomer emission and only the weakest excimer emission ($\lambda_{max} = 530$ nm; $\tau < 2$ ns). In contrast, despite forming a 2 : 2 complex with OA **1**, no dimerization is observed. ^{1}H NMR spectroscopy reveals a desymmetrization of the guest along its long axis, an observation that arises because the two copies of anthracene are π–π stacked but held in an out-of-register manner (Figure 35.2b). As a result, the emission spectrum of the complex reveals strong excimer emission ($\lambda_{max} = 510$ nm; $\tau < 263$ ns), but the integrity of the capsule frustrates the guests by holding them at the cusp of reaction. The excimer can emit, but cannot react.

The first example of controlling a reaction inside $\mathbf{1}_2$ involved the photolysis of dibenzyl ketones (Scheme 35.1) [36]. In free solution **4a** gave, via homolytic cleavage of one of the C(O)—C bonds and decarbonylation, products **5** (AA) **6** (BB), and **7** (AB) in the statistical 1 : 1 : 2 ratio. However, when compound **4a** was irradiated

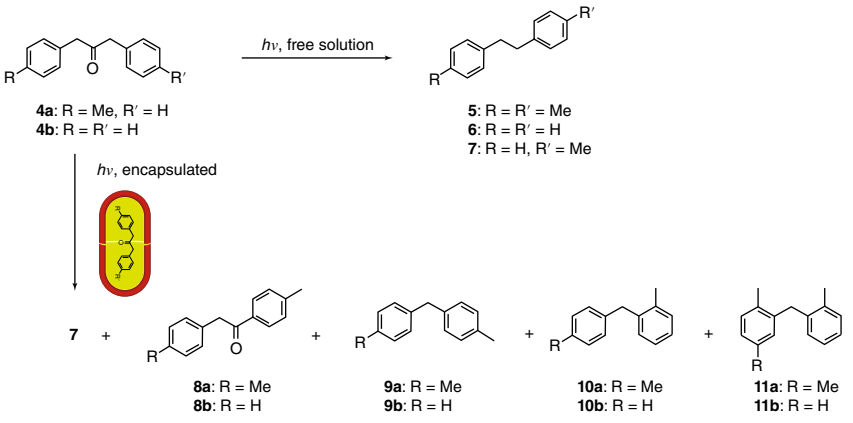

Scheme 35.1 Reaction manifold of dibenzyl ketones **4a** and **4b** within the OA capsule $\mathbf{1}_2$.

inside $\mathbf{1}_2$, only AB-type products (100% cage effect) were observed: specifically, 41% of decarbonylated **7**, 44% of rearranged ketone **8a**, and 15% of three decarbonylated and rearranged products **9a**–**11a**. Similar results were observed upon photolysis of **4b**: namely 38% of **6**, 49% of **8b**, and a combined 13% of **9b**–**11b**. The two ketone products formed in these encapsulation reactions (**8a** and **8b**) are formed via cleavage of the C(O)—C bond on the side of the unsubstituted aromatic ring to give a stabilized primary radical pair, intersystem crossing from the triplet to the singlet radical pair (spin memory loss), rapid reorientation of the unsubstituted benzyl radical, recombination, and a 1,5 H-atom shift. Presumably, both C(O)—C bonds are equally likely to cleave, but breaking the C—C bond on the side of the unsubstituted aromatic ring leads to rearrangement via rapid reorientation of the benzyl radical to give a thermodynamically lower energy state in which the benzyl/incipient methyl group better packs the pole region of the inner space. No such rearrangement is possible if the C—C bond on the other side of the carbonyl cleaves, and the resulting radicals may further react (vide infra) or may recombine to starting material and further feed the formation of **8a** and **8b**. The second major reaction pathway involves decarbonylation of the primary radical pair to form the secondary radical pair that mostly recombines to give **7**, but also to a much smaller extent, rearranged products **9a**/**b**–**11a**/**b**. Thus, the capsule formed by OA **1** not only exhibits a cage effect previously only observed in the solid state but also changes the relative stability of the primary and secondary radical pairs and orchestrates carbon frame rearrangement processes not observed in solution.

Further studies involved entrapped α-(*n*-alkyl) dibenzyl ketones, where the alkyl group was varied from Me to *n*-octyl (Figure 35.3) [37]. Each of the eight substrates formed 2 : 1 host–guest complexes with OA **1** but adopted three different packing motifs depending on the length of the alkyl groups (Figure 35.3a). For small R groups (R = Me, Et, *n*-Pr), the two phenyl rings of the guest occupy the pole regions of the capsule, while the alkyl group resides at the equatorial region (*Motif* 1). In contrast, for mid-sized R groups (R = *n*-Bu, *n*-pentyl, and *n*-hexyl), the dominating motif (*Motif* 2) is that in which the phenyl ring proximal to the R group (red) is displaced

by the alkyl group and resides in the equatorial region. Finally, for the largest R groups examined (R = *n*-heptyl and *n*-octyl), the guest primarily packs the cavity of the capsule such that the distal phenyl ring occupies the equatorial region of the capsule (*Motif* 3).

In free solution, the α-(*n*-alkyl) dibenzyl ketones primarily undergo the expected Norrish type I reactions to form (Figure 35.3b) decarbonylated AA (**6**), AB (**13**), and BB (**14**) products, and in the case of guests with alkyl groups possessing γ-hydrogens, smaller amounts of the Norrish type II products, dibenzyl ketone **4b**, and the corresponding cyclobutanols **15**. This range of products observed is consistent with multiple chemical channels in the triplet excited state surface.

However, encapsulated within the OA **1** dimer, the behavior of both primary and secondary radical pairs formed from the guests changed considerably. Over the whole range of guests, seven products were obtained in more than trace (>2%) amounts. The yields of the five major products within the pool of guests are summarized in Figure 35.3b. *En masse*, they once again demonstrate that the guests did not escape during reaction. The Norrish type I AB product **13** was found to be a significant product, but its yield decreased through the series R = Me through *n*-pentyl, but then increased significantly with the *n*-hexyl and *n*-heptyl derivatives. The opposite trend was seen with rearranged ketones **16** and **17**. Their overall yields increased for the series R = Me through *n*-pentyl, but were negligible for the *n*-hexyl and larger alkyl groups. It is interesting to note that the substrates with the smallest alkyl group tend to give very little of the product arising from α C–C cleavage on the unsubstituted side of the carbonyl (**16**), but that with the *n*-butyl and *n*-pentyl substrates this cleavage appears equally as likely as the corresponding bond cleavage on the substituted side of the carbonyl (**17**). Cleavage on the unsubstituted side is expected to be slower than cleavage on the substituted side (1° vs 2° benzyl radical respectively), so why does the former become significant with the *n*-butyl and *n*-pentyl guests? The hypothesis is that α C–C cleavage on the substituted side of the carbonyl group is still preferred, but that the formed 2° radical cannot reorientate from *Motif 2* and so recombines to starting material. However, if and when the unsubstituted α C–C does cleave, the less stable 1° benzyl radical can reorient to bring about rearrangement (**20**). These three products (**13**, **16**, and **17**) were not significant for the two largest guests possessing *n*-heptyl and *n*-octyl chains. Instead, Norrish type II chemistry dominated with dealkylation and the formation of dibenzyl ketone (**4b**) and to a smaller extent, cyclization to the corresponding butanol (**15**). This change of outcome can be explained by assuming that in *Motif 3* the 2° R-substituted benzyl radical is not able to rotate because of space restrictions (to yield **17**), and that there is no driving force for any 1° benzyl radical to rotate because the distal ring is located at the equatorial region. Concomitantly, γ-hydrogen abstraction may itself be facile because the γ-hydrogens in *Motif 3* are located close to the carbonyl chromophore.

The capsule $\mathbf{1}_2$ has also been used to control the oxidation of alkenes with singlet oxygen ($^1O_2$) [25]. Ene reactions involving the addition of $^1O_2$ to olefins to yield allylic hydroperoxides have been shown to involve addition of $^1O_2$ to the C=C bond

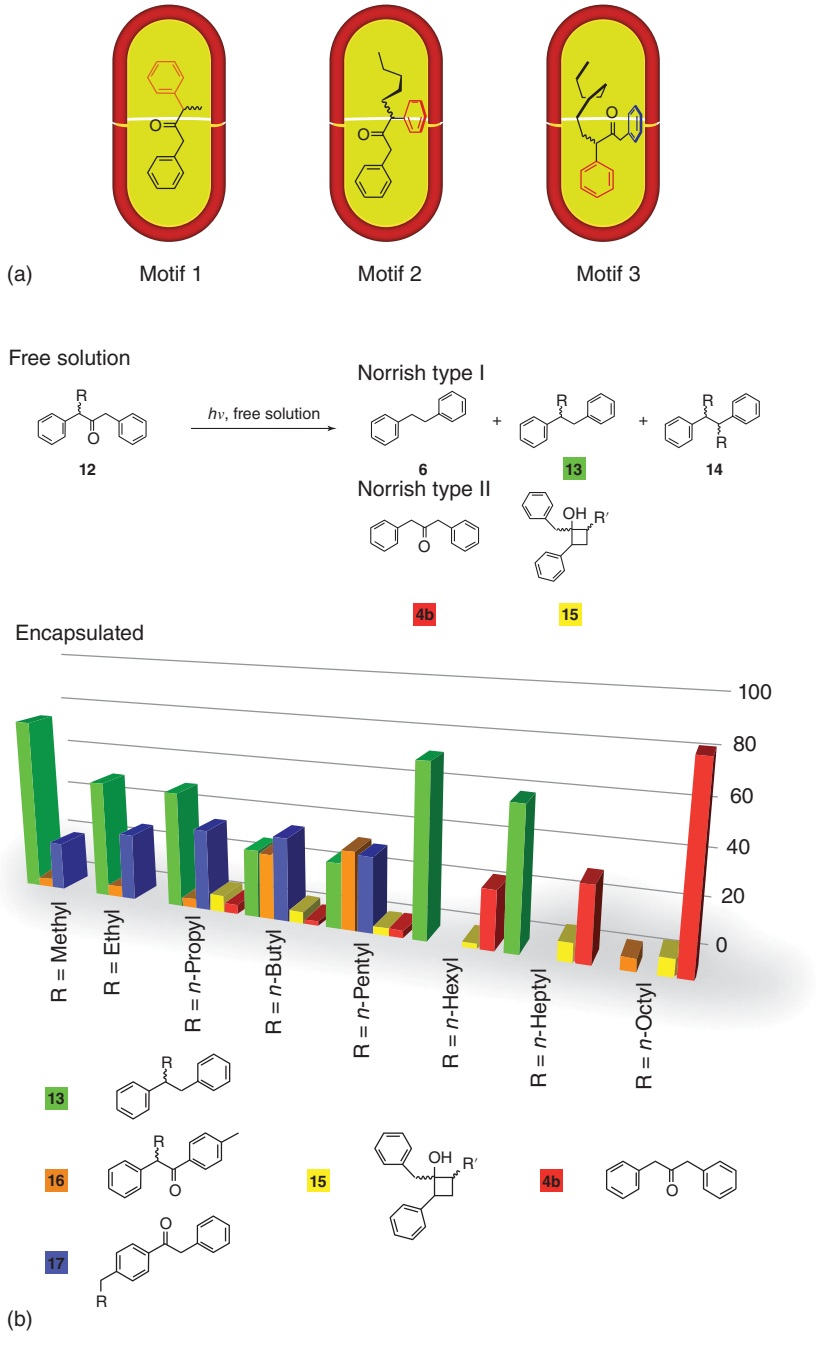

Figure 35.3 (a) Packing motifs of encapsulated α-(*n*-alkyl) dibenzyl ketones within $\mathbf{1}_2$. For clarity, proximal (to the alkyl group) and distal aromatic rings of the bound guest are highlighted in red and blue, respectively. Three different motifs are observed depending on the length of the alkyl groups. (b) Top: major products from the photochemistry of α-(*n*-alkyl) dibenzyl ketones in free solution. Bottom: distribution of the five key products from the photochemistry of α-(*n*-alkyl) dibenzyl ketones packed within $\mathbf{1}_2$.

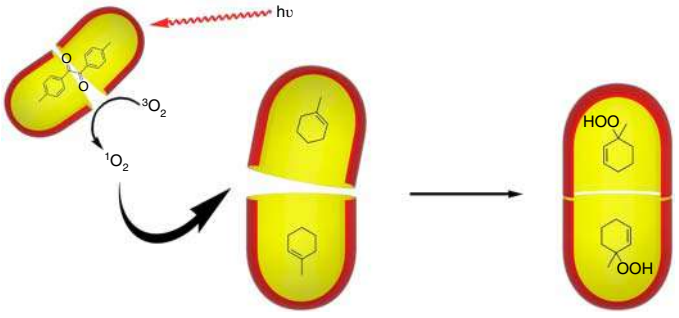

Figure 35.4 Controlled oxidation of encapsulated 1-methylcyclohexene within the dimer $\mathbf{1}_2$ using singlet oxygen ($^1O_2$). $^1O_2$ is generated (top left) by irradiation of the encapsulated sensitizer DMB at >310 nm. Capsule breathing allows $^3O_2$ to enter the *DMB complex, and after energy transfer, exit as $^1O_2$. Diffusion of $^1O_2$ into the 2 : 2 capsular complex allows abstraction of one of the most accessible allylic H_3-atom and the resultant formation of the 3° hydroperoxide.

and simultaneous abstraction of an allylic hydrogen. For substrates possessing multiple allylic positions, a mixture of allylic hydroperoxides is typically formed; it is difficult to control small and reactive species such as $^1O_2$.

Small guests such as 1-methylcyclohexene are known to form 2 : 2 capsular complexes with OA **1**, and in doing so adopt very specific orientations within the cavity. In this case, the two guests are oriented so as their methyl groups fill the pole region of the tapering cavity to form multiple Me· · ·π interactions with the host (Figure 35.4). Thus, it was hypothesized that in such an orientation only one of the most accessible H_3 allylic hydrogen atoms could be abstracted by $^1O_2$ and so bring about highly selective reaction. To test this, reaction of the complex was compared to that of the free guest in solution using Rose Bengal (RB) as the water-soluble sensitizer. This gave indiscriminate reaction; a mixture of the three peroxides arising from H-abstraction from the C-1 methyl, and C-3 and C-6 methylenes in 44%, 20%, and 36% yield respectively.

Reaction of encapsulated 1-methylcyclohexene could also be brought about using RB, but a more intriguing situation arose when the water-insoluble sensitizer DMB was used instead by encapsulating it within the OA **1** dimer. Prior to studying the oxidation process, two key experiments were performed. First, it was demonstrated by lifetime measurements in water and deuterated water that the $^1O_2$ generated by DMB.$\mathbf{1}_2$ spends most of its lifetime in the aqueous medium. Second, it was shown that mixing the capsular complexes of 1-methylcyclohexene and DMB did not lead to the formation of any hetero-guest capsular complex. Irradiation of the mixture of the sensitizer and substrate complexes with OA **1** at >310 nm led to a 90% yield of the peroxide arising from abstraction of the most accessible C-3 methylene. Thus, whereas reaction in free solution is indiscriminate, reaction of the complex is highly selective.

As discussed earlier, the rate constant for $^3O_2$-induced quenching of the *DMB.$\mathbf{1}_2$ complex was determined by monitoring its phosphorescence and T–T absorption as a function of oxygen concentration. The similar rate constants obtained by the two

approaches showed that the process was much slower than the diffusion rate constant, but much higher than the rate constant for energy transfer between $^3O_2$ and sensitizers within covalent cage hosts (where energy transfer is believed to occur through the walls of the host). As the $^1O_2$ phosphorescence kinetic profile revealed a dynamic rather than static quenching process between O_2 and encapsulated DMB, the measured quenching rate constants were concluded to represent capsule breathing controlling the rate at which O_2 can access the sensitizer. Evidently, the ability to generate $^1O_2$ arises because the rate of capsule opening and closing competes with the decay of *DMB inside the OA **1** dimer.

These three photochemistry examples demonstrate how the integrity of the capsule formed by OA **1** can be used to control guest binding motif, and hence bring considerable selectivity to otherwise unselective reactions. Readers wishing to examine other photochemical reactions within the OA **1** dimer are directed to this review [34].

35.6 Thermal Reactions

The dynamic nature of these capsular complexes means that there is a fine line between promoting reactions inside the capsule, and attenuating guest egression for reaction in free solution. The former is of course the focus here, but studies into preventing reaction by entrapment have taught us much about controlling guest reactivity.

Consider the situation where the guest exchange into and out of the capsule are relatively fast; comparable or perhaps faster than the entry rate of a reagent [38]. This is the case when small esters **18**–**22** (Figure 35.5a) are encapsulated, and the bulk media is a basic, hydrolytic solution. Here, the guests are seen to be protected to a degree-dependent on the relative affinity of each ester weighed by its reaction rate in free solution; guests that bind strongly to the capsule and react slowly in free solution appear well protected. Although the rate constants of hydrolysis of the free esters differed only by four, the relative affinity of esters **18**–**22** for the capsule ranged over 2 orders of magnitude (K_{rel}): **20** (1), **19** (1.8), **21** (10.7), **22** (16.4), and **18** (165.4). All of these guests adopted similar extended motifs (Figure 35.5a) with the two terminal methyl groups at each pole region of the capsule, and as a result two key factors influenced guest affinity. First, there is a general decrease in affinity when the ester group is located further from the equatorial region of the inner space and toward the pole region. There are likely steric factors arising from the width, rigidity, and preference for a *Z*-conformation of the ester group as it is forced to reside deeper in the capsule. In addition, the higher dielectric of the equatorial region of the inner space (vide infra) may simply be a more suitable environment for the polar ester group. Countering this effect are variations in the attractive $CH_3\cdots\pi$ interactions between the pole region walls of the host and the terminal methyl of the alkoxy group. These interactions are maximal when the C—H bonds are polarized by a proximal electronegative atom, and hence the strongest affinity observed was that of methyl ester **18**. However, this diminished rapidly as the number of bonds between the terminal methyl and the alkoxy oxygen increased, such that the ethyl

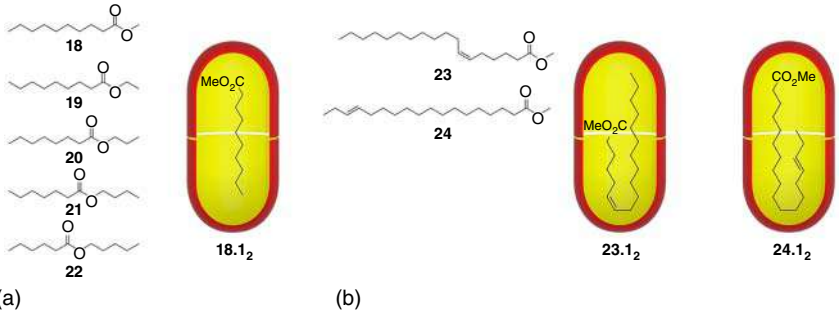

Figure 35.5 Selected ester guests demonstrating the importance of guest motif and capsule affinity in controlling hydrolysis. (a) Small esters **18**–**22** and binding motif of **18** within the OA **1** dimer. (b) Fatty acid esters **23** and **24** and their motifs within the OA **1** dimer.

(**19**) and propyl ester (**20**) bound the weakest. This extreme variation in affinity as a function of structure meant that it was possible to kinetically resolve many pairs of esters **18**–**22** by differential, supramolecular protection.

With larger esters, guest egression from the cavity is negligible. As a result, hydroxide entry/egression begins to manifest itself when the complexes are placed in a hydrolytic medium. Consider, for example, a series of 10 C18 mono-unsaturated fatty acid esters in which the position and stereochemistry of the C=C bond varied (e.g. **23** and **24**, Figure 35.5b) [39]. These esters and their corresponding carboxylates all formed 2 : 1 complexes with OA **1**. The latter all adopt a singular J-motif with the $-CO_2Me$ head group located in the equatorial region of the inner space; neither the position nor stereochemistry of the C=C double bond influenced guest motif. This was interpreted as an indicator that the equatorial region of the inner space possesses a higher dielectric than the pole region and is therefore ideal for housing the head group. In other words, because of capsule breathing the $-CO_2Me$ group can be partially solvated at the equatorial region. The lower polarity of the $-CO_2Me$ head group meant that this strong anchoring was diminished somewhat in the esters. As a result, three guest motifs were observed for this series, depending on the position and stereochemistry of the alkenyl C=C bond: (i) a dominant J-motif(*Me*) with the pole regions of the capsule, respectively, occupied by the terminal methyl of the alkenyl chain and a reverse turn in the alkenyl chain, and the $-CO_2Me$ group at the equatorial region, e.g. **23** (Figure 35.5b); (ii) a J-motif(*CO_2Me*), e.g. **24** (Figure 35.5b), and (iii) A U-motif where the ester head group and the alkenyl termini of the guest vie for occupancy of one pole region of the inner space, and the reverse turn in the alkenyl chain is housed in the opposing pole of the inner space. Investigating the hydrolysis of the 10 ester complexes revealed that, in contrast to small esters **18**–**22**, the reaction rates were not correlated with the guest affinity [40]. In fact, the strongest binders tended to undergo the fastest reaction and the weakest binders the slowest. Rather, esters that adopted a J-motif(*Me*) with the ester head group at the equatorial region tended to undergo faster reaction, whereas when the $-CO_2Me$ group was buried in the pole region it was relatively well protected. These studies demonstrate not only

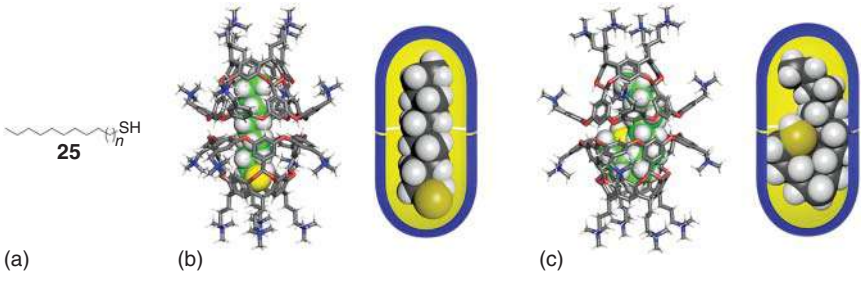

Figure 35.6 (a) Structure of *n*-alkyl thiols **25**. (b) Left: Molecular model of the complex formed by Positand-1 (**3**) and guest **25** ($n = 2$) with the host shown in ball-and-stick representation and the guest as a space-filling model. Right: schematic representation of the extended motif of guest **25** ($n = 2$) within Positand-1 (**3**) depicted as the blue bowl. (c) Molecular model and schematic representation of the complex formed by Positand-1 (**3**) and guest **25** ($n = 6$) in its J-motif(*Me*).

how functional groups can control guest motif and reactivity, but also how the overall guest affinity controls whether a guest reacts inside or outside the capsule.

One of the key features of OA **1** and Positand-1 **(3)** is that solubility is engendered by charge groups on their outer surfaces. Although these are remote from the inner space, the low dielectric of the walls of the hosts and the inner space in general mean that Coulombic forces can have a profound effect on guest reactivity. The equal but opposite EPFs of **1** and **3** are attenuated by the high dielectric of the water solvating them. Nevertheless, when charged intermediates and transition states (TSs‡) are formed within the capsules $\mathbf{1}_2$ and $\mathbf{3}_2$, they are greatly influenced by their respective EPF. This effect must be integrated with the effects from the overall heterogeneity of the inner space and by capsule breathing.

One of the most straightforward metrics to measure the effects of these different factors is acidity. How is the pK_a of a group affected by encapsulation? To probe this, we determined the acidity of a range of *n*-alkyl thiol guests (**25**, $n = 1$–9, Figure 35.6a) within OA (**1**) and Positand-1 (**3**) as a function of the aqueous media the capsules were dissolved in [41]. These thiols were selected because of their ideal acidity in free solution (p$K_a = \sim 10$), and because the bound thiol S–H group gave a clear signal in ^{1}H NMR spectroscopy. This technique showed that all the guests form 2 : 1 complexes with both **1** and **3**. For smaller guests such as **25** ($n = 2$) an extended motif was adopted (Figure 35.6b), while longer guests (Figure 35.6c) such as **25** ($n = 6$) adopted J-motifs(*Me*).

^{1}H NMR spectroscopy to monitor the deprotonation of the bound thiol allowed the determination of the pK_a of the guest. As anticipated, the thiols were more acidic encapsulated within $\mathbf{3}_2$ than in $\mathbf{1}_2$. ΔpK_a values between the two capsules ranged from 1.0 to 2.6 units for the different guests, i.e. with the positive capsule the thiolate was stabilized by between 6.3 and 14.8 kJ mol^{-1}. Within both capsules maximal pK_a values were seen for *n*-undecyl thiol **25** ($n = 2$) which packs the inner space with the thiol bound deeply in the pole region. Slightly shorter *n*-undecyl thiol **25** ($n = 1$) was marginally more acidic, but for guests longer than *n*-undecyl thiol **25** ($n = 2$) the pK_a value dropped sharply. This increase in acidity tracked with an increasing

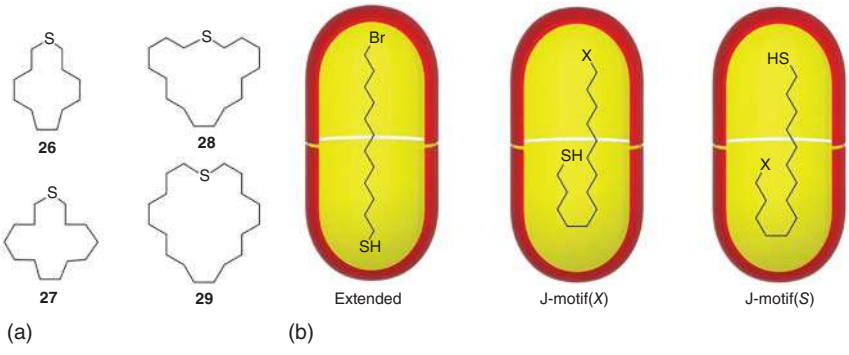

Figure 35.7 (a) The 13- to 19-membered macrocyclic thio-ether products **26–29** formed by reaction of α,ω thio-alkane halides within capsules $\mathbf{1}_2$ and $\mathbf{3}_2$. (b) The three motifs observed for the guest substrates: the extended motif for short guests, and the two J-motifs for the longer guests.

propensity to form a J-motif(*Me*) and was attributed to the thiol group being located in the (higher dielectric) equatorial region of the capsule (Figure 35.6c). Overall, within the capsule $\mathbf{1}_2$ ΔpK_a between the least and most acidic guests was 4.6 units, while in the case of positive capsule $\mathbf{3}_2$ ΔpK_a was 5.7 units.

The ionic strength of the external solution also affected the acidity of the encapsulated guests. Carboxylates are strongly solvated, and poor ion pairing was inferred from ζ potential measurements of capsular complexes involving OA **1**. Cesium ion was found to induce the largest pK_a in guests bound to $\mathbf{1}_2$, but the ΔpK_a value for bound *n*-tridecyl thiol **25** ($n = 4$) on going from 0 to 200 mM CsCl was only 0.2 units. On the other hand, trimethyl ammonium ions are weakly solvated and readily form ion pairs, and the largest observed ΔpK_a value for *n*-tridecyl thiol **25** ($n = 4$) bound to $\mathbf{3}_2$ was over 0.5 units over the range 0–10 mM $NaClO_4$. Thus, the biggest effector on pK_a is the guest motif, followed by the capsule charge, and then the nature of salts in solution.

The effects of guest motif and capsule charge on macrocyclization reactions has also been studied [42]. Specifically, the formation of 13- to 19-membered macrocyclic thio-ethers **26**–**29** (Figure 35.7a) from the corresponding α,ω thio-alkane halides has been studied inside capsules $\mathbf{1}_2$ and $\mathbf{3}_2$. Both hosts formed 2 : 1 host–guest complexes with both the starting materials and the products of reaction. As expected, the shorter substrates adopt an extended motif with the thiol and halide termini located deep in the pole regions of the capsules (Figure 35.7b), whereas longer substrates adopt both J-motif(*X*) and J-motif(*SH*), depending on the nature of the halogen atom.

In most cases, guest cyclization was initiated by the addition of excess NaOH. In sharp contrast to the formation of random polymer in free solution, cyclization within either capsule was quantitative. Interestingly, in the case of the formation of **28** inside $\mathbf{3}_2$, no base was required. Simply mixing the host and guest in water led to spontaneous and rapid cyclization.

For cyclizations that were slow enough to monitor by ^{1}H NMR spectroscopy, all followed apparent first-order kinetics. As anticipated, cyclizations within the negative capsule of OA **1** were slower than those within the capsule $\mathbf{3}_2$, but overall changes in rates as a function of guest length were very similar in the two capsules. Specifically, reaction was slowest with the shortest guest that preferred an extended motif; cyclization is difficult with the two termini of the substrate anchored to opposite poles of the capsule. In contrast, cyclization rates for macrocycle **27** were the fastest, a fact attributed to the preference for a J-motif that forces the two reacting termini of the substrates in close proximity. However, further increases in guest size slowed the rate of cyclization, an observation attributed to increased congestion within the inner space.

Acid–base titrations monitoring the SH signal for selected non-cyclizing guests devoid of a halogen atom demonstrated a lower pK_a of the thiol in guests adopting a J-motif (cf., pK_a of hexadecyl thiol ~6.3) [41]. Relatedly, measured cyclization rate constants as a function of base concentration confirmed complete guest deprotonation at 200 mM NaOH, and in the case of capsule $\mathbf{3}_2$, illustrated a rate retardation at very low base concentrations attributed to hydroxide preferentially binding to the outside of the capsule rather than deprotonating the guest.

That deprotonation of all guests was complete at 200 mM NaOH created a level "playing field" to allow Eyring analysis for the cyclization of selected host–thiolate combinations. The obtained activation thermodynamic parameters revealed the following. First, the half-life for cyclization to form **26** is 5×10^3 times shorter in the positive capsule $\mathbf{3}_2$, corresponding to a $\Delta G^{\ddagger}$ value 20 kJ mol^{-1} lower in $\mathbf{3}_2$ than in $\mathbf{1}_2$. This decrease in the reaction barrier was largely enthalpic in nature; $\Delta H^{\ddagger}$ was ~24 kJ mol^{-1} lower in $\mathbf{3}_2$. Second, in a comparison of the cyclization of a linear motif guest and a J-motif guest in capsule $\mathbf{1}_2$, the faster cyclization of the latter arises from a ~10 kJ mol^{-1} reduction in $\Delta G^{\ddagger}$ and a ~7 kJ mol^{-1} in $\Delta H^{\ddagger}$. These differences were attributed to the fact that to cyclize a guest in an extended motif, two anchoring points with the capsule must be broken, whereas in the J-motif only one anchor point must be severed.

Extensive EPF and TS‡ stabilization calculations collaborated the observed kinetics of cyclization and extended our understanding of the capsules $\mathbf{1}_2$ and $\mathbf{3}_2$. Thus, these studies revealed that the $\pm 16e$ charge of each capsule create a rather homogeneous field within the inner space, allowing the capsules to be modeled as Born spheres of approximate diameters of 12 Å, i.e. as hollow spheres whose net charge of $\pm 16e$ is uniformly smeared over their surfaces. Placement of these Born spheres in a dielectric continuum approximating that of water ($\varepsilon = 78$), and accounting for counter ion and buffer effects using Debye–Hückel theory, projected a free energy stabilization of a singly, negatively charged guest of 17.2 kJ mol^{-1} inside cationic $\mathbf{3}_2$ relative to the anionic capsule. This value differed by only ~3 kJ mol^{-1} from the corresponding Eyring data.

Overall, our study of thermal reactions reveals several key points. First, there is a fine line between guest and reagent affinity for the capsules which can be used to control the degree to which reaction occurs in the inner space, or in the external medium. This balance of substrate and reagent affinity is largely controlled by their

functionality, shape, and overall polarity, features of which feed into the nature of the capsule–guest noncovalent interactions, and the ability of the capsular complexes to "breath." Second, the preferred binding motif of a guest has a profound effect on physicochemical metrics such as pK_a and reaction rates, and therefore the net reaction outcome. Third, the nature of the water-solubilizing groups, and to a much smaller degree the external buffered medium, can be used to control reaction rates within the yocto-liter spaces.

35.7 Summary and Conclusions

The "Holy Grail" of enzyme mimicry is inspired by Nature [1–4]. Our approach is likewise. Toward understanding how noncovalent forces can be orchestrated to bring about efficient catalysis in water, our approach revolves around the self-assembly of supramolecular capsules possessing yocto-liter inner spaces. As we have described, a range of photochemical and thermal transformations can be carried out within these inner spaces. In each case, the host–guest relationship – on a macroscale the preferences for the guest to partition from the aqueous phase to the nonpolar inner space, and on an atomistic scale the different noncovalent interactions that can form between host and guest – play a key role in if, and how, the guest binds to the yocto-liter reaction site. The third partner in these systems – water – is also key here; not only does it engender the hydrophobic effect to boost partitioning to the reaction site, but it also allows (forces) the use of charged groups for solubilization that control the EPF that the inner space is immersed in.

Our research has revealed much about the control of reactions in tiny spaces, yet it is impossible to escape the endless questions that inevitably arise. Can the EPF be modulated and shaped to include gradients so that guest motif and reactivity can be better controlled? Does it help to have bigger inner spaces, or is the intimacy of the host–guest relationship lost? These and other questions have yet to be answered but provide motivations to delve deeply into this complex area.

Acknowledgments

YI and BCG gratefully acknowledge the financial support of the National Science Foundation (NSF CHE-1807101).

References

1 Zare, R. (2020). The quest to control chemical reactions using interfacial electric fields. *Chemistry World* 17 (10): 23.

2 Durrani, J. (2020). Artificial enzymes: catalysis by design. *Chemistry World* 17 (10): 38–39.

3 Kuah, E., Toh, S., Yee, J. et al. (2016). Enzyme mimics: advances and applications. *Chem. Eur. J.* 22 (25): 8404–8430.
4 Shaik, S., Mandal, D., and Ramanan, R. (2016). Oriented electric fields as future smart reagents in chemistry. *Nat. Chem.* 8 (12): 1091–1098.
5 Fried, S.D. and Boxer, S.G. (2017). Electric fields and enzyme catalysis. *Annu. Rev. Biochem.* 86 (1): 387–415.
6 Fried, S.D., Bagchi, S., and Boxer, S.G. (2014). Extreme electric fields power catalysis in the active site of ketosteroid isomerase. *Science* 346 (6216): 1510–1514.
7 Fried, S.D. and Boxer, S.G. (2015). Measuring electric fields and noncovalent interactions using the vibrational Stark effect. *Acc. Chem. Res.* 48 (4): 998–1006.
8 Warshel, A., Sharma, P.K., Kato, M. et al. (2006). Electrostatic basis for enzyme catalysis. *Chem. Rev.* 106 (8): 3210–3235.
9 Lynden-Bell, R.M., Morris, S.C., Barrow, J.D. et al. (2010). *Water and Life*. Boca Raton: CRC Press.
10 Ben-Amotz, D. (2016). Water-mediated hydrophobic interactions. *Annu. Rev. Phys. Chem.* 67: 617–638.
11 Bakker, H.J. (2012). Water's response to the fear of water. *Nature* 491: 533–534.
12 Chandler, D. (2007). Oil in troubled waters. *Nature* 445: 831–832.
13 Blokzijl, W. and Engberts, J.B.F.N. (1993). Hydrophobic effects. Opinions and facts. *Angew. Chem. Int. Ed.* 32: 1545–1579.
14 Ball, P. (2008). Water as an active constituent in cell biology. *Chem. Rev.* 108: 74–108.
15 Hillyer, M.B. and Gibb, B.C. (2016). Molecular shape and the hydrophobic effect. *Annu. Rev. Phys. Chem.* 67: 307–329.
16 Sharp, K. (2001). *Water: Structure and Properties*. eLS https://doi.org/10.1038/npg.els.0003116.
17 Shultz, M.J., Vu, T.H., Meyer, B., and Bisson, P. (2012). Water: a responsive small molecule. *Acc. Chem. Res.* 45: 15–22.
18 Ball, P. (2003). How to keep dry in water. *Nature* 423: 25–26.
19 Gan, H. and Gibb, B.C. (2012). Guest-controlled self-sorting in assemblies driven by the hydrophobic effect. *Chem. Commun.* 48 (11): 1656–1658.
20 Hillyer, M.B., Gan, H., and Gibb, B.C. (2018). Precision switching in a discrete supramolecular assembly: alkali metal ion-carboxylate selectivities and the cationic Hofmeister effect. *ChemPhysChem* 19 (18): 2285–2289.
21 Hillyer, M.B., Gibb, C.L.D., Sokkalingam, P. et al. (2016). Synthesis of water-soluble deep-cavity cavitands. *Org. Lett.* 18 (16): 4048–4051.
22 Liu, S., Whisenhunt-Ioup, S.E., Gibb, C.L.D., and Gibb, B.C. (2011). An improved synthesis of 'octa-acid' deep-cavity cavitand. *Supramol. Chem.* 23 (6): 480–485.
23 Giles, M.D., Liu, S., Emanuel, R.L. et al. (2008). Dendronized supramolecular nano-capsules: pH independent, water-soluble, deep-cavity cavitands assemble via the hydrophobic effect. *J. Am. Chem. Soc.* 130: 14430–14431.
24 Tang, H., de Oliveira, C.S., Sonntag, G. et al. (2012). Dynamics of a supramolecular capsule assembly with pyrene. *J. Am. Chem. Soc.* 134 (12): 5544–5547.

25 Natarajan, A., Kaanumalle, L.S., Jockusch, S. et al. (2007). Controlling photoreactions with restricted spaces and weak intermolecular forces: remarkable product selectivity during oxidation of olefins by singlet oxygen. *J. Am. Chem. Soc.* 129: 4132–4133.

26 Jayaraj, N., Jockusch, S., Kaanumalle, L.S. et al. (2011). Dynamics of capsuleplex formed between octaacid and organic guest molecules — photophysical techniques reveal the opening and closing of capsuleplex. *Can. J. Chem.* 89 (2): 203–213.

27 Liu, S., Russell, D.H., Zinnel, N.F., and Gibb, B.C. (2013). Guest packing motifs within a supramolecular nanocapsule and a covalent analogue. *J. Am. Chem. Soc.* 135 (11): 4314–4324.

28 Gibb, C.L.D. and Gibb, B.C. (2007). Straight-chain alkanes template the assembly of water-soluble nano-capsules. *Chem. Commun.*: 1635–1637.

29 Gan, H., Benjamin, C.J., and Gibb, B.C. (2011). Nonmonotonic assembly of a deep-cavity cavitand. *J. Am. Chem. Soc.* 133: 4770–4773.

30 Tang, D., Barnett, J.W., Gibb, B.C., and Ashbaugh, H.S. (2017). Guest controlled nonmonotonic deep cavity cavitand assembly state switching. *Phys. Chem. B* 121 (47): 10717–10725.

31 Gan, H. and Gibb, B.C. (2013). Guest-mediated switching of the assembly state of a water-soluble deep-cavity cavitand. *Chem. Commun.* 49 (14): 1395–1397.

32 Barnett, J.W., Tang, D., Gibb, B.C., and Ashbaugh, H.S. (2018). Alkane guest packing drives switching between multimeric deep-cavity cavitand assembly states. *Chem. Commun.* 54 (21): 2639–2642.

33 Barnett, J.W., Gibb, B.C., and Ashbaugh, H.S. (2016). Succession of alkane conformational motifs bound within hydrophobic supramolecular capsular assemblies. *J. Phys. Chem. B* 120 (39): 10394–10402.

34 Ramamurthy, V. (2015). Photochemistry within a water-soluble organic capsule. *Acc. Chem. Res.* 48: 2904–2917.

35 Kaanumalle, L.S., Gibb, C.L.D., Gibb, B.C., and Ramamurthy, V. (2005). A hydrophobic nanocapsule controls the photophysics of aromatic molecules by suppressing their favored solution pathways. *J. Am. Chem. Soc.* 127 (11): 3674–3675.

36 Kaanumalle, L.S., Gibb, C.L.D., Gibb, B.C., and Ramamurthy, V. (2004). Controlling photochemistry with distinct hydrophobic nanoenvironments. *J. Am. Chem. Soc.* 126 (44): 14366–14367.

37 Gibb, C.L.D., Sundaresan, A.K., Ramamurthy, V., and Gibb, B.C. (2008). Templation of the excited-state chemistry of α-(*n*-alkyl) dibenzyl ketones: how guest packing with a nanoscale supramolecular capsule influences photochemistry. *J. Am. Chem. Soc.* 130: 4069–4080.

38 Liu, S., Gan, H., Hermann, A.T. et al. (2010). Kinetic resolution of constitutional isomers controlled by selective protection inside a supramolecular nanocapsule. *Nat. Chem.* 2 (10): 847–852.

39 Wang, K. and Gibb, B.C. (2017). Mapping the binding motifs of deprotonated monounsaturated fatty acids and their corresponding methyl esters within supramolecular capsules. *J. Org. Chem.* 82: 4279–4288.

40 Wang, K., Jordan, J.H., and Gibb, B.C. (2019). Molecular protection of fatty acid methyl esters within a supramolecular capsule. *Chem. Commun.* 55 (78): 11695–11698.

41 Cai, X., Kataria, R., and Gibb, B.C. (2020). Intrinsic and extrinsic control of the pK_a of thiol guests inside yoctoliter containers. *J. Am. Chem. Soc.* 142 (18): 8291–8298.

42 Wang, K., Cai, X., Yao, W. et al. (2019). Electrostatic control of macrocyclization reactions within nanospaces. *J. Am. Chem. Soc.* 141: 6740–6747.

36

Chemical Catalyst-Promoted Regioselective Histone Acylation

Yuki Yamanashi and Motomu Kanai

The University of Tokyo, Graduate School of Pharmaceutical Sciences, 7-3-1 Hongo, Bunkyo-ku, Tokyo 113-0033, Japan

36.1 Introduction

Chemical methods to introduce post-translational modifications (PTMs) to native proteins in living cells have great potential in biology and medicine. In this chapter, we describe a chemical catalyst system that promotes histone-selective and regioselective acetylation in living cells. Challenges in developing such a chemical catalyst system reside in furnishing both reactivity and selectivity: the chemical catalyst must promote the target reaction to macromolecular, multifunctional substrates (i.e. nucleosomes and chromatin) through activating a nontoxic and stable reagent compatible with the aqueous cellular environment, where a number of off-target molecules and amino acid residues exist. An affinity-guided, supramolecular strategy is the foundation for tackling this challenge.

36.2 Chemical Catalyst-Mediated Synthetic Epigenetics

Histone PTMs, such as acetylation, methylation, and ubiquitination, play important roles in regulating gene expression of eukaryotic cells. Abnormal PTMs are intimately linked to many diseases, such as type 2 diabetes, Alzheimer disease, and various types of cancer [1–3]. Therefore, synthetic epigenetics aimed at epigenome editing through manipulation of histone PTMs is an upcoming field at the interface between chemistry and biology/medicine [4]. Several tools to manipulate histone PTMs have been developed, such as protein trans-splicing using native chemical ligation [5], genetic code expansion [6], dCas9-enzyme systems [7], post-translational mutagenesis [8, 9], synthetic modulator systems of epigenetic writers [10], and chemical catalyst-promoted histone modifications [11–14]. Chemical catalyst-promoted histone modifications have high potential for therapeutic applications as they are independent from endogenous enzymes and do not require genetic manipulations.

Supramolecular Catalysis: New Directions and Developments, First Edition.
Edited by Piet W.N.M. van Leeuwen and Matthieu Raynal.

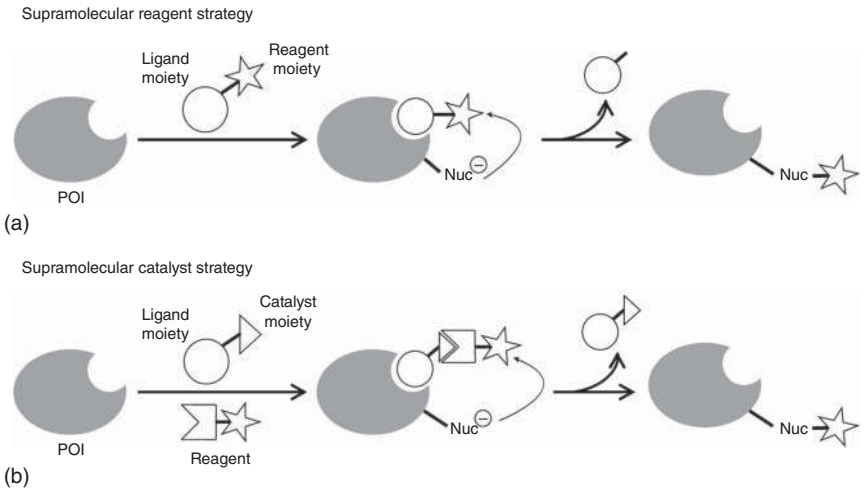

Figure 36.1 Supramolecular reagent and catalyst strategies for protein modifications.

36.3 Supramolecular Catalyst Strategy for Protein Modification

For modifying endogenous proteins, Hamachi developed an affinity-guided, supramolecular strategy [15]. In this strategy, the reagent or catalyst consists of two moieties: a ligand moiety for the protein of interest (POI) and a reagent or catalyst moiety for the reaction (Figure 36.1). By selectively delivering the reagent or catalyst moiety proximal to a specific amino acid residue of the POI by the ligand moiety, the reagent can label the POI with target protein- and regioselectivity.

Although the supramolecular reagent strategy (Figure 36.1a) using ligand–reagent conjugates [16] can label the POI both protein-selectively and regioselectively, the supramolecular catalyst strategy (Figure 36.1b) is more suitable for synthetic PTMs for several reasons. First, if activation of an endogenous reagent (e.g. acetyl CoA: Ac-CoA) is possible, the catalyst amount can be very small. This is especially preferable for therapeutic applications. Second, the supramolecular catalyst strategy has the ability to promote degrading reactions, such as demethylation, deacetylation, or oxygenation [17], which is not possible by the supramolecular reagent strategy.

36.4 Supramolecular Catalyst Strategy for Histone Acetylation In Vitro

Histone acetylation in cells is normally catalyzed by enzymes, histone acetyltransferases, using Ac-CoA as a reagent. To achieve selective lysine acetylation of histones without relying on histone acetyltransferases, we developed a chemical catalyst that activates Ac-CoA [11]. Prior to our study, there were no general catalysts that could activate Ac-CoA under physiological conditions. We first evaluated the acetylation

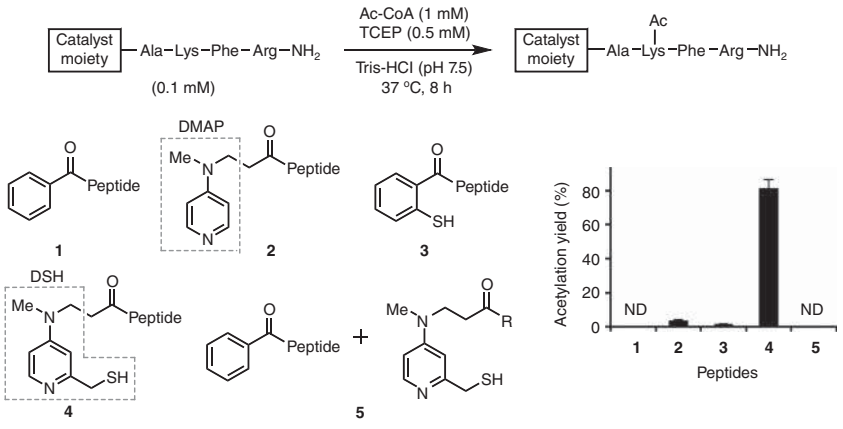

Figure 36.2 Studies using peptide models for identifying the appropriate catalyst moiety. Source: Amamoto et al. [11]. Reproduced with permission of American Chemical Society.

activity of several candidate catalyst moieties by using model peptides containing a catalyst moiety and a lysine residue (Figure 36.2), mimicking the intramolecularity of the supramolecular catalyst strategy.

Background acetylation by Ac-CoA itself did not occur without the aid of a catalyst moiety (**1**). 4-(Dimethylamino)pyridine (DMAP), a well-known nucleophilic acyl transfer catalyst [18], did not efficiently promote lysine acetylation (**2**). This low efficiency was likely due to the slow rate of the acyl pyridinium formation from Ac-CoA. Thus, we designed 4-(dimethylamino)pyridine-SH (DSH), which enabled a facile thiol–thioester exchange [19]. As intended, DSH promoted efficient lysine acetylation (**4**) [20]. It is also worth noting that DSH did not promote intermolecular acetylation (**5**). This property is important for achieving regioselective acetylation because acetylation can proceed only at lysine residues proximate to the DSH moiety.

Our proposed reaction mechanism involves three main steps (Figure 36.3): (i) formation of DSAc from DSH and Ac-CoA through a dynamic thiol–thioester exchange, (ii) formation of reactive acetyl pyridinium ion from DSAc through intramolecular S-to-N acyl transfer, and (iii) acetyl group transfer from an acetyl pyridinium ion to the amino group of a proximal lysine residue. The results of the density functional theory calculation supported our hypothesis.

Then, we designed catalysts to achieve histone-selective and regioselective acetylation, consisting of a catalyst moiety (DSH) and a ligand moiety binding to a specific region in a nucleosome (Figure 36.4). As the ligand moiety, we used two types of molecules. One is the *N*-terminus of Kaposi's sarcoma-associated herpes virus LANA (latency-associated nuclear antigen), which binds to an acidic patch of histones H2A–H2B [21]. The other one is a pyrrole-imidazole polyamide (PIP), which binds to DNA with a 5′-WGWWWW-3′ sequence, where W is A or T [22]. The ligand-conjugated DSH catalysts promoted regioselective histone acetylation in recombinant nucleosomes using Ac-CoA as a reagent (Figure 36.4); LANA-DSH catalyst **6** selectively acetylated lysine 120 in a histone H2B subtype (H2BK120); and PIP-DSH **7** catalyst selectively acetylated H4K77, H3K56, or H3K122 in

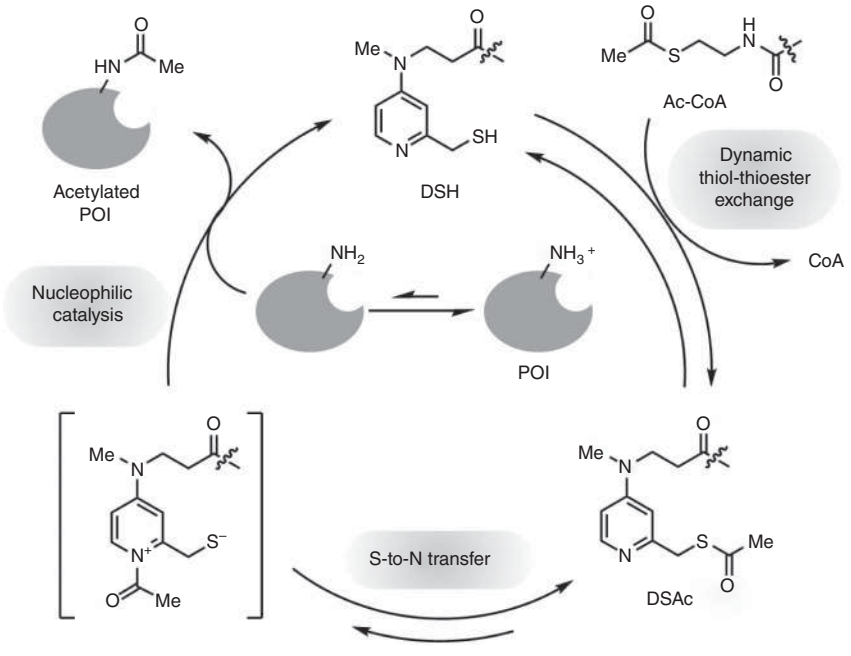

Figure 36.3 Proposed mechanism of DSH catalyst for lysine acetylation. Source: Based on Amamoto et al. [11].

nucleosomes 1–3, respectively, depending on the position of the DNA sequence recognized by PIP. Thus, the lysine residue existing proximal to the DSH moiety defined by the ligand moiety in the catalyst–substrate complex was regioselectively acetylated. Liquid chromatography tandem mass spectroscopy (LC–MS/MS) analysis allowed for quantitative evaluation of the yield and selectivity of the reaction with LANA-DSH **6**: H2BK120 was acetylated in 69% yield, with second proximate H2BK116 acetylated in 15% yield. An additional >50 lysine residues existing in the nucleosome were acetylated in only 0% to <3% yield.

Simply by switching the acyl donor (i.e. reagent) from Ac-CoA to other acyl group-containing thioesters, DSH was able to regioselectively introduce various natural and nonnatural acyl groups through the identical mechanism shown in Figure 36.3. Several acylation types have been identified in cellular chromatins, such as malonylation and butyrylation [23]. Therefore, our method will be useful for studying the biologic effects of various acylation PTMs, including nonnatural acylation.

36.5 Catalyst-Promoted Selective Acylation Targeting Proteins in Living Cells

Peptide ligands are generally unstable in living cells and not permeable to cell membrane (see Section 36.6). Therefore, we first studied the acylation of *Escherichia*

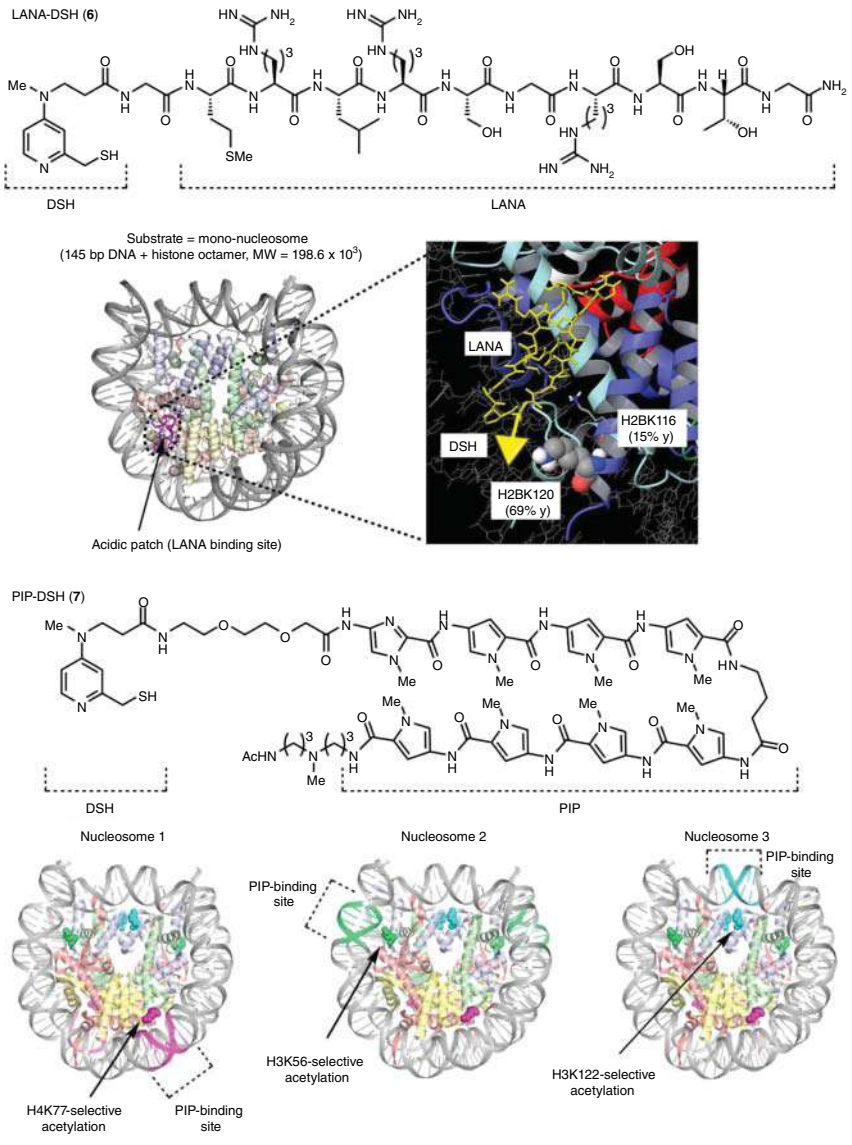

Figure 36.4 Regioselective histone acetylation by ligand-conjugated DSH *in vitro*. Source: Amamoto et al. [11]. Reproduced with permission of American Chemical Society.

coli dihydrofolate reductase (eDHFR), which binds with a cell permeable, stable small-molecule ligand trimethoprim (TMP) [24]. There are six lysine residues in eDHFR, and K32 exists proximal to the TMP-binding site (Figure 36.5a). TMP-DSH catalyst **8** regioselectively acetylated K32 of eDHFR-green fluorescent protein (GFP) *in vitro* in 94% yield using Ac-CoA (Figure 36.5b) [25]. The yield of acetylation for other lysine residues positioned far from the TMP-binding site (K38, K58, K76, K106, and K109) was less than 0.3%. TMP-DSH catalysts containing a shorter (**9**) or

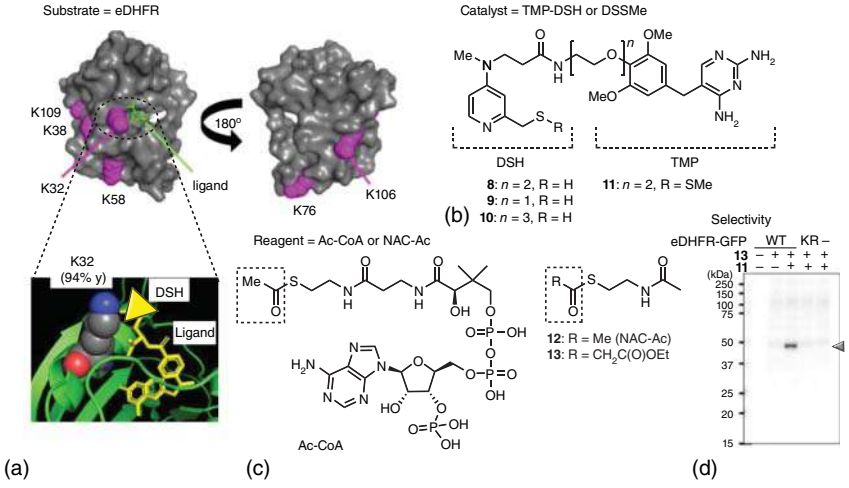

Figure 36.5 Catalyzed acylation of eDHFR. Source: Hamajima et al. [25]. Reproduced with permission of American Chemical Society.

longer (**10**) linker between the ligand and catalyst moieties were less effective than **8**, demonstrating the importance of the position of the DSH moiety relative to the lysine residue to be acetylated, which was defined by the ligand and linker length.

We next used catalyst **8** to examine the acetylation of eDHFR-GFP expressed in living cells. When using Ac-CoA as a reagent, however, the acetylation reaction hardly proceeded. The lack of reactivity for the in-cell reaction was due to the negligible cell membrane permeability of Ac-CoA, which contains anionic phosphate groups (Figure 36.5c). Consistent with this notion, when NAC-Ac **12** was used instead of Ac-CoA, the in-cell acetylation reaction proceeded in 11% yield based on quantitative analysis using LC–MS/MS. The yield was improved to 22% with pro-drugging catalyst **11**. Catalyst **11** furnished greater cell membrane permeability than **8**, while generating catalytically active **8** inside the cells through reduction by glutathione, which exists in a millimolar concentration. Using an ethyl malonyl donor **13** (10 mM) combined with catalyst **11** (25 μM), the in-cell acylation yield was ca. 40% at 37 °C for five hours.

To evaluate the selectivity of this catalyst system in cells, we conducted immunoblotting analysis of cell lysates after the reaction using anti-malonyl lysine antibody, which comprehensively visualized malonylated proteins (Figure 36.5d). Although malonylated proteins were not detected in the absence of both reagent **13** and catalyst **11** (lane 1), or hardly observed in the presence of only **13** (lane 2), malonylation of wild-type (WT) eDHFR-GFP (MW = 46.2×10^3, arrowhead) clearly proceeded in the presence of both **13** (10 mM) and **11** (25 μM) at 37 °C for five hours, concomitant with minimal malonylation of off-target proteins (lane 3). Therefore, the catalyst system selectively malonylated eDHFR-GFP in cells, where numerous off-target proteins exist. Further, malonylation was not detected when cells expressed the KR mutant eDHFR-GFP, where K32 was mutated to arginine (R) (lane 4). Therefore, K32 was again the reaction site for in-cell acylation. We

also demonstrated that the selective in-cell protein acylation by the supramolecular catalysis can be generalized to other proteins, such as HaloTag and endogenous Hsp90, which contain functional small molecule ligands in cells [25].

36.6 Chemical Catalyst-Promoted Regioselective Histone Acylation in Living Cells

The above results indicate that in-cell histone acetylation should be possible by supramolecular catalysis if the catalyst concentration in the cells is high enough. LANA-DSH catalyst **6** in combination with reagent **12**, however, failed to promote the acetylation reaction in cells. This was due to low cell membrane permeability and lability of the peptide LANA ligand in **6** to peptidase digestion. To overcome the permeability problem, we used a beads-loading method [26]. This method allowed the macromolecules to penetrate cells through a transiently disrupted cell membrane by glass bead treatment [27]. To overcome the stability problem, we synthesized pegylated LANA-conjugated DSH catalysts **14–16** by systematically changing the polyethylene glycol (PEG) length (Figure 36.6a). Conjugation with PEG implements peptides with resistance to peptidase digestion [28]. Various analytical techniques *in vitro* revealed that catalysts containing longer PEG chains are more resistant

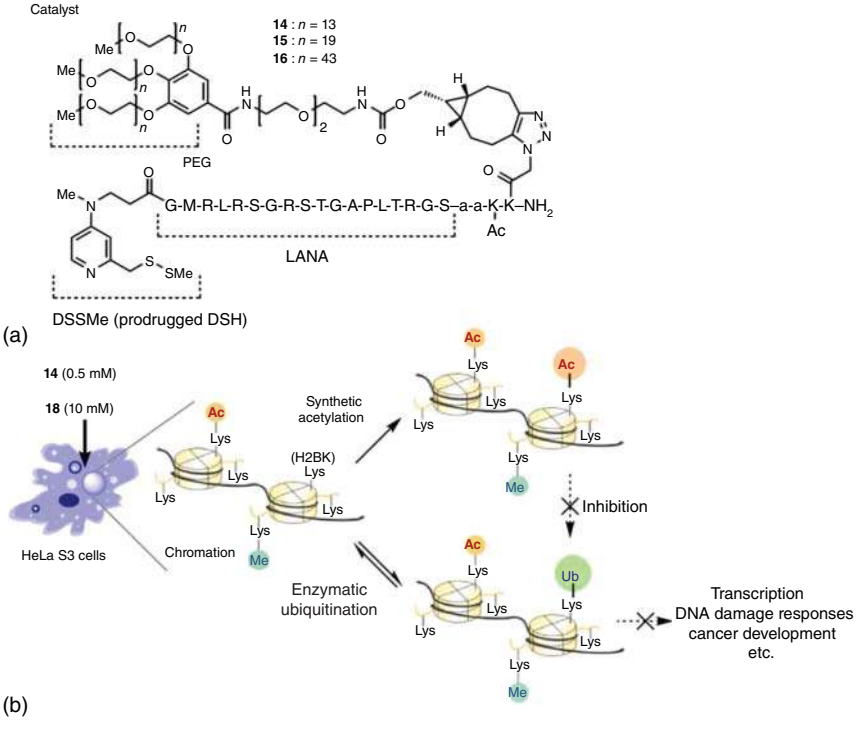

Figure 36.6 In-cell H2BK120 acetylation by PEG-LANA-DSSMe. Source: Based on Fujiwara et al. [13].

to peptidase digestion and thus more stable in cells (stability: **14** < **15** < **16**), but with lower binding affinity to nucleosomes and less catalytic activity (activity: **14** > **15** > **16**). Catalyst **14** containing the shortest PEG chains was optimal regarding the acetylation yield in living cells. Thus, when HeLa S3 cells were treated with catalyst **14** (0.5 mM) and reagent **12** (10 mM) at 37 °C for eight hours, the H2BK120 acetylation yield was as high as 51% for a cell fraction containing a high concentration of **14**. This is the first example of chemical catalyst-promoted epigenome manipulation in living cells without relying on genetic manipulation [13].

We then studied the impact of the synthetic histone acetylation in living cells on the epigenome and found a significant decrease in the level of H2BK120 ubiquitination (H2BUb). This phenomenon was likely due to competitive inhibition of enzyme (ubiquitin ligase)-promoted H2BUb by synthetic H2BK120 acetylation. Thus, the acetyl group introduced at H2BK120 by the chemical catalyst system worked as a protecting group of biomacromolecules in the cells (Figure 36.6b) [29]. Because H2BUb is an important histone modification that regulates transcription, the DNA damage response [30], and the development of a certain type of cancer [31, 32], our catalyst system acted as a novel H2BUb inhibitor, which may constitute a new anti-cancer strategy.

36.7 Concluding Remarks

On the basis of supramolecular catalysis strategy, we developed ligand-conjugated DSH catalysts that promote histone- and regioselective acylation *in vitro*. Optimizations for cell membrane permeability and metabolic stability of the catalyst system enable synthetic epigenome manipulation in living cells. Further improvements with regard to the reactivity and selectivity, as well as expansion of the reaction pattern, will enhance the applicability of chemical catalysts to intervene in physiological and pathological processes. Our goal is to realize catalyst-promoted synthetic epigenetics for therapeutic application (catalysis medicine).

References

1 Mirabella, A.C., Foster, B.M., and Bartke, T. (2016). Chromatin deregulation in disease. *Chromosoma* 125: 75–93.

2 Kundaje, A., Meuleman, W., Ernst, J. et al. (2015). Integrative analysis of 111 reference human epigenomes. *Nature* 518: 317–330.

3 Hyun, K., Jeon, J., Park, K., and Kim, J. (2017). Writing, erasing and reading histone lysine methylations. *Exp. Mol. Med.* 49: e324.

4 Yamatsugu, K., Kawashima, S.A., and Kanai, M. (2018). Leading approaches in synthetic epigenetics for novel therapeutic strategies. *Curr. Opin. Chem. Biol.* 46: 10–17.

5 Muller, M.M. and Muir, T.W. (2015). Histones: at the crossroads of peptide and protein chemistry. *Chem. Rev.* 115: 2296–2349.

6 Chin, J.W. (2014). Expanding and reprogramming the genetic code of cells and animals. *Annu. Rev. Biochem.* 83: 379–408.

7 Dominguez, A.A., Lim, W.A., and Qi, L.S. (2016). Beyond editing: repurposing CRISPR-Cas9 for precision genome regulation and interrogation. *Nat. Rev. Mol. Cell Biol.* 17: 5–15.

8 Yang, A., Ha, S., Ahn, J. et al. (2016). A chemical biology route to site-specific authentic protein modifications. *Science* 354: 623–626.

9 Wright, T.H., Bower, B.J., Chalker, J.M. et al. (2016). Posttranslational mutagenesis: a chemical strategy for exploring protein side-chain diversity. *Science* 354: 597–623.

10 Vaijayanthi, T., Pandian, G.N., and Sugiyama, H. (2018). Chemical control system of epigenetics. *Chem. Rec.* 18: 1833–1853.

11 Amamoto, Y., Aoi, Y., Nagashima, N. et al. (2017). Synthetic posttranslational modifications: chemical catalyst-driven regioselective histone acylation of native chromatin. *J. Am. Chem. Soc.* 139: 7568–7576.

12 Ishiguro, T., Amamoto, Y., Tanabe, K. et al. (2017). Synthetic chromatin acylation by an artificial catalyst system. *Chem* 2: 840–859.

13 Fujiwara, Y., Yamanashi, Y., Fujimura, A. et al. (2021). Live-cell epigenome manipulation by synthetic histone acetylation catalyst system. *Proc. Natl. Acad. Sci. U.S.A.* 118: e2019554118.

14 Kajino, H., Nagatani, T., Oi, M. et al. (2020). Synthetic hyperacetylation of nucleosomal histones. *RSC Chem. Biol.* 1: 56–59.

15 Koshi, Y., Nakata, E., Miyagawa, M. et al. (2008). Target-specific chemical acylation of lectins by ligand-tethered DMAP catalysts. *J. Am. Chem. Soc.* 130: 245–251.

16 Tsukiji, S., Miyagawa, M., Takaoka, Y. et al. (2009). Ligand-directed tosyl chemistry for protein labeling in vivo. *Nat. Chem. Biol.* 5: 341–343.

17 Ni, J., Taniguchi, A., Ozawa, S. et al. (2018). Near-infrared photoactivatable oxygenation catalysts of amyloid peptide. *Chem* 4: 807–820.

18 Litvinenko, L.M. and Kirichenko, A.I. (1967). Basicity and stereospecificity in nucleophile catalysis by tertiary amines. *Dokl. Akad. Nauk. SSSR* 176: 97–100.

19 Johnson, E.C.B. and Kent, S.B.H. (2006). Insights into the mechanism and catalysis of the native chemical ligation reaction. *J. Am. Chem. Soc.* 128: 6640–6646.

20 Yamatsugu, K., Furuta, M., Xi, S. et al. (2018). Kinetic analyses and structure-activity relationship studies of synthetic lysine acetylation catalysts. *Bioorg. Med. Chem.* 26: 5359–5367.

21 Barbera, A.J., Chodaparambil, J.V., Kelley-Clarke, B. et al. (2006). The nucleosomal surface as a docking station for Kaposi's sarcoma herpesvirus LANA. *Science* 311: 856–861.

22 Dervan, P.B. (2001). Molecular recognition of DNA by small molecules. *Bioorg. Med. Chem.* 9: 2215–2235.

23 Zhao, Y. and Garcia, B.A. (2015). Comprehensive catalog of currently documented histone modifications. *Cold Spring Harbor Perspect. Biol.* 7: a025064.

24 Miller, L.W., Cai, Y.F., Sheetz, M.P., and Cornish, V.W. (2005). In vivo protein labeling with trimethoprim conjugates: a flexible chemical tag. *Nat. Methods* 2: 255–257.

25 Hamajima, W., Fujimura, A., Fujiwara, Y. et al. (2019). Site-selective synthetic acylation of a target protein in living cells promoted by a chemical catalyst/donor system. *ACS Chem. Biol.* 14: 1102–1109.

26 Sato, Y., Stasevich, T.J., and Kimura, H. (2018). Visualizing the dynamics of inactive X chromosomes in living cells using antibody-based fluorescent probes. *Methods Mol. Biol.* 1861: 91–102.

27 McNeil, P.L. and Warder, E. (1988). Glass beads load macromolecules into living cells. *J. Cell Sci.* 88: 669–678.

28 Harris, J.M., Martin, N.E., and Modi, M. (2001). Pegylation: a novel process for modifying pharmacokinetics. *Clin. Pharmacokinet.* 40: 539–551.

29 Adamson, C. and Kanai, M. (2021). Integrating abiotic chemical catalysis and enzymatic catalysis in living cells. *Org. Biomol. Chem.* 19: 37–45.

30 Meas, R. and Mao, P. (2015). Histone ubiquitylation and its roles in transcription and DNA damage response. *DNA Repair (Amst)* 36: 36–42.

31 Daigle, S.R., Olhava, E.J., Therkelsen, C.A. et al. (2011). Selective killing of mixed lineage leukemia cells by a potent small- molecule DOT1L inhibitor. *Cancer Cell* 20: 53–65.

32 Wang, E., Kawaoka, S., Yu, M. et al. (2013). Histone H2B ubiquitin ligase RNF20 is required for MLL-rearranged leukemia. *Proc. Natl. Acad. Sci. U.S.A.* 110: 3901–3906.

37

Protein–Substrate Supramolecular Interactions for the Shape-Selective Hydroformylation of Long-Chain α-Olefins

Peter J. Deuss[1] *and Amanda G. Jarvis*[2]

[1] *University of Groningen, Chemical Engineering Department (ENTEG), Nijenborgh 4, Groningen, 9747 AG, The Netherlands*
[2] *University of Edinburgh, School of Chemistry, EaStCHEM, Joseph Black Building, David Brewster Road, Edinburgh, EH9 3FJ, UK*

37.1 Introduction

37.1.1 Introduction on Aqueous Phase Hydroformylation of Long-Chain α-Olefins

Hydroformylation stands out as a very important bulk chemical process with a global scale of operation of over 9 Mtonnes per year [1]. Its attractiveness arises from the transformation of an abundant feedstock, α-olefins obtained directly from the petrochemical industry to versatile aldehydes by an addition of hydrogen and carbon monoxide (synthesis gas) that can be readily obtained from steam methane reforming or coal/biomass gasification. The versatility of the aldehyde motif offers a great platform to access many other functional groups such as alcohols, amines, and carboxylic acids. Additionally, the transformation has a high atom economy, and several precious metal-based catalysts (typically, cobalt and rhodium complexes) can reach extremely high activity [2]. Hydroformylation of a terminal alkene forms the branched product or the typically desired linear product, depending on the position of the initial CO insertion (Figure 37.1). The ligand environment around the metal center is often used to steer the performance and selectivity, for example, rhodium–phosphine complexes can give very high linear selectivity. Today, the aldehydes that are produced by various operational hydroformylation processes are used not only for the synthesis of many bulk chemical products

☆ Dedicated to Professor Paul C. J. Kamer.
Dedication: The chapter is dedicated to Professor Paul C. J. Kamer who suddenly passed away on November 19, 2020. Professor Kamer was an excellent scientist with interests spanning from biochemistry to catalysis. He was an inspiration to many of his students, and both the authors are tremendously grateful to his mentorship and support in transitioning to independent careers. Here we celebrate the work of Professor Paul C. J. Kamer and his group on the development of artificial metalloenzymes focusing on the results obtained for hydroformylation.

Supramolecular Catalysis: New Directions and Developments, First Edition.
Edited by Piet W.N.M. van Leeuwen and Matthieu Raynal.

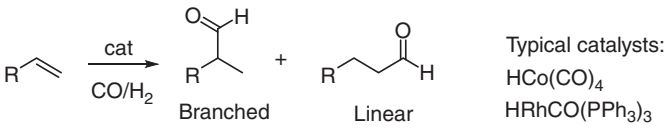

Figure 37.1 General reaction scheme for hydroformylation.

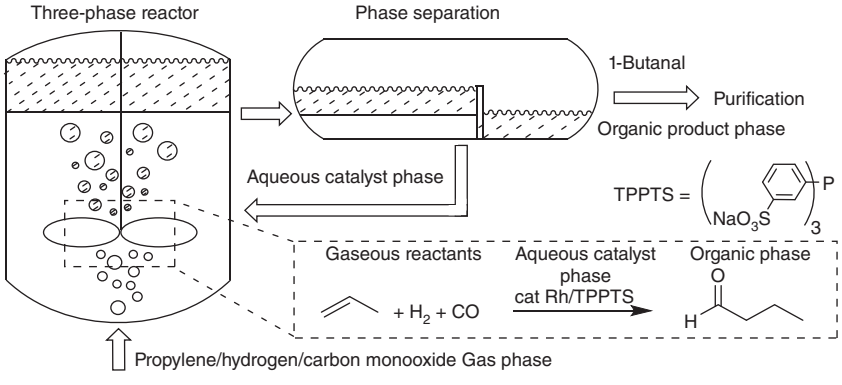

Figure 37.2 Schematic representation of the Ruhrchemie/Rhône-Poulenc process.

such as plasticizers and detergents but also for many specialty chemicals such as fragrances or pharmaceuticals.

Apart from the mentioned selectivity, there are many challenges for the operation of hydroformylation processes. The use of expensive precious metal complexes, their homogeneous nature, and the need for specific relatively expensive ligand environments to control activity and selectivity [3] mean that for industrial scale operation the process requires highly efficient solutions for integrated catalyst recycling. One very successful solution is demonstrated by the Ruhrchemie/Rhône-Poulenc process in which propylene gets converted to butanal (Figure 37.2) [4]. This process is operated in a three-phase system which utilizes a recyclable aqueous rhodium-TPPTS ligand system, gas-fed reactants, and an organic phase consisting mostly of the desired linear product (1-butanal) which can be readily separated and further purified. The key aspect is the low rhodium loss of only grams per year, which is very impressive for a process with a production capacity of multiple Mtonnes per year. These low losses are due to the high affinity of the applied rhodium-TPPTS complex for the aqueous phase allowing for easy recovery and recycling.

This aqueous phase hydroformylation process concept works well for ethylene and propylene. However, as the catalysis takes place in the aqueous phase, a process for higher alkenes suffers from the low solubility of these α-olefins in water which worsens in a logarithmic scale upon longer chain lengths (Figure 37.3) [5]. To make the catalytic reaction in the aqueous phase more efficient, many solutions have been explored. Examples are the use of cosolvents, surfactants, and catalyst complexes that can also partly dissolve in the organic phase (such as mono and disulfonated variants of TPPTS) [6]. Another solution is the use of inverse phase-transfer catalysts that can partly solubilize the hydrophobic substrate into the aqueous

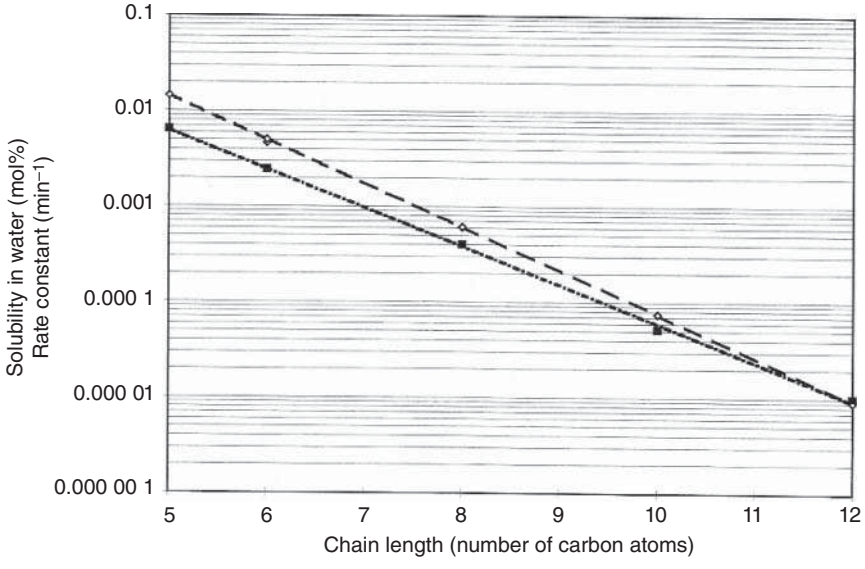

Figure 37.3 The solubility of linear α-olefins in water (solid line) correlated to the hydroformylation rate constant (dashed line). Source: Bahrmann et al. [5]. Reproduced with permission of John Wiley & Sons.

phase. For example, β-Cyclodextrins have been applied to induce significant rate enhancement for the Rh-TPPTS-catalyzed hydroformylation of dec-1-ene [7]. However, many such solutions lead to significant catalyst losses in the organic phase and/or a decrease in selectivity. The selectivity for the desired linear product over side products such as the branched and/or hydrogenation products is normally over 96% in aqueous phase hydroformylation using Rh-TPPTS. The formation of other active complexes such as monodentate ligand complexes or "naked" rhodium species is known to drop this selectivity toward 50% for long-chain α-olefins. Thus, the design of highly active and selective aqueous catalytic hydroformylation systems, which are modular and can be tuned for specific substrates such as hydrophobic long-chain olefins, is still a significant challenge that we, as part of the group of Professor P.C.J. Kamer, aimed to tackle by innovative rational catalyst design.

37.1.2 Shape Selective Artificial Metalloenzyme Catalyst Design

Shape selectivity has the potential to induce both substrate and product selectivity and is a powerful tool in catalysis. Enzymes are known to induce shape selectivity and are known to be tuneable in terms of activity and product selectivity using powerful tools such as directed evolution [8]. Thus, in the Kamer group, the design of enzyme-like catalysts for aqueous hydroformylation (i.e. hydroformylases) was envisioned. No enzymes in nature are known to have hydroformylase activity, which means that there is no starting point to apply methods such as directed evolution. Therefore, instead of trying to evolve a hydroformylase, the Kamer group decided to turn to artificial metalloenzymes (ArMs) that contained a synthetic metal ligand environment embedded in a tuneable protein environment.

In the early 2000s, a new field of research emerged that built on work from the 1970s by Whitesides and Kasier, which combined proteins and metals as hybrid catalysts for aqueous reactions [9]. These novel catalysts, later referred to as ArMs, used the supramolecular binding of biotin to avidin and streptavidin as the basis of their construction. Thomas Ward and coworkers showed that using this supramolecular approach and combining it with chemogenetic optimization gave quick access to new catalysts for enantioselective hydrogenation [10]. Using this approach, the hydrogenases developed were shown to be chemically tuneable, by varying the synthetic metal-binding site using existing knowledge from chemical catalysis. In addition, using biological tools such as site-directed mutagenesis allowed for the genetic tuning of the protein host to improve catalyst selectivity and activity. Since then, the Ward group and others have used this catalyst design strategy for a wide variety of reactions from Pd-catalyzed cross-coupling reactions [11] to mimicking the active sites of natural oxidases [12]. The bulk of this work relied on the supramolecular interaction of biotin and streptavidin for the introduction of the metal complex into the protein scaffold, positioning the resulting active site away from the binding site in a shallow pocket (Figure 37.4a).

In the Kamer group, we were interested in taking an alternative approach to ArM design where the molecular recognition properties of proteins were not used to introduce the metal complex but would be used to control substrate binding and direct reaction selectivity. This approach was inspired in part by the use of shape selectivity in heterogeneous catalysis, for example, selective α-oxidation of alkanes can be achieved by using porous materials containing appropriate size pores with catalysts embedded at key positions [13]. Many valuable homogeneous catalytic reactions are applied to linear aliphatic substrates and aim to control regioselectivity. By targeting protein scaffolds that can bind these types of substrates and by judicious placement of the metal active site, we hypothesized that we could create ArMs for a range of shape-selective catalytic transformations. The catalyst is then free to strategically interact with the supramolecularly bound substrate allowing the reaction to proceed selectively (Figure 37.4b).

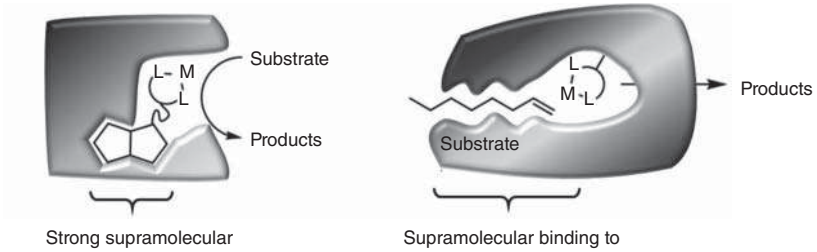

Figure 37.4 Contrasting approaches for metal binding site introduction to obtain artificial metalloenzymes: (a) supramolecular anchoring of the metal binding environment (b) site-selective covalent anchoring leaving the substrate binding site available for selective catalysis. M = metal, L = ligand.

37.2 Design of Protein Templates for Shape-Selective ArMs

To bring our vision to fruition, the first step was to identify protein scaffolds that can bind linear aliphatic substrates such as the targeted linear α-olefins. The Kamer group focused on binding proteins whose biological role was to bind hydrophobic molecules, such as sterols and long-chain fatty acids, and identified the steroid carrier protein-2L (SCP-2L) from the Human Multifunctional Enzyme 2 as a promising scaffold [14]. The crystal structure of this protein was reported and showed that the protein contained a hydrophobic tunnel of 18 Å by 10 Å that is ideal for binding linear apolar substrates such as long-chain terminal alkenes (Figure 37.5). In addition, the native protein contains no cysteine residues making it an ideal blank canvas to introduce cysteines at different positions for site-selective modification for the introduction of metal-binding sites.

We were able to obtain SCP-2L at a reasonable scale (25–60 mg l^{-1} media) via overexpression in *Escherichia coli* and purification by nickel-affinity chromatography [16]. With a method to express the native protein in good amounts in hand, the next step was to modify the scaffold to allow the anchoring of the desired metal–ligand environment for catalysis. A covalent modification strategy was chosen for this as it would allow us to control where within the protein we situated our ligand and to tune the positioning for optimal catalysis. Using the reported crystal structure

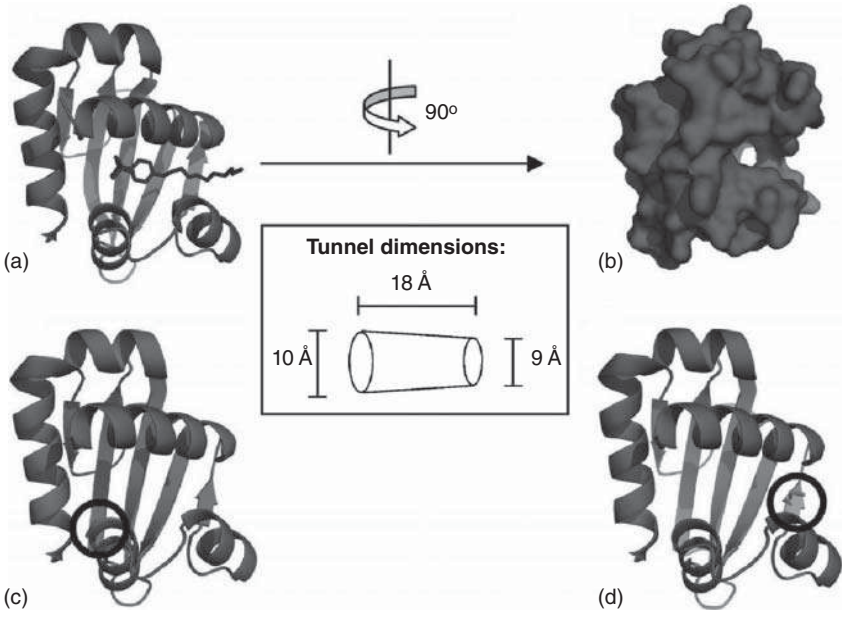

Figure 37.5 (a) Ribbon diagram of SCP-2L (pdb: 1IKT) using the presence of Triton X-100 in the apolar tunnel. (b) Space filled diagram of SCP-2L highlighting the apolar tunnel. (c) Position of V83C (denoted by circle). (d) Position of A100C (denoted by circle). Source: Deuss et al. [15]. Reproduced with permission of John Wiley & Sons.

of SCP-2L (pdb: 1IKT) and docking studies of various metal cofactors [16], the following residues, E14, W36, V82, V83, A100, Q111, were identified as potential sites to introduce a unique cysteine residue for modification which would situate the cofactor within the hydrophobic tunnel of SCP-2L. Following mutagenesis, plasmid optimization, protein expression, and purification, V83C and A100C were obtained in good yield (up to 75 mg l^{-1}) and taken forward for modification [15]. This was followed by W36C and Q111C in later years [17]. Substrate-binding studies on SCP-2L V83C confirmed that the binding affinity of the protein was not affected by the mutation (the binding affinity of 12-pyrene dodecanoic acid for SCP-2L is $K_d = 0.18\,\mu M$ (± 0.05), SCP-2L V83C $K_d = 0.18\,\mu M$ (± 0.07)). Furthermore, circular dichroism of V83C, A100C, and Q111C all showed the same tertiary structure by near UV CD spectroscopy, revealing no significant influence of these mutations on the protein folding.

37.3 Introduction of a Metal–Ligand Environment into SCP-2L

The successful introduction of unique cysteine residues into SCP-2L opened the door to site-selective covalent modification using metal complexes or ligands containing reactive groups such as maleimides, activated acids, alkyl halides, and iodoacetamides [18]. The Kamer group used these strategies to modify the unique cysteine in the mutant SCP-2Ls with a range of nitrogen-based ligands (Figure 37.6). Using carboxylic acid derived ligands, **N1** and **N2**, incomplete and multiple modifications were observed; therefore, the group turned to maleimide linkers for modification. Using this approach, a wide range of bi, tri, and tetradentate nitrogen ligands (examples shown in Figure 37.6 **N3–N7**) could be introduced selectively with quantitative conversions [15, 19]. Subsequent incubation with metal salts, e.g.

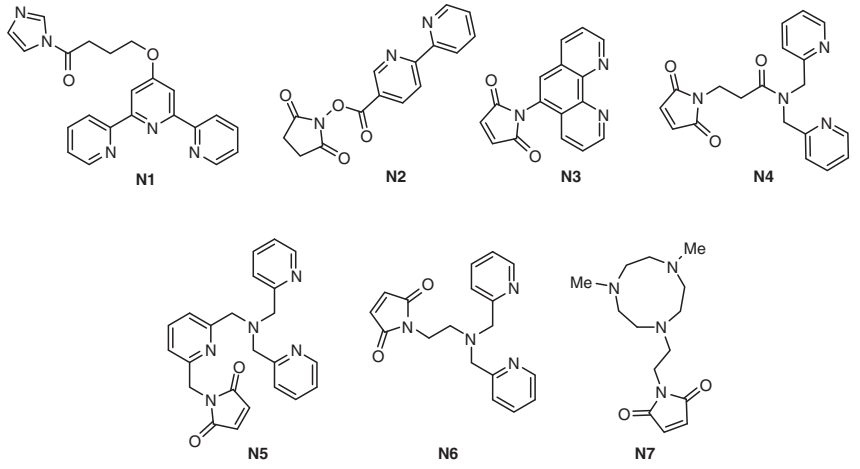

Figure 37.6 Nitrogen ligands used for protein modification.

$Cu(NO_3)_2$, led to the desired metalloproteins. Using metal complexes of the ligands directly in the modification led to mixed success with some complexes giving rise to modification, e.g. **N3**-Ru(*p*-cymene)(OH_2) [20], whereas **N4**-$Cu(NO_3)_2$ gave only protein dimers [15].

37.4 SCP-2L as a Catalytic Scaffold

The next step was to test these ArMs in catalysis to explore their reactivity and test whether the protein scaffold as designed could impart some selectivity. If the catalyst is located in the vicinity of the substrate-binding site, the supramolecular interaction of the protein environment with the substrate and catalyst is expected to affect catalytic performance.

As a model reaction, the asymmetric Diels–Alder reaction was chosen for screening SCP-2L-derived ArMs. SCP-2L mutants modified with **N3** and **N4** were incubated with copper nitrate and screened in the reaction of azachalcone (**1**) and cyclopentadiene (**2**) (Figure 37.7) [15]. Depending on the position of modification in the protein scaffold and the nitrogen ligand, different endo/exo ratios of product **3** were obtained and low enantioselectivities. SCP-2L V83C-**N3** gave a promising ee of 25%, while the use of SCP-2L A100C-**N4** gave high endo selectivity. These results clearly demonstrated the influence of the protein scaffold on the reaction.

Stereoselectivity is not the only criteria for selectivity in a reaction. More recently, the Kamer group looked at controlling reactivity in the oxidation of lignin model compounds with the aim of providing catalysts for selective lignin degradation [19]. When comparing the results from using the Fe(**N5**) complex either in a protein or by itself, it was found that in aqueous buffer the reaction only proceeded when the protein modified catalyst was used. Additionally, the protein scaffold appeared to control reactivity giving rise only to benzylic oxidation, whereas just using Fe(**N5**) in acetonitrile gave a mixture of products. Computational studies identified a nearby residue, Phe94, in close proximity to the metal center. When it was mutated to glutamic acid, it enhanced the yield of the reaction, potentially indicating that the active

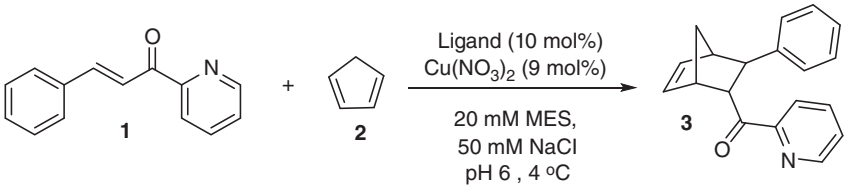

Ligand:	Conversion (%)	endo/exo ratio	ee (%)
SCP-2L V83C-**N3**	20	7.6	25
SCP-2L A100C-**N4**	76	17.6	–5

Figure 37.7 Asymmetric Diels–Alder reaction catalyzed by SCP-2L-based Cu-ArMs. Source: Based on Deuss et al. [15].

site can be tuned by amino acids in the primary coordination sphere of the metal just like in natural metalloenzymes.

Overall, both these examples showed that ArMs based on the SCP-2L could be synthesized by site-selective modification with a desired metal–ligand environment and used as tuneable catalysts. The next challenge was to see if the supramolecular binding of linear hydrophobic substrates within the protein scaffold could be utilized to achieve enhanced activity and regioselectivity with rhodium-catalyzed hydroformylation of long-chain linear α-olefins.

37.5 Phosphine Modification of Proteins

Transition metal complexes of phosphines are some of the most well-known and valuable homogeneous catalysts for both industrial and academic applications, including hydroformylation. To test the hypothesis that a protein scaffold could be used to control regioselectivity in hydroformylation, a method for incorporating phosphine–metal complexes was needed. Extending the approaches used above for nitrogen ligands to the introduction of phosphines into protein scaffolds was met with mixed success. 1,1′-Carbonyldiimidazole (CDI)-activated phosphino-carboxylic acids and their Rh complexes were successfully used for the modification of Photoactive Yellow Protein (PYP) and showed exclusive selectivity for the cysteine residue and good modification efficiencies (>90%) [20, 21]. However, for the desired protein scaffold SCP-2L, lysine residues were also modified using this modification method. Moving to using maleimides as the reactive linker, which was previously successful in overcoming this challenge, was not possible in the case of phosphines as the phosphorus can itself react with the maleimide to form an ylide. Therefore, an alternative strategy was required.

To enable the selective functionalization of SCP-2L, a 2-step approach was developed in which a maleimide linker is used to introduce a second reactive group (Figure 37.8). Maleimide-hydrazides were identified as potential linkers as a second reaction of the hydrazide with an aldehyde will readily occur and is compatible with phosphine groups. Using **4**, selective and complete modification of cysteine in a variety of proteins (SCP-2L, AppA, PYP) was obtained [22]. Subsequent reaction of protein-**4** with aldehydes **P1–6** led to a range of phosphine groups successfully being introduced to these proteins (Figure 37.8). The modified proteins were recovered in good yields for protein-**4**-**P1–4**; however, for **P5** and **P6**, the modification led to protein precipitation. The one exception to the efficient modification of SCP-2L was with SCP-2L W36C which regardless of conditions (pH, time, temperature) never reached more than 25% modification with **4**, potentially due to the buried nature of this residue or a loss in structure upon mutation of the tryptophan residue to cysteine [23].

The desired ArMs were predominantly formed via addition of a metal salt to the protein-**4**-**PX**, though complexes containing aldehydes can also be used directly in the second step to give access to metalloproteins (e.g. **P3-Au-Cl**) [24]. Formation of the modified proteins was confirmed by liquid chromatography mass spectrometry

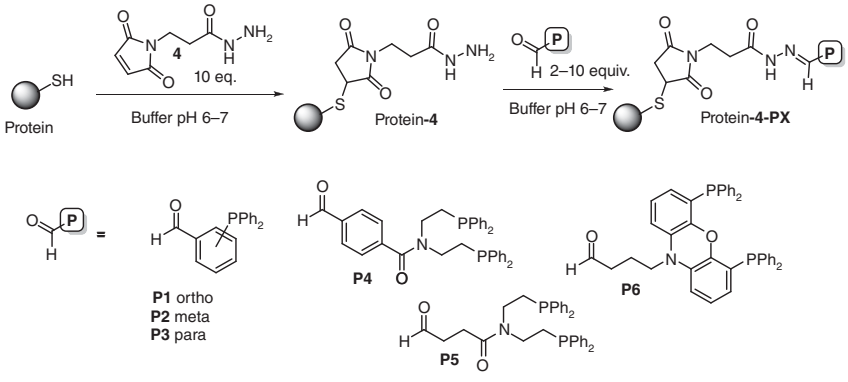

Figure 37.8 Introduction of phosphines via maleimide-hydrazide, **4**, into protein scaffolds by a two-step covalent modification strategy.

(LCMS) at each step, and ^{31}P nuclear magnetic resonance (NMR) was used to characterize the phosphine containing protein and confirm metal binding to the phosphorus. Only a slight change in K_d for Pyr-C12 binding was observed for the phosphine-modified proteins (SCP-2L-V83C-**X**-**P3** $K_d = 0.24\ (\pm 0.06)\ \mu M$), indicating that the binding properties of the protein remained intact upon modification.

37.6 Application in Biphasic Hydroformylation

Characterization of the SCP-2L-**4**-**PX** showed that the substrate-binding properties remained intact after modification, indicating that linear long-chain α-olefins can still bind within the protein tunnel and potentially orient the alkene toward the metal center and lead to preferential formation of the linear hydroformylation product (Figure 37.4b). The resulting aldehydes are more hydrophilic than the olefins which was hypothesized to lead to product/substrate exchange and turnover. For hydroformylation, the rhodium metalloproteins were obtained by the addition of $Rh(acac)(CO)_2$ to SCP-2L-**4**-**PX**. The catalytic activity of the rhodium metalloproteins was screened in the biphasic hydroformylation of 1-octene at 35 °C and 80 bar syngas (Figure 37.9a) [24]. Gratifyingly, several ArMs showed significant hydroformylation activity under these conditions [24]. The turnover number (TON) was dependent on the phosphine cofactor, with **P3** giving rise to the best activities, and negligible activity being obtained with **P1**. In addition, the position within the protein scaffold also affected the activity, with TON for SCP-2L-**4**-**P3** varying from 75 to 409 for SCP-2L V83C vs. SCP-2L A100C (Figure 37.9b). Control experiments showed that this activity was due to the rhodium protein and not leached rhodium which would be expected to give rise to higher TONs but lower selectivity (with $Rh(acac)(CO)_2$, TON = 530, 55% 1-nonanal). In comparison, impressive selectivities were obtained with the ArMs reaching up to 80% 1-nonanal, which strongly pointed toward the rhodium containing protein being responsible for catalyzing the reaction.

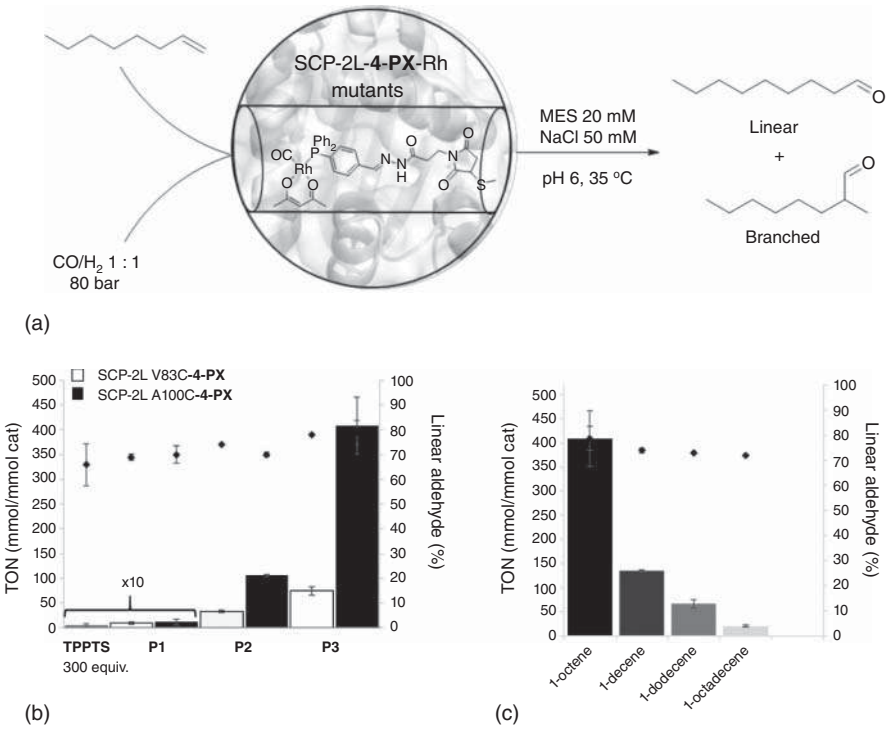

Figure 37.9 (a) Hydroformylation of 1-octene; (b) effect of phosphine ligand and protein scaffold on TON and linearity of aldehyde product; (c) hydroformylation of long-chain α-olefins using SCP-2L A100C-**4**-**P3**-Rh. Source: Jarvis et al. [24]. CC BY 4.0.

Comparing these results to the industrial water-soluble TPPTS/Rh system highlighted the benefit of combining rhodium catalysts with proteins. To achieve similar selectivities, over 300 equiv. TPPTS needed to be used to ensure the coordination of multiple ligands to metal centers, which led to significantly reduced TONs (~5 TON, 66% 1-nonanal). This is required as monodentate phosphine rhodium complexes rarely give selectivities of above 75% linearity, highlighting the significance of the remarkable selectivity obtained for these monodentate phosphine rhodium ArMs [2]. Simply adding the protein scaffold to reactions with Rh/TPPTS did not improve activity, showing that the increase in activity with SCP-2L-**4**-**P3** cannot simply be explained by the protein acting solely as a phase transfer agent. Overall, this demonstrated that the activity and selectivity of these catalysts can be attributed to their ability to bind the alkene substrate in the hydrophobic tunnel in close proximity to the introduced rhodium-phosphine center.

The rhodium hydroformylases are also active catalysts for longer chain α-olefins. Using SCP-2L A100C-**4**-**P3**-Rh the TON decreased by fourfold when increasing the substrate chain length from C8 to C10. This drop off in activity was less than expected if it was just dependent on substrate solubility (a 10-fold reduction is seen on increasing the chain length by two carbons for the Rh/TPPTS biphasic system, Figure 37.3), and the hydroformylases were still active with C12 and C18 alkenes

unlike the Rh/TPPTS system. A high linear selectivity of >70% was maintained across all the substrates (Figure 37.9c). These observations are attributed to the presence of a hydrophobic tunnel in the protein scaffold and its lipid-binding properties. Overall, rhodium phosphine-modified SCP-2Ls are linear-selective catalysts in the hydroformylation of long-chain alkenes. SCP-2L A100C-**4**-**P3**-Rh showed a rate enhancement of at least 10^3 compared to the traditional Rh/TPPTS system in the biphasic hydroformylation of 1-octene and 1-decene, highlighting the enzyme-like behavior of these hybrid catalysts.

Having shown that rhodium hydroformylases can be designed and prepared by the combination of a suitable protein scaffold with desirable substrate-binding properties and a synthetic rhodium phosphine environment, the Kamer group then went on to see if the hydroformylases could be further engineered in a similar manner to natural enzymes. Using crystal structures of the parent protein scaffolds (SCP-L V83C and SCP-2L A100C, pdb entries: 6Z1X and 6Z1W) and a 3DM database, potential mutations were identified that might increase the thermostability of the protein scaffold. On the introduction of two beneficial mutations, the thermostability of the protein scaffolds was improved by up to 16 °C compared to the parent scaffold [25]. Rhodium hydroformylases using these improved scaffolds showed increased stability under the reaction conditions leading to higher turnover numbers and allowed the reaction temperature to be increased to 45 °C without a detrimental effect on catalyst activity/stability. The results were particularly impressive with hydroformylases based on the parent scaffold SCP-2L V83C, giving rise to over a 10-fold increase in TON when using SCP-2L V83C+N31D+S56D-**4**-**P3**-Rh vs. SCP-2L V83C-**4**-**P3**-Rh at 45 °C over 48 hours (TON 402 vs. 27).

37.7 Structural Studies on the Rhodium Hydroformylases

Increasing our understanding of the rhodium hydroformylase structure is key to developing these catalysts further and maximizing the exploitation of the supramolecular binding of the substrates. While the Kamer group obtained crystal structures of the protein scaffolds SCP-2L V83C and A100C, to date we have been unable to obtain crystal structures of the modified protein scaffolds. Therefore, the group turned to a variety of other techniques to increase their understanding of the catalyst structure, including extended X-ray absorption fine structure (EXAFS) and NMR [17, 24]. Comparing the EXAFS spectra of A100C-**4**-**P3**-Rh and A100C-SeMet-**4**-**P3**-Rh, where all the methionines in the protein were replaced by selenomethionine, showed that a methionine residue is in close proximity to the rhodium center in the hydroformylase [24]. Alanine scanning mutagenesis of the methionines was conducted on the hydroformylases and the resulting catalysts screened in the hydroformylation of 1-octene. Only SCP-2L M105A+A100C-**4**-**P3**-Rh showed a significant difference in catalysis. However, further EXAFS experiments showed that this methionine was not responsible for the close Rh–S interaction, showing a possible discrepancy between the resting

state of the catalyst and the structure involved in the catalytic reaction [17]. In addition, no direct evidence for a methionine rhodium interaction was obtained via multinuclear NMR studies. However, clear and complex changes in the structure were observed upon modification of the protein scaffold with **4** and subsequently **P3** indicating that future studies should consider the whole polypeptide structure and not just the immediate environment of the rhodium. It is postulated that even small changes affect the conformation of the protein, including in amino acids distal from the active site, and this may affect the substrate-binding properties of the protein.

37.8 Concluding Remarks

This chapter described the design and synthesis of enzyme-like catalysts for the biphasic hydroformylation of long-chain linear α-olefins, a reaction not found in nature. The hydroformylases were obtained by engineering a protein scaffold (SCP-2L), with a selected hydrophobic-binding site suitable for binding such substrates, to contain a covalently anchored rhodium-phosphine environment. The designed enzymes led to significant rate enhancement compared to Rh/TPPTS and induced desirable linear selectivity.

This work can be used as a basis for the exploitation of ArMs design to be tailored to take on the challenge of converting biobased substrates overcoming current hurdles in the utilization of renewable carbon sources. To do this, it will be crucial to control the binding and release of substrates with the same potency as nature. Such a system will require tailored supramolecular catalyst–substrate interactions to attain desired activities and selectivities, and long-term stability will need to be improved for such systems to be applied competitively. Future work could look for ways to potentially carry out the whole process *in vivo* to allow bacteria to carry out hydroformylation bringing a traditionally industrial chemical process into the biosphere.

Acknowledgments

We would like to thank all previous members of the Kamer group that contributed to this work and numerous colleagues for discussions, aid with characterization and access to equipment. This work was supported by funding received from the EU through Marie Curie Excellence Grants, Artizyme Catalysis (MEXT-2004-014320), and a Marie Curie Individual Fellowship project ArtOxiZymes to A.G.J. (H2020-MSCA-IF-2014-657755). From the EPSRC through an EPSRC critical mass grant “Clean catalysis for sustainable development” (EP/J018139/1) and Sasol (CASE studentship to P.J.D.). The UK Catalysis Hub is kindly thanked for resources and support provided via our membership of the UK Catalysis Hub Consortium, which is funded by the EPSRC (EP/K014706/2, EP/K014668/1, EP/K014854/1, EP/K014714/1, and EP/M013219/1). A.G.J would also like to acknowledge the UKRI for the award of a Future Leaders Fellowship (MR/S017402/1).

References

1 Börner, A. and Franke, R. (eds.) (2016). *Hydroformylation: Fundamentals, Processes, and Applications in Organic Synthesis*. Weinheim: Wiley-VCH Verlag GmbH.

2 Van Leeuwen, P.W.N.M. (2004). *Homogeneous Catalysis: Understanding the Art*. Amsterdam: Springer.

3 Hanefeld, U. and Lefferts, L. (eds.) (2018). *Catalysis: An Integrated Textbook for Students*. Weinheim: Wiley-VCH Verlag GmbH.

4 Wiebus, E. and Cornils, B. (2006). Biphasic systems: water – organic. In: *Catalyst Separation, Recovery and Recycling. Chemistry and Process Design* (eds. D.J. Cole-Hamilton and R.P. Tooze), 105. Amsterdam: Springer.

5 Bahrmann, H., Bogdanovic, S., and van Leeuwen, P.W.N.M. (2004). *Aqueous Phase Organometallic Catalysis*, 2e (eds. B. Cornils and W. Herrmann), 391–409. Weinheim: Wiley-VCH.

6 Obrecht, L., Kamer, P.C.J., and Laan, W. (2013). Alternative approaches for the aqueous–organic biphasic hydroformylation of higher alkenes. *Catal. Sci. Technol.* 3: 541–551.

7 Monflier, E., Fremy, G., Castanet, Y., and Morteux, A. (1995). Molecular recognition between chemically modified β-cyclodextrin and dec-1-ene: new prospects for biphasic hydroformylation of water-insoluble olefins. *Angew. Chem. Int. Ed. Engl.* 34: 2269–2271.

8 Arnold, F.H. (2018). Directed evolution: bringing new chemistry to life. *Angew. Chem. Int. Ed.* 57: 4143–4148.

9 (a) Wilson, M.E. and Whitesides, G.M. (1978). Conversion of a protein to a homogeneous asymmetric hydrogenation catalyst by site-specific modification with a diphosphinerhodium(I) moiety. *J. Am. Chem. Soc.* 100: 306–307. (b) Yamamura, K. and Kaiser, E.T. (1976). Studies on the oxidase activity of copper(II) carboxypeptidase A. *J. Chem. Soc., Chem. Commun.* 20: 830–831. (c) Schwizer, F., Okamoto, Y., Heinisch, T. et al. (2018). *Chem. Rev.* 118: 142–231.

10 (a) Colllot, J., Gradinaru, J., Humbert, N. et al. (2003). Artificial metalloenzymes for enantioselective catalysis based on biotin–avidin. *J. Am. Chem. Soc.* 125: 9030–9031. (b) Letonder, C., Humbert, N., and Ward, T.R. (2005). Artificial metalloenzymes based on biotin–avidin technology for the enantioselective reduction of ketones by transfer hydrogenation. *Proc. Natl. Acad. Sci. U.S.A.* 102: 4683–4687. (c) Ward, T.R. (2011). Artificial metalloenzymes based on the biotin–avidin technology: enantioselective catalysis and beyond. *Acc. Chem. Res.* 44: 47–57.

11 Chatterjee, A., Mallin, H., Klehr, J. et al. (2016). An enantioselective artificial Suzukiase based on the biotin–streptavidin technology. *Chem. Sci.* 7: 673–677.

12 Mann, S.I., Heinisch, T., Ward, T.R., and Borovik, A.S. (2017). Peroxide activation regulated by hydrogen bonds within artificial Cu proteins. *J. Am. Chem. Soc.* 139: 17289–17292.

13 (a) Raja, R. et al. (2006). Highly efficient one-step conversion of cyclohexane to adipic acid using single-site heterogeneous catalysts. *Chem. Commun.*: 448–450. (b) Herron, N. and Tolman, C.A. (1987). A highly selective zeolite catalyst for hydrocarbon oxidation. A completely inorganic mimic of the alkane ω-hydroxylases. *J. Am. Chem. Soc.* 109: 2837–2839.

14 Haapalainen, A.M., van Aalten, D.M.F., Meriläinen, G. et al. (2001). Crystal structure of the liganded SCP-2-like domain of human peroxisomal multifunctional enzyme type 2 at 1.75 Å resolution. *J. Mol. Biol.* 313: 1127–1138.

15 Deuss, P.J., Popa, G., Slawin, A.M.Z. et al. (2013). Artificial copper enzymes for asymmetric Diels–Alder reactions. *ChemCatChem* 5: 1184–1191.

16 Deuss, P. J. (2011) Artificial metalloenzymes; modified proteins as tuneable transition metal catalysts. PhD thesis, University of St Andrews. https://research-repository.st-andrews.ac.uk/handle/10023/1923.

17 Iman, H.T., Jarvis, A.G., Cellorrio, V. et al. (2019). Catalytic and biophysical investigation of rhodium hydroformylase. *Catal. Sci. Technol.* 9: 6428–6437.

18 Lewis, J.C. (2013). Artificial metalloenzymes and metallopeptide catalysts for organic synthesis. *ACS Catal.* 3: 2954–2975.

19 Doble, M.V., Jarvis, A.G., Ward, A.C.C. et al. (2018). Artificial metalloenzymes as catalysts for oxidative lignin degradation. *ACS Sustainable Chem. Eng.* 6: 15100–15107.

20 den Heeten, R., Muñoz, B.K., Popa, G. et al. (2010). Synthesis of hybrid transition-metalloproteins via thiol-selective covalent anchoring of Rh-phosphine and Ru-phenanthroline complexes. *Dalton Trans.* 39: 8477–8483.

21 Laan, W., Muñoz, B.K., den Heeten, R., and Kamer, P.C.J. (2010). Artificial metalloenzymes through cysteine-selective conjugation of phosphines to photoactive yellow protein. *ChemBioChem* 11: 1236–1239.

22 Deuss, P.J., Popa, G., Botting, C.H. et al. (2010). Highly efficient and site-selective phosphane modification of proteins through hydrazone linkage: development of artificial metalloenzymes. *Angew. Chem. Int. Ed.* 49: 5315–5317.

23 Iman, H.T., Jarvis, A.G., Cellorrio, V. et al. (2019). Catalytic and biophysical investigation of rhodium hydroformylase. *Catal. Sci. Technol.* 9: 6428–6437.

24 Jarvis, A.G., Obrecht, L., Deuss, P.J. et al. (2017). Enzyme activity by design: an artificial rhodium hydroformylase for linear aldehydes. *Angew. Chem. Int. Ed.* 56: 13596–13600.

25 Doble, M.V., Obrecht, L., Joosten, H.-J. et al. (2021). Engineering thermostability in artificial metalloenzymes to increase catalytic activity. *ACS Catal.* 11, 3620–3627.

38

Supramolecular Assembly of DNA- and Protein-Based Artificial Metalloenzymes

Gerard Roelfes

University of Groningen, Stratingh Institute for Chemistry, Nijenborgh 4, 9747 AG Groningen, The Netherlands

38.1 Introduction

Artificial metalloenzymes have emerged as a promising approach to the biocatalysis of reactions that have no equivalent in Nature [1]. Artificial metalloenzymes are hybrids of catalytically active transition metal complexes that are embedded in a protein scaffold that is envisioned to supply to additional interactions that help achieve enzyme-like rate accelerations and (enantio-)selectivities. The embedding can be achieved using either covalent or supramolecular anchoring [2, 3].

Covalent anchoring has the advantage that it allows for precise control over the position of the metal complex inside the biomolecular scaffold. Often covalent anchoring is achieved by a chemical reaction linking the biomolecular scaffold to the ligand of the transition metal complex. While this approach has led to interesting applications, it is limited by the number of handling steps that are involved, thus severely limiting the possibilities for optimization. A recent development is the direct biosynthetic incorporation of noncanonical metal-binding amino acids in proteins using expanded genetic code methods such as stop codon suppression, using an orthogonal translation system [4, 5]. This method offers the advantage that the incorporation of the metal binding ligand is achieved during translation and no additional reaction and purification steps are needed. However, while a number of orthogonal translation systems for different metal binding amino acids are available, this is far from a general approach yet.

The supramolecular approach relies on self-assembly of the artificial metalloenzymes by exploiting noncovalent interactions between the transition metal complex and the biomolecular scaffold. This approach can again be subdivided in two subclasses. The first involves transition metal complexes that are conjugated to specific protein binders that "drag" the metal complex inside the protein. This so-called "Trojan horse Methodology" has proven very powerful and has been exploited often [1]. The best known example of this approach is based on the biotin/(strept-)avidin combination introduced by Whitesides and further developed with much success by the Ward laboratory [6–8].

Supramolecular Catalysis: New Directions and Developments, First Edition.
Edited by Piet W.N.M. van Leeuwen and Matthieu Raynal.

The alternative approach involves direct interaction of the metal complex with the biomolecular scaffold without using conjugated protein-binding moieties. This will be the focus of the present chapter, with a particular emphasis on our own work on DNA and protein-based artificial metalloenzymes.

38.2 DNA-Based Artificial Metalloenzymes

To date, no catalytic role has been reported for DNA in nature. However, DNA is an attractive scaffold for artificial metalloenzyme design because of its unique, programmable structure. Hence, we have investigated DNA-based artificial metalloenzymes [9, 10]. In our studies, we used natural double stranded DNA, i.e. salmon testes DNA, because it is cheap and readily available in large quantities. It should be noted that since our early work, many reports of catalysis with other DNA architectures have been reported, but those will not be discussed here [11–13].

The first design of DNA-based artificial metalloenzymes involved using a copper(II) complex of an aminomethylpyridine ligand conjugated via a short spacer to a DNA intercalator, i.e. 9-aminoacridine [14]. The aminoacridine moiety inserts itself between two DNA-base pairs and in this way forces the copper complex in close proximity to the DNA, in the chiral environment of the DNA grooves. This resulted in moderate enantioselectivities in the catalyzed Diels–Alder reaction, which was the first successful demonstration of the transfer of chirality from DNA to a catalyzed reaction. This design was later also found to be efficient and selective in oxa-Michael additions, including the enantioselective conjugate addition of water [15, 16]. This is a reaction for which there is no alternative using "conventional" small-molecule catalysts. Arguably, this first-generation design is a representation of the Trojan horse approach, albeit that the intercalation is not a specific one, as for example, the streptavidin/biotin interaction.

The second-generation design was based on simple polypyridine copper(II) complexes such as copper(II)-1,10-phenanthroline (Cu-phen), copper-2,2′-bipyridine (Cu-bipy), and Cu-4,4′-dimethyl-2,2′-bipyridine (Cu-dmbipy). These complexes bind with moderate affinity to DNA, with K_D's in the sub-millimolar range. Especially the salmon testes DNA/Cu-dmbipy system has proven to be a remarkably versatile catalyst: moderate to high ee's and significant rate accelerations were obtained in a range of Lewis acid-catalyzed reactions, including Diels–Alder reactions [17], fluorinations [18], hydrolytic epoxide ring opening [19], Michael additions [20, 21], vinylogous Friedel–Crafts alkylations of indoles (FC reaction) [22] and tandem Friedel–Crafts alkylations/enantioselective protonation reactions (FC/EP reaction) [23].

An intriguing question was why are DNA-based artificial metalloenzymes such good catalysts. This was not a priori clear because of rather weak affinity of the copper complexes for salmon testes, which means that under conditions of catalysis ~10% of the copper complex is unbound and can catalyze the reaction in racemic fashion. This issue was resolved by comparing the yields and reaction rates of the reactions with DNA to those without, i.e. with Cu-dmbipy alone [23–25]. In almost

all reactions, a significant DNA-induced rate accelerations were observed, ranging from ~6-fold to almost 1000-fold, in the case of the FC/EP reaction. Hence, the DNA-bound catalyst outcompetes the unbound copper complex.

Also, salmon testes DNA as scaffold can be considered to have random DNA sequence: every section on the DNA has a different sequence and, hence, presents a different microenvironment for the reaction. A study of self-complementary synthetic oligonucleotides revealed that the highest enantioselectivities were obtained when stretches of the consecutive G's (or C's) were present [19, 24]. Moreover, these sequences also provided the highest rate acceleration in catalysis. Hence, the copper complexes residing in these G tracts dominate the outcome of the catalysis.

Next the binding of both the copper complexes and substrates was investigated [26, 27]. It was shown that Cu(II)-dmbipy is a groove binder, whereas other polypyridine complexes displayed partial or complete intercalative binding. Moreover, it was observed in both spectroscopic and kinetic studies that the substrates bind to DNA as well. For example, the indoles in the FC/EP reaction showed weak but significant binding [23]. In a study of the indole concentration dependence of catalytic activity, it was found that at higher concentrations saturation occurred and the activity started leveling off. Direct spectroscopic evidence for intercalative binding was obtained for azachalcone derivatives.

Combined these observations suggest that effective molarity effects are (partly) responsible for the DNA-acceleration effect. The substrates and copper complexes all bind to DNA, and the high local concentrations of all the components favor their interaction and, as a result, catalysis. However, binding alone is not enough; the substrates also have to encounter one another. This explains the success of the Cu(II)-dmbipy-based catalysts. Cu(II)-dmbipy is a groove binder and can move along the DNA grooves where it encounters the substrates and effects the reaction (Figure 38.1). Hence, an important requirement for the copper complex is that it binds to the DNA, but not too tightly; the interaction should still allow for dynamic behavior. This may be a bit counterintuitive initially, but it explains why a moderate affinity, DNA groove binding copper complex outperforms the stronger binding (partly) intercalating ones in catalysis.

The catalytic scope of DNA-based artificial metalloenzymes was expanded to carbene transfer reactions, i.e. cyclopropanations [29]. A copper complex of a large polypyridine ligand was reduced in situ and employed in intramolecular cyclopropanation, although the activity and enantioselectivity were moderate.

A second design made use of cationic iron porphyrins, in particular meso-tetrakis(*N*-alkylpyridyl)porphyrins [28]. The best results in catalysis were obtained in the case of the N-methyl substituents at the ortho position with respect to the porphyrin ring (Fe-2TMepyP). In this case, DNA-accelerated catalysis was observed, resulting in tens of turnovers and up to 53% ee. Surprisingly, no external reducing agents were needed, and the reactions could be performed under ambient atmosphere. This is in contrast to most other artificial cyclopropanase enzymes. It was found that the DNA-accelerating effect especially relates to the metal carbenoid formation step. It was proposed that this was due to effective molarity effects: high

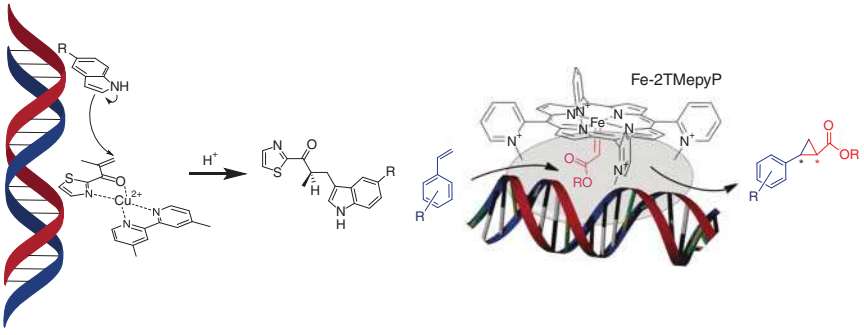

Figure 38.1 Left: Schematic representation of effective molarity effects in DNA-based catalytic FC/EP reactions and right: DNA-based catalytic enantioselective cyclopropanation. Source: Rioz-Martínez et al. [28]. Reproduced with permission of John Wiley & Sons.

local concentrations of the reagents in the hydrophobic areas between the bound iron porphyrin and the DNA (Figure 38.1).

38.3 Protein-Based Artificial Metalloenzymes

Supramolecular assembly has proven a powerful methodology for assembly of artificial metalloenzymes [1, 7]. However, relatively few examples rely on direct supramolecular assembly. One of the challenges is that it requires sufficiently strong interactions between protein and metal complex that do not block the catalytic site. Moreover, the binding site has to be sufficiently large to accommodate both the metal complex and still leave enough space for the substrates to bind and to undergo reaction. Early examples include the use of serum albumin proteins, which have a very large binding pocket and are well known to bind hydrophobic compounds [30, 31]. Another class is based on myoglobin. The heme cofactor is readily exchanged for another type of metal complex [32–36]. When using planar metal complexes, this leaves sufficient space for reactants, in particular after engineering of the distal site when using heme analogs.

We have introduced transcriptional regulators as an attractive class of protein scaffolds for artificial metalloenzymes design [37]. Our workhorse protein is the Lactococcal multidrug resistance Regulator (LmrR) [38, 39]. This protein is involved in the antibiotic resistance response of *Lactococcus lactis*. It is a homodimer that has an unusually large open hydrophobic pore at the dimer interface. In this pore hydrophobic compounds, e.g. drugs, can bind, which triggers the transcription/translation of membrane pumps. LmrR is a highly promiscuous binder: it is capable of binding many different compounds, especially those that are hydrophobic, planar, aromatic and cationic. A key role in the binding of these guests is played by two tryptophan residues in the middle of the pore, one from each monomer (W96 and W96′), which sandwich the guest molecule by using π-stacking interactions [39]. This binding mode is reminiscent of DNA intercalation, which is what first attracted our attention as we envisioned that copper(II) complexes

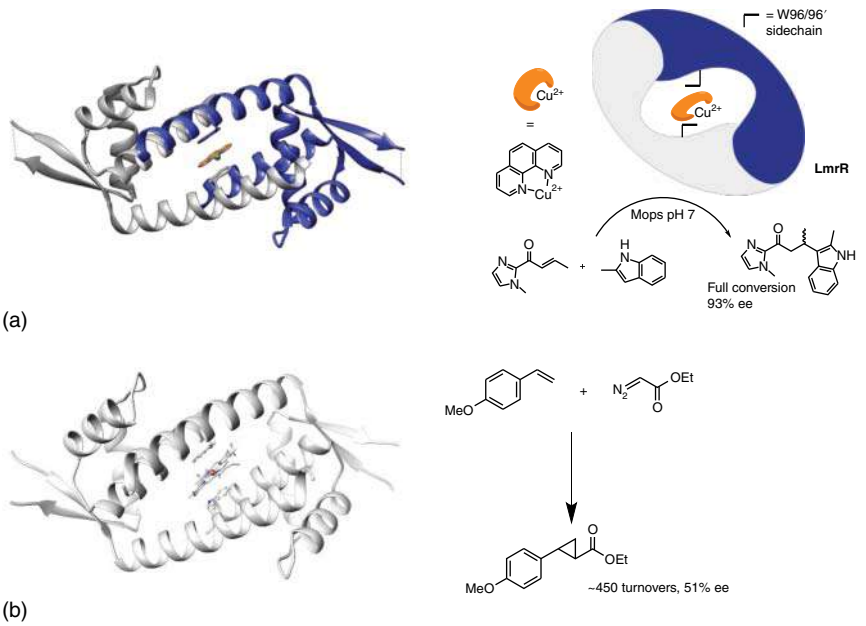

Figure 38.2 (a) X-ray crystal structure of LmrR with Cu-phen bound (PDB: 6R1L) and schematic representation of FC reaction catalyzed by the supramolecularly assembled LmrR-based artificial metalloenzymes. (b) X-ray crystal structure of LmrR with heme bound (PDB: 6FUU) and catalyzed cyclopropanation reaction.

of ligands such as 1,10-phenanthroline meet all the requirement for binding. We established that indeed Cu(II)-phenanthroline is capable of binding LmrR with micromolar affinity [40]. Based on fluorescence life time measurements it was concluded that indeed the copper complex binds to the central tryptophan moieties. Moreover, when mutating the central tryptophans for alanine (W96A), the binding affinity decreased with one order of magnitude. The binding was later confirmed by the x-ray crystal structure of LmrR with Cu(II)-phenanthroline bound (Figure 38.2) [41]. Indeed, the complex was found to reside between the two tryptophans with a distance typical of π stacking. The Cu(II) ion is facing the front entrance of the pore, where there are multiple glutamate and aspartate residues that provide electrostatic interactions, but no direct coordination was observed. This suggests the Cu(II) site is available for binding of substrates.

These self-assembled artificial metalloenzymes were evaluated in the catalysis of the vinylogous Friedel–Crafts alkylation reaction of indoles with α,β-unsaturated 2-acyl(*N*-methyl)imidazoles (FC reaction). The Friedel–Crafts product was obtained in good yields with excellent ee's of up to 93%. A significant protein-accelerated catalysis was found since without the protein present, i.e. with Cu(II)-phen alone, the yield was much lower. Also, using the LmrR_W96A mutant, a significantly lower yield and ee was observed, suggesting the catalysis indeed occurs by the Cu(II) complex bound between the tryptophans.

This was further supported by an alanine scan of the pore: the residues in or at the edge of the pore were mutated one-by-one to alanine (or another amino acid if the original residue was alanine), and the effect of this mutation in catalysis was determined. It was found that only mutation of residues around the central tryptophans had an effect, which could be either negative or positive, confirming the catalysis indeed takes place there. Interestingly, two mutations, i.e. M8A and A92E, already gave rise to markedly improved activity and selectivity. Especially the role of the A92E mutation was puzzling, as it also caused a dramatic increase in binding affinity of the Cu(II)-phenanthroline, with a K_D in the nanomolar range. A molecular dynamics (MD) study suggested that by changing alanine for glutamate, a hydrophobic interaction in the pore was disrupted and instead a new hydrogen bond interaction is formed. This causes that for significant amounts of time during the MD simulation, the pore adopts a more enlarged structure in which the indole rings of the central tryptophans become oriented parallel with respect to one another. This leads to a much better π-stacking interaction with the Cu(II) complex, which also is pulled more deeply into the pore.

The LmrR/Cu(II) assembly was also evaluated in a related reaction, the tandem Friedel–Crafts/enantioselective protonation (FC/EP reaction). In this reaction, an enone with a methyl substituent at the α position was used. This means that the chiral center is not created in the conjugate addition step, but in the subsequent protonation of the enolate intermediate. Proton transfer reactions are highly challenging because of the small size of a proton and the high rate of proton transfer processes. Yet, good yields and enantioselectivities were achieved in this reaction as well. This reaction proved critically dependent on the presence of protein as Cu(II)-phen proved to be minimally active. Interestingly, the same alanine scan of the pore revealed a completely different behavior: almost no effects were observed in catalysis upon mutation. The only mutation that had a noticeable negative effect was A92E, i.e. the same mutation that improved the catalysis in the FC reaction. The W96A mutation only had a marginal effect on the catalysis. This suggested that, in contrast to the FC reaction, this reaction does not occur in the pore close to the tryptophan residues, but somewhere else in or on the protein.

Competition experiments between α and β substituted enones showed that using the wild-type protein, both FC and FC/EP reactions occurred, albeit with a preference for the former. Introducing a single mutation, A92E, resulted in almost complete selectivity for the FC reaction. In contrast, the W96A mutation caused the FC/EP reaction to become the dominant reaction.

This behavior was rationalized by considering the dynamics of the binding of the metal cofactor. The K_D of the Cu(II) complex to the wild-type protein is in the micromolar range. Under the reaction conditions most, but not all of the complex is bound in the pore, where the FC reaction is the dominant reaction. A small but nonneglible fraction can bind at other locations of the protein, where the FC/EP reaction is dominant. The A92E mutation increases the binding affinity for the pore so much that no complex is available anymore to bind anywhere else. Hence, this mutant has become specialized for the FC reaction. In contrast, the W96A mutation abolishes the Cu(II)-phen-binding site. Hence, the fraction available for binding at the secondary locations is much higher, resulting in the FC/EP reaction becoming dominant.

LmrR has proven to be not only a good scaffold for copper(II) complexes, but the promiscuous pore also proved capable of binding heme with high affinity. The resulting artificial heme enzyme proved active in the abiological cyclopropanation of styrene derivatives with diazoethyl esters, giving rise to several hundreds of turnovers and up to 51% ee [42].

The X-ray crystal structure showed the heme to bind in the pocket, with the iron center between the indole moieties from the central tryptophans. No additional axial ligand was found. Based on this structure, it was hard to understand the catalytic activity, as the catalytic iron center was not accessible. An MD study showed the activity to be the result of the conformational dynamics of the LmrR protein: during significant amounts of time the α4 helix that lines the front entrance moves up and, as a result, one of the indole moieties moves away from the distal site toward the solvent. This makes the iron center accessible for the ethyl diazoacetate, allowing the iron-carbene intermediate to be formed. Moreover, the space created is large enough to also allow binding of the styrene. Even the calculated transition state of the cyclopropanation reaction nicely fitted in this cavity. This study emphasized the importance of conformational dynamics in enzyme design, an issue that is often ignored.

38.4 Synergistic Catalysis with Artificial Metalloenzymes

In parallel to the development of the supramolecular approach to the assembly of LmrR-based artificial metalloenzymes, we developed artificial metalloenzymes comprising genetically encoded noncanonical amino acids by using stop codon suppression methodology. First, this was used to incorporate bipyridine and hydroxyquinoline containing amino acids that can act as ligand for catalytic metal ions [4, 43–45]. Later, this was expanded to *p*-aminophenylalanine (pAF) that can engage in organocatalytic iminium ion activation mechanisms [46]. An attractive feature of using noncanonical amino acids is that they can be introduced site specifically by encoding them into the DNA using the amber stop codon. This allows the use of noncanonical amino acids in combination with supramolecularly introduced metal complexes, an approach known as synergistic catalysis. Using this principle, we designed an artificial enzyme that comprises two different abiological catalytic moieties [47]. It was shown that these can act in a synergistic fashion to achieve catalysis of Michael additions with high activity and ee's up to 98% ee (Figure 38.3). The pAF residue at position V15 in LmrR (LmrR_V15pAF) was used to activate the electrophile, i.e. the α,β-unsaturated aldehyde, by iminium ion formation. Simultaneously, the supramolecularly bound Cu-phen activates the nucleophile, by catalyzing the enolization on a 2-acyl(*N*-methyl)imidazole. Taking advantage of the binding of Cu-phen between the two central tryptophans, the nucleophile in this manner is delivered efficiently to one prochiral face of the α,β-unsaturated aldehyde. It was shown that indeed all the components, i.e. LmrR, pAF at position 15 and Cu-phen had to be present to achieve catalysis. A subsequent genetic optimization resulted in a mutant LmrR_V15pAF_M8A that gave a dr of 5 : 1 and an ee of up to >99% for the major diastereomer.

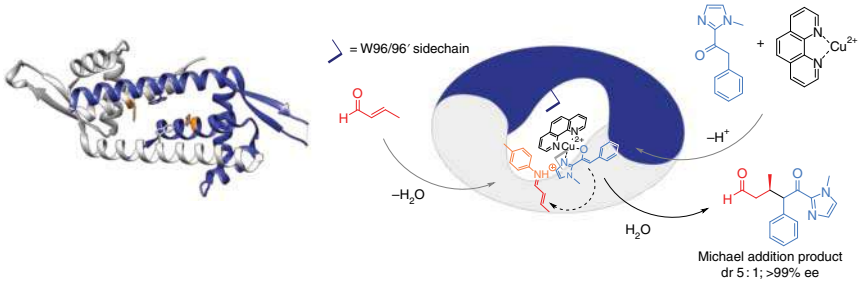

Figure 38.3 X-ray crystal structure of LmrR_V15pAF (PDB: 6I8N) [48] and schematic representation of the Michael addition reaction catalyzed by the LmrR-based synergistic artificial enzyme.

38.5 In Vivo Assembly and Application of LmrR-Based Artificial Metalloenzymes

The LmrR artificial metalloenzymes can also be assembled in vivo and applied in whole cell biocatalysis [49]. Assembly of artificial metalloenzymes had been achieved before in the periplasm and on the cell surface [50–52]. The cytoplasm is a more challenging environment, not in the least because of the presence of compounds such as glutathione that inactivate transition metal catalysts. Addition of Cu(II)-phen to *Escherichia coli* cells expressing LmrR was shown to give rise to assembly of the artificial metalloenzymes. Cell fractionation studies proved assembly indeed occurred in the cytoplasm. This was confirmed by an in-cell NMR study, which showed the same changes in the NMR as a result of binding of the paramagnetic Cu(II) complex occurred in vitro and in vivo. The cells containing the assembled artificial metalloenzymes were applied in the FC reaction of 2-methylindole and α,β-unsaturated 2-acyl(*N*-methyl)imidazoles. Compared to the isolated artificial metalloenzymes in vitro, the whole-cell catalysts gave rise to somewhat lower yields and ee's. But control experiments with cells expressing the unrelated protein SUMO, or in the absence of Cu-phen showed very little to no activity and selectivity. Moreover, testing the various mutants from the alanine scanning showed that the trends in activity and selectivity observed in vivo matched those of the artificial metalloenzymes in vitro. This suggested the feasibility of performing a directed evolution study using whole cells. Randomizing seven positions in the pore gave rise to the mutant LmrR_A92E_M8D that showed significantly increased activity and selectivity on various different indoles.

The fact that these artificial metalloenzymes were active in the cytoplasm was highly surprising. Control experiments in vitro showed that the artificial metalloenzymes are tolerant to millimolar concentrations of glutathione; only minor effects on catalysis were observed. It was proposed that the LmrR protein protects the copper(II) ion from reaction with glutathione. This may be due to the fact that the negatively charged front entrance provides electrostatic repulsion for the also negatively charged glutathione.

The possibility to assemble active artificial metalloenzymes in vivo is an important step toward the long-term goal of creating a "hybrid metabolism," that is, a biosynthetic pathway in vivo that is supplemented with unnatural chemistry [53].

38.6 Conclusions

Supramolecular assembly by using direct interactions between the catalytic metal complex and the biomolecular scaffold has proven to be a powerful approach to the creation of artificial metalloenzymes. This approach stands out due to its versatility and simplicity, as it relies on self-assembly, a process that is quite well understood. But it is becoming ever clearer that this should not be viewed as a static process. Indeed, among other things, our combined work on DNA and LmrR-based artificial metalloenzymes has revealed an important role for dynamics: both in binding the metal cofactor as in the biomolecular scaffold. This is an issue that has been mostly ignored to date, partly because it is also difficult to include this in the design process, but it has proven key to achieve high activities and selectivities in many systems.

Recent development in supramolecular assembly of artificial metalloenzymes is the combination with covalent anchoring approaches, especially the genetically encoded unnatural amino acids to achieve synergistic catalysis. This allows for an exquisite level of control over positioning, which results in high activities and selectivities.

Finally, the recent demonstration of in vivo assembly and application of supramolecular LmrR-based artificial metalloenzymes are an important step toward the next frontier, which is the integration of abiotic catalytic reactions in biosynthesis, leading to a "hybrid metabolism."

References

1 Schwizer, F., Okamoto, Y., Heinisch, T. et al. (2018). Artificial metalloenzymes: reaction scope and optimization strategies. *Chem. Rev.* 118 (1): 142–231.

2 Heinisch, T. and Ward, T.R. (2010). Design strategies for the creation of artificial metalloenzymes. *Curr. Opin. Chem. Biol.* 14 (2): 184–199.

3 Rosati, F. and Roelfes, G. (2010). Artificial metalloenzymes. *ChemCatChem* 2 (8): 916–927.

4 Drienovska, I. and Roelfes, G. (2020). Expanding the enzyme universe with genetically encoded unnatural amino acids. *Nat. Catal.* 3 (3): 193–202.

5 Yu, Y., Hu, C., Xia, L., and Wang, J. (2018). Artificial metalloenzyme design with unnatural amino acids and non-native cofactors. *ACS Catal.* 8 (3): 1851–1863.

6 Wilson, M. and Whitesides, G. (1978). Conversion of a protein to a homogeneous asymmetric hydrogenation catalyst by site-specific modification with a diphosphinerhodium(I) moiety. *J. Am. Chem. Soc.* 100 (1): 306–307.

7 Heinisch, T. and Ward, T.R. (2016). Artificial metalloenzymes based on the biotin-streptavidin technology: challenges and opportunities. *Acc. Chem. Res.* 49 (9): 1711–1721.

8 Liang, A.D., Serrano-Plana, J., Peterson, R.L., and Ward, T.R. (2019). Artificial metalloenzymes based on the biotin-streptavidin technology: enzymatic cascades and directed evolution. *Acc. Chem. Res.* 52 (3): 585–595.

9 Rioz-Martinez, A. and Roelfes, G. (2015). DNA-based hybrid catalysis. *Curr. Opin. Chem. Biol.* 25: 80–87.

10 Boersma, A.J., Megens, R.P., Feringa, B.L., and Roelfes, G. (2010). DNA-based asymmetric catalysis. *Chem. Soc. Rev.* 39 (6): 2083–2092.

11 Yum, J.H., Park, S., and Sugiyama, H. (2019). G-quadruplexes as versatile scaffolds for catalysis. *Org. Biomol. Chem.* 17 (44): 9547–9561.

12 Wang, C., Jia, G., Li, Y. et al. (2013). Na^+/K^+ switch of enantioselectivity in G-quadruplex DNA-based catalysis. *Chem. Commun.* 49 (95): 11161–11163.

13 Duchemin, N., Heath-Apostolopoulos, I., Smietana, M., and Arseniyadis, S. (2017). A decade of DNA-hybrid catalysis: from innovation to comprehension. *Org. Biomol. Chem.* 15 (34): 7072–7087.

14 Roelfes, G. and Feringa, B. (2005). DNA-based asymmetric catalysis. *Angew. Chem. Int. Ed.* 44 (21): 3230–3232.

15 Boersma, A.J., Coquiere, D., Geerdink, D. et al. (2010). Catalytic enantioselective syn hydration of enones in water using a DNA-based catalyst. *Nat. Chem.* 2 (11): 991–995.

16 Megens, R.P. and Roelfes, G. (2012). DNA-based catalytic enantioselective intermolecular oxa-Michael addition reactions. *Chem. Commun.* 48 (51): 6366–6368.

17 Roelfes, G., Boersma, A.J., and Feringa, B.L. (2006). Highly enantioselective DNA-based catalysis. *Chem. Commun.* (6): 635–637.

18 Shibata, N., Yasui, H., Nakamura, S., and Toru, T. (2007). DNA-mediated enantioselective carbon-fluorine bond formation. *Synlett* 24 (7): 1153–1157.

19 Dijk, E.W., Feringa, B.L., and Roelfes, G. (2008). DNA-based hydrolytic kinetic resolution of epoxides. *Tetrahedron: Asymmetry* 19 (20): 2374–2377.

20 Coquiere, D., Feringa, B.L., and Roelfes, G. (2007). DNA-based catalytic enantioselective Michael reactions in water. *Angew. Chem. Int. Ed.* 46 (48): 9308–9311.

21 Wang, J., Benedetti, E., Bethge, L. et al. (2013). DNA vs. mirror-image DNA: a universal approach to tune the absolute configuration in DNA-based asymmetric catalysis. *Angew. Chem. Int. Ed.* 52 (44): 11546–11549.

22 Boersma, A.J., Feringa, B.L., and Roelfes, G. (2009). Enantioselective Friedel–Crafts reactions in water using a DNA-based catalyst. *Angew. Chem. Int. Ed.* 48 (18): 3346–3348.

23 Garcia-Fernandez, A., Megens, R.P., Villarino, L., and Roelfes, G. (2016). DNA-accelerated copper catalysis of Friedel–Crafts conjugate addition/enantioselective protonation reactions in water. *J. Am. Chem. Soc.* 138 (50): 16308–16314.

24 Boersma, A.J., Klijn, J.E., Feringa, B.L., and Roelfes, G. (2008). DNA-based asymmetric catalysis: sequence-dependent rate acceleration and enantioselectivity. *J. Am. Chem. Soc.* 130 (35): 11783–11790.

25 Dijk, E.W., Boersma, A.J., Feringa, B.L., and Roelfes, G. (2010). On the role of DNA in DNA-based catalytic enantioselective conjugate addition reactions. *Org. Biomol. Chem.* 8 (17): 3868–3873.

26 Draksharapu, A., Boersma, A.J., Leising, M. et al. (2015). Binding of copper(II) polypyridyl complexes to DNA and consequences for DNA-based asymmetric catalysis. *Dalton Trans.* 44 (8): 3647–3655.

27 Draksharapu, A., Boersma, A.J., Browne, W.R., and Roelfes, G. (2015). Characterisation of the interactions between substrate, copper(II) complex and DNA and their role in rate acceleration in DNA-based asymmetric catalysis. *Dalton Trans.* 44 (8): 3656–3663.

28 Rioz-Martinez, A., Oelerich, J., Segaud, N., and Roelfes, G. (2016). DNA-accelerated catalysis of carbene-transfer reactions by a DNA/cationic iron porphyrin hybrid. *Angew. Chem. Int. Ed.* 55 (45): 14136–14140.

29 Oelerich, J. and Roelfes, G. (2013). DNA-based asymmetric organometallic catalysis in water. *Chem. Sci.* 4 (5): 2013–2017.

30 Mahammed, A. and Gross, Z. (2005). Albumin-conjugated corrole metal complexes: extremely simple yet very efficient biomimetic oxidation systems. *J. Am. Chem. Soc.* 127 (9): 2883–2887.

31 Reetz, M. and Jiao, N. (2006). Copper-phthalocyanine conjugates of serum albumins as enantioselective catalysts in Diels–Alder reactions. *Angew. Chem. Int. Ed.* 45 (15): 2416–2419.

32 Ohashi, M., Koshiyama, T., Ueno, T. et al. (2003). Preparation of artificial metalloenzymes by insertion of chromium(III) Schiff base complexes into apomyoglobin mutants. *Angew. Chem. Int. Ed.* 42 (9): 1005–1008.

33 Sreenilayam, G., Moore, E.J., Steck, V., and Fasan, R. (2017). Metal substitution modulates the reactivity and extends the reaction scope of myoglobin carbene transfer catalysts. *Adv. Synth. Catal.* 359 (12): 2076–2089.

34 Sreenilayam, G., Moore, E.J., Steck, V., and Fasan, R. (2017). Stereoselective olefin cyclopropanation under aerobic conditions with an artificial enzyme incorporating an iron-chlorin e6 cofactor. *Acs Catal.* 7 (11): 7629–7633.

35 Ohora, K., Meichin, H., Zhao, L. et al. (2017). Catalytic cyclopropanation by myoglobin reconstituted with iron porphycene: acceleration of catalysis due to rapid formation of the carbene species. *J. Am. Chem. Soc.* 139 (48): 17265–17268.

36 Key, H.M., Dydio, P., Clark, D.S., and Hartwig, J.F. (2016). Abiological catalysis by artificial haem proteins containing noble metals in place of iron. *Nature* 534 (7608): 534–537.

37 Roelfes, G. (2019). LmrR: a privileged scaffold for artificial metalloenzymes. *Acc. Chem. Res.* 52: 545–556.

38 Agustiandari, H., Lubelski, J., van den Berg van Saparoea, H.B. et al. (2008). LmrR is a transcriptional repressor of expression of the multidrug ABC transporter LmrCD in *Lactococcus lactis*. *J. Bacteriol.* 190 (2): 759–763.

39 Madoori, P.K., Agustiandari, H., Driessen, A.J.M., and Thunnissen, A.W.H. (2009). Structure of the transcriptional regulator LmrR and its mechanism of multidrug recognition. *EMBO J.* 28 (2): 156–166.

40 Bos, J., Browne, W.R., Driessen, A.J.M., and Roelfes, G. (2015). Supramolecular assembly of artificial metalloenzymes based on the dimeric protein LmrR as promiscuous scaffold. *J. Am. Chem. Soc.* 137 (31): 9796–9799.

41 Villarino, L., Chordia, S., Alonso-Cotchico, L. et al. (2020). Cofactor binding dynamics influence the catalytic activity and selectivity of an artificial metalloenzyme. *ACS Catal.* 10 (20): 11783–11790.

42 Villarino, L., Splan, K.E., Reddem, E. et al. (2018). An artificial heme enzyme for cyclopropanation reactions. *Angew. Chem. Int. Ed.* 57 (26): 7785–7789.

43 Drienovska, I., Rioz-Martinez, A., Draksharapu, A., and Roelfes, G. (2015). Novel artificial metalloenzymes by in vivo incorporation of metal-binding unnatural amino acids. *Chem. Sci.* 6 (1): 770–776.

44 Drienovska, I., Alonso-Cotchico, L., Vidossich, P. et al. (2017). Design of an enantioselective artificial metallo-hydratase enzyme containing an unnatural metal-binding amino acid. *Chem. Sci.* 8 (10): 7228–7235.

45 Drienovska, I., Scheele, R.A., Gutierrez de Souza, C., and Roelfes, G.A. (2020). Hydroxyquinoline-based unnatural amino acid for the design of novel artificial metalloenzymes. *ChemBioChem* 21 (21): 3077–3081.

46 Drienovska, I., Mayer, C., Dulson, C., and Roelfes, G. (2018). A designer enzyme for hydrazone and oxime formation featuring an unnatural catalytic aniline residue. *Nat. Chem.* 10 (9): 946–952.

47 Zhou, Z. and Roelfes, G. (2020). Synergistic catalysis in an artificial enzyme by simultaneous action of two abiological catalytic sites. *Nat. Catal.* 3 (3): 289–294.

48 Mayer, C., Dulson, C., Reddem, E. et al. (2019). Directed evolution of a designer enzyme featuring an unnatural catalytic amino acid. *Angew. Chem. Int. Ed.* 58 (7): 2083–2087.

49 Chordia, S., Narasimhan, S., Lucini Paioni, A. et al. (2021). In vivo assembly of artificial metalloenzymes and application in whole-cell biocatalysis. *Angew. Chem. Int. Ed.* 60: 5913–5920.

50 Jeschek, M., Reuter, R., Heinisch, T. et al. (2016). Directed evolution of artificial metalloenzymes for in vivo metathesis. *Nature* 537 (7622): –661, 665.

51 Grimm, A.R., Sauer, D.F., Polen, T. et al. (2018). A whole cell *E. coli* display platform for artificial metalloenzymes: poly(phenylacetylene) production with a rhodium-nitrobindin metalloprotein. *ACS Catal.* 8 (3): 2611–2614.

52 Ghattas, W., Dubosclard, V., Wick, A. et al. (2018). Receptor-based artificial metalloenzymes on living human cells. *J. Am. Chem. Soc.* 140 (28): 8756–8762.

53 Jeschek, M., Panke, S., and Ward, T.R. (2018). Artificial metalloenzymes on the verge of new-to-nature metabolism. *Trends Biotechnol.* 36 (1): 60–72.

Part VII

Supramolecular Allosteric Catalysts and Replicators

39

Switchable Catalysis Using Allosteric Effects

Michael Schmittel

University of Siegen, Department of Chemistry-Biology, Adolf-Reichwein Str. 2, D-57068, Siegen, Germany

39.1 Introduction

The crisp and general definition of allostery by Hilser [1] "*Allostery is the process by which biological macromolecules transmit the effect of binding at one site to another, often distal, functional site, allowing for regulation of activity*" spotlights the fact that allosteric effects, mostly in proteins, play a crucial role in controlling cellular pathways [2, 3]. A detailed systematics by Nussinov and coworkers [2] describing the relevant molecular mechanisms lastly provides a useful starting point for any allosteric system design.

Implementation of allosteric effects to regulate artificial catalysis in an ON/OFF or UP/DOWN manner has led to spectacular contributions from many groups [4–9], including Rebek and Würthner [10], Krämer and coworkers [11], Mirkin and coworkers [12, 13], Leigh and coworkers [5, 14], and Feringa and coworkers [5]. However, most of this work has been focusing on covalent or interlocked switches and even on knots [15], but not on supramolecular devices [16].

Impressive contributions by Mirkin have demonstrated the rewarding prospects of a supramolecular approach [17, 18]. Using his weak-link strategy [12, 17], a squaramide unit in the catalytic monomer was blocked from catalyzing a Friedel–Crafts reaction after opening the remote weak-link node. In the resulting semi-open structure, an ester group was sterically and conformationally freed for hydrogen bonding at the catalytic squaramide unit, a process that led to oligomerization and shut down of catalysis. Similarly, a Diels–Alder reaction was regulated [18]. Both processes mimic a strategy used by Nature, as enzyme oligomerization [2] involving hydrogen bonding at the active site is a frequently encountered motif for regulating catalytic activity [19].

What are the particular challenges in setting up allosteric control of catalysis using supramolecular multicomponent systems? Since the latter are held together by weak interactions, it is a nontrivial task to implement robust, reproducible, and reversible conformational transmission of the effector's binding event to the remote functional site. In the following, we will present two of our strategies.

Supramolecular Catalysis: New Directions and Developments, First Edition.
Edited by Piet W.N.M. van Leeuwen and Matthieu Raynal.

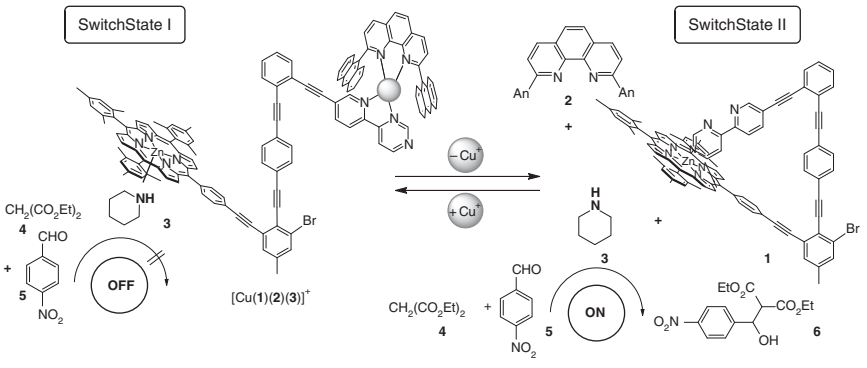

Figure 39.1 A nanoswitch regulating a Knoevenagel addition reaction. Source: Schmittel et al. [22].

39.2 Allosteric Regulation at Zinc Porphyrin Stations by Catalyst Release

The key feature of our first approach to allosteric regulation of catalysis is based on the firm but reversible binding of a catalytically active nitrogen heterocycle at a zinc porphyrin (ZnPor) site. A chemical input that leads to the relocation of an intramolecular arm onto the ZnPor unit causes the release of the catalyst from this site [20]. A significant variety of nitrogen heterocycles (= cat)$^+$ bind to ZnPor sites so strongly, e.g. piperidine ($\log K = 5.2$) [21], that at a given temperature the thermal dissociation of the cat→ZnPor complex is insignificant for promoting any catalytic transformation.

To illustrate the mode of regulation, let us have a look at the operation of nanoswitch **1** [22]. In SwitchState I, the toggling arm of nanoswitch **1** is firmly linked via an intermolecular heteroleptic copper(I) complex to phenanthroline **2** (Figure 39.1). At the same time, the ZnPor moiety is available for binding piperidine (**3**) that was selected as catalyst for the Knoevenagel reaction between diethyl malonate (**4**) and aldehyde **5**. In this state, no catalysis was registered. Upon removing the copper(I) ions from [Cu(**1**)(**2**)(**3**)]$^+$ by cyclam, the four-component system decayed and the azabipyridine toggling arm progressed onto the ZnPor unit, where it liberated piperidine (**3**) into solution that for its part turned on the Knoevenagel reaction (SwitchState II). Using alternate stoichiometric additions of copper(I) and cyclam, ON/OFF regulation was achieved over three cycles without loss of catalytic activity.

Intrasupramolecular walking was identified as another strategy to release and capture an organocatalyst at a ZnPor site. In the two-component assembly [**7**·**8**] (Figure 39.2), obtained from biped **8** and the ligand **7** [23], both ZnPor units of **7** were occupied by the picoline terminals of **8** and thus the added *N*-methyl pyrrolidine (**9**) was able to catalyze the conjugate addition between thiophenol and cyclopentenone **11**. Two sequential additions of 1 equiv of copper(I) ions made the biped walk with its picoline feet to the first and then second filled copper(I) phenanthroline station

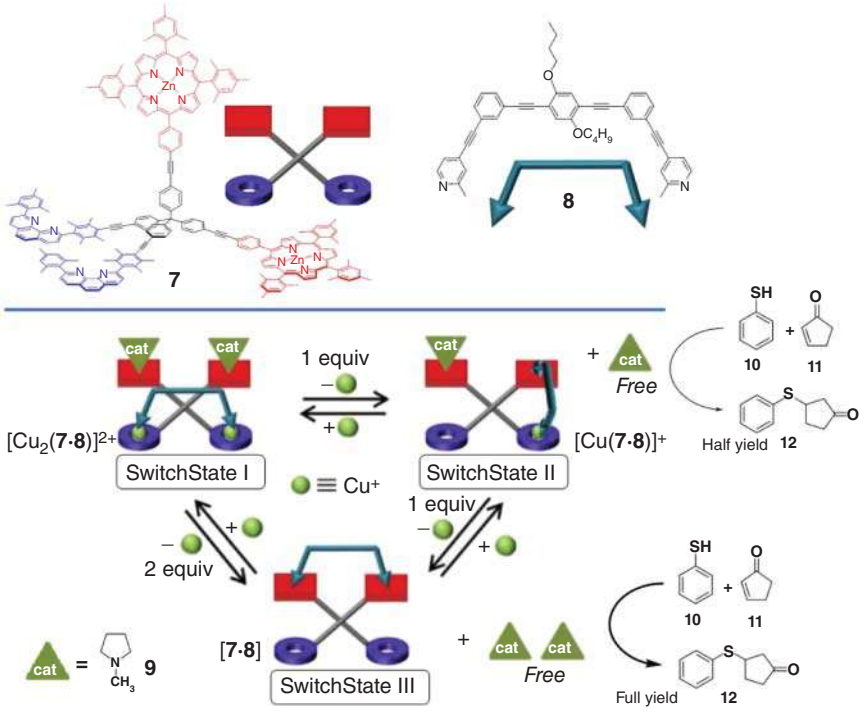

Figure 39.2 A multicomponent walker used for the stepwise regulation of a conjugate addition. Source: Adapted from Mittal et al. [23].

(Figure 39.2). The concomitant detachment of the feet from the ZnPor stations led to a proportionate binding of the catalyst at the freed ZnPor sites. The walking process was reversed by capturing the copper(I) ions with the electron-rich 2-ferrocenyl-9-mesityl-1,10-phenanthroline. Hence, in the forward walking, the transformation of $[\mathbf{7}\cdot\mathbf{8}] \rightarrow [Cu(\mathbf{7}\cdot\mathbf{8})]^{+} \rightarrow [Cu_2(\mathbf{7}\cdot\mathbf{8})]^{2+}$ led to an increasing seizure of the catalyst **9**, whereas the return process $[Cu_2(\mathbf{7}\cdot\mathbf{8})]^{2+} \rightarrow [Cu(\mathbf{7}\cdot\mathbf{8})]^{+} \rightarrow [\mathbf{7}\cdot\mathbf{8}]$ liberated *N*-methyl pyrrolidine (**9**). The effect on the catalytic reaction was that in SwitchState III the yield of **12** was roughly double that of SwitchState II, whereas in SwitchState I the conjugate addition between thiophenol (**10**) and cyclopentenone **11** was off [23].

An uncommon form of allosteric regulation [2] was achieved by the dimerization of $[Cu(\mathbf{13})(\mathbf{14})(\mathbf{15})]^{+}$ (Figure 39.3). In this four-component aggregate, the biped **14** with its two pyridine feet was bound to **13** via one copper(I) complexation and one N_{py}→ZnPor interaction [24]. The remaining ZnPor unit was utilized to bind the organocatalyst, pyrrolidine (**15**). In this state, catalysis of the Michael addition furnishing **18** was shut down. Upon removal of 1 equiv of copper(I) from 2 equiv of $[Cu(\mathbf{13})(\mathbf{14})(\mathbf{15})]^{+}$ a resorting took place that afforded the "dimeric" complex $[Cu(\mathbf{13})_2(\mathbf{14})_2]^{2+}$. Since all ZnPor units were occupied, the formerly bound catalyst **15** was now released into solution and catalyzed the formation of **18**. This catalytic

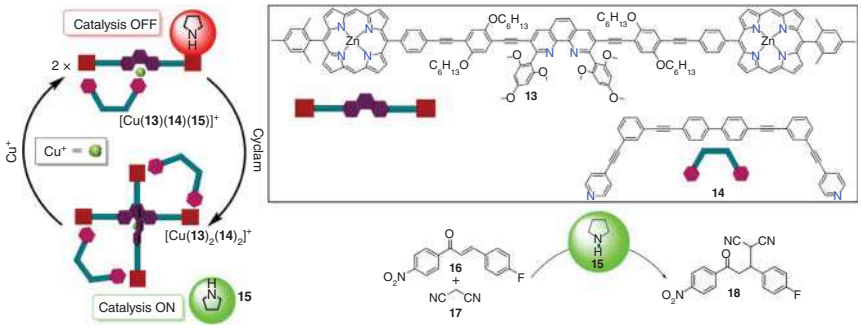

Figure 39.3 A dimerization reaction turning on a Michael addition. Source: Adapted from Saha et al. [24].

machinery combining dimerization and allosteric OFF/ON control of catalyst release worked well over two full cycles.

Already the walker in Figure 39.2, where the catalytic conversion was changed step by step in the walking process, represented a three-state switchable system. It was thus tempting to design a three-state switchable system that would even allow control of two different catalytic reactions. The key for achieving such a performance was the highly controlled triple self-sorting of a 10-component ensemble [25] (Figure 39.4).

At the center of this catalytic machinery, nanoswitch **23** was toggled between an intramolecular copper(I) complex (see $[Cu(\mathbf{23})]^+$ in SwitchStates I & II) and a three-component aggregate (see $[Cu(\mathbf{22})(\mathbf{23})]^+$ in SwitchState III). Intramolecular binding of the azabipyridine arm at the ZnPor unit in **23** was expected to release piperidine (**3**), i.e. the catalyst of the Knoevenagel reaction between **4** and **5**. Parallel, a click reaction was regulated in an ON/OFF manner by toggling between $[Cu(\mathbf{22})]^+$ (active catalyst) and $[Cu(\mathbf{22})_2]^+$ (inactive). In SwitchState I, a twofold completive [26] self-sorting of the key constituents **22**, **23** and Cu^+ = 1 : 1 : 2 furnished the complexes $[Cu(\mathbf{22})]^+$ and $[Cu(\mathbf{23})]^+$ (1 : 1). As a result, the click catalyzed process $\mathbf{19} + \mathbf{20} \rightarrow \mathbf{21}$ was turned ON, whereas the firm binding of piperidine (**3**) at $[Cu(\mathbf{23})]^+$ prevented any organocatalysis by **3**. Addition of phenanthroline **22** required a self-sorting of **22**, **23** and Cu^+ at a 2 : 1 : 2 ratio and led to SwitchState II. As this process afforded $[Cu(\mathbf{23})]^+ + [Cu(\mathbf{22})_2]^+$, the click catalysis was turned OFF due to the shielding of the copper(I) inside of complex $[Cu(\mathbf{22})_2]^+$. Another addition of **22** initiated a third self-sorting of **22**, **23** and Cu^+ now at a ratio of (3 : 1 : 2). Notably, aside of $[Cu(\mathbf{22})_2]^+$ this process afforded the intermolecular complex $[Cu(\mathbf{22})(\mathbf{23})]^+$, in which the azabipyridine arm toggled onto the ZnPor unit thus freeing the piperidine and turning ON the Knoevenagel reaction. The cycle was restarted (SwitchState III→I) by addition of 1 equiv of Cu^+ [25].

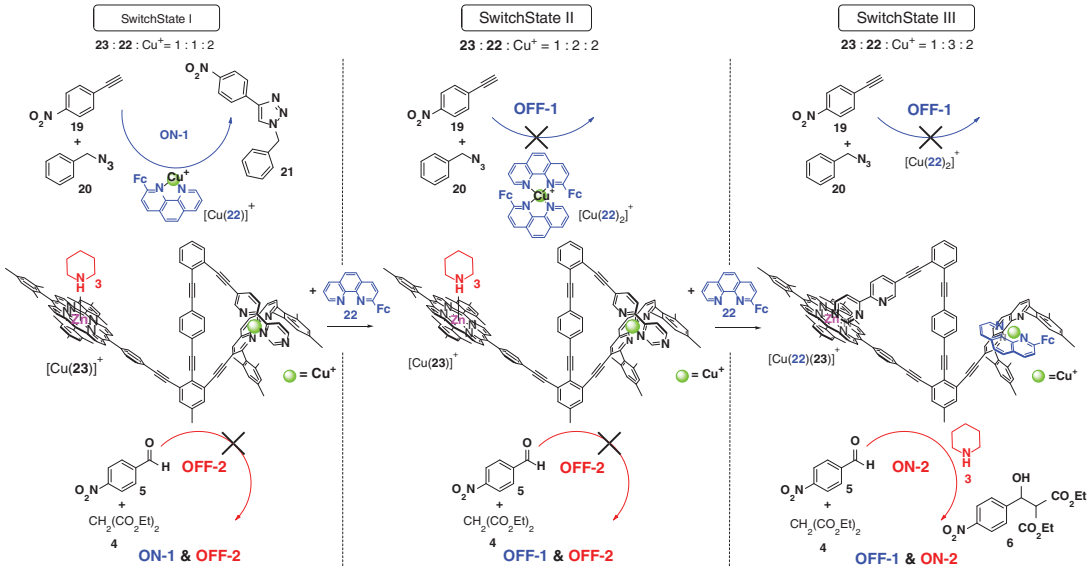

Figure 39.4 A three-state switching process regulating two catalytic processes. Source: Based on De et al. [25].

39.3 Allosteric Regulation of Catalysis at Copper(I) Sites

While we discussed above the release of an organocatalyst into solution, the ensuing examples will highlight how a catalytic copper(I) site is exposed after adding a chemical input that triggers the desired allosteric effects via dimerization.

The following ON/OFF toggling of catalysis is based on the dimerization of switch $[Cu(\mathbf{24})]^+$ [27]. When the intramolecular copper(I) complex $[Cu(\mathbf{24})]^+$, readily formed by adding copper(I) ions to ligand **24** (SwitchState I), was treated with 0.5 equiv of $Fe(ClO_4)_2$ the complexation afforded the "dimeric" complex $[Fe(Cu(\mathbf{24}))_2]^{4+}$ (SwitchState II). The highly exergonic complexation in the iron(II) bis-terpyridine interaction readily furnished the driving force for cleavage of the weaker copper(I) complex in $[Cu(\mathbf{24})]^+$. 4-*N*,*N*-Dimethylamino-2,2′:6′,2″-terpyridine as another strong complexation agent for iron(II) regenerated SwitchState I (Figure 39.5).

In the dimeric complex $[Fe(Cu(\mathbf{24}))_2]^{4+}$ both copper(I) ions were coordinatively unsaturated, an aspect that suggested to utilize them for driving the copper(I)-catalyzed cyclopropanation of cyclooctene (**25**) with the help of ethyl diazoacetate (**26**). As expected, the cyclopropanation was OFF in SwitchState I since the copper(I) was fully shielded inside the binding site of $[Cu(\mathbf{24})]^+$, whereas addition of 0.5 equiv of $Fe(ClO_4)_2$ led to formation of cyclopropane **27**. The modus operandi serves as a showcase how a metal-ion input (here Fe^{2+}) can turn ON catalysis by an entirely different metal ion. Moreover, the mechanism is similar to that of the (SARS-CoV) 3C-like protease (3Clpro) [28]. This enzyme is equally inactive in the monomeric state as its catalytic site is completely blocked, whereas in the homodimeric state the enzyme is functional owing to exposure of the active site.

A different sort of allosterically regulated catalysis was described recently [29] in a case of proximity catalysis that alike was based on the dimerization of switches. When the copper(I)-loaded switch $[Cu_2(\mathbf{28})]^{2+}$ was exposed to

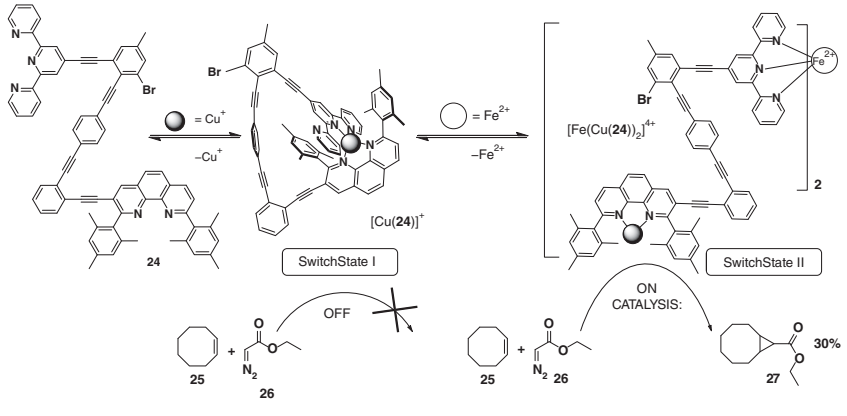

Figure 39.5 Reversible dimerization driving a copper(I)-catalyzed cyclopropanation. Source: Based on De et al. [27].

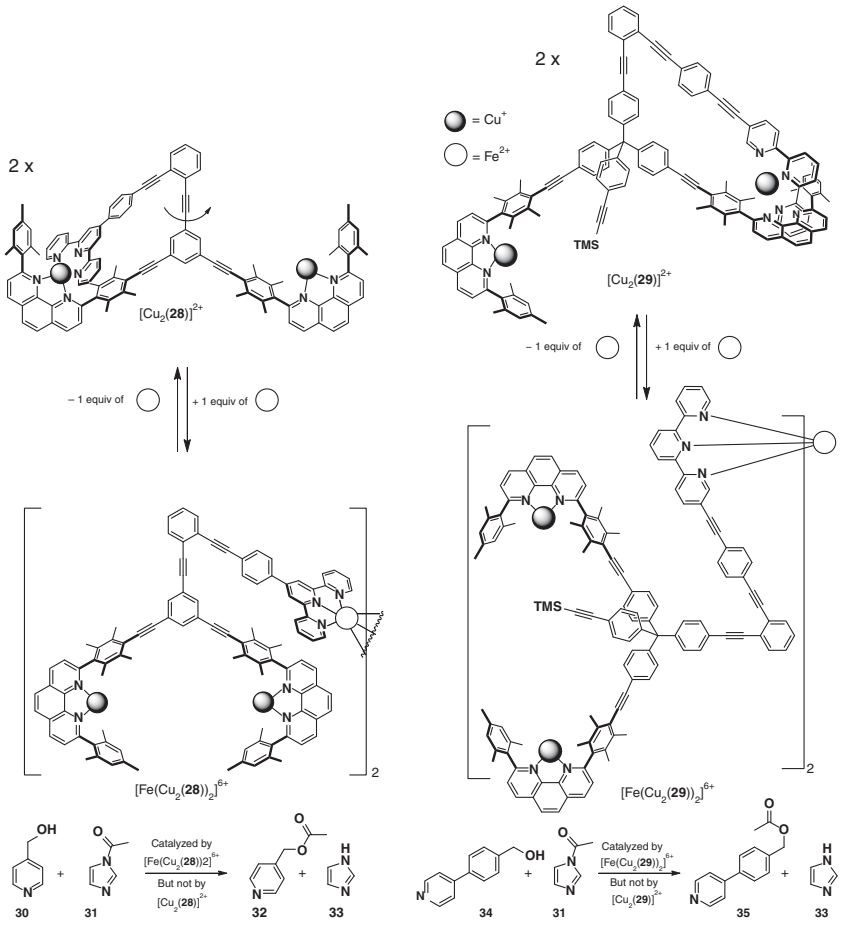

Figure 39.6 Reversible proximity catalysis of a catalyst duo. Source: Goswami et al. [29].

pyridine methanol (**30**) and the acetylation agent **31** (Figure 39.6), no reaction was registered. However, upon addition of iron(II) (0.5 equiv with regard to $[Cu_2(\mathbf{28})]^{2+}$), the dimeric complex $[Fe(Cu_2(\mathbf{28}))_2]^{6+}$ emerged whose cavity offered two copper(I) ions to pre-bind both **30** and **31** at a suitable reaction distance thus increasing the local concentration so that the acetylation $\mathbf{30} + \mathbf{31} \rightarrow \mathbf{32}$ rapidly took place. Thanks to a mechanistic study the corresponding hydrogen-bonded precursor complex was identified inside the cavity. Analogously, the larger switch **29** after dimerization catalyzed the acetylation of the larger substrate **34** due to size matching [29]. In separate experiments, both nanoswitches were toggled over 2.5 cycles by adding and removing the iron(II) ions with the effect that the catalysis was reversibly and reproducibly turned ON and OFF. Finally, the nanoswitches $[Cu_2(\mathbf{28})]^{2+}$ and $[Cu_2(\mathbf{29})]^{2+}$ were mixed with all the substrates and reagents (**30**, **31** & **34**). Upon addition of sub-stoichiometric amounts of iron(II) the reaction $\mathbf{31} + \mathbf{34}$ was selectively turned ON. Although the other reaction $\mathbf{30} + \mathbf{31}$ could not be selectively activated in the

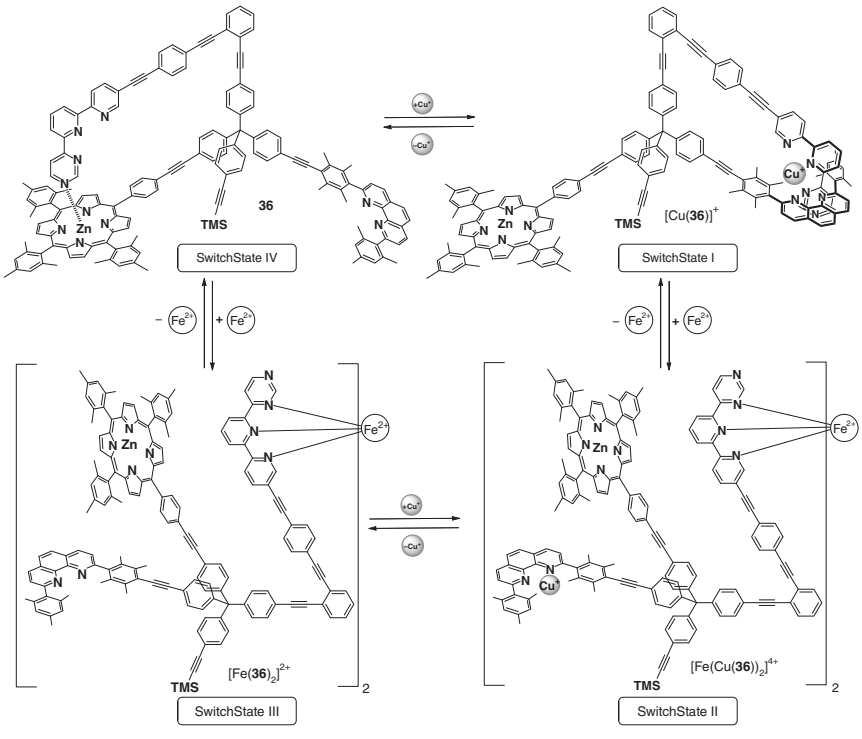

Figure 39.7 A four-state nanoswitch. Source: Gaikwad et al. [30].

mixture, this represents an advanced case of a switchable multicatalyst systems selecting between substrates of different size but basically identical reactivity.

Dimerization of the nanoswitch **36** finally opened the venue to a catalytic machinery that allowed regulation of a sequential two-step catalytic process. For control of both catalytic reactions, allosteric regulation and a combination of intra- vs. intermolecular complexation reactions were essential [30] as well as four distinct switching states. For this purpose, three orthogonal binding stations, i.e. a ZnPor, a sterically shielded phenanthroline, and an azaterpyridine unit, were attached at three arms in **36** (Figure 39.7). In SwitchState I, the copper(I) ion in $[Cu(\mathbf{36})]^+$ was deeply buried in a heteroleptic phenanthroline–terpyridine complex. Using the same dimerization strategy as above, addition of 0.5 equiv of iron(II) ions to $[Cu(\mathbf{36})]^+$ opened the intramolecular copper complex affording the "dimeric" $[Fe(Cu(\mathbf{36}))_2]^{4+}$ (SwitchState II). After successive removal of copper(I) and iron(II) ions, the copper(I)- and iron(II)-free compound **36** was obtained in SwitchState IV. As the only complex in the whole cycle, **36** is characterized by an intramolecular $N_{pym} \rightarrow$ ZnPor contact (pym = pyrimidine). The cycle was replicated several times without fatigue.

When the switching, as illustrated in Figure 39.7 [30], was conducted in the presence of piperidine (**3**) as a catalyst and the reactants **37**–**39** then the following outcome was observed (Figure 39.8): SwitchState I proved to be catalytically inactive

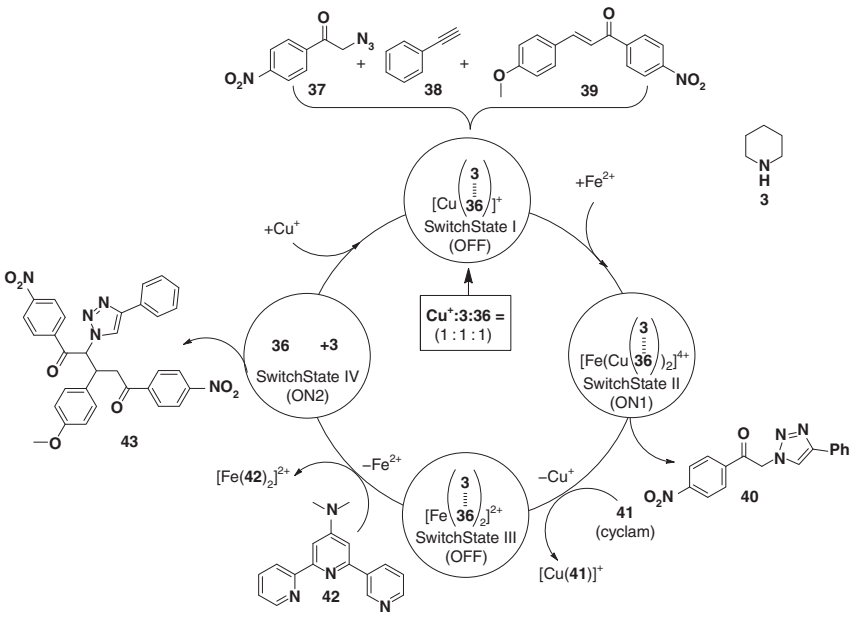

Figure 39.8 Sequential two-step catalysis in one-pot executed by nanoswitch **36** upon. inputs. Source: Gaikwad et al. [30].

as the organocatalyst **3** was firmly attached at the ZnPor unit of $[Cu(\mathbf{36})]^+$ and since the copper(I) ion was unavailable for catalysis. SwitchState II was obtained upon addition of iron(II). The dimeric complex $[Fe(Cu(\mathbf{36}))_2]^{4+}$ had the copper(I) ions exposed for catalysis. With the reactants **37**–**39** being present (Figure 39.8) now 50% of click product **40** was afforded. Insertion of cyclam (**41**) to strip off the copper(I) ions led to SwitchState III that represented an OFF state of catalysis, after that, added 4-*N*,*N*-dimethylamino-2,2′:6′,2″-terpyridine (**42**) removed iron(II) affording nanoswitch **36** (= SwitchState IV). As the azaterpyridine arm now toggled onto the ZnPor site, the so far firmly bound catalyst **3** (it was attached in SwitchStates I–III) was liberated into solution with the effect that the click product **40** underwent a catalyzed Michael addition affording **43** in 28% yield. Amazingly, the second cycle perfectly reproduced the yields of the first loop, demonstrating that intricate catalytic machinery with a total of eleven components may be operated in an interference-free manner [30].

39.4 Dynamic Allosteric Regulation of Catalysis

Only recently we have started to look into allosteric regulation of catalysis in highly dynamic supramolecular devices, however, since this issue is not associated with switchable catalysis, i.e. the topic of our chapter, it will only be peripherally treated. What do we understand by the term dynamic allosteric regulation of catalysis? Whereas in common allosteric control the effector will trigger conformational

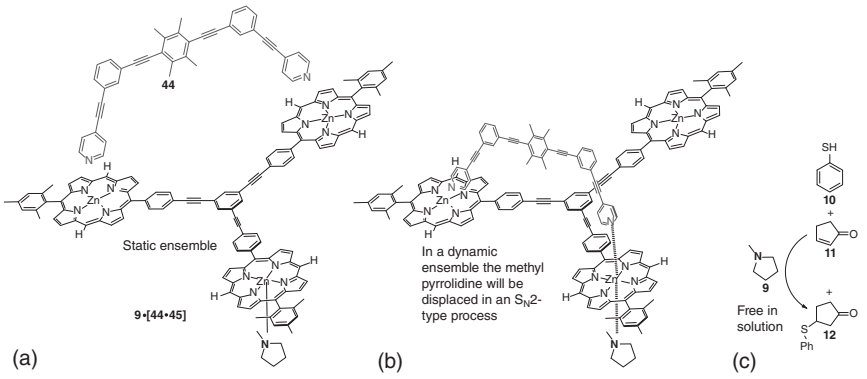

Figure 39.9 Dynamic allosteric effect accelerating a catalyzed conjugate addition [31].

changes that lead to a regulation of activity, in the dynamic variant of allosteric effects the conformational change is repetitively triggered by pure thermal dissociation in a degenerate system. We first discovered this effect in the slider-on-deck system [**44**·**45**] when it was associated with the organocatalyst **9** [31].

If the three-component system **9**·[**44**·**45**] would be static (Figure 39.9a), the binding of the catalyst **9** at the ZnPor site should be as efficient as in the OFF state that we have seen for instance with $[Cu_2(\mathbf{7}\cdot\mathbf{8})]^{2+}$. However, these slider-on-deck systems are highly dynamic due to an exchange of the biped's pyridine feet across the deck. With the organocatalyst **9** being available at one ZnPor of the deck at a given time, the sliding biped will detach the catalyst once the biped's foot steps onto the same ZnPor unit (Figure 39.9b) [20]. Actually, it was experimentally demonstrated that the faster the biped (using different bipeds) moved across the deck, the more of the catalyst was liberated into solution. In presence of the appropriate substrates, thus the catalysis of the conjugate addition of **10** + **11** → **12** was accelerated (Figure 39.9c). To sum up, the faster the catalytic machinery (the slider-on-deck) the faster is catalysis [31].

At this point, the logical question emerged whether dynamic allosteric effects may be advantageous for other kinds of molecular machines as well. Indeed, we detected that equally in catalytic machinery inhibited by product binding a faster machine speed stimulated a faster turn-over rate of the catalytic process [32]. For instance, at any given time in the dynamic four-component catalytic nanorotor **46** (Figure 39.10, left) one out of the two copper(I) centers will be available for click catalysis. If the product formed in the click reaction, e.g. **47**, is a good binding ligand for the catalytic copper center then in a static system the reaction would come to a stop after one turnover. In the highly dynamic rotor **46**, however, the rotator arm thermally dissociated from the opposite copper(I)-binding site (Figure 39.10, right) and moved onto the product-loaded copper(I) center. There, the rotator arm kicked out product **47** into solution. The copper(I) site, from which the rotator had departed, was now available for catalysis of the click reaction. It was demonstrated that both the turn-over rate of the click reaction and the liberation of the product were linearly correlated with the machine speed [32].

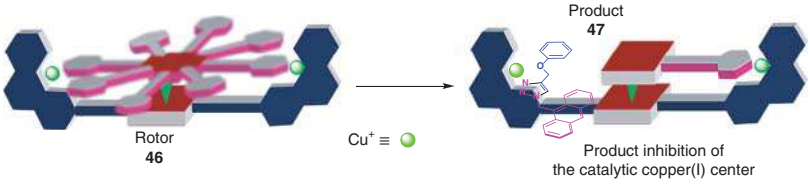

Figure 39.10 A rotating copper(I) catalyst for click reactions. Product **47** inhibiting the copper(I) center will be expelled by the rotator arm departing from the opposite and moving to the product-loaded site. Source: Biswas et al. [32]. Reproduced with permission of American Chemical Society.

39.5 The Future: From Allosteric Regulation of Catalysis in a Network to Smart and Autonomous Mixtures

A look at machines in the real world swiftly reveals which key elements are necessary for operation. For example, the minimum requirements for a machine involve not only the actual drive system with its moving parts but also control technology and a power supply. Such elaborate networked settings also work in the molecular world, as nature has been amply demonstrating by means of its highly regulated and autonomous machines [33, 34]. Since there are rewarding prospects for artificial machinery as well [35, 36], we have started to evaluate the use of allosteric effects [37] in networked processes. As these efforts are first steps toward interdependent multidevice machinery [38], the results are still modest in comparison to any biological archetypes.

For illustration a single example should suffice [39], which demonstrates ON/OFF regulation of catalysis in a network. Hereunto the cybernetic network, comprising the two nanoswitches **23** and **24**, the organocatalyst **9** and metal ions were chosen (Figure 39.11). The first networked state (NetState I) was the outcome of an incomplete self-sorting event that yielded the copper(I) nanoswitch complex $[Cu(\mathbf{24})]^+$, while switch **23** and *N*-methylpyrrolidine (**9**) were left uncoordinated in solution. To realize NetState II, a second self-sorting was required that emerged upon addition of iron(II) ions. Two nanoswitches **24** were now "dimerized" at the iron(II) via their terpyridine site yielding the iron complex $[Fe(\mathbf{24})_2]^{2+}$. Hereunto, the copper(I) complexation in $[Cu(\mathbf{24})]^+$ had to open up and the formerly bound copper(I) ions translocated to switch **23** where they found a stronger binding site. To finalize the complexation in $[Cu(\mathbf{23})]^+$, the switching arm of **23** had to depart from its ZnPor unit and to move to the copper(I) phenanthroline station. In this process, the zinc porphyrin station was freed and thus was able to bind the organocatalyst **9** ($\log K = 4.20$). The outcome of this double self-sorting was consequently utilized to turn ON/OFF a conjugate addition (Figure 39.11). In NetState I, the *N*-methylpyrrolidine (**9**) was available for catalysis of the conjugate addition, whereas in NetState II, catalyst **9** was firmly attached in $[Cu(\mathbf{9})(\mathbf{23})]^+$ and hence conjugate addition was OFF. Removal of the iron(II) ions regenerated NetState I. The switching protocol was successfully run over three cycles [39].

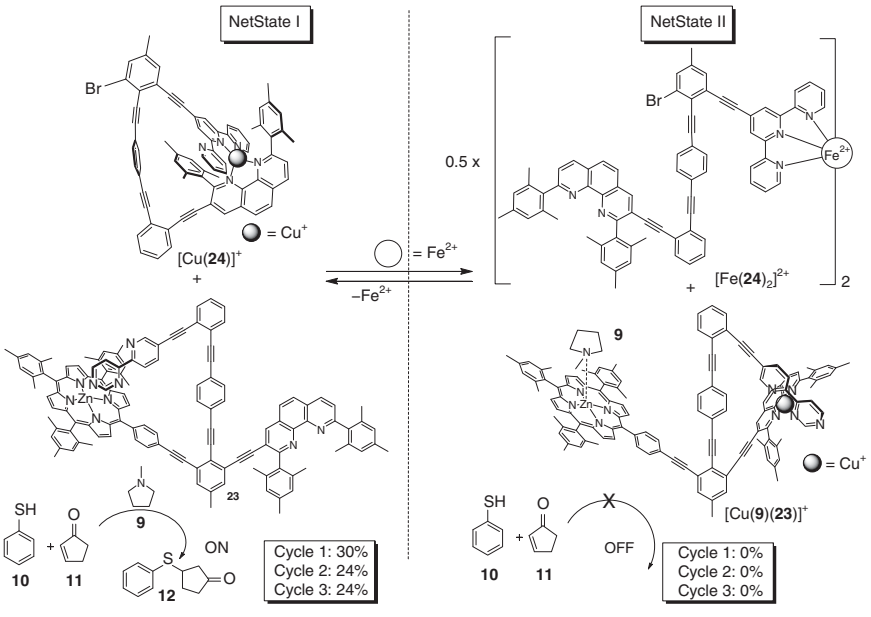

Figure 39.11 A networked ensemble of two nanoswitches operating via metal-ion communication for controlling a catalyzed conjugate addition. Source: Mittal et al. [39].

What are the steps to be addressed in the near future? There is an urgent need for implementing mechanisms that allow chemical fuels to act as power supply thus keeping the catalytic system out-of-equilibrium [40], for positive and negative feedback loops [41] to enable up- vs. downregulation and for higher levels of information handling [42], so that the smart mixture is able to autonomously make decisions.

39.6 Concluding Remarks

During the first two decades of developing allosteric control of catalysis, covalent and interlocked switches have been preferred as these – different to supramolecular multicomponent aggregates – are not prone to dissociation. More recent developments, however, have demonstrated that even weakly bound systems allow for reliable allosteric transmission of the effector's binding event to the distal functional site. In this respect, the prospects of creating new self-assembled multicomponent devices for regulating catalysis are bright and manifold.

Acknowledgments

Generous financial support by the DFG (Schm 647/19-2 and 647/20-2) is gratefully acknowledged. Moreover, we are indebted to the University of Siegen.

References

1 Motlagh, H.N., Wrabl, J.O., Li, J., and Hilser, V.J. (2014). The ensemble nature of allostery. *Nature* 508 (7496): 331–339.

2 Tsai, C.-J., Del Sol, A., and Nussinov, R. (2009). Protein allostery, signal transmission and dynamics: a classification scheme of allosteric mechanisms. *Mol. BioSyst.* 5: 207–216.

3 Doshi, U., Holliday, M.J., Eisenmesser, E.Z., and Hamelberg, D. (2016). Dynamical network of residue-residue contacts reveals coupled allosteric effects in recognition, catalysis, and mutation. *Proc. Natl. Acad. Sci. (PNAS)* 113: 4735–4740.

4 van Dijk, L., Tilby, M.J., Szpera, R. et al. (2018). Molecular machines for catalysis. *Nat. Rev. Chem.* 2: 117.

5 Vlatković, M., Collins, B.S.L., and Feringa, B.L. (2016). Dynamic responsive systems for catalytic function. *Chem. Eur. J.* 22 (48): 17080–17111.

6 Blanco, V., Leigh, D.A., and Marcos, V. (2015). Artificial switchable catalysts. *Chem. Soc. Rev.* 44: 5341–5370.

7 Raynal, M., Ballester, P., Vidal-Ferran, A., and van Leeuwen, P.W.N.M. (2014). Supramolecular catalysis. Part 2: artificial enzyme mimics. *Chem. Soc. Rev.* 43: 1734–1787.

8 Lüning, U. (2012). Switchable catalysis. *Angew. Chem. Int. Ed.* 51: 8163–8165.

9 Kovbasyuk, L. and Krämer, R. (2004). Allosteric supramolecular receptors and catalysts. *Chem. Rev.* 104: 3161–3187.

10 Würthner, F. and Rebek, J. Jr., (1995). Light-switchable catalysis in synthetic receptors. *Angew. Chem. Int. Ed.* 34: 446–448.

11 Fritsky, I.O., Ott, R., and Krämer, R. (2000). Allosteric regulation of artificial phosphoesterase activity by metal ions. *Angew. Chem. Int. Ed.* 39: 3255–3258.

12 Lifschitz, A.M., Rosen, M.S., McGuirk, C.M., and Mirkin, C.A. (2015). Allosteric supramolecular coordination constructs. *J. Am. Chem. Soc.* 137: 7252–7261.

13 Gianneschi, N.C., Bertin, P.A., Nguyen, S.T. et al. (2003). A supramolecular approach to an allosteric catalyst. *J. Am. Chem. Soc.* 125: 10508–10509.

14 de Bo, G., Leigh, D.A., McTernan, C.T., and Wang, S. (2017). A complementary pair of enantioselective switchable organocatalysts. *Chem. Sci.* 8: 7077–7081.

15 Marcos, V., Stephens, A.J., and Leigh, D.A. (2016). Allosteric initiation and regulation of catalysis with a molecular knot. *Science* 352 (6293): 1555–1559.

16 Czescik, J., Lyu, Y., Neuberg, S. et al. (2020). Host–guest allosteric control of an artificial phosphatase. *J. Am. Chem. Soc.* 142: 6837–6841.

17 McGuirk, C.M., Mendez-Arroyo, J., Am, L., and Mirkin, C.A. (2014). Allosteric regulation of supramolecular oligomerization and catalytic activity via coordination-based control of competitive hydrogen-bonding events. *J. Am. Chem. Soc.* 136: 16594–16601.

18 McGuirk, C.M., Stern, C.L., and Mirkin, C.A. (2014). Small molecule regulation of self-association and catalytic activity in a supramolecular coordination complex. *J. Am. Chem. Soc.* 136: 4689–4696.

19 Ali, M.H. and Imperiali, B. (2005). Protein oligomerization: how and why. *Bioorg. Med. Chem.* 13 (17): 5013–5020.

20 Favereau, L., Cnossen, A., Kelber, J.B. et al. (2015). Six-coordinate zinc porphyrins for template-directed synthesis of spiro-fused nanorings. *J. Am. Chem. Soc.* 137: 14256–14259.

21 Kirksey, C.H., Hambright, P., and Storm, C.B. (1969). Stability constants and proton magnetic resonance studies of zinc α,β,γ,δ-tetraphenylporphin and substituted pyridines. *Inorg. Chem.* 8: 2141–2144.

22 Schmittel, M., De, S., and Pramanik, S. (2012). Reversible ON/OFF nanoswitch for organocatalysis: mimicking the locking and unlocking operation of CaMKII. *Angew. Chem. Int. Ed.* 51: 3832–3836.

23 Mittal, N., Özer, M.S., and Schmittel, M. (2018). Four-component catalytic machinery: reversible three-state control of organocatalysis by walking back and forth on a track. *Inorg. Chem.* 57: 3579–3586.

24 Saha, S., Ghosh, A., Paululat, T., and Schmittel, M. (2020). Allosteric regulation of rotational, optical and catalytic properties within multicomponent machinery. *Dalton Trans.* 49: 8693–8700.

25 De, S., Pramanik, S., and Schmittel, M. (2014). A toggle nanoswitch alternately controlling two catalytic reactions. *Angew. Chem. Int. Ed.* 53: 14255–14259.

26 Saha, M.L. and Schmittel, M. (2012). Degree of molecular self-sorting in multicomponent systems. *Org. Biomol. Chem.* 10: 4651–4684.

27 De, S., Pramanik, S., and Schmittel, M. (2014). A monomer-dimer nanoswitch that mimics the working principle of the SARS-CoV 3CLpro enzyme controls copper-catalysed cyclopropanation. *Dalton Trans.* 43: 10977–10982.

28 Shi, J., Sivaraman, J., and Song, J. (2008). Mechanism for controlling the dimer-monomer switch and coupling dimerization to catalysis of the severe acute respiratory syndrome coronavirus 3C-like protease. *J. Virol.* 82: 4620–4629.

29 Goswami, A., Gaikwad, S., and Schmittel, M. (2021). A switchable catalyst duo for acyl transfer proximity catalysis and regulation of substrate selectivity. *Chem. Eur. J.* 27: 2997–3001.

30 Gaikwad, S., Goswami, A., De, S., and Schmittel, M. (2016). A metalloregulated four-state nanoswitch controls two-step sequential catalysis in an eleven-component system. *Angew. Chem. Int. Ed.* 55: 10512–10517.

31 Paul, I., Goswami, A., Mittal, N., and Schmittel, M. (2018). Catalytic three-component machinery: control of catalytic activity by machine speed. *Angew. Chem. Int. Ed.* 57: 354–358.

32 Biswas, P.K., Saha, S., Paululat, T., and Schmittel, M. (2018). Rotating catalysts are superior: suppressing product inhibition by anchimeric assistance in four-component catalytic machinery. *J. Am. Chem. Soc.* 140: 9038–9041.

33 Bielecki, A. (2015). The general entity of life: a cybernetic approach. *Biol. Cybern.* 109: 401–419.

34 Pfeuty, B. and Kaneko, K. (2009). The combination of positive and negative feedback loops confers exquisite flexibility to biochemical switches. *Phys. Biol.* 6: 46013.

35 Lancia, F., Ryabchun, A., and Katsonis, N. (2019). Life-like motion driven by artificial molecular machines. *Nat. Rev. Chem.* 3: 536–551.

36 Ma, P.-Q., Liang, C.-P., Zhang, H.-H. et al. (2018). A highly integrated DNA nanomachine operating in living cells powered by an endogenous stimulus. *Chem. Sci.* 9: 3299–3304.

37 Kremer, C. and Lützen, A. (2013). Artificial allosteric receptors. *Chem. Eur. J.* 19: 6162–6196.

38 Remón, P. and Pischel, U. (2017). Chemical communication between molecules. *ChemPhysChem* 18: 1667–1677.

39 Mittal, N., Pramanik, S., Paul, I. et al. (2017). Networking nanoswitches for ON/OFF control of catalysis. *J. Am. Chem. Soc.* 139: 4270–4273.

40 Biagini, C., Fielden, S.D.P., Leigh, D.A. et al. (2019). Dissipative catalysis with a molecular machine. *Angew. Chem. Int. Ed.* 58: 9876–9880.

41 Pramanik, S. and Aprahamian, I. (2016). Hydrazone switch-based negative feedback loop. *J. Am. Chem. Soc.* 138: 15142–15145.

42 Goswami, A., Paululat, T., and Schmittel, M. (2019). Switching dual catalysis without molecular switch: using a multicomponent information system for reversible reconfiguration of catalytic machinery. *J. Am. Chem. Soc.* 141: 15656–15663.

40

Supramolecularly Regulated Enantioselective Catalysts

Anton Vidal-Ferran[1,2]

[1] *Catalan Institution for Research and Advanced Studies (ICREA), Passeig de Lluís Companys 23, Barcelona, 08010, Spain*
[2] *University of Barcelona, Department of Inorganic and Organic Chemistry, Carrer Martí i Franquès 1-11, Barcelona, 08028, Spain*

40.1 Introduction

The use of supramolecular interactions in catalysis has become very popular in recent years and has contributed enormously to the development of efficient enantioselective catalysts [1–10]. This chapter primarily aims to highlight a specific aspect of the application of supramolecular interactions in catalysis: the generation of libraries of supramolecularly regulated enantioselective catalysts that retain most of the structural features of the backbone, while incorporating changes to their active sites that are determined by the structural characteristics of the regulation agent (RA) employed. The RA is a chemical species that is used to construct the catalyst and does not interact with the catalytic site, but with the catalytic system through supramolecular interactions. This produces a change in the three-dimensional structure of the catalyst with respect to that obtained with another RA. Supramolecular regulation involving major alterations of the structural or functional features of the catalyst falls outside the scope of this chapter. Supramolecular regulation in enantioselective catalysis seeks to override an important limitation: the lack of generality of enantioselective catalysts. It is common that a catalyst performing well for a particular set of substrates and/or reagents fails to provide good enantioselectivities with other substrate(s)/reagents(s). Thus, structural variation of the enantioselective catalyst is required to improve the outcome of the reaction. Supramolecular regulation has turned out to be an optimal strategy to produce libraries of enantioselective catalysts that not only preserve the main structural features but also incorporate structural peculiarities depending on the RA used. Overall, the aim is that one of the components of the library adapts to the stereochemical requirements of a given substrate and/or set of reagents [11].

The following paragraphs will highlight different strategies for *the use and efficacy of an RA to optimize the performance of a catalyst in terms of activity and enantioselectivity* via *supramolecular interactions between the RA and the catalyst*. As will

Supramolecular Catalysis: New Directions and Developments, First Edition.
Edited by Piet W.N.M. van Leeuwen and Matthieu Raynal.

be discussed later, the RA plays different roles in the selected examples. In some cases, the role of the RA is restricted to inducing a preferential chiral conformation of the whole catalyst, whilst in other cases, its role is to trigger significant changes in the conformation and/or rigidity of the whole catalytic system to yield better enantioselectivities. Not surprisingly, RAs have been called co-catalysts, chiral remote inducers, chiral cofactors, or "sergeants" in original publications. However, in all cases, they comply with the condition that they do not bind to the catalytic center; instead, they interact with the catalyst/ligand through supramolecular interactions at a site that is different from the catalytic center.

It should be noted that the selected examples presented here are not meant to be exhaustive. Due to space restrictions, a comprehensive review of all published examples is not possible. This perspective chapter highlights only published studies demonstrating the regulation ability of a set of RAs among an array of substrates.

40.2 Seminal Work

Ito and coworkers pioneered the field of supramolecular regulation in enantioselective catalysis by developing a catalyst that already incorporated the required stereogenic elements for biasing the production of one major enantiomeric product [12]. As indicated in Scheme 40.1, the authors designed palladium-based catalysts, derived from enantiopure diphosphine ligands, for enantioselective allylic substitutions. The enantioselective catalyst also contained a distal regulation site formed by an aza-crown-ether motif that was capable of interacting with an external RA through supramolecular interactions. The authors hypothesized that metal fluorides with cationic components of varying size could operate as RAs by influencing the relative arrangement of the nucleophile (i.e. the enolate of the starting α-nitro ketones) and the electrophilic allyl group. A library of supramolecular catalysts was prepared by combining the right amounts of the palladium precursor, the ligand **L1**, and an array of alkali metal fluorides (please refer to the original publication for further details on the choice of the chiral ligand). Ito and coworkers reported that the catalyst incorporating RbF as the RA produced higher conversion rates and enantioselectivities than those obtained in the absence of the RA or with other alkali metal fluorides (Scheme 40.1).

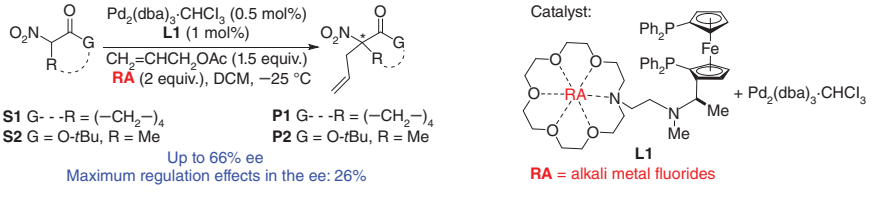

Scheme 40.1 The regulated catalyst for enantioselective allylic substitutions reported by Ito et al.

40.3 Supramolecular Regulation of a Preformed Enantioselective Catalyst

After the seminal and elegant design of a supramolecularly regulated enantioselective catalyst by Ito and coworkers, other groups further developed the concept of supramolecular regulation of bidentate metal complexes. This section highlights relevant examples in this area of research. As a comprehensive summary of all the published examples belonging to this category of supramolecularly regulated catalysts would fall beyond the space limit of this chapter, the following paragraphs highlight examples in which the final enantioselectivities surpassed 80% ee (enantiomeric ratio > 90 : 10) and the regulation effects caused an increase of at least 25% in the enantioselectivity for a given RA with respect to the non-regulated catalyst. Please refer to the comprehensive reviews on this area of research that have already been published [13–15].

Ooi and coworkers reported the enantioselective conjugated addition of azlactone **S3** to α,β-unsaturated ester surrogate **S4** (Scheme 40.2) that was catalyzed by hydrogen-bond assembled enantiopure ion organic pairs generated by combining enantiopure tetraamino phosphonium salts with phenols and phenoxides [16, Chapter 3]. It is interesting to note that the ability to bias the stereochemical outcome of the abovementioned transformation was attributed not only to the enantiopure component of the organic ion pair but also to the achiral phenol and phenoxide employed. In this regard, the achiral component can be considered the RA. Enantiopure phosphonium chlorides **L2** were synthesized from L-valine. The exchange of the chloride anion with hydroxide followed by neutralization with the corresponding phenol produced the target supramolecular catalyst. X-ray analysis revealed the structure of the final supramolecular assembly, which had incorporated one tetraamino-phosphonium moiety, two phenols, and one phenoxide anion (Scheme 40.2). This phenoxide group was readily replaced by the enolate of **S3**, which initiated the catalytic cycle. Ooi and coworkers studied the catalytic activity of these supramolecular assemblies in the enantioselective conjugate addition of the enolate of **S3**–**S4**. The stereoselectivity of the reaction could be tuned through the structural modification of the achiral component of the supramolecular aggregate (i.e. the phenol/phenoxide units), with 3,5-dichlorophenol (**RA6**) providing the highest enantioselectivity in the reaction between **S3** and **S4** (99% yield, 87% ee) [16].

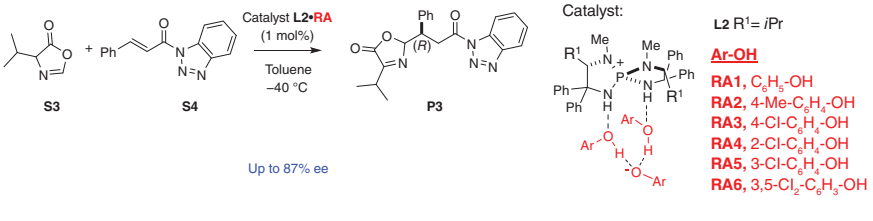

Scheme 40.2 The regulated catalyst for enantioselective conjugated additions reported by Ooi et al.

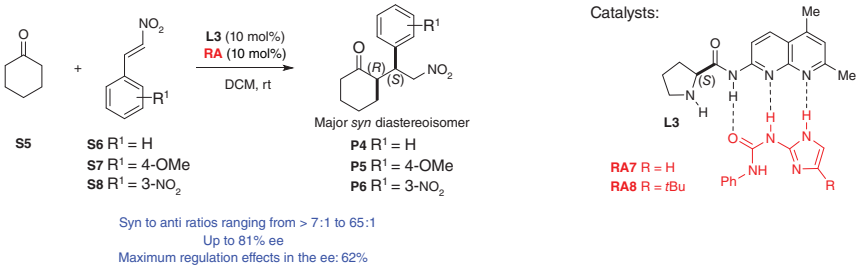

Scheme 40.3 The regulated catalyst for organocatalytic Michael additions reported by Clarke et al.

In addition to the previous example of supramolecular regulation in enantioselective organocatalysis by Ooi and coworkers, Clarke and coworkers reported an elegant example of regulation in the organocatalytic Michael additions of ketone enolates to nitroalkenes (Scheme 40.3) [17]. The authors designed ligands for enantioselective catalysis and a set of RAs, with the ligand and the RA presenting highly complementary hydrogen-bonding recognition motifs. Thus, highly precise self-assembled organocatalysts were obtained starting with the 2-amino-1,8-naphthyridine-based ligand **L3** and the 1-(1*H*-imidazol-2-yl)urea-based regulation agents **RA7**–**RA8** (Scheme 40.3). The authors envisioned that while **L3** would be responsible for the enantioselective catalysis due to the L-proline fragment, **RA7**–**RA8** would function as the RAs. Interestingly, Clarke and coworkers observed that the supramolecular assemblies derived from **L3** and **RA7**–**RA8** were more active in mediating the Michael additions under study than the proline-derivative **L3** alone. For instance, in the enantioselective Michael addition of cyclohexanone (**S5**) to β-nitrostyrene (**S6**), the use of the organocatalyst **L3**·**RA7** led to an enhancement in both the diastereoselectivity (from a 26 : 1 to a 65 : 1 *syn* to *anti* ratio of diastereomers) and the enantioselectivity (from 6% to 68% ee). Interestingly, the use of **RA8** instead of **RA7** led to the highest diastereo- and enantioselectivities in the Michael additions of **S5** to 4-methoxy- and 3-nitro-substituted β-nitrostyrenes (*syn* to *anti* ratio of 36 : 1 and 74% ee for **P5** and *syn* to *anti* ratio of >7 : 1 and 81% ee for **P6**) [17].

Following the work of Fan and He involving a regulation site based on a linear polyethyleneoxy motif [18], Vidal-Ferran and coworkers reported the use of α,ω-bisphosphites in rhodium-catalyzed enantioselective hydroformylations [19]. The studies were performed to identify the optimal ligand structure (i.e. the length of the polyethyleneoxy motif in the regulation site, the nature of the stereogenic elements, and the substitution pattern in the phosphite groups), with **L4** having the optimal ligand structure in the hydroformylation of linear alkenes (Scheme 40.4) [20]. In terms of the RAs, alkali metal salts were considered ideal candidates as they are known to be good polyether binders in organic solvents. Regarding the anionic component of the RA, the tetrakis[3,5-bis(trifluoromethyl)phenyl]borate anion (BArF) was demonstrated to be the best option, given its adequate solubility profile in organic solvents. Moreover, the alkali metal BArF salts provided higher selectivity toward the branched aldehyde than the tetrafluoroborate or perchlorate

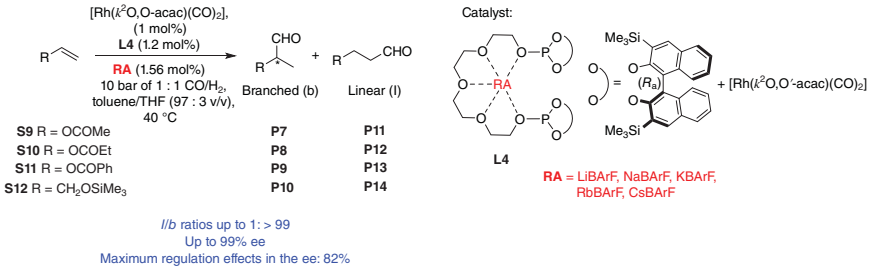

Scheme 40.4 The regulated catalyst for the enantioselective hydroformylations of linear alkenes reported by Vidal-Ferran et al.

counterparts [20]. Catalytic studies were first undertaken to evaluate the design principle and determine whether the chosen RA during the in situ generation of the catalysts was able to maximize the performance of the rhodium complexes derived from **L4** in terms of catalytic activity and enantioselectivity. Among the RAs tested, RbBArF had the largest regulation effects in the case of vinyl esters (99% conversion for **S9**–**S11**; *l*/*b* ratios up to 1 : >99 for **S9**–**S11**; 99% ee for **P7**–**P9**; and regulation effects in the ee of 64%, 63%, and 82% for **P7**, **P8**, and **P9**, respectively). The regulation approach worked to a lesser extent for the allyl alcohol derivative **S12** (modification of the *l*/*b* ratio from 41 : 59 to 82 : 18 and increase of 18% in the ee with RbBArF). The high activity of the catalytic system developed by Vidal-Ferran and coworkers was demonstrated by the increase in the substrate-to-catalyst (*S*/*C*) ratio in the hydroformylation of **S9** (vinyl acetate) from 100 (standard screening conditions) up to 1000 (0.1 mol% of catalyst), with almost no effect on catalytic performance (99% conversion, *l*/*b* ratio 1 : >99 and 97% ee in favor of (*S*)-**P7**). The addition of RbBArF not only increased the ee but also mediated a 4.4-fold increase in the TOF, with an *S*/*C* ratio of 1000 in the presence of RbBArF (from $TOF_{1/2} = 40\,h^{-1}$ in the absence of RbBArF to $TOF_{1/2} = 177\,h^{-1}$) [20]. Mechanistic studies were performed involving the continuous monitoring of the starting material **S9**, products **P7** and **P11**, and metal hydride intermediates, using an NMR flow probe [21]. Analysis of the reaction profile revealed a first-order dependence of the reaction rate with respect to the catalyst and the alkene, indicating that the olefin-hydride insertion was the rate- and stereo-determining step in the catalytic cycle. Computational studies provided insight into the structural changes induced by the RA, demonstrating that the ionic radius of the cation of the RA correlated with the width of the P-Rh-P angle (from 113° in the absence of the RA to c. 122° for Cs^+). Moreover, these studies revealed that the increase in the enantioselectivity resulted from the adaptation of the P-Rh-P angle to its optimal value to achieve high enantioselectivity [20].

The same regulation approach was applied by Vidal-Ferran and coworkers to the enantioselective hydroformylation of heterocyclic olefins, employing a structurally modified version of **L4** and alkali metal BArF salts as the RAs [22]. The most significant structural modification in the new ligand was the incorporation of a (R_a)-BINOL motif at the regulation site (**L5**, Scheme 40.5). High enantioselectivities

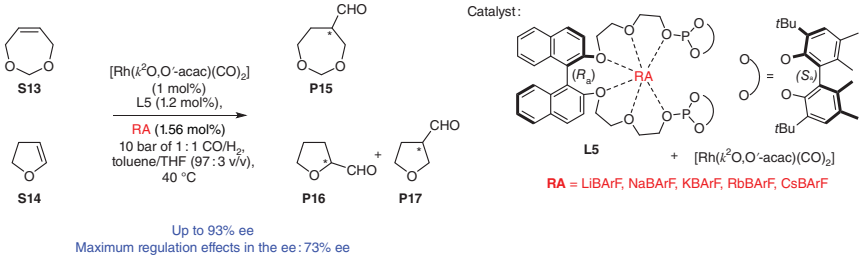

Scheme 40.5 The regulated catalyst for enantioselective hydroformylations of heterocyclic alkenes reported by Vidal-Ferran et al.

and regulation effects were observed in the hydroformylation of the heterocyclic olefins **S13** and **S14**, employing **L5** and alkali metal BArF salts as the RAs. The use of KBArF improved both the conversion (from 23% to >99%) and the enantioselectivity (73% increase in the ee, reaching 83% ee at 40 °C) in the hydroformylation of **S13**. The high activity of the rhodium complexes derived from **L5** enabled the hydroformylation reaction of **S13** to occur at room temperature with an excellent ee of 93%. KBArF was also the RA of choice for achieving high enantioselectivities in the hydroformylation of **S14** (2,3-dihydrofuran). The addition of KBArF changed the α-aldehyde vs. β-aldehyde ratio, leading mainly to the generation of the α-aldehyde **P16** (α- vs. β-aldehyde ratio of 3.6 : 1) and a much higher enantioselectivity with respect to the catalyst in the absence of the RA (84% vs. 13% ee).

Research efforts were dedicated by Fan, He, and coworkers to develop supramolecularly regulated catalysts for enantioselective Henry reactions (Scheme 40.6). The designed catalyst incorporated two chromium(III)-salen moieties (for the salen motif, see the fragment in bold in Scheme 40.6), which were separated by a polyether chain that acted as the regulation site [23]. The authors envisaged that the interaction between the polyether chain of the α,ω-bis(metallosalen) derivative and a polyether binder would bring the two chromium(III)-salen units together, generating the bimetallic catalyst **Cr(III)-L6**. The authors assessed the new catalyst in the Henry reaction between substituted benzaldehydes and nitromethane, demonstrating that the outcome of the reaction in terms of enantioselectivity could

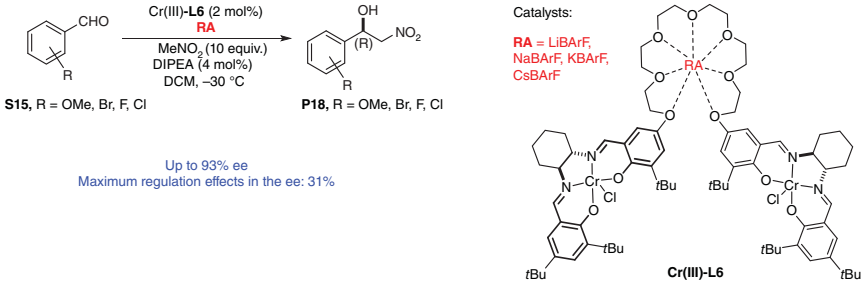

Scheme 40.6 The regulated catalyst for enantioselective Henry reactions reported by Fan, He et al.

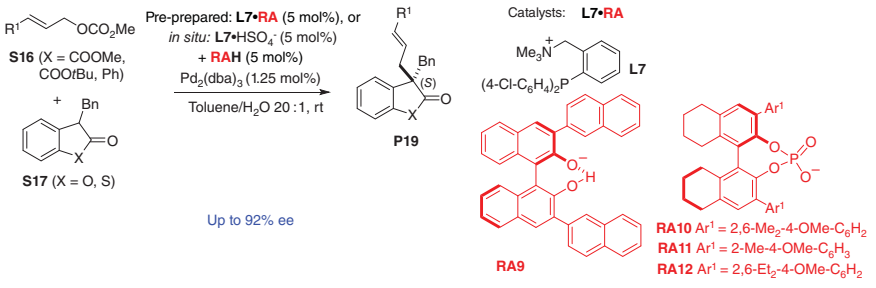

Scheme 40.7 The regulated catalyst for the allylation of lactones and thiolactones reported by Ooi et al.

be maximized by the RA chosen, with KBArF providing the highest enantioselectivities (mean enantioselectivity of 88% ee in an array of eight *o*-, *m*-, and *p*-substituted benzaldehydes). The regulation effects on the enantioselectivity were important (maximum increase in the enantioselectivity: from 53% to 81% ee), indicating the importance of the RA in this chemistry. The authors demonstrated that regardless of the electronic or positional nature of the substituents on the aromatic ring, the corresponding products were obtained with high enantioselectivities, with slightly higher ee values being obtained for the *o*-substituted substrates.

Ooi and coworkers designed a new class of interesting ligands in which a quaternary ammonium derivative was incorporated into the scaffold of an achiral phosphine ligand. The ammonium derivatives were combined with enantiopure [1,1′-biphenyl]-2,2′-bis(olate) derivatives or [1,1′-biaryl]-2,2′-diol-derived phosphoric acid derivatives that acted as the RAs, generating the ion-paired catalysts **L7**·**RA** (Scheme 40.7) [24, Chapter 3]. These supramolecularly regulated ligands were studied in the allylation of benzofuran-2(3*H*)-one and benzo[*b*]thiophen-2(3*H*)-one derivatives (**S17** with X = O or S, respectively). The structure of the ammonium derivatives was optimized. The combination of the ammonium derivative **L7** (Scheme 40.7) with the anionic components **RA9**–**RA12** produced efficient enantioselective catalysts in the allylation of **S17** with substituted allyl carbonates (R^1 = COOMe, COO*t*Bu or Ph; Scheme 40.7). The combination of **L7** and **RA10** enantioselectively generated the allylation product **P19** with R^1 = COOMe and X = O (90% ee), **P19** with R^1 = Ph and X = O (84% ee), **P19** with R^1 = COO*t*Bu and X = O (92% ee), and **P19** with R^1 = COO*t*Bu and X = S (79% ee) [24].

40.4 Supramolecular Regulation of a Prochiral Ligand or Catalyst

This approach is similar to that described in Section 40.3 in terms of generating a library of diverse enantioselective catalysts by supramolecularly assembling a ligand using an array of structurally diverse RAs. However, the supramolecularly regulated catalysts described in this section present one crucial difference with respect to those in the previous section: the initial ligand is achiral in the absence of the RA

and the use of an external chemical species (or RA) induces a well-defined chiral environment of the resulting supramolecular assembly. Overall, an enantiopure (or highly enantioenriched) supramolecular complex is formed through processes of chirogenesis [25] induced by the RA. A summary of the relevant examples using enantiopure small-sized RAs in enantioselective catalysis will be provided in this section. For the use of biomacromolecules in enantioselective catalysis, please refer to recent reviews [26–28, Chapter 38 of this book]. For the use of one-dimensional helical assemblies and enantiopure RAs (or "enantiopure sergeants," as referred to by the authors), please refer to Chapter 7 of this book.

Enantiopure bidentate phosphines are key ligands in transition metal-based enantioselective catalysis. Efficient synthetic methods and applications as enantioselective catalysts in pivotal chemical transformations have been reported for a myriad of enantiopure diphosphines. However, adaptation of the framework of the ligand to expand the scope of the substrate for a particular chemical transformation is associated with significant synthetic difficulties. Thus, strategies for synthesizing libraries of enantiopure diphosphines by the supramolecular assembly of an achiral and an enantiopure building block have been deemed a highly interesting strategy due to the lower cost of this strategy compared to standard covalent synthetic chemistry. Van Leeuwen and coworkers developed an elegant synthetic strategy for enantiopure supramolecular diphosphines, starting with an enantiopure diol derivative (acting as the enantiopure RA), $Ti(OiPr)_4$, and an achiral bidentate diphosphine ligand incorporating two (2-hydroxybenzylidene)amino groups [29]. The final supramolecular enantiopure diphosphine was assembled by reacting the three components in the presence of $[Rh(nbd)_2]BF_4$ without removing the generated isopropanol (for the structures of the initial components, see Scheme 40.8). The authors envisioned that the free isopropanol generated during the reaction of the diol or the achiral ditopic ligand with $Ti(OiPr)_4$ would confer reversibility properties on the assembly process, with the final supramolecular assembly being the same regardless of the order of addition of the reagents. The use of $[Rh(nbd)_2]BF_4$ in the supramolecular assembly process was highly beneficial as it acted as the template (for the structure of the final rhodium diphosphine complex Rh[(nbd)(**L8/L9·Ti·RA**)]BF_4, see Scheme 40.8). The assembly of the numerous combinations of diols and ditopic ligands, differing

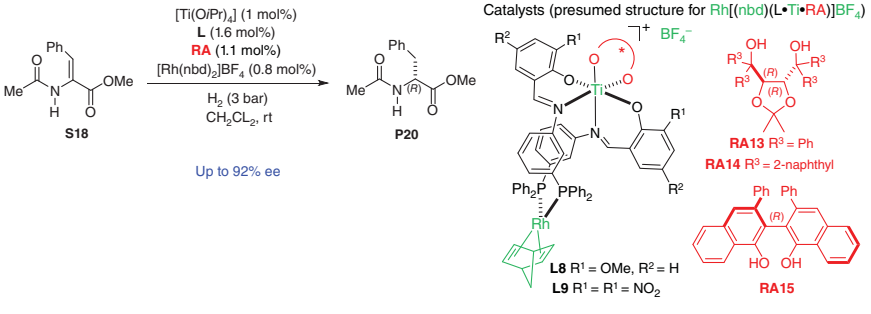

Scheme 40.8 The regulated catalyst for the enantioselective hydrogenation of functionalized alkenes reported by van Leeuwen et al.

in the nature of the substituents R^1 and R^2, was studied, showing efficient and selective formations of supramolecular diphosphines. These rhodium complexes were used as pre-catalysts in rhodium-catalyzed enantioselective hydrogenations of functionalized alkenes. Interestingly, the enantioselectivities in the hydrogenation of the substrate **S18** varied significantly as a function of the achiral diphosphine/diol pairs. Opposite configurations for the hydrogenation product **P20** were obtained when combining **L8** or **L9** with the same enantiopure regulation agent **RA14**. Under optimized conditions, the combination of **L8** and **RA13** generated the highest enantioselectivity in the formation of **P20** (92% ee). Moreover, the same catalyst was found to be the most efficient among the whole library for two other substrates [29].

Reek and coworkers published an elegant approach for generating libraries of enantioselective supramolecular catalysts. These authors designed an achiral diphosphine rhodium complex equipped with a binding site that recognized enantiopure RAs (called "*cofactors*" by the authors) [30]. With this strategy, the authors described the preparation of a library of enantioselective catalysts for asymmetric hydrogenations (Scheme 40.9). The ligand **L10** contained the diamidodiindolylmethane motif (the binding site for the RA) and phosphine binding groups for the generation of rhodium catalysts for enantioselective hydrogenations. As demonstrated by the authors, the rhodium complexes [Rh(nbd)(**L10**)]$^+$ were straightforwardly formed by mixing **L10** and $[Rh(nbd)_2]BF_4$. X-ray studies of the [Rh(nbd)(**L10**)]BF_4 complex showed that the tetrafluoroborate anion was bound to the diamidodiindolylmethane motif of the ligand in the solid state. Binding studies in solution demonstrated that enantiopure RAs with carboxylate groups easily displaced the tetrafluoroborate anion, as these had a much higher affinity for the diamidodiindolylmethane motif than the tetrafluoroborate anion. The authors exploited the high affinity of carboxylate anions for the diamidodiindolylmethane motif to generate a library of supramolecular enantioselective catalysts. Subsequent studies were performed to identify the optimal RA that produced the highest enantioselectivity in the hydrogenation of functionalized alkenes. Of the wide variety of enantiopure carboxylate-containing RAs tested, amino acid derivatives produced the best enantioselectivities in the hydrogenation of functionalized alkenes. Interestingly, Reek et al. reported that the substituents of the nitrogen group of the amino acid derivative had the greatest effect on enantioselectivity.

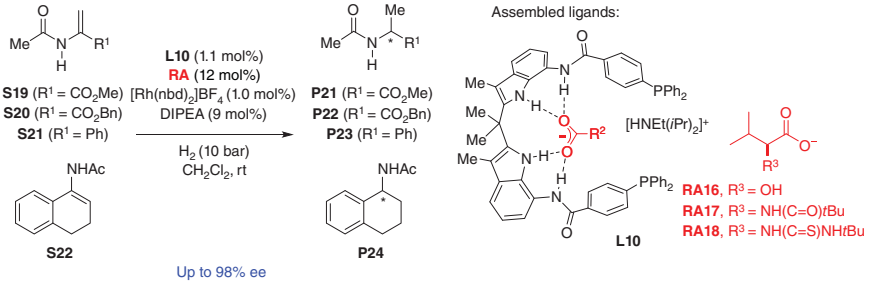

Scheme 40.9 The regulated catalyst for enantioselective hydrogenations reported by Reek et al.

The valine-derived regulation agent **RA18**, which incorporates a *tert*-butylthiourea group into the nitrogen group, provided the highest enantioselectivity in the hydrogenation of **S19**–**S21** (full conversion for the three substrates and 98%, 91%, and 82% ee for **S19**, **S20**, and **S21**, respectively). By contrast, the valine derivative **RA17**, which incorporates a *tert*-butylcarbamoyl group into the nitrogen group, was the RA of choice for the enantioselective hydrogenation of dihydronaphthalenyl acetamide (**S22**) (full conversion, 79% ee) [30].

40.5 Concluding Remarks

This chapter highlights two main supramolecular strategies for generating libraries of supramolecular enantioselective catalysts. The main characteristic of the members of each library of catalysts is that they retain most of the structural features of the backbone, while incorporating changes to their active sites that are determined by the structural characteristics of the RA. Two different categories of supramolecularly regulated enantioselective catalytic systems have been developed.

The first type of the regulated catalytic system possesses a catalytic site with a well-defined three-dimensional structure suitable for enantioselective catalysis and a distal regulation site containing a supramolecular motif capable of interacting with the RA. The regulation sites encompass (aza)-crown-ethers, tetraamino phosphonium, 2-amino-1,8-naphthyridine, polyethyleneoxy, and phosphanaminium motifs. A number of research groups have exploited the use of an array of structurally diverse binders (i.e. RAs) for the abovementioned regulation sites to generate libraries of enantioselective catalysts that are capable of geometric adaptation to the requirements of a given substrate for high enantioselectivity in a number of chemical transformations (e.g. palladium-catalyzed asymmetric allylic substitutions, conjugated additions including Michael reactions, rhodium-catalyzed hydroformylations, Henry reactions, and enolate allylations). It is interesting to note that this regulation strategy has been applied to both metal-catalyzed and organocatalytic chemical transformations.

The second type of supramolecularly regulated catalytic systems is generated from a prochiral unit that contains the catalytic site. The three-dimensional structure of the catalytic site is not well defined in the absence of an RA, and the addition of an enantiopure RA triggers chirogenesis from the RA to the carbon backbone containing the catalytic site. This type of catalytic system has not been applied as widely as that possessing a well-defined three-dimensional structure from the beginning. In this case, studies have demonstrated that efficient enantioselective hydrogenations can be obtained with unprecedented ease just by choosing the optimal enantiopure RA.

It should be noted that the selected examples herein are not comprehensive. Due to space limitations, this chapter highlights only the examples in which the final enantioselectivities surpassed 80% ee (enantiomeric ratio >90 : 10) and the regulation effects caused an increase of at least 25% in the enantiomeric excesses. Moreover, some interesting examples of supramolecular regulation have not been included

because the studies failed to demonstrate the regulation ability of the RAs among an array of substrates. We trust that the concepts that have been summarized and discussed in this chapter will pave the way for new designs of supramolecularly regulated catalysts and will encourage research groups to expand the structural diversity of the RAs in their studies to make this strategy more general and useful.

Acknowledgments

A. V.-F. thanks MICINN (PID2020-115658GB-I00) for the financial support.

References

1 Breit, B. (2005). Supramolecular approaches to generate libraries of chelating bidentate ligands for homogeneous catalysis. *Angew. Chem. Int. Ed.* 44: 6816–6825.
2 Goudriaan, P.E., van Leeuwen, P.W.N.M., Birkholz, M.-N., and Reek, J.N.H. (2008). Libraries of bidentate phosphorus ligands; synthesis strategies and application in catalysis. *Eur. J. Inorg. Chem.*: 2939–2958.
3 Meeuwissen, J. and Reek, J.N.H. (2010). Supramolecular catalysis beyond enzyme mimics. *Nat. Chem.* 2: 615–621.
4 Carboni, S., Gennari, C., Pignataro, L., and Piarulli, U. (2011). Supramolecular ligand–ligand and ligand–substrate interactions for highly selective transition metal catalysis. *Dalton Trans.* 40: 4355–4373.
5 Ohmatsu, K. and Ooi, T. (2015). Design of supramolecular chiral ligands for asymmetric metal catalysis. *Tetrahedron Lett.* 56: 2043–2048.
6 Dydio, P. and Reek, J.N.H. (2014). Supramolecular control of selectivity in transition-metal catalysis through substrate preorganization. *Chem. Sci.* 5: 2135–2145.
7 Fanourakis, A., Docherty, P.J., Chuentragool, P., and Phipps, R.J. (2020). Recent developments in enantioselective transition metal catalysis featuring attractive noncovalent interactions between ligand and substrate. *ACS Catal.* 10: 10672–10714.
8 Mote, N.R. and Chikkali, S.H. (2018). Hydrogen-bonding-assisted supramolecular metal catalysis. *Chem. Asian J.* 13: 3623–3646.
9 Tan, C.X., Chu, D.D., Tang, X.H. et al. (2019). Supramolecular coordination cages for asymmetric catalysis. *Chem. Eur. J.* 25: 662–672.
10 Li, X.Z., Wu, J.G., He, C. et al. (2019). Asymmetric catalysis within the chiral confined space of metal–organic architectures. *Small* 15: 1804770.
11 Vaquero, M., Rovira, L., and Vidal-Ferran, A. (2016). Supramolecularly fine-regulated enantioselective catalysts. *Chem. Commun.* 52: 11038–11051.
12 Sawamura, M., Nakayama, Y., Tang, W.-M., and Ito, Y. (1996). Enantioselective allylation of nitro group-stabilized carbanions catalyzed by chiral crown ether phosphine–palladium complexes. *J. Org. Chem.* 61: 9090–9096.

13 Raynal, M., Ballester, P., Vidal-Ferran, A., and van Leeuwen, P.W.N.M. (2014). Supramolecular catalysis. Part 1: non-covalent interactions as a tool for building and modifying homogeneous catalysts. *Chem. Soc. Rev.* 43: 1660–1733.

14 Raynal, M., Ballester, P., Vidal-Ferran, A., and van Leeuwen, P.W.N.M. (2014). Supramolecular catalysis. Part 2: artificial enzyme mimics. *Chem. Soc. Rev.* 43: 1734–1787.

15 van Leeuwen, P.W.N.M. (ed.) (2008). *Supramolecular Catalysis*. Weinheim: Wiley-VCH Verlag GmbH.

16 Uraguchi, D., Ueki, Y., and Ooi, T. (2009). Chiral organic ion pair catalysts assembled through a hydrogen-bonding network. *Science* 326: 120–123.

17 Fuentes, J.A., Lebl, T., Slawin, A.M.Z., and Clarke, M.L. (2011). Synthesis of organocatalysts using non-covalent chemistry; understanding the reactivity of ProNap, an enamine-type organocatalyst that can self-assemble with complementary co-catalysts. *Chem. Sci.* 2: 1997–2005.

18 Li, Y., Ma, B., He, Y. et al. (2010). Chiral metallacrown ethers for asymmetric hydrogenation: alkali-metal ion mediated enhancement of enantioselectivity. *Chem. Asian J.* 5: 2454–2458.

19 Mon, I., Jose, D.A., and Vidal-Ferran, A. (2013). Bis(phosphite) ligands with distal regulation: application in rhodium-mediated asymmetric hydroformylations. *Chem. Eur. J.* 19: 2720–2725.

20 Vidal-Ferran, A., Mon, I., Bauzà, A. et al. (2015). Supramolecularly regulated ligands for asymmetric hydroformylations and hydrogenations. *Chem. Eur. J.* 21: 11417–11426.

21 Martínez-Carrión, A., Howlett, M.G., Alamillo-Ferrer, C. et al. (2019). Kinetic treatments for catalyst activation and deactivation processes based on variable time normalization analysis. *Angew. Chem. Int. Ed.* 58: 10189–10193.

22 Rovira, L., Vaquero, M., and Vidal-Ferran, A. (2015). Asymmetric hydroformylation of heterocyclic olefins mediated by supramolecularly regulated rhodium–bisphosphite complexes. *J. Org. Chem.* 80: 10397–10403.

23 Ouyang, G.-H., He, Y.-M., and Fan, Q.-H. (2014). Podand-based dimeric chromium(III)–salen complex for asymmetric Henry reaction: cooperative catalysis promoted by complexation of alkali metal ions. *Chem. Eur. J.* 20: 16454–16457.

24 Ohmatsu, K., Ito, M., Kunieda, T., and Ooi, T. (2012). Ion-paired chiral ligands for asymmetric palladium catalysis. *Nat. Chem.* 4: 473–477.

25 Escárcega-Bobadilla, M.V. and Kleij, A.W. (2012). Artificial chirogenesis: a gateway to new opportunities in material science and catalysis. *Chem. Sci.* 3: 2421–2428.

26 Boersma, A.J., Megens, R.P., Feringa, B.L., and Roelfes, G. (2010). DNA-based asymmetric catalysis. *Chem. Soc. Rev.* 39: 2083–2092.

27 Park, S. and Sugiyama, H. (2010). DNA-based hybrid catalysts for asymmetric organic synthesis. *Angew. Chem. Int. Ed.* 49: 3870–3878.

28 Hyster, T.K. and Ward, T.R. (2016). Genetic optimization of metalloenzymes: enhancing enzymes for non-natural reactions. *Angew. Chem. Int. Ed.* 55: 7344–7357.

29 van Leeuwen, P.W.N.M., Rivillo, D., Raynal, M., and Freixa, Z. (2011). Enantioselective supramolecular catalysis induced by remote chiral diols. *J. Am. Chem. Soc.* 133: 18562–18565.

30 Dydio, P., Rubay, C., Gadzikwa, T. et al. (2011). "Cofactor"-controlled enantioselective catalysis. *J. Am. Chem. Soc.* 133: 17176–17179.

41

Emergent Catalysis by Self-Replicating Molecules

Kai Liu, Jim Ottelé, and Sijbren Otto

Stratingh Institute, University of Groningen, Centre for Systems Chemistry, Nijenborgh 4, Groningen 9747 AG, The Netherlands

41.1 Introduction

The ability of molecules or systems of molecules to produce copies of themselves has been of interest to the scientific community for over a century and is intimately linked to the concept of autocatalysis [1]. A single chemical reaction is *autocatalytic* if one of the products catalyzes the formation of itself (Figure 41.1a), which often gives rise to a sigmoidal growth curve (Figure 41.1b) [2]. Initially, only very little catalyst is present in such reactions; thus, the reaction proceeds slowly. The reaction speeds up progressively as more catalyst is produced until diminishing reactants slow it down again. Autocatalytic reactions are employed in various fields of research: from (bio)chemical oscillators and dissipative systems where they can be used to facilitate feedback loops [3–5] to molecular circuits in which they can aid in signal amplification [6, 7]. Furthermore, autocatalytic reactions play a central role in the research toward the origin of life [8, 9]. Indeed, the replication of molecules and of information stored within these is thought to be one of the essential processes required for life to emerge [10].

Autocatalysis and (self-)replication, while related, are not synonymous. Self-replication encompasses autocatalysis, but it demands an additional property: the transfer of information (e.g. molecular structures or sequences) to the next generation of replicators [11]. The additional requirement of information transfer has complicated the design of autocatalytic self-replicators. It is perhaps not surprising that the first report on a synthetic system capable of displaying self-replication did not materialize until the late 1980s, almost a century after the term "autocatalysis" was coined by the German chemist Wilhelm Ostwald. In this system, von Kiedrowski was able to demonstrate the nonenzymatic template-directed formation of an autocatalytic hexadeoxynucleotide from the condensation of two trimeric deoxynucleotides [12]. Other nucleotide-based replicators quickly followed [13], and self-replication was soon expanded to peptide-based [14] and fully synthetic systems [15]. Dynamic combinatorial replication has also been developed based

Supramolecular Catalysis: New Directions and Developments, First Edition.
Edited by Piet W.N.M. van Leeuwen and Matthieu Raynal.

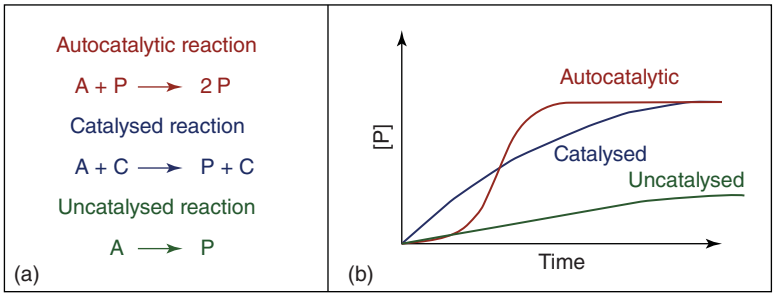

Figure 41.1 (a) Chemical reactions can be either autocatalytic, catalyzed, or noncatalyzed. (b) Conversions over time of these different types of reactions. Note that not only autocatalytic reactions can exhibit an exponential increase in the amount of product.

on the self-amplification of a particular component due to self-recognition in a molecular network in which different components can reversibly interchange with one another [16, 17].

To transit into more lifelike systems, it is essential that self-replicators develop additional functionalities beyond the ability to generate copies of themselves. A functionality that is particularly relevant in the concept of (early) evolution is catalysis, especially when it promotes the conversion of matter or energy into useful components. Such behavior can be considered a primitive manifestation of a metabolism [18]. Catalysis by self-replicating molecules can provide a bridge that will allow us to integrate replication and metabolism into a single system and can bring us one step closer to de novo life [11]. If self-replicators become catalytically active toward *another* chemical reaction, they may also start to influence the environment in which they exist. Additionally, if a product (e.g. a replicator building block or other precursor) of such a reaction is beneficial to the replicator's aptitude for self-replication, a positive feedback loop is created. In principle, replicators that are able to benefit from their catalytic capabilities should have greater dynamic kinetic stability to maintain themselves in far from equilibrium conditions, outcompeting those that do not [19, 20]. With continued evolution, catalytic capabilities may improve and expand, ultimately enabling further evolutionary transitions [21].

One way of tackling the integration of additional functionalities, such as catalysis, with the ability to self-replicate is to use a systems chemistry approach. Systems chemistry is an emerging field that bridges chemistry and biology. It focuses on how emergent properties can arise from networks of interacting molecules, where system-level properties are exhibited that cannot be attributed to any of the individual components of the system [22]. Molecular networks can facilitate chemical connectivity and active communication between the individual replication and catalytic subsystems, leading to the expression of complex and emergent behaviors such as feedback loops. The development of emergent catalysis in synthetic replicators can help overcome some of the limitations exhibited by canonical biomolecules (such as the challenge to combine the catalytic activity of RNA molecules with their ability to be replicated, where the former relies on folding, while the latter is hampered by folding [23]).

Supramolecular catalysis is becoming increasingly powerful [24], and its principles can be used to guide the design of catalytic activity in self-replicators. Noncovalent organization of binding and active sites is often used to design artificial enzyme mimics [25]. For a minimal replicator, the binding sites and catalytic moieties may be covalently attached to individual building blocks. During replication, these parts may be brought into close proximity, which can enhance catalytic activity. Indeed, self-assembly can be an efficient way to organize catalytic sites in a well-ordered manner, often leading to an enhanced reaction rate due to a local high concentration of reaction loci or cooperativity among functional groups [26]. Hydrophobic domains can similarly be incorporated, which can increase the binding affinity of apolar substrates or facilitate transition state stabilization [27]. Alternatively, postmodification of self-assembled structures (be they replicators or not) can endow catalytic activity by anchoring organic or inorganic catalysts to the assemblies. This approach may even lead to new features due to molecular recognition and structural preorganization [28]. Note that introducing catalysis in self-replicators should not have adverse effects on replication and that the conditions required for replication and catalysis must be compatible with one another.

41.2 Implementation of Organocatalysis in Self-Replicating Systems

In 2009, Rebek and coworkers reported that they could anchor functional groups on a previously developed autocatalyst [29, 30]. This system utilizes a bimolecular condensation reaction between an aldehyde and a thymine-derived amino acid to form the autocatalytic species. The amino acid was modified in such a way that it forms an imidazoline moiety upon condensation. This functional group is known to be a multipurpose organocatalyst and – more importantly – forms *during the process of autocatalysis* (Figure 41.2a). Thus, the mechanism of catalysis is coupled to the mechanism of autocatalysis (but not the other way around). Rebek and coworkers showed that the functionalized replicator was able to catalyze hydrogenation or nucleophilic addition to α,β-unsaturated aldehydes (Figure 41.2b). However, these reactions were performed in dichloromethane (DCM) and chloroform, respectively, while autocatalysis occurs in hot benzene. Here, the conditions for autocatalysis are not compatible with those needed for organocatalysis.

Nine years later, the first example of a system in which the replication of an RNA recombinase was coupled to catalytic activity was shown by Nghe and coworkers [31]. They utilized an RNA recombinase "*WXYZ*" that is able to promote the formation of itself by catalyzing the transesterification reaction of its constituent fragments WXY and Z. This system had previously been shown to exhibit autocatalytic behavior when the individual fragments W, X, Y, and Z were used as a precursor stock [32]. In their work, Nghe et al. modified the fragments WXY and Z by appending a 26-nucleotide foreign sequence at the 3′ end (resulting in WXY-mod and Z-mod). Remarkably, in systems that contained only modified fragments, unmodified fragments WXY and Z were reformed, which led to the formation of the autocatalyst

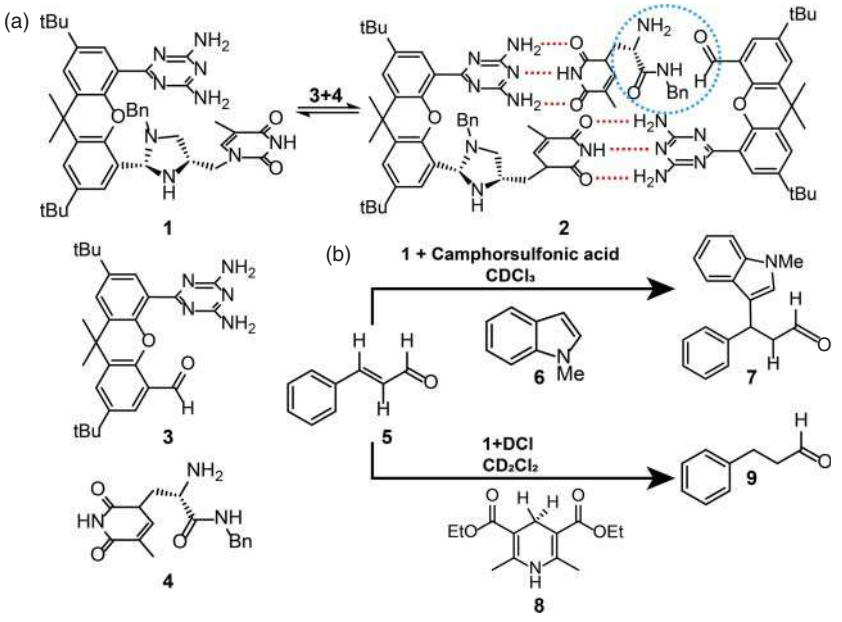

Figure 41.2 (a) Autocatalyst **1** can catalyze its own synthesis through the formation of a dimeric complex (**2**), where the recognition sites of **1** can bind with **3** and **4** by hydrogen bonds (red dashed lines) to promote the condensation reaction of the circled functional groups. (b) Self-replicator **1** acts as an organocatalyst for the Friedel–Crafts alkylation reaction (**5** + **6** → **7**) and the reduction of cinnamaldehyde (**5** + **8** → **9**).

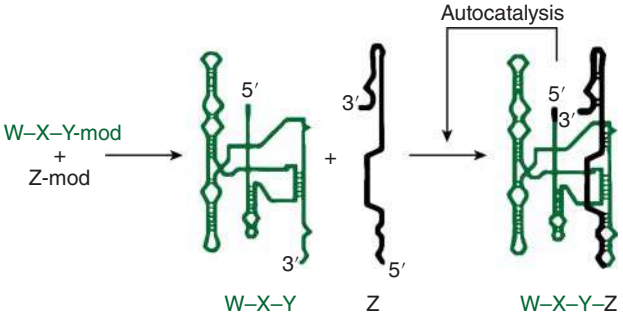

Figure 41.3 The *Azoarcus* ribozyme (W–X–Y–Z) can be synthesized from inactive RNA substrates (WXY and Z) in an autocatalytic process. The replicator can also cleave the modification (i.e. a short RNA fragment) on substrates W–X–Y–Mod and Z-mod to liberate more WXY and Z.

WXYZ (Figure 41.3). Indeed, the RNA ribozyme has been shown to rid itself of the undesirable modifications through a multistep pathway that is catalyzed by the ribozyme itself, endowing it with the ability to preprocess the available raw material to make it suitable for self-replication. Note that the replicator is derived from a product of biological evolution and is therefore not a completely synthetic system.

More recently, we have been able to integrate the self-replication of synthetic molecules with organocatalysis [33]. A building block that contains a pentapeptide

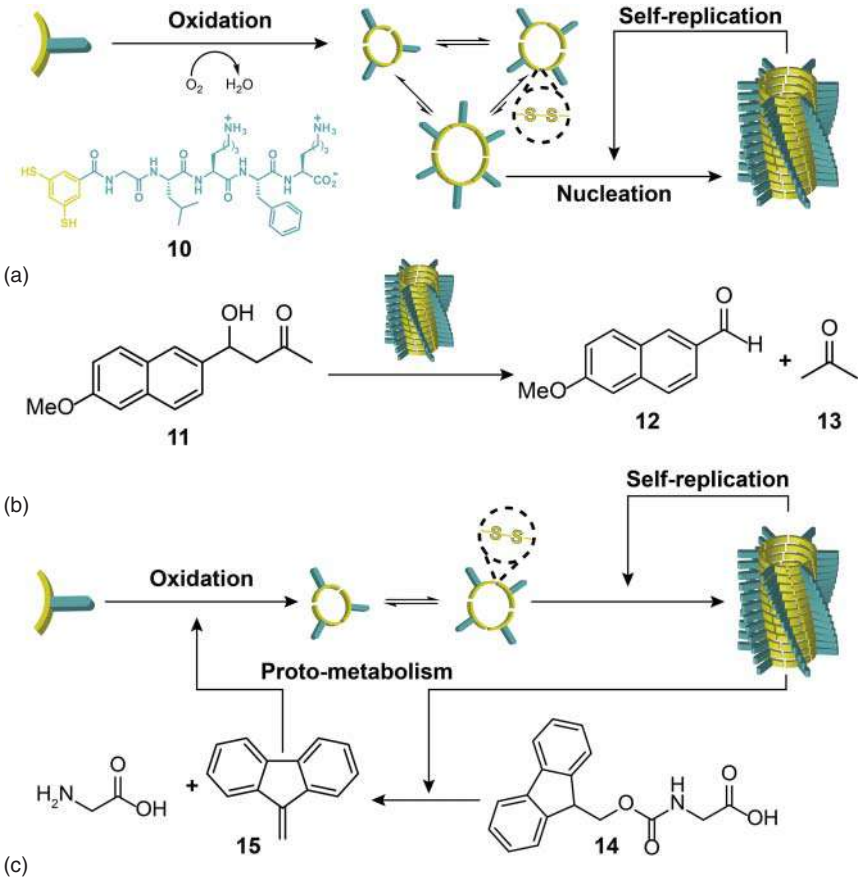

Figure 41.4 (a) Dithiol building block **10**, upon oxidation, produces a mixture of disulfide macrocycles that interconvert through a thiol-disulfide exchange. Nucleation followed by elongation and fragmentation enables the onset of the self-replication of hexamer macrocycle $(\mathbf{10})_6$. (b) Self-replicating $(\mathbf{10})_6$ fibers can catalyze the retro-aldol reaction that converts substrate **11** into aldehyde **12** and acetone **13**. (c) The same self-replicating $(\mathbf{10})_6$ fibers can also catalyze the cleavage of **14**. Product **15** speeds up the oxidation of **10** into the precursors of the replicator (e.g. $(\mathbf{10})_3$, $(\mathbf{10})_4$), introducing a positive feedback loop on self-replication.

(GLKFK) attached to a benzene-1,3-dithiol core was used to construct a dynamic combinatorial library (DCL). When dissolved in slightly basic aqueous media (borate buffer, pH 8.12), the thiol functional groups form disulfide bonds upon oxidation by atmospheric oxygen (Figure 41.4a). Since each building block contains two thiol groups, this results in the formation of various macrocycles. The reversible nature of the disulfide bond allows for exchange reactions between the macrocycles and introduces dynamicity to this system. After a certain lag time in which the various macrocycles equilibrate, the hexamer macrocycle can nucleate by stacking on top of another hexamer macrocycle. The stacking is stabilized by β-sheet formation of the pentapeptides and π–π stacking of the aromatic core moieties. The hexamers form supramolecular fibers that – upon mechanical agitation – can

fragment. As the fiber ends facilitate the formation of more hexamer macrocycles, the fragmentation pushes the self-replication into an exponential regime [17].

During the stacking process, lysine residues present in the pentapeptide are brought into close proximity. Lysine's ε-amino group has a pK_a of 10.2 and is therefore expected to be fully protonated in the nonassembled state at close-to-neutral pH. However, upon assembly the electrostatic repulsion experienced between the positively charged ammonium groups causes the pK_a of roughly 10% of the lysine residues to be reduced by three pK_a units. This resulted in a partial deprotonation of the ammonium groups of the lysine residues in the replicator assemblies and the formation of significant numbers of ε-amino groups in a rather hydrophobic environment generated by the neighboring amino acids. Amines with these characteristics are known to catalyze a variety of reactions by acting as a general base. We found that these supramolecular polymers were able to catalyze the retro-aldol reaction of methodol, while the building block and the unstacked macrocycles did not (Figure 41.4b). This reaction occurs through the formation of an iminium ion, which activates the carbon–carbon bond toward cleavage. Subsequently, the resulting enamine is hydrolyzed to regenerate the catalyst. In this system, the conditions for self-replication and catalysis are compatible with one another: a one-pot experiment was performed in which the building block of the replicator was mixed with the retro-aldol substrate. As soon as the self-replicator emerged from the mixture, the catalytic activity toward the retro-aldol reaction emerged with it, integrating catalysis with self-replication. The same self-replicating supramolecular structures were also found to be able to catalyze FMOC-glycine deprotection through a Brønsted-base-catalyzed hydrogen abstraction mechanism. This reaction resulted in the formation of CO_2, glycine, and dibenzofulvene (DBF) (Figure 41.4c). Interestingly, DBF is known to promote thiol oxidation [34]. Indeed, the liberation of DBF resulted in a faster rate of building block oxidation, which in turn, led to a higher replication speed. This not only resulted in the integration of self-replication and catalysis but also gave rise to a positive feedback loop through which catalysis enhanced autocatalysis.

41.3 The Implementation of Photocatalysis in Self-Replicating Systems

With the unique advantages of operation at room temperature and utilization of renewable solar light as the driving force, photocatalysis continues to be important in the field of catalysis. Nonbonding interactions can be used to control photocatalysis [35], as shown in natural photosystems where proteins work as a template to organize the pigments, electronic mediators, and catalytic centers into an efficient photocatalytic architecture [36]. Inspired by nature, we reasoned that supramolecular interactions between synthetic replicators and organic photocatalysts may tune their optical properties and photochemical pathways to generate emergent photocatalytic properties. We have successfully implemented this strategy in a synthetic

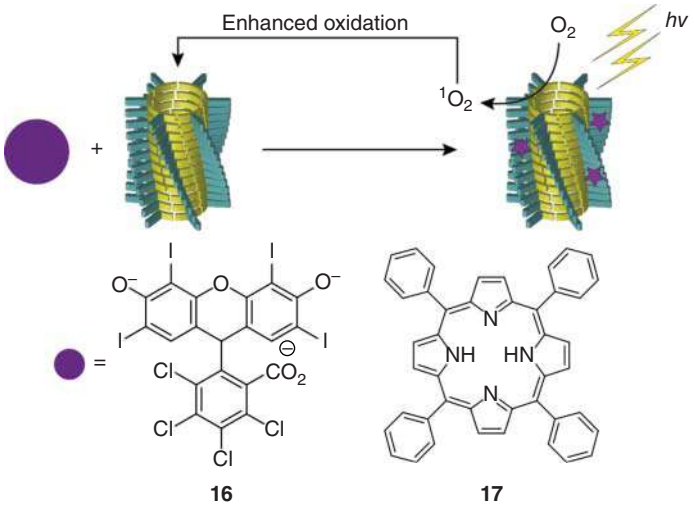

Figure 41.5 Self-replicating $(\mathbf{10})_6$ fibers can recruit photocatalytic cofactors (rose bengal **16** or tetraphenylporphyrin **17**) through noncovalent binding followed by the activation of their photoactivity. They form a fiber-cofactor complex that can convert $^3O_2$ into $^1O_2$ under light irradiation to accelerate thiol oxidation, resulting in a positive feedback on the mechanism of self-replication.

system in which the recruitment of cofactors activated these cofactors toward photocatalytic activity [37].

The same building block used to implement organocatalysis as described in Section 41.2 was an excellent candidate for the implementation of photocatalysis. The supramolecular binding of various photosensitizers with the replicator fibers was investigated (Figure 41.5). Water-soluble rose bengal was shown to form J-aggregates on the fiber surface due to intermolecular electrostatic and hydrophobic interactions. The J-aggregated rose bengal generated a new red-shifted absorption band at 590 nm, which was not present when nonassembled macrocycles were used. This enabled the possibility of selectively triggering the photoactivity of the fiber-rose bengal complex by irradiating with yellow (590 nm) light. The supramolecular recruitment strategy was also applied to the hydrophobic cofactor tetraphenylporphyrin. This well-known singlet oxygen photosensitizer was shown to have very low photoactivity in water, while its solubility was enhanced when replicator fibers were present due to its ability to bind to the hydrophobic surface of the fibers. Importantly, the replicator fibers are more efficient at activating tetraphenylporphyrin than nonassembled macrocycles, as confirmed by the enhanced absorbance and fluorescence of the dye when bound to the fibers, which was accompanied by an increased rate of singlet oxygen generation.

In both cases, the photocatalytic generation of singlet oxygen on the surface of the replicator fiber accelerated the oxidation of thiols present in the building blocks. Irradiation with light accelerated replication in the presence of building blocks and the cofactor. The rate of oxidation of building blocks increased as the fiber-cofactor complex accumulated due to enhanced singlet oxygen production. Thus, the

recruitment of the cofactor was found to have a positive feedback on self-replication due to emergent onset of photocatalysis. As energy (light) is harnessed to benefit the self-replicator, the process corresponds to a protometabolism: a rudimentary form of a metabolism in which energy is used to convert molecules in the environment to precursors that are utilized by the replicator to produce more of itself.

41.4 Conclusions and Outlook

The studies reported above show how the ability to catalyze chemical transformations can emerge spontaneously (and even by chance) from self-replicating systems. Currently, other chemical reactions that could be catalyzed by supramolecular structures are being investigated. The study of structure–function relationships is expected to increase our understanding of catalytic mechanisms and enhances our ability to engineer them for specific applications. The generation of replicator mutants (i.e. by mixing building blocks that contain different amino acids in the pentapeptide chain) may lead to active site modification, which in turn, can influence catalytic activity. The incorporation of energy harvesting and endergonic reactions (e.g. through the conversion of high-energy starting materials to lower energy products) in the catalytic processes would be the next step toward the implementation of a full-fledged metabolism. Although catalysis can increase the self-replication rate in the systems reported above, the replication processes are still under thermodynamic control. Another research direction is to operate the self-replicating systems away from equilibrium. The most promising way to approach this is to introduce a replication–destruction regime (e.g. by utilizing flow systems in which a continuous supply of building blocks is provided to the system while simultaneously flowing material out). In the context of evolution, it is also important to ensure that catalytic capabilities selectively benefit the replicators that are doing the catalysis and avoid parasitism, in which noncatalytic replicators benefit from catalysis. This could be facilitated through the formation of compartments or the generation of high local concentrations at surfaces [38]. With the generation of emergent functions in self-replication systems, we are getting closer to a chemical system capable of self-maintenance in out-of-equilibrium conditions with the prospect of evolution and by extension de novo life. Reaction networks or self-assembly pathways may also be coupled to the emergence of catalytic activity, potentially leading to additional emergent properties and complex functions (e.g. oscillations or pattern formations).

References

1 Lewis, G.N. (1905). Autocatalytic decomposition of silver oxide. *Proc. Am. Acad. Arts Sci.* 40: 719–733.

2 Bissette, A.J. and Fletcher, S.P. (2013). Mechanisms of autocatalysis. *Angew. Chem. Int. Ed.* 52: 12800–12826.

3 De Kepper, P., Epstein, I.R., and Kustin, K. (1981). A systematically designed homogeneous oscillating reaction: the arsenite-iodate-chlorite system. *J. Am. Chem. Soc.* 103: 2133–2134.

4 Semenov, S.N., Kraft, L.J., Ainla, A. et al. (2016). Autocatalytic, bistable, oscillatory networks of biologically relevant organic reactions. *Nature* 537: 656–660.

5 Semenov, S.N., Wong, A.S.Y., Van Der Made, R.M. et al. (2015). Rational design of functional and tunable oscillating enzymatic networks. *Nat. Chem.* 7: 160–165.

6 Yin, P., Choi, H.M.T., Calvert, C.R., and Pierce, N.A. (2008). Programming biomolecular self-assembly pathways. *Nature* 451: 318–322.

7 Zhang, D.Y., Turberfield, A.J., Yurke, B., and Winfree, E. (2007). Engineering entropy-driven reactions and networks catalyzed by DNA. *Science* 318: 1121–1125.

8 Pross, A. (2004). Causation and the origin of life. Metabolism or replication first. *Origins Life Evol. Biosphere* 34: 307–321.

9 Szathmáry, E. and Demeter, L. (1987). Group selection of early replicators and the origin of life. *J. Theor. Biol.* 128: 463–486.

10 Orgel, L.E. (1992). Molecular replication. *Nature* 358: 203–209.

11 Adamski, P., Eleveld, M., Sood, A. et al. (2020). From self-replication to replicator systems en route to de novo life. *Nat. Rev. Chem.* 4: 386–403.

12 von Kiedrowski, G. (1986). A self-replicating hexadeoxynucleotide. *Angew. Chem. Int. Ed.* 25: 932–935.

13 Zielinski, W.S. and Orgel, L.E. (1987). Autocatalytic synthesis of a tetranucleotide analogue. *Nature* 327: 346–347.

14 Lee, D.H., Granja, J.R., Martinez, J.A. et al. (1996). A self-replicating peptide. *Nature* 382: 525–528.

15 Kosikova, T. and Philp, D. (2017). Exploring the emergence of complexity using synthetic replicators. *Chem. Soc. Rev.* 46: 7274–7305.

16 Sadownik, J.W. and Philp, D. (2008). A simple synthetic replicator amplifies itself from a dynamic reagent pool. *Angew. Chem. Int. Ed.* 120: 10113–10118.

17 Colomb-Delsuc, M., Mattia, E., Sadownik, J.W., and Otto, S. (2015). Exponential self-replication enabled through a fibre elongation/breakage mechanism. *Nat. Commun.* 6: 1–7.

18 Muchowska, K.B., Varma, S.J., and Moran, J. (2020). Nonenzymatic metabolic reactions and life's origins. *Chem. Rev.* 120: 7708–7744.

19 Pascal, R. and Pross, A. (2019). Chemistry's kinetic dimension and the physical basis for life. *J. Syst. Chem.* 7: 1–8.

20 Pross, A. (2011). Toward a general theory of evolution: extending Darwinian theory to inanimate matter. *J. Syst. Chem.* 2: 1–14.

21 Szathmáry, E. and Smith, J.M. (1995). The major evolutionary transitions. *Nature* 374: 227–232.

22 Ashkenasy, G., Hermans, T.M., Otto, S., and Taylor, A.F. (2017). Systems chemistry. *Chem. Soc. Rev.* 46: 2543–2554.

23 Higgs, P.G. and Lehman, N. (2015). The RNA world: molecular cooperation at the origins of life. *Nat. Rev. Genet.* 16: 7–17.

24 van Leeuwen, P.W.N.M. (ed.) (2008). *Supramolecular Catalysis*. Weinheim: Wiley-VCH Verlag GmbH.

25 Raynal, M., Ballester, P., Vidal-Ferran, A., and van Leeuwen, P.W. (2014). Supramolecular catalysis. Part 2: artificial enzyme mimics. *Chem. Soc. Rev.* 43: 1734–1787.

26 Guler, M.O. and Stupp, S.I. (2007). A self-assembled nanofiber catalyst for ester hydrolysis. *J. Am. Chem. Soc.* 129: 12082–12083.

27 Serrano-Luginbühl, S., Ruiz-Mirazo, K., Ostaszewski, R. et al. (2018). Soft and dispersed interface-rich aqueous systems that promote and guide chemical reactions. *Nat. Rev. Chem.* 2: 306–327.

28 Schwizer, F., Okamoto, Y., Heinisch, T. et al. (2018). Artificial metalloenzymes: reaction scope and optimization strategies. *Chem. Rev.* 118: 142–231.

29 Park, T.K., Feng, Q., and Rebek, J. Jr., (1992). Synthetic replicators and extrabiotic chemistry. *J. Am. Chem. Soc.* 114: 4529–4532.

30 Kamioka, S., Ajami, D., and Rebek, J. (2010). Autocatalysis and organocatalysis with synthetic structures. *Proc. Natl. Acad. Sci. U.S.A.* 107: 541–544.

31 Arsène, S., Ameta, S., Lehman, N. et al. (2018). Coupled catabolism and anabolism in autocatalytic RNA sets. *Nucleic Acids Res.* 46: 9660–9666.

32 Draper, W.E., Hayden, E.J., and Lehman, N. (2008). Mechanisms of covalent self-assembly of the *Azoarcus* ribozyme from four fragment oligonucleotides. *Nucleic Acids Res.* 36: 520–531.

33 Ottelé, J., Hussain, A.S., Mayer, C., and Otto, S. (2020). Chance emergence of catalytic activity and promiscuity in a self-replicator. *Nat. Catal.* 3: 547–553.

34 Denes, F., Pichowicz, M., Povie, G., and Renaud, P. (2014). Thiyl radicals in organic synthesis. *Chem. Rev.* 114: 2587–2693.

35 Vallavoju, N. and Sivaguru, J. (2014). Supramolecular photocatalysis: combining confinement and non-covalent interactions to control light initiated reactions. *Chem. Soc. Rev.* 43: 4084–4101.

36 Croce, R. and Van Amerongen, H. (2014). Natural strategies for photosynthetic light harvesting. *Nat. Chem. Biol.* 10: 492–501.

37 Santiago, G.M., Liu, K., Browne, W.R., and Otto, S. (2020). Emergence of light-driven protometabolism on recruitment of a photocatalytic cofactor by a self-replicator. *Nat. Chem.* 12: 603–607.

38 Eigen, M. and Winkler-Oswatitsch, R. (1992). *Steps Towards Life: A Perspective on Evolution*. Oxford: Oxford University Press.

Index

Supramolecular Catalysis: New Directions and Developments, First Edition.
Edited by Piet W.N.M. van Leeuwen and Matthieu Raynal.

b

f

g

h

i

j

k

q

u